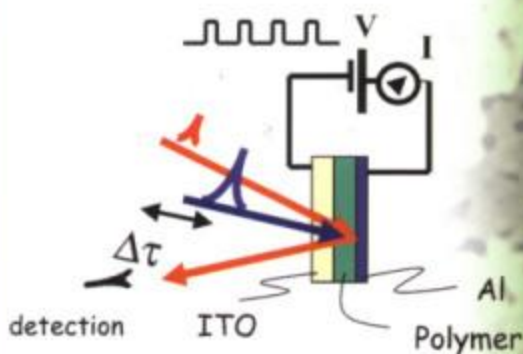
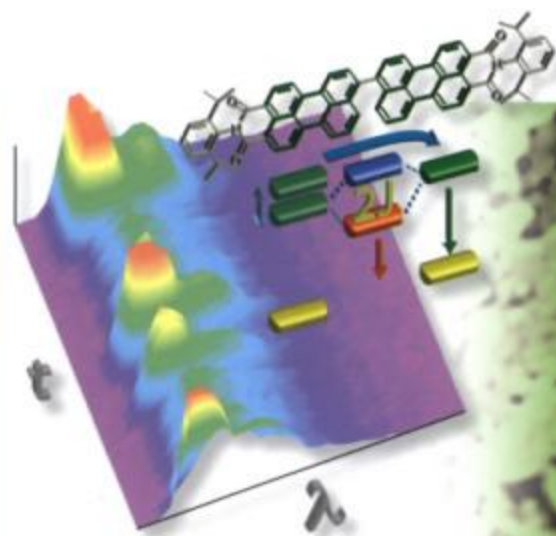


Edited by  
Guglielmo Lanzani

WILEY-VCH

# Photophysics of Molecular Materials

From Single Molecules to Single Crystals



**Photophysics of  
Molecular Materials**

*Edited by  
Guglielmo Lanzani*

# Photophysics of Molecular Materials

From Single Molecules to Single Crystals

*Edited by*

*Guglielmo Lanzani*



WILEY-  
VCH

WILEY-VCH Verlag GmbH & Co. KGaA

## Editors

### **Guglielmo Lanzani**

Dipartimento di Fisica  
Politecnico di Milano  
Milano  
Italy  
e-mail: [guglielmo.lanzani@fisi.polimi.it](mailto:guglielmo.lanzani@fisi.polimi.it)

## Cover

*Right:* Confocal laser scanning micrograph (CLSM) of a tetracene thin film.

*Top left:* Jumps between excitonic coupling and Förster type energy transfer in a single molecular dimer.

*Bottom left:* Layout for ultrafast optoelectronic probing experiments.

All books published by Wiley-VCH are carefully produced. Nevertheless, authors, editors, and publisher do not warrant the information contained in these books, including this book, to be free of errors. Readers are advised to keep in mind that statements, data, illustrations, procedural details or other items may inadvertently be inaccurate.

**Library of Congress Card No.:** applied for  
**British Library Cataloguing-in-Publication Data**  
A catalogue record for this book is available from the British Library.

## **Bibliographic information published by Die Deutsche Bibliothek**

Die Deutsche Bibliothek lists this publication in the Deutsche Nationalbibliografie; detailed bibliographic data is available in the Internet at <<http://dnb.ddb.de>>.

© 2006 WILEY-VCH Verlag GmbH & Co. KGaA, Weinheim

All rights reserved (including those of translation into other languages).  
No part of this book may be reproduced in any form – nor transmitted or translated into machine language without written permission from the publishers. Registered names, trademarks, etc. used in this book, even when not specifically marked as such, are not to be considered unprotected by law.

Printed in the Federal Republic of Germany.  
Printed on acid-free paper.

**Typesetting** Kühn & Weyh, Satz und Medien, Freiburg

**Printing** Strauss GmbH, Mörlenbach

**Bookbinding** Litges & Dopf Buchbinderei GmbH, Heppenheim

**ISBN-13:** 978-3-527-40456-8

**ISBN-10:** 3-527-40456-2

## Contents

### List of Contributors XV

- 1 Introduction 1**  
*Guglielmo Lanzani*
  
- 2 Optical Microscopy and Spectroscopy of Single Molecules 5**  
*Christian Hübner and Thomas Basché*
  - 2.1 Introduction 5
  - 2.2 Photophysical Principles of Single-Molecule Fluorescence Detection 6
    - 2.2.1 The Single Molecule as a Three-Level System 6
    - 2.2.2 Dipole–Dipole Coupled Oscillators 10
      - 2.2.2.1 Weak Coupling 11
      - 2.2.2.2 Strong Coupling 12
  - 2.3 Experimental Techniques 13
    - 2.3.1 Signal-to-Noise Considerations 13
    - 2.3.2 Room-Temperature Single-Molecule Spectroscopy 14
      - 2.3.2.1 Epifluorescence Microscopy 14
      - 2.3.2.2 Total Internal Reflection (TIR) Microscopy 18
      - 2.3.2.3 Scanning Confocal Optical Microscopy 18
      - 2.3.2.4 Two-Photon-,  $4\pi$ - and STED Microscopy 21
      - 2.3.2.5 Scanning Near-Field Optical Microscopy 22
    - 2.3.3 Single-Molecule Spectroscopy at Cryogenic Temperatures 23
      - 2.3.3.1 The Laser System 24
  - 2.4 Applications 27
    - 2.4.1 Photon Antibunching 27
    - 2.4.2 Photon Bunching 29
    - 2.4.3 Electronic Coupling Between Molecules 32
    - 2.4.4 Single Molecules as Antennas: Orientation 41

<b>3</b>	<b>Optical Properties of Single Conjugated Polymer Chains (Polydiacetylenes)</b>	<b>49</b>
	<i>Michel Schott</i>	
3.1	Introduction	49
3.1.1	Motivation for the Study	49
3.1.2	Choice of the Experimental System	50
3.1.3	The Isolated Polydiacetylene Chain, Isolated in its Monomer Crystal Matrix	50
3.1.4	Organization of the Chapter	55
3.2	A Short Survey of Some PDA Properties	55
3.2.1	Possible Electronic Structures of a PDA chain	56
3.2.1.1	The Colors of PDA	56
3.2.1.2	Ground-State Conformational Differences	58
3.2.1.3	Color Transitions	60
3.2.2	Spectroscopy of Bulk PDA Crystals	60
3.2.2.1	Reflection and Absorption	61
3.2.2.2	Electroreflectance	62
3.2.2.3	Fluorescence	63
3.2.2.4	Two-Photon Absorption	64
3.3	The Chosen DA	64
3.3.1	The Materials and How They Fulfill the Criteria	64
3.3.2	The Samples	67
3.4	Spectroscopy of Isolated Blue Chains	67
3.4.1	Visible Absorption Spectra	67
3.4.1.1	Room-Temperature Absorption and Determination of the Polymer Content $x_p$	67
3.4.1.2	Low-Temperature Absorption Spectra	69
3.4.1.3	Temperature Dependence	71
3.4.2	Electroabsorption	73
3.4.2.1	Results	73
3.4.2.2	Properties of the Exciton	75
3.4.2.3	Exciton Binding Energy	77
3.4.2.4	Properties of Electron and Hole	77
3.4.2.5	Electroabsorption at Higher Polymer Concentration	79
3.4.3	Fluorescence	79
3.4.3.1	Emission Spectra	79
3.4.3.2	Lifetime of the Emitting State	80
3.4.3.3	Risetime of the Emission: Relaxation Within the Singlet Manifold	82
3.4.4	Nonradiative Relaxation of the $^1B_u$ Exciton	82
3.4.4.1	Introduction. Experimental Method	82
3.4.4.2	Spectra and PA Decay Kinetics	83
3.4.4.3	Photobleaching	86
3.4.4.4	Nature of the Gap States	88
3.4.5	The Lowest Triplet State	88

3.4.5.1	Assignment of the 1.35-eV Photoinduced Absorption	88
3.4.5.2	Triplet Generation Processes	89
3.4.5.3	Triplet Energies and Triplet–Triplet Transition	91
3.4.5.4	Triplet Transport Properties	92
3.4.6	A High-Energy Exciton	93
3.4.7	Summary and Discussion	96
3.4.7.1	Summary of the Main Results Obtained on Isolated Blue PDA Chains	96
3.4.7.2	Exciton Size and Binding Energy	98
3.4.7.3	Influence of Electronic Correlations	98
3.4.7.4	Comparison with Blue Bulk PDA Crystals	99
3.5	Red Chain Spectroscopy	103
3.5.1	Another Emission in 3BCMU Crystals	103
3.5.1.1	Low-Temperature Emission Spectrum	103
3.5.1.2	Excitation Spectra	104
3.5.2	Absorption Spectroscopy	105
3.5.2.1	Absorption at 15 K	105
3.5.2.2	Electroabsorption	107
3.5.3	Emission and Absorption Temperature Dependence	108
3.5.4	Red Chain Exciton Relaxation	109
3.5.4.1	Quantum Yield	109
3.5.4.2	Fluorescence Decay Time	111
3.5.4.3	Radiative Lifetimes	112
3.5.4.4	Nonradiative Lifetimes	113
3.6	Study of a Single Isolated Red Chain: a Polymeric Quantum Wire	116
3.6.1	Feasibility of Studying a Single Isolated Red Chain. Experimental Method	116
3.6.2	One Exciton per Chain. Lineshape Analysis	117
3.6.2.1	The Vibronic Lines. A One-Dimensional Exciton Band	117
3.6.2.2	The Zero-Phonon Line. Exciton Coherence Time and Scattering Process	121
3.6.2.3	Lorentzian Component of the Vibronic Linewidth. Optical Phonon Coherence	123
3.6.3	Spatial Extension of the Emission	124
3.6.3.1	The Method and a Typical Image	124
3.6.3.2	Different Spatial Distributions. The Effect of Disorder	125
3.6.3.3	Origin of the Spatial Distribution	127
3.6.4	Several Excitons on a Chain. Effect of Excitation Power	127
3.6.4.1	Absorption Cross-Section for a Single Chain	127
3.6.4.2	Nonresonant Excitation	128
3.6.4.3	Resonant Excitation. Exciton–Photon Interaction	129
3.6.5	Summary	130
3.6.5.1	Summary of the Results on Red PDA Isolated Chains	130
3.6.5.2	What We Would Like to Know About Red Chains but Do Not Yet	131
3.7	Answered and Open Questions	131

- 3.7.1 The Nature and Properties of Excited States 132
- 3.7.2 Exciton–Phonon Interactions 134
- 3.7.3 Electronic Correlations 135
- 3.7.4 Influence of Disorder 136
- Appendix
- 3.A The DA Solid-State Polymerization Reaction 137
- 3.A–1: General Description 137
- 3.A–2: Structural Requirements 138
- 3.A–3: Energetics and Elementary Steps 141
- 3.B Structural Properties of 3B and 4B Monomers 142
- 3.B–1: Phase Transitions 143
- 3.B–2: Crystal Structures 143
- 3.B–3: Unit Cell Parameters Along the Chain Direction 144
- 3.C Origin of the Weak Absorption Lines in Blue Chains 145
  
- 4 Morphology-Correlated Photophysics in Organic Semiconductor Thin Films by Confocal Laser Microscopy and Spectroscopy 153**  
*Maria Antonietta Loi, Enrico Da Como and Michele Muccini*
- 4.1 Introduction 153
- 4.2 Principles of Confocal Laser Scanning Microscopy 154
- 4.3 Photoluminescence Imaging and Time-Resolved Local Spectroscopy 158
- 4.3.1 The Setup 158
- 4.3.2 Morphology Correlated Spectroscopy 159
- 4.3.3 Optical Sectioning 160
- 4.3.4 Comparison Between Topographic and Photoluminescence Imaging 161
- 4.4 Supramolecular Organization in Organic Semiconductor Ultra-Thin Films 164
- 4.5 Imaging and Spectroscopy of Organic Bulk Heterojunctions and Correlation with Optoelectronic Device Properties 171
- 4.6 Conclusions 178
  
- 5 Spectroscopy of Long-Lived Photoexcitations in  $\pi$ -Conjugated Systems 183**  
*Markus Wohlgenannt, Eitan Ehrenfreund and Z. Valy Vardeny*
- 5.1 Introduction 183
- 5.1.1 Basic Properties of  $\pi$ -Conjugated Polymers 183
- 5.1.2 Optical Transitions of Photoexcitations in Conducting Polymers 188
- 5.1.3 Optical Transitions of Solitons in Polymers with Degenerate Ground State 189
- 5.1.4 Optical Transitions of Charged Excitations in NDGS Polymers 190
- 5.1.4.1 The Polaron Excitation 190
- 5.1.4.2 The Bipolaron Excitation 190

5.1.4.3	The $\pi$ -Dimer and the Delocalized Polaron Excitations	192
5.1.5	Optical Transitions of Neutral Excitations in NDGS Polymers	193
5.1.5.1	Singlet Excitons	194
5.1.5.2	Triplet Excitons	194
5.1.5.3	Polaron Pairs	195
5.1.6	Infrared Active Vibrational Modes	195
5.2	Experimental Methods	198
5.2.1	Photomodulation Spectroscopy of Long-Lived Photoexcitations	198
5.2.2	Optically Detected Magnetic Resonance Techniques	200
5.2.2.1	The Electron Spin	201
5.2.2.2	Electron Spin Resonance	202
5.2.2.3	Basic Principles of $\mu$ -Wave Resonant Transitions	202
5.2.2.4	ESR Signal Strength and Population Statistics of Spin-Up and Spin-Down Levels	203
5.2.3	Magnetic Resonance Spectroscopy of Long-Lived Photoexcited States in $\pi$ -Conjugated Polymers	204
5.2.3.1	The ODMR Setup	205
5.3	Recombination, Relaxation and Generation Processes	207
5.3.1	Mono- and Bimolecular Recombination Mechanisms	207
5.3.2	Recombination Kinetics	208
5.3.2.1	Steady-State Case	208
5.3.2.2	Frequency Response	210
5.3.2.3	Generalized Coordinates	210
5.3.2.4	Dispersive Kinetics: Frequency Domain	213
5.3.2.5	Lifetime Distribution for Dispersive Processes	215
5.3.2.6	Inhomogeneous Distribution of Recombination Lifetimes: General Case	216
5.3.3	Polaron Recombination and Quantum Efficiency of OLEDs	218
5.3.3.1	Polaron Recombination in OLEDs	218
5.3.3.2	Spin-Dependent Exciton Formation Cross-Sections	220
5.4	Photoinduced Absorption: Spectroscopy and Dynamics	220
5.4.1	Red Polythiophenes: Regio-Regular, Regio-Random	220
5.4.1.1	Photomodulation Studies of RRa-P3HT	222
5.4.1.2	Photomodulation Studies in RR-P3HT	224
5.4.1.3	The Polaron Relaxation Energy	225
5.4.1.4	The Spectral Anti-Resonances	228
5.4.2	Recombination Kinetics	230
5.4.2.1	Poly( <i>p</i> -phenylenebipyridinevinylene)	230
5.4.2.2	Poly(phenylenevinylene)	235
5.4.3	Photophysics of a Blue-Emitting Polyfluorene	237
5.4.3.1	Electronic Structure of PFO Phases	239
5.4.3.2	Photoexcitation Dynamics in PFO	240
5.4.4	Measuring the Conjugation Length Using Photoinduced Absorption Spectroscopy	241

5.5	ODMR Spectroscopy: Measurement of Spin-Dependent Polaron Recombination Rates	243
5.5.1	Spin-Dependent Exciton Formation Probed by PADMR Spectroscopy	243
5.5.2	Spin-Dependent Exciton Formation Probed by PLDMR Spectroscopy	246
5.5.3	Quantitative Modeling of Spin-Dependent Recombination Spectroscopy	248
5.5.4	Material Dependence of Spin-Dependent Exciton Formation Rates	249
5.5	The Relation Between Spin-Dependent Exciton Formation Rates and the Singlet Exciton Yield in OLEDs	251
5.6	Conclusion	252
<b>6</b>	<b>Charge Transport in Disordered Organic Semiconductors</b>	<b>261</b>
	<i>V. I. Arkhipov, I. I. Fishchuk, A. Kadashchuk and H. Bässler</i>	
6.1	Introduction	261
6.2	Charge Generation	262
6.3	Charge Carrier Hopping in Noncrystalline Organic Materials	265
6.3.1	Outline of Conceptual Approaches	265
6.3.1.1	The Continuous Time Random Walk (CTRW) Formalism	265
6.3.1.2	The Gill Equation	266
6.3.1.3	The Hopping Approach	267
6.3.1.4	Monte Carlo Simulation	267
6.3.1.5	The Effective Medium Approach	270
6.3.1.6	Effect of Site Correlation	270
6.3.1.7	Polaron Transport	272
6.3.2	Stochastic Hopping Theory	273
6.3.2.1	Carrier Equilibration via Downward Hopping	275
6.3.2.2	Thermally Activated Variable-Range Hopping: Effective Transport Energy	277
6.3.2.3	Dispersive Hopping Transport	281
6.3.2.4	Equilibrium Hopping Transport	283
6.3.2.5	The Effect of Backward Carrier Jumps	285
6.3.2.6	Hopping Conductivity in Doped Organic Materials	286
6.3.2.7	Coulomb Effects on Hopping in a Doped Organic Material	289
6.3.3	Effective-Medium Approximation Theory of Hopping Charge-Carrier Transport	295
6.3.3.1	The EMA Theory Formulations	297
6.3.3.2	Miller–Abrahams Formalism	298
6.3.3.3	Temperature Dependence of the Drift Mobility	299
6.3.3.4	Electric Field Dependence of the Drift Mobility	303
6.3.3.5	Hopping Transport in Organic Solids with Superimposed Disorder and Polaron Effects	306

6.3.3.6	Low-Field Hopping Transport in Energetically and Positionally Disordered Organic Solids	308
6.3.3.7	Charge Carrier Transport in Disordered Organic Materials in the Presence Of Traps	314
6.4	Experimental Techniques	318
6.4.1	Charge Carrier Generation	318
6.4.1.1	Generation Versus Transport Limited Photocurrents	318
6.4.1.2	Delayed Charge Carrier Generation	320
6.4.1.3	Optically Detected Charge Carrier Generation	320
6.4.2	Experimental techniques to measure charge transport	321
6.4.2.1	The Time-of-Flight Technique	321
6.4.2.2	Space Charge-Limited Current Flow	323
6.4.2.3	Determination of the Charge Carrier Mobility Based Upon Carrier Extraction by Linearly Increasing Voltage (CELIV)	325
6.4.2.4	Charge Carrier Motion in a Field-Effect Transistor (FET)	326
6.4.2.5	The Microwave Technique	327
6.4.2.6	Charge Carrier Motion Probed by Terahertz Pulse Pulses	327
6.5	Experimental Results	328
6.5.1	Analysis of Charge Transport in a Random Organic Solid with Energetic Disorder	328
6.5.2	The Effect of Positional Disorder	339
6.5.3	Trapping Effects	342
6.5.4	Polaron Effects	347
6.5.5	Chemical and Morphological Aspects of Charge Transport	350
6.5.6	On-Chain Transport Probed by Microwave Conductivity	356
6.6	Conclusions	358
<b>7</b>	<b>Probing Organic Semiconductors with Terahertz Pulses</b>	<b>367</b>
	<i>Frank A. Hegmann, Oksana Ostroverkhova and David G. Cooke</i>	
7.1	Introduction	367
7.2	What is a Terahertz Pulse?	371
7.3	Generating and Detecting Terahertz Pulses	373
7.4	Terahertz Time-Domain Spectroscopy (THz-TDS)	377
7.5	Conductivity Models	381
7.6	THz-TDS Measurements of Conducting Polymers and Carbon Nanotubes	391
7.7	Time-Resolved Terahertz Spectroscopy (TRTS)	393
7.8	TRTS Measurements of Transient Photoconductivity in Organic Semiconductors	404
7.9	Conclusion	419

**8 Strong Exciton Polaritons in Anisotropic Crystals: Macroscopic Polarization and Exciton Properties 429**

*Gerhard Weiser*

- 8.1 Introduction 429
- 8.2 Interaction of Light and Matter: Excitons and Polaritons 432
  - 8.2.1 Quantum Mechanics of Electrons Interacting with Light 432
    - 8.2.1.1 Excited Electrons and Harmonic Oscillators 432
    - 8.2.1.2 From Excitons to Polaritons 434
  - 8.2.2 Dielectric Theory 439
    - 8.2.2.1 Maxwell's Equations, Fields and Energy Flux 439
    - 8.2.2.2 The Dielectric Tensor and Optical Properties 442
    - 8.2.2.3 Local Oscillators and Macroscopic Polarization 444
- 8.3 Fundamental Properties of Polaritons: Dispersion  $\Omega(k)$  446
  - 8.3.1 Polaritons in Isotropic Solids 446
    - 8.3.1.1 Localized Electronic States 446
    - 8.3.1.2 Delocalized Electrons: Spatial Dispersion of Polaritons 450
  - 8.3.2 Polaritons in Anisotropic Solids: Directional Dispersion 453
    - 8.3.2.1 Polaritons in Uniaxial Crystals 453
    - 8.3.2.2 Biaxial Crystals and Axial Dispersion 457
- 8.4 Experimental Results 458
  - 8.4.1 Non-Classical Absorption of Light 458
  - 8.4.2 Polaritons in Uniaxial Crystals 460
    - 8.4.2.1 Graphite 460
    - 8.4.2.2 Dye Single-Crystal CTIP 462
    - 8.4.2.3 TCNQ, Tetracyanoquinodimethane 469
  - 8.4.3 Polaritons in Biaxial Crystals 471
    - 8.4.3.1 Dye Crystal TTI. Bis(*N*-ethylthiazolin-2-yl)trimethine Cyanine Iodide 471
    - 8.4.3.2 Ionic Crystals of the Dye BDH [1,7-Bis(dimethylamino)heptamethinium] 476
  - 8.4.4 Polaritons in Thin Films of Nanocrystalline Domains 482
    - 8.4.4.1 Single Crystals of *a*-Sexithiophene (T6) 483
    - 8.4.4.2 Nanocrystalline Films 487
- 8.5 Conclusion 492

**9 Sub-5 fs Spectroscopy of Polydiacetylene 497**

*Takayoshi Kobayashi, Mitsuhiro Ikuta and Yoshiharu Yuasa*

- 9.1 Introduction 497
  - 9.1.1 Ultrafast Spectroscopy 497
  - 9.1.2 Characteristic Spectroscopic Properties of Polymers 498
  - 9.1.3 Polydiacetylenes 498
- 9.2 Experimental 501
  - 9.2.1 Sample 501
  - 9.2.2 Laser System 501

- 9.2.3 Data Analysis 502
- 9.3 Results and Discussion 502
- 9.3.1 Peak Tracking Analysis 502
- 9.3.2 Bleaching and Induced Absorption Spectra 509
- 9.3.3 Vibrational Thermalization in the Ground and Excited States 511
- 9.3.4 Singular Value Decomposition for the Analysis of Mode Dependence of Vibronic Coupling in the Excited and Ground States 513
- 9.4 Conclusion 521

## **10 Ultrafast Optoelectronic Probing of Excited States in Low-Dimensional Carbon – Based $\pi$ -Conjugated Materials 525**

*T. Virgili, J. Cabanillas-Gonzales, L. Lüer and G. Lanzani*

- 10.1 Introduction 525
- 10.2 Physics Background: Excited States in Low-Dimensional Conjugated Carbon Materials 526
- 10.3 Electromodulation of Steady-State Fluorescence in Organic Solids 530
- 10.3.1 Introduction 530
- 10.3.2 Electric Field-Assisted Photoluminescence Up-Conversion 533
- 10.4 Electric Field-Assisted Pump–Probe 537
- 10.4.1 Interpretation of the Pump–Probe Experiment 537
- 10.4.2 Interpretation of the Electric Field-Assisted Pump–Probe Experiment 540
- 10.4.3 Review of Experimental Results 541
- 10.4.3.1 Methyl-Substituted Ladder-Type Poly(*p*-Phenylene) (m-LPPP) 541
- 10.4.3.2 Polyfluorene 545
- 10.4.3.3 Fluorene Trimers (3F8) 549
- 10.4.3.4 Oligo(phenylenevinylene)s 551
- 10.5 Photocurrent Cross-Correlation: Real-Time Tracing of Mobile Charge Carrier Formation 555
- 10.5.1 Experimental Setup 556
- 10.5.2 Photocurrent Cross-Correlation: the Signal 556
- 10.5.3 Precursor Populations and the Precursor-Specific Free Carrier Yield 557
- 10.5.4 Stimulated Emission Dumping 558
- 10.5.5 Formation of Mobile Charge Carriers by Re-Excitation (Pushing) of Singlet Excitons 563
- 10.5.6 Mobile Charge Carrier Generation by Re-Excitation of Charged States (Detrapping) 568

**Index 573**

## List of Contributors

### ***Vladimir I. Arkhipov***

IMEC  
MCP/PME  
Kapeldreef 75  
3001 Leuven  
Belgium

### ***Thomas Basché***

Institut für Physikalische Chemie  
Johannes-Gutenberg-Universität  
Jakob-Welder-Weg 11  
55099 Mainz  
Germany

### ***Heinz Bässler***

Institute of Physical, Nuclear and  
Macromolecular Chemistry  
Philipps-Universität Marburg  
Hans-Meerwein-Strasse  
35032 Marburg  
Germany

### ***Juan Cabanillas-Gonzalez***

Dipartimento di Fisica  
Politecnico di Milano  
Piazza Leonardo da Vinci 32  
20133 Milano  
Italy

### ***David G. Cooke***

Department of Physics  
University of Alberta  
Edmonton  
Alberta T6G 2J1  
Canada

### ***Enrico Da Como***

Istituto per lo Studio dei Materiali  
Nanostrutturati (ISMN)  
Consiglio Nazionale delle Ricerche (CNR)  
via P. Gobetti 101  
40129 Bologna  
Italy

### ***Eitan Ehrenfreund***

Physics Department  
Technion-Israel Institute of Technology  
Haifa 32000  
Israel

### ***Ivan I. Fishchuk***

Department of Theoretical Physics  
Institute of Nuclear Research  
National Academy of Sciences of  
Ukraine  
Prospekt Nauki 47  
03680 Kiev  
Ukraine

**Frank A. Hegmann**

Department of Physics  
University of Alberta  
Edmonton  
Alberta T6G 2J1  
Canada

**Christian Hübner**

Fachbereich Physik  
Martin-Luther-Universität Halle-  
Wittenberg  
Hoher Weg 8  
06120 Halle (Saale)  
Germany

**Mitsuhiro Ikuta**

Department of Physics  
Graduate School of Science  
University of Tokyo  
7-3-1 Hongo  
Bunkyo-ku  
Tokyo 113-0033  
Japan

**Andrey Kadashchuk**

Institute of Physics  
Department of Photoactivity  
National Academy of Sciences of Ukraine  
Prospekt Nauki 46  
03028 Kiev  
Ukraine  
and  
IMEC  
MCP/PME  
Kapeldreef 75  
3001 Leuven  
Belgium

**Takayoshi Kobayashi**

Department of Physics  
Graduate School of Science  
University of Tokyo  
7-3-1 Hongo  
Bunkyo-ku  
Tokyo 113-0033  
Japan

**Guglielmo Lanzani**

Dipartimento di Fisica  
Politecnico di Milano  
Piazza Leonardo da Vinci 32  
20133 Milano  
Italy

**Maria Antonietta Loi**

Istituto per lo Studio dei Materiali  
Nanostrutturati (ISMN)  
Consiglio Nazionale delle Ricerche (CNR)  
via P. Gobetti 101  
40129 Bologna  
Italy

**Larry Lüer**

IFN-CNR  
Politecnico di Milano  
Piazza Leonardo da Vinci 32  
20133 Milano  
Italy

**Michele Muccini**

Istituto per lo Studio dei Materiali  
Nanostrutturati (ISMN)  
Consiglio Nazionale delle Ricerche (CNR)  
via P. Gobetti 101  
40129 Bologna  
Italy

**Oksana Ostroverkhova**

Department of Physics  
Oregon State University  
301 Weniger Hall  
Corvallis  
Oregon 97331-6507  
USA

**Michel Schott**

Institut des NanoSciences de Paris  
Université Pierre et Marie Curie  
et Université Denis Diderot  
Campus Boucicaut  
140 rue de Lourmel  
75015 Paris  
France

**Z. Vally Vardeny**

Physics Department  
University of Utah  
Salt Lake City  
Utah 84112  
USA

**Tersilla Virgili**

IFN-CNR  
Politecnico di Milano  
Piazza Leonardo da Vinci 32  
20133 Milano  
Italy

**Gerhard Weiser**

Department of Physics and  
Center of Material Sciences  
Philipps-Universität Marburg  
Renthof 5  
35037 Marburg  
Germany

**Markus Wohlgenannt**

Department of Physics and Astronomy  
The University of Iowa  
Iowa City  
Iowa 52242-1479  
USA

**Yoshiharu Yuasa**

Department of Physics  
Graduate School of Science  
University of Tokyo  
7-3-1 Hongo  
Bunkyo-ku  
Tokyo 113-0033  
Japan

## 1

**Introduction***Guglielmo Lanzani*

The field of organic semiconductors is very old. Melvin Calvin, introducing a first comprehensive text on the subject, *Organic Semiconductors*, by Felix Gutman and Lawrence E. Lyons, published by John Wiley & Sons in 1966, says: “*It was just over thirty years ago that I became aware of the idea that electronic conduction might be observed in organic materials and might play a role in their biological function*”. This places the birth of the field somewhere between 1930 and 1940, when quantum mechanics was still young, inorganic semiconductors were in their early stages and physics was having a fantastic evolution. The book by Gutman and Lyons collects the results obtained from World War II until 1966. In spite of the size and completeness of their text, these authors already acknowledged at that time that a much larger, encyclopedic effort would have been required to cover the field fully. Since then much work has been done, making the “encyclopedia” even further out of reach. Important discoveries occurred in more recent years, especially conjugated polymers leading to the Nobel Prize in Chemistry in 2000. The continuous discovery of new classes of materials, new applications and new tools for investigation has kept the field in a state of flux, in spite of its long history. So in 2005 many of the issues reported in 1966 are still valid, such as the demand for a large interdisciplinary approach, the effort of physicists to develop a theory for weakly bounded systems and that of chemists for understanding property–structure relationships. Amid the spectacular development in science and technology of organic semiconductors, allowed by an exponential increase in the number of active researchers in the field, in both academies and industrial laboratories, many questions remain open.

When I decided to undertake the challenge of editing a book on molecular materials, I had one point fixed in my mind: to make something different from the cutting-and-pasting of published papers. I felt that a monograph was needed that puts new and exciting experimental techniques on a common footing whenever possible, showing their foundations, limitations and interconnections. This will help to intensify and specify communication among experts in different experimental fields.

I asked all the authors of this book to write a broad, exhaustive tutorial on their subject, with original contents, explanation and views. Something that could actu-

ally help the newcomers, instruct the students, support the researchers, not become obsolete too soon and yet have up-to-date contents. It sounds like a mammoth task and indeed it was. Of course, selection was needed, to keep the contents sufficiently focused while preserving these general aims. For instance, the book contains reviews mainly on experimental results, interpretation is based on relatively simple models, except for a few cases, and theory is not included. There are already many excellent books on quantum chemistry. A painful screening had to be done, to select a few topics out of a huge amount of high-quality work existing in the field. One unquestionable criterion guiding this process was, again, avoiding overlap with other reviews. Yet the bibliography received special attention, to compensate for deficiencies and provide as broad as possible review for consultation. I hope most of the existing literature is properly quoted in the references and I apologize in advance for missing any contributions.

In any dynamic science there are many areas of controversy. Experiments, however, “never deceive”, as Leonardo da Vinci said. Interpretation is often that of the authors, yet I hope the reader will have the opportunity to elaborate her or his own point of view.

Radiation–matter interaction is at the foundation of material science, since it is an integral constituent of the principal material characterization tools. Photophysics is the keystone of the subject. The wealth of processes that it includes may be useful for the interpretation of results and also for the design of new device concepts. This is particularly true for organic semiconductors, which have the properties to be highly reactive to light stimuli. Indeed, natural chromophores, light-harvesting systems or emitters are all based on  $\pi$ -conjugated carbon molecules. Mimicking nature has led to the amazing development of plastic electronics.

The book starts with molecular photophysics (Chapter 2). This is one important piece of the story of organic optoelectronics, for such materials often behave as molecular solids. In addition, single-molecule devices are at the heart of molecular electronics, refreshing old molecular concepts for future technology. While basic topic can be a century old, the experimental results reported here are updated to state-of-the-art techniques for single-molecule spectroscopy. This is an attractive way to collect information on molecular dynamics, which reveals surprises and opens up new perspectives towards nanotechnology. The innovative way in which molecular dynamics is investigated, probing single events of isolated species and not averages over large ensembles, provides a new point of view for looking at molecular photophysics. Next are presented studies on single polymer chains, a nascent field (Chapter 3). Here the system investigated has a large size, challenging the concept of localized states suitable to describe molecules and introducing the concepts and tools of the solid state, yet in low dimensions. Such a borderline area is very fertile for new ideas about how to describe phenomena which are neither typical of covalent solids nor of isolated molecules. Quantum confinement, from three- to one-dimensional space, has dramatic effects on the nature and dynamics of excited states, as is well known from inorganic nanostructure investigations. In spite of a high electronic density, screening is much less effective than in higher dimensions and correlation takes over. The resulting tight

bounded exciton states resemble more a molecular than a wave-like crystal excitation. Soft lattice and strong electron–phonon coupling, typical of organic semiconductors, gives an extra twist to the subject.

Once the building blocks, molecules and polymers, are known, one can move on to the solid state, where they interact. An interesting mixing of notions gets involved here, depending on the intermolecular coupling regime. In the weak-coupling regime, localized, molecular states are still a valid description of the elementary excitations. However, in solids new phenomena may occur: energy (excited states) can migrate, incoherently, giving rise to energy transfer, or dissociate, forming charge-transfer states. In the medium coupling regime, intermolecular “resonance” interaction may lead to delocalization of the wavefunction, thus generating completely new excitations with respect to the starting component, described as Frenkel excitons, which cohabit with localized states. In the strong coupling regime, typical of covalent bonding, weakly bound electron–hole pairs can be formed, named Wannier–Mott excitons, or sometimes delocalized charge carriers can appear. Morphology plays a crucial role in modulating the degree of intermolecular interaction. Starting from the molecular structure, it is still a challenge to predict how this happens and to what extent. A number of empirical rules, sometime true recipes, were developed over time. Yet it is well known that even the same molecular species can give rise to a variety of aggregation states, depending on a number of parameters not always under control. We then introduce, in Chapter 4, a specifically designed technique for addressing the relationship between photophysics and morphology, based on the local probing of the optical properties through confocal microscopy.

Elementary excitation dynamics, including generation, relaxation and deactivation, are the next step. First we address long-lived excitations in Chapter 5, which usually appear only in the solid state, where intermolecular processes are responsible for either their generation or slower recombination. Typically long-lived excitations are triplet states and charged states. On this time scale, typically milliseconds, a wealth of characterization techniques are available, including the magnetic degree of freedom, which is of critical importance in some assignments. The scenario one can obtain is fairly exhaustive. The phenomena considered here are those occurring in most optoelectronic devices, which work in quasi-steady-state conditions. Charged excitations, rarely encountered in isolated systems, become important. They play a key role in many applications, so charge transport is the next topic to be considered (Chapter 6), and the discussion is focused on transport in disordered media, suitable for most carbon-based  $\pi$ -conjugated materials. Free carriers, however, are rarely encountered, if they exist at all in soft condensed matter. The place to look for them is the far-infrared region, where “Drude-like” contributions to the radiation–matter interaction may arise. Using electromagnetic pulses in the THz frequency range can do this. It is a difficult experiment, yet appealing and new to this field. The basics and a review of results are reported in Chapter 7. The case of highly ordered systems, as in crystalline specimens, is addressed in Chapter 8. Strong intermolecular interactions lead to wavefunction delocalization, generating new, collective excitations, which involves

all the molecules in the crystal and carry properties peculiar to the crystal and not the constituents. Excitons and polaritons have to be considered. Their peculiar properties are discussed comprehensively and some exemplifying cases are reported. In the last two chapters (9 and 10), ultrafast spectroscopy is introduced. Early time dynamics embody fundamental properties of the materials. The branching ratio of the nascent population into a number of subspecies, which determines the final performance of the material, occurs within 100 fs. We consider standard pump–probe experiments with extreme time resolution and finally electric field-assisted pump–probe experiments, which are carried out on device structures. The latter provide a useful and rather unusual tool for investigating elementary excitation dynamics, which offers a straightforward way of comparison with the better known inorganic semiconductor counterpart.

Advance in science is a collective process, which nowadays involves millions of people. Even in our specific subject the number of active researchers is very large and steady increasing. The essential step that keeps the whole machine running is information exchange within the community. I hope that the publication of this book will contribute to this process.

## 2

# Optical Microscopy and Spectroscopy of Single Molecules

Christian Hübner and Thomas Basché

### 2.1

#### Introduction

Since its first demonstration [1], single-molecule spectroscopy (SMS) has seen rapid development, which is evidenced by the ever-increasing number of publications and groups working in the field of SMS. The research topics covered range from fundamental quantum optical experiments to applications in molecular biology and material and nano-science. Along with this research diversity, technical progress has culminated in the commercial availability of standardized versions of optical microscopes with single-molecule sensitivity. Considering these developments, it seems natural that SMS is one important topic to be covered in a modern book on *Photophysics of Molecular Materials*. Actually, basic photophysical parameters of organic dye molecules as time constants of triplet and singlet decay or energy transfer efficiencies (in molecular aggregates) can easily be accessed by SMS. Although some of the corresponding experiments are “just” the single molecule version of well-known experiments with large ensembles of molecules, there are many experiments, which work exclusively at the single-molecule level.

The main intention of this chapter is to introduce different experimental techniques of SMS and some underlying elementary photophysical principles. Many aspects considered here have already been treated in the literature and two SMS textbooks [2, 3] and a series of review articles [4–14] are available for in-depth reading on specific topics. In addition, we will attempt to highlight the benefits of SMS considering selected applications, which have some relation to other material covered in this book.

Regarding applications, we will completely omit SMS in life sciences, because the huge variety of biological issues would simply exceed the limits of this chapter. Most aspects of single-molecule fluorescence experiments discussed here, however, hold also in the field of life sciences. The interested reader who has an application of SMS to a biological problem in mind will therefore profit from the understanding of its basic principles. Another experimental realization of single-molecule detection that will not be dealt with here is single-molecule detection in solution, which is also mainly employed in bio-oriented research. In this context,

fluorescence correlation spectroscopy (FCS) is sometimes regarded as a single-molecule technique. FCS, however, is not a strict single-molecule method, because it is by definition averaging over a large number of single-molecular events.

Whereas SMS in the early years was mainly performed at cryogenic temperatures, the field of room-temperature SMS is now growing rapidly. SMS under ambient conditions is also referred to as single-molecule detection (SMD). In order not to confuse the reader with two acronyms, we use SMS for both low-temperature and room-temperature experiments.

What makes single-molecule fluorescence so appealing to scientists in the fields of quantum optics and physical, chemical, material and life sciences? One of the magic words in this context is *heterogeneity*. If all molecules of an ensemble were to behave identically in space and time, the study of the properties of single molecules would not give any extra information as compared with an ensemble experiment. If there is any heterogeneity, however, be it of temporal or spatial nature, the observation of isolated entities may provide a wealth of information, which otherwise is hidden in the ensemble average. The great interest of life scientists in single-molecule experiments is due to the notorious heterogeneity of biological systems, which renders them ideal targets for SMS.

On the other hand, nanostructured materials constructed in a bottom-up approach need to be investigated on the nanoscale. Nanoscopic probes are desired here and fluorescence properties such as excited-state lifetime or emission wavelength of single molecules, which are determined by their surroundings, can report on heterogeneities on molecular scales. Ultimately, a single molecule may be a device by itself, a switch, a motor or a light source.

Besides this application-driven interest, single-molecule fluorescence is fascinating from a fundamental point of view. The temporal behavior of photon emission is of particular interest from this perspective. Furthermore, single molecules in a classical picture represent nanometer-sized antennas, the properties of which are worth investigating.

This chapter is organized as follows. In Section 2.2 some photophysical principles of single molecule fluorescence detection are presented. Section 2.3 deals with the experimental techniques. Selected applications of SMS are covered in Section 2.4.

## 2.2

### Photophysical Principles of Single-Molecule Fluorescence Detection

#### 2.2.1

##### The Single Molecule as a Three-Level System

Most fluorescent organic molecules – referred to as fluorophores – can be approximately treated as three-level systems, with the electronic ground state and the first electronically excited state, both being singlet states and an excited triplet state

(see Fig. 2.1). From the electronic ground state ( $S_0$ ) the molecule can be brought into the first electronically excited state ( $S_1$ ) by interaction with the laser field. The Rabi frequency  $\Omega_R \equiv \pi \vec{d} \cdot \vec{E} / h$  determines the interaction strength between the electric field of the light wave and the molecule and thus the pump rate between the electronic ground and first excited state in the electric dipole approximation. Here,  $\vec{d}$  is the electronic transition dipole,  $\vec{E}$  is the amplitude of the electric field of the interacting laser light and  $h$  is Planck's constant. The depopulation of  $S_1$  occurs with rate constant  $k_{21}$ , which is the sum of the radiative rate constant and the rate constants of the radiationless transitions given by internal conversion to  $S_0$  and intersystem crossing (ISC) to  $T_1$ . Because for the present we consider a resonant interaction between the purely electronic  $S_0$ - $S_1$  transition and the laser field, the molecule can be pumped back to the electronic ground state by stimulated photon emission. Of particular importance for the photodynamics of a single molecule is ISC from  $S_1$  to  $T_1$ , which occurs with low probability with rate constant  $k_{23}$ . From  $T_1$  the molecule eventually relaxes to the ground state. As was the case for singlet relaxation, the rate constant  $k_{31}$  of triplet relaxation is given by the sum of radiationless and radiative transitions (phosphorescence). Typically, molecules suitable for SMS do not show phosphorescence, because the radiative rate for the spin-forbidden  $T_1 \rightarrow S_0$  transition is very small. Because single-molecule optics at present is mainly based on fluorescence detection, good single-molecule fluorophores are characterized by a high fluorescence quantum yield. Accordingly, in such molecules the radiative rate constant for singlet decay is larger than the rate constants for the radiationless transitions.

The quantum-mechanical treatment of the three-level system interacting with the exciting laser can be accomplished in the framework of the density matrix formalism using optical Bloch equations. The density matrix equations in the rotating wave approximation then read [12,15]:

$$\begin{aligned} \dot{\rho}_{11} &= k_{21}\rho_{22} + k_{31}\rho_{33} + i\Omega_R(\rho_{21} - \rho_{12}) \\ \dot{\rho}_{22} &= -k_{21}\rho_{22} - k_{23}\rho_{22} - i\Omega_R(\rho_{21} - \rho_{12}) \\ \dot{\rho}_{12} &= [i(\omega - \omega_0) - T_2^{-1}]\rho_{12} + i\Omega_R(\rho_{22} - \rho_{11}) \\ \dot{\rho}_{33} &= k_{23}\rho_{22} - k_{31}\rho_{33} \end{aligned} \quad (2.1)$$

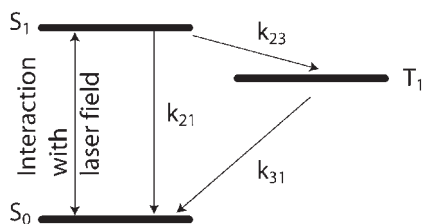


**Fig. 2.1** Reduced Jablonski diagram of the three-level system describing a fluorescent molecule.  $S_0$  and  $S_1$  are the electronic ground and first electronically excited singlet state of the fluorophore, respectively, and  $T_1$  is the

first electronically excited triplet state.  $k_{21}$  is the spontaneous decay rate from  $S_1$  and  $k_{23}$  and  $k_{31}$  are the intersystem and reverse intersystem crossing rates, respectively.

with  $\omega$  and  $\omega_0$  the laser and the molecule's resonance frequency and  $T_2$  the dephasing time.

The steady-state and time-dependent solutions of the set of differential equations in Eqs. (2.1) are appropriate to describe single-molecule behavior at low temperature, when the laser is in resonance with the purely electronic  $S_0$ – $S_1$  transition and phase relaxation processes are slowed. The corresponding results are well documented in the literature [12, 15]. At room temperature, owing to the rapid loss of phase coherence, the off-diagonal elements of the density matrix can be neglected for many applications. The temporal evolution of the system is then described by occupation probabilities or populations  $[n_i(t)]$  of electronic states only. In a typical room-temperature single-molecule experiment, molecules are excited into a vibrational level of  $S_1$ . In large polyatomic molecules vibrational relaxation occurs on the picosecond to sub-picosecond time-scale, which is 3–4 orders of magnitude faster than the time constants of other relevant transitions. Therefore, under typical experimental conditions stimulated emission must not be considered and the three-level system can be described by the following set of simple rate equations:

$$\begin{pmatrix} \dot{n}_1 \\ \dot{n}_2 \\ \dot{n}_3 \end{pmatrix} = \begin{pmatrix} -k_{12} & k_{21} & k_{31} \\ k_{12} & -(k_{21} + k_{23}) & 0 \\ 0 & k_{23} & -k_{31} \end{pmatrix} \begin{pmatrix} n_1 \\ n_2 \\ n_3 \end{pmatrix} \quad (2.2)$$

where  $k_{12} = \sigma I$  is excitation rate from the singlet ground state  $S_0$  to a vibrational level of  $S_1$  and depends on the wavelength-dependent absorption cross-section  $\sigma$  and the laser intensity  $I$ . The solution of this system of differential equations for the stationary case yields the emission rate for a given set of rate constants. Here we will give only the maximum emission rate  $R_\infty$  for an infinite excitation intensity, which depends on the excited state relaxation rate  $k_{21}$  and on the ISC rates  $k_{23}$  and  $k_{31}$ , respectively:

$$R_\infty = \frac{k_{21} + k_{23}}{1 + \frac{k_{23}}{k_{31}}} \Phi_f \quad (2.3)$$

with  $\Phi_f$  the quantum yield of fluorescence. When stimulated emission is considered, as would be the case for the density matrix Eqs. (2.1), the term in the denominator in Eq. (2.3) reads  $2 + k_{23}/k_{31}$ . This can be intuitively understood, because owing to the pumping from  $S_1$  to  $S_0$  the population of the first excited state cannot exceed the population of the electronic ground state.

The maximum emission rate is clearly limited by the ratio  $k_{23}/k_{31}$ , a fact that is frequently referred to as the triplet bottleneck. Whereas ensemble fluorescence spectroscopy usually is done far from saturation of the fluorescence transition, the triplet bottleneck limits the emission rate for the high excitation rates achieved in SMS. The stationary emission intensity  $I_{\text{em}}$  as a function of the excitation intensity  $I_{\text{exc}}$  is as follows:

$$I_{\text{em}} \propto \frac{I_{\text{exc}}}{I_{\text{exc}} + I_{\text{sat}}} \quad (2.4)$$

where  $I_{\text{sat}}$  is the saturation intensity according to

$$I_{\text{sat}} = \frac{R_{\infty}}{\sigma} \left( 1 + \frac{k_{23}}{k_{31}} \right) \quad (2.5)$$

For low excitation intensities, the emitted fluorescence light increases linearly with the excitation intensity and saturates for high excitation powers. This has consequences for the “ideal” excitation intensity, i.e. the excitation intensity with the best signal-to-noise ratio (see Section 2.3.1).

The solution of the system of differential Eqs. (2.2) under the initial conditions  $n_1(t=0) = 1$ ;  $n_2(t=0) = n_3(t=0) = 0$  provides the time evolution of the occupation probability of the first electronically excited singlet state  $n_2(\tau)$ , which is related to the fluorescence intensity autocorrelation function or second-order autocorrelation function:

$$g^{(2)}(\tau) = \frac{\langle n(t)n(t+\tau) \rangle}{\langle n(t) \rangle^2} = \frac{n_2(\tau)}{n_2(\tau \rightarrow \infty)} \quad (2.6)$$

where  $n(t)$  is the number of photons detected at time  $t$  and the brackets denote averaging over  $t$ . In the short time limit ( $t \approx 1/k_{21} \ll 1/k_{23}$ ) the solution of Eq. (2.2) gives [16]

$$g^{(2)}(\tau) = 1 - e^{-(k_{12}+k_{21})\tau} \quad (2.7)$$

This regime is called the antibunching regime, because it leads to a separation of emitted photons in time or, in other words, to a lower probability to detect a photon after a time  $\tau$  if a photon was detected at time ( $\tau = 0$ ) as compared with detecting a photon after infinite time. In the intensity autocorrelation function, antibunching is manifested by a decay to zero when  $\tau$  approaches zero (see Fig. 2.2).

In the triplet time regime ( $t \approx 1/k_{23} \approx 1/k_{31} \gg 1/k_{21}$ ) from Eq. (2.3) it follows that [16]

$$g^{(2)}(\tau) = 1 + \frac{k_{23}^{\text{eff}}}{k_{31}} e^{-(k_{23}^{\text{eff}}+k_{31})\tau} \quad (2.8)$$

where  $k_{23}^{\text{eff}}$  is the effective intersystem crossing rate, given by

$$k_{23}^{\text{eff}} = \frac{k_{12}}{k_{21} + k_{12}} \cdot k_{23} \quad (2.9)$$

As a result, the probability of detecting a second photon after time  $\tau$  is higher than the probability of detecting a second photon after  $\tau \rightarrow \infty$ . This time regime is therefore called the bunching regime. The (normalized) autocorrelation curve is larger than unity in the bunching regime, from where it decays to unity in the infinite time limit (see Fig. 2.2). The antibunching and the bunching regimes are

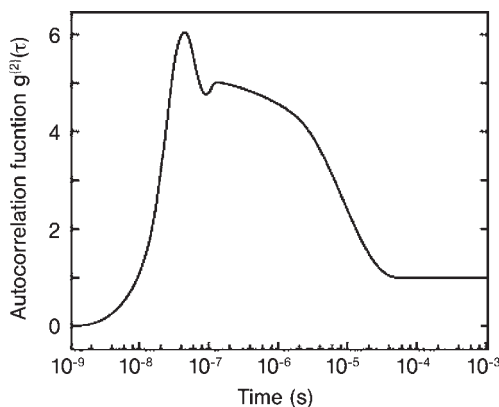


**Fig. 2.2** Simulated intensity autocorrelation function for a single pentacene molecule at low temperature showing photon antibunching at short times and photon bunching at longer times. Additionally, Rabi oscillations are visible in the short time region. Adapted from Ref. [17].

temporally well separated, because the excited-state relaxation rate is typically much higher than the triplet population and relaxation rates.

The respective solution of the density matrix Eqs. (2.1) taking into account coherent interactions between the laser field and the molecule leads to oscillations of  $g^{(2)}(\tau)$  in the short time regime, which are called Rabi oscillations (see Fig. 2.2). Those oscillations are rapidly damped out at room temperature owing to rapid loss of phase coherence.

The temporal properties of photon emission of single molecules thus differ significantly from other light sources such as lasers or thermal emitters. Both photon antibunching and photon bunching can be intuitively understood: There is a finite time for an excitation–emission cycle separating the photons in time, and the molecule shows periods where emission occurs due to singlet cycling, separated by dark periods when it is shelved in the triplet state.

### 2.2.2

#### Dipole–Dipole Coupled Oscillators

Multichromophoric aggregates recently became attractive targets for single-molecule fluorescence experiments driven by the interest in the study of energy transfer mechanisms in those systems (cf. Section 2.4.3). We will therefore present a brief overview of electronic coupling in molecular aggregates, in which one or more excitations are present. For the sake of clarity and simplicity we will limit our discussion to Coulombic interactions taking into account only the leading dipole–dipole term in the point multipole expansion. Consequently, electronic wavefunction overlap and electron exchange between the molecules are not considered. Although this often is a good approximation for strong, dipole allowed

electronic transitions, more advanced approaches exist, which can be found in the literature [18]. When the chromophores are in close proximity, the interaction between the transition dipoles may give rise to coherent excitation transfer, i.e. exciton states delocalized over the aggregate. This situation will be referred to as the strong coupling case. The weak coupling regime is described by incoherent energy transfer or hopping between localized states. A well-known example of such a process is fluorescence resonance energy transfer (FRET) or Förster energy transfer, which typically occurs between molecules separated by several nanometers.

### 2.2.2.1 Weak Coupling

Without dwelling on the details, we now summarize the results of Förster's theory of energy transfer between two chromophores. If one of the two chromophores – the donor – is excited, its energy may be transferred to the second chromophore – the acceptor – through dipole–dipole interaction. In order to make this transfer the dominant one, three requirements need to be fulfilled: (i) the electrostatic field of the donor that decreases with  $1/r^3$  has to be stronger than the radiative electric field that decreases with  $1/r$ , which is the case for short donor–acceptor distances in the nanometer range, (ii) there must be a component of the electrostatic field of the donor in the direction of the acceptor transition dipole and (iii) emission transitions of the donor have to be in resonance with absorption transitions of the acceptor. The transfer rate  $k_t$  then reads

$$k_t = \frac{1}{\tau_0} \left( \frac{r_0}{r} \right)^6 \quad (2.10)$$

The Förster radius  $r_0$ , being the distance between both chromophores at which the transfer rate equals the inverse of the excited state lifetime  $\tau_0$ , is given by

$$r_0 = 0.211 [\kappa^2 n^{-4} Y_{\beta}^D J_{\lambda}]^{1/6} \quad (2.11)$$

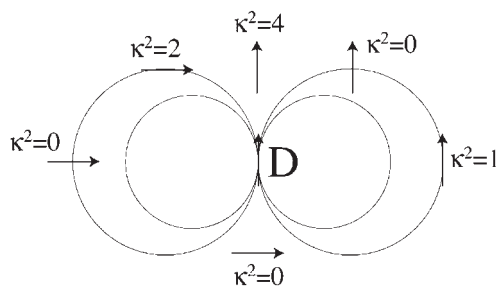


**Fig. 2.3** Orientation factors  $\kappa^2$  for Förster-type energy transfer for different geometries of donor/acceptor orientations. The donor emission transition dipole is depicted as an arrow in the center with some electric field

lines. Acceptor absorption transition dipole positions/orientations with the respective orientation factors are shown.  $\kappa^2$  attains its maximum of  $\kappa^2 = 4$  for in-line orientation of the dipoles.

where  $0 < \kappa^2 < 4$  is the orientation factor taking into account the relative orientation of the donor emission and the acceptor absorption dipole, respectively. Figure 2.3 exemplarily summarizes some cases of relative orientations with the respective orientation factors emphasizing the importance of the connection vector between the chromophores: chromophores with parallel dipole axes may show no transfer at all and there can be efficient transfer even for chromophores with orthogonal dipole axes.

The overlap integral  $J_\lambda = \int \varepsilon(\lambda) f(\lambda) \lambda^4 d\lambda$  goes over the wavelength range where the normalized donor fluorescence spectrum  $f(\lambda)$  overlaps with the acceptor absorption spectrum  $\varepsilon(\lambda)$ . It should be emphasized that the donor and the acceptor chromophores may be chemically identical or dissimilar. In fact, Förster's original derivation was based on chemically identical chromophores [19]. In most applications, however, dedicated donor and acceptor chromophores are used, because they allow for measurement of the transfer rate by spectroscopic means thus enabling – at least in principle – a distance determination on a molecular scale [20].

#### 2.2.2.2 Strong Coupling

Introductory treatments of the strong coupling case for a simple molecular dimer can be found in a seminal paper by Kasha et al. [21] and in a more recent review by Knoester [22]. In the point-dipole approximation the excitation transfer interaction  $J$  represents the interaction energy due to exchange of excitation energy between the two molecules in the dimer. The excitation becomes delocalized over both chromophores and the system now possesses new eigenstates:

$$|\pm\rangle = (|1\rangle \pm |2\rangle) / \sqrt{2} \quad (2.12)$$

with energies

$$E_\pm = \omega_0 \pm J \quad (2.13)$$

where  $|1\rangle$  and  $|2\rangle$  are the excited states of the two isolated chromophores with transition energy  $\omega_0$ . Depending on the orientation of the transition dipoles of the individual chromophores, the oscillator strength is redistributed amongst the transitions to the two new eigenstates. In the collinear case, all oscillator strength is carried by the lower exciton state (J-aggregates); for parallel transition dipoles all oscillator strength is carried by the upper exciton state (H-aggregates). Note that the orientations of the transition dipoles of the dimer eigenstates differ from those of the individual molecules.

The transition from the ground state of the dimer to the state where both chromophores are excited cannot be realized by single-photon absorption. A two-photon absorption process, however, can bring the dimer into the doubly excited state, from where it can relax by simultaneous emission of two photons.

So far we have considered the case of a homogeneous dimer with degenerate transition energies. Under typical experimental conditions, however, the dimer is

interacting with a heterogeneous environment, inducing shifts of the transition frequencies of the individual chromophores. In the presence of static disorder the exciton levels  $\Omega_{\pm}$  in the dimer then become

$$\Omega_{\pm} = \frac{(\omega_1 + \omega_2)}{2} \pm \sqrt{\left[\frac{(\omega_1 - \omega_2)}{2}\right]^2 + J^2} \quad (2.14)$$

with  $\omega_1, \omega_2$  being the transition frequencies of the monomers. In the limit of large static disorder ( $|(\omega_1 - \omega_2)/2| \gg |J|$ ) the excitation is localized, whereas for  $|(\omega_1 - \omega_2)/2| \ll |J|$  the excitation is delocalized.

## 2.3 Experimental Techniques

### 2.3.1 Signal-to-Noise Considerations

The essential requirement for all single molecule fluorescence experiments is that the weak signal from the single molecule rises above the noise due to photon statistics of the signal itself and from the background. There are two main sources of background, the signal from the detector if no light is present, which is referred to as the dark signal, and background induced by laser illumination of the sample. Whereas the dark signal is constant, the laser-induced background scales in a first approximation linearly with the excitation intensity. The signal-to-noise ratio (SNR) can be approximated by [23]

$$SNR = \frac{\eta_{\text{det}} R t_{\text{int}}}{\sqrt{(\eta_{\text{det}} R + C_b P + N_d) t_{\text{int}}}} \quad (2.15)$$

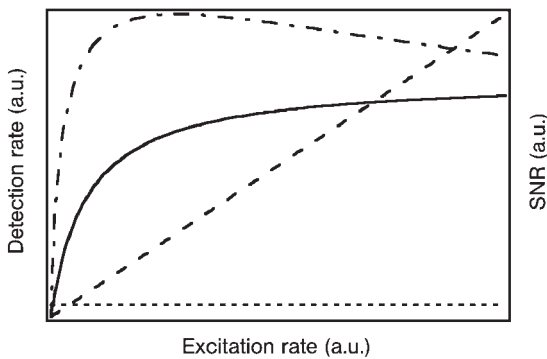


**Fig. 2.4** Modeled signal (solid line), dark signal (dotted line), laser-induced background (dashed line) and signal-to-noise ratio (dashed-dotted line) for single-molecule fluorescence detection.

with  $\eta_{\text{det}}$  the overall detection efficiency,  $R$  the emission rate,  $t_{\text{int}}$  the integration time of photon counting,  $C_{\text{b}}$  the number of background photons proportional to the exciting laser power and  $N_{\text{d}}$  the dark count rate. Obviously, a high count rate and detection efficiency in addition to a low background and dark count rate are advantageous. Figure 2.4 illustrates the signal-to-noise as a function of the excitation rate.

Because the fluorescence signal itself saturates at high excitation intensities, there is an optimal excitation rate with the best signal-to-noise for a given integration time for single-photon counting. If high time resolution is of interest, higher excitation rates are generally required in order to count enough photons within the short integration time. Chromophores with a high maximum emission rate – low intersystem crossing quantum yield and short triplet lifetime – are therefore wanted for SMS. High excitation rates usually imply – at least under ambient conditions – a very limited time frame for the experiment because the possible number of photocycles until irreversible photodestruction occurs is reached rapidly. To summarize, the best-suited excitation intensity has to be carefully adapted to each particular experiment taking into account saturation effects, time resolution, photostability of the chromophores and allowed time for the experiment.

### 2.3.2

#### Room-Temperature Single-Molecule Spectroscopy

##### 2.3.2.1 Epifluorescence Microscopy

Epifluorescence microscopy was, in spite of its simplicity, only recently applied to single-molecule investigations, mainly owing to its lower capability of background suppression. It is, however, well suited for applications where (i) a thin film sample is available and (ii) a temporal resolution in the millisecond range is sufficient. The main advantage of epifluorescence microscopy over scanning microscopy techniques is the short acquisition time for a complete image and its capability to record transient intensities of many molecules in parallel. The film thickness for epifluorescence studies should not exceed the focal depth of the microscope (about 500 nm), because out-of-focus molecules would otherwise contribute significantly to the background signal. With cameras that can be gated in the picosecond range, higher time resolutions can be achieved also in epifluorescence microscopy, but only at the expense of a considerable loss of photons, which is unfavorable in view of the small number of photons emitted by a single molecule.

Both commercial and home-built microscopes are used for single-molecule epifluorescence microscopy and spectroscopy (Fig. 2.5). Lasers are the excitation sources of choice owing to the high photon flux needed for sufficient excitation rates. To illuminate an area of  $30\ \mu\text{m}$  in diameter at  $1\ \text{kW cm}^{-2}$ , the laser should have an average power of 10 mW. For homogeneous illumination of the field of view, the microscope objective is usually overfilled with the Gaussian mode that is provided directly by the laser or after passing a spatial filter.

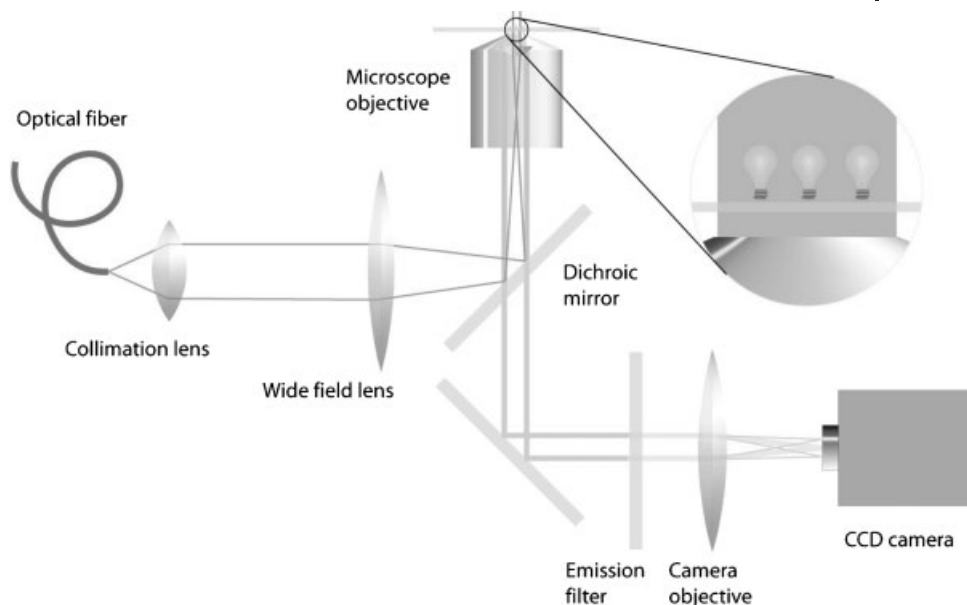


**Fig. 2.5** Schematic view of an epifluorescence microscope used for SMS. The laser light is focused into the back focal plane of the microscope objective.

Whenever possible, oil-immersion microscope objectives should be used. It is not primarily the slightly better resolution that can be achieved with the higher NA of oil-immersion objectives but rather the higher geometric collection efficiency, if the molecules are located close to an interface between a higher refractive index (the film in which the molecules are embedded) and lower refractive index (air) medium. If the molecule is located in the medium with the higher refractive index, e.g. a polymer film on top of a microscope cover-slip, total internal reflection at the polymer/air interface drastically enhances the signal collected by the oil-immersion microscope objective that detects the light through the cover-slip. This back-reflected light cannot be seen by an air objective from the low refractive index side. Even if the molecules are located in the lower refractive index medium, e.g. water on top of a glass cover-slip, a large fraction of fluorescence light is emitted in the direction of the critical angle for total internal reflection (see Fig. 2.6) [24].

Amongst the parts of an epifluorescence microscope used for SMS that demand the highest possible quality are the optical filters, which separate the excitation from fluorescence, i.e. the dichroic beamsplitter and the emission filter. The dichroic should feature a steep edge, a high transmission for the fluorescence (anti-reflective coating of the back side) and, if polarization resolution is required, a low polarization dependence of the edge position. Moreover, there is considerable change of the polarization state of the light reflected off the dichroic mirror, which has to be taken into account if polarization-sensitive techniques are used (cf. Section 2.4.4).

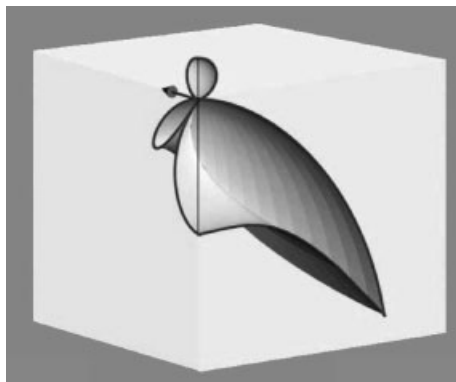


**Fig. 2.6** Spatial distribution of the emission of a dipole close to an interface between two media with different refractive indices. The medium with the lower refractive index is located below the dipole, which is symbolized by the arrow. Adapted from Ref. [24].

As emission filters, mainly holographic notch filters were employed in the early years of SMS. Owing to the significant improvements in the production of dielectric mirrors with steep edges, an optical density of 5–6 at the excitation wavelength and an unsurpassed transmission for the fluorescence, however, such filters are nowadays widely used in SMS. Another advantage, especially of the dielectric filters produced by sputtering, is their greater ruggedness as compared with holographic notch filters.

The heart of an epifluorescence microscope used for SMS is the camera that images the fluorescence light. Although the bare eye is, after adaptation to the dark for at least half an hour, capable of seeing the fluorescence of a single molecule through the binocular of the microscope, quantitative investigations require a camera for imaging. To choose amongst the various types of cameras, the exact requirements of the application should be considered.

The main parameters the decision should be based on are (i) quantum efficiency, (ii) dark signal, (iii) readout noise and (iv) other sources of noise. The highest quantum efficiencies in excess of 90% are achieved with back-illuminated charge coupled device (CCD) cameras. Front illuminated CCD cameras with micro-lens arrays come close to this number. Intensified CCDs (ICCDs) have typically lower quantum yields ranging from 10% to 35% depending on the cathode material of the image intensifier.

The dark signal of CCDs depends on the operation temperature. CCDs for low light applications are therefore cooled by Peltier elements or with liquid nitrogen. With Peltier cooling temperatures of  $-75^{\circ}\text{C}$  are achievable, which is sufficient for most applications. The dark signal of ICCDs depends on the photocathode material and on the temperature of the photocathode. As a rule of thumb, photocathodes with higher quantum efficiency usually also have a higher dark signal. Cooling of the photocathode as is realized in photomultiplier tubes would reduce

the dark signal in ICCDs. However, to date no SM fluorescence studies employing an ICCD with a cooled intensifier have been reported.

The readout process of all CCDs is a source of excess noise. At low integration times it is the main noise source, rendering impossible the detection of single photons with conventional CCDs. If single photons are to be detected with a camera, an amplification of the signal prior to readout is mandatory. The image intensifier of an ICCD serves this purpose.

Recently, a new class of CCDs has been developed, featuring an amplification register where the charges produced by impinging photons are multiplied by an avalanche process. Amplification factors as high as 2000 are reached in these electron-multiplying CCD (EMCCD) cameras. A single photon can thus produce 2000 electrons, well in excess of readout noise (typically a few electrons).

Other sources of noise are clock-induced charges (generated by the clock pulses that shift the charges to the readout register) and amplification noise in ICCDs and EMCCDs. In ICCDs two sources contribute to amplification noise: the electron multiplication process in the micro-channel plate and the phosphor that converts the electrons back into photons to be detected by the CCD. The latter is absent in electron-bombardment ICCDs, where the electrons are directly detected by the CCD chip. Direct electron bombardment, however, leads to rapid degradation of the CCD itself. ICCDs typically show the highest noise levels of all camera types. On the other hand, ICCDs allow fast gating down to the picosecond range. The background in experiments using pulsed excitation can thus be reduced by application of a time gate, i.e. rejecting scattered photons that arrive with the laser pulse.

Clock-induced charges contribute significantly to the noise of EMCCDs, because they are amplified like charges generated by photons. The stochastic nature of the amplification process in the gain register is another source of noise. Both noise sources are absent in conventional CCDs, which therefore show the lowest noise level of all camera types if enough photons are collected within the integration time to overcome the readout noise limit.

To summarize the considerations above, in all applications, where enough photons are provided within the integration time (strong signal or long integration times), conventional CCDs are the cameras of choice. If a small number of photons are to be detected within the integration time, EMCCDs are best suited. ICCDs are nowadays mainly used in applications requiring fast-gated operation.

Another aspect to be considered regarding the signal-to-noise ratio is the size of the image, i.e. the point spread function (PSF) of a single molecule. The best signal-to-noise ratio is achieved if this image fits the size of one camera pixel. In the home-built microscope used by the authors a commercially available zoom photo-objective allows for adjustment of the image size. Together with the binning capabilities of the CCD it provides a very high degree of flexibility.

Spectral resolution in epifluorescence can be made available by different means. If no fast dynamics are to be studied, images with different optical filters can be taken subsequently. If better time resolution is required, a dichroic beamsplitter sandwiched with a mirror that is slightly tilted can be placed in front of the cam-

era objective in such a way that two images appear on the CCD chip [25]. Similarly, a transmission grating with a low divergence can be placed in front of the camera objective, thus producing a low-resolution spectrum of each molecule [26, 27]. This method, however, requires spatially well-separated molecules.

In order to determine the polarization of the emitted light, a Wollaston prism can be placed in front of the camera objective. In this case, two images representing orthogonal polarizations appear on the CCD. More sophisticated detection schemes allowing for three-dimensional orientation determination will be discussed in Section 2.4.4.

### 2.3.2.2 Total Internal Reflection (TIR) Microscopy

If a thin-film sample is not available, the background due to out-of-focus molecules can be removed by excitation of the molecules with the evanescent field at an interface at which total internal reflection occurs. This evanescent field penetrates a few tens of nanometers into the medium with the lower refractive index, e.g. water. Two variants of TIR microscopy are possible, namely excitation through the microscope objective or excitation via a prism attached to the sample. The objective-type TIR microscopy has the advantage that the fluorescence can be collected more efficiently, as pointed out in the previous section. TIR fluorescence excitation using a prism on the other hand has the advantage of an extremely low laser background.

### 2.3.2.3 Scanning Confocal Optical Microscopy

The workhorse for SMS at room temperature is scanning confocal optical microscopy (SCOM). The authors will not give a complete overview of SCOM but rather a brief introduction and will focus on the actual problems to be considered if SCOM is to be applied to SM fluorescence studies. For more detailed descriptions of SCOM the reader is referred to dedicated textbooks [28, 29].

Figure 2.7 shows the outline of a typical SCOM used for SMS. The excitation laser is focused by a microscope objective to a diffraction-limited spot in the sample. In order to obtain a nearly diffraction-limited focus, the central part of an as perfect as possible Gaussian mode is directed to the microscope objective. The Gaussian mode is realized by spatial filtering, either at a pinhole or in a single-mode optical fiber. The authors use single-mode optical fibers for this purpose, because of their additional advantage of high flexibility and because they usually deliver better modes. A quarter- and a half-wave plate, both placed in rotation mounts in front of the fiber, allow for the adjustment of any state of polarization entering the microscope objective. The fiber has to be fixed on the optical table to avoid variations in the birefringence of the fiber due to bending. A simple yet efficient means to adjust the excitation power is to cut the laser beam by a movable metal sphere in front of the fiber. As a general rule, optical elements should be placed in front of the fiber whenever possible given that they have no impact on mode quality there.

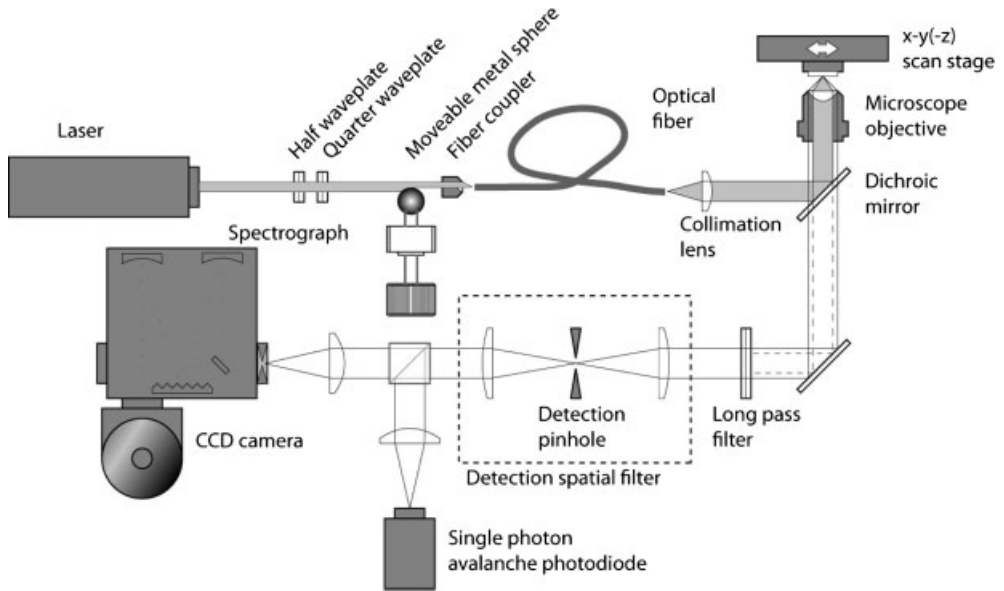


**Fig. 2.7** Scheme of a sample scanning confocal optical microscope. The spatial filter in the detection path can be omitted and instead the active area of the detector employed as a pinhole. Adapted from Ref. [30].

A lens then collimates the light emerging from the optical fiber. Achromats of the highest possible quality are recommended here. High-quality photo-objectives are also well suited for collimation of the laser light and the use of zoom objectives even allows for variation of the degree of overfilling the microscope objective aperture. In order to maintain the high mode quality of the excitation light, the dichroic mirror should have a surface flatness of better than  $\lambda/10$ . Such a surface quality usually requires a substrate thickness of at least 3 mm, which in most cases does not fit into commercial microscopes. The overall higher flexibility of home-built microscopes at present renders them superior to commercial microscopes for most applications with the exception of studies where cells need to be imaged simultaneously by conventional microscopy.

It is recommended to check the polarization state of the excitation light after reflection at the dichroic mirror in view of the fact that the polarization is usually influenced by the dichroic. Typical excitation powers in confocal single-molecule fluorescence range from few hundreds of nanowatts to few microwatts.

A microscope objective focuses the collimated laser light down to a diffraction-limited spot in the sample. For the microscope objective oil-immersion types are preferable for the reasons discussed in Section 2.3.2.1. In order to create a diffraction-limited spot from the collimated beam of light infinity-corrected microscope objectives are used. The microscope objective collects the fluorescence from the sample and directs it to the detectors.

An emission filter suppresses back-reflected excitation light. As already discussed, high-quality dielectric mirrors are nowadays superior to holographic notch filters that were used to date. Again, the substrate quality is of great importance; the emission filter in particular should not have a wedge to avoid beam deviation.

The confocal principle requires spatial filtering of the emitted light by a detection pinhole in order to suppress out-of-focus fluorescence. In principle, the same spatial filter can be used for excitation and emission. In this case, the spectral separation of excitation/emission is realized before the spatial filter. In most microscopes, however, a second pinhole is placed in the detection path. If the best optical resolution is the aim, the size of the pinhole in this spatial filter is chosen to match the full width at half-maximum (FWHM) of the detection point spread function (PSF). This leads, however, to a considerable loss of photons, which is unfavorable in SMS. Therefore, the diameter of the detection pinhole for SMS is chosen to approximate the diameter where the detection PSF has dropped to  $1/e^2$ . The fluorescence light may be split according to the spectrum by a dichroic and/or according to the polarization by a polarizing beam splitter before it is focused on to the detectors. Single-photon avalanche photodiodes (SPADs) are the detectors of choice owing to their higher quantum efficiency ( $\sim 80\%$  maximum QE) as compared with photomultiplier tubes (PMTs). The active area of the SPADs with a diameter of  $\sim 180\ \mu\text{m}$  can be used as a pinhole if a focusing lens of appropriate focal length is used, so that a dedicated detection pinhole can be omitted. This has the advantage of a reduced number of optical elements in the detection path that need to be aligned and that might give rise to a loss of photons.

Further optical elements are required for a beam scanning or laser scanning SCOM, namely a telecentric lens system and a scan mirror (cf. Section 2.3.3.2). A sample scanning SCOM has several advantages, in particular (i) a reduced number of optical elements, (ii) an image size that is only limited by the scan range of the scanning stage and (iii) significant reduction of optical aberrations. The superiority of a beam scanning over a sample scanning SCOM, on the other hand, lies in the faster achievable scan speed and in the possibility of placing the sample in a cryostat where sample scanning might be difficult to realize. Commercially available SCOMs usually work with beam scanning, whereas most of the home-built room-temperature microscopes used for SMS employ scan stages for sample scanning. The authors make use of a closed-loop piezoelectric  $x$ - $y$  scan stage for sample scanning and an additional closed-loop piezo-translator to move the microscope objective in the axial direction for focusing. The sample, which is usually prepared on a microscope cover-slip, is fixed on the sample holder by magnets. In order to perform experiments *in vacuo* or in well-defined atmospheres, the authors use a custom-made sample holder where the cover-slip is held by vacuum grease below a chamber that can be evacuated or flushed with the adapted atmosphere.

Spectral resolution can be realized by the use of dichroic beam splitters and multiple detectors or by directing the fluorescence light on to the entrance slit of a CCD-equipped spectrometer. If the requirements for spectral resolution are not too high, a grating can simply be placed in the parallel beam and the spectrum is imaged by a photo-objective equipped CCD camera or a multi-anode PMT.

In order to be able to perform epifluorescence microscopy with the same microscope, a mirror replaces the grating used for spectroscopy so that imaging with the CCD is possible. A lens is flipped into the excitation path in order to focus the laser light into the back focal plane of the microscope objective, thus generating a collimated beam of light illuminating the whole sample in wide-field mode. The focal length of the lens is chosen in such a way that the illuminated area matches the field of view of the microscope objective.

As pointed out in Section 2.3.1, a high signal-to-background ratio is crucial for reliable data analysis of SM fluorescence data. The main sources of background are scattering (including Raman scattering), background fluorescence, and detector dark signal. At the typical excitation powers in room temperature SMS the background signal is dominated by contributions caused by laser illumination – scattering and background fluorescence – if the dark count rate of the detectors does not drastically exceed  $100 \text{ counts s}^{-1}$ , which is the case for SPADs.

Special care has to be taken for sample preparation. The cover-slips on which the samples are prepared have to be cleaned thoroughly. A very efficient and reliable method for removal of fluorescent contaminants from the cover-slips is heating to  $510\text{--}515^\circ\text{C}$  for at least 1 h in a furnace. Fused silica cover-slips can be heated to  $1000^\circ\text{C}$ , which leads to substrates with a complete lack of fluorescent contaminants, whereas glass cover-slips heated to  $515^\circ\text{C}$  still show one to two fluorescent spots in a  $25 \mu\text{m}^2$  area under typical SMS conditions.

#### 2.3.2.4 Two-Photon-, $4\pi$ - and STED Microscopy

Several techniques can be applied to improve the resolution of a confocal microscope. In this section, a brief overview is given of techniques that enhance the resolution, but are based on the confocal principle. They are therefore capable of imaging in the bulk of the sample in contrast to the near-field method introduced in the next section, which is limited to the surface of the sample.

The excitation volume can be further reduced if two-photon excitation (TPE) is applied [31–34]. The simultaneous absorption of two photons with half the energy (twice the wavelength) of the excitation energy from the ground to the first electronically excited state leads to the excitation of the molecule. The quadratic dependence of the excitation rate on the excitation power is responsible for a reduction of the dimensions of the excitation volume by a factor of  $\sqrt{2}$ , which is of the same order as if a confocal detection pinhole was employed. The confocal pinhole is therefore usually absent when TPE is used. The additional advantage of TPE is the relatively large spectral spacing between excitation and fluorescence, which facilitates filtering. The low energy used for excitation additionally reduces background. These advantages are, however, partly compensated for by the higher quantum yield of photodestruction.

In order to increase the resolution of confocal microscopes beyond what can be achieved with TPE, two other techniques have been developed,  $4\pi$  microscopy and stimulated emission depletion (STED) microscopy [35–37]. In  $4\pi$  microscopy, the aim is to excite the molecule from the complete steradian. Two high-NA micro-

scope objectives are employed for this purpose. There has to be a well-defined phase relation between the waves coming from the two microscope objectives. The length of the optical path for one microscope objective is therefore adjustable with nanometer precision. As a result, the extension of the excitation volume in the direction of the optical axis is significantly reduced. Owing to its technical complexity and to the fact that the sample has to be accessible from both sides,  $4\pi$  microscopy is so far not routinely applied.

STED microscopy [38] is a double pulse technique. The first pulse is used for excitation in the confocal volume. The second pulse is focused to a doughnut-shaped intensity distribution around the confocal volume and depletes the excitation by stimulated emission. The nonlinear response of this depletion mechanism “sharpens” the border of the excitation volume, which results in a reduction of the excitation volume as compared with a diffraction-limited focus. This recently developed technique has to be adapted to the particular chromophores under investigation and is highly demanding with respect to alignment.

#### 2.3.2.5 Scanning Near-Field Optical Microscopy

Scanning near-field optical microscopy (SNOM) was the first microscopy technique that was applied to room-temperature SMS [39], in spite of the fact that it is probably the most demanding microscopic technique. The excitation volume in SNOM is reduced by confining the electromagnetic field by a geometric feature smaller than the wavelength of the excitation light. This geometric feature is either an aperture [39] or a sharp metal tip [46]. The aperture is realized at the end of a tapered optical fiber [39] or at the very end of a glass tetrahedron [116], both being coated with aluminum in order to confine the field. In apertureless SNOM, the locally enhanced field at the end of a sharp metal tip is utilized. Recently, a combination of both techniques was demonstrated, with a small tip grown at the edge of an aperture formed by the end of an optical fiber [40].

Because the optical near-field is confined to the closest vicinity of the probe, the latter has to be held at a small (of the order of the size of the probe, a few tens of nanometers) distance to the sample as in atomic force microscopy. SNOM is therefore limited to the detection of fluorescence from single molecules located very close to the surface of the sample. As in atomic force microscopy, the tip can be in permanent contact to the sample or the amplitude or phase of an oscillating probe is used to control the tip-sample distance. The fluorescence is usually detected by a microscope objective similar to SCOM through the (transparent) sample. Besides the main advantage of a significantly increased resolution there are two other benefits offered by SNOM: the detection efficiency is increased because there is no dichroic mirror in the detection path and the background is drastically reduced owing to the smaller excitation volume. Additionally, the topography of the sample can be simultaneously imaged, providing valuable extra information. For an in-depth description of the SNOM technique the reader is referred to dedicated textbooks [41].

## 2.3.3

**Single-Molecule Spectroscopy at Cryogenic Temperatures**

The microscopic techniques presented so far were based on the spatial isolation of single molecules. In principle, each of these experiments could also be conducted in a cryogenic setting. Such experiments are especially appealing when chromophores are used, which exhibit sharp zero-phonon transitions (lifetime-limited linewidth) at low temperatures. Under these conditions single chromophores can be isolated by their specific optical transition frequencies (zero-phonon lines) which are addressed selectively by a narrow linewidth laser source. The ability of spectral selection allows the number of molecules present in the excitation volume to be much larger than one. Single-molecule spectroscopy in solids at low temperatures fundamentally rests on the inhomogeneous broadening of optical transitions of guest molecules in solids. Owing to strains, dislocations, point defects or statistically varying electric fields in the host material, the dopant molecules experience different environments leading to an inhomogeneous distribution of their homogeneously broadened absorption lines. Detailed accounts on these fundamental aspects can be found in various review articles [2, 5–13, 42].

Historically, the first spectroscopic experiments with single molecules were done at low temperatures applying the principle of frequency selection. In 1989, Moerner and Kador reported the detection of a single pentacene molecule in a *p*-terphenyl crystal using frequency double-modulation absorption spectroscopy with quantum-limited sensitivity [1]. By employing fluorescence excitation spectroscopy in a small sample volume combined with very efficient detection of the fluorescence light, Orrit and Bernard [43] one year later achieved a dramatic increase in signal-to noise ratio for single pentacene molecules in *p*-terphenyl. This clear improvement rendered fluorescence excitation spectroscopy the preferred method to investigate single molecules in low-temperature solids. Although the experiments using a liquid helium cryostat and narrow-band dye lasers are relatively complicated, the advantages of spectral selectivity together with a low background level and with a drastically increased photostability facilitated the detection of the faint light emitted by a single molecule.

Different excitation and detection schemes can be used for low-temperature SMS, e.g. excitation by a focusing lens or through an optical fiber and detection with a parabolic mirror [44], microscopic imaging with an intensified camera [45] and confocal detection. A comprehensive overview over many of the techniques can be found in two textbooks [2, 3]; owing to the limited space here we will concentrate on the confocal scheme, which will be described in the second part of this section. The next part briefly deals with the laser system that delivers the narrow-band excitation light.

### 2.3.3.1 The Laser System

Typical excitation sources in low-temperature SMS are (actively stabilized) linear or ring dye lasers pumped by an argon ion laser or a frequency-doubled Nd:YAG laser. If shorter wavelengths are wanted, the third harmonic of high-power Nd:YAG lasers or comparable light sources can be used to pump the dye laser. Actively stabilized cw dye lasers allow single-mode operation with a bandwidth in the range of several megahertz, where the frequency can be continuously and reproducibly scanned over a range of  $\sim 30$  GHz. In order to achieve the narrow-band emission it has to be ensured that just one out of the possible resonator modes exceeds the lasing threshold. This is achieved by a combination of birefringent filters and Fabry–Perot étalons. A temperature-stabilized external reference cavity is used for closed-loop stabilization of the length of the laser cavity via a scanning Brewster plate and a piezo-driven mirror. Long-term drifts of the laser frequency can be compensated for with the aid of a frequency-stabilized He–Ne laser as a frequency standard [47].

### Low-temperature confocal microscopy

The outline of a low-temperature laser scanning confocal microscope is shown in Fig. 2.8. The light from the dye laser is coupled into a polarization-preserving single-mode optical fiber. The light coming from the fiber is collimated to a beam of diameter  $\sim 2$  mm, which corresponds to the aperture of the electro-optic modulators (EOM) that are used to stabilize the intensity and control the polarization of the excitation light. After the EOMs the beam is expanded to the final diameter of about three times the aperture diameter of the microscope objective. After reflection off the dichroic mirror the light is directed to the laser-scanning unit consisting of a scan mirror and a telecentric lens system. Angular motions of the scan mirror result in  $x/y$  displacements of the focus that is generated by the microscope objective within the sample. A gimbal mount mirror moved by stepping motors permits a resolution and a scan speed that are sufficient for spatial addressing of single molecules.

An optical cryostat with an axial window at the bottom is used to cool the sample to cryogenic temperatures. Owing to the usually short working distance of the microscope objective the latter has to be placed close to the sample in the cryostat. The sample can be moved within the cryostat in the axial direction with respect to the fixed microscope objective for focusing. The desired properties of the microscope objective are different from those for room-temperature SMS. The microscope objective has to be selected to withstand the low temperatures and the extreme temperature changes it is exposed to inside the cryostat. Anti-reflection coatings and the cement between the lenses of the microscope objective are usually not designed for these harsh environmental conditions and degrade rapidly with each cooling–heating cycle. Relatively cheap microscope objectives are therefore preferentially used. Those objectives, however, do not meet the optical quality requirements for optimal excitation and collection of the fluorescence. Recently, custom-made microscope objectives specifically designed for the use inside a liquid helium cryostat have become available. The fluorescence collected by

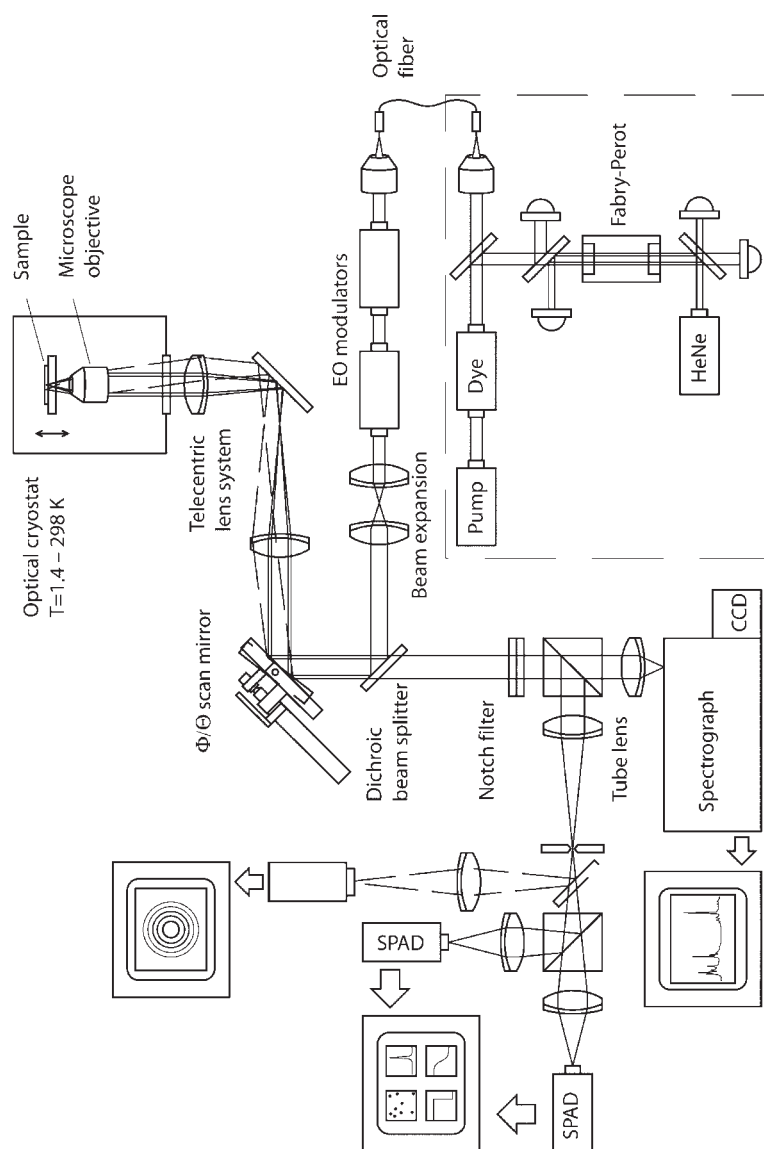


**Fig. 2.8** Schematic view of a low-temperature laser scanning confocal microscope. Adapted from Ref. [48].

the microscope objective passes the telecentric lens system and the dichroic mirror and after additional filtering by an emission filter (cf. Section 2.3.2.3) is directed to the detectors. The recording of fluorescence excitation spectra has been a major application in low-temperature single-molecule spectroscopy. In Fig. 2.9, excitation spectra of terrylene in *p*-terphenyl samples with decreasing concentration of the terrylene chromophores are displayed. In this case an excitation spot of around  $5\ \mu\text{m}$  was produced by focusing the dye laser beam with a single lens [49].

The emission light was collected by a parabolic mirror. Similar results can certainly be obtained with the confocal setup described before, which in general is more flexible. Here, however, we want to emphasize that the spectral selection criterion is sufficient for single-molecule detection at low temperatures provided that certain limits regarding concentration and excitation volume are followed.

The spectra in Fig. 2.9 demonstrate that single-molecule excitation lines can be recorded for very different concentrations of the impurity molecules. In Fig. 2.9a the data from the sample with the highest concentration are presented. In this case, where in an absolute sense the concentration is already very low ( $\sim 10^{-9}$  mol·mol<sup>-1</sup>), there is still a maximum of the inhomogeneous distribution observable. Single-molecule excitation lines are clearly discernible in the wings of the distribution. In Fig. 2.9b the concentration of absorbers is less so that excitation lines of single absorbers can be isolated over almost the whole frequency range. Finally, samples can be prepared where in the spatial volume probed by the laser the excitation line of only one chromophore is observable (see Fig. 2.9c).

Having isolated the excitation line of a single chromophore, a variety of different optical experiments can be performed. The narrow excitation line is a high-resolution spectroscopic probe ( $\nu/\Delta\nu > 10^7$ ) being extremely sensitive to the truly local environment (nanoenvironment) of the chromophore. The detailed investigation of static and dynamic aspects of the guest–host interaction is therefore one important aspect of low-temperature studies. There is also the possibility of exciting the molecule at a fixed frequency and disperse the fluorescence emission by a monochromator or spectrograph. Employing CCD cameras the vibrationally resolved fluorescence spectrum of a single molecule can be gathered in a single exposure. Such experiments were typically done by excitation into the zero-phonon line of the purely electronic transition. Consequently, the corresponding transition in emission is missing in the fluorescence spectra, which contain the longer

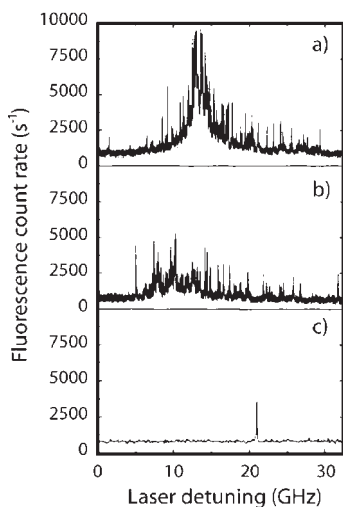


**Fig. 2.9** Fluorescence excitation spectra of terrylene in *p*-terphenyl samples with different dopant concentrations. The concentration decreases from (a) to (c). Whereas in (a) the inhomogeneous line shape is still visible, in (c) the homogeneous line of just one molecule appears in the whole spectral range. Adapted from Ref. [42]

wavelength vibronic transitions. Employing a combination of confocal microscopy and high-resolution spectroscopy, emission spectra following excitation into the vibrational manifold of the singlet excited state of a single absorber can be easily acquired [50, 51]. Spatial isolation of the chromophores by confocal imaging guarantees that indeed only one molecule is excited at a time. Spectral selection only would be difficult here, because the  $S_0$ - $S_1$  vibronic transitions are orders of magnitude broader than the purely electronic transition leading to increased spectral overlap of chromophores.

The combination of confocal microscopy and frequency-selective single-molecule spectroscopy at low temperatures is also a powerful tool for the investigation of multichromophoric aggregates, because it allows one to individually address molecules whose spatial distance is much smaller than the optical resolution of the imaging system [52–54]. A prominent example is the spectral isolation of individual BChl *a* chromophores within the B800 band of spatially isolated photosynthetic antenna complexes [55]. In a similar approach, single chromophores were addressed in the frequency domain within spatially isolated multichromophoric dendrimers [51, 56].

## 2.4 Applications

### 2.4.1 Photon Antibunching

One of the most intriguing statistical properties of the emission of isolated quantum systems is photon antibunching. It reflects the fact that a single emitter cannot deliver two photons simultaneously in one  $S_1 \rightarrow S_0$  transition and that there is a finite time between two  $S_1 \rightarrow S_0$  cycles. The distribution of time lags between consecutively emitted photons, which approximates the intensity correlation function  $g^2(t)$  at short times, upon cw excitation follows the equation [16]

$$g^{(2)}(\tau) = 1 - e^{-(k_{12}+k_{21})\tau} \quad (2.16)$$

where  $k_{12}$  is the excitation rate and  $k_{21}$  is the inverse of the excited state lifetime. The time lag between two photons is on the order of the excited state lifetime for moderate excitation rates.

Photon antibunching in the fluorescence emission of a single molecule was first observed at liquid helium temperature [17]. Because very short time differences between two photon arrivals need to be measured in order to observe photon antibunching, two detectors are necessary to circumvent the dead time limitation imposed by the detectors. In a Hanbury-Brown and Twiss (HBT) detection scheme the light is split by a 50:50 beamsplitter and then directed to two detectors [57]. The signals of the two detectors are fed either to dedicated correlation electronics or to fast start–stop electronics for time-correlated single-photon

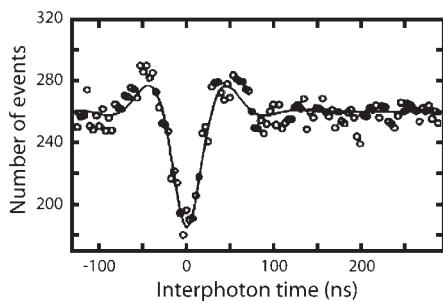


**Fig. 2.10** Inter-photon time histogram for a single pentacene molecule in *p*-terphenyl showing a pronounced dip at  $t = 0$  indicative of photon antibunching. The autocorrelation curve additionally exhibits Rabi oscillations. Adapted from Ref. [17].

counting. Because start-stop electronics is only capable of measuring positive times, the signal of one detector is usually delayed. Both combinations of events, arrival of the first photon on detector A and the second on detector B and vice versa, can thus be recorded. Photon pairs, however, where two subsequent photons hit the same detector, which account for half of the total number of events, cannot be analyzed. Figure 2.10 shows the photon time-lag histogram of the fluorescence from a single pentacene molecule embedded in a *p*-terphenyl crystal detected at liquid helium temperature in an HBT detection scheme with fast start-stop electronics [17]. A pronounced dip at zero time is characteristic of photon antibunching. High excitation rates are necessary to achieve a sufficient number of photon pairs with a short time lag before photobleaching occurs. The higher photostability at low temperatures in a liquid helium cryostat facilitated the demonstration of photon antibunching in the first experiments.

With the improvements of the signal-to-noise ratio due to advantages in confocal and optical near-field microscopy and the availability of detectors with high quantum efficiency, it was possible to observe photon antibunching for molecules adsorbed on a glass surface under ambient conditions [58]. However, care has to be taken when using SPADs for fluorescence detection in an HBT detection scheme. SPAD detectors tend to emit light in the infrared region upon the avalanche process after detection of a photon. Without precautions this light flash can be detected by the other SPAD leading to a peak in the photon distance histogram. A short-pass filter placed in front of one SPAD suppresses this effect.

As detailed above, high excitation rates are mandatory in photon-antibunching experiments in order to achieve high coincidence count rates. A high coincidence count rate can, however, also be achieved with pulsed excitation taking advantage of the high peak powers. The photon distance histogram in this case is sampled at temporal positions spaced by the pulse period. If only the value  $g^{(2)}(t = 0)$  is of interest [59], i.e. there is no need to obtain the complete photon distance histogram, pulsed excitation is therefore preferable. Figure 2.11 shows an example of the interphoton distance histogram for single Cy5 molecules excited with a pulsed

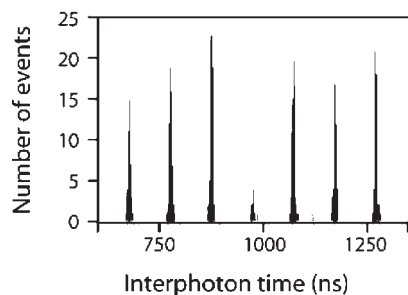


**Fig. 2.11** Photon time lag histogram for a single Cy5 molecule bound to a DNA strand excited by a pulsed laser. The central peak corresponds to two photons emitted during the same laser pulse, whereas the other peaks to photons emitted in subsequent laser pulses. Adapted from Ref. [59].

laser featuring a pulse width of  $<100$  ps. The histogram is governed by the temporal distance between the laser pulses, with the central peak at zero time lag almost missing indicative of photon antibunching.

Photon antibunching with pulsed excitation is potentially applied in single photon sources for e.g. photon-based quantum information processing [60–62]. Another method that was demonstrated to deliver triggered single photons is rapid adiabatic passage of the resonance frequency of single chromophores at low temperatures [63]

## 2.4.2

### Photon Bunching

A very appealing subject when studying the fluorescence properties of single fluorescent molecules is the chance of direct observation of quantum jumps. Intersystem crossing (ISC) from the singlet to the triplet manifold and the reverse represents quantum jumps between different quantum states of the molecule. In ensemble fluorescence experiments, ISC can be indirectly observed as fluorescence fading after pulsed excitation. At the single-molecule level quantum jumps can be directly followed as an on–off behavior of the transient fluorescence intensity of a single chromophore – photons are emitted in bunches separated by dark periods when the chromophore is shelved in the triplet state.

Photon bunching in the fluorescence of a single molecule was demonstrated for the first time by the autocorrelation method already in the first single-molecule fluorescence experiment by Orrit and Bernard [43] at cryogenic temperatures for the system pentacene in *p*-terphenyl. The same group reported a more detailed study of photon bunching 2 years later [47]. The intensity autocorrelation functions shown in Fig. 2.12 follow single exponential decays as expected. The apparent intersystem crossing rate depends on the branching ratio between the fluorescence and the intersystem crossing rate, i.e. the quantum yield of intersystem crossing and on the singlet cycling frequency. Consequently, the single-exponen-

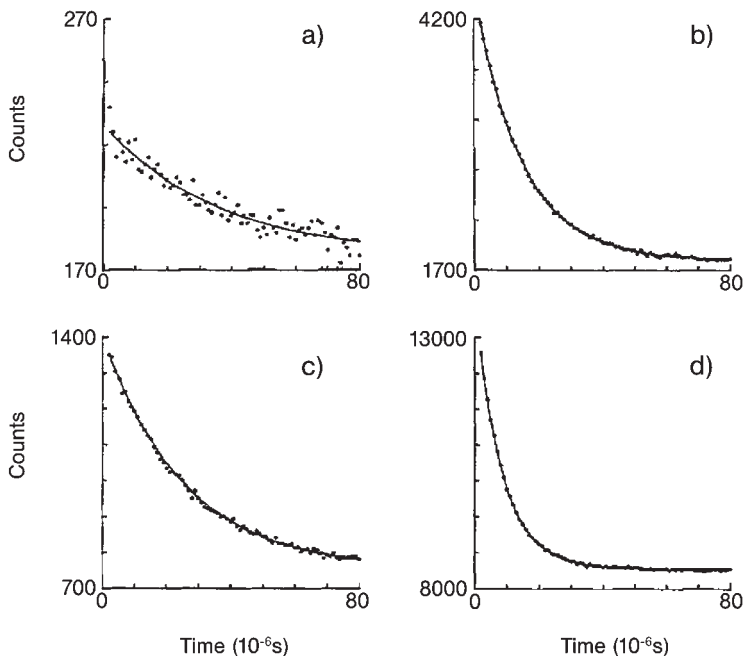


**Fig. 2.12** Intensity correlation functions of the fluorescence of a single pentacene molecule in *p*-terphenyl for increasing excitation intensities from (a) to (d): 0.75, 3, 7.5 and 30 mWcm<sup>-2</sup>. The decays can be fitted by

single exponentials, the time constants of which become shorter with increasing laser power owing to a higher apparent intersystem crossing rate. Adapted from Ref. [47].

tial decay of the intensity correlation function shortens with increasing excitation rate, because intersystem crossing to the triplet state occurs faster.

Basché et al. succeeded in the direct observation of singlet–triplet quantum jumps in the fluorescence of single terrylene molecules doped into a *p*-terphenyl crystal that was placed in a liquid helium cryostat [64].

A few years after the low-temperature experiments, photon bunching – or triplet blinking – was observed also in room-temperature single-molecule fluorescence [16, 65–67, 117]. The transient fluorescence intensity of a single Texas red fluorophore linked to a DNA strand immobilized on a silanized microscope cover-slip is shown in Fig. 2.13a. Pronounced quantum jumps between two intensity levels are visible. The low-intensity level corresponds to the background intensity and is therefore referred to as the “off-state” in contrast to the “on-state” from which fluorescence is detected. For a quantitative analysis the on-state and off-state are discriminated on the basis of a threshold criterion. The histograms of the number of photons detected in the on-state and of the off-state duration shown in Fig. 2.13b and c follow a single-exponential decay. The decay constants of these single exponentials provide the average number of photons detected before ISC occurs and the triplet lifetime, respectively. From the former number the intersystem crossing quantum yield can be calculated [65].

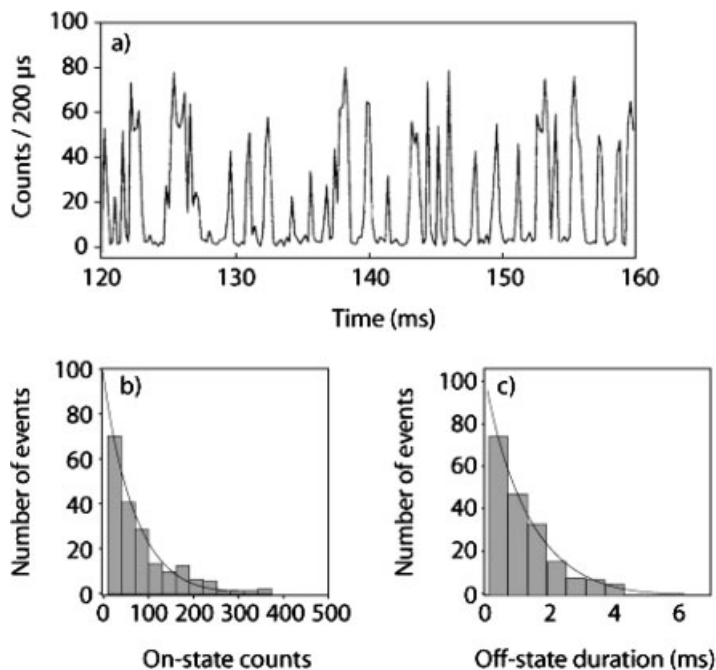


**Fig. 2.13** (a) Transient fluorescence intensity of a single Texas red fluorophore linked to a DNA strand immobilized on a silanized microscope cover-slip. The intensity clearly jumps between two levels, an on-state and an off-state. Histograms of (b) on-state

counts and (c) off-state duration, both following single-exponential decays. From the time constants the intersystem crossing quantum yield and the triplet state lifetime are obtained. Adapted from Ref. [65].

The first room-temperature observation of photon bunching triggered numerous studies of this phenomenon, with the main focus put on the influence of oxygen on the intersystem crossing process [67–71].

Veerman et al. found a time-varying triplet lifetime of single DiI chromophores embedded in a PMMA matrix [67]. They attributed these temporal variations to fluctuations of the local oxygen concentration. Oxygen is a well-known quencher of excited triplet states [71, 72]. Several groups elaborated this effect in a controlled manner [68–70]. It was shown that the presence of oxygen drastically shortens the triplet lifetime, but leads on the other hand to rapid photodestruction [68]. The triplet lifetimes for different molecules varied by over one order of magnitude in the presence of oxygen, giving rise to the conclusion that the accessibility of the molecules for oxygen is strongly heterogeneous in the sample.

Strong enhancement of the fluorescence signal upon oxygen exposure was also found for single conjugated polymer molecules doped into a host material [70]. Schindler et al. identified triplet shelving in conjunction with singlet–triplet annihilation as the bottleneck limiting the maximum emission rate from the fluores-

cing polymers. The oxygen dependence of the triplet lifetime of single fluorophores might be utilized in local oxygen-sensing applications [73].

Photon bunching reports on transitions of single fluorophores between states of different multiplicity by observation of fluorescence photons. Recently, the phosphorescence light of single metalloporphyrins was directly detected and oxygen quenching studied [74]. Mei et al. found a broad distribution of oxygen quenching rates, which they assigned to variations of the local oxygen concentration.

Brouwer et al studied the dependence of intersystem crossing on the isotopic composition of the chromophore pentacene doped into a *p*-terphenyl crystal [75]. The variations of the  $S_1 \rightarrow T_1$  intersystem crossing rate are discussed in terms of the isotope dependence of the zero-point energy of both electronic states.

Data analysis of the fluctuating fluorescence intensity due to photon bunching can be carried out by two different means: By the autocorrelation analysis or by compilation of histograms of on/off time durations [66,76]. The autocorrelation analysis has the advantage that the autocorrelation function is obtained without any additional parameter from the transient fluorescence intensity or by using dedicated correlation electronics. However, knowledge of the on-state and off-state intensity is required in order to calculate the triplet lifetime and the apparent intersystem crossing rate from the autocorrelation function. The great advantage of the correlation analysis is that long-time fluctuations of e.g. the intersystem crossing rate immediately show up in the correlation function and higher order correlation functions may provide additional information about the dynamics of the system [76].

In contrast to autocorrelation analysis, from the on/off state duration histograms the transition rates can be directly calculated. However, the criterion to assign an intensity level to an on-state or off-state, respectively, is not easy to find. High signal-to-background ratios are of the utmost importance here. As for the time resolution, triplet lifetimes shorter than the photon count binning time can be extracted in principle, if the on-state periods are significantly longer than the binning time.

Autocorrelation analysis can nowadays be performed on single-photon arrival data via software using clever algorithms [77]. This offers the advantage of maximum flexibility of data treatment, i.e. the autocorrelation function can be calculated in the temporal regions of interest.

For both types of analysis, the fluorescence rate has to be independently measured or photon-bunching experiments have to be performed for different excitation rates in order to obtain the actual intersystem crossing rate  $k_{23}$  (cf. Section 2.2.1).

### 2.4.3

#### Electronic Coupling Between Molecules

The transfer of electronic excitation energy is a crucial process in multichromophoric aggregates such as conjugated polymers and light-harvesting complexes of bacteria and green plants. Experiments with individual aggregates are increasing

our understanding of the electronic coupling mechanisms in such systems and how these depend on the structure and geometry of the aggregates and their immediate environment [59, 69, 78–87].

One striking observation in single-molecule investigations of multichromophoric aggregates has been the occurrence of collective dark states in their fluorescence emission, which has been reported for virtually every system studied. These dark states are a typical single-molecule signature of interacting chromophores. Typically, such dark states are due to efficient energy funneling into a dark trap state, which might be a triplet state or a charged species formed by photochemical transformations. Other signatures of collective behavior of electronically coupled chromophores are cooperative spontaneous emission (superradiance) and photon antibunching. In 1996 Ambrose and colleagues reported the observation of photon antibunching in B-phycoerythrin, a protein containing 34 bilin chromophores, where efficient singlet–singlet annihilation is thought to turn multiple excitations at different chromophoric sites into a single excitation [88].

Although a wealth of information has been obtained about electronic coupling in complex aggregates, here we want to concentrate on the simplest type of molecular aggregates, i.e. molecular dimers, which in recent years have been increasingly considered for single-molecule studies. Such simple model systems are especially attractive because the analysis of experimental data and the theoretical treatment is more easily accomplished than for complex aggregates with many electronic levels and larger structural flexibility. By applying appropriate synthetic concepts, the distance and orientation between two given chromophores can be varied in a fairly controlled manner via rigid linkers of variable length. In doing so, the electronic coupling strength between the chromophores can be adjusted.

In Fig. 2.14, two examples of simple molecular dimers are shown. In one of the dimers the two monomers (perylene monoimide) are directly connected via a single bond (BPM) whereas in the other one they are separated by the benzil motif (b\_BPM), which leads to differences in the electronic coupling strengths between the two dimers. The close proximity of the monomers in the first case gives rise to excitonic band splitting, which was rationalized by changes in the bulk absorption spectra [89] with respect to the monomer spectra and by a shortening of the fluorescence lifetime in agreement with previous experiments [90, 91] and with theo-

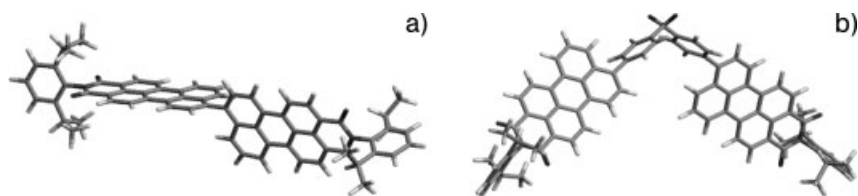


**Fig. 2.14** Structures of the electronic ground states of two molecular dimers as obtained by quantum chemical calculations. (a) Biperylenemonoimide (BPM) with two directly

linked perylenemonoimide chromophores. (b) Benzilic biperylenemonoimide (b\_BPM) with the benzil motif as a spacer between the monomers.

retical considerations [92, 93]. For a system of  $N$  coupled oscillators the radiative rate  $k_{\text{rad}}$  of the aggregate should scale with  $N$ . Therefore, if the excitation is completely delocalized, the radiative rate of a dimer should be twice the value of the monomer yielding a superradiance coherence factor  $L_S$  of 2. [ $L_S = k_{\text{rad}}(\text{dimer})/k_{\text{rad}}(\text{monomer})$  and  $L_S < N$  for incomplete excitation delocalization.] For the benzil structure (b\_BPM) the electronic interactions are governed by Förster-type energy hopping between the monomers.

Fluorescence intensity trajectories at the single molecule level showed one-step and two-step bleaching behavior which appeared to be very similar for both dimers [51]. However, emission spectra recorded simultaneously with the trajectories indicated spectral changes which allowed for distinguishing between weakly (b\_BPM) and strongly coupled dimers (BPM). In the latter case the spectral shape changes significantly when excitonic coupling is lifted after photochemical transformation of one of the monomers [51].

Simultaneous measurements of fluorescence intensities, lifetimes and emission spectra of BPM as a function of time were performed. In Fig. 2.15 complete data sets are shown for two individual BPM dimers. In both cases the fluorescence intensity has dropped to a lower level after a reversible dark state, indicating that one of the chromophores has bleached [51]. Also, in both cases the fluorescence lifetime  $\tau_f$  has increased after the bleaching event, when emission occurs from a single chromophore. An important difference, however, was given by the ratio of the fluorescence lifetimes, which showed that  $L_S$  was different for the two dimers. The value of  $L_S = 1.8$  for the data in Fig. 2.16a is close to  $L_S = 2$  as would be expected for full excitation delocalization. The discrepancy was partly attributed to the fact that the fluorescence quantum yields of the dimer and the monomer might be slightly different. In addition, the so far unknown ratio of static disorder to the coupling strength (see below and Section 2.2.2) determines the degree of excitation delocalization. Nevertheless, the results gave convincing evidence that the fluorescence lifetime changes in Fig. 2.15a are due to cooperative spontaneous emission in the BPM dimer. As expected, the lifetime changes were accompanied by a slight blue shift and changes of the vibronic structure of the emission spectra. The lower  $L_S$  value (1.5) for the dimer the data of which are shown in Fig. 2.15b was attributed to a regime of intermediate coupling, where the electronic excitation is not fully delocalized. Indeed, by investigating 30 isolated BPM dimers  $L_S$  values ranging from 1 to 1.8 were found, reflecting the interplay between the coherent excitation transfer interaction and static disorder.

Besides variations in intermolecular coupling between different dimers, interestingly also temporal variations for a single dimer have been observed. In Fig. 2.16a and b the fluorescence intensity and spectra of a single dimer are plotted as a function of time. At the beginning of the experiment spectrum 1 indicates emission from a localized state. After some time the shape and position of the emission spectrum changed instantaneously, now representing the coherent coupling case. With advancing time several additional transitions from localization to delocalization and vice versa were observed until irreversible photobleaching occurred. It is well known that fluctuations of the nuclear coordinates of the guest-host

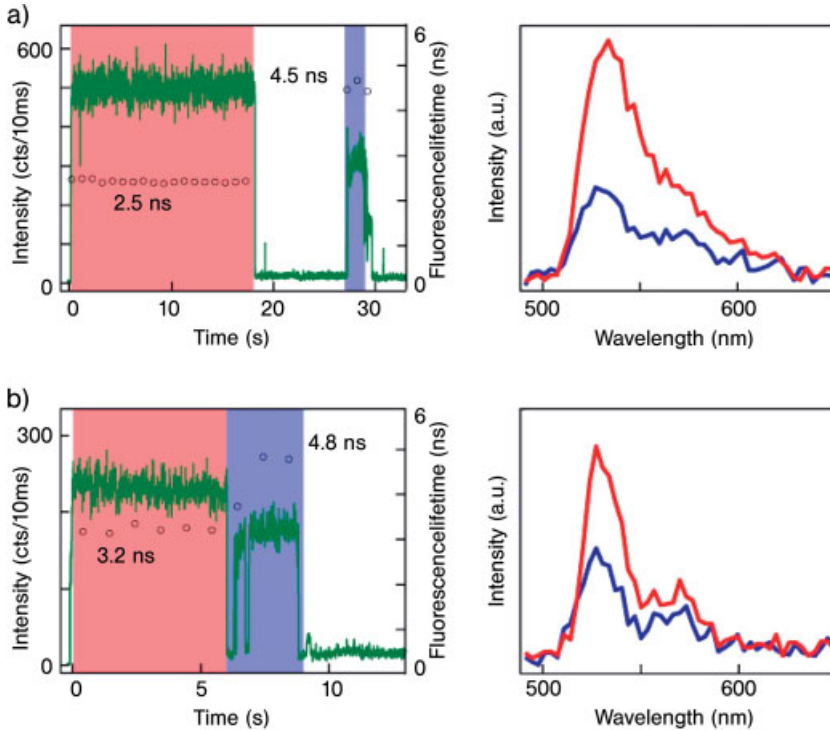


**Fig. 2.15** Room-temperature measurements of the fluorescence lifetimes and spectra of two single BPM dimers embedded in a thin polymer film (zeonex) before and after one of the PM chromophores has bleached. (a) Left: the signal drop after the dark state (~18–27 s) in the fluorescence intensity trajectory indicates the bleaching of one of the PM chromophores [51]. After the bleaching event the fluorescence lifetime (○) has increased from 2.5 to 4.5 ns, yielding a superradiance coherence size factor  $L_s = 1.8$ . Right: Fluorescence spectra recorded during the time intervals marked by the corresponding color in the intensity trajectory.

The spectrum recorded after the bleaching event shows a small blue shift and a change in vibronic structure. (b) Similar sequence of events as described for (a). For this BPM dimer, however, we find  $L_s = 1.5$ . Additionally, the spectral changes are much less pronounced as compared to the data in (a). The excitation light source was a frequency-doubled Ti-Sa laser ( $\lambda = 457$  nm) delivering light pulses with a width of about 1 ps. Single exponentials were fitted to the fluorescence decay curves by maximum likelihood estimation [94] to determine the fluorescence lifetimes. Adapted from Ref. [89].

system occurring on a broad range of time scales can lead to appreciable shifts (10–20 nm) of the electronic spectra. Accordingly, the authors assumed that shifts of the transitions frequencies of the two chromophores induced transitions from the localized to the delocalized state and vice versa [89]. Similar fluctuations at 1.4 K had been deduced from polarization-dependent measurements within the eight-membered B800 ring of light-harvesting complexes [95].

As just pointed out, cooperative spontaneous emission (superradiance) is a prominent signature of intermolecular coherence or the exciton delocalization

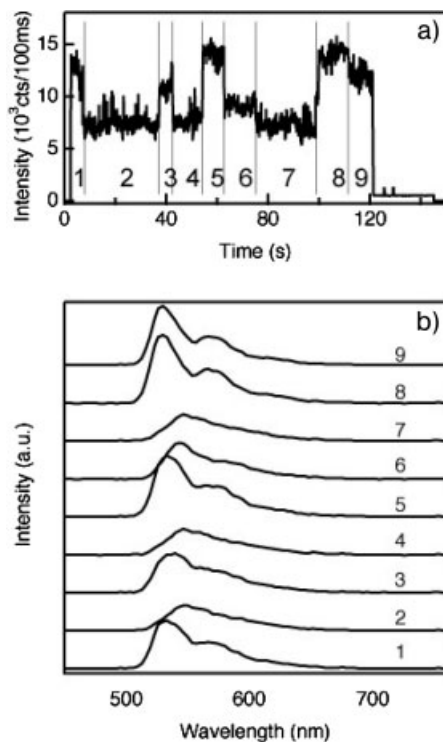


**Fig. 2.16** Temporal variations of the electronic coupling strength of individual BPM dimers. (a) Fluorescence intensity trajectory of a single BPM dimer. (b) Fluorescence spectra recorded during the time intervals numbered correspondingly in (a). The fluctuations

in spectral shape and position reflect transitions between localized (1, 3, 5, 8, 9) and delocalized states (2, 4, 6, 7) of the dimer. These measurements were conducted at room temperature. Adapted from Ref. [89].

length. In addition to the fluorescence lifetime data reported above, superradiant emission had previously been inferred from linewidth measurements at low temperature. Hettich et al. investigated coherent optical dipole–dipole coupling between two terrylene molecules embedded in a *p*-terphenyl crystal [96]. By employing the Stark effect under a scanning probe electrode, the two molecules were found to be localized in the crystal lattice at a distance of 12 nm. Single-molecule linewidth measurements on both lines provided spectral evidence for superradiance at one transition and subradiance at the other transition. The coherent electronic dipole coupling was also proven by another type of experiment invoking two-photon excitation of both molecules. By increasing the excitation intensity, a third line in addition to the two one-photon resonances appeared in the fluorescence excitation spectrum of the coupled molecules (Fig. 2.17). The central resonance frequency which was approximately located at the middle frequency of the two one-photon-resonances clearly indicated that both molecules were simultaneously excited via a two-photon process. This nonlinear signature of cooperative

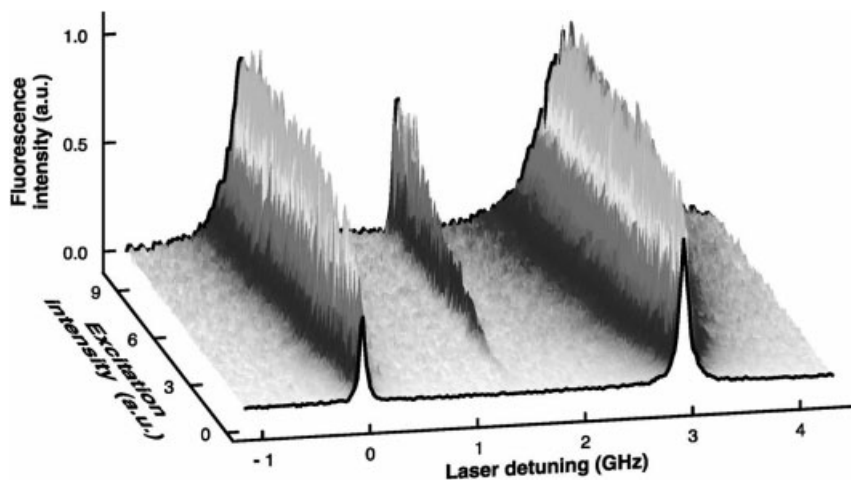


Fig. 2.17 Fluorescence excitation spectra of two electronically coupled terrylene molecules in a *p*-terphenyl-crystal as a function of the excitation intensity. The central resonance appears by simultaneous excitation of both molecules via a two-photon process. From Ref. [96].

behavior, which was experimentally demonstrated for the first time in this work [96], is another hallmark of the electronic dipole coupling between molecules. The observation of photon antibunching for the one-photon transitions and photon bunching for the two-photon transition provided further quantitative evidence for the cooperativity. Hettich et al. emphasized the entanglement of the molecular eigenstates achieved via electronic coupling and discussed schemes to establish how its degree might be effectively controlled [96].

The strong coupling regime has also been accessed in molecular trimers where three perylenediimide molecules are covalently linked in a linear fashion, leading to a collinear arrangement of three transition dipoles. Measurements of the fluorescence lifetimes of the intact trimer, dimer (one chromophore bleached) and the monomer (two chromophores bleached) gave clear differences between the three states with the shortest lifetimes observed for the trimer [97]. Consequently, Hernando et al. concluded that dipole–dipole coupling between the proximate chromophores leads to cooperative spontaneous emission (superradiance) in the oligomers. In comparison with the BPM dimer discussed before, an interesting feature of the trimer is that two different photodegradation pathways, leading to the dimer, exist. When one of the outer chromophores of the trimer bleaches, a dimer is formed with two nearby chromophores representing the strong coupling regime. Bleaching of the central chromophore of the trimer leads to a situation where two more distant chromophores are only weakly coupled (incoherent energy hopping). This behavior could be nicely recovered in the distribution of fluorescence lifetimes of the dimer, which was found to be bimodal. By carefully analyzing the lifetime data and taking into account static disorder, Hernando et al. could show that the photodegradation probabilities of their trimer

followed the contribution of each chromophore to the collective excited state of the system [97].

In addition to the strong, also the weak coupling regime has been studied in molecular dimers by single molecule spectroscopy. As mentioned before, by increasing the distance between two perylenemonoimide chromophores (b\_BPM, see Fig. 2.14), the excitation energy is transferred by incoherent hopping amongst the molecules. In such a weakly coupled dimer pronounced photon antibunching was reported [98]. Actually, no difference in the antibunching behavior as compared with an isolated chromophore was found. This observation was accounted for by a resonant coupling between the  $S_1 \rightarrow S_0$  transition of one electronically excited chromophore and an  $S_1 \rightarrow S_n$  transition of the other one, thus quickly removing a doubly excited state. This process is known as singlet–singlet annihilation [99].

In order to study energy transfer mechanisms involving triplet states, transient fluorescence intensities were recorded for the b\_BPM dimer. The transient fluorescence intensity plotted in Fig. 2.18 exhibits transitions between two intensity levels before one of the chromophores bleaches – photon bunching similar to a single chromophore. Naively, one would have expected more intensity levels because two chromophores are involved. The process of singlet–triplet annihilation, however, leads to the quenching of the fluorescence of one chromophore whilst the other chromophore resides in the triplet manifold.

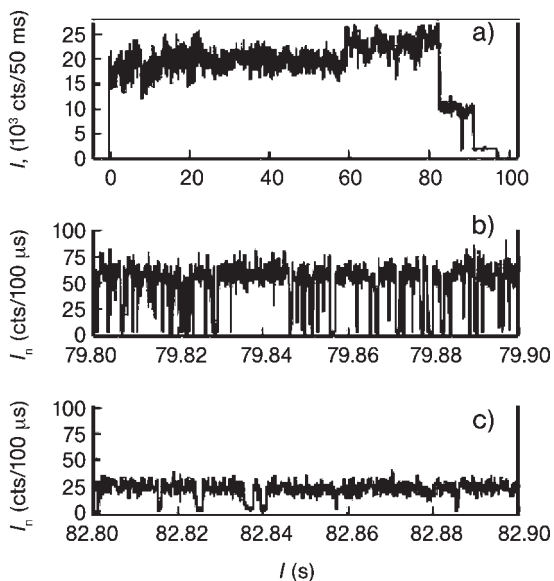


**Fig. 2.18** Transient fluorescence intensity of an isolated b\_BPM dimer (see Fig. 2.15). (a) The whole time course of the fluorescence with a bin time of 50 ms demonstrating two-step photo bleaching. Blow-ups

(b) before and (c) after the first intensity drop at 82 s for a bin time of 100  $\mu$ s showing pronounced switching between two intensity levels. From Ref. [98].

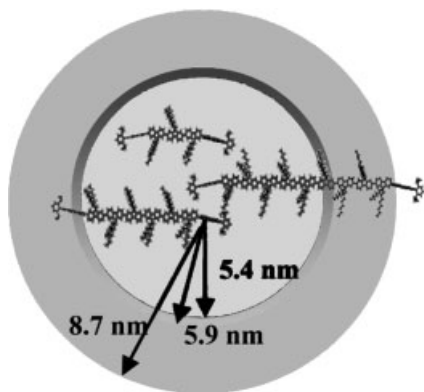


**Fig. 2.19** Structures of perylenemonoimide dimers with different spacers and calculated Förster radii for energy transfer to the  $S_0 \rightarrow S_1$  transition (energy hopping, inner circle), the  $S_1 \rightarrow S_n$  transition (singlet–singlet annihilation, middle circle) and the  $T_1 \rightarrow T_n$  tran-

sition (singlet–triplet annihilation, outer circle). The structures were obtained by force-field calculations and the Förster radii were calculated based on measured transient absorption spectra. Adapted from Ref. [101].

Furthermore, a shortening of the triplet lifetime in the dimer as compared with the monomer was observed, which is due to accelerated reverse ISC from higher excited triplet states. This behavior is very similar to that reported for dendrimers bearing identical chromophores at the rim [100].

Following up their work on multichromophoric dendrimers, Hofkens and co-workers studied Förster-type energy transfer pathways in bichromophoric molecules composed also of two perylenemonoimide chromophores [100, 101]. Different spacers were used to control the spatial arrangement of the chromophores. In one case, the spacer consisted of fluorene oligomers of various numbers of repeat units, starting with a trimer, over a hexamer to a polymer with 56 repeat units on average (Fig. 2.19) [101]. This resulted in interchromophore distances of 3.4, 5.9 and on average 42 nm, respectively. A rigid dendrimer was used as a spacer in another study [100].

In all systems, a two-step photobleaching behavior was seen in agreement with results reported in other studies on dimeric compounds [51, 89, 98] indicative of successive photodegradation of the two chromophores (Fig. 2.20a and b). Another common feature observed in the transient fluorescence intensities of all compounds was the occurrence of collective dark states before the first bleaching step, i.e. before chemical modification of either of the two chromophores. Two types of collective off-states were detected: frequent off-states on a microsecond time-scale (Fig. 2.20a) and very rare off-states on a millisecond to second time-scale (Fig. 2.20d). The exponentially decaying distribution of the short off-states gave rise to the assumption that triplet states were involved. From nanosecond transient ensemble absorption spectra the Förster radii for energy transfer from the  $S_1 \rightarrow S_0$  transition of one chromophore to the  $S_1 \rightarrow S_n$  transition and to the  $T_1 \rightarrow T_n$  of the other chromophore were obtained. The Förster radii implicate efficient energy

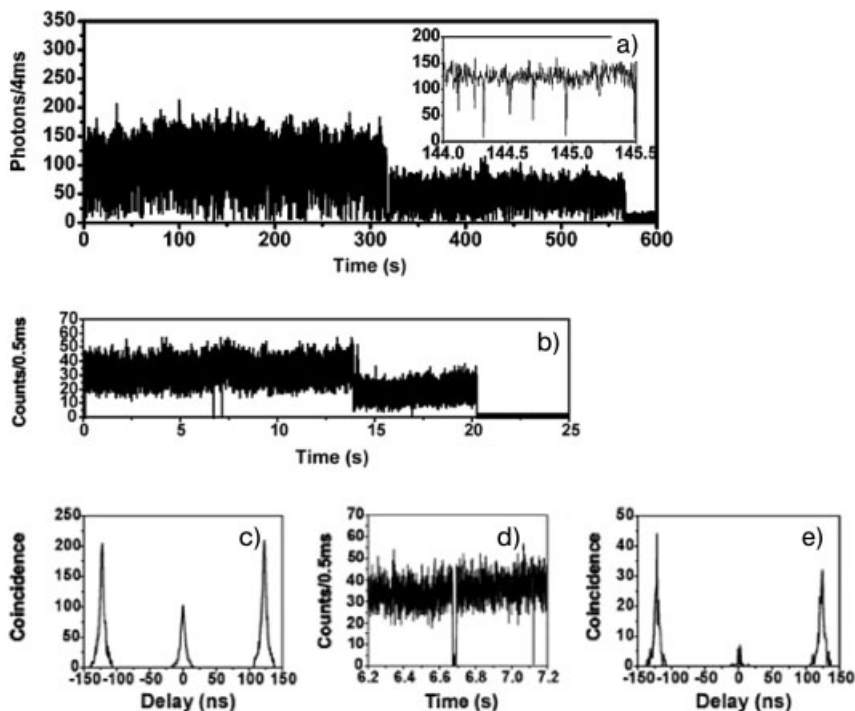


**Fig. 2.20** (a, b) Transient fluorescence intensities of single dimeric molecules with a dendrimer (a) and a polyfluorene ( $\langle n \rangle = 56$ ) (b) as a spacer between the two perylenemide chromophores. The insets in (a) and (d) show temporal blow-ups exhibiting collective off-states, which are more pronounced in the dendrimer system.

Interphoton time histograms of the dimer with the polyfluorene spacer (c) before and (e) after the first bleaching step with pulsed excitation show intermediate photon antibunching indicating less efficient singlet–singlet annihilation. Adapted from Refs. [100] and [101].

transfer to the  $T_1 \rightarrow T_n$  transition in all compounds in the case of collinear transition dipoles ( $\kappa^2 = 4$ , cf. Fig. 2.3). The short collective off-states could therefore be explained by efficient singlet–triplet annihilation. As the mechanism underlying the rare long off-states, the formation of a radical anion was proposed [100].

In order to unravel the singlet–singlet annihilation pathway, photon-pair distance measurements were performed with pulsed excitation. While pronounced antibunching for the dimers with the trimeric and hexameric fluorene spacers as well as for the dendrimer spacer was observed, the peak at  $t = 0$  was considerably higher for the polyfluorene spacer (Fig. 2.20c) in agreement with the calculated Förster radius for singlet–singlet-annihilation (Fig. 2.19).

Because of the importance of the relative orientation of the chromophores for the transfer efficiency, interchromophore angles were additionally measured for the dimers with the terfluorene and the dendrimer spacer by modulating the polarization of the incident laser light [100, 102]. This technique, however, is only

capable of measuring the transition dipole direction projected on to the sample plane. Comparison with simulations, however, allows the conclusion to be drawn that in the dendrimer system different conformers are present [100].

#### 2.4.4

#### Single Molecules as Antennas: Orientation

Besides the unique statistical properties of the photon stream emanating from a single-quantum emitter, single-molecule emission and absorption are interesting also from a classical point of view. The transition dipole of a single chromophore can be classically treated as an oscillating dipole. The emission of a linear dipole is linearly polarized and anisotropic. Along the same lines, absorption at a dipole shows identical anisotropy, i.e. a linear dipole can absorb only the parallel component of the electric field, or, in other words, light polarized perpendicular to the dipole axis cannot be absorbed. This anisotropy can be used to determine the orientation of the nanoscopic antenna of the molecule by optical means.

The simplest approach is to determine just the component of the transition dipole perpendicular to the optical axis (the “in-plane” component). This can be done by different means. If the polarization of the exciting light is rotated, the modulated excitation rate leads to a modulated fluorescence emission. When using a high NA microscope objective, the modulation depth without precautions is not 100% owing to polarization scrambling induced by refraction in the microscope objective. In particular, the out-of plane component is considerably excited. This method is best suited if the molecules have a fixed orientation or reorient in a jump-like fashion. Such a jump of the orientation is observed as a change of the modulation phase [103]. If the rotation is synchronized with the pixel clock of the SCOM, orientational jumps can be easily visualized [104].

In order to determine the orientation of the emission dipole, an analyzer can be rotated in the detection path. This method, however, leads to a considerable loss of photons and has a low time resolution. The more efficient and faster approach is to split the emitted light into two orthogonally polarized components. From the dichroic ratio  $(I_S - I_P)/(I_S + I_P)$  the in-plane orientation can be determined with a twofold degeneracy. Montali et al. determined the orientation of single conjugated polymer molecules in a polymer blend due to tensile deformation by this technique [105].

Several methods have been proposed and demonstrated to overcome the limitation to the in-plane angle, i.e. to determine the three-dimensional orientation. Sepiol et al. demonstrated a method in which the intensity distribution of the fluorescence light collected by an immersion mirror objective in planes before and behind the image plane is used to determine the angular orientation of the emission transition dipole [106]. A similar approach for the orientation determination of the emission dipole is the direct imaging of emission patterns [107, 108]. By slightly defocusing, intensity patterns characteristic for the orientation of the emission dipole are imaged by a CCD camera. The in-plane and out-of-plane angles are determined by fitting a model function to the recorded images. The

photons that are emitted by the molecule are therefore spread over several pixels on the camera, which results in a weaker signal and therefore a lower signal-to-noise ratio. Consequently, longer integration times or stronger excitation as compared with imaging where one pixel corresponds to the detection PSF are necessary.

For the determination of the absorption transition dipole orientation, Sick et al. used annular illumination through a high NA microscope objective where the low NA region is blocked by a circular beam stop [109]. The strong component of the electric field in the focus parallel to the polarization of the incoming light is therefore reduced. The magnitudes of the longitudinal component and the component perpendicular to the polarization of the incoming light, both resulting from the high NA of the microscope objective, are then comparable to the parallel component. The excitation rate of the single molecule is proportional to the electric field projected on to the absorption dipole. This leads to single-molecule excitation patterns characteristic of the orientation of the absorption transition dipole (Fig. 2.21a). The scanned image of an arbitrarily oriented chromophore reflects its orientation (Fig. 2.21b and c), which can subsequently be determined by a fitting procedure. It has to be emphasized that in this technique no detection pinhole is used in order not to cut the excitation patterns. Debarre et al. enhanced this method by additional use of phase modulation [110].

With this technique, the relative angle between the donor and the acceptor absorption dipole in single fluorescence resonance energy transfer pairs was measured by dual-color excitation of the donor and the acceptor chromophore [111]. The donor and the acceptor were addressed individually by excitation at the respective wavelengths. A fit of the experimentally obtained excitation patterns to model functions with the in-plane and out-of-plane angles as parameters allowed the determination of the three-dimensional orientations of both chromophores

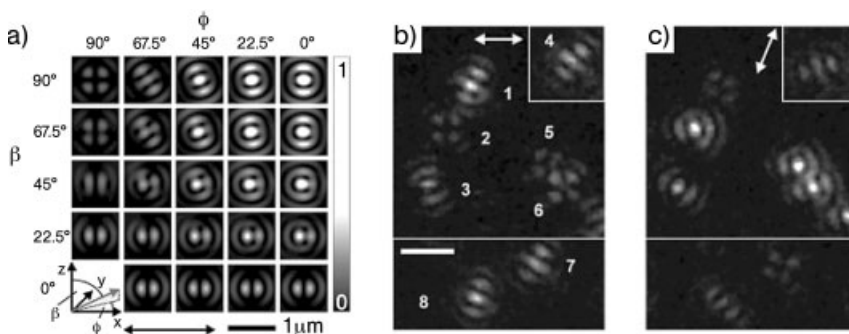


**Fig. 2.21** (a) Calculated single-molecule excitation patterns using annular illumination. The columns differ in the in-plane  $\phi$  and the rows in the out-of-plane angle  $\beta$  as sketched in the lower left corner. (b, c) Experimental excitation patterns as obtained by scanning a sample with single DiI molecules embedded

in a polymer film through the focus of a microscope objective illuminated with a hollow beam of the two depicted polarization directions. Panels (b) and (c) show the same area on the sample. The scale bar is 1  $\mu\text{m}$ . Adapted from Ref. [109].

for each individual pair [111]. The conformational state of individual molecules can therefore be directly determined.

Prummer et al. followed a different approach for the orientation determination. They alternatively illuminated the sample from different angles (therefore they called their technique “tomography”) and with linearly polarized light of two orthogonal polarizations [112], which gives three-dimensional orientation information about the absorption transition dipole. Vacha and Kotani used alternating epifluorescence and total internal reflection (TIR) excitation, taking advantage of the strong component of the electric field perpendicular to the sample plane in TIR [113].

A very elegant detection scheme delivering the full orientation information without fitting and without alternating excitation was proposed by Fourkas [114]. The emitted light is analyzed with respect to its polarization in three directions using three detectors. A simple calculation provides both the in-plane and out-of-plane angles based on the signal of the three detectors. Inspired by this proposal, an even simpler approach for shot-noise limited orientation determination was demonstrated [115]. By annular splitting of the emitted light by means of an aperture mirror the ratio of the light emitted into high NA directions in relation to the light emitted close to the optical axis can be measured (Fig. 2.22a), providing information about the out-of-plane angle of the emission transition dipole. The

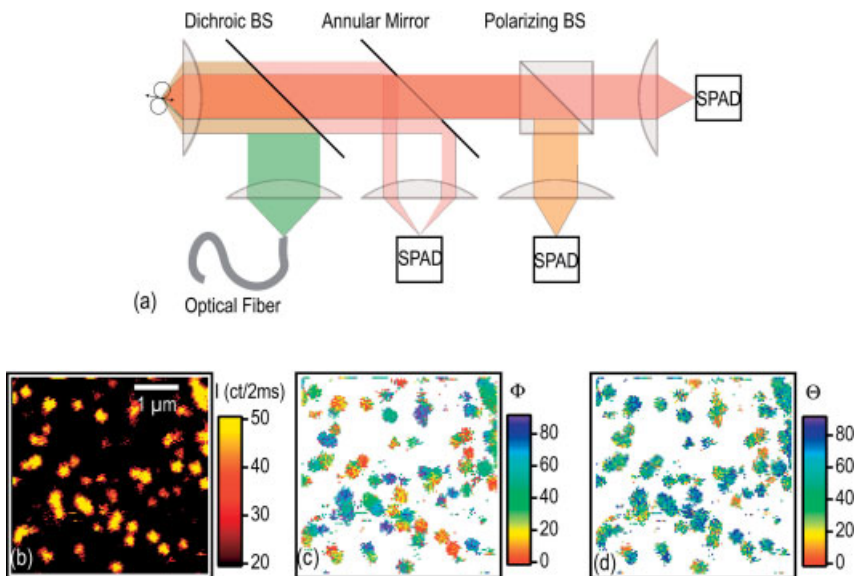


**Fig. 2.22** (a) Detection scheme for orientation determination. The aperture in the mirror corresponds to a detection cone with a cone angle of  $51^\circ$ . (b) Intensity image, (c) in-plane angle image and (d) out-of-plane angle image of PDI molecules embedded in a

PMMA film in a color-coded image. The angles were calculated for fluorescence counts above a threshold set to three times the background counts. Adapted from Ref. [115].

in-plane angle is measured conventionally by splitting the light passing through the aperture mirror into orthogonally polarized components. For each pixel in a raster-scanned SCOM image the orientation can thus be directly calculated (Fig. 2.22c and d) from the signals of the three detectors. With this method the study of hindered rotational diffusion and conformational flexibility with the full angular information and high time resolution is possible.

## References

- 1 W. E. Moerner, L. Kador, *Phys. Rev. Lett.* **62**, 2535–2538 (1989).
- 2 T. Basché, W. E. Moerner, M. Orrit, U. P. Wild (Eds.), *Single-Molecule Optical Detection, Imaging, Spectroscopy*, VCH, Weinheim, 1997.
- 3 R. Rigler, M. Orrit, T. Basché, *Single Molecule Spectroscopy, Nobel Conference Lectures*, Springer Series in Chemical Physics, Vol. 67, Springer, Berlin, 2002.
- 4 W. P. Ambrose, P. M. Goodwin, J. H. Jett, A. Van Orden, J. H. Werner, R. A. Keller, *Chem. Rev.* **99**, 2929–2956 (1999).
- 5 F. Kulzer, M. Orrit, *Annu. Rev. Phys. Chem.* **55**, 585–611 (2004).
- 6 X. Michalet, S. Weiss, *C. R. Phys.* **3**, 619–644 (2002).
- 7 W. E. Moerner, T. Basché, *Angew. Chem. Int. Ed. Engl.* **32**, 457–476 (1993).
- 8 W. E. Moerner, R. M. Dickson, D. J. Norris, *Adv. At. Mol. Opt. Phys.* **38**, 193–236 (1998).
- 9 W. E. Moerner, *J. Phys. Chem. B* **106**, 910–927 (2002).
- 10 W. E. Moerner, D. P. Fromm, *Rev. Sci. Instrum.* **74**, 3597–3619 (2003).
- 11 M. Orrit, J. Bernard, R. Brown, B. Lounis, *Prog. Opt.* **35**, 61–144 (1996).
- 12 T. Plakhotnik, E. A. Donley, U. P. Wild, *Annu. Rev. Phys. Chem.* **48**, 181–212 (1997).
- 13 P. Tamarat, A. Maali, B. Lounis, M. Orrit, *J. Phys. Chem. A* **104**, 1–16 (2000).
- 14 X. S. Xie, J. K. Trautman, *Annu. Rev. Phys. Chem.* **49**, 441–480 (1998).
- 15 T. Basché, S. Kummer, C. Bräuchle, *Single-Molecule Optical Detection, Imaging, Spectroscopy*, VCH, Weinheim, 1997, pp. 31–67.
- 16 L. Fleury, J. M. Segura, G. Zumofen, B. Hecht, U. P. Wild, *Phys. Rev. Lett.* **84**, 1148–1151 (2000).
- 17 T. Basché, W. E. Moerner, M. Orrit, H. Talon, *Phys. Rev. Lett.* **69**, 1516–1519 (1992).
- 18 G. D. Scholes, in *Resonance Energy Transfer*, edited by D. L. Andrews, A. A. Demidov, Wiley, Chichester, 1999, pp. 212–240.
- 19 T. Förster, *Ann. Phys. Berlin* **6**, 166–175 (1946).
- 20 L. Stryer, R. P. Haugland, *Proc. Natl. Acad. Sci. USA* **58**, 719 (1967).
- 21 M. Kasha, H. R. Rawls, M. A. El-Bayoumi, *Pure Appl. Chem.* **11**, 371–392 (1965).
- 22 J. Knoester, *Proceedings of the International School of Physics “Enrico Fermi”, Course CXLIX: Organic Nanostructures: Science, Applications*, edited by V. M. Agranovich, G. C. La Rocca, IOS Press, Amsterdam, 2001, pp. 149–186.
- 23 T. Basché, W. P. Ambrose, W. E. Moerner, *J. Opt. Soc. Am. B* **9**, 829–836 (1992).
- 24 J. Enderlein, *Chem. Phys. Lett.* **308**, 263–266 (1999).
- 25 M. Mörtelmaier, E. J. Kogler, J. Hesse, M. Sonnleitner, L. A. Huber, G. J. Schutz, *Single Mol.* **3**, 225–231 (2002).
- 26 J. Y. Lee, H. W. Li, E. S. Yeung, *J. Chromatogr. A* **1053**, 173–179 (2004).
- 27 S. A. Empedocles, D. J. Norris, M. G. Bawendi, *Phys. Rev. Lett.* **77**, 3873–3876 (1996).
- 28 P. M. Conn, *Confocal Microscopy*, Academic Press, San Diego, 1999.
- 29 A. Diaspro, *Confocal and Two-Photon Microscopy*, Wiley-Liss, New York, 2002.
- 30 F. Koberling, PhD Thesis, Johannes-Gutenberg-Universität Mainz, 2001.

- 31 A. Van Orden, H. Cai, P. M. Goodwin, R. A. Keller, *Anal. Chem.* **71**, 2108–2116 (1999).
- 32 M. K. Lewis, P. Wolanin, A. Gafni, D. G. Steel, presented at the Technical Digest, San Francisco, CA, 1998 (unpublished).
- 33 E. Rothenberg, Y. Ebenstein, M. Kazes, U. Banin, *J. Phys. Chem. B* **108**, 2797–2800 (2004).
- 34 G. Chirico, F. Cannone, A. Diaspro, *J. Phys. D Appl. Phys.* **36**, 1682–1688 (2003).
- 35 S. W. Hell, M. Dyba, S. Jakobs, *Curr. Opin. Neurobiol.* **14**, 599–609 (2004).
- 36 V. Westphal, L. Kastrop, S. W. Hell, *Appl. Phys. B* **77**, 377–380 (2003).
- 37 V. Westphal, C. M. Blanca, M. Dyba, L. Kastrop, S. W. Hell, *Appl. Phys. Lett.* **82**, 3125–3127 (2003).
- 38 T. A. Klar, M. Dyba, S. W. Hell, *Appl. Phys. Lett.* **78**, 393–395 (2001).
- 39 E. Betzig, R. J. Chichester, *Science* **262**, 1422–1428 (1993).
- 40 H. G. Frey, S. Witt, K. Felderer, R. Guckenberger, *Phys. Rev. Lett.* **93**, 2004 (2004).
- 41 D. Courjon, *Near-Field Microscopy, Near-Field Optics*, Imperial College Press, London, 2003.
- 42 T. Basché, C. Bräuchle, *Ber. Bunsen-Ges. Phys. Chem. Chem. Phys.* **100**, 1269–1279 (1996).
- 43 M. Orrit, J. Bernard, *Phys. Rev. Lett.* **65**, 2716–2719 (1990).
- 44 L. Fleury, P. Tamarat, B. Lounis, J. Bernard, M. Orrit, *Chem. Phys. Lett.* **236**, 87–95 (1995).
- 45 F. Güttler, T. Irngartinger, T. Plakhotnik, A. Renn, U. P. Wild, *Chem. Phys. Lett.* **217**, 393–397 (1994).
- 46 J. Azoulay, A. Debarre, A. Richard, P. Tchenio, *J. Microsc.* **194**, 486–490 (1999).
- 47 J. Bernard, L. Fleury, H. Talon, M. Orrit, *J. Chem. Phys.* **98**, 850–859 (1993).
- 48 F. Kulzer, PhD Thesis, Johannes-Gutenberg-Universität Mainz, 2000.
- 49 W. P. Ambrose, T. Basché, W. E. Moerner, *J. Chem. Phys.* **95**, 7150–7163 (1991).
- 50 A. Kiraz, M. Ehrl, C. Bräuchle, A. Zumbusch, *J. Chem. Phys.* **118**, 10821–10824 (2003).
- 51 T. Christ, F. Petzke, P. Bordat, A. Herrmann, E. Reuther, K. Müllen, T. Basché, *J. Luminesc.* **98**, 23–33 (2002).
- 52 E. Betzig, *Opt. Lett.* **20**, 237–239 (1995).
- 53 A. M. van Oijen, J. Köhler, J. Schmidt, M. Muller, G. J. Brakenhoff, *Chem. Phys. Lett.* **292**, 183–187 (1998).
- 54 Y. Durand, A. Bloess, A. M. van Oijen, J. Köhler, E. J. J. Groenen, J. Schmidt, *Chem. Phys. Lett.* **317**, 232–237 (2000).
- 55 A. M. van Oijen, M. Ketelaars, J. Köhler, T. J. Aartsma, J. Schmidt, *Chem. Phys.* **247**, 53–60 (1999).
- 56 R. Metivier, T. Christ, F. Kulzer, T. Weil, K. Müllen, T. Basché, *J. Luminesc.* **110**, 217–224 (2004).
- 57 R. Hanbury-Brown, R. Q. Twiss, *Nature* **177**, 27 (1956).
- 58 W. P. Ambrose, P. M. Goodwin, J. Enderlein, D. J. Semin, J. C. Martin, R. A. Keller, *Chem. Phys. Lett.* **269**, 365–370 (1997).
- 59 K. D. Weston, M. Dyck, P. Tinnefeld, C. Muller, D. P. Herten, M. Sauer, *Anal. Chem.* **74**, 5342–5349 (2002).
- 60 B. Lounis, W. E. Moerner, *Nature* **407**, 491–493 (2000).
- 61 S. G. Lukishova, A. W. Schmid, A. J. McNamara, R. W. Boyd, C. R. Stroud, *IEEE J. Sel. Top. Quantum Electron.* **9**, 1512–1518 (2003).
- 62 T. H. Lee, P. Kumar, A. Mehta, K. W. Xu, R. M. Dickson, M. D. Barnes, *Appl. Phys. Lett.* **85**, 100–102 (2004).
- 63 C. Brunel, B. Lounis, P. Tamarat, M. Orrit, *Phys. Rev. Lett.* **83**, 2722–2725 (1999).
- 64 T. Basché, S. Kummer, C. Bräuchle, *Nature* **373**, 132–134 (1995).
- 65 T. Ha, T. Enderle, D. S. Chemla, P. R. Selvin, S. Weiss, *Chem. Phys. Lett.* **271**, 1–5 (1997).
- 66 W. T. Yip, D. H. Hu, J. Yu, D. A. VandenBout, P. F. Barbara, *J. Phys. Chem. A* **102**, 7564–7575 (1998).
- 67 J. A. Veerman, M. F. Garcia Parajo, L. Kuipers, N. F. van Hulst, *Phys. Rev. Lett.* **83**, 2155–2158 (1999).
- 68 C. G. Hübnner, A. Renn, I. Renge, U. P. Wild, *J. Chem. Phys.* **115**, 9619–9622 (2001).
- 69 P. Tinnefeld, V. Buschmann, K. D. Weston, M. Sauer, *J. Phys. Chem. A* **107**, 323–327 (2003).

- 70 F. Schindler, J. M. Lupton, J. Feldmann, U. Scherf, *Adv. Mater.* **16**, 653–+ (2004).
- 71 D. S. English, A. Furube, P. F. Barbara, *Chem. Phys. Lett.* **324**, 15–19 (2000).
- 72 K. Kawaoka, A. U. Khan, D. R. Kearns, *J. Chem. Phys.* **46**, 1842 (1967).
- 73 N. Opitz, P. J. Rothwell, B. Oeke, P. S. Schuille, *Sens. Actuators B* **96**, 460–467 (2003).
- 74 E. W. Mei, S. Vinogradov, R. M. Hochstrasser, *J. Am. Chem. Soc.* **125**, 13198–13204 (2003).
- 75 A. C. J. Brouwer, J. Köhler, A. M. van Oijen, E. J. J. Groenen, J. Schmidt, *J. Chem. Phys.* **110**, 9151–9159 (1999).
- 76 R. Verberk, M. Orrit, *J. Chem. Phys.* **119**, 2214–2222 (2003).
- 77 M. Wahl, I. Gregor, M. Patting, J. Enderlein, *Opt. Expr.* **11**, 3583–3591 (2003).
- 78 A. M. van Oijen, M. Ketelaars, J. Köhler, T. J. Aartsma, J. Schmidt, *Science* **285**, 400–402 (1999).
- 79 L. M. Ying, X. S. Xie, *J. Phys. Chem. B* **102**, 10399–10409 (1998).
- 80 M. A. Bopp, Y. W. Jia, L. Q. Li, R. J. Cogdell, R. M. Hochstrasser, *Proc. Natl. Acad. Sci. USA* **94**, 10630–10635 (1997).
- 81 D. A. VandenBout, W. T. Yip, D. H. Hu, D. K. Fu, T. M. Swager, P. F. Barbara, *Science* **277**, 1074–1077 (1997).
- 82 W. T. Yip, D. H. Hu, J. Yu, D. A. VandenBout, P. F. Barbara, *J. Phys. Chem. A* **102**, 7564–7575 (1998).
- 83 T. Gensch, J. Hofkens, A. Heirmann, K. Tsuda, W. Verheijen, T. Vosch, T. Christ, T. Basché, K. Müllen, F. C. De Schryver, *Angew. Chem. Int. Ed.* **38**, 3752–3756 (1999).
- 84 Y. Zhao, T. Meier, W. M. Zhang, V. Chernyak, S. Mukamel, *J. Phys. Chem. B* **103**, 3954–3962 (1999).
- 85 M. Maus, R. De, M. Lor, T. Weil, S. Mitra, U. M. Wiesler, A. Herrmann, J. Hofkens, T. Vosch, K. Müllen, F. C. De Schryver, *J. Am. Chem. Soc.* **123**, 7668–7676 (2001).
- 86 J. Hernando, M. van der Schaaf, E. van Dijk, M. Sauer, M. F. Garcia-Parajo, N. F. van Hulst, *J. Phys. Chem. A* **107**, 43–52 (2003).
- 87 P. Tinnefeld, J. Hofkens, D. P. Herten, S. Masuo, T. Vosch, M. Cotlet, S. Habuchi, K. Müllen, F. C. De Schryver, M. Sauer, *ChemPhysChem* **5**, 1786–1790 (2004).
- 88 M. Wu, P. M. Goodwin, W. P. Ambrose, R. A. Keller, *J. Phys. Chem.* **100**, 17406–17409 (1996).
- 89 M. Lippitz, C. G. Hübner, T. Christ, H. Eichner, P. Bordat, A. Herrmann, K. Müllen, T. Basché, *Phys. Rev. Lett.* **92**, 103001 (2004).
- 90 S. Deboer, D. A. Wiersma, *Chem. Phys. Lett.* **165**, 45–53 (1990).
- 91 R. Monshouwer, M. Abrahamsson, F. van Mourik, R. van Grondelle, *J. Phys. Chem. B* **101**, 7241–7248 (1997).
- 92 T. Meier, Y. Zhao, V. Chernyak, S. Mukamel, *J. Chem. Phys.* **107**, 3876–3893 (1997).
- 93 Y. Zhao, T. Meier, W. M. Zhang, V. Chernyak, S. Mukamel, *J. Phys. Chem. B* **103**, 3954–3962 (1999).
- 94 L. Brand, C. Eggeling, C. Zander, K. H. Drexhage, C. A. M. Seidel, *J. Phys. Chem. A* **101**, 4313–4321 (1997).
- 95 C. Hofmann, M. Ketelaars, M. Matsushita, H. Michel, T. J. Aartsma, J. Köhler, *Phys. Rev. Lett.* **90**, 013004 (2003).
- 96 C. Hettich, C. Schmitt, J. Zitzmann, S. Kuhn, I. Gerhardt, V. Sandoghdar, *Science* **298**, 385–389 (2002).
- 97 J. Hernando, J. P. Hoogenboom, E. van Dijk, J. J. Garcia-Lopez, M. Grego-Calama, D. N. Reinhoudt, N. F. van Hulst, M. F. Garcia-Parajo, *Phys. Rev. Lett.* **93**, 236404 (2004).
- 98 C. G. Hübner, G. Zumofen, A. Renn, A. Herrmann, K. Müllen, T. Basché, *Phys. Rev. Lett.* **91**, 093903 (2003).
- 99 A. Y. Borisov, R. A. Gadonas, R. V. Danielius, A. S. Piskarskas, A. P. Razjivin, *Febs Lett.* **138**, 25–28 (1982).
- 100 T. Vosch, M. Cotlet, J. Hofkens, K. Van der Biest, M. Lor, K. Weston, P. Tinnefeld, M. Sauer, L. Latterini, K. Müllen, F. C. De Schryver, *J. Phys. Chem. A* **107**, 6920–6931 (2003).
- 101 J. Hofkens, M. Cotlet, T. Vosch, P. Tinnefeld, K. D. Weston, C. Ego, A. Grimsdale, K. Müllen, D. Beljonne, J. L. Bredas, S. Jordens, G. Schweitzer, M. Sauer, F. De Schryver, *Proc. Natl. Acad. Sci. USA* **100**, 13146–13151 (2003).

- 102 F. Jackel, S. De Feyter, J. Hofkens, F. Kohn, F. C. De Schryver, C. Ego, A. Grimdale, K. Müllen, *Chem. Phys. Lett.* **362**, 534–540 (2002).
- 103 T. Ha, T. Enderle, D. S. Chemla, P. R. Selvin, S. Weiss, *Phys. Rev. Lett.* **77**, 3979–3982 (1996).
- 104 K. D. Weston, L. S. Goldner, *J. Phys. Chem. B* **105**, 3453–3462 (2001).
- 105 A. Montali, A. R. A. Palmans, M. Eglin, C. Weder, P. Smith, W. Trabesinger, A. Renn, B. Hecht, U. P. Wild, *Macromol. Symp.* **154**, 105–116 (2000).
- 106 J. Sepiol, J. Jasny, J. Keller, U. P. Wild, *Chem. Phys. Lett.* **273**, 444–448 (1997).
- 107 A. P. Bartko, R. M. Dickson, *J. Phys. Chem. B* **103**, 11237–11241 (1999).
- 108 M. Böhmer, J. Enderlein, *J. Opt. Soc. Am. B* **20**, 554–559 (2003).
- 109 B. Sick, B. Hecht, L. Novotny, *Phys. Rev. Lett.* **85**, 4482–4485 (2000).
- 110 A. Debarre, R. Jaffiol, C. Julien, D. Nutarelli, A. Richard, P. Tchenio, F. Chaput, J. P. Boilot, *Eur. Phys. J. D* **28**, 67–77 (2004).
- 111 C. G. Hübner, V. Ksenofontov, F. Nolde, K. Müllen, T. Basché, *J. Chem. Phys.* **120**, 10867–10870 (2004).
- 112 M. Prummer, B. Sick, B. Hecht, U. P. Wild, *J. Chem. Phys.* **118**, 9824–9829 (2003).
- 113 M. Vacha, M. Kotani, *J. Chem. Phys.* **118**, 5279–5282 (2003).
- 114 J. T. Fourkas, *Opt. Lett.* **26**, 211–213 (2001).
- 115 J. Hohlbein, C. G. Hübner, *Appl. Phys. Lett.* **86**, 121104 (2005).
- 116 U. C. Fischer, J. Koglin, H. Fuchs, *J. Microsc.* **176**, 231–237 (1994).
- 117 S. M. Nie, D. T. Chiu, R. N. Zare, *Science* **266**, 1018–1021 (1994).

### 3

## Optical Properties of Single Conjugated Polymer Chains (Polydiacetylenes)

*Michel Schott*

### 3.1

#### Introduction

#### 3.1.1

##### Motivation for the Study

The initial motivation of the work presented in this chapter was to develop a model experimental system for the study of electronic properties of conjugated polymers (CP). When this work began and still to a large extent today, all actual solid CP samples were highly disordered, sometimes showing different types of disorder at different scales (for a discussion see, for instance, Ref. [1]), while theoretical studies almost always considered single infinite and perfectly regular chains in vacuum or in some cases crystals of such chains. Hence it was not easy to relate theoretical concepts and predictions to experimental facts. Consequently, several basic physical questions remained open, the main ones being the roles played by electron–phonon and by electron–electron interactions, both being expected to be very important in quasi 1D systems: might the latter be treated perturbatively and, if not, how should they be treated?

To take just an example, the role played by neutral excited states (excitons) in CP spectroscopy was not initially recognized; then, the debate shifted to the exciton binding energy  $E_b$ . The values most commonly inferred from experiments clustered around 0.5 eV, but there were claims of nearly zero binding energy [2].

This has been related to a more fundamental problem, the importance of correlations in determining the electronic properties of CP.  $E_b$  is an inappropriate quantity for assessing the importance of correlations, because of two effects which have a major influence on it that were overlooked until very recently: the effect of lateral confinement, in other words how close to one dimension the actual physical system is, and the contribution of polarization of the surrounding medium. This will be considered in Section 3.4.7.2.

Electron correlations were initially minimized. For instance, the Su–Schrieffer–Heeger (SSH) Hamiltonian for polyacetylene, which was used in a number of theoretical studies, explicitly includes electron–phonon interactions, but not electronic correlations [3]. The same point of view was taken in a later review of CP [4], despite the fact that as early as 1973 [5] it had been shown that electron correlations are enough to open in polyenes a gap comparable to experimental values. Later reviews (see, for instance, Ref. [6]) considered the importance of correlations and nowadays several Hubbard-type treatments are explicitly aimed at the study of CP (see, for instance, Refs. [7–9]). A problem is that each of these theoretical approaches successfully explains part of the available experimental results; some of these results are explained by different conflicting theories: reading Ref. [10] is striking.

In this context, our aim was to develop an experimental conjugated polymer system that would provide an ordered reference state for single CP chain properties. Experimental results obtained on such a system would be directly comparable to theory, in two ways: accurate data on a well-defined system would provide precise tests for theoretical calculations and, perhaps more important, they would hopefully assist physical understanding.

### 3.1.2

#### Choice of the Experimental System

We look for a linear, regular conjugated polymer chain, long enough to be considered as infinite and “isolated” in the sense that it is without interaction with other similar chains. This cannot be obtained in vacuum so such a chain must be surrounded by a dielectric solid medium. To study the electronic properties of the chain itself, the interaction with the matrix must be minimized. This implies that the medium has no electronic state close to a similar one (neutral or ionized) of the chain and its excitation energies are much higher than those of the chain. Van der Waals-type interactions are of course always present and will manifest themselves, for instance, by corrections to transition energies due to polarization of the surrounding medium. The choice of a crystalline matrix will ensure that the chain will be in a periodic potential with constant mean value along the whole chain length. However, the coupling with matrix phonons cannot be avoided. The effect of this interaction is considered in Section 3.6.2.3.

Since we want to study an isolated chain or at least an ensemble of identical isolated chains, their concentration in the matrix must be kept low enough and this low concentration must be stable in time. It will be characterized below as a polymer content by weight  $x_p$ .

### 3.1.3

#### The Isolated Polydiacetylene Chain, Isolated in its Monomer Crystal Matrix

The chain of polydiacetylene (PDA) dispersed in its monomer diacetylene (DA) single crystal matrix, to such a high dilution that the chains are isolated, meaning

that they do not interact at all with one another, provides such a system. A short survey of PDA properties is given in Section 3.2.

This chapter is devoted to the description and discussion of our present understanding of the spectroscopic properties of such chains. In principle, the system can be modified, so as to allow the study of interchain interactions (by increasing in a controlled way the polymer concentration in the matrix) or the influence of disorder (by introducing an amount of disorder which nature and extent would be quantifiable, if not controlled *a priori*). Such possible extensions are beyond the scope of this review. PDA chains could provide this ordered reference state, thanks to their peculiar polymerization process, a topochemically controlled reaction occurring in the solid crystalline phase of the corresponding monomer, the so-called 1-4 addition [11]. A DA monomer consists of a reactive part  $-C\equiv C-C=C-$ , the  $C_4$  group, capped by substituents, the side-groups. This reaction is discussed in more details (although still in a cursory way) in Appendix A. Here we shall rather consider the reasons why DA polymerization can lead to the type of system we are looking for.

The formation of a polymer chain can be thought of as consisting of three types of reactions: an *initiation*, in which a reactive entity is formed from neutral monomers, a sequence of *propagation* steps, in which a neutral monomer is added to the reactive end of the growing chain, and *termination*, by deactivation of the reactive ends. The final result of the 1-4 addition polymerization of DA is a PDA chain consisting of alternating double, single and triple CC bonds as shown in

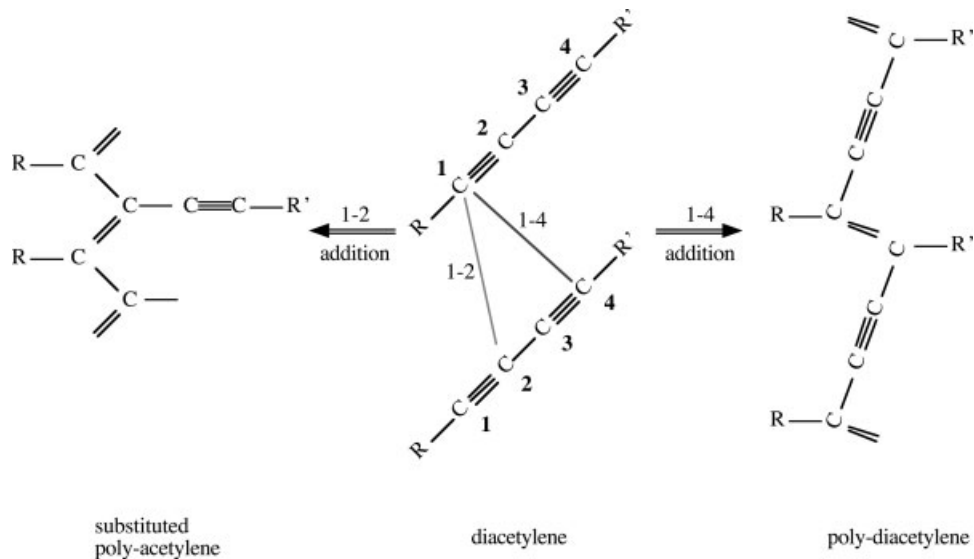
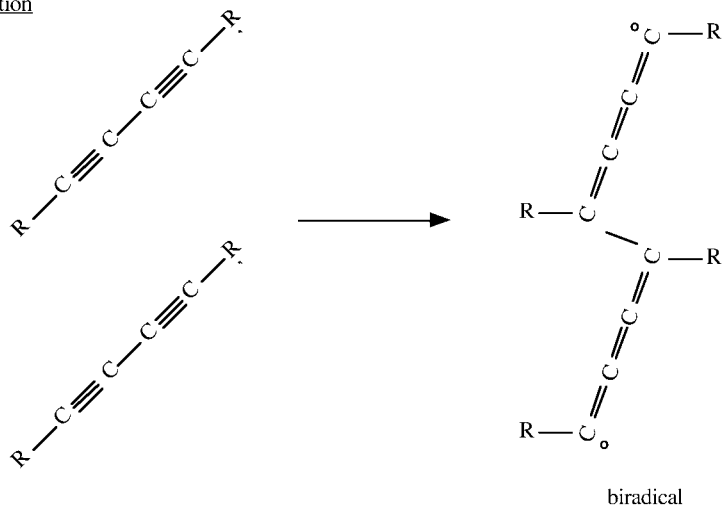


**Figure 3.1** Polymerization reactions of diacetylenes. 1-4 addition (formation of a bond between atoms 1 and 4 of successive monomers), specific to the solid state, yields the

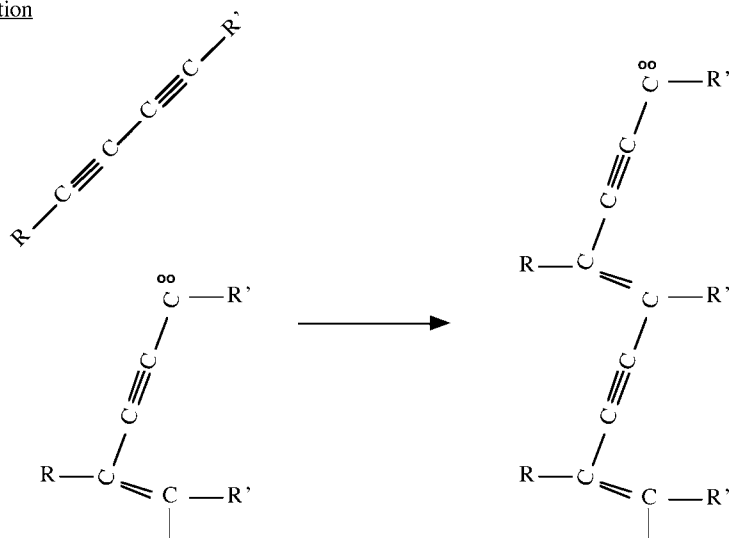
PDA polymers discussed in this chapter. In other situations, polymerization may lead to substituted polyacetylenes via 1-2 addition.

Fig. 3.1. Nontopochemical polymerization, in solution for instance, usually leads to a polyacetylene, via 1–2 addition [12], also shown in Fig. 3.1. The schemes for thermal or UV irradiation initiation and propagation are shown in Fig. 3.2. Initiation produces a biradical, but the active ends quickly transform into a carbene, at the hexamer stage [13], so propagation is essentially a carbene reaction. Obviously, the geometries of the two reactions in the solid state are very similar, so most conditions for efficient reaction will be similar for both.

a) Initiation



b) Propagation



**Figure 3.2** Reaction schemes of the solid-state formation of PDA: (a) initiation (leading to a butatrienic biradical); (b) propagation (via carbene chain ends).

No atom is added or removed in this reaction, only new bonds are formed between neighboring atoms, so the reaction is diffusionless; electrons are redistributed among C–C bonds of the resulting chain and only small atomic displacements occur.

An important point is that in all PDA crystal structures, the chain geometries are nearly identical, irrespective of the side-groups and the spectroscopic properties of all PDA crystals, in the region where the chain absorbs, fall in two well-defined classes, as discussed in Section 3.2.1. Hence it is reasonable to assume that any PDA chain is representative of its whole class.

The reaction leads to an increase in the number of the conjugated unsaturated bonds, so the energy levels move to lower energy and the absorption spectrum shifts towards the visible: PDA is a conjugated polymer absorbing in the visible whereas the  $C_4$  group, containing only two conjugated triple bonds, does not absorb light below 4.5 eV (see Fig. 3.28). This is illustrated in Fig. 3.3. In the case of 3BCMU monomer shown in Fig. 3.3, the DA absorption is dominated by the  $C_4$  group up to about 5.5 eV, where side-group absorption begins. In many other DA the side-groups contain aromatic rings the absorption of which is dominant, but still almost always confined to the UV, at much higher energy than the polymer absorption.

This property will be very useful for the study of the spectroscopic properties of an isolated PDA chain within its DA monomer crystal, since the matrix will only act as a transparent dielectric.

We are looking for generic properties of the chains, representative of the bulk PDAs, apart from the effect of chain interactions. The isolated chain geometry in the matrix should then be close to that of the chain in the bulk polymer crystal, hence the requirement that the distance  $d_m$  between two neighboring reacting DA

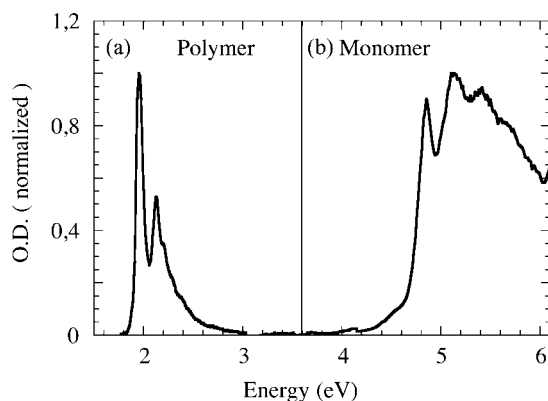


**Figure 3.3** Absorption spectra at room temperature of the DA monomer 3BCMU (b) and of the corresponding polymer (a). The two spectra are independently normalized to 1 at 5.1 and 1.92 eV, respectively (beyond

5.1 eV, the monomer absorption is saturated). In the spectral region shown, the 3BCMU monomer absorption is dominated by the  $C_4$  group (see Section 3.4.6).

molecules in the chain propagation direction in the crystal must be close to the repeat unit length  $d_p$  of the chain in its equilibrium geometry. All propagation steps are then geometrically identical, hence the successive repeat units of the chain have identical geometries. This situation permits chain propagation over long distances (see Appendix A), so that the effectively infinite chain limit is accessible. A counter example is given by the well-studied DA known as pTS or TS6, in which the difference between  $d_m$  and  $d_p$  is 6% at room temperature, so that at low polymer content the chains are very short and under high tensile strain [14].

However,  $d_m$  is never strictly equal to  $d_p$ , so some strain may accumulate in the growing chain, which in principle may enforce a periodic relaxation similar to the Frenkel–Kontorova process in thin films [15]. If the strain remains low enough, such relaxation will not occur, hence the chain will form a well-ordered one-dimensional periodic structure. Moreover, this structure will be embedded in a periodic potential of the same periodicity as the chain, owing to the surrounding dielectric crystal. Of course, if the chain is removed from the matrix, for instance by dissolution of the crystal, the perfect geometric regularity disappears and is, for entropic reasons, almost impossible to recover: cast films are highly disordered.

This process is known to produce, in the most favorable cases, macroscopic single crystals of PDA of high quality (for reviews, see Refs. [16, 17]). It occurs homogeneously within the monomer crystal, not by growth of a pure polymer phase. Hence the first few chains formed may be expected to be as good as those in a pure polymer crystal (as shown below, they may in fact be more perfect) and far enough from one another if their concentration is low enough. However, the formation of long and perfectly regular PDA chains at very small polymer content requires relatively strict structural and electronic conditions and in fact only few DA monomers do so.

The required conditions are discussed in Appendix A. They guide the proper choice of the DA monomers in which polymerization will be effected and the PDA chains will be diluted. Briefly, the main criteria for choosing the DA monomer are:

1. The isolated chain limit requires  $x_p$  close to zero; an average interchain distance of 100 nm in a random distribution of chains corresponds to  $x_p \approx 10^{-4}$ . This value must be stable in time, so thermal polymerization should not occur at room temperature.
2. Long and unstrained chains require  $d_m$  close to  $d_p = 4.9 \text{ \AA}$ .
3. The DA must form high quality macroscopic crystals.
4. One wants to be able to measure the chain length by usual methods of polymer physical chemistry, such as light scattering. Hence the corresponding PDA must be soluble in not too exotic solvents. Disordered films can be cast from such solutions.
5. Optical absorption by the side-groups should not occur in the range of PDA absorption.

To summarize, our reference ordered experimental system will consist in PDA chains diluted ( $x_p \approx 0$ ) in the corresponding DA monomer crystal. Apart from Section 3.6, which presents a study of single, individual, chains, all the experimental results presented and discussed below were obtained on ensembles of isolated chains. The crystalline character of the monomer matrix ensures that all chains in the ensemble are symmetry related and nearly identical, with nearly identical surroundings imposing on them the same periodic potential. The differences between chains are only due to unavoidable residual matrix disorder such as dislocations or elastic strain.

### 3.1.4

#### Organization of the Chapter

This chapter will be organized as follows. In Section 3.2, the properties of PDA that are important for the following presentation will be briefly presented. The topochemical polymerization reaction is further discussed in Appendix A. The chosen DA, 3BCMU and 4BCMU, are presented in Section 3.3 and the reasons for that choice will be given. Structural information on these monomer crystals is given in Appendix B. The following sections present and discuss spectroscopic studies on isolated PDA chains dispersed in their monomer crystal matrix. Section 3.4 deals with ensembles of “blue” chains. These results are fairly complete, so an extended discussion of them is given in the last part of the section. Section 3.5 deals with ensembles of “red” chains and Section 3.6 with the study of a single red chain by microphotoluminescence. It will be shown that such chains are a very high-quality organic quantum wire, with the expected properties of a quasi 1-D semiconducting system. This part of the work is still in progress. Finally, a survey of some answers obtained and some open problems are given in Section 3.7.

## 3.2

### A Short Survey of Some PDA Properties

The DA form a large family of molecules with general formula  $R-C\equiv C-C\equiv C-R'$ . The side-groups R and R' can be different or identical and may have a large variety of molecular formulae. DA are usually formed by coupling of monoacetylenic compounds such as  $R-C\equiv C-H$  or  $R'-C\equiv C-Br$ ; several general coupling methods have been developed [18, 19] and probably more than 1000 different DA have been prepared, but only some of them can be polymerized into the corresponding PDA of formula  $(=CR-C\equiv C-CR'=)_n$  as shown in Fig. 3.1.

The usual denominations of the DA mentioned in this chapter (acronyms of their complicated exact chemical denominations) and the corresponding side-group formulae are given in Table 3.1. The PDA related to a monomer M will be called poly-M.

**Table 3.1** Some usual diacetylenes: acronyms of the PDA mentioned in the text and their side-group formulas. The two side-groups are identical in all the PDA cited (for other PDA, see Refs. [16] and [17]).

Acronym	Side-group formula
3BCMU	$-(\text{CH}_2)_3-\text{OCONH}-\text{CH}_2-\text{COOC}_4\text{H}_9$
4BCMU	$-(\text{CH}_2)_4-\text{OCONH}-\text{CH}_2-\text{COOC}_4\text{H}_9$
DCH (or DCHD)	$-\text{CH}_2-\text{carbazole}$
ETCD (or 4U-2)	$-(\text{CH}_2)_4-\text{OCONH}-\text{CH}_2-\text{C}_2\text{H}_5$
PTS (or TS6 or TSHD)	$-\text{CH}_2-\text{OSO}_2-\text{C}_6\text{H}_4-\text{CH}_3$
pFBS	$-\text{CH}_2-\text{OSO}_2-\text{C}_6\text{H}_4-\text{F}$
TCDU	$-(\text{CH}_2)_4-\text{OCONH}-\text{C}_6\text{H}_5$

### 3.2.1

#### Possible Electronic Structures of a PDA chain

##### 3.2.1.1 The Colors of PDA

As shown in Fig. 3.1, the polymerization reaction generates a long string of conjugated alternating double and triple CC bonds. Such an extended conjugated system has low-lying excited states with large transition dipole moments from the ground state: PDA solids are deeply colored. In contrast, monomer crystals are usually colorless, their UV absorption being in general determined by the side-groups.

The absorption threshold of PDA varies widely, with the first maximum at wavelengths  $\lambda_{\text{max}}$  between 650 and 520 nm at room temperature, but the  $\lambda_{\text{max}}$  values mostly cluster around 620–630 and 540 nm. So, one conventionally considers two types of PDA crystals, corresponding to two different electronic structures, so-called “blue” and “red”. This terminology is now well established and we shall use it, but it is somewhat confusing: “blue” crystals absorb in the red (630 nm) but much less in the blue and “red” crystals absorb in the green and are transparent in the red; so, at small  $x_p$  a “blue” crystal appears blue in transmission or diffuse reflection and a “red” one appears red. Typical absorption spectra in the visible are shown in Fig. 3.4.

Figure 3.4 also shows a “yellow” spectrum peaking at 480 nm, corresponding to the absorption of soluble isolated PDA chains in a good solvent. They are semi-rigid coils, so-called wormlike chains, with a rather long persistence length of 16 nm [20]. In this disordered state, geometric distortions and fluctuations of the chain backbone localize the excitation over lengths much shorter than the chain length, hence the blue-shifted absorption. The overall absorption band is then the sum of many absorptions corresponding to different localization lengths, the shorter ones absorbing at shorter wavelengths; this is confirmed by resonance

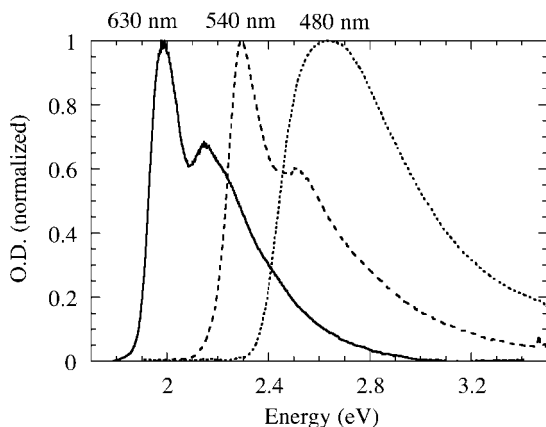


**Figure 3.4** Typical room-temperature absorption spectra of PDA. Solid line: a 4BCMU crystal containing a small concentration of poly-4B blue chains. Dashed line: a red gel of poly-4B in toluene at a concentration of ~1%.

Dotted line: a yellow solution of poly-4B in chloroform. Spectra are normalized at the wavelength of maximum absorption indicated at the top of the figure.

Raman scattering, since the observed Raman frequencies become larger as the excitation wavelength is swept through the absorption band towards shorter wavelengths [21]. This effect is universal in conjugated polymers [22], which are always disordered in the solid state. This is not the case of the blue and red PDA crystals, in which the Raman frequencies are independent of the excitation wavelength, so there is no distribution of conjugation lengths, hence no localization by static disorder, in crystalline PDA (this may not be true in amorphous films).

This red/blue dichotomy is not limited to bulk PDA crystals, it is also observed in cast films, gels, LB films and generally in all bulk PDA phases. As we shall see, isolated chains dispersed in their monomer matrix also can be blue (Section 3.4) or red (Sections 3.5 and 3.6).

The dichotomy is not strict, however, and cases are found of PDA with  $\lambda_{\max}$  anywhere between 540 and 620 nm or at longer or shorter wavelengths. This is particularly true of partially polymerized crystals at low  $x_p$ . Very short oligomeric chains may explain this in some cases. But at low  $x_p$  the distance  $d$  in the mixed crystal is close to  $d_m$  so the chains are strained, either in tension ( $d_m > d_p$ ) or in compression ( $d_m < d_p$ ). The effect of such strain on transition energies has been studied by applying a tension to a pTS single crystal whisker [23], showing that the transition energy increases linearly with strain at a rate 37 meV per % strain. Another way of applying a variable strain on an isolated chain is to vary the temperature, since  $d_m$  will decrease with  $T$  while  $d_p$  stays approximately constant [24]; for instance, in the octadienediol (ODD) crystal, the isolated chain  $\lambda_{\max}$  increases from 548 to 621 nm as  $T$  decreases from 300 to 10 K [25]. The case of 4BCMU, corresponding to compression, is discussed in Section 3.4.2.

A better criterion for identifying red and blue chains seems to be the values of the ground-state vibrational frequencies, as accurately determined by resonance

Raman scattering (RRS) [26] even at very low  $x_p$ . The most useful normal mode corresponds essentially to the double bond stretch (D mode). In all blue (red) PDA, D is at about  $1450 \pm 10$  ( $1510 \pm 10$ )  $\text{cm}^{-1}$ . The difference in frequencies is much larger than the strain-induced shifts in the blue phase (no data are available for the red phase) [27]. Hence these frequencies are sensitive tests of the nature of the chain ground state, red or blue; for instance, in the case of ODD, the Raman frequencies leave no doubt that the chains dispersed in the monomer crystal are “blue” despite their short  $\lambda_{\text{max}}$  at room temperature.

### 3.2.1.2 Ground-State Conformational Differences

RRS shows that the conjugation is the same all along the chain, since there is a single vibrational frequency for each normal mode, not a distribution as in solution, so the difference in  $\lambda_{\text{max}}$  must correspond to different ground-state conformations.

Early on in the study of PDA, the red/blue dichotomy was associated with two different ways of distributing the  $\pi$  electrons among the CC bonds, namely the so-called “enyne” and “butatriene” structures shown in Fig. 3.5, the enyne being associated with the blue spectrum and the butatriene with the red spectrum.

This is now known to be incorrect; the bond length alternation pattern is the same for all chains and is the one expected for the enyne. Moreover, theoretical calculations do not show even a local ground-state energy minimum at the expected butatriene geometry [28].

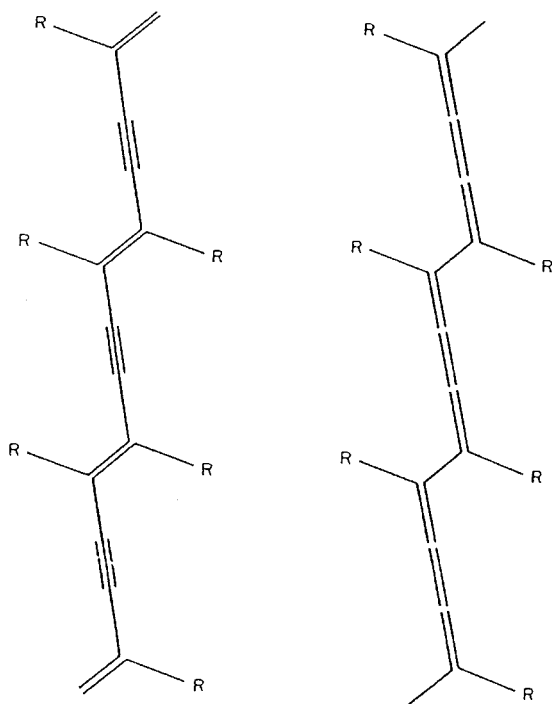


**Figure 3.5** Enyne (left) and butatrienic (right) structures of the polydiacetylene chain (from Ref. [17], where bond lengths of model compounds can be found).

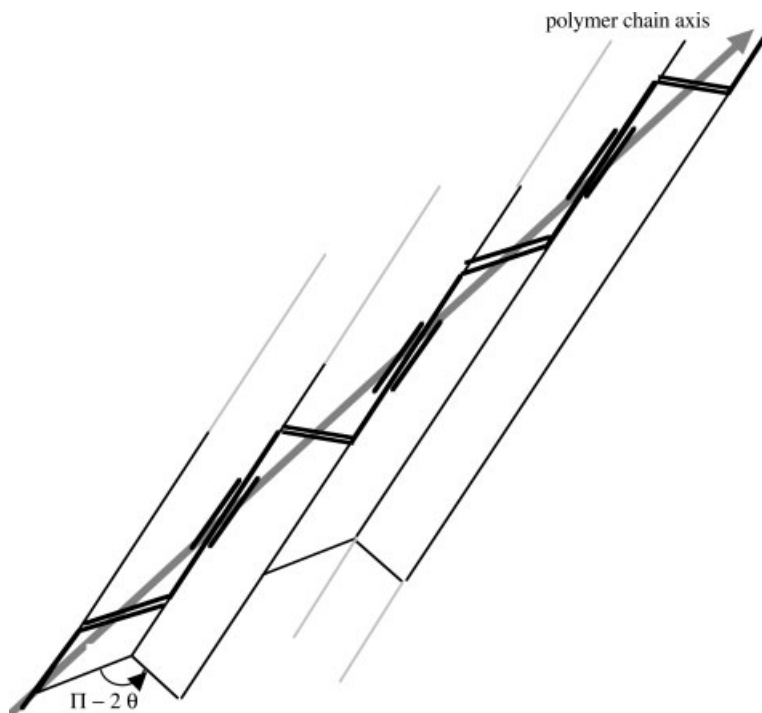


**Figure 3.6** Scheme of the proposed red chain structure. Successive repeat units are alternatively tilted by an angle  $\pm\theta$  relative to the average plane. The gray line indicates the polymer chain axis.

The structural difference is therefore small and still not definitely established. The best crystallographic study of a red PDA crystal [29] fails to show any significant difference in chain geometries. A model for red chains shown in Fig. 3.6 has been proposed.

It is assumed that in the red chain successive repeat units are tilted by an angle  $\theta$  alternatively above and below the main plane, whereas the blue chain is known to be planar [16, 17]. Therefore, the unit cell contains one repeat unit in blue chains and two in red chains. This model is supported by solid-state  $^{13}\text{C}$  NMR experiments on another PDA, poly-ETCD, which has the same  $(\text{CH}_2)_4$  spacer between chain and H-bonds as in 3BCMU and 4BCMU (see Fig. 3.9) and which exists in both the red and blue phases [30]; they confirm that the red chain has the same overall structure as the blue chain, but with slightly different chemical shifts, which are probably accounted for by slightly different ground-state electronic structures. This model is in fact compatible with present crystallographic results: the cell doubling produces weak satellites, which would probably pass unnoticed unless specifically looked for; and the chain C atoms would occupy two positions above and below the main plane with half occupancy probability. If not

explicitly introduced in the refinements, this would be mimicked by an elongated thermal motion perpendicular to the average chain plane.

Simple quantum chemical considerations show that the excited-state energy increases with  $\theta$  and reach the experimental red chain value for  $\theta \approx 20\text{--}30^\circ$ ; the gap increases and the widths of the bands decrease as coupling between successive monomers decreases [31].

All red chains have approximately the same transition energy, hence they should all have approximately the same  $\theta$  angle, so there must be a minimum of the total energy at  $\theta \approx 20\text{--}30^\circ$ . This minimum is not provided by the electronic energy of the conjugated chain, which varies monotonically with  $\theta$ , therefore it must correspond to a particular side-group geometry which, in some PDA but not all, leads to an overall energy minimum for the red conformation. Here again  $^{13}\text{C}$  NMR results [30] are useful. They indicate that the  $(\text{CH}_2)_4$  spacer has different well defined conformations in the two phases, both well known in alkane chains [32].

### 3.2.1.3 Color Transitions

Poly-ETCD is just one example of a bulk PDA showing a reversible first-order transition between a low- $T$  blue phase and a high- $T$  red phase (see, for instance, Refs. [33, 34]). Irreversible transitions are also known, for instance in single-crystal thin films of poly-4BCMU. Such transitions have been much studied in LB films or membranes, where they have been considered for applications in biological or chemical sensors, with optical detection [35]. The transition can also be triggered by light. The photoinduced transition is sometimes permanent, sometimes reversible and seems to require the generation of charge carriers on the chain [36]. This interesting topic is outside the scope of this chapter.

## 3.2.2

### Spectroscopy of Bulk PDA Crystals

Only a few PDA crystals have been well studied and about ten others less thoroughly, but this is enough to establish that all PDA share most of their spectroscopic properties. There is much more information on blue PDA, since they are more common and form better crystals than the red ones (less ordered condensed phases such as cast films or gels have very similar properties, but will not be discussed here). These standard properties will be briefly recalled, to allow easy comparison with those of the isolated chains, so that the generic character of the latter can be evaluated.

Since all known PDA structures are centrosymmetric, the electronic or vibrational states must have either  $u$  or  $g$  symmetry, that is, be either allowed or forbidden in one-photon absorption (or emission) with the reverse selection rule in two-photon absorption.

### 3.2.2.1 Reflection and Absorption

All PDA crystals show a very intense absorption in the visible, strongly polarized parallel to the chain direction, so one usually measures the reflection spectrum, from which in some cases the absorption was obtained by Kramers–Kronig transformation [37], although a few spectra of extremely thin single crystals [38] and diffuse reflection spectra of dispersed powders [39] have been published. Room-temperature spectra are broad, but there is some narrowing on cooling. Typical spectra of blue and red PDA at low  $T$  ( $\sim 10$  K) are shown in Fig. 3.7 for light polarized parallel to the chain direction.

The blue PDA spectrum consists of a strong origin (zero-phonon) band at about 1.86 eV for poly-DCH (the exact value varies somewhat for different PDA between 1.86 and 2 eV) and several well-resolved vibronic replicas. The maximum absorption coefficient is of the order of  $10^6$  cm $^{-1}$  and the overall oscillator strength is  $\sim 1$ . The absorption near 3.6–3.8 eV is due to the carbazole side-groups of DCH. In the red PDA poly-TCDU the zero-phonon band is at 2.3 eV, again with weaker, but much less well-resolved, vibronic satellites. Although the overall shapes of the two exciton absorption spectra are similar, the red spectrum is less well resolved, possibly because of poor crystal quality. Absorption spectra for light polarized perpendicular to the chains cannot be obtained in the same way, since the corresponding reflectivity changes are too small, but is measurable directly on a sufficiently thin single crystal; such crystals can be obtained for instance by limiting the polymerization to a thin surface region (less than 1  $\mu$ m) using low-energy electrons irradiation [40]. Spectra thus obtained are almost identical with those calculated from the reflectivity for the parallel polarization. The dichroic ratio is large, of the order of  $10^2$ .

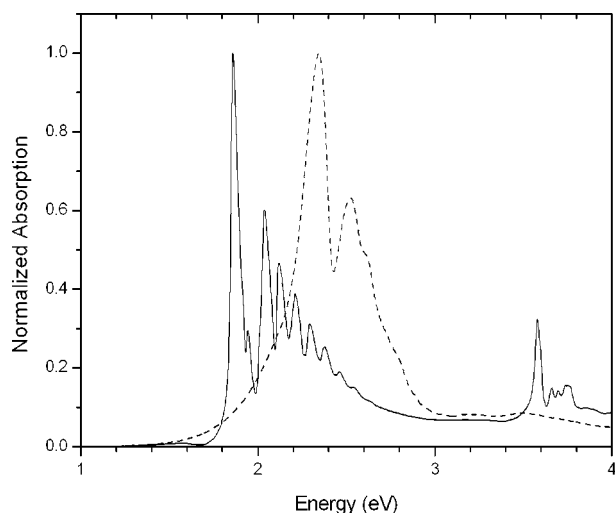


**Figure 3.7** Absorption spectra of blue and red PDA crystals calculated from experimental reflection spectra by Kramers–Kronig inversion. Solid line: blue poly-DCH. Dashed line: red poly-TCDU. Courtesy G. Weiser.

### 3.2.2.2 Electroreflectance

These spectra are entirely explained by a single excitonic transition, the corresponding band to band transition is not visible there, nor is any other excitonic transition. Hence the usefulness of electroreflectance, since an electric field may

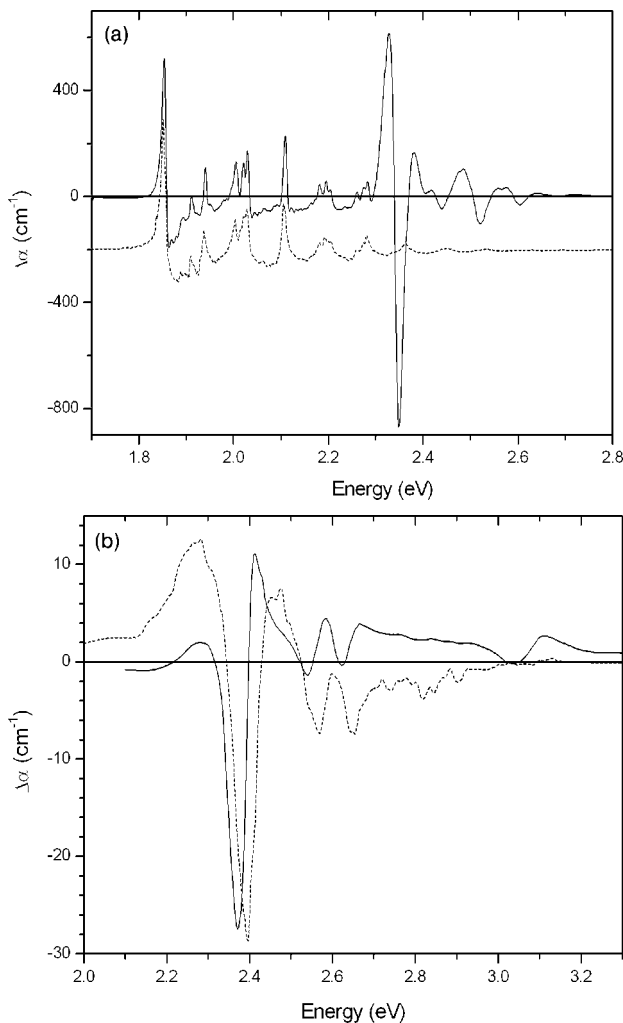


**Figure 3.8** Electroabsorption spectra (solid lines) of blue and red PDA crystals calculated from experimental electroreflectance (EA) spectra by Kramers–Kronig inversion. Dashed lines are first derivatives of the absorption spectra shown in Fig. 3.7, displaced vertically for clarity. Courtesy G. Weiser. (a) Blue poly-DCH. Below 2.3 eV, the EA spectrum is identical with the first

derivative of the absorption. Above 2.3 eV, a very strong EA signal appears, which does not correspond to any feature in absorption. (b) Red poly-TCDU. The EA spectrum is similar to, although not identical with, the first derivative of the absorption. The high-energy signal prominent in (a) is not present here; only a weak undulation near 3 eV is observed.

strongly modulate the absorption at the band edge (Franz–Keldysh effect; see, for instance, Ref. [41]). Again, electroabsorption spectra are derived from reflectivity data by Kramers–Kronig inversion [37], leading to spectra as shown in Fig. 3.8.

The lower energy part of these spectra, below 2.3 eV for blue PDA and below 2.8 eV for red TCDU, is almost identical with the first derivative of the absorption spectra shown in Fig. 3.7; this corresponds to a Stark shift of the excitonic transition, with at most a very small change of its oscillator strength. The large electric field modulation corresponds to a highly polarizable exciton, about  $7000 \text{ \AA}^3$ , in blue PDA, from which an exciton radius of about 10–12 Å can be estimated [37]. There are only two values available for red PDA,  $\sim 4300 \text{ \AA}$  for a bulk PDA [42] and  $\sim 6000 \text{ \AA}$  for a thin film [43]. They are comparable to those for blue PDA, perhaps slightly smaller.

The large oscillations above 2.2 eV in the poly-DCH spectrum are due to a very strong Franz–Keldysh (FK) effect. They yield a very accurate determination of the exciton binding energy  $E_b = 0.475 \text{ eV}$ ; the reduced carrier effective mass is about 0.1 and the coherence length of the carriers is large, tens of nanometers. In other blue PDA, the oscillations are much less resolved, but similar values of the parameters can be inferred, in particular  $E_b \approx 0.52 \pm 0.05 \text{ eV}$ . The FK signal is very sensitive to the carriers coherence length (which determines their acceleration in the applied electric field). Even a small amount of disorder, particularly in a quasi-1-D system, strongly reduces the electroabsorption. Apparently poly-DCH is exceptional among bulk PDA, for an unknown reason.

There is nothing similar to FK oscillations in the red crystal spectrum. A small feature is seen near 3 eV in red TCDU, consisting of a negative band followed by a positive band at higher energy, without correspondence in the derivative of the absorption. Since it is known that red TCDU crystals are far from perfect, this feature is assigned to the band to band transition, leading to a red exciton binding energy of about 0.6 eV [42], but it has also been interpreted as corresponding to an  $A_g$  state [44]. A similar feature is also observed in thin red poly-4BCMU crystalline films, which are also imperfect [45].

### 3.2.2.3 Fluorescence

The transition from the  $B_u$  exciton level to the ground state is strongly allowed: the radiative lifetime, based on the measured oscillator strength, should be at most a few nanoseconds. Yet, fluorescence from PDA crystals is said to be almost absent in blue phases (quantum yield  $\eta < 10^{-5}$  [46]) and weak in red phases (yields from  $10^{-4}$  to  $>10^{-2}$  [47] are quoted). These low values, and the results of picosecond time-resolved experiments which reveal that the ground state is recovered in about 2 ps, have been explained in the past by instantaneous self-trapping of the  $B_u$  exciton, according to the theory by Rashba [48] and Toyozawa [49], followed by rapid internal conversion to the ground state through crossing of the potential energy surfaces [50]. As will be shown in Sections 3.4 and 3.5, this explanation now seems unlikely and the very weak fluorescence of blue phases should rather be associated to the presence in the optical gap of “dark”  $A_g$  excited states, as in polyenes [51].

### 3.2.2.4 Two-Photon Absorption

Transitions between the  $A_g$  ground state and  $A_g$  excited states may be allowed in two-photon absorption. Several such  $A_g$  states have been located in that way in PDA crystals. In blue PDA there is at least one  $A_g$  state slightly below the  $B_u$  exciton level, possibly two [52], explaining the very weak fluorescence. There is also a state, often called  $mA_g$  in the literature, approximately 0.4 eV above the  $B_u$  exciton, which plays an important part in the nonlinear optical properties of both blue and red PDA [53, 54]; such a state is found in fact in almost all conjugated polymers. Red crystals have been less studied and some experiments do not find any  $A_g$  singlet state below the  $B_u$  one [55], whereas some others do in a (strongly disordered) cast film [56]. This question will be considered again in Section 3.5.4.4.

## 3.3

### The Chosen DA

#### 3.3.1

#### The Materials and How They Fulfill the Criteria

The monomers chosen for this study were 3BCMU and 4BCMU, which will be abbreviated as 3B and 4B. They were prepared for the first time by Patel [57]. Their molecular formulae are given in Table 3.1. A schematic view of the molecular structure of a poly-3B chain is shown in Fig. 3.9.

The  $-\text{CO}-\text{NH}-$  parts of their side-groups can form intermolecular H-bonds which may have several useful consequences: ensuring an intermonomer distance close to 4.9 Å, favorable to the growth of nearly unstrained chains; forming 1-D linear H-bond strings, ensuring that there will be a single propagation direction; increasing the activation energy for thermal initiation hence suppressing room temperature thermal polymerization. The  $-(\text{CH}_2)_n-$  and terminal butyl segments favor solubility of the corresponding PDA.

These monomers meet the requirements for obtaining long highly regular and isolated chains of the corresponding PDA in their single crystal matrix:

1. *Absence of thermal reactivity:* Both DA are thermally unreactive at room temperature. Close to its melting-point ( $T_m = 345$  K), 4B shows limited reactivity, but the maximum polymer content that can be produced is about 0.3%, probably owing to the presence of defects where the activation energy is decreased compared with its bulk value.
2. *Controlled radiation-induced polymerization:* As detailed in Appendix B, the structural conditions for efficient propagation under irradiation are fulfilled. Both DA polymerize readily under UV, X or  $\gamma$ -ray irradiation above  $\sim 200$  K. At lower  $T$ , long-lived “precursor” states are formed, but chain propagation does not occur. Thus, low- $T$  crystal structures can be obtained by conventional X-ray diffraction, whereas for room

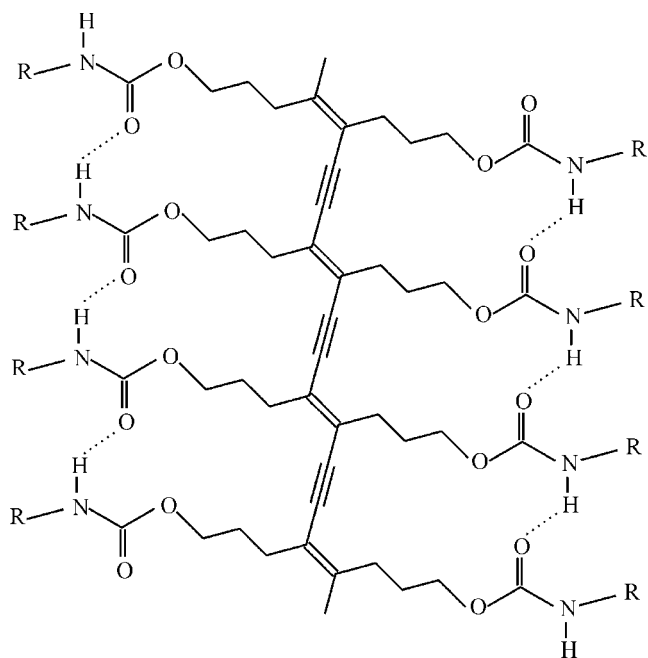


**Figure 3.9** Molecular structure of poly-3BCMUs. The conjugated chain is at the center of a ribbon, with two lines of H-bonds between CONH parts of the side-groups running parallel to it. R stands for the outer part of the side-groups:  $-\text{CH}_2\text{COOC}_4\text{H}_9$ .

The molecule as a whole is not planar in the crystal, but the chain and the H-bond lines still are parallel and in the same plane.

The 4BCMUs molecule has four  $\text{CH}_2$  units between the chain and the O atom, instead of three.

*T* studies neutron diffraction must be used. It is therefore possible to prepare crystals with a stable concentration  $x_p \leq 10^{-4}$  and to increase the polymer content at will in a controlled way. The visible absorption spectra have been calibrated [58], allowing accurate and easy determination of  $x_p$  in any crystal (see Section 3.4.1.1).

- Long chains and solubility:** Poly-3B and poly-4B are soluble in common organic solvents yielding “yellow” solutions, allowing the determination of molecular weights and internal chain structure. A previous measurement by size-exclusion chromatography yielded  $M_w = 2.6 \times 10^6$  for poly-4B chains formed at  $x_p < 0.1$  [58], a factor of two larger than earlier values for chains from much more polymerized crystals (see, for instance, Ref. [20]). However, recent light scattering measurements for chains formed at  $x_p < 0.03$  have given even much higher values of  $M_w$  for both poly-3B and poly-4B, up to  $2 \times 10^7$  and  $1.5 \times 10^7$ , respectively [59]; care was taken in these measurements to avoid chain scission, which appar-

ently affected previous studies, since the chains are so long: up to about  $20\ \mu\text{m}$  or  $4 \times 10^4$  monomer units. Hence it is clear that as far as electronic properties are concerned such chains are effectively infinite. These chains form in solution semi-rigid coils (“wormlike chains”) with a persistence length of  $\sim 16\ \text{nm}$  at room temperature. It was shown that the rigid segment of these chains is the  $C_4$  group itself [20], so that torsion occurs between each successive monomer; the measured persistence length corresponds to an average torsion angle of slightly more than  $10^\circ$ . The accumulation of such torsions with variable and fluctuating angles is the cause of electronic localization on these chains in solution, hence the spectral blue shift and the large inhomogeneously broadened width of the absorption band corresponds to the distribution of torsion angles that are possible. Therefore, yellow PDA chains are in some sense a reference disordered state, the average disorder being determined by a single parameter, the persistence length. The local conformations of the chains in solution and in the crystal are very similar: the repeat unit length is the same [20] and the bond lengths are the same as in the crystal [60].

4. *Existence of both blue and red chains:* Bulk solid phases of poly-3B and poly-4B exist in both blue and red configurations. In 3B, bulk crystals cannot be polymerized beyond  $x_p \approx 0.6$ , but the monomer–polymer mixed crystals are all blue and single-crystal films are also blue. In poly-4B, bulk crystals are blue and single-crystal films can be blue or red. Phases prepared from solution, i.e. cast films or gels, are red for poly-4B and predominantly blue for poly-3B. Poly-4B melts at  $\sim 110\ ^\circ\text{C}$  to a probably nematic red phase, which yields a red solid on cooling [61]. The equilibrium form therefore seems to be the blue one for poly-3B and the red one for poly-4B. As we shall see, isolated chains in 4B are blue, whereas they can be either blue or red in 3B.
5. *Favorable spectral properties:* The absorption spectra at low  $x_p$  are very dichroic; the transition moment practically coincides with the chain axis (see Section 3.4.1). This allows easy optical determination of the chain direction and orientation of the crystals, even at  $x_p \approx 10^{-5}$ .

The side-groups contain no  $\pi$  electron, so the lowest energy optical transition in the pure monomer belongs to the  $C_4$  group, at  $272\ \text{nm}$  ( $4.56\ \text{eV}$ ) at room temperature (see Section 3.4.6 and Fig. 3.28). Hence the chosen DA have the further advantage of providing the widest possible range for the study of the optical properties of the isolated chains without interference from matrix absorption. More-

over, some exchange interaction has been suspected in other DA between the chain and conjugated rings belonging to the side-groups, separated from the chain by a single  $\text{CH}_2$ , for instance carbazole in DCH, somewhat influencing the chains electronic properties. Any such interaction is absent in 3B and 4B.

### 3.3.2

#### The Samples

In this work, single crystals of 3B and 4B monomers containing less than  $x_p = 10^{-3}$  were studied, except for the high-energy exciton (Section 3.4.6) and the measurement of molecular weight (see above), where values up to 0.07 and 0.03, respectively, were used.

These crystals were grown from solutions in acetone or methyl isobutyl ketone at 4 °C in the dark, by slow evaporation of the solvent. The as-grown crystals were very slightly colored, owing to the formation of a very small amount of polymer during crystal growth, presumably due to cosmic radiation. They were subsequently kept at 260 K in the dark. Samples were indefinitely stable, the polymer content increasing only very slowly with time.

Crystals were typically 30–500  $\mu\text{m}$  thick with an area of 0.2–1  $\text{cm}^2$ . The chain direction was parallel to the well-developed face, which was the plane of a lamella (see Appendix B). These platelets had very uniform thickness and good surface quality, as shown by the observation of well-developed interference fringes throughout the visible and UV, corresponding to the total thickness of the platelet. AFM images showed large atomically flat regions, several micrometers in size and steps having a height of 2.7 nm or multiples of that value: this is the thickness of a lamella.

## 3.4

### Spectroscopy of Isolated Blue Chains

#### 3.4.1

##### Visible Absorption Spectra

##### 3.4.1.1 Room-Temperature Absorption and Determination of the Polymer Content $x_p$

A typical absorption spectrum at room temperature of a 3B crystal with low polymer content ( $x_p < 10^{-3}$ ) is shown in Fig. 3.10.

The direction of the chains in the crystal is known from the crystal structure (cf. Appendix B) and the recorded absorption is maximum with light polarized parallel to that direction (hereafter called “parallel polarization”). This spectrum is dominated by a band peaking at 1.95 eV with a width of  $\sim 50$  meV (FWHM). Smaller vibronic absorption bands are seen at higher energy. The spectrum shape is independent of  $x_p$  up to at least  $x_p \approx 0.05$ . 4B crystals give very similar spectra, but the peaks are slightly broader (see Fig. 3.12b).

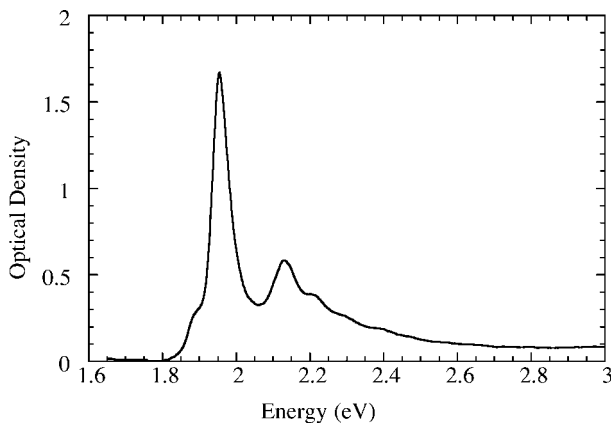


**Figure 3.10** Absorption spectrum of isolated poly-3B chains in a 69- $\mu\text{m}$  thick 3BCMU monomer crystal at 300 K with  $x_p \approx 5.5 \times 10^{-4}$ .

The absorption is so highly dichroic that spectra polarized parallel and perpendicular to the chain direction cannot be obtained accurately on the same sample. Upon increasing the polymer content, spectra in the // polarization quickly become saturated but absorption in the  $\perp$  polarization becomes high enough to be studied. No difference in the absorption spectrum shape is observed whatever the polarization; in particular, the wavelengths of maximum absorption  $\lambda_{\text{max}}$  are the same in both polarizations within experimental uncertainty.

#### Determination of polymer content using the absorption spectrum

These room temperature absorption spectra give a nondestructive spectroscopic method of determining the exact polymer content by weight  $x_p$  in a given crystal, as follows [58]. From yellow chloroform solutions containing a known concentration of either poly-3B or poly-4B, the absorption coefficients  $a_{\text{max}}$  at  $\lambda_{\text{max}}$  can be derived:

$$\begin{aligned} \text{for poly-3B at } \lambda_{\text{max}} = 482 \text{ nm, } E_{\text{max}} = 2.57 \text{ eV: } & a_{\text{max}} = (43 \pm 2) \times 10^3 \text{ L mol}^{-1} \text{ cm}^{-1}; \\ \text{for poly-4B at } \lambda_{\text{max}} = 470 \text{ nm, } E_{\text{max}} = 2.64 \text{ eV: } & a_{\text{max}} = (42 \pm 2) \times 10^3 \text{ L mol}^{-1} \text{ cm}^{-1}. \end{aligned}$$

Once these values of  $a_{\text{max}}$  for solutions are known, the exact polymer contents in a series of crystals were deduced from the optical densities of the corresponding chloroform solutions and the total crystal weight. The correspondence between the absorbance in the solid state (given by the room temperature absorptions) and  $x_p$  is then obtained in the whole  $x_p$  range where the spectrum shape, in // or  $\perp$  polarization, does not change. One can extrapolate to  $x_p = 1$ , that is to a hypothetical fully polymerized crystal in which the chains would have kept the optical properties of the isolated chains. Absolute maximum absorption coefficients of polymer chains in the solid state are then derived and can be used to determine non-destructively  $x_p$  in any crystal:

$$\begin{aligned} \text{for poly-3B at 635 nm or 1.95 eV: } & \alpha_{\parallel} = (1.0 \pm 0.2) \times 10^6 \text{ cm}^{-1}, \\ & \alpha_{\perp} = (1.6 \pm 0.4) \times 10^3 \text{ cm}^{-1}; \\ \text{for poly-4B at 626 nm or 1.98 eV: } & \alpha_{\parallel} = (7.4 \pm 1.8) \times 10^5 \text{ cm}^{-1}, \\ & \alpha_{\perp} = (2.0 \pm 0.3) \times 10^3 \text{ cm}^{-1}. \end{aligned}$$

The dichroic ratios derived from these values are 650 and 350 for the poly-3B and poly-4B, chains respectively. In fact, the transition dipole moments should lie in the chain plane, whereas one measures their component parallel to the surface, so the true value of  $\alpha_{\perp}$  is larger and the real dichroism smaller than the values above. From the crystal structures (Appendix B), the correction is by about a factor of two.

This is an intense transition and by integration of the zero-phonon absorption line an oscillator strength of the order of 0.5 is found.

### 3.4.1.2 Low-Temperature Absorption Spectra

All the experimental work described in this chapter originated from the observation that isolated 3B and 4B chains dispersed in their single-crystal monomer matrix at very low  $x_p$  have well-resolved low-temperature absorption spectra, with absorption bands much narrower than in the corresponding bulk PDA and in conjugated polymers generally [62, 63].

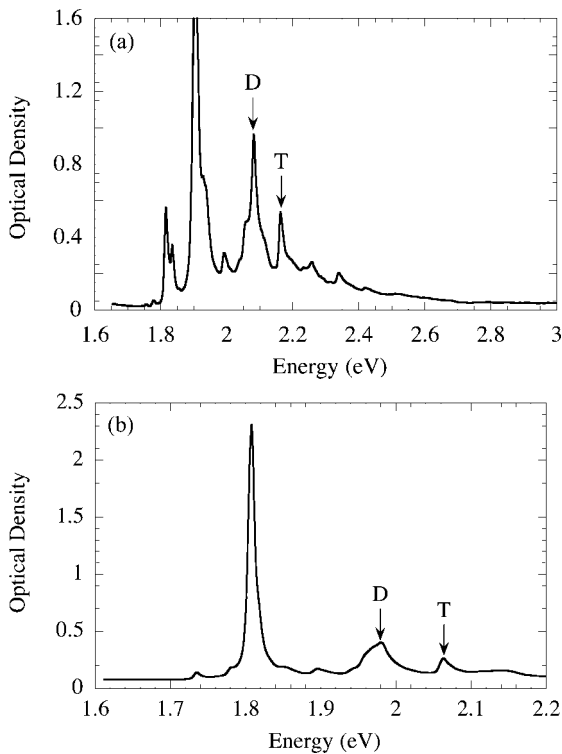
All experiments in this section were performed on such highly dilute chains, with light polarized // to the chain direction, except where mentioned otherwise, in particular in Sections 3.4.2.5 and 3.4.6.

Figure 3.11 shows these spectra at 15 K for poly-3B and poly-4B isolated chains. The main absorption line peaks at  $E_0 = 1.901$  eV (652 nm) for the poly-3B chains with a FWHM  $\approx 8$  meV and at  $E_0 = 1.808$  eV (686 nm) for 4B with a FWHM  $\approx 9$  meV; we are therefore dealing here with “blue” PDA chains. The area of this line is approximately the same at 300 K and at low temperature. This allows us to estimate the absorption coefficients at low  $T$  from the room  $T$  values and the respective widths. For poly-3B chains  $\alpha_{\parallel}$  (10 K) =  $(6 \pm 1) \times 10^7 \text{ cm}^{-1}$  and for poly-4B  $\alpha_{\parallel}$  (10 K) =  $(7.5 \pm 2) \times 10^7 \text{ cm}^{-1}$ .

Most published absorption spectra of other conjugated polymers were recorded at room temperature, but it is generally stated that only a modest narrowing (if any) occurs upon cooling. Isolated PDA chains in their single-crystal monomer matrix are therefore a unique system and offer the opportunity of much more accurate spectroscopic work.

The overall spectrum contains much weaker vibronic replicas of that main line. Thus the Franck–Condon factor of the transition is large, suggesting that the equilibrium geometry of the corresponding excited state is very close to that of the ground state. The observed vibrational frequencies are slightly lower than and very close to those of the corresponding ground state, measured on the same samples by resonance Raman spectroscopy (RRS).

Therefore, excited and ground states have very similar potential curves. The two main vibronic lines correspond to the double and triple bond stretching frequen-



**Figure 3.11** Low-temperature absorption spectra of blue chains. (a) Poly-3B in 3B.  $T = 15$  K. Same crystal as in Fig. 3.10. The four weak and narrow lines on the low-energy side of the most intense (zero-phonon) exciton absorption peak at 1.90 eV correspond to

minority chain populations discussed in Appendix C. (b) Poly-4B in 4B.  $T = 17$  K. The 103- $\mu\text{m}$  thick crystal contained  $x_p \approx 8 \times 10^{-4}$ . Note again two weak lines below the 1.81-eV absorption peak.

cies [26], labeled D and T, respectively, in Fig. 3.11. Further, the RRS frequencies are close to those measured on the corresponding bulk PDAs, confirming the blue character of the chains.

Absorption spectra were recorded in the  $\perp$  polarization on slightly more polymerized samples,  $x_p \approx (1-7) \times 10^{-3}$ . Their shape is identical with those of the  $//$  spectra shown in Fig. 3.11 and the dichroic ratio is the same as at room temperature. The very high dichroism shows that all transition moments are almost strictly parallel and oriented along the chain direction

This absorption system is the only one observed in the whole spectrum up to 4 eV, where another one appears (see Section 3.4.6). Several other electronic states are theoretically predicted for PDA in this spectral range, but they are of  $g$  symmetry if the material has a center of symmetry. This is the case for both 3B and 4B monomer crystals and also poly-4BCMU (3BCMU does not polymerize completely). It seems reasonable to assume that isolated chains also have a center of symmetry, so their states are of  $g$  or  $u$  symmetry: the level seen in absorption near 2 eV

is then the first  $B_u$  excited state labeled  $1^1B_u$ . This symmetry will be assumed throughout this review and it will be seen that it agrees with all observations to-date on isolated chains in 3B and 4B monomer crystals.

Note that in both materials several well-resolved weak lines are observed on the low-energy side of the main absorption line. It has been established that these lines correspond to electronic transitions of different blue chain populations at lower concentration. Experimental results concerning these populations are summarized in Appendix C. Since there is no interaction between these chains and the majority population of chains and since no new physical properties appear in these populations, the results pertaining to these lines will not be discussed in the main text of this review.

### 3.4.1.3 Temperature Dependence

The zero-phonon line energy  $E_0$  and width  $\Gamma_0$  have been studied as a function of temperature for both materials. The results for both types of chains between 5 and 325 K are compared in Fig. 3.12.

$E_0$  and  $\Gamma_0$  both steadily increase with  $T$ . More or less marked discontinuities appear at 227 and 319 K in poly-4B and near 160 K in poly-3B, at the temperatures of first-order transitions of the monomer crystals (Appendix B). Similar discontinuities are also observed at the same temperatures in D and T ground-state vibrational frequencies measured by RRS. Thus, both the ground-state geometry and the electronic transition energies are slightly affected by the monomer crystal phase transitions. This effect is probably both geometric (the unit cell parameters and the molecular packing change slightly, thus affecting the chain ground-state geometry) and electrostatic (the unit cell volume changes, hence the matrix polarizability and dielectric constant, thus affecting the van der Waals interactions).

The temperature dependences in the two materials are similar at low  $T$ . The  $\Gamma_0$  values are almost equal up to 200 K; and the  $E_0$  values, although they differ by  $\sim 0.1$  eV, have similar increases up to  $\sim 150$  K. At higher temperature,  $E_0$  and  $\Gamma_0$  continue to increase slowly in poly-3B, but much faster in poly-4B; therefore, at the monomer melting-point  $E_0 = 2.1$  eV and  $\Gamma_0 = 160$  meV, more than three times the poly-3B value.

These differences can be attributed to the structural differences of the monomers. In 4B, the chains are under quasi uniaxial compression (see Appendix B) and the strain decreases from 3.3% at low  $T$  to about 1% at room temperature. Since it is known that the transition energy in poly-pTS varies linearly with tensile strain at approximately the same rate (see Section 3.2.1.1), the large variation in 4B chains is likely to be due to changing strain. In 3B, the monomer unit cell parameter differs from the chain equilibrium repeat unit length by  $<0.5\%$  at all temperatures and this effect is absent.

The  $T$  dependence of the zero-phonon lineshape was therefore studied quantitatively on 3B to eliminate any possible influence of strain. The area of the zero-phonon absorption line keeps constant with temperature. The oscillator strength is therefore constant. The areas of the main vibronic lines also seem to keep con-

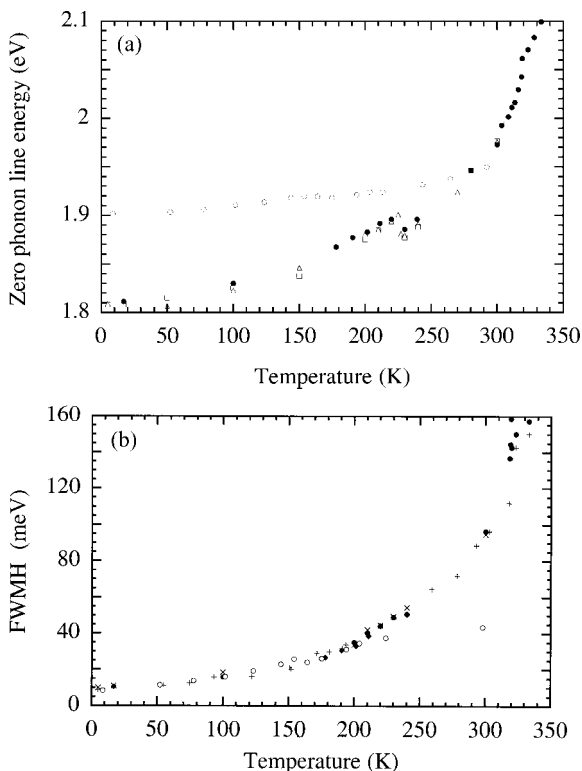


**Figure 3.12** Temperature dependences of (a) the zero-phonon transition energy  $E_0$  and (b) the zero-phonon linewidth  $\Gamma_0$ . Open circles: poly-3B in 3B. Other symbols: several series of measurements on poly-4B in 4B; these

series are given to emphasize the fact that the rapid increase above 150 K is not due to sample-dependent effects such as inhomogeneous broadening, but is intrinsic.

stant, so the Franck–Condon factor is not temperature dependent. The main exciton absorption line is well fitted by the sum of a strong Lorentzian and,  $\sim 7.5$  meV above, a weaker Lorentzian satellite with the same width. This satellite most probably corresponds to a phonon sideband, since RRS spectra show around  $60\text{ cm}^{-1}$  a resonant low-energy phonon, therefore corresponding to chain normal modes [25]. It is not possible to fit the experimental spectrum using Gaussian profiles with physically meaningful intensities and widths. Hence the lineshapes are governed by homogeneous broadening in the studied temperature range. It will be shown in Section 3.4.3.2 that the times derived from the widths are shorter than the excited-state lifetime at all temperatures. The widths are therefore governed by the loss of coherence of the excited state involved.

## 3.4.2

**Electroabsorption**

Electroreflectance measurements have brought important information on bulk PDA crystals: it was shown that the strong electronic transition in the visible is an excitonic one, with the exciton having a large polarizability; and on the best samples (poly-DCH, for instance) a well-resolved signal was observed at higher energy, characteristic of a Franz–Keldysh effect, showing that the gap is around 2.5 eV, hence an exciton binding energy of about 0.5 eV [37, 64]. In these measurements, the electroabsorption spectrum was deduced from the reflectance and electroreflectance spectra by Kramers–Kronig transformation.

3.4.2.1 **Results**

In monomer crystals containing a small enough concentration of isolated polymer chains, the absorbance is low enough and electroabsorption spectra can be directly recorded, as shown in Fig. 3.13 for 3B [65]. Electroabsorption is observed only when the applied electric field  $F$  is oriented // to the chain direction. The light was also polarized along the same direction in these experiments, since in  $\perp$  polarization the absorption at small  $x_p$  is too low to allow recording of an EA spectrum (see, however, Section 3.4.2.5).

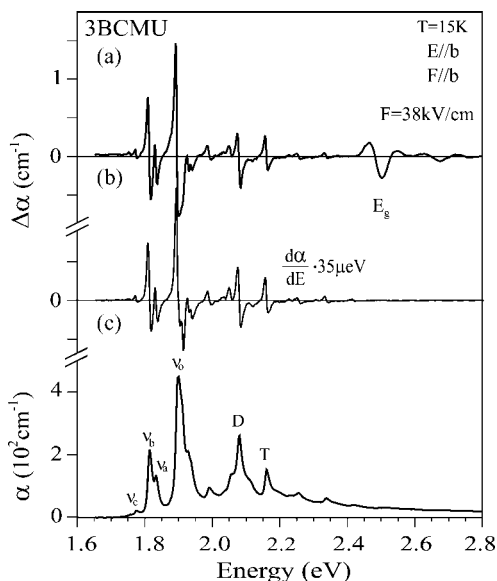


**Figure 3.13** Electroabsorption spectrum for parallel polarization of poly-3BCMU isolated chains at 15 K (a), compared with the first derivative (b) of the absorption spectrum (c);

the  $v_0$  line is saturated in this spectrum. The Stark shift used for the calculation of the derivative was  $35 \mu\text{eV}$  at an applied field of  $38 \text{ kV cm}^{-1}$ .

The spectra consist of two parts, below and above 2.4 eV respectively.

Below 2.4 eV the very well-resolved spectrum is identical with the first derivative of the absorption spectrum, except at the position of the main absorption line, where the absorption is slightly saturated. Hence the absorption spectrum shifts as a whole towards the red without change in shape or intensity. This is also true for the weak lower energy bands below the main absorption band, which were shown to correspond to minority populations of slightly different blue chains (Appendix C).

Above 2.4 eV, the first derivative absorption spectrum is featureless, while large well resolved oscillations are observed in electroabsorption. The signal is in fact very intense: at a field  $F = 40 \text{ kV cm}^{-1}$ , the change in absorbance at 2.5 eV is  $\Delta\alpha \approx 0.3 \text{ cm}^{-1}$  (see Fig. 3.15), in a sample in which  $\alpha \approx 27 \text{ cm}^{-1}$  at the same energy. This is a relative absorbance change of about 1%, more than two orders of magnitude larger than what is observed below 2.4 eV. The true ratio is even larger, since the absorption in this energy range is dominated by exciton multiphonon vibronic transitions. This is related to the dimensionality of the chain: the Franz–Keldysh effect is much enhanced in 1-D [66].

Except for a much better resolution, the full electroabsorption spectra are very similar to those deduced from the electroreflectance spectra of bulk PDA [37] and can be interpreted in the same way, except for the weak low-energy bands which are not seen in the bulk polymer spectra, either because of the poorer resolution or because all chains have become equivalent in the fully polymerized crystals.

The lower energy part of the spectrum is entirely explained by a field-induced shift of an excitonic transition and its associated vibronic transitions. The shape of the signal is independent of the magnitude of the applied electric field  $F$  and its amplitude is proportional to  $F^2$ , as shown in Fig. 3.14 (the other curve is discussed shortly). All this indicates that the field is only a small perturbation here.

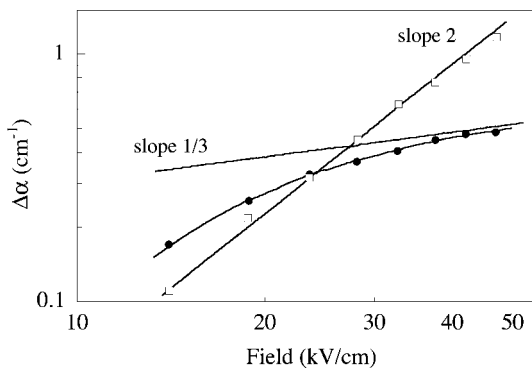


**Figure 3.14** Variation of the amplitude  $\Delta\alpha$  of the electroabsorption as a function of applied electric field  $F$ . Open squares: data in the low-energy region, increasing as  $F^2$ . Closed circles: data at the maximum near 2.5 eV, tending towards a variation as  $F^{1/3}$  at high field. From Ref. [65].

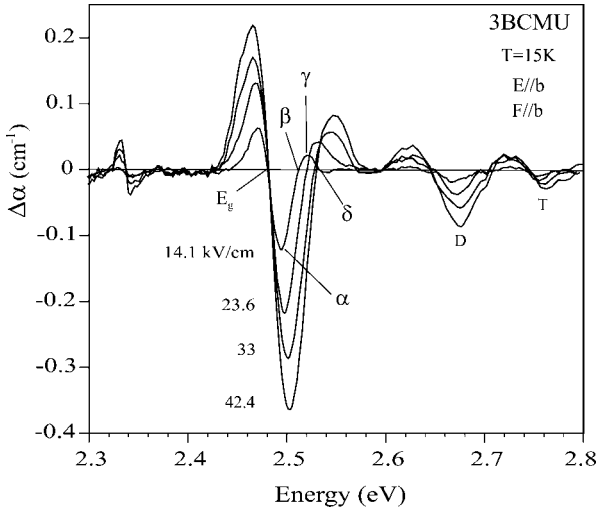


**Figure 3.15** Variation of the electroabsorption spectrum around 2.5 eV with applied field  $F$  between 14 and 42  $\text{kVcm}^{-1}$ . The lowest energy zero crossing, independent of  $F$ ,

marks the gap  $E_g$ . Other zero crossings  $\beta$  and  $\delta$ , and extrema  $\alpha$  and  $\gamma$ , shift with  $F$ , as shown in Fig. 3.14. D and T mark vibronic replicas.

In contrast, the shape of the high energy part changes with  $F$  as shown in Fig. 3.15. The lowest energy zero crossing stays at a constant energy, while the other zero crossings or turning points (labeled  $\beta$ ,  $\gamma$  and  $\delta$  in Fig. 3.15) shift to higher energies with increasing  $F$ , varying as  $F^{2/3}$  [65]. The signal amplitude grows sublinearly with  $F$ , tending to a  $F^{1/3}$  variation at high  $F$ , as shown in Fig. 3.14.

This is very well accounted for by the Franz–Keldysh effect at the edge of a quasi-one-dimensional continuum of free carriers associated with the lower lying exciton. The  $F^{2/3}$  dependence of the spectrum shape is a specific signature of the FK effect. In the high-field limit where the applied field is the dominant perturbation to the continuum states, the amplitude of the signal should indeed increase as  $F^{1/3}$  as shown in Fig. 3.14, a limit rarely approached in semiconductors, but clearly reached here.

Less well-structured electroreflectance signals observed on some bulk PDA had earlier been assigned to electric field enhancement of a forbidden transition to an  $A_g$  state [44, 67]. The present results allow this interpretation to be excluded.

### 3.4.2.2 Properties of the Exciton

The field-induced energy shift  $\Delta E_x$  of the exciton state  $x$  results from virtual transitions to all levels  $l_i$  to which  $x$  is coupled via one-photon-allowed transitions of transition dipole  $\mu_{xl}$ :

$$\Delta E_x = \sum_{l_i} \frac{|\mu_{x,l_i} F|}{E_x - E_{l_i}}$$

where  $E_x$  is the unperturbed exciton energy and  $E_{l_i}$  that of state  $l_i$ . Assuming that the isolated chain has a center of symmetry, the states  $l_i$  must have  $g$  symmetry, they do not appear in the absorption spectra presented above and since the spectrum shifts to the red the dominant ones must be at higher energy than the exciton. Such states can belong to the ionization continuum associated with it which produces the FK oscillations near 2.5 eV or be the  $g$  state observed in two-photon absorption spectra just below the continuum threshold [52, 68]. Replacing for simplicity the sum over  $l_i$  by a single level  $l$ , one then obtains

$$\Delta E_x = \frac{|\mu \cdot F|}{E_x - E_l} = \frac{p}{2} F^2$$

where  $p$  is the polarizability of the exciton state which is given by the virtual transitions to all states  $l_i$  and  $\mu$  is the transition dipole moment between  $x$  and  $l$ , hence a determination of  $p$  and  $\mu$  with an uncertainty of about 10% (Table 3.2).

**Table 3.2** Properties of the exciton in blue isolated chains. The last line shows the data for a bulk PDA crystal for comparison. The last column shows the transfer of oscillator strength from the exciton. Data from Refs. [37] and [65].

	Transition energy (eV)	Binding energy (eV)	Polarizability $p$ ( $\text{\AA}^3$ )	Dipole moment $\mu$ (e $\text{\AA}$ )	Oscillator strength transfer
3BCMU chains	1.896	0.586	$7120 \pm 700$	12	$3.8 \times 10^{-5}$
4BCMU chains	1.810	0.568	$6480 \pm 650$	11.3	$3.6 \times 10^{-5}$
DCH bulk	1.856	0.478	$8200 \pm 850$	11.7	

The dipole corresponds to 2–3 times the unit cell length, hence the exciton is fairly extended, with a Bohr radius of 10–15  $\text{\AA}$ , and it should thus have a relatively small effective mass. The reduced effective mass of the carriers estimated from the FK effect is about 0.05 (Section 3.4.2.4), compatible with an exciton effective mass of the order of 0.1. This value of the Bohr radius is close to the exciton radius calculated by Suhai [69]. A similar effective mass will be found for the red chains exciton from a completely different experiment (see Section 3.5.4.3). The polarizabilities are large compared with theoretical or experimental numbers quoted for other conjugated polymers, of the order of  $1000 \text{\AA}^3$  [70].

The differences between the two materials are small and not significant, despite the fact that at 15 K the poly-4B chains are under a 3% compressive strain, whereas the poly-3B chains are not. The measured properties are therefore robust and can be taken as generic for the PDA.

The coupling between  $x$  and  $l$  also brings up a transfer of oscillator strength from the allowed  $0 \rightarrow x$  transition to the forbidden  $0 \rightarrow l$  transitions, but it is of the order of  $\Delta E_x/(E_x - E_l) \approx (2-5) \times 10^{-5}$ , too small to affect the lineshape of the exciton electroabsorption spectrum, in agreement with the observed pure quadratic Stark effect. It is also too small to be detected as an increase in absorption in the region of the Franz–Keldysh signal. Indeed, the positive and negative parts of the signal in Fig. 3.15 cancel at low  $F$ , indicating a redistribution of oscillator strength in the same spectral range, that is, within the ionization continuum states, rather than a borrowing from other spectral regions. A small increase in the integrated absorption in the region of the Franz–Keldysh signal region becomes observable at the highest values of  $F$  only.

### 3.4.2.3 Exciton Binding Energy

The position of the lowest energy zero in the FK signal, marked  $E_g$  in Fig. 3.15, yields an accurate determination of the ionization bandgap  $E_g = 2.482$  eV (at 15 K) in 3B and 2.378 eV (at 40 K) in 4B, hence of the exciton binding energy  $E_b$  of 586 and 568 meV, respectively (Table 3.2). This value of  $E_b$  is slightly larger than those measured in the same way in bulk PDA: 480 meV in poly-DCH, 510 meV in poly-pTS [37]. PDA are the only conjugated polymer class in which  $E_b$  has been experimentally determined without ambiguity and to such a high accuracy up to now. It is not, however, directly comparable to theoretical values calculated by various methods for single PDA chains or other conjugated polymers [71], which almost always give very much larger  $E_b$ . However, such calculations do not take into account the effects of the surrounding (dielectric) medium, in our case a well-ordered monomer crystal. Polarization of that medium by the free electron–hole pair on the chain produces a much larger correction than the one produced by a bound pair (an exciton) and once this is taken into account the calculated exciton binding energy  $E_b$  is reduced to values close to the experimental ones. We return to this problem in Section 3.4.7.

### 3.4.2.4 Properties of Electron and Hole

Observation of well-defined FK oscillations is most useful in yielding information about the properties of charge carriers in a single well-ordered conjugated polymer chain, that are otherwise hard to obtain. This requires analysis of the FK oscillation lineshape [41]; the modulation is much larger for a quasi-1-D band, hence the fact that even very weak absorption bands yield an easily measurable electroabsorption signal [66].

The variation  $\Delta a$  of the absorbance at energy  $E$  is a function of the ratio of the energy difference  $E - E_g$  to a “scaling energy”  $\hbar\theta$  given by

$$\hbar\theta = \left[ \frac{(e\hbar F)^2}{2m^*} \right]^{1/3}$$

in which the only adjustable parameter is  $m^*$ , the reduced mass of the pair. Hence, plotting the energy shift of characteristic points of the electroabsorption signal, labeled  $\alpha$  to  $\gamma$  in Fig. 3.4.6, as a function of  $F^{2/3}$  should and indeed do, yield straight lines, which slope gives an estimate of  $m^* \approx 0.05 \pm 0.01$ . The same value was obtained in the same way on bulk poly-DCH, the only bulk PDA on which good enough data were obtained [37, 64]. This value is consistent with the hole effective mass  $m^* \approx 0.1$  inferred from angle-resolved UPS experiments on single crystal films of poly-4BCMU [72].

This analysis cannot be extended to larger values of  $E - E_g$ , since new features, labeled D and T on Fig. 3.15, appear at about  $E_g + 163$  and  $E_g + 250$  meV in 3B (165 meV and 260 meV in 4B); these are assigned to vibronic replicas of the band to band transition.

The electric field is not the only possible source of broadening of the FK electroabsorption spectra. Inhomogeneous broadening can be neglected here, since from the combination of absorption (Section 3.4.1) and fluorescence (Section 3.4.3) results it is known to amount to much less than 10 meV for the exciton transition and there is no obvious reason for it to be much larger for the band to band transition. However, the finite lifetime of the electronic state prepared by light absorption is significant: the extension in energy of the FK oscillations is related to the coherence length of the band states [73]. This extension is at least 70 meV at  $23 \text{ kV cm}^{-1}$ , a field at which the FK oscillations are entirely below the D feature at  $E_g + 165$  meV (Fig. 3.15).

This leads to a carrier coherence length of at least 35 nm, that is, more than 70 repeat units. A mean free path of that length is not easy to achieve in a quasi-1-D system such as an isolated PDA chain. It indicates very high structural perfection and, indeed, even a small amount of disorder is enough to decrease the FK signal and eventually wash it out: see data on 4B at higher  $x_p$  in Section 3.4.2.5 below.

Loss of coherence may be due to inelastic scattering, as will be found for excitons in red chains (Section 3.6.2.2); in this case the quantities deduced from the FK signal, effective mass and coherence length, are directly relevant to the carrier transport properties. However, loss of coherence may also correspond to polaron formation. The word "polaron" is ubiquitous in the conjugated polymer literature and it is widely accepted that lattice relaxation very rapidly dresses the charge carriers, although there is no direct experimental evidence of that. The results presented in Section 3.4.3 and even more convincingly in Sections 3.5 and 3.6, show that such lattice relaxation does not occur for singlet excitons, contrary to earlier expectations. Polaron formation would greatly affect the carrier transport properties, but contradictory conclusions have been drawn from transport experiments in bulk PDA. The question thus remains open and FK results only place a lower limit for the time needed for polaron formation to begin, if it occurs at all.

### 3.4.2.5 Electroabsorption at Higher Polymer Concentration

Electroabsorption measurements are possible at much higher polymer concentration up to  $x_p \approx 0.1$ , using light polarized perpendicular to the chain direction; as mentioned above, the absorption spectra are the same in // and  $\perp$  polarizations for such values of  $x_p$ . Experiments were carried out at  $T \approx 10$  K both on 3B and 4B [74]. An EA signal is observed only for the electric field // to the chains.

In the exciton energy range, the EA spectra are not much dependent on  $x_p$ . They are still completely accounted for by a quadratic Stark shift and the exciton polarizabilities thus derived are, to  $\pm 10\%$  accuracy of their determination, equal to the values found above for very dilute chains. The exciton energies and absorption linewidths increase slightly, the effect being slightly larger in 4B, probably owing to changes with polymer content of the mismatch between chain and matrix.

The Franz–Keldysh signal is still well developed in 3B, leading to the determination of a bandgap  $E_g = 2.50$  eV, and hence an exciton binding energy  $E_b \approx 580$  meV, equal to the value at lower  $x_p$ . In contrast, in 4B the signal, although still present (as shown by comparison with the first derivative of the absorption) is much decreased.  $E_g$  and  $E_b$  are less accurately determined but again are only slightly different from their value for highly dilute chains. This indicates that elastic stresses built into the 4B crystal due to the mismatch between the monomer unit cell and the polymer repeat unit dimensions cause enough disorder to limit the coherence length of the generated carriers, whereas this effect is much weaker in 3B. Still, the stresses in 4B remain small enough hardly to distort the diffraction Bragg peaks, showing how sensitive to disorder the Franz–Keldysh signal is; it is therefore not surprising that the FK oscillations can be observed only in high-perfection chains and not in most bulk PDA crystals nor in any other conjugated polymer.

At a polymer concentration  $x_p \approx 0.07$  and assuming a random distribution of the chains in the matrix, the probability that two chains are nearest neighbors within a crystal lamella is about 0.15. Still, no effect of interchain interaction is obvious in the spectra, indicating that these interactions must be weak. This is a subject for further studies.

## 3.4.3

### Fluorescence

#### 3.4.3.1 Emission Spectra

Bulk blue PDA are considered to be nonfluorescent [46]. When dispersed in their crystalline monomer matrix, blue poly-BCMU chains emit a weak fluorescence, easily studied at low  $T$ . Figure 3.16 shows the fluorescence spectrum at 2 K of poly-4B chains excited at 514.5 nm. This wavelength was chosen to avoid overlapping of strong RRS lines.

The corresponding absorption spectrum is shown as a dotted line. The emission spectrum is close to a mirror image of it, except for the region of the zero-phonon line, where reabsorption is important. The vibronic lines are better resolved in emission, so the exact position of the D and T vibronic emission lines can be de-

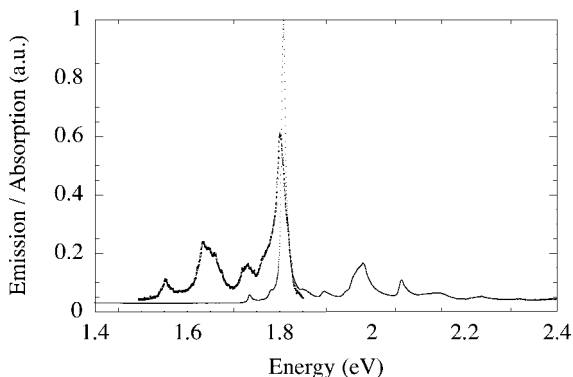


**Figure 3.16** Fluorescence emission spectrum at 2 K of poly-4B chains (open squares) compared with the absorption spectrum of the same 4B crystal (line and points).

terminated accurately. The corresponding vibrational energies are known from RRS data, so the zero-phonon emission line energy can be derived: it coincides within a few tenths of an meV with that of the zero-phonon absorption line: there is no Stokes shift.

Similar spectra and results are obtained for poly-3B chains.

This emission is therefore the resonance fluorescence of the  ${}^1B_u$  exciton of the polymer chain, without any geometric relaxation in the excited state.

#### 3.4.3.2 Lifetime of the Emitting State

The quantum yield of this emission is no doubt small, so the lifetime is expected to be short. Time-resolved data were obtained by the fluorescence up-conversion method [75]. For experimental details, see Ref. [76].

The emission spectrum shape is constant during the decay, and it is therefore the same well-defined state that emits. The decay is exponential over more than two decades, as seen in Fig. 3.17.

The measured effective lifetimes  $\tau$  at 20 K are as follows:

for poly-3B chains  $\tau = 135 \pm 10$  fs;

for poly-4B chains  $\tau = 130 \pm 5$  fs.

Their temperature dependence is given in Fig. 3.18 in the range 15–150 K. The lifetime  $\tau$  remains approximately constant in poly-3B, but in poly-4B it starts to decrease above about 50 K, reaching 100 fs at 180 K. Such short lifetimes account for about half of the zero-phonon absorption linewidth at the lowest temperatures. On the other hand, the absorption lineshapes between 50 and 150 K are well fitted by Lorentzians [76], suggesting that they correspond to a decreasing exciton coherence time and not to a dramatic increase in inhomogeneous broadening (the situation above 150 K in 4BCMU is less clear). A small residual inhomogeneous contribution to the linewidth is certainly present, but it cannot be larger than a few

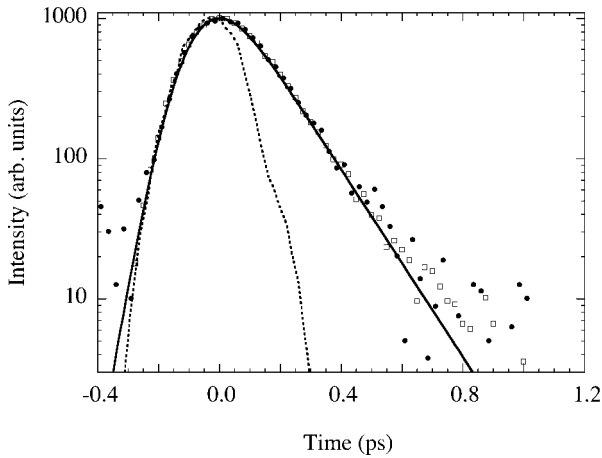


**Figure 3.17** Temporal variation of the fluorescence. The dotted line is the instrumental response. The solid line is a convolution of this response with an exponential of decay time 130 fs. Two sets of data are shown as open squares and filled circles. From Ref. [76].

meV; hence the exciton energy cannot vary by more than this value over the whole length of a single chain, of the order of  $20\ \mu\text{m}$ .

The measured lifetimes can be compared with the expected radiative lifetime of a molecular transition of oscillator strength of  $\sim 1$ , a few nanoseconds. The fluorescence quantum yield can be estimated on that basis to be  $5 \times 10^{-5}$  to  $10^{-4}$  (this is not necessarily correct if the chains behave as quantum wires, see Section 3.5.3). The exciton relaxation is therefore dominantly nonradiative. The corresponding processes are discussed below in Sections 3.4.4 and 3.4.5.

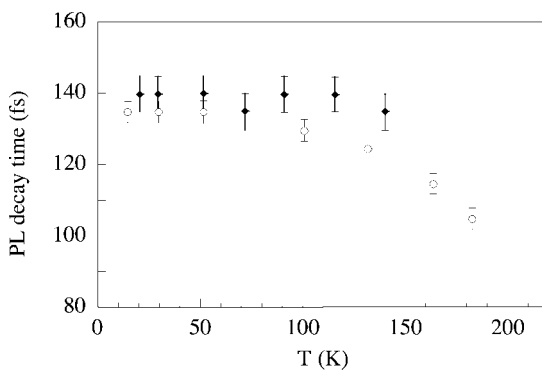


**Figure 3.18** Temperature dependence of the fluorescence lifetime in chains of poly-3B (diamonds) and poly-4B (open circles), from fits as shown in Fig. 3.17, with the corresponding uncertainties. From Ref. [76].

To summarize, the emitting state is a well-defined one, although short-lived, and, as shown by the resonant character of the emission, it is the excited state prepared by the absorption. These results do not agree with the instantaneous self-trapping exciton model [48, 49], which has been used [50] to account for the lack of fluorescence in bulk PDA.

### 3.4.3.3 Risetime of the Emission: Relaxation Within the Singlet Manifold

In these experiments, the exciting photon energy is close to that of the vibronic D line in absorption. The emission originates from the relaxed (zero-phonon) exciton level, so the time needed for the excitation to relax to that level should show up as a fluorescence risetime. As seen in Fig. 3.17, it is barely different from the instrument response. A fit yields an upper limit of  $\sim 40 \pm 20$  fs for the relaxation from the vibronic D line to the zero-phonon level.

### 3.4.4

#### Nonradiative Relaxation of the $^1B_u$ Exciton

##### 3.4.4.1 Introduction. Experimental Method

The very fast nonradiative decay evidenced by the very short fluorescence lifetime is unlikely to be due to direct internal conversion to the ground state. In the statistical limit, valid for large molecules, of the molecular theory of nonradiative relaxation [77], the probability of such a process is an exponentially decreasing function of the number of phonons which must be generated to transform the whole electronic energy into vibrational energy in the ground-state manifold. Hence the dominant relaxation channel is generally the one involving the highest energy phonon only. Since this phonon in the PDA chain is the normal mode we call T (the triple bond stretch) of about 265 meV, the exciton energy corresponds approximately to its seventh harmonic. It is highly unlikely that such a process can be fast enough to account for the measured lifetime.

This implies that the relaxation proceeds through one (or several) intermediate excited state(s) at lower energy. The absence of one-photon absorption below the exciton transition shows that there is no lower lying singlet excited state of  $u$  symmetry. Besides the lowest  $1^3B_u$  triplet, corresponding to the  $B_u$  singlet exciton, which certainly lies in the optical gap, two other types of candidates are a  $2^1A_g$  singlet or a self-trapped state produced by geometric relaxation around the  $B_u$  singlet exciton (the fluorescence results only show that self-trapping cannot be instantaneous, not that it cannot eventually occur). None of them is expected to be efficiently radiatively coupled to the ground state, so they cannot be studied in emission.

Therefore, subpicosecond pump–probe experiments were performed on 3B and 4B monomer crystals containing  $x_p < 10^{-3}$  polymer by weight. In such experiments, an intense monochromatic pulse (the pump) generates  $^1B_u$  excitons, which then decay through one or more intermediate excited states. Most experiments were carried out with an initial singlet density of 1 per 200 chain repeat units, but

this ratio could be varied from 1:1000 to 1:10, without any effect on the results except that the triplet yield is superlinear in pump fluence. Absorption by the excited states is measured by a second broadband subpicosecond pulse (the probe) delayed by a time  $\theta$ ; two types of phenomena can be studied:

1. Each excited state has its characteristic absorption spectrum, which can be recorded; this is photoinduced absorption (PA).
2. The presence of the excitations “depletes” the ground state, so the ground-state absorption leading to the exciton is decreased; this is photoinduced bleaching (PB).

The absorption of the probe light at a given wavelength is increased by PA and decreased by PB. By recording the spectra at different delays  $\theta$ , the relaxation kinetics of the various excited states are obtained. The PB kinetics are that of ground-state repopulation, whereas the kinetics of each PA band are due to the rise and decay of the corresponding excited state.

Details on the experimental setup can be found in the original paper [78]. Briefly, the temporal resolution was  $\sim 100$  fs and the probe pulse duration was  $<150$  fs. The pump photon energy could be chosen within the exciton absorption range or below and was kept below the known carrier generation threshold at about 2.5 eV, so only states within the  $^1B_u$  exciton manifold were directly excited. Ionized states would only be produced by multiquanta processes and be superlinear in pump intensity. Triplet generation, discussed in Section 3.4.5, indeed may require participation of such processes, but no such effect was detected in the PA and PB spectra discussed in this section. The probe spectral range lay between 1.25 and 2.3 eV, but the region between 1.5 and 1.65 eV could not be studied. The setup allowed the simultaneous acquisition of the whole photoinduced spectrum, which is important to obtain accurately the narrow lines of the PB component.

#### 3.4.4.2 Spectra and PA Decay Kinetics

Figures 3.19 and 3.20 show two examples of the absorbance change, between 1.65 and 2.1 eV and between 1.25 and 1.50 eV, respectively, for an optically thin 4B crystal ( $x_p$  at most a few  $10^{-4}$ ). These are raw spectra, uncorrected for the probe pulse chirp, but all data used in the following discussion have been corrected for the chirp.

In Fig. 3.19, the delay time given is taken at 1.81 eV. The sharp negative peaks are due to PB of the exciton transition and the positive background is due to PA of the state or states present at 1 ps. The small negative peak at  $\sim 1.76$  eV corresponds to the bleaching of a low-energy line (see Fig. 3.11) which is the exciton transition of a minority population of chains (see Appendix C). This state does not belong to the majority population, the only one considered below; in particular, it does not participate to the relaxation of the exciton of the majority chains. This is true of all these low-energy transitions in both materials. In contrast, these minority excitons

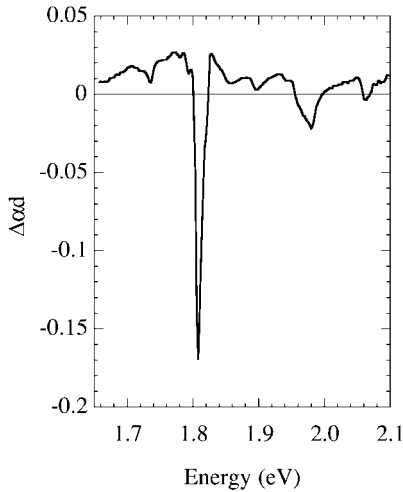


**Figure 3.19** Changes of absorbance in the exciton transition region, 1 ps after the pump pulse. The negative peaks are the bleaching of the exciton absorption; the positive signal is photoinduced absorption of various transient excited states. From Ref. [78].

behave very much like the majority one: this has been demonstrated directly in these pump–probe experiments, as shown in Appendix C.

In Fig. 3.20, spectrum (a) is taken at  $\theta = 335$  fs and spectrum (b) at  $\theta = 1.3$  ps (both at 1.35 eV). The spectra correspond to PA only and have two components: a quickly decaying background and a longer living Lorentzian line at about 1.35 eV. The latter is due to triplet–triplet absorption and will be discussed in Section 3.4.5. None of the PA features in Figs. 3.19 and 3.20 can be associated with the exciton, which has completely disappeared even at  $\theta = 335$  fs.

The kinetics of the PA background in the spectral range of Fig. 3.20 is given in Fig. 3.21: it is well accounted for by the sum of two components, a major one appearing within the pump pulse duration and decaying exponentially with a life-

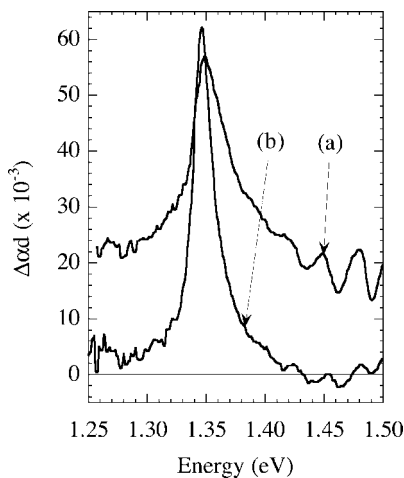


**Figure 3.20** Photoinduced absorption of the poly-4B chains in the near IR recorded 335 fs (a) and 1 ps (b) after the pump pulse. A fast-decaying PA background is present at 335 fs. The narrow line remaining at longer times is a triplet–triplet transition. Note the slight spectral shift and the narrowing of that line. From Ref. [78].

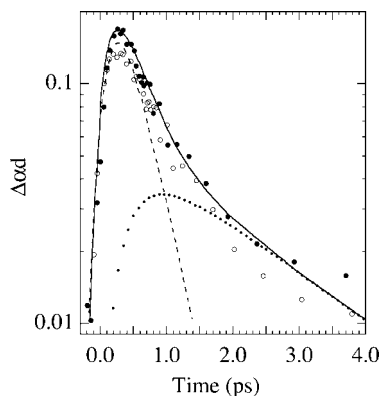


**Figure 3.21** Decay kinetics of the PA background in Fig. 3.20. Dashed line: convolution of the instrumental response with an exponential of decay time 450 fs. Dotted line: signal with a risetime of 450 fs and a decay time of 2 ps. Solid line: sum of these two components with appropriate relative intensities. Open and filled circles correspond to two experiments. From Ref. [78].

time of  $450 \pm 100$  fs and a second one, seven times weaker, appearing with a risetime of 450 fs and decaying with a lifetime of about 2 ps.

Two excited states are therefore involved, which we shall call  $X_1$  and  $X_2$ , respectively, and from the kinetics it is clear that  $X_2$  is produced by the relaxation of  $X_1$ . The  $X_1$  PA is a broad band peaking at 1.40 eV, with a threshold below 1.25 eV and a low-energy half-width of 80 meV. This absorption is intense: since the number of generated excitons is known, a lower limit of the absorption cross-section can be calculated assuming that all excitons decay through  $X_1$ : the total cross-section for the range 1.2–1.5 eV is  $\sigma(X_1) \approx 3 \times 10^{-16} \text{ cm}^2$ . For such a broad absorption band, this implies an oscillator strength  $>1$ . The same results are obtained with 3B.

A similar kinetic analysis carried out at a probe wavelength just below the exciton absorption shows that the PA appears there with a risetime of 450 fs, so it is only due to  $X_2$  and it decays in 1.7–2 ps, which is therefore the lifetime of  $X_2$ . The total absorption cross-section for the range 1.6–1.9 eV is  $\sigma(X_2) \approx 8 \times 10^{-16} \text{ cm}^2$ . Again, this is a strongly allowed transition.

Nowhere between 1.65 eV and the exciton energy does one see a PA that could be associated with an absorption by the exciton and the formation of a biexciton; it is either too small or absent.

PA is also present above the exciton transition, but there the kinetics must take into account simultaneously PA and photobleaching, which is discussed just below. The two components can be sorted out because the PB spectrum is identical with the exciton absorption spectrum, so PB dominates at the absorption lines positions and its contribution at other wavelengths can be calculated and subtracted from the observed response, yielding the pure PA component. At 1.965 eV, for instance, a strong PA by the exciton is observed, together with absorptions by  $X_1$  and  $X_2$ , with relative absorption cross-sections  $\sigma_0:\sigma_1:\sigma_2 = 5:1:2$ .

The final states of the absorptions by  $X_1$  and  $X_2$  lie about 3 eV above ground state and must be of  $u$  symmetry. Such states are therefore also connected to the ground state by symmetry-allowed one-photon transitions. Theoretical calculations on oligomers [79] indeed predict a  ${}^1B_u$  state at an energy compatible with a 3 eV value for an infinite chain. However, the one-photon absorption spectrum of

isolated PDA chains, which is otherwise well resolved, is structureless in that energy region, only showing the high-energy tail of the  $B_u$  exciton absorption, corresponding to highly vibrationally excited levels and its associated ionization continuum (see Section 3.4.6, Fig. 3.28).

### 3.4.4.3 Photobleaching

Let us consider now the PB signal. The kinetics for the zero-phonon line and for its D and T vibronic replicas can be accounted for by the sum of the bleaching recovery, which is the same for all lines (as expected) and different PA contributions (the other vibronic lines are too weak for a quantitative analysis). The excited states to be taken into account in the analysis are the exciton,  $X_1$  and  $X_2$  and the triplet. However, the triplet decay follows a  $t^{1/2}$  law after  $\sim 3$  ps (Section 3.4.5.4) and this is not observed in the PB decay, so triplets seem to be formed in too low concentration to contribute significantly to bleaching and they will not be included in the modeling. The absence of a triplet contribution to PB leads to an upper limit for the triplet yield of a few percent.

In modeling photobleaching, one must consider not only the number density of a given excited state  $X_i$ , but also its bleaching efficiency  $\phi_i$ , which will be expressed as a number of repeat units of the chain which do not take part in the absorption from the ground state if one  $X_i$  state is present. So, when the  ${}^1B_u$  exciton with bleaching efficiency  $\phi_0$  decays into  $X_1$ , which in turn decays into  $X_2$ , photobleaching persists since the ground state has not been regenerated but its magnitude changes if  $\phi_0 \neq \phi_1 \neq \phi_2$ . Indeed, changes are seen on the PB decay curve as shown in Fig. 3.22 for 3B.

A complicated shape at short time ( $\leq 2$  ps) is followed by a sequence of two exponentials with time constants 1.7 and 20 ps (the latter being longer in 4B). The shorter time is consistent with the lifetime of  $X_2$  but the longer one shows that yet

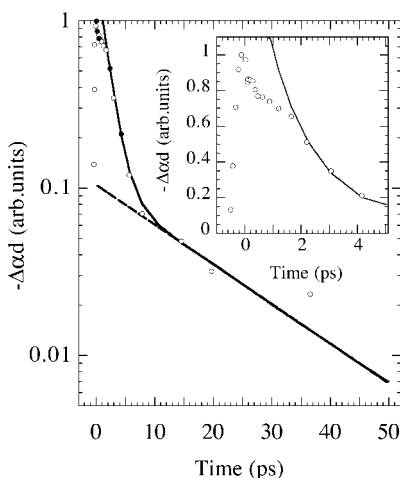


**Figure 3.22** Photobleaching at the exciton energy (1.90 eV) of poly-3B chains. The inset shows the short time signal. The solid line is a sum of two exponentials with decay times 1.7 and 20 ps. Open and filled circles are the results of two experiments.

another state – which will be called Y – also participates in the ground-state recovery. State Y may either belong to the same relaxation channel as  $X_1$  and  $X_2$ , being populated from  $X_2$  and decaying to the ground state, or it may act in parallel to state  $X_1$  and/or  $X_2$ , being populated directly from the exciton or from  $X_1$  and decaying to the ground state. The former is unlikely, since the ratio of the initial values of the fast and slow exponential should be the ratio  $\phi_2:\phi_Y$  of the bleaching efficiencies of the corresponding states, implying (see below) that  $\phi_Y < 1$ , which does not seem reasonable.

The PB decays were therefore fitted with the assumption that Y does not belong to the main decay channel, but is a derivation in parallel to it, using as parameters the bleaching efficiencies of all states involved defined above. The lifetimes are not adjustable parameters, since those of the exciton and of  $X_1$  are known and those of  $X_2$  and Y are fairly accurately determined by the decay times of the two exponentials in Fig. 3.22. A good fit to all experiments is obtained. An example is shown on Fig. 3.23.

Since the number of excitons generated can be calculated from the pump intensity and the known  $x_p$ , the initial value of the PB yields the bleaching efficiency  $\phi_0$  of the exciton,  $\phi_0 \approx 5$ , corresponding to a length of  $\sim 2.5$  nm. This is close to the exciton size deduced in Section 3.4.2. The 450-fs decay time of  $X_1$  does not show up in the decay, indicating that  $X_1$  and  $X_2$  have comparable bleaching efficiencies. The fit shown in Fig. 3.22 corresponds to  $\phi_1$  and  $\phi_2 = 2 \pm 1$ , about half of  $\phi$ .

The possible nature of these states will now be discussed.

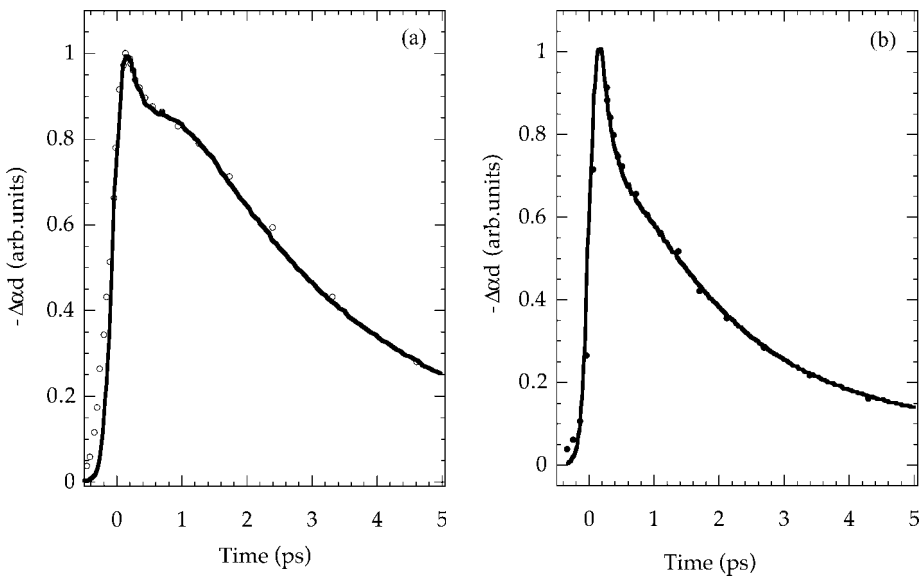


**Figure 3.23** Overall fits using the model and parameter values given in the text. (a) Poly-3B: fit of the results shown in Fig. 3.22. (b) Poly-4B.

#### 3.4.4.4 Nature of the Gap States

The exciton relaxation in bulk PDA phases, including disordered films, notably of poly-3B and poly-4B, has been discussed previously in terms of instantaneous self-trapping [50], based on the theoretical work of Rashba [48]. The existence of resonance fluorescence shows that self-trapping, if it occurs at all, cannot be instantaneous, but does not preclude the possibility of delayed self-trapping.

On the other hand, two-photon absorption experiments have shown the presence of at least one and possibly two [52]  $A_g$  states in poly-pTS crystal and in a Langmuir–Blodgett multilayer film [80]. These excited states are not self-trapped states (they are observed independently of the creation of  $B_u$  excitons) and can be populated from the higher lying  $B_u$  exciton by internal conversion. This relaxation process is well documented in polyenes, in which the  $B_u$  state lifetime is  $\sim 100$  fs [81], comparable to the exciton lifetime in PDA (Section 3.4.3). Hence  $A_g$  states are natural candidates for  $X_1$  and  $X_2$ .

The lifetime of the Y state is comparable to that of the  $B_u$  triplet as deduced from the decay of the PA at 1.3 eV. However, Y cannot be that triplet for several reasons: its contribution to PB is  $\sim 0.1 \pm 0.02$  whatever the pump photon energy, whereas the triplet yield is at least 50 times smaller when the pump is resonant with the exciton absorption than it is above 2.0 eV; in addition, the Y state concentration is linear in pumping fluence, whereas the triplet yield is non-linear (see Section 3.4.5).

However, there must be an  $A_g$  triplet, related to the  $A_g$  singlet states  $X_1$  and  $X_2$  from which it would be populated by intersystem crossing. This would provide another decay channel, branching off the main one at  $X_1$  or  $X_2$  (or both), with a rate constant of a few  $10^{10} \text{ s}^{-1}$ . Such an assignment for Y would be compatible with the experimental results. However, this  $^3A_g$  state must not significantly populate the  $^3B_u$  triplet: such an internal conversion would generate individual  $^3B_u$  triplets on a chain, not triplet pairs and such triplets would have long lifetimes (microseconds) since they would not disappear by fusion, but by ordinary intersystem crossing processes to the ground state; one should then observe intense triplet–triplet absorption and residual exciton bleaching for such long times, which is not the case. The assignment of Y to an  $A_g$  triplet therefore remains mere conjecture.

### 3.4.5

#### The Lowest Triplet State

##### 3.4.5.1 Assignment of the 1.35-eV Photoinduced Absorption

The 1.35-eV PA line can be recorded at least up to a 50-ps delay time, long after the PA from all states studied above have disappeared, except state Y. There only remains at these times a relatively narrow Lorentzian line at 1.345 eV ( $\Gamma = 12.5$  meV) in 4B [and at 1.360 eV ( $\Gamma = 14.8$  meV) in 3B] at 20 K, shown in Fig. 3.24 [82]. These values of the width  $\Gamma$  correspond to an excited state lifetime of about 40 fs.

A similar PA exists in all bulk blue PDA near 1.4 eV and has been unambiguously identified as a T–T\* absorption by the effects of microwaves or magnetic

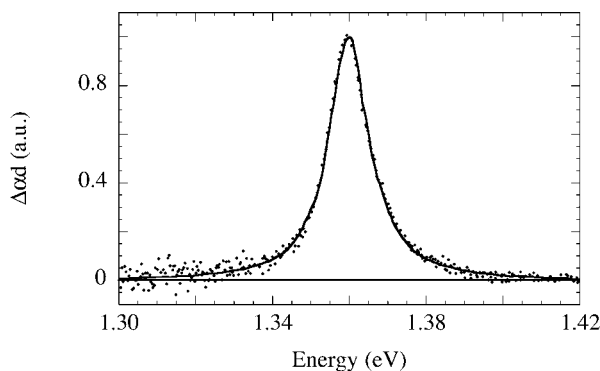


**Figure 3.24** Line shape of the 1.36 eV  $TT^*$  absorption in poly-3B chains, after background decay. Dots are experimental results and the solid line is a Lorentzian fit centered at 1.360 eV with a 14.8-meV width. From Ref. [82].

fields (see, for instance, Refs. [83, 84]). It is reasonable to assume that the absorption at 1.35 eV seen here in isolated chains is due to the same  $T-T^*$  transition. Hence triplets are formed by excitation in the singlet exciton absorption range and their density can be monitored by this PA line.

The variation of its intensity with pump fluence allows one to determine the triplet generation processes at work and from the estimate of the triplet generation yield, the strength of the  $T-T^*$  transition can be evaluated. The time dependence of the PA intensity gives information on the triplet decay process and on its transport properties.

#### 3.4.5.2 Triplet Generation Processes

The variation of the triplet yield with incident photon energy within the singlet absorption range is shown in Fig. 3.25 for 4B (similar results are obtained for 3B). Since the yield is not independent of pump fluence, the values are given for the same number of photons absorbed for all wavelengths.

The yield is very small at 1.8 eV, the zero-phonon line energy, it increases exponentially up to 2 eV, then stays constant or slowly increases linearly up to 2.5 eV.

The only triplet generation process that is fast enough to compete with the very fast relaxation within the singlet manifold (Section 3.4.3.3) is fission of a singlet into two triplets of total spin zero. This is a spin-allowed and fast process, well documented in molecular solids [85], and in a study of triplet generation in polycrystalline poly-DCH films it was concluded that they are produced by fission with a threshold of  $\sim 2.15$  eV at room temperature [86].

At low temperature, fission only occurs for singlets which energy is larger than twice the triplet energy (the unrelaxed energy, before the triplet undergoes self-trapping, if it occurs at all). A natural explanation of the energy threshold at 2.0 eV in Fig. 3.25 is that fission occurs above it but not at the relaxed exciton energy 1.8 eV. However, some triplet generation occurs upon pumping at 1.8 eV, so

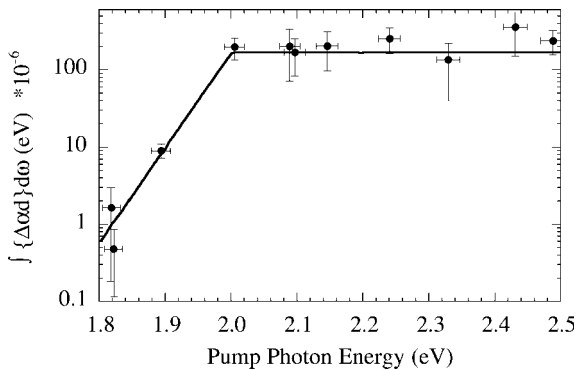


**Figure 3.25** Triplet yield deduced from  $TT^*$  transition intensities as a function of the energy of pump photons. The solid line is a guide for the eye, emphasizing the exponen-

tial increase up to 2.0 eV, then an almost constant, possibly slightly increasing, value. From Ref. [82].

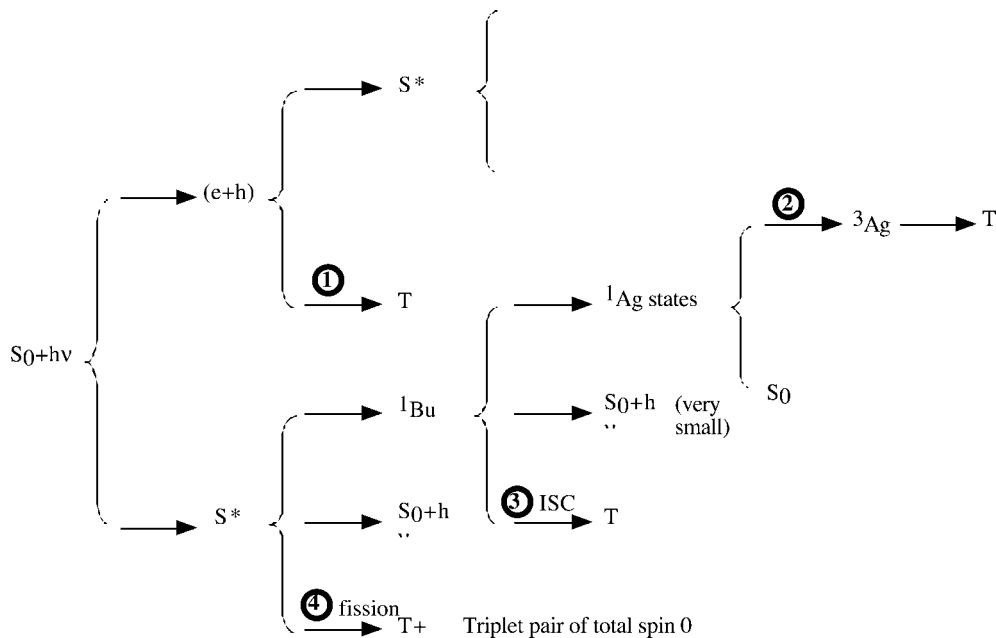


**Figure 3.26** Scheme of triplet generation processes.  $S^*$  is a “hot” singlet;  $T$  is the lowest triplet, presumed to be  $1^3B_u$ ;  $(e+h)$  is an electron-hole pair. The products of  $S^*$  at the top of the figure are the same as those

shown in the lower part. The threshold of process 1 is at least  $\sim 2.5$  eV, that of processes 2 and 3 is the exciton energy and that of process 4 is determined from Fig 3.25 (see text), around 2 eV.

another process must also be present. The yield there is proportional to the square of pump fluence, so it is a two-quantum process and intersystem crossing from the exciton,  $X_1$  or  $X_2$  is excluded (probably because it cannot compete efficiently with the very short lifetime of these states). The only possible process at 1.8 eV is therefore fission of high-energy singlets that are generated by absorption of the pump photons by the states that are present during the pump duration, essentially the exciton itself, with maybe a small contribution of  $X_1$ . The triplet yield above 2.0 eV increases slightly faster than linearly with the pump fluence, so exciton photoexcitation is also present at higher energies. This agrees with the observation that PA above the exciton energy is mainly due to photon absorption by the exciton itself, with an energy threshold near the exciton energy. Therefore, triplet generation occurs according to the general scheme shown in Fig. 3.26.

### 3.4.5.3 Triplet Energies and Triplet–Triplet Transition

The existence of fission above threshold and its absence at the exciton energy give upper and lower limits for the energy of the triplet states generated by fission, presumably the lowest energy triplet:

in 3B chains:  $0.95 \text{ eV} < E(T) < 1.05 \text{ eV}$ ,

in 4B chains:  $0.90 \text{ eV} < E(T) < 1 \text{ eV}$ ,

barely above midgap in both types of chains.

The symmetry of the triplet formed by fission requires clarification, however. Both the  $B_u$  and  $A_g$  triplets may be present in the optical gap. Theoretical calculations on oligomers [87] place the lowest  ${}^3A_g$  state much above the lowest  ${}^3B_u$  state (and of course below the lowest excited singlet  $A_g$  state), but there is no experimental proof of this ordering. However, the T–T\* transition is strongly allowed, so it must either be of the type  $u \rightarrow g$  or  $g \rightarrow u$ . Two-photon absorption and electroabsorption reveal a singlet  $A_g$  state just below the ionization threshold. It seems therefore most probable that T\* is the corresponding  ${}^3A_g$  triplet, so the lowest triplet must be the  $B_u$  one. If so, the  $B_u$  singlet–triplet exchange splitting is close to 0.9 eV, significantly larger than usually found in other conjugated polymers [88], and the  $A_g$  splitting is much smaller. Several theoretical calculations describe the lowest  ${}^1A_g$  excited singlet of polyenes as corresponding to a pair of  ${}^3B_u$  triplets and predict that its energy is about twice the  ${}^3B_u$  energy (see, for instance, Ref. [89]). If the above reasoning is correct, this is not verified in PDA, unless  ${}^1A_g$  is very close to  ${}^1B_u$ .

Assuming for  $E(T)$  the mean of the possible range of energies given above, the energy of the excited  $A_g$  triplet T\* is then 2.30 eV in 4B and 2.36 eV in 3B, to be compared with the gap values  $E_g$  of 2.38 and 2.48 eV, respectively (Section 3.4.2). The corresponding singlet  $A_g$  state, often called  $mA_g$ , also being below  $E_g$ , the exchange splitting of these two states has to be smaller than 0.1 eV.

The discussion of PB lead above to the conclusion that the triplet generation yield is less than a few percent. The initial absorbance of the T–T\* transition then yields a lower limit of its oscillator strength at least 10 times larger than that of the exciton transition. A similar conclusion had been reached earlier in a study of bulk poly-4B crystals [89].

#### 3.4.5.4 Triplet Transport Properties

The T-T\* absorption disappears in about 100 ps, much faster than reported in bulk PDA in which the triplet lifetime is tens or hundreds of microseconds (see, for instance, Ref. [86]). This short lifetime is easily explained by the strict one-dimensional confinement of the triplet in isolated chains since the lowest lying excited state of the matrix is the triplet of the C<sub>4</sub> group around 3 eV [90]. Moreover, the absorption does not decay exponentially in time and tends to a  $t^{-1/2}$  dependence at long times, characteristic of one-dimensional diffusion [91].

To account for the experimental decay law, the following model was therefore used: triplet motion is assumed to be diffusive, with a hopping rate  $W$  (s<sup>-1</sup>) and triplets situated on the same site (or equivalently on nearest neighbor sites) can annihilate by fusion with a rate  $A$ . Triplets are created by fission in pairs of total spin zero and it is known that they can form again a singlet by fusion upon re-encounter [85]. At time zero, two triplets are generated on the same site. Spin relaxation is neglected, considering the very short times involved, but it would not significantly influence the results, since the fusion of two triplets into an excited triplet is also energetically possible and is spin allowed for several of the spin states of the triplet pair [85]. This problem is analytically soluble [82] (for a similar problem, see also Ref. [92]). A very good fit is obtained over the whole decay for both materials. The result for 3BCMU, using a hopping time  $W^{-1} = 12.5$  ps and a fusion rate  $A = 4 \times 10^{11}$  s<sup>-1</sup>, is shown in Fig. 3.27.

The ratio  $A/W$  is obtained to a very good accuracy (a few percent). Note that the triplets of the same pair do not separate by more than a few sites between successive encounters, so even if several pairs are created simultaneously on the same chain, they can be considered independently of one another: the same decay kinetics should be observed up to fairly high triplet densities on a chain. The probability of fusion of two triplets is high:  $A/(A + 2W) = 0.7$ .

This model is general and does not specify which kind of triplet is moving or which kind of singlet is produced in the fusion reaction. The model only assumes

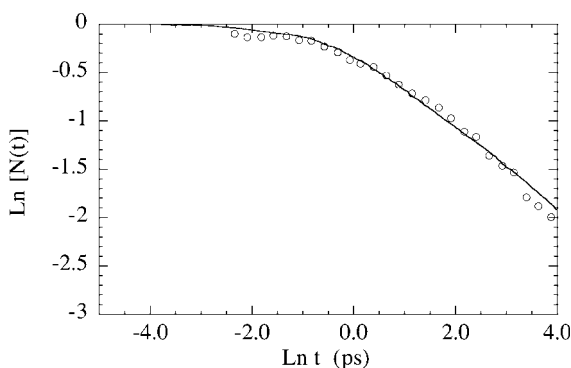


**Figure 3.27** Temporal dependence of the TT\* absorption, in a log-log plot. Open circles: experiment. Solid line: best fit using the 1-D fission-recombination model. Slope at long times is  $t^{-1/2}$ . From Ref. [82].

that fusion is energetically possible, and therefore that self-trapping, if it occurs, decreases the triplet energy by less than half the difference between the energy of the triplet and that of the singlet exciton produced by the fusion process. Information of this question is provided by the temporal dependence of the T–T\* transition energy and width. The energy decreases by  $\sim 4.5$  meV during the first picosecond, any further change being  $<1$  meV. The variation can be fitted to an exponential decay of time constant 350 fs. Simultaneously, the width decreases from 20 to 12 meV. There are two possible explanation for these shifts. Since almost all the energy deposited in the crystal by the pump pulse is very quickly transformed in vibrational energy, the process being completed in 2 ps, the observed shifts could be thermal; but red shifts upon heating are unusual. Self-trapping would also explain the shifts. Any process significantly shorter than the instrumental time resolution of  $\sim 100$  fs would not be detected. Therefore, if self-trapping occurs, either it causes a change in the transition energy of at most 5 meV or the process is almost completed in  $<100$  fs, which does not seem very likely. However, these results do not directly demonstrate that triplet self-trapping occurs in isolated PDA chains.

The nature of the singlet exciton produced by fusion was not specified either. The case of PDA chains is unusual: this singlet can be either the  $^1B_u$  state or one of the  $A_g$  states within the optical gap, both channels being energetically possible if the triplet is not self-trapped. If trapping occurs, fusion into the  $^1B_u$  exciton then requires that the trapping energy be  $<50$  meV; fusion into an  $A_g$  state would only require that it be at most a few tenths of an eV, assuming that the lowest  $A_g$  state is 0.4 eV below the  $B_u$  exciton, as observed in poly-PTS crystals [52]. A study of residual PA just below the exciton energy where only  $X_2$  absorbs, and/or of delayed fluorescence, at times up to 100 ps, would be useful, but difficult.

A diffusion coefficient can be deduced from  $W$  if the hopping length is known. The fine structure tensor of the PDA triplet, measured on other PDAs, indicates a triplet size of about two repeat units [83, 84]. A hopping length of  $\sim 1$  nm can then be chosen, leading to a diffusion coefficient at 20 K of about  $10^{-4}$  cm<sup>2</sup> s<sup>-1</sup>, which does not change much up to 80 K. This explains the slight motional narrowing of the triplet EPR spectra [84, 93].

### 3.4.6

#### A High-Energy Exciton

The absorption from the strong exciton transition and its associated ionization continuum studied in Sections 3.4.2 and 3.4.3 extends to higher energies as a slowly decreasing, structureless band, strongly polarized parallel to the chain direction. No feature that could be associated with another electronic transition is observed either in polarization below about 4 eV or in absorption or electroabsorption.

Side-groups of DAs often absorb in the near-UV region, obscuring possible chain transitions. 3B and 4B monomers are particularly useful since their lowest electronic transitions are those of the  $C_4$  group itself, all side-group transitions

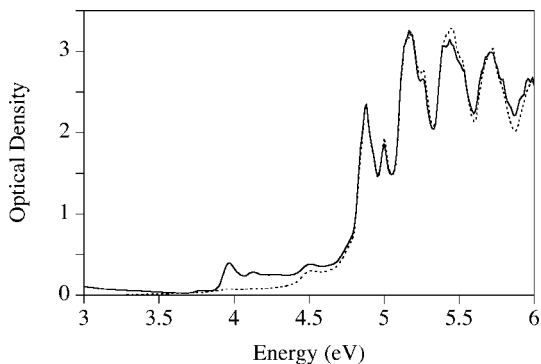


**Figure 3.28** Near-UV absorption of 3B crystals. Dotted line: crystal with  $x_p \approx 10^{-4}$ . Solid line: crystal with  $x_p \approx 10^{-3}$ . From Ref. [74].

appearing at significantly higher energy. In the “pure” monomer ( $x_p < 10^{-4}$ ), the UV absorption starts with a very weak band ( $a = 50 \text{ cm}^{-1}$ ) at 4.512 eV (275 nm), followed by strong structured absorption starting near 5 eV [74]. All this is accounted for by known transitions of the diacetylene molecule [94]. For  $x_p > 10^{-3}$ , another absorption appears at about 4 eV [74], as shown in Fig. 3.28.

This absorption grows linearly with  $x_p$  up to at least  $x_p = 0.07$  and is therefore an absorption of PDA isolated chains. Typical spectra at 10 K are shown in Fig. 3.29 in polarization perpendicular to the chains. Its properties are, however, different from those of the  $^1B_u$  exciton absorption:

1. It is preferentially polarized perpendicular to the chain direction:  $a_{\perp}/a_{\parallel} \approx 3$ .
2. It is much weaker.
3. The spectra in 3B and 4B are more different in intensity and shape.

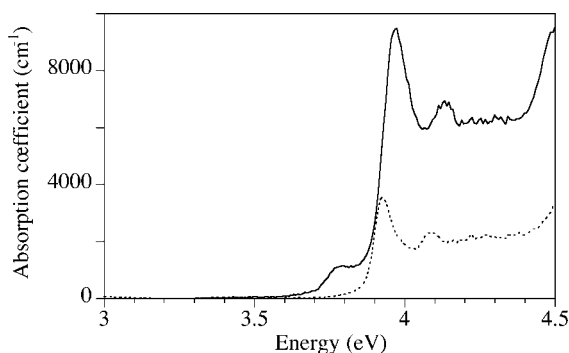


**Figure 3.29** UV absorption, polarized perpendicular to the chain direction, of poly-3B (solid line) and poly-4B (dotted line). The absorption coefficients are calculated as given in the text. From Ref. [74].

A weak band appears at 3.775 eV in 3B only, followed at higher energy by a strong band at 3.965 eV (linewidth  $\Gamma = 80$  meV); the corresponding values in 4B are 3.93 eV and  $\Gamma = 53$  meV. A vibronic D replica appears 168 meV above. The maximum absorption coefficients, for a hypothetical crystal made of isolated chains having the same spectrum, are  $9500$  and  $3600$   $\text{cm}^{-1}$  in 3B and 4B respectively.

Electroabsorption provides further insight. Spectra are typical of a quadratic Stark effect as for the lower lying exciton. This transition is therefore also excitonic, with a comparable polarizability. However, the EA spectra are shifted relative to the derivative of the absorption by 27 and 16 meV in 3B and 4B, respectively, which is not the case at 1.9 eV (Section 3.4.2). A much better fit is obtained by adding a component with the lineshape of the second derivative of the absorption. Fits with the first derivative only and with both components are shown in Fig. 3.30 for 4BCMU

The second-derivative component can be interpreted as due to a coupling with the continuum associated with the lower lying exciton, which, as seen in Fig. 3.28, extends within the range of the UV exciton absorption, this coupling leading to an exchange of oscillator strength. The fit shown in Fig. 3.30 corresponds to an exciton polarizability  $5300 \pm 500 \text{ \AA}^3$ , about two-thirds of the value obtained in Section 3.4.3. Hence this is a strongly polarizable excited state. The second-derivative part corresponds to a large charge-transfer dipole of  $4 \pm 0.5 e \text{ \AA}$ .

All these properties lead to the assignment of the absorption to a transition between a level of the  $\pi$  electrons localized on the acetylenic bonds and the lowest delocalized  $\pi^*$  electron or else between the delocalized  $\pi$  electrons and an empty state of the acetylenic bonds. Note that angle-resolved UPS experiments have shown that the top of the valence band is about 2.5 eV above the second highest (flat) band [72], an energy difference close to that between the two excitons.

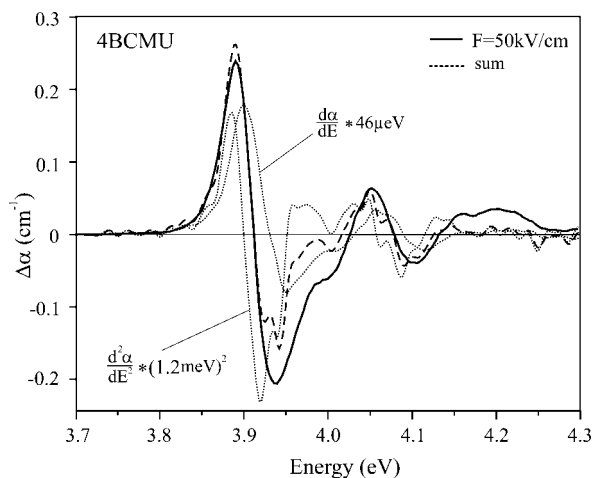


**Figure 3.30** Electroabsorption spectrum of the high-energy exciton (solid line) and its fit with a sum of a first and a second derivative of the absorption (both as dotted lines). The sum is given by the dashed line.

Acetylenic  $\pi$  electrons are usually neglected in theoretical studies of PDA electronic structure: PDA are often treated as a kind of polyene. The fact that the transition found here is more than 2 eV above the lowest lying  $B_u$  exciton which involves only delocalized  $\pi$  electrons validates this approximation for low-lying excited states, although one should of course include all  $\pi$  electrons in a complete description.

### 3.4.7

#### Summary and Discussion

##### 3.4.7.1 Summary of the Main Results Obtained on Isolated Blue PDA Chains

All data are consistent with the assumption that isolated blue chains in their single-crystal monomer matrix are centrosymmetric, as are chains in the bulk PDA crystals. Results for 3B and 4B are very similar, so they may be taken as generic for all blue PDA isolated chains.

The intense absorption in the visible is an excitonic transition with an oscillator strength of  $\sim 1$ . The exciton emits a resonance fluorescence with a very short lifetime ( $\sim 130$  fs) and a very small yield. Therefore:

1. There is no instantaneous self-trapping, but kinetically slower self-trapping is not excluded by this sole result.
2. The exciton relaxation proceeds essentially via non radiative channels.

The exciton is of intermediate size, its Bohr radius being 10–15 Å.

The gap (the threshold for electron–hole pair generation) is  $\sim 2.5$  eV, hence an exciton binding energy of  $\sim 0.58$  eV. The absorption to states of the ionization continuum is small: the spectrum remains dominated by exciton vibronic transitions in the corresponding energy range. The reduced mass of the electron–hole pair is  $< 0.1$  and the coherence length of these states is at least 30 nm. This places a lower limit for the time needed to form polarons from the generated free carriers (if polaron formation occurs at all).

The nonradiative relaxation of the exciton proceeds through several states in the optical gap. These states are not seen in one-photon absorption, hence are not singlet states of  $u$  symmetry. The dominant channel proceeds via two  $A_g$  singlet states in series, with lifetimes of 450 fs and  $\sim 1.7$  ps, respectively. This conclusion rests on the results of two photon-absorption (TPA) measurements on bulk PDA crystals and on the similarity of PDA excitation decay with that observed in polyenes. Transition to these states, which are directly accessible from the ground state by TPA, does not require a large lattice relaxation and it is in that sense distinct from the self-trapping process. A longer ground-state recovery time, of the order of 20–40 ps, is observed, so there must still be another minor decay channel, corresponding to an as yet unknown process. No evidence of a bound biexciton state is observed (however, a small energy range between 1.5 and 1.65 eV could not be studied).

The exciton lifetime explains only part of the experimental width of the absorption lines. The major component above 30 K is a reduced exciton coherence time. The contribution of inhomogeneous broadening is small (a few meV).

The triplets are generated essentially by fission of nonrelaxed singlet states into a pair of triplets of total spin zero. At most a few percent of the singlet excitons decay via fission. The energy threshold for fission is close to the  ${}^1B_u$  exciton energy, hence the energy of the triplets generated in that way is barely above half the singlet energy; therefore, the singlet–triplet splitting is large, 0.9–1 eV. Fission is an efficient process in competition with the very fast relaxation from vibrationally excited singlet states, which has a rate constant of  $>10^{13} \text{ s}^{-1}$ . Triplet pairs recombine rapidly into a singlet state. The triplet motion is diffusive with a diffusion coefficient  $D_T \approx 10^{-4} \text{ cm}^2 \text{ s}^{-1}$ , below 80 K.

All excited states, the  ${}^1B_u$  singlet, the  ${}^1A_g$  states in the gap and the  ${}^3B_u$  triplet, have very strong absorptions to higher lying states, possibly within the ionization continuum of the  ${}^1B_u$  singlet: these absorptions are about one order of magnitude stronger than those from the ground state.

The scheme of excited states of isolated blue PDA chains is shown in Fig. 3.31.

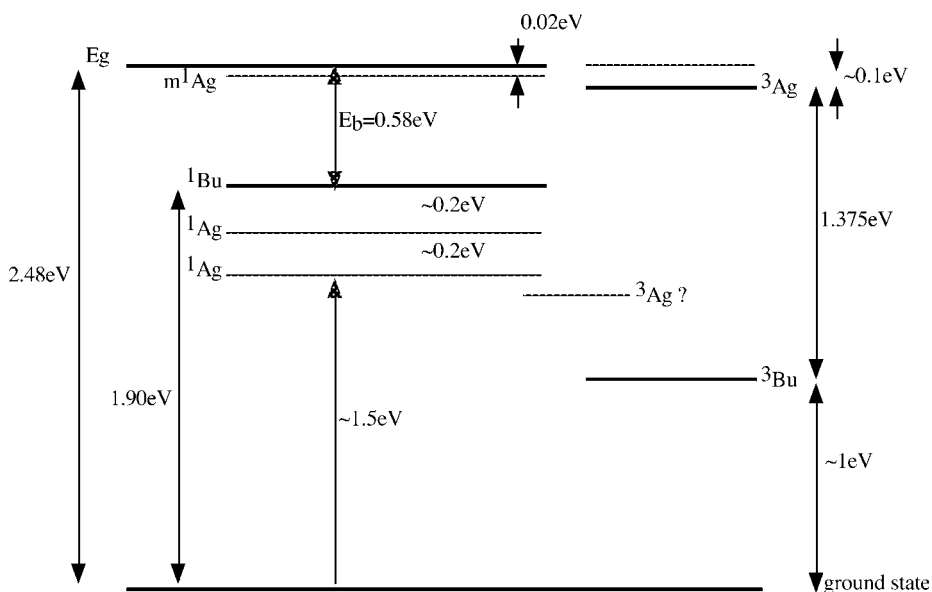


**Figure 3.31** Scheme of excited states in poly-3B chains up to 2.5 eV. Heavy lines are experimentally determined values, thin lines are approximate positions inferred in the text.

### 3.4.7.2 Exciton Size and Binding Energy

A large exciton binding energy  $E_b$  and small oscillator strength of the ionization continuum have been related theoretically to the importance of electron correlations [95].

$E_b$  has been calculated in several different ways for single chains of many conjugated polymers, including PDA, and the calculated values always turn out to be much larger than experimental values when they are known [71]. This is due at least in part to the neglect of the influence of the surrounding medium electronic polarizability, as has long been known in the case of molecular crystals [85]. Several recent papers have considered this correction and in the case of PDA values close to the experimental values reported above, not only for  $E_b$ , but also for the exciton Bohr radius  $R_x$  or polarizability  $p$ , have been obtained [96].

However, one should not forget that a PDA isolated chain may be the most nearly one-dimensional wire conceivable, since its lateral dimensions are of the order of a carbon atom radius. Even though the exciton radius is still relatively small, it is larger than the lateral size of the wire by one order of magnitude, so a PDA isolated chain is indeed electronically a quasi-1-D system. It was shown long ago that an H atom or an exciton have pathological properties in strict 1-D: their binding energy diverges and their size is zero [97]. These divergences are removed by a finite lateral dimension, however small. The problem has been treated exactly, taking into account Coulombic interactions within the framework of many-body semiconductor theory [98]. The effect of the matrix can be included by the image charge method [99]. Application to a poly-3B chain may not be possible, since the chain is one atom wide; however, calculation leads for  $E_b$  and  $R_x$  to values close to the experimental ones [100]. This suggests that the large value of  $E_b$  and small value of  $R_x$  are due at least in part to lateral confinement effects.

The triplet exciton radius has been estimated to be  $\sim 0.5$  nm, based on experimental fine and hyperfine structures [83, 84]. The possible influence of lateral confinement on this radius has never been considered.

### 3.4.7.3 Influence of Electronic Correlations

A recurring problem in the theoretical treatment of electronic properties of conjugated polymers is the importance of electronic correlations [6]: is their role secondary, so that they can be introduced perturbatively if needed [4], or should they be taken into account from the start? Several experimental facts have been related to this question, but, following the discussion above, mostly the ordering of exciton states, i.e. the relative energies of  $B_u$  and  $A_g$  states, will be considered. A detailed discussion is outside the scope of this chapter.

In polyenes, the same ordering of excited states as in PDA is experimentally observed and has been accounted for early on by a quantum chemical calculation including extensive doubly excited configurations, as a way of taking into account correlations [87, 101]. Recent calculations on PDA place the lowest  $A_g$  excited state above the  $B_u$  one, failing to reproduce the experimental ordering [96, 102]. The latter authors proposed that lattice relaxation depresses the lowest  $A_g$  state to

below the  $B_u$  state, but this does not account for the discrepancy, since two-photon absorption experiments measure vertical transition energies and place the  $A_g$  state or states below the  $B_u$  exciton [52]. This might indicate that correlations are important in PDA and not sufficiently taken into account in these calculations. Recent work on the application of the Hubbard model to conjugated polymers may be to the point [7, 8, 103] and the singlet–triplet splitting and transport properties of the triplet may be relevant. We shall return to the problem of correlations in Section 3.7.

#### 3.4.7.4 Comparison with Blue Bulk PDA Crystals

Isolated chains are directly comparable to chains in bulk PDA crystals and only these phases will be considered in the discussion. Even so, the literature on the spectroscopy of PDA crystals is fairly abundant and a critical review of it would exceed the size of this chapter. We shall look for similarities between chains in bulk or isolated as evidence that the properties of the latter are indeed generic, and for differences that might come from interchain interactions in bulk PDA: PDA crystals have generally been considered as ordered assemblies of quasi-1-D systems with very weak interactions. The system studied here may offer an opportunity to test this assumption.

All blue chains in their polymer single crystal have indistinguishable geometries as determined by diffraction methods [16, 17] and indeed very similar vibrational ground-state frequencies as measured by RRS [26]. Hence it is meaningful to speak of “the blue chain in a bulk polymer crystal”. Slight differences in blue PDA crystal properties should therefore be related to different environments provided by the side-groups, different distances and relative orientations of neighboring chains leading to different interactions and possibly to different types and degrees of disorder.

The bond lengths and angles of an isolated chain cannot be measured directly, but the similarities of vibrational ground-state frequencies with those of the bulk polymer indicate nearly identical geometries, even though the repeat unit lengths may differ by a few percent from the relaxed value.

We shall now compare the exciton energy levels, the relaxation schemes and briefly what is known of the ionized states and triplet states.

#### Energy levels

Many properties of the  $^1B_u$  exciton in bulk PDA are very similar to the isolated chains ones: the polarizability and Bohr radius [37], the oscillator strength and, in the case of 4BCMU at least, the absorption dichroism [104]. These properties are not known accurately (they are to  $\pm 10\%$ ) and the isolated chain values fall within the range of the bulk values. Exciton energies  $E_0$  or binding energies  $E_b$  are much more accurately known and differences among bulk PDA are therefore significant. For instance, at low  $T$  (10–15 K),  $E_0$  is 1.865 eV in poly-DCH and 1.965 eV in poly-pFBS, as calculated from reflectance spectra [37]. The other known bulk crystal values fall within that range.

An obvious reason for variations of the transition energy between different PDA is the effect of different dielectric constants and of the presence or absence of permanent dipoles in the side-groups on van der Waals corrections to the energy. The poly-3B isolated chain value  $E_0 = 1.901$  eV falls within the range of values in bulk PDA and the slightly smaller value for 4BCMU,  $E_0 = 1.810$  eV, is convincingly explained by the compressive mismatch imposed by the monomer crystal (Appendix B): a 3% tensile strain on poly-pTS induces a 100-meV increase in  $E_0$  [23].

The relative variations of  $E_b$  among bulk PDA is larger than for  $E_0$  and there are fewer, and often less reliable, data. The smallest value is again that of poly-DCH,  $E_b = 0.478$  eV, and values up to 600 meV have been reported [42]. Again, the isolated chain values fall within that range.

Overall, isolated chains are therefore a good model for all PDA. However, the effects of interchain interactions specific of bulk crystals should be considered.

### Interchain interactions

There are two types of interactions: electrostatic (van der Waals) and quantum mechanical (exchange). There is not much independent experimental information on either.

Several theoretical studies [105–108] predict that van der Waals interactions between parallel conjugated chains should be

- “anomalously” weak
- long range (decreasing as  $r^{-3}$  or even more slowly, instead of  $r^{-6}$ )
- sensitive to relative orientation of neighboring chains.

To compare the isolated chain in its monomer matrix with the corresponding bulk polymer one has to compare the effect of a neighboring chain with that of the stack of monomers it replaces, so it seems difficult to make at this stage quantitative predictions.

Quantum mechanical interactions imply close proximity since the overlap integrals usually decrease with distance  $r$  approximately as  $\exp(-r/0.5 \text{ \AA})$ . If  $r$  is small enough, a 3-D exciton band is formed or at least a 2-D one in a lamellar crystal such as 3B or 4B. This band will have a saddle point at  $k = 0$  and a minimum at the Brillouin zone boundary, since the dispersion of the band in the  $\perp$  direction corresponds to interaction between parallel dipoles. This is important since it would create a new nonradiative pathway specific of the bulk crystal. However, interchain interactions will generally be too small and several processes can localize the excitation on one chain (see the discussion in Ref. [109]), so instead of band formation, interchain hopping will possibly occur [110]. Indeed, the effect of interchain interactions has rather been described up to now in terms of “spatially indirect excitons” [111] or “interchain polarons” [112], meaning a state in which an electron resides on a chain and a hole on a neighboring chain. This interpretation has been disputed, however, and discussing it is not within the scope of this chapter.

Direct evidence of the effect of interchain interactions on optical properties of conjugated polymer films has recently been given for regioregular poly-3-hexyl-

thiophene [113], where the smallest interchain distance is  $\sim 3.8 \text{ \AA}$ . This distance is usually much larger in PDA, for instance  $6.45 \text{ \AA}$  in poly-DCH [114] or close to  $7 \text{ \AA}$  in poly-pFBS [16], all at 300 K. In 3BCMU crystals at low temperature, the distance between nearest neighbor chains would be  $<4.5 \text{ \AA}$  within a lamella (Appendix B), so some such interaction may well be observable in some PDA. However, there is no compelling evidence for it yet.

### Spectral linewidths

An obvious difference between isolated and bulk chains spectra is the linewidths. Room-temperature widths are comparable, but in the bulk there is not much narrowing at low  $T$ . The electroabsorption results on poly-DCH suggest a high quality crystal, so it is not likely that the low- $T$  linewidth in that case,  $24 \text{ meV}$  [37], is due to inhomogeneous broadening. Such a width would correspond to a coherence time of a few tens of femtoseconds. It was shown above that the low- $T$  width in 3B and 4B has a constant part due to the exciton lifetime and a  $T_2$ -type contribution that increases approximately linearly with  $T$ . The larger bulk width might then correspond to a shortened exciton lifetime.

### Relaxation processes

The exciton relaxation kinetics in bulk blue crystals has been studied by several authors using various methods. Here there seem to be differences in the decay of the exciton itself, but not much in the subsequent decay of the states in the optical gap (triplets are considered separately below).

A significant difference is that isolated chains fluorescence is easily observed whereas bulk blue PDA phases are generally said to be “nonfluorescent”. A very low fluorescence has been detected at room temperature, from which a quantum yield of  $\leq 10^{-5}$  was inferred [46]. This is  $\sim 10$  times less than for isolated chains (see Section 3.5.4.1). However, we have observed at 2 K fluorescence from single crystal films of poly-4B prepared by low-energy electron irradiation [115].

Concerning the exciton decay kinetics, a time of  $1.7\text{--}2 \text{ ps}$  at low  $T$  is always observed (see, for instance, Ref. [116]), shortened to  $1.3\text{--}1.6 \text{ ps}$  around room temperature [117, 118]. The situation for the shorter decay times identified above is more confused. The temporal variation of PA during the first picosecond was noted, but the existence of two separate states was not understood, so the  $450 \text{ fs}$  time was not found. In addition, a short time of  $100\text{--}140 \text{ fs}$  was observed in PA and PB at or near room temperature, but is not mentioned at 10 K [118].

The main experimental difference between isolated chains and bulk phases therefore seems to be the estimated room-temperature fluorescence quantum yield. If the  $100\text{--}140 \text{ fs}$  time is the room-temperature exciton lifetime in the bulk, a quantum yield of  $<10^{-5}$  implies a radiative lifetime  $\geq 10 \text{ ns}$ , not in agreement with the estimated oscillator strength of the transition. It will be shown in Section 3.5.3 that the radiative lifetime of the red chain exciton is estimated as  $\sim 1 \text{ ns}$  at room temperature, increasing by a factor of  $\sim 5$  between 10 and 300 K, owing to the quasi-one-dimensional character of the isolated chain. It therefore seems that either the measured  $100\text{--}140 \text{ fs}$  time is not the exciton lifetime or the fluorescence

quantum yield is larger than thought, possibly because the linewidths are large and a very weak structureless emission spectrum may have passed unnoticed.

A longer time is also observed, but only in some experiments, for instance  $11 \pm 5$  ps at room temperature in poly-DCH [118].

Clearly, the situation in bulk phases is similar to that in isolated chains, but is not well understood and should be evaluated again in the light of the present results on isolated chains.

### **Ionized states**

In contrast to the exciton Stark effect, which is not much different in isolated chains and in bulk PDA, the Franz–Keldysh (FK) signal is weakened and may even disappear in bulk PDA, despite the fact that the exciton linewidths are not significantly different (compare, for instance, Refs. [37, 44, 67] with Ref. [65]). It is most likely a consequence of the less perfect intrachain order rather than a loss of 1-D character. This is demonstrated by results on crystals with  $x_p \approx 0.05$  (Section 3.4.6), where the FK signal is much attenuated in poly-4B chains, whereas it is almost unchanged in poly-3B chains, in correlation with the observed slight decrease of order in the former. Hence the FK signal is indeed highly sensitive to intrachain order. This is not surprising, since large FK signals observed in isolated chains or poly-DCH crystals rest on the long coherence length of the carriers,  $\geq 30$  nm, compared with the exciton Bohr radius of  $\sim 1$  nm.

### **Triplet states**

The triplet generation process by fission and the T–T absorption near 1.4 eV also occur in bulk PDA [93]. The absorption linewidth is, however, somewhat larger, of the order of 20–30 meV at 4 K [93, 119]. However, the experimental triplet lifetime is much longer in bulk PDA, from 15 to several hundred  $\mu$ s instead of  $\sim 100$  ps. Yet one would expect the fusion process by 1-D diffusion of the triplets of the generated pair to be active in bulk phases as well. On the contrary, it seems that the generated triplets decay to the ground state individually instead of forming higher energy excitons (singlets or triplets) by fusion. It is not likely that interchain transfer is the cause of this difference: in order to allow most triplets to escape that fusion, the interchain hopping rate should be at least  $10^{11}$  s<sup>-1</sup>, comparable to the intrachain one, whereas there is evidence that the interchain hopping time in poly-pTS at low  $T$  is longer than or comparable to the triplet lifetime, several microseconds [93]. The discrepancy might perhaps be eliminated if, in fact, in the bulk PDA experiments, triplets were generated, one at a time, by carrier recombination rather than by fission. This again is an unsolved problem.

In conclusion, chains in bulk PDA single crystals are weakly interacting quasi-1-D systems similar to the isolated chains. However, except possibly in poly-DCH, the intrachain order in the bulk crystals is not perfect and this has a strong effect on the coherence of the excitations and therefore probably on the intrachain transport properties, which are as yet poorly known.

The interchain interactions seem small, but their strength cannot at present be evaluated, nor their effect on the dynamics of interchain transport.

### 3.5 Red Chain Spectroscopy

#### 3.5.1

#### Another Emission in 3BCMU Crystals

Apart from the resonance fluorescence of blue chains (Section 3.4.3), another emission is observed at higher energy in 3B crystals, provided that the excitation wavelength is shorter than about 540 nm [120]. No such emission is observed in 4B.

##### 3.5.1.1 Low-Temperature Emission Spectrum

Figure 3.32 shows the total emission spectrum of 3B at low temperature (15 K) under excitation at 501.7 nm. Below 1.9 eV there is the blue chain fluorescence discussed in Section 3.4.3. At higher energy, several much more intense and narrow emission lines are present, with an origin line peaking at 543.2 nm (2.282 eV). This zero-phonon line is very narrow ( $\Gamma \approx 1.5$  meV at 15 K) and symmetrical. The two main vibronic lines at 2.093 and 2.014 eV are broadened on their high-energy side. They are shifted from the zero-phonon line by 189 and 268 eV, respectively. These shifts differ from those of the D and T vibronic lines in the emission spectrum of blue chains by a few percent only.

As shown in Table 3.3, they are indeed very close to those observed in red bulk PDA Raman spectra. This spectrum therefore corresponds to emission of PDA chains in the “red” conformation; these chains will from now on be referred to as “red chains”.

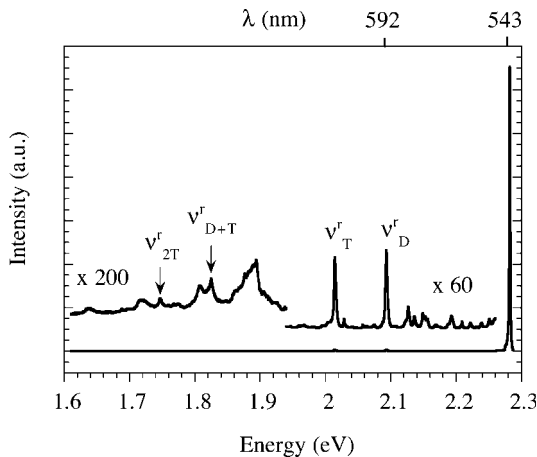


**Figure 3.32** Complete emission spectrum of a 3B crystal excited at 501.7 nm at 10 K. The low-energy part, below 1.9 eV, shows the blue chain emission multiplied by 200. The  $v_i^r$  identify the new vibronic emission lines. Note that  $v_{2,D}^r$  is missing.

**Table 3.3** Vibrational frequencies of red poly-3B chains compared with some typical red PDA phases.

		$\nu_b$	$\nu_T$
Poly-3B isolated chains	Ground state (Raman)	1525 cm <sup>-1</sup> , 189.1 meV	2160 cm <sup>-1</sup> , 267.8 meV
	<sup>i</sup> B <sub>u</sub> exciton (absorption)	186 meV	
Poly-DCH-HS <sup>a</sup>	Ground state (Raman)	1518 cm <sup>-1</sup> , 188.2 meV	
Poly-4B red, 110 C <sup>b</sup>	Ground state (Raman)	1517 cm <sup>-1</sup> , 188.1 meV	2105 cm <sup>-1</sup> , 261 meV

a Ref. [163].

b Ref. [61].

In fact, a few narrow features which appear in Fig. 3.32 within the blue chain fluorescence spectrum can be assigned to vibronic harmonic or combinations belonging to the red chains emission spectrum, for instance D + T or 2T. Note the absence of the 2D harmonic which should appear near 1.904 eV, but is totally reabsorbed since it falls within the blue exciton absorption line at 1.90 eV. This reabsorption indicates that the red chains emission is indeed a volume emission and not a surface one.

### 3.5.1.2 Excitation Spectra

Excitation spectra were obtained by measuring the intensity of an emission line while scanning the excitation wavelength at constant incident photon number. These spectra give the main features of the absorption spectrum. This is useful since, as discussed in Section 3.5.2.1, the direct measurement of the absorption corresponding to the red chain emission is hardly possible. However, an excitation spectrum reproduces the exact absorption spectrum only provided the fluorescence quantum yield is independent of excitation wavelength, implying that no extra nonradiative relaxation channel opens at some energy within the absorption region. An example of such a channel is the singlet exciton fission as discussed in Section 3.4.5 for blue chains.

The low-temperature excitation spectrum, in the origin region, of the D emission line at 2.093 eV is shown in Fig. 3.33a. It peaks at 543.2 nm (2.282 eV) indicating, as in the case of blue chain fluorescence, a resonance emission (for this reason, it is not possible to record in that spectral range the emission in the zero-phonon line itself). The absorption threshold near 2.282 eV is in the expected range for red PDA chains, confirming our assignment to emission from chains in the red conformation.

The vibronic structure of the excitation spectrum of the zero-phonon line at higher excitation energy is shown in Fig. 3.33b [121]. It shows two intense and well-resolved vibronic absorptions corresponding to the D and T lines, at ~2.46 and ~2.54 eV (width ≤10 meV), followed by much less intense overtones and com-

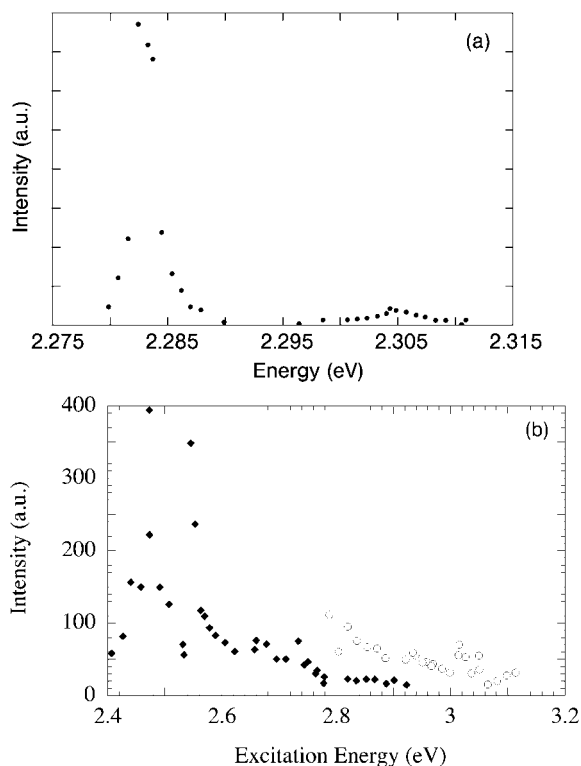


**Figure 3.33** Excitation spectrum of the new emission: (a) In the origin region, showing the zero-phonon line at 2.283 eV and a vibronic line at 2.305 eV, corresponding to a  $135\text{ cm}^{-1}$  chain phonon, (b) At higher energy,

showing in particular two intense vibronic absorptions corresponding respectively to  $\nu_D$  (188 meV above the zero-phonon line) and  $\nu_T$  (261 meV). The intensity scale for the circles has been multiplied by 4.

binations. The excited-state vibrational frequencies deduced from their positions are very close to those measured in the emission spectrum, as in the case of blue chains. Note that the 2D overtone is present in this spectrum, demonstrating that its absence in the emission spectrum is indeed due to reabsorption. The relative intensities are similar to those of the emission lines shown in Fig. 3.32, so emission and excitation are close to be mirror images of each other.

### 3.5.2

#### Absorption Spectroscopy

##### 3.5.2.1 Absorption at 15 K

When studying the visible absorption spectrum of a 3B crystal (see, for instance, Fig. 3.10), no structure corresponding to the excitation spectrum shown above is obvious. However, a careful study in the region of interest near 2.28 eV confirms

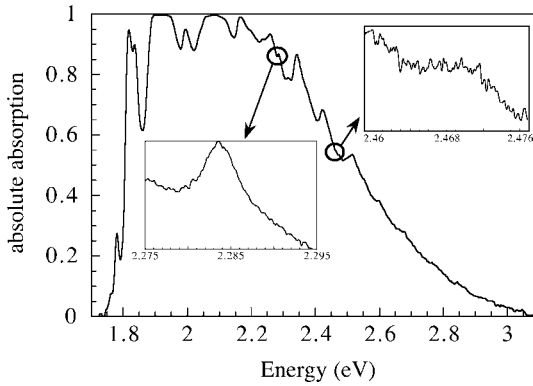


**Figure 3.34** Absorption spectrum of a slightly photopolymerized 3B crystal, plotted as a fraction of the incident light absorbed. The spectrum is almost entirely due to blue chains. A weak narrow line is observed at

2.283 eV (inset), resonant with the emission origin line. A even weaker feature is observed at 2.47 eV, coincident with the  $\nu_D$  line in Fig. 3.33b.

the presence of a weak and narrow absorption line at 2.282 eV, several orders of magnitude weaker than the dominant blue exciton absorption at 1.90 eV (Fig. 3.34). An even weaker feature is observed at the position expected for the D vibronic absorption, at 2.47 eV.

The absorption line at 2.282 eV after subtraction of the blue absorption contribution is compared in Fig. 3.35 with the corresponding emission line. It has a width of 1.6 meV in this case, comparable to the emission linewidth, but that width is sample dependent in the range 1.5–3 meV, indicating that inhomogeneous broadening is present at the 1-meV level. The D line at 2.47 eV has a width of about 4.5 meV, which is therefore probably homogeneous, corresponding to a  $\sim 100$ -fs lifetime of this excited state. The maximum absorption coefficient of the D line is

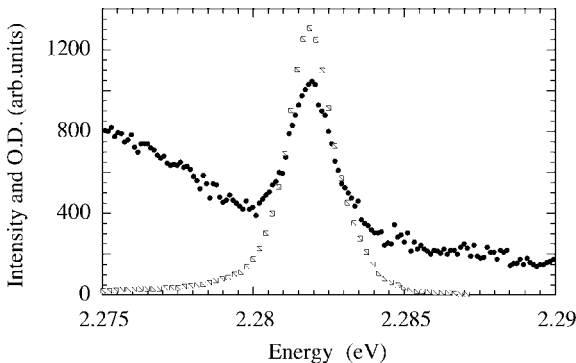


**Figure 3.35** Coincidence of the absorption (filled circles) and emission (squares) lines.

one-tenth of that of the zero-phonon absorption line. Note that the 501.7-nm argon laser line falls within the D linewidth at low temperature.

It is clear from Fig. 3.34 that the red chain absorption is  $10^3$ – $10^4$  times weaker than the blue one. Assuming similar oscillator strengths, the red chain concentration in 3B crystals is therefore at least  $10^3$  times smaller than the blue chain concentration  $x_p$ . Yet the red emission is much more intense than the blue one, hence the fluorescence yield is expected to be large and its experimental determination can be attempted (see Section 3.5.4.1). The exciton relaxation processes are consequently very different from those studied in Section 3.4.4 for blue chains.

### 3.5.2.2 Electroabsorption

The small width of the red chain absorption zero-phonon line allows to detect an electroabsorption signal as shown in Fig. 3.36, with electric field and light polarization both // to the chain direction [122]. The spectrum, although very weak, has the derivative lineshape expected for a Stark shift of an exciton transition. Its intensity is compatible with a red chain exciton polarizability very similar to that of the blue one as discussed in Section 3.4.2.

The red chain absorption is always too small to allow the observation, even qualitative, of any Franz–Keldysh effect, so there is no direct measurement of the gap for red isolated chains. Based on the interpretation of measurements on poly-TCDU red crystals (see Section 3.2.2.2), one would expect it at about 2.9–3 eV [42].

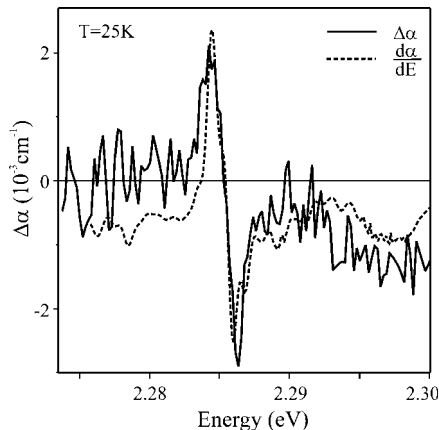


**Figure 3.36** Electroabsorption spectrum (solid curve) of red poly-3BCMU chains at 25 K, in the range of their zero-phonon absorption line, compared with the derivative of the absorption (dotted curve).

## 3.5.3

**Emission and Absorption Temperature Dependence**

Emission spectra can be studied up to room temperature whereas absorption can be followed only up to about 70 K. At all temperatures where absorption spectra can be recorded, the respective zero-phonon lines peak at the same wavelength confirming a resonant emission. It seems reasonable to assume that it keeps resonant at all temperatures.

This emission is still fairly intense at 300 K, although the integrated intensity has decreased by more than one order of magnitude compared with 15 K. The energies of the emission lines shift to the blue and their widths increase with increasing  $T$  in much the same way as the blue absorption in the same 3B crystals, with a more pronounced step at the phase transition temperature near 150 K. This is shown in Fig. 3.37 for the zero-phonon origin line of the spectra.

It is generally accepted that the blue chain geometry in bulk PDA is almost independent of temperature, as suggested by the very small changes in exciton energy or vibrational ground-state frequencies with temperature (see Section 3.4.1.3). In 3B monomer also, the changes of isolated blue chain Raman frequencies between 15 and 300 K remain small: from 1460 to 1450  $\text{cm}^{-1}$  for D and from 2104 to 2078  $\text{cm}^{-1}$  for T, also suggesting that the chain geometry is hardly changing in the whole temperature range. The blue shift of their absorption energy is therefore essentially due to the temperature dependence of the polarization of the monomer matrix, since the unit cell volume increases from 2500 to 2650  $\text{\AA}^3$  (see Appendix B), leading to a variation of the van der Waals corrections to the transition energy.

The parallelism of the curves in Fig. 3.37 then suggests that the red chain geometry as well is independent of  $T$ : the red chains conformation is a well defined locally stable minimum, differing from the blue chain conformation in a way which is not yet firmly established.

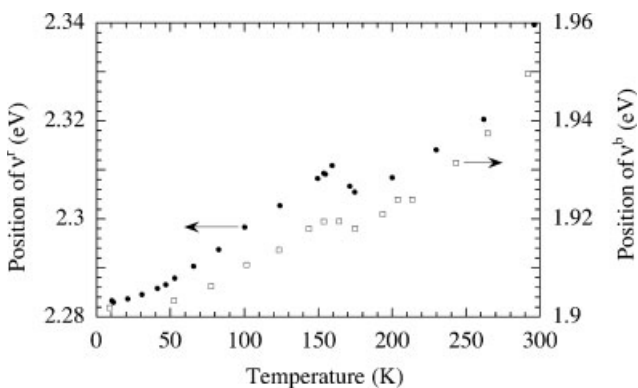


**Figure 3.37** Comparison of the temperature dependences of the energies of the red chain zero-phonon line  $v^r$  (filled circles) and the blue chain exciton absorption  $v^b$  (squares) in 3B.

Figure 3.38 shows that the  $T$  dependences of the widths are parallel, the line-width of the red emission being about 6 meV smaller than the blue absorption. This cannot be due to dissimilar inhomogeneous broadening: it was shown above (Section 3.4.1.3) that the blue chain absorption lines are Lorentzian above about 40 K and it will be shown below (Section 3.6.2.2) that the width of the emission of an ensemble of red chains becomes homogeneously broadened above 40 K. The difference is due at least in part to the contribution of the very small effective lifetime of the blue exciton, which corresponds to a width  $\geq 4$  meV. As discussed in Section 3.4.3.2, another source of homogeneous broadening becomes dominant in blue chains as  $T$  increases and it must correspond to shortened coherence time of the exciton. It will be shown in Section 3.6.2.2 that the same process dominates the red chain emission at least up to 50 K and that it corresponds to a coupling with longitudinal acoustic phonons of the monomer matrix. It then seems likely that for blue chains also the same process is operative with a similar efficiency.

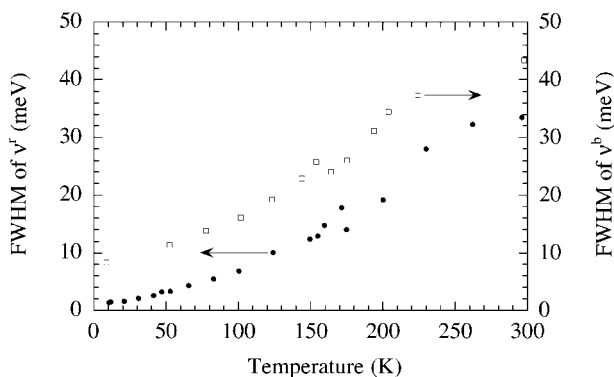


**Figure 3.38** Comparison of the temperature dependences of the widths of the red chain zero-phonon line  $v^r$  (filled circles) and the blue chain exciton absorption  $v^b$  (squares) in 3B.

### 3.5.4

#### Red Chain Exciton Relaxation

The emission intensity is large enough to allow the experimental determination of both fluorescence quantum yield  $\eta$  and emission lifetime  $\tau$ . Once  $\eta$  and  $\tau$  are known, the radiative ( $k_r$ ) and nonradiative ( $k_{nr}$ ) decay rate constants or their inverses the corresponding lifetimes  $\tau_r$  and  $\tau_{nr}$  become accessible.

##### 3.5.4.1 Quantum Yield

The parameter  $\eta$  is defined as the ratio of the number of emitted photons to the number of photons absorbed by the red chains. The main difficulty arises from the presence of the majority blue chain population which absorption is by far

dominant (see Fig. 3.34). The usual comparative method with an emitting standard using an integrating sphere cannot be used here. Moreover, the experimental determination of the number of absorbed photons can only be done where absorption is measurable, that is, at the zero-phonon line absorption wavelength and only up to about 80 K. This implies that fluorescence detection cannot be applied at the resonance wavelength, where most of the light is emitted.

Three quantities must therefore be measured accurately: the total number of photons absorbed at the zero-phonon line wavelength, the total number of photons emitted in the D emission line and the ratio of this emission to the total emission. The experimental details are described in Ref. [123].

Absolute values of  $\eta$  were obtained at 2 temperatures:

$$\eta = 0.30 \pm 0.05 \text{ at } 15 \text{ K};$$

$$\eta = 0.20 \pm 0.05 \text{ at } 40 \text{ K}.$$

The overall variation of  $\eta$  with  $T$  shown in Fig. 3.39 was obtained by measuring relative values of  $\eta$  [124] at different temperatures and adjusting to the two known absolute values. Relative values of  $\eta$  were derived from the spectral integration of the D emission line excited at the resonance absorption wavelength at each temperature. The emission intensities were then scaled to an equal number of absorbed photons, including corrections for the absorption of incident and emitted light by blue chains. The total intensity emitted in all lines, and in particular the dominant zero-phonon line, was then calculated using the measured ratio  $I_D/I_0$  as a function of temperature ( $I_D$  and  $I_0$  are the respective integrated intensities of the D and zero-phonon lines at a given temperature). The quantum yield is a monotonic decreasing function of  $T$  in the whole range where the measurement of the red chains absorbance is possible.

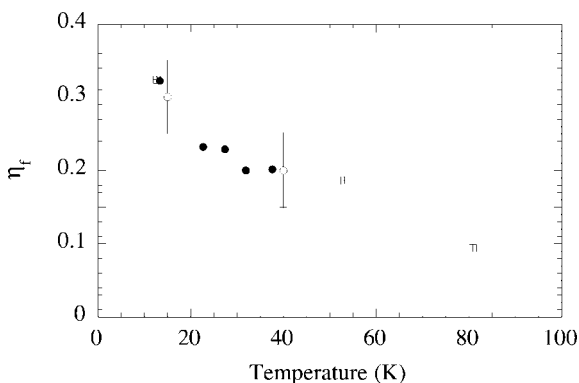


**Figure 3.39** Temperature dependence of the fluorescence yield. The open circles are absolute values, with their uncertainties. The other symbols correspond to two series of measurements of relative yields, scaled to the absolute values.

### 3.5.4.2 Fluorescence Decay Time

Decay times were measured using picosecond exciting pulses at the wavelength of the D absorption line near 500 nm, with excitation intensities of  $\leq 10^{-1} \text{ W cm}^{-2}$ , low enough to avoid any nonlinear effects. The emission in the zero-phonon line was detected with a streak camera [124].

A typical temporal variation of the fluorescence at 14 K is shown in figure 3.40.

The risetime is identical with the instrument response, so the actual emission risetime is shorter than a few picoseconds. The decay is well fitted over more than two decades by a single exponential and this is true at all  $T$ . The decay shown at 14 K gives  $\tau = 94 \pm 2 \text{ ps}$ ;  $\tau$  was measured at several temperatures between 13 and 120 K and the results are shown in Fig. 3.41. The temperature dependence of  $\tau$  is unusual, first increasing up to 50 K and then decreasing rapidly.

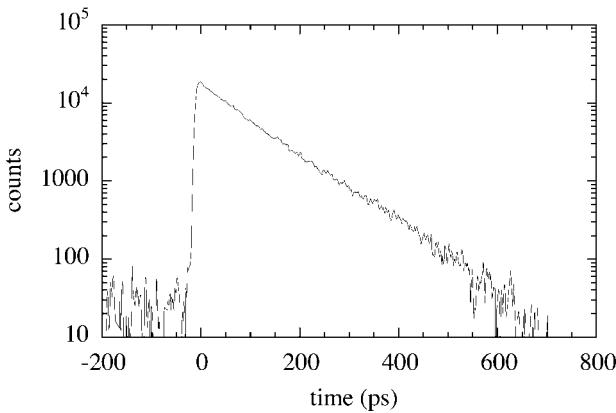


Figure 3.40 Typical fluorescence decay kinetics at  $T = 14 \text{ K}$ .

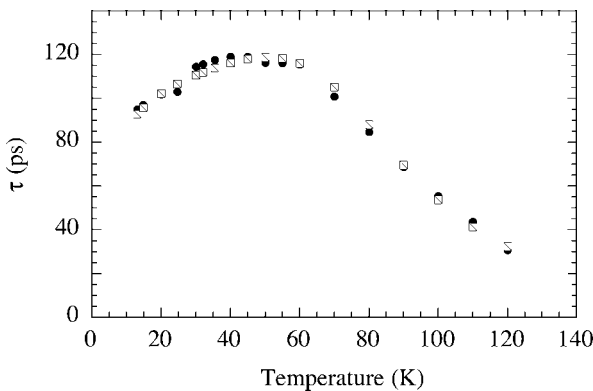


Figure 3.41 Measured fluorescence lifetimes as a function of  $T$  (filled circles) compared with values calculated using the parameters given in the text (squares).

### 3.5.4.3 Radiative Lifetimes

Once  $\tau(T)$  and  $\eta(T)$  are known, radiative  $\tau_r$  and nonradiative  $\tau_{nr}$  lifetimes can be derived at all temperatures, since  $\tau_r = \tau/\eta$  and  $\tau_{nr} = \tau/(1 - \eta)$ .

$\tau(T)$  increases monotonically from about 300 ps at 13 K to about 850 ps at 80 K. In the same  $T$  range, the oscillator strength of the exciton transition remains constant. Therefore, the exciton cannot be considered as a single emitting level where  $\tau_r$  would remain constant.

On the contrary, the observed behavior is explained assuming that the exciton is described as a one-dimensional band of states of well defined momentum  $k$ . The only  $k$  states that are radiatively coupled to the ground state are those where  $k$  is smaller than the photon momentum  $\approx 0$  and the population with temperature of nonradiant, higher lying, states with  $k \neq 0$  decreases the overall radiation rate. Theory predicts that for a 1 D exciton band  $\tau_r = AT^{1/2}$ . The measured values of  $\tau_r$  follow this law as shown in Fig. 3.42, with  $A = 80 \pm 20 \text{ ps K}^{-1/2}$ .

An explicit calculation of  $\tau_r$  has been carried out in the case of semiconducting quantum wires [125]. Assuming the applicability of that calculation to the type of polymeric quantum wire studied here (which admittedly is bold, but we are just looking for orders of magnitude), the expression for the radiative lifetime:

$$\tau_r = \frac{2m_0\epsilon_0}{3aE_{\text{ex}}^0} \frac{1}{f_L} \sqrt{\left(\frac{k_b T}{\pi E_1}\right)}$$

can be used to estimate the exciton effective mass  $m_{\text{ex}}^*$  which is the only unknown quantity in the above expression. This expression corresponds to an infinite coherence length, so it only yields an upper limit of the exciton effective mass.  $E_{\text{ex}}^0 = 2.28 \text{ eV}$  is the exciton energy at  $k=0$  and its dependence on  $T$  is neglected in the  $T$  range considered.  $E_1$ , given by

$$E_1 = \frac{\hbar k_{\text{ex}}^2}{2m_0 m_{\text{ex}}^*}$$

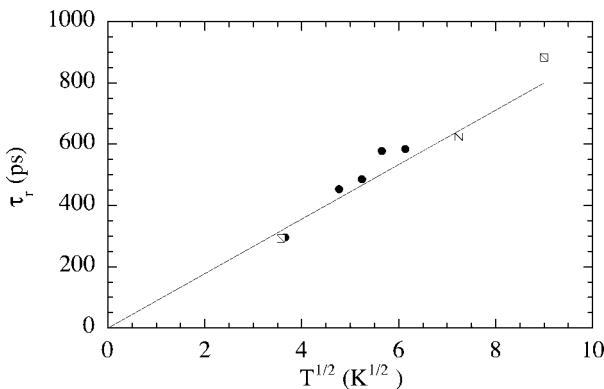


**Figure 3.42** Temperature dependence of the radiative lifetime. Two series of measurements are shown.

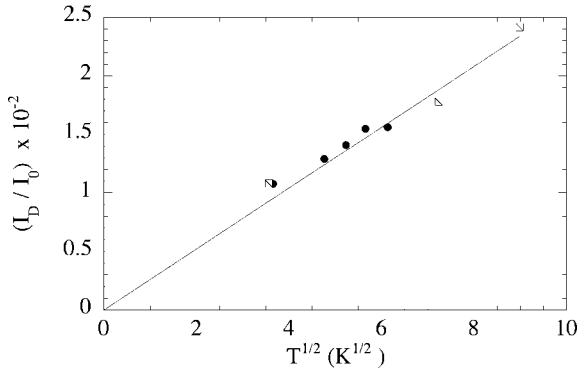


**Figure 3.43** Temperature dependence of the ratio of the integrated intensity  $I_D$  of the D vibronic emission to the integrated intensity  $I_0$  of the zero-phonon line.

is the energy of the exciton band level for which the momentum  $\mathbf{k}_{\text{ex}}$  is equal to the emitted photon momentum.  $f_L$  is the exciton absorption oscillator strength per unit length of chain. It can be evaluated for blue chains by integrating the exciton absorption spectrum,  $f \approx 0.5$  per repeat unit of the chain and using the repeat unit length of  $5 \times 10^{-10}$  m. This yields  $f_L \approx 10^9 \text{ m}^{-1}$ .

In this equation, the only unknown is the exciton effective mass  $m_{\text{ex}}^*$ , which may then be estimated from the measured value of  $A$ :  $0.1 \leq m^* \leq 0.3$ , where the large uncertainty is due to the fact that several quantities in the equation are only approximately known. This value of  $m_{\text{ex}}^*$  is to be compared with that estimated for the “blue” exciton, from electroabsorption measurements,  $m^* \approx 0.1$  (Section 3.4.2). Moreover, angle-resolved UPS experiments lead to a hole effective mass  $m_{\text{h}}^* \approx 0.1$  [72].

In an exciton band, any  $k$  state is radiatively coupled to the state of same  $k$  in the D vibrational band (or any other such band) of the ground state. Exciton states of all  $k$  thus contribute to the total D line emission, whereas only those near  $k = 0$  contribute to the zero-phonon line emission. Assuming that the emission probabilities to the D band are independent of  $k$  (which seems reasonable, since only states of small  $k$  are populated at the studied temperatures), the corresponding radiative lifetime is not  $T$  dependent, so the ratio  $I_D/I_0$  is predicted to vary as  $T^{1/2}$ . Our experimental data fit such a law, as shown in Fig. 3.43.

Emission from  $k \neq 0$  states also accounts for the asymmetric broadening of the D emission line and its increase with temperature (see also Section 3.6.2.1).

#### 3.5.4.4 Nonradiative Lifetimes

The nonradiative lifetime can be calculated using  $\tau_{\text{nr}} = \tau/(1 - \eta)$  up to 80 K. But  $\tau$  could be measured up to about 150 K; assuming that the relation  $\tau_r = AT^{1/2}$  still holds up to 150 K,  $\tau_{\text{nr}}$  was calculated from the experimental values of  $\tau$  between 80 and 150 K. The results are shown in Fig. 3.44.

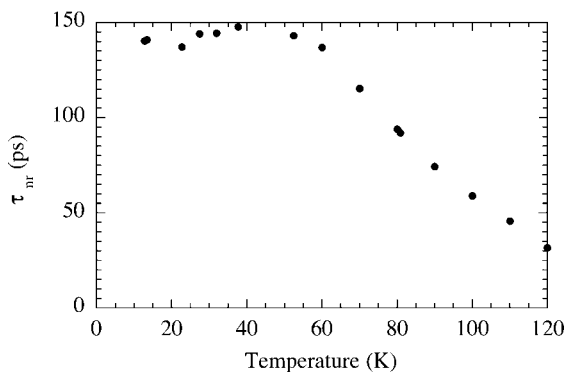


**Figure 3.44** Temperature dependence of the nonradiative lifetime.

There are two  $T$  ranges. Below 50 K,  $\tau_{\text{nr}}$  is practically independent of  $T$ ,  $\tau_{\text{nr}} = 145 \pm 10$  ps or a rate constant of  $7 \times 10^9 \text{ s}^{-1}$ . Above 50 K,  $\tau_{\text{nr}}$  starts to decrease, down to  $\tau_{\text{nr}} \approx 30$  ps at 120 K. The effective lifetime  $\tau$  could only be estimated at higher  $T$ ; it seems to stabilize above 250 K at  $\tau \approx 5\text{--}10$  ps. This would also be approximately the value of  $\tau_{\text{nr}}$  around room temperature.

This variation can be fitted assuming that, in addition to a  $T$ -independent term, there is an exponential term with an activation energy  $\Delta E \approx 40$  meV and pre-exponential factor of  $\sim 1\text{--}2 \times 10^{11} \text{ s}^{-1}$ . This factor would be the infinite temperature limit of the corresponding rate constant and corresponds to the effective lifetime  $\tau$  at 300 K.

In discussing these variations, one should take into account all  $k$  states of the exciton band. A  $T$ -independent term implies that all  $k$  states that are thermally populated at least up to 50 K have similar nonradiative rate constants: if only the  $k \approx 0$  states were active,  $\tau_{\text{nr}}$  should be proportional to  $T^{1/2}$  as  $\tau_r$ . An increase in the relaxation rate (decrease in  $\tau_{\text{nr}}$ ) above 50 K implies that higher lying  $k$  states have larger relaxation rates than the lower ones. This may be either because the rate of the same process operative a lower  $T$  abruptly increases beyond a certain value of  $k$  or because a second nonradiative channel opens at an energy about 40 meV above the bottom of the exciton band. The latter seems more likely and there are in fact several potential candidates for this second process. In that case, there are two nonradiative channels for the exciton.

The  $T$ -independent process can be accounted for by relaxation to a lower lying excited state, as for blue chains. However, since its rate constant is three orders of magnitude smaller than for blue chains it is highly unlikely that the final state for this process would be a lower excited singlet  $A_g$  state. The process should therefore be either intersystem crossing to a lower lying triplet or direct internal conversion to the ground state. There is at least one  $B_u$  triplet in the optical gap, but the position of the lowest triplet  $A_g$  state is not known. This triplet corresponds to the singlet  $A_g$  state which was in the blue chain gap and has been pushed to higher energy in the red chains. In either case, one would expect a smaller rate constant. However, a recent theoretical study of phenylethyne oligomers, which share

with the PDA the presence of a triple bond in the chain, suggests that the presence of acetylenic orbitals and a departure of the chain from planarity might greatly enhance the intersystem crossing [126].

There are several possible origins for the temperature dependent process, which will only be mentioned here:

- Singlet exciton fission into two triplets, as observed in blue chains; in that case the lowest triplet would be in red chains close to the middle of the optical gap as in blue chains.
- Another exciton band having its  $k = 0$  state 50 meV above the  $B_u$  singlet, for instance an  $A_g$  exciton, as found within the optical gap in blue chains, could open a new intersystem or internal conversion channel.

A further experimental study of these questions would require direct measurement of densities of triplets or other transient excited states and their time dependence by pump-probe spectroscopy. However, this is not possible at present on red chains, since any signal would be obscured by the much more intense signal from the blue chains.

The nonradiative rate constant extrapolated to infinite temperature from the above measurements is  $\approx 10^{11} \text{ s}^{-1}$ . This is two orders of magnitude smaller than the blue exciton decay rate into excited  $A_g$  states. Hence, either the thermally activated channel is not a decay into an  $A_g$  state or the  $B_u \rightarrow A_g$  nonradiative transition is much slower in the red than in the blue chains. This would be unexpected and require a theoretical explanation. However, the transition in red chains is from  $k$  states in the exciton band which are not close to  $k = 0$  and the above reasoning implicitly assumed that the transition matrix elements do not vary much with  $k$ . To explain all observed results, they would have to increase steeply as  $k \rightarrow 0$ .

The actual nonradiative relaxation rate, and hence the fluorescence yield, of various red PDA phases would depend sensitively on the value of  $\Delta E$ , as long as it is positive. In contrast,  $\tau$  should not, if  $\Delta E < 0$ , depend much on which red phase is studied. There are some experimental data on fluorescence yields in red phases and on the existence or not of a two-photon absorbing state below the  $B_u$  exciton. Single-crystal films of red poly-4B, prepared by irradiation with low-energy electrons [115], have a fluorescence lifetime of a few picoseconds at 300 K and an estimated fluorescence yield  $\leq 10^{-2}$ , not very temperature dependent [127]. Comparable values have been reported in other red PDA. For instance, a substituted poly-DCH which forms red solutions has a fluorescence yield at room temperature of  $\sim 10^{-2}$  [128]. In spin-cast films of the same material, an  $A_g$  state was observed in two-photon absorption  $\sim 150$  meV below the  $B_u$  exciton [129]. Similarly, a yield  $\eta \approx (2 \pm 1) \times 10^{-2}$  at room temperature was reported for Langmuir-Blodgett multilayers [47] and again two-photon absorption has been observed below the red exciton in a similar material [130]. Taken together, these observations suggest that the nonradiative decay rate constant of the red exciton into an  $A_g$  state might indeed be much smaller than for blue chains

Clearly, more experimental work is needed.

## 3.6

## Study of a Single Isolated Red Chain: a Polymeric Quantum Wire

## 3.6.1

## Feasibility of Studying a Single Isolated Red Chain. Experimental Method

A rough estimate of the average lateral distance between red chains, assumed to be randomly distributed in the 3B crystal, is  $\sim 1 \mu\text{m}$ . It is therefore in principle possible to excite a single red chain at the focus of a microscope objective and to collect its emission through the same objective: this is a microphotoluminescence ( $\mu\text{PL}$ ) experiment [131]. The spatial resolution of this experiment is  $1\text{--}3 \mu\text{m}$  and its spectral resolution  $50\text{--}100 \mu\text{eV}$ . Moreover, red chain emission at low  $T$  has other attractive features, a high yield and an intense zero-phonon line, so the fluorescence signal from a single chain may well be large enough. In this section, the results obtained to date in such experiments will be presented and discussed. All experiments have used continuous excitation; no time-resolved study is available.

Spectra recorded in usual macroluminescence of an ensemble of red chains discussed above and in  $\mu\text{PL}$  are compared in Fig. 3.45 [131]. Panel (a) shows a typical zero-phonon emission line at  $2.282 \text{ eV}$  from an ensemble of chains at  $10 \text{ K}$ , excited at  $501.7 \text{ nm}$ . It is not Lorentzian and its  $\text{FWHM} = 2 \text{ meV}$ . Panel (b) shows the  $\mu\text{PL}$  emission of a crystal containing a fairly high red chain concentration (inferred from the macroluminescence intensity of that crystal), under the same excitation conditions: several (at least eight, some overlapping) narrow lines with unequal heights are seen, within the energy range spanned by the macroluminescence emission line. Panel (c) shows the same from a crystal with a low concentration of

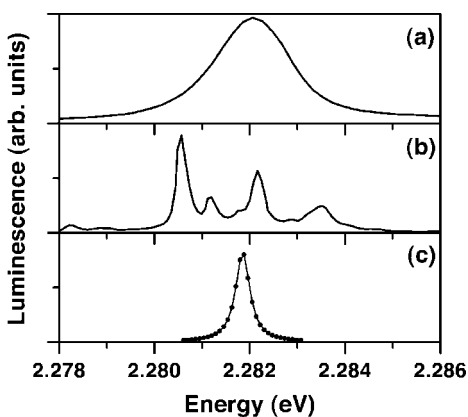


**Figure 3.45** Comparison of the zero-phonon emission line at  $15 \text{ K}$  of an ensemble of red poly-3BCMU chains, studied in Section 3.5 (a), with microfluorescence spectra, when several individual chains are simultaneously

excited (b) and when there is a single chain in the excited region (c). The spectrum (c), solid line, is compared with a Lorentzian fit (dots).

red chains: the emission is a single narrow line; the dots are a Lorentzian fit with  $\text{FWHM} = 500 \mu\text{eV}$ . Clearly in this case a single chain is excited, emitting a homogeneously broadened luminescence line. Panel (b) is therefore understood as the emission of several individual red chains, unequally excited by the incoming beam because they unequally overlap it, all lines having the same width.

Two kinds of experimental conditions can be achieved. The chain can be excited “resonantly” within the zero-phonon absorption line (near 2.282 eV at 10 K) creating a purely electronic excitation, or “nonresonantly” at higher energy, where the absorption creates a vibronic excitation. In resonant excitation, it is not possible to study the zero-phonon emission, which is at the same energy and has the same polarization as the excitation beam, so only vibronic emission lines can be studied, whereas in nonresonant excitation, all lines can be studied.

The excitation processes are not identical for the two types of experiments. In resonant excitation, an exciton in its  $k \approx 0$  state is created directly and subsequently evolves by phonon scattering as shown below or by photon emission. In nonresonant excitation, a composite vibronic state of total momentum  $\sim 0$  is created first, which then has to produce a zero-energy exciton. In the time-resolved experiments reported in Section 3.5.4, no fluorescence risetime has ever been detected, so the radiant  $k \approx 0$  exciton states are populated within at most a few picoseconds. In fact, most nonresonant excitations used the 501.7-nm argon laser line which, as can be seen in Fig. 3.34, falls within the homogeneous linewidth of the D absorption line at all temperatures used, which indicates a lifetime of the order of 100 fs. In similar excitation conditions, the blue fluorescence risetime is at most 40 fs (Section 3.4.3.3), so the  $k \approx 0$  exciton states are populated almost instantaneously and then can evolve as they do under resonant excitation. The differences in the initial excitation processes will therefore be neglected.

### 3.6.2

#### One Exciton per Chain. Lineshape Analysis

Since the lifetime of an exciton is  $\sim 100$  ps, it is possible to create  $\sim 10^9$  excitons per second on a single chain and still keep conditions in which there is never more than one exciton present on the chain. It will then emit  $>10^8$  photons per second, most of them in the zero-phonon line, and  $\geq 10^6$  in each of the most intense vibronic emission lines, the D and T ones.

##### 3.6.2.1 The Vibronic Lines. A One-Dimensional Exciton Band

Figure 3.46 shows two vibronic D lineshapes at 15 and 40 K under the same conditions as above. These lines are much broader than the zero-phonon line, with a high-energy side broadening asymmetrically as  $T$  increases.

It was concluded in Section 3.5.4.2 that the radiative lifetime of the zero-phonon line showed the  $T^{1/2}$  dependence predicted for a quasi-one-dimensional system, in the whole  $T$  range studied; the states radiating in the zero-phonon transition became diluted as  $T$  increases in nonradiative ones, which however did contribute

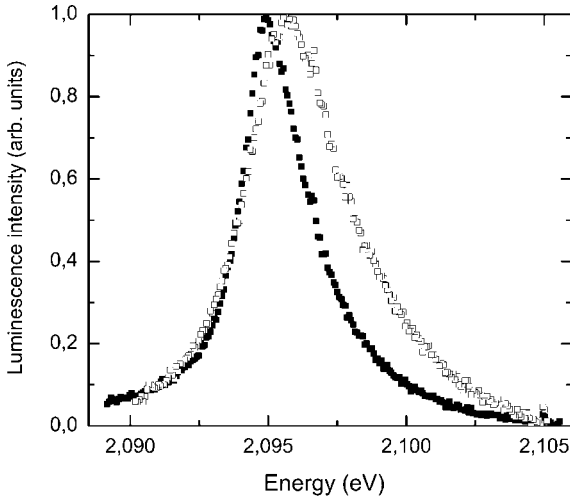


**Figure 3.46** The D line vibronic lineshape at 15 K (filled squares) and 43 K (circles).

to the vibronic emissions. This is easily understood in a band model by looking at the scheme in Fig. 3.47.

In a quasi-1-D system, only the exciton band states with momentum  $k \approx 0$ , in fact  $k \leq q$  the photon momentum, are radiatively coupled to the ground state. These states are confined to a very narrow range near the band minimum at  $k = 0$ . But any  $k$  state in the band may in principle be radiatively coupled to any vibrational level of the ground state, since the generation of a phonon with the same momentum  $k$  will ensure momentum conservation. This is the origin of the  $T^{1/2}$  dependence of  $\tau_r$  and of the increase in the relative contribution of vibronic emission as  $T$  increases that are observed.

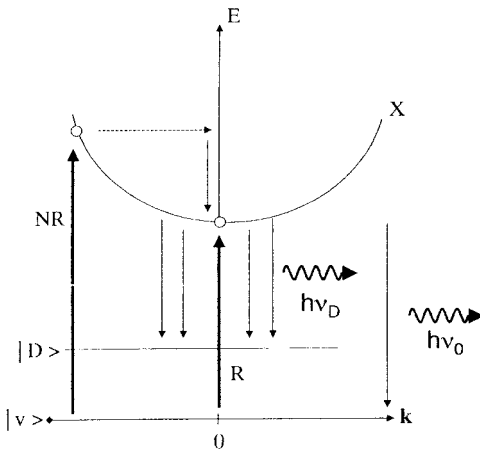


**Figure 3.47** Excitation and emission of a single chain. The arrow labeled R corresponds to resonant excitation within the zero-phonon absorption line, the arrow NR to nonresonant excitation (usually within the D absorption line). Emission  $h\nu_0$  from the exciton band X to the ground state  $|v\rangle$  can only occur at  $k = 0$ , whereas emission  $h\nu_D$  to the ground state vibrational band  $|D\rangle$  can be from any  $k$  state.

The emission shown in Fig. 3.46 comes from a single chain, without any inhomogeneous broadening, as verified on the corresponding zero-phonon line. It is therefore possible to analyze its lineshape as that of a perfectly ordered system.

Such lineshapes can be quantitatively accounted for all  $T$  and all vibronic lines as coming from a thermalized exciton population. This means fitting it with the equation

$$I(E) = \frac{A}{(E - E_0)^2 + \Gamma_{\text{vib}}^2} \left[ \text{DOS} \exp - \left( \frac{E - E_0}{kT} \right) \right]$$

where  $I(E)$  is the emission intensity at photon energy  $E$ . The factor  $A$  and the energy  $E_0$  are fixed by the experimental position and intensity of the emission maximum,  $\text{DOS}$  is the chosen density of states function,  $T$  is the *crystal* temperature, independently measured, and  $\Gamma_{\text{vib}}$  is a Lorentzian width, the only adjustable parameter.

The assumptions made in writing this equation are as follows:

1. The exciton is in thermodynamic equilibrium with its surroundings, the 3B crystal matrix. Hence the ensemble of excitons (all successively generated on the same chain), the emission of which is recorded during the experiment, follow a Boltzmann distribution among the accessible states. This is not in fact an assumption, since it will be proved in Section 3.6.2.2 by analysis of zero-phonon lineshapes.
2. There is a continuum of  $k$  states. If each repeat unit of the chain contributes one state to the band and assuming  $5 \times 10^4$  units and a 1-eV bandwidth, the average distance between states is  $20 \mu\text{eV}$ , the density of states is then large enough. This would not be true if the chain was in fact a collection of "boxes", i.e. if conjugation lengths were much less than the chain total length; each box would then contain a smaller number of discrete states. Simulation of resulting lineshapes indicates that some structure would appear on the high-energy tail of the emission band for conjugation lengths smaller than about 400 nm [100]. But here again, this assumption is proved by the spatial resolution experiments discussed in Section 3.6.3.
3. The matrix elements for the optical transition to the D phonon band (in the case of the figure) are assumed independent of  $k$ . This is not unreasonable, since even at the highest  $T$  used of 50 K, the thermally populated  $k$  exciton states extend only into a small fraction of the Brillouin zone and the point at  $k=0$  is not singular.
4. All homogeneous broadening processes are lumped into the single parameter  $\Gamma_{\text{vib}}$ . In a vibronic D emission, for instance, the final state contains a D phonon which has a finite coherence time, so it will contribute to  $\Gamma_{\text{D}}$  in addition to the contri-

bution of the finite coherence time of the initial state (which is the only contribution to the zero-phonon line). Hence  $\Gamma_{\text{vib}}$  can vary from one vibronic line to another. The fitting equation assumes that  $\Gamma_{\text{vib}}$  is independent of  $k$ . This is probably not strictly true, but the sum over  $k$  within the range  $\Gamma_{\text{vib}}$  is probably sufficient to reduce this effect to an undetectable level in the present experiments. The temperature dependence of  $\Gamma_{\text{D}}$  will be discussed below after that of  $\Gamma_0$ .

Results of such a fit are shown in Fig. 3.48 [132]. Panel (a) shows an experimental result at  $T = 43$  K, with the fit using a 1-D DOS in a parabolic band, proportional to  $(E - E_0)^{-1/2}$ , with the well known singularity at the origin. The agreement with experiment is very good; this is quantified in panel (b), where the relative errors (dots) are plotted. Also shown are the relative errors (open circles) for the “best” fit using a constant, energy-independent DOS (as in a 2-D system). All fits with a 1-D DOS, for all vibronic lines of all samples and at all temperatures are of the same quality.

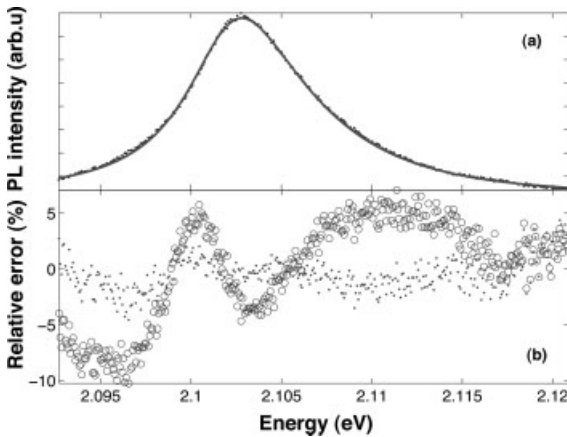


**Figure 3.48** Lineshape of the D emission line at 2.102 eV, at 43 K, and its fit using a 1-D density of states function. (a) Experimental results (points) and the fit (solid line). (b) Relative error using the 1-D DOS (points) and a constant density of states (open circles).

This directly demonstrates that the exciton in red PDA chains should not be considered as an energy level (as is usually done in discussing the properties of conjugated polymers), but that a whole exciton band has to be taken into account. It confirms the conclusions proposed in Section 3.5 that one is actually dealing with a broad exciton energy *band*. The chain is actually a well-behaved quantum wire.

### 3.6.2.2 The Zero-Phonon Line, Exciton Coherence Time and Scattering Process

The measured linewidth of  $500\mu\text{eV}$  ( $4\text{ cm}^{-1}$ ) at 10 K is much too large to correspond to the exciton lifetime of about 85 ps at that temperature. It is therefore determined by a coherence time limited by intraband scattering processes.

The loss of coherence can be due to transitions between different  $k$  states of the band. Since the radiant states which coherence time determines the zero-phonon linewidth lie at the bottom of the band, they only can absorb energy, making a transition to a higher lying  $k \neq 0$  state. The only available excitations at low enough  $T$  are acoustic phonons. Chain acoustic phonons are 1-D excitations as excitons are and conservation of 1-D momentum implies that the only allowed transition is between  $k=0$  and  $k=k_{1\text{-D}}$  as shown in Fig. 3.49.

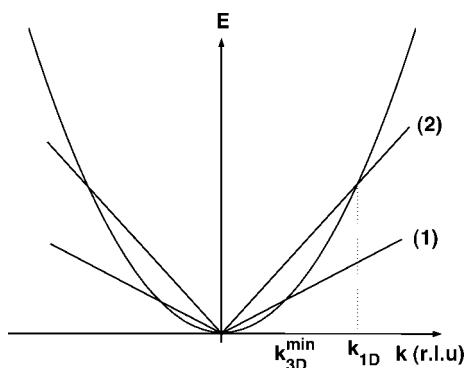


**Figure 3.49** Energy dispersion of the exciton band (parabola) of the 3 D matrix longitudinal acoustic phonons (1) and of the 1-D chain longitudinal acoustic phonons (2).

$k_{1\text{-D}}$  is the only accessible  $k$  point of the exciton band with 1-D phonons, whereas all points beyond  $k_{3\text{-D}}^{\text{min}}$  are accessible with 3-D phonons.

This transition cannot thermalize the exciton population, so the effect of 3-D phonons of the 3B crystal matrix must be considered. A sufficiently strong interaction will assure that the exciton will acquire the temperature of the lattice, as observed.

The experimental data are shown in Fig. 3.50 [132]. The zero-phonon linewidth increases approximately linearly with  $T$ , but has a finite limiting value as  $T \rightarrow 0$ ; the lowest experimentally attained  $T$  was 6 K.

One possible approach is to treat the exciton–phonon interaction in the deformation potential approximation commonly used in semiconductors for that purpose [133]. Since 3B is a centrosymmetric crystal (Appendix B), only 3-D longitudinal acoustic (LA) phonons need be taken into account [134]. In this model, the 1-D character of the exciton only imposes that the component of the momentum parallel to the chain direction be conserved, hence a cutoff: interaction with all 3-D phonons with  $k > k_{3\text{-D}}^{\text{min}}$  is allowed. Besides parameters that are already approximately known such as the sound velocity which determines  $k_{3\text{-D}}^{\text{min}}$ , the

exciton Bohr radius (taken as similar to that of blue chains) and its effective mass (deduced from radiative lifetimes, see Section 3.5.4.3), the only adjustable parameter is the deformation potential  $D_p$  itself. Calculation [129] shows that a quantitative fit is obtained (solid line in Fig. 3.50) for  $D_p \approx 6$  eV, a reasonable value, provided a constant term of  $\sim 150 \mu\text{eV}$  is added. This term cannot be due entirely to the finite spectral resolution of the experiment, which is rather  $50\text{--}100 \mu\text{eV}$ ; so it indicates that this description breaks down at low enough  $T$ . One possible cause is that at low enough  $T$  very small residual potential fluctuations finally localize the exciton. Extension of these experiments to lower  $T$  is in progress.

One should not give too much credit to the quantitative aspects of the fit. The chain stiffness is very different from that of the surrounding medium (see, for instance, Ref. [132] for blue chains), so it is actually for the phonons a linear defect – somewhat similar to a dislocation core –. Hence the momentum conservation rule might not be strict, the scattering rate might be larger and a different microscopic quantitative approach might be more appropriate. It is best to conclude that the 1-D exciton certainly is scattered among the band  $k$  states by interaction with 3-D LA phonons, thus ensuring exciton thermalization in a time short compared with the exciton lifetime, except possibly at temperatures much lower than 6 K.

The coherence time of  $<2$  ps is therefore a fundamental feature of the system, which places strict constraints on any possible application, in quantum computing for instance.

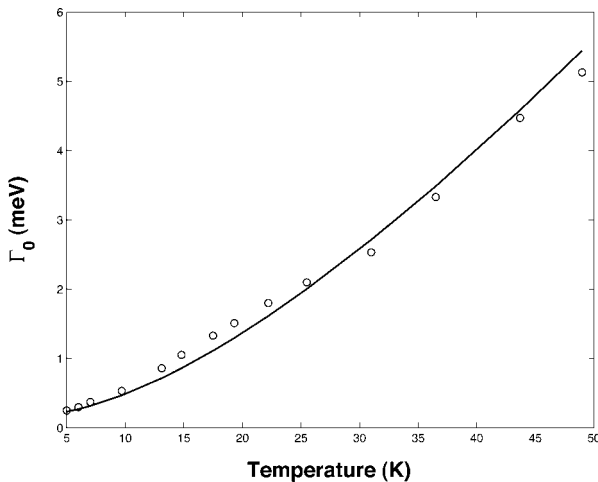


**Figure 3.50** Temperature dependence of the zero-phonon emission linewidth (circles) and the corresponding fit (solid curve).

### 3.6.2.3 Lorentzian Component of the Vibronic Linewidth. Optical Phonon Coherence

The empirical parameter  $\Gamma_D$  and the measured zero-phonon linewidth  $\Gamma_0$  are compared as a function of  $T$  in Fig. 3.51.

It is tempting to consider  $\Gamma_D$  as the sum of a component  $\Gamma_0$  associated with the initial state and a component  $\Gamma_D - \Gamma_0$  corresponding to the D phonon coherence time. This can only be an approximation, since for most of the initial states  $k$  is not zero and such states can be scattered by phonon emission, not only absorption, so they should have a shorter coherence time than the  $k \approx 0$  states. Hence  $\Gamma_D - \Gamma_0$  is only an upper limit of the final state contribution and the corresponding time a lower limit of the phonon coherence time. However, some qualitative conclusions are possible:

- The parallel variation with  $T$  of dots and circles suggests that the phonon coherence time is only weakly temperature dependent.
- The values deduced from the crosses for different vibronic lines vary between 300 fs (for D and T) and 600 fs (for the  $1200\text{-cm}^{-1}$  phonon). These values are in all cases close to those measured by CARS for blue chains in another PDA [136, 137]. This is another indication of the similarities of the ground states of blue and red chains.

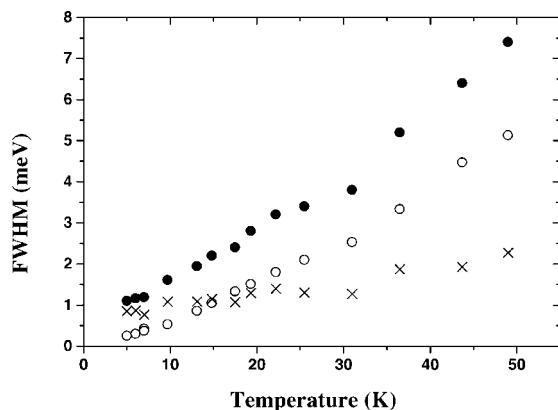


**Figure 3.51** Temperature dependence of the zero-phonon linewidth  $\Gamma_0$  (open circles) compared with the Lorentzian linewidth  $\Gamma_D$  used in fitting the D emission line (solid circles). The crosses are the differences between these two values.

## 3.6.3

**Spatial Extension of the Emission**3.6.3.1 **The Method and a Typical Image**

By adapting an imaging spectrometer to the  $\mu$ PL setup, it is possible to record a 2-D “artificial image” in which the ordinate axis is a space coordinate, here chosen along the chain direction and the abscissa is a spectral coordinate as in an ordinary spectrometer. The image thus shows along each horizontal line the spectrum of the light emitted at the point of the chain corresponding to the ordinate of that line. Such an image is shown in Fig. 3.52.

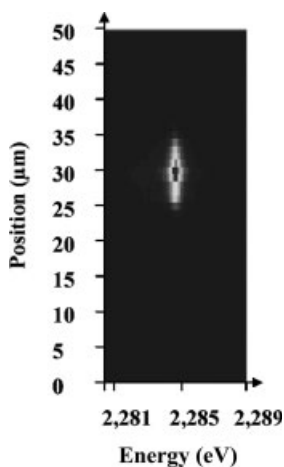


**Figure 3.52** Spatial image of the emission of a single chain.

This is the zero-phonon emission line of a chain excited (at 501.7 nm) at the ordinate  $z = 32 \mu\text{m}$  over a length of  $\sim 2 \mu\text{m}$ . It shows several striking results:

Although the excitation was limited to  $z = 32 \pm 1 \mu\text{m}$ , light is emitted everywhere between 27 and 33  $\mu\text{m}$ , a much longer distance. It is tempting to interpret this image as that of a 6  $\mu\text{m}$  long chain emitting over its whole length.

Spectral cuts taken at different  $z$  are identical, peaking at 2.2849 eV with  $\text{FWHM} = 600 \mu\text{eV}$  ( $T$  was about 11 K). Therefore, the energy of the bottom of the exciton band, the emitting level, is the same everywhere on the chain to better than  $\pm 100 \mu\text{eV}$  and its coherence time is the same everywhere.

Moreover, the image is independent of excitation power up to at least  $10^4 \text{ Wcm}^{-2}$ . At higher power, the spatial extension remains unchanged and the spectra are still the same at all positions, but the energy and width increase slightly in a way corresponding to a heating of the order of 1 K of the crystal.

These observations validate the second assumption made in the fit of vibronic emission lineshapes in Section 3.6.2.1.

In another experiment, a chain which emitted over a length of  $\sim 25 \mu\text{m}$  was excited successively at several different positions along its length. The spatial dis-

tribution of the emission was always the same, independent of the excitation position. This indicates that the spatial distribution of the emission is an equilibrium one, reached in a time short compared with the exciton lifetime.

### 3.6.3.2 Different Spatial Distributions. The Effect of Disorder

Not all images show all the properties of that shown in Fig. 3.52. There are in fact three classes of images:

1. Light is emitted at a single  $\lambda$  everywhere, but the spatial distribution does not show a broad maximum near the center of the emitting segment. Rather, the emission intensity is more or less constant over most of the segment length. An example is shown in Fig. 3.53.
2. The emission spectrum is the same everywhere, but the intensity shows large spatial variations, with regions of low intensity separating several, up to four, highly emitting segments several micrometers long, as shown in Fig. 3.54. Note that in all cases these segments are long enough to behave as quantum wires (1-D systems) and not as quantum boxes. This image spans a 150-meV spectral range. It shows on the right the D emission line and at 589.7 nm a single spot, which is the D resonance Raman line of the blue chains at  $1450\text{ cm}^{-1}$ . Since the Raman signal is excited only within the incident light spot, this gives the approximate size of the excited region and its position along the red chain:  $z = 39\text{ }\mu\text{m}$ . The red chain emits light over two segments, approximately  $\geq 7$  and  $\geq 10\text{ }\mu\text{m}$  long. At shorter wavelengths, five other vibronic emissions of the red chain are present, with much smaller intensities (as also seen in the macroluminescence spectrum, Fig. 3.45) and the same spatial pattern as

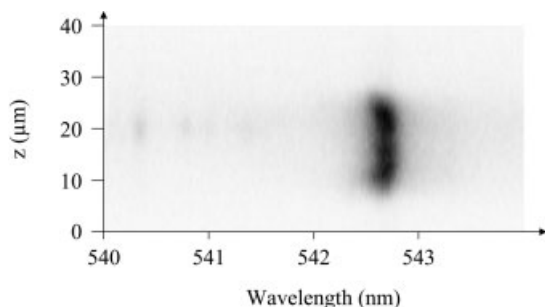


**Figure 3.53** Zero phonon emission of a chain emitting with approximately the same intensity over  $>15\text{ }\mu\text{m}$ .  $T = 8\text{ K}$ . Emission wavelength 542.8 nm. Excitation:

$\sim 5 \times 10^4\text{ W cm}^{-2}$  at 501.7 nm. The laser position is at  $z = 20$ , given by the faint line at 540.4 nm, which is the Raman D line of the blue chains.

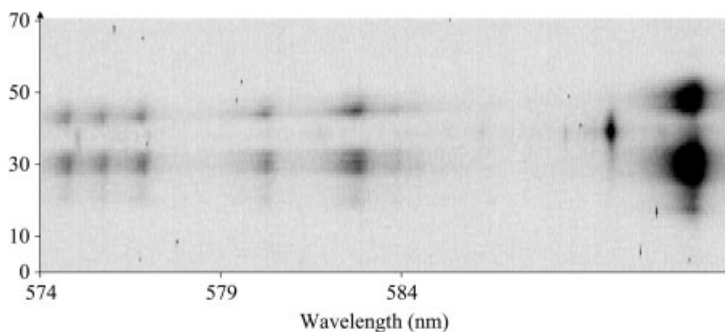


**Figure 3.54** Vibronic emission of a chain showing intense emission in two segments and a fainter third one at smaller  $z$ , overall spatial extension  $35\ \mu\text{m}$ . The D line is on the right, the single spot at  $589.8\ \text{nm}$  is the

Raman D line of the blue chains and marks the laser  $z$  position. Five other weaker vibronic emission bands are seen, all with the same spatial emission pattern.  $T = 15\ \text{K}$ . Excitation on the zero-phonon line  $\sim 700\ \text{W cm}^{-2}$ .

the D emission. One can notice that the  $580\text{-nm}$  vibronic line corresponding to the  $1200\text{-cm}^{-1}$  phonon has a slightly narrower emission spectrum. Further study of its shape and  $T$  dependence, as reported for the D line in Section 3.6.2.1, shows that the coherence time of the corresponding ground state phonon is indeed longer,  $\geq 600\ \text{fs}$ .

3. The emission spectrum varies spatially, in addition to spatial variations of the intensity. An example is given in Fig. 3.55.

In cases 1 and 2, the different emitting segments are aligned along the chain direction. These different segments cannot correspond to different chains, each directly excited with different efficiencies because of different positioning within the excitation region: the image does not discriminate different “lateral” positions, i.e. perpendicular to the chain direction. Therefore, in a multichain case they would all appear superimposed along  $z$ , possibly at different emission wavelengths owing to interchain disorder, and should all overlap the excitation region (such images are sometimes also seen). This means that all segments seen in Fig. 3.54 or 3.55 belong to the same chain, but only one of them contains the directly excited region and the others must be indirectly excited. In both figures, there is a gap of several micrometers between the emitting regions and its size is independent of  $T$ . Both the spot size and its drift in position as  $T$  is changed are much smaller, so the whole emission comes from a single chain with intrachain disorder. Moreover, the three parts of the chain shown in Fig. 3.55 equilibrate over low potential barriers during the exciton lifetime.

The length of the emitting segments is generally  $10\text{--}20\ \mu\text{m}$ , with some shorter ones such as in Fig. 3.52 and rarely longer. These lengths are lower limits of the actual chain length. Hence the red chain length distribution seems to be similar to the blue chain one directly measured by light scattering.

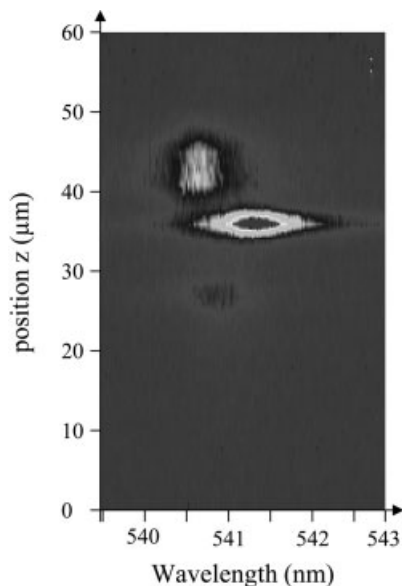


**Figure 3.55** Zero-phonon emission of a chain showing three segments emitting at different wavelengths.  $T = 30$  K. Excitation:  $100 \text{ W cm}^{-2}$  at  $501.7 \text{ nm}$ .

### 3.6.3.3 Origin of the Spatial Distribution

One may think that light is emitted from the whole of the chain because excitons are quickly transported over the whole chain length. In that case, excitons must be transported to a distance of  $\sim 10^{-3} \text{ cm}$  in a time short compared with  $100 \text{ ps}$ .

Diffusion seems unable to do so, since the required diffusion coefficient is  $\geq 10^4 \text{ cm}^2 \text{ s}^{-1}$ , an unreasonably large value (a value of  $D = 600 \text{ cm}^2 \text{ s}^{-1}$  recently found in GaAs/GaAlAs quantum wells was deemed “exceptionally large” [138]).

For ballistic transport of a wave packet, the group velocity must be  $\geq 10^8 \text{ cm s}^{-1}$ . This means that transport occurs only through states of high enough momentum. However, the required momentum corresponds to a kinetic energy larger than thermal energy at  $50 \text{ K}$ . Hence ballistic transport cannot explain the observations either.

The observations are thus unexplained, although it is tempting to see them as evidence of high spatial coherence of the exciton states. Again, this is a subject for future work. *Note added in proof:* Extended exciton spatial coherence has now been demonstrated by interference experiments (F. Dubin et al., submitted).

## 3.6.4

### Several Excitons on a Chain. Effect of Excitation Power

#### 3.6.4.1 Absorption Cross-Section for a Single Chain

Assuming that red and blue chain zero-phonon lines have similar oscillator strengths (the error is anyway at most a factor of 2), it is possible to estimate absorption cross-sections of the zero-phonon line per repeat unit of an individual

red chain at 10 K from the room-temperature absorption coefficient of an ensemble of blue chains (which is homogeneously broadened) and the ratio of the linewidths. A value of the order of  $\sigma_0 \approx 5 \times 10^{-14} \text{ cm}^2$  is found.

The corresponding value at 501.7 nm can be calculated from the absorbance of an ensemble of red chains since the D absorption line is certainly homogeneously broadened, its linewidth being about three times that of the inhomogeneously broadened zero-phonon line (see Section 3.5.2.1). At 10 K, the cross-section at 501.7 nm is lower by a factor of about 50 than that of the zero-phonon line.

Since the zero-phonon linewidth increases approximately as  $T$ ,  $\sigma_0$  is approximately proportional to  $T^{-1}$  between 10 and 50 K.

From these cross-sections, the average number of excitons simultaneously present on a single chain under known excitation conditions can be calculated.

#### 3.6.4.2 Nonresonant Excitation

The maximum power available at 501.7 nm at the focus of the microscope objective, that is, approximately within a circular spot with radius  $\sim 1 \mu\text{m}$ , corresponds to a flux of  $\sim 5 \times 10^5 \text{ W cm}^{-2}$  at the chain position. The flux was varied from  $10 \text{ W cm}^{-2}$ , where there is never more than one exciton on the chain, to its maximum value and the integrated intensities of the zero-phonon and D vibronic lines were recorded as a function of excitation power. The results (for 10 K) are shown as closed squares in Fig. 3.56.

The emission intensities are proportional to the excitation over the 4.5 orders of magnitude covered. The positions and widths of the zero-phonon line at low ( $320 \text{ W cm}^{-2}$ ) and high ( $3.5 \times 10^5 \text{ W cm}^{-2}$ ) power are compared in Fig. 3.57.

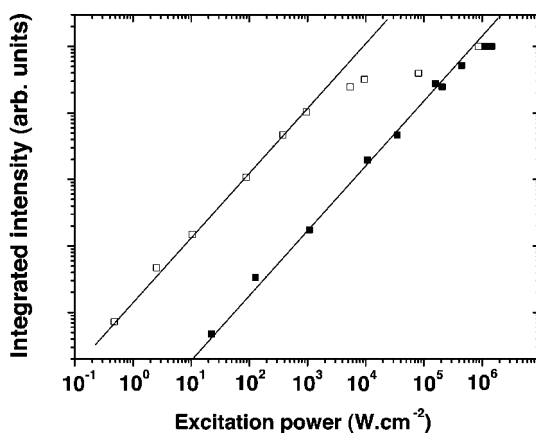


**Figure 3.56** Variation of the emitted fluorescence intensity as a function of excitation power. Solid squares, nonresonant excitation. Open squares, resonant excitation. The lines have slope 1.

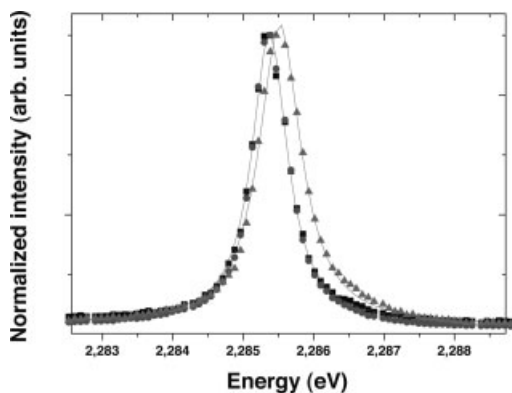


**Figure 3.57** Zero-phonon emission lineshape as a function of excitation power.  $T = 10$  K. Excitation at 501.7 nm. Solid circles,  $300 \text{ W cm}^{-2}$ ; open circles,  $6 \times 10^4 \text{ W cm}^{-2}$ ; stars,  $3.5 \times 10^5 \text{ W cm}^{-2}$ .

The changes are very modest and can entirely be accounted for by a 1 K increase in crystal temperature. This is small enough to allow neglecting the temperature dependence of the fluorescence yield in the data analysis.

It was shown above that the linewidth is determined by the lifetime of the radiant  $k \approx 0$  states, which is governed by intraband scattering due to the interaction of excitons with LA phonons of the matrix. This requires a sufficiently large population of such phonons: it was assumed above that the phonon density near the chain was not a limiting factor in the scattering. Figure 3.57 demonstrates that this remains true at high exciton density, despite the fact that excitons must absorb phonons to be scattered off the  $k \approx 0$  states.

These results also show that there is no exciton–exciton interaction leading to exciton quenching, for instance by some Auger effect, such as observed in molecular crystals [85]. Again, no evidence of biexciton formation, for instance a new line increasing nonlinearly with excitation power, was found.

### 3.6.4.3 Resonant Excitation. Exciton–Photon Interaction

In resonant excitation, the D-line emission is studied and the excitation wavelength is tuned to the maximum of that emission. It is then resonant to the zero-phonon transition of the particular chain under study (this energy varies, because of interchain disorder, within the inhomogeneous linewidth).

Results are displayed in Fig. 3.56 as open squares. The excitation power was again varied over more than four orders of magnitude, from  $0.2$  to  $4 \times 10^5 \text{ W cm}^{-2}$ .

The emission intensity is proportional to excitation power up to  $\sim 3 \times 10^2 \text{ W cm}^{-2}$  only, then it starts to saturate. This threshold corresponds to the same exciton density as at  $(1\text{--}2) \times 10^4 \text{ W cm}^{-2}$  under nonresonant excitation, where the emission intensity keeps increasing linearly up to an excitation power 30 times higher. Therefore, the sublinear variation shown in Fig. 3.56 cannot be due to exciton–

exciton interactions, since they should be the same at the same exciton density, irrespective of the exciton generation process.

The only difference between the two experiments is that the incoming photons are now tuned to resonance and have the same energy as the resonance fluorescence itself. In such a case, the lifetime of the emitting state (that is, the lifetime of the  $k \approx 0$  states, governed by intraband scattering, not the overall exciton lifetime governed by energy relaxation processes) is to be compared with the period of Rabi oscillations [139]. We consider that the observed onset of saturation corresponds to that situation. If so, the saturation threshold should increase rapidly with  $T$ , since it depends on the peak absorption cross-section and on the lifetime of the radiant states, which both decrease as  $T^{-1}$ . Preliminary results at higher temperature agree with that prediction.

### 3.6.5

#### Summary

##### 3.6.5.1 Summary of the Results on Red PDA Isolated Chains

3B monomer crystals emit an intense fluorescence that has been identified as the emission of a very dilute population of poly-3B isolated chains in the “red” configuration. The emission lines are very narrow, down to  $<2$  meV at low  $T$ . Most of the intensity (up to 90%) is in the zero-phonon line. This is a resonance emission: the zero-phonon emission wavelength coincides with the origin absorption band. In the corresponding absorption spectrum, the vibronic lines are also at least an order of magnitude smaller than the zero-phonon line and the excited-state vibrational frequencies are very close to the corresponding ground-state frequencies: the changes in geometry or bond stiffness upon excitation are therefore minimal. In that sense, the red and blue excitons are similar. All the properties of the absorption and the emission together make it possible to study the emission of a *single* isolated chain in a microfluorescence experiment.

The radiative lifetime is short (a few hundred picoseconds) and increases as  $T^{1/2}$  in the whole  $T$  range explored from 10 to 80 K, as expected for a one-dimensional exciton band. The exciton effective mass is small ( $\sim 0.1$ ), hence the band is broad (eV wide). This 1-D character is directly demonstrated by the spectral shape of the vibronic emission lines and its temperature dependence.

The exciton is strongly coupled to the 3-D LA phonons of the surrounding crystalline monomer matrix. The coupling produces efficient intraband scattering between  $k$  states, which thermally equilibrates the excitons with the lattice temperature on the picosecond time-scale and limit the lifetime of the radiant  $k \approx 0$  states to 2 ps or less, depending on  $T$ .

In microfluorescence, only a small fraction ( $2 \mu\text{m}$ ) of the total chain length (up to  $25 \mu\text{m}$ ) is directly excited by the incoming beam. However, the emitting region is always much larger and can span the whole chain length. The emission spatial and spectral shapes are generally independent of the excitation conditions, e.g. position of the exciting beam.

No indication of exciton–exciton interactions has been found yet.

Under resonant excitation conditions, a saturation of the vibronic emission is observed at high excitation power; this may correspond to the onset of experimental conditions in which the radiant state lifetime (not the overall lifetime of the exciton in the band) is becoming comparable to the Rabi oscillation period of the radiation field.

### 3.6.5.2 What We Would Like to Know About Red Chains but Do Not Yet

First and foremost, the exact conformation of red chains is still not definitely established. However, whatever the red conformation, spectroscopic data show that in 3B it is independent of  $T$ . Comparison of all known red phases suggests that it is the same in all of them; in the proposed model, the tilt angle is the same: it is a well-defined electronic structure of PDA chains. A crystallographic determination of the actual conformation will require the discovery of a high-quality red PDA crystal suitable for high-accuracy diffraction experiments.

Second, several experimental methods which yielded useful results on blue chains (exciton binding energies, Bohr radius and effective mass; nonradiative relaxation pathways including triplet exciton generation and transport) reported in Section 3.4, cannot be used in a system where the red chains are only a minority population, because their response (in electroabsorption or pump–probe experiments, for instance) cannot be sorted out from that of the majority blue chains, as can be done with fluorescence. Such experiments would require the discovery of a DA monomer in which long and unstrained isolated red chains were the only, or at least the majority, population at low  $x_p$ . TCDU, which produces red PDA crystals, does not meet these requirements, because the lattice mismatch between monomer and polymer is much too large [16]. This requirement is less strong than the previous one – for instance, 3B does not polymerize completely – but again such a system has not been found yet.

## 3.7

### Answered and Open Questions

The model system studied in this chapter was developed with the aim of contributing to the physical understanding of conjugated polymers and formulating questions for theoretical study. Here we try to examine to what extent it has been successful. This discussion will consider three points:

- the nature and properties of excited states (Section 3.7.1)
- the effects of exciton-phonon interactions (Section 3.7.2)
- the importance of electronic correlations (Section 3.7.3).

Of course, only one type of CP has been studied, the PDA, so one may ask how general the conclusions are. However, there is no obvious reason for thinking that PDA are fundamentally different from other CP. It may be that the importance of

correlations differs somewhat among conjugated polymers, being more important in PDA [8], but this should not much affect the exciton properties, and hence the spectroscopy. We believe that, if one were to know how to prepare other CP with the same degree of order as was obtained with PDA isolated chains, similar results would be obtained. The differences between the present results and those published on other CP are sometimes large, but there are also large differences between ordered and disordered PDA. Hence it may well be that most of these differences are related to disorder and possibly to interchain interactions in the cases where interchain distances are small enough. We shall briefly return to this problem in Section 3.7.4.

### 3.7.1

#### The Nature and Properties of Excited States

Results mostly concern the lowest  $B_u$  singlet exciton, which dominates the visible and near-UV optical properties of PDA chains. Despite the spectacular differences in the exciton relaxation processes between blue and red chains, their excitons seem to be similar: both spectra are dominated by a zero-phonon line bearing at least half of the total oscillator strength, the vibrational frequencies in the ground and excited states are almost equal, the polarizabilities and the exciton sizes are nearly equal and the  $T$  dependences of the linewidths (once corrected in the case of blue chains for the effect of the very short lifetime) are also similar, suggesting that in blue chains also the exciton coherence time should be governed by an interaction with LA phonons of the matrix, of similar strength.

1. This exciton is strongly bound. Lateral confinement, neglected up to now, certainly contributes significantly to the binding energy  $E_b$ : a PDA chain is probably the most nearly 1-D quantum wire possible, since it is a single line of carbon atoms. A calculation considering it as an ordinary semiconductor quantum wire (that is, in the weak coupling limit where excitons are Mott–Wannier excitons [9]) and taking into account the polarization of the surrounding matrix, leads to an estimated  $E_b$  close to the experimental value [96]. But electron correlations are known to be important in PDA, from the results in Section 3.4.4, and they also contribute to  $E_b$ , but in a nonintuitive way since larger  $U$  values lead to smaller  $E_b$  [8, 140]. The two effects may not be additive and their interplay needs to be clarified.
2. The exciton is a state of the whole chain or at least of a large part of it (several micrometers, as shown in Section 3.6.3.2), not localized on a short segment of it.  
A frequently used, but not rigorously defined, notion in CP is that of “conjugation length”, characterizing the size of the part of the chain which is involved in a  $\pi$ – $\pi^*$  optical transition, also called “chromophore” and often equated to the

length of the oligomer that would have the same transition energy; this length is therefore a ground-state property. That this can only be an approximate notion is demonstrated by the case of PDA isolated chains in solution, which are continuous curvature “worm-like” chains [20] and which absorption spectrum cannot be fitted by a discrete sum of absorption bands with reasonable linewidths [21].

The conclusions of this study of PDA isolated chains are totally unambiguous: in the most perfect chains, all repeat units are equivalent and the conjugation length is equal to the total length of the chain; at least this is always true of long segments of the chains, which still can be considered infinite. The characteristic 1-D density of states of the exciton band is directly visible on emission lineshapes and the radiative rate is that of a perfect 1-D system.

3. It is also often claimed that the “size of the excitation” is smaller than the conjugation length because the electron–phonon interaction further localizes the excited state. The size of the exciton is much smaller than the chain length, but this has nothing to do with phonon induced localization. It is due to a combination of lateral confinement and electronic correlations, as for the binding energy. There is strictly no geometric relaxation in the excited state. Moreover, the exciton size is not related to localization of the exciton: an exciton created at some point on the chain can be found anywhere over the whole chain length within a few picoseconds at most.
4. The exciton effective mass is small, hence the band is broad (several eV). Except for the threshold of the corresponding ionization continuum near 2.4 eV, no other state is observed in one-photon absorption or electroabsorption up to  $\sim 4$  eV, where another exciton involving the acetylenic  $\pi$  electrons appears (Section 3.4.6). One does not observe a (more or less) hydrogenoid series of levels converging to the ionization continuum. But there are other excitons, not accessible from the ground state by one-photon absorption, within that energy range: at least one  $A_g$  state is identified just below the onset of the associated continuum, and, in red chains at least, there is another  $A_g$  state, probably just above the bottom of the exciton band, corresponding to the state present in the blue chains gap. Also, several other states are predicted by theoretical calculations (see, for instance, Refs. [7–9]). The corresponding bands should then cross the  ${}^1B_u$  exciton band somewhere in the Brillouin zone and the actual exciton band structure is probably complex.

5. As for the singlets, there are two families of triplet states, respectively of  $B_u$  and  $A_g$  symmetries. The available experimental information only concerns the lowest  $B_u$  triplet. It appears to be different from its parent singlet, in that it may possibly self-trap and has a purely diffusive, relatively slow, transport. The singlet–triplet splitting is very large, almost equal to the triplet energy.

Triplets are efficiently generated by singlet fission. However, there are several nonradiative relaxation processes, one of which could be intersystem crossing (ISC) to a triplet. If so, the ISC rate would be much larger than calculated theoretically for other CP [126]. Further study of these properties would be useful.

### 3.7.2

#### Exciton–Phonon Interactions

There are several experimental manifestations of the importance of these interactions in PDA chains: fast intraband scattering by interaction with 3-D LA phonons or very high intensities of the 1-D chain modes in RRS. Note that in these two examples, very different types of phonons are involved.

In the CP literature, electron–phonon interactions are considered to be very important because they are assumed to lead to the Peierls instability [3] and more generally to self-trapping of charge carriers or excitons. This latter belief should be re-evaluated owing to the absence of self-trapping at least for the red chain singlet exciton and very likely in the blue one also, contrary to previous theoretical predictions for 1-D systems [48, 49]. LA phonons produce intraband scattering among  $k$  states, not self-trapping. The question was recently revisited by Silbey [109], who treated the case of a highly anisotropic 3-D exciton, interacting with 3-D phonons, the same as those used in Section 3.6.2.2 to explain the zero-phonon linewidth temperature dependence. An application to a PDA crystal lead to a vanishingly small predicted self-trapping energy, hence no trapping at all at nonzero temperatures. However, the result is not directly applicable to an isolated chain, which is “more 1-D” in the sense that there is no transfer matrix element with neighboring chains and that the lateral confinement is given by the single chain molecular structure and is of the order of the radius of one carbon atom. It would be worth reconsidering theoretically what happens in these more stringent conditions, both with 1-D, high-energy, chain optical phonons and with 3-D acoustic phonons.

One may conjecture that any observed localization of the singlet states in a conjugated polymer sample would rather be a consequence of disorder and not an intrinsic property of the CP chain itself. We return to this point in Section 3.7.4. Note, however, that the “weak” intrachain and interchain disorder, of the type which produces inhomogeneous broadening in macroscopic spectra and is evident in Figs. 3.54 and 3.55, does not lead to self-trapping.

The question of self-trapping of the lowest triplet in blue chains was left open in Section 3.4.5.4. If it indeed occurs, this difference with the singlet might be related to a much narrower triplet exciton bandwidth, leading according to theory [109] to a larger trapping energy. However, this might also reflect different internal structures of the two types of excitons: it is concluded, for instance, in [9] that the  $1^3B_u$ , but not the  $1^1B_u$  state, undergoes significant lattice relaxation, in the intermediate coupling regime thought to be appropriate for PDA.

If triplet self-trapping is shallow enough, triplets might trap at low temperature, but not at room temperature. There are not enough studies of the triplet properties to test this conjecture.

### 3.7.3

#### Electronic Correlations

This is a central question in CP physics. The experimental results presented in the previous sections have been discussed there in terms of conventional semiconductor theory applied to quantum wires, using the concept of Wannier–Mott excitons. In the presence of sizeable electron–electron interaction, a different approach in which the chain is considered as a Mott insulator may be more appropriate [7–9].

There has been an enormous amount of theoretical work on the electronic structure of CP, using various methods, taking electron correlations more or less fully into account, from the strong coupling limit of the Hubbard model [103] to the weak coupling limit of semiconductor theory. A review of that work would be beyond the scope of this chapter and beyond my own capabilities. Some results relevant to the present work are as follows. Excitons exist for a broad range of parameters [8]. They are of two types; in the weak coupling limit they are Wannier excitons as in conventional semiconductors; in the intermediate case, they are Mott–Hubbard excitons. Their spectroscopic signatures seem fairly similar and there is a lack of a crucial experiment.

The most direct evidence of the importance of correlations is the position of the first (and perhaps the second) excited  $A_g$  state below the  $B_u$  state in blue chains. Most calculations do not correctly predict this ordering of states. It has been claimed that the observed ordering might be due to much stronger lattice relaxation (self-trapping) of  $A_g$  states than of the  $B_u$  states [102]. Such relaxation may well exist, but it does not seem to explain the experimental results, since two-photon absorption corresponds to vertical transitions.

However, experiments do not only yield excited states energies. The presence and importance or the absence of lattice relaxation, the order of magnitude of the intrinsic (i.e. not determined by disorder) excitation size and their internal structure, their transport properties, etc., also depend on the correlations. Increasingly reliable results, some of them reported here, are produced by experiments and could be compared with theory.

Another point of interest is the intense fluorescence of red chains, indicating a different ordering of states. Theoretical studies usually consider the PDA chains

to be planar, as they are in the blue state. Experiment suggests that when the chain is forced to be nonplanar, the lowest  $A_g$  states shift to higher energy much faster than the  $B_u$  states and also that the lowest  $B_u$  triplet shifts at least as fast as the singlet. The reason for that is at present an open theoretical question: why do nonplanarity and/or unit cell doubling have that effect? The differences between PDA and CP containing phenyl rings, which are fluorescent [9], may also be related to this question.

Generally, the Hubbard model should be developed further, with qualitative predictions in mind, more interesting, in my view, than fitting the values of experimental parameters.

### 3.7.4

#### Influence of Disorder

Even a minimal deviation from perfect regularity has large effects in a quantum wire: a piece of experimental evidence is the high sensitivity of the Franz–Keldysh signal to a small amount of disorder (see Section 3.4.2.4). The 1-D exciton band of the perfect wire is replaced by a series of coupled quantum boxes; the emission wavelength varies from box to box along the chain and the  $\tau_r \propto T^{-1/2}$  law is no longer obeyed. This is generally the case in semiconductor quantum wires (see, for instance, Ref. [141]), in which variations of the wire width (by one atomic layer) are considered responsible for these effects.

Fluctuations of width cannot exist in a PDA chain (or more generally in a CP), but several other types of disorder are possible:

**Conformational changes.** Here the rigidity of the chain will be important. A flexible chain and a ladder polymer will behave differently. If the wire is not rigid, it may be curved and torsional fluctuations are not energy costly [142]. An extreme case is the isolated chain in a good solvent. Large geometric defects may also exist, such as entanglements.

**Variations of the potential due to the environment.** In a perfect crystal, including a bulk polymer crystal, this potential is periodic with the same period as that of the chain. In a real crystal, extended defects such as dislocations, stacking faults or slip planes will produce local potential extrema; such defects have been invoked above to account for observations such as multiple emitting regions on the same chain in microfluorescence (Section 3.6.3.2) or the existence of small absorption lines at energies lower than that of the exciton (Appendix C), but in neither case do they produce localization.

Disorder will first affect properties implying a long-range order: the necessity for reasoning in terms of bands, the spatial and temporal coherence of excitations (hence the sensitivity of the FK signal). Coherent transport is replaced by diffusion among localized states (boxes) distributed in space and energy. Such effects are already observed in imperfect crystals, despite the approximate long-range order present.

In a more highly disordered or an amorphous medium, van der Waals interactions with side-groups or other chains fluctuate in space, as well as quantum me-

chanical interchain interactions. In the extensive literature on CP fluorescence, related to the development of polymer light-emitting diodes, “aggregates” are often invoked to explain the observation of broad red-shifted emission bands qualitatively similar to excimer emission in several molecular crystals [85]. These aggregates are supposed to be regions of enhanced interchain interaction. Unfortunately, their structure is usually unknown.

The large fluctuations present in a highly disordered CP solid will not always, however, lead to localization at a scale comparable to the exciton size. It may be expected that long segments may keep an electronic structure comparable to that of the perfect chain, leading to fast energy transport and narrow spectral lines. An example of fast energy transport is given in Ref. [143]. Several other recent studies of single disordered chain spectroscopy show evidence of the role of disorder, but sometimes show narrow lines and evidence for “long” distance transport along the chain (see, for instance, Refs. [144, 145]), whereas others show no such effect and conclude that energy transfer is inefficient [146]. The transport is detected by the long-range effect of an impurity center on the chain or close to it, which quenches the emission by energy or charge transfer. Note that a theoretical treatment of charge carrier transport in doped CP rests on a similar combination of long-range intrachain transport and the effect of charge localized dopants [147]. In a recent paper, it is claimed that in fact, as suggested above, the nature of disorder and particularly whether the chain is rigid or not, plays a dominant role, rather than the details of the electronic structure of the particular CP studied [148].

The link between the properties of the perfect chain and of a disordered chain remains to be worked out. PDA may be good model experimental systems for that, since it already provides the ordered reference state for comparison.

## Appendix

### 3.A – The DA Solid-State Polymerization Reaction

#### 3.A-1:

##### General Description

The 1–4 addition reaction shown in Fig. 3.1 occurs only in the solid state. It requires a particular relative position of the reacting DA molecules, so it has structural requirements discussed below: this is a topochemical reaction, meaning that reactivity and reaction product geometry are entirely determined by the crystal structure [149].

The formation of a PDA polymer chain in a DA crystal may be seen as proceeding in three steps, as already mentioned in Section 3.1.3:

1. *Initiation*, in which an open-shell reactive entity is formed from two neighboring closed-shell DA molecules. This step is endothermic.
2. *Propagation*, in which a monomer molecule is added at the reactive end of a growing chain. This step is strongly exothermic, so polymerization is irreversible; however, it generally has a low activation energy, so propagation slows down and eventually stops at low temperature. Propagation is also topologically controlled. It stops if the monomer to be added does not meet the topological requirements for the reaction, for instance because the growing chain hits a fault, a twin, a dislocation or a surface or a slip plane, so that the next monomer to be added is misplaced. It also stops if it reaches an impurity the formula of which does not allow the addition reaction to proceed: a growing PDA chain will not in general incorporate chemical impurities, or any gross physical defect.
3. *Termination*: eventually, the reactive chain end will be inactivated by some internal reaction, since it is known to have a finite lifetime. This can occur after propagation has been stopped or else while the chain is still growing.

DA polymerization thus has strict topological and energetic requirements. It is therefore not surprising that only a minority of DA crystals do polymerize, often only partially. As polymerization proceeds, for  $0 < x_p < 1$ , the crystal can keep intact if a monomer-polymer solid solution of varying concentration is formed, that is, if reaction occurs more or less randomly in the bulk and not by nucleation and growth of a polymer phase at the expense of the monomer crystal. This will ensure that the few polymer chains formed at small  $x_p$  (say  $< 10^{-3}$ ) are dispersed in the matrix, so they are indeed not interacting with one another.

In the most favorable cases, polymerization goes to completion and a macroscopic polymer crystal, with typical dimensions of 0.1–10 mm, is formed (this is in fact the only known way for preparing polymer crystals of macroscopic size, as opposed to lamellae or spherulites generally produced in polymer crystallization). Only about 10 such cases are well documented. In a few of them, it has been shown that the unit cell indeed changes smoothly with  $x_p$  from its monomer values at  $x_p = 0$  to its polymer ones at  $x_p = 1$  (see, for instance, Refs. [16, 150, 151]) and in one case at least a complete structure of a mixed crystal at  $x_p = 0.2$  has been obtained [152].

### 3.A-2:

#### **Structural Requirements**

There are two types of such requirements: some apply to the crystal structures as a whole, others specify the geometry of the reaction center, i.e. of the two reacting carbon atoms and their vicinity.

**Macroscopic requirements.** A monomer–polymer solid solution without disruption of the crystal lattice requires that monomer and polymer have similar unit cell dimensions and that the polymer crystal structure has at least the monomer crystal symmetry elements (if not, a disordered structure will be formed). However, this latter constraint is not required if only the very beginning of the polymerization process is of interest, as for isolated chains as studied here.

In order to obtain long and unbranched chains, there must be only one direction of chain propagation in the monomer crystal; if not, a growing chain will quickly hit pre-existing chains in the other orientation. Hence, if there is a symmetry axis, it cannot be more than a twofold one. Most studied DA are “symmetrical”, meaning that the two side-groups are identical. They usually form centrosymmetric crystals of low symmetry, rarely orthorhombic (see Appendix B). The corresponding PDA crystals are also centrosymmetric.

The cohesive energy of DA crystals is generally dominated by van der Waals interactions with a significant contribution from hydrogen bonds if they can form. The  $C_4$  diacetylene group itself plays no special role and molecular packing within the unit cell is dominated by contributions of the side-groups. Hence there is a great variety of crystal structures, cell dimensions and molecular packing among DA crystals. Once the polymer is formed, the crystal contains parallel strings of covalent C–C bonds, which contribute an important part of the total crystal energy. Indeed, in all known PDA crystals the repeat unit distance along the chain is  $d_p = 4.89 \pm 0.02 \text{ \AA}$ , and this is generally assumed to be the equilibrium distance, and the bonds lengths and angles are almost the same for all PDA [16, 17]. Therefore, a polymerizable DA should contain parallel one dimensional stacks of monomers with a repeat distance of  $\sim 4.9 \text{ \AA}$ .

Since side-groups give the dominant contribution to crystal energy, their molecular structure is crucial in determining a DA crystal structure favoring polymerization. If one considers the known structures of PDA and reactive DA [16, 17], two types of interactions between side-groups seem particularly favorable: first, those forming intermolecular H-bonds, usually of the CONH type, the equilibrium distance of which [153] naturally leads to an intermolecular distance of  $\sim 4.9 \text{ \AA}$  in the crystal and which often arrange in 1-D lines (consider the case of proteins), thus simultaneously ensuring a favorable repeat unit distance and a single propagation direction – the DA chosen for the present study belong to this class – second, those containing aromatic rings, which tend to form 1-D stacks by  $\pi$ – $\pi$  interactions, as evidenced in the crystal structures of many aromatic molecules. The resulting repeat unit distance may in this case vary in a wider range, say between 4.5 and 5.3  $\text{\AA}$ , hence there is a large variation of reactivity in this class.

Further constraints come from the **microscopic aspects** of the 1–4 addition reaction.

The geometry of *initiation* is shown in Fig. 3.58.

Before reaction, the distance between the reacting carbon atoms is at least twice their van der Waals radius or 3.5  $\text{\AA}$ , and the bond formed has a length of about 1.5  $\text{\AA}$ . After reaction, these atoms will have moved towards axis (aa) by about 1  $\text{\AA}$ ,

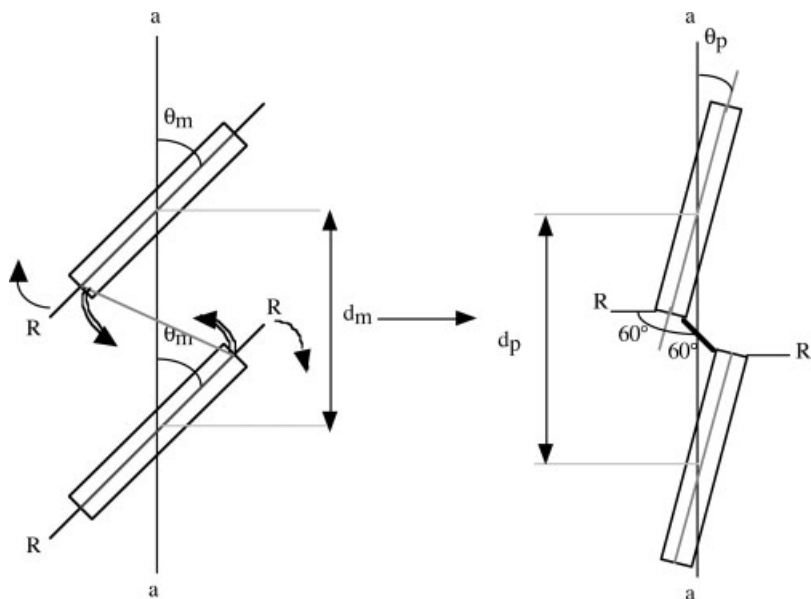


**Figure 3.58** Geometry of the initiation step:  $a$  is the chain direction. The angle of the  $C_4$  group with  $a$  changes from  $\theta_m$  to  $\theta_p$ , the first bonds to the side-groups  $R$  rotate oppositely and the distance between the  $C_4$  group centers changes from  $d_m$  to  $d_p$ .

thereby exerting a traction on the side-groups. They may also have shifted parallel to  $(aa)$  if the repeat distance  $d_m$  in the monomer is significantly different from  $d_p$ .

*Propagation* is the reaction of a reactive end of a growing chain with the next monomer (see Fig. 3.2). One can draw for it a figure similar to Fig. 3.58, so the microscopic requirements are similar for the two reactions since they imply the same kind of motions.

Hence two types of atomic displacements are to be considered: those of the reactive carbon atoms which make the reaction possible and the overall displacements of all atoms, including those of the side-groups, which must be small enough to keep the crystal structure intact. There are therefore two types of requirements: that the addition reaction can occur and that the ensuing deformations are in some way “absorbed” by the other atoms, mainly the side-groups. A general approach of topochemical reactions is the least motion principle, which states that the reaction only occurs if the root mean square displacement of all atoms is smaller than a critical value. Baughman [154] has shown that the observed reaction indeed corresponds to least motion of the four carbon atoms of the diacetylene moiety. One can also consider the closeness of the two reacting carbon atoms in the monomer structure as the dominant factor, the reaction occurring only if this distance is less than  $\sim 4 \text{ \AA}$  [16, 155]. This is illustrated in Fig. 3.59.

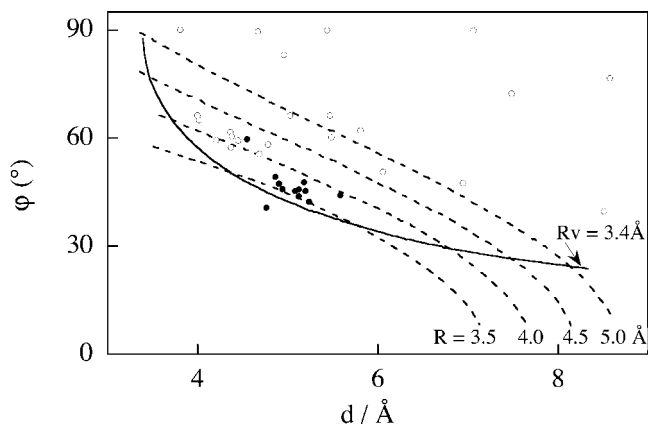


**Figure 3.59** Values of the parameters  $d$  and  $\phi$  for reactive diacetylenes (filled circles) and nonreactive diacetylenes (open circles). From Ref. [16].

The parameters  $d_m$  and  $\phi_m$  define the geometry of the monomer pair before reaction as shown in Fig. 3.58. The solid line is the locus of points  $(d_m, \phi_m)$  corresponding to van der Waals contact of the two parallel  $C_4$  groups and the dashed lines are locus of equal distances of the two reacting carbon atoms. It shows that reactive monomers which structure is known (black dots) are clustered in a very small region near  $d_m \approx 5 \text{ \AA}$  and  $\phi_m \approx 45^\circ$ . However, it says nothing about absolute reactivities: very small structural differences may correspond to large differences in polymerization rate.

If  $d_m$  is significantly larger than  $d_p$ , the growing chain will tend to be shorter than the columnar volume it should fill. The ensuing strain pattern is not favorable to chain propagation and indeed in this case the chains generated at low  $x_p$  are short and their absorption spectrum suggests that they are highly strained. This is the case of the much studied monomer pTS or of TCDU [14]. Such DA would not be suitable to the study of long and unstrained isolated chains. However, the reaction still may lead in that case to good-quality polymer single crystals, since the  $d$  values of the mixed crystals decrease smoothly towards  $d_p$ , owing to the stress generated by the chains, which are much stiffer than the monomer crystal [135]. As stated above, the requirements for a high-quality isolated PDA chain and a high-quality PDA crystal are not identical.

### 3.A-3:

#### Energetics and Elementary Steps

For generation of the reactive dimer, an energy input  $\Delta E_m$  is required. This can be done by heat (thermal polymerization) or by the absorption of radiation: UV, X- or  $\gamma$ -rays or electrons.

If  $\Delta E_{in} \leq 1$  eV, initiation is thermally possible not far above room temperature and in any case below the monomer melting-point; 1 eV is much less than the energy of the lowest excited state of the  $C_4$  group, a triplet, which is about 3 eV [91]. Therefore, in this case initiation proceeds from a highly vibrationally excited ground state. If  $\Delta E_{in} \geq 1$  eV, thermal initiation does not occur, except possibly at some defect sites. This seems to be the more general case, particularly among DA with H-bonds. In the latter case, reaction can only proceed from an electronically excited state of the  $C_4$  group.

One possibility is absorption of UV photons producing neutral excited states. The initial steps of this reaction have been studied in detail in the case of pTS [13]. It was shown that the reactive dimer is a biradical with an unpaired electron at each end of the  $C_8$  chain; this remains true as chains grow up to the hexamer (a  $C_{24}$  chain), where the electrons rearrange to a bicarbene structure, with two independent unpaired electrons at each end. Quantum chemical calculations nicely account for such behavior [156].

Propagation is exothermic, releasing between 1.0 eV in 4BCMU – a DA with H-bonds [157] – to 1.6 eV in pTS – a DA without H-bonds [158, 159] – per step, but there is a small activation energy for monomer additions ( $<0.4$  eV), so at low  $T$  the reaction can be slowed and stopped, allowing detailed studies of the reactive intermediates and also allowing X-ray structural studies.

It must be stressed that the energetics of the various steps do not depend only on what occurs at the reaction site itself; it is governed by the overall energetic changes in the crystal, including the effects of side-group motions. Their contribution may be significant if, for instance, H-bonds between side-groups are broken or modified, as noted above.

The fact that the reactive end is a carbene suggests that known carbene rearrangements may act as termination reactions. The best candidate in our opinion is the hydrogen transfer reaction  $-\bullet\text{C}-\text{CH}_2- \rightarrow -\text{CH}=\text{CH}-$  [130], but this remains a conjecture.

No such study of intermediate states has ever been carried out for polymerization using higher energy radiation. One may presume, however, that initiation will also proceed from ionic excited states  $C_4^+$  and  $C_4^-$  which are formed by these radiations in addition to proceeding from neutral excited states. Initiation processes are then expected to be different and also the growth of an ionized chain may differ from that of a neutral one.

### 3.B – Structural Properties of 3B and 4B Monomers

Since most of our structural results are not yet published, these properties are summarized here.

## 3.B–1:

**Phase Transitions**

In both DA there is a first-order phase transition below room temperature: at 155 K in 3B and at 226 K in 4B [63]. Crystals are grown and polymerized in the room-temperature phase, while most of the spectroscopic studies are done in the low-temperature phase. In 4B there is another first-order transition at 316 K, but the electronic properties in the high-temperature phase between 316 K and the melting temperature of 344 K were not studied. All transitions are first order, with hysteresis of a few degrees, but with a low transition enthalpy and the crystal is not destroyed, or even significantly degraded, by crossing them. In fact, the structural differences between solid phases are not great.

## 3.B–2:

**Crystal Structures**

In 3B, both phases are monoclinic,  $C2/c$  (No. 15). This is a fairly common space group among molecular crystals and DA. The low-temperature phase has been studied previously [161], but although the same space group is found, the unit cell parameters are not the same as those found in our crystals. Apparently, there is a possible polymorphism of 3B, which has not been investigated.

In 4B, the situation is more unusual: the room temperature phase is orthorhombic,  $Cmcm$  (No. 63). The low-temperature phase is monoclinic,  $P1c1$  (No. 7). Also unusual is the very large value of one unit cell dimension,  $>100$  Å. Both space groups are centrosymmetric.

Unit cell parameters are given in Table 3.4.

Both materials form lamellar crystals, with a lamella thickness of  $\sim 27$  Å, that is, half (in 3B) or one-quarter (in 4B) of the largest unit cell dimension. The  $C_4$  groups, and therefore the chains, lie in the center of the lamellae, with the side-groups rather extended on either side. Therefore, despite long side-groups, neigh-

**Table 3.4** Unit cells of 3BCMU and 4BCMU monomers.

	Space group	$a$ (Å)	$b$ (Å)	$c$ (Å)	$\beta$ (°)
<i>3BCMU</i>					
270 K	$C2/c$	9.041	4.877 <sup>a</sup>	59.64	90.25
110 K	$C2/c$	8.955	4.872 <sup>a</sup>	58.70	97.62
<i>4BCMU</i>					
296 K	$Cmcm$	109.26	11.344	4.813 <sup>a</sup>	90
15 K	$P1c1$	105.12	11.019	4.720 <sup>a</sup>	92.48

<sup>a</sup> Parameters corresponding to the chain direction.

boring chains can be fairly close: at low  $T$ , the interchain distance would be  $<4.5 \text{ \AA}$  in 3B and  $\sim 5.5 \text{ \AA}$  in 4B. A similar situation is also observed in other conjugated polymers, but on a local scale since they are less well ordered [1], for instance in regio-regular polyalkylthiophenes where the chain distance is even smaller,  $3.8 \text{ \AA}$  [113].

The  $C_4$  groups are close packed along the  $b$  axis in 3B and along  $c$  in 4B (this choice is a consequence of usual crystallographic conventions), so this is the chain direction. The corresponding side-groups are linked by two lines of H-bonds, one on each side (Fig. 3.9). The monomers lie on centers of symmetry. It is not enough to prove that an isolated chain within the crystal will be centrosymmetric as well, but this seems reasonable; all experimental results to date agree with that assumption.

3.B-3:

### Unit Cell Parameters Along the Chain Direction

Table 3.4 shows that in 3B parameter  $b$  is almost the same at 270 and 110 K and very close to the equilibrium repeat unit length in PDA of about  $4.89 \text{ \AA}$ . There is a small thermal expansion in the high- $T$  phase,  $\Delta b \approx 3 \times 10^{-5} \text{ K}^{-1}$ , so the value just above the phase transition is  $b = 4.863 \text{ \AA}$  and the thermal expansion in the low- $T$  phase is very small. Figure 3.60 shows the temperature dependence of the unit cell parameters of 3B and 4B in the chain direction.

This behavior is typical of a crystal containing a line of H-bonds, for expansion along the bond direction [162]. Hence the difference between the monomer distance and  $4.89 \text{ \AA}$  is always  $<0.03 \text{ \AA}$  or  $\sim 0.5\%$ . Such a small compressive strain would have only a minimal effect on the properties of the chain and isolated poly-3B chains in their monomer crystal can be considered relaxed.

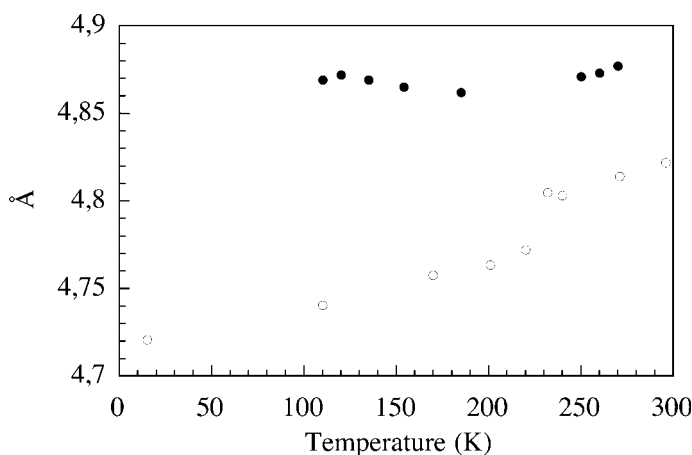


**Figure 3.60** Temperature dependence of the unit cell parameters in the direction of chain growth. Filled circles, 3B; open circles, 4B. Uncertainties are  $\pm 5 \times 10^{-3} \text{ \AA}$ .

In 4B, the  $c$  parameter is always significantly smaller than 4.89 Å and the corresponding thermal expansion is much larger,  $\Delta c \approx 6 \times 10^{-5} \text{ K}^{-1}$ , indicating much weaker H-bonds. Poly-4B chains are therefore always under significant compression, 1.6% at room temperature, increasing steadily as  $T$  decreases, to 3.6% at 15 K. Still, 4B is more reactive to  $\gamma$ -irradiation than 3B [58] and forms chains nearly as long as in 3B [59], so a slight compression seems to favor reactivity.

These different situations will influence the  $T$  dependence of the spectroscopic properties of isolated chains, as shown particularly in Section 3.4.2.

### 3.C – Origin of the Weak Absorption Lines in Blue Chains

Several weak absorption lines appear in both 3BCMU and 4BCMU below the intense transition to the  $^1B_u$  exciton (Fig. 3.11).

Resonance Raman spectra taken with excitation at the peaks of these lines show vibrational frequencies that differ from those of the main absorption and from one line to another; the differences amount to at most a few tens of wavenumbers. Therefore, these lines correspond to absorptions by chains having slightly different ground-state geometries. This suggests that each line is the exciton of a minor population of chains or parts of chains, which is slightly different from the major one.

All these different excitons behave in EA very much like the main absorption lines: they show a pure quadratic Stark effect of the same order magnitude as the major absorption (Fig. 3.13). This shows that there is no transfer of oscillator strength between them and the main transition, as expected for transitions related to spatially distinct chains. It also shows that these excitons are very similar to the major one, since they have the same polarizability, and so also the same exciton Bohr radius.

These absorption lead to resonance fluorescence; it is difficult to compare the yields, since these fluorescences are not subject to reabsorption (the optical density of these lines is too small at low  $x_p$ ) and since they are usually excited nonresonantly at energies where all populations absorb. That all populations absorb above the  $^1B_u$  exciton transition is shown, for instance, in Fig. 3.19, where the PB of the weak lines in 4BCMU is visible. Taking the relative bleachings as a measure of the relative absorptions at the pump wavelength and comparing the fluorescence intensities for excitation at the same wavelength indicates that the yields of the different resonance emissions corresponding to the different chain populations are comparable.

In one series of experiments, the pump was chosen resonant to one weak line in 3BCMU and PA–PB spectra and their time dependence were studied (Fig. 3.61).

There is absolutely no bleaching of the main absorption line, directly proving that the ground states of the two chain populations do not communicate. PB is also observed at wavelengths corresponding to the D and T vibronic transitions of the bleached line at  $\sim 1440 \text{ cm}^{-1}$  (178 meV) and  $2100 \text{ cm}^{-1}$  (260 meV). The time

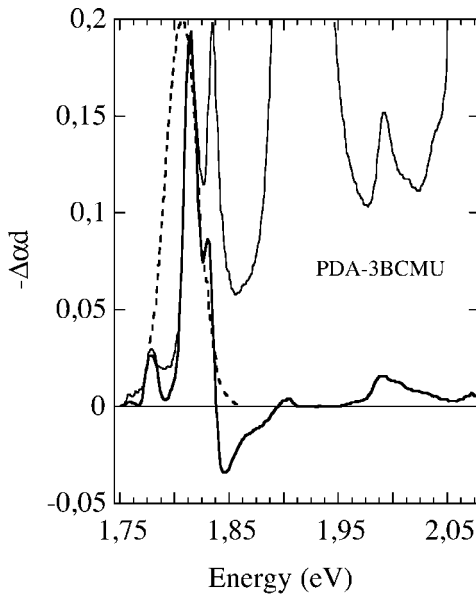


**Figure 3.61** Differential absorption spectrum upon pumping one of the weak transitions (thick line). The pump spectrum is the dotted line. The absorption spectrum is shown as a thin line. The pumped transition

is bleached and the weak bleaching at 1.99 eV is the corresponding D absorption line. No bleaching is observed at the exciton position 1.9 eV, showing that the two transitions do not share the same ground state.

decay of this PB spectrum shows the same characteristic times of  $1.8 \pm 0.1$  ps and about 30 ps, with the same intensity ratio of the two components as the major PB discussed in Section 3.4.4.3. Therefore, all excitons have similar relaxation decay schemes.

It seems likely that the minority populations are chains produced in the vicinity of an extended defect. Stacking faults are obvious candidates, since both monomer crystals are lamellar (Appendix B), but there are too many lines in 3BCMU to be entirely accounted for in this way. Hence other, unidentified, types of defects may also play a part.

Since the weak lines behave in all respects in much the same way as the main absorption, their properties were not studied further.

### Acknowledgments

The results reported in this chapter are the collective work of Prof. C. Lapersonne-Meyer, Dr. J. Berréhar and myself, together with three PhD students, S. Spagnoli, R. Lécoullier and F. Dubin, and a postdoctoral fellow, B. Kraabel. Working together has been a great pleasure and scientific stimulation. We have benefited from numerous collaborations, first of all with Prof. G. Weiser, University of Marburg,

and also with Dr. J.-D. Ganière and Dr. S. Haacke, Ecole Polytechnique Fédérale de Lausanne, Dr. D. Hulin and Dr. M. Joffre, ENSTA, Palaiseau, and within our laboratory with Dr. R. Grousson and Dr. V. Voliotis. We are very grateful to all of them.

I am very much indebted to Prof C. Lapersonne who contributed to the writing of part of the manuscript. I also would like to thank Dr. J. Berréhar, who prepared most of the figures, and Drs. T. Barisien, F. Dubin and V. Voliotis for the others.

## References

- 1 M. Schott, in *Organic Conductors: Fundamentals and Applications*, edited by J. P. Farges, Marcel Dekker, New York, 1994, Chap. XII, p. 539.
- 2 C. H. Lee, G. Yu, A. J. Heeger, *Phys. Rev. B* **47**, 5543 (1993); A. J. Heeger, D. Moses, in *Conjugated Oligomers, Polymers and Dendrimers: From Polyacetylene to DNA*, edited by J.-L. Brédas, DeBoeck, Brussels, 1999, p. 5.
- 3 W.-P. Su, J. R. Schrieffer, A. J. Heeger, *Phys. Rev. B* **22**, 2099(1980).
- 4 A. J. Heeger, S. Kivelson, J. R. Schrieffer, W.-P. Su, *Rev. Mod. Phys.* **60**, 781(1988).
- 5 A. A. Ovchinnikov, I. I. Ukrainskii, G. V. Kventsel, *Sov. Phys. Usp.* **15**, 575 (1973).
- 6 D. Baeriswyl, D. K. Campbell, S. Mazumdar, in *Conjugated Conducting Polymers*, edited by H. G. Kiess, Springer Series in Solid State Sciences, Vol. 102, Springer, Berlin, 1992, p. 7.
- 7 F. Gallagher, S. Mazumdar, *Phys. Rev. B* **56**, 15025 (1997).
- 8 F. H.L. Essler, F. Gebhard, E. Jeckelmann, *Phys. Rev. B* **64**, 125119 (2001); E. Jeckelmann, *Phys. Rev. B* **67**, 075106 (2003).
- 9 W. Barford, R. J. Bursill, R. W. Smith, *Phys. Rev. B* **66**, 115205 (2002).
- 10 N. S. Sariciftci (Editor), *Primary Photoexcitations in Conjugated Polymers: Molecular Exciton versus Semiconductor Band Model*, World Scientific, Singapore, 1997.
- 11 G. Wegner, *Z. Naturforsch., Teil B* **24**, 824 (1969).
- 12 F. Carré, N. Devylder, S. G. Dutremez, C. Guérin, B. J.L. Henner, A. Jolivet, V. Tomberli, *Organometallics* **22**, 2014 (2003).
- 13 H. Sixl, *Adv. Polym. Sci.* **63**, 49 (1984).
- 14 P. A. Albouy, D. N. Patillon, J.-P. Pouget, *Mol. Cryst. Liq. Cryst.* **93**, 239 (1983).
- 15 P. M. Chaikin, T. C. Lubensky, *Principles of Condensed Matter Physics*, Cambridge University Press, Cambridge, 1995, p. 602.
- 16 V. Enkelmann, *Adv. Polym. Sci.* **63**, 91 (1984).
- 17 M. Schott, G. Wegner, in *Nonlinear Optical Properties of Organic Molecules and Crystals*, edited by J. Zyss and D. S. Chemla, Vol. 2, Academic Press, Orlando, 1987, p. 3.
- 18 P. Cadot, M. Chodkiewicz, in *Chemistry of Acetylenes*, edited by H. G. Viehe, Marcel Dekker, New York, 1969, p. 597.
- 19 L. Brandsma, *Preparative Acetylenic Chemistry*, Elsevier, Amsterdam, 1998.
- 20 M. Rawiso, J.-P. Aimé, J.-L. Fave, M. A. Müller, M. Schott, M. Schmidt, H. Baumgartl, G. Wegner, *J. Phys. (Paris)* **49**, 861 (1988).
- 21 M. L. Shand, R. R. Chance, M. LePostollec, M. Schott, *Phys. Rev. B* **25**, 4431 (1982).
- 22 Y. Yacobi, E. Ehrenfreund, in *Light Scattering in Solids VI*, edited by M. Cardona, G. Güntherodt, Springer Topics in Applied Physics, Vol. 68, Springer, Berlin, 1991, p. 73.
- 23 D. N. Batchelder, D. Bloor, *J. Phys. C, Solid State Phys.* **11**, L629 (1978).
- 24 D. N. Batchelder, *J. Polym. Sci.* **14**, 1235 (1976).
- 25 J. Berréhar, M. Schott, unpublished results.
- 26 D. N. Batchelder, D. Bloor, *Adv. IR Raman Spectrosc.* **11**, 133 (1984).
- 27 D. N. Batchelder, D. Bloor, *J. Polym. Sci., Polym. Phys. Ed.* **17**, 569 (1979).

- 28 H. Katagiri, Y. Shimoi, S. Abe, *Chem. Phys.* **306**, 191 (2004); H. Katagiri, Y. Shimoi, S. Abe, *Nonlin. Opt.* **26**, 207 (2000).
- 29 A. Kobayashi, H. Kobayashi, Y. Tokura, T. Kanetake, T. Koda, *J. Chem. Phys.* **87**, 4962 (1986).
- 30 H. Tanaka, M. A. Gomez, A. E. Tonelli, M. Thakur, *Macromolecules* **22**, 1208 (1989).
- 31 V. Dobrosavljevic, R. M. Stratt, *Phys. Rev. B* **35**, 2731 (1987).
- 32 E. Helfand, *J. Chem. Phys.* **54**, 4651 (1971).
- 33 H. Eckhardt, C. J. Eckhardt, K. C. Yee, *J. Chem. Phys.* **70**, 5498 (1979).
- 34 S. Koshihara, T. Tokura, K. Takeda, T. Koda, A. Kobayashi, *J. Chem. Phys.* **92**, 7581 (1990).
- 35 See, for instance, D. J. Ahn, E.-H. Chae, G. S. Lee, H.-Y. Shim, T.-A. Chang, K.-D. Ahn, J.-M. Kim, *J. Am. Chem. Soc.* **125**, 8976 (2003).
- 36 S. Koshihara, T. Tokura, K. Takeda, T. Koda, *Phys. Rev. Lett.* **68**, 1148 (1992).
- 37 G. Weiser, *Phys. Rev. B* **45**, 14076 (1992).
- 38 B. I. Greene, J. F. Muller, J. Orenstein, D. H. Rapkine, S. Schmitt-Rink, M. Thakur, *Phys. Rev. Lett.* **61**, 325 (1988).
- 39 G. N. Patel, E. N. Duesler, D. Y. Curtin, I. C. Paul, *J. Am. Chem. Soc.* **102**, 461 (1980).
- 40 J. Berréhar, C. Lapersonne-Meyer, M. Schott, *Appl. Phys. Lett.* **48**, 631 (1986).
- 41 D. E. Aspnes, *Phys. Rev.* **147**, 554 (1966); **153**, 972 (1967).
- 42 G. Weiser, in *Primary Photoexcitations in Conjugated Polymers: Molecular Exciton versus Semiconductor Band Model*, edited by N. S. Sariciftci, World Scientific, Singapore, 1997, p. 318 (cf. p. 336).
- 43 G. Weiser, personal communication.
- 44 Y. Tokura, Y. Oowaki, T. Koda, R. H. Baughman, *Chem. Phys.* **88**, 437 (1984).
- 45 G. Weiser, A. Horvath, *Chem. Phys.* **227**, 153 (1998).
- 46 A. Yasuda, M. Yoshizawa, T. Kobayashi, *Chem. Phys. Lett.* **209**, 281 (1993).
- 47 J. Olmsted, III, M. Strand, *J. Phys. Chem.*, **87**, 4790 (1983).
- 48 E. I. Rashba, in *Excitons – Selected Chapters*, edited by E. I. Rashba and M. D. Sturge, North-Holland, Amsterdam, 1987, p. 273.
- 49 Y. Toyozawa, *Prog. Theor. Phys.* **26**, 29 (1961).
- 50 T. Kobayashi, in *Relaxation in Polymers*, edited by T. Kobayashi, World Scientific, Singapore, 1996, p. 1.
- 51 B. S. Hudson, B. E. Kohler, K. Schulten, in *Excited States*, edited by E. C. Lim, Vol. 6, Academic Press, New York, 1982, p. 1.
- 52 C. Lawrence, W. E. Torruellas, M. Cha, M. L. Sundheimer, G. I. Stegeman, J. Meth, S. Etamad, G. Baker, *Phys. Rev. Lett.* **73**, 597 (1994).
- 53 J. M. Leng, Z. V. Vardeny, B. A. Hooper, K. D. Straub, J. M. J. Madey, G. L. Baker, *Mol. Cryst. Liq. Cryst.* **256**, 617 (1994).
- 54 T. Manaka, T. Yamada, H. Hoshi, K. Ishikawa, H. Takezoe, A. Fukuda, *Synth. Met.* **84**, 963 (1997).
- 55 T. Manaka, T. Yamada, H. Hoshi, K. Ishikawa, H. Takezoe, *Synth. Met.* **95**, 155 (1998).
- 56 W. E. Torruellas, K. B. Rochford, R. Zanon, S. Aramaki, G. I. Stegeman, *Opt. Commun.* **82**, 94 (1991).
- 57 G. N. Patel, *ACS Polym. Prepr.* **19**, 154 (1978).
- 58 S. Spagnoli, J. Berréhar, C. Lapersonne-Meyer, M. Schott, M. Rawiso, A. Rameau, *Macromolecules* **29**, 5615 (1996).
- 59 T. Barisien, J. Berréhar, L. Legrand, M. Schott, to be published.
- 60 G. E. Babbitt, G. N. Patel, *Macromolecules* **14**, 554 (1981).
- 61 Z. Iqbal, N. S. Murthy, Y. P. Khanna, J. S. Szobota, R. A. Dalterio, F. J. Owens, *J. Phys. C, Solid State Phys.* **20**, 4283 (1987).
- 62 C. Lapersonne, J. Berréhar, M. Schott, S. Spagnoli, *Mol. Cryst. Liq. Cryst.* **256**, 423 (1994).
- 63 S. Spagnoli, J. Berréhar, C. Lapersonne-Meyer, M. Schott, *J. Chem. Phys.* **100**, 6195 (1994).
- 64 L. Sebastian, G. Weiser, *Phys. Rev. Lett.* **46**, 1156 (1981).
- 65 A. Horvath, G. Weiser, C. Lapersonne-Meyer, M. Schott, S. Spagnoli, *Phys. Rev. B* **53**, 13507 (1996).

- 66 G. Weiser, A. Horvath, H. J. Kolbe, *Proc. SPIE* **3145**, 152 (1997).
- 67 Y. Tokura, T. Koda, A. Itsubo, M. Miyabashi, K. Okuhara, A. Ueda, *J. Chem. Phys.* **85**, 99 (1986).
- 68 S. Polyakov, T. Pauchard, G. Stegeman, J. Berréhar, M. Schott, *J. Chem. Phys.* **118**, 4341 (2003).
- 69 S. Suhai, *Phys. Rev. B* **29**, 4570 (1984).
- 70 J.-W. van der Horst, P. A. Bobbert, P. H. L. de Jong, M. A. J. Michels, L. D. A. Siebbeles, J. M. Warman, G. H. Gelink, G. Brocks, *Chem. Phys. Lett.* **334**, 303 (2001).
- 71 See, for instance, M. Rohlfing, S. G. Louie, *Phys. Rev. Lett.* **82**, 1959 (1999).
- 72 W. R. Salaneck, M. Fahlman, C. Laperonne-Meyer, J.-L. Fave, M. Schott, M. Lögdlund, J.-L. Brédas, *Synth. Met.* **67**, 309 (1994).
- 73 A. Jaeger, G. Weiser, P. Wiedemann, I. Gyuro, E. Zielinski, *J. Phys. Condens. Matter* **8**, 6779 (1995).
- 74 J. Berréhar, C. Laperonne-Meyer, M. Schott, G. Weiser, *Chem. Phys.* **303**, 481 (2004).
- 75 J. Shah, *IEEE J. Quantum Electron.* **24**, 276 (1988).
- 76 S. Haacke, J. Berréhar, C. Laperonne-Meyer, M. Schott, *Chem. Phys. Lett.* **308**, 363 (1999).
- 77 A. Nitzan, S. Mukamel, J. Jortner, *J. Chem. Phys.* **63**, 713 (1975); R. Engelman, J. Jortner, *Mol. Phys.* **18**, 145 (1970).
- 78 B. Kraabel, M. Joffre, C. Laperonne-Meyer, M. Schott, *Phys. Rev. B* **58**, 15777 (1998).
- 79 M. Chandross, Y. Shimoi, S. Mazumdar, *Phys. Rev. B* **59**, 4822 (1999).
- 80 F. Kajzar, J. Messier, *Thin Solid Films* **132**, 11 (1985).
- 81 M. Mimuro, S. Akimoto, S. Takaichi, I. Yamazaki, *J. Am. Chem. Soc.* **119**, 1452 (1997).
- 82 B. Kraabel, D. Hulin, C. Aslangul, C. Laperonne-Meyer, M. Schott, *Chem. Phys.* **227**, 83 (1998).
- 83 L. Robins, J. Orenstein, R. Superfine, *Phys. Rev. Lett.* **56**, 1850 (1986).
- 84 C. Kollmar, W. Rühle, J. Frick, H. Sixl, J. U. von Schütz, *J. Chem. Phys.* **89**, 55 (1988).
- 85 M. Pope, C. E. Swenberg, *Electronic Processes in Organic Crystals and Polymers*, 2nd edn., Oxford University Press, Oxford, 1999.
- 86 C. Jundt, G. Klein, J. Le Moigne, *Chem. Phys. Lett.* **203**, 37 (1993).
- 87 P. Tavan, K. Schulten, *Phys. Rev. B* **36**, 4337 (1987).
- 88 A. Köhler, D. Beljonne, *Adv. Funct. Mater.* **14**, 11 (2004).
- 89 P. Gass, I. Abram, R. Raj, M. Schott, *J. Chem. Phys.* **100**, 88 (1994).
- 90 M. Bertault, M. Schott, P. Peretti, P. Ranson, *J. Luminesc.* **33**, 123 (1985).
- 91 F. Spitzer, *Principles of Random Walk*, Springer, Berlin, 1976.
- 92 D. C. Torney, H. M. McConnell, *J. Phys. Chem.* **87**, 1941 (1983).
- 93 H. Sixl, W. Rühle, in *Conjugated Polymeric Materials: Opportunities in Electronics, Optoelectronics and Molecular Electronics*, edited by J. L. Brédas and R. R. Chance, Kluwer, Dordrecht, 1990, p. 457.
- 94 G. Herzberg, *Electronic Spectra of Polyatomic Molecules*, Van Nostrand, New York, 1966.
- 95 S. Abe, *J. Phys. Soc. Jpn.* **58**, 62 (1989); S. Abe, W. P. Su, J. Yu, *Phys. Rev. B* **45**, 8264 (1992).
- 96 J. W. Van der Horst, P. A. Bobbert, M. A. J. Michels, H. Bässler, *J. Chem. Phys.* **114**, 6950 (2001).
- 97 R. Loudon, *Am. J. Phys.* **27**, 649 (1959).
- 98 M. Combescot, T. Guillet, *Eur. Phys. J. B* **34**, 9 (2003).
- 99 O. Betbeder-Matibet, M. Combescot, *Solid State Commun.* **94**, 221 (1994).
- 100 F. Dubin, PhD Thesis, Université Pierre et Marie Curie, Paris, 2004.
- 101 P. Tavan, K. Schulten, *J. Chem. Phys.* **85**, 6602 (1986).
- 102 A. Race, W. Barford, R. J. Bursill, *Phys. Rev. B* **67**, 245202 (2003).
- 103 W. Barford, *Phys. Rev. B* **65**, 205118 (2002).
- 104 R. R. Chance, G. N. Patel, J. D. Witt, *J. Chem. Phys.* **71**, 206 (1979).
- 105 E. Moore, B. Gherman, D. Yaron, *J. Chem. Phys.* **106**, 4216 (1997).
- 106 H. Sternlicht, *J. Chem. Phys.* **40**, 1175 (1964).
- 107 S. L. Tan, P. W. Anderson, *Chem. Phys. Lett.* **97**, 23 (1983).

- 108 Z. G. Soos, G. Hayden, P. C.M. McWilliams, S. Etemad, *J. Chem. Phys.* **93**, 7439 (1990).
- 109 R. Silbey, in *Conjugated Oligomers, Polymers, and Dendrimers: from Polyacetylene to DNA*, edited by J.-L. Brédas, DeBoeck, Brussels, 1999 p. 117.
- 110 S. Abe, *Synth. Met.* **85**, 1015 (1997).
- 111 M. Yan, L. J. Rothberg, F. Papadimitrakopoulos, M. E. Galvin, T. M. Miller, *Phys. Rev. Lett.* **72**, 1104 (1994).
- 112 E. Conwell, in *Primary Photoexcitations in Conjugated Polymers: Molecular Exciton versus Semiconductor Band Model*, edited by N. S. Sariciftci, World Scientific, Singapore, 1997, p. 99.
- 113 P. J. Brown, D. S. Thomas, A. Köhler, J. S. Wilson, J.-S. Kim, C. M. Ramsdale, H. Sirringhaus, R. H. Friend, *Phys. Rev. B* **67**, 064203 (2003).
- 114 P. A. Appar, K. C. Yee, *Acta Crystallogr. Sect. B* **34**, 957 (1977).
- 115 J. Berréhar, C. Lapersonne-Meyer, M. Schott, *Appl. Phys. Lett.* **48**, 631 (1986).
- 116 T. Kobayashi, *Synth. Met.* **71**, 1663 (1995).
- 117 J. M. Huxley, P. Mataloni, R. W. Schoenlein, J. G. Fujimoto, E. P. Ippen, G. M. Carter, *Appl. Phys. Lett.* **56**, 1600 (1990).
- 118 J. Kinugasa, S. Shimada, H. Matsuda, H. Nakanishi, T. Kobayashi, *Chem. Phys. Lett.* **287**, 639 (1998).
- 119 T. Hattori, W. Hayes, D. Bloor, *J. Phys. C* **17**, L881 (1984).
- 120 R. Lécuyer, J. Berréhar, C. Lapersonne-Meyer, M. Schott, *Phys. Rev. Lett.* **80**, 4068 (1998).
- 121 C. Blumer, J. D. Ganière, M. Schott, unpublished results.
- 122 S. Möller, G. Weiser, R. Lécuyer, C. Lapersonne-Meyer, *Synth. Met.* **116**, 153 (2001).
- 123 R. Lécuyer, J. Berréhar, C. Lapersonne-Meyer, M. Schott, J.-D. Ganière, *Chem. Phys. Lett.* **314**, 255 (1999).
- 124 R. Lécuyer, J. Berréhar, J.-D. Ganière, C. Lapersonne-Meyer, P. Lavallard, M. Schott, *Phys. Rev. B* **66**, 125205 (2002).
- 125 D. S. Citrin, *Phys. Rev. Lett.* **69**, 3393 (1994).
- 126 D. Beljonne, Z. Shuai, G. Pourtois, J.-L. Brédas, *J. Phys. Chem. A* **105**, 3899 (2001).
- 127 S. Spagnoli, J.-D. Ganière, M. Schott, unpublished results.
- 128 M. Alloisio, A. Cravino, I. Moggio, D. Comoretto, S. Bernocco, C. Cuni-berti, C. Dell'Erba, G. Dellepiane, *J. Chem. Soc., Perkin Trans. 2* **146** (2001).
- 129 D. Grando, G. Banfi, D. Comoretto, G. Dellepiane, *Chem. Phys. Lett.* **362**, 492 (2002).
- 130 P.-A. Chollet, F. Kajzar, J. Messier, *Synth. Met.* **18**, 459 (1987).
- 131 T. Guillet, J. Berréhar, R. Grousson, J. Kovensky, C. Lapersonne-Meyer, M. Schott, V. Voliotis, *Phys. Rev. Lett.* **87**, 087401 (2001).
- 132 F. Dubin, J. Berréhar, R. Grousson, T. Guillet, C. Lapersonne-Meyer, M. Schott, V. Voliotis, *Phys. Rev. B* **66**, 113202 (2002).
- 133 I.-K. Oh, J. Singh, *J. Luminesc.* **85**, 233 (2000).
- 134 V. M. Agranovich, O. A. Dubovskii, *JETP Lett.* **3**, 223 (1966).
- 135 R. J. Leyrer, W. Wetzling, G. Wegner, *Ber. Bunsenges. Phys. Chem.* **84**, 880 (1980).
- 136 T. Chen, A. Vierheilg, W. Kiefer, A. Materny, *Chem. Phys. Lett.* **312**, 349 (1999).
- 137 A. Vierheilg, T. Chen, P. Waltner, W. Kiefer, A. Materny, A. H. Zewail, *Phys. Chem. Chem. Phys.* **3**, 5408 (2001).
- 138 F. Pulizzi, W. H. A. Thijssen, P. C. M. Christianen, J. C. Maan, *Physica B* **298**, 441 (2001).
- 139 F. Dubin et al., to be published.
- 140 Z. Shuai, J. L. Brédas, S. K. Pati, S. Ramasesha, *Phys. Rev. B* **58**, 15329 (1998).
- 141 D. Y. Oberli, M.-A. Dupertuis, F. Reinhardt, E. Kapon, *Phys. Rev. B* **59**, 2910 (1999).
- 142 J. L. Brédas, A. J. Heeger, *Macromolecules* **23** 1150 (1990); G. Rossi, R. R. Chance, R. J. Silbey, *J. Chem. Phys.* **90**, 7594 (1989).
- 143 L. Chen, D. W. McBranch, H.-L. Wang, F. Wudl, D. G. Whitten, *Proc. Natl. Acad. Sci. USA* **96**, 12287 (1999).
- 144 T. Huser, M. Yang, L. J. Rothberg, *Proc. Natl. Acad. Sci. USA* **97**, 11187 (2000).

- 145 Z. Yu, P. F. Barbara, *J. Phys. Chem. B* **108**, 11321 (2004).
- 146 C. F. Wang, J. D. White, T. L. Lim, J. H. Hsu, S. C. Yang, W. S. Fann, K. Y. Peng, S. A. Chen, *Phys. Rev. B* **67**, 035202 (2003).
- 147 L. Zuppiroli, M. N. Bussac, S. Paschen, O. Chauvet, L. Forro, *Phys. Rev. B* **50**, 5196 (1994).
- 148 F. Schindler, J. M. Lupton, J. Feldmann, U. Scherf, *Proc. Natl. Acad. Sci. USA* **101**, 14695 (2004).
- 149 J. Kaiser, G. Wegner, E. W. Fischer, *Isr. J. Chem.* **10**, 157 (1972).
- 150 J. P. Aimé, PhD Thesis, Université Paris 7, 1983.
- 151 D. Bloor, R. J. Day, D. J. Ando, M. Motevalli, *Br. Polym. J.* **17**, 287 (1985).
- 152 J. P. Aimé, M. Schott, M. Bertault, L. Toupet, *Acta Crystallogr., Sect. B* **44**, 617 (1988).
- 153 A. Gavezzotti, G. Filippini, *J. Phys. Chem.* **98**, 4831(1994).
- 154 R. H. Baughman, *J. Polym. Sci., Polym. Phys. Ed.* **12**, 1511 (1974).
- 155 H. Bässler, *Adv. Polym. Sci.* **63**, 1 (1984).
- 156 C. Kollmar, H. Sixl, *J. Chem. Phys.* **88**, 1343 (1988).
- 157 H. Eckhardt, T. Prusik, R. R. Chance, *Macromolecules* **16**, 732 (1983).
- 158 R. R. Chance, M. L. Shand, *J. Chem. Phys.* **72** (1980).
- 159 M. Bertault, M. Schott, M. J. Brienne, A. Collet, *Chem. Phys.* **85**, 481 (1984).
- 160 A. Nickon, *Acc. Chem. Res.* **26**, 84 (1993).
- 161 V. Enkelmann, G. Wenz, M. A. Müller, M. Schmidt, G. Wegner, *Mol. Cryst. Liq. Cryst.* **105**, 11 (1984).
- 162 A. I. Kitaigorodsky, *Molecular Crystals and Molecules*, Academic Press, New York, 1973, p. 294.
- 163 E. Giorgetti, G. Margheri, S. Sottini, G. Toci, M. Muniz-Miranda, L. Moroni, G. Dellepiane, *Phys. Chem. Chem. Phys.* **4**, 2762 (2002).

## 4

# Morphology-Correlated Photophysics in Organic Semiconductor Thin Films by Confocal Laser Microscopy and Spectroscopy

*Maria Antonietta Loi, Enrico Da Como and Michele Muccini*

### 4.1 Introduction

Photoluminescence spectroscopy is one of the most informative and powerful techniques used to investigate electronic states in semiconductors. This is particularly true for organic semiconductors, in which electronic and optical properties are strongly anisotropic and dependent on the supramolecular arrangement. The supramolecular arrangement in organic semiconductors not only affects the fundamental electronic properties, but has also a strong influence on the performances of devices based on organic thin films. In fact, the nature of the organic/metallic or organic/dielectric interfaces and the morphological characteristics of thin films on the hundred-nanometer scale affect directly the operation of optoelectronic devices such as organic light-emitting devices [1, 2], field-effect transistors [3, 4], light-emitting transistors and photovoltaic cells [5, 6]. A straightforward consequence is that there is the need for analytical methods sensitive to chemical composition, morphology and molecular orientation on the hundred-nanometer scale. Owing to the severe requirements in terms of sensitivity, spatial resolution and not perturbing interactions with the sample, the ideal experimental technique does not exist. However, the development of photoluminescence spectroscopy as a local tool can be a significant step forward for a better understanding of the morphology-correlated electronic properties of organic semiconductor thin films and devices.

Both near- and far-field optical microscopies can allow local excitation and detection with spatial resolution below 1  $\mu\text{m}$ . Near-field microscopy can reach lateral resolution down to few nanometers [7, 8], while far-field microscopy [9] has a lower lateral resolution that can approach in the best cases 100 nm [10]. Near-field techniques are for their intrinsic nature potentially invasive. In fact, the use of metallic probes that approach the surface of the sample at distances of a few nanometers can cause relevant electronic perturbations, in particular when the sample is composed of soft matter, such as organic semiconductors and biological molecules. Variation of the photoluminescence lifetime of the molecules due to inter-

action with the metallic tip [11] and modification of the sample nature by heat transferred from the tip [12] have been reported.

In spite of the lower lateral resolution, far-field microscopies have the clear advantage of being less invasive and perturbing [13].

Confocal laser scanning fluorescence microscopy is, among far-field microscopy techniques, the one with the highest lateral resolution and offers in addition the possibility of performing three-dimensional sectioning, characteristics that prompted its great diffusion in biology and the life sciences. Its low interaction with the sample and the reasonably high spatial resolution mean that it can be used to achieve the local excitation and detection needed to develop a setup to perform morphology-correlated spatially resolved spectroscopy. Such a local spectroscopy tool has direct applications in areas such as material science and nanotechnology, but can also allow more quantitative investigations in the life sciences.

In this chapter, we report on the development of a setup for correlated spatially resolved spectroscopy and microscopy and on its application to organic semiconductor material science. The characteristics of the experimental setup are discussed and the imaging abilities are compared with those of a more standard morphological technique such as atomic force microscopy.

We then focus on two examples of the investigation of organic semiconductor thin films. In the first, the supramolecular organization in ultra-thin films (starting from sub-monolayer coverage) of a prototype organic semiconductor is revealed by the cross correlation of confocal laser scanning microscopy, spatially resolved photoluminescence spectroscopy and atomic force microscopy. In the second, we show how the determination of the microscopic structure of an organic bulk heterojunction by photoluminescence microscopy can shed light on the working mechanism and electronic properties of a bulk heterojunction-based device.

We demonstrate that confocal laser scanning microscopy and spectroscopy can be a key tool for material science and nanotechnology, as it may probe fundamental electronic and optical properties on the hundred-nanometer scale.

## 4.2

### Principles of Confocal Laser Scanning Microscopy

In far-field optical techniques, imaging is accomplished by focusing elements. In a microscope the objective lens forms a magnified image of the illuminated object that can then be examined with the eyepiece. If we consider the image of a single point, the light intensity is distributed around the focal point in a focal volume described by a point spread function (PSF). The extent of the PSF determines the resolution in far-field microscopy. In the ideal case where no aberrations are present, the resolution is limited by diffraction and is determined by the wavelength of light in the medium ( $\lambda n$ ) and the aperture angle of the lens  $NA = n \sin \nu$  ( $n$  is the

refractive index of the medium and  $\nu$  is the half angle of the lens aperture) and can be expressed by the Rayleigh theoretical resolution limit [14]:

$$RL = 0.61\lambda/NA \quad (4.1)$$

Much research has been devoted to developing tools able to image objects with a resolution lower than the Rayleigh limit. By confocal microscopy a resolution about 30% less than the Rayleigh limit is obtained [14]. This considerable advantage of confocal microscopy follows by the use of a point detector, obtained in practice by placing a circular pinhole in front of the photodetector that allows cutting the out-of-focus information from surrounding planes.

In the following we will concentrate on microscopy techniques based on photoluminescence (PL) emission, i.e. techniques where the optical excitation of the sample creates electronic excited states, which then emit light upon relaxation to the ground state.

In Fig. 4.1 is shown a schematic diagram of a PL confocal microscope working in reflection mode. The excitation light is focused on the sample surface by the objective, the photoluminescence emitted by the sample is collected by the same objective and directed through the pinhole to the detector after has been discriminated from the excitation light by the dichroic mirror. The pinhole in front of the detector allows one to select the signal arising exclusively from the in-focus plane of the sample. Owing to the absence of the out-of-focus signal, confocal microscopes provide not only an enhancement of lateral resolution with respect to non-confocal microscopes, but also the possibility of obtaining optical sectioning (three-dimensional imaging) of thick samples (see Fig. 4.5). The optical sectioning or depth discrimination has been the major motivation to prefer the confocal approach (in particular in the life sciences) over other far-field or near-field techniques, which do not have this capability.

The spatial resolution of the photoluminescence images depends on the confocal pinhole diameter, is proportional to the average between the emission and laser excitation wavelengths and is inversely proportional to the objective NA. A precise calculation of the PSF requires electromagnetic diffraction theory [9], but a good approximation for the in-plane ( $R_{xy}$ ) and depth ( $R_z$ ) resolution can be obtained by the following simplified equations:

$$R_{xy} \sim 0.37(\lambda^*/NA) \quad (4.2)$$

$$\text{with } \lambda^* \sim (\lambda_{\text{ex}}\lambda_{\text{em}})^{1/2}$$

$$R_z \sim 0.64\lambda/[n - (n^2 - NA^2)^{1/2}] \quad (4.3)$$

Equation (4.2) refers to the theoretical approximation for a pinhole aperture smaller than 0.25 Airy units (AU), where  $1 \text{ AU} = 1.22(\lambda_{\text{ex}}/NA)$  [15].

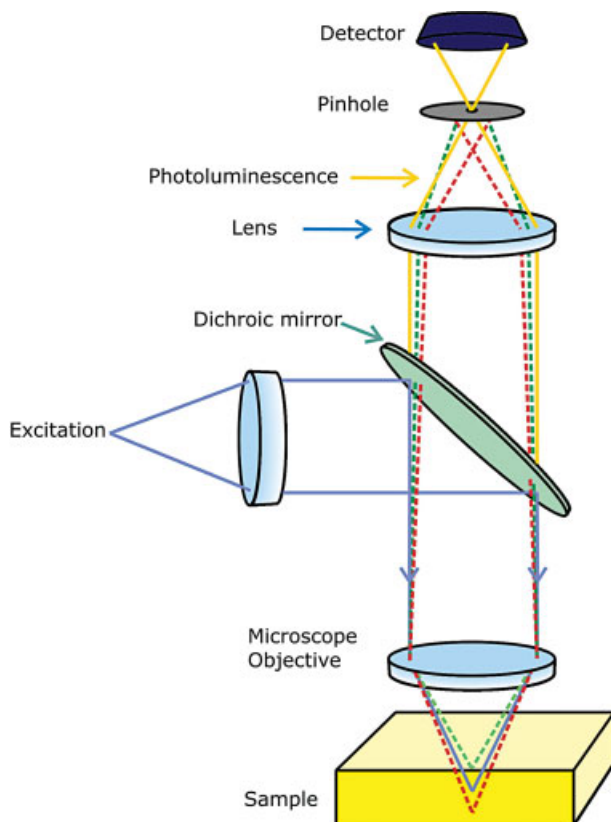


**Figure 4.1** Schematics of the working mechanism of the confocal fluorescence microscope. The pinhole serves as a spatial filter to prevent the out-of-focus PL from reaching the detector.

Several strategies have been pursued to improve the spatial resolution of confocal microscopes, among the most successful being the use of an objective lens with high numerical aperture [16] and the use of multi-photon absorption [17, 18] to exploit the intrinsic decrease of the PSF.

For example, by two-photon excitation it is possible to obtain lateral resolution down to  $\sim 100$  nm without using a pinhole, because the two-photon absorption is proportional to the square of the electromagnetic field intensity [19] and therefore occurs in only a small portion of the focused beam.

High effective numerical aperture objectives can be obtained by filling the space between the sample and the objective with a medium with high refractive index. Commonly this is achieved by the use of oil immersion objectives. Recently, the use of solid immersion lenses allows one to achieve resolutions down to 0.4 times the excitation wavelength [16]. Another very successful strategy to increase the total illumination aperture is to use the 4Pi technique [20]. Such a technique uses

two opposing objective lenses of high aperture, so that the spherical wavefronts are brought to constructive interference in the common focal point.

So far we have analyzed how it is possible to obtain a good optical image of a point of the object. In fact, whereas in conventional optical microscopy the image of the complete object field is obtained immediately, in confocal microscopy the image is generated by a point-by-point digital reconstruction. The entire image is built by raster scanning the object across the light source image or the light source image over the stationary object. Raster scanning the object is a choice generally more accurate for measuring distances and gives advantages such as less stringent requirements for the optical system and objective quality and constant resolution across the entire field of view [9]. The drawback of this scanning technique is that the acquisition of the final image of the object is fairly slow. The beam scanning approach is used when it is important to reduce the acquisition times. The beam can be scanned by using vibrating galvanometer mirrors, rotating wheels or acousto-optic beam deflectors. The drawbacks of scanning the beam are the increased complexity of the optical system and the less homogeneous quality of the image across the field of view [9].

Nowadays, confocal laser scanning microscopes (CLSM) where the laser beam is raster scanned across the sample are commercially available. In Fig. 4.2 is shown a schematic diagram of the typical scanning head for a CLSM. Such a scanning head can be attached to a standard optical microscope.

The raster scanning of the laser is achieved by using two galvanometric mirrors that direct the laser towards the sample. A dichroic mirror is used to discriminate the sample photoluminescence from the laser excitation.

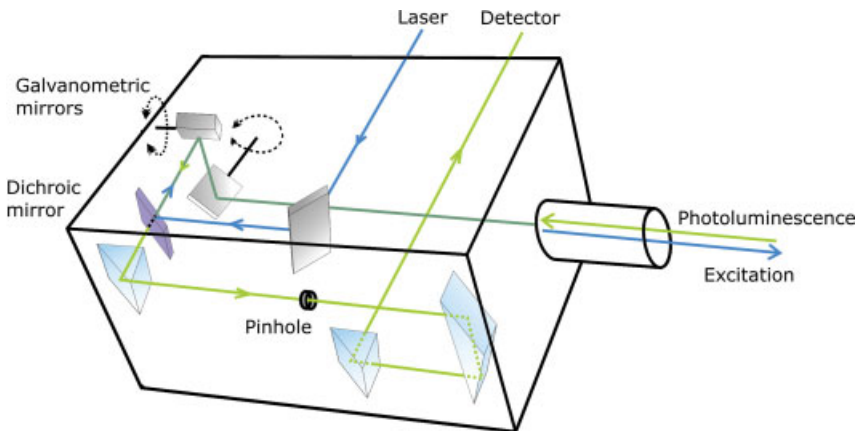


**Figure 4.2** Schematics of the laser scanning head of the CLSM. The incoming laser beam is reflected by the dichroic mirror and directed towards the sample by the two galvanometric mirrors. The sample photoluminescence transmitted by the dichroic mirror is

spatially filtered by the pinhole before reaching the detector. The object is scanned by the laser in a raster pattern, the PL signal from each point scanned by the laser is collected by the detector and the fluorescence image is reconstructed by a computer.



pulsed excitation. The pulsed excitation of the sample allows time-resolved photoluminescence measurements. The fundamental and the second harmonic of the pulsed laser are directly coupled into the scanning head with an optical system which guarantees good beam quality and efficient coupling with the scanning head. The setup is designed to reduce the laser path through the transmission optics in order to minimize the pulse temporal broadening before sample excitation. The laser pulse duration has been measured to be of the order of several hundred femtoseconds at the microscope focal plane.

The three cw excitation lasers are coupled either independently or contemporarily into the microscope through a multimode optical fiber. The imaging is achieved by detecting sample photoluminescence with three independent photomultipliers (PMTs) centered in complementary spectral windows of the visible range.

Time-resolved PL spectroscopy is performed by means of an Hamamatsu streak camera system with a temporal resolution of  $\sim 2$  ps, coupled to a monochromator.

To perform spectroscopic measurements, the laser is “parked” in a selected spatial position of the sample and the output PL signal collected by the confocal microscope is directed to the monochromator and the streak camera.

#### 4.3.2

#### Morphology Correlated Spectroscopy

In Fig. 4.4 is shown an illustrative example of the operation of the spatially resolved spectroscopy setup applied to an organic semiconductor thin film. Figure 4.4a shows a confocal PL image of a 50-nm thick tetracene film grown by high-vacuum sublimation [21]. The sample is excited with the second harmonic of the Ti:sapphire laser at 400 nm through a 40 $\times$  magnification oil immersion objective ( $NA$  1.3). The imaging is performed by detecting the PL signal with a photomultiplier tube, whose spectral window is centered at 515 nm. In the micrograph, areas of the sample with different intensity are not due to thickness differences but are mainly related to the local crystalline orientation of the film, which gives rise to photoluminescence intensity variations when excited with laser light with constant polarization [21].

Figure 4.4b reports the PL spectrum measured with the exciting laser focused in the sample area indicated in Fig. 4.4a. The corresponding PL time decay at 525 nm is reported in Fig. 4.4c.

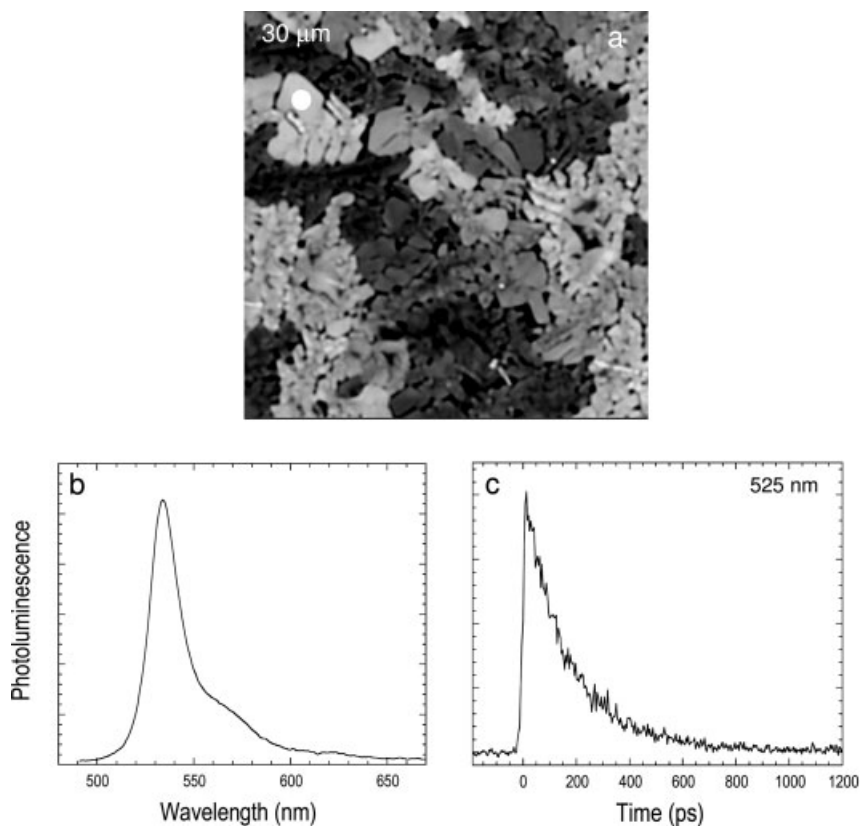


**Figure 4.4** (a) CLSM micrograph of a tetracene thin film. (b) Steady-state PL measured in the position indicated in (a). (c) Time-resolved PL decay at 525 nm measured in the position indicated in (a). Adapted from Ref. 21.

### 4.3.3

#### Optical Sectioning

In the previous paragraph we underlined that one of the main characteristics of confocal microscopy is the possibility of performing optical sectioning by imaging selected focal planes inside the sample (see Fig. 4.5a) [9].

In Fig. 4.5b is shown an example of optical sectioning applied to micro-structures [22] obtained in a blend film composed of poly(bisphenol A carbonate) and tris(8-hydroxyquinoline)aluminum(III) ( $\text{Alq}_3$ ) by the breath figures method [23, 24]. The photoluminescence CLSM micrograph of the film surface is reported together with the  $z$  section of the film measured by changing the focal plane inside the sample as shown in Fig. 4.5a. The  $z$  section allows the visualization of the structure of the pores without any mechanical cut.

## 4.3.4

**Comparison Between Topographic and Photoluminescence Imaging**

The experimental technique most commonly used for morphological investigations of thin films is atomic force microscopy (AFM). Such a technique uses as a measurable parameter the force between the tip and the sample surface and is therefore by definition a topographic technique [25].

As described previously, CLSM allows imaging of the sample surface by measuring the PL intensity. PL micrographs do not necessarily provide straightforward morphological information, but their analysis can lead to significant relations with the sample morphology.

In the following we will compare CLSM and AFM imaging to underline the differences and peculiarities of these techniques by showing some examples of applications to organic semiconductor thin films. It is important to highlight that AFM is an experimental technique that can be used in different acquisition modes, each having its own peculiarities [25]. The detailed analysis of the specific features of AFM is outside the scope of this work and therefore in the following we will rely on the general characteristics of the technique.

AFM has lateral resolution of a few nanometers (depending on the experimental conditions and on the sample nature) and  $z$  resolution in the ångström range [25]. CLSM is a far-field optical technique with a lateral resolution of a few hundred nanometers [see Eqs. (4.2) and (4.3)] and  $z$  resolution generally half the lateral resolution.

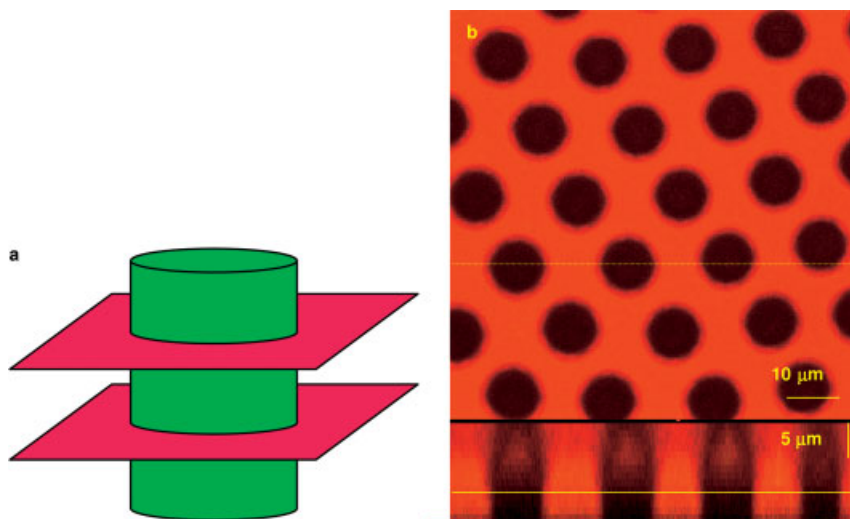


**Figure 4.5** (a) Sketch of the optical sectioning performed by CLSM. By moving the focus of the laser along the  $z$  direction it is possible to reconstruct the three-dimensional structure of an object. (b) CLSM

micrograph of a polycarbonate/ $\text{Alq}_3$  breath figure structure. The lower part of the image shows the optical section in the  $z$  direction as the surface is cut along the dashed line.

In Fig. 4.6a and b are shown, respectively, CLSM and AFM measurements of a sexithiophene film of 2-nm nominal thickness grown by vacuum sublimation at a rate of  $0.02 \text{ \AA s}^{-1}$ . The images recorded with the two techniques show the same apparent morphology, but whereas AFM shows islands of material with empty inter-island regions, the CLSM micrograph shows the PL signal confined in regions of the sample where AFM does not show the presence of material. This example, will be discussed in detail in the next paragraph, can be considered emblematic of the fact that in some experimental circumstances topographic techniques alone do not give complete and reliable information on thin film structure and molecular organization.

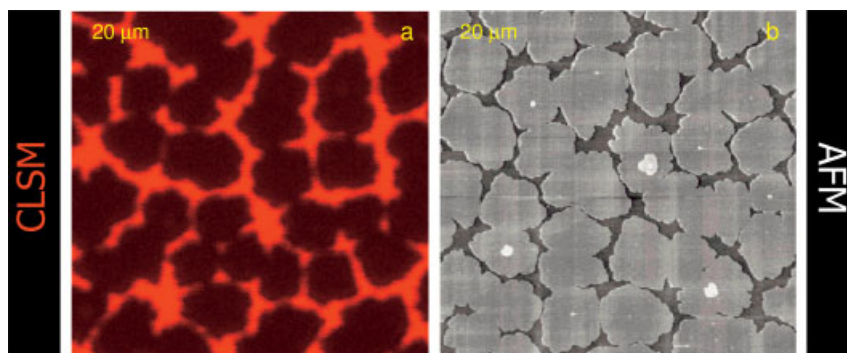


**Figure 4.6** (a) CLSM and (b) AFM images of vacuum-sublimed T6 films on  $\text{SiO}_2$ . The film growth conditions are rate  $0.02 \text{ \AA s}^{-1}$ , substrate temperature  $120 \text{ }^\circ\text{C}$  and nominal thickness 2 nm. AFM is measured in contact mode.

Figure 4.7a and c show the CLSM and AFM micrographs of a 30-nm thick film of T6 on quartz. The high  $z$ -axis sensitivity of AFM is demonstrated by the resolution of terraces (step height 2.5 nm) of T6, which originate from the layer-by-layer growth of the thin film. In Fig. 4.7a the terraces are not resolved by CLSM and only a slight inhomogeneity of the signal accounts for the thickness differences. Moreover, the CLSM micrograph shows areas of  $5\text{-}\mu\text{m}$  size where the PL signal is alternatively strong or low. Such a “mosaic”-like appearance does not compare with thickness effects shown by AFM and can be ascribed to polarization effects. The high PL signal indicates that the orientation of the crystalline macro domains is favorable to the absorption of the laser polarized light, whereas the lower signal indicates unfavorable crystalline orientation [21].

Figure 4.7b and d show the CLSM and AFM micrographs of a 30-nm thick film of T6 on graphite. The film grows following elongated structures that have a height profile up to 100 nm. Such an elevated step height is problematic for AFM and does not allow one to obtain images of good quality without artifacts. The step height is clearly not a problem for CLSM that at most would show out-of-focus objects as blurred.

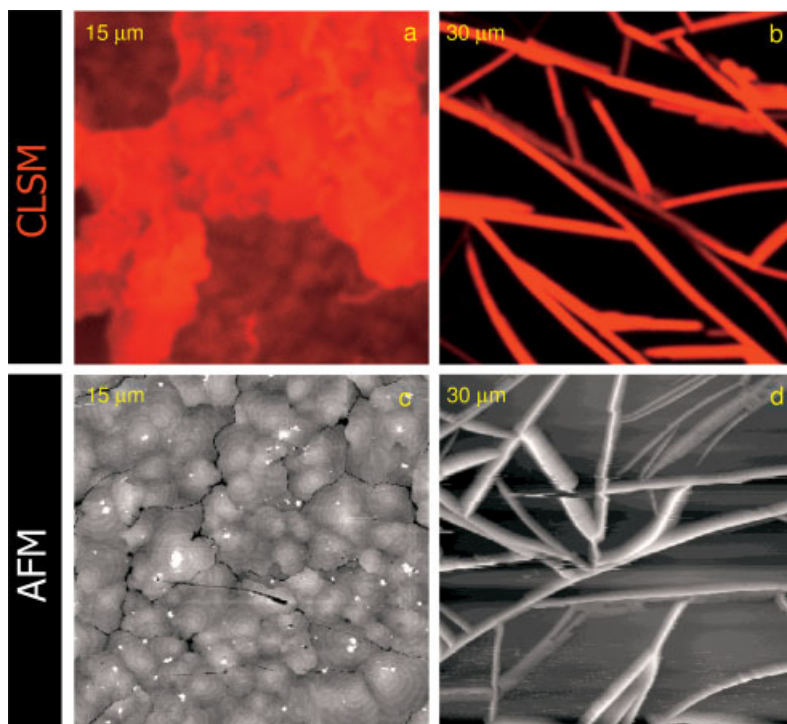


**Figure 4.7** (a, b) CLSM and (c, d) AFM images of T6 films vacuum sublimed on (a, c) quartz and (b, d) graphite. The film growth conditions are rate  $0.1 \text{ \AA s}^{-1}$ , substrate temperature  $180 \text{ }^\circ\text{C}$  and nominal thickness  $30 \text{ nm}$ . AFM is measured in contact mode.

It is important to note that, on the one hand, in the case of samples that are mechanically not stable AFM measurements can be affected by artifacts related to mechanical modifications of the sample induced by interaction with the tip. On the other hand, in CLSM the interaction with the laser light can cause irreversible degradation of the PL of the sample due to photochemical reactions.

Another important difference between the two techniques is the acquisition time, that can be relevant in the study of dynamic phenomena. To obtain a good-quality AFM image several minutes are necessary, whereas CLSM can provide a high-quality PL map in few seconds.

In conclusion, we have shown that a careful analysis of the PL micrograph measured by CLSM can give information on thin-film structure and morphology. In the following we will demonstrate how the correlation of different microscopy and spectroscopy techniques allows a deep understanding of the morphology and molecular organization of organic ultra-thin films.

## 4.4

**Supramolecular Organization in Organic Semiconductor Ultra-Thin Films**

In this section we show how the cross correlation of photoluminescence microscopy, spatially resolved PL spectroscopy and AFM allows to determine the morphology and supramolecular arrangement of a prototypical organic semiconductor in ultra-thin films.

The physical properties of organic semiconductors, in particular charge transport, which underlie electronic device operation, depend both on the molecular structure and on the supramolecular arrangement in the solid state [26, 27]. Although it has been demonstrated that the molecular properties can be tuned by chemical tailoring, the solid-state supramolecular arrangement is generally more difficult to control and appears to be one of the next challenges for material science.

Improvements in the charge transport properties are observed when the supramolecular order is maximized as in single crystals or in well-ordered thin films [28–30]. Field-effect mobilities of up to  $20 \text{ cm}^2 \text{ V}^{-1} \text{ s}^{-1}$  have been obtained using molecular single crystals [31], whereas for thin films the highest reported value is  $3 \text{ cm}^2 \text{ V}^{-1} \text{ s}^{-1}$  [29]. For technological applications, thin films are much more desirable than single crystals, and consequently the real goal is to obtain thin films with a well-defined supramolecular organization.

Among  $\pi$ -conjugated semiconductors, *a*-sexithiophene (T6) is one of the most studied systems, with regard to both fundamental properties[32, 33] and electronic applications[34, 35]. Since the first demonstration of oligothiophene-based field-effect transistors (FETs)[34, 36], hole mobility has been improved to up to  $4 \times 10^{-2} \text{ cm}^2 \text{ V}^{-1} \text{ s}^{-1}$  [37]).

Several attempts to correlate the transport properties of T6 thin films with morphology and molecular orientation [38] have been performed by means of crystallographic and morphological investigations. Early X-ray and electron diffraction studies showed that T6 molecules are oriented perpendicularly with respect to silicon dioxide substrates [39, 40]; such an arrangement favors charge transport in FET devices owing to the  $\pi$ -orbital overlap along the transport direction. However, all these studies were performed on films with thickness  $>20 \text{ nm}$ . The morphology of T6 thin films grown on different substrates has also been studied [40, 41] and the dependence of film morphology on the growth parameters has been investigated on a crystalline substrate such as ruby mica [41, 42]. Despite the wealth of investigations devoted to this topic, only very recently have the morphology and supramolecular organization in ultra-thin films of T6 on silicon dioxide been elucidated [43].

It is known that in organic FETs the interface between the oxide layer, acting as gate dielectric, and the organic active layer plays a fundamental role in the device operation and that, in particular, only the first two monolayers closest to the dielectric interface are relevant for charge transport [37].

The supramolecular organization in ultra-thin films (starting from sub-monolayer coverage) of T6 on silicon dioxide ( $\text{SiO}_2$ ) can be investigated by the cross correlation of CLSM, spatially resolved photoluminescence spectroscopy and AFM.

In Fig. 4.8a is shown the molecular structure of T6 and the unit cell of the single crystal. The low-temperature polymorph of crystalline T6 is monoclinic and belongs to the space group  $P2_1/n$  with four (non-equivalent) molecules in the unit cell [44, 45]. The four molecules in the cell arrange in a herringbone fashion in two molecular layers. The herringbone angle is  $\sim 66^\circ$  and is due to the repulsion of the  $\pi$ -electron clouds. The single-crystal surface corresponds to the  $bc$  plane of the unit cell. The intermolecular interactions between adjacent  $bc$  layers are weaker than the intra-layer ones.

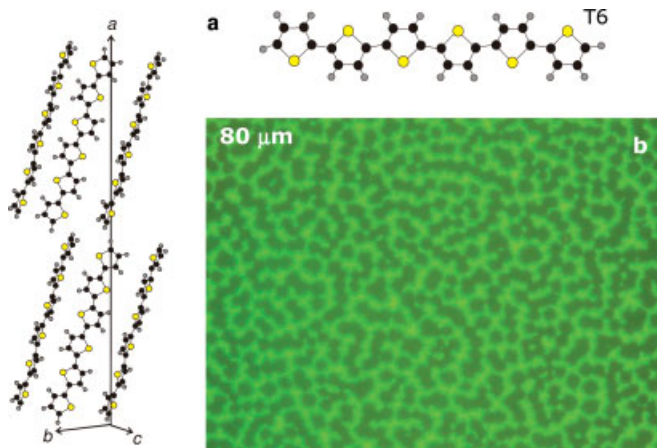


**Figure 4.8** (a) Molecular structure of  $\alpha$ -sexithiophene and unit cell of the single crystal. (b) PL wide-field micrograph of a 2-nm thick film of T6.

Figure 4.8b shows a photoluminescence wide-field micrograph of a 2-nm thick T6 film. The image in real colors shows the appearance, upon illumination with an Hg lamp, of dark areas surrounded by very bright green emitting regions.

T6 ultra-thin films were grown by sublimation in ultra-high vacuum (base pressure  $10^{-8}$  Pa) at a rate of  $0.02 \text{ \AA s}^{-1}$  on 100-nm thick thermal silicon dioxide on silicon. These deposition conditions give the highest field-effect charge mobility for T6 films [37]. During T6 growth the substrate was held at  $120^\circ\text{C}$ ; the film thickness was monitored by a quartz oscillator placed near the substrate.

Morphological measurements were performed with an AFM operating in contact mode using Si cantilevers.

Laser scanning confocal microscopy and spatially resolved photoluminescence spectroscopy were performed with the setup described in Section 4.3 using a  $60\times$  magnification objective with  $NA$  1.4. T6 films were excited with 488-nm  $\text{Ar}^+$  laser radiation.

In Fig. 4.9a–c are shown a series of AFM images of T6 ultra-thin films grown on  $\text{SiO}_2$  substrates. The films have a nominal thickness of 0.3, 0.8 and 2 nm (sub-monolayer coverage). The topography shown by all the reported sub-monolayer

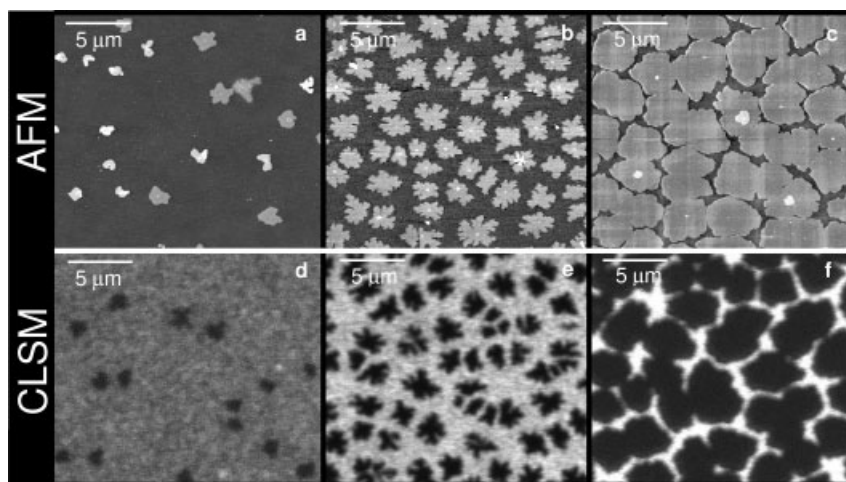


**Figure 4.9** (a–c) AFM and (d–f) CLSM images of T6 ultra-thin films on  $\text{SiO}_2$ . The film growth conditions are rate  $0.02 \text{ \AA s}^{-1}$ , substrate temperature  $120 \text{ }^\circ\text{C}$  and nominal thickness for (a, d) 0.3, (b, e) 0.8 and (c, f) 2 nm. The step height of the islands in the AFM images is  $\sim 2.5 \text{ nm}$ . Adapted from Ref. [43].

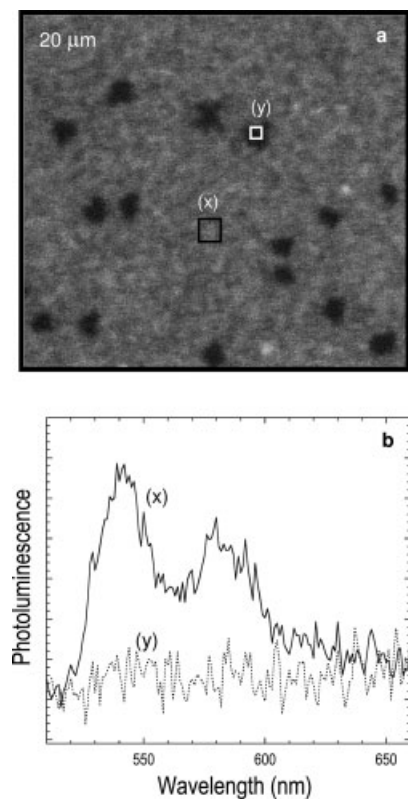
films is island-like and the height profile of the islands (lighter color) is around 2.5 nm, comparable to the length of the T6 molecule [45]. An increase of the island lateral dimension is observed on going from thinner (Fig. 4.9a) to the thicker films (Fig. 4.9c). AFM does not detect any presence of material in the inter-island region, even when operating in the most sensitive lateral force mode.

Figure 4.9d–f show CLSM images of the same samples investigated by AFM. The three CLSM images show the same “motif” of the topographical images but with inverted contrast: dark islands (low PL emission) and bright inter-island regions (high PL emission). It is important to note that no PL emission is shown by the  $\text{SiO}_2$  substrates before T6 deposition.

The high PL signal in the CLSM micrographs is limited to the inter-island regions (see Figs. 4.8b and 4.9) where AFM does not detect any material. AFM cannot distinguish features of vertical dimension comparable to the RMS roughness of the substrate. Consequently, we can estimate as the upper limit for the thickness of the inter-island region the RMS roughness of the  $\text{SiO}_2$  substrates, which is 0.2–0.3 nm.

The correlation of PL images and spatially resolved PL spectra with an in-plane spatial resolution of  $\sim 200 \text{ nm}$  allows to gain more detailed information on the molecular orientation and supramolecular organization in the islands and inter-islands regions.

In Fig. 4.10a the CLSM image of a 0.3-nm thick film of T6 is shown. The PL spectra in Fig. 4.10b were measured by parking the focused laser beam on a T6 island or on a portion of the inter-island region indicated in Fig. 4.10a.



**Figure 4.10** (a) CLSM PL image of a 0.3-nm thick T6 film on  $\text{SiO}_2$ , rate  $0.02 \text{ \AA s}^{-1}$ , substrate temperature  $120 \text{ }^\circ\text{C}$ . The regions indicated by (x) and (y) are those selected for the spatially resolved PL measurements reported in (b). The PL spectra in (x) and (y) are measured under the same experimental conditions. Adapted from Ref. [43].

The PL spectrum of the inter-island region is well resolved and shows limited broadening. The spectrum has a main peak at  $\sim 540 \text{ nm}$  ( $2.30 \text{ eV}$ ) and a second peak at  $\sim 580 \text{ nm}$  ( $2.14 \text{ eV}$ ). The vibronic distance is  $\sim 170 \text{ meV}$ , smaller than the  $181 \text{ meV}$  owing to the strongest C=C stretching mode ( $1459 \text{ cm}^{-1}$ ) measured in the T6 single crystal PL spectrum [46]. It is important to point out that similar spectra are found in all the inter-island regions of sub-monolayer thick films. The islands, under the same laser excitation power, have a PL intensity that is below the setup sensitivity (see Fig. 4.10b).

The relatively high PL intensity of the inter-island region is an indication that the transition dipole of the T6 molecule is efficiently coupled with the electrical field of the exciting laser impinging perpendicularly to the substrate. In contrast, in the case of the islands, poor dipole coupling results in low absorption of the light and an undetectable PL intensity. The T6 molecule is known to have the main optical transition dipole parallel to the long molecular axis [47]; a perpendicular (or almost perpendicular) arrangement of the molecules on the  $\text{SiO}_2$  substrate can justify the poor dipole coupling in the islands. Transition dipoles (i.e. T6 molecules) parallel to the substrate are needed to explain the high PL intensity signal arising from the inter-island regions.

As mentioned previously, the substrate roughness is of the order of 0.2–0.3 nm and topographical features with comparable vertical dimensions cannot be distinguished by AFM. Hence from the cross correlation of the CLSM and AFM measurements, we can infer that the T6 molecules in the inter-island region lie with their long axis parallel to the substrate and in the island are perpendicular to the substrate. A schematic diagram of the suggested film organization is reported in Fig. 4.13a.

More insight into the supramolecular organization in the inter-island regions is obtained by the comparison of the PL spectra of T6 in different aggregation forms. In Fig. 4.11 are shown the PL spectra of the inter-island areas in sub-monolayer films, the single crystal and T6 molecules dispersed in a poly(methyl methacrylate) (PMMA) matrix. The T6/PMMA matrix film was prepared by drop casting on a quartz substrate from a dioxane solution with a T6 concentration  $<10^{-5}$  M.

The PL spectrum of the inter-island region is blue shifted with respect to the single-crystal spectrum and red shifted with respect to the PMMA matrix spectrum. The difference from the PMMA/T6 spectrum proves that T6 molecules in the inter-island region are not randomly oriented and are subject to electronic interactions.

The fairly good spectral resolution and limited broadening, which is comparable to that of the single-crystal PL spectrum, reveals the high degree of molecular organization and order of the inter-island region. The vibronic intensity distribution of the inter-island spectrum does not coincide with the one of the single crystal that is characteristic of H-type aggregation [48]. We can conclude that the molecules in the inter-island region are not organized according to the single-crystal unit cell [44, 45] and that the dominant intermolecular interactions are not H-aggregate like.

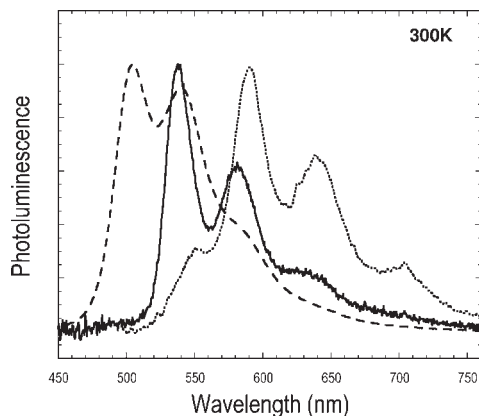


**Figure 4.11** Photoluminescence spectra of the inter-island region of a 0.3-nm thick T6 film (continuous line), of T6 molecules in a PMMA matrix (dashed line) and of a T6 single crystal (dotted line). The T6–PMMA matrix spectrum was excited at 400 nm.

The single-crystal PL spectrum (laser excitation at 488 nm) was measured in spatially resolved and backscattering configuration to minimize self-absorption. Adapted from Ref. [43].

In Fig. 4.12a and b CLSM and AFM images, respectively, of a 5-nm thick T6 film are shown. From AFM measurements the film is composed of two complete layers of T6 molecules for a total height profile of  $\sim 5$  nm. On top of these two layers (Fig 4.12b) there is the recurrence of the island “motif” forming a third and a fourth layer. The CLSM micrograph shows some bright regions that correspond to the thicker part of the film (towers). The islands forming the third and fourth layers of the film are only slightly visible under the brighter spots and the two underlying complete layers are very weakly emitting. The high PL intensity of the towers with respect to the surrounding areas can be explained by the greater thickness. In addition, it cannot be excluded that by increasing the film thickness the molecules of the top layers might undergo a small rotation of their long axis with respect to the normal to the surface. This would favor molecular excitation thanks to the larger component of their dipole moment parallel to the laser electric field. It is useful to note that in the single-crystal unit cell T6 molecules form an angle of roughly  $23^\circ$  with respect to the *a*-crystalline axis (see Fig. 4.8a) [45].

Figure 4.12c reports the spatially resolved PL spectrum measured on one of these towers. The spectrum is compared with that of the single crystal and shows the same features with the excitonic peak at  $\sim 590$  nm (2.1 eV) [49].

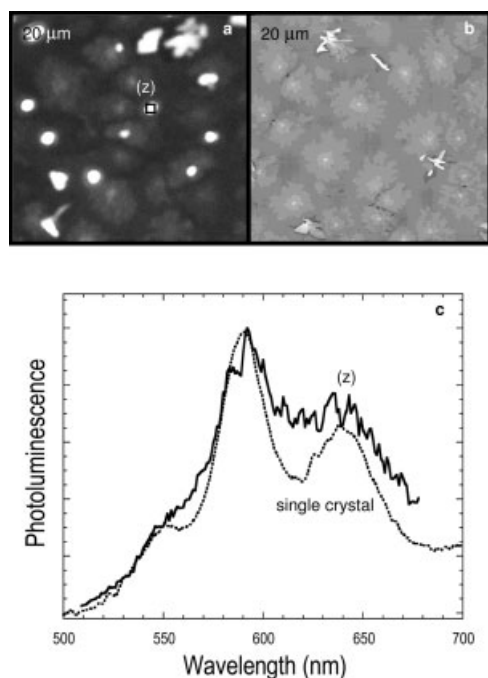


**Figure 4.12** T6 film of 5-nm nominal thickness on  $\text{SiO}_2$ , rate  $0.02 \text{ \AA s}^{-1}$ , substrate temperature  $120^\circ \text{C}$ . (a) CLSM image; (b) AFM image; (c) continuous line, spatially resolved PL spectrum measured at position (z) in (a); dotted line, PL spectrum of T6 single crystal. Adapted from Ref. [43].

Since the PL spectra of organic semiconductors are highly sensitive indicators of molecular packing, we can infer that in films thicker than two monolayers the T6 molecules organize as in the single crystal with a herringbone-like packing and a dominant H-aggregate interaction [32, 49].

In films formed by at least a complete layer, the characteristic spectrum of the inter-island region (Fig. 4.10b) is no longer detected.

This demonstrates that the molecules that in the sub-monolayer films lie flat on the substrate, as the deposition continues they undergo rotation of their long molecular axis until they all stand close to the perpendicular to the substrate in thicker films (Fig. 4.13b). A more detailed study of this mechanism is outside the scope of this contribution and will be reported elsewhere [50].

In conclusion, by CLSM and spectroscopy we have demonstrated that in sub-monolayer films of T6 on silicon dioxide there is the coexistence of two phases composed of molecules either perpendicular or parallel to the substrate (Fig. 4.13a and a'). When a complete layer of molecules is formed, all of them stand perpendicular to the substrate (Fig. 4.13b and b'). At a thickness greater than two complete layers, T6 molecules pack as in the single crystal. The results reported show that confocal spatially resolved PL microscopy and spectroscopy are power-

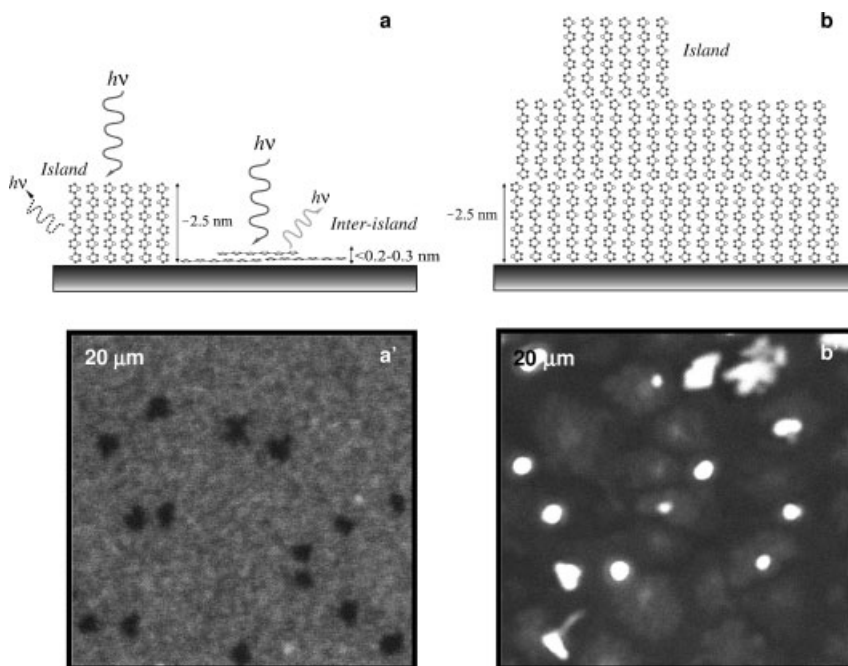


**Figure 4.13** (a') CLSM image of a sub-monolayer film of T6; (a) proposed sketch of the molecular organization in sub-monolayer films on SiO<sub>2</sub> substrates; (b') CLSM image of a T6 multi-layer film; (b) proposed sketch of the T6 molecular organization in multi-layer films on SiO<sub>2</sub> substrates.

ful techniques to determine the supramolecular organization in organic ultra-thin films.

## 4.5

### Imaging and Spectroscopy of Organic Bulk Heterojunctions and Correlation with Optoelectronic Device Properties

In this section, confocal microscopy is used to determine the microscopic structure of organic semiconductor bulk heterojunction thin films. The properties of devices based on bulk heterojunctions are extremely sensitive to the morphology and phase segregation of the active layer. CLSM can map PL intensity originated by different materials with a spatial resolution of  $\sim 200$  nm. This allows one to image the microscopic structure and the phase segregation of bulk heterojunctions within devices with the aim of correlating them with the device electrical characteristics.

Organic material science is a continuously growing field that nowadays is developing devices that are reaching market standards. Organic LEDs for display applications are market ready and FETs are being developed as switching devices for active-matrix LED displays [51], low-cost large-area flexible microelectronics [52–54] and hybrid electronics [55].

The combination in a single device of two functionalities, such as electrical switching and light emission, increases the number of applications of organic semiconductors and is a step towards the idea of completely integrated organic optoelectronics [56]. Such a device, namely a light-emitting field-effect transistor (LET), is characterized by light emission that correlates with the drain current and can be modulated by both the drain–source voltage and the gate voltage.

Recently, LETs with unipolar electrical characteristics (p-type transport) based on molecular semiconductors [57, 58] and polymers [59, 60] were reported. Ambipolar charge transport is a desirable property for organic semiconductors since it enables the fabrication of complementary logic circuits such as CMOS transistors with a single active layer [61, 62]. Moreover, ambipolar conduction can be crucial in light-emitting transistors to maximize exciton recombination through electron–hole balance as well as to adjust the position of the recombination region in the channel by tuning the gate voltage [63].

Although simultaneous p- and n-type conduction should be an intrinsic property of pure organic semiconductors, only a few materials are known to support both electron and hole conduction [64–66]. Organic semiconductors are generally unipolar and most of them exhibit p-type transport [67]. The limited number of ambipolar organic materials reported stimulated the search for alternative approaches to achieve simultaneous electron and hole transport in organic field-effect transistors [68, 69].

Bulk heterojunctions of solution-processed blends of a *p-type* polymer and *n-type* molecules such as fullerene and perylene were reported to give ambipolar conduction in FET configuration [62, 69, 70]. The validity of this approach has

been largely demonstrated in the fabrication of LEDs [71, 72] and solar cells [73, 74], showing its general importance for organic semiconductors.

Recently, we reported the first ambipolar organic LET [75]. The active layer is a vacuum-sublimed bulk heterojunction composed of *N,N'*-ditridecylperylene-3,4,9,10-tetracarboxylic diimide (P13) (*n-conductor*) and *a*-quinquethiophene (T5) (*p-conductor*).

Here we report on the bulk heterojunction approach for fine tuning of electron and hole mobility and also of electroluminescence intensity in field-effect devices. The electron and hole field-effect mobility and the light emission intensity are determined by the relative concentration of the two materials and by the microscopic structure of the bulk heterojunction, which can be imaged by CLSM.

In particular, by varying the volume ratio of the p- and n-type materials in the bulk heterojunction we identify three different working regimes for the ambipolar light-emitting field-effect devices. The first one is obtained for bulk heterojunctions composed of an excess of T5 and is characterized by ambipolar electrical conduction and absence of light emission. In the second working regime the active layer has a balanced composition and shows ambipolar electrical properties accompanied by light emission. For bulk heterojunctions composed of an excess of P13 the third regime characterized by unipolar (n-type) transport and electroluminescence emission is obtained.

The working mechanism of a T5–P13 bulk heterojunction LET is revealed by time-resolved photoluminescence measurements.

Devices were prepared using as a substrate a heavily doped, n-type Si wafer (doping level  $10^{18} \text{ cm}^{-3}$ ) with an aluminum back contact that acts as a gate electrode. The gate insulator consists of a thermally grown  $\text{SiO}_2$  layer with a thickness of 150 nm. The organic thin-film bulk heterojunctions with a thickness of about 50 nm were prepared by co-evaporation of T5 and P13 with variable volume ratios.

The base pressure during the vacuum sublimation of T5 and P13 was  $2 \times 10^{-7}$  mbar and the deposition rate was kept constant at  $0.1 \text{ \AA s}^{-1}$  for each material. The different volume ratios of T5 and P13 were obtained by reducing the flux of one of the components on the substrate with a mechanical chopper.

Source and drain Au contacts were thermally evaporated through a shadow mask with a thickness of about 40 nm. The channel length and width of the FET device were  $40 \mu\text{m}$  and  $55.1 \text{ mm}$ , respectively. For electrical characterization, the devices were transferred through air into an argon glove-box ( $<1 \text{ ppm O}_2, \text{ H}_2\text{O}$ ). The transistor output and transfer characteristics and the photocurrent were measured with a semiconductor parameter analyzer. The mobility values were extracted from the saturated drain in transfer configuration.

In Fig. 4.14 the molecular structures of T5 and P13 and the scheme of the FET device are shown.

Figure 4.15 shows CLSM micrographs of three different relevant bulk heterojunction compositions in the green and red spectral range. It is necessary to study the morphology and phase composition of the co-evaporated films with CLSM because the imaging of the co-evaporated films by AFM is problematic owing to the low mechanical stability of P13 upon interaction with the AFM tip.

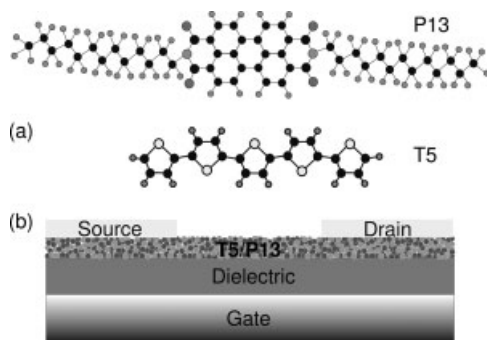


**Figure 4.14** (a) Molecular structures of the co-evaporated film components (T5 and P13); (b) schematic of the FET device structure.

CLSM measurements were performed with the setup described in Section 4.3.1; samples were excited with 488-nm  $\text{Ar}^+$  laser radiation. As the PL emission of T5 and P13 are spectrally separated [T5 PL peaks at 550 nm and of P13 at  $\sim 690$  nm; see Fig. 4.19a], it is possible to image the phase separation in the bulk heterojunction by selecting the detection windows to match the emission spectral range of each material. T5 photoluminescence is monitored in the spectral range centered at  $515 \pm 20$  nm (green channel), P13 is monitored in the spectral range for wavelength  $>600$  nm (red channel). The two spectral ranges are recorded with different amplifications to compensate for the low PL efficiency of T5, its low absorption at 488 nm and the smaller spectral detection window for the T5 emission range (green channel).

In Fig. 4.15 the red and green channels monitor the P13 and T5 emission, respectively.

It is important to note that P13 exhibits a considerably higher PL intensity than the weakly emitting T5. In Fig. 4.15a and a' CLSM micrographs of the co-evaporated film T5:P13 3:1 are presented. The morphology of the film is rather inhomogeneous and the bulk heterojunction is dominated by T5 clusters  $\sim 1 \mu\text{m}$  in size. In Fig. 4.15b and b' PL micrographs of the co-evaporated film with balanced T5:P13 composition are shown for the red and green spectral ranges, respectively. The film appears rather smooth; small T5 clusters are visible in the green channel (Fig. 4.15b'). On increasing the proportion of P13 to 75%, the surface of the bulk heterojunction appears smoother (see Fig. 4.15c). Also in this case, T5 forms small clusters but they are rather homogeneously distributed in the film (Fig. 4.15c'). In agreement with the observed tendency of T5 to form clusters in the bulk heterojunction, the T5 PL component in Fig. 4.19a shows typical solid-state features [76].

Figure 4.16 shows (a) the output and (b) the corresponding electroluminescence intensity of the bulk heterojunction LET composed of T5 and P13 with a volume ratio of 1:1. The transistor exhibits pronounced ambipolar behavior in the output and transfer characteristics, as discussed in detail in Ref. [75]. From the transfer

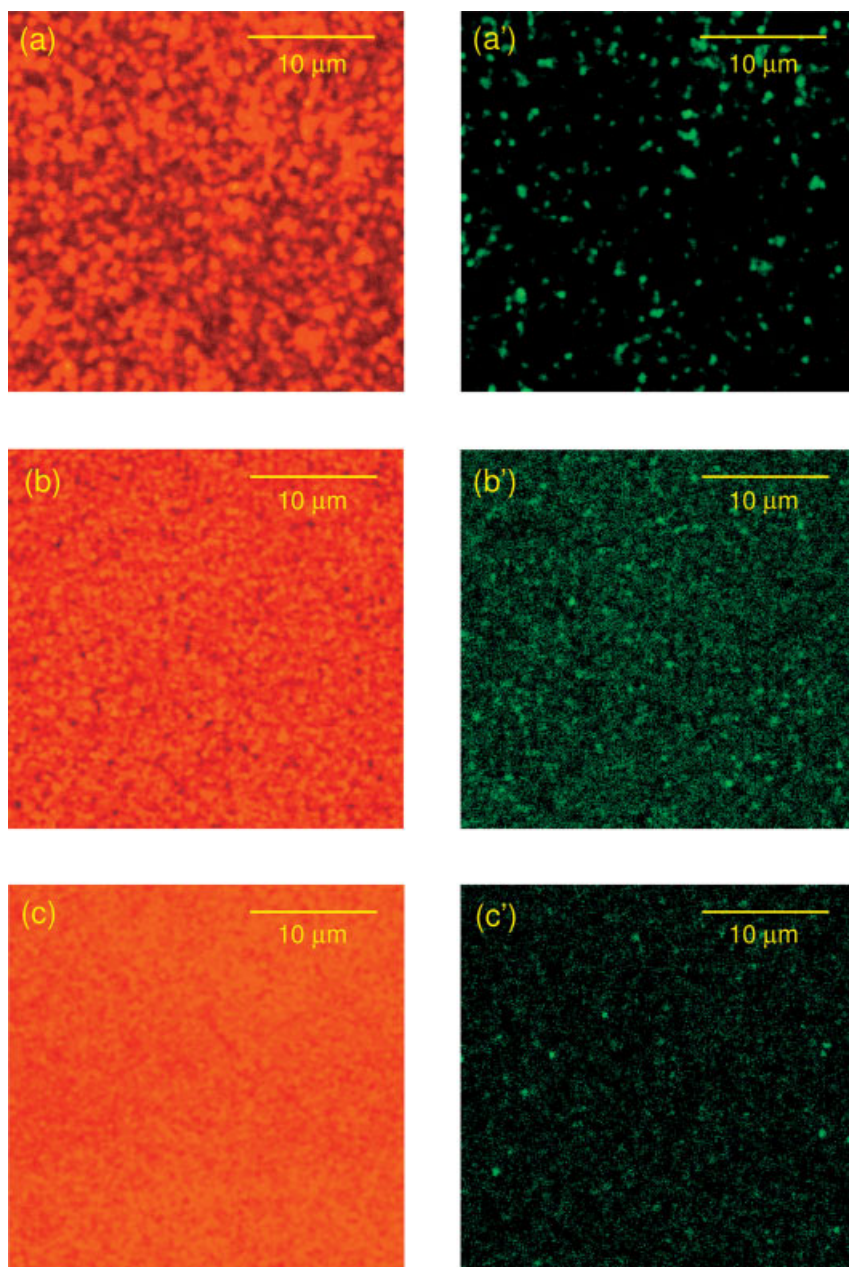


**Figure 4.15** CLSM micrograph of the co-evaporated films. (a) T5:P13 9:1 red channel (intensity amplified by a factor of 3 with respect to the other red channel images); (a') green channel; (b) T5:P13 1:1 red channel; (b') green channel; (c) T5:P13 1:3 red channel; (c') green channel.

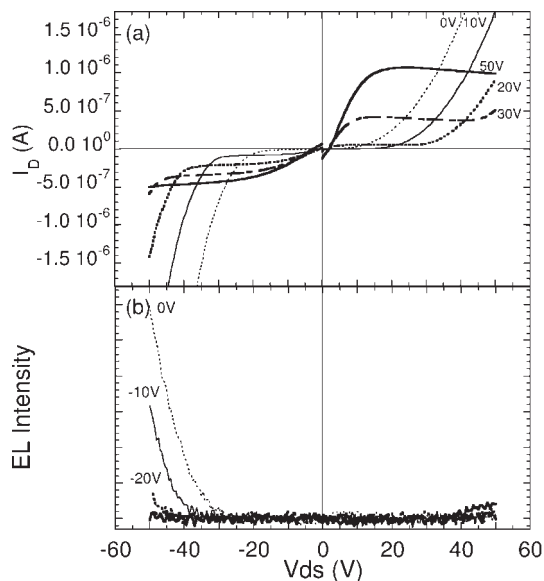


**Figure 4.16** T5:P13 1:1 (a) output characteristics and (b) electroluminescence intensity of the LET device for negative and positive drain-source bias. Adapted from Ref. [75].

curves reported in Fig. 4.17a, a hole mobility of  $5 \times 10^{-4} \text{ cm}^2 \text{ V}^{-1} \text{ s}^{-1}$  and an electron mobility of  $1 \times 10^{-3} \text{ cm}^2 \text{ V}^{-1} \text{ s}^{-1}$  is extracted. In the output characteristics for negative  $V_{DS}$  and  $V_G$ , the light output (Fig. 4.17b) is apparently correlated with the non-saturating drain current. The onset and magnitude of the electroluminescence correlate well with the drain current, whereas for positive bias voltages only weak emission is observed and no obvious correlation with the drain current seems to exist.

The influence of the composition of the bulk heterojunction on the mobility and EL intensity of the light-emitting transistors with a systematic variation of the T5:P13 volume ratio have been investigated. The devices with an excess of P13 exhibit both light emission and a unipolar electron current [77]. The devices with an excess of T5 show ambipolar charge-carrier transport but no light emission.

In Fig. 4.18 are reported the extracted mobilities of the different T5:P13 bulk heterojunction compositions and of the pure reference devices. When the relative concentration of the electron- or hole-transporting material is decreased there is a corresponding decrease in the electron or hole mobility. The electron mobility decreases by about one order of magnitude, whereas the hole mobility decreases by 1.5 orders of magnitude. At lower concentrations of P13, the electron mobility seems to level off, whereas at low percentages of T5 the hole mobility is below the detection limit.

By correlating the CLSM micrograph and the optoelectronic characteristics of the bulk heterojunction LETs with different T5:P13 compositions, it is possible to

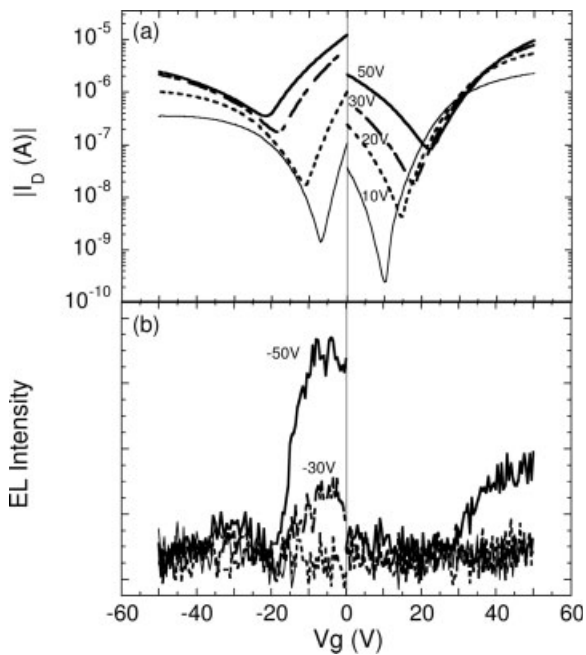


**Figure 4.17** T5:P13 1:1 (a) transfer characteristics and (b) electroluminescence intensity of the bulk heterojunction LET device. Adapted from Ref. [75].

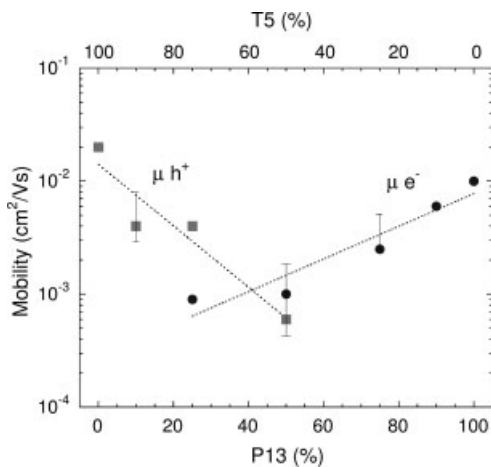


**Figure 4.18** Electron and hole field-effect mobilities for different bulk-heterojunction composition. Adapted from Ref. [77].

investigate the microscopic structure of the heterojunction and the resulting charge percolation. Whereas 25% of P13 in the bulk heterojunction is sufficient to have a continuous path for electrons that leads to a remarkable mobility, the same percentage of T5 is insufficient to produce comparable hole conduction. This can be explained by the different film growth behaviors of the two moieties. As shown in Fig. 4.15, T5 tends to form clusters, giving rise to a continuous pathway for holes only for bulk heterojunctions with proportions of T5 larger than 25%. In contrast, P13 is a highly surface-mobile molecule, hence even diluted concentrations lead to continuous pathways for electrons in the bulk heterojunction.

In Fig. 4.19a the PL spectra of bulk heterojunctions with different compositions are shown. The spectra are excited by the second harmonic of a Ti:sapphire laser at 400 nm where P13 has a minimum of absorbance and are dominated by P13 emission that has a main peak at  $\sim 690$  nm; the weak T5 PL is peaked at 550 nm. On increasing of the concentration of T5 in the heterojunction the PL intensity of P13 strongly decreases. Three orders of magnitude are lost by varying the concentration of P13 from 100 to 25%. Such a dramatic quenching cannot be due only to

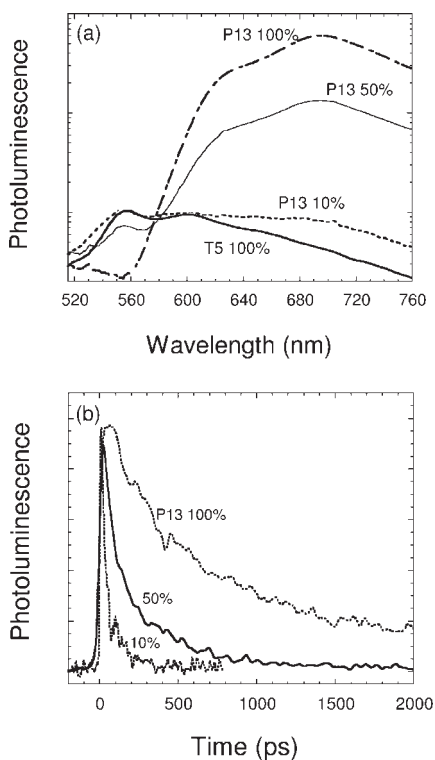


**Figure 4.19** (a) Steady-state PL intensity of co-evaporated films with different percentages of T5-P13; (b) photoluminescence transients at  $635 \pm 20$  nm of co-evaporated films. Excitation at 400 nm. Adapted from Ref. [77].

the decreased concentration of P13 in the film, but is an indication of the dissociation of excitons formed in P13 upon interaction with T5 molecules.

In Fig. 4.19b are reported the PL decays for the P13 film and two relevant heterojunctions, measured at the 635-nm peak of the P13 photoluminescence spectrum. The PL dynamics of the bulk heterojunction films are strongly dependent on T5 concentration. The decay of pure P13 is bi-exponential with a first decay time  $\tau_1 \approx 350$  ps and a tail with  $\tau_2 \approx 1.6$  ns, the film T5:P13 1:1 has a first decay time  $\tau_1 \approx 100$  ps and a second of  $\tau_2 \approx 700$  ps. On increasing the excess of T5 (T5:P13 3:1) the PL decay becomes extremely fast with  $\tau_1 \approx 20$  ps and  $\tau_2 \approx 150$  ps.

Such fast PL dynamics and quenching with increasing percentages of T5 in the bulk heterojunction is an indication of the dissociation of P13 excitons by hole transfer to the material with the lower ionization potential (T5). This process is in competition with exciton recombination and light emission in bulk heterojunctions and is therefore detrimental for LET functioning.

Indeed, the exciton separation taking place at high percentages of T5 explains why the bulk heterojunction device composed by T5:P13 3:1 has good ambipolar transport characteristics but no electroluminescence emission. Finally, whether charge separation or light emission is the predominant phenomenon in the P13–T5 mixtures depends critically on the ratio of the two components and on the microscopic structure of the bulk heterojunction.

By controlled co-evaporation of the *p-conductor* T5 and the *n-conductor* P13 it is possible to determine the microscopic structure of the bulk heterojunction and, consequently, to modulate the effect of the electronic interaction between the two moieties. The microscopic structure of the bulk heterojunction is revealed by confocal laser scanning microscopy; the correlation with time-resolved photoluminescence spectroscopy showed that excitons generated in P13 undergo dissociation when T5 molecules are in the close vicinity.

The electroluminescence emission for this device is the result of a trade-off between an extended percolation path for carriers that guarantees ambipolar transport and exciton formation and the electronic interaction between P13 and T5 molecules that causes exciton quenching.

#### 4.6 Conclusions

Confocal laser scanning microscopy is an extremely popular experimental technique in biology and the life sciences. Its diffusion derives from the fact that it is a high-resolution imaging technique using PL as measurable parameter, which allows fast acquisition and optical sectioning.

Here we have reported on the development of CLSM as a local spectroscopic tool able to perform spatially and time-resolved spectroscopy. The possibility of correlating PL imaging and spatially resolved spectroscopy favors a more quantita-

tive approach in biology and the life sciences and also the application of CLSM to other scientific fields such as nanotechnology and material science.

The combination of imaging and spatially and time-resolved spectroscopy applied to the study of organic semiconductor thin films can reveal fundamental excitonic processes and allow their correlation with the local molecular environment in thin films, heterojunctions and nanostructures.

We reported on the determination of the supramolecular organization of organic semiconductor ultra-thin films by correlation of CLSM photoluminescence imaging, spatially resolved spectroscopy and AFM. CLSM reveals the presence of molecules lying on the substrate that cannot be revealed by AFM.

Moreover, we found that by photoluminescence microscopy measurements it is possible to determine the microscopic structure of an organic bulk heterojunction and, by correlating these with the electronic properties of the devices, to understand their working mechanism.

### Acknowledgments

The authors acknowledge very fruitful collaboration with C. Rost, S. Karg, W. Riess, M. Murgia, F. Dinelli, M. Cavallini, R. Zamboni, F. Biscarini and C. Taliani. The valuable technical support of P. Fancello, P. Mei and T. Bonfiglioli is appreciated. This work was supported by the EU FET-IST program under contract IST-2001-38919 (PHOENIX), by EU-G5RD-CT2000-00349 (MONA-LISA) by the EU-IST-FET program under project IST-33057 (ILO) and the Italian ministry MIUR under project FIRB-RBNE033KMA.

### References

- 1 R. H. Friend, R. W. Gymer, A. B. Holmes, J. H. Burroughes, R. N. Marks, C. Taliani, D. D. C. Bradley, D. A. Dos Santos, J. L. Brédas, M. Lögdlund, W. R. Salaneck, *Nature* **397**, 121 (1999).
- 2 C. W. Tang, S. A. VanSlyke *Appl. Phys. Lett.* **51**, 913 (1987).
- 3 G. Horowitz, D. Fichou, X. Peng, Z. Xu, F. Garnier, *Solid State Commun.* **72**, 381 (1989).
- 4 C. D. Dimitrakopoulos, P. R. L. Malenfant, *Adv. Mater.* **14**, 99 (2002,)
- 5 S. E. Shaheen, C. J. Brabec, N. S. Sariciftci, F. Padinger, T. Fromherz, J. C. Hummelen, *Appl. Phys. Lett.* **78**, 841 (2001).
- 6 P. Peumans, S. Uchida, S. R. Forrest, *Nature* **425**, 158 (2003).
- 7 D. W. Pohl, W. Denk, M. Lanz, *Appl. Phys. Lett.* **44** 651 (1984).
- 8 F. Zenhausern, Y. Martin, H.K. Wickramasinghe, *Science* **269**, 1083 (1995).
- 9 T. Wilson, *Confocal Microscopy*, Academic Press, London, 1990.
- 10 M. Schrader, S.W. Hell, H.T.M. van der Voort, *Appl. Phys. Lett.* **69**, 3644 (1996).
- 11 R. X. Bian, R. C. Dunn, X. S. Xie, P. T. Leung, *Phys. Rev. Lett.* **75**, 4772 (1995).
- 12 P. J. Moyer, K. Walzer, M. Hietschold, *Appl. Phys. Lett.* **67**, 2129 (1995).
- 13 W. Denk, J.H. Strickler, W.W. Webb, *Science* **248**, 73 (1990).
- 14 M. Young, *Optics, Lasers*, Springer, Berlin, 2000.

- 15 M. W. Davidson, M. Abramowitz, *Optical Microscopy*, Olympus America, New York, 1999.
- 16 S. Moehl, H. Zhao, B. Dal Don, S. Wachter, H. Kalt, *J. Appl. Phys.* **93**, 6265 (2003).
- 17 W. Denk, J. H. Strickler, W. W. Webb, *Science* **248**, 73 (1990).
- 18 S. W. Hell, K. Bahlmann, M. Schrader, A. Soini, H. Malak, I. Gryczynski, J. R. Lakowicz, *J. Biomed. Opt.* **1**, 71 (1996).
- 19 O. Nakamura, *Microsc. Res. Tech.* **47**, 165 (1999).
- 20 M. Schrader, S. W. Hell, *J. Microsc.* **183**, 189 (1996).
- 21 F. Cicoira, C. Santato, F. Dinelli, M. Murgia, M. A. Loi, F. Biscarini, R. Zamboni, P. Heremans, M. Muccini, *Adv. Funct. Mater.* **15**, 375 (2005).
- 22 J. Gomez-Segura, M. Cavallini, M. A. Loi, E. Da Como, G. Ruani, M. Massi, M. Muccini, D. Ruiz-Molina, J. Veciana, F. Biscarini, unpublished.
- 23 L. Rayleigh, Breath figures. *Nature* **86**, 416 (1911).
- 24 M. Srinivasarao, D. Collings, A. Philips, S. Patel, *Science* **292**, 79 (2001).
- 25 W. A. Hofer, A. S. Foster, A. L. Shluger, *Rev. Mod. Phys.* **75**, 1287 (2003).
- 26 H. Sirringhaus, P. J. Brown, R. H. Friend, M. M. Nielsen, K. Bechgaard, B. M. W. Langeveld-Voss, A. J. H. Spiering, R. A. J. Janssen, E. W. Meijer, P. Herwig, D. M. De Leeuw, *Nature*, **401**, 685 (1999).
- 27 V. C. Sundar, J. Zaumseil, V. Podzorov, E. Menard, R. L. Willett, T. Someya, M. E. Gershenson, J. A. Rogers, *Science* **303**, 1644 (2004).
- 28 R. W. I. de Boer, T. M. Klapwijk, A. F. Morpurgo, *Appl. Phys. Lett.* **83**, 4345 (2003).
- 29 H. Klauk, M. Halik, U. Zschieschang, G. Schmid, W. Radlik, W. Weber, *J. Appl. Phys.* **92**, 5259 (2002).
- 30 G. Horowitz, M. E. Hajlaoui, *Adv. Mater.* **12**, 1046 (2000).
- 31 V. Podzorov, E. Menard, A. Borissov, V. Kiryukhin, J. A. Rogers, M. E. Gershenson, *Phys. Rev. Lett.* **93**, 086602 (2004).
- 32 M. Muccini, E. Lunedei, C. Taliani, D. Beljonne, J. Cornil, J. L. Brédas, *J. Chem. Phys.* **109**, 10513 (1998); M. Muccini, E. Lunedei, A. Bree, G. Horowitz, F. Garnier, C. Taliani, *J. Chem. Phys.* **108**, 7327 (1998).
- 33 M. A. Loi, C. Martin, H. R. Chandrasekhar, M. Chandrasekhar, W. Graupner, F. Garnier, A. Mura, G. Bongiovanni, *Phys. Rev. B* **66**, 113102 (2002).
- 34 G. Horowitz, D. Fichou, X. Peng, Z. Xu, F. Garnier, *Solid State Commun.* **72**, 381 (1989).
- 35 M. Mushrush, A. Facchetti, M. Lefenfeld, H. E. Katz, T. J. Marks, *J. Am. Chem. Soc.* **125**, 9414 (2003).
- 36 P. Ostoja, S. Guerri, M. Impronta, P. Zabberoni, R. Danieli, S. Rossini, C. Taliani, R. Zamboni, *Adv. Mater. Opt. Electron.* **1**, 127 (1992).
- 37 F. Dinelli, M. Murgia, P. Levy, M. Cavallini, F. Biscarini, *Phys. Rev. Lett.* **92**, 116802 (2004).
- 38 B. Servet, G. Horowitz, S. Ries, O. Lagorsse, P. Alnot, A. Yassar, F. Deloffre, P. Srivastava, R. Hajlaoui, P. Lang, F. Garnier, *Chem. Mater.* **6**, 1809, 1994.
- 39 P. Ostoja, S. Guerri, S. Rossini, M. Servidori, C. Taliani, R. Zamboni, *Synth. Met.* **54**, 447 (1993).
- 40 A. J. Lovinger, D. D. Davis, R. Ruel, L. Torsi, A. Dodabalapur, H. E. Katz, *J. Mater. Res.* **10**, 2558 (1995).
- 41 F. Biscarini, R. Zamboni, P. Samori, P. Ostoja, C. Taliani, *Phys. Rev. B* **52**, 14868 (1995).
- 42 M. Muccini, M. Murgia, F. Biscarini, C. Taliani, *Adv. Mater.* **13**, 355 (2001).
- 43 M. A. Loi, E. Da Como, F. Dinelli, M. Murgia, R. Zamboni, F. Biscarini, M. Muccini, *Nat. Mater.* **4**, 81 (2005).
- 44 W. Porzio, S. Destri, M. Maschera, S. Brückner, *Acta Polym.* **44**, 266 (1993).
- 45 G. Horowitz, B. Bachet, A. Yassar, P. Lang, F. Demanze, J.-L. Fave, F. Garnier, *Chem. Mater.* **7**, 1337 (1995).
- 46 A. Degli Esposti, M. Fantì, M. Muccini, C. Taliani, G. Ruani, *J. Chem. Phys.* **112**, 5957 (2000).
- 47 F. Kouki, P. Spearman, P. Valat, G. Horowitz, F. Garnier, *J. Chem. Phys.* **113**, 385 (2000).
- 48 M. Pope, C. E. Swenberg, *Electronic Processes in Organic Crystals*, Oxford University Press, New York, 1982.

- 49 M. A. Loi, A. Mura, G. Bongiovanni, Q. Cai, C. Martin, H. R. Chandrasekhar, M. Chandrasekhar, W. Graupner, F. Garnier, *Phys. Rev. Lett.* **86**, 732 (2001).
- 50 F. Dinelli, J.F. Moulin, M. A. Loi, E. Da Como, M. Massi, M. Murgia, M. Muccini, F. Biscarini, to be published.
- 51 T. N. Jackson, Y. Y. Lin, D. J. Gundlach, H. Klauk, *IEEE J. Sel. Top. Quantum Electron.* **4**, 100 (1998).
- 52 G. H. Gelinck, H. E. A. Huitema, E. Van Veenendaal, E. Cantatore, L. Schrijnemakers, J. B. P. H. Van der Putten, T. C. T. Geuns, M. Beenhakkers, J. B. Giesbers, B.-H. Huisman, E. J. Meijer, E. M. Benito, F. J. Touswlaager, A. W. Marsman, B. J. E. Van Rens, D. M. De Leeuw, *Nat. Mater.* **3**, 106 (2004).
- 53 C. D. Sheraw, L. Zhou, J. R. Huang, D. J. Gundlach, T. N. Jackson, M. G. Kane, I. G. Hill, M. S. Hammond, J. Campi, B. K. Greening, J. Francl, J. West, *Appl. Phys. Lett.* **80**, 1088 (2002).
- 54 P. Mach, S. J. Rodriguez, R. Nortrup, P. Wiltzius, J. A. Rogers, *Appl. Phys. Lett.* **78**, 3592 (2001).
- 55 T. Tsujimura, F. Libsch, P. Andry, *J. Soc. Int. Display*, **13**, 161 (2005).
- 56 H. Sirringhaus, N. Tessler, R. H. Friend, *Science* **280**, 1741 (1998).
- 57 A. Hepp, H. Heil, W. Weise, M. Ahles, R. Schmechel, H. von Seggern, *Phys. Rev. Lett.* **91**, 157406 (2003).
- 58 C. Santato, R. Capelli, M. A. Loi, M. Murgia, F. Cicoria, V. A. L. Roy, P. Stallinga, R. Zamboni, C. Rost, S. F. Karg, M. Muccini, *Synth. Met.* **146**, 329 (2004).
- 59 M. Ahles, A. Hepp, R. Schmechel, H. von Seggern, *Appl. Phys. Lett.* **84**, 428 (2004).
- 60 T. Sakanoue, E. Fujiwara, R. Yamada, H. Tada, *Appl. Phys. Lett.* **84**, 3037 (2004).
- 61 B. Crone, A. Dodabalapur, Y.-Y. Lin, R. W. Filas, Z. Bao, A. LaDuca, R. Sarpeshkar, H. E. Katz, W. Li, *Nature* **403**, 521 (2000).
- 62 E. J. Meijer, D. M. De Leeuw, S. Setayesh, E. van Veenendaal, B.-H. Huisman, P. W. M. Blom, J. C. Hummelen, U. Scherf, T. M. Klapwijk, *Nat. Mater.* **2**, 678 (2003).
- 63 M. Freitag, J. Chen, J. Tersoff, J. C. Tsang, Q. Fu, J. Liu, J. Avouris, *Phys. Rev. Lett.* **93**, 076803 (2004).
- 64 R. J. Chesterfield, C. R. Newman, T. M. Pappenfus, P. C. Ewbank, M. H. Haukaas, K. R. Mann, L. L. Miller, C. D. Frisbe, *Adv. Mater.* **15**, 1278 (2003).
- 65 T. Yasuda, T. Tsutsui, *Chem. Phys. Lett.* **402**, 395 (2005).
- 66 T. D. Anthopoulos, C. Tanase, S. Setayesh, E. J. Meijer, J. C. Hummelen, P. W. Blom, D. M. De Leeuw, *Adv. Mater.* **16**, 2174 (2004).
- 67 C. D. Dimitrakopoulos, P. R. L. Malenfant, *Adv. Mater.* **14**, 99 (2002).
- 68 A. Dodabalapur, H. E. Katz, L. Torsi, R. C. Haddon, *Appl. Phys. Lett.* **68**, 1108 (1996).
- 69 W. Geens, S. E. Shaheen, C. J. Brabec, J. Portmans, N. S. Sariciftci, *AIP Conf. Proc.* **544**, 516 (2000).
- 70 K. Tada, H. Harada, K. Yoshino, *Jpn. J. Appl. Phys.* **35**, L 944 (1996).
- 71 N. Corcoran, A. C. Arias, J. S. Kim, J. D. MacKenzie, R. H. Friend, *Appl. Phys. Lett.* **82**, 299 (2003).
- 72 M. M. Alam, C. J. Tonzola, S. A. Jenekhe, *Macromolecules* **36**, 6577 (2003).
- 73 S. E. Shaheen, C. J. Brabec, N. S. Sariciftci, F. Padinger, T. Fromherz, J. C. Hummelen, *Appl. Phys. Lett.* **78**, 841 (2001).
- 74 A. C. Arias, J. D. MacKenzie, R. Stevenson, J. J. M. Halls, M. Inbasekaran, E. P. Woo, D. Richards, R. H. Friend, *Macromolecules* **34**, 6005 (2001).
- 75 C. Rost, S. Karg, W. Riess, M. A. Loi, M. Murgia, M. Muccini, *Appl. Phys. Lett.* **85**, 1613 (2004).
- 76 M. A. Loi, A. Mura, G. Bongiovanni, C. Botta, G. Di Silvestro, R. Tubino, *Synth. Met.* **121**, 1299 (2001).
- 77 M. A. Loi, C. Rost-Bietsch, M. Murgia, S. Karg, W. Riess, M. Muccini, *Adv. Funct. Mater.*, in press (2005).

## 5 Spectroscopy of Long-Lived Photoexcitations in $\pi$ -Conjugated Systems

Markus Wohlgenannt, Eitan Ehrenfreund and Z. Valy Vardeny

### 5.1 Introduction

#### 5.1.1 Basic Properties of $\pi$ -Conjugated Polymers

$\pi$ -Conjugated polymer systems have been intensively studied during the last 25 years. They form a new class of semiconductor electronic materials with potential applications such as organic light-emitting diodes (OLEDs) [1], thin-film transistors (TFTs) [2], photovoltaic cells [3] and optical switches and modulators [4]. As polymers, these organic semiconductors have a highly anisotropic quasi-one-dimensional electronic structure that is fundamentally different from the structures of conventional inorganic semiconductors. This has two consequences: First, their chain-like structure leads to strong coupling of the electronic states to conformational excitations peculiar to the one-dimensional (1D) system [5], and second, the relatively weak interchain binding allows diffusion of dopant molecules into the structure (between chains), whereas the strong intrachain carbon-carbon bond maintains the integrity of the polymer [5]. In their neutral form, these polymers are semiconductors with an energy gap of  $\sim 2$  eV. However, they can be easily doped with various p- and n-type dopants, increasing their conductivity by many orders of magnitude; conductivities in the range of  $\sim 10^3$ – $10^4$  S cm $^{-1}$  are not unusual [6]. The discovery of the ability to dope these organic semiconductors into metallic conductivities led to the award of the 2000 Nobel Prize in Chemistry to Alan Heeger, Alan McDiarmid and Hideki Shirakawa.

The simplest example of the class of conducting polymers is polyacetylene, (CH) $_x$ , which is depicted in Fig. 5.1. It consists of weakly coupled chains of CH units forming a pseudo-1D lattice. The stable isomer is *trans*-(CH) $_x$ , in which the chain has a zigzag geometry; the *cis*-(CH) $_x$  isomer, in which the chain has a backbone geometry, is unstable at room temperature or under high illumination. Simple conducting polymers such as polyacetylene are planar, with three of the four carbon valence electrons forming sp $^2$  hybrid orbitals ( $\sigma$  bonds), while the fourth valence electron is in a  $\pi$  orbital perpendicular to the plane of the chain. The  $\sigma$

bonds are the building blocks of the chain skeleton and are thus responsible for the strong elastic force constant of the chain. The  $\pi$  orbitals form the highest occupied molecular orbitals (HOMOs) and the lowest unoccupied molecular orbitals (LUMOs), which together span an energy range of  $\sim 10$  eV [5]. *trans*-(CH) $_x$  is a semiconductor with a gap  $E_g \approx 1.5$  eV, which has two equivalent lowest energy states having two distinct conjugated structures [5]. Other polymers shown in Fig. 5.1, such as *cis*-(CH) $_x$ , polythiophene (PT), poly(*p*-phenylenevinylene) (PPV) and polyfluorene (PFO), have a non-degenerate ground-state structure and this can be formally described by adding an extrinsic gap component to the Peierls gap [5].

The properties and dynamics of optical excitations in conducting polymers are of fundamental interest because they play an important role in the potential applications. However, in spite of intense studies of the linear and nonlinear optical properties, the basic model for the proper description of the electronic excitations in conducting polymers is still controversial. One-dimensional semiconductor models [7], in which electron–electron (e–e) interaction has been ignored, have been successfully applied to interpret a variety of optical experiments in  $\pi$ -conjugated polymers [5]. In these models the strong electron–phonon (e–p) interaction leads to rapid self-localization of the charged excitations, the so-called polaronic effect. Then optical excitations across  $E_g$ , which is now the Peierls gap, are entirely different from the electron–hole (e–h) pairs of conventional semiconductors. Instead, the proper description of the quasiparticles in *trans*-(CH) $_x$  is 1D domain walls or solitons (S) that separate the two degenerate ground-state structures [5]. As a result of their translational invariance, solitons in *trans*-(CH) $_x$  are thought to play the role of energy- and charge-carrying excitations. Since the soliton is a topological defect, it can be either created in soliton–antisoliton (SS) pairs or be created in polyacetylene chains with odd numbers of CH monomers upon isomerization from *cis*-(CH) $_x$ . The same Hamiltonian that has predicted soliton excitations in *trans*-(CH) $_x$  predicts polarons as a distinct solution when a single electron is added to the trans chain [5]. For the non-degenerate ground-state (NDGS) polymers, adding an extrinsic gap component to the electron–phonon Hamiltonian results in polarons and bipolarons as the proper descriptions of their primary charge excitations. Singlet and triplet excitons have been also shown to play a crucial role in the photophysics of conducting polymers [8–13]. However, their existence in theoretical studies can be justified only when electron–electron interaction and correlation effects are added to the Hamiltonian [14, 15]. Recently, 2D type charge excitations or 2D polarons have been suggested to explain the properties of charge carriers in planar polymers and polymers that form lamellae such as regio-regular polyhexylthiophene [P(3HT)]. Some of the following sections deal with the variety of long-lived charge and neutral excitations in  $\pi$ -conjugated polymers and thus a brief summary of their physical properties is in order.

The e–e interaction is extremely important even in the simplest example of *trans*-(CH) $_x$  and therefore it is more comfortable to use the ‘exciton notation’ for the various excited states of  $\pi$ -conjugated polymers. In this notation the ground state is the  $1A_g$  state; the excited states are either even-symmetry excitons,  $nA_g$  or

odd-symmetry excitons,  $kB_u$ . The importance of the e–e interaction in *trans*-(CH)<sub>x</sub> can be concluded from the fact that the  $2A_g$  excited state (determined experimentally by two-photon absorption [16, 17]) is located below the first optically allowed excited state exciton, the  $1B_u$ . The e–e interaction cannot be ignored in any  $\pi$ -conjugated polymer and it has significant effects on various optical properties, such as photoluminescence (PL), electroabsorption (EA) and third-order optical susceptibilities. In cases where the bond alternation is relatively small, the ordering of the odd and even symmetry lowest excited states is  $E(2A_g) < E(1B_u)$  [18]. When the “effective” bond alternation is relatively large, the ordering of these states is reversed, resulting in a strong PL emission band. In PPV-type polymers, for instance, the benzene ring in the backbone structure gives rise to a large “effective” bond alternation for the extended  $\pi$  electrons [18] and therefore to high PL efficiency and improved OLED devices. Nevertheless, the Coulomb interaction among the  $\pi$  electrons, even when it is not dominant, leads to behavior qualitatively different from the prediction of single-particle Hückel model.

The soliton excitation in *trans*-(CH)<sub>x</sub> is an amphoteric defect that can accommodate zero, one or two electrons [5, 7, 19, 20]. The neutral soliton ( $S^0$ , spin-1/2) has one electron; positively and negatively charged solitons ( $S^\pm$ , spin-0) have zero or two electrons, respectively. Within the framework of the Su–Schrieffer–Heeger (SSH) model Hamiltonian [5], which contains e–p interactions but does not contain e–e or 3D interactions, it has been shown that a photoexcited e–h pair is unstable toward the formation of a soliton–antisoliton ( $S\bar{S}$ ) pair [21]. Subsequently, it was demonstrated [22] that as a consequence of the Pauli principle and charge conjugation symmetry in *trans*-(CH)<sub>x</sub>, the photogenerated soliton and antisoliton are oppositely charged. The study of photoexcited *trans*-(CH)<sub>x</sub>, however, has revealed several unexpected phenomena, which were not predicted by the SSH model of the soliton (for a review, see Ref. [23]). Most importantly, an overall neutral state as well as charged excitation have been observed; this neutral state has been correlated with  $S^0$  transitions [10]. This finding together with the absence [in undoped *trans*-(CH)<sub>x</sub>] of optical transitions at the midgap level, where transitions of neutral and charged solitons should have appeared according to the SSH picture, have shown that electron–electron interaction in *trans*-(CH)<sub>x</sub> cannot be ignored. In this case the electronic gap in *trans*-(CH)<sub>x</sub> is partially due to the electron correlations rather than entirely due to electron–phonon interaction as in the SSH model. Under these circumstances, the nature of the photoexcitations in *trans*-(CH)<sub>x</sub> may be very different from that predicted by the SSH Hamiltonian. These findings have stimulated photophysical research in *all* conducting polymers, mostly the NDGS polymers. The previous picture of photogeneration of bound soliton–antisoliton pairs in NDGS polymers has been modified. In contrast, photoexcitation of singlet and triplet excitons and/or polaron pairs [24, 25] has been demonstrated in many such conducting polymers.

The origin of the branching process that determines the relative photoproduction of neutral versus charged photoexcitations in the class of conducting polymers is not very well understood. One possible explanation of the branching process is offered by the Onsager theory, which has successfully explained charge

photoproduction in disordered materials and in molecular crystals [26]. The difficulty with this approach is that conducting polymers are quasi-1D semiconductors for which the Onsager theory based on the e–h Coulomb attraction may not be applicable. In addition, the application of this theory for 1D semiconductors results in negligible quantum efficiency for charge photoproduction under weak electric fields, contrary to experimental results. To solve this problem, it was suggested that the 1D–3D interplay is important in the photophysics of conducting polymers [27]. In the proposed model, *intrachain* excitation results in a neutral state, which is an exciton with relatively large binding energy, whereas *interchain* excitation may produce separate charges on the neighboring chains or polaron pair if the interchain geminate recombination is overcome. A demonstration [28] of the important role of interchain excitation was that long-lived charged excitations in oriented films are more efficiently photogenerated with light polarized perpendicular to the polymer chain direction than with light polarized parallel to it. On the other hand, the demonstration that charged polarons and bipolarons can be photogenerated in isolated PT and PPV chains [29, 30] in both solution and solid forms may challenge the common view of the unique importance of 3D interaction for charge photoproduction in conducting polymers.

In recent years, it has been recognized that many characteristics of the excited states of conjugated polymers are in essence very similar to those of the corresponding finite oligomers. *trans*- $\beta$ -carotene, for example, is a conjugated molecule that consists of a backbone of 11 double bonds, similar to *trans*-(CH)<sub>*x*</sub>, which has fixed length of about 22 carbons. Upon doping, it was observed that the charge is stored in a spinless stable configuration accompanied by structural relaxation [31]. Another example is the thiophene oligomers. Here, several oligomers ranging from bithiophene through sexithiophene [32–34] to octa- and decathiophene were studied. At low doping levels, the radical ions of all the oligomers show the characteristics of polarons (i.e. charged defect, with spin-1/2 accompanied by bond relaxation). Upon further doping, the di-ions show the characteristics of bipolarons (i.e. doubly charged spinless defects with stronger bond relaxation). In a recent study [35], the long-lived charge photoexcitations in sexithiophene (Fig. 5.1) were identified as polarons because of the similarity of their absorption spectrum to that of the radical cations. It therefore seems natural to use oligomers of various lengths to characterize the excited states of the longer polymers.

In this chapter, we review the studies of photoexcitations in *trans*-(CH)<sub>*x*</sub>, the representation of the degenerate ground-state polymers and NDGS polymers such as PT derivatives as well as those in the important PT oligomer *a*-sexithiophene; the backbone structure of these materials is depicted schematically in Fig. 5.1. We studied photoexcitations in such polymers in a broad time interval from femtoseconds to milliseconds and spectral range from 0.1 to 2.4 eV. However, in this chapter we review only our continuous wave (cw) studies, where the photoexcitations are generated in quasi-steady-state conditions. The main experimental technique described herein is photomodulation (PM), which gives information complementary to that obtained by photoluminescence (PL), which is limited to radiative processes, or photoconductivity (PC), which is sensitive to high-mobility photocar-

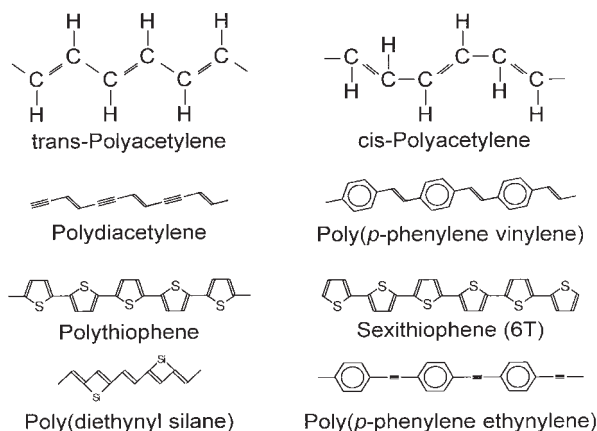


**Figure 5.1** Chemical structures of several common  $\pi$ -conjugated polymers and oligomers.

riers. The PM method, in contrast, is sensitive to nonequilibrium excitations in *all* states.

Among the various powerful techniques that have been used to investigate the long-lived photoexcitation properties in conducting polymers, perhaps the most controversial is the technique of light-induced electron spin resonance (LESR), which in principle has the potential to measure the spin of photoexcitations. The sensitivity of ESR machines is usually too low for LESR; the overall minimum number of spins that can be measured is only  $10^{11}$ . A back-of-the-envelope calculation using realistic dimensions of the type of  $\mu$ -wave cavities used in LESR and the light absorbance of conducting polymers (light penetration depth of  $\sim 1000$  Å) limits the minimum steady-state density of spin-carrying photoexcitations that can be detected in LESR to  $10^{17}$  cm $^{-3}$ . This relatively high photoexcitation density can be photogenerated if excitation lifetime is longer than about  $10^{-2}$  s and the generation quantum efficiency is higher than about 10%. These conditions are not easy to satisfy for most types of photoexcitations in conducting polymers. If attainable, they further require high laser excitation intensity and this leads to sample heating, which is the second problem associated with LESR: conducting polymers usually contain spin- $1/2$  defects (dangling bonds, ends of chains, etc.) of substantial density, on the order of  $10^{17}$  cm $^{-3}$  or larger. The modulation of the laser excitation intensity in LESR measurements causes temperature modulation, which in turn modulates the Curie susceptibility, leading to temperature artifacts in the magnetic resonance spectra. Double modulation, where the  $\mu$ -wave intensity and the laser excitation intensity are simultaneously modulated, does not help to reduce the heating problem, since the LESR and the thermal lifetimes are similar.

In this chapter, we discuss the powerful technique of photoinduced absorption-detected magnetic resonance (PADMR) [10], in which spin states and their correlated spectra in the PM can be simultaneously measured; this technique is far superior to LESR. The main idea in PADMR is the detection of changes in steady-

state photoexcitation density induced by  $\mu$ -wave absorption in resonance with Zeeman split sublevel electronic states. Since the changes are induced in the density of photoexcitations rather than in  $\mu$ -wave absorption, the effect can be measured with detectors in the visible to near-IR spectral ranges, with improved sensitivity of up to five orders of magnitude over that of  $\mu$ -wave detectors. Moreover, spectral information can also be gained in PADMR measurements, as the optical probe can be easily tuned.

### 5.1.2

#### Optical Transitions of Photoexcitations in Conducting Polymers

Perhaps the best way to detect and characterize long-lived photoexcitations in the class of  $\pi$ -conjugated polymers is to study their optical absorption [23]. As a consequence of their localization they give rise to gap states in the electron and phonon level spectra, respectively. The scheme of our experiments is the following. We photoexcite with above-gap light and then probe the optical absorption of the sample in a broad spectral range from the IR to visible; this has been dubbed the PM spectrum. In the PM spectrum we essentially obtain difference spectra, i.e. the difference in the optical absorption ( $\Delta a$ ) of the polymer when it contains a nonequilibrium carrier concentration and that in the equilibrium ground state. Therefore, the optical transitions of the various photoexcitations are of fundamental importance. In this section we discuss and summarize the states in the gap and associated electronic transitions of various photoexcitations in conducting polymers; the IR-active vibrations (IRAVs) related to the charged excitations will be only briefly summarized.

Rather than discussing the various electronic states in conducting polymers in terms of bands (valence and conducting bands, for example), which might be the proper description of the infinite chains or discrete levels with proper symmetries, which should be used for oligomers or other finite chains, we prefer the use of HOMO, LUMO and SOMO (singly occupied molecular orbital). In the semiconductor description of the infinite chain, HOMO is the top of the valence band, LUMO is the bottom of the conduction band and SOMO is a singly occupied state in the forbidden gap. In this case  $E_g = \text{LUMO} - \text{HOMO}$ . On the other hand, in the excitonic description of the correlated infinite chain, HOMO is the  $1A_g$  state and LUMO is the  $1B_u$  exciton [we deal mainly with luminescent polymers in this review, in which  $E(1B_u) < E(2A_g)$ ]. In this case  $E_g = E(1B_u)$ . In finite chains HOMO and LUMO are discrete (isolated) levels with definite symmetries. Among them the subscript 'g' stands for even (*gerade*) parity and 'u' stands for odd (*ungerade*) parity. These symbols are extremely important for possible optical transitions, since one-photon absorption can take place between states of *opposite* representations, such as  $g \rightarrow u$  or  $u \rightarrow g$ . This is true in the singlet manifold as well as in the triplet manifold.

We discuss separately excitations in degenerate and non-degenerate ground-state polymers.



$$\delta S^+ + \delta S^- = E_g + \Delta E_r - U_{\text{eff}} \quad (5.3)$$

$$2\delta S^0 = E_g + U \quad (5.4)$$

It is seen from Eq. (5.4) that we can determine  $U$  from a single transition ( $\delta S^0$ ) if  $E_g$  is known and charge conjugation symmetry exists. In the more general case in which  $S^0$  is replaced by a polaron level this transition should be associated with the SOMO level in the gap. We use this relation later to determine  $U$  in NDGS polymers from the optical transitions associated with the polaron levels in the gap.

#### 5.1.4

#### Optical Transitions of Charged Excitations in NDGS Polymers

The proper description of charged excitations in NDGS polymers has been the polaron ( $P^\pm$ ), which carries spin- $1/2$  and the spinless bipolaron ( $BP^\pm$ ). However, a third possible excitation has recently gained interest, namely the  $\pi$  dimer or the interchain BP [33].

##### 5.1.4.1 The Polaron Excitation

The states in the gap and the associated optical transitions for  $P^+$  are shown in Fig. 5.3a. The two polaron energy states in the gap are SOMO and LUMO, respectively, separated by  $2\omega_0(P)$ . Then three optical transitions,  $P_1$ ,  $P_2$  and  $P_3$ , are possible. In oligomers, the parity of the HOMO, SOMO, LUMO and LUMO + 1 levels alternate; they are  $g$ ,  $u$ ,  $g$  and  $u$ , respectively. Therefore, the transition  $P_3$  vanishes in the dipole approximation and the polaron excitation is then characterized by the appearance of two correlated optical transitions below  $E_g$ . Even for long chains in the Hückel approximation, transition  $P_3$  is extremely weak and therefore the existence of two optical transitions upon doping or photogeneration indicates that polarons were created. Unfortunately, polaron transitions have not been calculated for an *infinite* correlated chain. A possible disorder-induced relaxation of the optical selection rules may occur that may cause ambiguity as to the number of optical transitions associated with polarons in “real” polymer films.

##### 5.1.4.2 The Bipolaron Excitation

The states in the gap and the possible optical transitions for  $BP^{2+}$  are given in Fig. 5.3b. There are now two unoccupied energy states separated by  $2\omega_0(BP)$ : the LUMO and LUMO + 1, which are deeper in the gap than corresponding states for  $P^+$ . Two optical transitions are then possible:  $BP_1$  and  $BP_2$ . In short oligomers, again the parity of HOMO, LUMO and LUMO + 1 alternate ( $g$ ,  $u$  and  $g$ , respectively) and therefore the  $BP_2$  transition vanishes. In this case the BP is characterized by a single transition below  $E_g$ . We note that even in the approximation of an

infinite chain the  $BP_2$  transition is very weak. Electron correlation and disorder-induced relaxation of the optical selection rule, however, may cause the  $BP_2$  transition to gain intensity and therefore BP's with one strong transition at low energy and a second, weaker transition at higher energy should not be unexpected in "real" films.

The polaron and bipolaron transitions shown in Fig. 5.3 can also be used to calculate the important parameters  $U$ ,  $U_{eff}$  and  $\Delta E$ , defined earlier in Fig. 5.2 for solitons, using Eqs. (5.1)–(5.4). This is possible because the polaron SOMO level is singly occupied and is therefore equivalent to  $S^0$  in Fig. 5.2, whereas bipolaron levels are either unoccupied ( $BP^{2+}$ ) or doubly occupied ( $BP^{2-}$ ) and therefore are equivalent to the states  $S^+$  and  $S^-$ , respectively, in Fig. 5.2. However, there are two levels in the gap for  $P^+$  and  $BP^{2\pm}$  excitations and therefore we have to take into account their respective separation  $2\omega_0(P)$  and  $2\omega_0(BP)$  (Fig. 5.3a and b). The SOMO level of  $P^-$  is pushed up and that of  $P^+$  is pushed down by  $\omega_0(P)$  and the HOMO level of the  $BP^{2-}$  is pushed up and the LUMO level of  $BP^{2+}$  down by  $\omega_0(BP)$ . Then  $P_3 - \omega_0(P)$  is equivalent to transition  $\delta S^-$  in Fig. 5.2 and similarly  $BP_1 + \omega_0(BP)$  is equivalent to transition  $\delta S^-$  in Fig. 5.2. Now within the model presented in Section 5.1.4.1 we find

$$U_{eff} = P_1 - BP_1 + \Delta\omega_0 \quad (5.5)$$

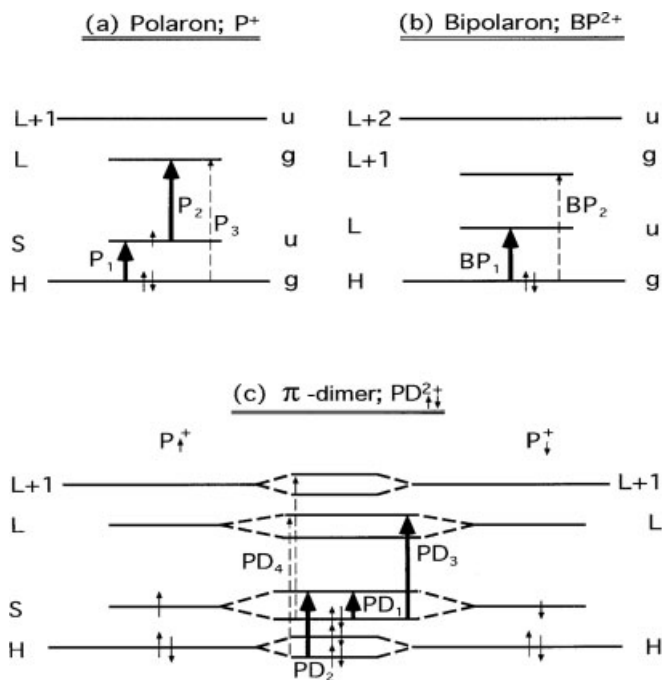


**Figure 5.3** Charged excitations in non-degenerate ground-state polymers. The various notations are explained in the text.

$$P_3 + BP_1 = E_g + \Delta E_r + \Delta\omega_0 \quad (5.6)$$

where  $\Delta E_r$  is the relaxation energy of the BP with respect to the polaron and  $\Delta\omega_0 = \omega_0(P) - \omega_0(BP)$ . Equations (5.5) and (5.6) are equivalent to Eqs. (5.1) and (5.2), respectively, but for NDGS polymers. Another useful relation follows from Eq. (5.4):

$$2P_1 + P_2 = E_g + U \quad (5.7)$$

In Eqs. (5.5)–(5.7) we used  $P_3 = P_1 + P_2$ .

#### 5.1.4.3 The $\pi$ -Dimer and the Delocalized Polaron Excitations

When two polarons come together on the same chain, then theory (Hückel approximation) predicts that they are unstable toward the formation of a bipolaron:



Whether this model is true in “real” polymers is still an open question. Nevertheless, BPs must appear in conducting polymers upon heavy doping, regardless of whether or not Eq. (5.8) is exothermic. When heavily doped, however, another type of charge excitation can be formed; an extrinsic bipolaron (as opposed to an intrinsic BP) or  $\pi$  dimer ( $PD^{2\pm}$ ), in which two polarons on different chains are coupled together. The PD excitations are spinless (Fig. 5.3c) and their formation has been recently proposed to explain the dramatic decrease in unpaired spins observed in  $FeCl_3$ -doped  $\alpha$ -sexithiophene at low temperatures [33]. Then the possibility that PD charge excitations can be photogenerated cannot be discarded. In addition, a polaron can be delocalized on two different chains, if the interchain distance is small. Such a situation occurs (see section 5.4.1) in lamellae of regio-regular poly(3-hexylthiophene) (RR-P<sub>3</sub>HT), where the chains are arranged parallel to each other with  $\pi$ -stacking possibility and this arrangement promotes charge delocalization in 2D. This situation has been described in the literature similar to the case of  $\pi$ -dimer excitations. Thus the following description of  $\pi$ -dimer excitations also accounts for delocalized polaron (DP) excitations in 2D-type polymers.

The energy levels of a  $PD^{2+}$  (or  $DP^+$ ), which are formed from the energy levels of two coupled  $P^+$  polarons (or two coupled polaron levels delocalized on different chains for DPs), are shown in Fig. 5.3c. As is clearly seen, the  $P^+$  level is split into two levels owing to the coupling, where the SOMO splitting is related to the charge-transfer overlap integral  $t_{CT}$ . There are now four possible transitions,  $PD_1$ – $PD_4$ , but transition  $PD_4$  is strictly forbidden in oligomers (similar to transition  $P_3$  of polarons in oligomers). Again we expect this transition to be weak in real polymers. We therefore conclude that  $PD^{2\pm}$  is characterized by three strong transitions: the charge transfer transition  $PD_1$  at the lowest energy and two other transitions,  $PD_2$  and  $PD_3$ , that are blue shifted with respect to the two equivalent

polaron transitions  $PD_1$  and  $PD_2$ . For the DP excitations we also expect three transitions,  $DP_1$ – $DP_3$ ; however, transition  $DP_2$  is weak. More on DP transition will be given in Section 5.4.1.

### 5.1.5

#### Optical Transitions of Neutral Excitations in NDGS Polymers

Upon photon absorption, a bound e–h pair or an exciton (X) is immediately generated. By definition the exciton is a neutral, spinless excitation of the polymer. Following photogeneration the exciton may undergo several processes: It may recombine radiatively by emitting light in the form of fluorescence (FL), which is the light source in OLED devices. It may also recombine non-radiatively through recombination centers by emitting phonons. Excitons may be also trapped ( $X_t$ ), either by a self-trapping process undergoing energy relaxation (this can be envisioned as a local ring rotation, etc.) or by a trapping process at defect centers. Excitons may also undergo an intersystem crossing into the triplet manifold, creating a long-lived triplet (T) state. Finally, an exciton may disassociate into a polaron pair (PP) either on the same chain (but on two different segments) or on two different chains. Since we are interested in long-lived photoexcitations in this chapter, we deal here only with trapped singlet excitons ( $X_t$ ), triplets (T) and polaron pairs (PP); their energy levels and possible optical transitions are shown in Fig. 5.4.

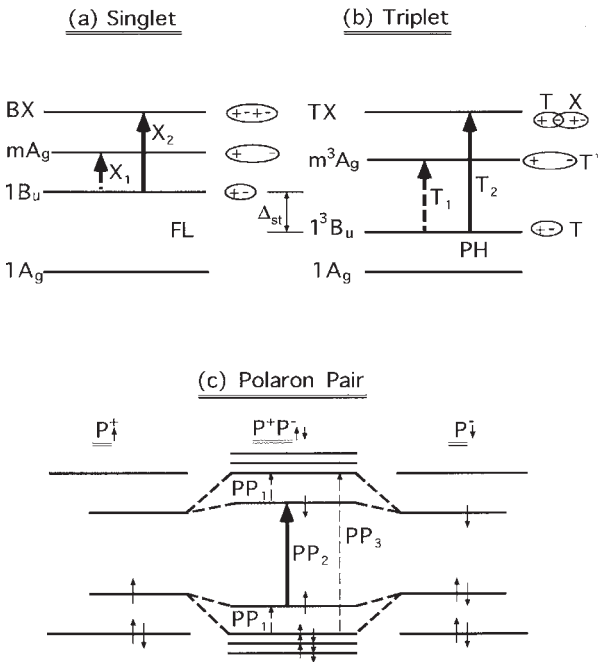


**Figure 5.4** Neutral excitations in non-degenerate ground-state polymers. The various notations are explained in the text.

For  $X_i$  and T we adopt here the correlated picture in which the notations for different many-body exciton levels, which follow the group theory representations, are  $A_g$  and  $B_u$ , respectively.

#### 5.1.5.1 Singlet Excitons

Two important exciton levels ( $1B_u$  and  $mA_g$ ) and a double excitation type level ( $BX$  or  $kA_g$ ) are shown in Fig. 5.4a [12]; their electron configurations are also shown for clarity. We consider  $mA_g$  to be an excited state above the  $1B_u$  level, whereas the  $BX$  or  $kA_g$  excited state may be due to a biexciton state, i.e. a bound state of two  $1B_u$  excitons. The  $mA_g$  level is known to have strong dipole moment coupling to  $1B_u$ , as deduced from the various optical nonlinear spectra of conducting polymers analyzed in terms of the “four essential states” model [36]. We therefore expect two strong optical transitions to form following the  $1B_u$  photogeneration:  $X_1$  and  $X_2$ , as shown in Fig. 5.4a. Due to exciton self-trapping, however, we do not know whether  $X_1$  would maintain its strength, since the relaxed  $1B_u$  state may no longer overlap well with the  $mA_g$  state.  $X_2$ , on the other hand, will be always strong regardless of the  $1B_u$  relaxation, since there is always room for a second exciton photogeneration on a chain following the photoproduction of the first exciton.

From two-photon absorption and electroabsorption spectra in soluble derivatives of PT and PPV polymers we know that  $mA_g$  is about 0.7 eV above  $1B_u$  [12, 37, 38]. We therefore expect the  $X_1$  transition to be in the mid-IR spectral range, at about 0.7 eV. The  $BX$  level, on the other hand, has not as yet been directly identified in conducting polymers, although a weak two-photon state, dubbed  $kA_g$ , was identified in recent nonlinear optical spectroscopy.

#### 5.1.5.2 Triplet Excitons

The most important electronic states in the triplet manifold are shown in Fig. 5.4b. The lowest triplet level is  $1^3B_u$ , which is lower than  $1B_u$  by the singlet-triplet energy splitting  $\Delta_{ST}$ . In principle,  $1^3B_u$  can directly recombine to the ground state by emitting photons (leading to phosphorescence, PH) or phonons. But the transition is spin-forbidden and therefore extremely weak, leading to the well-known long triplet lifetime. The other two levels shown in Fig. 5.4b are the  $m^3A_g$  level, which is equivalent to  $mA_g$  in the single manifold and the  $TX$  level, which is a complex composed of a triplet exciton and a singlet exciton bound together; their electronic configuration is also shown in Fig. 5.4b for clarity.

As in the case of single excitons, we expect for triplets two strong transitions  $T_1$  and  $T_2$  (Fig. 5.4b).  $T_1$  is into the  $m^3A_g$  level and from Figs. 5.4a and b it is clear that it is possible to estimate  $\Delta_{ST}$  from the relation

$$\Delta_{ST} = T_1 - X_1 \quad (5.9)$$

Since the  $m^3A_g$  and  $m^1A_g$  levels should not be far from each other.  $\Delta_{ST}$  has recently been directly measured in conducting polymers from phosphorescence

emission involving heavy atoms [39,39] and Eq. (9) has been actually confirmed. Unfortunately, we do not know whether  $T_1$  is indeed strong, since, as in singlet excitons, the relaxed triplet may not well overlap with the  $m^3A_g$  state, leading to a decrease in  $T_1$  intensity. In contrast, it is quite certain that transition  $T_2$  into the TX level is strong, because it is always possible to photogenerate a second (singlet) exciton close to a previously formed triplet exciton.

### 5.1.5.3 Polaron Pairs

A polaron pair (PP) [25] is a bound pair of two oppositely charged polarons,  $P^+$  and  $P^-$ , formed on two adjacent chains. In this respect it is similar to the  $\pi$ -dimer discussed previously, except that the binding energy is mainly Coulombic in the case of PP, in contrast to lattice relaxation for PD excitations. The stronger overlap leads to larger splitting of the  $P^+$  and  $P^-$  levels compared with those for PDs, as shown in Fig. 5.3c. Following the same arguments as those given before for polaron transitions, we expect three strong transitions  $PP_1$ – $PP_3$ . For a loosely bound PP these transitions are not far from transitions  $P_1$  –  $P_3$  of polarons. However, for tightly bound PP excitations we expect a single transition,  $PP_2$ , to dominate the spectrum, as  $PP_1$  is considered to be intraband with traditional low intensity and  $PP_3$  is close to the fundamental transition and therefore difficult to observe. In this case there are mainly two states in the gap and the excitation is also known as neutral BP ( $BP^0$ ) or polaronic exciton. We note, however, that  $PP_2$  transition is close in spirit to transition  $X_2$  discussed above for excitons, as a second electron is also promoted to the excited level in the case of PP. Then from the experimental point of view, it is not easy to identify and separate in the PM spectra the transitions of a trapped exciton ( $X_i$ ) from those of a tightly bound PP or  $BP^0$ . They may differ, however in their PADMR spectra, as discussed below in the following sections.

### 5.1.6

#### Infrared Active Vibrational Modes

The pristine  $\pi$ -conjugated polymer chain is neutral, free of excess charges. The neutral chain has a set of Raman-active  $A_g$  vibrations that are strongly coupled to the electronic bands via the e–p coupling. These vibrations have been dubbed amplitude modes (AM) [40] since they modulate the electronic gap  $2\Delta$ , in the notation of Peierls gap. The AM vibrations have been the subject of numerous studies and reviews since they play a crucial role in resonant Raman scattering dispersion with the laser excitation and therefore can show important properties of the coupled electronic levels. The most successful description of the AM type vibrations was advanced by Horovitz et al. [40] and its application to resonant Raman scattering by Ehrenfreund et al. [41].

When charges are added on to the chain some of the Raman active modes become IR-active vibrations (IRAV), since there is excess charge on the chain that may easily couple to electromagnetic radiation. The IRAVs that are manifested as

peaks in the absorption spectrum, accompany all the charge excitations mentioned above. Actually in various studies the appearance of photoinduced IRAVs is taken in the literature as evidence of photogenerated charge excitation onto the chain [41]. Usually the IRAVs have immense oscillator strength, which is actually comparable to the strength of the electronic transitions. The reason for this excess strength is the small kinetic mass of the correlated charge excitation that translates into a large dipole moment. Sometimes the IRAVs do not appear as peaks in the absorption but rather as dips or anti-resonances (ARs) [42, 43]. This happens when the electronic transitions overlap in energy with the IRAVs. In this case Fano resonance occurs between the two types of transitions, which results in the appearance of ARs. Despite the Fano-type AR, still the AM model can accurately describe the absorption spectrum, as was recently demonstrated for the ARs of DP excitations in P3HT [42, 43]. Here we want to briefly give several equations to describe both the doping induced and photoinduced IRAVs in some polymers, in addition to the ARs in the PM spectrum in other polymers.

An important ingredient of the AM model is that all IRAVs are interconnected and contribute to the same phonon propagator [41]. We therefore start by defining the pinned, many-phonon-propagator,  $D_a(\omega) = D_0(\omega)/[1 - a_p D_0(\omega)]$ , where  $a_p$  is the polaron-vibrational pinning parameter and  $D_0(\omega)$  is the bare phonon propagator. The latter is given [44] by  $D_0(\omega) = \sum_n d_{0,n}(\omega)$  and  $d_{0,n}(\omega) = \lambda_n / \lambda \{ (\omega_n^0)^2 / [\omega^2 - (\omega_n^0)^2 - i\delta_n] \}$ , where  $\omega_n^0$ ,  $\delta_n$  and  $\lambda_n$  are the bare phonon frequencies, their natural linewidth (inverse lifetime) and electron-phonon (e-p) coupling constant, respectively, and  $\sum \lambda_n = \lambda$ , which is the total e-p coupling. In the non adiabatic limit, for a polaron current coupling to phonons,  $f(\omega)$  influences the conductivity,  $\sigma(\omega)$  [and hence also shows up in the absorption spectrum, since  $Re(\sigma) \approx a$ ]; there is a correlated contribution,  $g(\omega)$  from the most strongly coupled phonons via the e-p coupling. The function  $g(\omega)$  is given in the random phase (RPA) approximation by [40, 45]

$$g(\omega) = \omega^2 / E_r^2 [-\lambda D_a(\omega) f^2(\omega)] / [1 + 2\lambda D_a(\omega) \Pi_\phi(\omega)] \quad (5.10)$$

where  $E_r$  is the polaron relaxation energy  $\Pi_\phi(\omega)$  is the phonon self mass correction due to the electrons, which can be approximated for charge density wave (CDW) by the relation

$$2\lambda \Pi_\phi(\omega) = 1 + c(\omega) \quad (5.11)$$

In the charge density wave (CDW) approximation,  $c(\omega)$  is given by

$$c(\omega) = \lambda \omega^2 f(\omega) / E_r^2 \quad (5.12)$$

but since for  $\omega > E_r$ ,  $f(\omega)$  changes slowly over the phonon linewidth, we may take it to be a constant,  $C$ . The RPA terms in Eq. (5.10) contain the sharp structure of  $D_a(\omega)$ , whereas additional non-RPA terms contribute a smooth background term.

In general, the conductivity spectrum,  $\sigma(\omega)$ , is given by [40]

$$\sigma(\omega) = (\omega_p^2/4\pi i\omega)[d(\omega) + g(\omega) - 1] \quad (5.13)$$

where  $\omega_p$  is the plasma frequency, which is proportional to the photoinduced carrier density and  $[d(\omega) - 1]$  is the response in the absence of phonons that also includes non-RPA terms. In the CDW approximation  $d(\omega) = f(\omega)$  [46]. Hence the sharp structure of Eq. (5.13) can be written as

$$\sigma(\omega) \approx [1 + D_0(\omega)(1 - a')]/[1 + D_0(\omega)(1 + C - a)] \quad (5.14)$$

where  $a'$  is a constant that replaces a smooth electronic response; in the CDW approximation [46] we have  $a' = a_p$ , which was defined above for the trapped polaron excitation.

The poles of Eq. (5.14), which can be found from the relation  $D(\omega) = -(1 - a_p + C)^{-1}$ , give peaks (or IRAVs) in the conductivity (absorption) spectrum. These absorption bands are very strong and can be taken as a signature of charges added to the chain. On the other hand, the zeros in Eq. (5.14), which can be found by the relation  $D_0(\omega) = -(1 - a_p)^{-1}$ , give the indentations (or ARs) in the conductivity (absorption) spectrum. It is therefore apparent that the ARs are due to the formation of quantum interference between the phonons and the electron optical transition in the conductivity spectrum.

To see the effect of the non-adiabatic limit on the PA spectrum, we calculated [42] the conductivity spectrum, including the IRAVs for polarons with both low and high  $E_r$ , as seen in Fig. 5.5. For these calculations we used the phonon param-

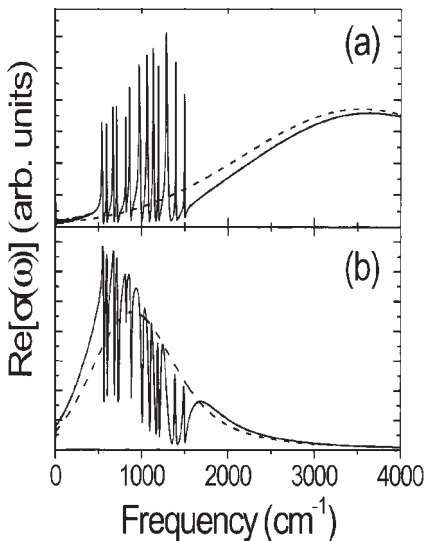


**Figure 5.5** Calculated PA spectrum (solid line) using the CDW response function [40]  $f(\omega)$  (broken line) with onset  $2A$  at (a)  $3600 \text{ cm}^{-1}$  and FWHM of  $2400 \text{ cm}^{-1}$ ; and (b)  $800 \text{ cm}^{-1}$  and FWHM of  $800 \text{ cm}^{-1}$ .

eters of RR-P3HT [46] with 13 strongly coupled vibrational modes and approximated the electronic band contribution,  $f(\omega)$ , by the CDW response function [46], where the CDW gap  $2\Delta = E_r$  and  $E_r$  is associated with the polaron relaxation energy that governs the  $P_1$  band. It is seen that when  $\omega \ll E_r$ , then only IRAVs with positive peaks can be observed (Fig. 5.5a); this happens since  $C$  in Eq. (5.14) is negligibly small and consequently ARs are not formed. However, when  $E_r$  is small so that the CDW band overlaps with the IRAVs, then quantum interference occurs that gives rise to ARs in the spectrum (Fig. 5.5b); in this case the ARs are more dominant than the IRAVs that occur on their high-energy side.

## 5.2

### Experimental Methods

The relatively small spectroscopic changes induced by the application of interband photons proved to be a powerful tool in the study of photoexcitations in  $\pi$ -conjugated systems, due to their localized nature and strong extinction coefficient. Since the first report [43] of photoinduced solitons in  $(\text{CH})_x$ , a variety of photoexcitation species, such as polaron-like charged species as well as triplet excitons [10, 35, 47–53], have been extensively studied by the measurement of the photoinduced changes in the sample transmission. The electronic spin properties of these photoexcitations have been studied by placing the samples in a magnetic field and applying a resonant microwave radiation as a second modulation, thereby measuring the spin character of the photoinduced species.

In this section we describe experimental methods used to study the long lived photogenerated species in  $\pi$ -conjugated systems.

#### 5.2.1

##### Photomodulation Spectroscopy of Long-Lived Photoexcitations

In this method, two optical beams are used: a pump beam which excites the  $\pi$ -conjugated polymer, generating photoexcitation species and a probe beam which measures the changes  $\Delta T$  of the sample transmission  $T$  due to the probe beam. A sketch of the experimental setup is shown in Fig. 5.6. It allows for measurements of the modulated PA spectra as a function of temperature, pump intensity,  $I_L$ , pump modulation frequency,  $\nu$  and pump photon energy,  $E$ .

Let us assume a sample in the form of a film of thickness  $d$  illuminated by a pump beam with a photon flux  $I_L(t)$ , which is modulated at a frequency  $\omega$ . The intensity profile of the pump beam in the film is  $I_L(x, t) = I_L(t)\exp(-a_L x)$ , where  $d$  is measured from the front surface and  $a_L$  is the film absorption coefficient at the pump photon energy. This intensity profile gives rise to an inhomogeneous photoexcitation density,  $N(x)$ , which in turn produces variations,  $\Delta a(E, x, t)$ , in the film absorption coefficient at the probe energy  $E$ :

$$\Delta a(E, x, t) = \sigma(E)N(x) \quad (5.15)$$

where  $\sigma$  is the cross-section for absorption at energy  $E$  due to the photoexcited species. Writing the probe beam profile in the sample as  $I_{\text{probe}}(x) = I_{\text{probe}} \exp(-ax)$ , the measured  $\Delta T/T$  can readily be written as

$$-\frac{\Delta T}{T}(E, t) = 1 - \exp\left[-\int_0^d \Delta\alpha(E, x, t) dx\right] = 1 - \exp\left[-\sigma(E) \int_0^d N(x, t) dx\right] \quad (5.16)$$

In practice,  $\Delta T/T \ll 1$  and Eq. (5.16) can thus be written as

$$-\frac{\Delta T}{T}(E, t) \approx \int_0^d \Delta\alpha(E, x, t) dx = -\sigma(E) \int_0^d N(x, t) dx \quad (5.17)$$

Hence  $-\Delta T/T$  measures the photoinduced absorption (PA) of the sample.

The above expression does not include any changes in the transmission due to the effect of the pump beam on the refractive index; these changes are usually much smaller in  $\pi$ -conjugated polymers than the PA itself.

Equation (5.17) takes a very simple form for thin samples,  $a_L d \ll 1$ , where  $\Delta\alpha(E, x, t)$  and  $N(x, t)$  may be regarded as uniform throughout the thickness of the sample:

$$-\frac{\Delta T}{T}(E, t) \approx \Delta\alpha d = \sigma(E) N(t) d \quad (5.18)$$

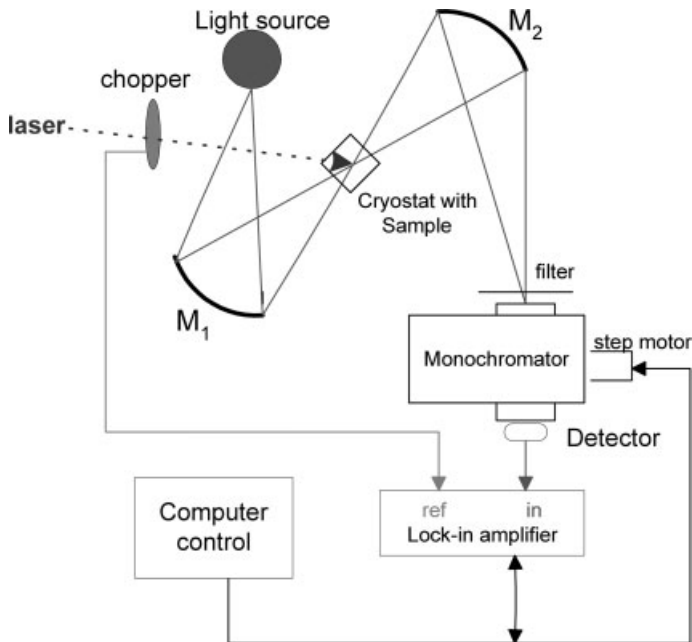


Figure 5.6 Typical setup for frequency-dependent photomodulation spectroscopy.

The above equations show that the dependence of the PA on the pump intensity,  $I_L$ , and its modulation frequency,  $\omega$ , yields the kinetics of the photogenerated species.

In the photomodulation technique, the kinetics of the photogenerated species are followed by measuring the modulated signal using a lock-in technique in which both the in-phase ( $I$ ) and quadrature ( $Q$ ) components are simultaneously obtained. Since the lock-in measures only the first harmonics at frequency  $\nu$ , the fully modulated excitation can be written simply as

$$G(t) = (g/2) \times (1 + \cos\omega t) \quad (5.19)$$

where  $\omega = 2\pi\nu$ . In Eq. (5.19),  $g$  is the generation rate, which is proportional to the pump intensity:  $g = \eta I_L [1 - \exp(-a_L d)]/d$ , where  $\eta$  is the quantum efficiency for generating photoexcitations. For thin samples,  $g \approx \eta a_L I_L$ . The measured in-phase and quadrature components of the PA are then proportional to the corresponding components of the photoexcitation density,  $N(t)$ :

$$\begin{aligned} N_I &= \int_{\text{period}} N(t) \cos(\omega t) dt \\ N_Q &= \int_{\text{period}} N(t) \sin(\omega t) dt \end{aligned} \quad (5.20)$$

Measuring the dependence of the  $I$  and  $Q$  components on the pump intensity and modulation frequency provides useful information regarding the recombination mechanisms and characteristic lifetime of the photoexcitations.

### 5.2.2

#### Optically Detected Magnetic Resonance Techniques

Optically detected magnetic resonance (ODMR) techniques are extensions of the more common (conventional) electron spin resonance (ESR) techniques. ODMR measures changes in the optical absorption and/or emission that occur as a result of electron spin transitions. Since the ground state in conjugated polymers is almost always spin-0, usually only excited states are studied and therefore spin transition-induced changes in PA are detected rather than changes in ground-state absorption. (Conventional) ESR, on the other hand, uses microwave absorption for detecting the occurrence of electron spin resonance. When applied to  $\pi$ -conjugated semiconductor films, ODMR techniques can be used for assigning the correct spin quantum number to the optical absorption bands of long-lived photoexcitations and/or for studying spin-dependent reactions that may occur between these photoexcitations. The following are examples of typical questions that ODMR spectroscopy can provide answers for:

1. Given is a certain optical absorption band: Is this absorption band due to a singlet (i.e. spin-0) state, a doublet state (i.e. spin- $1/2$ ) or a triplet state (i.e. spin-1)? As an example, ODMR has been used for distinguishing between the absorption

bands of singly charged (polarons, spin- $1/2$ ) and doubly charged (bipolarons, spin-0) excitations [54] (see Section 5.1.4).

- Does the lifetime of triplet excitons depend on the magnetic quantum number? Does the recombination rate between oppositely charged polarons depend on their relative spin-orientation? We will see that the latter question is important for optimizing the performance of OLEDs (see Section 5.3.3).

One major advantage of ODMR over ESR is a much higher sensitivity in the detection of resonant processes, because the energy range of the detected photons in ODMR is much higher (some eV) than the microwave energies that monitor ESR (some meV). Much better detectors with higher detectivity exist for photons in the eV range than in the meV range. A significant increase in the sensitivity of ODMR when compared with ESR also results from differences in the spin polarization; in our ODMR experiments we have typically obtained spin polarizations exceeding the thermal equilibrium polarization by at least one order of magnitude. A detailed discussion of ODMR techniques and the ODMR spectrometer is given in later sections. Let us now first review the basic concepts of ESR.

### 5.2.2.1 The Electron Spin

In addition to a given, intrinsic value for their rest mass,  $m$ , and charge,  $e$ , electrons have an intrinsic angular momentum, called spin, characterized by quantum number,  $s = 1/2$ . In the pattern of other quantized angular momenta, the total spin angular momentum is given by (see Figure 5.7)

$$S = \sqrt{s(s+1)}\hbar = \frac{\sqrt{3}}{2}\hbar \quad (5.21)$$

The  $z$ -component of the spin vector is given by

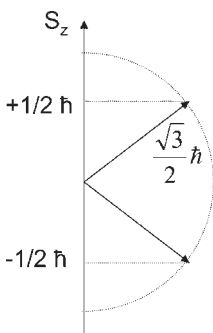


**Figure 5.7** Electron spin: shown are the two possible states for  $S_z$  and the spin vector,  $\vec{S}$ . The length of  $\vec{S}$  equals  $\frac{\sqrt{3}}{2}\hbar$ .

$$S_z = \pm \frac{1}{2} \hbar \quad (5.22)$$

The magnetic moment associated with the electron spin is

$$\vec{\mu}_s = -\frac{e}{2m} g \vec{S} \quad (5.23)$$

where  $g$  is called the Landé factor and has the value  $g = 2.00232\dots$  (for comparison  $g = 1$  for orbital angular momentum). The precise value of  $g$  was predicted by relativistic quantum mechanics in the Dirac equation and was measured in the Lamb shift experiment.

### 5.2.2.2 Electron Spin Resonance

ESR is the fundamental technique for spin measurements. In this technique, different spin projection states are split by an external field (Zeeman splitting); this is actually the simplest case since also internal fields may contribute to the splitting in general. In ESR resonant  $\mu$ -wave absorption indicates the electron spin resonance between  $\mu$ -wave frequency and Zeeman splitting. The basic features of magnetic resonance as described in the following apply both to ESR and to ODMR.

### 5.2.2.3 Basic Principles of $\mu$ -Wave Resonant Transitions

A charged particle with an angular momentum  $\vec{L}$  has a magnetic dipole moment  $\vec{\mu}$  given by

$$\vec{\mu} = g \frac{e}{2m} \vec{L} \quad (5.24)$$

where  $e$  and  $m$  are the charge and the mass of the particle, respectively. For orbital angular momenta  $g$  is exactly 1. However, for spin angular momenta  $g$  is a characteristic number reflecting the nature of the paramagnetic center and its environment. For a free electron  $g$  is  $g_e = 2.0023\dots$ . If a magnetic dipole  $\vec{\mu}$  is inserted into an applied magnetic field  $\vec{H}$  it will experience a torque  $\vec{T}$  given by

$$\vec{T} = \vec{\mu} \times \vec{H} \quad (5.25)$$

The torque is defined as a change of angular momentum in time:  $\vec{T} = d\vec{L}/dt$ . Together with Eqs.(5.24) and (5.25), this leads to the governing equation of motion of a magnetic dipole in a magnetic field:

$$\begin{aligned} \frac{d\vec{L}}{dt} &= g \frac{q}{2m} \vec{L} \times \vec{H} \\ &= \gamma \vec{L} \times \vec{H} \end{aligned} \quad (5.26)$$

where  $\gamma$  is the gyromagnetic ratio that is related to  $g$  by:  $\gamma = g\beta/\hbar$ .  $\beta$  is the Bohr magneton,  $\beta = e\hbar/2m$ . From the solution of Eq. (5.26), it follows that the magnetic dipole will precess around the magnetic field axis with the frequency  $\omega_L = \gamma H$ , the Larmor (precession) frequency. Note that this precession occurs because the quantum mechanical (spin) angular momentum vector is tilted with respect to the  $z$ -axis, given by the direction of  $\vec{H}$  (see Fig. 5.7).

The energies of the spin projection states follow from the Zeeman Hamiltonian:

$$H_{\text{Zeeman}} = \frac{\beta}{\hbar} \vec{H} \overset{\leftrightarrow}{g} \vec{S} \quad (5.27)$$

where  $\overset{\leftrightarrow}{g}$  is a second-order tensor and reduces to the Landé factor  $g$  in isotropic media. The eigenenergies are obtained as

$$E = g\beta m_s H \quad (5.28)$$

The orientation of spin angular momenta in an applied magnetic field is quantized in the direction of the magnetic field and takes integer values between  $-I$  and  $+I$ , where  $I$  is the spin of the paramagnetic species defined through the absolute value of the spin:  $|\vec{S}| = \sqrt{I(I+1)}\hbar$ . Transitions between two Zeeman levels are possible under the emission or the absorption of photons with energies equal to the difference of the Zeeman levels. The energy needed or released in such a transition is absorbed by, or emitted as, a photon of an energy equal to the level splitting:

$$\hbar\omega = g\beta H \quad (5.29)$$

where  $\omega$  is the Larmor frequency and  $\hbar\omega$  is the photon energy of the resonant  $\mu$ -wave radiation. For electrons in laboratory magnetic fields of typically several thousand Gauss it follows for that the photon frequency  $\omega$  is of the order of  $10^{10}$  Hz – a microwave frequency.

The interaction of the microwaves with the spins is given by the interaction of the microwave magnetic field  $H_1$  and the magnetic moment of the spin system. It can easily be shown that the matrix element connecting two Zeeman levels with quantum numbers  $m_s$  and  $m_s'$  has only nonzero elements for microwave magnetic fields perpendicular to the external field and for  $m_s = m_s' \pm 1$  (magnetic dipole transition rule) [55]. The resonant microwave frequency and magnetic field are therefore related by Eq. (5.29) and the external applied magnetic field must be directed in an axis perpendicular to the microwave magnetic field vector.

#### 5.2.2.4 ESR Signal Strength and Population Statistics of Spin-Up and Spin-Down Levels

The incoming  $\mu$ -wave radiation,  $\hbar\omega$ , absorbed by the electrons in the lower Zeeman energy level will induce these electrons to jump into the higher energy state. The incoming radiation, however, also causes the electrons in the higher energy level to jump down to the lower level, a phenomenon called stimulated emission.

Since the coefficients of absorption and stimulated emission are equal, no net ESR signal would be observed if the spin population were equally distributed between these two levels. At thermal equilibrium, however,  $n_1$ , the population of the ground state, exceeds  $n_2$ , the population of the excited state, and a net absorption of microwave radiation takes place.

The population ratio of these two states at the temperature  $T$  can in most cases be described by the Boltzmann distribution:

$$\frac{n_1}{n_2} = e^{-\frac{\Delta E}{kT}} \quad (5.30)$$

where  $k$  is the Boltzmann constant. A material containing atomic magnetic moments satisfying this Boltzmann distribution is called paramagnetic. Since  $\Delta E = \hbar\omega$  at resonance the sensitivity of this technique is improved by using a high applied frequency. In practice, the most common frequencies in ESR are those in the well-developed radar wavebands. In addition, low operating temperatures are also beneficial for signal enhancement.

### 5.2.3

#### **Magnetic Resonance Spectroscopy of Long-Lived Photoexcited States in $\pi$ -Conjugated Polymers**

The ground state of  $\pi$ -conjugated systems is almost always spin-0 since the valence electrons occupy the bonding orbitals in spin-up and spin-down pairs. The ground state is therefore uninteresting for ESR measurements. However, it is meaningful to study the spin of excited states, such as those which occur upon photoexcitation (see Section 5.2.1) or electrical excitation in OLEDs. The ODMR experiments that we will discuss below employ photoexcitation where a powerful (several milliwatts) laser is used to excite the sample. There are several possibilities for optically detecting the occurrence of magnetic resonance. For example, one may use the sample fluorescence emission. In this particular technique, dubbed photoluminescence-detected magnetic resonance (PLDMR), the magnetic resonance is detected through a resonant change in the fluorescence intensity. Here we will mostly focus on another technique, dubbed photoinduced absorption-detected magnetic resonance (PADMR), where the magnetic resonance is detected through a resonant change in the PA. The PADMR experimental setup therefore consists of, in addition to the magnetic resonance part of the setup, two optical light beams: the laser or pump beam that photoexcites the sample and the probe light beam by which the magnetic resonance is detected. Tuning the probe beam's wavelength allows the selection of the particular absorption band to be studied.

### 5.2.3.1 The ODMR Setup

Figure 5.8 shows a schematic drawing of the experimental setup used for PADMR. It consists of three parts:

1. A laser is used for photoexciting the sample (pump beam). As in PA spectroscopy, this laser excitation results in the photogeneration of polarons, triplet excitons and possibly other long-lived excitations.
2. A tungsten halogen lamp, that has a broad spectrum, is used as the probe beam. Upon modulation of the laser beam, modulated changes in the sample film's transmission spectrum occur owing to photoinduced absorption. The monochromator allows tuning of the probe beam wavelength and thereby selection of a certain PA band whose spin state is to be studied.
3. A magnetic resonance part similar to a conventional ESR spectrometer. It consists of an optical access resonator, located between the poles of a superconducting electromagnet, and a microwave source and modulator. Since the magnetic resonance is detected optically, the microwave bridge that is usually necessary for detection of the resonance is not needed in the PADMR experiment.

The thin-film sample is mounted in a high- $Q$  3-GHz cylindrical microwave cavity (see Fig. 5.8). The sample position is in the middle of the cavity, where the mag-

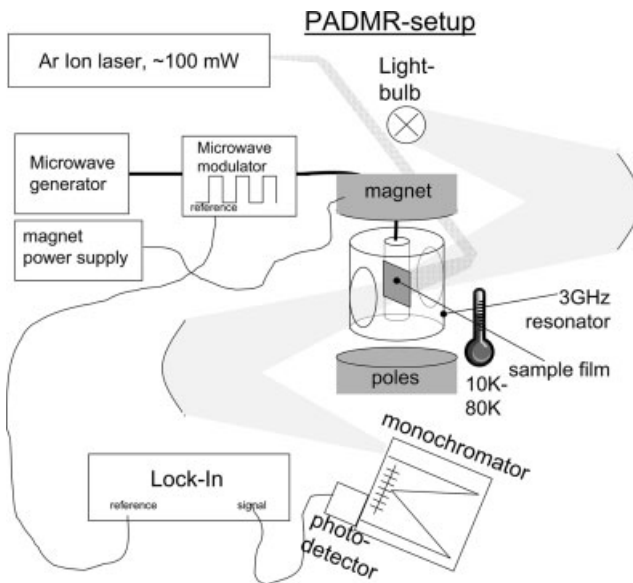


**Figure 5.8** Schematic setup for optically detected magnetic resonance (ODMR).

netic field amplitude has its maximum and the electric field ideally is zero. The cavity is mounted in a helium-cooled cryostat in the center of a superconducting magnet that provides the external magnetic field between 0 G and 30 kG. Microwaves of 3 GHz are generated by a commercial UHV signal generator and fed through cables into a modulator. This modulator is controlled by a signal generator modulating the microwaves between 100 and 20 kHz with a square wave. The modulated microwaves are fed into an amplifier and through cables to the cryostat, where they are coupled into the cavity with a dipole antenna.

The sample is constantly illuminated with a laser beam (argon ion gas laser). The tungsten halogen probe light is focused on to the sample inside the cavity. The sample is cooled with helium through a needle valve from a helium reservoir within the cryostat. The probe light is dispersed with a single-grating monochromator and detected with the same solid-state detectors as used in the PL and PA measurements.

In PADMR we measure the changes,  $\delta T$ , that are induced in the PA spectrum,  $\Delta T$ , by magnetic resonance [56]. Two types of PADMR spectra are possible: the H-PADMR spectrum where  $\delta T$  is measured at a fixed probe wavelength,  $\lambda$  as the magnetic field  $H$  is scanned and the  $\lambda$ -PADMR spectrum where  $\delta T$  is measured at a resonant  $H$  while  $\lambda$  is scanned. For the detailed description, see Ref. [56]. The PLDMR [57] technique is closely related to PADMR: PLDMR measures changes,  $\delta PL$ , induced in PL (rather than PA) upon magnetic resonance. We note that PA, PADMR and PLDMR can all be measured using the same setup and under identical conditions, allowing accurate comparison between results of the three methods. We note that ODMR experiments are performed at low temperature (typically 10 K), mainly for two reasons: (a) the photoexcitation lifetime is strongly temperature dependent and is sufficiently long for study using cw spectroscopy only at temperatures below typically 100 K; (b) the spin-lattice relaxation time is strongly temperature dependent and becomes very long at low temperatures, such that the spin alignment is conserved during the modulation period of the experiments.

ODMR is an excited-state dynamic technique that is not based on spin states in thermal equilibrium. In this respect it is not similar to ESR, whose signal follows the Boltzmann statistics (see Section 5.2.2.4). In fact, in ODMR we have generally observed much larger spin polarizations than would arise from the thermal equilibrium population of the Zeeman levels. In fact, this situation is well known from the study of amorphous silicon and it was concluded that this non-thermal equilibrium magnetic resonance response arises because of spin-dependent recombination rates of the photoexcitations [58]. Therefore, any spectroscopy of photoexcitations, such as PL or PA and electroluminescence [59] in optics or photoconductivity (PC) in transport measurements, will be altered under resonance. In general, it is thus possible to monitor resonant changes in PL (PLDMR), PA (PADMR) and PC (electrically detected magnetic resonance or EDMR). By combining ESR with PL or PA the monitored energies to observe resonance are shifted from the microwave region (as in ESR) to higher energies, which may even be in the optical range (therefore the name optically detected magnetic resonance), leading to a sensitivity that is greatly enhanced (several orders of magni-

tude). However, whereas in ESR the actual concentration of paramagnetic centers is measured, it is the resonant changes in recombination rates that are observed in the ODMR techniques.

### 5.3 Recombination, Relaxation and Generation Processes

#### 5.3.1 Mono- and Bimolecular Recombination Mechanisms

PA dependencies on the modulation frequency,  $\omega$ , and excitation intensity,  $I_L$ , have usually been utilized to determine the photoexcitations lifetime,  $\tau$ , and the recombination mechanism. These are important characteristic properties that influence the photophysics and other opto-electronic responses, which figure in device applications based on these materials. In particular, the monomolecular recombination (MR) and bimolecular recombination (BR) processes may unravel the generation mechanism of the photoexcitation species, which, however, occurs at much earlier times than that of the cw measurements. Carrier MR kinetics in PCP hints at a possible geminate generation process, where the hole and electron polarons ( $P^\pm$ ) come from a common excitation parent. Carrier BR kinetics, on the other hand, indicate the dominance of distant pair recombination dynamics, with important implications for optically detected magnetic resonance and photoconductivity spectroscopy. Furthermore, isolated triplet excitons (TE) are expected to recombine via an MR process, whereas TE–TE annihilation provides a bimolecular channel for recombination. Hence a combined MR and BR process may be expected in such a case.

When the disorder in the film is not severe then the PA dynamics are clear: near the steady state, where  $\omega\tau < 1$ , the PA magnitude gently decreases with increasing  $\omega$ , whereas for frequencies above  $\omega\tau \approx 1$  (away from the steady state) the signal decrease inversely with  $\omega$  [35]. In addition, the PA scales linearly with  $I_L$  for MR kinetics, whereas a  $\sqrt{I_L}$  dependence is expected for BR kinetics near the steady state. This simple approach, however, does not work out in reality because of complications related to the disorder and inhomogeneity known to exist in most PCP films. First, the long-lived photoexcitations may be associated with deep traps in the film; in this case the traps might be partially saturated at high  $I_L$  showing a sub-linear dependence on  $I_L$ , where, in fact, the kinetics may still be due to MR [52]. Second, there may be a broad distribution of recombination rates, which may prevent steady-state conditions from being reached experimentally and this precludes the use of the above intensity dependence criterion.

## 5.3.2

**Recombination Kinetics**

In order to emphasize the main issues described above, it is useful to study characteristic simple cases for which the photoexcitation density,  $N(t)$ , is governed by a single rate equation:

$$dN/dt = G(t) \cdot S(N_0) - U(N) \quad (5.31)$$

where  $G(t)$  is given by Eq. (5.19). Equation (5.31) includes, through the function  $S(N_0)$ , defect limited cases in which, due to trap filling,  $N$ , tends to saturate at high  $I_L$ .  $N_0$  is the trap density that gives rise to the saturation term  $S(N_0)$  and  $U$  specifies the recombination mechanism. We will restrict ourselves to MR and BR processes. A combined process which includes both mechanisms may be given by the following  $U$  and  $S(N_0)$  terms:

$$U = N/\tau + bN^2 \quad (5.32)$$

$$S = (1 + g\tau/N_0)^{-1} + [1 + (g\tau_{BR}^0/N_0)^2]^{-1} \quad (5.33)$$

where  $\tau^{-1}$  is the MR characteristic recombination rate. In Eq. (5.33),  $\tau_{BR}^0$  is the  $I_L$  (or  $\gamma$ )-dependent effective recombination rate in the absence of saturation:

$$(\tau_{BR}^0)^{-1} = \sqrt{gb} \quad (5.34)$$

The linear MR or quadratic BR processes are obtained by setting  $b = 0$  or  $1/\tau = 0$ , respectively, in Eqs. (5.32) and (5.33). Note that the familiar MR or BR are specific cases of the defect-limited processes in the limits  $b, g\tau/N_0 \rightarrow 0$  or  $1/\tau, g/bN_0^2 \rightarrow 0$ , respectively, in Eqs. (5.32) and (5.33) (see also [60, 61]).

**5.3.2.1 Steady-State Case**

For experiments conducted at  $\omega = 0$ , the steady state, density is obtained by setting  $dN/dt = 0$  in Eqs. (5.31)–(5.33):

$$N_{ss} = \frac{1}{2b\tau} \left[ \sqrt{1 + 4g^*b\tau^2} - 1 \right] = g^* \tau_{eff}^s \quad (5.35)$$

where  $g^* = gS$  and  $S$  is given by Eq. (5.33). In Eq. (5.35),  $\tau_{eff}^s$  is defined as

$$\tau_{eff}^s = \tau \frac{\sqrt{1 + 4(\tau/\tau_{BR}^s)^2} - 1}{2(\tau/\tau_{BR}^s)^2} \quad (5.36)$$

where  $(\tau_{\text{BR}}^s)^{-1} = \sqrt{g^*b}$  is an effective BR-like recombination rate in the presence of the saturation mechanism defined by Eq. (5.33). As expected, for any combination of MR and BR processes,  $N_{\text{ss}}$  approaches  $N_0$  at very high generation rate values. When the saturation effect is negligible, Eq. (5.35) takes the form

$$N_{\text{ss}} = \frac{1}{2b\tau} [\sqrt{1 + 4gb\tau^2} - 1] = g\tau_{\text{eff}} \quad (5.37)$$

where  $\tau_{\text{eff}}$  is given by

$$\tau_{\text{eff}} = \tau \frac{\sqrt{1 + 4(\tau/\tau_{\text{BR}}^0)^2} - 1}{2(\tau/\tau_{\text{BR}}^0)^2} \quad (5.38)$$

where  $\tau_{\text{BR}}^0$  is given by Eq. (5.34).

The separate defect-limited MR and BR steady-state densities are

$$\text{DMR: } N_{\text{ss}} = \frac{g\tau}{1 + g\tau/N_0} \quad (5.39)$$

$$\text{DBR: } N_{\text{ss}} = \frac{g\tau_{\text{BR}}^0}{\sqrt{1 + (g\tau_{\text{BR}}^0/N_0)^2}} \quad (5.40)$$

each of which saturates at  $N_0$  as  $g \rightarrow \infty$ . As a summary of the above discussion, we show in Fig. 5.9 the dependence of  $N_{\text{ss}}$  on  $\gamma$  for DMR and DBR. It is seen that for negligible saturation,  $g/g_0 < 1$ ,  $N_{\text{ss}} \propto g$  for MR and  $N_{\text{ss}} \propto g^{1/2}$  for DBR. For extreme saturation cases,  $g/g_0 \gg 1$ ,  $N_{\text{ss}}$  approaches  $N_0$ .

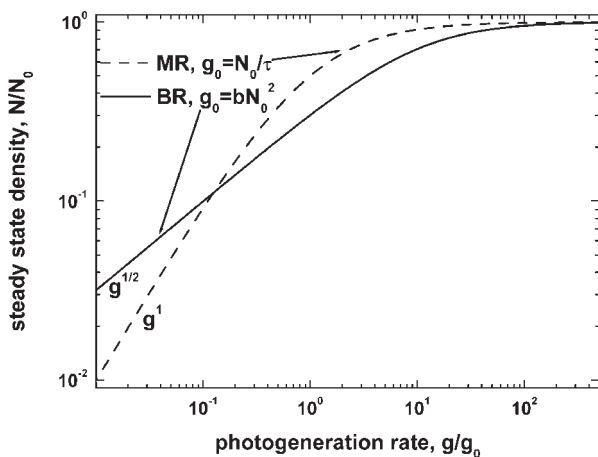


**Figure 5.9** Excitation intensity dependence at steady state in the presence of saturation for BR (solid line) and MR (dashed line).

### 5.3.2.2 Frequency Response

When the modulation frequency is finite, the in-phase and quadrature components are obtained experimentally using phase-sensitive lock-in detection. For the DMR process it is straightforward to show that  $N_I(\omega)$  and  $N_Q(\omega)$  are given by

$$N_I(\omega) = g^* \tau / (1 + \omega^2 \tau^2), \quad N_Q(\omega) = \omega \tau N_I \quad (5.41)$$

where  $g^* = gS$ .

Replacing  $\tau$  by  $\tau_{BR}$  in Eq. (5.41), we get for the general DBR process a modulation frequency dependence that is very close to the one found by numerically solving Eqs. (5.31)–(5.33). The modulation frequency dependence is shown in Fig. 5.10. For both processes,  $N_Q(\omega) \propto \omega$  at very low frequencies, reaching a maximum at  $\omega_{max} = \tau_{eff}^{-1}$  and  $N_I = N_Q$  at this frequency. At higher frequencies,  $\omega > \omega_{max}$ ,  $N_I < N_Q$ . The asymptotic behavior, for each of the components, is a power law decrease:  $\omega^{-\beta}$ , where  $\beta = 2$  or  $1$ , for the  $I$  or  $Q$  components, respectively. This dependence on the frequency is characteristic for both MR and BR processes and their combination. Furthermore, even for a finite-width Gaussian (or Lorentzian) distribution of recombination rates it can be shown that the asymptotic behavior does not change.

In the next sections we study the dependence of  $N_I$  and  $N_Q$  on the pump intensity,  $I_L$ , which is very different for the different processes.

### 5.3.2.3 Generalized Coordinates

In order to treat the dependences of the PA on  $I_L$  and  $\omega$  for the various recombination processes on an equal footing, we define two generalized coordinates,  $\mu$  and  $\chi$ :

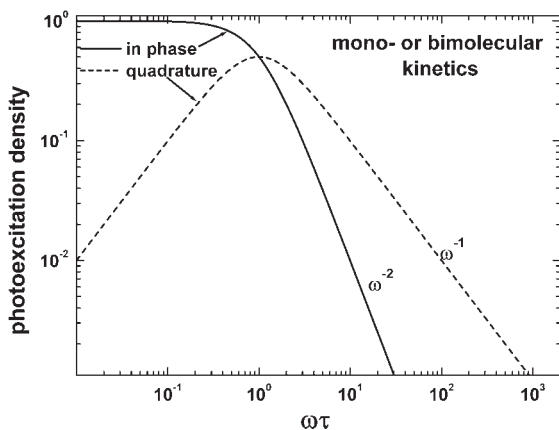


**Figure 5.10** The PA modulation frequency dependence for non-dispersive kinetics for both MR and BR. Solid line, in-phase component; dashed line, quadrature component.

$$\mu^* = N/g^* \omega (\tau_{\text{eff}}^s)^2 \tag{5.42}$$

$$\chi^* = 1/(\omega \tau_{\text{eff}}^s)^2 \tag{5.43}$$

where  $\tau_{\text{eff}}^s$  is defined in Eq. (5.35). The two components of  $\mu^*$ , namely  $\mu_I^*$  and  $\mu_Q^*$ , are plotted in Fig. 5.11 versus  $\chi^*$ , for both MR and BR. It is seen that for each  $\mu^*$  component there exists a *universal* curve, which is approximately given by  $\mu_I^* = (\chi^*)^{3/2}/(1 + \chi^*)$ ,  $\mu_Q^* = \chi^*/(1 + \chi^*)$  that *uniformly* describes all recombination processes, including defect limited MR, BR and their combination.

The importance of this plot is that it clearly distinguishes the various dynamic regimes:  $\chi > 1$ , i.e. close to steady state, and  $\chi < 1$ , away from steady state. There is, however, an important point which has to be taken into account. The variable  $g^*$  in Eqs. (5.42) and (5.43) is *not* the photogeneration rate  $\gamma$ , which is proportional to the applied pump intensity,  $I_L$ . In order to analyze measured data in a universal way, it is more practical to define the generalized coordinates using the actual generation rate  $\gamma$  instead of  $g^*$ , as follows:

$$\mu = N/g\omega \tau_{\text{eff}}^2 \tag{5.44}$$

$$\chi = 1/(\omega \tau_{\text{eff}})^2 \tag{5.45}$$

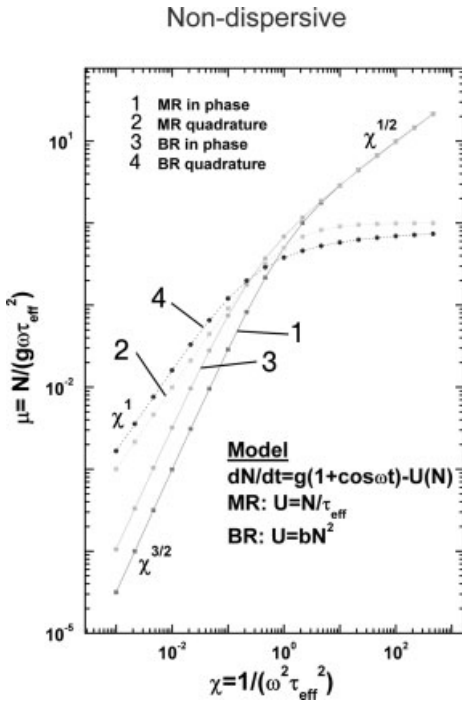
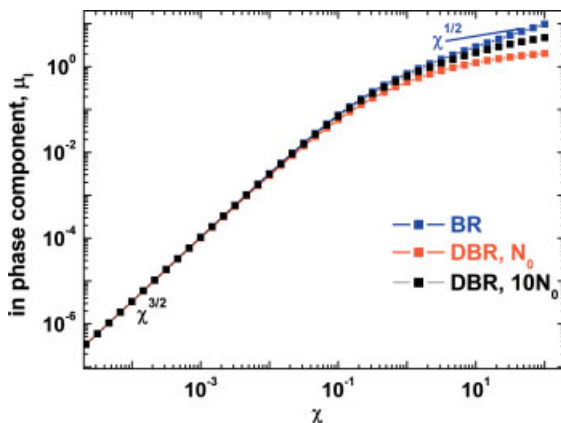


Figure 5.11 PA kinetics plotted in generalized coordinates,  $\mu$  versus  $\chi$ , for MR and BR.

Strictly, the universal curves shown in Fig. 5.11 now describe the dependence of  $\mu$  on  $\chi$  for *saturationless* recombination kinetics. However, for “moderate” saturation cases, the universality described above still holds for most of the dynamic range. In Fig. 5.12, the in-phase component of  $\mu$ , is plotted versus  $\chi$ , for the case of “moderate” saturation; i.e.  $g\tau_{\text{eff}}/N_0 < 1$ , for several values of  $N_0$ . As can be seen, except near the steady state, the universality is retained in the full dynamic range. Since extreme saturation cases are not generally observed with the relatively low pump intensity used in the photomodulation spectroscopy technique, we limit ourselves hereafter to only moderate saturation. Furthermore, since the effect of saturation is mostly apparent in the steady state, the cases of extreme saturation can be analyzed using Eqs. (5.36)–(5.40), which are appropriate for the steady state.



**Figure 5.12** PA kinetics for moderate saturation,  $g\tau_{\text{eff}}/N_0 < 1$ , plotted in generalized coordinates,  $\mu$  versus  $\chi$ , for three values of saturation densities:  $N_0$  (lower curve),  $10N_0$  (middle curve) and pure BR (or  $N_0 \rightarrow \infty$ ) (upper curve).

Focusing now on the dependence of the PA on the pump intensity ( $I_L$  or  $\gamma$ ), we can draw the following conclusions from the above analysis:

- *MR*. PA is *linear* in  $\gamma$  over the entire dynamic range (Fig. 5.9).
- *MR or BR with saturation near the steady state* ( $\chi \gg 1$ ). PA is *sublinear* approaching a fixed value at high  $I_L$  values (Fig. 5.9).
- *BR near steady state* ( $\chi \gg 1$ ). PA is *sublinear*.  $PA_I \propto I_L^{1/2}$ , whereas  $PA_Q$  approaches independence of  $I_L$  at high  $I_L$  (Fig. 5.9).
- *BR away from the steady state* ( $\chi \ll 1$ ). In-phase component is *superlinear*.  $PA_I \propto I_L^{3/2}$ , whereas the quadrature component is *linear*.  $PA_Q \propto I_L$  and is independent of the bimolecular recombination rate  $b$  (Fig. 5.13).

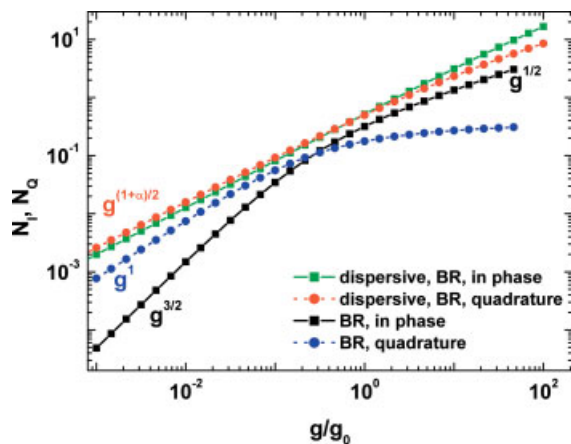


**Figure 5.13** Excitation intensity dependence at finite modulation frequencies for non-dispersive and dispersive BR.

This behavior should be observed only in cases where the recombination rates for the MR and BR processes are uniquely defined. When a distribution of recombination rates are present in the sample, we expect a broader transition range of  $\mu$  ( $\chi$ ) around  $\chi \approx 1$  compared with that in Fig. 5.11. In the next sections we shall treat special cases of recombination rate distribution.

#### 5.3.2.4 Dispersive Kinetics: Frequency Domain

One of the most intriguing results of the preceding analysis is the superlinear pump intensity dependence of the PA away from the steady state in the BR case:  $PA_I \propto I_L^{3/2}$ . Such a behavior is rarely observed. This distinct BR superlinear behavior may be masked owing to a radical recombination rate distribution, such as “dispersive recombination” [62]. One of the key signatures of the latter mechanism is the gentle high-frequency fall-off of the PA:  $\propto \omega^{-a}$  ( $a < 1$ ), compared with  $N_I \propto \omega^{-2}$  for the uniform recombination rate case, Eq. (5.41). In many PCP the modulated PA shows such high-frequency behavior [35, 49, 63–65]. We therefore extend the “generalized coordinates” ( $\mu$  and  $\chi$  introduced above) approach in order to separate the various kinetic regimes in this case also.

Since films of conjugated polymers, in general, are very inhomogeneous at the molecular level, they resemble amorphous materials. The dynamics of photoexcitations in amorphous materials is governed in many cases by a “dispersive” (or diffusive) process [66, 67]. In a dispersive process, the response,  $N(\omega)$ , of the system to a modulated excitation depends non-trivially on a fractional power of the (modulation) frequency,  $\omega$  [66, 68]. For the sake of simplicity, we consider the Cole–Cole model [66], which is one of the simplest non-trivial mechanisms found in amorphous materials:

$$N(\omega) = \frac{N_{ss}^0}{1 + (i\omega\tau_0)^a} \quad (5.46)$$

where  $a < 1$ ,  $\tau_0$  is a “mean” lifetime and  $N_{ss}^0$  is the steady-state response at zero frequency. In Eq. (5.46), the system response,  $N$ , is written as a complex function whose real (imaginary) part is the  $I$  ( $Q$ ) component. The response  $N(\omega)$  in Eq. (5.46) was originally assigned to the dielectric response of the system [66, 68]. Here, we assume that the PA response can be written in the form given in Eq. (5.46) identifying  $N(\omega)$  with the density of the photogenerated species undergoing relaxation/recombination processes following a modulated photoexcitation at frequency  $\omega$ . We identify  $N_{ss}^0$  in Eq. (5.46) with an “average” steady-state photoexcitation density at zero frequency, such that  $N_{ss}^0 = g^*\tau_0$ , where  $g^* \equiv gS$  [see Eq. (5.33) for the definition of the saturation parameter  $S$ ]. For the MR process  $\tau_0$  is independent of the excitation intensity, whereas for the combined MR and BR we assume the typical excitation intensity dependence  $\tau_0^{-1} = \sqrt{g^*b_0}$ , where  $b_0$  is a “mean” BR-like recombination rate. The in-phase and quadrature PA components are then given by

$$N_I(\omega) = \text{Re}[N(\omega)] = \frac{g^*\tau_0[1 + (\omega\tau_0)^a \cos(\pi a/2)]}{1 + 2(\omega\tau_0)^a \cos(\pi a/2) + (\omega\tau_0)^{2a}} \quad (5.47)$$

$$N_Q(\omega) = -\text{Im}[N(\omega)] = \frac{g^*\tau_0(\omega\tau_0)^a \sin(\pi a/2)}{1 + 2(\omega\tau_0)^a \cos(\pi a/2) + (\omega\tau_0)^{2a}} \quad (5.48)$$

In Fig. 5.14 we show the expected frequency response for a dispersive recombination process, for  $a = 0.6$ . It is seen that (a) the  $Q$  component shows a maximum at  $\omega_{max} \approx \tau_0^{-1}$  and (b) at  $\omega \gg \omega_{max}$ , both the  $Q$  and  $I$  components decrease *sublinearly* with  $\omega$ :  $PA_{I,Q} \propto \omega^{-\beta}$ , where  $\beta_Q \approx \beta_I \approx a$ . It is important to note here that such a sub-linear frequency dependence is not limited to the above Cole–Cole mechanism.

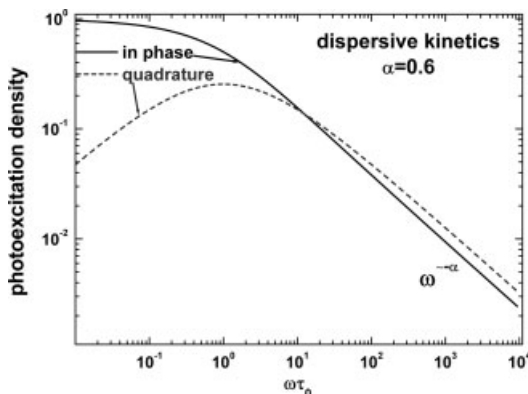
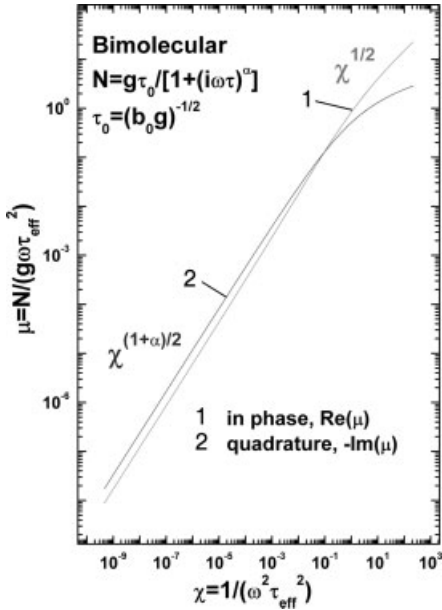


Figure 5.14 The PA modulation frequency dependence for dispersive kinetics.



**Figure 5.15** PA kinetics plotted in generalized coordinates,  $\mu$  versus  $\chi$ , for dispersive kinetics.

Other dispersive models, such as the Davidson–Cole [69] and Havriliak–Negami [70], also show the unique sublinear frequency dependence.

For the dispersive process we define the generalized coordinates,  $\mu$  and  $\chi$ , as above, with  $\tau_0$  replacing  $\tau_{\text{eff}}$  in Eqs. (5.44) and (5.45). Using Eq. (5.46), we plot  $\mu_I$  and  $\mu_Q$  versus  $\chi$  in Fig. 5.15 (for  $a = 0.6$ ). We note that for  $\omega\tau_{\text{eff}} > 1$ , both  $N_I$  and  $N_Q$  behave similarly, with an  $a$ -dependent *sublinear*  $\chi$ -dependence, for both MR and BR processes. This sublinear dependence contradicts the superlinear  $\chi^{3/2}$  dependence for non-dispersive recombination processes discussed above (Fig. 5.13).

We turn now to examine the PA  $I_L$  dependence, which shows some interesting features for the dispersive BR case, as shown in Fig. 5.13a. In the higher  $\gamma$  regime (where  $gb_0/\omega^2 \gg 1$ , i.e., near the steady state),  $N_I \propto \sqrt{g}$  (as for the regular saturationless non-dispersive BR process) and  $N_Q \propto g^{1/2(1-a)}$  (i.e., weak dependence, similar to the non-dispersive case). In the lower  $\gamma$  regime (where  $gb_0/\omega^2 \ll 1$ , away from steady state),  $N_Q \propto g^{(1+a)/2}$ , whereas  $N_I$  behaves similarly (for  $a < 1 - 2(gb_0/\omega^2)^{2a}/\pi$ ). The striking superlinear dependence ( $N_I \propto g^{3/2}$ ), expected for the “regular” (i.e.  $a \equiv 1$ ) BR process away from the steady state, is totally masked away by the lifetime distribution in these inhomogeneous systems (see the next section).

### 5.3.2.5 Lifetime Distribution for Dispersive Processes

The dispersive response described in the preceding section is phenomenological in the sense that Eq. (5.46) was not derived from a rate equation, but rather was invoked in order to account for the experimentally observed peculiar sublinear fre-

quency and pump intensity dependences, away from the steady state. However, the origin of the empirical expression, Eq. (5.46), can be traced to an inhomogeneous distribution of recombination rates.

Following Ref. [71], we define the lifetime distribution function  $\Gamma(\ln\tau)$  by the equation

$$N(\omega) = \int_{-\infty}^{\infty} \frac{g\tau'}{1 + i\omega\tau'} \Gamma(\ln\tau') d(\ln\tau') \quad (5.49)$$

where  $\gamma$  is the generation rate,  $N(\omega)$  is given by Eq. (5.46) and  $\int_{-\infty}^{\infty} \Gamma(\ln\tau') d(\ln\tau') = 1$ . Hence the dispersive process is described by a single lifetime recombination process combined with a lifetime distribution function  $\Gamma(\ln\tau')$ . The single lifetime process may, for instance, be a monomolecular process or a more general bimolecular process, for which  $\tau'$  may be expressed as  $\tau'^{-1} = \sqrt{gb'}$ . Hence the peculiar sublinear frequency dependence at high modulation frequencies results then from an extremely wide distribution in which the presence of very short lifetimes prevents a truly “away from steady state” situation. The distribution function,  $\Gamma$ , can be extracted from the photogenerated density,  $N(\omega)$ , using the inverse transform of Eq. (5.49) [71]. Hence by measuring the PA as a function of the modulation frequency and pump intensity one can, in principle, extract the inhomogeneous distribution of recombination lifetimes. It should be noted, however, that owing to the experimentally limited range of modulation frequencies and pump intensities, the distribution function  $\Gamma$  can be determined only on a finite range of recombination rates.

### 5.3.2.6 Inhomogeneous Distribution of Recombination Lifetimes: General Case

In the general inhomogeneous case, it is useful to define the lifetime distribution function by Eq. (5.49), where the real (“in-phase”) and imaginary (“quadrature”) components of  $N(\omega)$  are given by Eq. (5.41). Since the frequency response for both MR and BR processes is practically identical (see Section 5.3.2.2), the above definition of the lifetime distribution function may be applicable for both processes, with  $\tau$  being dependent on pump intensity for the BR case [see Eq. (5.34)]. Examining Eq. (5.49), we may conclude the following:

The broader the distribution is, the broader is the “transition” region from the “low frequency” (or “near steady state”) to the “high frequency” (or “away from steady state”). In this extended transition region, a weaker frequency dependence [relative to the “normal” case, Eq. (5.41)] could be observed for both in-phase and quadrature components.

For a finite width distribution, the “normal” frequency dependence [Eq. (5.41)] should be observed outside the transition region, i.e. for either  $\omega \gg \tau_{\min}^{-1}$  or  $\omega \ll \tau_{\max}^{-1}$ , where  $\tau_{\min, \max}^{-1}$  are the low and high cutoffs of the distribution.

As an illustration, we consider a step distribution function defined by

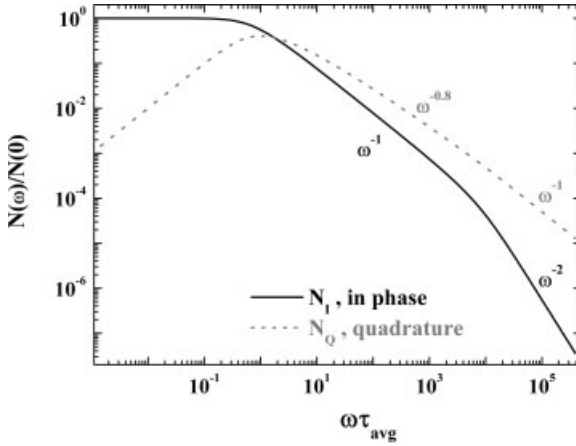


**Figure 5.16** The modulation frequency response for a finite step lifetime distribution function [Eqs. (5.50)–(5.52)], plotted as  $N_{I,Q}$  versus  $\omega\tau_{\text{avg}}$ , with  $\ln(\tau_{\text{max}}/\tau_{\text{min}}) = 10$ .  $\tau_{\text{avg}}$  is the average lifetime.

$$\Gamma(\ln\tau) = \begin{cases} 1/\ln(\tau_{\text{max}}/\tau_{\text{min}}), & \ln\tau_{\text{min}} < \ln\tau < \ln\tau_{\text{max}} \\ 0, & \text{otherwise} \end{cases} \quad (5.50)$$

With this distribution function, the response  $N(\omega)$  [Eq. (5.49)] can be easily calculated:

$$N_I(\omega) = \frac{g}{\omega \ln(\tau_{\text{max}}/\tau_{\text{min}})} [\tan^{-1}(\omega\tau_{\text{max}}) - \tan^{-1}(\omega\tau_{\text{min}})] \quad (5.51)$$

$$N_Q(\omega) = \frac{g}{2\omega \ln(\tau_{\text{max}}/\tau_{\text{min}})} \ln\left(\frac{1 + \omega^2 \tau_{\text{max}}^2}{1 + \omega^2 \tau_{\text{min}}^2}\right) \quad (5.52)$$

In Fig. 5.16 we show the predicted PA response for the finite step lifetime distribution [Eqs. (5.50)–(5.52)]. We see that in the transition region,  $\omega\tau_{\text{avg}} \approx [1, \omega\tau_{\text{max}}]$ , both  $N_I$  and  $N_Q$  fall off more slowly relative to the homogeneous case (Fig. 5.10), indicating a situation in which only a portion of the sample is at a truly “high-frequency” limit. At higher frequencies, a truly high-frequency limit is achieved for the whole sample and the “normal” homogeneous response is observed. Similar behavior is obtained for the pump intensity dependence of the PA for the BR process (not shown), where the  $g^{3/2}$  dependence (Fig. 5.10) is seen only for very low pump intensities and/or very high frequencies. In the broad transition region, where a truly high-frequency limit has not been achieved yet, an  $N_{I,Q} \propto g^{-1}$  dependence is obtained for both the in phase and quadrature components.

## 5.3.3

**Polaron Recombination and Quantum Efficiency of OLEDs**5.3.3.1 **Polaron Recombination in OLEDs**

Commercial interest in organic semiconducting materials, both small molecules and polymers, is to a large extent motivated by the electroluminescent property of many  $\pi$ -conjugated compounds. Research in the use of  $\pi$ -conjugated compounds as the active semiconductors in light-emitting diodes has advanced rapidly (for a review, see Ref. [72]). Organic light-emitting diodes (OLEDs) are now approaching efficiencies and lifetimes sufficient for the commercial market for, e.g., large-area flexible displays or panel lighting. Organic electroluminescence (EL) was first reported for anthracene single crystals in the 1960s [73, 74]. Efficient EL was demonstrated in the 1980s by Tang and Van Slyke in two-layer sublimed molecular film devices [75]. These devices consisted of a hole-transporting layer of an aromatic diamine and an emissive layer of 8-hydroxyquinoline aluminum (Alq<sub>3</sub>). Indium tin oxide (ITO) is used as the transparent hole-injecting electrode, through which the electroluminescence is harvested, and a magnesium–silver alloy as the electron-injecting electrode. A large number of other molecular materials have been used as the charge-transporting or emissive layer in OLEDs.

EL from conjugated polymers was first reported in 1990 [1], using poly(*p*-phenylenevinylene) (PPV). The main advantage of using polymers, compared with small  $\pi$ -conjugated molecules, is their potential for large-scale, low-cost production using solution processing techniques.

The processes responsible for EL were established in the early studies: positive and negative polarons are first injected from the electrodes into the luminescent layer. The polarons then migrate through this layer and can form neutral, bound excitons, either spin singlet or triplet. The *internal* electroluminescence quantum efficiency,  $\eta_{EL}$ , can therefore be defined as a product of three factors [72, 76]:

$$\eta_{EL} = \eta_1 \eta_2 \eta_3.$$

1.  $\eta_1$  is the fraction of emitted photons per optically active exciton formed
2.  $\eta_2$  is the fraction of optically active excitons per total number of excitons and
3.  $\eta_3$  is the fraction of excitons formed per charge carrier flowing in the external circuit.

In hydrocarbon materials usually only singlet states luminesce, triplet states usually being non-emissive [39]. The maximum possible efficiency of fluorescence-based (only singlet states are emissive) OLEDs is therefore determined by the fraction of injected electrons and holes that recombine to form emissive spin-singlet excitons, rather than non-emissive triplet excitons.

An assumption often employed until recently is that excitons are formed in the ratio one singlet to three triplets, since only one singlet combination can be formed from the addition of two spin- $1/2$  charge carriers, however, the triplet state

is threefold degenerate (see Fig. 5.17). This is correct only if the polaron recombination process by which these excitons form were spin-independent and then the maximum quantum efficiency,  $\eta_{\max}$ , of OLEDs would be limited to  $\eta_2 = 25\%$  [72], even if  $\eta_1$  and  $\eta_3$  where both equal to unity. The validity of this 25% spin-degeneracy statistic was tested in an Alq<sub>3</sub> device and a singlet fraction of  $22 \pm 3\%$  was found [77], in good agreement with expectations. Much research has therefore been focused on finding schemes where both spin states, singlet and triplet excitons, can be used for light-emission in OLEDs. Such schemes generally involve materials, primarily organometallic complexes, having significant spin-orbit coupling to promote the spin-flip needed for optical emission. The most prominent schemes for harvesting triplet excitons involve either using phosphorescence emission directly or using Förster transfer from the triplet state of the “phosphorescent sensitizer” to the singlet state of a fluorescent guest complex [78]. A recent report by Adachi et al. demonstrated an impressive internal phosphorescence efficiency of 87% [79]; in such devices the external efficiency is then mostly determined by the light out-coupling efficiency of the device.

The triplet harvesting scheme has proven very successful, but a surprising recent discovery indicates that in OLEDs made from  $\pi$ -conjugated polymers a considerably higher number of singlet excitons are generated than expected from spin-degeneracy statistics (i.e. 25%) and triplet harvesting might not always be necessary. The original report gave a singlet fraction of  $\sim 50\%$  [80] in a PPV-based device and a similar result was soon thereafter obtained by another laboratory [81]. To explain the large singlet yield, the original report also speculated that either the exciton binding energy is weak or that singlet bound states are formed with higher probability than triplets. To our knowledge, all subsequent studies have considered the second alternative, since it is by now well established that the splitting between the lowest singlet and triplet excitons is typically 0.7 eV [39], so that at least the triplet exciton is strongly bound. The singlet exciton binding ener-

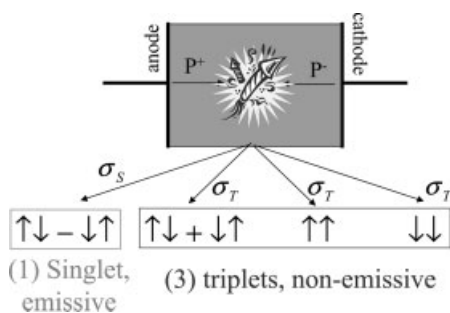


**Figure 5.17** Spin-dependent exciton formation in OLEDs: The OLED device is drawn schematically as a single layer sandwich device. Upon application of forward bias, positive ( $P^+$ ) and negative ( $P^-$ ) polarons are injected. Polaron recombination is symbolized

as a firework; the possible spin states for the resulting exciton are shown. Assigning different exciton formation cross-sections for the singlet ( $\sigma_S$ ) and triplet ( $\sigma_T$ ) channels allows for spin-dependent exciton formation.

gy is therefore also expected to be relatively large. The exact value for the singlet exciton binding energy has, however, remained a matter of intense discussion and ongoing research. (see, e.g., Ref. [82] for a review)

Recently, Baldo and co-workers [83] used a novel technique employing reverse bias measurements of photoluminescent efficiency to determine the excitonic singlet–triplet formation statistics of electroluminescent organic thin films. Using this method, the singlet fractions in thin films of two organic emissive materials commonly used in organic light-emitting devices, Alq<sub>3</sub> and poly[2-methoxy-5-(2-ethylhexyloxy)-1,4-phenylenevinylene] (MEH-PPV), were found to be  $20 \pm 1$  and  $20 \pm 4\%$ , respectively. These results are in apparent contradiction to reports by others claiming that the singlet fraction is much larger than 25% in polymer devices. We must therefore conclude that the current understanding of exciton formation statistics in polymeric and low molecular weight organic electroluminescent materials is still incomplete and that the notion that  $\eta_{\max} > 25\%$  is widely, but currently not universally, accepted.

### 5.3.3.2 Spin-Dependent Exciton Formation Cross-Sections

To accommodate the possibility that singlets and triplets form with different probabilities, Shuai et al. [76] introduced the spin-dependent exciton formation cross-sections,  $\sigma_S$  and  $\sigma_T$ , for singlet and triplet formation, respectively (see also Fig. 5.17). They also postulated that  $\eta_2 = \sigma_S / (\sigma_S + 3\sigma_T)$  (this relation can be derived from a simple rate-equation model [84]). For  $\sigma_S = \sigma_T$  we retrieve  $\eta_2 = 25\%$ , the spin-statistical limit; however, if it turns out that  $\sigma_S > \sigma_T$  then efficiencies larger than 25% would be possible. Indeed, a number of recent reports have indicated that  $\eta_{\max}$  in OLEDs ranges between 22 and 83% [77, 80, 81, 84–87] and the reason for this variation is under investigation. Recent experimental and theoretical work has mostly stated the problem in terms of spin-dependent exciton formation rates, rather than formation cross-sections. In our work we will assume that the exciton formation cross-sections are proportional to the exciton formation rates that we will measure experimentally using PADMR (see Section 5.5).

## 5.4

### Photoinduced Absorption: Spectroscopy and Dynamics

#### 5.4.1

##### Red Polythiophenes: Regio-Regular, Regio-Random

Relatively high mobilities, of the order of  $0.1 \text{ cm}^2 \text{ V}^{-1} \text{ s}^{-1}$ , have recently been obtained with regioregular substituted poly(3-hexylthiophene) (RR-P3HT) (see Fig. 5.18) in FETs [88]. Such films were also successfully used in FETs to drive OLEDs based on polymers, which demonstrated an all-organic display pixel [89]. The reason for the dramatic increase in carrier mobilities is that self-organization of RR-P3HT chains results in a lamellar structure perpendicular to the film sub-

strate [88]. In such lamellae, two-dimensional (2D) sheets are formed having strong interchain interaction due to the short interchain interlayer distance of the order of 3.8 Å. Delocalization of the charge carrier among the lamellae has been invoked as the reason for the high interlayer mobility. Recent optical studies of RR-P3HT films, where delocalized polaron excitations on adjacent chains were measured using charge-induced optical techniques in FETs [88, 90], and also direct photogeneration in thin films [91], have confirmed this assumption. In contrast, P3HT films cast from polymer chains having regiorandom (RRa-) order (see Fig. 5.18a, inset) form ordered lamellae to a lesser degree and the field-effect carrier mobilities obtained in FETs based on this polymer are consequently much smaller [88]. The main reason for the reduced carrier mobility is the lack of sufficiently strong interchain or inter-lamellae interaction that is caused by the chain-like film morphology.

Figure 5.18 shows the absorption and PL spectra of RRa-P3HT and RR-P3HT films at room temperature [92]. The strong absorption band at photon energies

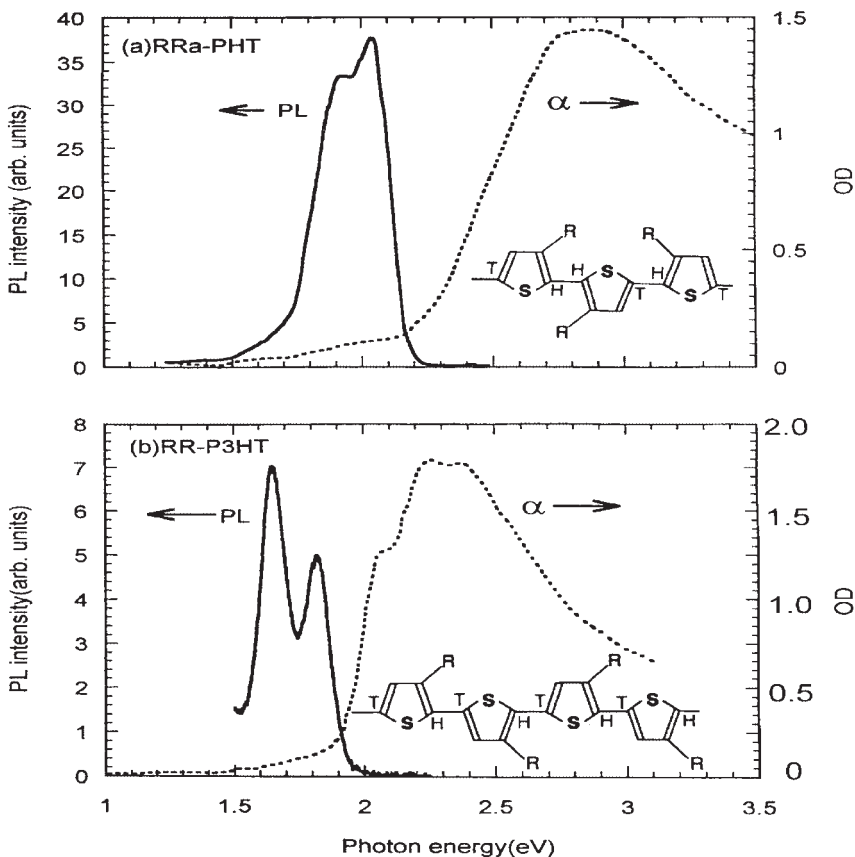


**Figure 5.18** Photoluminescence and absorption spectra of a regio-random P3HT film (a) and of a regio-regular P3HT film (b).

over the energy-gap is due to  $\pi$ - $\pi^*$  transitions and according to Kasha's rule, the PL emission comes from the lowest exciton in the system. We note the red shift of the RR-P3HT absorption and PL bands with respect to those in RRa-P3HT, which is caused by the superior order in the lamellae structures [88]. The planar order leads to polymer chains with longer conjugations with fewer defects, such as twists and radicals on the chains. In addition, the absorption and the PL bands of the RR-P3HT film show pronounced structures due to phonon replicas, indicating that the polymer chains in this film are more homogeneous than those in RRa-P3HT films. In spite of the superior order, we measured in RR-P3HT an order of magnitude *decrease* in the PL quantum efficiency,  $\eta$ ; in RRa-P3HT we measured  $\eta \approx 8\%$ , whereas in RR-P3HT we measured  $\eta < 0.5\%$ . The PL quantum efficiency decrease in RR-P3HT cannot be explained by an increase in the non-radiative decay rate, because this film contains fewer defects and intersystem crossing to the triplet manifold is absent (see below). We conjecture, therefore, that the PL decrease in RR-P3HT is due to a weaker *radiative* transition of the lowest lying excitons in this film. A similar conclusion was also reached for excitons in RR-P3HT chains that form aggregates when dissolved in a poor solvent [93]. The weaker optical transition in the RR-P3HT films may be due to a larger interchain contribution for the lowest excitons in the lamellae compared with the usual intrachain excitons in RRa-P3HT. Indeed, an interlayer separation of 3.8 Å in RR-P3HT lamellae causes a stronger interchain–interlayer interaction, as recently calculated using numerical quantum-chemical methods [94, 95]. For an H-aggregate chain configuration this interaction leads to splitting of the HOMO and LUMO levels, so that the lower, red-shifted LUMO level becomes optically forbidden [94]. The weak PL that is still detected in RR-P3HT may be due to defects that are present in the film, which relax the optical selection rules. This model may explain the weak PL in RR-P3HT, and also its red shift. The higher split LUMO level is optically allowed in this model [94] and may be directly seen in absorption, which should be blue shifted respect to the PL. Hence from the Stokes shift of the 0–0 transition in absorption and PL spectra (Fig. 5.18b) we obtain an upper limit for the LUMO splitting in RR-P3HT of 250 meV, in good agreement with recent model calculations [94, 95].

#### 5.4.1.1 Photomodulation Studies of RRa-P3HT

Figure 5.19a shows that a strong PA band, T, at 1.45 eV dominates the PM spectrum in RRa-P3HT films [91]. At larger amplification ( $\times 30$ ) we also observed a PA band  $P_1$  at 0.5 eV. This band is correlated with a series of narrow lines below about 200 meV that are considered to be IRAVs that are made ir-active owing to the induced charges on the chains (Fig. 5.5a). The two PA bands have different dynamics as measured by their distinctive different dependences on the laser excitation intensity,  $I$ , and modulation frequency,  $f$ . Whereas the band T has a linear  $I$  dependence and a well-defined lifetime (of about 1 ms), the band  $P_1$ , in contrast, has a sublinear  $I$  dependence and does not have a unique lifetime. Actually, it has a wide distribution of lifetimes ranging from a few milliseconds to a few seconds.

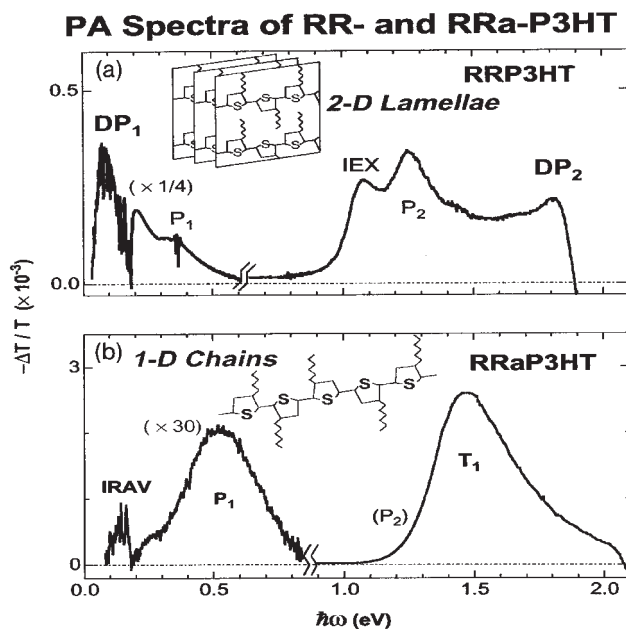


**Figure 5.19** Photoinduced absorption spectra of a regio-regular P3HT film (a) and a regio-random P3HT film (b). Note that  $P_1$  and IRAV bands are multiplied by a factor of 30.

We conclude, therefore, that the two PA bands are due to two different types of photoexcitations. Similar PA bands have been found in many other polymers and are therefore very well understood. The T band is due to a strong optical transition in the triplet manifold that is from the lowest lying triplet,  $1^3B_u$ , to the  $m^3A_n$  state, as discussed in the Introduction, and is therefore a signature of triplet excitons. For this assignment we have strong experimental evidence using the PADMR technique.

We measured (Fig. 5.20a) the  $\lambda$ -PADMR spectrum at resonant magnetic field,  $H_{\nu/2} = 430$  G, corresponding to  $g \approx 5.1$ , which is due to microwave transitions between two triplet sublevels with a substantial zero-field splitting (dubbed “half-field” [96]). We found [97] that the PADMR spectrum contains a single negative  $\delta T$  band at 1.45 eV, which is similar to the PA spectrum. This unambiguously shows that the T band is due to triplet excitons. The long-lived triplets are formed via intersystem crossing to the triplet manifold with a time constant of the order of 5 ns [98]. In addition to the T band we also measured a weak PA band ( $P_1$ ) in the mid-IR spectral range. The PA band  $P_1$  is the low-energy absorption band of intra-chain polarons (Fig. 5.19) and its correlation with the photoinduced IRAVs shows that the underlying photogenerated species are indeed charged. The higher polaron band ( $P_2$  in Fig. 5.19) should appear in the visible/near-IR spectral range, but is not observed here. This happens since the much stronger T band in the PM spectrum probably overshadows it.

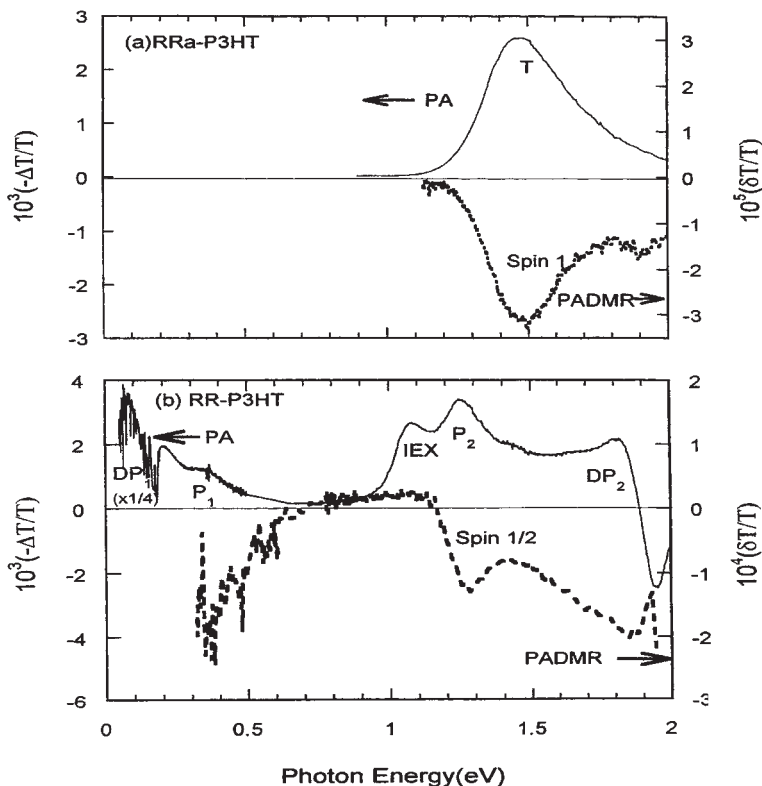


**Figure 5.20** PA and spin-1 PADMR spectrum of regio-random P3HT (a). PA and spin-1/2 PADMR spectrum of regio-regular P3HT (b)

#### 5.4.1.2 Photomodulation Studies in RR-P3HT

The cw PA spectrum of RR-P3HT films (Fig. 5.19b) is much richer [91]. It contains two PA bands, DP<sub>1</sub> at 0.1 eV and DP<sub>2</sub> at 1.8 eV, that are due to 2D delocalized polarons in the lamellae (Fig. 5.21) [88, 90, 91], as well as PA bands P<sub>1</sub> at 0.35 eV and P<sub>2</sub> at 1.25 eV, that are due to localized intrachain polarons in the disordered portions of the film [91]. In agreement with this assignment the two DP bands have the same dynamics; also the two P bands have the same dynamics, which are not correlated with those of the DP bands. We note that DP<sub>1</sub> is red shifted with respect to P<sub>1</sub>, whereas DP<sub>2</sub> is blue shifted with respect to P<sub>2</sub>. Moreover, the sum rule  $E(\text{DP}_1) + E(\text{DP}_2) = E(\text{P}_1) + E(\text{P}_2)$  approximately holds [91, 97]. An interaction model depicted in Fig. 5.21 explains both the energy shift of the DP bands with respect to the P bands and the experimentally demonstrated sum rule. In this model the strong interchain interaction of the DP specie splits the two intrachain polaron levels in the gap in such a way that the lower (upper) optical transition becomes optically allowed. Another feature in the PM spectrum (Fig. 5.19b) is a PA band dubbed IEX at 1.1 eV that was tentatively identified [91, 97] as due to trapped interchain singlet excitons in the lamellae.

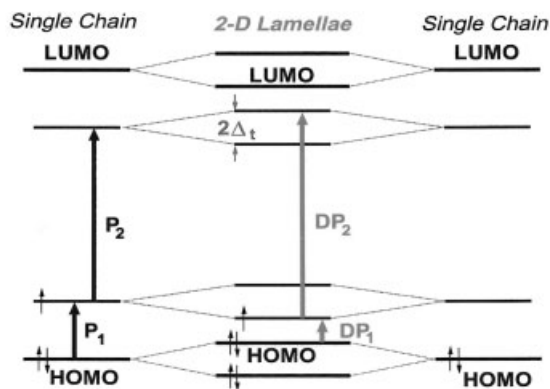


**Figure 5.21** Schematic level diagram for 1D polarons (left and right) and the 2D delocalized polaron (middle) that results from interchain interaction.

The  $\lambda$ -PADMR spectrum measured in RR-P3HT at resonant field that corresponds to  $g \approx 2$  due to spin- $1/2$  carriers is shown in Fig. 5.20b [92] and confirms the previous assignments of the various PA bands [91]. This spectrum shows that, except for the IEX band, all other PA bands in the PM spectrum are associated with spin- $1/2$  carriers. In particular,  $DP_2$  may now be associated with spin- $1/2$  polarons. It is also seen in Fig. 5.20b that IEX is not associated with any spin- $1/2$  excitation, in agreement with its previous assignment [97] that it results from trapped spin *singlet* excitons.

Using PADMR at  $H_{1/2}$  that corresponds to  $g \approx 5.1$  of triplet species [92], long-lived spin-1 excitations *have not* been found in RR-P3HT films. This shows that long-lived triplet excitons are not easily generated in RR-P3HT lamellae. In RR-P3HT solutions, in contrast, long-lived photogenerated triplets do exist and an intersystem crossing (ISC) time constant of about 5 ns was determined [98]. We therefore conjecture that the delocalized interchain interlayer excitons in the lamellae do not easily turn into localized intrachain triplet excitons in RR-P3HT via ISC. This is further strong evidence that the primary photoexcitations in RR-P3HT are not the ordinary intrachain excitons, as found in many other polymer films. Instead, they are delocalized among adjacent layers, similar to the delocalized polarons in the lamellae studied before [88, 90, 91], with a consequent suppression of ISC into the triplet manifold. We note that ISC suppression was also observed recently in aggregates of long oligothiophenes below the aggregate formation temperature [99]. ISC suppression might therefore be a general consequence of enhanced interchain interaction.

#### 5.4.1.3 The Polaron Relaxation Energy

Polaron excitations in polymers have two correlated optical bands below the gap [100]; these are  $P_1$  in the mid-IR and  $P_2$  in the near-IR spectral range (see Fig. 5.22,

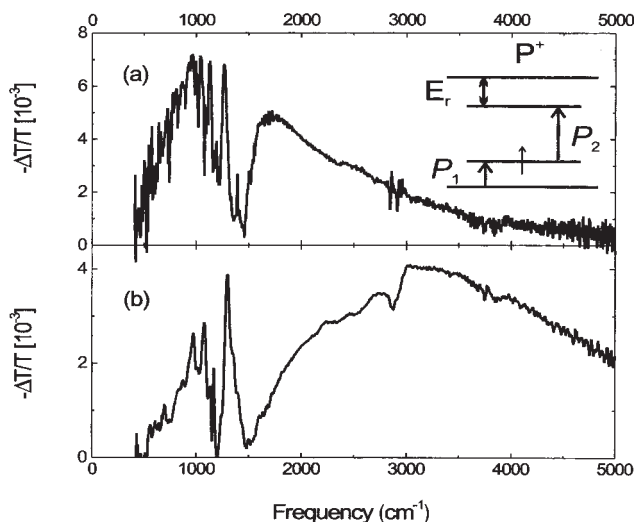
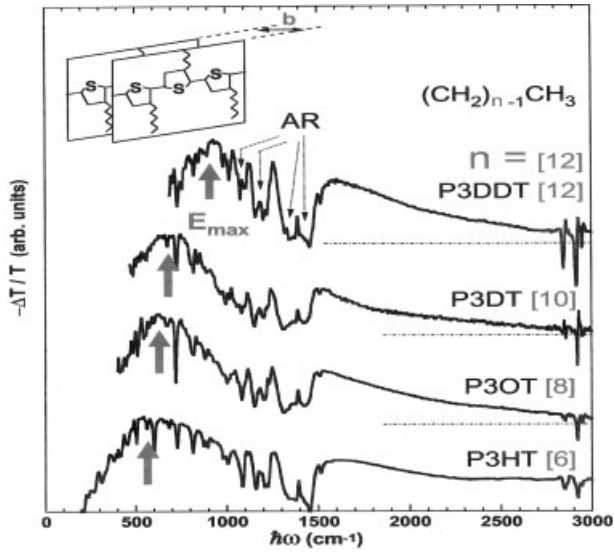


**Figure 5.22** PA spectra, obtained using an FTIR spectrometer, of two RR-P3AT films that were measured at 20 K; one is RR-P3HT (a) and the other is RR-P3AT that has a very long alkyl side-group (b).

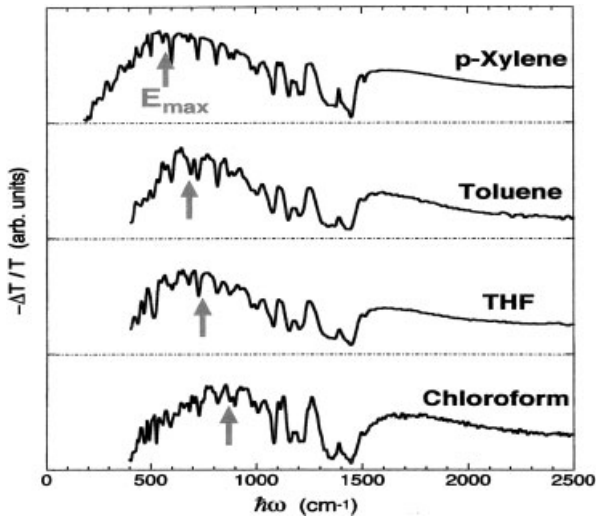
inset).  $P_1$  for a positive polaron is an optical transition from the HOMO band into the lower intragap polaron level, whereas for a negative polaron it is a transition between the upper intragap polaron level into the LUMO band;  $P_1$  is thus directly related to the polaron relaxation energy,  $E_r$ .  $P_2$ , in contrast is the optical transition between the two intragap polaron levels and is thus related to the separation between them [100] (see Fig. 5.22, inset).

Figure 5.22 [42] shows the PA spectra of two RR-P3AT films that were measured at 20 K; one is RR-P3HT (Fig. 5.22a) and the other is RR-P3AT that has a very long alkyl side-group (Fig. 5.22b). We note that whereas RR-P3HT forms lamellae in the film [88], the second polymer chains do not form lamellae, because of the very long attached side-group. One of the pronounced differences between the two PA spectra in Fig. 5.22 is the PA bands marked  $DP_1$  and  $P_1$ ; in RR-P3HT  $DP_1$  peaks at about  $1000\text{ cm}^{-1}$  and is due to the DP species [91], whereas  $P_1$  peaks at about  $3000\text{ cm}^{-1}$  in the less ordered polymer film and is due to intrachain polarons, similar to the case of RRa-P3HT discussed above. We therefore conclude that the polaron relaxation energy,  $E_r$  is substantially smaller in the more ordered film.

In fact the peak  $E_{\text{max}}$  of the  $DP_1$  band is very sensitive indicator for the polaron relaxation energy and thus can be closely monitored to study the film morphology. We assume that  $E_r$  is smaller the more ordered are the polymer chains in the film; this is caused by the stiffer environment in the ordered films. For example, the size of the alkyl size group may determine  $E_r$  in RR-P3AT films through the chain stiffness. In Fig. 5.23 we show the  $DP_1$  band in several P3AT films,  $(\text{CH}_2)_{n-1}\text{CH}_3$  with  $n = 6-12$  [91]. It is seen that  $DP_1$  blue shifts as  $n$  increases, indicating that larger polaron relaxation occurs in lamellae formed with P3AT with a larger side-



**Figure 5.23** PA spectra, obtained using an FTIR spectrometer, of several films of RR-polythiophene polymer with alkyl side-group substituents of different lengths. Note that  $E_{\text{max}}$  increases with the side-group length,  $n$ .



**Figure 5.24** PA spectra, obtained using an FTIR spectrometer, of several films of RR-P3HT cast from different solvents.

group. One explanation for the increase in  $E_r$  with  $n$  is the increase in the interlayer distance,  $b$ , with  $n$  [91] as depicted in Fig. 5.23, inset. In fact, very long side-groups destroy lamellae formation as for the P3AT film shown in Fig. 5.22.

Different solvents may also play an important role in controlling the interchain interaction, which in turn controls lamellae formation in the film. The order and size of the lamellae determine  $E_r$  and therefore RR-P3HT films spun from different solvents may show slightly different  $E_{\max}$  for the DP<sub>1</sub> band. This is shown in Fig. 5.24, where the DP<sub>1</sub> band obtained in films spun from different solvents is depicted [101]. It is seen that films prepared from solutions of solvents with high boiling temperatures,  $T_B$ , such as *p*-xylene ( $T_B = 138$  °C) has a lower  $E_{\max}$  than films prepared with solvents of low  $T_B$  such as chloroform ( $T_B = 61$  °C) [101]. Bao et al. [102] found in their FET fabrication made of RR-P3HT polymers that the film quality and field-effect mobility are strongly correlated with the choice of solvents. Also, in the picosecond work of Nguyen et al. [103] it was shown that the polymer film morphology changes with the solvent and spin casting speed. Similarly, the RR-P3HT polymer chains in our case are probably more planar and neatly arranged in *p*-xylene solutions, resulting in more ordered lamellae and consequently smaller polaron relaxation. In contrast, the RR-P3HT chains tend to be more coiled in chloroform solutions, hence the lamellae in films cast from this solvent are less ordered and consequently  $E_r$  is larger.

#### 5.4.1.4 The Spectral Anti-Resonances

The most striking difference between the two PA spectra illustrated in Fig. 5.22 is the sharp photoinduced features at frequencies below about  $1600\text{ cm}^{-1}$  that are due to photoinduced IRAVs. Whereas in the less ordered film the photoinduced IRAVs appear as positive absorption lines (Fig. 5.22b), they appear as dips or anti-resonances (ARs) superimposed on the DP<sub>1</sub> PA band in the ordered film (Fig. 5.22a) [91]. These AR dips are apparently caused by the overlap between the IRAV lines and the DP<sub>1</sub> band. Moreover, the AR spectrum (Fig. 5.22a) contains much sharper dips and consequently is much richer than the positive photoinduced IRAV spectrum.

Photoinduced AR lines are not unique to RR-P3HT, which happens to form lamellae in the cast films [88]. In fact, we found that ARs are a generic phenomenon in ordered films, where the polaron P<sub>1</sub> band overlaps with the IRAVs. Figure 5.25a–d show the PA spectra of several other ordered polymer films [42]. In all of them photoinduced ARs superimposed on P<sub>1</sub> are apparent. In some polymers the separation between positive IRAVs and negative ARs is difficult, especially where the overlap with the P<sub>1</sub> band is less pronounced (Fig. 5.25a–c). We also note that in PPE there exists a prominent AR at much higher frequency (at about  $2100\text{ cm}^{-1}$ ) than in the other polymers, which is probably related to the modified C–C triple bond stretching vibration associated with this polymer chain. Also the literature contains other examples of photoinduced ARs in the PA spectra, such as in polydiacetylene single crystals [104, 105], for example, and other polymer films where the AR phenomenon was not recognized [106]. We conclude that

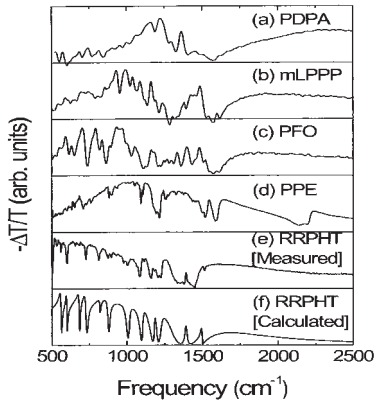


**Figure 5.25** PA spectra, obtained using an FTIR spectrometer, of several films of different well-ordered polymers [(a)–(e)]. (f) The calculated spectrum for RR-P<sub>3</sub>HT.

photoinduced ARs are as common as photoinduced positive IRAVs and therefore an appropriate model to describe this phenomenon was recently advanced.

We have analyzed the AR spectrum using the amplitude mode (AM) model [44, 41], which has had spectacular success in explaining the resonant Raman scattering (RRS) dispersion in addition to photoinduced and doping-induced IRAVs in PCP [41]. In all of these previous applications of the AM model it was explicitly assumed that the adiabatic approximation holds true. This was correct since the Raman line frequencies are much smaller than the optical gap and the IRAV frequencies were much smaller than the energy of the photoinduced or doping-induced electronic bands. This approximation, however does not hold in the case where the ir-active lines overlap with the electronic transition; a modification to the AM model to include the non-adiabatic limit was summarized in the Introduction [42]. We took into account both vibronic and electronic transitions, in addition to the quantum interference between the two types of photoexcitations.

To see the effect of the non-adiabatic limit on the PA spectrum, we calculated [42] the conductivity spectrum, including the IRAVs for polarons with both low and high  $E_r$ , as seen in Fig. 5.5. For these calculations we used the phonon parameters of RR-P3HT with 13 strongly coupled vibrational modes and approximated the electronic band contribution,  $f(\omega)$ , by the CDW response function, where the CDW gap  $2\Delta = E_r$  and  $E_r$  is associated with the polaron relaxation energy that governs the  $P_1$  band. It is seen that when  $\omega \ll E_r$ , then only IRAVs with positive peaks can be observed (Fig. 5.5a); this happens since  $C$  in Eq. (5.14) is negligible small and consequently ARs are not formed. However, when  $E_r$  is small so that the CDW band overlaps with the IRAVs, then quantum interference occurs that gives rise to ARs in the spectrum (Fig. 5.5b); in this case the ARs are more dominant than the IRAVs that occur on their high-energy side. We note the qualitative similarity of the experimental data (Fig. 5.22) with the model (Fig. 5.4), which shows that our approach catches the essence of the AR phenomenon.

To have a more quantitative fit to the experimental PA spectrum of RR-P3HT, we used both resonant Raman scattering (RRS) and doping induced absorption spectra of this polymer film to determine the 13 bare phonon frequencies and

their corresponding e–p couplings [42]. The advantage of using the AM model is that the same phonon propagator,  $D_0(\omega)$ , which determines the photoinduced AR and IRAV frequencies, also determines the RRS and doping induced IRAV frequencies [41]. The RRS frequencies are the solution of the equation  $D_0(\omega) = -(1 - 2\lambda)^{-1}$ , where  $\lambda$  is the effective e–p coupling, whereas the doping-induced IRAV frequencies are correspondingly given by the equation  $D_0(\omega) = -(1 - a_p)^{-1}$ , where  $a_p$  is the pinning parameter associated with the doping-induced polarons [44]. The phonon parameters of RR-P3HT obtained are given in Ref. [42] and were used to calculate, via the AM model, the doping induced IRAV, RRS and photoinduced IRAV and AR frequencies [42].

The actual fit to the RR-P3HT photoinduced AR *spectrum* is seen in Fig. 5.25(f) and can be compared with the measured spectrum (Fig. 5.25e). The excellent agreement between theory and experiment was obtained by using the CDW absorption band to represent the polaron  $P_1$  band with  $E_r = 2\Delta = 900 \text{ cm}^{-1}$ . For this fit a distribution in  $2\Delta$  of about 60% and a distribution in  $a$  of 12% around  $a = 0.38$ , with  $C = -0.08$  was necessary. The disorder and inhomogeneity that still exist in RR-P3HT films in spite of the lamella formation justify the parameter distributions.

In view of the excellent agreement between theory and experiment that is seen in Fig. 5.25e and f, we conjecture that the AM model and a continuum electronic band for  $P_1$  such as the CDW can quantitatively describe the AR phenomenon in ordered polymer films. This conclusion strongly indicates that the photoinduced polaron band in such materials is *continuous*. Since the polaron PA band involves optical transitions between a localized level in the gap and the HOMO and LUMO levels in the charge manifold of these polymers (Fig. 5.22), we therefore conclude that these levels in ordered polymers are in fact *continuous bands* [107, 108]. In such bands electrons can be readily accelerated due to external forces, similarly as in inorganic semiconductors and hence the treatments of ordered polymers in OLEDs and FETs via band bending to form depletion and accumulation layers as in more regular semiconductors are, *a posteriori*, justified.

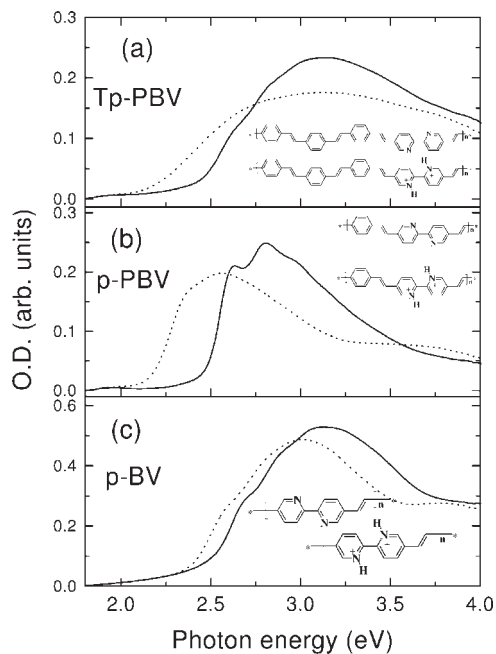
#### 5.4.2

##### Recombination Kinetics

###### 5.4.2.1 Poly(*p*-phenylenebipyridinevinylene)

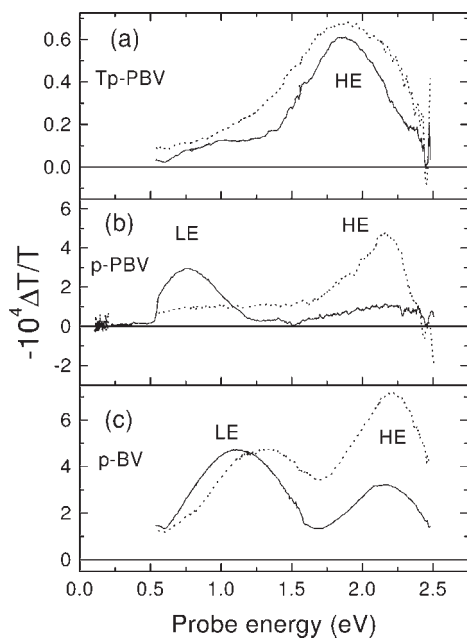
The  $\pi$ -conjugated polymers described here are optically tunable derivatives of pyridylene/vinylene polymers (see Fig. 5.26 for their molecular structure). These derivatives can be tuned reversibly via protonation–deprotonation (P–DP) processes [109]. The PA spectra of the two forms revealed two types of photoexcited species, whose density or absorption intensity depend on the protonation state of the polymer.

Figure 5.26 shows the absorption spectra of films of the above polymers both in their free-base (solid lines) and fully protonated (dotted lines) forms. The free-base form appears to be less inhomogeneous, since its spectrum is sharper than



**Figure 5.26** The optical absorption spectra of Tp-PBV (a), p-PBV (b) and p-BV (c) films in their free-base (solid line) and fully protonated (dotted line) forms. The chemical

structures shown in (a), (b) and (c) are for the free-base (top) and protonated (bottom) forms of each of the films.



**Figure 5.27** The PA spectra for Tp-PBV (a), p-PBV (b) and p-BV (c) films in their free-base (solid line) and fully protonated (dotted line) forms. The HE and LE bands are marked.

that of the protonated films. Figure 5.27 shows the PA spectra of the films both in their free-base (solid lines) and fully protonated (dotted) lines forms. Both the free-base and protonated polymer spectra contain two bands: a low-energy (LE) band and a high-energy (HE) band. However, the two PA spectra are very distinct from each other. In the free-base film of p-PBV (Fig. 5.27b), the LE band (peak position at  $\sim 0.8$  eV) is much stronger than the HE band (peak position at  $\sim 2.2$  eV), whereas in the protonated film, the relative intensities are reversed, indicating that the two bands have different origins. Note that no absorption due to photoinduced IRAVs, characteristic of charged polarons, were not observed either for free base or for the protonated samples. The missing IRAV lines indicate that the LE and HE bands originate from optical transitions due to neutral photoexcited species, such as triplet excitons.

### The kinetics of the HE band: non-dispersive bimolecular recombination

In Fig. 5.28, we show the modulation frequency dependence of the HE band for the two forms of all three polymers. It shows the characteristic non-dispersive kinetic behavior expected for both the  $I$  and  $Q$  components. The  $Q$  component (solid circles) reaches its maximum at frequency  $\nu_{\max}$  (in the range 130–260 Hz for all samples) where the  $I$  component (solid squares) reduces to half of its zero frequency value. At higher modulation frequencies,  $\omega \equiv 2\pi\nu > 2\pi\nu_{\max}$ , both the  $I$  and  $Q$  components decrease as a power law:  $\omega^{-\beta}$ , with  $\beta = 2$  and  $1$ , respectively. The solid and dotted lines in Fig. 5.28 represent a fit of the single recombination rate equation, Eq. (5.41), to the experimental HE data. We conclude that the recombination mechanism is either a mono- or bimolecular recombination process with no appreciable recombination rate distribution.

We can gain more insight into the recombination process by plotting directly the PA versus  $I_L$  for both near steady-state conditions ( $\omega\tau_{\text{eff}} \ll 1$ ) and away from the steady state ( $\omega\tau_{\text{eff}} \gg 1$ ). In Fig. 5.29 we show the in-phase PA component of the HE band of p-PBV versus the normalized pump intensity for low and high  $\omega$ . The superlinear dependence at 400 Hz is clearly seen, whereas at 140 Hz it is sub-linear, as expected for a BR process.

### The kinetics of the LE band: dispersive case

The LE band behaves differently with respect to the modulation frequency and pump intensity, as shown in Fig. 5.30 for p-PBV and p-BV. Comparing Figs. 5.28 and 5.30, we observe three main differences in the modulation frequency dependence between the LE and HE bands: (a) The maximum of the  $Q$  component in LE is much less apparent than in HE; (b) the  $I$  component in LE does not level off at low  $\omega$  as in HE; and (c) at high frequencies both the  $I$  and  $Q$  components of LE decrease very gently, as  $\omega^{-\gamma}$ , with  $\gamma < 1$  (as marked in Fig. 5.30) compared with the much stronger dependence for HE (see Fig. 5.28). We conclude that the two PA bands indeed have different origins and that the LE kinetics are dispersive. We therefore used Eqs. (5.47) and (5.48) to fit the  $I$  and  $Q$  components of the LE band. The results of the fit are shown in Fig. 5.30 as solid and dashed lines, respectively, along with the values of  $a$  obtained by these fits. The different values of  $a$  are pos-

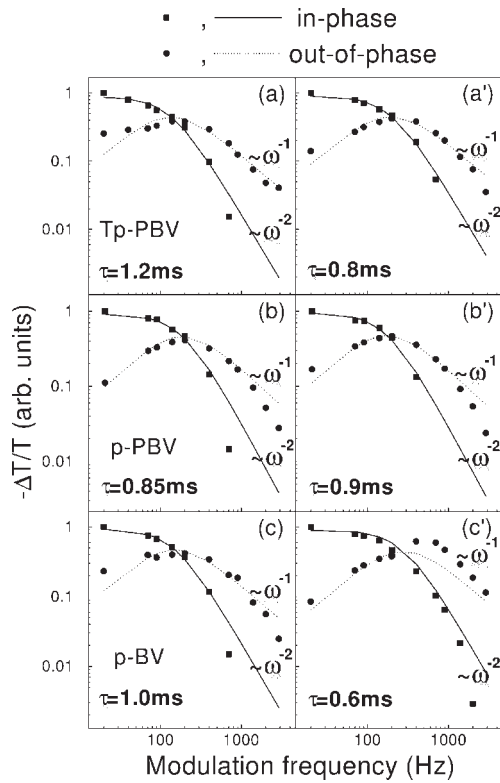


**Figure 5.28** The modulation frequency dependence of the HE band shown in Fig. 5.27: (a)–(c) protonated form; (a')–(c') free base form. Solid square (circle) symbols represent the in-phase (quadrature) data. The lines are fits to Eq. (5.41). Note the log–log scale.

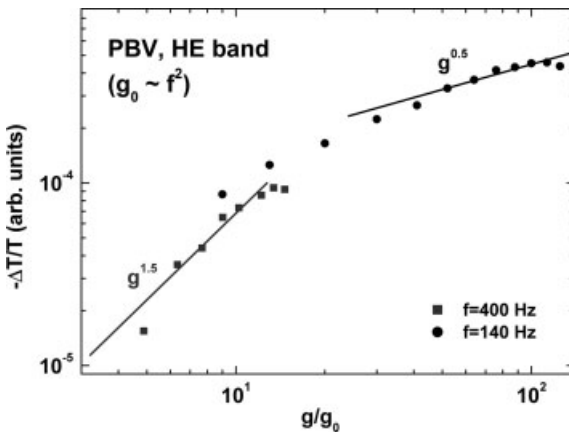


**Figure 5.29** The dependence of the in-phase PA of the HE band in PBV on the pump intensity for low and high frequencies, showing a  $g^{1.5}$  dependence at 400 Hz and a  $g^{0.5}$  dependence at 140 Hz, as expected for BR.

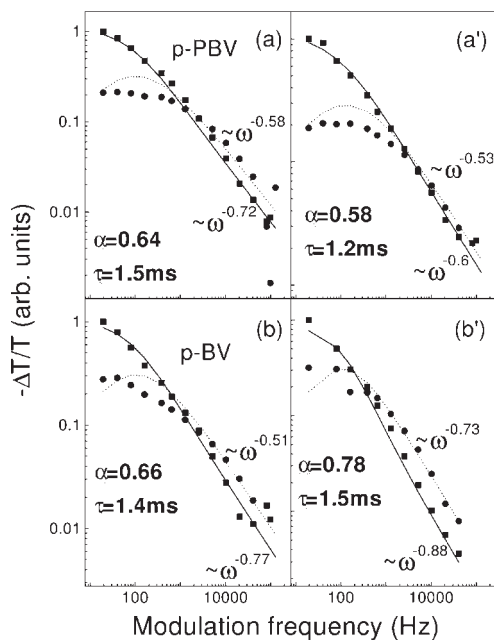


**Figure 5.30** The modulation frequency dependence of the LE band shown in Fig. 5.27: (a), (b) protonated form; (a'), (b') free base. Solid square (circle) symbols represent

the in-phase (quadrature) experimental data. The lines are fits to the dispersive relaxation process [Eqs. (5.47) and (5.48)]. Note the log–log scale.

sibly associated with the amorphous nature of the different films. The smaller value of  $a$  found for the protonated form possibly indicates more disorder [109, 110]. The very good fits support the assumption of dispersive mechanism for the photoexcitation dynamics.

In Fig. 5.31b we show, in generalized coordinates, the PA experimental dependence of the low-energy (LE) band of p-PBV (Fig. 5.27b), which was shown above to have dispersive recombination kinetics. Note the similarity of the in-phase and quadrature components away from the steady state. The overall similarity of Fig. 5.31a and b demonstrates the usefulness of the plot. We also note that by plotting the experimental data in these generalized coordinates, one can distinguish between dispersive mechanisms and “regular” mechanisms (for which there is no or a relatively narrow lifetime distribution).

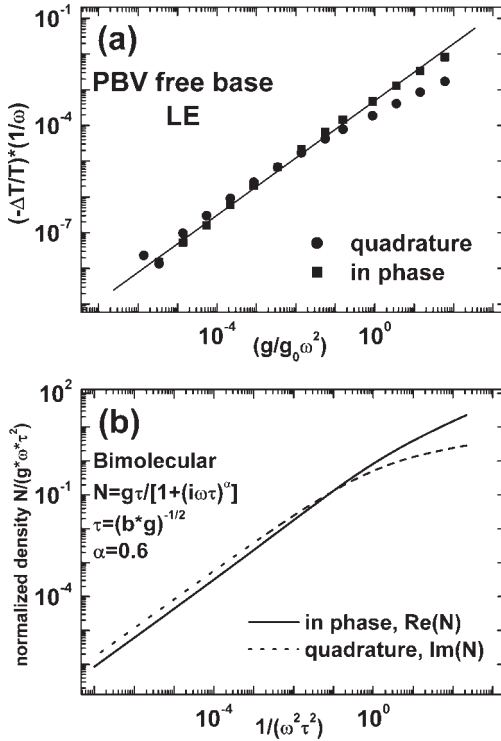


**Figure 5.31** The kinetics of the LE band in PBV (free base) plotted in generalized coordinates,  $\mu$  versus  $\chi$ , showing the dispersive nature of the LE band. Note the log–log scale. (a) Experimental results for the in-phase and quadrature components. The

slope of the straight line is 0.8, which corresponds to BR dispersive kinetics with  $\alpha = 0.6$ , as shown in (b). (b) Theoretical results for a BR dispersive kinetics with  $\alpha = 0.6$  and a slope of  $(1 + \alpha)/2 = 0.8$  for  $\chi \ll 1$ .

#### 5.4.2.2 Poly(phenylenevinylene)

##### Triplet excitons

Another example of the usefulness of the generalized coordinates concept is the triplet exciton (TE) band in poly(phenylenevinylene) (PPV) films. PPV films show strong TE band at around 1.5 eV [111]. The modulation frequency and pump intensity dependences were measured over a dynamic range of more than five decades [112]. The PA intensity dependence shows sublinear behavior, indicating a BR process. Figure 5.32 shows the data plotted (as symbols) in generalized coordinates [Eqs. (5.44) and (5.45)] appropriate for a BR process; i.e.  $\mu \propto -\Delta T/T/\omega$  and  $\chi \propto I_L/\omega^2$ . The initial experimental dependence at the lowest  $\chi$  values is  $\mu \propto \chi^\gamma$  with  $\gamma \approx 0.7$  and  $\approx 0.9$  for the quadrature and in-phase components, respectively. The solid and dashed lines are fits to the data using the BR dispersive model with a dispersive parameter of  $\alpha = 0.75$ . Hence the TE recombination process in PPV

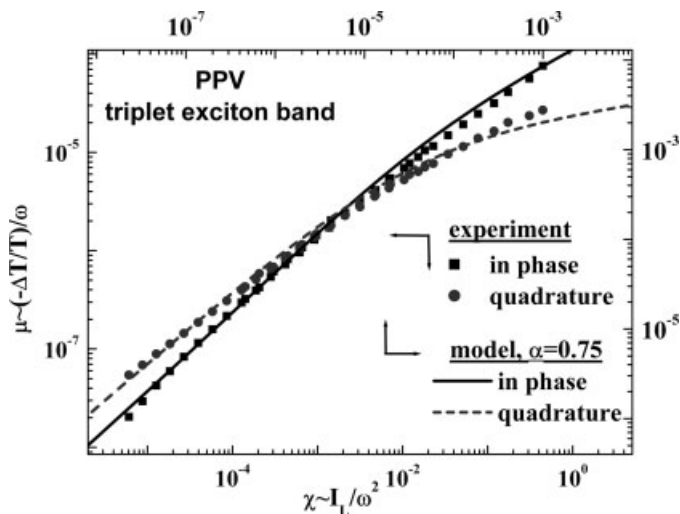


**Figure 5.32** The kinetics of the TE band in PPV plotted in generalized coordinates,  $\mu$  versus  $\chi$ . Symbols, experimental data; lines, dispersive model calculation, using Eqs. (5.47) and (5.48) with  $\alpha = 0.75$ .

is bimolecular with dispersive kinetics, which means that there is a wide distribution of BR rates, with pump intensity-dependent average lifetime.

### Polarons

In addition to the TE neutral photoexcitation mentioned above, PPV shows charge photoexcitations in the form of polarons [111]. The polaron kinetics was studied by following its modulation frequency dependence at various pump intensities [112]. In Fig. 5.33 (symbols) we show the data at two representative pump intensities. Two important features can immediately be recognized. First, the frequency at which the maximum of the  $\Theta$  component occurs,  $\nu_{\max}$ , scales approximately as the square root of the pump intensity [ $\nu_{\max} \approx 0.16$  kHz in (a) and  $\approx 1$  kHz in (b)]. This observation points out towards a BR process. Second, the crossing of the I and  $\Theta$  components (see Fig. 5.33a) occurs at  $\nu \gg \nu_{\max}$ , as expected for dispersive processes (compare Figs. 5.10 and 5.14). The solid lines in Fig. 5.33a are fits of the dispersive BR kinetics to the low pump intensity data, using  $\alpha = 0.59$  and  $\tau_0 = 1.0 \times 10^{-3}$  s. Using the same dispersive parameter,  $\alpha = 0.59$ , and scaling  $\tau_0$  by the inverse square root of the intensity ratio, we show in Fig. 5.33b (solid lines) the calculated  $\Theta$  and I components. As can be seen, the calculated curves describe fairly adequately the experimental frequency dependence. The magnitude of the  $\Theta$  component, however, should be scaled by a uniform factor of  $\sim 1.8$  in order to fit the high pump intensity experimental data (dashed line, Fig. 5.33b). In spite of the magnitude discrepancy of the  $\Theta$  component (which may be the result of experimental calibration), we conclude that the photoexcited polarons in PPV undergo a BR dispersive process, similar to TE in PPV, but with a smaller dispersive parameter.

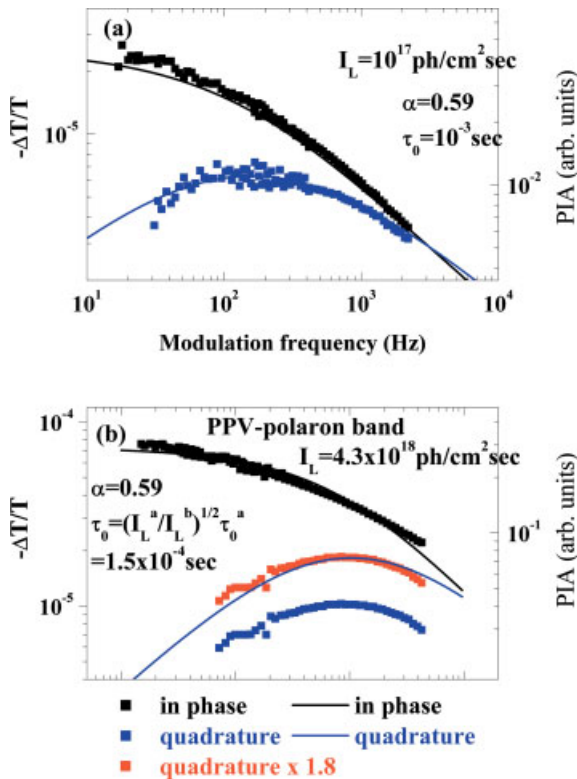


**Figure 5.33** The modulation frequency dependence of the polaron band in PPV, for low pump intensity (a) and high pump intensity (b). Symbols, experimental data (left

scale); lines, BR dispersive model fits using  $\alpha = 0.59$  (right scale). The broken line in (b) is the calculated quadrature component scaled by a factor of 1.8.

#### 5.4.3

#### Photophysics of a Blue-Emitting Polyfluorene

Polyfluorene (PFO) derivatives are known [113–115] for having excellent quantum efficiencies, high mobilities and exceptional thermal and chemical stability in inert environments. In particular, poly(9,9-dioctylfluorene) has emerged as an attractive material for display applications owing to efficient blue emission [116, 117] and hole mobility  $>3 \times 10^{-4} \text{ cm}^2 \text{ V}^{-1} \text{ s}^{-1}$  with trap-free transport [118]. Recently PFO has been recognized as an attractive material for magnetoresistive devices [119].

PFO has also been found to exhibit a complex morphological behavior and the relation between morphology and photophysical properties have been studied [120]. In the melt, polyfluorenes show liquid crystalline phases that can be aligned and quenched into the glassy state, which has led to the fabrication of highly polarized electroluminescence devices [121, 122]. Examples of harnessing struc-

tural versatility to manipulate electronic and optical properties in PFO are the observation of fast hole transport in glassy liquid crystalline monodomains [123] and the variation of lasing properties with phase morphology [124]. PFO films display several different phases [120]: Spin coating a PFO film from solution produces a glassy sample with spectroscopic characteristics typical of conjugated polymers. A different phase that has been called the  $\beta$ -phase has been detected upon cooling a glassy film on a substrate to 80 K or below and slowly reheating it to room temperature or exposing a film to the vapor of a solvent or swelling agent [125, 126]. We note that mesomorphic behavior is seen also in other conjugated polymer families containing alkyl side-chain substituents [127–129] although the exact details are both backbone and side-chain specific.

The spectroscopic properties of the glassy and  $\beta$ -phase PFO differ characteristically from one another. Figure 5.34a shows the absorption and emission spectra of as-spun PFO, purchased from H. W. Sands and measured in our laboratory. Similar results were also obtained in PFO purchased from American Dye Source [130]. It is seen that the  $\pi$ - $\pi^*$  transition of the glassy phase is featureless. The emission spectrum is similar to the mirror image of the absorption spectrum, but, in contrast to the absorption spectrum, the vibronic progressions are clearly resolved. Remarkably, the  $\beta$ -phase sample, obtained from the as-spun sample by

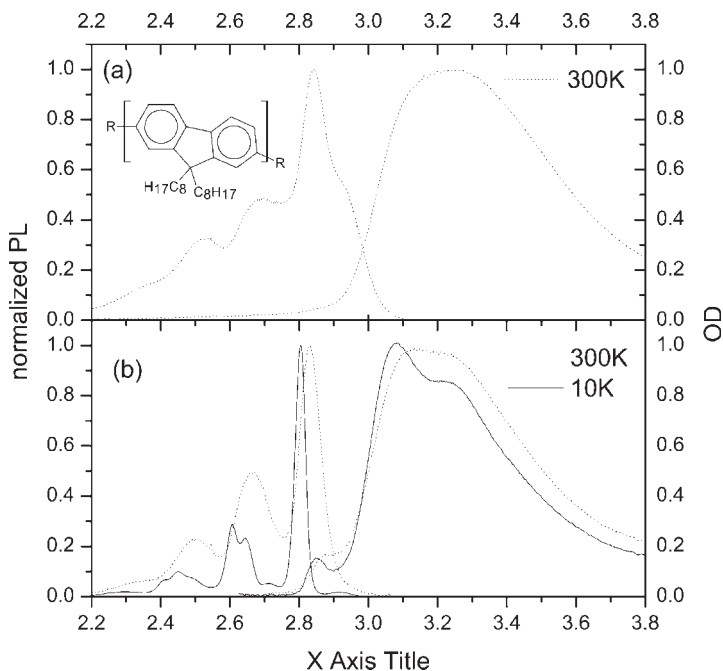


**Figure 5.34** The photoluminescence and absorption spectra of a glassy PFO film (a) and that of a  $\beta$ -phase containing sample (b) that was obtained from the glassy sample by

exposure to solvent vapor (toluene) for several hours. Dotted lines are for room temperature, solid lines for 10 K. The polymer was purchased from H. W. Sands.

exposure to toluene vapor, shows well-resolved features in the absorption spectrum. This is indicative of reduced disorder in the sample and resulting reduced inhomogeneous broadening in the spectrum. This behavior has been correlated with the degree of intrachain ordering in the different phases [120]. X-ray fiber diffraction measurements of the glassy phase have shown that the parallel-to-chain coherence length matches the length of persistence in solution [126] ( $85 \pm 10 \text{ \AA}$ ) as well as the effective conjugation length in solution [131]. Hence the effective conjugation length (CL) in glassy PFO is conformationally limited. However, the CL of the  $\beta$ -phase is much longer [120]. In summary, the rich phase morphology of PFO provides a unique opportunity to study the influence of film morphology on the photophysics of conjugated polymers without the need for chemical modification. In the following, we consider the electronic structure of PFO films by absorption and PL. Photoexcitation dynamics were studied by PA spectroscopy.

#### 5.4.3.1 Electronic Structure of PFO Phases

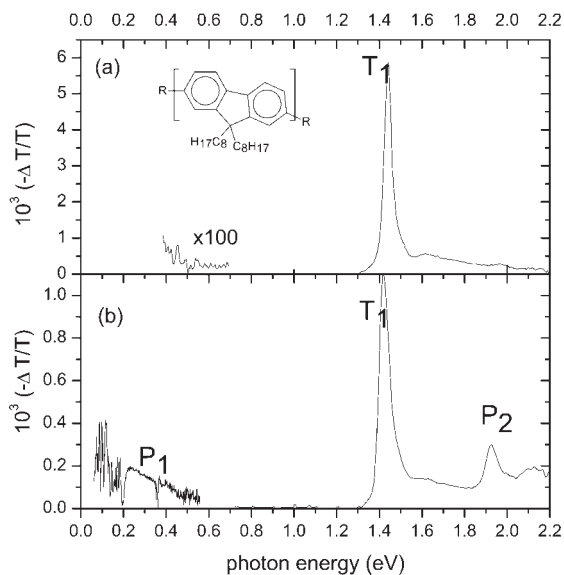
Figure 5.34a shows the absorption and PL spectra of a PFO film spin cast from toluene solution. The absorption begins at 2.8 eV and reaches a peak at 3.23 eV. The lowest energy absorption band is 0.5 eV wide with no apparent vibronic structure. The PL spectrum exhibits a clear vibronic structure with peaks at 2.84, 2.68 and 2.52 eV. Another band at higher energies is visible although it is suppressed because it overlaps with the absorption spectrum. Both absorption and emission spectra can roughly be modeled as an electronic 0–0 transition at 3.1 and 3.0 eV, respectively, together with vibronic progressions. The width (standard deviation) of the individual progressions is 0.05 and 0.1 eV for emission and absorption, respectively.

Figure 5.34b, dotted line, shows the absorption and PL spectra of a PFO film following exposure to toluene vapor for several hours. A new absorption band at 2.88 eV with some vibronic structure is superimposed upon the original absorption spectrum and the PL spectrum has also red shifted and developed a more pronounced vibronic structure. The fine structure becomes even more pronounced at 10 K: three clear peaks are observed in the absorption spectrum, namely at 2.85, 3.08 and 3.24 eV. Note that this progression does not correspond to a single phonon frequency. The PL spectrum at 10 K shows a triplet substructure in each of the vibronic progressions observed at 300 K. The described spectroscopic observations suggest the following conclusions about the nature of the  $\beta$ -phase in PFO: Interchain dipole–dipole interaction effects cannot account for changes in the absorption and PL spectra of PFO upon  $\beta$ -phase formation. If the absorption peak at 2.85 eV were due to Davydov splitting of the main absorption band, there should be a corresponding blue-shifted absorption peak and reduced fluorescence yield [132]. J-aggregate formation causes significant narrowing of the absorption and emission spectra, whereas only a slight narrowing is observed in the PL. Interchain aggregation can lead to excimer emission [133, 134], which is characterized by a reduction of the PL quantum yield and a structureless PL that

is red shifted by 0.5 eV or more with respect to the fluorescence [135]. The spectroscopic evidence therefore supports the conjecture that the  $\beta$ -phase is an intrachain state with extended conjugation. However, the observed red shift of absorption is even greater than what can be accounted for by extrapolation of a series of oligofluorenes to infinite CL [131]. This could be explained assuming that neighboring fluorine units in the  $\beta$ -phase chains assume a more planar conformation than that in glassy samples or solutions, and/or that part of the red shift in the spectra is caused by a delocalization of the  $\pi$ -wavefunctions over neighboring chains as a result of increased interchain order. Similar conclusions were reached in regard to the polaron wavefunction in PFO in E4. Quenching experiments by Winokur et al. [128] showed that formation of the  $\beta$ -phase corresponds first and foremost to intrachain relaxation. However, once the PFO chains have adopted this more planar conformation, then interchain ordering and crystallization can take place.

#### 5.4.3.2 Photoexcitation Dynamics in PFO

Figure 5.35 shows the PA spectrum of (a) the as-spun sample and (b) the  $\beta$ -phase containing sample obtained by thermal cycling of the as-spun film. The PA spectrum of the as-spun sample is dominated by an unusually sharp (standard deviation = 20 meV) and strong transition at 1.44 eV with a weak sideband at 1.62 eV. There was no evidence for photoinduced infrared-active vibrations that accompany charged excitations [136–138]. We accordingly assign the PA band at 1.44 eV to excited state absorption of triplet excitons. To the best of our knowledge, this tran-



**Figure 5.35** (a) PA spectrum of an as-spun PFO film. (b) PA spectrum of a thermally cycled PFO film. The PFO was obtained from Dow Chemical.

sition is the sharpest triplet excited-state absorption feature ever observed for a conjugated polymer. A sharp transition accompanied by a relatively weak and broad vibronic sideband is characteristic of an optical transition where there is little geometric relaxation between the two states (small Huang–Rhys factor). Such a narrow linewidth also requires there to be very little inhomogeneous broadening of the transition, indicative of a material with low energetic disorder. The PA below 1.4 eV is fairly weak.

The PA spectrum of the thermally cycled sample is shown in Fig. 35b. The triplet PA band is about five times weaker than in the glassy sample. The red shift of the  $T_1$  band upon  $\beta$ -phase formation is very minor compared with that observed in absorption and PL. Two new PA bands appear at 1.93 and below 0.5 eV. These PA bands have the same dependence on pump power and modulation frequency and are accompanied by a series of sharp infrared-active vibrations (that appear as anti-resonances, i.e. negative dips rather than peaks) below 0.2 eV. The PA spectrum below 0.5 eV was measured using a Fourier transform infrared (FTIR) spectrometer. All of these results are characteristic of polarons, charged excitations with spin- $1/2$ . The assignment was confirmed by PADMR measurements [139]. We accordingly assign these PA bands to the  $P_1$  and  $P_2$  transitions of polarons. The vibronic progression of the  $P_2$  band is consistent with a Huang–Rhys factor of 0.65 and a phonon energy of 0.19 eV, which is therefore different than that of the PL emission. Comparison of the PA below 0.5 eV of the two samples shows that the polaron yield is  $\sim 10$ – $15$  times stronger in the thermally cycled sample than in the as-spun sample. We conjecture that the polaron photogeneration is more efficient at the boundaries between as-spun and  $\beta$ -phase PFO, related to the red shift of the optical gap in  $\beta$ -phase PFO.

#### 5.4.4

#### Measuring the Conjugation Length Using Photoinduced Absorption Spectroscopy

Finally, we want to outline another application of PA spectroscopy. We have previously shown that the polaron PA spectrum – in particular the low energy band – can be employed for accurately estimating the CL in  $\pi$ -conjugated polymer films [140]. Although the molecular weight of polymers is typically much larger than that of oligomers, nevertheless it is established that the polymer should be viewed as a string of effectively independent segments, separated by chemical or physical defects. The length of these segments is called the conjugation length (CL). The CL can be much shorter than the physical polymer chain length.

Our spectroscopic technique is illustrated in Fig. 5.36, which shows the peak photon energies of the  $P_1$  transition in a large variety of oligomers versus the oligomer length,  $L$ .

It is seen that the  $P_1$  transition in each of the oligomer classes red shifts as  $L$  increases; specifically  $P_1 = P_{1,\infty} + \text{constant}/L$ . This scaling relation is ubiquitous in oligomers: the optical gap (i.e. the singlet exciton energy) [141], triplet exciton energy [142] and also the  $P_2$  transition each obey such a scaling relationship. The striking observation in Fig. 5.36 is that the  $P_1$  data for most oligomers all fall on a

“universal” line. This observation is fully appreciated when compared with similar plots for the optical gap, where large differences between the various oligomer classes exist (e.g. 4 eV for 5P, but 3 eV for 5T). However, the data for the alkoxy-substituted OPV apparently do not follow the “universal” scaling law. This observation can be explained by the localization of the positive charge caused by alkoxy substitution. To the best of our knowledge, the reason for the universal behavior of  $P_1$  in a large class of materials is currently not theoretically understood. We anticipate that a theoretical understanding of this “universal” behavior may result in much additional insight into the physics of conjugated oligomers and polymers.

The observations in Fig. 5.36, together with the identification that the CL of a polymer is the length of the “equivalent” oligomer, clearly suggest that  $P_1$  can be used as a *universal and sensitive* measure of the CL of polymer films (caution is necessary when dealing with alkoxy-substituted polymers). Specifically, we may use the following method for obtaining the effective CL of polymer films: we measure  $P_1$ , say by using the PA technique, then invert the universal relation  $P_1(\text{CL})$ .

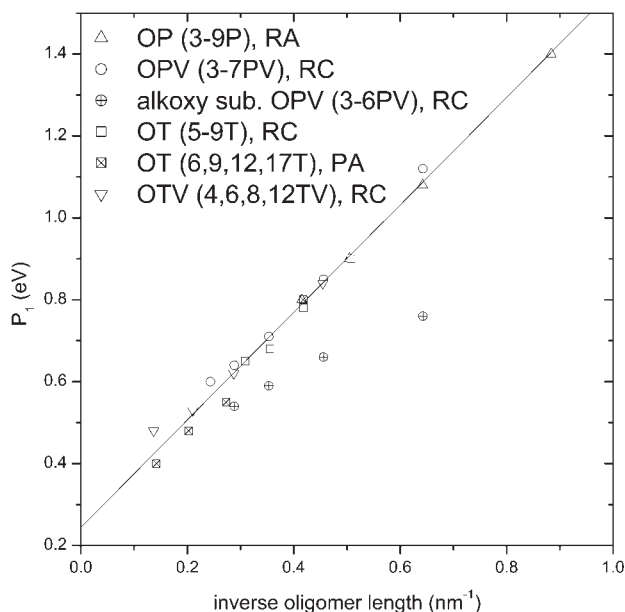


**Figure 5.36** The peak photon energies of the  $P_1$  polaron transition in a variety of oligomers, namely solutions of (unsubstituted) oligophenyls [OP, radical anion (RA)], alkyl-substituted (AS) oligophenylenevinylens [OPV, radical cation (RC)], alkoxy-substituted

OPV (RC), end-capped oligothiophenes (OT, RC), films of AS OT (PA), AS oligothiophenevinylens (OTV, RC). The solid line is a fit to the data excluding the data for the alkoxy-substituted OPV.

## 5.5

### ODMR Spectroscopy: Measurement of Spin-Dependent Polaron Recombination Rates

In this section we discuss the ODMR technique we used to measure the ratio  $r \equiv k_S/k_T = \sigma_S/\sigma_T$  in a large variety of  $\pi$ -conjugated polymer and oligomer thin films.  $k_S$  is the rate of formation of singlet excitons from polaron recombination and  $k_T$  is the respective triplet exciton formation rate (see Section 5.3.3). The goal of our experiments is to determine whether  $r > 1$ , as has been suggested by recent measurements of  $\eta_{\max}$  in OLEDs, and to determine the material dependence of  $r$ . Once the material dependence of  $r$  is understood, this aids *a priori* selection of a  $\pi$ -conjugated material as the active layer for highly efficient OLEDs. In addition, we anticipate that our study will provide valuable insight into the physics of polaron recombination and exciton formation.

#### 5.5.1

##### Spin-Dependent Exciton Formation Probed by PADMR Spectroscopy

Our technique uses both PA (Section 5.2.1) and PADMR spectroscopy (Section 5.2.2). We therefore studied the spin-dependent recombination of *photogenerated* polarons in thin films rather than polarons injected into OLED devices. The latter experiment would be more desirable since it studies exciton formation under conditions identical with OLED operation. We note that in principle it is possible to use our technique directly in OLED devices, but it has been shown that in such measurements electrode interface effects [59] and spin randomization make a quantitative interpretation very involved at best. Measurements on films are also less time consuming, easier and more general (also non-luminescent materials can be studied) and this allowed us to study a large number of materials and examine the materials dependence of  $r$ .

We start with a brief discussion of two example PA spectra: Figures 5.37a and 5.38a show typical PA spectra in oligomer and polymer films, respectively. Figure 5.37a was measured in a thin film of a soluble oligothiophene [143] (12T, see Fig. 5.37a, inset); the spectrum in Fig. 5.38a is for methylated ladder-type poly(*p*-phenylene) [144] (mLPPP, see Fig. 5.38a, inset). In both spectra the characteristic two bands due to polarons ( $P_1$  and  $P_2$ ) are assigned, whereas the triplet exciton absorption is a single band ( $T_1$ ).

The effect of spin-dependent polaron recombination (exciton formation) on the PA bands in the photomodulation spectrum can be studied by the spin- $1/2$  PADMR technique. In this technique we measure the changes,  $\delta T$ , that are induced in  $\Delta T$  by spin- $1/2$  magnetic resonance.  $\delta T$  is proportional to  $\delta n$  that is induced in the photoexcitation density,  $n$ , due to changes in the spin-dependent polaron recombination rates. In PA and PADMR spectroscopy, charge-transfer (CT) or recombination reactions occur between neighboring  $P^+$  and  $P^-$ ; the product of CT reactions are neutral excitons, either spin-singlet or -triplet. The CT reaction rate  $R_p$  between spin parallel pairs ( $\uparrow\uparrow$ ,  $\downarrow\downarrow$ ) is therefore proportional to  $2k_T$ ,

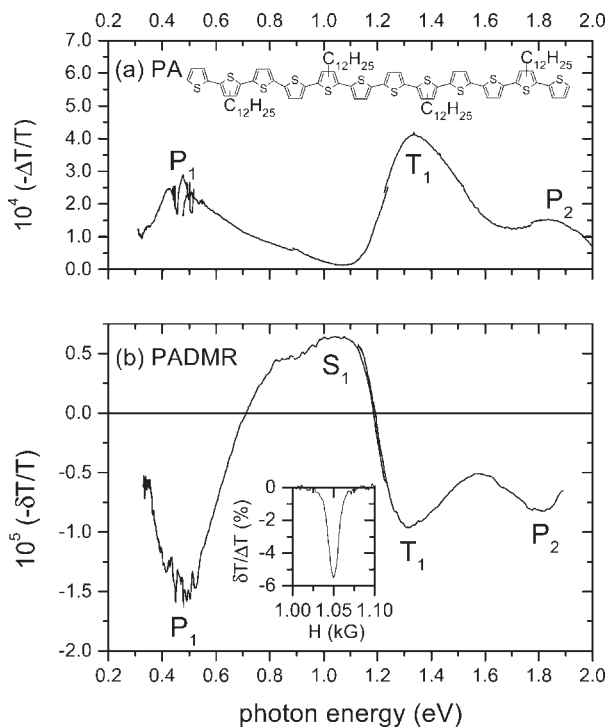


**Figure 5.37** (a) The PA spectrum of 12T (inset); (b) the PADMR spectrum at magnetic field  $H = 1.05$  kG corresponding to  $S = 1/2$  resonance [see inset in (b)]. Both spectra (a) and (b) show two bands ( $P_1$  and  $P_2$ ) due

to polarons,  $T_1$  is due to triplet absorption.  $S_1$  is assigned to singlets. The PA was measured at 80 K, with excitation by 488-nm radiation from an Ar<sup>+</sup> laser (500 mW); the PADMR spectrum was measured at 10 K.

whereas the CT reaction rate  $R_{AP}$  between spin antiparallel pairs ( $\uparrow\downarrow, \downarrow\uparrow$ ) is proportional to  $(k_S + k_T)$ , where the proportionality constant is the same in both cases [84]. These relations are obtained as follows (see Fig. 5.17): antiparallel pairs may form either the  $\uparrow\downarrow - \downarrow\uparrow$  (total spin singlet state) or  $\uparrow\downarrow + \downarrow\uparrow$  combination (total triplet), whereas parallel pairs form only total triplet pairs ( $\uparrow\uparrow$  or  $\downarrow\downarrow$ ) (The spins of the two polarons are assumed independent for the following reason:  $\mu$ -wave-induced spin flips from parallel spin to antiparallel spin alignment are only energetically possible in the case of negligible exchange interaction.)

This general picture of PADMR can be quantitatively formulated as follows. Consider parallel and antiparallel pairs with respective generation rates  $G_P$  and  $G_{AP}$  and recombination rates  $R_P$  and  $R_{AP}$ . Using simple rate equations we have previously shown [56] that the PADMR signal is then given as (see also Section 5.5.3)

$$\frac{\delta n}{n} = \frac{R_{AP} - R_P}{R_{AP} + R_P} \quad \text{for geminate polaron pairs} \quad (5.53)$$

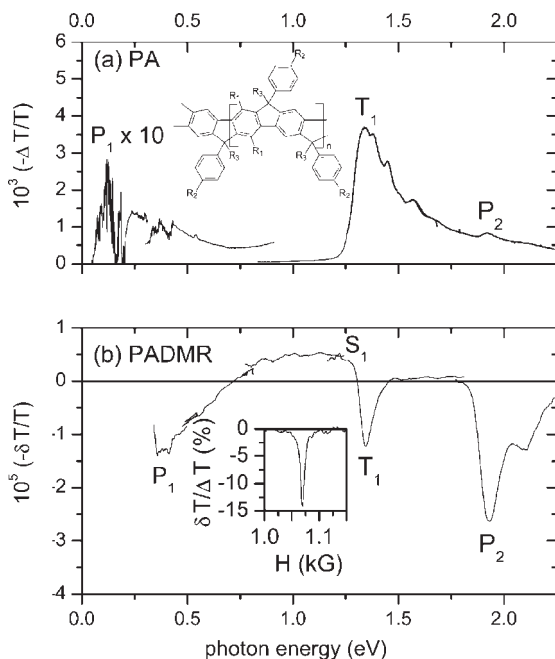


**Figure 5.38** (a) The PA spectrum of mLPPP (inset); (b) the PADMR spectrum at magnetic field  $H = 1.06$  kG corresponding to  $S = 1/2$  resonance [see inset in (b)]. Both spectra (a) and (b) show two bands ( $P_1$  and  $P_2$ ) due

to polarons,  $T_1$  is due to triplet absorption.  $S_1$  is assigned to singlets. The PA was measured at 80 K, with excitation by 457-nm radiation from an  $Ar^+$  laser (300 mW); the PADMR spectrum was measured at 10 K.

$$\frac{\delta n}{n} = - \left( \frac{R_{AP} - R_P}{R_{AP} + R_P} \right)^2 \quad \text{for non-geminate polaron pairs} \quad (5.54)$$

In the case of a geminate pair, the photoexcited negative and positive particles are correlated following photon absorption, hence their spins are in antiparallel configuration (i.e.  $G_P = 0$ ). The reason for that is that the ground state is a spin singlet and the photon absorption process conserves spin. In the case of non-geminate pairs, the individual spins are uncorrelated; spin-parallel and spin-antiparallel pairs are produced with equal probability, therefore  $G_P = G_{AP}$ . As we will show below, polaron recombination in cw PA and PADMR spectroscopy is non-geminate (see also Refs. [111, 145, 146] and Section 5.5.1). Our hypothesis is that  $k_S > k_T$  in  $\pi$ -conjugated compounds and therefore  $R_{AP} > R_P$  and spin-parallel pairs prevail at steady-state conditions. Under *saturated* magnetic resonance conditions (the PADMR signals increase as the power of the  $\mu$ -wave source is increased, but saturate at the highest power levels; experimental data reported here are for this saturation regime), the polaron pair densities with parallel and antiparallel spins become equal. (Correctly speaking,  $\mu$ -wave absorption and stimulated emission lead to frequent spin-flips and thereby to rapid interconversion of parallel and

antiparallel pairs. Therefore, the classification into parallel and antiparallel pairs becomes meaningless under resonance. Saturation conditions therefore refer to the situation that a large number of spin-flips occur during the pair lifetime.) It then follows that the PADMR measurements detect a reduction,  $\delta n$  (which is proportional to  $\delta T$ ) in the polaron pair density  $n$  (which is proportional to  $\Delta T$ ), since slowly recombining parallel pairs are converted to more efficiently recombining antiparallel pairs. At the same time, the density of triplet excitons also decreases as a result of the decrease in the density of parallel polaron pairs, whereas the singlet exciton density increases as a result of the increase in the density of antiparallel polaron pairs. The last statement is very directly related to  $k_S > k_T$ .

There is another, equivalent, way of understanding the ODMR experiment: ODMR techniques are modulation experiments where the resonant  $\mu$ -wave field is periodically turned on and off. Since the experiment is performed at low temperature, spin alignment is conserved during the half-wave with  $\mu$ -wave field off and polaron recombination/exciton formation obeys spin statistics. However, during the half-wave with  $\mu$ -wave field on, spin- $1/2$  resonance leads to rapid spin-flips of the recombining polarons. Spin alignment is therefore not conserved and each pair may choose whether to form singlet or triplet exciton. It can easily be shown [84, 86] that this leads to enhanced formation of the exciton with larger formation rate (leading to a positive ODMR signal), at the expense of the more slowly forming exciton (that gives a negative ODMR). In addition, the overall polaron recombination rate is enhanced, since the fast channel becomes allowed for all polaron pairs. *In summary,  $k_S > k_T$  implies the observation of a resonant reduction in polarons and triplet excitons and an increase in singlet exciton density.*

The spin- $1/2$  PADMR spectra (Figs. 5.37b and 5.38b) clearly show the negative magnetic resonance response at  $P_1$ ,  $P_2$  and  $T_1$ , which are due to a reduction in the polaron and triplet densities, in agreement with our expectations. The PADMR spectra therefore provide strong evidenced that  $r > 1$  in these  $\pi$ -conjugated compounds. We also tentatively assign the positive PA band in the  $\lambda$ -PADMR spectra ( $S_1$ ) to excess (trapped) singlet exciton absorption expected from the above discussion (see also Ref. [139]).

### 5.5.2

#### Spin-Dependent Exciton Formation Probed by PLDMR Spectroscopy

In the previous section, we showed that the triplet exciton density is reduced upon resonance and explained this as a consequence of  $k_S > k_T$ . However, in order to complete our argument, we still have to demonstrate that the singlet population is enhanced upon resonance. We can show this by observing the resonantly enhanced fluorescence emission that is a result of the increase in singlet exciton population. Therefore, PLDMR studies were performed [111] on films of two representative  $\pi$ -conjugated polymers, namely PPV and regio-random poly(3-hexylthiophene) (RRa-P3HT). Films of these polymers show, at the same time, relatively high intensities for both the PA spectrum and PL emission. In many other materials, since PA and PL are competing processes, either the PA or PL intensi-

ties are weak. A positive PLDMR spin- $1/2$  resonance that is a mirror-image of the PADMR resonance is observed in all the films we have studied.

We have been able to advance the notion that the enhanced PL is a result of spin-dependent polaron recombination [111]. (We note that alternative mechanisms other than spin-dependent exciton formation have been employed for explaining the positive PLDMR resonance. In particular, a model of exciton quenching by polarons, developed in detail by List et. al. [57], can explain many of the results of PLDMR spectroscopy.) This can be shown by a comparison between the polaron recombination kinetics and the PLDMR signal kinetics. To this end, the dependences of the polaron PA and PLDMR signals on the laser intensity were studied [111]. Figure 5.39 shows the experimentally determined dependences of PL,  $\delta$ PL and polaron PA band  $P_1$  (where  $-\Delta T/T \propto N$ ) on the laser intensity,  $\Phi$ , in a PPV film. We first discuss the polaron kinetics. Figure 5.39 shows that the polaron PA signal scales as  $\Phi^{1/2}$  at large  $\Phi$ , which shows that polaron recombination follows a rate equation law with bimolecular recombination kinetics (see Section 5.3). We note that we found that the polaron PA signal scales as  $\Phi^{1/2}$  at large  $\Phi$  in all the films we studied. (We note that the observed bimolecular kinetics for polaron recombination naturally implies *non-geminate* spin pairing. However, conventionally bimolecular recombination is viewed as a process where each polaron has a choice of several recombination partners and thereby the recombination rate increases with polaron density. This view then apparently contradicts the concept of pairing, where each polaron remains faithful to one part-

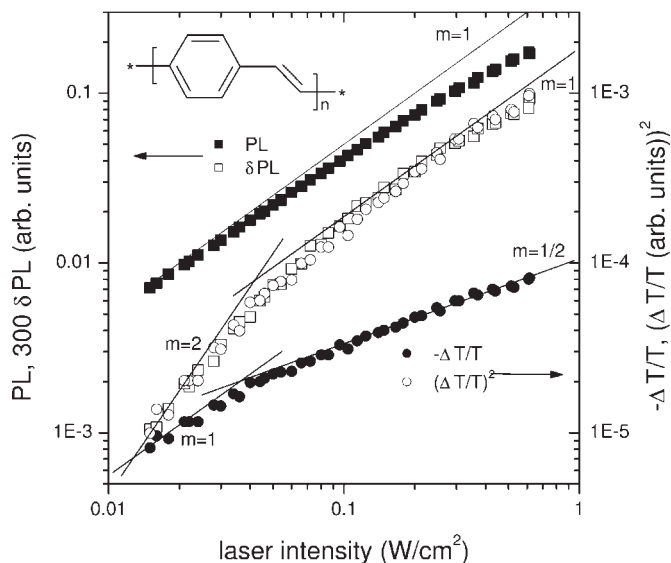


**Figure 5.39** The laser intensity dependences of the photoluminescence (PL, solid squares), the magnetic resonance effect on the photoluminescence ( $\delta$ PL, open squares),

the polaron PA band measured at 0.55 eV ( $-\Delta T/T$ , solid circle) and its square (open circles, rescaled) in a PPV film measured at 10 K. The modulation frequency was 1 kHz.

ner, that appears necessary for the observation of ODMR from polarons. We currently do not have an explanation for this apparent contradiction.)

In order to identify the mechanism responsible for the PLDMR signal, we explored the relation between  $N$  and  $\delta\text{PL}$ . Importantly in Fig. 5.39, we see that  $(\Delta T/T)^2$  coincides with high accuracy with the laser intensity dependence of  $\delta\text{PL}$ , i.e.  $\delta\text{PL} \propto N^2$ . We have thus shown that  $\delta\text{PL}$  is proportional to the recombination term in the polaron rate equation (see Section 5.3) and this relationship between  $\delta\text{PL}$  and  $N^2$  directly implies that  $\delta\text{PL}$  is a result of a magnetic resonance effect on the bimolecular and thus *non-geminate* polaron recombination. The positive sign of the H-PLDMR then shows that the singlet exciton density is enhanced upon magnetic resonance.

### 5.5.3

#### Quantitative Modeling of Spin-Dependent Recombination Spectroscopy

In the previous sections, we have shown that the PADMR and PLDMR results are in agreement with the qualitative expectations from a spin-dependent exciton formation model. Moreover, a *quantitative* rate equation model has been developed [139] that allows the determination of the value of  $r$  from the PADMR and PA spectra. The model is based on rate equations that describe the polaron dynamics. Since polaron recombination and exciton formation are spin dependent, two types of rate equations are needed: One describes the spin-dependent “free” dynamics during the half-cycle of modulation when the microwave field is turned off, the other the dynamics under the boundary condition introduced by spin- $1/2$  magnetic resonance, i.e. that the pair densities of polarons recombining with parallel and antiparallel spins are equal. For simplicity these equations are written for steady-state conditions,  $dn(t)/dt = 0$ , i.e. the photoexcitation density is constant in time and given by the equilibrium reached between photogeneration and spin-dependent recombination.

The general structure of the rate equations is as follows: the l.h.s. is the change of the photoexcitation density with time (here set to zero because of steady-state conditions), the first term on the r.h.s. is the generation term as a result of laser photon absorption ( $\Phi$  is the absorbed laser photon flux) and the last term of the r.h.s. is the recombination term. [In the previous section we established that under the present experimental conditions polarons form non-geminate recombination-pairs with their nearest neighbors and that the overall polaron recombination rate is proportional to the total polaron density. Importantly, our ODMR data imply that the recombination partners remain correlated with each other during most of their lifetime: if the polarons changed their recombination partner the spin polarization would be destroyed, since, on average, half of their new partners have parallel spin and half have antiparallel spin. Since after their formation the recombination kinetics of polaron pairs is not influenced by other polarons, we therefore describe them using monomolecular kinetics, albeit with an overall recombination rate proportional to the total polaron density. Since the *total* polaron population changes little ( $\delta N/N$  is typically 10%), we drop the explicit den-

sity dependence in the rate equations below. We note that the nature of the lifetime-long correlation of the non-geminately formed recombination pairs is at present not well understood.]

$$0 = \frac{\eta}{2} \Phi - R_p N_p \quad (5.55)$$

$$0 = \frac{\eta}{2} \Phi - R_{AP} N_{AP} \quad (5.56)$$

$$0 = \eta \Phi - \frac{R_{AP} + R_p}{2} \tilde{N} \quad (5.57)$$

Equations (5.55) and (5.56) describe the spin-dependent, non-geminate polaron pair dynamics and Eq. 7 describes the dynamics under saturated resonance condition during the half-cycle of modulation when the microwave field is turned on.  $\eta$  is the photogeneration quantum efficiency for the polaron pairs. In Eqs. (5.55) and (5.56),  $N_p$  and  $N_{AP}$  are the densities of parallel and antiparallel pairs, respectively, and  $R_p$  and  $R_{AP}$  are their respective recombination rates. In Eq. (5.57),  $\tilde{N}$  is the total population under saturated spin- $1/2$  resonance conditions. We adopt the notation that densities under resonance conditions will be marked with a tilde ( $\tilde{\phantom{x}}$ ). The solutions to the above rate equations are given in form of a fractional change in population density upon spin- $1/2$  resonance:

$$\left. \frac{\delta N}{N} = \frac{\delta T}{\Delta T} \right|_{PI} = - \left( \frac{r-1}{r+3} \right)^2 \quad (5.58)$$

In Eq. (5.58), the relations  $R_{AP} \propto k_S + k_T$  and  $R_p \propto 2k_T$  were used. Most importantly, Eq. (5.58) allows the determination of  $r$  from the experimentally obtained ratio  $\delta T/\Delta T$  of polarons; explicitly:

$$r \equiv \frac{k_S}{k_T} = \frac{1 + 3\sqrt{\left| \frac{\delta T}{\Delta T} \right|}}{1 - \sqrt{\left| \frac{\delta T}{\Delta T} \right|}} \quad (5.59)$$

Quantitative PA and PADMR experiments have been performed in a large number of materials [84, 86] with the goal of studying the material dependence of  $r$ . The results of this study are now presented.

#### 5.5.4

##### Material Dependence of Spin-Dependent Exciton Formation Rates

Understanding the material dependence of  $r$  is of great importance, since in principle it allows *a priori* selection of materials capable of high EL quantum efficiencies. We performed quantitative PADMR studies in a large number of  $\pi$ -conjugated polymers and oligomers and applied Eq. (5.59) to calculate  $r$  from the experimentally determined  $\delta T/\Delta T$ .

In Fig. 5.40 we show  $r$  measured in a large variety of  $\pi$ -conjugated materials versus  $P_1$ . Since  $P_1$  is a linear function of  $1/CL$  (see Fig. 5.36), we may actually plot  $r$  versus  $1/CL$ , as is also shown in Fig. 5.40 (upper axis) [specifically, we used the following method for obtaining the CL of the polymer films: we measured  $P_1$  by using the PA technique, then inverted the universal relation  $P_1(CL)$ , obtained as the solid line fit shown in Fig. 5.36]. We obtain the important result that  $r$  is determined mostly by the conjugation length. In particular,  $r$  increases with CL and  $r \approx 1$  for short oligomers and monomers.

We note that negative values for  $1/CL$  are encountered for several polymers that have the lowest  $P_1$  transitions. (In the present scheme these polymers would therefore be assigned a conjugation-length “larger than infinity”. We have shown [140] that the exceptionally low photon energy for the  $P_1$  band results from a delocalization of polarons not only along the conjugated polymer backbone, but also along neighboring chains in the perpendicular directions.)

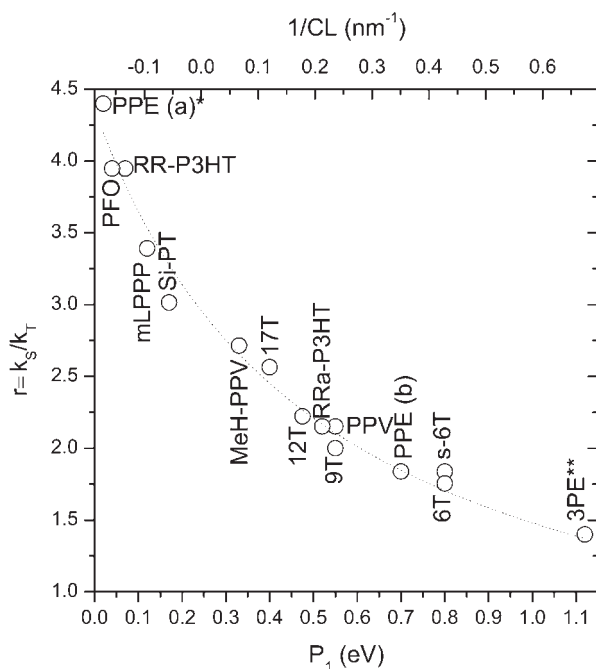


**Figure 5.40** The ratio  $r = k_s/k_T$  of spin-dependent exciton formation cross-sections in various polymers and oligomers as a function of the peak photon energy of the  $P_1$  transition (lower x-axis).  $r$  is also shown as a function of the inverse conjugation length  $1/CL$  (upper x-axis), which was determined from  $P_1$  (see text for discussion). The line through the data points is a linear fit. \*The  $P_1$  band of

this polymer does not show a clear peak in the PA spectrum; the  $P_1$  band extends to the longest wavelengths measured. \*\*The length of this oligomer was calculated. In addition to the chemical names defined in the text, 3PE stands for the PPE trimer, PPE for poly(phenylene-ethynylene) and Si-PT for silicon-bridged polythiophene. For details, see original publications.

The data in Fig. 5.40 clearly suggest that  $r$  is apparently independent of the detailed chain backbone structure or film morphology. A generally accepted theoretical explanation for the (approximately) universal dependence of  $r$  on the CL has not yet emerged. Several recent theories that model spin-dependent exciton formation suggest reasons for the CL dependence, including:

1. The lowest singlet exciton lies higher in energy than the lowest triplet exciton. The singlet and triplet energies depend on the CL. A model of vibrational energy relaxation then predicts that  $r$  increases with increasing CL [147]. Models based on inter-chain electron transfer arrive at similar conclusions [148, 149].
2. Selection rules exist that couple the charge separated state only to the lowest singlet and triplet exciton state [148, 150]. According to a simplified formalism suggested by Tandon et al. [148], the exciton formation rate can be obtained from the Schrödinger equation that describes the direct transition from the state of separated polarons to the low-lying exciton states. The spin-dependent yield therefore decreases with increasing energy difference between polaron pair and low-lying exciton states. Such models predict that  $r$  increases with increasing CL.
3. The energy release that is required by the above-mentioned selection rules implies that exciton formation is a multi-phonon emission process. Multi-phonon emission probabilities are given in terms of the (polaron) Huang–Rhys factor [150]. Since the polaron Huang–Rhys factor measures the polaron's relaxation energy which is closely related to  $P_1$ , then such theories predict that  $r$  decreases with increasing Huang–Rhys factor and therefore  $P_1$  [151].

## 5.5

### The Relation Between Spin-Dependent Exciton Formation Rates and the Singlet Exciton Yield in OLEDs

In summary, our ODMR studies reveal that singlet excitons form at a larger rate than triplet excitons and that the ratio  $r$  of the rates increases with the CL. This result is important for OLED applications, since  $r$  may be directly related to  $\eta_{\max}$  in OLEDs. However, the experimental conditions of the ODMR experiments are different in several respects from those found during exciton formation in OLEDs. Whereas OLEDs are normally operated at room temperature, our ODMR experiments are performed at temperatures below 80 K, typically at 10 K. In addition, the large electric fields that are applied to OLEDs are absent in ODMR and exciton formation in OLEDs may occur near polymer/electrode or organic heterojunction interfaces. The relation between spin-dependent exciton formation rates and the singlet exciton yield in OLEDs therefore has to be studied experimentally.

First steps in this direction have been taken: Wilson et al. [85] found that the singlet-to-triplet exciton ratio in OLEDs made from a Pt-containing polymer is larger than that in OLEDs made from the corresponding monomer. This result is qualitatively consistent with our findings using ODMR. In order to substantiate this connection, we performed [152] a quantitative comparison of ODMR and the technique of Wilson et al. [85]. We measured the spin- $1/2$  ODMR response of a  $\pi$ -conjugated polymer sample and its corresponding monomer [both closely related to the materials used by Wilson et al. It would be desirable to perform the ODMR measurements on the Pt-containing compounds that were used by Wilson et al. However, the heavy Pt atom induces strong spin-orbit coupling that actually leads to spin randomization even during the half-wave of modulation where the  $\mu$ -wave field is turned off. We therefore chose to perform our ODMR measurements on materials with a very similar structure except the Pt-containing group] and found that the ODMR response of the polymer sample was roughly 30 times stronger than that of the monomer. This shows that whereas exciton formation is spin dependent in the polymer, it is approximately spin independent in the monomer. Based on ODMR, we predict a singlet exciton yield of  $\sim 60$  and  $\sim 30\%$  in the polymer- and monomer-based OLEDs, respectively. These predictions are very close to the values measured by Wilson et al. [85] in working OLEDs, namely 57 and 22% for the polymer and monomer, respectively. We consider the very good agreement obtained between two different, independent experimental approaches to be an indication that  $r$  values measured by ODMR can be used for predicting singlet yields in OLEDs. However, such comparisons will have to be completed for a larger number of materials to strengthen this claim.

## 5.6

### Conclusion

Perhaps the best way to detect and characterize long-lived photoexcitations in the class of  $\pi$ -conjugated polymers is to study their optical absorption. The main experimental technique we employed is cw photomodulation (PM).

In Section 5.3 we modeled recombination and generation processes using rate equations that treat both mono- and bimolecular recombination mechanisms (MR and BR, respectively). We (approximately) solved these rate equations to obtain PM dependences on the modulation frequency,  $\omega$ , and excitation intensity,  $I_L$ , taking into account also moderate saturation due to trap filling. Our analysis of the rate equation led us to introduce the concept of generalized coordinates that allows reduction of the various recombination kinetics to a single “universal” plot. Focusing first on the dependence of the PA on the pump intensity ( $I_L$  or  $\gamma$ ), we can draw the following conclusions from our analysis:

- MR: PA is linear in  $\gamma$  over the entire dynamic range.
- MR or BR with saturation near the steady state: PA is sublinear, approaching a fixed value at high  $I_L$  values.

- *BR near steady state*: PA is sublinear: in-phase component  $PA_I \propto I_L^{1/2}$ , whereas quadrature component  $PA_Q$  approaches  $I_L$  independence at high  $I_L$ .
- *BR away from the steady state*: In-phase component is superlinear,  $PA_I \propto I_L^{3/2}$ , whereas the quadrature component is linear,  $PA_Q \propto I_L^1$ , and is independent of the bimolecular recombination rate  $\beta$ .

We found that in a dispersive process, the response,  $N(\omega)$ , of the system to a modulated excitation depends non-trivially on a fractional power of the (modulation) frequency,  $\omega$ . We found that: (a) the  $Q$  component shows a maximum at  $\omega_{\max} \approx \tau_0^{-1}$ , where  $\tau_0$  is an “average” lifetime; (b) at  $\omega \gg \omega_{\max}$ , both the  $Q$  and  $I$  components decrease *sublinearly* with  $\omega$ :  $PA_{I,Q} \propto \omega^{-\beta}$ , where  $\beta_Q \approx \beta_I \approx a$ . With regard to the modulation frequency dependence of the PA signal in the case of dispersive recombination, we found that:

- The broader the distribution is, the broader is the “transition” region from the “low frequency” (or “near steady state”) to the “high frequency” (or “away from steady state”).
- For a finite width distribution, the “normal” frequency dependence should be observed outside the transition region, i.e. for either  $\omega \gg \tau_{\min}^{-1}$  or  $\omega \ll \tau_{\max}^{-1}$  where  $\tau_{\min, \max}^{-1}$  are the low and high cutoffs of the distribution.

In Section 5.4 we reported on an extensive experimental study of absorption, photoluminescence, PA spectra and dynamics in a variety of  $\pi$ -conjugated polymer films ranging from the red-emitting polythiophenes (RRa-P3HT and RR-P3HT) to the blue-emitting polyfluorenes (PFO).

The spectroscopic properties of the ordered RR-P3HT films differ characteristically from those of the disordered RRa-P3HT films. Studying the absorption and PL spectra of RRa-P3HT and RR-P3HT films at room temperature, we found a red shift of the RR-P3HT absorption and PL bands with respect to those in RRa-P3HT, which is caused by the superior order in the lamellae structures. In spite of the superior order, we measured in RR-P3HT an order of magnitude *decrease* in the PL quantum efficiency. The PL quantum efficiency decrease in RR-P3HT cannot be explained by an increase in the non-radiative decay rate and we conjecture, therefore, that the PL decrease in RR-P3HT is due to a weaker *radiative* transition of the lowest lying excitons in this film.

The cw PA spectrum of RR-P3HT films is much richer than that of RRa-P3HT. It contains two PA bands,  $DP_1$  at 0.1 eV and  $DP_2$  at 1.8 eV, that are due to 2D delocalized polarons in the lamellae, in addition to PA bands  $P_1$  at 0.35 eV and  $P_2$  at 1.25 eV, that are due to localized intrachain polarons in the disordered portions of the film. We find that  $DP_1$  blue shifts as the length  $n$  of the alkyl side-chains increases, indicating that larger polaron relaxation occurs in lamellae formed with P3AT with a larger side-group. We therefore conjecture that very long side-groups destroy lamellae formation.

We find that whereas in the less-ordered film the photoinduced IRAVs appear as positive absorption lines, they appear as dips or anti-resonances (AR) superimposed on the DP<sub>1</sub> PA band in the ordered film. These AR dips are apparently caused by the overlap between the IRAV lines and the DP<sub>1</sub> band. Moreover, the AR spectrum contains much sharper dips and consequently is much richer than the positive photoinduced IRAV spectrum.

PFO has been found to exhibit a complex morphological behavior. Spin coating a PFO film from solution produces a glassy sample. A different phase that has been called the  $\beta$ -phase has been detected upon either thermal cycling or exposure to solvent vapor. The rich phase morphology of PFO provides a unique opportunity to study the influence of film morphology on the photophysics of conjugated polymers without the need for chemical modification. The spectroscopic properties of the glassy and  $\beta$ -phase PFO differ characteristically from one another. We found that the  $\pi$ - $\pi^*$  absorption transition of the glassy phase is featureless. Remarkably, the  $\beta$ -phase sample shows well-resolved features in the absorption spectrum. This is indicative of reduced disorder in the sample. In addition, the  $\pi$ - $\pi^*$  transition in the  $\beta$ -phase is red shifted compared with that in the glassy phase. We showed that the spectroscopic evidence supports the conjecture that the  $\beta$ -phase has extended conjugation. However, the observed red shift of absorption is even greater than what can be accounted for by extrapolation of a series of oligofluorenes to infinite CL. This could be explained by assuming that neighboring fluorine units in the  $\beta$ -phase chains assume a more planar conformation than that in glassy samples or solutions, and/or that part of the red shift in the spectra is caused by a delocalization of the  $\pi$ -wavefunctions over neighboring chains as a result of increased interchain order. The polaron PA band in PFO showed similar characteristics to the DP<sub>1</sub> band in RR-P3HT, namely very low relaxation energy and IRAVs that appear as anti-resonances. We conjecture that the formation of the  $\beta$ -phase corresponds to formation of a planar chain with extended conjugation. Once the PFO chains have adopted this more planar conformation, then interchain ordering and crystallization can take place, resulting in increased importance of interchain interaction and delocalization of the wavefunctions. The PA spectra of both the as-spun sample and the  $\beta$ -phase containing sample are dominated by an unusually sharp (standard deviation = 20 meV) PA band that we assign to excited state absorption of triplet excitons.

We studied the recombination kinetics in derivatives of pyridylene/vinylene polymers. These derivatives can be tuned reversibly via protonation–deprotonation (P–DP) processes. The PA spectra of the two forms revealed two types of photoexcited species, whose densities depend on the protonation state of the polymer. We analyzed the measured PM kinetics using the methods we developed in Section 5.3.2. We find that the kinetics of the high-energy (HE) band obeys non-dispersive bimolecular recombination kinetics, whereas the kinetics of the low-energy (LE) band shows dispersive kinetics. In addition, we analyzed the recombination kinetics of triplet excitons and polarons in films of PPV and extract a value for the dispersive parameter  $\alpha = 0.75$  and 0.6, respectively.

In Section 5.4.4 we described a spectroscopic technique that allows measurement of a polymer's conjugation length. This method is based on measurement of the peak photon energies of the  $P_1$  transition. Revisiting doping induced absorption spectra of doped oligomer solutions measured by others, we found that the peak photon energy of the low-energy polaron transition is a universal and sensitive measure of the oligomer length. This observation provides us with a sensitive measure of the conjugation length in polymer thin films using standard photoinduced absorption spectroscopy. We find that the wavefunction extend of polarons in polymer films may be similar to that in oligomers in some materials, but polarons are very much more extended in other polymer films, presumably depending on quality and purity of the polymer material. In some materials, the polaron wavefunction can even be delocalized over neighboring chains.

Using spin- $1/2$  PADMR spectroscopy, we presented direct evidence in Section 3.5 that polaron recombination is spin dependent and that singlet excitons form with a larger rate constant than triplet excitons, i.e.  $k_S > k_T$ . These claims are justified based on a large body of experimental data measured using photoinduced absorption-detected and photoluminescence-detected magnetic resonance spectroscopy, respectively. Completing a quantitative ODMR study in a large variety of  $\pi$ -conjugated polymers and oligomers, we obtained the important result that  $r = k_S/k_T$  is determined mostly by the conjugation-length. In particular,  $r$  increases with CL and  $r \approx 1$  for short oligomers and monomers.

## Acknowledgments

The work was supported by the US–Israel Binational Science Foundation and Israel Science Foundation (Technion), by the Carver Foundation and NSF ECS 04-23911 (Iowa) and by DOE ER-46109 (Utah).

## References

- 1 J. H. Burroughes, D. D. C. Bradley, A. R. Brown, R. N. Marks, K. Mackay, R. H. Friend, P. L. Burn, A. B. Holmes, *Nature* **347**, 539 (1990).
- 2 F. Garnier, R. Hajlaoui, A. Yassar, P. Srivastava, *Science* **265**, 1684 (1994).
- 3 M. Granström, K. Petritsch, A. C. Arias, A. Lux, M. R. Anderson, R. H. Friend, *Nature* **395**, 257 (1998).
- 4 S. Etamad, G. L. Baker, Z. G. Soos, in *Molecular Nonlinear Optics, Materials, Physics, Devices*, edited by J. Zyss, Academic Press, San Diego, 1994, p. 433.
- 5 A. J. Heeger, S. Kivelson, J. R. Schrieffer, W. P. Su, *Rev. Mod. Phys.* **60**, 781 (1988).
- 6 T. Skotheim, editor, *Handbook of Conducting Polymers*, Marcel Dekker, New York, 1986.
- 7 W. P. Su, J. R. Schrieffer, A. J. Heeger, *Phys. Rev. Lett.* **42**, 1698 (1979).
- 8 L. Robins, J. Orenstein, R. Superfine, *Phys. Rev. Lett.* **56**, 1850 (1986).
- 9 L. S. Swanson, J. Shinar, K. Yoshino, *Phys. Rev. Lett.* **65**, 1140 (1990).
- 10 X. Wei, B. C. Hess, Z. V. Vardeny, F. Wudl, *Phys. Rev. Lett.* **68**, 666 (1992).
- 11 R. Kersting, U. Lemmer, R. F. Mahrt, K. Leo, H. Kurz, H. Bassler, E. O. Göbel, *Phys. Rev. Lett.* **70**, 3820 (1993).
- 12 M. Leng, S. A. Jeglinski, X. Wei, R. E. Benner, Z. V. Vardeny, F. Guo,

- S. Mazumdar, *Phys. Rev. Lett.* **72**, 156 (1994).
- 13 M. Yan, L. J. Rothberg, F. Papadimitrakopoulos, M. E. Galvin, T. M. Miller, *Phys. Rev. Lett.* **72**, 1104 (1994).
- 14 Z. G. Soos, S. Ramasesha, *Phys. Rev. B* **29**, 5410 (1984).
- 15 P. Tavan, K. Schulten, *Phys. Rev. B* **36**, 4337 (1987).
- 16 F. Kajzar, S. Etemad, G. L. Baker, J. Mesnier, *Synth. Met.* **17**, 563 (1987).
- 17 B. E. Kohler, C. Spangler, C. Westfield, *J. Chem. Phys.* **89**, 5422 (1988).
- 18 Z. G. Soos, S. Ramasesha, D. S. Galvao, *Phys. Rev. Lett.* **71**, 1609 (1993).
- 19 Z. Vardeny, J. Tauc, *Phys. Rev. Lett.* **54**, 1844 (1985).
- 20 Z. Vardeny, J. Tauc, *Philos. Mag.* **B 52**, 313 (1985).
- 21 W. P. Su, J. R. Schrieffer, *Proc. Natl. Acad. Sci. USA* **77**, 5626 (1980).
- 22 R. Ball, W. P. Su, J. R. Schrieffer, *J. Phys. C* **44**, 429 (1983).
- 23 J. Orenstein, in *Handbook of Conducting Polymers*, edited by T. Skotheim, Marcel Dekker, New York, 1986, p. 1297.
- 24 M. Yan, L. J. Rothberg, F. Papadimitrakopoulos, M. E. Galvin, M. Miller, *Phys. Rev. Lett.* **72**, 1104 (1994).
- 25 H. A. Mizes, E. M. Conwell, *Phys. Rev. B* **50**, 11243 (1994).
- 26 D. M. Pai, R. C. Enck, *Phys. Rev. B* **11**, 5163 (1975).
- 27 A. S. Siddiqui, *J. Phys. C* **17**, 683 (1984).
- 28 P. D. Townsend, R. H. Friend, *Synth. Met.* **17**, 361 (1987).
- 29 L. Rothberg, T. J. Jedju, S. Etemad, G. L. Baker, *Phys. Rev. B* **36**, 7529 (1987).
- 30 C. Botta, S. Luzzalli, R. Tubino, D. D. C. Bradley, R. H. Friend, *Phys. Rev. B* **48**, 14809 (1993).
- 31 E. Ehrenfreund, D. Moses, A. J. Heeger, J. Cornil, J. L. Brédas, *Chem. Phys. Lett.* **196**, 84 (1992).
- 32 D. Fichou, G. Horowitz, B. Xu, F. Garnier, *Synth. Met.* **39**, 243 (1990).
- 33 P. Bauerle, U. Segelbacher, K. U. Gaud, D. Huttenlocher, M. Mehring, *Angew. Chem. Int. Ed. Engl.* **32**, 76 (1993).
- 34 G. Zotti, G. Schiavon, A. Berlin, G. Pagani, *Chem. Mater.* **5**, 620 (1993).
- 35 J. Poplawski, E. Ehrenfreund, J. Cornil, J. L. Brédas, R. Pugh, M. Ibrahim, A. J. Frank, *Mol. Cryst. Liq. Cryst.* **256**, 407 (1994).
- 36 G. Guo, S. Mazumdar, S. N. Dixit, F. Kajzar, F. Jarka, Y. Kawabe, N. Peyghambarian, *Phys. Rev. B* **48**, 1433 (1993).
- 37 C. J. Baker, O. M. Geisen, D. D. C. Bradley, *Chem. Phys. Lett.* **201**, 127 (1993).
- 38 N. Periasamy, R. Danieli, G. Ruani, R. Zamboni, C. Taliani, *Phys. Rev. Lett.* **68**, 919 (1992).
- 39 A. Köhler, J. S. Wilson, R. H. Friend, *Adv. Mater.* **14**, 701 (2002).
- 40 B. Horovitz, H. Gutfreund, M. Weger, *Phys. Rev. B* **17**, 2796 (1978).
- 41 E. Ehrenfreund, Z. Vardeny, O. Braffman, B. Horovitz, *Phys. Rev. B* **36**, 1535 (1987).
- 42 R. Österbacka, X. M. Jiang, C. P. An, B. Horovitz, Z. V. Vardeny, *Phys. Rev. Lett.* **88**, 226401 (2002).
- 43 J. Orenstein, G. L. Baker, *Phys. Rev. Lett.* **49**, 1043 (1980).
- 44 B. Horovitz, *Solid State Commun.* **41**, 729 (1982).
- 45 M. Rice, *Phys. Rev. Lett.* **37**, 36 (1976).
- 46 X. M. Jiang, R. Österbacka, O. Korovyanko, C. P. An, B. Horovitz, R. A. J. Janssen, Z. V. Vardeny, *Adv. Funct. Mater.* **12**, 587 (2002).
- 47 J. Orenstein, Z. Vardeny, G. L. Baker, G. Eagle, S. Etemad, *Phys. Rev. B* **30**, 786 (1985).
- 48 Z. Vardeny, E. Ehrenfreund, O. Braffman, M. Nowak, H. Schaffer, A. J. Heeger, F. Wudl, *Phys. Rev. Lett.* **56**, 671 (1986).
- 49 K. E. Ziemelis, A. T. Hussain, D. D. C. Bradley, R. H. Friend, J. Rühle, G. Wegner, *Phys. Rev. Lett.* **66**, 2231 (1991).
- 50 J. Poplawski, E. Ehrenfreund, Z. V. Vardeny, A. J. Epstein, *Synth. Met.* **54**, 113 (1992).
- 51 J. Poplawski, E. Ehrenfreund, J. Cornil, J. L. Brédas, R. Pugh, M. Ibrahim, A. J. Frank, *Synth. Met.* **69**, 401 (1995).
- 52 P. A. Lane, X. Wei, Z. V. Vardeny, J. Poplawski, E. Ehrenfreund, M. Ibrahim, A. J. Frank, *Synth. Met.* **76**, 57 (1996).
- 53 P. A. Lane, X. Wei, Z. V. Vardeny, J. Poplawski, E. Ehrenfreund, M. Ibra-

- him, A. J. Frank, *Chem. Phys.* **210**, 229 (1996).
- 54 P. A. Lane, X. Wei, Z. V. Vardeny, *Phys. Rev. Lett.* **77**, 1544 (1996).
- 55 A. Abragam, *Electron Paramagnetic Resonance of Transition Ions*, Clarendon Press, Oxford, 1970.
- 56 Z. V. Vardeny, X. Wei, *Handbook of Conducting Polymers I*, Marcel Dekker, New York, 1997, Chapt. 22.
- 57 E. J. W. List, C. H. Kim, A. K. Naik, U. Scherf, G. Leising, W. Graupner, J. Shinar, *Phys. Rev. B* **64**, 155204 (2001).
- 58 S. Depinna, B. C. Cavenett, I. G. Austin, T. M. Searle, M. J. Thompson, J. Allison, P. G. Lecomber, *Philos. Mag. B* **46**, 473 (1982).
- 59 N. C. Greenham, J. Shinar, J. Partee, P. A. Lane, O. Amir, F. Lu, R. H. Friend, *Phys. Rev. B* **53**, 13528 (1996).
- 60 M. Westerling, C. Vijila, R. Österbacka, H. Stubb, *Phys. Rev. B* **67**, 195201 (2003).
- 61 M. Westerling, C. Vijila, R. Österbacka, H. Stubb, *Chem. Phys.* **286**, 315 (2003).
- 62 O. Epshtein, G. Nakhmanovich, Y. Eichen, E. Ehrenfreund, *Phys. Rev. B* **63**, 125206 (2001).
- 63 H. S. Woo, S. C. Graham, D. A. Halliday, D. D. C. Bradley, R. H. Friend, P. L. Burn, A. B. Holmes, *Phys. Rev. B* **46**, 7379 (1992).
- 64 M. G. Roe, J. M. Ginder, P. E. Wigen, A. J. Epstein, M. Angelopoulos, A. G. MacDiarmid, *Phys. Rev. Lett.* **60**, 2789 (1988).
- 65 N. S. Sariciftci, L. Smilowitz, Y. Cao, A. J. Heeger, *J. Chem. Phys.* **98**, 2664 (1993).
- 66 K. S. Cole, R. H. Cole, *J. Chem. Phys.* **9**, 341 (1941).
- 67 G. Pfister, H. Scher, *Adv. Phys.* **27**, 747 (1978).
- 68 K. L. Ngai, C. T. White, *Phys. Rev. B* **20**, 2475 (1979).
- 69 D. W. Davidson, R. H. Cole, *J. Chem. Phys.* **19**, 1484 (1951).
- 70 S. Havriliak Jr., S. Negami, *J. Polym. Sci., Part C: Polym. Symp.* **14**, 99 (1966).
- 71 A. Bello, E. Laredo, M. Grimau, *Phys. Rev. B* **60**, 12764 (1999).
- 72 R. H. Friend, R. W. Gymer, A. B. Holmes, J. H. Burroughes, R. N. Marks, C. Taliani, D. D. C. Bradley, D. A. D. Santos, J. L. Brédas, M. Löglund, W. R. Salaneck, *Nature* **397**, 121 (1999).
- 73 M. Pope, H. Kallmann, P. Magnante, *J. Chem. Phys.* **38**, 2042 (1963).
- 74 W. Helfrich, W. G. Schneider, *Phys. Rev. Lett.* **14**, 229 (1965).
- 75 C. W. Tang, S. A. Van Slyke, *Appl. Phys. Lett.* **14**, 913 (1987).
- 76 Z. Shuai, D. Beljonne, R. J. Silbey, J. L. Brédas, *Phys. Rev. Lett.* **84**, 131 (2000).
- 77 M. A. Baldo, D. F. O'Brien, M. E. Thompson, S. R. Forrest, *Phys. Rev. B* **60**, 14422 (1999).
- 78 M. A. Baldo, M. E. Thompson, S. R. Forrest, *Nature* **403**, 750 (2000).
- 79 C. Adachi, M. A. Baldo, M. E. Thompson, S. R. Forrest, *J. Appl. Phys.* **90**, 5048 (2001).
- 80 Y. Cao, I. D. Parker, G. Yu, C. Zhang, A. J. Heeger, *Nature* **397**, 414 (1999).
- 81 J.-S. Kim, P. K. H. Ho, N. C. Greenham, R. H. Friend, *J. Appl. Phys.* **88**, 1073 (2000).
- 82 N. S. Sariciftci, editor, *Primary Photoexcitations in Conjugated Polymers; Molecular Excitons vs. Semiconductor Band Model*, World Scientific, Singapore, 1997.
- 83 M. Segal, M. A. Baldo, R. J. Holmes, S. R. Forrest, Z. G. Soos, *Phys. Rev. B* **68**, 075211 (2003).
- 84 M. Wohlgenannt, K. Tandon, S. Mazumdar, S. Ramasesha, Z. V. Vardeny, *Nature* **409**, 494 (2001).
- 85 J. S. Wilson, A. S. Dhoot, A. J. A. B. Seeley, M. S. Khan, A. Köhler, R. H. Friend, *Nature* **413**, 828 (2001).
- 86 M. Wohlgenannt, X. M. Jiang, Z. V. Vardeny, R. A. J. Janssen, *Phys. Rev. Lett.* **88**, 197401 (2002).
- 87 A. S. Dhoot, D. S. Ginger, D. Beljonne, Z. Shuai, N. C. Greenham, *Chem. Phys. Lett.* **360**, 195 (2002).
- 88 H. Siringhaus, P. J. Brown, R. H. Friend, M. M. Nielsen, K. Bechgaard, B. M. W. Langeveld-Voss, A. J. H. Spiering, R. A. J. Janssen, E. W. Meijer, P. Herweg, D. M. de Leeuw, *Nature* **401**, 685 (1999).
- 89 H. Siringhaus, N. Tessler, R. H. Friend, *Science* **280**, 1741 (1998).

- 90 P. J. Brown, H. Sirringhaus, M. Harrison, M. Shkunov, R. H. Friend, *Phys. Rev. B* **63**, 125204 (2001).
- 91 R. Österbacka, C. P. An, X. M. Jiang, Z. V. Vardeny, *Science* **287**, 839 (2000).
- 92 O. J. Korovyanko, R. Österbacka, X. M. Jiang, Z. V. Vardeny, R. A. J. Janssen, *Phys. Rev. B* **64**, 235122 (2001).
- 93 G. Rumbles, I. D. W. Samuel, C. J. Collison, P. F. Miller, S. C. Moratti, A. B. Holmes, *Synth. Met.* **101**, 158 (1999).
- 94 J. Cornil, D. Beljonne, J. P. Calbert, J. L. Brédas, *Adv. Mater.* **13**, 1053 (2001).
- 95 D. Beljonne, J. Cornil, H. Sirringhaus, P. J. Brown, M. Shkunov, R. H. Friend, J. L. Brédas, *Adv. Funct. Mater.* **11**, 229 (2001).
- 96 R. Österbacka, M. Wohlgenannt, D. Chinn, Z. V. Vardeny, *Phys. Rev. B* **60**, R11253 (1999).
- 97 R. Österbacka, C. P. An, X. M. Jiang, Z. V. Vardeny, *Synth. Met.* **116**, 317 (2001).
- 98 B. Kraabel, D. Moses, A. J. Heeger, *J. Chem. Phys.* **103**, 5102 (1995).
- 99 J. J. Apperloo, R. A. J. Janssen, P. R. L. Malenfant, J. M. J. Fréchet, *J. Am. Chem. Soc.* **123**, 6916 (2001).
- 100 K. Fesser, A. Bishop, D. K. Campbell, *Phys. Rev. B* **27**, 4804 (1983).
- 101 X. M. Jiang, C. P. An, R. Österbacka, Z. V. Vardeny, *Synth. Met.* **116**, 203 (2001).
- 102 Z. Bao, A. Dodabalapur, A. Lovinger, *Appl. Phys. Lett.* **69**, 4108 (1996).
- 103 T. Nguyen, I. Martini, J. Liu, B. Schwartz, *J. Phys. Chem. B* **104**, 237 (2000).
- 104 F. Pratt, K. S. Wong, W. Hayes, D. Bloor, *J. Phys. C* **20**, L41 (1987).
- 105 F. L. Pratt, K. S. Wong, W. Hayes, D. Bloor, *J. Phys. D* **20**, 1361 (1987).
- 106 Y. H. Kim, D. Spiegel, S. Hotta, A. J. Heeger, *Phys. Rev. B* **38**, 5490 (1988).
- 107 L. Sebastian, G. Weiser, *Phys. Rev. Lett.* **46**, 1156 (1981).
- 108 I. G. Hill, A. Kahn, Z. G. Soos, R. A. Pascal Jr, *Chem. Phys. Lett.* **327**, 181 (2000).
- 109 Y. Eichen, G. Nakhmanovich, V. Gorelik, O. Epshtein, J. M. Poplawski, E. Ehrenfreund, *J. Am. Chem. Soc.* **120**, 10463 (1998).
- 110 G. Nakhmanovich, O. Epshtein, V. Gorelik, J. M. Poplawski, J. Oiknine-Schlesinger, E. Ehrenfreund, Y. Eichen, *Synth. Met.* **101**, 269 (1999).
- 111 M. Wohlgenannt, C. Yang, Z. V. Vardeny, *Phys. Rev. B* **66**, R241201 (2002).
- 112 M. Wohlgenannt, PhD Thesis, University of Utah, 2001.
- 113 M. Leclerc, *J. Polym. Sci., Part A* **39**, 2867 (2001).
- 114 D. Neher, *Macromol. Rapid Commun.* **22**, 1366 (2001).
- 115 G. Zeng, W. L. Yu, S. J. Chua, W. Huang, *Macromolecules* **35**, 6907 (2002).
- 116 A. Grice, D. D. C. Bradley, M. T. Bernius, M. Inbasekaran, W. W. Wu, E. P. Woo, *Appl. Phys. Lett.* **73**, 629 (1998).
- 117 C. I. Wilkinson, D. G. Lidzey, L. C. Palielis, R. B. Fletcher, S. J. Martin, X. H. Wang, D. D. C. Bradley, *Appl. Phys. Lett.* **79**, 171 (2001).
- 118 M. Redecker, D. D. C. Bradley, M. Inbasekaran, E. P. Woo, *Appl. Phys. Lett.* **73**, 1565 (1998).
- 119 T. L. Francis, O. Mermer, G. Veeraraghavan, M. Wohlgenannt, *New J. Phys.* **6**, 185 (2004).
- 120 A. J. Cadby, P. A. Lane, H. Mellor, S. J. Martin, M. Grell, C. Giebeler, D. D. C. Bradley, M. Wohlgenannt, C. An, Z. V. Vardeny, *Phys. Rev. B* **62**, 15604 (2000).
- 121 M. Grell, D. D. C. Bradley, M. Inbasekaran, E. P. Woo, *Adv. Mater.* **9**, 798 (1997).
- 122 M. Grell, W. Knoll, D. Lupo, A. Meisel, T. Miteva, D. Neher, H. G. Nothofer, U. Scherf, A. Yasuda, *Adv. Mater.* **11**, 671 (1999).
- 123 M. Redecker, D. D. C. Bradley, M. Inbasekaran, E. P. Woo, *Appl. Phys. Lett.* **74**, 1400 (1999).
- 124 M. N. Shkunov, R. Österbacka, A. Fujii, K. Yoshino, Z. V. Vardeny, *Appl. Phys. Lett.* **74**, 1648 (1999).
- 125 M. Grell, D. D. C. Bradley, X. Long, T. Chamberlain, M. Inbasekaran, E. P. Woo, M. Soliman, *Acta Polym.* **49**, 439 (1998).

- 126 M. Grell, D. D. C. Bradley, G. Ungar, J. Hill, K. S. Whitehead, *Macromolecules* **32**, 5810 (1999).
- 127 L. A. Harrah, J. M. Zeigler, *J. Polym. Sci., Polym. Lett. Ed.* **23**, 209 (1985).
- 128 M. J. Winokur, D. Spiegel, Y. H. Kim, S. Hotta, A. J. Heeger, *Synth. Met.* **28**, C419 (1989).
- 129 S. D. D. V. Rughooputh, S. Hotta, A. J. Heeger, F. Wudl, *J. Polym. Sci., Polym. Phys. Ed.* **25**, 1071 (1987).
- 130 M. J. Winokur, J. Slinker, D. L. Huber, *Phys. Rev. B* **67**, 184106 (2003).
- 131 G. Klaerner, R. D. Miller, *Macromolecules* **31**, 2007 (1998).
- 132 M. Pope, C. E. Swenberg, *Electronic Processes in Organic Crystals and Polymers*, Oxford University Press, New York, 1982.
- 133 G. Cerullo, S. Stagira, M. Nisoli, S. D. Silvestri, G. Lanzani, G. Kranzelbinder, W. Graupner, G. Leising, *Phys. Rev. B* **57**, 12806 (1998).
- 134 U. Lemmer, S. Heun, R. F. Mahrt, U. Scherf, M. Hopmeier, U. Siegner, E. O. Göbel, K. Müllen, H. Bassler, *Chem. Phys. Lett.* **240**, 373 (1995).
- 135 S. A. Jenekhe, J. A. Osaheni, *Science* **265**, 765 (1994).
- 136 D. Moses, A. Dogariu, A. J. Heeger, *Chem. Phys. Lett.* **316**, 356 (2000).
- 137 D. Moses, A. Dogariu, A. J. Heeger, *Phys. Rev. B* **61**, 9373 (2000).
- 138 U. Mizrahi, I. Shtrichman, D. Gershoni, E. Ehrenfreund, Z. V. Vardeny, *Synth. Met.* **102**, 1182 (1999).
- 139 M. Wohlgenannt, Z. V. Vardeny, *J. Phys: Condens. Matter* **15**, R83 (2003).
- 140 M. Wohlgenannt, X. M. Jiang, Z. V. Vardeny, *Phys. Rev. B* **69**, 241204 (2004).
- 141 J. S. de Melo, L. M. Silva, L. G. Arnaut, R. S. Becker, *J. Chem. Phys.* **111**, 5427 (1999).
- 142 A. P. Monkman, H. D. Burrows, I. Hamblett, S. Navarathnam, M. Svensson, M. R. Andersson, *J. Chem. Phys.* **115**, 9046 (2001).
- 143 R. A. J. Janssen, N. S. Sariciftci, A. J. Heeger, *Synth. Met.* **70**, 1343 (1995).
- 144 U. Scherf, K. Müllen, *Makromol. Chem.* **112**, 489 (1991).
- 145 M. Wohlgenannt, *Phys. Status Solidi A* **201**, 1188 (2004).
- 146 O. Epshtein, Y. Eichen, E. Ehrenfreund, M. Wohlgenannt, Z. V. Vardeny, *Phys. Rev. Lett.* **90**, 046804 (2003).
- 147 S. Karabunarliev, E. R. Bittner, *Phys. Rev. Lett.* **90**, 057402 (2003).
- 148 K. Tandon, S. Ramasesha, S. Mazumdar, *Phys. Rev. B* **67**, 045109 (2003).
- 149 D. Beljonne, A. Ye, Z. Shuai, J. L. Brédas, *Adv. Funct. Mater.* **14**, 684 (2004).
- 150 W. Barford, *Phys. Rev. B* **70**, 205204 (2004).
- 151 M. Wohlgenannt, O. Mermer, *Phys. Rev. B* **71**, 165111 (2005).
- 152 C. Yang, Z. V. Vardeny, A. Köhler, M. Wohlgenannt, M. K. Al-Suti, M. S. Khan, *Phys. Rev. B* **70**, 241202 (2004).

## 6

# Charge Transport in Disordered Organic Semiconductors

V. I. Arkhipov, I. I. Fishchuk, A. Kadashchuk and H. Bässler

### 6.1

#### Introduction

Mechanisms of photogeneration and transport of charge carriers are fundamentally important for understanding electronic phenomena in organic systems. These processes basically determine how and, particularly, how efficiently optical energy can be converted to electrical current and vice versa. On a nanometer scale, this is the subject of optodynamics in biological systems and photosynthesis. The study of steady-state and transient photoconductivity is the method of choice in order to delineate the pathway for charge transfer and, more generally, for photovoltaic energy conversion in organic devices.

It turned out that the conceptual understanding of photoconductivity was stimulated a great deal by concomitant technological developments. One of them was the discovery of electrophotography, which in the meantime became a mature technology with an enormous economic impact. Early on it was recognized that those photoreceptors have to be large-scale and, therefore, amorphous thin films, which allows breakdown effects caused by grain boundaries between crystallites to be avoided. It was also recognized that spatial randomness lowers the mobility of charge carriers by orders of magnitude. Fortunately, a fairly modest mobility of  $10^{-5}$ – $10^{-4}$   $\text{cm}^2 \text{V}^{-1} \text{s}^{-1}$  is enough for xerography because the development of the latent picture is set up by the mechanical machinery rather than by the transit time of charges across the photoreceptors that today are mostly molecularly doped polymers.

However, the next generation of optoelectronic devices will be all-electronic and their ultimate response time will no longer be determined by the system mechanics but by the motion of the charge itself. Prominent examples are light-emitting diodes (LEDs), field-effect transistors (FETs) and photovoltaic cells. The current bottlenecks for their large-scale industrial application are their lifetime, on the one hand, and the magnitude of the charge carrier mobility, on the other. The latter is particularly important for FETs because the on–off ratio depends on it, and also for photovoltaic cells because it determines the fraction of the charge carriers collected.

The active elements in organic optoelectronic devices are the layers of either vapor-deposited  $\pi$ -bonded oligomeric molecules or  $\pi$ -conjugated main chain polymers. Both have their advantages and disadvantages. Vapor-phase deposition permits one to fabricate multilayer structures more easily and at improved purity while polymers can be more easily spin-coated and they are more resistant towards crystallization. In the meantime, it has been well established that disorder is the main obstacle to improving that aspect of the device performance which is related to charge carrier mobility. There is currently an endeavor to reduce disorder while still retaining noncrystallinity of the samples and to explore the structure–mobility relationship.

The aim of this chapter is to review the current achievements regarding the experimental and theoretical understanding of charge transport in random organic photoconductors with particular attention to conjugated polymers. The field is huge and full coverage is not attempted. Instead, we want to highlight recent developments in addition to an outline of the basic phenomena, focusing on charge transport rather than on charge generation because the latter process has already been reviewed recently [1]. Therefore, only key results will be summarized in the experimental section.

## 6.2

### Charge Generation

There has been a lively, if controversial, discussion about the mechanism(s) by which absorption of a photon in a conjugated polymer produces charge carriers. It has been generally agreed that, in conventional organic solids, such as molecular crystals, molecular glasses made up by oligomers and molecularly doped polymers, in which the host acts as an inert binder, absorbed photons generate singlet or – after intersystem crossing – triplet neutral excitations [2]. In an undiluted system they can move incoherently and can be considered as Frenkel-type excitons. Transfer of one of the constituent charges to an adjacent chromophore, thus creating a charge-transfer state, requires additional energy, as does the subsequent escape of the electron–hole pair from its mutual Coulombic potential. The difference between the energy of fully separated charges and the singlet exciton energy is referred to as the exciton binding energy  $E_b$  and is of the order of 1 eV.

Because the dielectric constants of conventional molecular solids including  $\pi$ - and  $\sigma$ -bonded conjugated polymers, are basically the same i. e. 3 ÷ 4 their optoelectronic properties should be similar. However, the observation that, in  $\pi$ -conjugated polymers, onset of photoconduction coincides with the absorption edge has been taken as evidence that (i) the exciton binding energy in these materials is  $\sim kT$  at room temperature and (ii) the optical absorption is a valence-to-conduction band transition in terms of inorganic semiconductor theory rather than of concepts relevant for molecular crystals and organic solids in general [3]. The only exception from this notion were polydiacetylenes, in which photoconductivity starts about 0.5 eV above the (excitonic) absorption edge [4, 5]. Meanwhile, there is abundant experimental evidence against this hypothesis and in favor of the molec-

ular approach. A summary of more recent advances in this field will be given below. Regarding details, the reader is referred to recent reviews [1, 6].

It is well known that, in the bulk of molecular solids, a vibrationally relaxed exciton needs an energy  $\gg kT$  at room temperature in order to dissociate in a pair of free charges [2]. Therefore, intrinsic photoconduction should commence at higher photon energies only. This is confirmed by experiments on pure anthracene crystals, in which photoinjection from the electrodes was eliminated [7]. However, unless special precautions are taken there is always some photogeneration occurring close to the absorption edge, notably if the illuminated electrode is biased positively [8]. It is caused by exciton dissociation at the electrode when the electron is transferred to the electrode and the remaining hole is only weakly bound to its image charge in the metal. In principle, this process should be symmetric with respect to the electrode polarity. The reason why it is not is charge carrier trapping at the interface. In systems with moderately low oxidation potentials, there are always inadvertent oxidation products serving as deep electron traps [8, 9]. By the way, measurements of the yield of that type of extrinsic photocurrent as a function of photon energy, i.e. of the penetration depth of the incident light, have been used as a probe of the diffusion length of the excitons that can reach the electrode [10]. Unfortunately, this method yields meaningful results only if that diffusion length is comparable to the light penetration depth. There is clear evidence that in conjugated polymers electrode-sensitized photoconduction does play a role [11]. However, the effect should be present but, in fact, is absent in polydiacetylenes because of the extremely short exciton lifetime in these materials. It is also strongly reduced in diode structures carrying semi-transparent metal electrodes because dipole-allowed transfer of an exciton to metal electrons competes effectively with its dissociation decay at the interface. An effect that is complementary to exciton dissociation at an electrode is sensitized photoinjection from an optically excited dye molecule absorbed at the interface. It depends on the redox properties of the interface and can be used to extend the spectral range of the photoelectric sensitivity towards lower quantum energies [2]. A recent example is sensitized hole injection from a perylene diimide into a dendrimer [12].

Dissociation of excitons in the bulk can occur when the sample is deliberately or inadvertently doped by dopants with either high electron affinity or very low oxidation potential. In the course of its diffusion, an exciton can transfer one of its charges to the dopant. Photovoltaic power conversion using  $\pi$ -conjugated polymers rests upon this process [13–18]. To be efficient, it has to ensure that (1) every exciton reaches a dopant, (2) the generated electron–hole pairs dissociate into free carriers rather than recombine geminately [19, 20] and (3) both sorts of charges are mobile and are collected by the built-in electric field that is determined by the difference of the workfunctions of the electrodes. Meeting the first condition is facilitated by thorough mixing, e.g. blending, in a donor–acceptor system [21]. Strategies to improve the yield of the electron–hole pair dissociation are currently under debate [20, 22].

The condition under which a vibrationally relaxed singlet exciton can dissociate is that the relevant rate constant is comparable to the rate of exciton decay to the

ground state. Since in molecular crystals the energy of a charge-transfer state is  $\sim 0.5$  eV larger than that of a singlet exciton [23], thermally activated dissociation is noncompetitive. In  $\pi$ -conjugated polymers this process is feasible provided that an electric field is applied that is sufficiently strong to compensate for the energy mismatch. The reason why in this respect conjugated polymers behave differently from molecular crystals is that, in the former, the size of the on-chain exciton is already comparable to the intermolecular separation [24]. Therefore, the excess energy needed to transfer a charge from an excited chain element to an adjacent chain is lower than that of classic molecular crystals. Fluorescence quenching in  $\pi$ -conjugated polymers by electric fields as large as  $1 \text{ MV cm}^{-1}$  [25, 26] provides unambiguous evidence that a neutral singlet exciton can dissociate into a pair of charges, if coulombically bound, although this process is endothermic at zero field. Transient absorption of the created charges proves that dissociation occurs within the entire lifetime of the singlet excitons [27].

At photon energies some 0.5–1.0 eV above the optical gap, the yield of intrinsic photogeneration increases, indicating that an excess of quantum energy facilitates dissociation. This is equivalent to autoionization of a higher Franck–Condon state which is a well-known phenomenon in molecular crystals [2, 28]. Experimental signatures of the phenomenon are the photocarrier generation commencing at a photon energy close to the sum of the exciton energy and the exciton binding energy and weak temperature dependence of the photogeneration yield at moderate electric fields. Two theoretical frameworks have been proposed which are complementary regarding their time domains. The work by Arkhipov et al. [29] is a quasi-equilibrium theory and assumes that the excess energy relative to that of a relaxed exciton is funneled into local vibrational heat bath of a chain element. For a short time, the local temperature is significantly higher than the ambient temperature which facilitates thermally activated dissociation of the electron–hole pair in terms of a Boltzmann process. The Basko and Conwell model [30], on the other hand, assumes that ejection of an electron from the excited chain segment against the Coulombic forces occurs before any thermalization occurs. The recent experiments by Gulbinas et al. [31], in which a film of a ladder-type poly(phenylene) was excited with a 150-fs pulse of 4.66-eV photons, i.e.  $\sim 2$  eV above the  $S_1 \leftarrow S_0$  0–0 transition, revealed, in fact, a fast onset of charge generation that has not been observed upon exciting at a photon energy of 0.4 eV above the optical gap [27]. The effect decays on a time-scale of 1 ps, i.e. it lasts much longer than the duration of the primary pulse. When exciting MeLPPP with 3.2-eV photons, i.e. 0.5 eV above the  $S_1 \leftarrow S_0$  0–0 transition and monitoring the evolution of the charges with sub-20 fs time resolution, Gadermaier et al. [32] also observed a fast component of photoresponse that decayed on a 1 ps time-scale while the redistribution of the initial vibrational energy is believed to be completed within 10 fs or less. This would argue in favor of the Arkhipov et al. model. In reality, it is likely that there is a superposition of both processes, i.e. there is instantaneous direct dissociation of hot Franck–Condon states followed by somewhat slower dissociation of excitons while the chain is still vibrationally hot.

The excess energy needed to dissociate an exciton can also be supplied via two-photon absorption or via a sequential process. The work of Silva et al. [33] showed that in the work by Moses et al. [34], intended to prove that a bare singlet exciton has enough energy to dissociate into free carriers, two-photon absorption or step-wise excitation by two photons or bimolecular exciton fusion dominated. By the way, a sequential process need not be ultra-fast. It is well established that a metastable coulombically bound geminate electron-hole pair is generated by a one-photon process with a little excess energy [35, 36], and it can subsequently dissociate by interaction with a mobile singlet or triplet exciton. The decay of geminate pairs is a random process featuring a power law extending from the sub-ns to  $\mu$ s range. Accordingly, release of one of charges comprising the geminate pair by interaction with an exciton can span a large dynamic range [37–40]. It is fair to state, however, that unraveling the complexities of sequential photodissociation is a real challenge for experimentalists.

### 6.3 Charge Carrier Hopping in Noncrystalline Organic Materials

#### 6.3.1 Outline of Conceptual Approaches

##### 6.3.1.1 The Continuous Time Random Walk (CTRW) Formalism

The incentive for studying the photoconductivity of disordered semiconductors started several decades ago when amorphous chalcogenides were introduced as photoreceptors in electrophotography. They combine photoconductivity in an appropriate spectral range with high dielectric strength, mechanical stability and low-cost manufacture. It has been recognized, however, that in this class of materials charge transport is orders of magnitude slower than in crystalline semiconductors, which may seriously affect the response of a device. An obvious obstacle against improvement of their performance was a missing understanding of this phenomenon. The intuitive notion has been that this is a genuine signature of disorder. A milestone in this endeavor turned out to be the development of the formalism of continuous time random walks (CTRW) in an amorphous network by Lax, Montroll and Scher [41–45]. It is based on the idea that one can cast the effect of disorder in a material by formally replacing the conventional exponential waiting time distribution of a charge carrier at any translationally symmetric site of a crystalline semiconductor by an algebraic distribution of waiting times of the form  $\psi(t) \sim t^{-(1+\alpha)}$ , with  $0 < \alpha < 1$  being a dispersion parameter, while retaining the crystalline structure of the sample. This introduces a hierarchy of sites regarding their ability to transfer a charge carrier to an adjacent site thus opening faster and slower routes for charge transport. This concept was able to explain the phenomenon of transit time dispersion that was encountered upon measuring a time of flight signal excited at a well-defined starting time including the self-similarity

of the shapes of photocurrent transient pulses. The approach was heuristic in the sense that the origin of the algebraic waiting time distribution remained unspecified.

Later, however, it was recognized that the concept of multiple trapping within a manifold of trapping sites featuring an exponential distribution of energies is a concrete example of the CTRW formalism [46–51]. It does lead to dispersive transport with a dispersion parameter  $a = T/T_0$ , where  $kT_0$  is the characteristic energy of the trap distribution. This affords an interpretation of experimental transport data for amorphous hydrogenide silicon- and chalcogenide-like systems in which the density of states (DOS) distribution is, indeed, featuring an exponential for whatever reason.

### 6.3.1.2 The Gill Equation

The CTRW approach has also been applied to charge transport in molecularly doped polymers because their experimental signatures, especially the observation of dispersive transport, are similar [52, 53]. The intuitive notion has been that the dispersion is a reflection of the static fluctuation of the distances among the transport sites. This issue initiated some controversy because it was argued that the variation of the jump distances could hardly explain the magnitude of the observed effects [54–56]. Another argument against the notion that positional disorder alone controls transport was the measurement of the charge carrier mobility as a function of temperature and electric field. Numerous studies on a broad class of molecularly doped polymers such as polycarbonate doped with derivatives of triphenylamine [57, 58] and hydrazone [59] or main-chain polymers such as polysilanes [60, 61], members of the polyphenylenevinylene family [62] and polyvinylcarbazole [63], revealed (i) activated behavior of the charge carrier mobility yielding an activation energy of 0.4–0.6 eV independent of chemical constitution and synthesis if analyzed in terms of the Arrhenius equation, (ii) a field dependence of the mobility resembling the Poole–Frenkel law,  $\ln\mu \sim SF^{1/2}$ , over an extended range of electric fields [64] and (iii) a deviation of both the magnitude of  $S$  and its temperature dependence from the prediction of the Poole–Frenkel theory even including a reversal of sign of  $S$  above a certain temperature [65]. This led Gill [66] to introduce his famous equation:

$$\mu(F, T) = \mu_0 \exp\left(-\frac{\Delta_0 - \beta F^{1/2}}{kT_{\text{eff}}}\right), \quad \frac{1}{T_{\text{eff}}} = \frac{1}{T} - \frac{1}{T^*} \quad (6.1)$$

where  $T^*$  is the temperature at which extrapolations of the  $\log\mu$  versus  $1/T$  lines intersect. However, apart from the fact that Eq. (6.1) has no theoretical foundation, its application to experimental data analysis caused serious problems. The key difficulty is the assumption of the original form of the Poole–Frenkel effect. It implies that transport is limited by traps that are charged when empty. However, the independence of the temperature coefficient of the mobility on chemical composition combined with the ubiquitous occurrence of the  $\ln\mu \sim F^{1/2}$  behavior casts

serious doubts on the dominance of impurity effects. One can safely exclude that chemically different systems contain (i) the same amount of traps having (ii) the same depths relative to the transport level and (iii) being charged when empty. Instead, one has to conclude that the above features reflect a recurrent intrinsic transport property of the that class of system. This, in turn, renders multiple trapping models inadequate for rationalizing charge carrier motion except in systems such as polyvinylcarbazole that is known to contain extrinsic traps of physical origin, i.e. incipient dimers. Another inherent problem of the Gill approach is its failure to account for the transition to dispersive transport at lower temperatures

### 6.3.1.3 The Hopping Approach

Owing to the weak intermolecular coupling, valence and conduction bands of molecular crystals are narrow, typically 0.1 eV or less [2]. As a consequence, the mean free path of a charge carrier between subsequent phonon scattering events is of the order of the lattice parameter itself, at least at room temperature. Given the disorder present in noncrystalline organic solids such as molecularly doped polymers, it is straightforward to assume that an elementary transport event in such systems is the transfer of a charge carrier between adjacent transporting molecules or segments of a main-chain polymer, henceforth called transport sites. In chemical terms this is a redox process involving chemically identical yet physically different moieties. The dependence of the charge carrier mobility on temperature and electric field must reflect the dependence of that elementary step on  $T$  and  $F$ . Its activation energy will, in general, be the sum of inter- and intramolecular contributions. The former arises from the physical inequivalence of the hopping sites due to local disorder and is an inherent property of any amorphous organic solid. The latter is due to the change in molecular conformation upon removal or addition of an electron from/to the transport site. Transfer of a charge requires a concomitant activated transfer of the molecular distortion, i.e. transfer of a polaron. The essential difference among transport models is related to the relative importance of both contributions. The hopping model assumes that the coupling of the charge carrier to intra-or intermolecular modes is weak and the activation energy of transport reflects the static energetic disorder of the hopping sites. The (small) polaron model, on the other hand, considers the disorder energy being negligible relative to the molecular deformation energy.

### 6.3.1.4 Monte Carlo Simulation

The easiest way to model charge transport in a random organic solid is via Monte Carlo simulation [67]. This can be considered as an idealized experiment carried out on a sample of arbitrarily adjustable degree of disorder and devoid of any accidental complexity. It allows one to determine which level of sophistication is required to reproduce the properties of a real-world sample and, by comparison with theory, to check the validity of approximations involved in a theoretical formalism that is based on the same physical principles. The essential input parameter

is the width of the distribution of hopping states (DOS). It is usually assumed to be of Gaussian shape:

$$g(E) = \frac{1}{\sqrt{2\pi}\sigma} \exp\left(-\frac{E^2}{2\sigma^2}\right) \quad (6.2)$$

Because in organic solids optical absorption generates neutral rather than charged excitations, there is no direct experimental proof of this assumption. However, it is known that inhomogeneously broadened absorption profiles of molecules embedded in a glassy matrix are of Gaussian shape. The reason is that the lattice polarization energy of an excited molecule, i.e. the gas to solid shift energy, depends on many internal coordinates, each varying randomly. Therefore, the central limit theorem applies that predicts a Gaussian envelope function regardless whether the interaction energy is of the dipole–dipole or, rather, of charge–dipole type [68, 69].

The simplest ansatz for the hopping rate is that of Miller and Abrahams [70]:

$$v_{ij} = v_0 \exp\left(-2\gamma a \frac{r_{ij}}{a}\right) \exp\left[-\frac{|E_j - E_i| + (E_j - E_i)}{2kT}\right] \quad (6.3)$$

where  $r_{ij}/a$  is the relative jump distance between hopping sites  $i$  and  $j$ ,  $\gamma$  the so-called inverse wavefunction location radius, although strictly it is the coupling matrix element between the sites,  $a$  the mean intersite distance and  $v_0$  the frequency factor (attempt-to-jump frequency). It is a one-phonon approximation and assumes spherically symmetric sites. To consider that in a disordered medium (i) the intersite distance and, more importantly, (ii) coupling among the transport molecules, that are usually non-spherical, are subject to local variation, the overlap parameter  $2\gamma a = \Gamma$  can also be subjected to a distribution. This is referred to as positional or off-diagonal disorder. Operationally, one can account for this type of disorder by splitting the intersite coupling parameter  $\Gamma_{ij}$  into two specific site contributions,  $\Gamma_i$  and  $\Gamma_j$ , each taken from a Gaussian probability density of variance  $\sigma_r$ . The variance of  $\Gamma_{ij}$  is then  $\Sigma = 2\sqrt{\sigma_r}$ . This is an arguable procedure because it implies a certain type of correlation because all jumps starting from a given site  $i$  are affected by specifying  $\Gamma_i$ . The assumption of a Gaussian-type probability density for  $\Gamma_{ij}$  appears to be more critical since, as Slowik and Chen [71] have shown, the overlap parameter is a strong and complicated function of the mutual orientation of the interacting molecules. In the absence of any explicit knowledge about the actual distribution of  $\Gamma_{ij}$  a Gaussian appears nevertheless to be a zero-order choice, in particular since the relative fluctuation  $\Sigma/2\gamma a$  required to fit experimental data will turn out to hardly be in excess of 0.3. In any event,  $\Sigma$  should be considered as an operationally defined measure of the off-diagonal disorder that cannot be directly translated into a microscopic structural property, in contrast to the parameter  $\sigma$  that characterizes energetic, i.e. diagonal, disorder.

Since the simulation work is well documented in the literature [67, 72] only the main results will be summarized briefly.

1. Upon starting in a random site within the DOS, a charge carrier tends to relax towards tail states featuring a logarithmic decay law  $\Delta E \propto \ln t$ . Concomitantly, the diffusivity of the particle decreases with time. This gives rise to dispersive transport of charge carriers.
2. Depending on the magnitude of the energetic disorder parameter,  $\hat{\sigma} = \sigma/kT$ , quasi-equilibrium is established sooner or later. The equilibrium occupational DOS is also a Gaussian of width  $\sigma$ , but off-set from the center of the intrinsic DOS by an energy  $-\sigma^2/kT$  as predicted by analytic theory.

$$\langle E_{eq} \rangle = \lim_{t \rightarrow \infty} \langle E(t) \rangle = \frac{\int_{-\infty}^{\infty} dE E g(E) \exp(-E/kT)}{\int_{-\infty}^{\infty} dE g(E) \exp(-E/kT)} = -\frac{\sigma^2}{kT} = -\hat{\sigma} \sigma \quad (6.4)$$

3. The relaxation of an ensemble of non-interacting charge carriers has a crucial effect on their motion at arbitrary temperature. Since the mean energy of charge carriers under quasi-equilibrium decreases with decreasing temperature, the activation energy needed for a jump to a site close the transport energy (see below) is no longer a temperature-independent quantity as it is in an energetically discrete sample but increases with decreasing  $T$ .
4. The superposition of an external electric field will tilt the DOS. Therefore, the local activation energy will, on average, be lowered and the charge carrier mobility will increase except in case of positional disorder, when a carrier may be forced to execute a detour involving an up-hill jump against the field. At large electric field, when the gain in the electrostatic potential overcompensates energy disorder, the drift velocity of a packet charge carriers must saturate because transport becomes unidirectional and the asymmetric jump rate implied by the Miller–Abrahams assumption prevents its increase in a down-hill jump.

In the intermediate field range the  $T$  and  $F$  dependences of the charge carrier mobility are predicted to be

$$\mu(\hat{\sigma}, F) = \mu_0 \exp \left[ -\left( \frac{2}{3} \hat{\sigma} \right)^2 \right] \times \begin{cases} \exp[C(\hat{\sigma}^2 - \Sigma^2)F^{1/2}], & \Sigma \geq 1.5 \\ \exp[C(\hat{\sigma}^2 - 2.25)F^{1/2}], & \Sigma < 1.5 \end{cases} \quad (6.5)$$

where  $C$  is a numerical constant. For  $a = 0.6$  nm,  $C = 2.9 \times 10^{-4} \text{ cm}^{1/2} \text{ V}^{-1/2}$ . It features a Poole–Frenkel-type of field dependence of  $\mu$  and offers an understanding of the coefficient  $S$  in the Gill equation [Eq. (6.1)] in terms of a superposi-

tion of energetic and positional disorder including the case when  $S < 0$ .

5. Even under quasi-equilibrium conditions, the diffusive spreading of an initially  $\delta$ -shaped sheet of charge carriers drifting across a sample is anomalously large. This is an inherent signature of the disorder induced broadening of the waiting time distribution. It is accompanied with a field-induced increase of the Einstein  $\mu/D$  ratio whose value in a discrete system is  $e/kT$  [73].
6. At weak electric fields, hopping within an intrinsically broadened DOS and multiple trapping in a system with a discrete transport level and an energetically disperse distribution of trapping levels are formally equivalent [74].
7. Moderately deep traps outside of the intrinsic DOS can be modeled by renormalization of the DOS [75, 76].

#### 6.3.1.5 The Effective Medium Approach

The first analytical treatment of hopping charge carrier transport in an amorphous solid with Gaussian DOS under the condition of an otherwise empty DOS was carried out by Movaghar et al. [77] using the effective medium approximation (EMA). In this approximation, the higher order correlation effects, appearing when summing over all paths that a particle can take from site  $i$  to site  $j$ , lead to an effective reduction of the site density after each jump. In undiluted systems it describes the hopping process in an appropriate way except at low temperatures when the system becomes frustrated because intermediate thermally activated jumps that may be required for further relaxation are frozen [78, 79]. This limitation applies to charge carriers that migrate via short-range exchange interaction to singlet excitation that couple via longer ranged dipole–dipole interaction. It turned out that the temperature dependence of the charge carrier transport under quasi-equilibrium conditions is in quantitative agreement with Monte Carlo simulation as is the temporal course of relaxation [77, 78]. A compelling direct spectroscopic test of the correctness of the predictions of the EMA approach has recently been reported [80] employing site-selective excitation of singlet excitons in  $\pi$ -conjugated polyfluorene whose motion is the mirror image of charge-carrier hopping in an inhomogeneously broadened density-of-states distribution.

#### 6.3.1.6 Effect of Site Correlation

A weak point of previous Monte Carlo simulations was the limited range of the Poole–Frenkel-type field dependence of the charge carrier mobility. It has not been observed until the field reaches  $(3\text{--}5) \times 10^5 \text{ V cm}^{-1}$ . This is in disagreement with experiments that consistently bear out a  $\ln \mu \propto F^{1/2}$  behavior already at fields below  $10^5 \text{ V cm}^{-1}$ . The work of Gartstein and Conwell [81] demonstrated, however, that this problem can be solved by introducing correlation between the energies of

spatially close sites. Their simulation shows that this idea leads to an extended range of validity of the Poole–Frenkel law. Such an assumption is physically reasonable because the static fluctuations of the site energies are due to the interaction of a charge carrier with permanent and induced dipoles. This must extend the Poole–Frenkel regime of  $\mu(F)$  towards lower fields because the field dependence arises from the drop of the electrostatic potential,  $eFl$ , across a relevant length  $l$  of the hopping system relative to  $kT$ . With uncorrelated site energies  $l$  is identical with the mean intersite distance. Correlation increases the length scale, thereby decreasing the critical field.

Dunlap et al. [82] developed a 1D analytical treatment of hopping transport in the presence of correlation. Later they extended that work to the 3D case [83]. This extension is important because in a 3D system a charge carrier might circumvent an obstacle more easily. Extensive simulations demonstrated, however, that the basic features of the correlated disorder model (CDM) are retained on extending the treatment to 3D. CDM shares some features with the conventional Gaussian disorder model (GDM). However, it turns out that essential transport properties of CDM are insensitive to the way in which detailed balance is included in the hopping rate. The same Poole–Frenkel-type field dependence occurs with symmetric (small-polaron-like) rates or asymmetric Miller–Abrahams rates. On the basis of their simulation, Novikov et al. [83] proposed the following empirical relation for  $\mu(F, T)$ :

$$\mu(F, T) = \mu_0 \exp \left[ - \left( \frac{3}{5} \hat{\sigma}_d \right)^2 + C_0 \left( \hat{\sigma}_d^{3/2} - \Gamma \right) \left( \frac{eaF}{\sigma_d} \right)^{1/2} \right] \quad (6.6)$$

where  $C_0 = 0.78$  and  $\Gamma = 2$ . The latter describes positional disorder.  $\sigma_d$  is the DOS width caused by randomly positioned permanent dipoles. However, extensive experimental studies by Borsenberger and co-workers [72, 84] on charge transport in polymers molecularly doped with hole-transporting molecules carrying various polar substituents proved that, although a random distribution of dipoles does contribute to the total magnitude of disorder manifested in charge transport, there is a significant contribution of the van der Waals coupling among randomly positioned nonpolar transport sites. A measurement of  $\mu$  as a function of the dipole moment is able to discriminate between the polar and the nonpolar contributions. Observing a Poole–Frenkel-type field dependence of  $\mu$  down to moderate fields confirms that the effect of site correlation is not confined to random dipolar fields. This is plausible because the van der Waals interaction between nonspherical molecules is evidently an inter- rather an intra-site effect. Rakhmanova and Conwell [85] treated this case by performing Monte Carlo simulations in which they modeled correlation by introducing inhomogeneity in the manifold of apolar hopping sites with two different  $\sigma$ -values. The Poole–Frenkel-type field dependence was recovered while the temperature dependence acquired an Arrhenius form.

### 6.3.1.7 Polaron Transport

There has been a lively discussion of whether or not charge transport in random organic solids is predominately controlled by disorder or by (small) polaron effects [58, 86–88]. Without any doubt, a moving charge carrier is always accompanied by a structural distortion. The question relates to the magnitude of the effect. Unfortunately, there is no unambiguous spectroscopic probe of the magnitude of the configurational change on adding or removing an electron to or from a molecule, while neutral excitations are, in fact, amenable to spectroscopic probing. Upon optical absorption there is always some readjustment of bond length, equivalent to coupling to molecular vibration(s), because it changes the electron distribution. This is evidenced by the vibrational satellites that accompany a purely electronic 0–0 transition in an absorption spectrum. A measure of the coupling strength is the Huang–Rhys factor  $S_{HR}$ , which determines the energy change between the unrelaxed and the relaxed configuration of an excited chromophore [89]. In rigid organic molecules,  $S_{HR}$  is of the order of unity, implying a structural relaxation energy  $E_p \approx 0.15$  eV. In a molecule that has a torsional degree of freedom,  $E_p$  is larger. An example is biphenyl, where the phenyl rings favor a twisted configuration in the electronic ground state whereas in the excited state it tends to become planar. An earlier site-selective fluorescence study of various polyarylenevinylenes, that differ with regard to the moment of inertia of the intramolecular torsional displacement, documented that effect and delineated the existence of light and heavy polarons in  $\pi$ -conjugated polymers [90]. A subsequent time-resolved study confirmed this notion and showed that coupling to a torsional mode in a polybiphenylvinylene-type polymer slows energy transfer among the polymer chains [91].

Since neutral and charged excitations share common features with regard to coupling of an electronic state to an intramolecular displacement, charge carriers in organic solids have to be polaron-like [92]. This has been revealed by comparative studies employing site-selective fluorescence spectroscopy on the one hand and temperature-dependent hole transport on the other [93, 94]. They demonstrated that, depending on the degree of structural relaxation, the polaronic contribution to the activation energy in charge transport has to be taken into account but the disorder contribution is always dominant. This is in agreement with quantum calculations on oligomeric model compounds of polythiophene and PPV that bear out a polaron binding energy of typically 0.1–0.2 eV [95, 96].

A model based solely on polaron effects fails to describe charge transport because the required fit parameters turn out to be unphysical [97]. In the adiabatic limit the activation energy  $\Delta$  for polaronic transport is

$$\Delta = \frac{E_p}{2} - J \quad (6.7)$$

where  $J$  is the electronic transfer integral [86, 88]. Therefore, if representative values of  $\Delta$  range between 0.3 and 0.6 eV, one had to postulate  $E_p$  of 0.6–1.2 eV. Except in the case of strong coupling to an on-chain torsional mode, such values are unacceptably large and in disagreement with both quantum chemical calculations [95, 96] and theoretical analyses of charge transport in molecular crystals

that predict  $E_p \leq 0.15$  eV only [92]. Any contribution of  $J$  to  $\Delta$  is negligible anyhow. Additional arguments against the predominance of polaron effects are (i) the unrealistically large value of the charge carrier mobility if extrapolated to  $T \rightarrow \infty$  invoking an Arrhenius law and (ii) the observation of dispersive transport at lower temperatures because the relaxation energy of the molecular skeleton as a result of adding to or removing a charge from a monomer/polymer is supposed to be a discrete rather than a random quantity.

### 6.3.2

#### Stochastic Hopping Theory

If the carrier jump rate,  $v_{ij}$  is known as a function of distance and energy difference between hopping sites  $i$  and  $j$ , the hopping master equation can be readily written for the occupational probability,  $f_i$ , of any site of the system as

$$\frac{df_i}{dt} = \sum_{j \neq i} v_{ji} f_j - f_i \sum_{j \neq i} v_{ij} \quad (6.8)$$

Since exponentially decaying tails are typical for wavefunctions of localized carriers and energetically upward carrier jumps require Boltzmann-type thermal excitation, the Miller–Abrahams jump rate, given by Eq. (6.3) offers a good universal approach to  $v_{ij}$  in organic materials. Under certain conditions Eq. (6.8) can be solved analytically. An example is an ordered system of monoenergetic hopping sites in which nearest-neighbor jumps are the dominant transport mode. Under such conditions Eq. (6.8) is simply equivalent to the conventional continuity equation for the carrier density with the drift and diffusion terms and the mobility and diffusion coefficient determined by the lattice constant  $a$ , the nearest-neighbor jump rate  $\nu$  and the temperature as  $\mu = e\nu a^2/kT$  and  $D = \nu a^2$ , where  $e$  is the elementary charge. Note that these  $\mu$  and  $D$  obey the Einstein relation.

In principle, this equation can also be solved, either analytically or numerically, for every site of a reasonably large random hopping system if the location and energy of all sites are fixed and known. That solution should then yield full information about charge carrier kinetics within the system. However, this solution would tell us very little about charge transport in a real disordered material. The reason is that, in order to calculate any macroscopic value in a random system, one has to average the solution of Eq. (6.8) over all possible realizations of this system. Theoretically, this is the most difficult part of the problem and differences between analytical theories of carrier hopping in disordered systems essentially originate from different approaches to the averaging procedure.

Percolation-type theories [98] rest on the notions that (i) the Miller–Abrahams carrier jump rate decreases exponentially with increasing distance between hopping sites, which implies the major role of hopping between nearest-neighbor sites, and (ii) in a positionally random system distances between nearest hopping sites vary strongly. Therefore, one can suggest that the most difficult jumps between nearest neighbors separated by the longest distance  $r_{\max}$  control the total

hopping time and, concomitantly the hopping mobility,  $\mu \sim \exp(-2\gamma r_{\max})$ . The longest distance scales with the average inter-site distance  $a$  as  $r_{\max} = \lambda a$ , with  $\lambda = 1.39$  and  $\lambda = 1.47$  for 3D and 2D random hopping systems, respectively [98]. However, extension of the percolation argument to hopping in energetically disordered materials is not straightforward. The reason is that, at variance with a random system of *monoenergetic* sites, in a system with energy disorder the jump rates  $v_{ij}$  and  $v_{ji}$  strongly differ from each other unless the sites  $i$  and  $j$  occasionally have the same energy [99]. As a result, the nearest-neighbor jumps are no longer dominant and the mobility is determined by the temperature-controlled trade-off between weaker activated jumps over larger distances and stronger activated jumps over smaller distances [100].

This interplay is traditionally considered in terms of the variable-range hopping theory [100]. This approach suggests that a carrier localized in a site of energy  $E$  will most probably make the fastest possible, i.e. jump to a site of energy  $E'$  over distance  $r$  characterized by the minimum possible value of the hopping parameter  $u$  [99]:

$$u(r, E, E') = 2\gamma r + \frac{\eta(E' - E)}{kT} \quad (6.9)$$

where  $\eta$  the unity step-function. The distance-dependent factor in Eq. (6.9) is completely symmetric, i.e. the distance between hopping sites similarly controls the rate of forth and back jumps. Therefore, a site that is remote from all its neighbors in a positionally random system of monoenergetic hopping sites cannot be considered as a trap for carriers because the trapping time would be equal to the release time, i.e. it is equally difficult for a carrier to be released and trapped by such an isolated localized state [47]. However, this is not the case for an energetically random system. While energetically upward jumps require thermal activation, downward jumps imply dissipation of the excess energy via phonon emission. The former takes a much longer time than the latter and, therefore, the rates of forth and back jumps are, on average, very different. This asymmetry makes the effect of energy disorder much more important as far as charge transport characteristics are concerned. If the average jump rate  $\langle v \rangle$  and distance  $\langle r \rangle$  are somehow calculated for all hopping sites of a system, one can straightforwardly calculate macroscopic carrier transport characteristics such as the mobility and diffusion coefficient. Moreover, based on the average hopping rate, derivation of hopping transport equations for macroscopic charge carrier density becomes feasible.

In order to calculate the hopping mobility in an energetically disordered system, one has first to average minimum possible values of the hopping parameter  $u$  for sites of a given energy  $E$ , which should yield the average jump rate as a function of energy,  $\langle v_E \rangle$ . This calculation can be based on the Poisson statistics as outlined below. In a positionally random system of localized states, the average number of target sites for a starting site of energy  $E$ , whose hopping parameters are not larger than  $u$ ,  $n(E, u)$ , can be calculated as [99,101]

$$n(E, u) = \frac{4\pi}{3} \left( \frac{u}{2\gamma} \right)^3 \left[ \int_{-\infty}^E dE' g(E') + \int_E^{E+kTu} dE' g(E') \left( 1 - \frac{E' - E}{kTu} \right)^3 \right] \quad (6.10)$$

By considering the number of hopping neighbors as a function of the hopping parameter and applying Poisson statistics, one can calculate the probability density  $w(E,u)$  that the nearest hopping neighbor of a site of the energy  $E$  will be characterized by the hopping parameter  $u$ . The result is

$$w(E,u) = \exp[-n(E,u)] \frac{\partial n(E,u)}{\partial u} \quad (6.11)$$

By its definition the function  $w(E,u)$  is the distribution function of the hopping parameter. Using it for the calculation of the average hopping parameter  $\langle u \rangle(E)$  yields

$$\langle u \rangle(E) = \int_0^{\infty} du u \exp[-n(E,u)] \frac{\partial n(E,u)}{\partial u} = \int_0^{\infty} du \exp[-n(E,u)] \quad (6.12)$$

It is interesting that different possible hopping regimes can be seen already in the structure of the  $n(E,u)$  function. The first integral in the right-hand side of Eq. (6.10) accounts for deeper sites whereas the second one corresponds to possible jumps to shallower states. Based on relative contributions of these terms to the total number of hopping neighbors, one can distinguish between DOS regions where either downward or upward hopping dominates at a given temperature. Depending on which portion of the DOS is mainly populated, two different transport regimes are possible. Downward hopping is typical for an earlier stage of energetic relaxation of photogenerated carriers, especially at low temperatures. Upward hopping describes both the later stage of carrier equilibration controlled by thermally activated hopping and equilibrium transport.

### 6.3.2.1 Carrier Equilibration via Downward Hopping

By its nature, equilibration of charge carriers is a non-equilibrium transient process that cannot be described in terms of (time-dependent) carrier mobility and diffusivity. One reason is that, in energetically disordered systems, the conventional Fokker–Planck-type continuity equation is valid only if energy relaxation of carriers is practically finished. This is obviously not the case for the regime of downward hopping. Another reason is that average jump distance increases in the course of energetic relaxation and so does the gain or loss of electrostatic energy in external electric field. Therefore, even a weak-to-moderate electric field will sooner or later cause a large distortion of the DOS distribution, which is equivalent to the strong-field effect in quasi-equilibrium transport.

One of the most important characteristics of the carrier equilibration process is the rate of energy relaxation, i.e. the time-dependent energy distribution of the state occupational probability  $f(E,t)$ . It can be calculated by averaging the probability density of Eq. (6.11) with the Poisson probability to still occupy at the time  $t$  a site, whose nearest neighbor has the hopping parameter  $u$ , yielding

$$f(E, t) = \int_0^{\infty} du \frac{\partial n(E, u)}{\partial u} \exp[-n(E, u)] \exp[-v_0 t \exp(-u)] \approx \exp[-n(E, \ln(v_0 t))] \quad (6.13)$$

In the regime of low-temperature downward hopping relaxation, Eq. (6.13) reduces to [102,103]

$$f(E, t) = \exp \left[ -\frac{4\pi}{3} (2\gamma)^{-3} [\ln(v_0 t)]^3 \int_{-\infty}^E dE' g(E') \right] \quad (6.14)$$

In order to calculate the density of occupied states, one has to multiply the DOS distribution by the occupational probability and normalize the product to the total carrier density. The results of this calculation for a Gaussian DOS function are shown in Fig. 6.1. With increasing relaxation time, the energy distribution of carriers shifts to deeper states and narrows although the lower tail of the distribution always follows the DOS function while the upper tail is governed by the probability for a given hopping site to be still occupied at a given time. The maximum of the carrier distribution,  $E_m(t)$ , is governed by the occupational probability given by Eq. (6.14) and can be found from the following transcendental equation:

$$\frac{4\pi}{3} (2\gamma)^{-3} [\ln(v_0 t)]^3 \int_{-\infty}^{E_m(t)} dE' g(E') = 1 \quad (6.15)$$

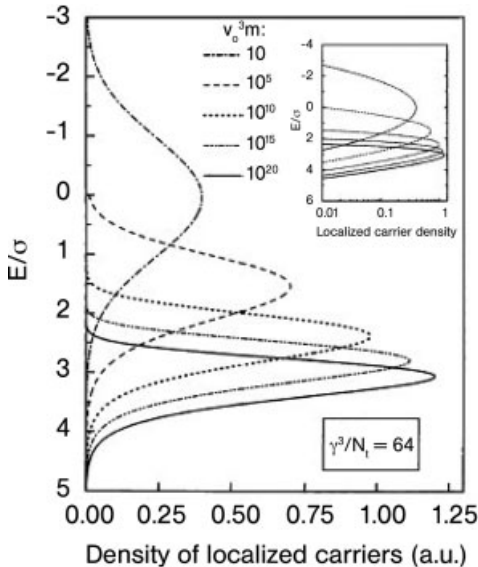


**Figure 6.1** Low-temperature energy relaxation of carriers in a random hopping system with a Gaussian DOS distribution. Whereas the lower tail of the localized carrier energy distribution always follows the DOS function, the width of the upper tail decreases with time.

Evaluating the integral in the left-hand side of Eq. (6.15) for a Gaussian DOS function and solving the transcendental equation yields

$$E_m(t) \approx \sigma \sqrt{2 \ln \left\{ \frac{N}{12\sqrt{2\pi}\gamma^3} [\ln(v_0 t)]^3 \right\}} \quad (6.16)$$

Since energy relaxation of charge carriers proceeds via carrier jumps, this process also leads to some diffusive spreading of the charge carrier packet. According to Poisson statistics, the hopping parameter  $u$ , characteristic of jumps at a time  $t$ , is given by the condition  $v_0 t \exp(-u) = 1$ , which yields the jump rate  $v = v_0 \exp(-u) = 1/t$ . The jump distance,  $r_j$ , can be estimated from the condition  $r_j(t) = u(t)/2\gamma = \ln(v_0 t)/2\gamma$ . The increased rate of carrier packet dispersion,  $d\sigma_d/dt$ , can be estimated as  $d\sigma_d/dt = vr_j^2/3 = [\ln(v_0 t)]^2/12\gamma^2 t$ . Integrating this equation yields [103]

$$\sigma_d(t) = \frac{1}{36\gamma^2} [\ln(v_0 t)]^3 \quad (6.17)$$

According to Eq. (6.17), the root-mean-square (r.m.s.) of the carrier packet,  $\sqrt{\sigma_d}$ , increases with time much more slowly than  $\sqrt{t}$  that is typical for equilibrium diffusion. The reason is that the average number of hopping neighbors accessible via downward jumps strongly decreases with relaxation time and, concomitantly, hopping slows very rapidly. On the basis of Eq. (6.17), the effective time-dependent diffusion coefficient can be introduced via  $D(t) = d\sigma_d(t)/dt$ . A common way to calculate the (time-dependent) weak-field carrier mobility would be the use of the Einstein relation. However, the Einstein relation does not work under non-equilibrium conditions [104]. Moreover, it has been shown that, at variance with carrier-packet spreading, the average weak-field carrier velocity in the downward hopping regime depends upon the DOS distribution. In a system with an exponential DOS the center of gravity of a carrier packet,  $\langle x \rangle$ , shifts along the field as [103]

$$\langle x \rangle(t) = \frac{eF}{36\gamma^2 E_0} [\ln(v_0 t)]^3 \quad (6.18)$$

where  $E_0$  is the characteristic energy of the exponential DOS. Defining the mobility as  $\mu(t) = (1/F)d\langle x \rangle(t)/dt$  yields  $\mu/D = e/E_0$  [104] instead of  $e/kT$  as predicted by the Einstein equation. This result is not really surprising because the latter was derived for equilibrium transport while the temperature cannot play any role in the low- $T$  downward hopping. It should be emphasized, however, that the validity of this expression is restricted in time because sooner or later jumps become so long that the gain in electrostatic energy on any jump substantially tilts the DOS, which leads to nonlinear field effects.

### 6.3.2.2 Thermally Activated Variable-Range Hopping: Effective Transport Energy

At a finite temperature, downward hopping of a charge carrier must be terminated at some time when the nearest hopping neighbor of this carrier will have a

larger energy and, therefore, the next jump of this carrier will require thermal activation. In order to analyze this transport regime we have to turn back to Eqs. (6.10) and (6.12). After a jump to a shallower state, a carrier will have a much wider choice of hopping sites for subsequent jumps. Therefore, energetically upward jump will constitute a rate-limiting step of the thermally activated hopping regime. By neglecting the contribution of deeper hopping neighbors in Eq. (6.10) and making the following replacement of variables:

$$E_{ir} = E + kTu \quad (6.19)$$

one can represent the average number of hopping neighbors of a site of energy  $E$  as a function of the energy  $E_{ir}$ :

$$n(E, E_{ir}) = \frac{\pi}{6} (\gamma kT)^{-3} \int_E^{E_{ir}} dE' g(E') (E_{ir} - E')^3 \quad (6.20)$$

After an upward jump, the carrier can either jump further to other sites or return back to the previously occupied state. In order to ensure further hopping, a carrier must, on average, have probed more than one hopping neighbor. As suggested by the percolation theory, further hopping is granted if more than one nearest hopping neighbor of a given hopping site is taken into consideration such that  $n(E, E_{ir}) = \beta$ , where  $\beta$  is the percolation parameter. The use of this condition in Eq. (6.20) yields the following transcendental equation for the energy  $E_{ir}$ :

$$\int_E^{E_{ir}} dE' g(E') (E_{ir} - E')^3 = \frac{6\beta}{\pi} (\gamma kT)^3 \quad (6.21)$$

If the DOS distribution decreases with energy faster than  $|E|^{-4}$  then (i) the value of the integral in the left-hand side of Eq. (6.21) depends only weakly on the lower bound of integration for sufficiently deep starting sites and (ii) a major contribution to the integral comes from states with energies around  $E_{ir}$  and, therefore, Eq. (6.21) can be reduced to [101]

$$\int_{-\infty}^{E_{ir}} dE g(E) (E_{ir} - E)^3 = \frac{6\beta}{\pi} (\gamma kT)^3 \quad (6.22)$$

The physical meaning of the effective transport level follows from this equation. It demonstrates that target sites for thermally assisted upward carrier jumps are located around the energy  $E_{ir}$ , independent of the energy of starting sites. Therefore, for any starting site the hopping parameter for the most probable jump of a carrier, occupying this site, can be calculated from Eq. (6.19). Substituting the result into the Miller–Abrahams equation for the thermally activated hopping rate, one obtains

$$v = v_0 \exp(-u) = v_0 \exp\left(-\frac{E_{tr} - E}{kT}\right) \quad (6.23)$$

which is identical with the carrier release rate in the model of trap-controlled carrier transport with the energy  $E_{tr}$  playing the role of the mobility edge. This analogy was first discovered in Monte Carlo simulations of the variable-range hopping [105] and was later demonstrated analytically [106].

The temperature dependence of the effective transport energy in a hopping system with a Gaussian DOS distribution is illustrated in Fig. 6.2 parametric in the DOS width. A remarkable feature of these results is that, at some temperature, every curve crosses the zero energy level at which the DOS has a maximum. At first glance this seems to be an artifact. Even at very high temperatures, carriers can hardly jump to states above  $E = 0$  where the density of states is relatively low and decreases steeply with increasing energy. In order to resolve this puzzle, one may consider the asymptotic behavior of  $E_{tr}$  and higher temperatures and/or low

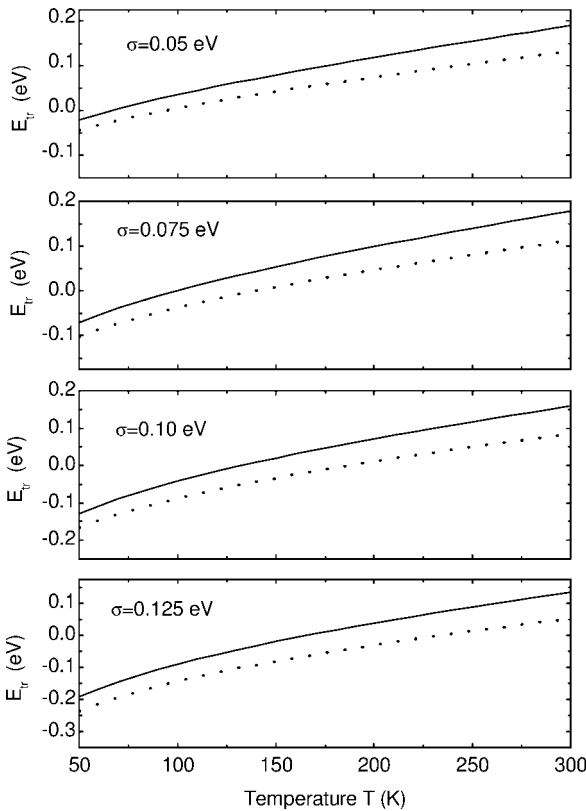


**Figure 6.2** Temperature dependence of the effective transport energy in a disordered hopping system with a Gaussian DOS distribution. The data shown by the solid and

dashed lines are calculated from Eqs. (6.47) and (6.22), respectively, for an inverse localization radius of  $10 \text{ nm}^{-1}$  and a total density of hopping sites of  $10^{22} \text{ cm}^{-3}$ .

concentration of localized states. The latter condition corresponds to strongly diluted hopping systems. Solving Eq. (6.22) at  $T \rightarrow \infty$  and/or  $N \rightarrow 0$  yields

$$E_{tr} = kT \left( \frac{6\beta\gamma^3}{\pi N} \right)^{\frac{1}{3}} \quad (6.24)$$

This result is still puzzling: the transport energy linearly increases with temperature *above* the maximum of the DOS distribution. Substituting this equation into Eq. (6.23) leads to the following high-temperature and low-concentration asymptotic expression for the hopping rate:

$$v = v_0 \exp \left[ - \left( \frac{6\beta\gamma^3}{\pi N} \right)^{\frac{1}{3}} \right] \exp \left( \frac{E}{kT} \right) \quad (6.25)$$

which clarifies the situation. Equation (6.25) proves that, on the one hand, carriers do jump to states around  $E = 0$  through barriers with thickness  $\sim N_i^{-1/3}$  and, on the other hand,  $E_{tr}$  can be interpreted as a genuine level of most probable jumps only while this energy is still well below the DOS maximum.

The similarity between the effective transport level in a disordered hopping system and the mobility edge in an amorphous material with both extended and localized states for charge carriers allows the use of trap-controlled transport formalism for the analysis of variable range hopping. In order to complete the analogy, one has to calculate the carrier mobility at the effective transport level. If a carrier currently occupies a state of energy around  $E_{tr}$ , its next jump will most probably be made to a deeper state. By estimating the average squared distance  $r_j^2$  of such a

jump as  $r_j^2 = \left[ \int_{-\infty}^{E_{tr}} dE g(E) \right]^{-\frac{2}{3}}$  and the concomitant jump rate  $v_j$  as

$$v_j = v_0 \exp \left[ -2 \left( \frac{3\beta}{4\pi} \right)^{\frac{1}{3}} \gamma r_j \right] = v_0 \exp \left\{ -2 \left( \frac{3\beta}{4\pi} \right)^{\frac{1}{3}} \gamma \left[ \int_{-\infty}^{E_{tr}} dE g(E) \right]^{-\frac{1}{3}} \right\} \quad (6.26)$$

one obtains the following expression for the diffusion coefficient  $D_{tr}$  at the effective transport level:

$$D_{tr} = v_j r_j^2 = v_0 \left[ \int_{-\infty}^{E_{tr}} dE g(E) \right]^{-\frac{2}{3}} \exp \left\{ -2 \left( \frac{3\beta}{4\pi} \right)^{\frac{1}{3}} \gamma \left[ \int_{-\infty}^{E_{tr}} dE g(E) \right]^{-\frac{1}{3}} \right\} \quad (6.27)$$

At weak and moderate electric fields the carrier mobility  $\mu_{tr}$  and diffusion coefficient  $D_{tr}$  are related by the Einstein equation which yields

$$\mu_{tr} = \frac{ev_0}{kT} \left[ \int_{-\infty}^{E_{tr}} dE g(E) \right]^{-\frac{2}{3}} \exp \left\{ -2 \left( \frac{3\beta}{4\pi} \right)^{\frac{1}{3}} \gamma \left[ \int_{-\infty}^{E_{tr}} dE g(E) \right]^{-\frac{1}{3}} \right\} \quad (6.28)$$

Equations (6.22), (6.23), (6.27) and (6.28) for the effective transport energy, thermally-activated jump rate, carrier diffusivity and mobility at the transport level, respectively, virtually reduce the variable-range hopping problem to much simpler trap-controlled band transport problem. This simplification is possible only when the hopping kinetics are fully controlled by thermally activated upward jumps, i.e. when the regime of energetically downward hopping is terminated. This happens when the most of carriers are already localized below the effective transport level, i.e. when the energy level  $E_m(t)$ , determined by Eq. (6.15), crosses the effective transport level.

### 6.3.2.3 Dispersive Hopping Transport

The onset of thermally activated hopping regime does not yet indicate that the process of carrier thermalization within an inhomogeneously broadened DOS distribution is completed. Although the hopping kinetics are controlled by carrier jumps from deeper states to the effective transport level, the carrier energy distribution continues to shift towards the deeper tail of the DOS. This transport regime is known as non-equilibrium or dispersive transport [43]. Before an equilibrium energy distribution is established most carriers occupy so-called 'currently deep traps', i.e. states from which their jumps are still unlikely at a time  $t$  [50, 107]. The density of such states,  $g_d(E, t)$ , obviously, depends upon time. In order to find this function one should again exploit the Poisson distribution of probabilities [108]. The average rate of carrier jumps from a state of energy  $E$  is given by Eq. (6.23). If this state has been occupied at the time  $t = 0$  the probability of this state still being occupied by the same carrier at a time  $t$ ,  $w(E, t)$  is given by

$$w(E, t) = \exp \left[ -v_0 t \exp \left( -\frac{E_{tr} - E}{kT} \right) \right] \quad (6.29)$$

According to its definition, the density of currently deep states can be calculated as a product of the DOS function and the probability that a state is a currently deep trap at the time  $t$ , which yields

$$g_d(E, t) = g(E) \exp \left[ -v_0 t \exp \left( -\frac{E_{tr} - E}{kT} \right) \right] \quad (6.30)$$

The occupational probability of currently deep states,  $f_d(E, t)$ , can be defined as the density of carriers, localized in these states,  $\rho_d(E, t)$ , normalized to  $g_d(E, t)$ , as

$$f_d(E, t) = \frac{\rho_d(E, t)}{g_d(E, t)} \quad (6.31)$$

Since no carrier can be released from currently deep traps, their occupancy is changed only due to carrier jumps to these states from hopping sites that belong to the effective transport level. Concomitantly, the equation for the occupational probability takes the form

$$\frac{\partial f_d(E, t)}{\partial t} = v_j \left[ \int_{-\infty}^{E_r} dE g(E) \right]^{-1} p_{tr}(t) \quad (6.32)$$

where  $p_{tr}$  is the density of carriers occupying sites at the effective transport level. Substituting Eq. (6.31) into Eq. (6.32) and integrating over time, one obtains

$$\rho_d(E, t) = v_j \left[ \int_{-\infty}^{E_r} dE g(E) \right]^{-1} g_d(E, t) \int_0^t dt' p_{tr}(t') \quad (6.33)$$

Under the dispersive transport regime, most carriers occupy currently deep traps and, therefore, integrating both sides of Eq. (6.33) over energy yields the relationship between total carrier density  $p$  and the density of carriers occupying states around  $E_r$  [50, 108]:

$$p(t) = \frac{1}{\tau(t)} \int_0^t dt' p_{tr}(t') \quad (6.34)$$

where the function  $\tau(t)$  is defined as

$$\begin{aligned} \frac{1}{\tau(t)} &= v_j \left[ \int_{-\infty}^{E_r} dE g(E) \right]^{-1} \int_{-\infty}^{E_r} dE g_d(E, t) \\ &= v_j \left[ \int_{-\infty}^{E_r} dE g(E) \right]^{-1} \int_{-\infty}^{E_r} dE g(E) \exp \left[ -v_0 t \exp \left( -\frac{E_r - E}{kT} \right) \right] \end{aligned} \quad (6.35)$$

Since all carrier jumps proceed via the effective transport level, the continuity equation for the carrier density should be written as

$$\frac{\partial p}{\partial t} + \mu_{tr} \nabla(\mathbf{F} p_{tr}) - D_{tr} \Delta p_{tr} = 0 \quad (6.36)$$

Combining Eqs. (6.34)–(6.36) and integrating over time yields the dispersive continuity equation of the form [50]

$$p(\mathbf{r}, t) + \mu_{tr} \tau(t) \nabla[\mathbf{F}(\mathbf{r}) p(\mathbf{r}, t)] - D_{tr} \tau(t) \Delta p(\mathbf{r}, t) = p(\mathbf{r}, 0) \quad (6.37)$$

where  $p(\mathbf{r},0)$  is the carrier density at  $t=0$ .

Remarkably, this *transport* equation does not contain time derivatives, implying that time dependences of all transport characteristics are fully governed by the function  $\tau(t)$ , i.e. by the DOS distribution and temperature. In order to illustrate basic features of this equation we consider non-equilibrium carrier hopping in constant electric field neglecting the space-charge effects. Solving Eq. (6.37) with the initial condition  $p(x,0) = \sigma_0\delta(x)$  yields an *exponential* rather than Gaussian shape of the carrier packet:

$$p(x,t) = \frac{\sigma_0}{\sqrt{[\mu_{tr}F\tau(t)]^2 + 4D_{tr}\tau(t)}} \times \begin{cases} \exp\left(\frac{\mu_{tr}F}{2D_{tr}} \left[ \sqrt{1 + \frac{4D_{tr}}{(\mu_{tr}F)^2\tau(t)} + 1} \right] x\right), & x \leq 0, \\ \exp\left(-\frac{\mu_{tr}F}{2D_{tr}} \left[ \sqrt{1 + \frac{4D_{tr}}{(\mu_{tr}F)^2\tau(t)} - 1} \right] x\right), & x > 0 \end{cases} \quad (6.38)$$

This solution has several distinctions as compared with normal equilibrium transport. (i) The presence of an electric field does not change the packet shape, which makes it difficult to distinguish between the drift and diffusion contributions to the carrier dynamics. (ii) The maximum of charge carrier density is stuck at the plane  $x=0$  where the carriers were initially generated. (iii) The field-assisted spreading of the carrier packet always dominates at larger times and the r.m.s. of the packet,  $x_{r.m.s.}$ , is equal to the packet mean  $\langle x \rangle$ :

$$\langle x \rangle(t) = x_{r.m.s.}(t) = \mu_{tr}F\tau(t) \quad (6.39)$$

Because of this anomalously large dispersion of the carrier packet, the non-equilibrium transport regime is commonly referred to as dispersive transport. Since, on average, carriers slow down in a constant electric field, the current, observed in a time-of-flight (TOF) experiment, decreases monotonically with time even before carriers are ejected across the back electrode which gives rise to the so-called anomalous (or dispersive) TOF current transients [109]. Although it is notoriously difficult to measure the carrier drift mobility from such data, it turned out that, under certain conditions and assumptions, the DOS distribution can be identified from the shape of the post-transit TOF current [110].

#### 6.3.2.4 Equilibrium Hopping Transport

The dispersive transport regime terminates when the majority of carriers are equilibrated and their energy distribution  $\rho_{eq}$  is determined by the Fermi–Dirac function as

$$\rho_{eq}(E) \propto \frac{g(E)}{1 + \exp\left(\frac{E - E_F}{kT}\right)} \quad (6.40)$$

where  $E_F$  is the Fermi energy. In disordered organic materials the total density of localized states is normally orders of magnitude larger than the carrier density unless the material is heavily doped. Therefore, only the very deep tail of the DOS distribution can be completely filled by carriers. Furthermore, if the DOS is Gaussian, the total density of fully occupied states below the Fermi level is *much smaller* than the total carrier density such that most carriers are localized in states above  $E_F$  and, concomitantly, their energy distribution is described by the Boltzmann statistics, which yields

$$\rho_{eq}(E) \propto g(E) \exp\left(-\frac{E}{kT}\right) \quad (6.41)$$

Below, our consideration of equilibrium hopping will be based on the Boltzmann statistics unless specified differently.

Employing the concept of effective transport energy, one can derive the following continuity equation for equilibrium hopping transport [49]:

$$\frac{\partial p(x, t)}{\partial t} + \mu_{eq} \frac{\partial}{\partial x} [F(x, t)p(x, t)] - (D_{eq} + D_f) \frac{\partial^2 p(x, t)}{\partial x^2} = 0 \quad (6.42)$$

where  $\mu_{eq}$  and  $D_{eq}$  are equilibrium hopping mobility and diffusion coefficient, respectively, and  $D_f$  is the field-assisted diffusion coefficient [49, 111]. The first two coefficients are the conventional hopping mobility and diffusivity controlled by the distribution of localized states below the effective transport level. These states virtually play the role of energetically distributed traps in the model of trap-controlled band transport. The values of  $\mu_{eq}$  and  $D_{eq}$  are determined by the following equations:

$$\mu_{eq}(T) = \mu_{tr}(v_0/v_j) \left[ \int_{-\infty}^{E_r} dE g(E) \exp\left(\frac{E}{kT}\right) \right]^{-1} \int_{-\infty}^{E_r} dE g(E) \quad (6.43)$$

$$D_{eq}(T) = D_{tr}(v_0/v_j) \left[ \int_{-\infty}^{E_r} dE g(E) \exp\left(\frac{E}{kT}\right) \right]^{-1} \int_{-\infty}^{E_r} dE g(E) \quad (6.44)$$

For a Gaussian DOS distribution, Eq. 6.43 yields the dependences of the mobility upon temperature and density of hopping sites that can be rather accurately represented in factorized form as

$$\mu = \mu_0 \exp\left(-\frac{b\gamma}{N_t^{1/3}}\right) \exp\left[-\left(\frac{c\sigma}{kT}\right)^2\right]$$

with the parameter  $b \cong 1.05$  being almost independent of the temperature and the parameter  $c$  changing from 0.59 at  $N_t = 10^{22} \text{ cm}^{-3}$  to 0.68 at  $N_t = 10^{18} \text{ cm}^{-3}$  in good quantitative agreement with the results of Monte Carlo simulations ( $c = 0.67$ ) and predictions of the effective medium model ( $c = 0.64$ ).

The occurrence of field-assisted diffusion is a remarkable feature of charge transport in disordered materials. This additional broadening of the carrier packet originates from the stochastic nature of hopping in a random system of localized states. Although variation of both the time and distance of every individual carrier jump contributes to the field-assisted diffusion, the effect of the former variation is much larger than that of the latter. Therefore, the field-assisted diffusion coefficient increases strongly with increasing energetic disorder and decreasing temperature as

$$D_f(T) = v_0 (\mu_{tr} F / v_j)^2 \left[ \int_{-\infty}^{E_{tr}} dE g(E) \right]^2 \times \left[ \int_{-\infty}^{E_{tr}} dE g(E) \exp\left(\frac{E}{kT}\right) \right]^{-3} \int_{-\infty}^{E_{tr}} dE g(E) \exp\left(\frac{2E}{kT}\right) \quad (6.45)$$

Interestingly, the coefficient  $D_f$  is universally proportional to the squared electric field independent of the DOS distribution in a particular material. It is also worth noting that, at variance with conventional diffusion, the field-assisted spreading of the carrier packet occurs only in the field direction and, since this effect is due to local stochastic variations of the hopping drift velocity, it cannot lead to carrier backflow against the external field.

### 6.3.2.5 The Effect of Backward Carrier Jumps

The approach outlined in the previous sections disregards repeated carrier jumps between two accidentally close hopping neighbors both of which are isolated from other localized states. Although such jumps can be responsible for a.c. conductivity, they do not contribute to the d.c. current. Therefore, after jumps to sites of the energy around  $E_{tr}$ , some carriers will just return to initially occupied deep states and such jumps should not be considered as jumps to the effective transport level. In order to account for this effect one must calculate the probability of a backward jump from a site of a given energy [101].

After an upward jump over the distance  $r$ , a carrier will, most probably, not return to the starting site if there is another hopping neighbor of the target site with a hopping parameter that is smaller than  $2\gamma r$  *outside* the sphere of radius  $r$  centered at the starting site. The average number of such neighbors,  $n_b(E, r)$ , increases with increasing  $E$  or  $r$  as

$$n_b(E, r) = 2\pi \int_0^r d\xi \xi^2 \int_{\arccos(\xi/2r)}^{\pi} d\vartheta \sin \vartheta \int_{-\infty}^{E+2\gamma kT(r-\xi)} dE' g(E') \\ = \frac{\pi r^3}{12} \left\{ 11 \int_{-\infty}^E dE' g(E') + \int_E^{E+2kT\gamma r} dE' g(E') \left[ 8 \left( 1 - \frac{E' - E}{2kT\gamma r} \right)^3 + 3 \left( 1 - \frac{E' - E}{2kT\gamma r} \right)^4 \right] \right\} \quad (6.46)$$

Since the round-trip carrier jumps do not contribute to transport and relaxation, only those hopping neighbors should be accounted for from which carrier jumps back to initially occupied starting sites are improbable. This condition leads to the following equation for the effective transport energy that accounts for backward carrier jumps:

$$4\pi \int_{-\infty}^{E_{tr}} dE g(E) \int_0^{(E_{tr}-E)/2\gamma kT} dr r^2 \{1 - \exp[-n_b(E, r)]\} = 1 \quad (6.47)$$

The effect of backward carrier jumps on the temperature dependence of the effective transport energy is illustrated by solid lines in Fig. 6.2 for a random hopping system with Gaussian DOS distributions of different widths  $\sigma$ . Dashed lines in this figure show the temperature dependences of the effective transport energy calculated from Eq. (6.22) without accounting for backward jumps. Evaluating the high-temperature asymptote of  $E_{tr}$  from Eq. (6.47) yields

$$E_{tr} = \left(\frac{32}{11}\right)^{\frac{1}{6}} kT \left(\frac{6\gamma^3}{\pi N}\right)^{\frac{1}{3}} \cong 1.2kT \left(\frac{6\gamma^3}{\pi N}\right)^{\frac{1}{3}} \quad (6.48)$$

indicating that the backward carrier jumps cause the genuine transport energy to be 20% higher than that calculated disregarding the possibility of backward jumps.

### 6.3.2.6 Hopping Conductivity in Doped Organic Materials

The above consideration of hopping in disordered systems pertains to situations in which a charge carrier moves within an empty density-of-states distribution.

In this section, we consider variable-range hopping at high carrier densities when the tail states of the DOS are completely filled by carriers and transport is controlled by carrier jumps from states around the Fermi level.

It will be assumed that the countercharges reside somewhere out of the hopping system. An example is an organic thin-film transistor in which high carrier density in the channel is balanced by countercharges accumulated in the gate.

Under such circumstances, the equilibrium energy distribution of carriers has to be described by the Fermi–Dirac distribution as in Eq. (6.40). The Fermi energy is related to the total carrier density,  $p$ , by the condition

$$p = \int_{-\infty}^{\infty} dE \rho_{eq}(E) = \int_{-\infty}^{\infty} \frac{dE g(E)}{1 + \exp[(E - E_F)/kT]} \quad (6.49)$$

Consideration of variable-range carrier hopping at high carrier densities can again be based on the effective transport energy concept. However, one should bear in mind that Eq. (6.22) for  $E_{tr}$  was derived for low carrier densities, i.e. disregarding the trap-filling effect. This effect can easily be incorporated if the DOS function in the integrand of Eq. (6.22) is replaced by the density of vacant sites  $g(E) - \rho_{eq}(E)$ . The result is

$$\int_{-\infty}^{E_{tr}} dE \frac{g(E)(E_{tr} - E)^3}{1 + \exp[-(E - E_F)/kT]} = \frac{6}{\pi} (\gamma kT)^3 \quad (6.50)$$

It is worth noting that, in materials with a Gaussian DOS distribution, the position of the Fermi level is not always essential for the charge transport characteristics because, under realistic conditions, the majority of charge carriers can occupy weakly filled states above the Fermi level. Therefore, the equilibrium mobility can be affected by filling of deep localized states only at sufficiently high carrier densities.

The effect of the filling on the effective transport energy in a hopping system with a Gaussian DOS distribution is illustrated in Fig. 6.3. The value of  $E_{tr}$  remains practically unaffected by filling of deep states until the total carrier density reaches 1–10% of the total density of hopping sites. Although those high doping levels can be achieved electrochemically [112], they are hardly relevant to practical device applications. At lower carrier densities one can still use the zero carrier density value of  $E_{tr}$  given by Eq. (6.22).

Since the occurrence of the effective transport energy virtually reduces the problem of variable-range hopping to the trap-controlled transport model, the weak-field equilibrium mobility  $\mu$  can be estimated as

$$\mu = \frac{ev_0}{kTp} \left[ \int_{-\infty}^{E_{tr}} dE g(E) \right]^{-\frac{2}{3}} \int_{-\infty}^{E_{tr}} \frac{dE g(E)}{1 + \exp[(E - E_F)/kT]} \exp\left(\frac{E - E_{tr}}{kT}\right) \quad (6.51)$$

in which the Fermi energy  $E_F$  is related to the total carrier density  $p$  by Eq. (6.49).

Equations (6.49)–(6.51) describe the mobility as a function of the charge carrier concentration. The calculated dependences are shown by solid lines in Fig. 6.4 together with experimental data obtained on electrochemically doped PHT films of

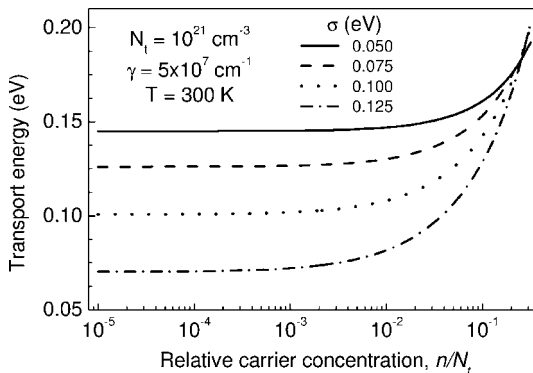


**Figure 6.3** Dependence of the effective transport energy in a disordered hopping system with a Gaussian DOS distribution on the equilibrium carrier concentration.

54, 70, 81 and 97% of regioregularity [112]. It should be noted that electrochemical doping induces both free charge carriers and immotile counterions. The effect of the latter on the DOS distribution and carrier mobility will be discussed below. In regioregular PHT, the interchain carrier jumps along the stacking direction have been suggested as a predominant conductivity mode. In terms of hopping transport, this implies the occurrence of a double-peak Gaussian distribution [113]:

$$g(E) = \frac{N_1}{\sqrt{2\pi}\sigma_1} \exp\left(-\frac{E^2}{2\sigma_1^2}\right) + \frac{N_2}{\sqrt{2\pi}\sigma_2} \exp\left(-\frac{E^2}{2\sigma_2^2}\right) \quad (6.52)$$

in which the first narrow peak describes ordered regions and the second corresponds to an amorphous phase, i.e.  $\sigma_2 \gg \sigma_1$ . For materials with relatively high degrees of regioregularity one should also assume that  $N_1 > N_2$ . At large relative densities of charge carriers, i.e. at  $n > 0.01(N_1 + N_2)$ , the agreement is very satisfactory. It is also remarkable that the experimental results for systems with different degrees of regioregularity can be fitted under the premise of an undistorted Gaussian-shaped DOS distribution. However, one has to assume unusually large widths of the DOS distribution in the disordered phase,  $\sigma_2 = 0.25\text{--}0.34\text{ eV}$ , although the parent conjugated polymer features a low degree of disorder. This indicates that the DOS distribution may deviate from Gaussian and its width must increase strongly with increasing density of charge carriers such that variations of the energy levels of the hole-transporting moieties, caused by different degrees of regioregularity, are smeared out. This effect is illustrated in Fig. 6.5, which shows the carrier-concentration dependence of the Gaussian DOS width that is required for fitting the carrier-concentration dependence of the mobility in 54% regioregularity PHT within the entire experimental range of carrier concentrations. The apparent width increases by a factor of two from 0.15 eV at low carrier concentration to 0.35 eV at  $n/N_i \approx 0.03$  and practically saturates at larger carrier densities.

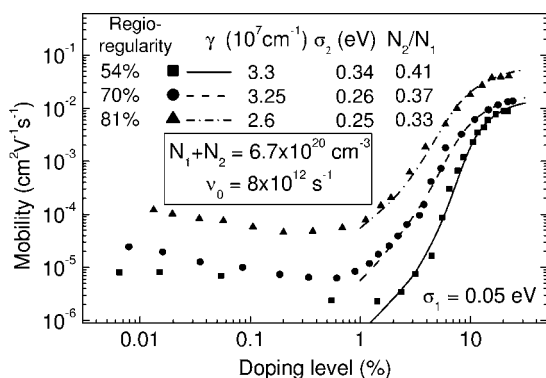


**Figure 6.4** Dependence of the equilibrium hopping mobility on the dopant concentration in a disordered organic semiconductor. Experimental points are taken from Ref. [112].

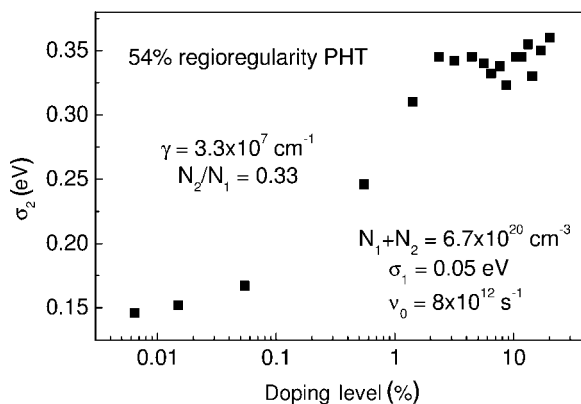


**Figure 6.5** Variation of the apparent DOS width required for the fit of the experimentally observed dopant concentration dependence of the mobility shown in Fig. 6.4.

These results imply a very strong effect of the Coulomb interactions on the energy disorder in doped organic semiconductors. It was already recognized that the dipole–dipole interaction between randomly located and oriented dipoles is one of the major causes of energy disorder in organic materials [82]. Increasing regioregularity can suppress this type of disorder and, concomitantly, improve the mobility at low carrier concentrations as one can see from Fig. 6.4. However, a higher density of randomly distributed ionized dopants generates a random Coulomb potential distribution, which effectively broadens the DOS distribution. This effect occurs together with filling of deep traps. At relatively low carrier densities the Coulomb DOS broadening dominates while most carriers still occupy sites above the Fermi level. Under these conditions, the mobility decreases with increasing carrier concentration. At higher carrier densities the Coulomb-induced DOS broadening almost saturates while the energy distribution of localized carriers becomes shallower, which leads to a higher average jump rate and steeply increasing mobility with further increase in carrier density. The effect on the hopping mobility of the Coulomb interaction between ionized dopants and charge carriers will be considered in the following section.

### 6.3.2.7 Coulomb Effects on Hopping in a Doped Organic Material

Experimentally, it is known that an impurity can serve as, for instance, an electron acceptor in an organic semiconductor even if the LUMO of the dopant is  $\sim 1$  eV above the HOMO of the host molecules. Intuitively, it is not clear how the charge transfer can occur from a host molecule to a dopant under such circumstances. In order to clarify the situation one should bear in mind that both HOMO and LUMO energies are defined for isolated charges disregarding Coulomb interactions and/or intrinsic fields. However, in amorphous organic materials, charge transfer from a host molecule to a dopant should directly produce a strongly Cou-

lombically bound short geminate pair rather than a free carrier. The size of such a pair is equal to the intermolecular distance, which is typically 0.6–1.0 nm. The Coulomb binding energy of this pair is then 0.5–0.8 eV if the permittivity retains its typical macroscopic value of 3 and 0.8–1.2 eV if the permittivity goes down to 2 at such short distances. If this energy gain is sufficient to compensate for the charge-transfer energy, the geminate pair of charges rather than a neutral dopant and a neutral host molecule will form the ground state in a doped material.

Even if a carrier has been transferred from a dopant to a host molecule, it cannot immediately contribute to the d.c. conductivity owing to the Coulomb interaction that still bounds it to the parent dopant ion. A carrier can be released from a Coulomb trap in the course of a multi-jump Onsager-like process facilitated by the external electric field. Exact analytical consideration of this process, including correlations between energies and positions of hopping sites within Coulomb potential wells, is hardly feasible and one has to formulate a simplified model that still retains essential details of the carrier kinetics. We suggest a model based on the following simplifications: (i) every collective Coulomb trap surrounding a localized counter ion is replaced by a single deep localized state nearest to the ionized dopant and (ii) the energy of this site is a sum of the intrinsic disorder energy and the electrostatic energy  $\Delta$  counted from the top of the potential barrier which is formed by the Coulomb and external fields as

$$\Delta = \sqrt{\frac{e^3 F}{\pi \epsilon_0 \epsilon}} - \frac{e^2}{4\pi \epsilon_0 \epsilon a} \quad (6.53)$$

Under these assumptions, the effective DOS distribution in a doped material takes the form

$$g(E) = \frac{N_i - N_d}{N_i} g_i(E) + \frac{N_d}{N_i} g_i \left( E + \frac{e^2}{4\pi \epsilon_0 \epsilon a} - \sqrt{\frac{e^3 F}{\pi \epsilon_0 \epsilon}} \right) \quad (6.54)$$

If not specified otherwise, in the following we assume that the material is macroscopically neutral, i.e. that the average density of carriers is equal to the concentration of dopants. The field dependence of the mobility, calculated with the DOS distribution given by Eq. (6.54) at a moderate concentration of dopants  $N_d = 10 \text{ cm}^{-3}$ , is shown in Fig. 6.6 parametric in temperature. A Gaussian distribution of the width  $\sigma = 100 \text{ meV}$  has been used as an intrinsic DOS distribution. Although the curves follow the Poole–Frenkel-type  $\log \mu \propto F^{1/2}$  dependence, at weaker fields they tend towards saturation at stronger fields. Figure 6.7 illustrates the temperature dependence of the mobility at different external fields. Although both the doping-induced Coulomb traps and the intrinsic DOS distribution affect this dependence, most carriers are localized in the former, which gives rise to an almost perfect Arrhenius temperature dependence with the slope affected by the external field. As shown in the inset in Fig. 6.7, an attempt to visualize these data on a  $\log \mu$  versus  $1/T^2$  plot fails to yield straight lines, indicating that the mobility

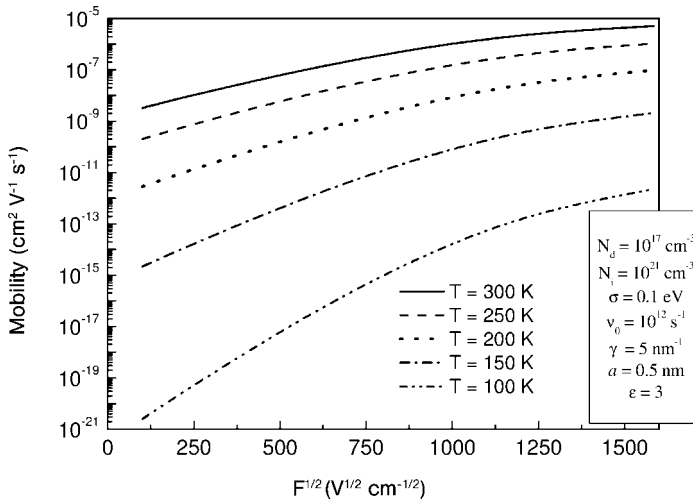


**Figure 6.6** Field dependences of the charge carrier mobility in a doped disordered organic semiconductor at different temperatures.

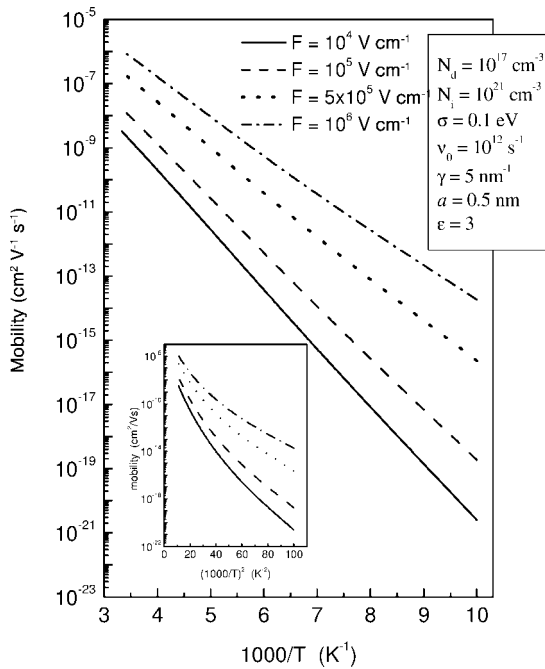


**Figure 6.7** Temperature dependence of the mobility in a doped disordered organic material. The inset shows the same set of curves replotted in  $\log u$  versus  $1/T^2$  axes.

is effectively controlled by carrier jumps from states around the Fermi level [114–116]. One should expect that, at lower temperatures, the effective transport level should approach the Fermi level and the temperature dependence of the mobility has to almost level off featuring the Mott  $T^{-1/2}$  law.

Figure 6.8 illustrates the dopant concentration dependence of the mobility parametric in the width of the intrinsic Gaussian DOS distribution. These dependences are strikingly different in materials with weak and strong energy disorder, i.e. with small and large values of the DOS width. While doping a weakly disordered system suppresses the mobility, the latter increases with doping level in strongly disordered materials. It should be noted, however, that the mobility always decreases with doping more weakly than  $1/N_d$  and, therefore, the conductivity, which is proportional to the product of  $\mu$  and  $N_d$ , increases upon doping even in materials with small DOS widths.

In order to understand why the mobility in weakly and strongly disordered materials is so differently affected by doping, one should bear in mind that dopants provide both charge carriers and deep Coulomb traps. If these traps are deeper than those states that control the mobility in the pristine material, the deep Coulomb traps will still trap majority of doping-induced carriers and their mobility has to be smaller than the carrier mobility in the undoped material. The electrostatic energy of a Coulomb trap can be estimated from Eq. (6.53) as 0.5 eV in a field of  $1 \text{ MV cm}^{-1}$  with  $a = 0.5 \text{ nm}$  and  $\epsilon = 3$ . However, the effective depth of a Coulomb trap is smaller because carriers can escape from this trap by jumps via localized states with energies below the maximum of the DOS distribution [103, 105, 106, 115]. The activation energy of the mobility can be estimated from the curves plotted in Fig. 6.7 and for the field of  $1 \text{ MV cm}^{-1}$  this energy is only 0.36 eV.

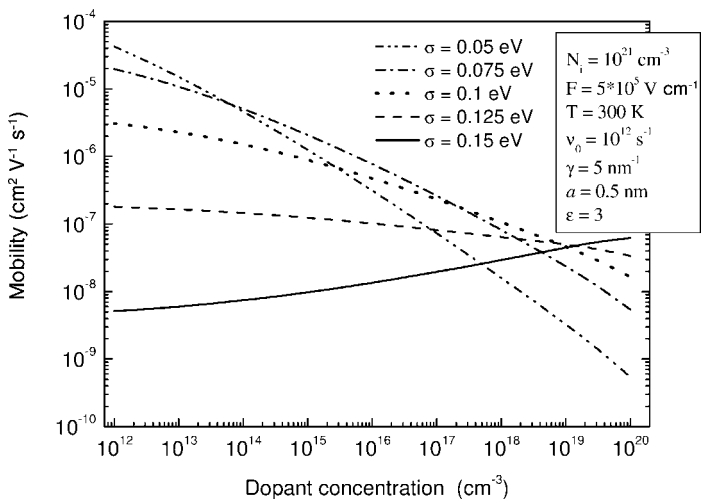


**Figure 6.8** Dependence of the carrier mobility on the concentration of dopants in materials with different variations of the intrinsic DOS distribution.

In a pristine material with a Gaussian DOS the distribution of localized carriers has a maximum at the energy  $E_m$  of  $\sigma_i^2/kT$  below the maximum of the intrinsic DOS function. In a strongly disordered material with  $\sigma_i = 120$  meV, the energy  $E_m$  is as large as 0.6 eV at room temperature. This energy is larger than the activation energy of the Coulomb traps and carriers can easily leave the latter and fill the deep tail of the intrinsic DOS at energies below and *above*  $E_m$ . Concomitantly, the Fermi level elevates which leads to increasing mobility upon doping. In other words, disordered organic materials can be efficiently doped by introducing virtually deep Coulomb traps because free equilibrated carriers fill states in the deep tail of the intrinsic DOS distribution that are even deeper than the Coulomb traps. It should also be noted that, at high doping levels, Coulomb potential wells of neighboring dopants strongly overlap, which leads to smoothing of the potential landscape. Under such circumstances, the effect of trap filling takes over and the mobility steeply increases even in weakly intrinsically disordered materials [112, 114].

If the activation energy of the dopant-induced Coulomb traps is larger than  $E_m$ , most doping-induced carriers are still localized within Coulomb potential wells of ionized dopants and in the deep tail states *below*  $E_m$ . The dominant effect of doping is then creation of additional deep states in the DOS and, concomitantly, the mobility decreases with increasing  $N_d$ . However, this decrease is weaker than  $1/N_d$  and the conductivity, determined by the product of the mobility and carrier density, still increases with increasing dopant concentration.

It is known from both experimental studies and theoretical considerations that the mobility must strongly increase at high doping levels [105, 114, 116]. However, this effect cannot be analyzed within the framework of the present model because the latter is valid only at relatively low doping levels when the Coulomb potential

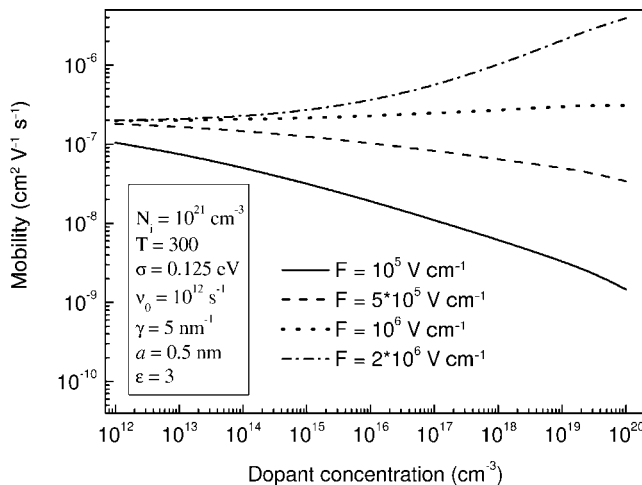


**Figure 6.9** Dependence of the carrier mobility on the concentration of dopants at different external fields.

wells of ionized dopants do not overlap. The increase of the mobility at high values of  $N_d$  is associated with filling of deep tail states by carriers. This is possible only if adding new dopants do not create new deep Coulomb traps, which is the case at very high dopant concentration when Coulomb potential wells already strongly overlap and additional ionized dopants smoothen rather than roughen the potential landscape [114].

Since the effective depth of Coulomb traps is controlled by the external field, one should expect different dopant-concentration dependences of the mobility at weak and strong electric fields. This effect is illustrated in Fig. 6.9. Indeed, at weak external fields, Coulomb potential wells are deep and ionized dopants serve as deep traps for carriers. Strong external fields reduce the barrier for carrier release from Coulomb traps, making them shallower, and, thereby, increasing the density of free carriers and the average carrier mobility. It is interesting that the effect of the external field on the effective depth of a Coulomb trap does not depend upon the field direction. Therefore, carriers in the channel of an organic FET should not experience the Coulomb trapping by dopant ions due to a strong vertical field and their mobility along the channel should increase with doping level even if the lateral field is weak.

It should be noted that the results discussed above were obtained under the assumption that the density of charge carriers is equal to the density of dopants, i.e. that the field-driven carrier ejection from a sample is fully compensated by charge injection and vice versa. This condition can be violated if a blocking contact is used, which is typical for the TOF measurements. Upon application of an external electric field, all mobile carriers will sooner or later be extracted from the sample and only Coulomb traps surrounding counter ions will remain in the bulk. In a heavily doped material this will result in the formation of a zone at the blocking

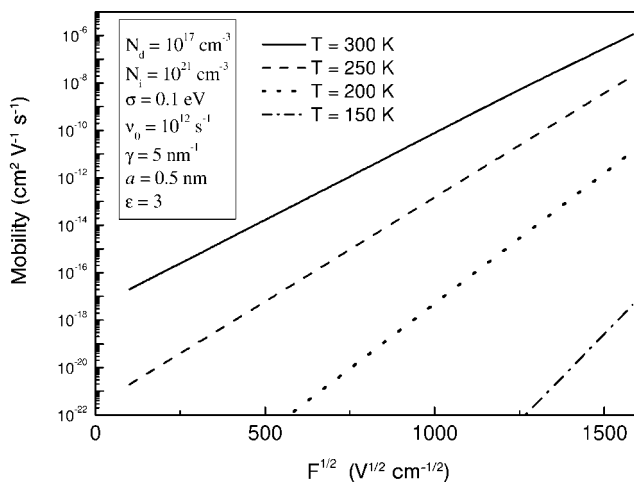


**Figure 6.10** Field dependences of the single-carrier (TOF) carrier mobility in a doped disordered organic material at different temperatures.

contact that is depleted of mobile carriers. However, in an accidentally doped (apparently pristine) material with a low density of dopant ions, the field can still remain almost constant. In order to simulate the TOF mobility, measured in such samples, one has to use the DOS distribution given by Eq. (6.54) and assume the density of photogenerated carriers much smaller than the dopant concentration. The use of this model yields the mobility that is orders of magnitude smaller than at higher carrier densities and reveals a perfect Poole–Frenkel field dependence within the entire field range, as illustrated in Fig. 6.10. This result offers a plausible explanation of the notorious difference [114, 116] between both the magnitudes and field dependences of the field-effect and space-charge limited current mobility on the one hand and the mobility measured in TOF experiments on the other.

### 6.3.3

#### Effective-Medium Approximation Theory of Hopping Charge-Carrier Transport

Effective medium approximation (EMA) theories attempt to identify self-consistently an ordered system having the same macroscopic transport properties as the actual disordered system under study. They have been applied to the study of electronic processes in different solids such as polycrystalline materials and disordered materials. The basis of the continuum EMA theory was set in the 1930s in order to describe conductivity in classical binary random mixtures and subsequently this approach has attracted a considerable attention [117]. The classical mixture model assumes a random mixture of conducting and isolating materials whose conductivity is described by classical charge transport theories. The fundamental idea of the EMA is to determine the electric field in a representative small element of the material, which is embedded in an *effective medium* with still unknown conductivity. By setting the averaged deviation from the true conductivity to be zero, the effective conductivity can be determined. Hence the effective medium is considered as homogeneous and the field inside the medium is equal to the average external field. Let us assume that  $\sigma_e$  is the effective conductivity as derived by the EMA for a random mixture consisting of spherical particles and consider a sphere of conductivity  $\sigma_i$  with the electrical field  $\mathbf{F}_i$  inside the sphere embedded in an infinite medium of effective conductivity  $\sigma_e$  under an applied uniform electric field  $\mathbf{F}_0$ . The effective value  $\sigma_e$  must be determined by the condition that the ensemble-averaged value  $\delta\mathbf{F}_i = \mathbf{F}_i - \mathbf{F}_0$  vanishes ( $\langle\delta\mathbf{F}_i\rangle = 0$ ). The assumption of the EMA and the ergodic hypothesis, which assumes that an ensemble average can be replaced by a spatial average, yields an equation for the electric field in the mixture, from which it follows that  $\langle(\sigma - \sigma_e)/(\sigma + 2\sigma_e)\rangle = 0$ , where the angular brackets denote the spatial averaging.

The best verification of an analytical theory is a direct comparison with computer simulation results as the simulation actually solves the model as it stands whereas a real experiment can include processes not accounted for. It was found that the EMA predicts successfully the effective conductivity in binary mixtures, with the exception of the vicinity of percolation threshold where the approxima-

tion method breaks down and one should rather use either a percolation-type theory or a higher degree of approximations within the EMA method.

Later, the EMA method was used to describe hopping conductivity in disordered inorganic and organic semiconductors with localized electronic states [77, 78, 118–120] and hereafter we shall focus on results relevant to amorphous organic solids. In the simplest case, a disordered system is modeled by a cubic isotropic lattice consisting of point-like localized sites randomly distributed in energy and randomly displaced from their positions in the lattice sites. Hopping transitions with the jump rate  $W_{ij}$  are conventionally considered only between nearest-neighbor hopping sites.

The jump rate  $W_{ij}$  between hopping sites is usually described by the Miller–Abrahams (MA) formalism for materials with a weak electron–phonon coupling (single-phonon approximation) or by the Marcus jump rate equation when polaron effects are important (multi-phonon approximation). As was discussed in preceding sections, the energy of hopping sites in a disordered organic solid is subject to random variation generally described by a Gaussian distribution with a width  $\sigma$ . The energy disorder leads to an asymmetric energy-dependent jump rate  $W_{ij} \neq W_{ji}$ , whereas earlier developments in the EMA method mainly concerned a symmetrical jump rate  $W_{ij} = W_{ji} = W$ . In the latter case, the randomization of  $\Omega$  is governed by the positional disorder and the effective jump rate  $W_e$  at  $F_0 \rightarrow 0$  is determined by the well-known equation  $\langle (W - W_e)/(W + 2W_e) \rangle = 0$ , which, by the way, resembles the above-mentioned equation for the effective conductivity  $\sigma_e$ . Here the angular brackets denote the positional configurational averaging. Calculation of  $W_e$  becomes considerably more complicated at strong electric fields. The hopping conductivity in the presence of a strong electric field (field dependence of  $W_e$ ) was first studied by Böttger and Bryksin [118], who developed a simple (single-parameter) EMA theory that accounted for only the positional disorder and were able to show a negative differential drift velocity, i.e. a region for which the drift velocity decreased with increasing electric field. A more general, fully self-consistent EMA theory was suggested by Parris and Bookout [121] and allowed three independent parameters, but it failed to predict the negative differential drift velocity, even though that computer simulation studies did reveal such an effect in materials with positional disorder. It was therefore concluded that EMA theories based on idea of embedding a single bond defect in an otherwise uniform system are not able to reproduce the negative differential mobility in positionally disordered systems.

Movaghar and co-workers [77, 78, 119, 120] developed an EMA theory based on the MA equation for the jump rate to describe conductivity, energy- and time-dependent diffusivity and energy relaxation of excitations by accounting for solely the energetic disorder. The theoretical results were found to be in good agreement with computer simulation data on the time dependence of the energy relaxation of excitations over a broad temperature range except at very low temperatures where the EMA theory overestimates the decay channels available for every jump. In this case, as in the vicinity of the percolation threshold, one should use percolation-type theories or higher approximations within the EMA method. It turned

out that the conventional two-site cluster EMA is not sufficient for an adequate description of the drift mobility, while accounting for contributions from the clusters containing more than two sites (closed-loop contribution) to the effective drift mobility  $\mu_e$  [77, 120] led to an equation for the temperature dependence of mobility similar to that obtained by computer simulation studies,  $\mu_e = \mu_0 \exp[-(2\sigma/3k_B T)^2]$ .

Recently, the application of EMA method was extended further by Fishchuk et al [122, 123] to describe various aspects of non-dispersive charge transport in disordered organic materials using the MA and the Marcus jump rates and the results are discussed below. The theory is shown to be readily applicable to relevant experiments.

### 6.3.3.1 The EMA Theory Formulations

As shown in the Section 6.2.2, one can use the hopping master equation to describe the occupational density  $\rho_i$  of a site  $i$  ( $\rho_i \ll 1$ ) in a hopping transport system with localized states:

$$\frac{d\rho_i}{dt} = \sum_j W_{ji}\rho_j - \rho_i \sum_j W_{ij} \quad (6.55)$$

where  $W_{ij}$  is a jump rate between sites  $i$  and  $j$ . Under thermodynamic equilibrium, which occurs in the nondispersive charge carrier transport regime, we have  $d\rho_i/dt = 0$ .

Let us replace in this case the disordered medium by some effective ordered medium (cubic lattice with spacing  $a$ ), where all  $W_{ij}$  are replaced by the effective hopping rate  $W_e$  and all  $\rho_i$  by uniform value  $\rho_0$ . The effective value  $W_e$  must be determined by the condition that the configuration-averaged value of  $\delta\rho_i = \rho_i - \rho_0$  vanishes ( $\langle\delta\rho_i\rangle = 0$ ) when any  $W_e$  in an effective medium is replaced by the random  $W_{ij} \neq W_{ji}$  for any neighboring sites along one of cubic axes. Such calculations in the two-site approximation yield [122, 123]

$$\left\langle \frac{W_{12} - W_e}{\frac{W_{12} + W_{21}}{2} + 2W_e} \right\rangle = 0, \quad \left\langle \frac{W_{21} - W_e}{\frac{W_{12} + W_{21}}{2} + 2W_e} \right\rangle = 0 \quad (6.56)$$

In the case when only positional disorder (different  $r_{ij}$ ) is present but the energetic disorder is neglected ( $\varepsilon_1 = \varepsilon_2$ ), so that  $W_{12} = W_{21} = W$ , Eq. (6.56) reduces to the well-known form  $\langle(W - W_e)/(W + 2W_e)\rangle = 0$ . Then one needs to choose a certain form of  $W_{12}$  and  $W_{21}$ . If the configuration averaging in both Eqs. (6.56) is done correctly then one must obtain the same value of  $W_e$  from both equations. As was shown in Ref. [122], one needs to average the energy of the starting state and the target state over the asymptotic occupational density of states (ODOS) and over the DOS, respectively, in both Eqs. (6.56).

To generalize both Eqs. (6.56) to the case of arbitrary electric fields, one can use [123] the procedure developed by Parris and Bookout [121], where the full self-consistency was performed by EMA to calculate kinetic characteristics of a disordered system for arbitrary electric fields. In our case, the full self-consistency under the electric field,  $F$ , directed along the  $OX$ -axis leads to the following set of equations [123]:

$$\left\langle \frac{W_{12}^+ - W_e^+}{Q} \right\rangle = 0, \left\langle \frac{W_{21}^- - W_e^-}{Q} \right\rangle = 0, \left\langle \frac{W_{12} - W_e}{\frac{W_{12} + W_{21}}{2} + \left(\frac{1}{M} - 1\right) W_e} \right\rangle = 0 \quad (6.57)$$

where

$$Q = W_e + \left( \frac{W_{12}^+ + W_{21}^- - W_e^+ + W_e^-}{2} \right) M_1 + \left( \frac{W_{12}^- - W_{21}^+ - W_e^+ - W_e^-}{2} \right) M_2 \quad (6.58)$$

$$M = \frac{1}{(2\pi)^3} \int d\Omega_{\mathbf{k}} (1 - \cos k_y) \frac{F_1}{F_2} \quad (6.59)$$

$$M_1 = \frac{1}{(2\pi)^3} \int d\Omega_{\mathbf{k}} (1 - \cos k_x) \frac{F_1}{F_2}, M_2 = \frac{\delta}{(2\pi)^3} \int d\Omega_{\mathbf{k}} \sin^2 k_x \frac{1}{F_2} \quad (6.60)$$

$$F_1 = \eta(1 - \cos k_x) + (1 - \cos k_y) + (1 - \cos k_z), F_2 = F_1^2 + \delta^2 \sin^2 k_x \quad (6.61)$$

$$\eta = \frac{W_e^+ + W_e^-}{2W_e}, \delta = \frac{W_e^+ - W_e^-}{2W_e} \quad (6.62)$$

The set of three Eqs. (6.57) allow the calculation of three effective parameters,  $W_e^+$ ,  $W_e^-$  and  $W_e$ , which describe the effective drift velocity along, opposite to and normal to the electric field direction, respectively. For zero field  $F \rightarrow 0$  one obtains the set of Eqs. (6.56). However, calculation of the above effective parameters for arbitrary fields by Eqs. (6.57) is a very complicated task. Therefore, we shall restrict our considerations to the ranges of relatively weak and strong electric fields where the effective values can be calculated.

### 6.3.3.2 Miller–Abrahams Formalism

As mentioned above, the Miller–Abrahams (MA) jump rate [70] has been used extensively to interpret hopping transport in disordered organic solids. The key point of the MA model is an expression to describe an intersite jump rate  $W_{ij}$  for a charge carrier between sites  $i$  and  $j$  in the single-phonon approximation. It assumes a weak overlap of the electronic wavefunction between neighboring hopping sites  $i$  and  $j$  with energy  $\varepsilon_i$  and  $\varepsilon_j$  at the intersite distance  $r_{ij} = |\mathbf{r}_{ij}|$ , so that  $|\varepsilon_j - \varepsilon_i| \gg 2I_{ij}$ , where  $I_{ij} = I_0 \exp(-r_{ij}/b)$  is the integral of overlap and  $b$  is the

localization radius of a charge carrier. The principal result of the original paper by Miller and Abrahams [70] to determine jump rates in the case of uncorrelated site energies and arbitrary spacing  $\varepsilon_j - \varepsilon_i$  can be written as

$$W_{ij} = W_1 \frac{k_B T}{\hbar} \frac{\frac{|\varepsilon_j - \varepsilon_i|}{2k_B T}}{\sinh\left(\frac{|\varepsilon_j - \varepsilon_i|}{2k_B T}\right)} e^{-\frac{\varepsilon_j - \varepsilon_i}{2k_B T}} \quad (6.63)$$

where  $W_1 = A(k_B T/\hbar) \exp(-2a/b)$  and  $A$  is a constant. In the case of moderate-to-large degree of the energetic disorder, when  $|\varepsilon_j - \varepsilon_i| \gg 2k_B T$ , Eq. (6.63) reduces to

$$W_{ij} = W_2 \exp\left[-\frac{|\varepsilon_j - \varepsilon_i| + (\varepsilon_j - \varepsilon_i)}{2k_B T}\right] \quad (6.64)$$

where  $W_2 = v_0 \exp(-2a/b)$  and  $v_0 = A|\overline{\varepsilon_j - \varepsilon_i}|/\hbar$ . Here  $|\overline{\varepsilon_j - \varepsilon_i}|$  is the average energy spacing of sites  $i$  and  $j$ . It should be mentioned that only Eq. (6.64) for the inter-site jump rates has been commonly used in analytical theories and also in computer simulations of charge carrier transport in disordered organic systems in the framework of the MA formalism. Hereafter we shall refer all results obtained by using Eq. (6.63) as *approach I* and results obtained from Eq. (6.64) as the (approximate) *approach II*.

### 6.3.3.3 Temperature Dependence of the Drift Mobility

In this section, we consider the temperature dependence of charge carrier drift mobility using the MA jump rate within the above-mentioned *approaches I* and *II*. In the case of *approach I*, the jump rates  $W_{12}$  and  $W_{21}$  can be obtained from Eq. (6.63). Then, assuming  $(W_{12} + W_{21})/2W_1 \geq 1$  and in the case of large degree of the energetic disorder from the Eq. (6.56) one obtains

$$X_e = \left\langle \frac{\exp\left(-\frac{\varepsilon_2 - \varepsilon_1}{2k_B T}\right)}{\cosh\left(\frac{|\varepsilon_2 - \varepsilon_1|}{2k_B T}\right)} \right\rangle \left/ \left\langle \frac{\tanh\left(\frac{|\varepsilon_2 - \varepsilon_1|}{2k_B T}\right)}{\frac{|\varepsilon_2 - \varepsilon_1|}{2k_B T}} \right\rangle \right. \quad (6.65)$$

where  $X_e = W_e/W_1$  and  $\varepsilon_1$  and  $\varepsilon_2$  are the energies of the starting and target state, respectively. The ODOS and DOS distributions are assumed to be Gaussians with variance  $\sigma$  in forms

$$P(\varepsilon_1) = \left(1/\sigma\sqrt{2\pi}\right) \exp\left\{-\frac{1}{2}[(\varepsilon_1 - \varepsilon_0)/\sigma]^2\right\}$$

and

$$P(\varepsilon_2) = \left(1/\sigma\sqrt{2\pi}\right) \exp\left\{-\frac{1}{2}(\varepsilon_2/\sigma)^2\right\}$$

where  $\varepsilon_0 = -\sigma^2/k_B T$ . After performing the configuration averaging in Eq. (6.65), one obtains

$$X_e = \frac{i_0}{i_1} \quad (6.66)$$

where

$$i_0 = \frac{1}{2\pi} \int_{-\infty}^{\infty} dt_1 \int_{-\infty}^{\infty} dt_2 \varphi_0(t_1, t_2) \exp\left[-(t_2 - t_1) \frac{x}{2}\right], \quad (6.67)$$

$$i_1 = \frac{1}{2\pi} \int_{-\infty}^{\infty} dt_1 \int_{-\infty}^{\infty} dt_2 \frac{\varphi_0(t_1, t_2)}{\varphi_1(t_1, t_2)}$$

Here

$$\varphi_0(t_1, t_2) = \frac{\exp\left\{-\frac{1}{2}[(t_1 + x)^2 + t_2^2]\right\}}{\cosh\left(|t_2 - t_1| \frac{x}{2}\right)}, \quad \varphi_1(t_1, t_2) = \frac{|t_2 - t_1| \frac{x}{2}}{\sinh\left(|t_2 - t_1| \frac{x}{2}\right)} \quad (6.68)$$

Assuming the validity of Einstein's law relating the drift charge carrier mobility  $\mu_e$  to the effective diffusivity  $D_e = a^2 W_e$  for a disordered organic system,  $\mu_e = ea^2 W_e/k_B T = \mu_1 X_e$  and  $\mu_1 = A(ea^2/\hbar) \exp(-2a/b)$  is obtained, where  $\mu_1$  is a temperature-independent parameter.

Let us consider *approach II*. In this case  $W_{12}$  and  $W_{21}$  can be obtained from Eq. (6.64). Then, assuming  $\frac{1}{2} < (W_{12} + W_{21})/2W_2 < 1$ , from Eq. (6.56) one can obtain a simplified expression for  $Y_e$ :

$$Y_e = \left\langle \frac{\exp\left(-\frac{\varepsilon_2 - \varepsilon_1}{2k_B T}\right)}{\cosh\left(\frac{|\varepsilon_2 - \varepsilon_1|}{2k_B T}\right)} \right\rangle \left/ \left\langle \frac{\exp\left(\frac{|\varepsilon_2 - \varepsilon_1|}{2k_B T}\right)}{\cosh\left(\frac{|\varepsilon_2 - \varepsilon_1|}{2k_B T}\right)} \right\rangle \right. \quad (6.69)$$

where  $Y_e = W_e/W_2$ . Performing the configuration averaging as in the *approach I*, yields

$$Y_e = \frac{i_0}{i_2} \quad (6.70)$$

where  $i_0$  is determined by Eq. (6.67) and  $i_2$  by

$$i_2 = \frac{1}{2\pi} \int_{-\infty}^{\infty} dt_1 \int_{-\infty}^{\infty} dt_2 \frac{\varphi_0(t_1, t_2)}{\varphi_2(t_1, t_2)}, \quad \varphi_2(t_1, t_2) = \exp\left(-|t_2 - t_1| \frac{x}{2}\right) \quad (6.71)$$

If we take into account that  $\cosh(|t_2 - t_1|x/2) \exp(-|t_2 - t_1|x/2) \cong 1$ , we obtain the approximate expression  $Y_e = \langle W_{12} \rangle / W_2$  [122]

$$Y_e = \frac{1}{\sqrt{\pi}} \int_{-\infty}^{\infty} dt e^{-t^2} \left[ 1 + \operatorname{erf} \left( t - \frac{1}{\sqrt{2}} x \right) \right] \quad (6.72)$$

where  $\operatorname{erf}(x) = (2/\sqrt{\pi}) \int_0^x dt e^{-t^2}$  is the error function. In this case the effective drift mobility  $\mu_e/\mu_0 = Y_e$ , where  $\mu_0 = (ea^2\nu_0/k_B T) \exp(-2a/b)$  is a temperature-dependent parameter. The results for  $X_e$  and  $Y_e$  obtained in the framework of *approaches I and II*, respectively, are valid for small values of  $\sigma/k_B T$  only, i.e. when the two-site cluster approximation is adequate.

In the case of large values of  $\sigma/k_B T$ , one can use a simple method to calculate  $\mu_e$  within the framework of the present EMA theory suggested in Ref. [123]. It assumes that charge carrier transport occurs only via thermal excitation of a carrier to the effective transport energy level [106, 113, 115]  $\varepsilon_{tr}$ . The  $\varepsilon_{tr}$  level within the Gaussian-shaped DOS [cf. function  $P(\varepsilon_2)$ ] can be calculated from the equation  $\int_{-\infty}^{\varepsilon_{tr}} P(\varepsilon_2) d\varepsilon_2 = p_c$ , where  $p_c$  is the site percolation threshold. For a three-dimensional hopping system  $p_c = 0.312$  and  $\varepsilon_{tr} \cong -\sigma/2$  are obtained. Adopting this concept and using the Gaussian distribution for the starting ODOS states  $P(\varepsilon_1)$  and the function  $P(\varepsilon_2) = \delta(\varepsilon_2 - \varepsilon_p)$  for target states, one obtains

$$Y_e = \frac{i'_0}{i''_1} \quad (6.73)$$

where

$$i'_0 = \frac{1}{\sqrt{2\pi}} \int_{-\infty}^{\infty} \varphi(t) \frac{\exp(t\frac{x}{2})}{\cosh(t\frac{x}{2})} dt, \quad i''_1 = \frac{1}{\sqrt{2\pi}} \int_{-\infty}^{\infty} \varphi(t) \frac{\exp(|t|\frac{x}{2})}{\cosh(t\frac{x}{2})} dt \quad (6.74)$$

$$\varphi(t) = \exp \left[ -\frac{1}{2} (t - c + x)^2 \right], \quad c = -\frac{\varepsilon_{tr}}{\sigma} = \frac{1}{2} \quad (6.75)$$

If for  $i'_0$  and  $i''_1$  one uses the simplification  $\cosh(tx/2) \cong \exp(|t|x/2)$ , then  $Y_e$  reads

$$Y_e = \frac{1}{2} \left\{ e^{-\frac{1}{2}x^2 + cx} \left[ 1 - \operatorname{erf} \left( \frac{c}{\sqrt{2}} \right) \right] + \left[ 1 - \operatorname{erf} \left( \frac{x-c}{\sqrt{2}} \right) \right] \right\} \quad (6.76)$$

Using the expression for  $Y_e$  under the condition  $x \gg 1$ , one obtains

$$\mu_e \cong \frac{1}{2} \mu_0 \exp \left[ -\left( \frac{\sqrt{2}}{2} \frac{\sigma}{k_B T} \right)^2 \right] \quad (6.77)$$

Figure 6.11 presents the temperature dependence of the effective mobility calculated within *approach I* [123] for a weak (curve 3) and strong energetic disorder (curve 1), while the results of calculation within the approximated *approach II* are given by curves 4 and 2. Curves 2, 3 and 4 in Fig. 6.11 were calculated with Eqs.

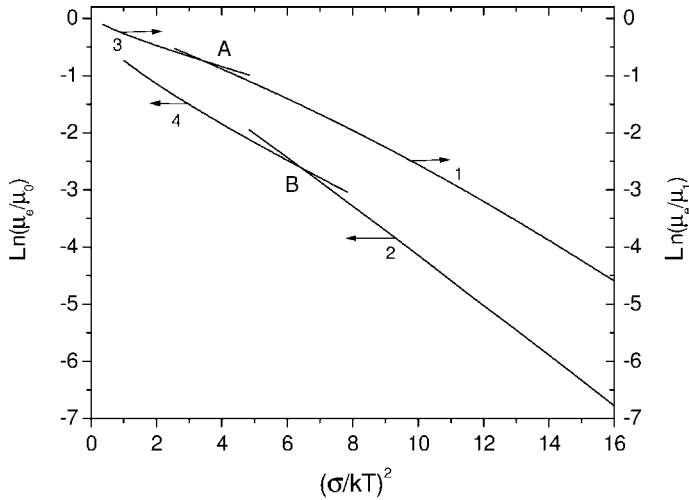


**Figure 6.11** Temperature dependence of the effective charge carrier drift mobility  $\ln(\mu_e/\mu_0)$  calculated in the framework of the exact *approach I* (curves 1 and 3) and  $\ln(\mu_e/\mu_0)$  calculated within the approximated *approach II* (curves 2 and 4) for a broad range of  $\sigma/k_B T$

values. Curves 1 and 2 were calculated by taking into account of the existence of the effective transport energy level in the case of large  $\sigma/k_B T$  values. The intersection points A and B define the transition from a weak to strong energetic disorder.

(6.73), (6.66) and (6.70), respectively (for calculation of curve 1, see Ref. [123]). As one can see, curve 3 gives the weakest temperature dependence and could be approximated by the expression  $\mu_e \cong \mu_1 \exp[-(4\sigma/9k_B T)^2]$ . In the case of large energetic disorder, curve 1 can be approximated by  $\mu_e \cong \mu_1 \exp[-(3\sigma/5k_B T)^2]$  and curve 2 by  $\mu_e \cong \mu_0 \exp[-(2\sigma/3k_B T)^2]$ . Interestingly, a similar coefficient of 3/5 was obtained recently for the temperature dependence of zero-field mobility using a computer simulation of charge transport using a correlated disorder model [83] [cf. Eq. (6.6)]. This implies that at low energetic disorder the exact MA expression gives a notably *weaker* temperature dependence of the carrier mobility. Note that the above curves intersect and the intersection points can be considered as a demarcation between the regions of weak and strong disorder. The physical difference between *approaches I* and *II* is that the latter is restricted to the condition when  $|\varepsilon_1 - \varepsilon_2| \gg 2k_B T$  is valid, whereas the former is valid for the whole range of energies  $\varepsilon_1$  and  $\varepsilon_2$  when performing the configuration averaging, i.e. the former approach can properly account charge carrier jump rates for any energy spacing of neighboring hopping sites.

Remarkably, employing *approach I* the present EMA theory was able to describe the very weak temperature dependence of charge carrier mobility observed within the temperature range  $150 < T < 393$  K in a conjugated polymer (MeLPPP) with exceptionally weak disorder [124] (see Section 6.5.1 for details). The experimental results can be fitted reasonably well by Eq. (6.66) employing *approach I* and assuming  $\sigma = 0.0335$  eV and  $\mu_1 = 1.41 \times 10^{-3} \text{ cm}^2 \text{ V}^{-1} \text{ s}^{-1}$  as fitting parameters [123].

Note that a similar  $\sigma$  value was also obtained by the Gaussian fit of the low-energy portion of absorption spectrum of MeLPPP [124].

#### 6.3.3.4 Electric Field Dependence of the Drift Mobility

For a range of relatively weak electric fields where  $M_2 \ll M_1$  and  $2W_e \leq W_e^+ + W_e^- \ll W_{12}^+ + W_{21}^-$  are valid, Eqs. (6.57) yield the effective values  $W_e^+$  and  $W_e^-$ :

$$W_e^+ = \left\langle \frac{W_{12}^+}{W_{12}^+ + W_{21}^-} \right\rangle \left/ \left\langle \frac{1}{W_{12}^+ + W_{21}^-} \right\rangle \right., W_e^- = \left\langle \frac{W_{21}^-}{W_{12}^+ + W_{21}^-} \right\rangle \left/ \left\langle \frac{1}{W_{12}^+ + W_{21}^-} \right\rangle \right. \quad (6.78)$$

For strong electric fields where  $W_e^+ \gg W_e^-$ , we have  $\eta = \delta = W_e^+/2W_e \gg 1$  and  $M_1 = M_2 = 1/2\eta$ . Then, the effective values  $W_e^+$  and  $W_e^-$  are

$$W_e^+ = 1 \left/ \left\langle \frac{1}{W_{12}^+} \right\rangle \right., W_e^- = \left\langle \frac{W_{21}^-}{W_{12}^+} \right\rangle \left/ \left\langle \frac{1}{W_{12}^+} \right\rangle \right. \quad (6.79)$$

In the general case, the effective hopping drift mobility can be calculated without resorting to the Einstein relation, but using the definition

$$\mu_e = a \frac{W_e^+ - W_e^-}{F} \quad (6.80)$$

The EMA calculation of charge transport under a relatively weak electric field in a weakly energetically disordered organic system was performed in Ref. [123] using *approach I*. Replacing  $\varepsilon_2 - \varepsilon_1$  by  $\varepsilon_2 - \varepsilon_1 - eaF$  ( $e > 0$ ) in Eq. (6.63), one obtains expressions for  $W_{21}^-$  and  $W_{12}^+$ . Then from Eq. (6.78) one can obtain the values  $X_e^\pm = W_e^\pm/W_1$ . When performing a configurational averaging one should take into account that in the expression for  $X_e^+$  the values  $\varepsilon_1$  and  $\varepsilon_2$  are energies of starting and target state (i.e. they are described by ODOS and DOS distributions, respectively) and the reverse in the expression for  $X_e^-$ . Appropriate configurational averaging in Eq. (6.78) leads to

$$X_e^\pm = \frac{i_0^\pm}{i_1^\pm} \quad (6.81)$$

where

$$i_0^\pm = \frac{1}{2\pi} \int_{-\infty}^{\infty} dt_1 \int_{-\infty}^{\infty} dt_2 \varphi_0^\pm(t_1, t_2) e^{-(t_2 - t_1 \mp f) \frac{x}{2}}, i_1^\pm = \frac{1}{2\pi} \int_{-\infty}^{\infty} dt_1 \int_{-\infty}^{\infty} dt_2 \frac{\varphi_0^\pm(t_1, t_2)}{\varphi_1^\pm(t_1, t_2)} \quad (6.82)$$

and

$$\varphi_0^\pm(t_1, t_2) = \frac{\exp\left\{-\frac{1}{2}[(t_1 + x)^2 + t_2^2]\right\}}{\cosh\left(|t_2 - t_1 \mp f| \frac{x}{2}\right)}, \varphi_1^\pm(t_1, t_2) = \frac{|t_2 - t_1 \mp f| \frac{x}{2}}{\sinh\left(|t_2 - t_1 \mp f| \frac{x}{2}\right)} \quad (6.83)$$

where  $f = eaF/\sigma$ . In the asymptotic case of a strong electric fields, from Eq. (6.79) one obtains  $X_e^+$  and  $X_e^-$  and it turns out that the effective charge carrier mobility is field independent:

$$\mu_e = \mu_1 \quad (6.84)$$

It should be noted that in such asymptotic cases Eq. (6.84) can also be obtained from Eq. (6.81). Thus Eq. (6.81) is able to describe the electric field dependence of the mobility  $\mu_e$  over a broad field range in solids under the premise of weak energetic disorder.

Figure 6.12 compares the results of the EMA theory with experimental charge carrier mobility of poly(9,9-dioctylfluorene) (PFO) [125, 126] (circles) measured at room temperature over a larger field range. Note that in the electric field range employed we have  $0.48 < f < 7.68$ , i.e. the cases of both weak and strong fields are covered. When  $x \rightarrow 0$  one obtains  $\mu_e \rightarrow \mu_1$  over the whole range of electric field, i.e. the drift charge carrier mobility is field independent. This is indeed observed for molecular organic crystals except for very low temperatures [1], where coherent effects become important.

Let us, for the sake of comparison, consider the field dependence of the charge mobility in an organic system with large energetic disorder ( $x = \sigma/k_B T \gg 1$ ) within *approach II*. Replacing  $\varepsilon_2 - \varepsilon_1$  by  $\varepsilon_2 - \varepsilon_1 - eaF$  in Eq. (6.64), one obtains expressions for  $W_{12}^+$  and  $W_{21}^-$ . First we consider the case of relatively weak fields.

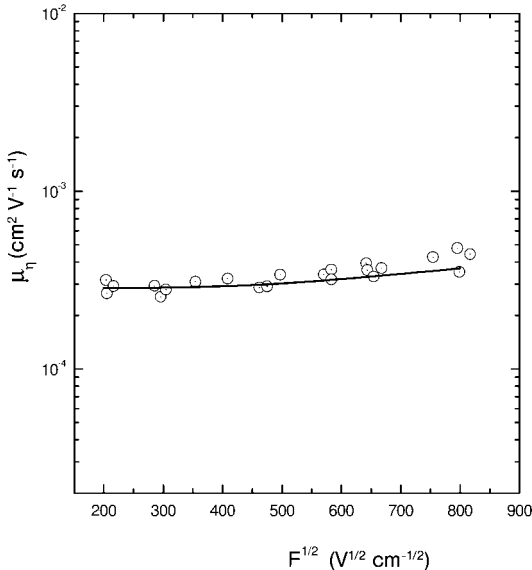


**Figure 6.12** Experimental field dependence of the hole mobility measured in PFO measured at room temperature [125, 126]. Theoretical fit by Eqs. (6.33) and (6.34) with the

following parameters  $a = 3$  nm,  $\sigma = 0.025$  eV,  $T = 300$  K ( $x = 0.97$ ) and  $\mu_1 = 4.4 \times 10^{-4}$  cm<sup>2</sup> V<sup>-1</sup> s<sup>-1</sup> is given by solid line.

Similarly to the procedure for obtaining Eq. (6.72), we use here approximate expressions [122]  $W_e^+ = \langle W_{12}^+ \rangle$  and  $W_e^- = \langle W_{21}^- \rangle$  instead of Eqs. (6.78). Since we consider the case of strong energetic disorder, we can take into consideration that transport occurs only via the effective energy level  $\varepsilon_r$ . After appropriate configuration averaging one obtains

$$Y_e^\pm = \frac{1}{2} \left\{ e^{-\frac{1}{2}(x-c\mp f)^2 + \frac{1}{2}(c\pm f)^2} \left[ 1 - \operatorname{erf}\left(\frac{c\pm f}{\sqrt{2}}\right) \right] + \left[ 1 - \operatorname{erf}\left(\frac{x-c\mp f}{\sqrt{2}}\right) \right] \right\} \quad (6.85)$$

where  $Y_e^\pm = W_e^\pm / W_2$ . Using the  $Y_e^+$  and  $Y_e^-$  values, one can calculate the effective drift mobility. In case when  $1/x \ll f \ll x$  (relatively weak electric fields), one obtains

$$\mu_e = \mu_2 \exp \left[ - \left( \frac{\sqrt{2}}{2} \frac{\sigma}{k_B T} \right)^2 + \frac{\sigma}{k_B T} \frac{eaF}{\sigma} - \frac{1}{2} \left( \frac{eaF}{\sigma} \right)^2 \right] \quad (6.86)$$

where  $\mu_2 = \mu_0 / \sqrt{2\pi} x f^2$  is a power function of the electric field.

In the case of strong electric fields ( $f \gg x$ ) and large energetic disorder, using Eqs. (6.79) one obtains

$$\mu_e = \mu_0 \frac{k_B T}{eaF} \quad (6.87)$$

Note that in this asymptotic case Eq. (6.87) can also be obtained from Eqs. (6.85). Hence Eqs. (42) obtained for  $Y_e^+$  and  $Y_e^-$  describe the electric field dependence of the mobility  $\mu_e$  over a broad field range in organic solids with moderate to large energetic disorder.

As was mentioned in Section 6.2.1.6, the correlated disorder model (CDM) has recently attracted much attention owing to its ability to explain the Poole–Frenkel type of field dependence of mobility in the range of relatively weak electric fields. One could account for the energetic correlation effects using the method described in Ref. [123]. For that,  $eaF/\sigma$  should be replaced by  $\sqrt{x/2} \sqrt{eaF/\sigma}$  in Eq. (6.86) and the result reads

$$\mu_e = \mu_2 \exp \left[ - \left( \frac{\sqrt{2}}{2} \frac{\sigma}{k_B T} \right)^2 + \frac{\sqrt{2}}{2} \left[ \left( \frac{\sigma}{k_B T} \right)^{\frac{3}{2}} - \left( \frac{\sigma}{k_B T} \right)^{\frac{1}{2}} \right] \sqrt{\frac{eaF}{\sigma}} \right] \quad (6.88)$$

which can be compared with the empirical expression derived from computer simulations [83, 127]:

$$\mu_e \propto \exp \left[ - \left( 0.60 \frac{\sigma}{k_B T} \right)^2 + 0.78 \left[ \left( \frac{\sigma}{k_B T} \right)^{\frac{3}{2}} - 2 \right] \sqrt{\frac{eaF}{\sigma}} \right] \quad (6.89)$$

Good agreement between the result obtained by EMA calculation for a 3D strongly disordered system [Eq. (6.88)] and the results of computer simulation given by the empirical Eq. (6.89) should be noted. It is a demonstration that the EMA approach is able to recover the field dependence of the charge carrier mobility in a quantitative fashion.

### 6.3.3.5 Hopping Transport in Organic Solids with Superimposed Disorder and Polaron Effects

The strong electron–phonon coupling causes carrier self-trapping and creates a quasi-particle, a polaron, which can move to an adjacent molecule only by carrying along the associated molecular deformation. The importance of polaron effects for charge transport in organic disordered materials is still under debate because purely polaron models eventually fail to describe consistently charge transport because of their principle limitation related to the magnitude of physical parameters such as polaron activation energy  $E_a = E_p/2$  and transfer integral  $J$  (see Section 6.5.4 for more details). However, it is believed that for some organic systems the deformation energy might be comparable to the disorder energy and therefore the description of charge transport in such materials should account for superposition of disorder and polaron effects.

In the case of polaron hopping transport, the nonadiabatic small polaron hopping rate given by Marcus theory [128, 129] could be used (hereafter *Marcus jump rate*):

$$W_{ij} = \frac{J^2}{\hbar} \sqrt{\frac{\pi}{4E_a k_B T}} \exp\left(-\frac{E_a}{k_B T}\right) \exp\left[-\frac{\epsilon_j - \epsilon_i}{2k_B T} - \frac{(\epsilon_j - \epsilon_i)^2}{16E_a k_B T}\right] \quad (6.90)$$

Recently, Fishchuk et al. [130] formulated an EMA theory to describe polaron transport in a disordered organic system using the Marcus jump rate given by Eq. (6.90). The effective polaron mobility can be obtained by substituting Eq. (6.90) into Eqs. (6.78) and (6.80); the result in the presence of an electrical field is

$$\mu_e = \mu_3 \exp\left(-\frac{E_a}{k_B T}\right) \frac{1}{f\bar{x}} \left(\frac{Y_e^+}{Z_e^+} - \frac{Y_e^-}{Z_e^-}\right) \quad (6.91)$$

Here

$$\mu_3 = \frac{ea^2}{k_B T} W_3, \quad W_3 = \frac{J^2}{\hbar} \sqrt{\frac{\pi}{4E_a k_B T}} \quad (6.92)$$

$$Z_e^\pm = \frac{\exp\left[-\frac{1}{2}(x \mp f)^2\right]}{q} \frac{1}{2} \left\{ \exp\frac{1}{2}\left(\frac{x \mp 2f}{2q}\right)^2 \left[1 + \operatorname{erf}\left(\frac{x \mp 2f}{2\sqrt{2}q}\right)\right] + \exp\frac{1}{2}\left(\frac{3x \mp 2f}{2q}\right)^2 \left[1 - \operatorname{erf}\left(\frac{3x \mp 2f}{2\sqrt{2}q}\right)\right] \right\} \quad (6.93)$$

where  $q = \sqrt{1 - xy/8}$  and  $y = \sigma/E_a$ . Equation (6.91) is valid when  $(\sigma/E_a)(\sigma/k_B T)/8 < 1$ . In the limiting case of zero electric field ( $F \rightarrow 0$ ), one obtains from Eqs. (6.91) [130]

$$\mu_e = \mu_3 \frac{1}{2q} \exp \left[ -\frac{E_a}{k_B T} - \frac{1}{8q^2} \left( \frac{\sigma}{k_B T} \right)^2 \right] \quad (6.94)$$

In the condition when  $(\sigma/E_a)(\sigma/k_B T)/8 \ll 1$  ( $q \cong 1$ ), one can derive the apparent effective Arrhenius activation energy of the polaron mobility as

$$E_{\text{eff}} = -k_B [d \ln \mu_e / d(1/T)] = E_a + \frac{1}{4} \frac{\sigma^2}{k_B T} \quad (6.95)$$

where  $E_{\text{eff}}$  is the sum of contributions from the energetic disorder and the polaron formation (polaron activation energy). As one can see, this equation differs somewhat from the conventional expression  $E_{\text{eff}} = E_a + (8/9)\sigma^2/k_B T$  [67], which was used for estimating the material parameters  $E_a$  and  $\sigma$  from the temperature dependence of the mobility (for more discussion, see below). Employment of Eq. (6.95) for the analysis of experimental data gives a twice-larger parameter  $\sigma$  than that obtained using the above conventional expression.

Eqs. (6.91) can be used for calculating the electric field dependence of polaron mobility in a broad range of arbitrary fields (as mentioned above, we shall limit ourselves to the field range  $1/x \ll f \ll x/2$ ). It should be mentioned that this field range is at least twice smaller than that considered above for the derivation of Eq. (6.88). From Eq. (6.91), after taking into account the correlation effects, the result can be approximated well by the following expression [130]

$$\mu_e = \mu_4 \exp \left\{ -\frac{E_a}{k_B T} - \frac{1}{8q^2} \left( \frac{\sigma}{k_B T} \right)^2 + \frac{1}{2\sqrt{2}q^2} \left[ \left( \frac{\sigma}{k_B T} \right)^{\frac{3}{2}} - \left( \frac{\sigma}{k_B T} \right)^{\frac{1}{2}} \right] \sqrt{\frac{eaF}{\sigma}} \right\} \quad (6.96)$$

where  $\mu_4 = \mu_3 q / \sqrt{2\pi x f^2}$  is a power function of the electric field. It should be noted that Eq. (6.96) agrees well with the empirical expression derived from computer simulations [131]:

$$\mu_e = \mu_0 \exp \left\{ -\frac{E_a}{k_B T} - 0.31 \left( \frac{\sigma}{k_B T} \right)^2 + 0.78 \left[ \left( \frac{\sigma}{k_B T} \right)^{\frac{3}{2}} - 1.75 \right] \sqrt{\frac{eaF}{\sigma}} \right\} \quad (6.97)$$

The value  $\mu_4 = 2.45 \times 10^{-3} \text{ cm}^2 \text{ V}^{-1} \text{ s}^{-1}$  determined for the parameters taken from Ref. [130] is close to the value of  $\mu_0 = 3.60 \times 10^{-3} \text{ cm}^2 \text{ V}^{-1} \text{ s}^{-1}$  calculated in Ref. [131]. Further, Eq. (6.96) corresponds to the Poole–Frenkel type of dependence  $\ln \mu \propto \sqrt{F}$ .

The present theory suggests an important test, which, in principle, could be used for distinguishing between polaron and polaron-free transport [130]. It appears that slopes of the electric field dependence of the mobility [Poole–Frenkel

(PF) factors], defined as  $\beta' = \partial \ln(\mu_e/\mu_2)/\partial \sqrt{F}$ , varies almost linearly with  $T^{-3/2}$  in the case of polaron-free transport when the MA formalism is applicable and  $\beta = \partial \ln(\mu_e/\mu_4)/\partial \sqrt{F}$  deviates significantly from linearity with  $T^{-3/2}$  for the polaron transport. Hence the presence of such a deviation should imply the presence of polarons in the system under study. Further, the present polaron model can quantitatively explain the observed magnitudes of temperature- and field-dependent polaron mobilities assuming reasonable values of polaron binding energies and transfer integrals. Importantly, the Poole–Frenkel-type field dependence of mobility  $\ln \mu \propto \sqrt{F}$  occurs for both the bare charge carrier and the polaron transport provided that energetic correlation effects have been taken into account. Also, the super-Arrhenius type of temperature dependence of the drift mobility  $\ln \mu \propto 1/T^2$  can be observed for polaron transport provided that the polaron activation energy is relatively small. The results of the present EMA theory are found also to be in good agreement with experimental results obtained for some  $\sigma$ -conjugated polysilanes where polaron formation was straightforwardly demonstrated (see Section 6.5.4 for further discussion).

#### 6.3.3.6 Low-Field Hopping Transport in Energetically and Positionally Disordered Organic Solids

In the present section we considered the influence of superimposed energetic and positional disorder on the field dependence of drift mobility in disordered organic solids using jump rate expressions based either on Miller–Abrahams or Marcus models [132]. It is assumed that the two-site transition rate is an exponential function of both an energetic barrier height and an intersite distance. In the following we assume that energetic and positional disorders are independent and that the effective transition rates determined by the random-energy and random-position contributions can be factorized. As it will be showed below, such an assumption allows considerable simplification of the analytical calculations and good agreement of the obtained results with the charge transport computer simulation data over a broad field range justifies that the above assumption is acceptable. Under these premises, the two-site transition rates  $Z_{12}^+(Z_{21}^-)$  and the effective transition rates  $Z_e^+(Z_e^-)$  along (opposite to) the electrical field direction can be written as

$$Z_{12}^+ = W_{12} Q_{12}^+, Z_{21}^- = W_{21} Q_{21}^- \quad (6.98)$$

$$Z_e^+ = W_e Q_e^+, Z_e^- = W_e Q_e^- \quad (6.99)$$

where  $W_{12}(W_{21})$  and  $W_e$  are energetic disorder components of the two-site and effective transition rates, respectively, in zero electric field. The values  $Q_{12}^+(Q_{21}^-)$  and  $Q_e^+(Q_e^-)$  are positional disorder components of the two-site and effective transition rates, respectively, along (opposite to) the electrical field direction.

EMA theory can be used to calculate  $W_e$  by either of two equivalent equations (6.56). The  $Q_e^+(Q_e^-)$  values can also be calculated in the framework of the EMA method [123]:

1. At relatively weak electric fields when  $\eta = (Q_e^+ + Q_e^-)/2Q_e > 1$  and  $\delta = (Q_e^+ - Q_e^-)/2Q_e < 1$ , the following set of equations can be derived:

$$\begin{aligned} Q_e^+ &= \left\langle \frac{Q_{12}^+}{Q_{12}^+ + Q_{21}^-} \right\rangle \left/ \left\langle \frac{1}{Q_{12}^+ + Q_{21}^-} \right\rangle \right., \\ Q_e^- &= \left\langle \frac{Q_{21}^-}{Q_{12}^+ + Q_{21}^-} \right\rangle \left/ \left\langle \frac{1}{Q_{12}^+ + Q_{21}^-} \right\rangle \right., \left\langle \frac{Q_e - Q_e^-}{Q_e + 2Q_e^-} \right\rangle = 0 \end{aligned} \quad (6.100)$$

Equations (6.100) are similar to Eqs. (6.78). Angular brackets in Eqs. (6.100) denote positional configuration averaging. The last of Eqs. (6.100) corresponds to zero electric field when  $Q_{12}^+ \rightarrow Q_{21}^- \rightarrow Q_e$ . As follows from the sum rule [121], the charge carrier drift in this case is essentially a three-dimensional (isotropic) motion.

2. At high electric fields when  $\eta \cong \delta \cong Q_e^+/2Q_e \gg 1$ , one obtains

$$Q_e^+ = 1 \left/ \left\langle \frac{1}{Q_{12}^+} \right\rangle \right., Q_e^- = \left\langle \frac{Q_{21}^-}{Q_{12}^+} \right\rangle \left/ \left\langle \frac{1}{Q_{12}^+} \right\rangle \right. \quad (6.101)$$

In this case, the sum rule suggests a quasi-one-dimensional (directed) character of charge carrier drift. When accounting for energetic and positional disorder, the general expression (6.80) for the drift mobility transforms to

$$\mu_e = \mu_{e0} \frac{Q_e^+ - Q_e^-}{\lambda} \quad (6.102)$$

where  $\mu_{e0} = ea^2 W_e/k_B T$  is the zero-field effective drift mobility determined solely by the energetic disorder (its calculation was described above) and  $\lambda = eaF/k_B T$ .

Further theoretical treatment requires choosing an explicit expression for the two-site transition rates  $Z_{12}^+(Z_{21}^-)$  in addition to functions describing energetic and positional disorder. To take into account the positional disorder, we use the approach suggested by Gartstein and Conwell [81, 133], i.e. instead of  $W_2$  and  $W_3$  we choose that  $W_2 \exp(\xi)$  in the MA model and  $W_3 \exp(\xi)$  in the Marcus model. Here  $\xi$  describes positional disorder in pairs of sites and it changes uniformly within the range  $-\xi_0 \leq \xi \leq \xi_0$ . Hence for the probability density  $P(\xi)$  we imply  $P(\xi) = \frac{1}{2}\xi_0$  if  $abs(\xi) \leq \xi_0$  and  $P(\xi) = 0$  if  $abs(\xi) > \xi_0$ .

Calculations of drift mobility led to the following results [132]:

1. In the Miller–Abrahams model for the range of relatively weak electric fields using Eqs. (6.100) and (6.102) one obtains

$$\mu_e = \mu_{e0} Q_e \frac{M^+ - M^-}{N\lambda} \frac{\ln A}{\xi_0 - \frac{1}{2} \ln A} \quad (6.103)$$

where

$$\begin{aligned} M^+ &= \exp\left(-\frac{|x^2 - \lambda| - x^2 - \lambda}{2}\right), & M^- &= \exp(-\lambda), \\ N &= \exp\left(-\frac{|x^2 - \lambda| - x^2}{2}\right) \cosh\left(\frac{\lambda}{2}\right) \end{aligned} \quad (6.104)$$

$$A = \frac{N \exp(\xi_0) + 2Q_e}{N \exp(-\xi_0) + 2Q_e}, \quad Q_e = \frac{1}{2} \frac{\exp(\xi_0) - \exp(-\frac{1}{3}\xi_0)}{\exp(\frac{2}{3}\xi_0) - 1} \quad (6.105)$$

At relatively high electric fields using Eqs. (6.100) and (6.101) one obtains

$$\mu_e = \mu_{e0} \frac{M^+}{\lambda} \frac{\xi_0}{\sinh(\xi_0)} \quad (6.106)$$

As above, we can account for the energetic correlation effects by substitution of the parameter  $\lambda$  by  $x\sqrt{x/2}\sqrt{eaF/\sigma}$  in Eq. (6.103). Then, for instance, for a disordered system devoid of positional disorder ( $\xi_0 \rightarrow 0$ ), one obtains

$$\mu_e \propto \exp\left[\frac{1}{\sqrt{2}} \left(\frac{\sigma}{k_B T}\right)^{\frac{3}{2}} \sqrt{\frac{eaF}{\sigma}}\right] \quad (6.107)$$

2. In the Marcus model for the range of relatively weak electric fields, one obtains

$$\mu_e = \mu_{e0} Q_e \frac{X_e^+ - X_e^-}{\lambda} \quad (6.108)$$

where

$$X_e^\pm = \frac{M^\pm}{N^\pm} \frac{\ln A^\pm}{\xi_0 - \frac{1}{2} \ln A^\pm}, \quad A^\pm = \frac{N^\pm \exp(\xi_0) + 2Q_e}{N^\pm \exp(-\xi_0) + 2Q_e} \quad (6.109)$$

$$M^\pm = \exp\left[\pm \frac{\lambda}{2} (1 + 4x^2 d) - dx^2\right],$$

$$N^\pm = \exp(\pm 2x^2 d \lambda - dx^2) \cosh\left(\frac{\lambda}{2}\right), \quad d = \frac{k_B T}{16E_a} \quad (6.110)$$

Using Eq. (6.101) for the range of strong electric fields, one obtains

$$\mu_e = \mu_{e0} \frac{M^+}{\lambda} \frac{\xi_0}{\sinh(\xi_0)} \quad (6.111)$$

We can also account for the energetic correlation effects in Eq. (6.108). For a disordered system devoid of positional disorder ( $\xi_0 \rightarrow 0$ ), Eq. (6.108) gives

$$\mu_e \propto \exp \left[ \frac{1}{2\sqrt{2}} \left( \frac{\sigma}{k_B T} \right)^{\frac{3}{2}} \sqrt{\frac{eaF}{\sigma}} \right] \quad (6.112)$$

The results obtained suggest the validity of the Poole–Frenkel law  $\ln \mu_e \propto \sqrt{F}$  in an experimentally important electric field range, but with a twice-smaller coefficient than in Eq. (6.107).

Figure 6.13 shows the field dependences of drift mobility for an organic material with strong energetic disorder and different degrees of the positional disorder, which were calculated assuming the MA jump rate by Eq. (6.103) for a broad range of electric fields (curves 1, 2 and 3) and by Eq. (6.106) for high electric fields (curves 1', 2' and 3') (note that curves 1 and 1' overlap). These results suggest that a three-dimensional (3D) disordered system can be treated as an essentially one-dimensional (1D) system at sufficiently high electric fields (curves 1, 2 and 3 in Fig. 6.13 approach curves 1', 2' and 3', respectively, in the high-field region).

Employment of the Marcus jump rate for calculation of the field dependences of the mobility for a system with strong energetic disorder and different degrees

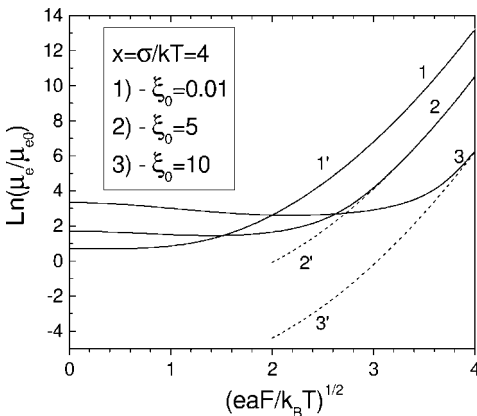


**Figure 6.13** Field dependences of mobility,  $\ln(\mu_e/\mu_{e0})$  versus  $\sqrt{eaF/k_B T}$ , for a disordered organic material with strong energetic disorder and different degrees of the positional disorder as calculated by Eq. (6.103)

assuming Miller–Abrahams jump rates for a broad range of electric fields (curves 1, 2 and 3) and by Eq. (6.106) for high electric fields only (curves 1', 2' and 3').

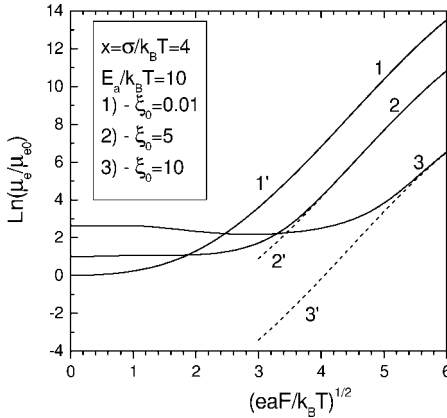


**Figure 6.14** Field dependences of mobility,  $\ln(\mu_e/\mu_{e0})$  versus  $\sqrt{eaF/k_B T}$ , calculated using Eq. (6.108) assuming Marcus jump rate for a system with strong energetic dis-

order and different degree of the positional disorder over a broad range of electric fields (curves 1, 2 and 3) and by Eq. (6.111) for high electric fields only (curves 1', 2' and 3').

of positional disorder is demonstrated in Fig. 6.14. The field dependences were calculated with Eq. (6.108) (Marcus model) for a broad range of electric fields (curves 1, 2 and 3) and Eq. (6.111) for high electric fields only (curves 1', 2' and 3'). As in the previous case of the MA jump rate, Fig. 6.14 suggests that at sufficiently high electric fields a 3D disordered system can be treated as a 1D system.

Note that in previous computer simulations due to Bässler and co-workers [134], the positional disorder was described by a Gaussian with variance  $\Sigma$ . Comparing the effective mobility for the limiting case of  $F \rightarrow 0$  with computer simulation data [134], one can obtain a relation between these parameters of positional disorder as  $\xi_0 = (3/2)\Sigma^2$ .

The results of the calculations are found to be in good agreement with relevant experimental results. Figure 6.15 presents the field dependence of charge carrier drift mobility measured in a  $\sigma$ -conjugated polymer poly(di-*n*-butylsilylene) (DNBSi) (symbols) [135] where hole mobility is first observed to *decrease*, then clearly to go through a *minimum* and then to *increase* as the field is progressively increased. Hence there is a certain intermediate electric field at which the field dependence of drift mobility shows a minimum. This effect clearly cannot be explained by a transition from diffusion- to drift-controlled transport since, for instance, at  $T = 294$  K and a film thickness of  $8 \mu\text{m}$  the critical electric field would be  $F_{cr} = 95 \text{ V cm}^{-1}$ , which is outside the experimental field range used. The theoretical calculation performed without accounting for the energetic correlation effects by Eq. (6.108) assuming a Marcus jump rate (solid curves) agree reasonably well with experimental data (Fig. 6.15) when one assumes  $\sigma = 0.05 \text{ eV}$ ,  $E_a = 0.05 \text{ eV}$ ,  $a = 10 \text{ nm}$ ,  $\xi_0 = 10$  and  $\mu_{e0} = \mu_0 \exp(-E_a/k_B T - x^2/8q^2)$ , where  $\mu_0 = 0.19 \times 10^{-3} \text{ cm}^2 \text{ V}^{-1} \text{ s}^{-1}$ ,  $q = \sqrt{1 - xy/8}$  and  $y = \sigma/E_a$ . Note that parameter  $a$  here also implies an effective hopping distance and it differs from the intermolecular distance, which is typically  $0.6\text{--}1 \text{ nm}$ . Hence the Marcus model allows one to

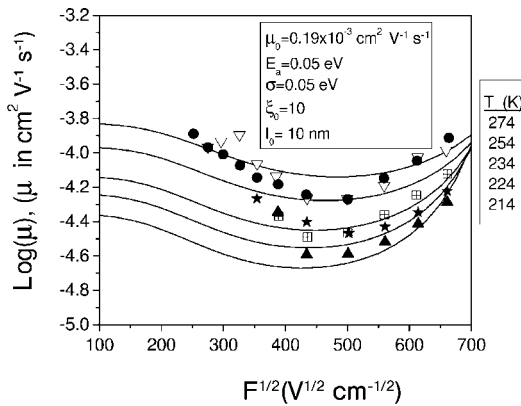


**Figure 6.15** Experimental field dependence of charge carrier drift mobility measured in poly(di-*n*-butylsilylene) (DNBSi) (symbols) [135] for different temperatures. The theoretical calculation performed using Eq. (6.108) assuming the Marcus model for the same temperatures are given by solid curves.

reproduce successfully the temperature dependence of mobility at reasonable material parameters. Another example of fitting experimental results on the field dependence of mobility measured at different temperatures in 1,1-bis(di-4-tolylaminophenyl)cyclohexane (TAPC) doped in polycarbonate (PC) [134] by the present theory assuming the MA jump rate is discussed in Section 6.5.2.

The key result of this treatment is that the negative field dependence of drift mobility in the low-field range is an inherent property of hopping transport in disordered solids rather than an artifact. Hence it can be theoretically reproduced using either Miller–Abrahams or Marcus models for characteristic parameters of the investigated material and under specified measurement conditions. Further, as was recently demonstrated [136], the influence of the diffusion-controlled transport at low fields on measured TOF mobility suggested in Refs. [73, 136] is irrelevant for the phenomena observed. The physical reason for the appearance of the negative field dependence of charge mobility in hopping transport systems is the same as predicted earlier by percolation transport theories. According to these, in a hopping system with large positional disorder the fastest percolation passes whose direction is not aligned with the direction of the external electric field are transformed at higher fields in such a way as to diminish jumps against the field. Therefore, the carrier is forced to make the difficult jumps, resulting in decreasing mobility with increasing electric field. In other words, the modified percolation passes at higher field have larger resistivity resulting in negative differential hopping conductivity observed in inorganic semiconductors [137, 138]. A similar explanation was suggested by computer simulation studies [67].

### 6.3.3.7 Charge Carrier Transport in Disordered Organic Materials in the Presence Of Traps

Traditionally, the Hoesterey–Letson formalism [139] is used to describe charge carrier transport in trap-containing materials and it provides a reasonable zero approximation to describe trapping. The key predictions of the formalism are the following: (i) the mobility scales with relative trap concentration as  $c^{-1}$  and (ii) the concentration at which the mobility is decreased by a factor of two is  $c_{1/2} = \exp(-E_t/k_B T)$ . These predictions, however, are not always in agreement with experimental data [75, 76]. This is not unexpected as the formalism was originally developed for systems devoid of disorder and it is based on a discrete trap depth, an assumption which is probably unrealistic for disordered organic solids. Therefore, a theoretical approach which can adequately account for the effects of disorder needs to be developed.

In the present section, a self-consistent EMA theory is considered to describe charge transport in the presence of trapping [140]. The disordered medium is replaced by an effective ordered medium (cubic lattice of sites with constant spacing  $a$ ). Each lattice site can be either a trap or intrinsic transport (hopping) site with a relative concentration  $c$  or  $1 - c$ , respectively. We take into account only the site energetic disorder and assume a Gaussian DOS distribution of intrinsic transport sites. Trap states are also distributed in energy according to a Gaussian function, but they are offset to lower energies with respect to the center of the intrinsic DOS by  $-E_t$  ( $E_t > 0$ ). Hence the cumulative DOS in this case is a superposition of two Gaussians. The case  $c = 0$  implies a trap-free disordered system, whereas  $c = 1$  means that charge carrier transport occurs only via the traps.

First let us calculate the parameter  $W_e^+ = \langle W_{12}^+ \rangle$  in the presence of an electrical field, where  $W_{12}^+$  has the Miller–Abrahams form (*approach II*). The normalized cumulative DOS distribution function for a trap-containing disordered system was chosen as follows:

$$P(\varepsilon_2) = \frac{1-c}{\sigma_0\sqrt{2\pi}} \exp\left[-\frac{1}{2}\left(\frac{\varepsilon_2}{\sigma_0}\right)^2\right] + \frac{c}{\sigma_1\sqrt{2\pi}} \exp\left[-\frac{1}{2}\left(\frac{\varepsilon_2 + E_t}{\sigma_1}\right)^2\right] \quad (6.113)$$

Here, it is assumed that the energy distributions of the density of transport and trap states are described by Gaussian functions of width  $\sigma_0$  and  $\sigma_1$ , respectively. To obtain an expression for  $P(\varepsilon_1)$  in the form of an ODOS, one should normalize the product of  $P(\varepsilon_1)$  [presented in a form similar to Eq. (6.113)] and  $\exp(-\varepsilon_1/k_B T)$  to unity. When calculating  $W_e^-$ , one should take into account that the energies  $\varepsilon_2$  and  $\varepsilon_1$  in the expression for  $\langle W_{21}^- \rangle$  correspond to ODOS and DOS distribution function, respectively. Then we can use Eq. (6.80) for the effective mobility  $\mu_e$ .

In the case of a large degree of energetic disorder ( $\sigma_0/k_B T \gg 1, \sigma_1/k_B T \gg 1$ ) using the concept of the effective transport (percolation) energy level and in the limiting case where  $f \rightarrow 0$  ( $F \rightarrow 0$ ) and deep traps, we obtain

$$\mu_e = \mu_e(0) \frac{[1 + c^2 \exp(xy)]}{1 + c \{ \exp[xy + \frac{1}{2} x^2 (\eta^2 - 1)] \}} \quad (6.114)$$

where  $\mu_e(0) = \mu_e(c=0) = \mu_5 x \exp(-x^2/2)$ ,  $\eta = \sigma_1/\sigma_0$ ,  $\mu_5 = (ea^2 v_0/\sigma_0) \exp(-2a/b)$  and  $y = E_t/\sigma_0 \gg 1$ .

Let us find a trap concentration  $c_{1/2}$  at which the charge mobility drops by a factor of 2,  $\mu_e/\mu_e(0) = \frac{1}{2}$ , under the condition  $c \ll 1$ . It is easy to see that

$$c_{\frac{1}{2}} \cong \exp \left[ -\frac{E_t}{k_B T} - \frac{1}{2} \left( \frac{\sigma_0}{k_B T} \right)^2 (\eta^2 - 1) \right] \quad (6.115)$$

Then, at  $c \gg c_{1/2}$ , one has

$$\mu_e = \mu_e(0) \frac{1 + c^2 \exp(xy)}{c} \exp \left[ -xy - \frac{1}{2} x^2 (\eta^2 - 1) \right] \quad (6.116)$$

From Eq. (6.116), one can obtain the critical trap concentration  $c_{cr}$  at which the effective charge carrier mobility reaches the minimum value  $\mu_e^m$ :

$$c_{cr} = \exp \left( -\frac{1}{2} \frac{E_t}{k_B T} \right) \quad (6.117)$$

$$\mu_e^m = \mu_e(0) 2c_{cr} \exp \left[ -\frac{1}{2} x^2 (\eta^2 - 1) \right] \quad (6.118)$$

Let us rewrite Eq. (6.116) in the form

$$\mu_e = \mu_e(0) c \frac{1 + (c/c_{cr})^2}{(c/c_{cr})^2} \exp \left[ -\frac{1}{2} x^2 (\eta^2 - 1) \right] \quad (6.119)$$

For trap concentrations in the range  $c_{1/2} \ll c \ll c_{cr}$ , from Eq. (6.119) and the expression for  $\mu_e(0)$  we obtain

$$\mu_e = \mu_2 c^{-1} \left( \frac{\sigma_0}{k_B T} \right) \exp \left[ -\frac{E_t}{k_B T} - \frac{1}{2} \left( \eta \frac{\sigma_0}{k_B T} \right)^2 \right] \quad (6.120)$$

Further, for trap concentrations in the range  $c_{cr} \ll c \leq 1$ , Eq. (6.119) leads to

$$\mu_e = \mu_2 c \left( \frac{\sigma_0}{k_B T} \right) \exp \left[ -\frac{1}{2} \left( \eta \frac{\sigma_0}{k_B T} \right)^2 \right] \quad (6.121)$$

Hence, at  $c_{cr}$ , one expects a transition from trap-controlled to the trap-to-trap hopping transport, i.e.  $c_{cr}$  is the transition point between trap-controlled and trap-to-

trap hopping transport which are described by Eqs. (6.120) and (6.121), respectively.

Theoretical treatment of mobility over a broad temperature range reveals a critical temperature  $T_{cr}$  at which the transition from trap-controlled to trap-to-trap hopping transport regime occurs. The expression for  $T_{cr}$  at a concentration  $c$  can be obtained from Eq. (6.117) as  $T_{cr} = -E_t/2k_B \ln c$ . The temperature dependence of charge carrier mobility calculated with Eq. (6.114) for different values of  $\eta$  is presented in Fig. 6.16. The asymptotic behavior of the mobility in the temperature range  $T > T_{cr}$  (trap-controlled transport regime) and in the range  $T < T_{cr}$  (trap-to-trap transport regime) can be described by Eqs. (6.120) and (6.121), respectively. By using Eq. (6.114), one can estimate  $E_t$  and  $\sigma_1$  from the experimental data on the temperature dependence of charge mobility. On the other hand, it can be seen from Eq. (6.115) that, for  $T < T_{cr}$ , the activation energy of charge mobility contains only the contribution from the width of the energy trap distribution  $\sigma_1 = \eta\sigma_0$ , because transport proceeds at such temperatures via traps. From Fig. 6.16a, one can see that the temperature dependence of charge mobility in the trap-containing disordered system depends considerably on  $\eta$ . For instance, at  $\eta < 1$ , i.e. when the width of the energy distribution of traps  $\sigma_1$  is smaller than the width of the energy distribution of intrinsic hopping sites  $\sigma_0$ , the decrease in mobility with decrease in temperature in the range  $T < T_{cr}$  (curve 2 in Fig. 6.16a) becomes less pronounced in comparison with that for a trap-free system (curve 1). This can lead to a situation where the charge mobility in a trap-containing system at a certain temperature might even exceed that in the trap-free material. For purposes of comparison, curve 5 in Fig. 6.16a shows the temperature dependence of charge mobility calculated from the Hoesterey–Letson formalism [139] neglecting the energetic disorder. In this case, for trap concentrations  $c \gg c_{1/2}$ , one has  $\ln(\mu_c/\mu_2) = -\ln c - (E_t/\sigma_0)\sqrt{(\sigma_0/k_B T)^2}$ . Here, the activation energy of the mobility  $E_a$  is equal to the trap depth  $E_a = E_t$ . On the other hand, the present EMA theory, which accounts for the disorder effects, predicts the apparent activation energy of charge mobility to exceed  $E_a = E_t + \eta^2\sigma_0^2/k_B T$  over the trap concentration range  $c_{1/2} \ll c \ll c_{cr}$  ( $T > T_{cr}$ ). For trap concentrations  $c_{cr} \ll c \leq 1$  ( $T < T_{cr}$ ), one obtains  $E_a = \eta^2\sigma_0^2/k_B T$ . This is illustrated in Fig. 6.16b, where curves 3 and 5 in Fig. 6.16a are replotted in the Arrhenius coordinates (curves 3' and 5', respectively). The present theory has been applied to fit experimental results on charge carrier mobility measured in different trap-contained disordered organic materials (see Section 6.5.3) including also the temperature dependence of hole mobility measured in the conjugated polymer poly(phenylenevinylene ether) [141].

The important implication of this study is that the effect of deep traps in a disordered organic photoconductor cannot be described in terms of the conventional Hoesterey–Letson model which predicts an Arrhenius-type temperature dependence of the charge carrier mobility where the activation energy is simply the trap depth  $E_t$ . The calculations support a notion that effect of traps can be quantitatively accounted for by introduction of the effective disorder parameter,  $\sigma_{eff}$ , and

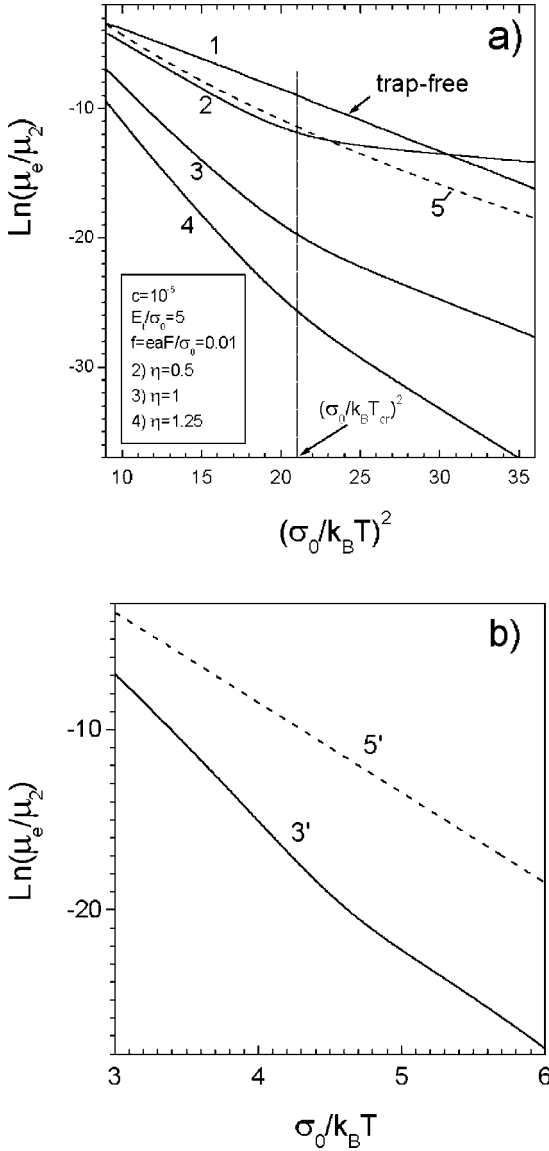


**Figure 6.16** (a) The calculated by Eq. (6.114) temperature dependence of charge mobility in the trap-free (curve 1) and trap-containing disordered systems for different parameters  $\eta = \sigma_1/\sigma_0 = 0.5$  (curve 2), 1 (curve 3) and 1.25 (curve 4) plotted in  $\text{Ln}(\mu_e/\mu_2)$  versus

$(\sigma_0/k_B T)^2$  representation. The  $\mu(T)$  dependence calculated with the Hoestery-Letson formalism is given for comparison (curve 5). (b) The same curves 3 and 5 but re-plotted in  $\text{Ln}(\mu_e/\mu_2)$  versus  $\sigma_0/k_B T$  representation (curves 3' and 5', respectively)

an expression for  $\sigma_{\text{eff}}$  being a function of the trap depth and trap concentration [140]:

$$\left(\frac{\sigma_{\text{eff}}}{\sigma_0}\right)^2 = 1 + 2\left(\frac{k_B T}{\sigma_0}\right)^2 \ln \left\{ \frac{1 + c \exp\left\{ \frac{E_t}{k_B T} + \frac{1}{2} \left(\frac{\sigma_0}{k_B T}\right)^2 \left[ \left(\frac{\sigma_1}{\sigma_0}\right)^2 - 1 \right] \right\}}{1 + c^2 \exp\left(\frac{E_t}{k_B T}\right)} \right\} \quad (6.122)$$

Note that the Eq. (6.122) is valid for whole concentration range ( $0 \leq c \leq 1$ ) whereas the previously suggested expression based on the Hoesterey–Letson formalism [75, 76]:

$$\left(\frac{\sigma_{\text{eff}}}{\sigma_0}\right)^2 = 1 + 2\left(\frac{k_B T}{\sigma_0}\right)^2 \left[ \ln c + \frac{E_t}{k_B T} \right] \quad (6.123)$$

is restricted to the concentration range  $c_{1/2} \ll c \ll c_{cr}$ .

Hence the EMA theory is able to account quantitatively for a variety of basic features of charge carrier transport in disordered organic materials containing traps. It turns out that both relaxation of the ensemble of majority charge carriers within the combined intrinsic and extrinsic density of state distribution and the occurrence of trap-to-trap migration alter the  $\mu(T)$  dependence significantly, notably at lower temperature when the apparent activation energy can become  $< E_t$ . Ultimately,  $\mu(T)$  is controlled by the width of the distribution of trap levels. If it is narrower than that of the intrinsic DOS, the  $\mu(T)$  dependence flattens and eventually the mobility in the trap containing system can even exceed that of the undoped system.

## 6.4 Experimental Techniques

### 6.4.1 Charge Carrier Generation

#### 6.4.1.1 Generation Versus Transport Limited Photocurrents

A photocurrent is proportional to the product of the charge carrier concentration, their mobility and the electric field. In the absence of any other loss of carriers except their discharge at the electrodes, the stationary concentration is the number of carriers generated per unit time multiplied by the time needed to traverse the sample, i.e. the transit time  $t_m$ , that is inversely proportional to the product of mobility and electric field. In this case the transport velocity cancels and the stationary photocurrent

$$j = e\eta I \quad (6.124)$$

is a measure of the number of absorbed photons  $I$  and the efficiency  $\eta$  of photoionization regardless of how fast or slowly the carriers reach the electrode(s). Any field dependence of the photocurrent is, therefore, controlled by the field dependence of the primary photodissociation event. If excitation occurs by a light pulse that is short relative to the carrier transit time the photocurrent measured for  $t < t_{tr}$  is determined by the product of the number of carriers generated and their transport velocity while

$$\int_0^{\infty} dt j(t) = e\eta \int_0^{\infty} dt I(t) \quad (6.125)$$

In this case both  $\eta$  and the carrier mobility  $\mu$  can be determined independently.

The above concept fails at high light intensities when the number of charge carriers generated approaches or even exceeds the capacitor charge sitting at the electrodes. In the case of unipolar charge production, for instance by efficient injection, the current becomes space charge limited (see Section 6.4.2.2), i.e. transport limited. Upon photoexcitation in the bulk of the sample the generated space charge is bipolar and bimolecular electron-hole recombination can occur before carriers reach the exit contacts. The following simple calculation provides a clue at which carrier concentration and, concomitantly, which current density this process is becoming important. The rate of recombination between electrons and holes at concentrations  $n_-$  and  $n_+$  is

$$\frac{dn_{\pm}}{dt} = \frac{dn_{\pm}}{dt} = -Rn_+n_- \quad (6.126)$$

where  $R$  is the bimolecular recombination rate constant. The condition that the recombination dominates over discharge is that  $Rn_{+/-}$  must exceed the reciprocal carrier transit time of the faster moving charge, usually the hole, i.e.

$$Rn_+ > \frac{\mu_+F}{d} \quad (6.127)$$

By using Langevin's relation:

$$\frac{R}{\mu} = \frac{e}{\epsilon_0\epsilon} \quad (6.128)$$

and assuming

$$j \simeq j_+ = en_+\mu_+F \quad (6.129)$$

then Eq. (6.127) translates into the condition

$$j > \frac{\epsilon_0 \epsilon \mu_+ F^2}{d} \quad (6.130)$$

which is reminiscent of Child's law (see Section 6.4.2.2). In other words, recombination becomes rate limiting whenever the total current exceeds the hypothetical space charge-limited current of majority carriers. In a light-emitting diode one wants this condition to be fulfilled under premise of balanced injection [142].

A cautionary note is appropriate regarding optical charge carrier generation in samples with coplanar electrodes as compared with sandwich-type diode structures. In the former case current flow is confined to a thin layer comparable to the skin depth of absorption whereas the electrode gap is usually comparatively large. Therefore, the critical photocurrent normalized to the cross-section of current flow can be orders of magnitude lower than in a sandwich cell. In this case the decay of a transient photocurrent generated by a short light pulse would not probe carrier extraction from the dielectric but rather its bimolecular recombination. Another complication is related to the recognition that electrons photoinjected from the sample surface can contribute significantly to the total current and can obscure the genuine photogeneration yield [143].

#### 6.4.1.2 Delayed Charge Carrier Generation

In organic solids, photogeneration is a two-step process involving a precursor state such as a geminately bound electron-hole pair [1]. In molecular crystals, geminate recombination of those pairs is very fast and it may require THz probing to delineate the pair lifetime. In disordered organic solids, e.g. molecularly doped or conjugated polymers, geminate pairs can be metastable and their ultimate dissociation can be time delayed. Since full separation requires escapes from the Coulombic potential and, concomitantly, is assisted by an electric field, delayed field collection is the method of choice to monitor this process. One excites the sample at zero electric field and measures the number of the charges collected after a defined delay time, taking care to compensate for the RC response of the sample, however. An early example of such an experiment is the work of Mort et al. [144] on polyvinylcarbazole. The technique has meanwhile been developed by Popovic [145, 146]. It has recently been extended to a conjugated polymer by the Rothberg group [26] by disentangling field-dependent primary generation of geminate pairs and their subsequent separation.

#### 6.4.1.3 Optically Detected Charge Carrier Generation

Because a charged molecule is an electronically different moiety, it has its own absorption spectrum. Optically generated charges are, therefore, amenable to transient absorption via the relative change of transmission upon photoexcitation. Meanwhile such studies are becoming almost routine, employing typically 150-fs long light pulses from a frequency-doubled Ti-sapphire laser for primary excitation and a white-light continuum for subsequent probing. The typical response

time of such a system is of the order of 1 ps [27, 147]. It is worth noting, however, that one would detect both free and coulombically bound charges because the Coulombic electric field acting on a pair of charges will hardly affect their absorption spectrum. By the way, free charge carriers moving in an external electric field are also amenable to optical probing [148].

A comment on the interpretation of the transient absorption appears to be appropriate. In earlier work on conjugated polymers it became common practice to describe their excited states in terms of the semiconductor band model. This implies that a photon raises an electron from the valence to the conduction band of the polymer [2, 149]. The generated pair couples quickly to phonons, thus creating polarons and bipolarons. In this picture, the transient absorption spectrum of, say, a positive polaron is the energy transition between the valence band and the localized state occupied by a photogenerated positive polaron. Meanwhile there is consensus that the molecular model is more appropriate [150]. In this model the transient absorption is the Franck–Condon-type absorption spectrum of a radical cation or a radical anion after the backbone of the neutral chain has relaxed to the its new equilibrium configuration in response of the changed electron distribution [151]. A textbook example is the action spectrum of optical detrapping of a positive charge trapped at a tetracene molecule doped into an anthracene lattice [152]. It turns out to be identical with the known absorption spectrum of the tetracene radical cation in solution. In conjugated polymers, absorption spectra of positive and negative polarons, i.e. radical cations and anions, overlap [153] and comprise an IR band near 0.6 eV and a higher band somewhere between 1.8 and 2.0 eV, i.e. well below the  $S_1$ – $S_0$  0–0 transition of the neutral polymer [151]. They are electronic Franck–Condon transitions including a 0–0 transition coupled to vibronic satellites not probing, however, the energy gained when a chromophore relaxes into its new configuration upon charging.

## 6.4.2

### Experimental techniques to measure charge transport

#### 6.4.2.1 The Time-of-Flight Technique

The classical method to study charge transport is the time-of-flight (TOF) technique, originally introduced by Kepler [154] and LeBlanc [155]. The sample is sandwiched between two parallel electrodes, one of which has to be semitransparent. The bias determines the polarity of the charge carriers. A short light pulse generates a  $\delta$ -shaped sheet of charge carriers that traverses the sample and gives rise to a current that remains constant until the carrier packet reaches the exit electrode and sharply drops thereafter provided that the dielectric relaxation time  $\epsilon_0\epsilon/\sigma_c$ , where  $\sigma_c$  is the conductivity, is much greater than the carrier transit time. An inflection point of the transient photocurrent indicates arrival of the carriers at the exit contact at time  $t_{tr} = d/\mu F$  and allows one to infer their mobility. A current plateau for  $t < t_{tr}$  indicates that (i) charge carrier generation is completed by  $t \ll t_{tr}$ , (ii) no carriers are lost during their motion and (iii) their velocity is independent

of time. Under such circumstances, only diffusion broadens the spatial carrier profile and causes a relative spread  $\Delta t_{tr}$  of the transit times:

$$\Delta t_{tr} = t_{tr} \sqrt{\frac{2kT}{eV}} \quad (6.131)$$

where  $V$  is the applied voltage. For  $V = 500$  V and  $T = 290$  K,  $\Delta t_{tr}/t_{tr} = 10^{-2}$ . Equation (6.131) is based on the validity of the Einstein relation  $D/\mu = kT/e$  between the carrier mobility and their diffusion constant  $D$ .

Usually experimental TOF signals feature broader tails even if the reciprocal RC time of the circuit is much less than the transit time. There are several possible contributions to this phenomenon:

1. Optical excitation generates a sheet of carriers with finite spatial width, notably if it occurs intrinsically, i.e. within an escape depth comparable to the penetration depth  $a^{-1}$  of the incident light. To avoid this effect, the sample thickness had to be much greater than  $a^{-1}$ , i.e. several micrometers. This is incompatible with sample fabrication via spin-coating. One possibility to overcome this limitation is to inject charge carriers from a thin optically excited sensitizing layer such as a selenium layer or a dye layer [72], the conditions being that (i) the absorption edge of the sensitizer is red shifted relative to that of the sample, (ii) the HOMO of the sensitizer had to be below that of the sample for hole injection whereas for electron injection the LUMO had to be above that of the sample and (iii) injection had to be much faster than the subsequent carrier transport. A recent example of sensitized hole injection is the work of Markham et al. [12] on a 520-nm thick layer of a spin-coated film of a bisfluorene dendrimer.
2. The TOF method requires non-interacting charge carriers because any space charge inside the sample can distort the TOF signal. To limit space charge effects it has become practice to limit the number of migrating carriers to 5% of the capacitor charge, i.e.  $\sim 10^{10}$  charge carriers  $\text{cm}^{-2}$  in an electric field of  $10^5$  V  $\text{cm}^{-1}$ , equivalent to a concentration of  $10^{13}$   $\text{cm}^{-3}$  in a 10- $\mu\text{m}$  thick sample.
3. In principle, the above formalism applies to systems containing moderately deep traps too, provided that the traps are monoenergetic, implying that carrier trapping and release processes are kinetically of first order with well-specified rates. An example is hole transport in an anthracene crystal doped with tetracene [139]. However, there is often trapping by shallow physical defects that are not monoenergetic. This gives rise to a dispersion of carrier release times and, concomitantly, broadens a TOF signal. This phenomenon becomes

ubiquitous in random systems and, in the extreme case, can lead to dispersive transport (see Section 6.3.2). In this case one has to resort to double logarithmic plots of TOF signals in order to distinguish between capturing of carriers by deep traps prior to their arrival at the exit contact and a decreasing carrier velocity because carriers encounter progressively deeper states within the manifold of shallow traps.

The TOF method has been extended by introducing temporarily intermittent charge transport. The idea is to remove the electric field for a fixed time interval while the carriers are still inside the bulk of the sample in order to allow carriers attain quasi equilibrium before leaving the sample [72, 156]. Although not widely known, this method could be applied profitably to the study of dispersive transport because one can monitor the relaxation of carriers towards quasi equilibrium.

#### 6.4.2.2 Space Charge-Limited Current Flow

If a semiconductor is contacted with an electrode that, by virtue of a low-energy barrier at the interface, is able to supply an unlimited number of one of the types of charge carriers, the current is limited by its own space charge. This reduces the electric field at the injecting electrode to zero. This is approximately realized when the number of carriers per unit area inside the sample equals the capacitor charge  $\epsilon_0 \epsilon V / ed$ . This charge traverses the sample of thickness  $d$  during the transit time  $t_{tr} = d^2 / \mu V$ . The maximum unipolar space charge-limited current should, therefore, be equal to  $j_{SCL} \approx \epsilon_0 \epsilon \mu V^2 / d^3$ . This simplistic calculation ignores the inhomogeneous distribution of the electric field in the bulk of the sample. The correct value of the stationary space charge limited current (SCLC), derived by employing Poisson's equation and the continuity equation, is

$$j_{SCL} = \frac{9}{8} \frac{\epsilon_0 \epsilon \mu V^2}{d^3} \quad (6.132)$$

which is known as Child's law [157, 158]. In the presence of traps,  $\mu$  has to be replaced by the effective mobility  $\mu_{\text{eff}}$ , calculated from the sum of the carrier transit time in the absence of trapping and the time a carrier spends in traps. In the case of monoenergetic traps,

$$\mu_{\text{eff}} = \mu \left[ 1 + c \exp\left(\frac{E_t}{kT}\right) \right]^{-1} \quad (6.133)$$

where  $E_t$  is the trap depth and  $c$  the fraction of molecules that act as traps [139]. The situation becomes more complicated if the traps are distributed in energy. For an exponential distribution of traps,

$$g(E) = \frac{H}{kT_c} \exp\left(-\frac{E}{kT_c}\right) \quad (6.134)$$

where  $H$  is the total number of traps per unit volume and per unit energy range and  $kT_c$  is a measure of the width of the trap distribution,

$$j_{\text{SCL}} \propto \frac{F^{l+1}}{d^l} \quad (6.135)$$

with  $l = T_c/T$  [157]. The stronger field dependence as compared with Child's law is a signature of the rising quasi-Fermi level and, concomitantly, the lowering of the activation energy for thermally assisted trap release. If the number of trapped charged carriers approaches the number of traps the regime of trap-filled transport is entered at a characteristic field  $F_{\text{TFL}} = 2eH/3\epsilon_0\epsilon$ .

It is obvious that the measurement of a steady-state SCL current affords the possibility of determining the carrier mobility. This technique has been applied successfully to films of  $\pi$ -conjugated polymers [159] and molecular glasses [160] as examples of organic solids without deep traps. The SCLC formalism has also been applied to trap-containing  $\pi$ -conjugated systems [161]. In general, however, one has to examine relevant experimental results carefully in order to avoid any misinterpretation of the data. Specifically, one has to ascertain that an observed superlinear current-field relation is, indeed, due to SCL current flow rather than to field-assisted carrier injection. An unambiguous indication would be the thickness dependence of the current at a given electric field. In practice, however, the experimentally accessible thickness range is fairly limited, particularly if the sample morphology can change with increasing the sample thickness. A timely example of the intricacies one confronts when applying the SCLC technique is the work of de Boer et al. [162] on tetracene single crystals.

Another problem possibly encountered in cw-SCL current flow relates to the effect of deep traps at low concentration whose capture time exceeds the carrier transit time but which might become important under steady-state conditions. An elegant way to circumvent this ambiguity is to measure a transient SCL current upon applying a step voltage to the injecting electrode. In this case the current increases with time because the moving front of the carrier packet experiences an increasing electric field due to the field redistribution caused by the space charge drifting across the sample. It gives rise to a cusp in the current at a time  $t_{\text{cusp}} = 0.78t_{\text{tr}}$  [163]. For  $t > t_{\text{cusp}}$  the current can either settle at a constant value or decay slowly because of deep trapping. The technique of transient SCL current is applicable to thin samples because injection occurs at the very interface between dielectric and electrode. However, decreasing the sample thickness is accompanied by an increase of the RC time of the circuit and one has to compensate for this effect. Needless to say, the current cusp monitoring the arrival of the carrier front would be eroded if transport were dispersive. The studies of Abkowitz and Pai [164] and, later, Poplavskyy et al. [160] are examples of the successful application of the SCLC technique to systems that are devoid of deep traps and feature non-dispersive hopping transport.

A variant of the transient SCLC method is the xerographic discharge technique. By this method the free surface of a sample is charged by a corona discharge.

Exposing it to a short light flash injects a sheet of charge carriers into the bulk of the sample. As the charge drifts across the sample the surface potential decreases. From its time dependence both the mobility and the efficiency of charge generation can be inferred [165, 166].

#### 6.4.2.3 Determination of the Charge Carrier Mobility Based Upon Carrier Extraction by Linearly Increasing Voltage (CELIV)

Measurement of the charge carrier mobility via the TOF method requires that the dielectric relaxation time,  $\tau_{rd} = \epsilon_0 \epsilon / \sigma_c$ , exceeds the carrier transit time. On applying an electric field of  $10^5 \text{ V cm}^{-1}$  to a  $1\text{-}\mu\text{m}$  thick sample and assuming that the residual dark conductivity is determined by  $\sigma_c = en\mu$ , this leads to a critical dark charge carrier concentration  $n < 3 \times 10^{15} \text{ cm}^{-3}$ . It is worth noting that this condition is equivalent to the condition that the residual ohmic current originating from impurity ionization is less than the hypothetical unipolar space charge-limited current (see Section 6.4.2.2). For the above set of parameters and assuming  $\mu = 10^{-6} \text{ cm}^2 \text{ V}^{-1} \text{ s}^{-1}$ ,  $j_{\text{SCL}} = 3 \mu\text{A cm}^{-2}$ . In molecular crystals, molecularly doped polymers and nominally undoped conjugated polymers, this condition is easily fulfilled. In those systems the experimentally observed dark currents hardly ever exceed  $10^{-8} \text{ A cm}^{-2}$  provided that (i) the electrodes are only weakly injecting and (ii) deliberate or unintentional doping by strong electron donors or acceptors is absent. Examples of doped organics are conjugated polymers with low ionization potential, such as polythiophene, unintentionally doped by oxygen or by oxidation products [167].

The CELIV method, introduced by Juška and co-workers [168, 169], is a technique to measure (i) charge carrier mobilities in systems with shorter dielectric relaxation times and (ii) the residual, if spurious, bulk conductivity. The idea is to apply two sequential voltage pulses of triangular shape under reverse bias to a sandwich-type diode with at least one non-injecting electrode. The instantaneous rise of the current on applying the first voltage pulse is due to the (geometric) capacitance of the sample. The initial slope of the following current pulse is a measure of the bulk conductivity:

$$\sigma_c = \epsilon_0 \epsilon \left. \frac{d[j/j(0)]}{dt} \right|_{t=0} \quad (6.136)$$

while the time  $t_{\text{max}}$  at which the current features a maximum is a measure of the carrier mobility:

$$\mu = \frac{2d^2}{3At_{\text{max}}^2 [1 + 0.36\Delta j/j(0)]} \quad (6.137)$$

where  $V(t) = At$  is the time-dependent voltage pulse and  $\Delta j = j(t_{\text{max}}) - j(0)$ . The derivation of Eq. (6.137) involves the integration of the Poisson and continuity equations taking into account that the spatial distribution of the electric field inside

the sample changes with time. The second voltage pulse is used to monitor recovery of equilibrium after the first voltage pulse.

When interpreting mobility data derived from a CELIV experiment, one should recognize, however, that CELIV and TOF methods are different in principle. In the former case the applied electric field acts on charge carriers that are already present under equilibrium conditions whereas TOF probes carriers that are photo-excited and – at least in disordered systems – suffer energetic relaxation while migrating towards the exit contact.

#### 6.4.2.4 Charge Carrier Motion in a Field-Effect Transistor (FET)

In an organic FET [170, 171], the current flowing between source and drain electrodes in a coplanar arrangement is modulated by a perpendicularly applied gate voltage,  $V_g$ , across an insulating layer, usually  $\text{SiO}_2$  or  $\text{Al}_2\text{O}_3$ . The gate voltage induces a unipolar charge near the interface of the semiconductor and insulator that has been injected from either anodic or cathodic drain electrode, depending on the polarity of  $V_g$ . That charge is moving under the action of the drain voltage  $V_d$  and is eventually replenished from the electrode. Because the number of carriers is known, their mobility can be extracted from the measured drain current  $I_d$ . In the linear regime,

$$\mu = \frac{L}{WC(V_g - V_T)} \frac{I_d}{V_d} \quad (6.138)$$

where  $W$  and  $L$  are the length of the electrodes and their separation, respectively,  $C$  is the capacitance and  $V_T$  the threshold voltage. There is a problem because the spatial distribution of the voltage drop across the transistor is controlled by both  $V_d$  and  $V_g$  and is not constant because the drain potential varies along the conducting channel. A finite contact resistance would also affect the transfer characteristics. Working in the linear regime minimizes this problem [172]. However, there are generic problems encountered when comparing mobility values derived from FET and TOF experiments. In a FET the charge carriers are localized in a very thin, if not monomolecular, layer of the semiconductor next to the insulator. Because of the energetic disorder of the hopping sites in a random organic material, tail states of the DOS are already filled by the capacitor charges. If the DOS is not affected by the presence of the surface of the insulator this will decrease the activation energy for transport and, concomitantly, increase  $\mu$  [114, 173, 174]. At the same time, the presence of that interfacial charge will roughen the energy landscape because of the more or less randomly positioned Coulombic centers [114]. This should lead to an opposing decrease of  $\mu$ . Apart from state filling effects, the shape of the DOS near the interface can be different from that in the bulk because of the likely presence of a dipole layer at the surface of the insulator that tends to broaden the DOS.

Another factor is the morphology of the dielectric layer next to the interface. This is particularly important for polymeric systems in which the polymer chains

tend to deposit parallel to the surface. There is a current endeavor to reduce the disorder by parallel chain alignment in order to increase the FET mobility because large-scale application of polymeric FETs requires higher mobilities [175]. In any event the value of the charge carrier mobility derived from FET characteristics is an operationally determined quantity that does not need to be identical with the value derived from a TOF experiment.

#### 6.4.2.5 The Microwave Technique

Conventional time-resolved mobility experiments usually monitor charge motion across the entire sample. In random media this implies hopping transport mediated by capture and release of carriers at tail states of the DOS while the early time transport, i.e. prior to trapping, is not amenable. A method to cover the time window between carrier generation and onset of trapping is the flash photolysis time-resolved microwave conductivity technique (FR-TRMC) developed by the Warman-de Haas group in Delft [176–178]. The idea is to create charge carriers inside a bulk sample by a several nanoseconds long pulse of 3-MeV electrons from a van der Graaf accelerator and to probe the induced conductivity, i.e. the imaginary part of the dielectric function, via the attenuation of the microwave power when the microwave radiation propagates through the medium. The frequency of the microwave field is on the order of 30 GHz, the power output is typically 100 mW and the microwave field is of the order of  $100 \text{ V cm}^{-1}$ . This implies that the probing electric field is much lower than in a usual TOF experiment and the average net displacement of the carriers is very small whereas the diffusion length of a carrier can be significant. Note that on the time-scale of 10 ps, equivalent to a quarter-wave of 25-GHz radiation, the diffusion length  $l_{\text{diff}} = (2Dt)^{1/2}$  of a charge carrier with a mobility of  $1 \text{ cm}^2 \text{ V}^{-1} \text{ s}^{-1}$ , i.e. a diffusion constant of  $2.5 \times 10^{-2} \text{ cm}^2 \text{ s}^{-1}$ , is 7 nm. The radiation-induced conductivity is  $\Delta\sigma_c = en(\mu_+ + \mu_-)$ , where  $n$  is the number of carriers generated. In order to evaluate the combined electron and hole mobilities requires knowledge of  $n$ . Since ionization efficiencies of high-energy electrons are fairly insensitive to the chemical structure of organic molecules, this information has been inferred from radiation studies on liquid alkanes for which charge carrier mobilities are known from TOF experiments, thus allowing a critical assessment of the compatibility of both techniques. One should keep in mind, though, that the FR-TRMC technique probes the motion of charges after a time set by the duration of the electron pulse. Any ultra-fast response would not be recovered.

#### 6.4.2.6 Charge Carrier Motion Probed by Terahertz Pulse Pulses

The most recent advancement in ultra-fast monitoring of charge carrier motion in an organic solid is THz pulse spectroscopy [179]. It pushes the time window of carrier probing into the picosecond range. Instead of exciting charge carriers by a nanosecond electron pulse as is done in FR-TRMC (see Section 6.4.2.5), 100-fs pulses from an amplified Ti-sapphire laser are applied. The same laser is used to

generate THz pulses with a center frequency of 1 THz. Measuring the change in transmission upon charge carrier generation as a function of the delay time probes the transient change of the sample conductivity and, provided that the efficiency of carrier generation is known, yields the mobility within a temporal window of 1–40 ps. Related experiments were done on crystals of functionalized pentacene and, quite recently, on a II-conjugated polymer [180].

## 6.5

### Experimental Results

#### 6.5.1

#### Analysis of Charge Transport in a Random Organic Solid with Energetic Disorder

One of the generic differences between inorganic and organic glasses is the form of the DOS distribution. In the former, e.g. in chalcogenide glasses, there is a band of extended states and an exponential distribution of localized band-tail states separated by a so-called mobility edge. In the latter, all states are localized and form a Gaussian-type DOS (see Section 6.3.1). In inorganic glasses, transport of charge carriers proceeds via multiple trapping and it is entirely dispersive because the Boltzmann-type equilibrium distribution of carriers is impossible for an exponential DOS. In organic glasses, transport of randomly generated charge carriers is dispersive at short times and becomes non-dispersive when they have relaxed towards quasi-equilibrium. In that transport mode the temperature dependence features an  $\exp[-(T_0/T)^2]$  law, where  $kT_0 = (2/3)\sigma$ . An example is the temperature dependence of the hole mobility in 1,1-bis[(di-4-tolylamino)phenyl]cyclohexane (TAPC) glass plotted in the conventional Arrhenius-type  $\ln\mu$  versus  $T^{-1}$  form and on a  $\ln\mu$  versus  $T^{-2}$  scale (Fig. 6.17) [181]. There is a systematic deviation from straight-line behavior in the former case that is eliminated in the  $\ln\mu$  versus  $T^{-2}$  representation. It is obvious, though, that good data quality is required in order to discriminate between the two plots. An additional criterion is provided by extrapolating  $\mu$  towards  $T \rightarrow \infty$ . The maximum value for  $\mu_0$  should be the mobility in the material in the crystalline phase, i.e. typically  $0.1\text{--}1\text{ cm}^2\text{ V}^{-1}\text{ s}^{-1}$ . Higher values obtained by plotting  $\mu(T)$  on an Arrhenius scale and extrapolating to  $T \rightarrow \infty$  are, therefore, unphysical.

The key parameter that determines the transport properties of a random organic solid is the width of the DOS,  $\sigma$ , that is inferred from the temperature dependence of the mobility. It not only determines the magnitude of  $\mu$  at a given temperature but also the temperature,  $T_c$ , at which transport becomes dispersive. Since the carrier equilibration time increases with decreasing temperature much faster than the transit time [77], a transition from non-dispersive to dispersive transport will be observed in a TOF experiment as the temperature decreases. Its signatures are (i) the loss of an inflection point in a TOF transient if plotted on a linear current versus time plot and (ii) a negative slope in a  $\ln\mu$  versus  $T^{-2}$  plot because carriers that do not have occupational DOS relaxed completely to equilibrium need, on

average, more thermal excitation for transport at longer times. A textbook example of this phenomenon is the transition from non-dispersive to dispersive hole transport in a glass of *p*-diethylaminobenzaldehyde diphenylhydrazone (DEH) (Fig. 6.18) [182] at a critical temperature where  $d \ln \mu / dT^{-2}$  changes (Fig. 6.19). It is remarkable that both the shape of the transient TOF signal and its displacement on the time axis are determined by only the  $\sigma$ -value inferred from the  $\mu(T)$  dependence at temperatures above  $T_c$ . The transition from non-dispersive to dispersive transport also depends on the sample thickness because in a thinner sample the

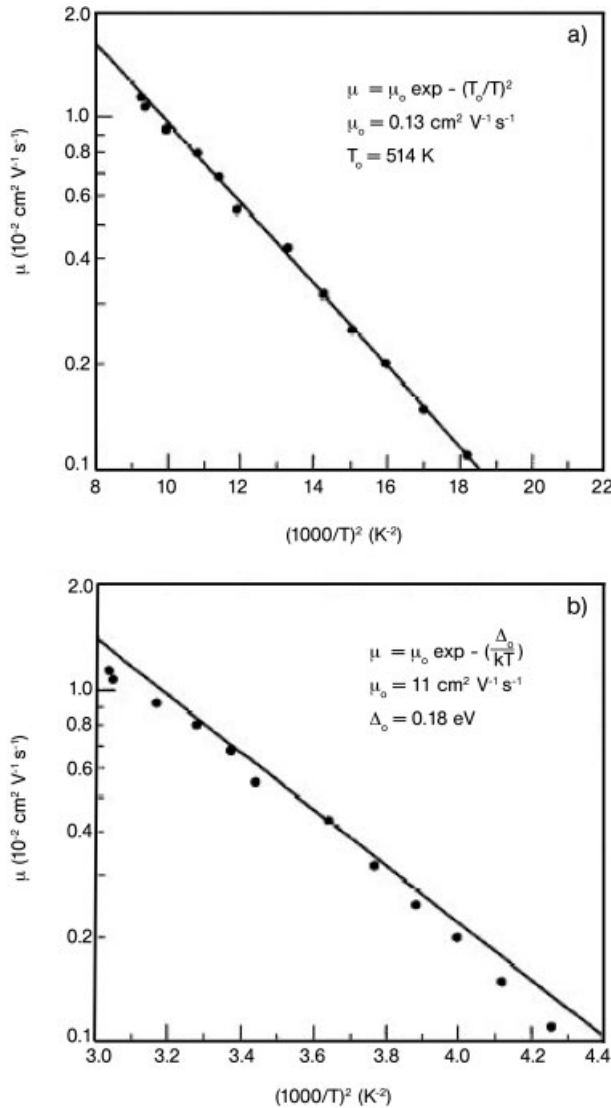


**Figure 6.17** The logarithm of the low-field mobility versus  $T^{-2}$  (a) and vs  $T^{-1}$  (b).

carriers have less time to attain quasi-equilibrium before recombining at the counterelectrode. It is obvious that mobility inferred from a  $\log \mu$  versus  $\log t$  plot is an operationally determined quantity only and depends on experimental parameters such as sample thickness and electric field.

A recent example of the straightforward application of the disorder model is the work of Poplavskyy and Nelson [160] on amorphous films of a fluorenylamine derivative with a spiro linkage between two fluorene units. This kind of compound is interesting because the spiro linkage prevents the formation of incipient sandwich-like dimers of planar  $\pi$ -bonded molecules that can act often as traps for both singlet excitations and charge carriers. By the same token the insertion of a spiro linkage suppresses crystallization. The materials under study were solvent-cast films of methoxyspirofluorenylamine (spiro-MeOTAD), whose ionization potential is 5.2 eV. In order to check whether or not the transport properties depend on film thickness, the hole mobility was measured either on up to 4- $\mu\text{m}$  thick films using the TOF method or on films as thin as 135 nm employing the transient SCLC technique (see Section 6.4.2.2). In the latter case holes were injected from a dispersion of poly(3,4-ethylenedioxythiophene) and poly(styrene-

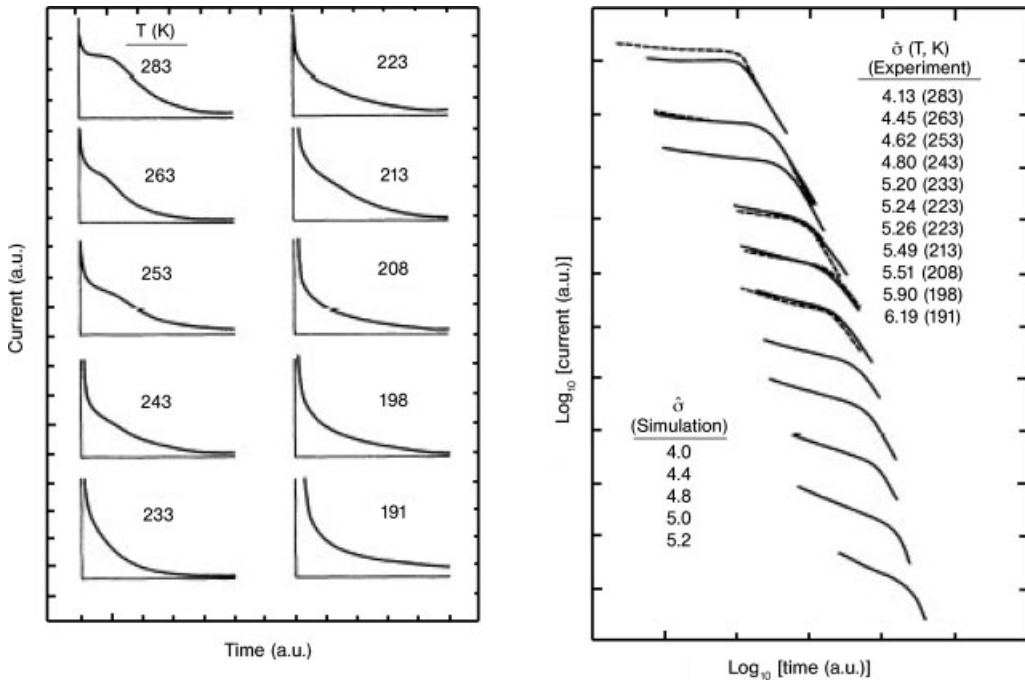


**Figure 6.18** (a) Experimental transients, parametric in temperature at  $6 \times 10^5 \text{ V cm}^{-1}$ . (b) Comparison between experimental (full curves) and simulated (dashed) transients. The field was  $6 \times 10^5 \text{ V cm}^{-1}$ . The

simulations are for  $n_z = 8000$ , except that  $\sigma/kT = 5.2$  has been extrapolated from the data for  $n_z \leq 4000$ . The experimental transient for  $\sigma/kT = 4.45$  is coincident with the simulation for  $\sigma/kT = 4.4$ .

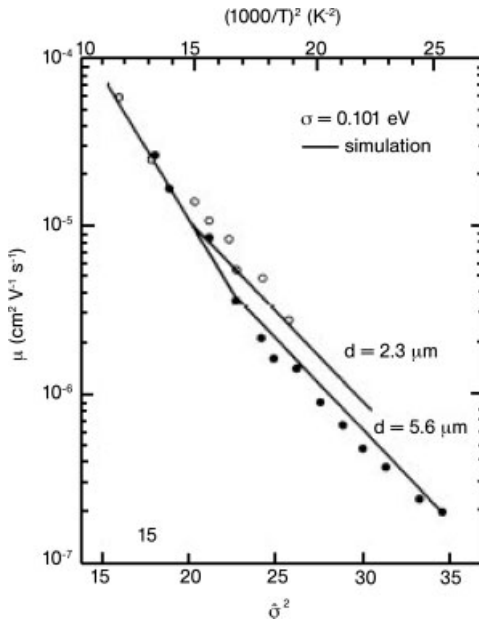


**Figure 6.19** Hole mobilities in DEH evaluated from the relationship  $\mu = d/E\langle t_T \rangle$ . Here  $\langle t_T \rangle$  was determined from the intersection of the asymptotes in either double linear or the double logarithmic representation.

sulfonic acid) (PEDOT/PSS) anode that turns out to form an ohmic contact in the dark. The TOF signals showed perfect horizontal plateaus. In the SCLC case a cusp was observed that monitored the arrival of the front of mobile charges. Additionally, the steady-state SCLC current was measured and the mobility was determined via Child's law.

It was gratifying that, within a factor of two, all methods yielded a consistent  $\mu(F)$  dependence (Fig. 6.20), implying that  $\mu$  was independent of thickness (Fig. 6.21). This proves that the morphology of the film does not change within the thickness range between a few hundred nanometers and several micrometers. It is remarkable that the values of the mobility probed by steady-state SCL conductivity and by transient techniques were the same. This testifies to the absence of deep extrinsic traps outside the intrinsic DOS. From the  $\mu(F, T)$  data, the width of the DOS was determined as 0.101 eV, the positional disorder parameter  $\Sigma$  was 2.3–2.7 and  $\mu_0$  was  $0.047 \text{ cm}^2 \text{ V}^{-1} \text{ s}^{-1}$ .

It turned out that the substituents on the peripheral phenylene groups have an influence on the above parameters. Replacements of the methoxy groups by either hydrogen or methyl groups decreases  $\sigma$  to a value of 0.08 eV and  $\mu_0$  to 0.01–0.016  $\text{cm}^2 \text{ V}^{-1} \text{ s}^{-1}$  [183]. Bach et al. [183] related the higher value of  $\mu_0$  in the methoxy-substituted molecule to the increase in the effective overlap of the wavefunctions of neighboring molecules. Such an effect was earlier observed in methoxy-

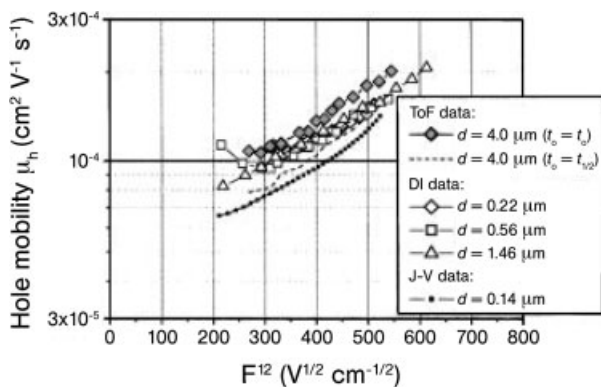


**Figure 6.20** Hole mobilities in spiro-MeOTAD measured by three different methods at room temperature.

TPD with respect to TPD [*N,N'*-diphenyl-*N,N''*-bis(3-methylphenyl)-1,1'-biphenyl-4,4'-diamine] itself. This was qualitatively explained by the electron-donating effect of the  $\text{OCH}_3$  side-group that leads to a higher negative charge density at the HOMO, which results in a higher effective spatial extension of this orbital.

However, there is an alternative explanation for the above phenomenon, which is related to positional disorder. If there is a distribution of electronic coupling matrix elements among the hopping sites, additional hopping paths can be opened on the premise that a carrier choosing the fastest route will win. Therefore, the prefactor mobility increases with  $\Sigma$  as  $\exp(\Sigma^2/2)$  [184]. An increase in  $\mu_0$  by a factor of 3 would imply an increase in  $\Sigma$  by a factor of 1.5. On average, this is

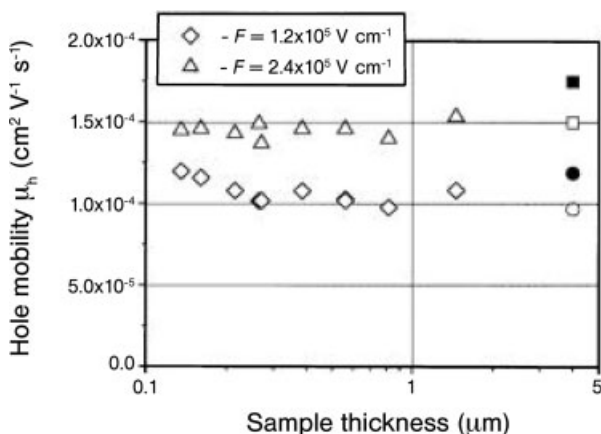


**Figure 6.21** Dependence of transient mobilities (TOF and DI methods) on the sample thickness at two different electric fields at room temperature. TOF data ( $d = 54 \text{ mm}$ ) are shown for two different transit times:  $t_0$  (open symbols) and  $t_{1/2}$  (filled symbols).

consistent with the experimental results. Obviously, caution is in order when trying to extract too much information from a limited amount of experimental data.

The width of the DOS is a measure of the variation of the polarization energy of a charged molecule inside the matrix. Below the glass transition the system can be considered as being frozen [185]. Therefore, that energy is the energy of interaction between a charge and static as well as induced dipoles that are oriented randomly. Concomitantly,  $\sigma$  is composed of a dipolar and van der Waals terms as  $\sigma = \left(\sigma_{\text{vdw}}^2 + \sigma_{\text{dip}}^2\right)^{1/2}$  [73, 186]. Even in an apolar matrix there can be a dipolar contribution to  $\sigma$  if the molecule carries bond dipoles that cancel vectorially in the absence of extrinsic charges, because the interaction energy between a charge and the ensemble of bond dipoles is finite even if that molecule is randomly oriented.

The original disorder formalism has been applied to conjugated polymers. Inhomogeneously broadened absorption spectra prove unambiguously that they belong to the class of random organic solids, but it remains to be checked whether or not the distribution of hopping sites can be described by a Gaussian function because there are on-chain and off-chain contributions. In the oligomer approach [187] the chain is an ensemble of segments each consisting of several repeat units whose length, usually called the effective conjugation length  $L_{\text{eff}}$ , is limited by topological faults that interrupt or, at least, weaken the conjugation of the  $\pi$ -electrons in the case of a  $\pi$ -type conjugated polymer and that of the  $\sigma$ -bonds in a polysilene. Invoking the simplest particle-in-the-box formalism translates a statistical variation of  $L_{\text{eff}}$  into a distribution of single carrier HOMO and LUMO as well as exciton states by extrapolating the presumed linear relation between excitation energy of an oligomer versus reciprocal chain length. However, a recent theoretical approach based on the density-matrix renormalization group indicates that this linear extrapolation is unjustified and a quadratic law is more appropriate for extrapolation to the infinite chain limit [188]. In addition to intra-chain disorder there is off-chain disorder, i.e. the variation of the electronic polarization energy of a chain segment caused a random inter-chain packing effect. Anyhow, the HOMO and LUMO energy states of chain segments inside a bulk polymer film will depend on a large number of internal coordinates each varying randomly. Therefore, the central limit theorem should apply, implying that the statistical variation obeys a Gaussian envelope function. This is supported by the Gaussian low energy tail of the  $S_1 \leftarrow S_0$  0–0 exciton transition and by the observation that the exciton dynamics can be described in terms of spectral diffusion with an excitonic DOS of Gaussian shape [189].

An example of the successful employment of the unmodified disorder model is the interpretation of the data obtained on a spin-cast ca 1- $\mu\text{m}$  thick film of a phenylamino-PPV derivative (PAPPV) [124]. In a TOF experiment, the charge carriers were generated by dissociation at the ITO/polymer interface of singlet states created by an 8-ns laser pulse. Figures 6.22 and 6.23 show the absorption and fluorescence spectra of the film and two representative TOF signals recorded at higher (311 K) and lower (153 K) temperature, respectively. They testify to transit time dispersion occurring at lower  $T$ . The hole mobility was determined via the inter-

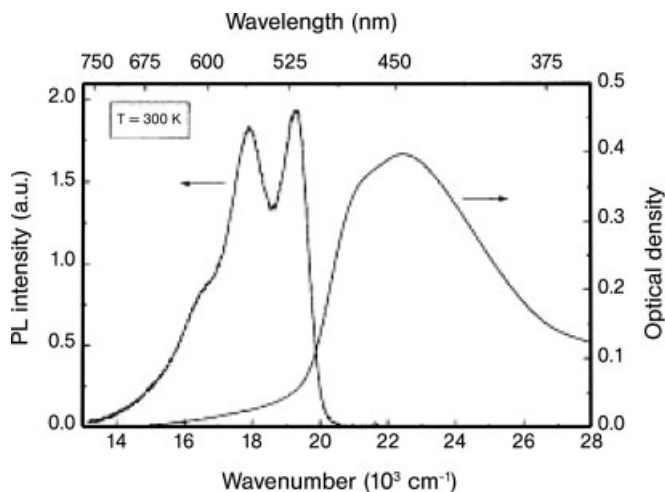


**Figure 6.22** Absorption and fluorescence spectra of PAPPV.

section of the pre- and post-transit time asymptotes of the current plotted either on a linear or a double logarithmic scale. The temperature dependence of the mobility was plotted on a  $\ln \mu$  versus  $T^{-2}$  scale for two different values of the electric field. Above 153 K,  $\mu(T)$  follows a  $\ln \mu \sim (T_0/T)^2$  law with  $T_0 = 396$  K, i.e.  $\sigma = 52$  meV for the lower field (Fig. 6.24). Extrapolating  $\mu(T)$  to  $T \rightarrow \infty$  yields  $\mu_0 = 10^{-2} \text{ cm}^2 \text{ V}^{-1} \text{ s}^{-1}$ . Onset of transit time dispersion is accompanied by a decrease in the absolute value of  $d \ln \mu / dT^{-2}$ , which is a signature of carriers not having attained quasi-equilibrium. It is gratifying that the transition occurs within 10 K of the critical temperature predicted by simulation. The field dependence of  $\mu$  is also in accordance with the disorder model featuring a  $\ln \mu \sim \beta F^{1/2}$  law with  $\beta$  increasing as  $T$  decreases.

The situation is different for the methyl-substituted ladder-type polyphenylene (MeLPPP) [124]. Based on absorption and the well vibronically resolved fluorescence spectra of a neat film (Fig. 6.25), this is the least disordered conjugated polymer. Fitting the low-energy tail of the  $S_1 \leftarrow S_0$  0–0 transition yields  $270 \text{ cm}^{-1}$  for the disorder parameter of the excitonic transition [124]. However, on annealing the sample at  $150^\circ \text{C}$  for several hours a broad low-energy feature is seen in the emission spectrum, indicating that exciton traps of either structural or photochemical origin are created. In the unannealed sample the TOF signals are almost molecular crystal-like, proving that, indeed, disorder effects are weak. Interestingly, the field dependence of the hole mobility does not feature a  $\ln \mu \sim F^{1/2}$  (Fig. 6.26) behavior, and the temperature dependence does not bear out a  $\ln \mu \sim T^{-2}$  law. The latter dependence is only recovered for the annealed sample yielding a  $\sigma$  value of 50 meV (Fig. 6.27). In the unannealed sample the temperature dependence of  $\mu$  is fairly weak. If plotted on an Arrhenius scale one could arrive at an activation energy of  $\sim 22$  meV. Remarkably, extrapolating  $\mu(T)$  to  $T \rightarrow \infty$  yields  $\mu_0 \approx 3 \times 10^{-3} \text{ cm}^2 \text{ V}^{-1} \text{ s}^{-1}$ . It appears that in the neat sample the  $\mu(F, T)$  dependence can-

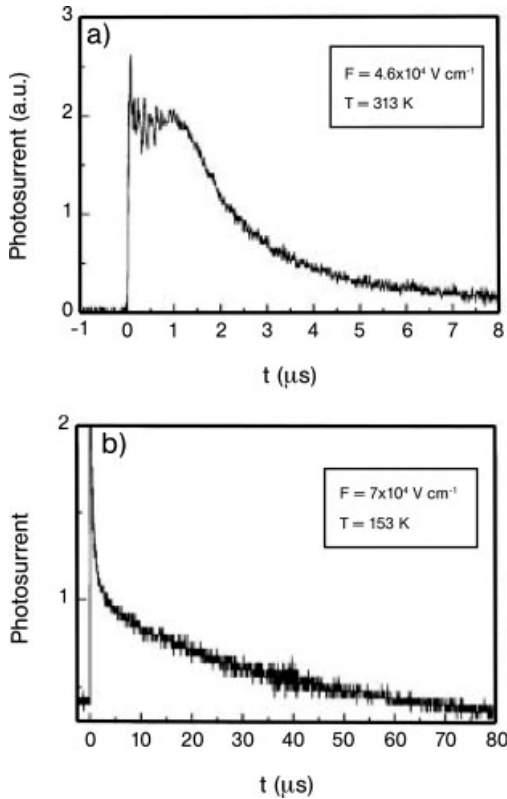


**Figure 6.23** TOF signals of PAPPV in the nondispersive (a) and dispersive (b) transport regimes.

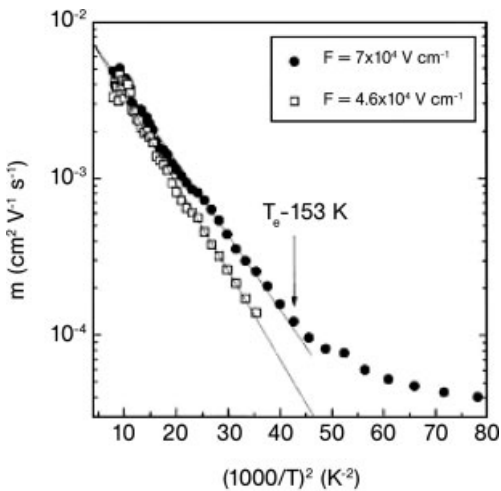


**Figure 6.24** Temperature dependence of the mobility  $\mu$  of PAPPV.  $\log \mu$  is plotted against  $T^{-2}$ . The arrow marks the transition from nondispersive to dispersive transport.

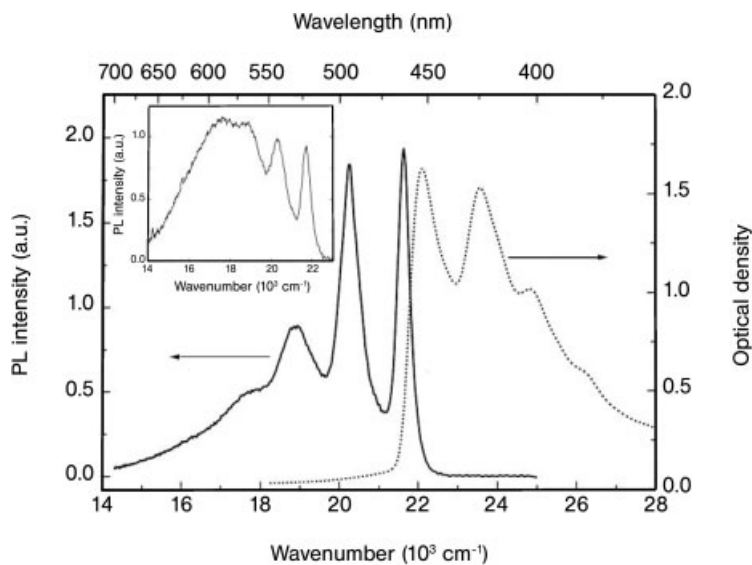


**Figure 6.25** Room temperature absorption and fluorescence spectra of MeLPPP films. The inset shows the fluorescence spectrum of the annealed MeLPPP film.

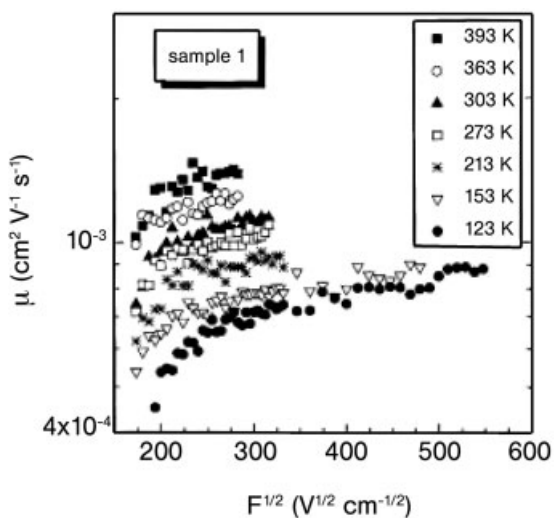


**Figure 6.26** Electric field dependence of the hole mobility of MeLPPP sample 1 at different temperatures. Data plotted on a  $\log \mu$  versus  $F^{1/2}$  scale. For clarity, the data at 333, 243 and 183 K are not shown.

not be explained in terms of the conventional disorder model. More recently, theoretical work by Fishchuk et al. [123] indicated that the simplified version of the Miller–Abrahams-type jump rate is no longer adequate at weak disorder because it ignores phonon emission. When employing the exact Miller–Abrahams rate the  $\mu(F,T)$  data can indeed be fitted invoking a disorder parameter of 33 meV (Fig. 6.27, solid line in the lower plot).

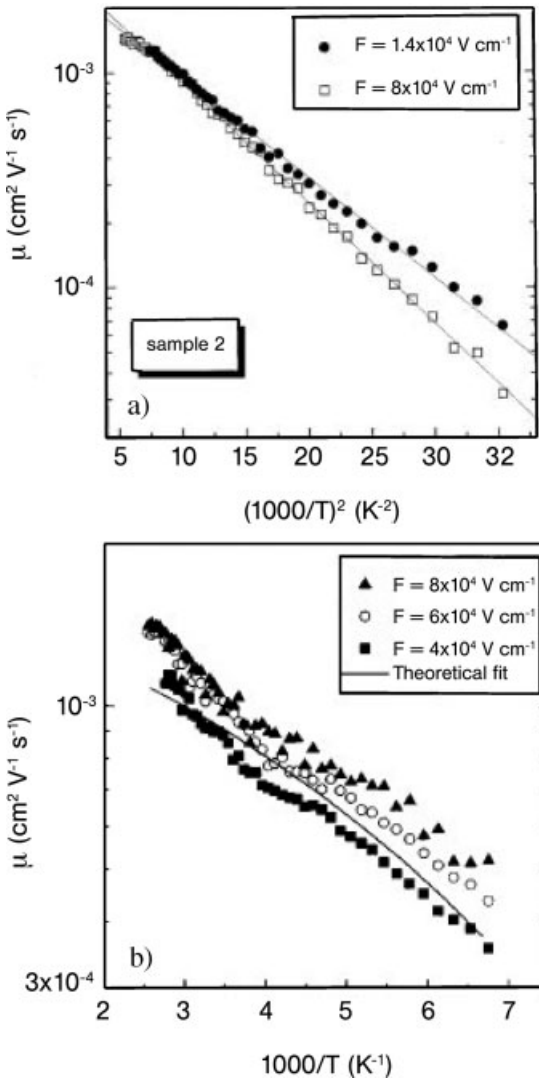


**Figure 6.27** Logarithm of the mobility versus  $T^{-2}$  for MeLPPP sample 2 (a) and Arrhenius plot of the hole mobility of MeLPPP sample 1 parametric in electric field (b). The solid line in (b) is theoretical fit by Eq. (6.66) within

the framework of *approach I* (see Section 6.2.3.3). The parameters used for the calculation are  $\sigma = 0.0355 \text{ eV}$  and  $\mu_1 = 1.4 \times 10^{-3} \text{ cm}^2 \text{V}^{-1} \text{s}^{-1}$ .

There are two important implications of the results obtained for MeLPPP. The comparison between the  $\mu(T)$  dependences in neat and annealed samples proves that this temperature dependence is indeed controlled by structural disorder and is not due to polaron formation because the latter would be rather a generic feature of an individual polymer chain. The second implication is that even in a very weakly disordered material  $\mu(T)$  does not extrapolate at  $T \rightarrow \infty$  to a value characteristic of a molecular crystal. Obviously, neither energetic disorder nor any polaron contribution to the carrier jump rate is sufficient to explain why the mobility is much lower than in a molecular crystal. A possible explanation is related to the oscillatory motion of a charge carrier within each conjugated segment of a polymer chain that comprises typically 10 repeat units or more. Since the chains are never perfectly aligned, inter-chain hopping should occur preferentially at crossing points only where electronic coupling is optimal. This would imply that delocalizing charge carriers in a well-ordered polymer chain is counterproductive for inter-chain hopping that limits transport in a bulk film unless chains can be aligned on a mesoscopic scale via side group ordering [175].

Another class of conjugated polymers with comparatively high mobility is the polyfluorenes (PFOs). On a 3- $\mu\text{m}$  thick film of 9,9-dioctyl-substituted PFO, TOF transients feature well-developed plateaus. At 300 K the hole mobility was  $(3\text{--}4) \times 10^{-4} \text{ cm}^2 \text{ V}^{-1} \text{ s}^{-1}$  virtually independent of electric field [125]. This is a signature of both a high degree of purity and moderate if low disorder. An interesting aspect of that particular material is its ability to form a liquid crystalline (nematic) phase. A PFO film was deposited on a substrate with a 30-nm thick polyimide film, rubbed with a nylon cloth to generate surface alignment of the layer. After heating in vacuum to 200 °C and rapid quenching, the film acquired a glassy morphology with no indication of crystallite formation that might cause dielectric breakdown along grain boundaries. It turned out that in the ordered phase the hole mobility was  $8.5 \times 10^{-3} \text{ cm}^2 \text{ V}^{-1} \text{ s}^{-1}$ , i.e. chain alignment raises the mobility by a factor of 30, indicating that nematic alignment was preserved. This is further clear evidence for the crucial importance of disorder [126].

In an attempt to combine the good charge-transporting properties of triarylamine-based glass with the processability of a soluble polymer, Redecker et al. [190] synthesized five dioctylfluorene–triarylamine conjugated polymers. All of them feature hole mobilities ranging between  $3 \times 10^{-4}$  and  $3 \times 10^{-3} \text{ cm}^2 \text{ V}^{-1} \text{ s}^{-1}$  at a field of  $2.5 \times 10^5 \text{ V cm}^{-1}$  and 295 K. These values of the mobility are larger than the value accepted for TPD dispersed in a polycarbonate binder at the same concentration and even exceeds that of an undiluted glassy film of TPD. This indicates that the fluorene moiety has significance beyond that of a simple chemical linkage between triarylamine transport sites. Obviously, conjugated fluorene moieties participate in the transport process, most probably facilitating intra-chain transport among the triarylamine units that have a lower oxidation potential than that of the PFO.

## 6.5.2

## The Effect of Positional Disorder

In Sections 6.3.2 and 6.3.3, the effect of positional disorder on charge transport was dealt with from a theoretical perspective. Its experimental signature is the negative field dependence of the mobility at moderate electric fields and the observation of a mobility minimum at a certain electric field. Starting from the work of Peled and Schein [65], where the decrease in the hole mobility with increasing electric field in a pyrazoline-doped polycarbonate was first reported, some molecularly doped [72, 134] and conjugated [135, 191] polymers have been shown to feature a negative field dependence, notably at elevated temperatures. A well-documented example is the field-dependent hole mobility measured at variable temperatures in TAPC doped into polycarbonate (Fig. 6.28). As mentioned in Section 6.3.1, positional disorder arises from fluctuations of the intersite coupling due to variation of either intersite distances or the overlap between the corresponding electronic orbitals. Under the condition that thermally activated jumps are the rate-limiting step, the motion of a charge carrier in a rough energy landscape is controlled by activated jumps towards sites close to the statistically defined transport energy [106, 113]. At weak to moderate electric fields transport is in accor-

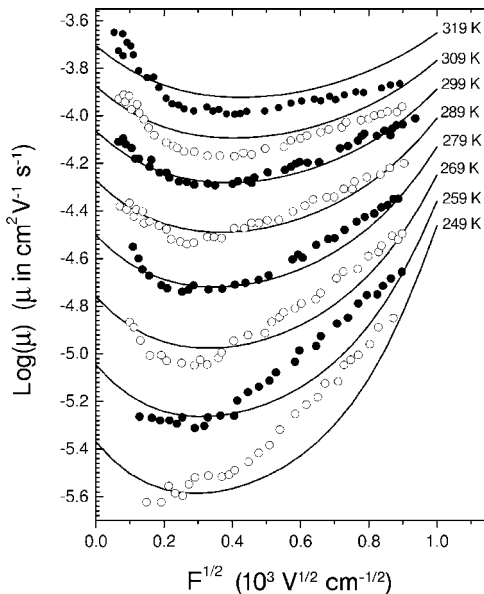


**Figure 6.28** Experimental field dependences of mobility in 1,1-bis(di-4-tolylaminophenyl)-cyclohexane (TAPC) doped in polycarbonate measured at different temperatures (symbols). The theoretical calculations performed by Eq. (6.103) from Ref. [132] assuming the

Miller–Abrahams model (see Section 6.3.3.6) for the same temperatures are given by solid curves. The following parameters were used for calculation:  $\sigma = 0.095$  eV,  $\xi_0 = 7.5$ ,  $l_0 = 3$  nm and  $\mu_0 = 3.2 \times 10^{-3}$  cm<sup>2</sup> V<sup>-1</sup> s<sup>-1</sup>.

dance with the Einstein relation between drift and diffusion. As the field increases, the activation energy is lowered by the drop of the electrostatic potential between the hopping sites. Therefore, the mobility should increase while the diffusive character of mobility is still retained. This is no longer the case when, on average, the drop of the electrostatic potential gained upon every jump is comparable to or even exceeds the energy difference between hopping sites for an along-field jump. In that case, the dwell time of a carrier on a site approaches the reciprocal rate for that jump because jumps against the field direction are gradually eliminated. Accordingly, the transport velocity must saturate with field. This implies a hyperbolic decrease in the carrier mobility because it is controlled by energetically downward jumps that are not accelerated with increasing field.

The situation is more complex if positional disorder becomes important. In that case a carrier can avoid an energetically unfavorable site by executing a detour around that site. This resembles motion in a percolating cluster and leads to an increase in the overall carrier mobility at moderate fields. However, the interplay between drift and diffusion is field dependent, as it is in the case of pure energetic disorder, because the excess motional freedom that a carrier gains by following the detour path is gradually eliminated at higher fields. Importantly, however, the critical field for that effect is dictated by the decrease in the electrostatic potential across the percolating cluster, i.e. the degree of positional disorder, rather than by the intersite distance. This leads to an S-like  $\log\mu$  versus  $\beta F^{1/2}$  dependence. At very low fields,  $\mu$  is constant and tends to decrease as the field increases. Eventually,  $\beta$  reverses sign when the additional carrier loops are blocked and the effect of energetic disorder takes over. At the highest electric fields,  $\mu$  decreases again owing to the drift velocity saturation.

The above qualitative reasoning was based upon a hopping concept involving Miller–Abrahams-type jump rates. However, the phenomenological transport characteristics can similarly be rationalized in terms of Marcus-type jump rates (see Section 6.3.3.6). The recent theoretical work by Fishchuk et al. [132] employing the effective medium approach shows that the shape of the  $\mu(F)$  dependence is independent of the choice of the particular hopping rate. Furthermore, the decrease in  $\mu$  at very low electric fields can, in principle, be recovered by invoking the Marcus jump regime. However, a detailed analysis of mobility data for a system where structural site relaxation is important indicates that unrealistically large values of the reorganization energy are required in order to explain the decrease in the hole mobility at very high electric fields, while a hopping approach yields reasonable fit parameters.

In Fig. 6.28, experimental data on the  $\mu(F, T)$  in the TAPC/PC system are compared with theoretical EMA results. Except at low fields, the agreement is good. Not only does this confirm the validity of that theory, it also proves that the negative field dependence together with the observation of a minimum of  $\mu(F)$  is a genuine feature of random organic solids in which both energetic and positional disorder are important and the structural correlation length exceeds the nearest-neighbor jump distance. This conclusion is particularly important because it has been argued that this phenomenon is accidental in the sense that at low electric

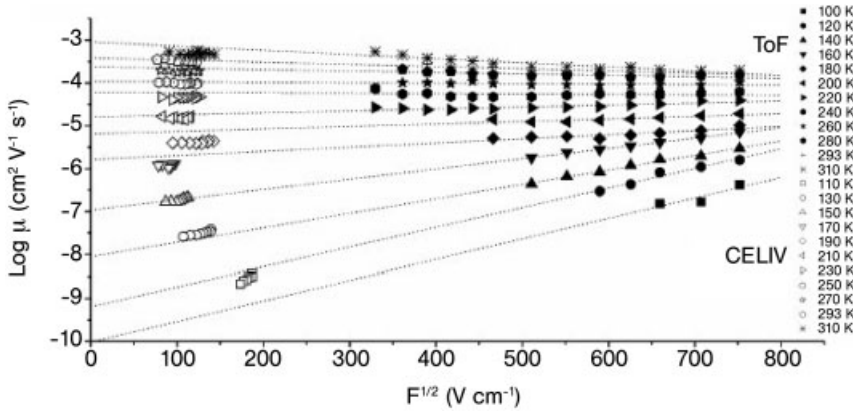


**Figure 6.29** Temperature and electric field dependences of the mobility determined by both TOF and CELIV experimental techniques.

fields transport is solely diffusive and carrier drift in electric field does not contribute to the displacement of charge carriers [73, 136]. There is recent independent proof against that claim. It is based on the comparison between mobility data recovered via either the TOF or the CELIV techniques (see Section 6.4.2.3). Remember that in a TOF experiment there is a thin sheet of carriers, generated next to an illuminated electrode, that drifts across the sample and broadens by diffusion. In the CELIV technique, one monitors carriers generated homogeneously

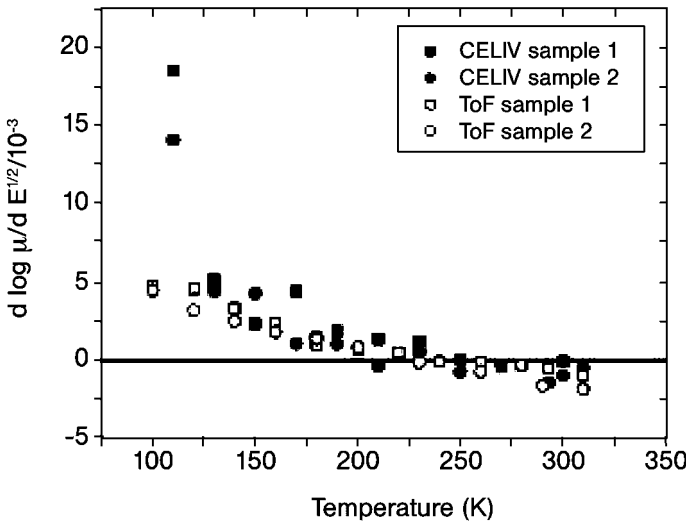


**Figure 6.30** Slope of the electric field dependence of mobility versus temperature determined by the CELIV technique and TOF technique. Results for two samples are shown.

throughout the sample by moderate doping. Therefore, there can be no further significant diffusion spread of the ensemble of carriers. Mozer et al. [192] studied both hole transport in an undoped film of poly(3-alkylthiophene) employing the TOF technique and in the same sample via CELIV after oxygen doping that raised the conductivity. It turned out that both sets of data were mutually consistent although the fields applied in these experiments were different (Fig. 6.29). As one can see from Fig. 6.30, extrapolated slopes,  $d\ln(\mu/\mu_0)/dF^{1/2}$ , as functions of temperature are, within experimental error, identical except at the lowest temperatures at which the TOF signal became dispersive. These experiments confirm that the negative field dependence of  $\mu(F)$  at weak/moderate fields and the concomitant mobility minimum at intermediate fields is a generic feature of organic hopping system in which the spatial correlation length exceeds the inter-site distance considerably.

### 6.5.3

#### Trapping Effects

In molecular solids, charge carrier hopping is a ubiquitous phenomenon. Unfortunately, it is notoriously difficult to identify and quantify how traps affect electronic transport. In molecular crystals, the situation is easier to tackle because near room temperature transport occurs via temperature-independent hopping among isoenergetic adjacent molecules. This leads to the Hoesterey–Letson equation that predicts how a relative concentration  $c$  of traps, whose energy levels are off-set from the mean transport energy, i.e. the valence or conduction band states, by the trap energy  $E_t$ , affects the carrier mobility:

$$\mu(T, c) = \mu_0 \left[ 1 + c \exp\left(\frac{E_t}{kT}\right) \right]^{-1} \quad (6.139)$$

where  $\mu_0$  is the intrinsic mobility. The trap depth  $E_t$  is set by the difference between the HOMO (LUMO) levels of host and guest for holes (electrons) [193]. This is a characteristic feature of organic solids in which the identity of the molecular constituent is preserved because intermolecular interactions are weak. The determination of trap distributions in both oligomeric and polymeric systems by applying the technique of thermally stimulated currents confirms the notion that these systems behave electronically no different from more conventional organic solids [75, 194]. However, in a random organic solid the situation is more complex because both the intrinsic hopping states and the traps feature inhomogeneously broadened DOS distributions that overlap. Since the temperature dependence of transport is set by the energy difference between occupied and transport states, each being dependent on the DOS itself, it can no longer be simply determined by a Boltzmann factor with the activation energy being the difference of the HOMO/LUMO levels of host and guest. It is plausible that, qualitatively, the functional dependences of  $\mu$  on field and temperature are retained if the energy difference  $E_t$  between the centers of the intrinsic and extrinsic DOS is moderate, say 2–3 times

the width of the intrinsic DOS because then the tail of the joint DOS is again a Gaussian whose effective width  $\sigma_{\text{eff}}$  depends on  $c$  and  $E_t$ . Detailed hole transport measurements on molecular glasses of tri-*p*-tolylamine (TTA) doped with various concentrations of derivatives of TTA, in which either one, two or three  $\text{CH}_3$  groups in the para position of the phenyl groups were replaced by  $\text{OCH}_3$  groups, which raised the HOMO levels, confirmed this notion [75, 76]. In this case, the expected trap energies can be inferred from cyclovoltammetric measurements. It turns out that a first-order amendment of the Gaussian disorder model is sufficient to explain the experimental data.

The frustrating aspect of the above formalism is that from the  $\mu(F, T)$  data alone one is unable to draw conclusions on the presence or absence of moderately shallow traps unless the experiments are extended towards lower temperatures. That kind of experiment can, indeed, delineate trapping but their analysis requires more sophisticated theoretical modeling in terms of either the effective medium approach (Section 6.3.3) or a stochastic hopping approach using the concept of the effective transport energy. A successful fit to the concentration dependence of the hole mobility in the above TTA glasses in terms of the EMA approach by Fishchuk et al. [140] demonstrates quantitative agreement between theory and experiment (Fig. 6.31) (see Section 6.3.3.7 for more details). Another example of application of that formalism is presented in Fig. 6.32, showing the hole mobility in a PPV–ether system in which phenylvinyl moieties are coupled with ether linkages. The clue to unraveling the hopping effect is provided by the change in the slope of the  $\ln\mu$  versus  $T^{-2}$  temperature dependence. Data analysis yielded the parameters  $\sigma_0 = 0.084$  eV,  $\sigma_t = 0.066$  eV,  $E_t = 0.25$  eV,  $c = 0.0115$  and  $\mu_0 = 1.4 \times 10^{-2} \text{ cm}^2 \text{ V}^{-1} \text{ s}^{-1}$ , where  $\sigma_0$  and  $\sigma_t$  are variances of the intrinsic and trap DOS, respectively. Figure 6.16 further illustrates the theoretical temperature dependence of the mobility in a hopping system with low concentration ( $c = 10^{-5}$ ) of moderately deep traps ( $E_t/\sigma_0 = 5$ ) at moderate electric field, parametric in the ratio of the widths of the intrinsic and trap DOSs plotted on  $\ln\mu$  versus  $T^{-2}$  and  $\ln\mu$  versus  $T^{-1}$  scales. It turns out that in the  $\ln\mu$  versus  $T^{-2}$  plot the  $T$ -dependences becomes weaker and approach the dependence predicted by the simple Hoesterey–Letson model provided that  $\sigma_0/\sigma_t = 1$ . This, too, is expected because at low  $T$  the rate-limiting step is the activation of a charge carrier from a trap DOS towards the intrinsic DOS and this is determined by the offset of HOMO/LUMO levels of host and guest. It is remarkable, though, that this dependence becomes even weaker if  $\sigma_0/\sigma_t < 1$  as in Fig. 6.16, in which the case  $\sigma_0/\sigma_t = 0.5$  is shown. There are two reasons of this effect. (i) If the trap DOS is narrower than the intrinsic DOS, hopping can proceed directly via trapping states at an appropriate concentration of the latter. As a result, the  $\mu(T)$  dependence flattens and eventually the mobility in the trap-containing system can even exceed that of the trap-free system. (ii) If the occupational DOS is swept across the distribution of traps levels the relaxation towards the tail states is diminished and, concomitantly, the decrease of the mobility upon lowering the temperature is also diminished. A cautionary note is in order if in such a system the temperature dependence of  $\mu$  is measured within a narrow temperature range.

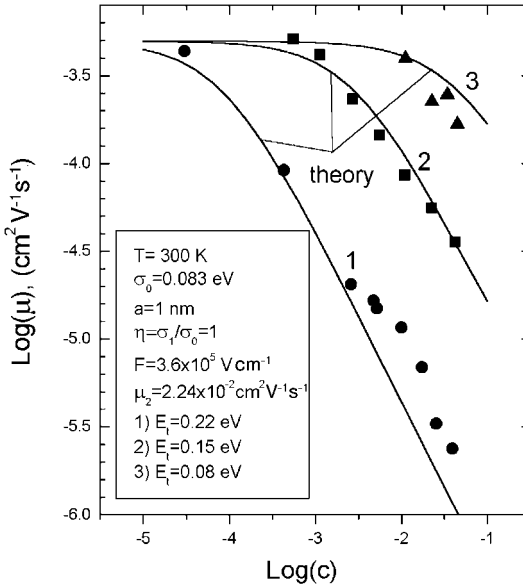


**Figure 6.31** Concentration dependence of the hole mobility in TTA-doped polystyrene-containing traps of different depth. Traps are due to DTA ( $E_t = 0.08$  eV), DAT ( $E_t = 0.15$  eV)

and TTA ( $E_t = 0.22$  eV). Measurements are shown by symbols and calculations by solid lines. Material parameters are shown in the inset.

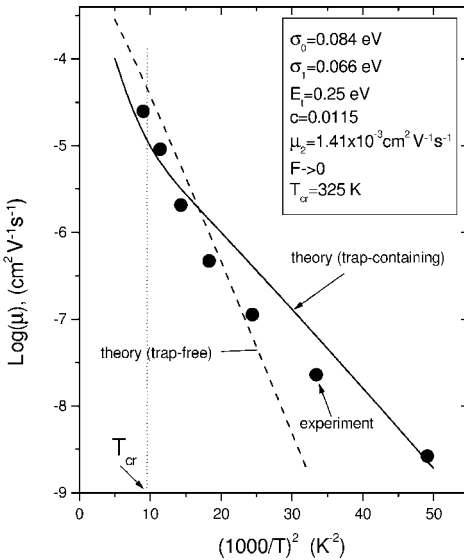


**Figure 6.32** Temperature dependence of the zero-field hole mobility (symbols) measured in PPV-ether [Ref. 141] and that calculated by the EMA theory (solid line) [140].

In that case, one might recover only the flatter portion of the  $\mu(T)$  curve. Its extrapolation towards  $T \rightarrow \infty$  would yield an accidentally low value of  $\mu_0$ .

Another peculiarity of trap-containing organic solids is the concentration dependence of the mobility at higher concentrations of traps. It turns out that beyond a relative molar concentration of 0.05–0.1,  $\mu$  features a minimum and rises again at higher concentrations. The reason is again the commencement of direct trap-to-trap transport that overcompensates thermally activated release of carriers to the intrinsic transport states. This effect becomes the more important as the trap energy  $E_t$  increases. The effect resembles percolation above the critical percolation threshold although the critical concentration at which  $\mu(c)$  increases is lower than the classic percolation theory would predict. The reason is that percolation theory is based on a hard-core interaction potential among the transport sites whereas in organic systems the transfer matrix elements among the molecules vary exponentially in distance. Therefore, the critical percolation limit is eroded [195]. Experimentally, the effect is well documented in the literature. Examples are the studies by Pai et al. [196] on polyvinylcarbazole doped with TPD and by Borsenberger et al. [197] on di-*p*-tolylphenylamine (DPT)-doped polystyrene containing different concentrations of *p*-diethylaminobenzaldehyde diphenylhydrazone (DEH) that forms a hole trap with a nominal trap depth of 0.32 eV (Fig. 6.33).

The latter concept is readily extended to bipolar transport in donor–acceptor systems such as polyvinylcarbazole (PVC) and trinitrofluorenone (TNF) [66]. As the

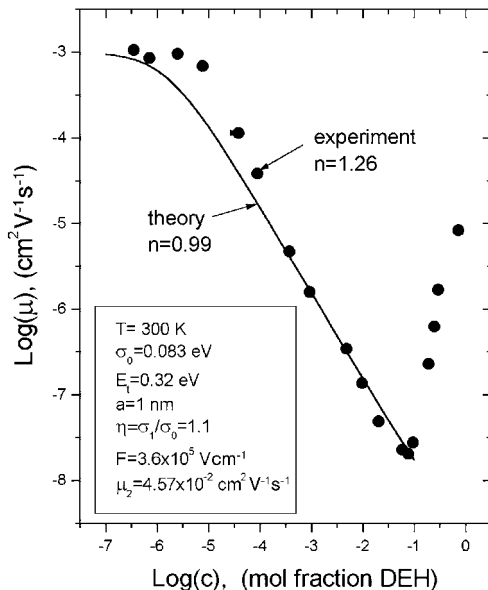


**Figure 6.33** Concentration dependence of the hole mobility measured in DPT-doped polystyrene containing different concentration of traps due to DEH (symbols) and calculated by the EMA theory (solid line).

concentration of TNF increases, the hole mobility decreases because of the dilution of the hole-transporting sites. At the same time, the electron mobility increases. More recently, Pacios et al. [198] studied bipolar transport in polyfluorene-[6,6]-phenyl-C<sub>61</sub>-butyric acid methyl ester (PCBM) blend films. Figure 6.34 shows TOF signals measured for the pure polymer (sample denoted A) and different blends plotted on a double logarithmic scale. The upper curves are for holes and the lower curves for electrons. The hole signals show at least a shoulder in the  $j(t)$  plots indicating that the ensemble of holes is approaching quasi-equilibrium. In the electron case this is only true for the PCBM blends with composition 20:1 and 3:1 whereas in a highly diluted and highly concentrated electron transporting subsystem transport is fully dispersive. It is remarkable that in the pure polyfluorene phase both hole and electron mobilities are similar, indicating that transport is intrinsic and determined by the structural disorder. As the strong electron acceptor PCBM is introduced it acts as an electron trap at low concentration whereas at higher concentrations motion among the PCBM moieties prevails. In this context see also the work by Choulis et al. [199].

It is a general observation that in most of the hole-transporting compounds electron transport is not detectable in TOF studies and vice versa. The reason is the mutual position of the HOMO and LUMO levels of inadvertent traps relative to those of the host material. In order to transport holes (electrons) unaffected by (deep) trapping, a material should have a high-lying HOMO (low-lying LUMO),

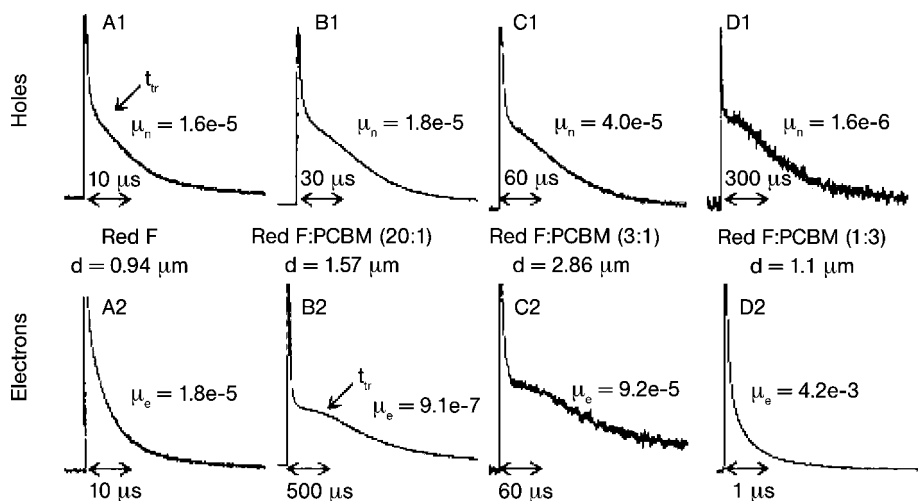


**Figure 6.34** Transient TOF currents measured for the pure polymer and the three different blends. Signals are plotted on a linear scale (temporal scale bars are indicated, current magnitude is on an arbitrary scale). The upper curves are for holes (positive bias applied to the ITO anode) and the lower

curves for electrons (negative bias applied to the ITO anode). The curve labels (e.g. A1, A2) are used for identification purposes in the text. Electron and hole mobility ( $\text{cm}^2 \text{V}^{-1} \text{s}^{-1}$ ) and film thicknesses are also quoted for easier comparison.

i.e. low oxidation potential (low reduction potential) so that accidental impurities act as antitraps. Oxygen and oxidation products have in general low reduction potentials and, concomitantly, act as electron traps. The obvious strategy for increasing the electron mobility in a material is, therefore, to lower its reduction potential in order to overcompensate any possible impurity. An example is the work of Redecker et al. [200] on starburst phenylquinoxalines. By the same token injection of electrons from a cathode is facilitated. Unfortunately, when trying to lower both oxidation and reduction potentials of the active molecule(s) of an optoelectronic device, one has to pay a price because a diminished HOMO–LUMO gap decreases the energy of, for instance, photons emitted by an OLED.

#### 6.5.4

##### **Polaron Effects**

As mentioned in Section 6.3, any change in the electronic state of a molecular site in a random organic solid, e.g. by generating a neutral exciton and/or a charge carrier, must give rise to a conformational readjustment upon which the molecular skeleton is locked into a new quasi-equilibrium structure. Unfortunately, there is no experimental tool to measure the concomitant relaxation energy, i.e. the polaron binding energy, directly. At the beginning of the work on  $\pi$ -conjugated polymers, it was believed that the transient absorption spectrum upon optical excitation does yield that information. This rested on the supposed validity of the semiconductor band model implying that optical absorption creates a pair of charge carriers coupled to phonons. Within the framework of this concept, the difference between the band gap absorption and the bathochromically shifted transient absorption spectrum is the polaron binding energy [201].

Meanwhile, it is known that in a molecular system the transient absorption after optical excitation is due to a (charged) radical anion/cation or a (neutral) singlet/triplet excitation [38, 147, 202, 203]. They are Franck–Condon-type transitions starting from the already optically excited states and do not reflect any conformational change occurring when the chromophore is converted from the ground state to the first excited or charged state. However, there is an indirect spectroscopic probe of that conformational change. These are the vibronic absorption and luminescence spectra of the chromophore. The relative intensities of the vibronic lines, quantified by the Huang–Rhys-factor, is a measure of the displacement of the minima of the molecular potential in the ground and excited states, noting, however, that the only entity that is amenable to that spectroscopic probing is the neutral exciton because there is no direct photoionization. In order to assess the formation of charged polarons, one has to rely on the simulation of the conformational change occurring when an electron–hole pair comprising an exciton or a single charge carrier is generated. In  $\pi$ -conjugated polymers, in which the electron–hole separation in the neutral singlet exciton is comparable to or even larger than the length of the repeat unit, this simulation is almost quantitative. This is borne out by the comparison between the excitonic relaxation energy, inferred from the Huang–Rhys factor, on the one hand and the result of the quan-

tum chemical calculation of the energies of radical anions/cations on the other. In more or less rigid systems, the latter is of the order of 0.2–0.3 eV and is identified as the conformational binding energies of a pair of charges [203]. Note, however, that a more recent calculation of the structural relaxation energy of oligo(phenylenevinylene)s upon removing an electron yielded significantly smaller values, ranging from 0.106 eV for the monomer to 0.022 eV for the oligomer consisting of 12 repeat units [204].

It is obvious that those energies must increase when a chromophore can couple to a torsional degree of freedom. A characteristic example is the biphenyl group as an element in the repeat unit of a conjugated polymer. In the ground state both rings form a dihedral angle of ca. 40° whereas in the excited state the system is coplanar as evidenced by the erosion of the  $S_1 \leftrightarrow S_0$  0–0 transition, a concomitant loss of the vibronic resolution and a significant Stokes shift between the absorption and fluorescence maxima. This effect is diminished when the moments of inertia of the phenyl rings is increased by attachment of pendant groups. Figure 6.35 shows a set of site-selectively measured fluorescence spectra of a series of poly(arylenevinylene)s [90]. They prove that the excited singlet state is accompanied by a chain deformation, which originates from coupling to a torsional mode. The fact that the configuration of a chromophore differs in the ground and excited states implies a reduction of the matrix element for excitation transfer, i.e. an exciton or a charge carrier becomes heavier. As a consequence, the time-scale of transfer of a singlet excitation is shifted towards longer times when in a PPV derivative the central phenylene group is replaced by a biphenylene group [91].

In order to assess the importance of a polaron effect on charge carrier motion, one has to resort to a careful measurement of the temperature dependence of the carrier mobility in conjunction with a theoretical analysis. Basically, the disorder

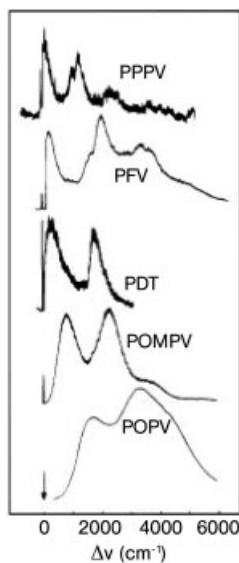


**Figure 6.35** Quasi-resonant fluorescence spectra of a series of conjugated polymers. The abscissa scale is relative to the laser energy.

contribution to transport should scale with  $\mu \sim \exp[-(T_0/T)^2]$  whereas the polaron contribution should be simply activated. In a first-order approach [205], this strategy was used to disentangle both contributions in a film of polymethylphenylsilylene (PMPS) [206]. In such a material the polaron contribution to transport might be significant because the polymer chain is single bonded and raising an electron from a  $\sigma$  to an unbonded  $\sigma^*$  orbital should cause a major conformational change. Analyzing the  $\mu(F, T)$  data in the limit of  $F \rightarrow 0$  in terms of

$$\mu(T) = \mu_0 \exp \left[ - \left( \frac{3}{2} \frac{\sigma}{kT} \right)^2 - \frac{E_p}{2} \right] \quad (6.140)$$

yielded  $\sigma = 0.070$  eV, the polaron binding energy  $E_p = 0.16$  eV and  $\mu_0 = 0.1$  cm<sup>2</sup> V<sup>-1</sup> s<sup>-1</sup>. The above simple approach has recently been put on firmer theoretical grounds by Arkhipov et al. using a stochastic approach [205]. Applying the more sophisticated EMA formalism by Fishchuk et al. [130] yields  $\sigma = 0.086$  eV and  $E_a = E_p/2 = 0.145$  eV. This shows that the simplistic approach captures the gist of the phenomenon but the EMA formalism yields additional information on the matrix element  $J$  for the inter-chain hopping and the hopping distance,  $J = 8$  meV and  $a = 1.2$  nm, respectively. The quality of the fitting procedure is illustrated in Figs. 6.36 and 6.37. Similar experiments were performed on a polysilylene in which the pendant phenyl group was replaced with a biphenyl group. As expected, the torsional freedom of the latter causes an increase in the polaron binding energy ( $E_p = 0.44$  eV) and also the degree of disorder ( $\sigma = 0.096$  eV).

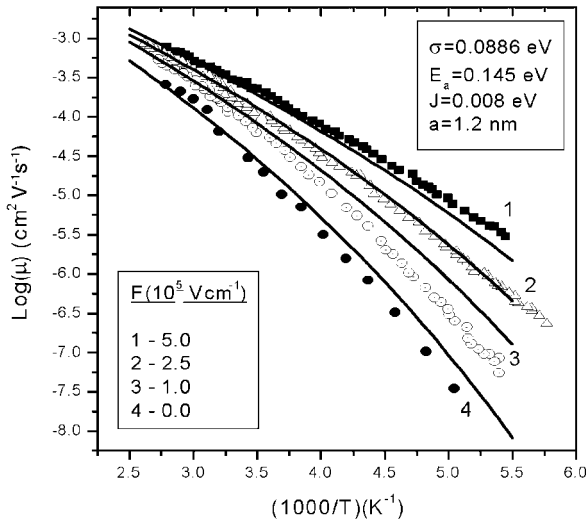


**Figure 6.36** Temperature dependences of the drift mobility  $\mu_e$  in PMPSi calculated with the use of Eq. (23) from Ref. [130] for several electric fields (solid lines). Experimental data from Ref. [206] are given by symbols.

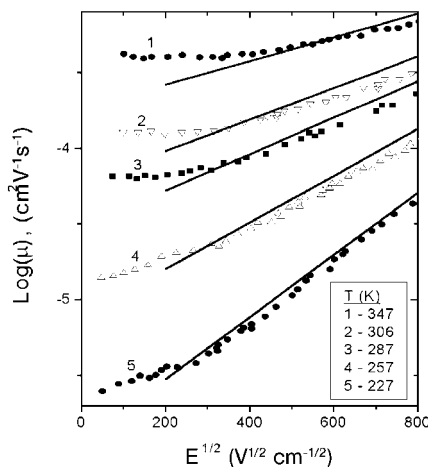


**Figure 6.37** Field dependences of the drift mobility  $\mu_e$  in PMPsi calculated by Eq. (23) from Ref. [130] for several temperatures. All parameters used in the calculations were the same as in Fig. 6.36. Symbols show the experimental data and lines the calculated dependences.

### 6.5.5

#### Chemical and Morphological Aspects of Charge Transport

In the course of the endeavor to optimize the performance of optoelectronic devices, there has been an intense search into the development of materials with improved charge transport properties. In this section only some relevant strategies are outlined and no attempt is made to cover the field. An example is the relationship between the molecular structure of members of the biphenylamine family and their hole-transporting properties in the glassy phase [207]. These materials are of commercial interest because of their low oxidation potential, which facilitates hole injection from anodes such as ITO. For the same reason, fewer inadvertent impurities are likely to have trapping levels above the manifold of the intrinsic hole-transporting states.

In Shirota's group [208] in Osaka, a large series of compounds were synthesized paying particular attention to moderate glass transition temperatures and, concomitantly, good film-forming properties. Among them were the ortho-, meta- and para-substituted tritolylamines (TTAs) and biphenyldiamines (BPDs). Their molecular structures are shown in Fig. 6.38. The hole mobilities measured at 295 K and at a field of  $1 \times 10^5 \text{ V cm}^{-1}$  are summarized in Table 6.1. It is obvious that the  $\mu$  values depend greatly on the position of the phenyl group in the biphenyl moiety. In the ortho- and para-isomers of TTA and BPD the mobility is larger than in the meta-isomers by more than one order of magnitude. The analysis of the electric field and temperature dependences of the mobility in terms of the conventional disorder model showed that the controlling parameter is the energetic disorder

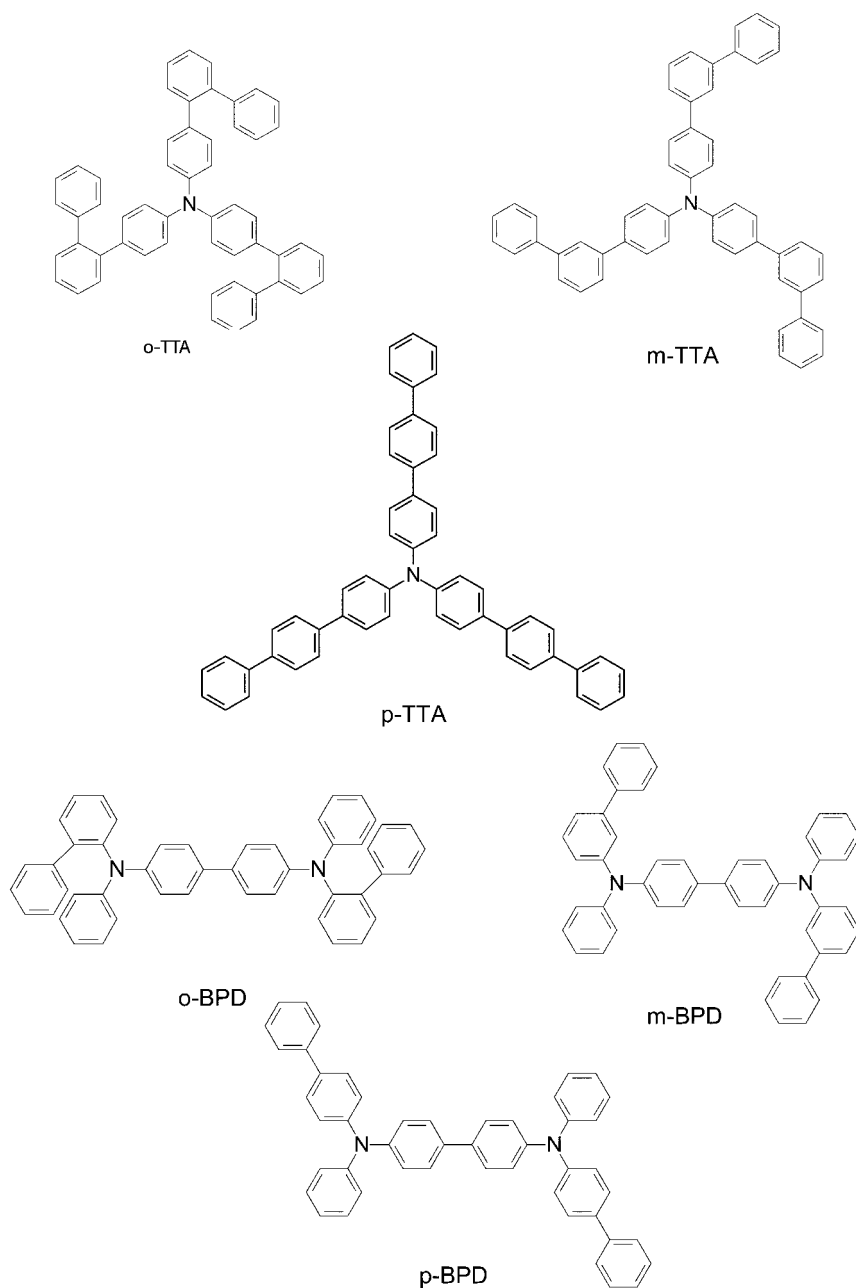


**Figure 6.38** Molecular structures of ortho-, meta- and para-substituted tritolyamines (TTAs) and biphenyldiamines (BPDs).

**Table 6.1** Hole mobilities measured in the ortho-, meta-, and para-substituted tritolylamines (TTAs) and biphenyldiamines (BPDs).

Material	$\mu_h/\text{cm}^2 \text{V}^{-1} \text{s}^{-1}$
<i>m</i> -MTDATA	$3.0 \times 10^{-5} \text{ }^a$
<i>o</i> -MTDAB	$3.0 \times 10^{-3} \text{ }^b$
<i>p</i> -DPA-TDAB	$1.40 \times 10^{-4} \text{ }^b$
MTBDAB	$2.5 \times 10^{-5} \text{ }^b$
<i>m</i> -MTDAPB	$1.6 \times 10^{-5} \text{ }^b$
<i>o</i> -TTA	$7.9 \times 10^{-4} \text{ }^a$
<i>m</i> -TTA	$2.3 \times 10^{-5} \text{ }^a$
<i>p</i> -TTA	$8.8 \times 10^{-4} \text{ }^a$
<i>o</i> -BPD	$6.5 \times 10^{-4} \text{ }^a$
<i>m</i> -BPD	$5.3 \times 10^{-5} \text{ }^a$
<i>p</i> -BPD	$1.0 \times 10^{-3} \text{ }^a$
BMA-3T	$2.8 \times 10^{-5} \text{ }^a$
BMA-4T	$1.0 \times 10^{-5} \text{ }^a$

Measured at an electric field of

<sup>a</sup> $1.0 \times 10^5 \text{ V cm}^{-1}$  and

<sup>b</sup> $2.0 \times 10^5 \text{ V cm}^{-1}$  at 293 K.

parameter  $\sigma$ . That value increases in the series *o*-TTA (0.059 eV) < *p*-TTA (0.071 eV) < *m*-TTA (0.093 eV) and *o*-BPD (0.071 eV) < *p*-BPD (0.075 eV) < *m*-BPD (0.105 eV). Arguably, this is related to torsional displacement along the C–C and C–N bonds that influence the molecular structure, the geometric change being correlated with the energetic disorder. Because of the restricted internal rotation in the biphenyl moiety in the ortho-isomer, on the one hand, and the smaller number of conformers resulting from bond rotation for the symmetrical para-isomer, on the other, the variation of the molecular geometry is smaller for the ortho- and para-isomers as compared with the meta-isomer.

The above effect is related to the smoothness of the torsional potential of the phenyl groups. More torsional motion, if frozen, increases disorder, but specific inter-site packing effects are not involved. This is no longer the case for the alkoxy-substituted polyphenylenevinylenes [209] (Fig. 6.39). Experimental values for the hole mobility as a function of electric field and temperature feature  $\ln\mu \propto F^{1/2}$  and  $\ln\mu \propto T^{-2}$  laws (Fig. 6.40) with the parameters listed in Table 6.2. It is obvious that the decrease in conjugation on replacing as little as 11% of the phenylenevinylene by non-conjugated ethylidene group, i.e. conjugation defect, lowers the mobility drastically. The effect originates from the increasing, on average, distance

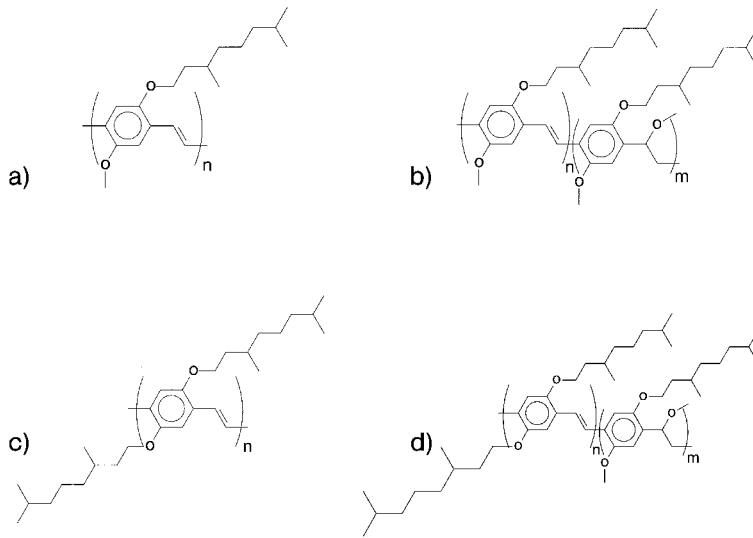


**Figure 6.39** Chemical structures of the polymers studied: (a) Fully conjugated  $OC_1C_{10}$ -PPV; (b) partially conjugated  $OC_1C_{10}$ -PPV with  $n:m = 9:1$ ; (c) dialkoxy-PPV with two

$C_{10}H_{21}$  side-groups ( $OC_{10}C_{10}$ -PPV); (d) fully conjugated PPV copolymer synthesized from  $OC_{10}C_{10}$ -PV and  $OC_1C_5$ -PV units in the ratio  $n:m = 3:1$ .

$a$  between the  $\pi$ -bonded hopping sites, which was inferred by analyzing the data within the framework of the correlated disorder model (see Section 6.3.1.6). Different values of mobility in interrupted PPV chains (systems A, C and D) have to be accounted for by structural changes imposed by the side-groups. The presence of the two bulky  $OC_{10}H_{21}$  side-chains ( $OC_{10}C_{10}$ -PPV) results in a large increase in the absolute value and a decrease in the activation energy of  $\mu$  as compared with  $OC_1C_{10}$ -PPV; see Fig. 6.40. The lower activation of  $\mu$  shows that the energetic disorder in  $OC_{10}C_{10}$ -PPV is significantly less than in  $OC_1C_{10}$ -PPV. This difference can be understood in view of the possible couplings between monomer units of the two polymers. The asymmetric substitution of the  $OC_1C_{10}$  monomer during synthesis allows three possible dimer configurations in  $OC_1C_{10}$ -PPV, whereas in the

**Table 6.2** Material parameters derived from field and temperature dependences of the mobility in the alkoxy-substituted poly-phenylenevinylenes.

Sample	$\mu$ , [ $m^2/Vs$ ]	$\sigma$ [meV]	$C$ [( $m/V$ ) $^{1/2}$ ]	$a$ [nm]	$L$ [nm]
A	$5.1 \times 10^{-9}$	112	$4.0 \times 10^{-5}$	1.2	0.3
B	$4.0 \times 10^{-10}$	121	$4.3 \times 10^{-5}$	1.7	0.3
C	$1.6 \times 10^{-7}$	93	$3.8 \times 10^{-5}$	1.1	0.5
D	$1.5 \times 10^{-7}$	99	$4.0 \times 10^{-5}$	1.2	0.5

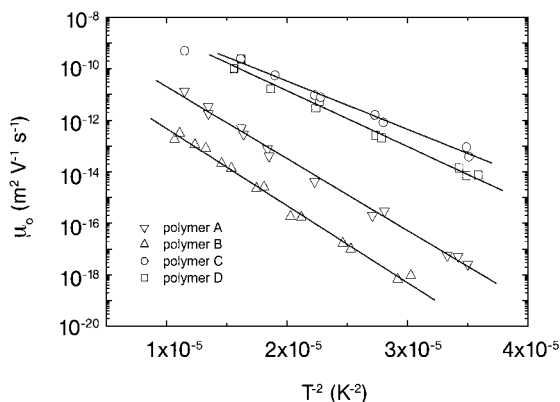


**Figure 6.40** Temperature dependence of the zero-field mobility of the four PPV derivatives studied. The data are fitted with the  $\ln \mu_0 \propto T^{-2}$  law for hopping transport in a Gaussian DOS. The parameters derived for the different compounds are listed in Table 6.2.

case of the OC<sub>10</sub>C<sub>10</sub> polymer every coupling of two monomers results in the same dimer (OC<sub>10</sub>C<sub>10</sub>-PPV is a regioregular and stereoregular polymer). In comparison with OC<sub>10</sub>C<sub>10</sub>-PPV, the increased configurational freedom of the OC<sub>1</sub>C<sub>10</sub> polymer will give rise to a larger energetic spread between the electronic levels of individual chain segments. A second effect of the regularity of OC<sub>10</sub>C<sub>10</sub>-PPV is the decreased conformational freedom of individual chains, which probably also decreases energetic disorder. Furthermore, it can be expected that a high degree of regularity enhances the ordering in the solid state.

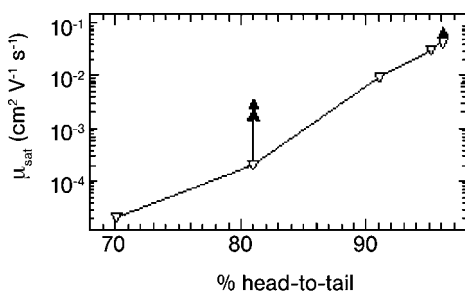


**Figure 6.41** Charge carrier mobility of P3HT FETs with different microstructures. Dependence of the room temperature mobility on the regioregularity for spin-coated (downward triangles) and solution-cast (upward triangles) top-contact P3HT FETs (channel length  $L = 75 \mu\text{m}$ , channel width  $W = 1.5 \text{mm}$ ). Measurements were per-

formed in vacuum ( $p < 1 \times 10^{-6} \text{mbar}$ ) to prevent charge trapping by adsorbed atmospheric impurities. The mobility of top-contact FETs with Au source–drain contacts evaporated after deposition of the polymer is higher, typically by a factor of two, than that of bottom-contact devices.

The exceptional propensity for self-alignment of alkyl side-groups in conjugated polymers offers a challenging opportunity to improve charge transfer. To this end, Siringhaus et al. [175] studied hole transport in a FET in which the active layer is a 70–100-nm spin-coated film of regioregular poly-3-hexylthiophene. Regioregularity denotes the percentage of stereoregular head-to-tail attachments of the hexyl side-chains to the 3-position of the thiophene and induces self-organization. It results in a lamellar structure with the two-dimensional conjugated sheets formed by inter-chain stacking. Grazing incidence X-ray diffraction revealed that in a sample with high regioregularity (>91%) and low molecular weight the preferential orientation of ordered domains is with the (100)-axis normal to the film and the (010)-axis in the plane of the film, whereas in samples with low regioregularity (81%) the ordering is reversed.

The ability to induce different orientations allows one to establish a direct correlation between the direction of the  $\pi$ - $\pi$  stacking and the in-plane mobility in the FET – see Fig. 6.41. At 295 K, the highest mobilities of  $0.05$ – $0.1 \text{ cm}^2 \text{ V}^{-1} \text{ s}^{-1}$  were observed for the sample with the highest regioregularity and the largest size of crystallites with in-plane orientation of the (010)-axis. For spin-coated samples with low regioregularity, in which the (010)-axis is normal to the film, the mobility is only  $2 \times 10^{-4} \text{ cm}^2 \text{ V}^{-1} \text{ s}^{-1}$ . The large FET mobility anisotropy, caused by different preferential orientations of the ordered microcrystalline domains, is clear evidence that the transport is no longer dominated by the remaining amorphous regions of the polymer film but is starting to reflect the charge transport in ordered polymer domains. The residual disorder in the film manifests itself in a thermally activated mobility at lower temperatures similar to trap-controlled transport in a molecular crystal. Unfortunately, the experiment does not allow the mobility to be extracted in a hypothetical P3HT crystal. IR spectroscopy indicates that the increased intra-chain coupling in the ordered domains gives rise to some charge delocalization among adjacent chains, i.e. transport acquires 2D features with a reduced degree of polaronic relaxation [210]. Examples of mobility enhancement by self-ordering include studies on hole transport in polyfluorenes in the nematic phase (see Section 6.5.1) and on oligosilanes [211].

Another recent assessment of the effect of sample morphology, i.e. structural disorder, on hole transport was made by Inigo and co-workers [212, 213]. They compared TOF studies with photoluminescence as well as small-angle X-ray scattering (SAXS) measurement on  $3.7\text{-}\mu\text{m}$  thick MEH-PPV films prepared by solution casting from either toluene (TL) or chlorobenzene (CB) solution. The temperature-dependent TOF experiment covered the range 235–325 K. Both sets of  $\mu(F, T)$  data can be analyzed successfully in terms of the unmodified disorder model yielding  $\sigma$ -values for the variance of the DOS distribution of  $92 \pm 2$  and  $63 \pm 1 \text{ meV}$  for the CB- and TL-cast films, respectively. Despite the large difference in the  $\sigma$ -values, the hole mobility at 295 K and  $F = 1.6 \times 10^5 \text{ V cm}^{-1}$  is  $\sim 3 \times 10^{-6} \text{ cm}^2 \text{ V}^{-1} \text{ s}^{-1}$  in the TL case and  $\sim 1 \times 10^{-6} \text{ cm}^2 \text{ V}^{-1} \text{ s}^{-1}$  in the CB case, i.e.  $\mu^{(\text{TL})}/\mu^{(\text{CB})}$  is only 3. The reason is that in the CB case the large degree of positional disorder compensates for the effect of larger energetic disorder as inferred from the stronger  $\mu(F)$  dependence. Whereas the fluorescence spectra of both samples are almost indistinguishable, the

two-dimensional SAXS patterns obtained with X-rays parallel and perpendicular to the film surface bear out different morphologies. The CB-cast film has smaller ordered domains and more order/disorder interfaces than the TL-cast film along the vertical direction. This translates into a larger distance fluctuation between hopping sites in the CB-cast film and, concomitantly, a larger positional disorder.

#### 6.5.6

#### On-Chain Transport Probed by Microwave Conductivity

The microwave technique affords the possibility of measuring charge transport on a nanometer scale at electric fields as low as  $100 \text{ V cm}^{-1}$ . If experiments are done on polymers in dilute solution where aggregation is negligible and on oriented bulk systems, it provides a handle on on-chain versus off-chain transport. An example is hole transport in aligned polyfluorene films [214, 215]. The alignment can be achieved by spin-coating the polymer on to a rubbed polyimide layer followed by annealing at a temperature slightly above the solid-to-mesophase transition. Using this approach, films have been produced with anisotropies of  $>15$  in optical absorption and  $>20$  in electroluminescence. It was also found that in FETs alignment increases the mobility along the polymer axis and the in-plane anisotropy of transport was close to the optical dichroic ratio [216]. By performing microwave experiments on the same kind of sample, the Delft group [217] confirmed the above conclusion. The on-chain mobility turned out to be  $0.15 \text{ cm}^2 \text{ V}^{-1} \text{ s}^{-1}$  with an on-chain to off-chain ratio of 7. The latter value is a lower limit for the intrinsic anisotropy for charge transport because any contribution to the photoconductivity originating in the isotropic regions of the sample would make a larger fractional contribution to transport in the direction of chain alignment.

For non-aligned bulk polymers of the alkoxyphenylenevinylene family the mobilities derived from measurements of radiation-induced microwave conductivity are at least one order of magnitude lower and depend on morphology. For unsymmetrical dialkoxy-substituted compounds high-temperature annealing has a substantial positive effect on the hole mobility. Its values range from  $2.5 \times 10^{-3} \text{ cm}^2 \text{ V}^{-1} \text{ s}^{-1}$  for MEH-PPV to  $3.6 \times 10^{-2} \text{ cm}^2 \text{ V}^{-1} \text{ s}^{-1}$  for the dioctadecyloxy derivative with an intriguingly weak temperature dependence between  $-50$  and  $+150$  °C. Saturation of vinylene residues that interrupt conjugation decreases the mobility [218]. It is remarkable that in the bulk phase of MEH-PPV  $\mu$  is one order of magnitude lower than in a liquid solution (Fig. 6.42), indicating that this is a general phenomenon. This is obviously a signature of disorder being static in a bulk film but dynamic in solution where rapid conformational sampling can occur.

The maximum mobility values observed in  $\pi$ -conjugated polymers are those in crystalline polydiacetylene [219]. There was an early TOF study on a thin single crystal of poly(toluenesulfonate-diacetylene) cut in a way such that the polymer axis was at an angle of  $\sim 70^\circ$  relative to the crystal faces. It yielded a mobility of (supposedly) electrons of  $4.8 \pm 1.5 \text{ cm}^2 \text{ V}^{-1} \text{ s}^{-1}$  [220]. After a lively and controversial discussion, that order of magnitude has been confirmed by microwave experiments [219, 221]. The latter experiments discarded earlier claims [222] that the on-

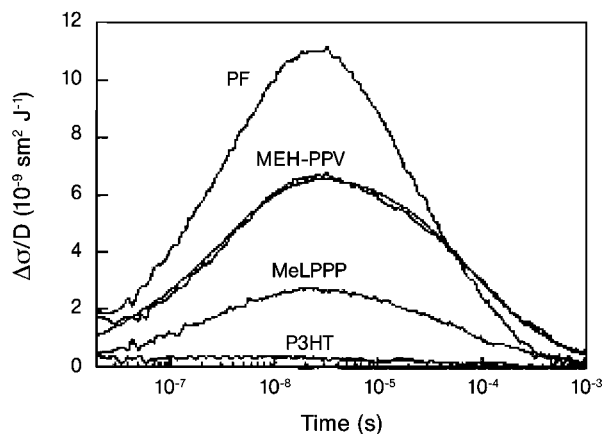


**Figure 6.42** Dose-normalized changes in the microwave conductivity on pulse-radiolysis of dilute, oxygen-saturated benzene solutions of the  $\pi$ -bond conjugated-carbon polymers. In all cases the monomer unit concentration was close to 1 mM. The transients were obtained using single 5- or 10-ns pulses

and were monitored from 10 ns to 1 ms using a transient digitizer with a pseudo-logarithmic time base. The smooth full line drawn through the data for MEH-PPV is an example of calculated fits from which the hole mobility was determined.

chain mobility is order of magnitude higher. In PR-TRMC experiments, done on a single crystal of poly(toluenesulfonate-diacetylene), turning the crystal through  $360^\circ$  with respect to the electric field vector confirmed earlier results indicating that the mobility is highly anisotropic [223]. The anisotropy is  $\geq 10^2$  and strongly affected by the method of monomer crystal growth and the polymerization routes, indicating that the crystallographic quality of a sample is important, but noting, however, that the inter-chain transport is not much different in samples with different morphology. Incidentally, it appears that the inter-chain mobility is comparable to that of a film of ladder-type polyphenylene (MeLPPP) if extrapolated to  $T \rightarrow \infty$ . On the other hand, one may conjecture that the on-chain mobility of conjugated polymers can be raised to a value comparable to that of polydiacetylene, i.e. several  $\text{cm}^2 \text{V}^{-1} \text{s}^{-1}$ , provided that the intra-chain disorder can be reduced by either chemical or physical means [218].

Based on theoretical studies and measurements of the Franz-Keldysh effect in single polydiacetylene crystals [224], it has been concluded that the effective mass of charge carriers in a  $\pi$ -conjugated chain is around 0.05 free electron mass [24]. This would imply a mobility comparable to that in an inorganic semiconductor such as silicon in which  $\mu = 10^3 \text{ cm}^2 \text{V}^{-1} \text{s}^{-1}$ . The reason why the experimentally determined mobility is much lower, i.e. comparable to that in conventional molecular crystals at room temperature, is that an optically excited charge carrier is rapidly dressed with a phonon cloud and moves in the form of a small polaron. Coupling of singlet excitons to phonons in noncrystalline  $\pi$ - and  $\sigma$ -conjugated polymers has, indeed, been confirmed by site-selective fluorescence spectroscopy in

matrix-isolated chains at low temperatures. Whereas in oligomers of planarized *p*-phenylenes zero phonon lines have been observed, they are absent in the polymers [225]. Instead, the  $S_1 \leftarrow S_0$  0–0 transitions features a linewidth of a few meV, indicating coupling to low-energy chain phonons [188, 225].

Dynamic disorder must be even more important in solutions than single crystals. The fact that in an aligned bulk PFO film  $\mu$  is a factor of 5 less than in solution and decreases by an additional one or even two orders of magnitude on going from an ordered to a random phase is a stringent test that static disorder limits the mobility. Since in PR-TRMC experiments transport is probed on a length scale at which neither hopping via impurities is occurring nor can grain boundaries between domains play a role, that value of the mobility is a genuine feature of a chemically pure but conformationally defective polymer.

Recently, interesting results on polaron transport in dilute fluid solution of poly(thienylenevinylene) have been reported by Prins et al. [226]. It turns out that the hole and electron mobilities are almost identical,  $\mu^+ = 0.38 \text{ cm}^2/\text{Vs}$  and  $\mu^- = 0.23 \text{ cm}^2/\text{Vs}$ . This proves that the ubiquitously observed asymmetry of the mobilities is only caused by trapping of one sort of carriers.

It is a remarkable and important consistency test for the disorder model that both the off-chain mobility in aligned PFO samples and the mobility in a random polymer, i.e.  $\sim 10^{-2} \text{ cm}^2 \text{ V}^{-1} \text{ s}^{-1}$ , agree with the values inferred from TOF experiments on macroscopic distances when extrapolating to  $T \rightarrow \infty$ . It confirms that  $\mu_0$  is a measure of inter-chain hopping at an earlier stage of transport, i.e. before relaxation towards the tail states of the DOS. Note that if one were to extrapolate  $\mu(T)$  to  $T \rightarrow \infty$  based on an Arrhenius-type temperature dependence, one would end up with a prefactor mobility that is two or three orders of magnitude larger.

## 6.6

### Conclusions

Disorder effects are essential for understanding basic charge transport processes in random organic materials ranging from diluted molecularly doped systems to dense small-molecule materials and further to conjugated polymers, each group incorporating a broad variety of chemically and morphologically different materials. Although microscopic electronic structure is obviously different in these groups of materials, it turns out that the variable-range hopping concept provides a universal theoretical basis for the description of electrical conductivity in nearly all disordered organic solids. The reason is that (i) intermolecular interactions are too weak and polarization effects too strong for the formation of extended electronic states, (ii) the structure of electronic wavefunctions inside molecules or conjugated segments does not play a crucial role in the charge transfer between molecules or conjugated segments and (iii) the tails of wavefunctions outside molecules/conjugated segments can be fairly well universally approximated by exponential functions. Depending on the relative importance of the energetic disorder

and polarization effects, either the Miller–Abrahams or Marcus expression for the carrier hopping rate should be used.

This notion is fully supported by similar Poole–Frenkel-like field and  $1/T^2$  temperature dependences of the carrier mobility universally observed in different groups of disordered organic solids. Furthermore, a clear correlation between energetic and positional disorder, on the one hand, and the magnitude and field and temperature dependence of the mobility, on the other, has been found in nearly all experimentally studied systems. This result indicates a superior role in the charge transport of morphology and intermolecular coupling as compared with intramolecular electronic structure. Since all electronic states in disordered organic solids are localized, nanoscale fluctuations of electrostatic potential may strongly affect charge transport characteristics. These fluctuations can be caused by both dipole (or quadrupole) moments of randomly located/oriented molecules and charged defects or impurities. The former possibility implies a strong effect on charge transport of the material polarity whereas the latter indicates an important role of accidental or intentional doping by electron donors or acceptors. It should be noted that random potential fluctuations, i.e. correlation between energies and positions of localized states, have been shown to yield a Poole–Frenkel-like field dependence of the mobility measured in TOF experiments.

In general, two types of interactions contribute to energetic disorder, namely (i) van der Waals interaction via varying distances between and mutual orientations of nearest molecular moieties and (ii) long-range potential fluctuations. Apart from polaronic effects, the presence of charge carriers can hardly have a strong effect on the material morphology that suggests the van der Waals-type disorder being independent of charge carrier density. However, the random electrostatic potential landscape can be entirely changed in the presence of a sufficiently large density of excess charge carriers in the bulk. This ‘landscape-smoothing’ effect may be responsible for the lack of the field dependence of the mobility calculated from  $I$ – $V$  curves measured under SCLC conditions.

Experimentally, it has long been known that the mobility measured in a disordered organic material at low carrier densities, typical for TOF and SCLC measurements, is much smaller than that obtained at high carrier densities, i.e. the field-effect mobility. A straightforward explanation of this effect is the role of deep traps that can control the TOF and SCLC mobility but are completely filled in the channel of a FET. However, the threshold carrier densities are normally much higher than the possible concentrations of deep traps. This suggests filling of intrinsic deep sites and a concomitant upward shift of the Fermi level within the intrinsic DOS distribution. Remarkably, doping of a disordered organic solid is not simply equivalent to increasing carrier density. The Coulomb interaction between ionized dopants and charge carriers enhances the energetic disorder and strongly broadens the DOS in the doped material.

In this review, we outlined two theoretical approaches to variable-range hopping. The stochastic approach is based on the effective transport level concept and allows the hopping problem to be reduced to a set of equations describing band transport controlled by a broad distribution of localized states. This approach can

be easily extended to the analysis of space charge effects, carrier recombination, charge injection, etc., and, therefore, it is useful for modeling of various organic devices. The effective medium approximation based on appropriate averaging of either the Miller–Abrahams or Marcus hopping rate can account for both energetic and positional disorder in organic materials, the presence of polaron effects and extrinsic traps. It allows one to obtain the Poole–Frenkel-type field dependence of the charge carrier mobility from moderate to large electric fields and can reproduce the negative field dependence of drift mobility at low-fields for certain material parameters. The EMA approach is particularly relevant for the study of hopping transport in organic materials with reduced energetic disorder.

### Acknowledgments

Financial support from the European Union through the project NAIMO, IP 500355, from NATO grant PST.CLG 978952 and from the Fonds der Chemischen Industrie is gratefully acknowledged.

### References

- 1 V.I. Arkhipov, H. Bässler, *Phys. Status Solidi A* **201**, 1152 (2004).
- 2 M. Pope, C. E. Swenberg, *Electronic Processes in Organic Crystals, Polymers*, 2nd edn, Oxford University Press, Oxford, 1999.
- 3 A. Heeger, in *Primary Photoexcitation in Conjugated Polymers: Molecular Exciton versus Semiconductor Band Model*, edited by N. S. Sariciftci, World Scientific, Singapore, 1997, p. 20–54.
- 4 K. Lochner, H. Bässler, B. Tieke, G. Wegner, *Phys. Status Solidi B* **88**, 653 (1978).
- 5 K. Pakbaz, C. H. Lee, A. J. Heeger, T. W. Hagler, D. McBranch, *Synth. Met.* **64**, 295 (1994).
- 6 V. I. Arkhipov, H. Bässler, in *Handbook of Luminescence, Display Materials, Devices*, Vol. 1, edited by H. S. Nalwa, L. S. Rohwer, American Scientific Publishers, Los Angeles 2003, p. 279–342.
- 7 K. Kato, C. L. Braun, *J. Chem. Phys.* **72**, 172 (1980).
- 8 R.R. Chance, C.L. Braun, *J. Chem. Phys.* **59**, 2269 (1973); **64**, 3573 (1976).
- 9 D. Hertel, H. Bässler, S. Möller, H. Tillmann, H. H. Hörhold, *Mol. Cryst. Liq. Cryst.* **355**, 175 (2001).
- 10 B. Mulder, *Philips Res. Rep.* **4**, 1 (1968).
- 11 S. Barth, H. Bässler, H. Rost, H. H. Hörhold, *Phys. Rev. B* **56**, 3844 (1997).
- 12 J. P. J. Markham, T. D. Anthopoulos, I. D. W. Samuel, G. J. Richards, P. L. Burn, C. Im, H. Bässler, *Appl. Phys. Lett.* **81**, 3266 (2002).
- 13 A. J. Heeger, *J. Phys. Chem. B* **105**, 8475 (2001).
- 14 C. J. Brabec, N. S. Sariciftci, J. C. Hummelen, *Adv. Funct. Mater.* **11**, 15 (2001).
- 15 J. J. Halls, R. H. Friend, in *Clean Electricity from Photovoltaics*, edited by M.D Archer, R. Hill, Imperial College Press, London, 2001, p. 377.
- 16 D. M. Russell, A. C. Arias, R. H. Friend, C. Silvaa, C. Ego, A. C. Grimsdale, K. Müllen, *Appl. Phys. Lett.* **80**, 2204 (2002).
- 17 L. Kulikovskiy, D. Neher, E. Mecher, K. Meerholz, H.-H. Hörhold, O. Ostroverkhova, *Phys. Rev. B* **69**, 125216.
- 18 I. Riedel, V. Dyakonov, *Phys. Status Solidi A* **201**, 1332 (2004).

- 19 M. C. Scharber, N. A. Schultz, N. S. Sariciftci, C. J. Brabec, *Phys. Rev. B* **67**, 085202 (2003).
- 20 A. Nollau, M. Hoffmann, T. Fritz, K. Leo, *Thin Solid Films*, **368**, 130 (2000).
- 21 A. C. Morteani, A. S. Dhoot, J.-S. Kim, C. Silva, N. C. Greenham, C. Murphy, E. Moons, S. Ciná, J. H. Burroughes, R. H. Friend, *Adv. Mater.* **15**, 1708 (2003).
- 22 V. I. Arkhipov, E. V. Emelianova, H. Bässler, *Chem. Phys. Lett.* **372**, 886 (2003).
- 23 L. Sebastian, G. Weiser, G. Peter, H. Bässler, *Chem. Phys.* **75**, 103 (1983).
- 24 J. W. van der Horst, P. A. Bobbert, M. A. J. Michels, H. Bässler, *J. Chem. Phys.* **114**, 6950 (2001).
- 25 B. Schweitzer, V. I. Arkhipov, H. Bässler, *Chem. Phys. Lett.* **304**, 365 (1999).
- 26 D. Hertel, E. V. Soh, H. Bässler, L. J. Rothberg, *Chem. Phys. Lett.* **361**, 99 (2002).
- 27 V. Gulbinas, Y. Zaushitsyn, V. Sundstrom, D. Hertel, H. Bässler, A. Yartsev, *Phys. Rev. Lett.* **89**, 107401 (2002).
- 28 N. E. Geacintov, M. Pope, *J. Chem. Phys.* **47**, 1194 (1967).
- 29 V. I. Arkhipov, E. V. Emelianova, H. Bässler, *Phys. Rev. Lett.* **82**, 1321 (1999).
- 30 D. M. Basko, E. M. Conwell, *Phys. Rev. B* **66**, 155210 (2002).
- 31 V. Gulbinas, Y. Zaushitsyn, H. Bässler, A. Yartsev, V. Sundstrom, *Phys. Rev. B* **70**, 035215 (2004).
- 32 C. Gadermaier, G. Cerullo, C. Manzoni, U. Scherf, E. J. W. List, G. Lanzani, *Synth. Met.* **139**, 605 (2003).
- 33 C. Silva, A. S. Dhoot, D. M. Russell, M. A. Stevens, A. C. Arias, J. D. MacKenzie, N. C. Greenham, R. H. Friend, S. Setayesh, K. Müllen, *Phys. Rev. B* **64**, 125211 (2001).
- 34 D. Moses, A. Dogariu, A. J. Heeger, *Chem. Phys. Lett.* **316**, 356 (2000).
- 35 B. Schweitzer, V. I. Arkhipov, U. Scherf, H. Bässler, *Chem. Phys. Lett.* **313**, 57 (1999).
- 36 Y. V. Romanovskii, V. I. Arkhipov, H. Bässler, *Phys. Rev. B* **64**, 033104 (2001).
- 37 J. G. Müller, U. Lemmer, J. Feldmann, U. Scherf, *Phys. Rev. Lett.* **88**, 147401 (2002).
- 38 G. Lanzani, G. Cerullo, D. Polli, A. Gambetta, M. Zavelani-Rossi, C. Gadermaier, *Phys. Status Solidi A* **201**, 1116 (2004).
- 39 V. I. Arkhipov, E. V. Emelianova, H. Bässler, *Chem. Phys. Lett.* **383**, 166 (2004).
- 40 V. I. Arkhipov, E. V. Emelianova, H. Bässler, *Chem. Phys. Lett.* **340**, 517 (2001).
- 41 E. W. Montroll, H. Scher, *J. Stat. Phys.* **9**, 101 (1973).
- 42 H. Scher, M. Rax, *Phys. Rev. B* **7**, 491 (1973).
- 43 H. Scher, E. W. Montroll, *Phys. Rev. B* **12**, 2455 (1975).
- 44 G. Pfister, H. Scher, *Adv. Phys.* **27**, 747 (1978).
- 45 J. Klafter, R. Silbey, *Phys. Rev. Lett.* **44**, 55 (1980).
- 46 A. I. Rudenko, *J. Non.-Cryst. Solids* **22**, 215 (1976).
- 47 M. Pollak, *Philos. Mag.* **36**, 1157 (1977).
- 48 F. W. Schmidlin, *Phys. Rev. B* **16**, 2362 (1977).
- 49 A. I. Rudenko, V. I. Arkhipov, *Philos. Mag. B* **45**, 177 (1982).
- 50 V. I. Arkhipov, A. I. Rudenko, *Philos. Mag. B* **45**, 189 (1982).
- 51 A. A. Jakobs, K. W. Keln, *Phys. Rev. B* **48**, 8780 (1993).
- 52 J. Mort, G. Pfister, S. Grammatica, *Solid State Commun.* **18**, 693 (1976).
- 53 G. Pfister, S. Grammatica, J. Mort, *Phys. Rev. Lett.* **37**, 1360 (1976).
- 54 J. M. Marshall, *Philos. Mag. B* **38**, 335 (1978).
- 55 G. Schönherr, H. Bässler, M. Silver, *Philos. Mag. B* **44**, 369 (1981).
- 56 B. Ries, H. Bässler, *Phys. Rev. B* **35**, 2295 (1987).
- 57 D. M. Pai, J. F. Yannis, M. Stolka, D. Renfer, W. W. Limburg, *Philos. Mag. B* **48**, 505 (1983).
- 58 L. B. Schein, D. Glatz, J. C. Scott, *Phys. Rev. Lett.* **65**, 472 (1990).
- 59 L. B. Schein, A. Rosenberg, S. L. Rice, *Philos. Mag. B*, **61**, 10835 (1990).
- 60 M. A. Abkowitz, M. J. Rice, M. Stolka, *Philos. Mag. B*, **61**, 25 (1990).

- 61 K. Yokoyama, M. Yokoyama, *Philos. Mag. B* **61**, 59 (1990).
- 62 P. Strohriegel, D. Haarer, *Macromol. Chem. Macromol. Symp.* **44**, 85 (1991).
- 63 E. Müller-Horsche, D. Haarer, H. Scher, *Phys. Rev. B* **35**, 1273 (1987).
- 64 S. J. Santos Lemus, J. Hirsch, *Philos. Mag. B* **53**, 25 (1986).
- 65 A. Peled, L. B. Schein, *Chem. Phys.* **153**, 422 (1988).
- 66 W. G. Gill, *J. Appl. Phys.* **43**, 5033 (1972).
- 67 H. Bässler, *Phys. Status Solidi B* **175**, 15 (1993), and references cited therein.
- 68 T. P. Carter, M. Manavi, W. E. Moerner, *J. Chem. Phys.* **89**, 1768 (1998).
- 69 L. Kador, *J. Chem. Phys.* **95**, 5574 (1991).
- 70 A. Miller, E. Abrahams, *Phys. Rev.* **120**, 745 (1960).
- 71 J. H. Slowik, I. Chen, *J. Appl. Phys.* **54**, 4467 (1983).
- 72 P. M. Borsenberger, D. S. Weiss, *Organic Photoreceptors for Xerography*, Marcel Dekker, New York, 1998.
- 73 A. Hirao, H. Nishizawa, H. Sugiuchi, *Phys. Rev. Lett.* **75**, 1787 (1995).
- 74 B. Hartenstein, H. Bässler, A. Jakobs, K. W. Kehr, *Phys. Rev. B* **54**, 8574 (1996).
- 75 U. Wolf, H. Bässler, P. M. Borsenberger, W. T. Grünbaum, *Chem. Phys.* **222**, 259 (1997).
- 76 P. M. Borsenberger, W. T. Grünbaum, U. Wolf, H. Bässler, *Chem. Phys.* **234**, 277 (1998).
- 77 B. Movaghar, M. Grünwald, B. Ries, H. Bässler, D. Würtz, *Phys. Rev. B* **33**, 5545 (1986).
- 78 B. Movaghar, B. Ries, M. Grünwald, *Phys. Rev. B* **34**, 5575 (1986).
- 79 R. Richert, H. Bässler, B. Ries, B. Movaghar, M. Grünwald, *Philos. Mag. Lett.* **59**, 95 (1989).
- 80 S. C. J. Meskers, J. Hübner, M. Oestreich, H. Bässler, *J. Phys. Chem. B* **105**, 9139 (2001).
- 81 Yu. N. Gartstein, E. M. Conwell, *Chem. Phys. Lett.* **217**, 41 (1994).
- 82 D. H. Dunlap, P. E. Parris, V. M. Kenkre, *Phys. Rev. Lett.* **77**, 542 (1996).
- 83 S. V. Novikov, D. H. Dunlap, V. M. Kenkre, P. E. Parris, A. V. Vannikov, *Phys. Rev. Lett.* **81**, 4472 (1998).
- 84 J. A. Sinicropi, J. R. Cowdery-Corvan, E. H. Magin, P. M. Borsenberger, *Proc. SPIE*, **2850**, 202, (1996).
- 85 S. V. Rakhmanova, E. M. Conwell, *Appl. Phys. Lett.* **76**, 3822 (2000).
- 86 L. B. Schein, *Philos. Mag. B* **65**, 795 (1992).
- 87 D. H. Dunlap, V. M. Kenkre, *Chem. Phys.* **178**, 67 (1993).
- 88 D. Emin, *Phys. Rev. B* **46**, 9419 (1992).
- 89 H. Bässler, B. Schweitzer, *Acc. Chem. Res.* **32**, 173 (1999).
- 90 R. F. Mahrt, H. Bässler, *Synth. Met.* **45**, 107 (1991).
- 91 K. Brunner, A. Tortschanoff, C. Warmuth, H. Bässler, H. F. Kauffmann, *J. Chem. Phys.* **104**, 3781 (2000).
- 92 E. A. Silinsh, V. Capek, *Organic Molecular Crystals: Interaction, Localization, Transport Phenomena*, API Press, New York, 1994.
- 93 R. F. Mahrt, J. Yang, H. Bässler, *Chem. Phys. Lett.* **192**, 576 (1992).
- 94 S. Heun, H. Bässler, P. Borsenberger, *Chem. Phys.* **200**, 265 (1995).
- 95 Z. Shuai, J. L. Bredas, W. P. Su, *Chem. Phys. Lett.* **228**, 301 (1994).
- 96 D. Beljonne, J. Cornil, J. L. Bredas, R. H. Friend, *Synth. Met.* **76**, 61 (1996).
- 97 V. M. Kenkre, D. H. Dunlap, *Philos. Mag. B* **65**, 831 (1992).
- 98 B. I. Shklovskii, A. L. Efros, *Electronic Properties of Doped Semiconductors*, Springer, Berlin, 1984.
- 99 M. Pollak, *J. Non-Cryst. Solids* **11**, 1 (1972).
- 100 N. F. Mott, *J. Non-Cryst. Solids* **1**, 1 (1968).
- 101 V. I. Arkhipov, E. V. Emelianova, G. J. Adriaenssens, *Phys. Rev. B* **64**, 125125 (2001).
- 102 M. Grünwald, B. Movaghar, *J. Phys.: Condens. Matter* **1**, 2521 (1989).
- 103 V. I. Arkhipov, G. J. Adriaenssens, *J. Phys.: Condens. Matter* **8**, 7909 (1996).
- 104 S. D. Baranovskii, T. Faber, F. Hensel, P. Thomas, G. J. Adriaenssens, *J. Non-Cryst. Solids* **200**, 214 (1996).
- 105 M. Grünwald, P. Thomas, *Phys. Status Solidi B* **94**, 125 (1979).
- 106 D. Monroe, *Phys. Rev. Lett.* **54**, 146 (1985).
- 107 V. I. Arkhipov, A. I. Rudenko, M. S. Iovu, S. D. Shutov, *Phys. Status Solidi A* **54**, 67 (1979).

- 108 V. I. Arkhipov, *J. Non-Cryst. Solids* **163**, 274 (1993).
- 109 M. E. Scharfe, *Phys. Rev. B* **2**, 5025 (1970).
- 110 G. F. Seynhaeve, R. P. Barclay, G. J. Adriaenssens, J. M. Marshall, *Phys. Rev. B* **39**, 10196 (1989).
- 111 R. Richert, L. Pautmeier, H. Bässler, *Phys. Rev. Lett.* **63**, 547 (1989).
- 112 X. Jiang, Y. Harima, K. Yamashita, Y. Tada, J. Ohshita, A. Kunai, *Chem. Phys. Lett.* **364**, 616 (2002).
- 113 A. Kadashchuk, Yu. Skryshevskii, A. Vakhnin, N. Ostapenko, V. I. Arkhipov, E. V. Emelianova, H. Bässler, *Phys. Rev. B* **63**, 115205 (2001).
- 114 V. I. Arkhipov, P. Heremans, E. V. Emelianova, G. J. Adriaenssens, H. Bässler, *Appl. Phys. Lett.* **82**, 3245 (2003).
- 115 V. I. Arkhipov, P. Heremans, E. V. Emelianova, G. J. Adriaenssens, H. Bässler, *J. Phys.: Condens. Matter* **14**, 9899 (2002).
- 116 C. Tanase, P. W. M. Blom, D. M. de Leeuw, E. J. Meijer, *Phys. Status Solidi A* **201**, 1236 (2004).
- 117 M. Hori, F. Yonezawa, *J. Phys. C: Solid State Phys.* **10**, 229 (1977).
- 118 H. Böttger, V. V. Bryksin, *Phys. Status Solidi B*, **96**, 219 (1979).
- 119 B. Movaghar, W. Schirmacher, *J. Phys. C: Solid State Phys.* **14**, 859 (1981).
- 120 M. Grünwald, B. Pohlmann, B. Movaghar, D. Würtz, *Philos. Mag. B* **49**, 341 (1984).
- 121 P. E. Parris, B. D. Bookout, *Phys. Rev. B*, **53**, 629 (1996).
- 122 I. I. Fishchuk, *Philos. Mag. B* **81**, 576 (2001).
- 123 I. I. Fishchuk, D. Hertel, H. Bässler, A. Kadashchuk, *Phys. Rev. B* **65**, 125201 (2002).
- 124 D. Hertel, H. Bässler, U. Scherf, H. H. Hörhold, *J. Chem. Phys.* **110**, 9214 (1999).
- 125 M. Redecker, D. D. C. Bradley, M. Inbasekaran, E. P. Woo, *Appl. Phys. Lett.* **73**, 1565 (1998).
- 126 M. Redecker, D. D. C. Bradley, M. Inbasekaran, E. P. Woo, *Appl. Phys. Lett.* **74**, 1400 (1999).
- 127 S. V. Novikov, D. H. Dunlap, V. M. Kenkre, *Proc. SPIE* **3471**, 181 (1998).
- 128 R.A.Marcus, *J. Chem. Phys.* **24**, 966 (1956).
- 129 R.A.Marcus, *Rev. Mod. Phys.* **65**, 599 (1993).
- 130 I. I. Fishchuk, A. Kadashchuk, H. Bässler, S. Nešpurek, *Phys. Rev. B* **67**, 224303 (2003).
- 131 P. E. Paris, V. M. Kenkre, D. H. Dunlap, *Phys. Rev. Lett.* **87**, 126601 (2001).
- 132 I. I. Fishchuk, A. Kadashchuk, H. Bässler, M. Abkowitz, *Phys. Rev. B* **70**, 245212 (2004).
- 133 Yu. N. Gartstein, E. M. Conwell, *J. Chem. Phys.* **100**, 9175 (1994).
- 134 P. M. Borsenberger, L. Pautmeier, H. Bässler, *J. Chem. Phys.* **94**, 5447 (1991).
- 135 M. A. Abkowitz, *Philos. Mag. B* **65**, 817 (1992).
- 136 H. Cordes, S. D. Baranovskii, K. Kohary, P. Thomas, S. Yamasaki, F. Hensel, J.-H. Wendorff, *Phys. Rev. B* **63**, 094201 (2001).
- 137 Nguen Van Lien, B. I. Shklovskii, *Solid State Commun.* **67**, 233 (1988).
- 138 H. Böttger, V.V.Bryksin, *Philos. Mag. B* **42**, 297 (1980).
- 139 D. C. Hoesterey, G. M. Letson, *Phys. Chem. Solids* **24**, 1609 (1963).
- 140 I. I. Fishchuk, A. K. Kadashchuk, H. Bässler, D. S. Weiss, *Phys. Rev. B* **66**, 205208 (2002).
- 141 C. Im, H. Bässler, H. Rost, H. H. Hörhold, *J. Chem. Phys.* **113**, 3802 (2000).
- 142 U. Albrecht, H. Bässler, *Chem. Phys.* **199**, 207 (1995).
- 143 B. R. Wegewijs, G. Dicker, J. Piris, A. A. Garcia, M. P. de Haas, J. M. Warman, *Chem. Phys. Lett.* **332**, 79 (2000).
- 144 J. Mort, M. Morgan, S. Grammatica, J. Noolandi, K. M. Hong, *Phys. Rev. Lett.* **48**, 1411 (1982).
- 145 Z. D. Popovic, *Chem. Phys. Lett.* **100**, 227 (1983).
- 146 Z. D. Popovic, *J. Chem. Phys.* **78**, 1552 (1983).
- 147 W. Graupner, G. Cerullo, G. Lanzani, M. Nisoli, E. J. W. List, G. Leising,

- S. De Silvestri, *Phys. Rev. Lett.* **81**, 3259 (1998).
- 148 M. Redecker, H. Bässler, *Appl. Phys. Lett.* **69**, 70 (1996).
- 149 K. Fesser, A. R. Bishop, D. K. Campbell, *Phys. Rev. B* **27**, 4804 (1983).
- 150 H. Bässler, in *Primary Photoexcitation in Conjugated Polymers: Molecular Exciton versus Semiconductor Band Model*, edited by N. S. Sariciftci, World Scientific, Singapore, 1997, p. 51–98.
- 151 M. Deussen, H. Bässler, *Synth. Met.* **54**, 49 (1993).
- 152 H. Rohrbacher, N. Karl, *Phys. Status Solidi A* **29**, 517 (1975).
- 153 C. W. Spangler, T. J. Hall, *Synth. Met.* **44**, 85 (1991).
- 154 R. G. Kepler, *Phys. Rev.* **119**, 1226 (1960).
- 155 O. H. LeBlanc, *J. Chem. Phys.* **33**, 626 (1960).
- 156 B. Polischuk, S. O. Kasap, A. Baillie, *Appl. Phys. Lett.* **63**, 183 (1993).
- 157 P. Mark, W. Helfrich, *J. Appl. Phys.* **33**, 305 (1962).
- 158 M. A. Lampert, P. Mark, *Current Injection in Solids*, Academic Press, New York, 1970.
- 159 P. W. M. Blom, M. J. M. deJong, J. J. M. Vlegaar, *Appl. Phys. Lett.* **68**, 3308 (1996).
- 160 D. Poplavskyy, J. Nelson, *J. Appl. Phys.* **93**, 341 (2003).
- 161 A. J. Campbell, D. D. C. Bradley, D. G. Lidzey, *J. Appl. Phys.* **82**, 6326 (1997).
- 162 R. W. I. de Boer, M. Jochemsen, T. M. Klapwijk, A. F. Morpurgo, J. Niemax, A. K. Tripathi, J. Pflaum, *J. Appl. Phys.* **95**, 1196 (2004).
- 163 A. Many, G. Rakavy, *Phys. Rev.* **126**, 1980 (1962).
- 164 M. A. Abkowitz, D. Pai, *Philos. Mag. B* **53**, 193 (1986).
- 165 D. Pai, *J. Imaging Sci. Technol.* **4**, 135 (1997).
- 166 T. K. Daubler, V. Cimrova, S. Pfeiffer, H. H. Horhold, D. Neher, *Adv. Mater.* **11**, 1274 (1999).
- 167 N. T. Binh, M. Gailberger, H. Bässler, *Synth. Met.* **47**, 77 (1992).
- 168 G. Juška, K. Arlauskas, M. Viliunas, J. Kocka, *Phys. Rev. Lett.* **84**, 4946 (2000).
- 169 G. Juška, K. Arlauskas, M. Viliunas, K. Genevicius, R. Österbacka, H. Stubb, *Phys. Rev. B* **62**, R16235 (2000).
- 170 J. H. Burroughes, C. A. Jones, R. H. Friend, *Nature* **335**, 137 (1988).
- 171 F. Garnier, G. Horowitz, X. Z. Peng, D. Fichou, *Synth. Met.* **45**, 163 (1991).
- 172 G. Horowitz, P. Lang, M. Mottaghi, M. Aubin, *Adv. Funct. Mater.* **14**, 1069 (2004).
- 173 E. J. Meijer, C. Tanase, P. W. M. Blom, E. van Veenendaal, B.-H. Huisman, D. M. de Leeuw, T. M. Klapwijk, *Appl. Phys. Lett.* **80**, 3838 (2002).
- 174 C. Tanase, E. J. Meijer, P. W. M. Blom, D. M. de Leeuw, *Phys. Rev. Lett.* **91**, 216601 (2003).
- 175 H. Sirringhaus, P. J. Brown, R. H. Friend, M. M. Nielsen, K. Bechgaard, B. M. W. Langeveld-Voss, A. J. H. Spiering, R. A. J. Janssen, E. W. Meijer, P. Herwig, D. M. de Leeuw, *Nature* **401**, 685 (1999).
- 176 P. R. Infelta, M. P. De Haas, J. M. Warman, *Radiat. Phys. Chem.* **10**, 353 (1977).
- 177 J. M. Warman, M. P. De Haas, A. Hummel, *Chem. Phys. Lett.* **22**, 480 (1973).
- 178 F. C. Grozema, PhD Thesis, Delft University, 2003.
- 179 F. A. Hegmann, R. R. Tykwinski, K. P. H. Lui, J. E. Bullock, J. E. Anthony, *Phys. Rev. Lett.* **89**, 227403 (2002).
- 180 E. Hendry, M. Koeberg, J. M. Schins, H. K. Nienhuys, V. Sundström, L. D. A. Siebbeles, M. Bonn, *Phys. Rev. B* **71**, 125201 (2005).
- 181 P. M. Borsenberger, L. Pautmeier, R. Richert, H. Bässler, *J. Chem. Phys.* **94**, 8276 (1991).
- 182 P. M. Borsenberger, L. T. Pautmeier, H. Bässler, *Phys. Rev. B* **46**, 12145 (1992).
- 183 U. Bach, K. De Cloedt, H. Spreitzer, M. Grätzel, *Adv. Mater.* **12**, 1060 (2000).
- 184 L. Pautmeier, B. Ries, R. Richert, H. Bässler, *Chem. Phys. Lett.* **143**, 459 (1988).
- 185 P. M. Borsenberger, H. Bässler, *Phys. Status Solidi B* **170**, 291 (1992).
- 186 W. T. Gruenbaum, E. H. Magin, P. M. Borsenberger, *Jpn. J. Appl. Phys.* **35**, 2704 (1996).

- 187 G. Wegner, K. Müllen, editors, *Electronic Materials: the Oligomer Approach*, Wiley-VCH, Weinheim, 1998.
- 188 J. Rissler, *Chem. Phys. Lett.* **395**, 92 (2004).
- 189 S. C. J. Meskers, J. Hübner, M. Oestreich, H. Bässler, *J. Phys. Chem.* **105**, 9139 (2001).
- 190 M. Redecker, D. D. C. Bradley, M. Inbasekaran, W. W. Wu, E. P. Woo, *Adv. Mater.* **11**, 241 (1999).
- 191 A. J. Mozer, N. S. Sariciftci, *Chem. Phys. Lett.* **389**, 438 (2004).
- 192 A. J. Mozer, N. S. Sariciftci, A. Pivrikas, R. Österbacka, G. Juška, H. Bässler, *Phys. Rev. B* in press.
- 193 N. Karl, Festkörperprobleme, edited by H. J. Queisser, Pergamon/Vieweg, Braunschweig, 1974, Vol. 14, p. 261 in *Defect Control in Semiconductors*, Vol. 2, edited by K. Sumino, North-Holland, Amsterdam, 1990, p. 1725.
- 194 N. von Malm, J. Steiger, H. Heil, R. Schmechel, H. von Seggern, *J. Appl. Phys.* **92**, 7564 (2002); R. Schmechel, Habilitationsschrift, Darmstadt University, 2004.
- 195 B. Ries, H. Bässler, M. Silver, *Philos. Mag. B* **54**, 141 (1986).
- 196 D. M. Pai, J. F. Yanus, M. Stolka, *J. Phys. Chem.* **88**, 4717 (1984).
- 197 P. M. Borsenberger, E. H. Magin, S. A. Visser, *Jpn. J. Appl. Phys.* **37**, 1945 (1998).
- 198 R. Pacios, J. Nelson, D. D. C. Bradley, C. J. Brabec, *Appl. Phys. Lett.* **83**, 4764 (2003).
- 199 S. A. Choulis, J. Nelson, Y. Kim, D. Poplavskyy, T. Kreouzis, J. R. Durrant, D. D. C. Bradley, *Appl. Phys. Lett.* **83**, 3812 (2003).
- 200 M. Redecker, D. D. C. Bradley, M. Jandke, P. Strohriegel, *Appl. Phys. Lett.* **75**, 109 (1999).
- 201 A. J. Heeger, S. Kivelson, J. R. Schrieffer, W. P. Su, *Rev. Mod. Phys.* **60**, 781 (1988).
- 202 M. Deussen, H. Bässler, *Chem. Phys.* **164**, 247 (1992).
- 203 Z. Vardeny, E. Ehrenfreund, O. Braffman, B. Horowitz, H. Fujimoto, J. Tanaka, M. Tanaka, *Phys. Rev. Lett.* **57**, 2995 (1986).
- 204 J. Cornil, D. Beljonne, J. L. Bredas, *J. Chem. Phys.* **103**, 834 (1995); F. C. Grozema, L. P. Candeias, M. Swart, P. Th. van Duijnen, J. Wildeman, G. Hadziioanou, L. D. A. Siebbeles, J. M. Warman, *J. Chem. Phys.* **117**, 11366 (2002).
- 205 V. I. Arkhipov, P. Heremans, E. V. Emelianova, G. J. Adriaenssens, H. Bässler, *Chem. Phys.* **288**, 51 (2003).
- 206 H. Bässler, P. M. Borsenberger, R. J. Perry, *J. Polym. Sci., Part B: Polym. Phys.* **32**, 1677 (1994).
- 207 R. D. Hreha, C. P. George, A. Haldi, B. Domercq, M. Malagoli, S. Barlow, J.-L. Brédas, B. Kippelen, S. R. Marder, *Adv. Funct. Mater.* **13**, 967 (2003).
- 208 J. Shirota, *J. Mater. Chem.* **10**, 1 (2000).
- 209 H. C. F. Martens, P. W. M. Blom, H. F. M. Schoo, *Phys. Rev. B* **61**, 7489 (2000).
- 210 P. J. Brown, H. Sirringhaus, M. Harrison, M. Shkunov, R. H. Friend, *Phys. Rev. B*, **63**, 125204 (2001).
- 211 H. Okumoto, T. Yatabe, M. Shimomura, A. Kaito, N. Minami, Y. Tanabe, *Adv. Mater.* **13**, 72 (2001).
- 212 A. R. Inigo, C. H. Tan, W. Fann, Y.-S. Huang, G.-Y. Perng, S.-A. Chen, *Adv. Mater.* **13**, 504 (2001).
- 213 A. R. Inigo, H.-C. Chiu, W. Fann, Y.-S. Huang, U.-S. Jeng, T.-L. Lin, C.-H. Hsu, K.-Y. Peng, S.-A. Chen, *Phys. Rev. B* **69**, 075201 (2004).
- 214 M. Grell, D. D. C. Bradley, M. Inbasekaran, E. P. Woo, *Adv. Mater.* **9**, 798 (1997).
- 215 T. Miteva, A. Meisel, W. Knoll, H. G. Nothofer, U. Scherf, D. C. Müller, K. Meerholz, A. Yasuda, D. Neher, *Adv. Mater.* **13**, 565 (2001).
- 216 H. Sirringhaus, R. J. Wilson, R. H. Friend, M. Inbasekaran, W. Wu, E. P. Woo, M. Grell, D. D. C. Bradley, *Appl. Phys. Lett.* **77**, 406 (2000).
- 217 F. C. Grozema, T. J. Savenije, M. J. W. Vermeulen, L. D. A. Siebbeles, J. M. Warman, A. Meisel, D. Neher, H.-G. Nothofer, U. Scherf, *Adv. Mater.* **13**, 1627 (2001).
- 218 F. C. Grozema, L. D. A. Siebbeles, J. M. Warman, S. Seki, S. Tagawa, U. Scherf, *Adv. Mater.* **14**, 228 (2002).
- 219 H. Zuilhof, H. M. Barentsen, M. V. Dijk, E. J. R. Sudholter, R. J. O. M. Hoofman, L. D. A. Siebbeles, M. P. de Haas, J. M. Warmann in *Supramolecular Photo-*

- sensitive, *Electroactive Materials*, edited by H. S. Nalwa, Academic Press, Orlando, FL, 2001, p. 339–439
- 220 B. Reimer, H. Bässler, *Phys. Status Solidi B* **85**, 145 (1978).
- 221 G. P. van der Laan, M. P. de Haas, D. M. de Leeuw, D. Bloor, J. Tsibouklis, *Synth. Met.* **69**, 35 (1995).
- 222 K. J. Donovan, E. G. Wilson, *Philos. Mag. B* **44**, 9 (1981).
- 223 R. J. O. M. Hoofman, L. D. A. Siebbeles, M. P. de Haas, A. Hummel, D. Bloor, *J. Chem. Phys.* **109**, 1885 (1998).
- 224 L. Sebastian, G. Weiser, *Phys. Rev. Lett.* **46**, 1156 (1981).
- 225 T. Pauck, H. Bässler, J. Grimme, U. Scherf, K. Müllen, *Chem. Phys.* **210**, 219 (1996).
- 226 P. Prins, L. P. Candeias, A. J. J. M. van Breemen, J. Sweelssen, P. T. Herwig, H. F. M. Schoo, L. D. A. Siebbeles, *Adv. Mater.* **17**, 718 (2005).

## 7

**Probing Organic Semiconductors with Terahertz Pulses**

Frank A. Hegmann, Oksana Ostroverkhova and David G. Cooke

## 7.1

**Introduction**

There is growing interest in using organic semiconductors for applications in electronics and photonics [1–8]. In particular, organic semiconductor thin films offer several advantages over traditional silicon technology, including low-cost processing, the potential for large-area flexible devices, high-efficiency light emission and widely tunable properties through functionalization of the molecules in the material.

Field-effect organic thin-film transistors (OTFTs) based on conjugated polymers or oligomers typically have mobilities much less than  $0.1 \text{ cm}^2 \text{ V}^{-1} \text{ s}^{-1}$  owing to the high degree of disorder in the polymer films [3, 9], but higher mobilities have been reported for small oligomers [10, 11]. Most of the work on OTFTs, however, has concentrated on vacuum-deposited, polycrystalline pentacene thin films which, owing to the higher degree of order in the films and better  $\pi$ -orbital overlap between molecules, have higher room temperature mobilities on the order of  $1 \text{ cm}^2 \text{ V}^{-1} \text{ s}^{-1}$  and have been used in a variety of device structures [3, 12–17]. Since higher carrier mobilities result in faster switching times for transistor circuits, pentacene film morphology and its influence on carrier mobility and other properties have been extensively studied [17–23]. The polycrystalline morphology of the pentacene thin films typically results in a thermally activated carrier mobility where the mobility decreases as the temperature is lowered [12, 19, 20], but an almost temperature-independent carrier mobility has also been observed [12].

In order to gain a better understanding of the *intrinsic* properties of organic semiconductors, many groups have performed field-effect (OFET), time-of-flight (TOF) or space-charge-limited current (SCLC) measurements on high-purity single-crystal samples of naphthalene [24–28], anthracene [29], tetracene [30–35], pentacene [35–38], rubrene [32, 35, 39–43], perylene [25–28] and other organic molecular crystals [25–28, 44, 45]. Room temperature mobilities as high as  $20 \text{ cm}^2 \text{ V}^{-1} \text{ s}^{-1}$  for rubrene [42] and  $35 \text{ cm}^2 \text{ V}^{-1} \text{ s}^{-1}$  for pentacene [38] have been reported recently. Furthermore, in many of the studies the mobility was observed to increase as the temperature decreased over some temperature range, indicative of band-like

transport observed in many inorganic semiconductors [24–32, 38, 42]. For example, ultrapure naphthalene shows an increase in mobility from about  $1 \text{ cm}^2 \text{ V}^{-1} \text{ s}^{-1}$  at room temperature to more than  $100 \text{ cm}^2 \text{ V}^{-1} \text{ s}^{-1}$  below 30 K with  $\mu \propto T^{-n}$ , where  $n = 2.90$  for holes and 1.40 for electrons [24]. (The expected behavior for scattering of electrons from acoustic phonons is  $\mu \sim T^{-1.5}$ . In silicon, for example, other scattering mechanisms give  $\mu \sim T^{-2.42}$  near 300 K [46].) However, the nature of band-like transport for charge carriers in organic molecular crystals, which was first observed experimentally more than 25 years ago [47], is still not understood and has been the focus of many recent theoretical investigations [48–58]. The electronic properties, band structure and exciton energies in oligoacenes have also been extensively studied theoretically over the past few years [59–66]. Understanding the nature of charge carrier transport in organic semiconductors such as the oligoacenes is not only of fundamental interest but would also be useful for the optimization of these materials in applications.

One of the most successful photonics applications of thin-film organic semiconductors has been light-emitting devices for flexible display technology based on conjugated polymers such as poly(*p*-phenylenevinylene) (PPV) [67–71]. More recently, light emission from tetracene thin-film FETs has been observed [72–74]. Other applications include polymer lasers [8, 75–77], efficient organic photovoltaics [6, 78–82] and sensitive, high-speed organic photodetectors [80, 83–87]. However, despite much progress in organic photonics, the nature of photocarrier generation and subsequent photocarrier transport in organic semiconductors is not completely understood and remains controversial even today [88–97]. The generation of mobile charge carriers in photoexcited organic materials occurs over femtosecond to picosecond time-scales, and so ultrafast pump–probe experiments are essential for improving our understanding of fundamental optoelectronic processes in organic semiconductors. Ultrafast photoexcitation dynamics and charge carrier generation have been studied with femtosecond laser sources using optical pump–optical probe techniques in conjugated polymers [88–114], polycrystalline pentacene [115] and thiophene [116] thin films, and thiophene [116–118] and perylene [119, 120] single crystals.

Many experiments on conjugated polymers support the molecular exciton model where the primary photoexcitations are strongly bound excitons which can dissociate into mobile charge carriers by various mechanisms over picosecond and sub-picosecond time-scales [88, 89]. The primary photoexcitations in organic molecular crystals are also believed to be tightly bound excitons (or Frenkel excitons) [48, 49, 117]. For example, the photogeneration of free charge carriers by electric-field-induced dissociation of primary excitons [98, 99, 107, 108] may occur over 10–100-ps time-scales. On the other hand, hot exciton dissociation can produce free charge carriers over faster time-scales within 100 fs [100, 101, 106]. Singlet exciton fission into pairs of triplet excitons with a characteristic time constant of about 80 fs has also been explored in pentacene thin films [115]. In general, the molecular exciton model predicts higher rates of exciton dissociation into charge carriers at higher temperatures, higher electric fields and at higher pump photon energies above the onset for charge generation, which depends on the size of the

exciton binding energy [48, 49, 88]. (Note that the hot exciton model also predicts a temperature independent charge carrier generation rate if the excess photon energy is much larger than the thermal energy in the system [100, 101, 106].) The exact values for the exciton binding energies in organic semiconductors, however, are not completely known [66, 92]. In Si and GaAs, the exciton binding energies are around 15 and 5 meV, respectively. In naphthalene, the singlet exciton binding energy may be as high as 1 eV with a HOMO–LUMO gap (or bandgap) of about 5 eV [66]. In pentacene, the singlet exciton binding energy is lower than that in naphthalene and is in the range of 0.1–0.5 eV, with a bandgap of 2.2 eV [61, 66]. In many conjugated polymer organic semiconductors, 0.5 eV is a typical singlet exciton binding energy [121] with bandgaps on the order of 2 eV, but binding energies around 60 meV for PPV have also been reported [121, 122]. A high exciton binding energy makes it difficult for dissociation to occur and so charge photogeneration efficiencies (or quantum efficiencies)  $\eta \ll 1$  have been reported. A low exciton binding energy, therefore, generally results in more efficient dissociation of primary excitons into separated charge carriers.

In the semiconductor band model, the primary photoexcitations are mobile charge carriers that are created with high efficiency directly from the light absorption process [90–92], as is the case in inorganic semiconductors such as Si and GaAs. In this model, the generation of charge carriers does not occur through some secondary process involving dissociation of excitons. Primary photoexcitation of charge carriers (or polarons) with quantum yields as high as 10% ( $\eta \approx 0.1$ ) within 100-fs time-scales and in zero electric field have been observed in MEH-PPV films using ultrafast pump–probe techniques [90–92]. Photogeneration of charged polarons with efficiencies near 20% and within 100-fs time-scales has also been observed in polythiophene films [104]. A charge photogeneration efficiency that is roughly independent of the pump wavelength for photon energies larger than the absorption onset has also been reported, which is contrary to some of the predictions of the molecular exciton model [90–92, 123].

Even though ultrafast pump–probe experiments that use probe photon energies in the mid-infrared to visible range (0.1–3 eV) may be sensitive to the *presence* of charge carriers in organic semiconductors with a time resolution  $< 0.1$  ps, they *cannot* sense if those carriers are mobile or provide direct insight into the nature of the photocarrier transport. Photoconductivity measurements, on the other hand, are sensitive to the presence of mobile charge carriers and can provide fundamental insight into the nature of photoexcitations and charge carrier transport in organic semiconductors. Steady-state (DC or low-frequency) photoconductivity measurements have revealed wavelength-independent [123] and temperature-independent [124] charge generation efficiencies in PPV films consistent with the semiconductor band model, but other studies have agreed with the molecular exciton (Onsager) model showing that the quantum yield increases with temperature, electric field and photon energy [125]. Steady-state photoconductivity in anthracene single crystals has been studied extensively [48, 49, 126–128], where the onset for optical absorption is at 3.2 eV but the onset for photoconductivity occurs at about 3.9 eV owing to the large exciton binding energy [126, 128]. DC

photoconductivity measurements in tetracene [129, 130], pentacene [129–131], functionalized pentacene [132, 133] and rubrene [134] single crystals, and polycrystalline pentacene thin films [135] have also been performed. In recent measurements on single-crystal pentacene samples, the photocurrent yield was observed to increase from 0.1% close to the HOMO–LUMO gap at 2.2 eV (560 nm) to about 50% at 2.9 eV (430 nm) [131]. Amorphous-like band tails were also observed below 2.2 eV in these high-purity pentacene single crystals, but their origin is currently unknown [131].

Transient photoconductivity measurements that use fast oscilloscopes connected to samples via voltage-biased electrodes allow carrier mobilities to be measured using time-of-flight techniques [28] and can provide information on photo-carrier trapping and recombination times. Transient photoconductivity in PPV and PDA films has also been measured with 50-ps time resolution using Auston switch transmission line geometries [136, 137]. A fast voltage transient with an initial exponential decay time of 100 ps and a temperature-independent amplitude from 300 K down to 15 K was observed, followed by a slow component with a decay time >600 ps and an amplitude that was reduced at lower temperatures. The fast component was attributed to photogenerated polarons and the slow component to bipolaron formation. Transient photoconductivity experiments with sub-nanosecond or nanosecond time resolution have also been performed in anthracene [138–140], pentacene [141] and sexithiophene [142] single crystals and C<sub>60</sub> films [143]. However, it may not always be so easy to pattern contacts onto samples and the metal–organic interface at the contact may complicate interpretation of the transient photoconductivity results. Contactless transient photoconductivity measurements with nanosecond time resolution have recently been achieved using time-resolved microwave conductivity (TRMC) techniques [144–146], which have been used to measure the mobility of photogenerated carriers in polymer thin films and along the conjugated backbone of isolated polymer chains in solution.

Considering the ultrafast time-scales discussed above for charge carrier photo-generation, a non-contact technique for probing transient photoconductivity in organic semiconductors with *sub-picosecond* time resolution would be desirable. Such a technique does exist and is referred to as time-resolved terahertz spectroscopy (TRTS), which is the main focus of this chapter. TRTS is a relatively new ultrafast pump–probe technique that uses terahertz pulses to directly probe the conductivity induced by a pump pulse in a material. Recently, time-resolved terahertz spectroscopy has been used to probe transient photoconductivity in pentacene and functionalized pentacene thin films and single crystals as well as other organic molecular crystals [147–153], and has revealed photogeneration of mobile charge carriers over sub-picosecond time-scales and band-like carrier transport in both single-crystal and polycrystalline thin film samples. TRTS measurements of transient photoconductivity in PPV films and isolated PPV polymer chains in solution have also been performed recently [154, 155]. The purpose of this chapter is to describe the technique of time-resolved terahertz pulse spectroscopy and show how it can be used to probe the nature of photoexcitations and carrier transport in organic semiconductors.

## 7.2

## What is a Terahertz Pulse?

Within the context of time-resolved terahertz spectroscopy (TRTS), a terahertz (THz) pulse can be described as a free-space-propagating, approximately single-cycle electromagnetic transient with a pulse duration on the order of 1 ps. The electric field versus time of a typical terahertz pulse measured in the laboratory is shown in Fig. 7.1. The Fourier amplitude spectrum of such a pulse, therefore, is centered around 1 THz and has a bandwidth on the order of 1 THz, as shown in the inset of Fig. 7.1, hence the name “terahertz pulse”. The broad spectrum of the THz pulse allows spectroscopy to be performed on materials typically within the range of terahertz frequencies from 0.2 to 3 THz. A frequency of 1 THz corresponds to a wavelength of  $300\ \mu\text{m}$ , which is in the far-infrared region of the spectrum. Table 7.1 provides a list of useful conversions between commonly used spectroscopic units from the microwave to visible regions. A photon with a frequency of 1 THz has an energy of 4.1 meV, which is less than the characteristic thermal energy of  $k_{\text{B}}T = 25\ \text{meV}$  at room temperature (see Table 7.2) and much smaller than typical bandgap energies of 1–3 eV in organic and inorganic semiconductors. Typical optical phonon energies in materials are in the mid-infrared range above 5 THz, but many other optically active vibrational modes appear below 5 THz, especially in organic materials (see Section 7.4). Terahertz pulses, therefore, generally probe low-energy excitations in materials with characteristic energies below 15 meV. In particular, free-carrier (intra-band) absorption makes THz pulses ideal probes of conduction in materials, as discussed in more detail in Section 7.5.

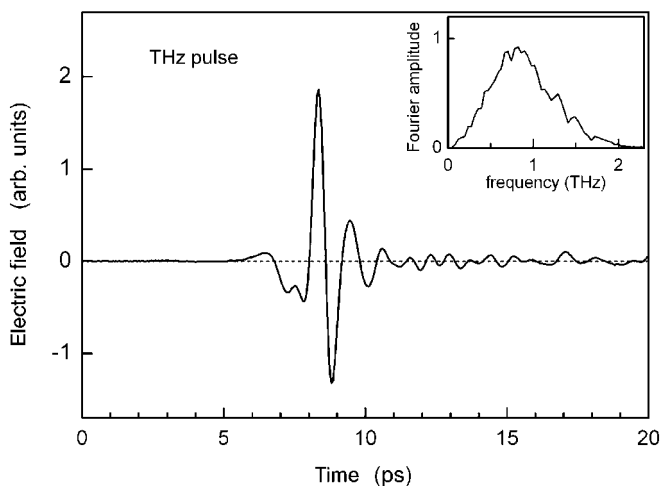


**Figure 7.1** Example of a terahertz (THz) pulse in the time domain. The corresponding Fourier transform is shown in the inset with a center frequency of 1 THz and a bandwidth of about 1 THz.

**Table 7.1** Conversion table for the terahertz frequency region expressed in other units.  $f$ , frequency;  $\nu$ , wavenumber;  $hf$ , photon energy;  $\lambda$ , wavelength. The box encloses the range typically studied in most terahertz pulse experiments.

$f$ (THz)	$\nu$ (cm <sup>-1</sup> )	$hf$ (meV)	$\lambda$ (μm)	EM spectrum
0.01	0.33	0.041	30000	Microwave (cm)
0.1	3.3	0.41	3000	Microwave (mm)
<b>0.2</b>	<b>6.7</b>	<b>0.83</b>	<b>1500</b>	Far-infrared (THz region)
<b>0.5</b>	<b>17</b>	<b>2.1</b>	<b>600</b>	
<b>1.0</b>	<b>33</b>	<b>4.1</b>	<b>300</b>	
<b>1.5</b>	<b>50</b>	<b>6.2</b>	<b>200</b>	
<b>2.0</b>	<b>67</b>	<b>8.3</b>	<b>150</b>	
<b>2.5</b>	<b>83</b>	<b>10.3</b>	<b>120</b>	
<b>3.0</b>	<b>100</b>	<b>12.4</b>	<b>100</b>	
5.0	167	20.7	60	
10	333	41.4	30	
30	1000	124	10	Mid-infrared
100	3333	414	3	
300	10000	1240	1	Near-infrared
600	20000	2480	0.5	Visible

**Table 7.2** Conversion from thermal energies to terahertz frequencies.  $T$ , Temperature;  $k_B$ , Boltzmann's constant;  $f$ , frequency.

$T$ (K)	$k_B T$ (meV)	$f$ (THz)
10	0.86	0.21
48	4.14	1.00
100	8.62	2.08
144	12.4	3.00
295	25.4	6.15

Terahertz time-domain spectroscopy or THz-TDS (see Sections 7.4 and 7.6), takes advantage of the ability to detect coherently the amplitude and phase of THz pulses in the time domain for determining the real and imaginary components of the frequency-dependent complex conductivity of materials without having to resort to Kramers–Kronig analysis used in more traditional Fourier transform infrared (FTIR) spectroscopic techniques [156–158]. THz-TDS, therefore, is essentially a new and improved spectroscopic tool for the far-infrared region of the spectrum. Time-resolved terahertz spectroscopy (TRTS), discussed in Sections 7.7 and 7.8, is a pump–probe technique that takes advantage of the short pulse duration of THz pulses to probe transient conductivity in photoexcited materials with sub-picosecond time resolution [159]. The use of THz pulses in security or imaging applications will not be discussed here, but some very good reviews of THz pulse techniques, experiments and applications can be found in Refs. [156–159].

### 7.3

#### Generating and Detecting Terahertz Pulses

The two most common techniques for generating THz pulses are the current-surge mechanism in a photoconductive switch [156–163] and optical rectification in a non-linear crystal [156–159, 164, 165], as illustrated in Fig. 7.2a and b, respectively. In the photoconductive switch source shown in Fig. 7.2a, the region between two voltage-biased electrodes on a semi-insulating (SI) GaAs substrate, for example, is illuminated with a laser pulse from a femtosecond laser source ( $\lambda < \lambda_G = 870 \text{ nm}$  for the bandgap in GaAs). The laser pulse generates a transient photocurrent with current density  $J = \sigma E$  in the semiconductor wafer between the electrodes and the resulting acceleration of the photogenerated charge carriers produces a THz pulse that is emitted out the other side of the substrate with an electric field in the far-field given by  $E_{\text{THz}} \propto dJ/dt$ . The gap between the electrodes can be as small as  $20 \mu\text{m}$  with a voltage bias of 20 V for photoconductive antennas or 2 mm–2 cm for large-aperture sources with voltage biases up to 20 kV. The smaller gap photoconductive antennas typically use a silicon lens on the back of the wafer to help couple out and collimate the THz pulses and are illuminated using mode-locked femtosecond laser sources producing 800-nm, 100-fs pulses at repetition rates around 80 MHz. Typical average THz beam powers are around 10 nW, but the peak THz pulse power is  $\sim 100 \mu\text{W}$  with  $\sim 0.1 \text{ fJ}$  per THz pulse ( $\sim 50\,000$  THz photons) [161]. The resulting electric field is of the order of  $E_{\text{THz}} \approx 3 \text{ V cm}^{-1}$  at a 1-mm focus, but higher electric fields up to  $85 \text{ V cm}^{-1}$  have recently been achieved [166]. Large-aperture photoconductive sources illuminated by 1-kHz repetition rate Ti:sapphire amplifier systems have achieved THz pulse energies up to  $0.8 \mu\text{J}$  and  $E_{\text{THz}} \approx 350 \text{ kV cm}^{-1}$  at the focus [167, 168].

For the optical rectification source shown in Fig. 7.2b, a femtosecond laser pulse passes through a second-order (non-centrosymmetric) non-linear optical crystal such as ZnTe and produces a rectified polarization transient  $P$  inside the crystal that follows the envelope of the laser pulse. This polarization transient generates a

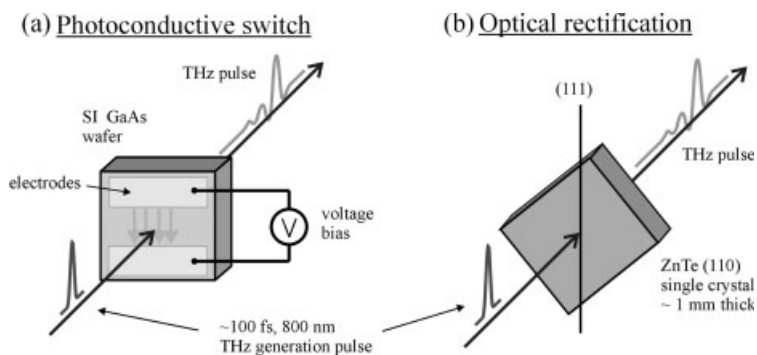


**Figure 7.2** Typical methods used for generating THz pulses. (a) Current surge mechanism from an optically activated photoconductive switch element, such as voltage-biased semi-

insulating (SI) GaAs. (b) Optical rectification in a non-linear optical crystal which lacks inversion symmetry. ZnTe is often used for this type of THz pulse source.

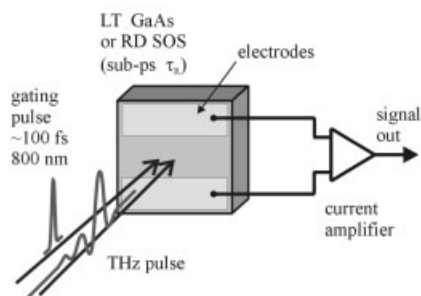
THz pulse that radiates out the other side of the ZnTe wafer with  $E_{\text{THz}} \propto d^2P/dt^2$  in the far field. This is in essence similar to the current surge mechanism discussed above since  $J \propto dP/dt$ . Optical rectification is the zeroth-order term in the non-linear polarization response of a material with no inversion symmetry to the electric field of an intense laser pulse and its magnitude is proportional to the second-order susceptibility  $\chi^{(2)}$  of the material. Optical rectification can also be thought of as difference frequency mixing between the higher and lower frequency components of the incoming femtosecond laser pulse. For example, a 60-fs, 800-nm laser pulse with a bandwidth of 15 nm could potentially produce a THz pulse by optical rectification in a non-linear crystal with a bandwidth of about 7 THz. However, the THz pulse bandwidths that are observed are limited not only by the frequency response of the detection setup but also phase matching conditions for optical rectification at the source, which depend on the interaction length of the laser pulse and THz pulse through the crystal. There may also be absorption of the higher frequency components of the THz pulse due to phonons in the source crystal above 5 THz (i.e. 5.4 THz in ZnTe) [165]. ZnTe happens to have good phase matching for THz pulse generation by optical rectification of 800-nm laser pulses, and crystal thicknesses around 0.5-mm are commonly used. Other crystals such as GaAs, CdTe and InP have also been studied [164] and broader bandwidths can be achieved by sending shorter laser pulses through thinner crystals. In one experiment, THz pulses generated by optical rectification of 10-fs, 780-nm laser pulses in a 20- $\mu\text{m}$  thick GaSe crystal had frequency components beyond 120 THz ( $\lambda \approx 2.5 \mu\text{m}$ ) [169], which is almost in the near-infrared region of the spectrum (see Table 7.1).

Efficient THz pulse generation by optical rectification in organic single crystals of 4-*N*-methylstilbazolium tosylate (DAST) has been extensively studied [170–172] and THz pulse emission from poled polymers has also been observed [173]. MBANP organic crystals were found to be better than ZnTe in generating THz pulses by optical rectification at 800 nm, and on-resonance excitation with 400-nm

pulses also generated THz pulses which provided a means for studying charge-transfer dynamics in these materials [174]. In fact, THz pulses emitted from either photoconductive or optical rectification sources can provide information on dynamics inside the source material itself. Ultrafast carrier dynamics in low-temperature-grown (LT) GaAs has been studied by examining the THz pulse that is emitted from a photoconductive switch made from LT-GaAs [175]. THz pulse emission due to photoexcited intramolecular charge transfer between donor and acceptor sites in polar molecules aligned by an external electric field in solution has also been investigated [176, 177]. More recently, THz generation from photoconductive switches made from PPV [178], MEH-PPV [179] and pentacene [149] films has been observed. Since  $E_{\text{THz}} \propto dJ/dt$ , then the fact that THz pulses are even observed from these voltage-biased samples shows that charge carrier generation must occur over sub-picosecond time-scales, as observed for SI-GaAs photoconductive sources. In biased MEH-PPV films, the THz pulse emission revealed that the time for charge carrier generation was  $<200$  fs, but that it occurred with an efficiency of only 1% through hot exciton dissociation [179].

The electric field of the THz pulse as a function of time can be measured using ultrafast gated-detection techniques [156, 157]. In photoconductive sampling [160–163], as shown in Fig. 7.3a, the THz pulse is focused to a region between two electrodes on a semiconductor substrate with its polarization oriented across the two electrodes. The semiconductor material is made to have a very short, sub-picosecond carrier recombination or trapping time, which is possible using LT-GaAs or radiation-damaged silicon on sapphire (RD-SOS). If the gap between the electrodes is illuminated with a laser pulse from the same femtosecond laser source that generated the THz pulse in the first place, then the semiconductor material will be made momentarily conducting, or “gated”, for a time  $<1$  ps as determined by the carrier trapping time in the material. If the THz pulse arrives at the same time as the gating pulse, then the electric field of the THz pulse will drive current through the circuit in a direction that depends on the polarity of the THz pulse at that time at the gated detector. Since this is a repetitive sampling system, an average DC current will be driven through the circuit which is representative of the amplitude and polarity of the THz pulse electric field at that time delay between the THz pulse and the gating pulse. Changing the delay of the gating pulse with respect to the arrival of the THz pulse at the detector will allow the temporal profile of the THz pulse to be mapped out. The recovery time of the gated semiconductor material back to the insulating state (i.e. the time it takes to “close the gate” again) will limit the ultimate bandwidth of the system, but bandwidths up to 5 THz can be achieved using photoconductive sampling techniques [163]. Despite the low average power in the THz beam generated by some photoconductive switch sources, as discussed above, the gated detection technique results in an excellent signal-to-noise ratio better than  $10^4:1$  in the measured electric field of the THz waveform [156, 157]. This is because the detector is actually only “on” for a very short period of time and, when it is on, it is always sampling the same part of the THz waveform.

## (a) Photoconductive sampling



## (b) Free-space electro-optic sampling

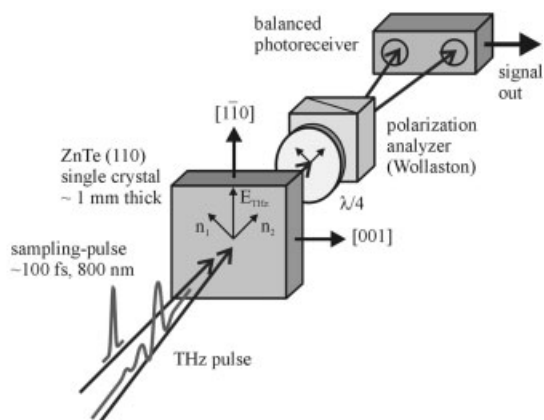


**Figure 7.3** Two techniques used for detecting THz pulses are (a) photoconductive sampling and (b) free-space electro-optic sampling. In both techniques, a time-delayed “gating” pulse is used to sample the electric field of the THz pulse.

A second commonly used gated-detection technique known as free-space electro-optic sampling (FSEOS) or simply electro-optic EO detection, is described in Fig. 7.3b [156, 157, 165, 169, 180–186]. In this detection technique, the electric field of the THz pulse induces a birefringence in the ZnTe detector crystal by the Pockels effect. A sampling laser pulse travels collinearly with the THz pulse and samples the optical birefringence induced by the THz pulse in the ZnTe crystal. The polarization state of the sampling pulse is analyzed by a balanced photodetector system that provides a difference signal proportional to the THz pulse electric field [181, 183, 184]. The EO detection technique is non-resonant and therefore very fast, and it is the only way to coherently detect THz pulses with frequency components higher than 5 THz [169, 182]. EO sampling is also much easier to implement in a THz pulse setup than photoconductive sampling techniques that require lithography and a silicon lens for improved coupling. ZnTe is the most popular choice as an EO detection element for 800-nm laser sources [157, 186], but EO detection in other materials such as GaSe [169], CdTe, GaP, InP, GaAs [186] and DAST [187] has also been explored and comparisons with photoconductive sampling techniques have been made [188]. The detection bandwidth is reduced as the thickness of the EO crystal is increased owing to phase matching issues between the THz pulse and the sampling pulse, but a ZnTe detector 0.5 mm thick can give detection bandwidths out to 4 THz. Systems that use a 1-kHz amplified Ti:sapphire laser source typically use a 0.5-mm thick ZnTe crystal for the THz pulse source (optical rectification) and a 0.5–1-mm thick ZnTe crystal as an EO detector element.

There has been an enormous amount of effort in the terahertz community improving and finding new THz pulse sources [157, 189–191], as well developing

new techniques for manipulating or detecting THz pulses [157, 192, 193]. Some recent developments in terahertz pulse techniques include THz pulse propagation along long metal-wire waveguides up to 1 m in length with low attenuation and very low group velocity dispersion [194, 195], THz transmission through subwavelength apertures [196], and terahertz near-field imaging of surfaces with nanometer-scale resolution (150 nm) using sharp metal tips [197–199].

## 7.4

### Terahertz Time-Domain Spectroscopy (THz-TDS)

The broad bandwidth of THz pulses allows them to be used for far-infrared spectroscopy of materials typically in the range 0.2–3 THz with the best sensitivity near 1 THz, but 0.1–5 THz is also possible in standard systems and up to 120 THz in more advanced systems [169]. Above 5 THz, however, more traditional FTIR spectroscopic techniques tend to have a better signal-to-noise ratio but do not offer the advantages of coherent detection achieved in THz-TDS [156, 157, 200].

A schematic of a THz-TDS setup is shown in Fig. 7.4. A laser pulse from a femtosecond laser source is divided into two beams by a beamsplitter. One beam is used to generate the THz pulse at the THz source and the other beam is used to sample (or gate) the electric field of the THz pulse at the THz detector. The THz pulse travels in free space between the source and detector and is collimated and focused onto a sample by front-surface (gold-coated) off-axis parabolic mirrors. The sampling laser pulse has an appropriate optical delay imposed on it so that it arrives at the detector at the same time as the THz pulse, and since the laser pulse used for gated detection is derived from the same laser pulse used to generate the THz pulse in the first place, then there is no timing jitter associated with the THz detection process. An optical delay stage on the sampling pulse beam is used to map out the time-dependent electric field of the THz pulse arriving at the detector by repeatedly sampling the same point on the THz waveform until the delay stage is moved to a new position and a new point on the THz waveform. Lock-in detection is typically used by chopping the THz source beam. In general, the setup is purged with dry nitrogen in order to avoid absorption of the THz pulse due to water vapor in the air, but even without purging, pathlengths longer than 1 m are still easily crossed by the THz pulse in a normal laboratory environment. Since the wavelength at 1 THz is 300  $\mu\text{m}$ , then the spot size at the focus at the sample is  $\sim 1$  mm in diameter (FWHM) depending on the  $F$ -number of the optics and quality of alignment of the off-axis parabolic mirrors. Lower frequency components (longer wavelengths) of the THz pulse will have a larger spot size at the focus, but most of the THz pulse can pass through a 2-mm aperture. The THz pulse spot size in THz-TDS requires that the face of the sample be larger than  $3 \times 3$  mm, but smaller samples can be accommodated by placing apertures in front of the sample at the focus with some loss of the lower frequency components due to frequency-dependent spatial filtering of the THz pulse.

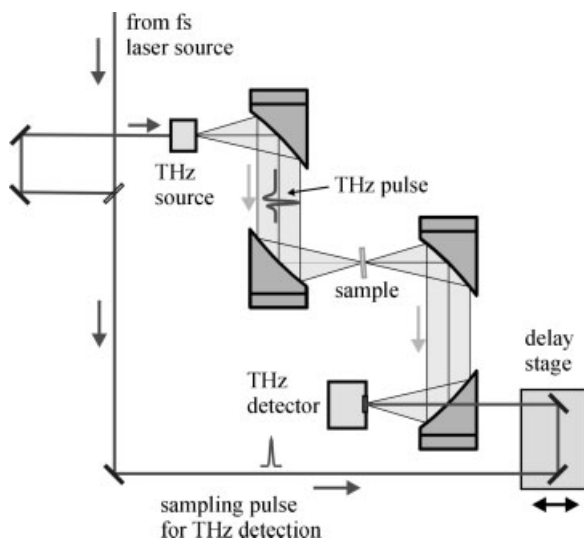


**Figure 7.4** Schematic of THz pulse setup used for THz time-domain spectroscopy (THz-TDS).

To perform THz-TDS on a sample, the time-domain waveforms of the THz pulse with the sample in place at the focus [sample waveform,  $E_s(t)$ ] and the sample removed [reference pulse,  $E_0(t)$ ] are measured. This is illustrated in Fig. 7.5a in a THz-TDS experiment by Walther et al. [201] on 9-*cis*-retinal embedded in polyethylene disks, where the sample (dashed line) and reference (solid line) time-domain THz waveforms are shown in the upper part of Fig. 7.5b. Note that the sample THz waveform is delayed in time by about 1.5 ps with respect to the reference THz waveform and slightly reduced in amplitude. The extra delay time (or phase delay) experienced by the THz pulse through the sample provides an estimate of the index of refraction of the sample and the drop in amplitude is due to the absorption coefficient of the sample in addition to reflection losses. The Fourier amplitude spectra of the corresponding time-domain waveforms are shown in the lower part of Fig. 7.5b. The Fourier transforms of the sample and reference waveforms each contain phase and amplitude information for each Fourier component that can be used to calculate, respectively, the refractive index  $n_s$  and absorption coefficient  $a$  of the sample as a function of frequency  $\omega$ . Dividing the sample Fourier transform  $E_s(\omega)$  by the reference Fourier transform  $E_0(\omega)$ , we have

$$\frac{E_s(\omega)}{E_0(\omega)} = \frac{|E_s(\omega)|e^{i\phi_s(\omega)}}{|E_0(\omega)|e^{i\phi_0(\omega)}} = (|t|e^{i\phi})e^{-\frac{a}{2}d}e^{i\frac{2\pi}{c}d(n_s-1)} \quad (7.1)$$

where  $\omega = 2\pi f$ ,  $\phi_s$  and  $\phi_0$  are the phases of the sample and reference Fourier components, respectively,  $d$  is the sample thickness,  $c$  is the speed of light and the pre-factor  $|t|e^{i\phi}$  takes into account reflection losses from both faces of the sample.

Note that oscillations in the Fourier spectra due to étalon effects can be removed simply by windowing the time-domain waveforms to eliminate multiple THz pulse reflections in the sample (for large  $d$ ). The refractive index and absorption coefficient are then given as

$$n_s = \frac{c}{\omega d} [\phi_s(\omega) - \phi_0(\omega) - \Phi] + 1$$

$$a = -\frac{2}{d} \ln \left[ \frac{|E_s(\omega)|}{|t||E_0(\omega)|} \right] \quad (7.2)$$

Figure 7.5c shows  $n_s$  and  $a$  for the *9-cis*-retinal sample extracted from the THz-TDS data in Fig. 7.5b at 298 and 10 K. Cooling the sample sharpens the features in the spectra, such as the absorption peaks near 43 and 54  $\text{cm}^{-1}$ , which were attributed to collective torsional vibrations of the molecules. Comparing the spectra obtained for two other retinal isomers revealed some variation in the torsional mode frequency that depended on the conformation of the molecule [201].

Another study looked at torsional modes in polycrystalline oligo(*p*-phenylenes) and found that THz-TDS is a sensitive probe of phase transitions at lower temperatures in these materials [202]. THz-TDS has become a very useful technique for detecting low-energy IR-active vibrational modes in large molecules that can shift depending on the conformation of the molecule as well as the molecular environment. Looking for “fingerprints” of specific molecules within the THz region of

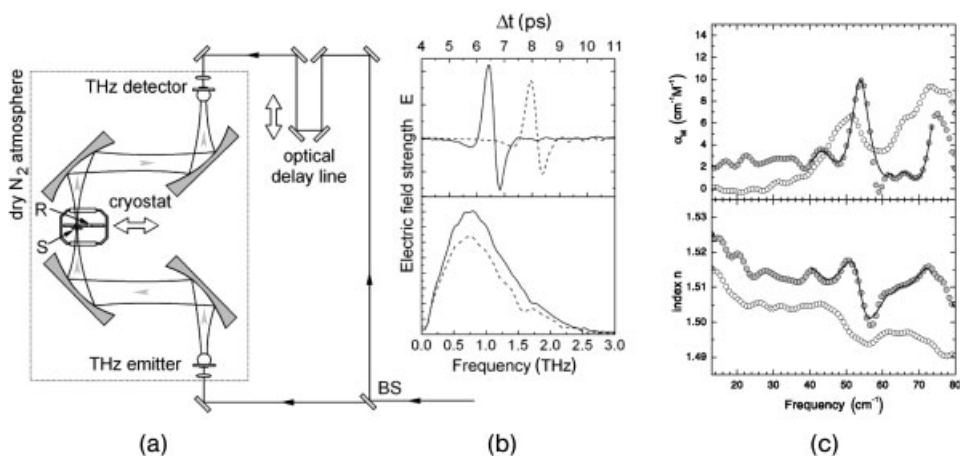


**Figure 7.5** (a) Example of a THz-TDS setup with an optical cryostat that can be moved from side-to-side for obtaining sample (S) and reference (R) THz pulse waveforms. (b) Time-domain THz pulse signals and corresponding frequency-domain spectra for the reference THz pulse (solid line) and the THz pulse transmitted through a sample contain-

ing *9-cis*-retinal (dashed line). (c) The molar absorptivity,  $a_m$ , and the refractive index,  $n$ , extracted from the THz data for the sample at 298 K (open circles) and 10 K (filled circles). The frequency scale in (c) is from 0.4 to 2.4 THz. Reproduced from Ref. [201], with permission. See Ref. [201] for more details on the solid line fit to the data in (c).

the spectrum, therefore, has become an extremely active area of research. Besides studies on conjugated molecules [201, 202], THz-TDS has been used to examine vibrational modes in polymer films [203, 204] and organic crystals [205, 206], biomolecules such as DNA and RNA [207–214], pharmaceutical materials [215] and even explosives [216, 217].

Once  $n_s$  and  $a$  are known in a material, then the optical properties of that material can be expressed using other optical parameters such as the complex dielectric constant  $\hat{\epsilon}(\omega)$  or complex conductivity  $\hat{\sigma}(\omega)$  through the following relations [218–220]:

$$\begin{aligned}\hat{n} &= n_s + ik \\ a &= \frac{2\kappa\omega}{c} \\ \hat{\epsilon} &= \epsilon_1 + i\epsilon_2 = \hat{n}^2 = 1 + \frac{i\hat{\sigma}}{\epsilon_0\omega} \\ \hat{\sigma} &= \sigma_1 + i\sigma_2 \\ \epsilon_1 &= n_s^2 - \kappa^2 \\ \epsilon_2 &= 2n_s\kappa \\ \sigma_1 &= \epsilon_2\epsilon_0\omega \\ \sigma_2 &= -(\epsilon_1 - 1)\epsilon_0\omega\end{aligned}\tag{7.3}$$

where  $\epsilon_0$  is the permittivity of free space and  $\kappa$  is the extinction coefficient. Note that the complex conductivity  $\hat{\sigma}$  can also be used to describe vibrational modes in materials in addition to the conductivity of free charges, which is described further in Section 7.5, but the choice of whether to express optical properties of a material in terms of  $\hat{n}$ ,  $\hat{\epsilon}$  or  $\hat{\sigma}$  usually depends on the particular field of study or how the model being used for comparison has been written historically. In other words, THz-TDS results are not always expressed in terms of  $n_s(\omega)$  and  $a(\omega)$ , and often  $\sigma_1(\omega)$  and  $\sigma_2(\omega)$  are used.

Over the past 20 years, THz-TDS has been used to investigate the far-infrared optical properties of a wide variety of material systems. There has been much THz-TDS research investigating dielectric relaxation in liquids, which can be interpreted in terms of the Debye model, since the characteristic rates at which molecules interact with each other in liquids are in the terahertz range [221–227]. There have also been THz-TDS studies of nanometer-sized water pools [228].

As discussed in the next section, THz-TDS is ideal for probing the contribution of mobile charge carriers to the complex conductivity of a material. Numerous THz-TDS studies have examined the nature of charge carrier transport in doped Si [161, 162, 229–231] and GaAs [162, 232, 233], mapped carrier concentrations and mobilities in a GaAs wafer [234], measured the superconducting energy gap

in superconductors such as Nb [235] and MgB<sub>2</sub> [236] thin films, investigated the temperature dependence of the quasiparticle scattering rate below the superconducting transition temperature ( $T_c$ ) in high- $T_c$  superconductors [237–239], observed Josephson plasma resonances along the  $c$ -axis in thallium-based high- $T_c$  superconductors [240–242], tested Fermi liquid theory in ferromagnetic metals [243] and explored hopping conduction in nanoporous doped crystals [244]. More recently, THz-TDS has been used to probe the nature of carrier transport in conducting organic materials such as polypyrrole [245], poly-3-methylthiophene [246, 247], doped MEH-PPV [248] and single-walled carbon nanotubes [249, 250], which is discussed further in Section 7.6. The next section describes some of the models that are used to describe conductivity in materials.

## 7.5 Conductivity Models

As discussed above, THz-TDS measurements can be used to determine the complex conductivity of a material in the far-infrared region of the spectrum. This section discusses some of the theoretical models for the complex conductivity of materials that can be used to interpret the data for  $\sigma_1$  and  $\sigma_2$  obtained from THz-TDS experiments. There are many such models, which apply to both mobile *and* bound charges in materials. Analysis of the frequency dependence of  $\sigma_1$  and  $\sigma_2$  can be used to distinguish between the various models and help identify the nature of the observed conductivity. Many of the characteristic features of these models for typical materials are in the terahertz region of the spectrum, which makes THz-TDS ideal for probing the nature of conductivity in materials.

The most commonly used model for describing the conductivity of mobile charge carriers in materials is the Drude model [219, 220, 251, 252]. In the steady-state (DC) or at low frequencies, the Drude model assumes that charge carriers such as electrons or holes are free to move in an electric field with drift velocity  $v_D = \mu E$ , where  $\mu$  is the carrier mobility and  $E$  is the electric field. The carrier mobility is given by

$$\mu = \frac{e\tau}{m} \quad (7.4)$$

where  $e$  is the electric charge,  $m$  is the mass of the carrier and  $\tau$  is the Drude relaxation time associated with scattering of the charge carriers. Since the current density is  $J = \sigma_{DC}E = nev_D$ , where  $n$  is the carrier concentration (carrier density) and  $\sigma_{DC}$  is the steady-state conductivity of the material, then

$$\sigma_{DC} = ne\mu = \frac{ne^2\tau}{m} = \varepsilon_0\omega_p^2\tau \quad (7.5)$$

where  $\omega_p$  is the plasma frequency for the charge carrier density in the material ( $\omega_p^2 = ne^2/\epsilon_0 m$ ). In the Drude model,  $\tau$  is assumed to be a constant value independent of the carrier energy at a given temperature. This is equivalent to saying that  $\tau$  is independent of the frequency  $\omega = 2\pi f$  of the applied electric field. If the external electric field is removed from a current-carrying conductor, then the current decays exponentially with a time constant given by the Drude relaxation time. Scattering of charge carriers, as determined by the Drude relaxation time, introduces a damping term to the equations of motion for the charge carriers. The frequency dependence of the conductivity in the Drude model is therefore

$$\begin{aligned}\hat{\sigma} &= \sigma_1 + i\sigma_2 = \frac{\sigma_{\text{DC}}}{1 - i\omega\tau} \\ \sigma_1 &= \frac{\sigma_{\text{DC}}}{1 + (\omega\tau)^2} \\ \sigma_2 &= \frac{\sigma_{\text{DC}}\omega\tau}{1 + (\omega\tau)^2}\end{aligned}\quad (7.6)$$

Note that at  $\omega = 0$  (DC), we have  $\sigma_1 = \sigma_{\text{DC}}$  and  $\sigma_2 = 0$ , such that the complex conductivity is purely real. For short relaxation times such that  $\omega\tau \ll 1$ , then  $\sigma_2 \approx 0$  and  $\sigma_1 \approx \sigma_{\text{DC}}$ .

The Drude conductivity in the terahertz frequency range and normalized to  $\sigma_{\text{DC}}$  is shown in Fig. 7.6 for several relaxation times from 500 down to 10 fs. Note that from Eq. (7.6),  $\sigma_2/\sigma_1 = \omega\tau$ , so the “crossover” frequency where  $\sigma_1 = \sigma_2$  is given by  $f_c = 1/2\pi\tau$ . As shown in Table 7.3, typical Drude relaxation times in metals [251] such as copper and gold are about 30 fs at room temperature and as high as 210 fs at 77 K, which puts the crossover frequency  $f_c$  at 5.3 and 0.76 THz, respectively. Electrons in the conduction band of n-type Si [229] and GaAs [232] have Drude relaxation times higher than 160 fs, which gives  $f_c < 1$  THz. Charge carriers in graphite [253] and photoexcited sapphire ( $\text{Al}_2\text{O}_3$ ) [254] also have  $f_c$  below 1.7 THz. Since the curvatures of  $\sigma_1$  and  $\sigma_2$  near  $f_c$  in the Drude model are very distinctive and depend solely on the value of  $\tau$ , and since  $f_c$  typically lies within the frequency range covered by terahertz pulses from 0.2 to 3 THz (see Section 7.2), then THz-TDS is ideal for probing conductivity in many metals and semiconductors. Even if the carriers have relaxation times as small as 10 fs, the frequency dependence of  $\sigma_1$  and  $\sigma_2$  (Fig. 7.6f) has enough variation below 3 THz that Drude parameters can be extracted from a comparison of the Drude model with the THz-TDS data. This would be the case for materials such as  $\text{Ba}_{0.8}\text{K}_{0.4}\text{BiO}_3$ , a superconducting compound with  $T_c = 31$  K [255], and conducting polypyrrole [245]. However, there are many other materials such as conducting polymeric sulfur nitride  $[(\text{SN})_x]$  [48] and even elemental lead (Pb) [251] that have Drude relaxation times  $< 2$  fs at room temperature. In this case, where  $\omega\tau \ll 1$  at 1 THz, we have  $\sigma_2 \approx 0$  and  $\sigma_1$  roughly independent of frequency and equal to  $\sigma_{\text{DC}}$  over the frequency range  $< 3$  THz, which makes it difficult to fit a Drude model to the THz-TDS data in order to extract a relaxation time from the curvature of the plots. How the transmission of a THz pulse depends on the complex conductivity of a material will be discussed later in Section 7.7.

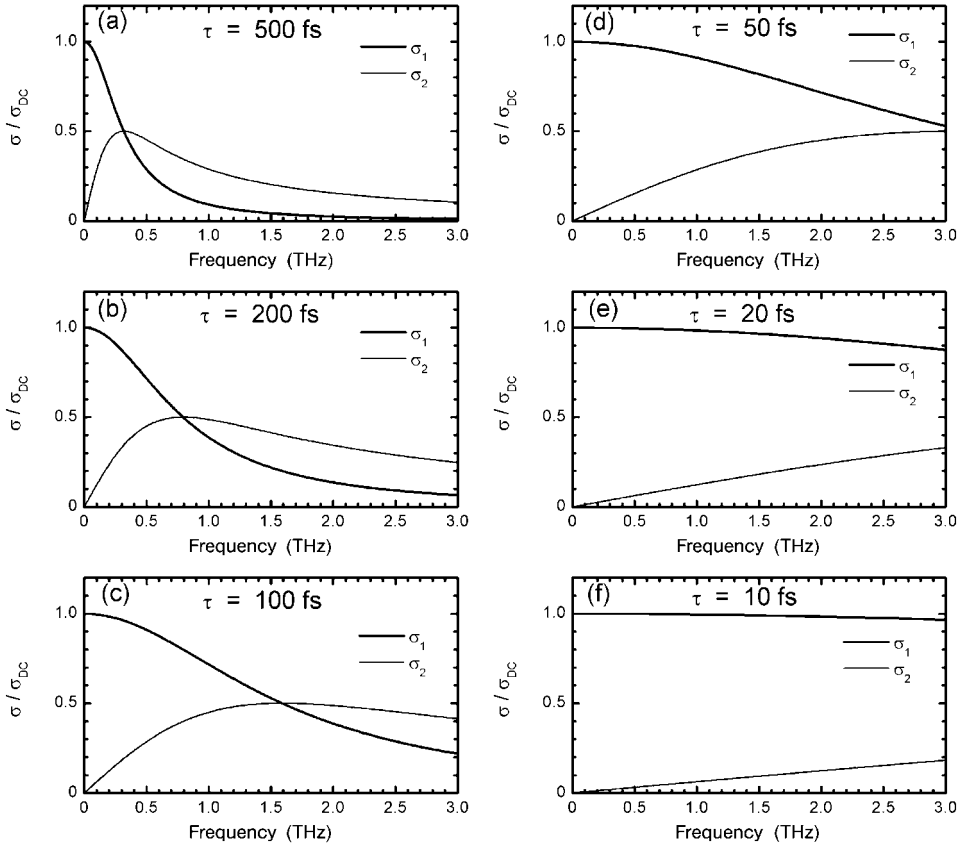


**Figure 7.6** Drude conductivity in the THz frequency region for Drude relaxation times  $\tau$  of (a) 500, (b) 200, (c) 100, (d) 50, (e) 20 and (f) 10 fs. The real ( $\sigma_1$ ) and imaginary ( $\sigma_2$ ) compo-

nents of the Drude conductivity are normalized to the DC ( $f = 0$ ) value of  $\sigma_{DC} = ne^2\tau/m$ . The crossover frequency where  $\sigma_1 = \sigma_2$  is given by  $f_c = 1/2\pi\tau$ .

It was mentioned in Section 7.1 that ultrapure naphthalene single crystals have mobilities close to  $1 \text{ cm}^2 \text{ V}^{-1} \text{ s}^{-1}$  at room temperature and  $>100 \text{ cm}^2 \text{ V}^{-1} \text{ s}^{-1}$  below 30 K [24] and that polycrystalline pentacene films have mobilities around  $1 \text{ cm}^2 \text{ V}^{-1} \text{ s}^{-1}$ . As shown in Table 7.3 using Eq. (7.4), a mobility of  $1 \text{ cm}^2 \text{ V}^{-1} \text{ s}^{-1}$  for carriers with an effective mass  $m$  equal to the free electron mass  $m_e$  would give a Drude relaxation time of 0.57 fs, which is very short but not too far removed from the Drude relaxation times for Pb and (SN)<sub>x</sub> at room temperature. For a mobility of  $100 \text{ cm}^2 \text{ V}^{-1} \text{ s}^{-1}$ , however, the Drude relaxation time would increase to 57 fs, placing  $f_c$  at 2.8 THz and within the THz pulse bandwidth. It should be pointed out that the same 57 fs relaxation time can be obtained using a carrier mobility of  $10 \text{ cm}^2 \text{ V}^{-1} \text{ s}^{-1}$  and a carrier effective mass of  $m = 10m_e$ . Therefore, in general, fitting the Drude model to the measured conductivity requires three parameters: the carrier density  $n$ , the effective mass  $m$  and the relaxation time  $\tau$ . Sometimes  $m$  is

**Table 7.3** Examples of Drude relaxation times  $\tau$  in selected materials. The last three entries are calculated Drude relaxation times for carriers with mobility  $\mu$  and effective mass  $m$ , where  $m_e$  is the free electron mass. The crossover frequency where  $\sigma_1 = \sigma_2$  is given by  $f_c = 1/2\pi\tau$ .

Material (or carrier mobility)	Conditions	Drude relaxation time, $\tau$ (fs)	$f_c = 1/2\pi\tau$ ( $\sigma_1 = \sigma_2$ ) (THz)	Reference
Au	273 K	30	5.3	251
Au	77 K	120	1.3	251
Cu	273 K	27	5.9	251
Cu	77 K	210	0.76	251
Pb	273 K	1.4	114	251
Pb	77 K	5.7	28	251
n-Si	295 K; $4 \times 10^{14} \text{ cm}^{-3}$ ; $\sim 2000 \text{ cm}^2 \text{ V}^{-1} \text{ s}^{-1}$	295	0.54	229
n-GaAs	295 K; $7.8 \times 10^{15} \text{ cm}^{-3}$ ; $\sim 4300 \text{ cm}^2 \text{ V}^{-1} \text{ s}^{-1}$	165	0.96	232
Graphite	295 K	200	0.8	253
Al <sub>2</sub> O <sub>3</sub> (single-crystal sapphire)	295 K ( $\mu_e \approx 600 \text{ cm}^2 \text{ V}^{-1} \text{ s}^{-1}$ )	95	1.7	254
Ba <sub>0.8</sub> K <sub>0.4</sub> BiO <sub>3</sub> ( $T_C = 31$ K)	295 K	15	11	255
Polypyrrole (conducting)	295 K ( $\sigma = 215 \Omega^{-1} \text{ cm}^{-1}$ )	12.6	13	245
(SN) <sub>x</sub> (single crystal)	295 K; along backbone	$\sim 1$ – $2.6$	$\sim 160$ – $60$	48
$\tau = m\mu/e$	$\mu = 1 \text{ cm}^2 \text{ V}^{-1} \text{ s}^{-1}$ ; $m = m_e$	0.57	280 (1.1 $\mu\text{m}$ )	
$\tau = m\mu/e$	$\mu = 100 \text{ cm}^2 \text{ V}^{-1} \text{ s}^{-1}$ ; $m = m_e$	57	2.8	
$\tau = m\mu/e$	$\mu = 10 \text{ cm}^2 \text{ V}^{-1} \text{ s}^{-1}$ ; $m = 10m_e$	57	2.8	

known, as is the case for many semiconductors such as GaAs and so only two parameters are needed for the Drude fit ( $n$  and  $\tau$ ). This can be straightforward if  $\sigma_1$  and  $\sigma_2$  vary sufficiently over the frequency range of the THz pulse such that  $\tau$  can be determined from the curvature of the data or by using the expression  $\tau = \sigma_2/\sigma_1\omega$ . If this is not true, as is the case for  $\omega\tau \ll 1$  such that  $\sigma_1$  is roughly constant ( $= \sigma_{\text{DC}}$ ) and  $\sigma_2 \approx 0$ , then  $n$ ,  $m$  and  $\tau$  cannot be determined independently by fits of the Drude model to the THz-TDS data.

Conductivity in a material may also arise from the polarization of bound charges by an external electric field with frequency  $\omega$  according to the Lorentz oscillator model [218–220, 252]. The conductivity for a Lorentz oscillator is given by

$$\begin{aligned}\sigma_1 &= \frac{\varepsilon_0 \omega_{\text{pL}}^2 \omega^2 (1/\tau_{\text{L}})}{(\omega_{\text{L}}^2 - \omega^2)^2 + (\omega/\tau_{\text{L}})^2} \\ \sigma_2 &= -\frac{\varepsilon_0 \omega_{\text{pL}}^2 \omega (\omega_{\text{L}}^2 - \omega^2)}{(\omega_{\text{L}}^2 - \omega^2)^2 + (\omega/\tau_{\text{L}})^2}\end{aligned}\quad (7.7)$$

where  $\omega_{\text{L}}$  is the center frequency of the oscillator,  $\tau_{\text{L}}$  is the lifetime of the oscillator and  $\omega_{\text{pL}}$  is indicative of the strength of the oscillator. [Note that Eq. (7.6) for the Drude conductivity is obtained from Eq. (7.7) for the Lorentz model by setting  $\omega_{\text{L}} = 0$ ,  $\tau_{\text{L}} = \tau$  and  $\omega_{\text{pL}} = \omega_{\text{p}}$ . In other words, the Drude model is the same as a Lorentz model with the center resonance frequency moved to  $\omega_{\text{L}} = 0$ .] Whereas  $\sigma_2$  is always positive for free carriers in the Drude model,  $\sigma_2$  for bound charges in the Lorentz oscillator model is *negative* for  $\omega < \omega_{\text{L}}$ . This is illustrated in Fig. 7.7 for Lorentz oscillators with center frequencies  $f_{\text{L}}$  at 2 THz (8.3 meV) and 15 THz (62 meV) and with lifetimes of 0.5 ps (1.3 meV). Lorentz oscillators are typically used to model vibrational modes in materials, as discussed in Section 7.4 for THz-TDS studies on biomolecules. Note that if the center frequency of the Lorentz oscillator is at frequencies much higher than those accessible by the bandwidth of the THz pulse, then the THz pulse will see a complex conductivity that is almost purely imaginary with  $\sigma_1 \approx 0$  and a negative  $\sigma_2$  that scales linearly with frequency, as shown in Fig. 7.7d. That is, in the limit  $\omega \ll \omega_{\text{L}}$  and  $\omega \ll 1/\tau_{\text{L}}$ , we have

$$\sigma_2 \approx -\frac{\varepsilon_0 \omega_{\text{pL}}^2}{\omega_{\text{L}}^2} \omega \quad (7.8)$$

and so the low-frequency dielectric constant associated with the Lorentz oscillator using Eq. (7.3) is  $\varepsilon_1 \approx 1 + (\omega_{\text{pL}}/\omega_{\text{L}})^2$ , which is larger than 1 and frequency independent. In this case, the dielectric constant can also be defined as

$$\hat{\varepsilon} = \varepsilon_1 + i\varepsilon_2 = \varepsilon_{\infty} + \frac{i\hat{\sigma}}{\varepsilon_0 \omega} \quad (7.9)$$

where  $\varepsilon_{\infty}$  is the background dielectric constant that contains contributions to  $\varepsilon_1$  from Lorentz oscillators at higher frequency and  $\hat{\sigma}$  is due to any additional conductivity introduced into the material, for example, by doping or photoexcitation. Lorentz oscillators that are not at higher frequencies (i.e. they do not satisfy  $\omega \ll \omega_{\text{L}}$  and  $\omega \ll 1/\tau_{\text{L}}$ , where  $\omega$  spans the frequency range of the THz pulse) or oscillators that are introduced into the material (which might be due to excitons), must still be included in the expression for  $\hat{\sigma}$  in Eq. (7.9). The total conductivity of the material can then be expressed as a summation of the Drude and Lorentz components as  $\sigma_{\text{Total}} = \sigma_{\text{Drude}} + \sigma_{\text{Lorentz}}$ , which is referred to as the “Drude–Lorentz” model.

The Lorentz oscillator model can also be used to describe the dielectric polarization of excitons at frequencies less than that associated with the binding energy of the exciton. The Drude model for mobile charge carriers and the Lorentz model for bound charge carriers are very distinct from each other, which can be used to

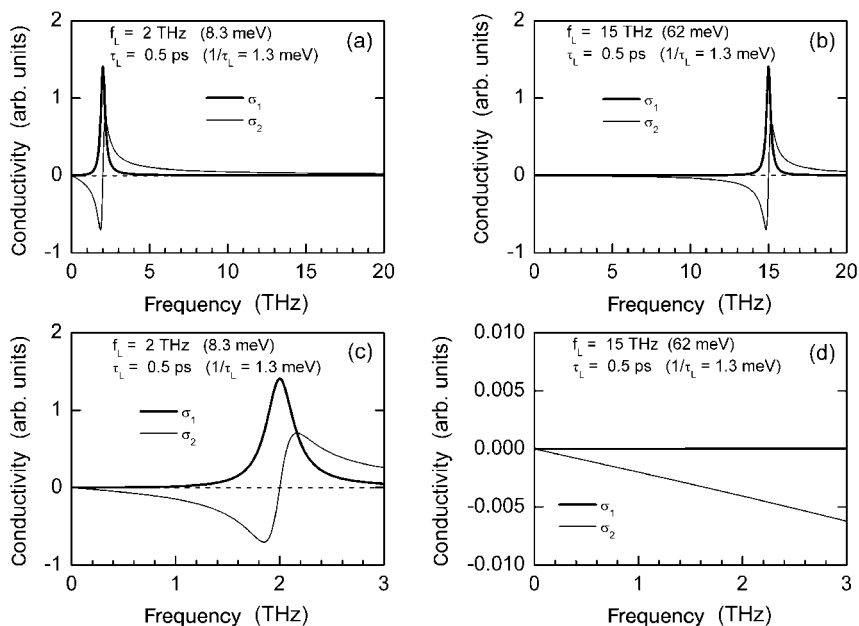


**Figure 7.7** Conductivity of Lorentz oscillators with center frequencies  $f_L$  at (a) 2 THz and (b) 15 THz. Both oscillators have the same damping term of  $1/\tau_L = 1.3$  meV, where

$\tau_L = 0.5$  ps is the lifetime of the oscillator. Expanded views of the low frequency regions below 3 THz are shown in (c) and (d) for the 2- and 15-THz oscillators, respectively.

identify the nature of primary photoexcitations in organic semiconductors, as discussed in Section 7.1. The exciton binding energy in GaAs is around 5 meV ( $f_L = 1.2$  THz), which is well within the bandwidth of THz pulses and so contributions to the conductivity due to the presence of excitons in GaAs can easily be identified using THz-TDS. However, a Lorentz oscillator describes resonance in a system with two discrete levels, which may be the case for an internal transition of the exciton from a 1s to 2p state, but cannot describe dissociation of the exciton for photon energies greater than the binding energy. In other words, the THz photons with energies greater than the binding energy excite the bound exciton states to a continuum of states above the energy gap of the material, which means that  $\sigma_1$  will continue to be significant for  $\omega > \omega_L$ . In one terahertz pulse (TRTS) experiment looking at photoexcited carriers in GaAs quantum wells at low temperatures, the time over which excitons formed from the photoexcited electron-hole gas was observed to be on the 100-ps time-scale [256]. This was done by looking at the time evolution of the frequency-dependent conductivity from a Drude-like free-carrier response at early times to a Lorentz-oscillator-like response due to excitons at later times [256]. In organic semiconductors such as pentacene and PPV, the exciton binding energies are in the range 0.06–1 eV, as discussed in Section 7.1. The Lorentz oscillator associated with an exciton with a binding energy of 60 meV has a center frequency of  $f_L = 15$  THz, which is illustrated in Fig. 7.7b

over frequencies up to 20 THz and in Fig. 7.7d in the THz pulse bandwidth range up to 3 THz. If the conductivity data from a THz-TDS experiment were similar to those shown in Fig. 7.7(d), then it would not be possible to extract the binding energy of the exciton using the low-frequency limit of the Lorentz oscillator model given in Eq. (7.8) unless  $\omega_{\text{pl}}$  was known exactly.

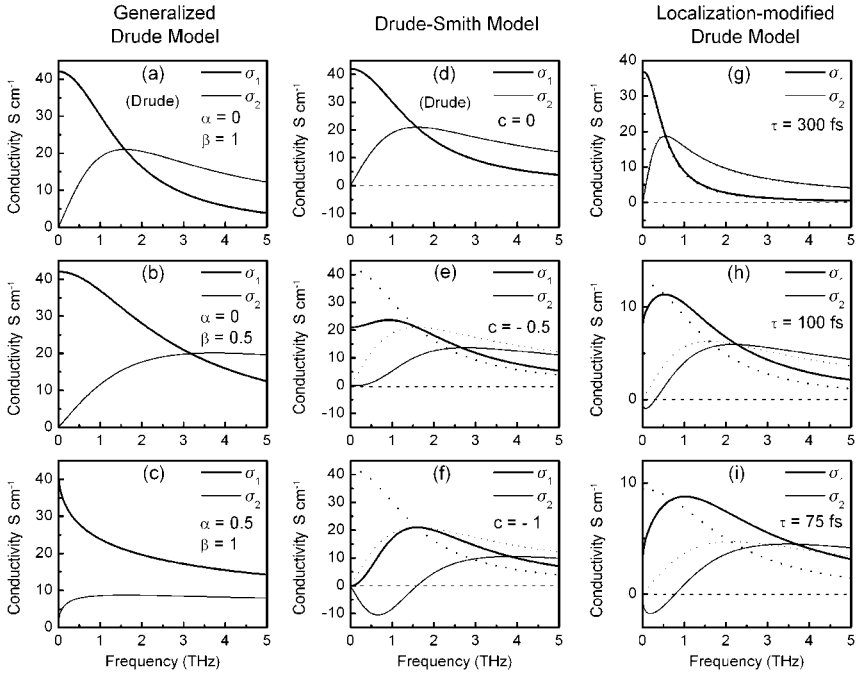
One might argue that a negative  $\sigma_2$  at low frequencies is sufficient for showing that the observed conductivity in a material is due to the presence of polarizable excitons in the system, regardless of the fact that the excitons may have binding energies above 15 THz. However, a negative  $\sigma_2$  does *not* necessarily imply an excitonic contribution in the system. There are other conductivity models that can predict negative values of  $\sigma_2$  at low frequencies, as discussed below, and these models should be considered when fitting THz-TDS data.

Figure 7.8 shows examples of three different models that deviate from the Drude model. The conductivity in the generalized Drude model [229, 257, 258] is given by

$$\hat{\sigma} = \frac{\sigma_{\text{DC}}}{\left[1 - (i\omega\tau)^{1-a}\right]^\beta} \quad (7.10)$$

where  $a$  and  $\beta$  are positive constants. Setting  $a = 0$  and  $\beta = 1$  gives the Drude model in Eq. (7.6), as shown in Fig. 7.8a. Setting  $a = 0$  but allowing  $\beta$  to vary gives the Cole-Davidson model, as shown in Fig. 7.8b with  $\beta = 0.5$ . The Cole-Cole model sets  $\beta = 1$  and varies  $a$ , as shown in Fig. 7.8c for  $a = 0.5$ . In the Drude model, it is assumed that the relaxation time  $\tau$  is independent of frequency. This assumption, in general, is not correct and the generalized Drude model effectively allows a distribution of scattering times for better fits to the conductivity data. Careful THz-TDS measurements on doped silicon at room temperature revealed a complex conductivity that deviated slightly from the Drude model and had a better fit to a Cole-Davidson model, as shown in Fig. 7.9 for n- and p-type wafers, with  $\beta = 0.91$  ( $n = 2.3 \times 10^{16} \text{ cm}^{-3}$ ) and 0.86, respectively [229]. This was the first time a Cole-Davidson model was used to describe the conductivity of charge carriers in a crystalline semiconductor, suggesting that fractal-like conductivity can also be found in seemingly ordered materials. Higher resistivity n-type wafers exhibited slightly lower values for  $\beta$  down to 0.84 for  $n = 4.0 \times 10^{14} \text{ cm}^{-3}$ . Highly doped wafers ( $n > 10^{17} \text{ cm}^{-3}$ ) were more Drude-like with the best fit being close to  $\beta = 1$ , which was opposite to what was seen in photoexcited GaAs wafers where  $\beta$  was typically larger than 0.8 but converged to 1 at low carrier concentrations [257]. A Cole-Cole model with  $a \approx 0.5$  was used to characterize the conductivity of photoexcited carriers in low-temperature grown GaAs (LT-GaAs) [258]. Like the Drude model, the generalized Drude model cannot produce a negative  $\sigma_2$ .

Another modification of the Drude model has been developed recently by Smith [259, 260] and is referred to as the Drude-Smith model. The conductivity in the Drude-Smith model is given by



**Figure 7.8** Frequency dependence of the conductivity according to various models that deviate from the Drude model (see text for details). For both the generalized Drude model (a–c) and the Drude–Smith model (d–f),  $\tau = 100$  fs. The generalized Drude model reduces to the Drude model for  $a = 0$  and  $\beta = 1$ , as shown in (a). The Drude–Smith

model reduces to the Drude model for  $c = 0$ , as shown in (d). The dotted lines in (e) and (f) are the same Drude response from (d) and are plotted for comparison. The dotted lines in (g–i) represent Drude responses for the scattering times indicated and are plotted for comparison to the localization-modified Drude model.

$$\hat{\sigma} = \frac{\sigma_{\text{DC}}}{1 - i\omega\tau} \left[ 1 + \sum_n \frac{c_n}{(1 - i\omega\tau)^n} \right] \quad (7.11)$$

which is the Drude model multiplied by a correction term (in square brackets) that takes into account possible backscattering of charge carriers. The coefficients  $c_n$  represent how much of the carriers original velocity remains after  $n$  collisions, but taking only the first term ( $n = 1$ ) gives

$$\begin{aligned} \hat{\sigma} &= \frac{\sigma_{\text{DC}}}{1 - i\omega\tau} \left[ 1 + \frac{c}{1 - i\omega\tau} \right] \\ \sigma_1 &= \frac{\sigma_{\text{DC}}}{[1 + (\omega\tau)^2]^2} [1 + (\omega\tau)^2 + c(1 - (\omega\tau)^2)] \\ \sigma_2 &= \frac{\sigma_{\text{DC}} \omega\tau}{[1 + (\omega\tau)^2]^2} [1 + (\omega\tau)^2 + 2c] \end{aligned} \quad (7.12)$$

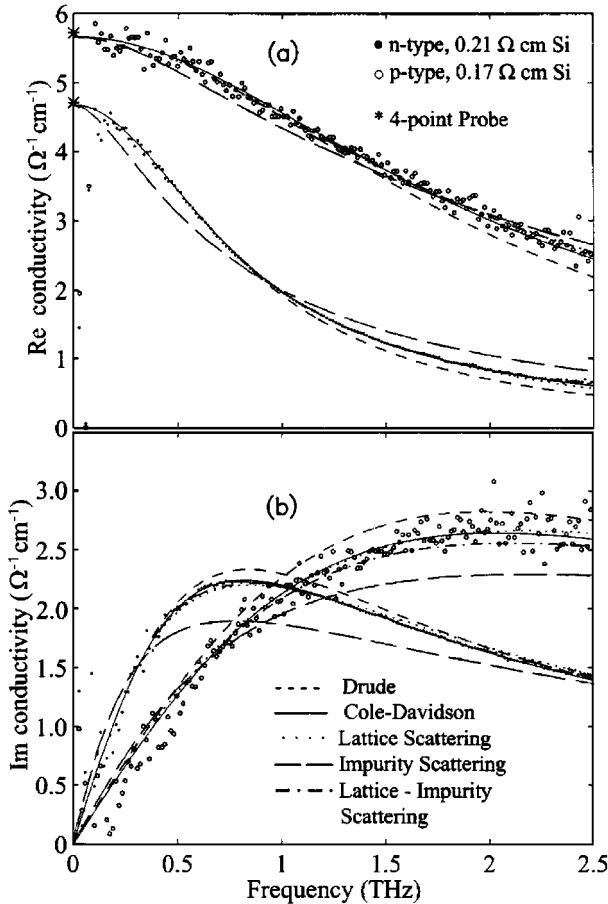


**Figure 7.9** THz-TDS measurements of the complex conductivity of n-type (solid circles) and p-type (open circles) silicon. The lines are fits to the data by various theoretical models. The data do not exactly follow a Drude-type behavior. The best fit to the data is with the

Cole–Davidson model (which is the same as the generalized Drude model with  $a = 0$ ) where  $\beta = 0.91$  for n-type and  $\beta = 0.86$  for p-type. Reproduced from Ref. [229], with permission.

where  $-1 \leq c \leq 0$ . The Drude–Smith model reduces to the Drude model for  $c = 0$ , as shown in Fig. 7.8d. As  $c$  becomes more negative, the low frequency part of  $\sigma_1$  is suppressed, as shown for  $c = -0.5$  in Fig. 7.8e. The new zero-frequency conductivity is given by  $\sigma(\omega = 0) = \sigma_{\text{DC}}(1 + c)$ . Setting  $c = -1$ , as shown in Fig. 7.8f, results in a complete suppression of  $\sigma_1$  at low frequencies such that  $\sigma_1(0) = 0$  and makes  $\sigma_2$  go negative at low frequencies. A value of  $c = -1$  in the Drude–Smith model represents complete backscattering of carriers, which would correspond to carrier localization. The Drude–Smith model with a value of  $c = -0.99994$  was used recently to describe the conductivity observed from TRTS measurements of photoexcited car-

riers in InP nanoparticle arrays [261]. TRTS measurements of transient photoconductivity in dye-sensitized nanocrystalline TiO<sub>2</sub> also used the Drude–Smith model with  $c = -0.93$  to fit the conductivity data observed 3 ps after photoexcitation of the sample [262].

The last conductivity model discussed here is the localization-modified Drude model [246, 247, 263, 264] given by

$$\sigma_1 = \frac{\sigma_{\text{DC}}}{1 + (\omega\tau)^2} \left[ 1 - \frac{C}{(k_{\text{F}}l)^2} \left( 1 - \frac{l}{L_{\omega}} \right) \right] \quad (7.13)$$

where  $k_{\text{F}}$  is the Fermi wavevector,  $l$  is the mean free path of the carriers,  $C$  is a constant of order 1 and  $L_{\omega}$  is the distance over which the carriers can diffuse within a period of the incident radiation. The localization-modified Drude model has been used extensively to describe disorder-induced metal–insulator transitions in conducting polymers [263, 264]. The  $k_{\text{F}}l$  term is a measure of how many lattice spacings a carrier travels before being scattered, since for a free electron Fermi gas in a metal  $k_{\text{F}} \approx 1/a$ , where  $a$  is the lattice constant. If  $k_{\text{F}}l \gg 1$ , then there is coherent transport over many lattice spacings and the material is metallic. If  $k_{\text{F}}l < 1$ , then the carriers are localized around the atomic sites and the material is an insulator. The metal–insulator transition in the material occurs when  $k_{\text{F}}l \approx 1$ , which is also known as the Ioffe–Regel criterion. The mean free path can also be expressed as  $l = v_{\text{F}}\tau$ , where  $v_{\text{F}}$  is the Fermi velocity and  $\tau$  is the Drude relaxation time, and also in terms of a carrier diffusion coefficient  $D = l^2/3\tau$ . We now have  $L_{\omega} = (D/\omega)^{1/2}$ , so that Eq. (7.13) can be rewritten as

$$\sigma_1 = \frac{\sigma_{\text{DC}}}{1 + (\omega\tau)^2} \left[ 1 - \frac{B}{\tau^2} + (3\omega)^{1/2} \frac{B}{\tau^{3/2}} \right] \quad (7.14)$$

where  $B = C/(k_{\text{F}}v_{\text{F}})^2$  is a constant. Equation (7.14) is plotted in Fig. 7.8g, h and i for relaxation times  $\tau$  of 300, 100 and 75 fs, respectively, with the corresponding Drude response (dotted lines) for the same relaxation times. [Note that  $\sigma_2$  in the localization-modified Drude model is obtained through Kramers–Kronig analysis using the expression for  $\sigma_1$  in Eq. (7.14) [246].] The suppression of  $\sigma_1$  at low frequencies due to localization is evident, in addition to a  $\sigma_2$  that is negative at low frequencies for short scattering times. This is similar to the Drude–Smith model, but the scaling of  $\sigma_1$  as a function of frequency is different. At low frequencies ( $\omega\tau < 1$ ),  $\sigma_1 \sim \omega^2$  in the Drude–Smith model for  $c = -1$ , whereas  $\sigma_1 \sim \omega^{1/2}$  in the localization-modified Drude model [263].

Lastly, the measured conductivity for a composite material made from a mixture of conducting and insulating components can be modeled using effective medium theories [265], as long as the component length scales are much smaller than the wavelength of the probing radiation. Extracting the conductivity of the conducting component alone from these models can be difficult, however. Effective medium theory has been used to understand TRTS measurements of transient

photoconductivity in CdSe nanoparticles dispersed in toluene [266] and carbon nanotube films [267]. THz-TDS measurements of the dielectric constant of porous silicon [268] and carbon nanotube films [249, 250, 269], which is discussed further in the next section, have also used effective medium theory to model the measured conductivity.

## 7.6

### THz-TDS Measurements of Conducting Polymers and Carbon Nanotubes

Conducting polymers acquire their conductivity from the addition of dopants to an originally insulating organic semiconductor material [270–272]. The conductivities in some conducting polymers can be fairly high ( $\sim 10^4 \text{ S cm}^{-1}$ ), approaching values around 2% that of copper, and their discovery was recognized by the 2000 Nobel Prize in Chemistry [273]. Despite the large amount of work in this field over the past 25 years, however, the nature of the metallic state in conducting polymers is still not understood [273–279]. In particular, the metal–insulator transition has been extensively studied, which can be investigated by adjusting the doping levels in the polymer system [263, 264, 280–284]. Indeed, probing the low-frequency response in the far-infrared region of the spectrum has helped to identify the nature of carrier transport in the metallic regime for conducting polymers in terms of localized or Drude-like behavior, and both conventional FTIR [263, 264, 276, 280, 282, 283] and THz-TDS [245–248] techniques have been used.

Many of the studies have focused on  $\text{PF}_6$ -doped polypyrrole, but the interpretation of the nature of the metallic state has not been consistent and has been described in terms of a localization-modified Drude model [263, 264] or a more Drude-like response [245, 276]. Figures 7.10a and b show the real and imaginary components of the conductivity, respectively, obtained by THz-TDS on  $\text{PF}_6$ -doped polypyrrole film with a room temperature DC conductivity of  $215 \text{ S cm}^{-1}$  [245, 247]. The measured conductivity follows a Drude response (solid lines) with a Drude relaxation time  $\tau = 12.6 \text{ fs}$ , a carrier density  $n = 1 \times 10^{20} \text{ cm}^{-3}$  and a mobility  $\mu = 13 \text{ cm}^2 \text{ V}^{-1} \text{ s}^{-1}$ . As can be seen by the dot-dashed line in Fig. 7.10a, the localization-modified Drude model does not fit the data for  $\sigma_1$ .

On the other hand, THz-TDS experiments on conducting poly-3-methylthiophene films with  $\sigma_{\text{DC}} = 7.5 \text{ S cm}^{-1}$  at room temperature show a reasonable fit of the conductivity data to a localization-modified Drude model, as shown in Figs. 7.10c and d [246, 247]. Note the suppression of  $\sigma_1$  at low frequencies in Fig. 7.10c and the negative  $\sigma_2$  in Fig. 7.10d, which is very different from a simple Drude response. The fits give a relaxation time  $\tau = 8 \text{ fs}$ , a carrier density of  $n = 1.3 \times 10^{19} \text{ cm}^{-3}$  and a mobility  $\mu = 8.2 \text{ cm}^2 \text{ V}^{-1} \text{ s}^{-1}$ . A value of  $k_{\text{Fl}} \approx 0.8$  can be estimated from the data given in Ref. [246] for conducting poly-3-methylthiophene, which is close to the metal–insulator transition. For the experiments that showed a localization-modified Drude response for the metallic state of doped polypyrrole, a value of  $k_{\text{Fl}} \approx 1.3$  was reported in films with  $\sigma_{\text{DC}} \approx 350 \text{ S cm}^{-1}$  [264]. However, as mentioned above, a Drude response was seen in conducting polypyrrole with

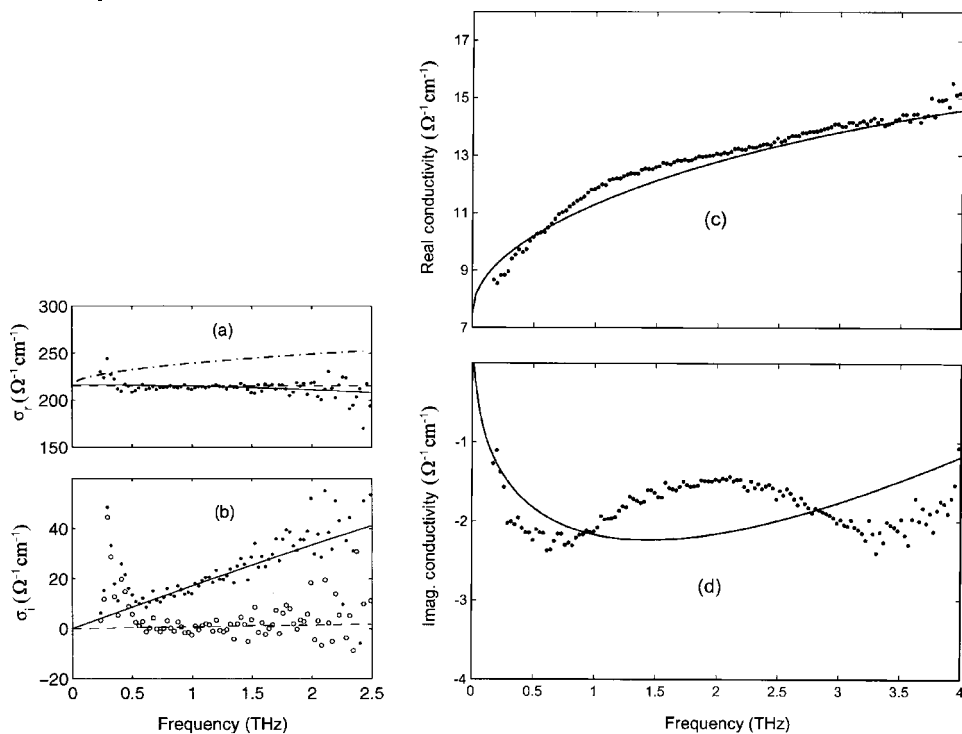


**Figure 7.10** Real (a) and imaginary (b) components of the complex conductivity of a conducting polypyrrole film as measured by THz-TDS. In (b), the extracted  $\sigma_2$  ( $\sigma_i$ ) is very sensitive to the choice of background dielectric constant, as shown by the solid circles for  $\epsilon_\infty = 70$  and the open circles for  $\epsilon_\infty = 40$ . The solid line is a Drude fit to the data with  $\omega_p/2\pi = 70$  THz,  $\tau = 12.6$  fs ( $f_c = 12.6$  THz) and  $\epsilon_\infty = 70$ . The dashed line represents a Drude response using parameters close to those

obtained in Ref. 263 with  $\omega_p/2\pi = 334$  THz,  $\tau = 0.55$  fs ( $f_c = 288$  THz) and  $\epsilon_\infty = 40$ . The dot-dash line is from a localization modified Drude model. Reproduced from Ref. [245], with permission. The complex conductivity of a conducting poly-3-methylthiophene film as measured by THz-TDS is shown in (c) and (d). The solid line represents a fit to the data using a localization-modified Drude model with  $\tau = 8$  fs. Reproduced from Ref. [246], with permission.

roughly the same [276] or slightly lower [245] room temperature conductivity, so whether or not the metallic state for polypyrrole is Drude-like is not clear. Interestingly, recent THz-TDS measurements of the conductivity in  $\text{FeCl}_3$ -doped MEH-PPV films with  $\sigma_{\text{DC}} \approx 0.1 \text{ S cm}^{-1}$  did not show a Drude or localization-modified Drude response but could be modeled simply by using a single Lorentz oscillator centered at 4 THz (16.5 meV) and with a large damping term of  $1/2\pi\tau_L = 4$  THz ( $\tau_L \approx 40$  fs) [248]. It is believed that intra-chain localization of carriers in these doped MEH-PPV films is very strong, putting these films on the insulating side of the metal–insulator transition [248].

THz-TDS measurements of aligned films of conducting single-walled carbon nanotubes (SWNTs) have also been performed recently [249, 250]. A schematic of

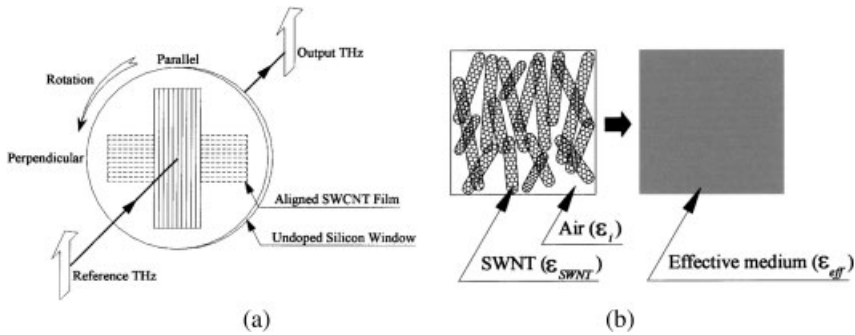


**Figure 7.11** (a) Schematic of the THz-TDS experiment for measuring the anisotropic conductivity of aligned single-walled carbon nanotubes (SWNTs). (b) Representation of aligned SWNT film on the silicon window as

an effective medium ( $\epsilon_{\text{eff}}$ ) of carbon nanotubes ( $\epsilon_{\text{SWNT}}$ ) embedded in an air medium ( $\epsilon = 1$ ). Reproduced from Ref. [250], with permission.

the experiment is shown in Fig. 7.11a, where the polarization of the THz pulse is used to probe the conductivity parallel and perpendicular to the alignment direction of the carbon nanotubes. The film was modeled as an effective medium of carbon nanotubes in air, as described in Fig. 7.11b. A Maxwell–Garnett effective medium model is used to fit the data, as shown in Fig. 7.12, where the contribution from the SWNTs with a filling factor of 0.9 is modeled using a Drude–Lorentz response [250]. The relatively weak anisotropy observed in the response is believed to be due to enhanced electromagnetic coupling between the carbon nanotubes in the perpendicular direction. A Drude relaxation time of 136 fs is obtained for the SWNTs in the parallel direction. The Lorentz oscillator center frequency is 2.40 THz with a damping term of 4.56 THz, which corresponds to a phonon mode along the  $c$ -axis of the nanotube [250].

## 7.7 Time-Resolved Terahertz Spectroscopy (TRTS)

As discussed above, THz-TDS experiments use the broad bandwidth of THz pulses to perform spectroscopy of materials in the far-infrared region of the spectrum. However, the short duration of THz pulses also makes it possible to perform time-resolved studies of *transient* conductivity in materials with *sub-picosecond* time resolution [156, 159]. This unique ultrafast pump–probe technique, which was first introduced in the mid-1980s [285] but has rapidly grown as a powerful research tool over the past 5 years [159], is commonly referred to as time-resolved terahertz spectroscopy or TRTS, to differentiate it from THz-TDS where the sample is *not* photoexcited with a pump pulse. TRTS, therefore, essentially probes transient photoconductivity in materials with sub-picosecond ( $\sim 0.4$  ps) time resolution.

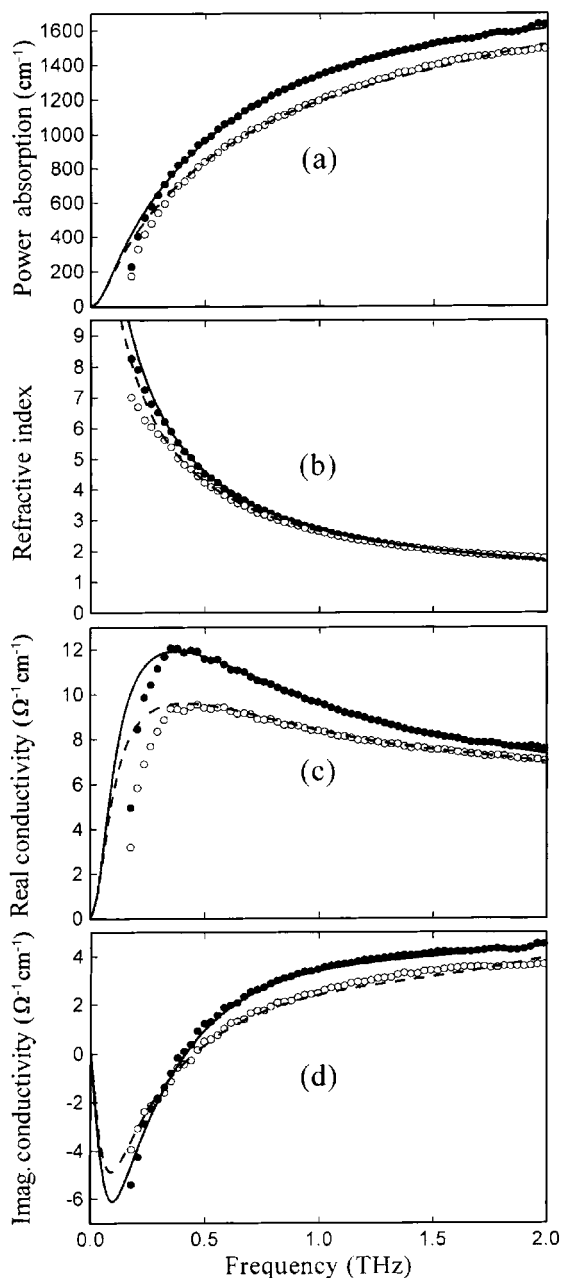


**Figure 7.12** THz-TDS measurements of the (a) power absorption, (b) refractive index, (c) real part of the conductivity and (d) imaginary part of the conductivity for aligned SWNTs parallel (solid circles) and perpendicular (open circles) to the alignment direction. The conductivity anisotropy is about 1.4. The solid and dashed lines are fits to the parallel and perpendicular directions, respec-

tively, using a Maxwell–Garnett effective medium theory, with the SWNT component following a Drude–Lorentz model and with a filling factor of 0.9. In the parallel direction,  $f_c$  for the Drude component is  $1/2\pi\tau = 1.17$  THz and the Lorentz oscillator component has  $f_L = 2.40$  THz and  $1/2\pi\tau_L = 4.56$  THz. Reproduced from Ref. [250], with permission.

TRTS experiments have been used to explore transient carrier dynamics in bulk inorganic semiconductors such as GaAs [257, 285–289], ZnTe and CdTe [290], and also insulators such as sapphire [254] and  $\text{TiO}_2$  [262, 291, 292]. Picosecond carrier relaxation times have been studied in LT-GaAs [258, 293], radiation-damaged silicon-on-sapphire (RD-SOS) [294–296], amorphous Si [296], microcrystalline Si [297] and proton-bombarded InP [298]. Non-contact measurements of transient photoconductivity have also been performed in semiconductor nanostructures such as GaAs quantum wells [256, 299], self-assembled InGaAs [300–302] and ErAs [303] quantum dots, and InP [261], CdSe [266] and Si [267] nanoparticles. TRTS has been very useful for probing non-equilibrium superconductivity in high- $T_c$  compounds [304–306] and  $\text{MgB}_2$  [307], and also transient carrier dynamics in colossal magnetoresistance materials [308]. Solvation dynamics and transport properties in liquids have also been extensively explored with TRTS [309–313]. TRTS measurements of transient photoconductivity in organic semiconductors were first reported in functionalized pentacene single crystals in 2002 [147], followed by more studies on pentacene single crystals [153], pentacene and functionalized pentacene thin films [148–152], and other organic molecular crystals [152]. Recently, TRTS experiments have investigated transient conductivity in MEH-PPV thin films [154, 155] and solutions [155], and also carbon nanotube films [267]. The theoretical foundations behind the TRTS technique have also been thoroughly discussed [257, 310, 314–317].

A schematic of a TRTS setup is shown in Fig. 7.13. It is very similar to the THz-TDS setup shown in Fig. 7.4, except that a third beam is split off from the laser source to act as a pump pulse for photoexcitation of the sample. Delay stage B is used to control the relative delay time between the THz probe pulse and the optical

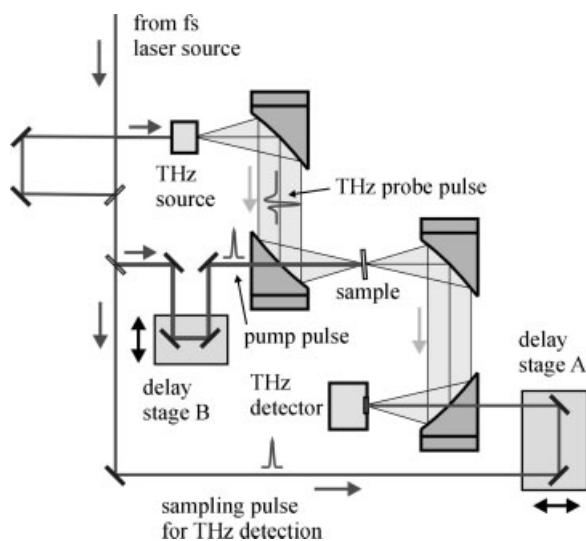


**Figure 7.13** Schematic of THz pulse setup used for time-resolved THz spectroscopy (TRTS).

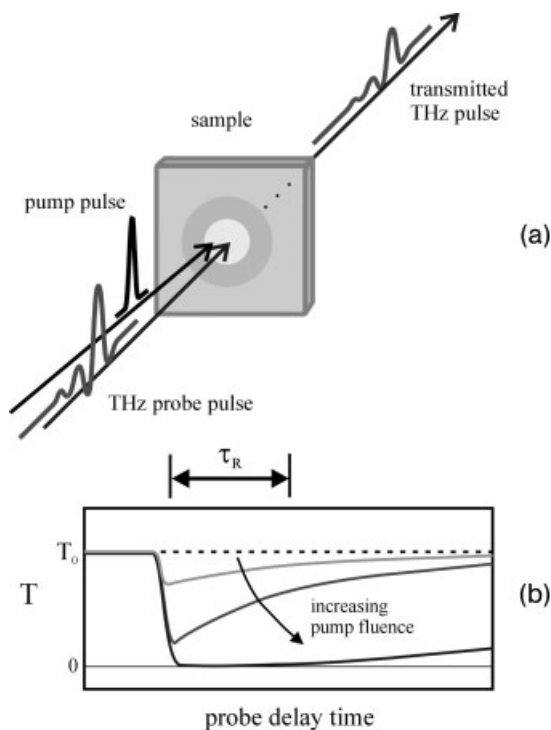


**Figure 7.14** (a) Schematic of a TRTS experiment using optical pump pulses and THz probe pulses. (b) The transmission of the THz pulse is typically reduced upon generation of conductivity in the sample by the pump pulse. In highly conductive samples

and at high pump fluence, the transmission of the THz pulse through the sample can be reduced to zero.  $T_0$  is the peak transmission of the THz pulse through the unexcited sample.

pump pulse arriving at the sample and delay stage A is used to scan over the transmitted THz wave form. Figure 7.14a describes the optical pump–THz probe technique where a pump pulse photoexcites a sample which is later probed by a THz pulse. The transient photoconductivity induced in the sample decreases the amplitude of the transmitted THz pulse, as shown in Fig. 7.14b. Increasing the pump fluence further attenuates the transmitted THz pulse and at high fluences (and in samples with high carrier mobilities) the transmission of the THz pulse can be completely blocked. The change in amplitude and phase of the transmitted THz pulse compared to the THz wave form transmitted through the unexcited sample can be used to extract the complex conductivity induced by the pump pulse in the sample.

The TRTS measurement technique is described further in Fig. 7.15. In Fig. 7.15a, a normally insulating (or semiconducting) material with refractive index  $N$  is excited by a pump pulse within an optical penetration depth  $d$  of the sample surface. The THz pulse arrives at the sample after a delay time  $\Delta t$  with

respect to the pump pulse (delay stage B in Fig. 7.13 controls the delay time  $\Delta t$ ). A delay time of  $\Delta t = 0$  corresponds to the pump pulse and the main peak of the THz pulse arriving at the same time at the sample, with positive delay times corresponding to the THz pulse arriving at the sample after the pump pulse. The THz pulse wave form,  $E_0(t)$ , transmitted through the unexcited sample at negative delay times (or with the pump beam blocked), is shown in Fig. 7.15b (delay stage A in Fig. 7.13 scans the time  $t$  for the THz wave form). Figure 7.15c shows the THz pulse wave form,  $E_S(t)$ , transmitted through the photoexcited sample at positive delay times. By chopping the pump beam in Fig. 7.13, the modulation in the transmitted THz pulse wave form  $\Delta E(t) = E_S(t) - E_0(t)$  due to photoexcitation of the sample by the pump pulse can be measured through lock-in detection techniques. An indication of transient absorption of the THz pulse in the sample can be seen by plotting  $-\Delta E(t)$ , as shown in Fig. 7.15d.

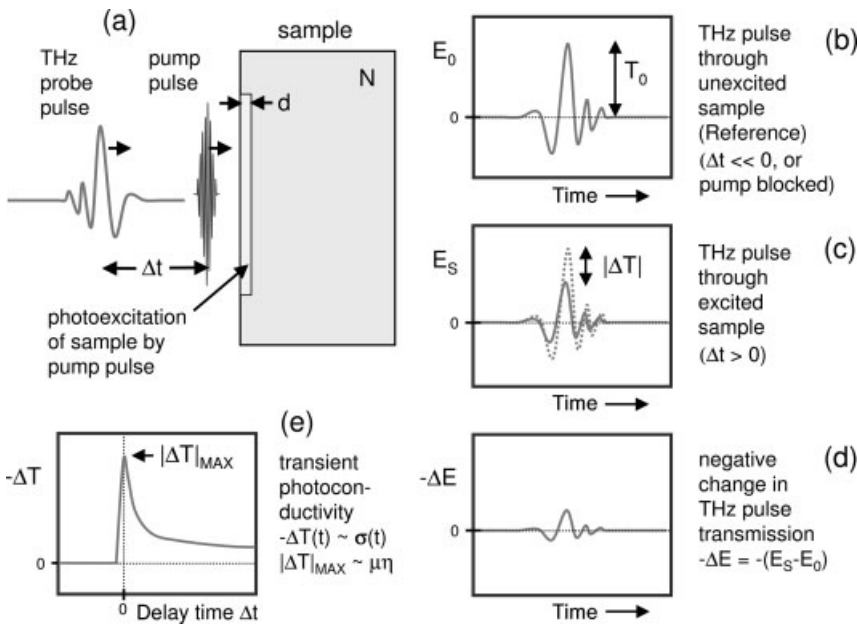


**Figure 7.15** Schematic of typical measurements made in TRTS experiments (see text for more details).

If we assume that the thickness of the optically excited region in the sample is much smaller than the wavelength of the THz radiation (i.e.  $d \ll \lambda$  or  $n_s \omega d/c \ll 1$ ) and that  $d$  is much less than the overall sample thickness, then we can use the thin-film approximation for the amplitude transmission of electromagnetic radiation through a thin conducting film with conductivity  $\hat{\sigma}$  on a semi-infinite insulating substrate with a refractive index  $N$  of [156, 235–239, 295]

$$T_s(\omega) = \frac{E_s(\omega)}{E_i(\omega)} = \frac{2}{1 + N + Z_0 \hat{\sigma}(\omega) d} \quad (7.14a)$$

where  $Z_0$  is the impedance of free space ( $Z_0 = 377 \Omega$ ),  $E_s(\omega)$  is the Fourier transform of  $E_s(t)$  and  $E_i(\omega)$  is the incident THz field on the sample [Eq. (7.14a) applies for normal incidence with the incident THz pulse traveling in vacuum or air]. The transmission through the unexcited sample with  $\hat{\sigma} = 0$  is therefore

$$T_0(\omega) = \frac{E_0(\omega)}{E_i(\omega)} = \frac{2}{1 + N} \quad (7.15)$$

so that

$$\frac{T_s(\omega)}{T_0(\omega)} = \frac{E_s(\omega)}{E_0(\omega)} = \frac{1 + N}{1 + N + Z_0 \hat{\sigma}(\omega) d} \quad (7.16)$$

where any reflections of the THz pulse from the second sample–air interface cancel out. The negative differential transmission as a function of frequency is then

$$-\frac{\Delta E(\omega)}{E_0(\omega)} = \frac{Z_0 \hat{\sigma}(\omega) d}{1 + N + Z_0 \hat{\sigma}(\omega) d} \quad (7.17)$$

A fairly simple way to extract the real and imaginary components of the conductivity  $\hat{\sigma}$  of the photoexcited layer in the sample at a given delay time is to invert Eq. (7.16) as follows:

$$\frac{E_s(\omega)}{E_0(\omega)} = \frac{E_0(\omega)}{E_0(\omega) + \Delta E(\omega)} = \left[ 1 + \frac{Z_0 \sigma_1(\omega) d}{1 + N} \right] + i \left[ \frac{Z_0 \sigma_2(\omega) d}{1 + N} \right] \quad (7.18)$$

The real and imaginary components of the Fourier transforms of the THz wave forms, therefore, can be used to directly find  $\sigma_1$  and  $\sigma_2$  in the photoexcited layer of the sample.

If the scan window for the THz wave form has a temporal width  $t_w$  and a time-step increment  $t_s$  between each data point in the wave form, then the corresponding Fourier spectrum (FFT) has a frequency resolution of  $\Delta f = 1/t_w$  and a maximum frequency of  $f_{\text{Max}} = 1/(2t_s)$ . Time-step increments of 50 fs will give  $f_{\text{Max}} = 10$  THz, which is large enough for typical THz pulses with bandwidths up to 4 THz. A THz scan window width of 10 ps will give a frequency resolution of 100 GHz ( $\Delta f = 0.1$  THz), which is also reasonable. Increasing the window size, of course, will improve the frequency resolution in the Fourier spectrum, but having a long scan window for the THz wave forms is problematic if the transient photoconductivity in the sample is varying significantly over that time window [304]. In other words, what happens if the front end of the THz pulse “sees” a different conductivity than the tail end? This issue has been addressed in the literature using numerical (finite-difference time domain) or analytical techniques to deter-

mine the complex conductivity in a photoexcited sample even if the conductivity changes over the time-scale of the THz pulse [155, 257, 258, 310, 314–317]. Experimentally, this can be accomplished by adding a third delay stage to the TRTS setup in Fig. 7.13 for the THz source beam. The THz wave form is obtained by scanning this stage while keeping a fixed delay time between the pump pulse and the THz sampling pulse. Each point on the THz wave form, therefore, passes through the sample at the same delay time after the initial photoexcitation of the sample by the pump pulse [310]. After completing each scan, the delay time between the pump and sampling pulses is changed so that the conductivity of the sample as a function of delay time can be determined (also known as a 2-D scan).

Acquiring complete THz wave form scans for a series of delay times after excitation of the sample by the pump pulse can be very time consuming. A simpler and faster mode of operation in TRTS experiments which provides valuable insight into carrier relaxation dynamics (but *not* the frequency-dependent conductivity) is to sample only the modulation in the *peak* of the transmitted THz pulse. This optical pump–THz probe technique, which is used extensively in TRTS measurements, is similar to traditional optical pump–optical probe experiments that monitor the modulation in the transmitted probe pulse intensity as a function of delay time. Optical pump–THz probe experiments are done by keeping delay stage A of the TRTS setup in Fig. 7.13 for the THz sampling beam fixed on the peak electric field component of the THz pulse transmitted through the sample, which is labeled  $T_0$  in Fig. 7.15b. (Note that  $T_0$  in Fig. 7.15b is actually  $T_0 E_i$ , but  $E_i$  will cancel out in the equations given below.) Chopping the pump beam at positive delay times produces a modulation in the transmitted peak amplitude of the THz pulse, as indicated by  $|\Delta T|$  in Fig. 7.15c. Delay stage B is then scanned, which changes the relative delay time of the pump pulse with respect to the fixed THz probe pulse. A plot of  $-\Delta T$  versus delay time  $\Delta t$  can be obtained, as shown in Fig. 7.15e, which is representative of the transient photoconductivity in the photoexcited sample. The time resolution of this technique is around 0.3–0.5 ps, which is limited by the sampling response time of the THz detection system. This technique assumes that the phase shift in  $E_s(t)$  is small compared with  $E_0(t)$ , so that  $|\Delta T|$  is mainly due to amplitude modulation of the peak of the THz pulse rather than any temporal shifts of the THz waveform that would mimic amplitude modulation. The phase shift in the THz pulse will be small if the complex conductivity is predominantly real. For Drude conductivity, this is satisfied if  $\omega\tau < 1$ , such that  $\hat{\sigma} \approx \sigma_{DC} = ne\mu$  [see Eqs. (7.5) and (7.6)]. The time evolution of this conductivity is denoted by  $\sigma_{DC}(\Delta t) = \sigma(\Delta t) = \sigma$  and following Eq. (7.17) we now have for the negative differential transmission through the photoexcited sample

$$-\frac{\Delta T}{T_0} = \frac{Z_0 \sigma d}{1 + N + Z_0 \sigma d} = 1 - \frac{1 + N}{1 + N + Z_0 \sigma d} \quad (7.19)$$

The time dependence of the negative differential transmission, therefore, is determined by the transient photoconductivity induced in the sample.  $-\Delta T/T_0$  ranges from  $\sim 0$  for very small conductivities to a maximum value of 1 for very high con-

ductivities, in which case the transmission of the THz pulse is completely blocked by the photoexcited sample. The time-dependent conductivity of the sample is then [295]

$$\sigma = \left( \frac{1 + N}{Z_0 d} \right) \left( -\frac{\Delta T}{T_0} \right) \left[ \frac{1}{1 - (-\Delta T/T_0)} \right] \quad (7.20)$$

which for small modulations in the transmitted THz pulse becomes

$$\sigma \approx \left( \frac{1 + N}{Z_0 d} \right) \left( -\frac{\Delta T}{T_0} \right) \quad \text{for} \quad \left| \frac{\Delta T}{T_0} \right| \ll 1 \quad (7.21)$$

Therefore

$$\sigma \propto -\frac{\Delta T}{T_0} \quad (7.21a)$$

We see from Eq. (7.21) that the transient photoconductivity induced in the sample is directly proportional to the negative differential transmission of the THz pulse through the sample for small modulations (i.e.  $|\Delta T|/T_0 < 20\%$ ).

In general,  $\sigma(\Delta t) = n(\Delta t)e\mu(\Delta t)$ , but often the mobility is known and is independent of time [i.e.  $\mu(\Delta t) = \mu$ ] so that the time-dependent carrier concentration in a sample after excitation by a pump pulse can be written from Eq. (7.20) as [294–296, 303]

$$n(\Delta t) = \left( \frac{1 + N}{Z_0 d e \mu} \right) \left( -\frac{\Delta T}{T_0} \right) \left[ \frac{1}{1 - (-\Delta T/T_0)} \right] \quad (7.22)$$

If the mobility is *not* known, then Eq. (7.20) or (7.21) can only provide the product of the carrier concentration and the carrier mobility ( $n\mu$ ) from the measured  $-\Delta T/T_0$ . Furthermore, the charge generation efficiency,  $\eta$ , may be less than 100% so that  $n \rightarrow \eta n$ . At zero time delay, the maximum conductivity induced in the sample by the pump pulse is then

$$\sigma_{\text{Max}}(\Delta t = 0) = n e \mu = \eta n_{\text{Max}} e \mu = \eta \frac{F_{\text{Pump}}}{h f_{\text{Pump}} d} e \mu \quad (7.23)$$

where  $F_{\text{Pump}}$  is the pump beam fluence illuminating the sample,  $f_{\text{Pump}}$  is the frequency of the pump light,  $h$  is Planck's constant and  $n_{\text{Max}}$  is the maximum possible carrier concentration that could be generated by the pump pulse with  $\eta = 1$ . Assuming small modulations and combining Eqs. (7.21) and (7.23), the maximum value of  $|\Delta T|/T_0$  near  $\Delta t = 0$  can be used to determine the product of the charge carrier mobility and charge photogeneration efficiency from the equation [147–153]

$$\eta\mu \approx \frac{hf_{\text{Pump}}(1+N)}{Z_0 e F_{\text{Pump}}} \left| \frac{\Delta T}{T_0} \right|_{\text{Max}} \quad (7.24)$$

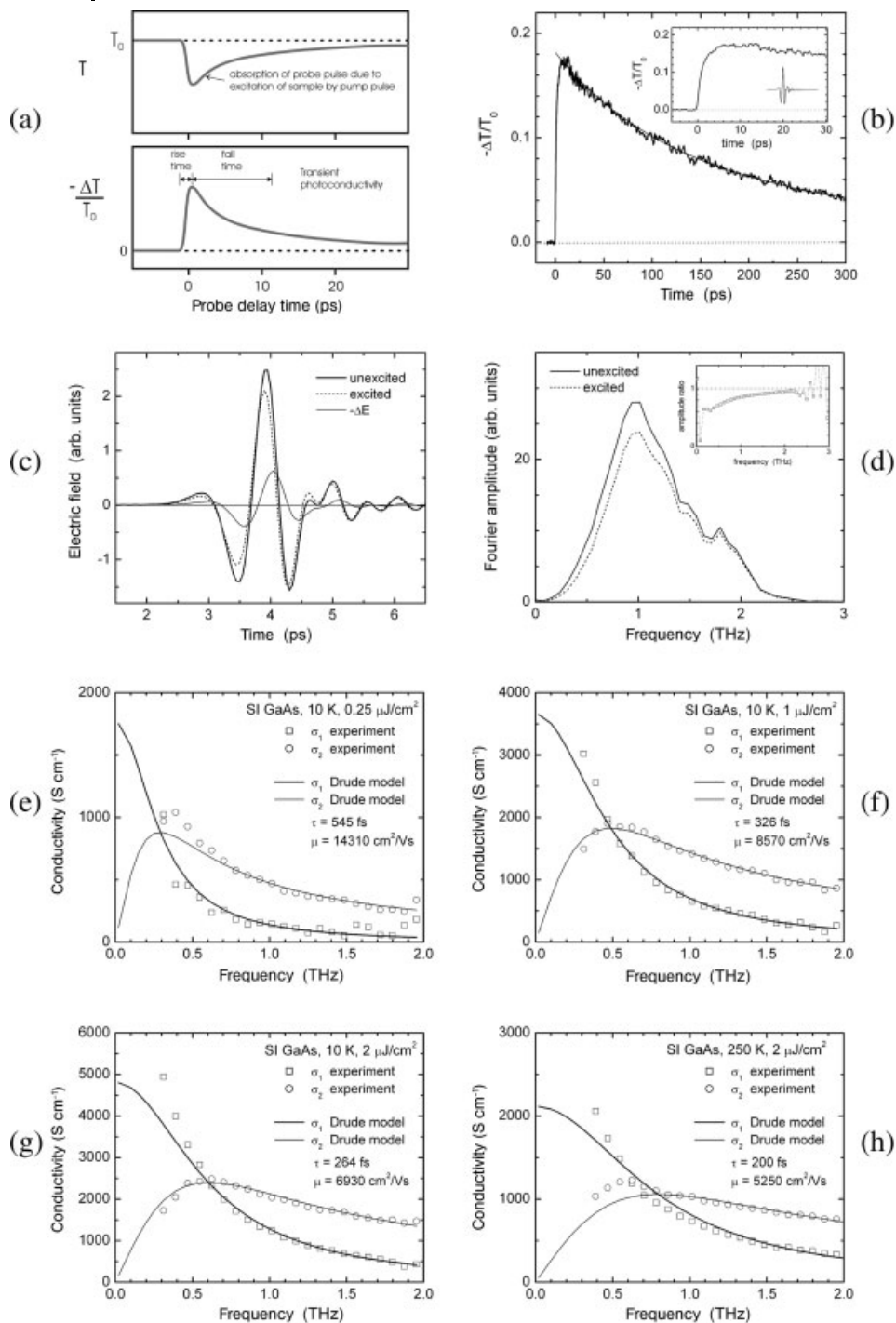
If  $\eta \approx 1$ , as in most inorganic semiconductors, Eq. (7.24) can then be used to determine the carrier mobility directly from the measurement of the differential transmission of the THz pulse at  $\Delta t = 0$ . If  $\eta < 1$ , as is believed to be the case for many organic semiconductors (as discussed in Section 7.1), then Eq. (7.24) can be used to find a *lower* limit for the carrier mobility by letting  $\eta = 1$ . Since the right-hand side of Eq. (7.24) is a constant value determined from experiment, then the product  $\eta\mu$  must also be constant. Having  $\eta < 1$  in Eq. (7.24) will result in a larger estimate for the carrier mobility  $\mu$  [147, 148, 153].

It is also worth noting that Eq. (7.24) assumes that all the pump fluence is absorbed in the sample but does *not* require any knowledge of the actual optical penetration depth (as long as it satisfies the thin-film approximation). This is because the transmission of the THz probe pulse is sensitive to the product  $nd$  in the sample, which is the number of carriers per unit area photoexcited by the pump pulse. If the sample is very thin, however, then Eq. (7.24) can be modified to account for transmission of the pump pulse through the sample as [148, 149, 151]

$$\eta\mu \approx \frac{hf_{\text{Pump}}(1+N)}{Z_0 e [1 - \exp(-ad)] F_{\text{Pump}}} \left| \frac{\Delta T}{T_0} \right|_{\text{Max}} \quad (7.25)$$

where  $d$  is now the sample thickness and  $a = 1/\delta$ , where  $\delta$  is the optical penetration depth of the pump pulse in the sample. Recently, lower limits for the mobilities of photogenerated charge carriers in pentacene and functionalized pentacene thin films were reported using Eq. (7.25) [148, 149], which will be discussed further in Section 7.8.

An example of a TRTS experiment using 400-nm pump pulses on an SI-GaAs wafer at 10 K is described in Fig. 7.16. Figure 7.16a illustrates how the peak of the transmitted THz probe pulse is suppressed after excitation by the pump pulse. The negative differential transmission  $-\Delta T/T_0$  represents the transient absorption of the THz probe pulse passing through the sample, as shown in Fig. 7.16b. The solid line is a biexponential fit to the decay of the transient signal due to carrier recombination with  $\tau_1 = 100$  ps and  $\tau_2 = 340$  ps. The inset of Fig. 7.16b zooms in on the rise time of the transient photoconductivity induced by the 400-nm pump pulse in the GaAs wafer. The rise time of the transient signal is around 4 ps, which is due to intervalley scattering from the low-mobility satellite valleys in GaAs to the high-mobility  $\Gamma$  valley at the zone center [257, 285, 290]. Pumping GaAs with 800-nm pulses gives a rise time less than 0.5 ps limited by the time resolution of the setup. The inset in Fig. 7.16b also shows the temporal position on the decay curve where a THz scan was taken for sampling the conductivity (delay time  $\Delta t = 20$  ps). The THz scans for the unexcited sample,  $E_0(t)$ , the excited sample,  $E_s(t)$  and the negative of the difference,  $-\Delta E(t)$ , are shown in Fig. 7.16c with corresponding Fourier spectra in Fig. 7.16d. The frequency dependence for  $\sigma_1$  and  $\sigma_2$ , which was found by inserting the complex Fourier transforms of the



wave forms shown in Fig. 7.16c into Eq. (7.18), is shown in Fig. 7.16e for low pump fluence by the open squares and open circles, respectively. The solid lines are a Drude model fit to the data for both  $\sigma_1$  and  $\sigma_2$  using just two parameters: the Drude relaxation time  $\tau$  and the DC conductivity  $\sigma_{DC}$ . The Drude model agrees well with the measured  $\sigma_1$  and  $\sigma_2$ , with  $\tau = 545$  fs. The corresponding mobility is  $14310 \text{ cm}^2 \text{ V}^{-1} \text{ s}^{-1}$ . At higher pump fluences, as shown in Fig. 7.16f, more carrier scattering is expected as seen by the reduction in relaxation time to 326 fs with a corresponding decrease in the carrier mobility to  $8570 \text{ cm}^2 \text{ V}^{-1} \text{ s}^{-1}$ . A further decrease in carrier mobility to  $6930 \text{ cm}^2 \text{ V}^{-1} \text{ s}^{-1}$  can be seen at even higher fluences in Fig. 7.16g with a good fit to the Drude model. At 250 K, but at the same pump fluence as Fig. 7.16g, the Drude relaxation time decreases to about 200 fs ( $\mu = 5250 \text{ cm}^2 \text{ V}^{-1} \text{ s}^{-1}$ ).

The Drude response observed in the transient photoconductivity of GaAs shown in the TRTS example in Fig. 7.16 is also seen in other TRTS studies of photoexcited GaAs wafers [287] and is close to the generalized Drude model response (see Section 7.5) also reported for photoexcited GaAs [257]. A Drude response is typically observed in the transient photoconductivity of many other materials studied by TRTS such as GaAs quantum wells [256], GaAs with embedded ErAs nanoislands [303], bulk single crystals of ZnTe [290], CdTe [290],  $\text{Al}_2\text{O}_3$  (sapphire) [254] and  $\text{TiO}_2$  (rutile) [292], high- $T_c$  superconductor thin films [305], liquid *n*-hexane and cyclohexane [312], and pentacene single crystals [153] and thin films [148]. As discussed in Section 7.5, deviations from Drude-like behavior in the transient photoconductive response are also observed in TRTS experiments, such as the generalized Drude model for GaAs [257] and LT-GaAs [258], the Drude–Smith model for InP nanoparticles [261] and nanocrystalline  $\text{TiO}_2$  [262], and dispersive behavior for photoexcited charge carriers in MEH-PPV films [154, 155]. Besides showing frequency-dependent conductivities, these TRTS experiments often look at carrier dynamics by showing the time dependence of the differential transmission  $-\Delta T/T_0$  of the peak of the THz pulse through the photoexcited sample, as

**Figure 7.16** Example of TRTS experiment on a 0.5-mm thick wafer of SI-GaAs mounted on a 1.5-mm diameter aperture at 10 K in an optical cryostat and excited by 400-nm, 100-fs pump pulses. The penetration depth of GaAs at 400 nm is  $\delta = 15$  nm and the effective mass of the electrons is  $0.067m_e$ . (a) Schematic of the transient absorption of the THz pulse with amplitude  $T_0$  at negative time delays in terms of the negative differential transmission  $-\Delta T/T_0$ , which is proportional to the transient photoconductivity in the sample. (b) Transient photoconductivity at 10 K and a pump fluence of  $2 \mu\text{J cm}^{-2}$ . The solid line is a bi-exponential fit to the decay with  $\tau_1 = 100$  ps and  $\tau_2 = 340$  ps. The inset shows the rise time

of the signal, which is limited by carrier scattering from the GaAs satellite valleys, and the temporal location of the THz pulse for the conductivity analysis shown in (c) to (h).

(c) THz pulse transmitted through the unexcited (solid line) and excited (dashed line) sample 20 ps after the arrival of the pump pulse. The corresponding Fourier transforms are shown in (d). The inset in (d) shows the ratio of the excited to unexcited transforms. The extracted conductivities for fluences of  $0.25$ ,  $1$  and  $2 \mu\text{J cm}^{-2}$  are shown in (e), (f) and (g), respectively. (h) Conductivity at 250 K and  $2 \mu\text{J cm}^{-2}$ . The best-fit Drude relaxation times  $\tau$  and corresponding electron mobilities  $\mu$  are also given.

shown in Fig. 7.16b. There are also many other TRTS studies that have focused solely on this latter method to explore ultrafast carrier dynamics in materials such as GaAs [285, 286], LT-GaAs [293], RD-SOS [294–296], amorphous Si [296], microcrystalline Si [297], proton-bombarded InP [298], self-assembled InGaAs quantum dots [300–302] and functionalized pentacene single crystals [147]. In some cases, THz wave forms were acquired at various delay times to demonstrate the absence of temporal shifts in the peak of the THz pulse [147, 294, 295]. In general, however, extracting the complex conductivity from the THz wave forms, as shown in Fig. 7.16e–h, is required in order to better understand the nature of transient photoconductivity in materials.

Lastly, carrier mobilities in organic semiconductors such as pentacene are typically much smaller than those in inorganic semiconductors, and so the transient THz differential transmission signals are expected to be much less in organic semiconductors compared with what is seen in higher mobility materials such as GaAs. This is evident from Eq. (7.21), where the negative differential transmission of the THz pulse is proportional to the transient conductivity, which is larger for higher carrier mobilities. Nevertheless, TRTS experiments on pentacene and functionalized pentacene thin films, which are discussed further in the next section, have been able to make (non-contact) measurements of carrier mobilities as low as  $0.01 \text{ cm}^2 \text{ V}^{-1} \text{ s}^{-1}$  [148, 149, 151].

## 7.8

### TRTS Measurements of Transient Photoconductivity in Organic Semiconductors

The first optical pump–terahertz probe measurements of transient photoconductivity in an organic semiconductor were reported by Hegmann et al. [147] in functionalized pentacene single crystals. The molecular structure of the functionalized pentacene (FPc) derivative is shown in Fig. 7.17a and is described in more detail by Anthony and co-workers [318, 319]. Whereas the stacking in pristine pentacene (Pc) crystals follows a “herringbone” structure [61], the TIPS (triisopropylsilylethynyl) side-groups in FPc force a more “brick-wall-like” packing structure with enhanced  $\pi$ -overlap between the faces of the pentacene units [318, 319], as shown in Fig. 7.17b. The stacking in the  $a$ – $b$  plane of the crystal can be seen in the crystallographic view down the  $c$ -axis in Fig. 7.17c. The view down the  $a$ -axis in Fig. 7.17d shows the large separation between the  $a$ – $b$  planes along the  $c$ -axis due to the TIPS side-groups. The  $a$ – $b$  plane of the crystal, therefore, has a much higher conductivity than that along the  $c$ -axis [318]. The TIPS side-groups also increase the solubility of the molecules, making it easier to grow large single crystals from solution [318, 319]. An example of an FPc crystal grown from a saturated THF solution at 4 °C is shown in Fig. 7.18a [147]. The  $a$ – $b$  plane forms the large face of the crystal with the  $c$ -axis along the thickness. Typical crystal dimensions were around  $2 \times 4 \text{ mm}$  on the face with a thickness around 0.5 mm. The large crystal size made it possible to mount the FPc crystals on a 1-mm diameter aperture in an optical cryostat for TRTS experiments, as shown in Fig. 7.18b. The single-crys-

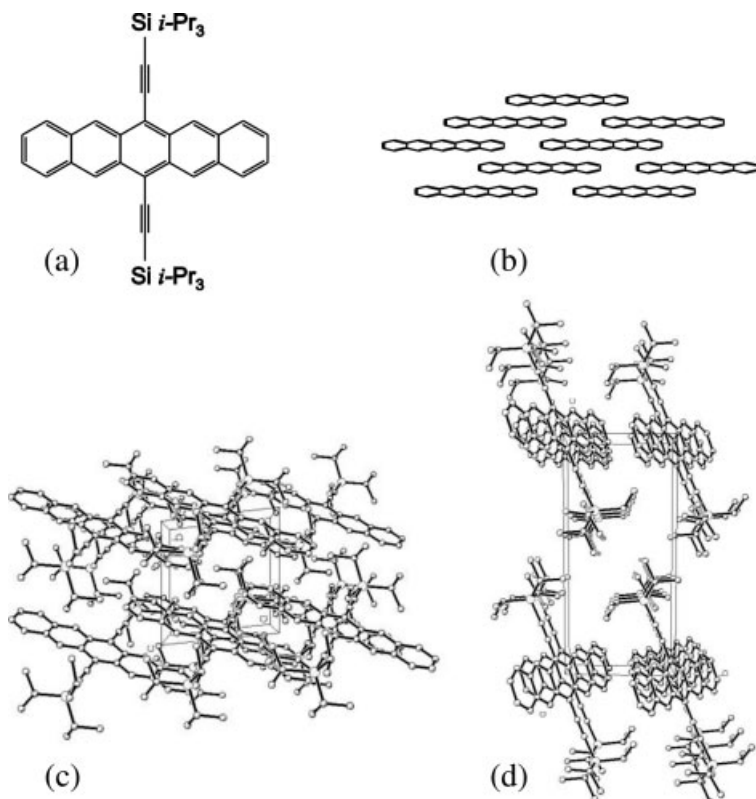


**Figure 7.17** (a) Molecular structure of TIPS functionalized pentacene (FPC). The TIPS (triisopropylsilyl) side-groups force stacking of the molecules into a brick-like pattern in the  $a$ - $b$  plane, as shown schematically in (b) and in the crystallographic view (c) looking

down the  $c$ -axis. (d) Crystallographic view down the  $a$ -axis of the FPC crystal. The crystal structures shown in (c) and (d) are courtesy of J. E. Anthony and S. R. Parkin at the University of Kentucky.

tal samples were excited with 800-nm, 100-fs pump pulses from an amplified Ti:sapphire laser source operating at a repetition rate of 1 kHz. Typical pump fluences were around  $2.5 \text{ mJ cm}^{-2}$ , with photoexcited carrier densities up to  $10^{18} \text{ cm}^{-3}$ . The THz probe pulses were focused through the 1-mm aperture and were able to pass through the unexcited sample with very little attenuation. The electric field of the THz pulses was within the  $a$ - $b$  plane of the FPC crystal, and so the THz pulses probed the transient photoconductivity within the  $a$ - $b$  plane. The cryostat windows were made of fused silica, which attenuated the higher frequency components of the THz pulse and the 1-mm diameter aperture attenuated the lower frequency components owing to the larger focal spot size at low frequencies. An example of a THz pulse from this experiment that was measured after having passed through the cryostat windows and the FPC single crystal sample mounted on the 1-mm aperture is shown in Fig. 7.1 [147].

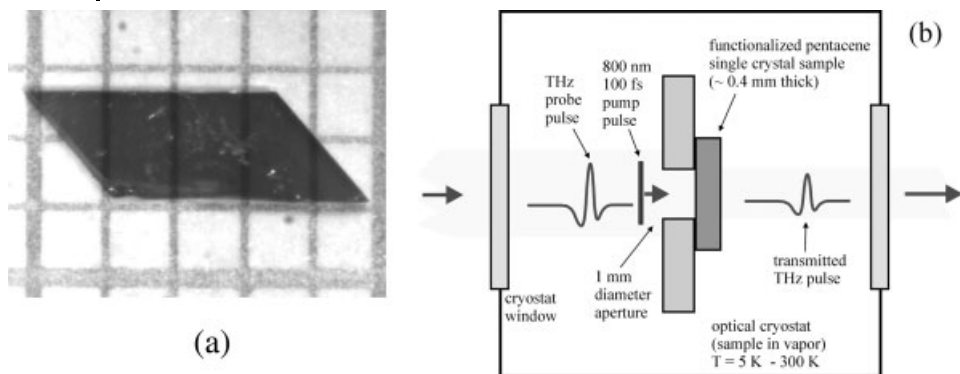


**Figure 7.18** (a) Photograph of a TIPS FPC single crystal grown from solution. The squares are  $1 \times 1$  mm. (b) Schematic of a TIPS FPC sample mounted on a 1-mm diameter aperture in an optical cryostat for TRTS experiments.

Before presenting the results of these experiments, it is important first to discuss the optical and electronic properties of TIPS FPC. The first optical absorption peak of TIPS FPC in solution is at  $\sim 645$  nm (1.92 eV) [132, 149–151]. When FPC is made into a solid thin film, the first absorption peak occurs close to 700 nm (1.77 eV) with an onset for absorption around 750 nm (1.65 eV) [148–151]. For a thick FPC single crystal, the optical absorption edge occurs at 800 nm (1.55 eV) [147, 148, 150] and so 800-nm pump pulses could be absorbed in thick single-crystal samples (but not FPC thin films). Steady-state photoconductivity measurements with an onset around 800 nm were also reported for TIPS FPC single crystals [132]. Interestingly, temperature-dependent resistivity measurements give a bandgap as small as 0.6 eV ( $\lambda_G = 2.1 \mu\text{m}$ ) for TIPS FPC [318], and electronic band structure calculations by Haddon et al. [59] estimate the bandgap at about 0.45 eV ( $\lambda_G = 2.8 \mu\text{m}$ ) along the *b*-axis. However, the optical absorption for  $\lambda > 850$  nm in FPC single crystals is small compared with the absorption for  $\lambda < 800$  nm. Other calculations estimate the energy gap for TIPS FPC to be 1.89 eV (656 nm) [64]. For comparison (as discussed in Section 7.1), the calculated bandgap for pentacene single crystals is about 2.2 eV ( $\lambda_G = 564$  nm) [61], but the first optical absorption peak in Pc thin films is at 670 nm (1.85 eV) with an onset near 700 nm (1.77 eV) [148, 149], which is due to singlet exciton absorption [48, 49, 61]. Recent steady-state photoconductivity measurements on Pc single crystals have observed a photocurrent yield of about 3% close to the first optical absorption peak at 1.85 eV, which was attributed to singlet-to-triplet exciton decay followed by interactions of triplet excitons with trapped carriers, but the exact origin of the photocurrent yield below 2.2 eV is not completely understood [131].

Returning to the TRTS experiments on FPC single crystals [147], the modulation in the transmission of the peak of the THz pulse is then measured as a function of delay time between the THz probe pulse and the optical pump pulse. According to Eq. (7.21), the transient photoconductivity in the sample is proportional to the

negative differential transmission  $-\Delta T/T_0$  of the main peak of the THz pulse. Figure 7.19 shows the transient photoconductivity induced by 800-nm, 100-fs pump pulses in an FPC single crystal as a function of temperature down to 10 K [147]. There was no significant temporal shift in the peak of the THz wave form upon excitation of the sample by the pump pulse. The transient signals have a fast initial decay over the first 2–3 ps and then decay more slowly at longer times. The exact origin of the decay dynamics is not understood. One reason might be fast carrier relaxation due to carrier trapping in defect states in these solution-grown samples, but preliminary TRTS measurements on high-purity pentacene and tetracene single crystals have shown similar fast decay times [152]. The slow decay over longer time-scales shows a power-law behavior (see Figs. 7.25 and 7.26), which is reminiscent of dispersive transport [147, 148, 150]. One of the main features of the TRTS results in Fig. 7.19, however, is that the magnitude of the transient photoconductivity signals increases as the temperature decreases. According to Eq. (7.24), the carrier mobility is proportional to the peak value of the negative differential transmission, and so this behavior is interpreted as evidence for band-like transport in these organic crystals where the mobility *increases* as the temperature *decreases*, as discussed in Section 7.1. Using Eq. (7.24), the lower limit for the carrier mobility (assuming  $\eta = 1$ ) is 1.6 and  $0.2 \text{ cm}^2 \text{ V}^{-1} \text{ s}^{-1}$  at 10 K and room temperature, respectively [147]. If the charge photogeneration efficiency is only 10% ( $\eta = 0.1$ ), as reported in MEH-PPV films [90–92] or in Pc single crystals above 2.5 eV [131], then the corresponding mobilities according to Eq. (7.24) would be 16 and  $2 \text{ cm}^2 \text{ V}^{-1} \text{ s}^{-1}$  at 10 K and room temperature, respectively. For comparison, room temperature FET measurements on evaporated FPC thin films exhibited mobilities up to  $0.4 \text{ cm}^2 \text{ V}^{-1} \text{ s}^{-1}$  [320], and recent FET measurements on solution-deposited FPC films showed mobilities as high as  $0.17 \text{ cm}^2 \text{ V}^{-1} \text{ s}^{-1}$  [321]. The TRTS

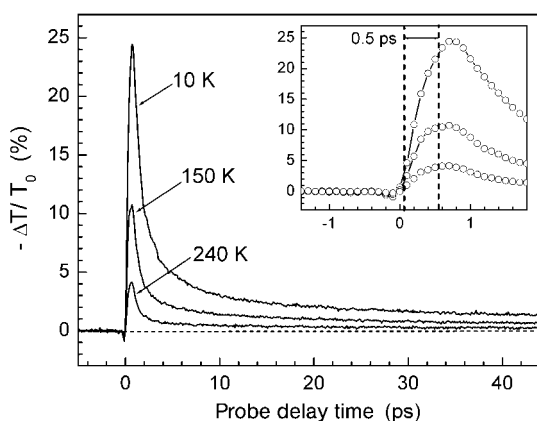


**Figure 7.19** TRTS measurements of transient photoconductivity in functionalized pentacene (TIPS FPC) single crystals as a function of temperature. 800-nm, 100-fs pump pulses

were used to excite the TIPS crystal. The fast, 0.5-ps rise time of the transient response (inset) is limited by the time resolution of the THz pulse setup. Adapted from Ref. [147].

results, therefore, are consistent with the FET measurements for carrier mobility in FPC. Furthermore, the rise time of the photoconductive signal is about 0.5 ps, as shown in the inset of Fig. 7.19, which is limited by the time resolution of the TRTS setup. The formation of mobile charge carriers in FPC, therefore, is expected to occur over time-scales shorter than 0.5 ps.

Similar TRTS studies have been performed by Ostroverkhova et al. [148, 149, 151] on polycrystalline, vacuum-deposited Pc and FPC thin films, as shown in Fig. 7.20. In this case, 580-nm (2.1-eV), 100-fs pulses from an optical parametric amplifier (OPA) were used to excite the films, which ensured that most of the pump pulse energy was absorbed within the films. As can be seen in Fig. 7.20a, the magnitude of the room temperature transient signals from the thin-film samples was typically much less than that observed from FPC single crystals, but both thin-film and single-crystal samples exhibited the same fast decay over the first few picoseconds. At first, single exponential decays were reported for the Pc and FPC thin-film samples [148], but more recent results have shown power-law decays in the FPC thin-film samples similar to what is seen in FPC single crystals [149]. Transient behavior in the thin film samples that more closely matches that of the single crystals is indicative of better film quality [149]. Using Eq. (7.25) and the peak values of the FPC crystal, Pc film and FPC film transient signals in Fig. 7.20a, the room temperature carrier mobility and charge photogeneration efficiency products are  $\mu\eta \approx 0.19, 0.02$  and  $0.025 \text{ cm}^2 \text{ V}^{-1} \text{ s}^{-1}$ , respectively [148]. In general, Pc films were found to have room temperature  $\mu\eta$  products in the range 0.02–0.04  $\text{cm}^2 \text{ V}^{-1} \text{ s}^{-1}$ , whereas FPC films were in the range of 0.01 to 0.06  $\text{cm}^2 \text{ V}^{-1} \text{ s}^{-1}$ , depending on the film morphology [149].

Figure 7.20b shows reference [ $E_0(t)$ ] and modulated [ $-\Delta E(t)$ ] THz wave forms near  $\Delta t = 0$  for a Pc thin film excited with 580-nm pump pulses at a fluence of about  $1 \text{ mJ cm}^{-2}$  [148]. The corresponding complex conductivity was extracted using Eq. (7.18) and is shown in Fig. 7.20c. The real part of the conductivity ( $\sigma_1$ ) is roughly frequency independent over the range from 0.5 to 2.5 THz and the imaginary component ( $\sigma_2$ ) is almost zero. This is indicative of a Drude-like response for a highly resistive metal with  $\omega\tau \ll 1$ , as shown in Fig. 7.6f. The fact that  $\sigma_2$  is not negative and that  $\sigma_1 \gg \sigma_2$  rules out the possibility that some Lorentz oscillator (i.e. exciton) is responsible for the observed transient photoconductivity in the sample [148] (see Section 7.5).

The temperature dependence of the  $\mu\eta$  product from TRTS experiments on a variety of organic semiconductor single crystals and thin films is shown in Fig. 7.21 [147, 148, 152]. In all cases, band-like transport is observed where the mobility increases as the temperature decreases. The data shown in Fig. 7.21 also represent the first measurement of band-like transport in Pc and FPC thin films [148]. The solid line in Fig. 7.21 is a power-law fit to the thin-film data of the form  $\mu\eta \propto T^{-n}$ , where  $n \approx 0.32$ . This is certainly not as large an exponent as  $n = 2.90$  obtained for high-purity naphthalene single crystals [24], but it is consistent with other TRTS results on Pc single crystals by Thorsmølle et al. [153], where band-like transport with  $n = 0.27$  was observed (see also Fig. 7.23). However, Ostroverkhova et al. [148, 152] observe band-like behavior in Pc and FPC single crystals that seems to follow an exponential temperature dependence given by

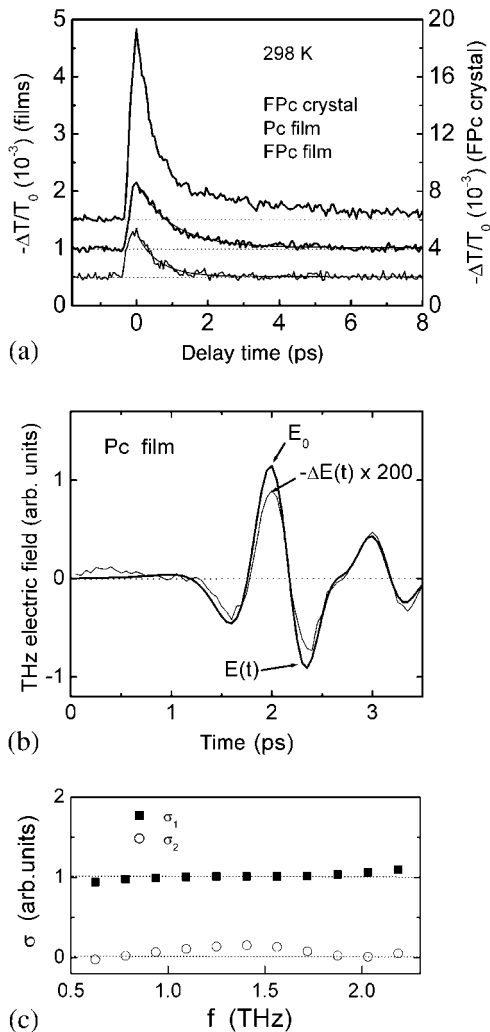


**Figure 7.20** (a) TRTS measurements of transient photoconductivity in pentacene (Pc) and functionalized pentacene (FPc) thin films and a FPc single crystal at room temperature using 580-nm, 100-fs pump pulses at a fluence  $F \approx 1 \text{ mJ cm}^{-2}$  (note the scale change for thin films versus single crystals). The THz

wave form transmitted through the unexcited sample (thick line) and the change in transmission  $-\Delta E$  upon excitation of the Pc thin film sample close to  $\Delta t = 0$  (thin line) is shown in (b). (c) Extracted values for the complex conductivity of the Pc thin film sample at room temperature. Adapted from Ref. [148].

$\mu\eta = 2.3\exp(-T/T^*) \text{ cm}^2 \text{ V}^{-1} \text{ s}^{-1}$ , where  $T^* = 115 \text{ K}$  (9.9 meV) (dashed line in Fig. 7.21). The nature of this exponential behavior in the band-like transport is not understood, especially since most theoretical models predict power-law behavior, as discussed in Section 7.1 [49, 51, 56]. There are, however, some theoretical models in the nearly small molecular polaron picture that predict exponential behavior

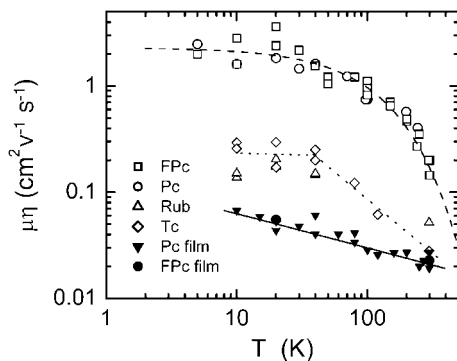


**Figure 7.21** Temperature ( $T$ ) dependence of the product of charge carrier mobility  $\mu$  and photogeneration efficiency  $\eta$  in functionalized pentacene (FPc), pentacene (Pc), rubrene (Rub) and tetracene (Tc) single crystals and Pc and FPc thin films. The product  $\mu\eta$  was extracted from the peak value of the transient photoconductivity in the TRTS experiments. The solid line is a power law fit,  $\mu\eta \sim T^{-n}$ , to

the thin-film data with  $n = 0.32$ . The dashed line is a single exponential fit to the FPc and Pc single crystal data of  $\mu\eta = 2.3\exp(-T/T^*)$   $\text{cm}^2 \text{V}^{-1} \text{s}^{-1}$ , where  $T^* = 115 \text{ K}$  (9.9 meV). The dotted line is a guide to the eye for the single-crystal Rub and Tc data, with the high-temperature portion plotted as  $\mu\eta \sim T^{-1}$ . Adapted from Ref. [152].

in the temperature dependence of the effective mass of molecular polarons at low temperatures of the form  $m(T) \approx m(0)\exp(T/T_0)$  [49, 51].

According to Fig. 7.21, the room temperature products  $\mu\eta$  for rubrene (Rub) and Pc single crystals are at best  $0.05$  and  $0.3 \text{ cm}^2 \text{V}^{-1} \text{s}^{-1}$ , respectively. However, FET measurements made on similar rubrene crystals have reported room temperature mobilities as high as  $20 \text{ cm}^2 \text{V}^{-1} \text{s}^{-1}$  [42] and SCLC measurements on similar Pc single crystals have shown mobilities up to  $35 \text{ cm}^2 \text{V}^{-1} \text{s}^{-1}$  at room temperature [38]. The TRTS results for the product  $\mu\eta$  would therefore suggest that the charge photogeneration efficiency is  $\eta \approx 0.003$  for rubrene and  $\eta \approx 0.008$  for Pc, but more work is needed to understand these results.

Finally, the room temperature product  $\mu\eta$  as a function of wavelength for FPc single crystals and Pc and FPc thin films is shown in Fig. 7.22. Approximately wavelength-independent behavior is observed for all the samples over a broad range of wavelengths right up to the onset of optical absorption in each sample [148], which is inconsistent with the molecular exciton model. Even though wavelength-independent photogeneration efficiency has been observed in MEH-PPV films [90–92, 123], most experiments on organic semiconductors report wavelength-dependent behavior with a threshold for charge generation above the onset of optical absorption determined by the exciton binding energy [48, 49, 88] (see also Section 7.1).

TRTS measurements on Pc single crystals by Thorsmølle et al. [153] are shown in Fig. 7.23. In these experiments, 400-nm, 50-fs pump pulses with fluences up to  $0.8 \text{ mJ cm}^{-2}$  from an amplified Ti:sapphire laser source were used to produce carrier densities up to  $1.1 \times 10^{18} \text{ cm}^{-3}$  in the Pc single crystal samples. Fast, sub-pico-second rise times and decay times are observed in the TRTS transients taken at

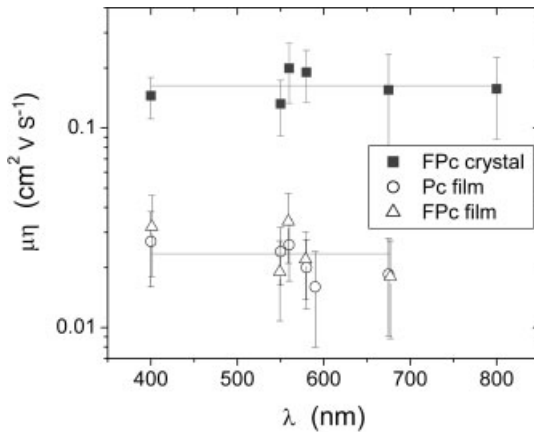


**Figure 7.22** Wavelength dependence of the product of charge carrier mobility  $\mu$  and photogeneration efficiency  $\eta$  in Pc thin films, FPc thin films and FPc single crystals. The solid lines are guides to the eye for a wavelength independent photoreponse. Adapted from Ref. [148].

20 K, as shown in Fig. 7.23a. The THz wave form scans in Fig. 7.23b reveal Drude-like behavior in Fig. 7.23c with a nearly frequency-independent  $\sigma_1$  and an approximately zero  $\sigma_2$ , as observed by Ostroverkhova et al. [148] in polycrystalline Pc thin films. Figure 7.23d shows band-like transport in the temperature dependence of the carrier mobility that follows a power-law behavior  $\mu \sim T^{-n}$ , where  $n \approx 0.27$ , which is close to  $n \approx 0.32$  observed by Ostroverkhova et al. [148] in polycrystalline Pc thin films but not in Pc single crystals [152] (Fig. 7.21). The lower limit for the carrier mobility at 30 K was found to be about  $0.4 \text{ cm}^2 \text{V}^{-1} \text{s}^{-1}$ , which is smaller than the product  $\mu\eta$  of about  $1.5 \text{ cm}^2 \text{V}^{-1} \text{s}^{-1}$  obtained in Pc single crystals at 30 K by Ostroverkhova et al. [152], as shown in Fig. 7.21. Thorsmølle et al. concluded that the transient photoconductivity observed in Pc single crystals was due to primary photoexcitations of mobile charge carriers.

One question that arises is how band-like transport can be observed by TRTS in polycrystalline Pc (and FPc) thin films that typically show thermally-activated or (at best) temperature-independent mobility under DC conditions [12, 19, 20]. The answer lies in the fact that TRTS measurements are non-contact *and* ultrafast, which enables the intrinsic properties within the grains of polycrystalline films to be measured over short time-scales before the carriers have a chance to relax through recombination or trapping at defect sites. The relaxation dynamics that follow over longer time-scales can also be probed by TRTS and provide useful information on carrier dynamics and transport in the system. Steady-state (DC) conductivity measurements with contacted samples, as shown in Fig. 7.24a, force current to travel through the grain boundaries between crystallites in the film. The grain boundaries are full of defect sites which tend to trap carriers and limit the current flow. As the temperature decreases, thermal excitation out of the traps

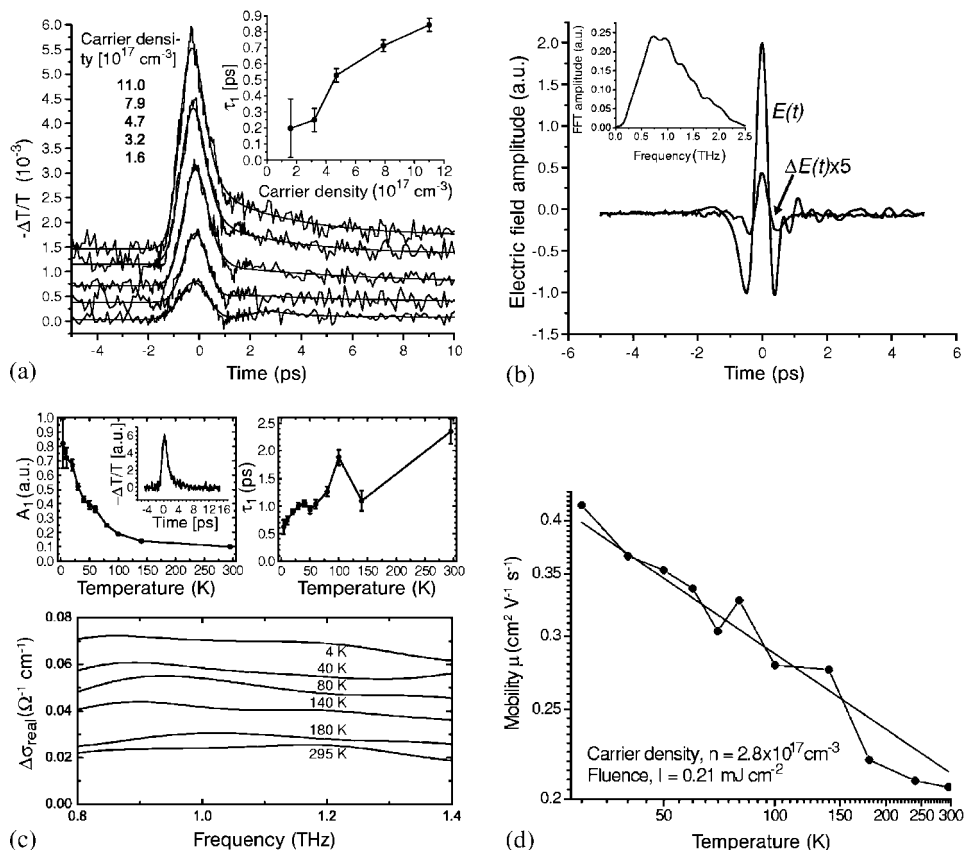


**Figure 7.23** (a) TRTS measurements of transient photoconductivity in pentacene (Pc) single crystals excited by 400-nm, 50-fs pump pulses at a temperature of 20 K and various fluences. The decay times from single-exponential fits to the transients are shown in the inset as a function of pump fluence. (b) The electric field of the THz pulse,  $E(t)$ , transmitted through the unexcited Pc sample and the change,  $-\Delta E(t)$ , in transmission due to excitation by the pump pulse at 4 K. The inset shows the Fourier transform of the THz

pulse. (c) Temperature dependence of the amplitude and decay times of the transient photoconductivity signals. The frequency dependence of the real part of the conductivity induced in the sample is also shown as a function of temperature. The change in the imaginary component of the conductivity was close to zero. (d) Transient carrier mobility as a function of temperature assuming  $\eta = 100\%$ . The solid line is a fit to the data to  $\mu \sim T^{-n}$ , where  $n = 0.27$ . Reproduced from Ref. [153], with permission.

becomes less likely and the conductivity of the film decreases. The nature of the contacts themselves can be problematic, and so DC conductivity measurements may end up probing the extrinsic properties of the film. On the other hand, TRTS measurements can probe the intrinsic conductivity within the individual crystallites, as depicted in Fig. 7.24b, where the high-frequency electric field of the THz probe pulse essentially “shakes” carriers back and forth within the crystallite rather than forcing them across the grain boundaries.

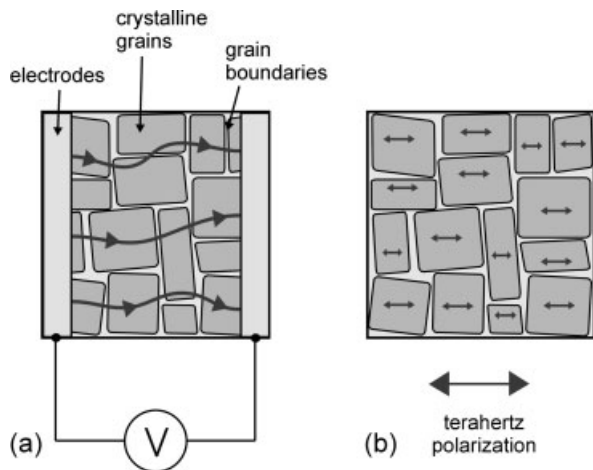


**Figure 7.24** Comparison between (a) steady-state (DC) and (b) THz measurements of the conductivity of polycrystalline organic semiconductor thin films.

The non-contact nature of TRTS experiments and the resolution-limited rise time of the TRTS transients observed in both single-crystal and thin-film samples implies that charge formation can occur in zero external electric field over time-scales less than 0.4–0.5 ps (see inset of Fig. 7.19 and Refs. [147] and [148]). This means that electric-field-induced exciton dissociation mechanisms with charge formation times from 10–100 ps [98, 99, 107, 108] (see Section 7.1) cannot apply. (The magnitude of the THz pulse electric field at the sample was  $<10^3 \text{ V cm}^{-1}$ , which is far too small to induce any significant dissociation of excitons.) The fact that the magnitude of the transient photoconductive response increases as the temperature decreases, as shown in Figs. 7.19, 7.21 and 7.23d disagrees with thermally induced exciton dissociation mechanisms that predict the opposite behavior. Hot exciton models predict a temperature-independent charge generation efficiency if the excess energy is larger than the thermal energy at higher temperatures, but such behavior is not seen here. Furthermore, the wavelength independence of the transient photoconductive response shown in Fig. 7.22 disagrees with hot exciton models that predict higher exciton dissociation rates at higher photon energies. The Drude-like response with a frequency-independent  $\sigma_1$  and a nearly zero  $\sigma_2$  seen at early times in Pc thin films [148] (Fig. 7.20c) and single crystals [153] (Fig. 7.23c) rules out the possibility that the transient photoconductivity signal is due to some kind of excitonic contribution. All these results suggest that mobile charge carriers are one of the primary photoexcitations in organic molecular crystals such as pentacene and functionalized pentacene and do not necessarily form as a result of some exciton dissociation process associated with the molecular exciton model (see Section 7.1).

Of course, more work is needed to understand the TRTS results. One outstanding issue is the nature of the power-law decay of the form  $\Delta t^{-\beta}$  observed in the

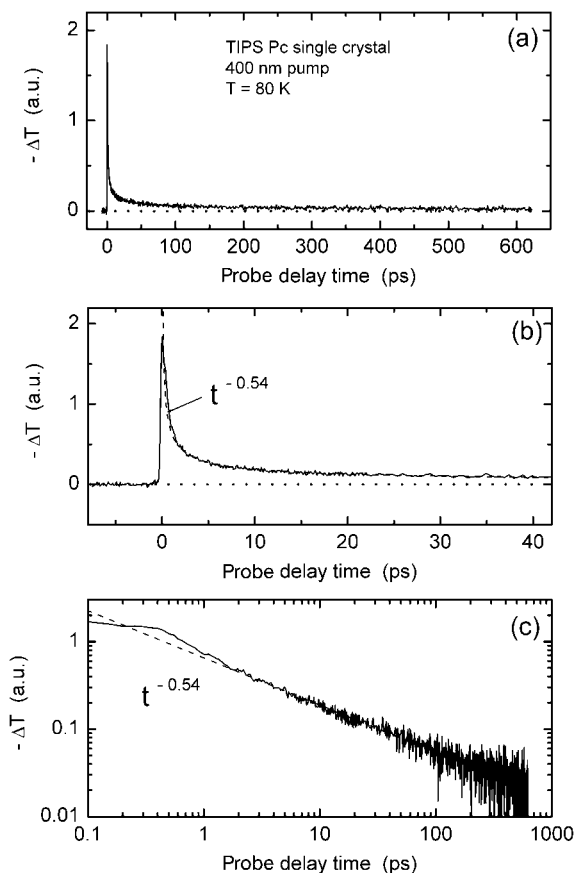


**Figure 7.25** (a) Long-time scan of transient photoconductivity in a TIPS FPC single crystal excited by 400-nm pump pulses at 80 K. (b) Closer look at early time-scales. The dashed line shows a simple power-law decay

of  $-\Delta T \sim t^{-0.54}$ . (c) Log-log plot of the same data showing a power-law decay over two orders of magnitude in time. Adapted from Ref. [150].

transient photoconductivity of FPC single crystals [147–149, 151] and thin films [148, 149, 151] at all temperatures. An example of this decay with the same power-law exponent of  $\beta = 0.54$  over two orders of magnitude in time is shown in Fig. 7.25 for 400-nm pump pulses photoexciting an FPC single crystal at 80 K [150]. Another example of transient photoconductivity in an FPC single crystal pumped with 400-nm pulses at 50 K is shown in Fig. 7.26. A power-law decay with  $\beta = 0.7$  is clearly seen in the inset of Fig. 7.26. The power-law exponent becomes slightly larger at lower temperatures, starting at  $\beta = 0.47$  near room temperature and reaching  $\beta = 0.7$  at 50 K before falling back slightly at 10 K [147]. The power-law decay has been attributed to dispersive carrier transport with a roughly temperature-independent exponent, similar to what has been observed in polyvinylcarb-

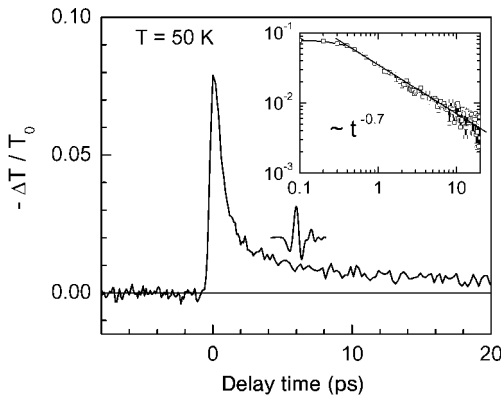


**Figure 7.26** TRTS measurement of transient photoconductivity in a TIPS FPC single crystal at 50 K. The sample was excited with 400-nm pump pulses at a fluence of about  $0.6 \text{ mJ cm}^{-2}$ . The sample was about  $200 \mu\text{m}$  thick, much larger than the optical penetration depth at 400 nm of  $\sim 1 \mu\text{m}$ . The corresponding initial photoexcited carrier density, assuming  $\eta = 1$ ,

would be  $1.2 \times 10^{19} \text{ cm}^{-3}$ . The THz waveform indicates where the conductivity of the sample was measured at a 6 ps delay time after the peak of the transient response. If the transient decay corresponds to a reduction in carrier density, then at 6 ps delay time  $n \approx 1.4 \times 10^{18} \text{ cm}^{-3}$ . The inset shows a power-law decay of the transient photoconductivity of  $t^{-0.7}$ .

azole [322], polyacetylene [323] and  $\text{C}_{60}$  thin films [45], owing to non-activated tunneling between isoenergetic sites [51, 324].

To examine this further, a THz pulse scan is taken 6 ps after photoexcitation by the pump pulse, as shown by the THz waveform in Fig. 7.26, which is well into the power-law decay region where the transient photoconductivity does not change significantly over the duration of the THz pulse. The frequency-dependent conductivities  $\sigma_1$  and  $\sigma_2$  extracted from the THz waveforms at this delay time are given in Fig. 7.27a. The dashed lines are guides to the eye showing an almost linear dependence extrapolating to zero for both a positive-valued  $\sigma_1$  and a negative-valued  $\sigma_2$ , which is obviously non-Drude-like. We now try to fit this data using some of the models presented in Section 7.5. Since dispersive carrier motion in disordered materials is related to carrier localization effects and considering the low-frequency behavior of the data, the first choice is the Drude–Smith model which is given in Eq. (7.12) and plotted in Fig. 7.8d–f for  $c$ -parameters from 0 (Drude model) to  $-1$  (complete carrier localization). From the pump laser fluence, the absorbed excitation density is  $1.2 \times 10^{19} \text{ cm}^{-3}$ , and if we assume  $\eta = 1$  we then have a maximum photoexcited charge carrier density of  $1.4 \times 10^{18} \text{ cm}^{-3}$  at a delay time of 6 ps (assuming  $n \propto -\Delta T$ ), which leaves  $\tau$ ,  $m$  and  $c$  as fitting parameters. The best attempt of a Drude–Smith fit to the data is shown in Fig. 7.27b with  $\tau = 31 \text{ fs}$ ,  $m = 3.7m_e$  and  $c = -0.94$ , which is very close to localized behavior. (The frequency range up to 8 THz is plotted to show what the model does at higher frequencies.) Even though the fit may be acceptable for  $\sigma_1$ , it does not seem to simultaneously fit the  $\sigma_2$  data. If the power-law decay in the transient photoconductivity is due to polarization of excitons, then it might be possible to fit the data to a Lorentz oscillator which also gives a posi-

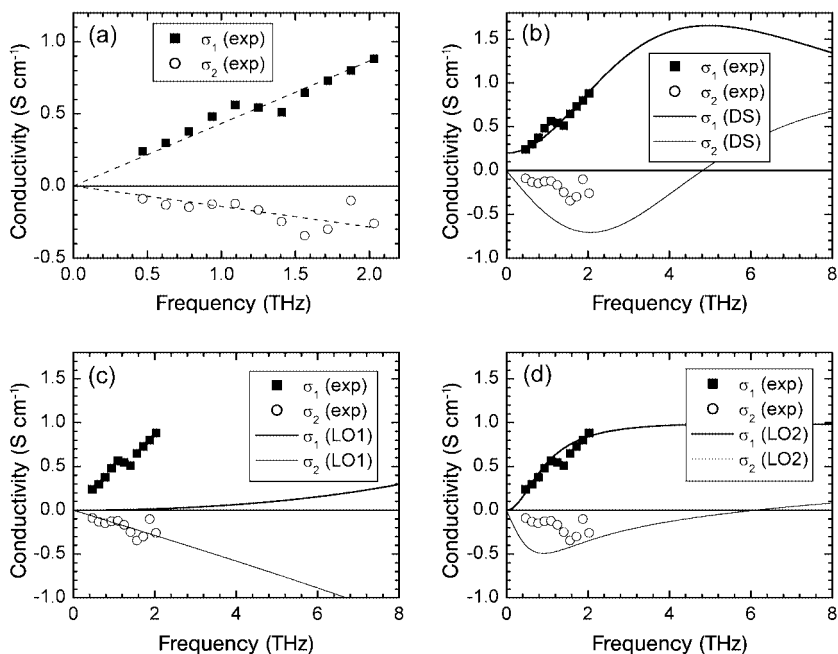


**Figure 7.27** (a) TRTS measurement of the real ( $\sigma_1$ , solid squares) and imaginary ( $\sigma_2$ , open circles) components of the complex conductivity of a TIPS FpC single crystal 6 ps after photoexcitation with 400-nm pump pulses at 50 K (see Fig. 7.26). The dashed lines are guides to the eye showing an almost linear frequency dependence for both components. (b) Attempt to fit  $\sigma_1$  of the experimental (exp) data with a Drude–Smith (DS)

model with  $c = -0.94$ ,  $\tau = 31$  fs,  $m = 3.7m_e$  and a photoexcited carrier density of  $n = 1.40 \times 10^{18} \text{ cm}^{-3}$ . (c) Comparison of the data with a Lorentz oscillator (LO1) with  $f_L = 24.2$  THz (100 meV) and  $\tau_L = 10$  fs ( $1/2\pi\tau_L = 15.9$  THz or 66 meV). (d) Attempt to fit  $\sigma_1$  of the data with a Lorentz oscillator (LO2) with  $f_L = 6.1$  THz (25.2 meV) and  $\tau_L = 4$  fs ( $1/2\pi\tau_L = 40$  THz or 165 meV).

tive  $\sigma_1$  and negative  $\sigma_2$  at low frequencies. Figure 7.27c and d show fits of the data to Lorentz oscillators with center frequencies (and damping times) of 24.2 THz (10 fs) and 6.1 THz (4 fs), respectively. The only way to make the Lorentz model come close to fitting the data is to use rather unrealistic damping times of a few femtoseconds in order to increase  $\sigma_1$  compared with  $\sigma_2$  which, if these were excitons, would be very short-lived. Other models can also be examined, including combinations of models, but Figs 7.26 and 7.27 have been included in this chapter to serve as an example of how difficult the modeling process can become with significant deviations from Drude-like behavior.

Deviations from Drude-like behavior have recently been observed in TRTS experiments by Hendry et al. [154, 155] studying transient photoconductivity in MEH-PPV films and solutions. As described in Fig. 7.28a, these experiments used 400-nm, 150-fs pump pulses to excite  $\sim 20\text{-}\mu\text{m}$  thick MEH-PPV polymer films on quartz substrates at 30 K. The absorbed excitation density was about  $8 \times 10^{20} \text{ cm}^{-3}$ ,

but only a small fraction of this absorbed excitation density was turned into mobile charge carriers [154, 155]. A fast initial decay with a time constant of 0.9 ps is seen in Fig. 7.28b, and a slower decay with a time constant around 200 ps is shown in Fig. 7.28c. (The rise time of the transient signal is 0.3 ps, limited by the time resolution of the setup.) The frequency-dependent conductivity measured 0.5 ps after photoexcitation is shown in Fig. 7.29a and does not exhibit a Drude-like response. The solid and dashed lines in Fig. 7.29a are fits to the data for  $\sigma_1$  and  $\sigma_2$ , respectively, according to a dispersive free charge transport model described by Grozema et al. [144], in which torsional disorder along the polymer backbones introduces carrier localization. The model seems to describe completely the conductivity data at this early time assuming the free carrier density is  $3.2 \times 10^{15} \text{ cm}^{-3}$ , which is  $\sim 10^5$  times less than the initial photoexcited density ( $\eta \approx 10^{-5}$ ). The model, however, overestimates the mobility along the polymer chains by not taking into account other disorder-inducing effects such as conjugation breaks along the chains, and so the upper limit for the charge photogeneration efficiency becomes  $\eta \approx 10^{-2}$ . At later times, as shown in Fig. 7.29b for a delay time of 10 ps after the initial photoexcitation, the conductivity is almost purely imaginary and can be described by dielectric polarization of excitons, as described by Eq. (7.8) in Section 7.5 and the dashed line fit to  $\sigma_2$  in Fig. 7.29b. Adding PCBM as an electron

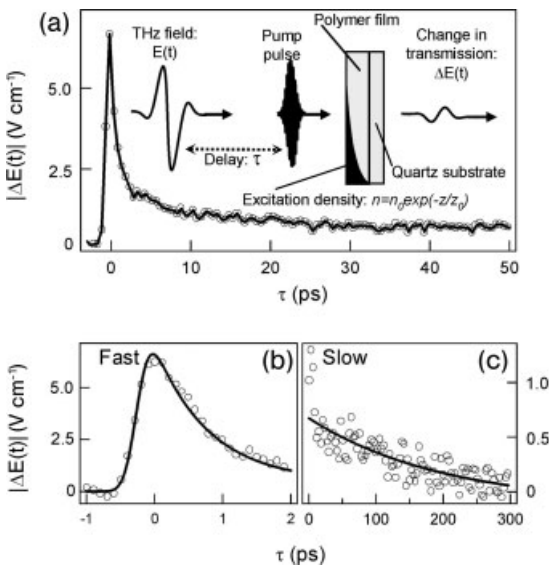


**Figure 7.28** (a) TRTS measurements of transient conductivity in MEH-PPV thin films excited with 400-nm, 150-fs pump pulses at a temperature of 30 K. The films were  $\sim 20 \mu\text{m}$  thick on quartz substrates. (b) A fast initial exponential decay with a time constant of

0.9 ps is observed, followed by a much slower exponential decay (c) with a time constant of about 200 ps. The absorbed pump density is  $\sim 8 \times 10^{20} \text{ cm}^{-3}$  within an optical penetration depth of  $\sim 100 \text{ nm}$ . Reproduced from Ref. [154], with permission.

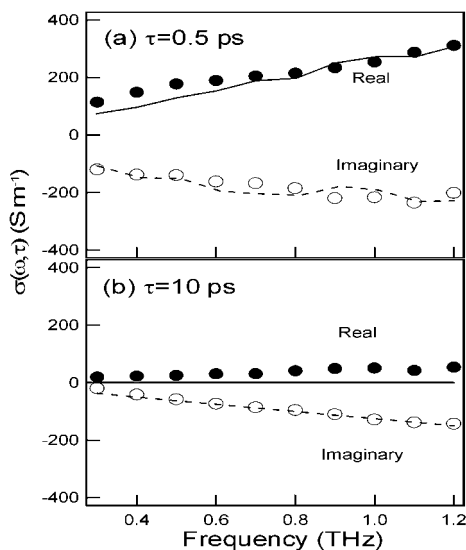


**Figure 7.29** (a) TRTS measurement of the complex conductivity of an MEH-PPV film 0.5 ps after photoexcitation with 400-nm, 150-fs pump pulses at 30 K (see Fig. 7.28). The lines are fits to the data according to a dispersive free charge transport model. Comparison of the model with the data suggests that the free charge density is about  $3.2 \times 10^{15} \text{ cm}^{-3}$  for an absorbed pump density

of  $\sim 8 \times 10^{20} \text{ cm}^{-3}$ , corresponding to low quantum efficiencies for free carriers. (b) Complex conductivity measured 10 ps after the initial excitation. The dashed line is a fit to  $\sigma_2$  of the data using a Lorentz oscillator model due to excitons with a binding energy of 0.8 eV (19.4 THz). Reproduced from Ref. [154], with permission.

scavenger in the MEH-PPV films resulted in a conductivity at a delay time of 10 ps that looked very similar in form to that obtained at 0.5 ps for the pristine MEH-PPV films, which confirmed that the conductivity data at 0.5 ps were due to cooled charge carriers. The initial photogeneration of charge carriers with an upper limit for the photogeneration efficiency of  $\eta = 10^{-2}$  was attributed to hot-exciton dissociation since the transient signals for free charge carriers were twice as large at pump wavelengths of 266 nm compared with 400 nm. The origin of the fast conductivity decay is not exactly known, but it may be due to charge carrier recombination or trapping at defect sites along the chain. Most of the initial photoexcited density ( $\sim 99\%$ ) is in the form of excitons which take a few picoseconds to migrate along the chains to find the lowest energy (and therefore most polarizable) sites. In another TRTS study by Hendry et al. [155], the charge photogeneration efficiency for MEH-PPV in solution ( $\eta \approx 10^{-5}$ ) was 100 times less than in solid films ( $\eta \approx 10^{-3}$ ). This was attributed to enhanced hot-exciton dissociation in solid films due to the proximity of neighboring chains.

## 7.9

## Conclusion

Understanding the nature of photoexcitations and carrier transport in organic semiconductors is not only of fundamental interest but is also vital for the development of applications in organic electronics and photonics. Mechanisms for charge carrier photogeneration and transport are some of the central issues being studied. Terahertz pulses are sensitive to the conductivity in a material and terahertz time-domain spectroscopy (THz-TDS) has been used to study the nature of conduction in conducting polymers and carbon nanotubes. Time-resolved terahertz spectroscopy (TRTS) is an ultrafast, non-contact technique that can be used to probe both the real and imaginary components of the transient photoconductivity in materials with sub-picosecond time resolution. TRTS has been used to study transient photoconductivity in organic molecular crystals, such as pentacene and functionalized pentacene single crystals and thin films, and semiconducting polymers. TRTS is a powerful research tool for probing organic semiconductors.

## Acknowledgments

We acknowledge support from the Natural Sciences and Engineering Research Council of Canada (NSERC), CFI, CIPI, ONR, iCORE and the Killam Trust. We acknowledge collaborations with J. E. Anthony, R. F. Egerton, S. R. Parkin, S. Shcherbyna and R. R. Tykwinski. We also thank V. Podzorov and M. E. Gershenson for supplying rubrene and tetracene single crystals and O. D. Jurchescu and T. T. M. Palstra for supplying pentacene single crystals.

## References

- 1 D. Voss, *Nature* **407**, 442 (2000).
- 2 S. R. Forrest, *Nature* **428**, 911 (2004).
- 3 C. D. Dimitrakopoulos, P. R. L. Malenfant, *Adv. Mater.* **14**, 99 (2002).
- 4 J. R. Sheats, *J. Mater. Res.* **19**, 1974 (2004).
- 5 G. Malliaras, R. Friend, *Phys. Today*, **58** (5), 53 (2005).
- 6 H. Hoppe, N. S. Sariciftci, *J. Mater. Res.* **19**, 1924 (2004).
- 7 N. Peyghambarian, R. A. Norwood, *Opt. Photon. News*, April, 28 (2005).
- 8 I. D. W. Samuel, G. A. Turnbull, *Mater. Today*, September, 28 (2004).
- 9 G. Horowitz, *Adv. Mater.* **10**, 365 (1998).
- 10 M. Halik, H. Klauk, U. Zschieschang, G. Schmid, W. Radlik, S. Ponomarenko, S. Kirchmeyer, W. Weber, *J. Appl. Phys.* **93**, 2977 (2003).
- 11 T. C. Gorjanc, I. Lévesque, M. D'Iorio, *Appl. Phys. Lett.* **84**, 930 (2004).
- 12 S. F. Nelson, Y.-Y. Lin, D. J. Gundlach, T. N. Jackson, *Appl. Phys. Lett.* **72**, 1854 (1998).
- 13 H. Klauk, D. J. Gundlach, T. N. Jackson, *IEEE. Electron Dev. Lett.* **20**, 289 (1999).
- 14 P. F. Baude, D. A. Ender, M. A. Haase, T. W. Kelley, D. V. Muyres, S. D. Theiss, *Appl. Phys. Lett.* **82**, 3964 (2003).
- 15 H. Klauk, M. Halik, U. Zschieschang, F. Eder, G. Schmid, C. Dehm, *Appl. Phys. Lett.* **82**, 4175 (2003).

- 16 M. Halik, H. Klauk, U. Zschieschang, G. Schmid, C. Dehm, M. Schütz, S. Malsch, F. Effenberger, M. Brunnbauer, F. Stellacci, *Nature* **431**, 963 (2004).
- 17 P. V. Pesavento, R. J. Chesterfield, C. R. Newman, C. D. Frisbie, *J. Appl. Phys.* **96**, 7312 (2004).
- 18 M. Shtein, J. Mapel, J. B. Benziger, S. R. Forrest, *Appl. Phys. Lett.* **81**, 268 (2002).
- 19 S. Veerlak, V. Arkhipov, P. Heremans, *Appl. Phys. Lett.* **82**, 745 (2003).
- 20 D. Knipp, R. A. Street, A. R. Völkel, *Appl. Phys. Lett.* **82**, 3907 (2003).
- 21 R. Ruiz, A. C. Mayer, G. G. Malliaras, B. Nickel, G. Scoles, A. Kazimirov, H. Kim, R. L. Headrick, Z. Islam, *Appl. Phys. Lett.* **85**, 4926 (2004).
- 22 G. Witte, C. Wöll, *J. Mater. Res.* **19**, 1889 (2004).
- 23 Z. Rang, M. I. Nathan, P. P. Ruden, R. Chesterfield, C. D. Frisbie, *Appl. Phys. Lett.* **85**, 5760 (2004).
- 24 W. Warta, N. Karl, *Phys. Rev. B* **32**, 1172 (1985).
- 25 W. Warta, R. Stehle, N. Karl, *Appl. Phys. A* **36**, 163 (1985).
- 26 N. Karl, K.-H. Kraft, J. Marktanner, M. Münch, F. Schatz, R. Stehle, H.-M. Uhde, *J. Vac. Sci. Technol. A* **17**, 2318 (1999).
- 27 N. Karl, *Synth. Met.* **133–134**, 649 (2003).
- 28 N. Karl, in *Organic Electronic Materials: Conjugated Polymers, Low Molecular Weight Organic Solids*, edited by R. Farchioni, G. Grosso, Springer, Berlin, 2001, . Chapters 6 and 8
- 29 A. N. Aleshin, J. Y. Lee, S. W. Chu, J. S. Kim, Y. W. Park, *Appl. Phys. Lett.* **84**, 5383 (2004).
- 30 R. W. I. de Boer, T. M. Klapwijk, A. F. Morpurgo, *Appl. Phys. Lett.* **83**, 4345 (2003).
- 31 R. W. I. de Boer, M. Jochemsen, T. M. Klapwijk, A. F. Morpurgo, J. Niemax, A. K. Tripathi, J. Pflaum, *J. Appl. Phys.* **95**, 1196 (2004).
- 32 R. W. I. de Boer, M. E. Gershenson, A. F. Morpurgo, V. Podzorov, *Phys. Status Solidi A* **201**, 1302 (2004).
- 33 V. Y. Butko, X. Chi, A. P. Ramirez, *Solid State Commun.* **128**, 431 (2003).
- 34 C. R. Newman, R. J. Chesterfield, J. A. Merlo, C. D. Frisbie, *Appl. Phys. Lett.* **85**, 422 (2004).
- 35 C. Goldmann, S. Haas, C. Krellner, K. P. Pernstich, D. J. Gundlach, B. Batlogg, *J. Appl. Phys.* **96**, 2080 (2004).
- 36 V. Y. Butko, X. Chi, D. V. Lang, A. P. Ramirez, *Appl. Phys. Lett.* **83**, 4773 (2003).
- 37 D. V. Lang, X. Chi, T. Siegrist, A. M. Sargent, A. P. Ramirez, *Phys. Rev. Lett.* **93**, 076601 (2004).
- 38 O. D. Jurchescu, J. Baas, T. T. M. Palstra, *Appl. Phys. Lett.* **84**, 3061 (2004).
- 39 V. Podzorov, V. M. Pudalov, M. E. Gershenson, *Appl. Phys. Lett.* **82**, 1739 (2003).
- 40 V. Podzorov, S. E. Sysoev, E. Loginova, V. M. Pudalov, M. E. Gershenson, *Appl. Phys. Lett.* **83**, 3504 (2003).
- 41 V. C. Sundar, J. Zaumseil, V. Podzorov, E. Menard, R. L. Willett, T. Someya, M. E. Gershenson, J. A. Rogers, *Science* **303**, 1644 (2004).
- 42 V. Podzorov, E. Menard, A. Borissov, V. Kiryukhin, J. A. Rogers, M. E. Gershenson, *Phys. Rev. Lett.* **93**, 086602 (2004).
- 43 Z. Rang, M. I. Nathan, P. P. Ruden, V. Podzorov, M. E. Gershenson, C. R. Newman, C. D. Frisbie, *Appl. Phys. Lett.* **86**, 123501 (2005).
- 44 M. Mas-Torrent, P. Hadley, S. T. Bromley, N. Crivillers, J. Veciana, C. Rovira, *Appl. Phys. Lett.* **86**, 012110 (2005).
- 45 R. Zeis, T. Siegrist, Ch. Kloc, *Appl. Phys. Lett.* **86**, 022103 (2005).
- 46 O. Madelung (Editor), *Semiconductors – Basic Data*, 2nd edn, Springer, Berlin, 1996.
- 47 L. B. Schein, C. B. Duke, A. R. McGhie, *Phys. Rev. Lett.* **40**, 197 (1978).
- 48 M. Pope, C. E. Swenberg, *Electronic Processes in Organic Crystals and Polymers*, 2nd edn., Oxford University Press, New York, 1999.
- 49 E. A. Silinsh, V. Čápec, *Organic Molecular Crystals: Interaction, Localization and Transport Phenomena*, American Institute of Physics, New York, 1994.
- 50 C. B. Duke, L. B. Schein, *Phys. Today*, February, 42 (1980).

- 51 E. A. Silinsh, A. Klimkans, S. Larsson, V. Capek, *Chem. Phys.* **198**, 311 (1995).
- 52 D. Emin, *Phys. Rev. B* **61**, 14543 (2000).
- 53 V. Coropceanu, M. Malagoli, D. A. da Silva Filho, N. E. Gruhn, T. G. Bill, J. L. Bredas, *Phys. Rev. Lett.* **89**, 275503 (2002).
- 54 L. Giuggioli, J. D. Andersen, V. M. Kenkre, *Phys. Rev. B* **67**, 045110 (2003).
- 55 Y. C. Cheng, R. J. Silbey, D. A. da Silva Filho, J. P. Calbert, J. L. Bredas, *J. Chem. Phys.* **118**, 3764 (2003).
- 56 K. Hannewald, P. A. Bobbert, *Appl. Phys. Lett.* **85**, 1535 (2004).
- 57 K. Hannewald, V. M. Stojanovic, J. M. T. Schellekens, P. A. Bobbert, G. Kresse, J. Hafner, *Phys. Rev. B* **69**, 075211 (2004).
- 58 K. Hannewald, P. A. Bobbert, *Phys. Rev. B* **69**, 075212 (2004).
- 59 R. C. Haddon, X. Chi, M. E. Itkis, J. E. Anthony, D. L. Eaton, T. Siegrist, C. C. Matheus, T. T. M. Palstra, *J. Phys. Chem. B* **106**, 8288 (2002).
- 60 E. V. Tsiper, Z. G. Soos, *Phys. Rev. B* **68**, 085301 (2003).
- 61 M. L. Tiago, J. E. Northrup, S. G. Louie, *Phys. Rev. B* **67**, 115212 (2003).
- 62 K. Hummer, P. Puschnig, C. Ambrosch-Draxl, *Phys. Rev. B* **67**, 184105 (2003).  
K. Hummer, P. Puschnig, C. Ambrosch-Draxl, *Phys. Rev. Lett.* **92**, 147402 (2004).
- 63 G. Brocks, J. van den Brink, A. F. Morpurgo, *Phys. Rev. Lett.* **93**, 146405 (2004).
- 64 A. Maliakal, K. Raghavachari, H. Katz, E. Chandross, T. Siegrist, *Chem. Mater.* **16**, 4980 (2004).
- 65 A. Troisi, G. Orlandi, *J. Phys. Chem. B* **109**, 1849 (2005).
- 66 K. Hummer, C. Ambrosch-Draxl, *Phys. Rev. B* **71**, 081202 (2005).
- 67 J. Shinar (Editor), *Organic Light-Emitting Devices: a Survey*, Springer, New York, 2004.
- 68 R. H. Friend, R. W. Gymer, A. B. Holmes, J. H. Burroughes, R. N. Marks, C. Taliani, D. D. C. Bradley, D. A. Dos Santos, J. L. Bredas, M. Logdlund, W. R. Salaneck, *Nature* **397**, 121 (1999).
- 69 M. A. Baldo, M. E. Thompson, S. R. Forrest, *Nature* **403**, 750 (2000).
- 70 Q. Xu, H. M. Duong, F. Wudl, Y. Yang, *Appl. Phys. Lett.* **85**, 3357 (2004).
- 71 D. Qin, Y. Tao, *Appl. Phys. Lett.* **86**, 113507 (2005).
- 72 A. Hepp, H. Heil, M. Ahles, R. Schmechel, H. von Seggern, *Phys. Rev. Lett.* **91**, 157406 (2003).
- 73 C. Santato, I. Mununza, A. Bonfiglio, F. Cicoira, P. Cosseddu, R. Zamboni, M. Muccini, *Appl. Phys. Lett.* **86**, 141106 (2005).
- 74 J. Reynaert, D. Cheyns, D. Janssen, R. Muller, V. I. Arkhipov, J. Genoe, G. G. Borghs, P. Heremans, *J. Appl. Phys.* **97**, 114501 (2005).
- 75 V. G. Kozlov, V. Bulovic, P. E. Burrows, S. R. Forrest, *Nature* **389**, 362 (1997).
- 76 D. Pisignano, M. Anni, G. Gigli, R. Cingolani, M. Zavelani-Rossi, G. Lanzani, G. Barbarella, L. Favaretto, *Appl. Phys. Lett.* **81**, 3534 (2002).
- 77 J. R. Lawrence, G. A. Turnbull, I. D. W. Samuel, *Appl. Phys. Lett.* **82**, 4023 (2003).
- 78 M. Granstrom, K. Petritsch, A. C. Arias, A. Lux, M. R. Andersson, R. H. Friend, *Nature* **395**, 257 (1998).
- 79 C. J. Brabec, N. S. Sariciftci, J. C. Hummelen, *Adv. Funct. Mater.* **11**, 15 (2001).
- 80 P. Peumans, A. Yakimov, S. R. Forrest, *J. Appl. Phys.* **93**, 3693 (2003).
- 81 J. Nelson, J. Kirkpatrick, P. Ravirajan, *Phys. Rev. B* **69**, 035337 (2004).
- 82 S. A. McDonald, G. Konstantatos, S. Zhang, P. W. Cyr, E. J. D. Klem, L. Levina, E. H. Sargent, *Nat. Mater.* **4**, 138 (2005).
- 83 G. Yu, Y. Cao, J. Wang, J. McElvain, A. J. Heeger, *Synth. Met.* **102**, 904 (1997).
- 84 P. Peumans, V. Bulovic, S. R. Forrest, *Appl. Phys. Lett.* **76**, 3855 (2000).
- 85 G. Matsunobu, Y. Oishi, M. Yokoyama, M. Hiramato, *Appl. Phys. Lett.* **81**, 1321 (2002).
- 86 R. Koeppel, J. G. Muller, J. M. Lupton, J. Feldman, U. Scherf, U. Lemmer, *Appl. Phys. Lett.* **82**, 2601 (2003).
- 87 J. Xue, S. R. Forrest, *J. Appl. Phys.* **95**, 1859, 1869 (2004).
- 88 N. S. Sariciftci (Editor), *Primary Photoexcitations in Conjugated Polymers: Molecular Exciton versus Semiconductor Band*

- Model*, World Scientific, Singapore, 1997, and references cited therein.
- 89 F. A. Hegmann, *Phys. Can.* **59**, March/April, 127 (2003), and references cited therein.
- 90 D. Moses, A. Dogariu, A. J. Heeger, *Phys. Rev. B* **61**, 9373 (2000).
- 91 P. B. Miranda, D. Moses, A. J. Heeger, *Phys. Rev. B* **64**, 081202(R) (2001).
- 92 P. B. Miranda, D. Moses, A. J. Heeger, *Phys. Rev. B* **70**, 085212 (2004).
- 93 B. Kraabel, V. I. Klimov, R. Kohlman, S. Xu, H.-L. Wang, D. W. McBranch, *Phys. Rev. B* **61**, 8501 (2000).
- 94 S. Xu, V. I. Klimov, B. Kraabel, H. Wang, D. W. McBranch, *Phys. Rev. B* **64**, 193201 (2001).
- 95 Z. An, C. Q. Wu, X. Sun, *Phys. Rev. Lett.* **93**, 216407 (2004).
- 96 V. Gulbinas, Y. Zaushitsyn, H. Bässler, A. Yartsev, V. Sundström, *Phys. Rev. B* **70**, 035215 (2004).
- 97 Y. Zaushitsyn, V. Gulbinas, D. Zigmantas, F. Zhang, O. Inganäs, V. Sundström, A. Yartsev, *Phys. Rev. B* **70**, 075202 (2004).
- 98 R. Kersting, U. Lemmer, M. Deussen, H. J. Bakker, R. F. Mahrt, H. Kurz, V. I. Arkhipov, H. Bässler, O. E. Göbel, *Phys. Rev. Lett.* **73**, 1440 (1994).
- 99 W. Graupner, G. Cerullo, G. Lanzani, M. Nisoli, E. J. W. List, G. Leising, S. D. Silvestri, *Phys. Rev. Lett.* **81**, 3259 (1998).
- 100 V. I. Arkhipov, E. V. Emelianova, H. Bässler, *Phys. Rev. Lett.* **82**, 1321 (1999).
- 101 V. I. Arkhipov, E. V. Emelianova, S. Barth, H. Bässler, *Phys. Rev. B* **61**, 8207 (2000).
- 102 G. Cerullo, G. Lanzani, S. D. Silvestri, H.-J. Egelhaaf, L. Lüer, D. Oelkrug, *Phys. Rev. B* **62**, 2429 (2000).
- 103 E. Frankevich, H. Ishii, Y. Hamanaka, T. Yokoyama, A. Fuji, S. Li, K. Yoshino, A. Nakamura, K. Seki, *Phys. Rev. B* **62**, 2505 (2000).
- 104 A. Ruseckas, M. Theander, M. R. Andersson, M. Svensson, M. Prato, O. Inganäs, V. Sundström, *Chem. Phys. Lett.* **322**, 136 (2000).
- 105 M. W. McCutcheon, J. F. Young, A. G. Pattantyus-Abraham, M. O. Wolf, *J. Appl. Phys.* **89**, 4376 (2001).
- 106 D. M. Basko, E. M. Conwell, *Phys. Rev. B* **66**, 155210 (2002).
- 107 J. G. Müller, U. Lemmer, J. Feldman, U. Scherf, *Phys. Rev. Lett.* **88**, 147401 (2002).
- 108 V. Gulbinas, Y. Zaushitsyn, V. Sundström, D. Hertel, H. Bässler, A. Yartsev, *Phys. Rev. Lett.* **89**, 107401 (2002).
- 109 For reviews, see C. Gadermaier, G. Lanzani, *J. Phys.: Condens. Matter* **14**, 9785 (2002); G. Lanzani, G. Cerullo, D. Polli, A. Gambetta, M. Zavelani-Rossi, C. Gadermaier, *Phys. Status Solidi A* **201**, 1116 (2004).
- 110 L. Lüer, H.-J. Egelhaaf, D. Oelkrug, C. Gadermaier, G. Cerullo, G. Lanzani, *Phys. Rev. B* **68**, 155313 (2003).
- 111 Q.-H. Xu, D. Moses, A. J. Heeger, *Phys. Rev. B* **68**, 174303 (2003).
- 112 X. Yang, T. E. Dykstra, G. D. Scholes, *Phys. Rev. B* **71**, 045203 (2005).
- 113 T. Virgili, D. Marinotto, C. Manzoni, G. Cerullo, G. Lanzani, *Phys. Rev. Lett.* **94**, 117402 (2005).
- 114 C.-X. Sheng, Z. V. Vardeny, A. B. Dalton, R. H. Baughman, *Phys. Rev. B* **71**, 125427 (2005).
- 115 C. Jundt, G. Klein, B. Sipp, J. L. Moigne, M. Joucla, A. A. Villaeys, *Chem. Phys. Lett.* **241**, 84 (1995).
- 116 D. Moses, J. Wang, A. Dogariu, D. Fichou, C. Vidélot, *Phys. Rev. B* **59**, 7715 (1999).
- 117 S. V. Frolov, Ch. Kloc, B. Batlogg, M. Wohlgenannt, X. Jiang, Z. V. Vardeny, *Phys. Rev. B* **63**, 205203 (2001).
- 118 F. Cordella, R. Orru, M. A. Loi, A. Mura, G. Bongiovanni, *Phys. Rev. B* **68**, 113203 (2003).
- 119 N. Tamai, C. F. Porter, H. Masuhara, *Chem. Phys. Lett.* **211**, 364 (1993).
- 120 T. Fujino, T. Tahara, *J. Phys. Chem. B* **107**, 5120 (2003).
- 121 M. Knupper, *Appl. Phys. A* **77**, 623 (2003).
- 122 D. Moses, J. Wang, A. J. Heeger, N. Kirova, S. Brazovski, *Synth. Met.* **125**, 93 (2002).
- 123 T. K. Däubler, V. Cimrová, S. Pfeiffer, H.-H. Hörhold, D. Neher, *Adv. Mater.* **11**, 1274 (1999).
- 124 D. Moses, J. Wang, G. Yu, A. J. Heeger, *Phys. Rev. Lett.* **80**, 2685 (1998).

- 125 S. Barth, H. Bässler, *Phys. Rev. Lett.* **79**, 4445 (1997).
- 126 K. Kato, C. L. Braun, *J. Chem. Phys.* **72**, 172 (1980).
- 127 M. Samoc, D. F. Williams, *J. Chem. Phys.* **78**, 1924 (1983).
- 128 E. A. Silinsh, H. Inokuchi, *Chem. Phys.* **149**, 373 (1991).
- 129 V. D. Zhukov, M. V. Kurik, Y. P. Piryatinskii, L. I. Tsikora, *Sov. Phys. Solid State* **25**, 594 (1983).
- 130 Z. Rang, A. Haraldsson, D. M. Kim, P. P. Ruden, M. I. Nathan, R. J. Chesterfield, C. D. Frisbie, *Appl. Phys. Lett.* **79**, 2731 (2001).
- 131 D. V. Lang, X. Chi, T. Siegrist, A. M. Sargent, A. P. Ramirez, *Phys. Rev. Lett.* **93**, 086802 (2004).
- 132 T. Tokomuto, J. S. Brooks, R. Clinite, X. Wei, J. E. Anthony, D. L. Eaton, S. R. Parkin, *J. Appl. Phys.* **92**, 5208 (2002).
- 133 J. S. Brooks, T. Tokomuto, E.-S. Choi, D. Graf, N. Biskup, D. L. Eaton, J. E. Anthony, S. A. Odom, *J. Appl. Phys.* **96**, 3312 (2004).
- 134 V. Podzorov, V. M. Pudalov, M. E. Gershenson, *Appl. Phys. Lett.* **85**, 6039 (2004).
- 135 J. Lee, S. S. Kim, K. Kim, J. H. Kim, S. Im, *Appl. Phys. Lett.* **84**, 1701 (2004).
- 136 D. Moses, M. Sinclair, A. J. Heeger, *Phys. Rev. Lett.* **58**, 2710 (1987).
- 137 C. H. Lee, G. Yu, D. Moses, A. J. Heeger, *Phys. Rev. B* **49**, 2396 (1994).
- 138 L. B. Schein, R. W. Anderson, R. C. Enck, A. R. McGhie, *J. Chem. Phys.* **71**, 3189 (1979).
- 139 D. Moses, *Solid State Commun.* **69**, 721 (1989).
- 140 R. Katoh, M. Kotani, *J. Chem. Phys.* **94**, 5954 (1991).
- 141 E. A. Silinsh, V. A. Kolesnikov, I. J. Muzikante, D. R. Balode, *Phys. Status Solidi B* **113**, 379 (1982).
- 142 G. Horowitz, F. Kouki, P. Valet, P. Delannoy, J. Roussel, *Phys. Rev. B* **59**, 10651 (1999).
- 143 R. Könenkamp, G. Priebe, B. Pietzak, *Phys. Rev. B* **60**, 11804 (1999).
- 144 F. C. Grozema, P. Th. van Duijnen, Y. A. Berlin, M. A. Ratner, L. D. A. Siebbeles, *J. Phys. Chem. B* **106**, 7791 (2002).
- 145 G. Dicker, M. P. de Haas, L. D. A. Siebbeles, J. M. Warman, *Phys. Rev. B* **70**, 045203 (2004).
- 146 G. Dicker, M. P. de Haas, L. D. A. Siebbeles, *Phys. Rev. B* **71**, 155204 (2005).
- 147 F. A. Hegmann, R. R. Tykwinski, K. P. H. Lui, J. E. Bullock, J. E. Anthony, *Phys. Rev. Lett.* **89**, 227403 (2002).
- 148 O. Ostroverkhova, D. G. Cooke, S. Shcherbyna, R. F. Egerton, F. A. Hegmann, R. R. Tykwinski, J. E. Anthony, *Phys. Rev. B* **71**, 035204 (2005).
- 149 O. Ostroverkhova, S. Shcherbyna, D. G. Cooke, R. F. Egerton, F. A. Hegmann, R. R. Tykwinski, S. R. Parkin, J. E. Anthony, *J. Appl. Phys.* **98**, 033701 (2005).
- 150 F. A. Hegmann, O. Ostroverkhova, J. Gao, L. Barker, R. R. Tykwinski, J. E. Bullock, J. E. Anthony, *Proc. SPIE* **5352**, 196 (2004).
- 151 O. Ostroverkhova, S. Shcherbyna, D. G. Cooke, R. Egerton, R. R. Tykwinski, J. E. Anthony, F. A. Hegmann, *Proc. SPIE* **5517**, 163 (2004).
- 152 O. Ostroverkhova, D. G. Cooke, S. Shcherbyna, R. F. Egerton, F. A. Hegmann, R. R. Tykwinski, J. E. Anthony, V. Podzorov, M. E. Gershenson, O. D. Jurchescu, T. T. M. Palstra, in *Optical Terahertz Science, Technology Topical Meeting on CD-ROM*, Optical Society of America, Washington, DC, 2005, TuB7.
- 153 V. K. Thorsmølle, R. D. Averitt, X. Chi, D. J. Hilton, D. L. Smith, A. P. Ramirez, A. J. Taylor, *Appl. Phys. Lett.* **84**, 891 (2004).
- 154 E. Hendry, J. M. Schins, L. P. Candéias, L. D. A. Siebbeles, M. Bonn, *Phys. Rev. Lett.* **92**, 196601 (2004).
- 155 E. Hendry, M. Koeberg, J. M. Schins, H. K. Nienhuys, V. Sundström, L. D. A. Siebbeles, M. Bonn, *Phys. Rev. B* **71**, 125201 (2005).
- 156 M. C. Nuss, J. Orenstein, "Terahertz time-domain spectroscopy (THz-TDS)" in *Millimeter and Submillimeter Wave Spectroscopy of Solids*, edited by G. Grüner, Springer, Berlin, 1998, and references cited therein, p. 7.

- 157 D. Mittleman (Editor), *Sensing with Terahertz Radiation*, Springer, Berlin, 2003, and references cited therein.
- 158 B. Ferguson, X.-C. Zhang, *Nat. Mater.* **1**, 26 (2002), and references cited therein.
- 159 C. A. Schmuttenmaer, *Chem. Rev.* **104**, 1759 (2004), and references cited therein.
- 160 M. van Exter, Ch. Fattinger, D. Grischkowsky, *Appl. Phys. Lett.* **55**, 337 (1989).
- 161 M. van Exter, D. Grischkowsky, *Phys. Rev. B* **41**, 12140 (1990).
- 162 D. Grischkowsky, S. Keiding, Ch. Fattinger, *J. Opt. Soc. Am. B* **7**, 2006 (1990).
- 163 P. Uhd Jepsen, R. H. Jacobsen, S. R. Keiding, *J. Opt. Soc. Am. B* **13**, 2424 (1996).
- 164 A. Rice, Y. Jin, X. F. Ma, X.-C. Zhang, D. Bliss, J. Larkin, M. Alexander, *Appl. Phys. Lett.* **64**, 1324 (1994).
- 165 A. Nahata, A. S. Weling, T. F. Heinz, *Appl. Phys. Lett.* **69**, 2321 (1996).
- 166 A. Dreyhaupt, S. Winnerl, T. Dekorsy, M. Helm, *Appl. Phys. Lett.* **86**, 121114 (2005).
- 167 D. You, R. R. Jones, P. H. Bucksbaum, D. R. Dykaar, *Opt. Lett.* **18**, 290 (1993).
- 168 E. Budiarto, J. Margolies, S. Jeong, J. Son, J. Bokor, *IEEE J. Quantum Electron.* **32**, 1839 (1996).
- 169 C. Kübler, R. Huber, S. Tübel, A. Leitenstorfer, *Appl. Phys. Lett.* **85**, 3360 (2004).
- 170 X.-C. Zhang, X. F. Ma, Y. Jin, T.-M. Lu, E. P. Boden, P. D. Phelps, K. R. Stewart, C. P. Yakymyshyn, *Appl. Phys. Lett.* **61**, 3080 (1992).
- 171 T. J. Carrig, G. Rodriguez, T. S. Clement, A. J. Taylor, K. R. Stewart, *Appl. Phys. Lett.* **66**, 10 (1995).
- 172 H. Hashimoto, H. Takahashi, T. Yamada, K. Kuroyanagi, T. Kobayashi, *J. Phys.: Condens. Matter* **13**, L529 (2001).
- 173 A. Nahata, D. H. Auston, C. Wu, J. T. Yardley, *Appl. Phys. Lett.* **67**, 1358 (1995).
- 174 J. J. Carey, R. T. Bailey, D. Pugh, J. N. Sherwood, F. R. Cruickshank, K. Wynne, *Appl. Phys. Lett.* **81**, 4335 (2002).
- 175 H. Nemeč, A. Pashkin, P. Kužel, M. Khazan, S. Schnull, I. Wilke, *J. Appl. Phys.* **90**, 1303 (2001).
- 176 M. C. Beard, G. M. Turner, C. A. Schmuttenmaer, *J. Am. Chem. Soc.* **122**, 11541 (2000).
- 177 M. C. Beard, G. M. Turner, C. A. Schmuttenmaer, *J. Phys. Chem. A* **106**, 878 (2002).
- 178 C. Soci, D. Moses, *Synth. Met.* **139**, 815 (2003).
- 179 E. Hendry, M. Koeberg, J. M. Schins, L. D. A. Siebbeles, M. Bonn, *Phys. Rev. B* **70**, 033202 (2004).
- 180 Q. Wu, M. Litz, X.-C. Zhang, *Appl. Phys. Lett.* **68**, 2924 (1996).
- 181 Z. G. Lu, P. Campbell, X. C. Zhang, *Appl. Phys. Lett.* **71**, 593 (1997).
- 182 Q. Wu, X.-C. Zhang, *Appl. Phys. Lett.* **71**, 1285 (1997).
- 183 G. Gallot, D. Grischkowsky, *J. Opt. Soc. Am. B* **16**, 1204 (1999).
- 184 P. C. M. Planken, H.-K. Nienhuys, H. J. Bakker, T. Wenckebach, *J. Opt. Soc. Am. B* **18**, 313 (2001).
- 185 N. C. J. van der Valk, T. Wenckebach, P. C. M. Planken, *J. Opt. Soc. Am. B* **21**, 622 (2004).
- 186 M. Nagai, K. Tanaka, H. Ohtake, T. Bessho, T. Sugiura, T. Hirosumi, M. Yoshida, *Appl. Phys. Lett.* **85**, 3974 (2004).
- 187 P. Y. Han, M. Tani, F. Pan, X.-C. Zhang, *Opt. Lett.* **25**, 675 (2000).
- 188 S.-G. Park, M. R. Melloch, A. M. Weiner, *Appl. Phys. Lett.* **73**, 3184 (1998).
- 189 J. N. Heyman, P. Neocleous, D. Hebert, P. A. Crowell, T. Müller, K. Unterrainer, *Phys. Rev. B* **64**, 085202 (2001).
- 190 J. F. Holzman, A. Y. Elezzabi, *Appl. Phys. Lett.* **83**, 2967 (2003).
- 191 M. Reid, I. Cravetchi, R. Fedosejevs, I. M. Tiginyanu, L. Sirbu, R. W. Boyd, *Phys. Rev. B* **71**, 081306(R) (2005).
- 192 J. Ahn, A. V. Efimov, R. D. Averitt, A. J. Taylor, *Opt. Express* **11**, 2486 (2003).
- 193 M. Walther, G. S. Chambers, Z. Liu, M. R. Freeman, F. A. Hegmann, *J. Opt. Soc. Am. B*, in press.
- 194 K. Wang, D. M. Mittleman, *Nature* **432**, 376 (2004).
- 195 T.-I. Jeon, J. Zhang, D. Grischkowsky, *Appl. Phys. Lett.* **86**, 161904 (2005).

- 196 D. Qu, D. Grischkowsky, W. Zhang, *Opt. Lett.* **29**, 896 (2004).
- 197 H.-T. Chen, R. Kersting, G. C. Cho, *Appl. Phys. Lett.* **83**, 3009 (2003).
- 198 K. Wang, D. Mittleman, N. C. J. van der Valk, P. C. M. Planken, *Appl. Phys. Lett.* **85**, 2715 (2004).
- 199 P. C. M. Planken, N. C. J. van der Valk, *Opt. Lett.* **29**, 2306 (2004).
- 200 P. Y. Han, M. Tani, M. Usami, S. Kono, R. Kersting, X.-C. Zhang, *J. Appl. Phys.* **89**, 2357 (2001).
- 201 M. Walther, B. Fischer, M. Schall, H. Helm, P. Uhd Jepsen, *Chem. Phys. Lett.* **332**, 389 (2000).
- 202 M. B. Johnston, L. M. Herz, A. L. T. Khan, A. Kohler, A. G. Davies, E. H. Linfield, *Chem. Phys. Lett.* **377**, 256 (2003).
- 203 S. Krishnamurthy, M. T. Reiten, S. A. Harmon, R. A. Cheville, *Appl. Phys. Lett.* **79**, 875 (2001).
- 204 N. Nagai, R. Fukasawa, *Chem. Phys. Lett.* **388**, 479 (2004).
- 205 M. Walther, K. Jensby, S. Keiding, H. Takahashi, H. Ito, *Opt. Lett.* **25**, 911 (2000).
- 206 J. Han, H. Xu, Z. Zhu, X. Yu, W. Li, *Chem. Phys. Lett.* **392**, 348 (2004).
- 207 M. Brucherseifer, M. Nagel, P. Haring Bolivar, H. Kurz, A. Bosserhoff, R. Büttner, *Appl. Phys. Lett.* **77**, 4049 (2000).
- 208 A. G. Markelz, A. Roitberg, E. J. Heilweil, *Chem. Phys. Lett.* **320**, 42 (2000).
- 209 B. M. Fischer, M. Walther, P. Uhd Jepsen, *Phys. Med. Biol.* **47**, 3807 (2002).
- 210 T. R. Globus, D. L. Woolard, T. Khromova, T. W. Crowe, M. Bykhovskaia, B. L. Gelmont, J. Hesler, A. C. Samuels, *J. Biol. Phys.* **29**, 89 (2003).
- 211 P. Y. Han, G. C. Cho, X.-C. Zhang, *Appl. Phys. Lett.* **25**, 242 (2000).
- 212 A. Markelz, S. Whitmire, J. Hillebrecht, R. Birge, *Phys. Med. Biol.* **47**, 3797 (2002).
- 213 M. Walther, B. M. Fischer, P. Uhd Jepsen, *Chem. Phys.* **288**, 261 (2003).
- 214 Y. C. Shen, P. C. Upadhy, E. H. Linfield, A. G. Davies, *Appl. Phys. Lett.* **82**, 2350 (2003).
- 215 C. J. Strachen, T. Rades, D. A. Newnham, K. C. Gordon, M. Pepper, P. F. Taday, *Chem. Phys. Lett.* **390**, 20 (2004).
- 216 F. Huang, B. Schulkin, H. Altan, J. F. Federici, D. Gary, R. Barat, D. Zimdars, M. Chen, D. B. Tanner, *Appl. Phys. Lett.* **85**, 5535 (2004).
- 217 D. J. Funk, F. Calgaro, R. D. Averitt, M. L. T. Asaki, A. J. Taylor, *Appl. Spectrosc.* **58**, 428 (2004); J. Barber, D. E. Hooks, D. J. Funk, R. D. Averitt, A. J. Taylor, D. Babikov, *J. Phys. Chem. A* **109**, 3501 (2005).
- 218 For a classic text on optical properties, see F. Wooten, *Optical Properties of Solids*, Academic Press, San Diego, CA, 1972.
- 219 For a more recent, extensive text on optical properties, see M. Dressel, G. Grüner, *Electrodynamics of Solids: Optical Properties of Electrons in Matter*, Cambridge University Press, Cambridge, 2002.
- 220 For an excellent introductory text, see M. Fox, *Optical Properties of Solids*, Oxford University Press, Oxford, 2001.
- 221 B. N. Flanders, R. A. Cheville, D. Grischkowsky, N. F. Scherer, *J. Phys. Chem.* **100**, 11824 (1996).
- 222 C. Rønne, P.-O. Åstrand, S. Keiding, *Phys. Rev. Lett.* **82**, 2888 (1999).
- 223 J. T. Kindt, C. A. Schmuttermaer, *J. Phys. Chem.* **100**, 10373 (1996).
- 224 D. S. Venables, C. A. Schmuttermaer, *J. Chem. Phys.* **108**, 4935 (1998).
- 225 M. L. T. Asaki, A. Redondo, T. A. Zawodzinski, A. J. Taylor, *J. Chem. Phys.* **116**, 10377 (2002).
- 226 B. L. Yu, F. Zeng, Q. Xing, R. R. Alfano, *Appl. Phys. Lett.* **82**, 4633 (2003).
- 227 B. L. Yu, Y. Yang, F. Zeng, X. Xin, R. R. Alfano, *Appl. Phys. Lett.* **86**, 061912 (2005).
- 228 J. E. Boyd, A. Briskman, V. L. Colvin, D. M. Mittleman, *Phys. Rev. Lett.* **87**, 147401 (2001).
- 229 T.-I. Jeon, D. Grischkowsky, *Phys. Rev. Lett.* **78**, 1106 (1997).
- 230 S. Nashima, O. Morikawa, K. Takata, M. Hangyo, *J. Appl. Phys.* **90**, 837 (2001).
- 231 J. Dai, J. Zhang, W. Zhang, D. Grischkowsky, *J. Opt. Soc. Am. B* **21**, 1379 (2004).

- 232 N. Katzenellenbogen, D. Grischkowsky, *Appl. Phys. Lett.* **61**, 840 (1992).
- 233 P. G. Huggard, J. A. Cluff, G. P. Moore, C. J. Shaw, S. R. Andrews, S. R. Keiding, E. H. Linfield, D. A. Ritchie, *J. Appl. Phys.* **87**, 2382 (2000).
- 234 D. M. Mittleman, J. Cunningham, M. C. Nuss, M. Geva, *Appl. Phys. Lett.* **71**, 16 (1997).
- 235 M. C. Nuss, K. W. Goossen, J. P. Gordon, P. M. Mankiewich, M. L. O'Malley, M. Bhushan, *J. Appl. Phys.* **70**, 2238 (1991).
- 236 R. A. Kaindl, M. A. Carnahan, J. Orenstein, D. S. Chemla, H. M. Christen, H.-Y. Zhai, M. Paranthaman, D. H. Lowndes, *Phys. Rev. Lett.* **88**, 027003 (2002).
- 237 S. D. Brorson, R. Buhleier, I. E. Trofinov, J. O. White, Ch. Ludwig, F. F. Balakirev, H.-U. Habermeier, J. Kuhl, *J. Opt. Soc. Am. B* **13**, 1979 (1996).
- 238 F. Gao, L. Carr, C. D. Porter, D. B. Tanner, G. P. Williams, C. J. Hirschmugl, B. Dutta, X. D. Wu, S. Etemad, *Phys. Rev. B* **54**, 700 (1996).
- 239 J. Corson, R. Malozzi, J. Orenstein, J. N. Eckstein, I. Bozovic, *Nature* **398**, 221 (1999).
- 240 V. K. Thorsmølle, R. D. Averitt, M. P. Haley, L. N. Bulaevskii, C. Helm, A. J. Taylor, *Opt. Lett.* **26**, 1292 (2001).
- 241 V. K. Thorsmølle, R. D. Averitt, M. P. Haley, M. F. Hundley, A. E. Koshelev, L. N. Bulaevskii, A. J. Taylor, *Phys. Rev. B* **66**, 012519 (2002).
- 242 V. K. Thorsmølle, R. D. Averitt, M. P. Haley, L. N. Bulaevskii, C. Helm, A. J. Taylor, *Physica B* **312–313**, 84 (2002).
- 243 J. S. Dodge, C. P. Weber, J. Corson, J. Orenstein, Z. Schlesinger, J. W. Reiner, M. R. Beasley, *Phys. Rev. Lett.* **85**, 4932 (2000).
- 244 H. Harimochi, J. Kitagawa, M. Ishizaka, Y. Kadoya, M. Yamanishi, S. Matsuishii, H. Hosono, *Phys. Rev. B* **70**, 193104 (2004).
- 245 T.-I. Jeon, D. Grischkowsky, A. K. Mukherjee, R. Menon, *Appl. Phys. Lett.* **77**, 2452 (2000).
- 246 T.-I. Jeon, D. Grischkowsky, A. K. Mukherjee, R. Menon, *Appl. Phys. Lett.* **79**, 4142 (2001); Erratum: *Appl. Phys. Lett.* **81**, 2902 (2002).
- 247 T.-I. Jeon, D. Grischkowsky, A. K. Mukherjee, R. Menon, *Synth. Met.* **135**, 451 (2003).
- 248 T.-I. Jeon, K.-J. Kim, A. K. Mukherjee, R. Menon, *Synth. Met.* **150**, 53 (2005).
- 249 T.-I. Jeon, K.-J. Kim, C. Kang, S.-J. Oh, J.-H. Son, K. H. An, D. J. Bae, Y. H. Lee, *Appl. Phys. Lett.* **80**, 3403 (2002).
- 250 T.-I. Jeon, K.-J. Kim, C. Kang, I. H. Maeng, J.-H. Son, K. H. An, J. Y. Lee, Y. H. Lee, *J. Appl. Phys.* **95**, 5736 (2004).
- 251 N. W. Ashcroft, N. D. Mermin, *Solid State Physics*, Saunders College, Philadelphia, 1976.
- 252 G. Burns, *Solid State Physics*, Academic Press, Boston, 1985.
- 253 H. R. Philipp, *Phys. Rev. B* **16**, 2896 (1977).
- 254 J. Shan, F. Wang, E. Knoesel, M. Bonn, T. Heinz, *Phys. Rev. Lett.* **90**, 247401 (2003).
- 255 A. V. Puchkov, T. Timusk, W. D. Mosley, R. N. Shelton, *Phys. Rev. B* **50**, 4144 (1994).
- 256 R. A. Kaindl, M. A. Carnahan, D. Hägele, R. Lövenich, D. S. Chemla, *Nature* **423**, 734 (2003).
- 257 M. C. Beard, G. M. Turner, C. A. Schmuttenmaer, *Phys. Rev. B* **62**, 15764 (2000).
- 258 M.C. Beard, G.M. Turner, C.A. Schmuttenmaer, *J. Appl. Phys.* **90**, 5915 (2001).
- 259 N. V. Smith, *Phys. Rev. B* **64**, 155106 (2001).
- 260 N. V. Smith, *Phys. Rev. B* **68**, 132406 (2003).
- 261 M. C. Beard, G. M. Turner, J. E. Murphy, O. I. Micic, M. C. Hanna, A. J. Nozik, C. S. Schmuttenmaer, *Nano Lett.* **3**, 1695 (2003).
- 262 G. M. Turner, M. C. Beard, C. A. Schmuttenmaer, *J. Phys. Chem. B* **106**, 11716 (2002).
- 263 K. Lee, R. Menon, C. O. Yoon, A. J. Heeger, *Phys. Rev. B* **52**, 4779 (1995).
- 264 K. Lee, A. J. Heeger, *Phys. Rev. B* **68**, 035201 (2003).

- 265 T. C. Choy, *Effective Medium Theory: Principles and Applications*, Clarendon Press, Oxford, 1999.
- 266 M. C. Beard, G. M. Turner, C. A. Schmuttenmaer, *Nano Lett.* **2**, 983 (2002).
- 267 H. Altan, F. Huang, J. F. Federici, A. Lan, H. Grebel, *J. Appl. Phys.* **96**, 6685 (2004).
- 268 S. Labbé-Lavigne, S. Barret, F. Garet, L. Duvillaret, J.-L. Coutaz, *J. Appl. Phys.* **83**, 6007 (1998).
- 269 J. Han, Z. Zhu, Z. Wang, W. Zhang, L. Yu, L. Sun, T. Wang, F. He, L. Liao, *Phys. Lett. A* **310**, 457 (2003).
- 270 A. B. Kaiser, *Rep. Prog. Phys.* **64**, 1 (2001).
- 271 R. Farchioni, G. Grosso (Editors), *Organic Electronic Materials: Conjugated Polymers and Low Molecular Weight Organic Solids*, Springer, Berlin, 2001.
- 272 P. Chandrasekhar, *Conducting Polymers, Fundamentals and Applications: a Practical Approach*, Kluwer, Dordrecht, 1999.
- 273 A. J. Heeger, *Rev. Mod. Phys.* **73**, 681 (2001); see also C. K. Chiang, C. R. Fincher, Jr., Y. W. Park, A. J. Heeger, H. Shirakawa, E. J. Louis, S. C. Gua, A. G. MacDairmid, *Phys. Rev. Lett.* **39**, 1098 (1977).
- 274 J. L. Brédas, G. B. Street, *Acc. Chem. Res.* **18**, 309 (1985).
- 275 A. J. Heeger, S. Kivelson, J. R. Schrieffer, W.-P. Su, *Rev. Mod. Phys.* **60**, 781 (1988).
- 276 R. S. Kohlman, J. Joo, Y. Z. Wang, J. P. Pouget, H. Kaneko, T. Ishiguro, A. J. Epstein, *Phys. Rev. Lett.* **74**, 773 (1995).
- 277 B. Chapman, R. G. Buckley, N. T. Kemp, A. B. Kaiser, D. Beaglehole, H. J. Trodahl, *Phys. Rev. B* **60**, 13479 (1999).
- 278 J. Joo, S. M. Long, J. P. Pouget, E. J. Oh, A. G. MacDiarmid, A. J. Epstein, *Phys. Rev. B* **57**, 9567 (1998).
- 279 V. N. Prigodin, A. N. Samukhin, A. J. Epstein, *Synth. Met.* **141**, 155 (2004).
- 280 R. S. Kohlman, J. Joo, Y. G. Min, A. G. MacDiarmid, A. J. Epstein, *Phys. Rev. Lett.* **77**, 2766 (1996).
- 281 A. J. Heeger, *J. Supercond.* **14**, 261 (2001).
- 282 G. Tzamalīs, N. A. Zaidi, C. C. Homes, A. P. Monkman, *Phys. Rev. B* **66**, 085202 (2002).
- 283 I. G. Romijin, H. J. Hupkes, H. C. F. Martens, H. B. Brom, A. K. Mukherjee, R. Menon, *Phys. Rev. Lett.* **90**, 176602 (2003).
- 284 H. C. F. Martens, H. B. Brom, *Phys. Rev. B* **70**, 241201(R) (2004).
- 285 M. C. Nuss, D. H. Auston, F. Capasso, *Phys. Rev. Lett.* **58**, 2355 (1987).
- 286 B. I. Greene, J. F. Federici, D. R. Dykaar, A. F. J. Levi, L. Pfeiffer, *Opt. Lett.* **16**, 48 (1991); P. N. Saeta, J. F. Federici, B. I. Greene, D. R. Dykaar, *Appl. Phys. Lett.* **60**, 1477 (1992).
- 287 M. Schall, P. U. Jepsen, *Opt. Lett.* **25**, 13 (2000).
- 288 R. Huber, F. Tauser, A. Brodschelm, M. Bichler, G. Abstreiter, A. Leitenstorfer, *Nature* **414**, 286 (2001).
- 289 F. Kadlec, H. Němec, P. Kužel, *Phys. Rev. B* **70**, 125205 (2004).
- 290 M. Schall, P. Uhd Jepsen, *Appl. Phys. Lett.* **80**, 4771 (2002).
- 291 C. A. Schmuttenmaer, G. M. Turner, M. C. Beard, *Proc. SPIE* **5223**, 64 (2003).
- 292 E. Hendry, F. Wang, J. Shan, T. F. Heinz, M. Bonn, *Phys. Rev. B* **69**, 081101(R) (2004).
- 293 S. S. Prabhu, S. E. Ralph, M. R. Melloch, E. S. Harmon, *Appl. Phys. Lett.* **70**, 2419 (1997).
- 294 K. P. H. Lui, F. A. Hegmann, *Appl. Phys. Lett.* **78**, 3478 (2001).
- 295 F. A. Hegmann, K. P. H. Lui, *Proc. SPIE* **4643**, 31 (2002).
- 296 K. P. H. Lui, F. A. Hegmann, *J. Appl. Phys.* **93**, 9012 (2003).
- 297 P. Uhd Jepsen, W. Schairer, I. H. Libon, U. Lemmer, N. E. Hecker, M. Birkholz, K. Lips, M. Schall, *Appl. Phys. Lett.* **79**, 1291 (2001).
- 298 C. Messner, H. Kostner, R. A. Höpfel, K. Unterrainer, *J. Opt. Soc. Am. B* **18**, 1369 (2001).
- 299 R. H. M. Groeneveld, D. Grischkowsky, *J. Opt. Soc. Am. B* **11**, 2502 (1994).
- 300 D. A. Yarotski, R. D. Averitt, N. Negre, S. A. Crooker, A. J. Taylor, G. P. Donati, A. Stintz, L. F. Lester, K. J. Malloy, *J. Opt. Soc. Am. B* **19**, 1480 (2002).
- 301 D. Turchinovich, K. Pierz, P. Uhd Jepsen, *Phys. Status Solidi C*, **0**, 1556 (2003).

- 302 D. G. Cooke, F. A. Hegmann, Yu. I. Mazur, W. Q. Ma, X. Wang, Z. M. Wang, G. J. Salamo, M. Xiao, T. D. Mishima, M. B. Johnson, *Appl. Phys. Lett.* **85**, 3839 (2004).
- 303 R. P. Prasankumar, A. Scopatz, D. J. Hilton, A. J. Taylor, R. D. Averitt, J. M. Zide, A. C. Gossard, *Appl. Phys. Lett.* **86**, 201107 (2005).
- 304 R. D. Averitt, G. Rodriguez, J. L. W. Siders, S. A. Trugman, A. J. Taylor, *J. Opt. Soc. Am. B* **17**, 327 (2000).
- 305 R. D. Averitt, G. Rodriguez, A. I. Lobad, J. L. W. Siders, S. A. Trugman, A. J. Taylor, *Phys. Rev. B* **63**, 140502(R) (2001).
- 306 R. D. Averitt, V. K. Thorsmølle, Q. X. Jia, S. A. Trugman, A. J. Taylor, *Physica B* **312–313**, 86 (2002)
- 307 J. Demsar, R. D. Averitt, A. J. Taylor, V. V. Kabanov, W. N. Kang, H. J. Kim, E. M. Choi, S. I. Lee, *Phys. Rev. Lett.* **91**, 267002 (2003).
- 308 R. D. Averitt, A. I. Lobad, C. Kwon, S. A. Trugman, V. K. Thorsmølle, A. J. Taylor, *Phys. Rev. Lett.* **87**, 017401 (2001).
- 309 R. McElroy, K. Wynne, *Phys. Rev. Lett.* **79**, 3078 (1997).
- 310 J. T. Kindt, C. A. Schmuttenmaer, *J. Chem. Phys.* **110**, 8589 (1999).
- 311 E. Knoesel, M. Bonn, J. Shan, T. F. Heinz, *Phys. Rev. Lett.* **86**, 340 (2001).
- 312 E. Knoesel, M. Bonn, J. Shan, F. Wang, T. F. Heinz, *J. Chem. Phys.* **121**, 394 (2004).
- 313 F. Kadlec, C. Kadlec, P. Kužel, P. Slavicek, P. Jungwirth, *J. Chem. Phys.* **120**, 912 (2004).
- 314 M. C. Beard, C. A. Schmuttenmaer, *J. Chem. Phys.* **114**, 2903 (2001)
- 315 H. Němec, F. Kadlec, P. Kužel, *J. Chem. Phys.* **117**, 8454 (2002).
- 316 D. Côté, J. E. Sipe, H. M. van Driel, *J. Opt. Soc. Am. B* **20**, 1374 (2003).
- 317 H. Němec, F. Kadlec, S. Surendran, P. Kužel, P. Junwirth, *J. Chem. Phys.* **122**, 104503 (2005); H. Nemeč, F. Kadlec, C. Kadlec, P. Kužel, P. Junwirth, *J. Chem. Phys.* **122**, 104504 (2005).
- 318 J. E. Anthony, J. S. Brooks, D. L. Eaton, S. R. Parkin, *J. Am. Chem. Soc.* **123**, 9482 (2001)
- 319 J. E. Anthony, D. L. Eaton, S. R. Parkin, *Org. Lett.* **4**, 15 (2002).
- 320 C. D. Sheraw, T. N. Jackson, D. L. Eaton, J. E. Anthony, *Adv. Mater.* **15**, 2009 (2003).
- 321 M. M. Payne, S. R. Parkin, J. E. Anthony, C.-C. Kuo, T. N. Jackson, *J. Am. Chem. Soc.* **127**, 4986 (2005).
- 322 F. C. Bos, D. M. Burland, *Phys. Rev. Lett.* **58**, 152 (1987).
- 323 S. Etemad, T. Mitani, M. Ozaki, T. C. Chung, A. J. Heeger, A. G. MacDiarmid, *Solid State Commun.* **40**, 75 (1981).
- 324 H. Scher, E. W. Montroll, *Phys. Rev. B* **12**, 2455 (1975); H. Scher, M. F. Shlesinger, J. T. Bendler, *Phys. Today* **44** (1), 26 (1991).

## 8

# Strong Exciton Polaritons in Anisotropic Crystals: Macroscopic Polarization and Exciton Properties

Gerhard Weiser

### 8.1

#### Introduction

Linear optical spectroscopy is a convenient and successful tool to derive the electronic structure of matter. The interaction of electrons with light is commonly considered as weak perturbation where the interaction  $H_1 = \vec{\mu}_{fg} \cdot \vec{E}$  of radiation field and transition dipole  $\vec{\mu}_{fg} = \langle f | e\vec{r} | g \rangle$  induces transitions between the ground state  $|g\rangle$  and excited state  $|f\rangle$  of the system. The transition probability and absorption constant obey Fermi's golden rule, being linear in the intensity of light, the density of states and the square of the transition dipole moment  $\mu_{fg}$ . Absorption peaks are attributed to the gap between the ground and excited states and the linewidth provides information on energy dissipation and structural inhomogeneity. The transition dipole reflects a change of the charge distribution and accounting for the different potential of ground and excited state leads to the concept of excitons. Two different descriptions emerged for delocalized and localized states. The Wannier model uses a local positive charge, the hole, to represent the electron removed from a homogeneous charge distribution in the ground state [1]. The local Coulomb potential introduces a hydrogen-like series of bound states below the gap to the free electron continuum and shifts oscillator strength from unbound states to bound states and to the lower range of unbound states [2]. The concept of Wannier excitons works well in high-mobility semiconductors where large spatial overlap of bonding and antibonding states creates wide energy bands. It is inappropriate for molecular solids where orbitals of different molecules overlap much less. With negligible hybridization of molecular orbitals electrons remain localized to the constituent molecules and the excited state is a Frenkel exciton with electron and hole residing on the same molecule [3]. The calculation of its properties turns out to be a veritable many-body problem in  $\pi$ -conjugated molecules since the  $\pi$ -electrons are resonant in energy and share a common but relatively small volume.

Although the electrons and holes are localized to a single molecule, Frenkel excitons interact in solids via their dipole moments. The dipole field of the mole-

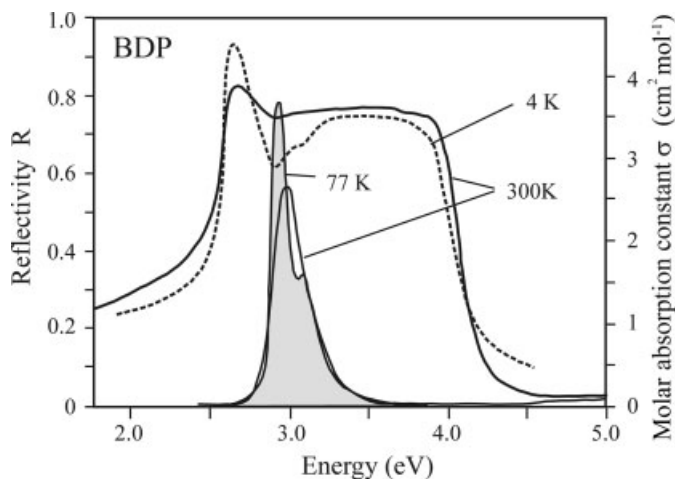


**Figure 8.1** Molar absorption of 1,5-bis(dimethylamino)pentamethinium perchlorate (BDP) in aqueous solution and reflectance spectra of a single crystal at room temperature [5] and at low temperature [6]. The shaded spectrum is a BDP spectrum in isobutanol–isopentane glass.

cules in a unit cell splits the molecular exciton into a multiplet. Polarization and strength of these Davydov components derive from superposition of the molecular dipoles and depend on the aggregation of the molecules while level splitting measures the strength of dipole–dipole interaction [4]. The superposition of molecular dipoles works well for excitons of weak or moderate oscillator strength but fails for strong transitions of  $\pi$ -conjugated bonds. Owing to their confinement to the small volume of conjugated bonds the  $\pi$ -electrons are strongly correlated and respond to light collectively, similar as the free-electron plasma in metals. A single exciton inherits much of the oscillator strength of  $\pi$ - $\pi^*$  transitions and solution spectra show a strong absorption band, which often is separated from other absorption bands.

In the solid state the exciton dipoles add up to a macroscopic polarization, which, increasing with the density of molecules, has a significant effect on the optical spectra. The earliest example reported is the reflectivity of the cationic dye BDP [1,5-bis(dimethylamino)pentamethinium perchlorate] [5,6], shown in Fig. 8.1. A more than 1 eV wide band of high reflectivity, dubbed “metallic”, is observed in polarized light that does not narrow at low temperature and is absent for orthogonal polarization of light. The spectrum of the single crystal is much broader than the absorption spectra of molecules dissolved in water or in isobutanol–isopentane glass at 77 K, which, except for the smaller linewidth at low temperatures, are similar. Such a striking difference in the spectral width in crystals and in solution was unexpected and in obvious contrast to the presumed insensitivity of molecular states to condensation. Attempts to explain the wide band of high reflectivity as the dielectric response of a free electron gas failed, but model-

ing the spectrum as response of a strong exciton was as unsatisfactory. Linewidth broadening washed out the sharp edges of the reflectance band and reduced its height rapidly. Increasing use of reflectance spectroscopy revealed that such spectra are common for single crystals of conjugated molecules with strong excitons and some examples have been extensively studied: cationic dyes [7, 8], neutral molecules such as TCNQ [9, 10], and in the case of perylene different crystal structures resulted in distinctly different spectra [11]. Kramers–Kronig analysis found the “metallic” reflectivity to be related to a strong and fairly narrow absorption band at its low-energy edge. However, different faces of the same crystal had very different reflectance spectra, sometimes even different color and Kramers–Kronig transformation produced absorption bands of different shape and peak position.

All these striking properties arise from the macroscopic polarization, which is an inherent part of excitons in solids, missed if the interaction of excitons and light is treated as perturbation. The optical spectra of solids derive from polaritons, composite particles of excitons and photons, and their difference from excitons cannot be neglected in the case of strong excitons. Soon after the polariton emerged as a valuable concept extensive reviews appeared on exciton polaritons in semiconductors [12], phonon polaritons [13, 14] and on the closely related surface polaritons [15], but none of these included the striking optical properties of single crystals of  $\pi$ -conjugated molecules.

Section 8.2 reviews the relation of excited electrons to harmonic oscillators, that of excitons and polaritons and to the dielectric response theory. Section 8.3 employs dielectric response theory to derive the fundamental properties of polaritons and to reveal the fundamental difference encountered in the evaluation of spectra of isotropic and anisotropic solids. Section 8.4 compares experimental data with polariton theory. Spectra of naphthalene are shown as an example of non-classical absorption, demonstrating the role of scattering in optical absorption. The dielectric theory is then applied to extract the properties of excitons from polariton spectra of increasing complexity. It will be shown that polaritons are also responsible for the loss of fine structure in the spectra of nanocrystalline films of  $\pi$ -conjugated molecules. Electroabsorption spectra of polaritons in oligothiophenes show that nonlinear spectroscopy recovers part of the spectral fine structure, which is not apparent in absorption spectra. Section 8.5 summarizes the deviations that are caused in spectra by polariton effects.

## 8.2

## Interaction of Light and Matter: Excitons and Polaritons

## 8.2.1

## Quantum Mechanics of Electrons Interacting with Light

## 8.2.1.1 Excited Electrons and Harmonic Oscillators

Absorption is an obvious result of the interaction of light and matter but the prime response of electrons is a coherent polarization  $\vec{P}$  induced by the electric field of light:

$$\frac{\partial^2 \vec{P}}{\partial t^2} + \omega_0^2 \vec{P} = \beta \vec{E}(t) \quad (8.1)$$

The equation of motion describes a harmonic polarization of eigenfrequency  $\omega_0$  which is driven by an electric field via a coupling constant  $\beta$ . Quantum mechanics describes harmonic oscillators, molecular vibrations and electromagnetic waves, by bosons of energy  $\hbar\omega$  but electrons are fermions whose resonance frequency is determined by the energy gap between the ground and excited states. It has been shown by Fano that a weakly excited system of fermions may be described by bosons representing a harmonic classical oscillators [16].

The starting point is a homogeneous material with oscillators of eigenfrequencies  $\omega_1, \omega_2, \dots, \omega_n$ , localized in the unit cell, as for instance eigenstates of non-interacting molecules. The Hamiltonian (without the irrelevant zero-point energy) of non-interacting oscillators is the sum of the energy of all oscillators, given by the frequencies  $\omega_n$  and quantum numbers  $N_{nj}$ :

$$H_B = \sum_{n,j} N_{nj} \hbar \omega_n = \sum_{n,j} b_{nj}^+ b_{nj} \hbar \omega_n, \quad b_n b_{n'}^+ - b_{n'}^+ b_n = \delta_{n'n} \quad (8.2)$$

The index  $j$  denotes the cell and the quantum number  $N_{nj}$  is represented by annihilation and creation operators  $b_n, b_n^+$  commuting like bosons. The number operator of bosons has an unlimited number of eigenvalues  $N_{nj} = 1, 2, \dots$ , but the classical harmonic oscillator has no higher harmonics. Since even for classical oscillators higher harmonics can be neglected for small amplitudes only, a weakly excited oscillator is equivalent to a vanishing probability of eigenvalues  $N_{nj} > 1$ .

The Hamiltonian of electrons of energy  $\hbar\omega_n$  looks similar but annihilation and creation operators  $a_n, a_n^+$  commute differently.

$$H_F = \sum_{n,j} N_{nj} \hbar \omega_n = \sum_{n,j} a_{nj}^+ a_{nj} \hbar \omega_n, \quad a_{nj} a_{nj}^+ + a_{nj}^+ a_{nj} = 1 \quad (8.3)$$

Electron states are either empty or singly occupied resulting in two eigenvalues  $N_{nj} = 0$  or 1, as the weakly excited system of harmonic oscillators and fermion operators  $a_{nj}$

are represented by  $2 \times 2$  matrices. In contrast, matrices representing bosons with unlimited occupancy of states have a corresponding number of rows and columns. On the other hand, in a weakly excited system the matrices  $(1 - b_{nj}^+ b_{nj}) b_{nj}$  agree with fermion matrices  $a_{nj}$  since elements related to quantum numbers  $N_{nj} > 1$  are zero. Replacing the operator  $a_{nj}$  by  $(1 - b_{nj}^+ b_{nj}) b_{nj}$  and  $a_{nj}^+$  by  $b_{nj}^+ (1 - b_{nj}^+ b_{nj})$  the fermion Hamiltonian is expressed by boson operators:

$$H_F = \sum_{nj} a_{nj}^+ a_{nj} \hbar \omega_n = \sum_{nj} b_{nj}^+ (1 - b_{nj}^+ b_{nj}) (1 - b_{nj}^+ b_{nj}) b_{nj} \hbar \omega_n = \sum_{nj} b_{nj}^+ b_{nj} \hbar \omega_n \quad (8.4)$$

The equivalence to the classical oscillator is obtained only after dropping the term  $b_{nj}^+ b_{nj}$  in both parentheses. This step, eliminating also terms of higher order, is justified for weak excitation where few oscillators are excited in a large number of cells. Under weak excitation the system of fermions is thus equivalent to classical oscillators. It is recalled that in dilute and weakly excited systems both Bose and Fermi distributions reduce to the classical Boltzmann distribution.

The Hamiltonian in Eq. (8.4) in general will include cross terms such as  $b_{nj}^+ b_{ni}$ , which, corresponding to excitation transfer into another cell, result in delocalized excited states. The operator  $B_r$  of delocalized excitations is expanded into linear combinations of local operators  $b_{nj}$  and the sum over the cell index  $j$  accounts for delocalization:

$$B_r = \sum_{nj} (c_{r,nj} b_{nj} + d_{r,nj} b_{nj}^+) \quad (8.5)$$

The operators  $B_r$  and their energy  $\hbar \omega_r$  describe the Hamiltonian of delocalized states representing for long-wavelength or wavevector  $k \rightarrow 0$  excitons:

$$H = \sum_r B_r^+ B_r \hbar \omega_r \quad (8.6)$$

Migration of a local excitation of non-interacting molecules requires interaction in the excited states. Optically excited states have transition dipoles and dipolar interaction to transition dipoles in neighboring cells spreads the excitation even if there is no other interaction of the electrons. Operators representing delocalized states, labeled by their wavevector  $k$ , are generated from local operators by proper choice of the expansion coefficients in Eq. (8.5), as for instance

$$c_{r,nj} = \frac{1}{\sqrt{N}} \exp(-ikr_j), \quad d_{r,ni} = 0 \quad (8.7)$$

where  $N$  is the number of cells, accounting for normalization and  $r_j$  denotes the position of cell  $j$ .

The operator  $B_r$  as delocalized eigenstate of a homogeneous system can be viewed as the normal mode of a system of coupled local oscillators. Normal modes

of wavevector  $k$  and frequency  $\omega_n$  are described by field amplitudes  $Q_{nk}$  and conjugated moments  $P_{nk}$ :

$$Q_{nk} = \sqrt{\frac{\hbar}{2\omega_n}}(B_{nk} - B_{n-k}^+), \quad P_{nk} = i\sqrt{\frac{\hbar\omega_n}{2}}(B_{nk}^+ + B_{n-k}) \quad (8.8)$$

Using these amplitudes the Hamiltonian acquires a more classical appearance:

$$H = \sum_n \hbar\omega_n \sum_k \frac{-1}{2} (P_{nk}P_{n-k} + \omega_n^2 Q_{nk}Q_{n-k}) \quad (8.9)$$

The operators derived from the coefficients in Eq. (8.7) represent propagating waves and are appropriate if spatial damping is to be considered [16]. Their combination  $Q_{nk} - Q_{n-k}$  and  $i(Q_{nk} + Q_{n-k})$  is Hermitian and representing stationary states is suitable to study temporal damping of an excited state.

Fano's equivalence of excited electrons and classical oscillators yields the same exciton polarization as a derivation that starts out from a free electron gas in homogeneous semiconductors [17]. Optical excitations correspond to density fluctuations, represented by fermion operators  $a_k$  and the equation of motion of the Fourier components  $q = k - k'$  of Coulomb-coupled local fluctuation leads to a hierarchy of multi-operator terms. Expansion to four-operator terms and factorizing the dominant contributions by two-operator terms corresponds to weak excitation and results in linear polarization involving two Coulomb coupled states  $|k\rangle$  and  $|k'\rangle$  which for  $k = k'$  represent excitons of wavevector  $q = 0$ .

### 8.2.1.2 From Excitons to Polaritons

Excitons in isotropic solids have either even or odd symmetry and being normal modes of long wavelength are transverse or longitudinally polarized. Transverse waves are even with respect to reflection on a plane perpendicular to the wavevector  $k$  while longitudinal waves change sign under that operation (Fig. 8.2). As in the case of phonons, different forces apply to transverse and longitudinal modes resulting in different energies of transverse and longitudinal excitons [18]. Quite early it was also suggested that exciting an exciton in anisotropic solids requires an energy that depends on the propagation of light [19]. An exciton is usually perceived as a purely electronic state excited by light. However, the exciton cannot be separated from its dipole moment, which permits not only coupling to light but also represents the polarization, defined by the volume density of transition dipoles. In an enlightening paper, Hopfield pointed out that perturbation theory is inappropriate to derive the optical response of solids [20]. An optically excited state must be derived as an eigenstate of a Hamiltonian, which consists of the electronic excitation  $H_{\text{exc}}$ , represented by excitons, the radiation field  $H_{\text{rad}}$ , represented by photons, and their interaction  $H_{\text{int}}$ . None of these terms can be treated as perturbation in describing the optical spectra of solids. Since such a coherent

state of light and delocalized excitons is closely related to coherent coupling of an atom to the radiation field, it is useful to consider first the resulting Rabi splitting of atomic levels.

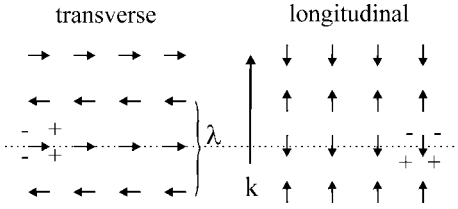


**Figure 8.2** Transverse and longitudinal polarized waves of wavelength  $\lambda$  in an isotropic medium. The amplitude of longitudinal modes changes sign under reflection on a plane perpendicular to the wavevector  $k$ .

Consider two levels at energy  $\hbar\omega_2$  and  $\hbar\omega_1$  that are coupled by the transition dipole  $\mu_{12}$  and the time-dependent field  $E \cos(\omega t)$ . The wavefunction of the coupled state is described as linear combination of the eigenstates  $\phi_1(r)$  and  $\phi_2(r)$ :

$$\Psi(r, t) = a_1(t)\exp(-i\omega_1 t)\phi_1(r) + a_2(t)\exp(-i\omega_2 t)\phi_2(r) \quad (8.10)$$

and the term  $\mu_{12}E(t)$ , coupling light and exciton of frequency  $\omega$  and  $\omega_0 = \omega_2 - \omega_1$ , respectively, results in a time dependence of the amplitudes  $a_1$  and  $a_2$ :

$$\begin{aligned} \frac{da_1}{dt} &= i\mu_{12} \frac{E}{2\hbar} \{ \exp[i(\omega - \omega_0)t] + \exp[i(\omega + \omega_0)t] \} a_2 \\ \frac{da_2}{dt} &= i\mu_{12} \frac{E}{2\hbar} \{ \exp[i(\omega - \omega_0)t] + \exp[i(\omega + \omega_0)t] \} a_1 \end{aligned} \quad (8.11)$$

Being interested in the resonant case, the rapidly oscillating term of frequency  $\omega + \omega_0$  is discarded, keeping the slowly varying part of frequency  $\omega - \omega_0$ . Replacing the derivative  $da_1/dt$  in the second derivative of  $a_2$  reveals the harmonic variation of the expansion coefficient  $a_2$  and an equivalent result is obtained for  $a_1$ :

$$\frac{d^2 a_2}{dt^2} = - \left| \frac{\mu_{12} E}{2\hbar} \right|^2 a_2 \quad (8.12)$$

The contributions of the ground and excited states to the excited state change periodically with frequency  $\omega_R/2$  and the atom oscillates with the Rabi frequency  $\omega_R$  between both states:

$$a_2(t) = a_2(0)\exp\left(\frac{\pm i\omega_R}{2} t\right) \quad \omega_R = \frac{|\mu_{12} \cdot E|}{\hbar} \quad (8.13)$$

The phase factor of the wavefunction  $\Psi(r,t)$  shows that under resonant conditions,  $\omega = \omega_0$ , both levels split by the Rabi frequency  $\omega_R$  and the spectrum  $\omega_0$  develops sidebands separated by  $\omega_R$  from the central line at  $\omega_0$ :

$$\Psi(r,t) = a_1(0)\exp\left[-i\left(\omega_1 \pm \frac{\omega_R}{2}\right)t\right]\phi_1(r) + a_2(0)\exp\left[-i\left(\omega_2 \pm \frac{\omega_R}{2}\right)t\right]\phi_2(r) \quad (8.14)$$

Under non-resonant conditions,  $\omega = \omega_0 - \eta$ , detuning modifies the level splitting and introduces an additional phase factor  $\exp(-i\eta t)$  resulting in opposite shifts of ground and excited states. The shift resembling the Stark effect in a static field is called the optical Stark effect [17]:

$$E_1 = \hbar\left(\omega_1 - \frac{\eta \pm \sqrt{\eta^2 + \omega_R^2}}{2}\right), \quad E_2 = \hbar\left(\omega_2 + \frac{\eta \pm \sqrt{\eta^2 + \omega_R^2}}{2}\right) \quad (8.15)$$

An excited atom decays with lifetime  $\tau$  by spontaneous emission of a photon within the bandwidth of the spectral line. Rabi oscillation and Rabi splitting are thus observed only if  $\omega_R$  exceeds the spectral linewidth, otherwise the energy of the excited atom is dissipated before it is coupled back to the radiation field. The Rabi frequency, being proportional to the transition dipole  $\mu_{12}$  and the radiation field  $E$ , increases with the square root of the photon density and is observed either in intense light or in a cavity. In a cavity photons of the resonator mode at  $\omega$  outnumber by far those from spontaneous emission and with negligible dissipation the energy of a resonant atom oscillates between the resonator mode and the atom. Stationary states of resonator mode and excited state are obtained by a linear combination of photon and excited atom and in the case of resonance,  $\omega = \omega_0$ , the degenerate levels of exciton and resonator split according to the coupling strength, which defines the Rabi frequency.

The Hamiltonian of coherently coupled excitons and light must account for excitons including their dipole moment, photons and their interaction:

$$\begin{aligned} H &= H_{exc} + H_{rad} + H_{int} \\ &= \sum_k E(k) \left( B_k^+ B_k + \frac{1}{2} \right) + \sum_k \hbar\omega(k) \left( A_k^+ A_k + \frac{1}{2} \right) + H_{int} \end{aligned} \quad (8.16)$$

Excitons of energy  $E(k)$ , including the corresponding dipole moment, are represented by boson operators  $B_k$  and should be regarded as field quanta of the polarization. They differ from the bare electron–hole pair, solutions of the stationary Schrödinger equation, by the dipole moment [21]. The operators  $A_k$  represent the photons of the radiation field and the interaction term couples photons and excitons to the coherent eigenstate. In anisotropic solids an additional index appears, denoting the polarization of exciton and photon.

The field quanta of the coherently coupled polarization and radiation are the polaritons, composite particles of excitons and photons. Energy brought into the system as photons or excitons will be redistributed since neither one is an eigenstate of the coupled system. Conservation laws of homogeneous media require that a photon of energy  $\hbar\omega(k)$  creates an exciton of the same energy and momentum while annihilation of an exciton creates that photon again. The latter is valid within the linear approximation of non-interacting excitons. Therefore, as a local excitation propagates, energy oscillates between the photon and the exciton until the polariton reaches the surface and is reflected or vanishes by emitting a photon. It is emphasized that exciton and photon cannot separate as the polariton wavepacket propagates. The interaction part  $H_{\text{int}}$  binding exciton and photon to a polariton is essential and can be written as [20, 22]

$$H_{\text{int}} = \frac{\hbar}{2} \sum_k F_k (A_k^\dagger B_k - A_k B_k^\dagger) \quad (8.17)$$

The coupling constant  $F_k$  of photon and exciton depends on the transition dipole moment, the volume density of oscillators  $N$  and the detuning of frequencies of photon and exciton,  $\omega_k$  and  $\Omega_k$ , respectively. It is convenient to express the coupling constant by quantities that are easily obtained from experiments:

$$F_k = \omega_p \sqrt{\frac{\omega_k}{\Omega_k}} f_k, \quad f_k = \frac{2m}{\hbar e^2} \Omega_k |\mu_k|^2, \quad \omega_p = \sqrt{\frac{e^2 N}{m \epsilon_0}} \quad (8.18)$$

The square root of the oscillator strength  $f_k$  replaces the transition dipole  $\mu_k$  and the plasma  $\omega_p$  accounts for the permittivity of vacuum  $\epsilon_0$  and the density  $N$  of oscillators. Compared with the atom in a cavity, photon and excited state exchanged their role since in a weakly excited solid a large number of oscillators couples to a few photons.

The time dependence follows the same scheme as shown for an atom and the polariton wavefunction is written as a linear combination of exciton and photon of energy  $\hbar\Omega_k$  and  $\hbar\omega_k$ , respectively:

$$\Psi(t) = \sum_k [c_k \exp(-i\omega_k t) A_k^\dagger + d_k \exp(-i\Omega_k t) B_k^\dagger] \quad (8.19)$$

The corresponding amplitudes  $c_k$  and  $d_k$  derive again from the equation of motion:

$$\frac{d}{dt} \Psi(t) = -iH\Psi(t) \quad (8.20)$$

and the interaction term determines the time dependence of the exciton and photon amplitudes of the polariton:

$$\begin{aligned}\frac{d}{dt}c_k &= -iF_k d_k \exp(-i\eta_k t), \quad \eta_k = \Omega_k - \omega_k \\ \frac{d}{dt}d_k &= -iF_k c_k \exp(i\eta_k t) - (\gamma_k d_k)\end{aligned}\tag{8.21}$$

Under resonance conditions the photon and exciton amplitudes oscillate with the Rabi frequency, determined by the plasma frequency and the oscillator strength of the exciton:

$$\omega_R^2 = \omega_p^2 f\tag{8.22}$$

The time derivative of the exciton amplitude includes a phenomenological relaxation rate  $\gamma_k$  to account for inelastic scattering, assuming that only excitons couple to other states of the system. As the excitons dissipate energy less is coupled back to the radiation field and observed as absorption of light.

The theory of Rabi coupling with only one component involved in energy dissipation yields an effective scattering rate  $\gamma$  of the polariton, which depends not only on the scattering rate  $\gamma_k$  of the exciton but also on the Rabi frequency [22, 23]:

$$\gamma = \frac{\gamma_k \omega_R^2}{(\Omega_k - \omega_k)^2 + \gamma_k^2 + \omega_R^2}\tag{8.23}$$

The dependence on the Rabi frequency accounts for the competition of coupling the exciton coherently to the radiation field or to dissipate its energy into an incoherent population of excited states. Most rapid scattering occurs under resonance condition ( $\Omega_k = \omega_k$ ) and two distinctly different cases emerge:

1. Weak coupling of exciton and photon ( $\omega_R \ll \gamma_k$ ): The exciton is scattered before its energy is coupled back to the radiation field and the energy  $W(t)$  of the polariton decays as

$$W(t) = W(0)\exp(-2\gamma t) = W(0)\exp\left(-\frac{\omega_p^2 f}{\gamma_k} t\right)\tag{8.24}$$

Consistent with Fermi's golden rule, the absorption of light increases with the oscillator strength  $f$  of the exciton and the density of states, which is proportional to  $\omega_p^2$ .

2. Strong coupling of exciton and photon ( $\omega_R \gg \gamma_k$ ): the energy of the polariton oscillates between photon and exciton and decays as

$$W(t) = W(0)\exp(-2\gamma t) = W(0)\exp(-2\gamma_k t)\tag{8.25}$$

Scattering of the polariton and thus the absorption rate of light are independent of the oscillator strength and determined by the scattering rate of excitons.

The absorption rate of light describes the temporal decay  $dW/dt$  of the energy of the stationary radiation field while the absorption constant  $a$  describes spatial damping ( $-dW/dx$ ) of the energy of a propagating wave. The loss increases exponentially with the transit time and the absorbance of light therefore increases exponentially with the thickness of the sample, defining the absorption constant. However, in the strong coupling case ( $\omega_R \gg \gamma_k$ ) the absorption constant does not depend on the oscillator strength but is determined by the exciton scattering rate until this rate is sufficiently fast to reach the weak coupling case ( $\omega_R \ll \gamma_k$ ). For increasing scattering rate polaritons should therefore show a transition from a reduced, non-classical absorption constant to one that follows Fermi's golden rule.

Hopfield assumed that polaritons are peculiar to excitons since excitation into continuum states creates a large number of virtual electron-hole pairs with the momentum of a photon that interfere destructively [20]. Such a principal difference between bound and unbound pairs disappears if bare electron-hole pairs and the electromagnetic field, now including polarization, are treated as coupled wave equations [24]. However, owing to the short lifetime of unbound pairs, polariton effects are observed only at energies below the exciton continuum, a small range in the case of Wannier excitons but large for strong Frenkel excitons in organic solids.

## 8.2.2

### Dielectric Theory

#### 8.2.2.1 Maxwell's Equations, Fields and Energy Flux

Dielectric theory considers that polaritons are normal modes of electromagnetic fields in matter where photons, the normal modes of vacuum, cannot persist. Since polaritons differ from photons by the polarization of matter [25], electrodynamics offers an alternative access to most properties of polaritons that is easily extended to anisotropic solids. Dielectric theory was used to confirm the first experimental evidence of polaritons by explaining an apparent violation of selection rules in hexagonal ZnO. Two narrow absorption lines appeared in the forbidden polarization of light  $E//c$  when by tilting the crystal the wavevector of light had a small component parallel to the optical axis  $c$  [26]. These lines arise from excitons allowed for  $E \perp c$  only, which couple to  $E//c$  owing to a small longitudinal component of the propagating wave. Consistent with the dielectric theory, the lines increased with the tilt angle and the transition energy was close to the longitudinal exciton of the allowed transition for  $E \perp c$ .

Maxwell's equations connect space and time derivatives of four vector fields, the electric field  $E$ , the displacement current  $D$  and the magnetic field  $H$  and induction  $B$  and relate them to space charge  $\rho$  and the current density  $j$ :

$$\nabla \times H - \frac{d}{dt} D = j \quad (8.26)$$

$$\nabla \times E + \frac{d}{dt} B = 0 \quad (8.27)$$

$$\nabla \cdot D = \rho \quad (8.28)$$

$$\nabla \cdot B = 0 \quad (8.29)$$

Material equations describe the linear response of matter to electric and magnetic forces and define the dielectric response function  $\varepsilon$ , the magnetic permeability  $\mu$  and the d.c. conductivity  $\sigma$ ;  $\varepsilon_0$  and  $\mu_0$  account for the permittivity and permeability of vacuum.

$$D = \varepsilon\varepsilon_0 E \quad (8.30)$$

$$B = \mu\mu_0 H \quad (8.31)$$

$$j = \sigma E \quad (8.32)$$

Henceforth only neutral solids ( $\rho = 0$ ) with negligible concentration of free carriers ( $\sigma = 0$ ) are considered, which reduces Maxwell's equations to homogeneous differential equations. We will further consider magnetically isotropic or non-magnetic solids.

The time dependence of the local energy density of electric and magnetic fields,  $W_e + W_m$ , is derived from the sum of the scalar product of Eqs. (8.26) and (8.27) with  $E$  and  $B$ , respectively, and a vector identity links the time derivative of the energy density to the divergence of the Poynting vector  $S = E \times H$ , providing the continuity equation of the energy flux [27]:

$$\frac{1}{2} \frac{d}{dt} (E \cdot D + H \cdot B) = E \cdot (\nabla \times H) - H \cdot (\nabla \times E) = -\nabla \cdot (E \times H) \quad (8.33)$$

$$\frac{d}{dt} (W_e + W_m) + \nabla \cdot S = 0 \quad (8.34)$$

Solutions of Maxwell's equation in homogeneous media are plane waves and the electric field is defined by an amplitude  $E_0$ , wavevector  $k$  and frequency  $\omega$ :

$$E = E_0 \exp(i(\vec{k} \cdot \vec{r} - \omega t)) = E_0 \exp\left(i \frac{n\omega}{c} \vec{r} \cdot \hat{s}\right) \exp(-i\omega t) \quad (8.35)$$

The refractive index  $n = \sqrt{\varepsilon\mu}$  accounts for the modified phase velocity  $c/n$  in matter and the unit vector  $\hat{s}$  is parallel to the wavevector and normal to the wavefront. The Poynting vector defines the unit vector  $\hat{v}$  of the energy propagation:

$$\hat{s} = \frac{\vec{k}}{|\vec{k}|} = \frac{c}{n\omega} \vec{k}, \quad \hat{v} = \frac{\vec{S}}{|\vec{S}|} = \frac{\vec{E} \times \vec{H}}{|\vec{E} \times \vec{H}|} \quad (8.36)$$

The orientation of the fields with respect to the wavevector is obtained by inserting plane waves into Maxwell's equations:

$$\begin{aligned} D + \frac{1}{\omega}(k \times H) &= 0 \quad \text{and} \quad k \cdot D = 0 \\ B - \frac{1}{\omega}(k \times E) &= 0 \quad \text{and} \quad k \cdot B = 0 \end{aligned} \quad (8.37)$$

$D$  and  $B$  are always orthogonal to the wavevector  $k$  but not the electric field  $E$ . The frequently applied condition  $\nabla \cdot E = 0$  results in transverse electric fields  $E \perp k$  but is valid only for isotropic media. Magnetic isotropy keeps also  $H$  transverse.

The energy current density is defined by the Poynting vector  $S = E \times H$  and deviates in anisotropic material from the wavevector as shown in Fig. 8.3. Parallel fields  $B$  and  $H$  define a common plane for the electric field  $E$ , the displacement current  $D$  and the unit vectors of phase and energy velocity,  $\hat{s}$  and  $\hat{v}$ , which are rotated by the angle  $\varphi$  between electric field and displacement current. The transverse component  $E_{\perp}$  of the electric field is found by the projection on to the displacement current:

$$\vec{D} = \frac{n^2 \epsilon_0}{\mu} \frac{\vec{E} \cdot \vec{D}}{|\vec{D}|} = -\frac{n^2 \epsilon_0}{\mu} \hat{s} \times (\hat{s} \times \vec{E}) = \frac{n^2 \epsilon_0}{\mu} [\vec{E} - \hat{s} \cdot (\hat{s} \cdot \vec{E})] = \epsilon \epsilon_0 \vec{E} \quad (8.38)$$

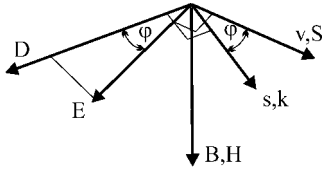


**Figure 8.3** Orientation of the fields of an electromagnetic wave in a non-magnetic medium with respect to unit vectors  $\hat{s}$  and  $\hat{v}$  of wavevector  $k$  and Poynting vector  $S$ .

The dielectric tensor  $\epsilon$  rotates the field and the refractive index therefore varies with the relative orientation of the electric field and the displacement current:

$$n^2 = \frac{c^2 k^2}{\omega^2} = \frac{\mu}{\epsilon_0} \frac{D^2}{\vec{E} \cdot \vec{D}} \quad (8.39)$$

The energy density  $W$  is obtained by integrating the continuity equation of the energy flux [Eq. (8.34)] and can be expressed by the projection of the Poynting vector on to the phase velocity:

$$W = \frac{n}{c} \hat{s} \cdot \vec{S} \quad (8.40)$$

### 8.2.2.2 The Dielectric Tensor and Optical Properties

The dielectric tensor rotates the displacement current with respect to the electric field:

$$D_i(\omega) = \varepsilon_0 \sum_{j=1}^3 \varepsilon_{ij}(\omega) E_j(\omega) \quad (8.41)$$

and the linear relation results in an energy density that is quadratic in the field strength and in ellipsoids representing surfaces of constant energy:

$$\frac{W}{\varepsilon_0} = \varepsilon_{11} E_1^2 + \varepsilon_{22} E_2^2 + \varepsilon_{33} E_3^2 + 2(\varepsilon_{12} E_1 E_2 + \varepsilon_{23} E_2 E_3 + \varepsilon_{31} E_3 E_1) \quad (8.42)$$

A real dielectric tensor  $\varepsilon_{ij}$  can be diagonalized, which is equivalent to using the principal axes of the ellipsoid as coordinates ( $x$ ,  $y$ ,  $z$ ). The energy density is then expressed by the diagonal elements of the dielectric tensor and the field amplitudes:

$$W = \varepsilon_0 \left( \varepsilon_x E_x^2 + \varepsilon_y E_y^2 + \varepsilon_z E_z^2 \right) = \frac{1}{\varepsilon_0} \left( \frac{D_x^2}{\varepsilon_x} + \frac{D_y^2}{\varepsilon_y} + \frac{D_z^2}{\varepsilon_z} \right) \quad (8.43)$$

Eliminating the magnetic fields in the Maxwells equations leads to a relation of displacement current, electric field and wavevector of a propagating wave:

$$\mu_0 \mu \vec{D} = -\frac{1}{\omega^2} \vec{k} \times (\vec{k} \times \vec{E}) = \frac{1}{\omega^2} [k^2 \vec{E} - (\vec{k} \cdot \vec{E}) \vec{k}] \quad (8.44)$$

Replacing the displacement current [Eq. (8.41)] provides a set of equations for the components  $E_j$  of the electric field, which shows that the polarization of the propagating wave depends on the orientation of the wave vector and the dielectric constants:

$$\sum_{i=1}^3 \left[ \frac{\omega^2}{c^2 k^2} \varepsilon_{ij}(\omega) - \delta_{ij} + s_i s_j \right] E_j(\omega) = 0 \quad (8.45)$$

The velocity of light enters via the identity  $\varepsilon_0 \mu_0 = c^{-2}$ . Transformation to the principal axes and the definition of the refractive index in Eq. (8.39) simplifies the evaluation of the polarization:

$$E_j = \frac{n^2 s_j (\vec{E} \cdot \hat{s})}{n^2 - \mu \varepsilon_j}, \quad j = x, y, z \quad (8.46)$$

The scalar product  $\hat{s} \cdot \vec{E}$  finally leads to the Fresnel equation, the fundamental equation of crystal optics, which describes ellipsoids of constant phase:

$$\frac{s_x^2}{n^2 - \mu\epsilon_x} + \frac{s_y^2}{n^2 - \mu\epsilon_y} + \frac{s_z^2}{n^2 - \mu\epsilon_z} = \frac{1}{n^2} = \frac{\omega^2}{c^2 k^2} \quad (8.47)$$

This equation is also obtained from Eq. (8.45) by the condition for non-vanishing electric field:

$$\det \left| \frac{\omega^2}{c^2 k^2} \epsilon_{ij}(\omega, \vec{k}) - \delta_{ij} + s_i s_j \right| = 0 \quad (8.48)$$

The Fresnel equation is quadratic in  $k^2$  and yields two waves  $\omega(\pm k)$  of orthogonal polarization, which are the normal modes of electromagnetic fields. Coupling photon and exciton to a polariton thus correspond to combining radiation field and the polarization to the displacement current and the dielectric susceptibility  $\chi$  therefore represents the exciton part of the polariton:

$$\vec{D} = \epsilon_0 \vec{E} + \vec{P}, \quad \vec{P} = \chi \epsilon_0 \vec{E} \quad (8.49)$$

Solving the Fresnel equation requires knowledge of the dielectric constant, which will be compared with better observable quantities, such as absorption constant, reflectivity and refractive index. Temporal damping of the electric field [Eq. (8.35)] corresponds to an imaginary part of frequency  $\omega$  but spatial damping should be described by an imaginary part of the refractive index  $\tilde{n} = n + i\kappa$ , resulting in an imaginary part of the wavevector  $k$  and exponential decay of the field and the intensity  $I$ :

$$\begin{aligned} \vec{E} &= \vec{E}_0 \exp\left(-\kappa \frac{\omega}{c} \hat{s} \cdot \vec{r}\right) \exp\left[i\left(n \frac{\omega}{c} \hat{s} \cdot \vec{r} - \omega t\right)\right] \\ I &= |\vec{E}|^2 = I_0 \exp(-ar) = I_0 \exp\left(-2 \frac{\kappa \omega}{c} \hat{s} \cdot \vec{r}\right) \end{aligned} \quad (8.50)$$

The absorption constant  $a$  is therefore directly related to the imaginary part of the refractive index:

$$a = 2 \frac{\omega}{c} \kappa \quad (8.51)$$

The complex refractive index implies a complex dielectric constant representing the dielectric response function for a given wavevector:

$$\epsilon \mu = [\text{Re}(\epsilon) + i\text{Im}(\epsilon)]\mu = \tilde{n}^2 = (n + i\kappa)^2 = (n^2 - \kappa^2) + i(2n\kappa) \quad (8.52)$$

Polaritons must be excited on the surface of the solid by incident photons. The continuity of the electric field component parallel to the surface and of the normal component of the displacement current imposes boundary conditions that are matched by partial reflection of an incident photon or polariton current:

$$E_r = rE_0 \quad E_t = tE_0 \quad (8.53)$$

The reflection and transmission coefficients  $r$  and  $t$  can also be obtained from the continuity of the time and spatial derivative of photon and polariton amplitudes at the interface. For normal incidence of light the boundary conditions lead to

$$r = \frac{1-n}{1+n} = \sqrt{R} \exp(i\theta), \quad t = \frac{2}{1+n} \quad (8.54)$$

where  $R$  is reflectivity of the surface and  $\theta$  accounts for the phase shift of the reflected field.

### 8.2.2.3 Local Oscillators and Macroscopic Polarization

The macroscopic polarization of a single crystal is the dipole  $\mu$  induced in the unit cell by the local electric field of frequency  $\omega$ , which is the sum of dipole moments induced in the molecules via their polarizability  $\beta$ . The polarizability of molecule in the ground state  $|g\rangle$  is a rather complicated tensor since it involves virtual transitions to all excited states  $|f\rangle$ . Virtual transitions are described by the transition dipole matrix elements  $\mu_{fg} = \langle f|er_j|g\rangle$  and an energy denominator, which accounts for detuning of the photon from the transition energy  $E_f - E_g$ .

$$\beta_{ij} = \sum_f \left( \frac{\langle g|er_i|f\rangle \langle f|er_j|g\rangle}{E_f - E_g - \hbar\omega} + \frac{\langle g|er_j|f\rangle \langle f|er_i|g\rangle}{E_f - E_g + \hbar\omega} \right), \quad r_j = x, y, z \quad (8.55)$$

The induced dipole depends on the orientation of the local field with respect to the transition dipoles  $\mu_{fg}$  and points into a different direction than the field unless the molecule or the unit cell is isotropic.

Owing to the energy denominator near resonance of a strong and spectrally isolated transition the corresponding transition dipole dominates the polarizability. The consequences of such a dominant transition are obvious in the example in Fig. 8.4, presenting a sexithiophene molecule with large transition dipole  $\mu_{fg}$  parallel to the molecular axis. This transition dominates the polarizability in the visible spectral range and the induced dipole  $\mu$  points along the molecular axis for any orientation of the incident electric field  $E$ , and the magnitude is given by the scalar product of transition dipole and field:

$$\vec{\mu} = \sum_j \beta_{ij} E_j \equiv \frac{|\langle f|\vec{\mu}_{fg} \cdot \vec{E}|g\rangle|^2}{\hbar^2 ((\omega_f - \omega_g)^2 - \omega^2)} \quad (8.56)$$

The induced dipole is a Lorentz oscillator as in classical physics and the molecular dipoles add up to the polarization of the cell. Equivalent to considering individual

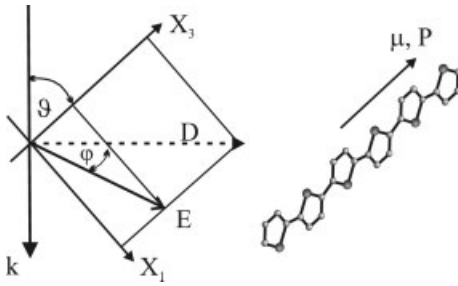


**Figure 8.4** Orientation of the electric field  $E$  and the displacement current  $D$  in a solid consisting of aligned molecules. The transition dipole moment  $\mu$  along the molecular axis introduces anisotropy and defines a principal axis of the dielectric tensor.

molecules is summing up the molecular transition dipoles to a polarizability of the unit cell.

The local electric field that induces polarization is not that of the radiation field but is altered by the field arising from the induced dipoles. For normal incidence of light, dipoles induced on the surface oscillate in phase and layers below maintain that property so that the wavevector of the polariton is normal to the surface. Plane-wise summation is therefore a convenient method of summation, converging rapidly so that after very few planes the sample acquires the optical properties of a semi-infinite solid [28, 29]. The dynamic modification of the local field is part of the propagating field but there is also a non-vanishing static part of the polarization ( $\omega = 0$ ) evident from the Lorentz oscillator in Eq. (8.56). That static field interacts with the dipole moments of the unit cell, resulting in some shift with respect to the transition energy of free molecules. If unit cells contain molecules of different orientation the static field splits the molecular exciton into a multiplet of Davydov components, each representing a superposition of molecular transitions compatible with the symmetry of the cell [4].

The solvent shift of molecules in solution results from polarization of the solvent and the local field at the site of diluted molecules can be estimated from isotropic Lorentz screening since the contribution of diluted molecules is negligible. In solids all polarization is created by exciton dipoles but the magnitude depends on the local field. The situation is particularly difficult in anisotropic solids. Let all molecules in Fig. 8.4 be parallel in an otherwise isotropic solid of dielectric constant  $\epsilon_1$ . The polarization is parallel to the dominant transition dipole  $\mu$  and it is favorable to use that direction as optical axis  $X_3$  of a uniaxial dielectric tensor. Below the resonance frequency the dielectric constant  $\epsilon_3$  is larger than  $\epsilon_1$  owing to the contribution of the molecular dipoles. The displacement current  $D$  is orthogonal to the wavevector  $k$  but the coplanar electric field has a longitudinal component,  $\epsilon_0 E_j = D_j/\epsilon_j$ , which increases as the resonance frequency of the exciton is approached [Eq. (8.56)]. The electric field therefore rotates owing to an increasing

$\varepsilon_3$  and at the resonance frequency of the exciton the field is orthogonal to the transition dipole due to the diverging value  $\varepsilon_3$ , leaving the polarization undefined.

The problem vanishes by going back to Maxwell's equation where the longitudinal electric field emerges as direct consequence of Coulomb's law in the absence of space charge:

$$\nabla \cdot \vec{D} = \varepsilon_0 \nabla \cdot \vec{E} + \nabla \cdot \vec{P} = 0 \rightarrow \nabla \cdot \vec{E} = -\frac{\nabla \cdot \vec{P}}{\varepsilon_0} \quad (8.57)$$

Any longitudinal component of the polarization creates a longitudinal electric field to maintain a transverse displacement current. The longitudinal electric field thus depends on the angle  $\vartheta$  between the transition dipole  $\mu$  and the wavevector  $k$  but it is always opposite to the polarization, generated by the induced dipole. Since the dipole is part of the optically excited state, coupling the transition dipole to the longitudinal field results in a blue shift of the optical resonance, representing a polariton of  $k \approx 0$ . Excitons–polaritons are therefore shifted to higher energy compared with that of bare excitons by an amount that increases with the longitudinal polarization. Since such a shift is absent in isotropic solids where all fields are transverse, the directional shift of the resonance of an exciton–polariton by a macroscopic longitudinal polarization is the most striking effect observed in the spectra of anisotropic solids.

### 8.3

#### Fundamental Properties of Polaritons: Dispersion $\Omega(\mathbf{k})$

##### 8.3.1

##### Polaritons in Isotropic Solids

###### 8.3.1.1 Localized Electronic States

All principal axes of the dielectric tensor are equivalent in isotropic solids and a single dielectric constant enters the Fresnel equation:

$$\varepsilon(\omega) - \frac{c^2 k^2}{\omega^2} = n^2(\omega) - \frac{c^2 k^2}{\omega^2} = 0 \quad (8.58)$$

The polarization  $P(\omega)$ , the product of induced dipole moment  $\mu_{\text{cell}}$  and density of the unit cells, is expressed by Lorentzians, each representing an exciton with transition dipole  $\mu_j$ :

$$\vec{P} = N \vec{\mu}_{\text{cell}} = N \sum_j \frac{\omega_j}{\hbar} \frac{|\mu_j|^2}{\omega_j^2 - \omega^2} \vec{E} = \chi \varepsilon_0 \vec{E} \quad (8.59)$$

Substituting the density of unit cells by the plasma frequency [Eq. (8.18)] yields a dielectric constant defined as sum of contributions of excitons to the susceptibility  $\chi = \varepsilon - 1$ :

$$\varepsilon(\omega) = 1 + \omega_p^2 \sum_j \frac{m\omega_j}{e^2 \hbar} \frac{|\mu_j|^2}{\omega_j^2 - \omega^2} = 1 + \sum_j \frac{\chi_j \omega_j^2}{\omega_j^2 - \omega^2} \quad (8.60)$$

The right-hand side defines the strength of exciton by the contribution  $\chi_j$  of the exciton to the static dielectric constant  $\varepsilon(0)$ , which is closely related to the oscillator strength  $f_j$  of the exciton, the transition dipole  $\mu_j$  and the plasma frequency  $\omega_p$ :

$$f_j = \frac{2m}{\hbar e^2} \omega_j |\mu_j|^2, \quad \chi_j = \frac{N}{\varepsilon_0} \frac{|\mu_j|^2}{\hbar \omega_j} = \frac{\omega_p^2 f_j}{\omega_j^2 2} \quad (8.61)$$

Inserting the dielectric constant into the Fresnel equation leads to the dispersion relation of the polaritons  $\omega(k)$  in an isotropic material:

$$\frac{c^2 k^2}{\omega^2} = n^2 = \varepsilon(\omega) = \varepsilon(\infty) + \sum_j \frac{\chi_j \omega_j^2}{\omega_j^2 - \omega^2} \quad (8.62)$$

The dielectric constant  $\varepsilon(\infty)$  accounts for the polarization contributed by transitions at higher energy and allows reducing the sum to transitions in the spectral range of interest. The dispersion  $E(k)$  in Fig. 8.5 considers a single transverse exciton TE at  $\hbar\omega_j = 2$  eV of strength  $\chi = 1$  in vacuum,  $\varepsilon(\infty) = 1$ . The exciton is localized and therefore its energy is independent of the wavevector. The photon has its linear dispersion and intersects at 2 eV the dispersion of the transverse exciton. Coupling of photon and exciton by the transition dipole of the exciton lifts that degeneracy and results in two polaritons branches  $\omega(k)$ , which are separated by an energy gap. The gap is the range of negative dielectric constant above the exciton energy [Eq. (8.62)] and corresponds to an imaginary wavevector  $k$ . Photons in the spectral range of the polariton gap cannot couple to a propagating wave and are reflected, resulting in the “metallic” reflectivity of the polariton stop band.

The lower polariton branch starts with linear dispersion but reduced phase velocity, which shows that even far from resonance photons remain coupled to the exciton. The group velocity  $d\omega/dk$  decreases as the frequency approaches resonance and vanishes at the transition energy of the localized exciton. The wavevector diverges ( $k \rightarrow \infty$ ) and this pole identifies the transition energy of the transverse exciton. The upper branch starts at the energy where the dielectric constant returns to positive values. At higher energy the upper branch approaches the photon dispersion curve, indicating that the exciton is no longer coupled into the propagating electromagnetic wave. Since  $\varepsilon = 0$  defines also longitudinal modes the upper branch is degenerate at  $k = 0$  with the longitudinal exciton LE. It is emphasized that the longitudinal exciton does not couple to light since the dipole moment is orthogonal to the transverse electric field of the propagating wave.

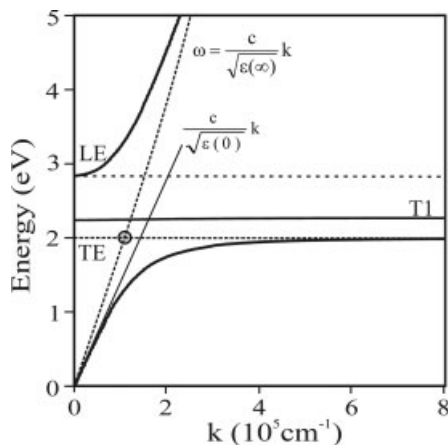


**Figure 8.5** Polariton dispersion resulting from dipolar coupling of a photon to a strong exciton of energy  $TE$ . The degeneracy (circle) is removed and a gap opens between  $TE$  and  $LE$ , the energy of the longitudinal exciton. An additional weak transition ( $T1$ ) opens another branch of small dispersion.

Coupling the exciton transition dipole to the longitudinal field arising from the polarization causes a gap between transverse and longitudinal excitons. Since only longitudinal excitons create such a field they are shifted to higher energy. Transverse and longitudinal excitons thus split by the same interaction of photon and exciton that causes the polaritons gap. The polariton gap increases with the contribution  $\chi$  of the exciton to the static dielectric constant,  $\epsilon(0) = \epsilon(\infty) + \chi$ . Inserting the frequency  $\omega_L$  of the longitudinal exciton into Eq. (8.62) yields the Lyddane–Sachs–Teller relation between transverse and longitudinal resonance frequency of an exciton,  $\omega_T$  and  $\omega_L$ , and the dielectric constant far below and above its resonance:

$$\left(\frac{\omega_L}{\omega_T}\right)^2 = 1 + \frac{\chi}{\epsilon(\infty)} = \frac{\epsilon(0)}{\epsilon(\infty)} \quad (8.63)$$

This relation is well known from phonon spectra. Since the local field is partially screened by the polarization arising from high-energy transitions the coupling strength  $\chi$  of the exciton to light is reduced by the high frequency dielectric constant  $\epsilon(\infty)$ . For the example presented, the energy of the  $LE$  exciton is 2.83 eV. The susceptibility  $\chi = 1$  of an exciton at  $\hbar\omega_j = 2$  eV and  $\epsilon(\infty) = 1$  corresponds to an oscillator strength  $f \approx 1$  and a transition dipole  $\mu = 2 e \text{ \AA}$  for a molecular volume of  $250 \text{ \AA}^3$ , which are common values for  $\pi$ -conjugated molecules.

Each transverse exciton provides a polariton branch. If another exciton dispersion crosses the polariton the degeneracy will be lifted again by a coupling transition dipole. If a weak exciton  $T1$ , for instance a vibronic satellite, falls into the polariton gap the wavevector becomes real again below the transition energy  $T1$

where  $\varepsilon(\omega)$  has a pole. That case is shown in Fig. 8.5 for a weak additional exciton ( $\chi = 0.1$ ) at 2.2 eV. The zero of  $\varepsilon(\omega)$  defines the longitudinal mode L1 and another polariton branch appears in energy range between L1 and T1. This range increases with the strength of the T1 exciton. The main branch changes little if the strength of the exciton at 2 eV is reduced to  $\chi = 0.85$  to keep the position of the upper longitudinal exciton LE. This interdependence of strong and weak transition shows that the polariton involves all excitons.

Transverse and longitudinal exciton energies inserted into Eq. (8.62) provide another representation of the dielectric constant [30, 31], the Kurosawa equation, which is very useful for determining the polariton resonance in anisotropic crystals:

$$\varepsilon(\omega) = \varepsilon(\infty) \prod_j \frac{L_j^2 - (\hbar\omega)^2}{T_j^2 - (\hbar\omega)^2} \quad (8.64)$$

The finite lifetime  $\tau = 1/\gamma$  of excitons introduces an imaginary part into the Lorentz oscillators and, resulting in an imaginary part of the wavevector, spatial attenuation of the polariton:

$$\frac{c^2 k^2}{\omega^2} = \tilde{n}^2 = \varepsilon(\infty) + \sum_j \frac{\chi_j \omega_j^2}{\omega_j^2 - \omega^2 - i\gamma_j \omega} \quad (8.65)$$

The full curve in Fig. 8.6 shows the same polariton as in Fig. 8.5 but with weak damping ( $\hbar\gamma = 5$  meV) of the excitons. The polariton dispersion, represented by the real part of the wavevector, is not much altered except for poles that are replaced by maxima. The imaginary part of the wavevector corresponds, except for a factor of 2, to the absorption spectrum, evident from Eqs. (8.51) and (8.52):

$$a = 2 \frac{\omega}{c} \kappa = \frac{c}{\omega} \frac{\text{Im}(\varepsilon)}{n} = 2\text{Im}(k) \quad (8.66)$$

Absorption maxima occur near the resonance frequency where the exciton amplitude and hence the scattering rate of the polariton is largest. The lineshape is asymmetric despite a dielectric response that is represented by Lorentzians. The distorted lineshape is due to significant dispersion of the refractive index near a strong spectral resonance. The reflectivity of the polariton shows the wide band of high reflectance but scattering reduces its height. The polariton branch related to the weak exciton at 2.2 eV causes a narrow dip in the band of high reflectivity. The dashed lines show the effect of stronger broadening by 50 meV of the weak exciton. The exciton polariton dispersion is hardly affected except for additional broadening around 2.2 eV but the reflectivity responds sensitively. The narrow dip fills up but remains narrow and, most noteworthy, broadening of the weak transition reduces the reflectance in the whole range of the band without affecting its

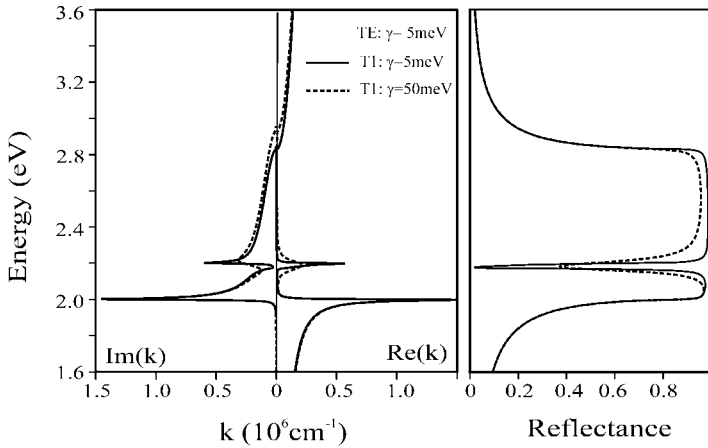


**Figure 8.6** Polariton dispersion as in Fig. 8.5. Spatial damping  $\gamma$  results in absorption  $\alpha = 2\text{Im}(k)$ . The polariton branch due to a weak exciton at 2.2 eV causes a narrow dip in

the high-reflectance band between the excitons of energy  $TE$  and  $LE$ . Increasing scattering of the weak transition  $T1$  affects the whole reflectance band.

width. The width of the reflectance, deriving from the macroscopic polarization in the solid, obviously cannot be reproduced by broadening an exciton, even if the Lorentzian describes the absorption spectrum of the molecules in the vapor phase fairly well [32].

Energy propagation is increasingly diffusive in the case of scattering and must be derived from the energy flux including energy loss terms [12]. Only in the weakly absorbing region does the energy propagate with the group velocity  $v = \nabla_k \omega(k)$  of excitons. Scattering, on the other hand, deposits energy into the solid, decreasing the reflectivity within the polariton gap.

### 8.3.1.2 Delocalized Electrons: Spatial Dispersion of Polaritons

The excitation energy of localized electrons migrates only by coupling the polarization into a propagating electromagnetic wave. Hybridization of the molecular orbitals, however, delocalizes the electrons and the resulting Bloch state provides an independent path of coherent energy migration. The kinetic energy resulting from the center of mass motion of an electron–hole pair increases the exciton energy and alters the resonance energy of the exciton to  $\hbar\Omega(k) = \hbar\omega_0 + (\hbar k)^2/2M$ . The resulting dependence of the dielectric function on the wavevector is called spatial dispersion of the polariton [33]:

$$\varepsilon(\omega, k) = \varepsilon(\infty) + \frac{\omega_0^2 \chi}{\Omega^2 - \omega^2} = \varepsilon(\infty) + \frac{\chi}{\left(1 + \frac{\hbar k^2}{2M \omega_0}\right)^2 - \left(\frac{\omega}{\omega_0}\right)^2} \quad (8.67)$$

Spatial dispersion effects are most pronounced for Wannier excitons in high-mobility semiconductors where the electron and hole have a small mass. Since the transition dipole is still determined by the spatial overlap of electron and hole, equivalent to finding the excited electron at the site of the hole [2], local response theory can be applied as long as the Bohr radius is small compared with the wavelength of light.

The kinetic energy of the exciton has a significant effect on solutions of the Fresnel equation:

$$\frac{c^2 k^2}{\omega^2} = \varepsilon(\infty) + \frac{\chi}{1 + \frac{\hbar k^2}{M \omega_0} - \left(\frac{\omega}{\omega_0}\right)^2} \quad (8.68)$$

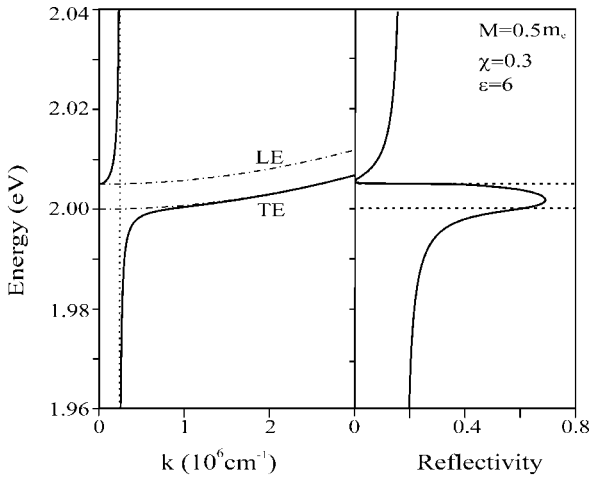
The term of order  $k^4$  in the Lorentz denominator of the exciton susceptibility is omitted since the kinetic energy is small compared with the transition energy  $\hbar\omega_0$ . The remaining dependence on the wavevector introduces a term  $k^4$  into the Fresnel equation and generates two polaritons of the same polarization.

Figure 8.7 shows the polariton dispersion near the crossing of photon and exciton dispersion, calculated for a Wannier exciton with common parameters: Exciton mass  $M = 0.5m_e$ , transition energy 2 eV, susceptibility  $\chi = 0.3$  and background dielectric constant  $\varepsilon(\infty) = 6$ . The splitting of transverse (TE) and longitudinal (LE) excitons is only 5 meV, consistent with the Lyddane–Sachs–Teller relation and the small ratio  $\chi/\varepsilon(\infty)$ . Resonant Raman scattering is commonly used to measure the polariton branches and confirm the expected dispersion [34]. The lower branch bends over from the linear photon-like dispersion into the exciton dispersion as in the case of localized excitons and the wavevector is real for all energies. The wavevector of the second branch is imaginary at low energy and becomes real at the energy of the longitudinal exciton, approaching photon-like dispersion at high energy.

Compared with the polariton in Fig. 8.5, which is based on localized excitons, the change in the dispersion seems small. However, the kinetic energy of the exciton closes the gap for electromagnetic waves, extending the lower branch beyond the energy of the longitudinal exciton. The reflectivity therefore stays below unity even in the absence of scattering. More serious is the problem arising from the presence of two polaritons of the same polarization at any energy. Incident photons now couple to two modes of refractive indices  $n_1$  and  $n_2$  even if one is imaginary below the energy of the longitudinal exciton. Since the boundary conditions of the electric field and displacement current are sufficient only to match photons to one polariton, an additional boundary condition is needed to match incident and reflected photons to two polaritons.

An obvious condition is a vanishing contribution of excitons to polarization at the interface  $P(r=0)$ , for instance by destructive interference of the polaritons [35]:

$$P_1(0) + P_2(0) = [n_1^2 - \varepsilon(\infty)]E_1 + [n_2^2 - \varepsilon(\infty)]E_2 = 0 \quad (8.69)$$



**Figure 8.7** Spatial dispersion of a polariton coupled to a mobile exciton of small oscillator strength. The  $k$  dependence of the exciton energy due to the center of mass motion of the exciton closes the polariton gap between transverse and longitudinal excitons of energy  $TE$  and  $LE$  and reduces the reflectivity.

More elaborate boundary conditions consider a repulsive potential that keeps the exciton away from the surface [33]. This unknown potential is usually replaced by an infinite barrier, creating an exciton-free layer of refractive index  $\sqrt{\varepsilon(\infty)}$  of a thickness comparable to the exciton Bohr radius. The boundary condition in Eq. (8.69) leads to an effective refractive index  $n^*$  which is real only above the longitudinal exciton where both modes propagate [33]:

$$n^* = \frac{n_1 n_2 + \varepsilon(\infty)}{n_1 + n_2}, \quad R = \left| \frac{1 - n^*}{1 + n^*} \right|^2 \quad (8.70)$$

The reflectivity in Fig. 8.7 has been calculated from Eq. (8.70). Scattering has been excluded but the reflectivity is well below unity in the polariton gap between transverse and longitudinal exciton, indicated by the dashed lines. The reflectivity increases with increasing mass of the exciton and for  $M \rightarrow \infty$ , corresponding to immobile excitons, the total reflectance within the polariton gap is recovered. The reduced reflectivity is due to energy transport by mobile excitons and is found for any boundary condition. The reflectivity decreases further if scattering dissipates more energy into the solid and in the case of an exciton-free layer the spectrum is found to be sensitive to the width of that layer [36, 37].

Most elaborate calculations solve the coupled equations of dipole moments, displacement currents and exciton amplitude near the surface and conjecture that  $\nabla \vec{P}$  should vanish at the surface while the condition  $P(0) = 0$  is adequate if excited states in a surface region differ from bulk states [38], a case that should apply to molecular solids where the transition energies are shifted by dipolar interaction,

which is different close to the surface. Spatial dispersion may be important in single crystals of conjugated polymers for a wavevector along the  $\pi$ -conjugation where electrons move freely. The weak intermolecular overlap in molecular solids, however, results in a large electron mass and spatial dispersion effects should be undetectable. Furthermore, the confinement of electron and hole to a single molecule increases the oscillator strength of Frenkel excitons and opens a wide polariton gap that cannot be closed by the kinetic energy of the exciton. Spatial dispersion effects are therefore neglected in discussing the effects arising from the anisotropy of the molecules.

### 8.3.2

#### Polaritons in Anisotropic Solids: Directional Dispersion

Unless wavevector and electric field coincide with principal axes of the dielectric tensor, the displacement current and electric field point in different directions. Multiplication of the Fresnel equation [Eq. (8.47)] with  $n^2 = (ck/\omega)^2$  yields the fundamental equation of crystal optics for an arbitrarily chosen set of orthogonal axes:

$$\left\{ \sum_{ij} \varepsilon_{ij} s_i s_j n^4 - \sum_l [\varepsilon_{ij} s_i s_j \varepsilon_{ll} - \varepsilon_{il} \varepsilon_{ij} s_i s_j] n^2 \right\} - \|\varepsilon_{ij}\| = 0 \quad (8.71)$$

Transformation to principal axes simplifies the equation to a form that can also be derived from the ellipsoid of constant phase [Eq. (8.48)]:

$$\varepsilon_1 s_1^2 (n^2 - \varepsilon_2)(n^2 - \varepsilon_3) + \varepsilon_2 s_2^2 (n^2 - \varepsilon_3)(n^2 - \varepsilon_1) + \varepsilon_3 s_3^2 (n^2 - \varepsilon_1)(n^2 - \varepsilon_2) = 0 \quad (8.72)$$

The equation is quadratic in  $n^2$  and has two solutions of orthogonal electric fields  $E$  [Eq. (8.48)]. The solutions depend on the orientation  $\hat{s}$  of the wavevector and optical spectra vary with orientation of the wavevector.

#### 8.3.2.1 Polaritons in Uniaxial Crystals

Crystals of uniaxial symmetry are the simplest cases of optical anisotropy since only one direction, defining the optical axis, has a dielectric constant  $\varepsilon$  that deviates from the value  $\varepsilon_{\perp}$  of the other principal axes. With two tensor components only the Fresnel equation factorizes and each factor yields a polariton:

$$(n^2 - \varepsilon_{\perp}) \left[ \varepsilon_{//} s_{//}^2 (n^2 - \varepsilon_{\perp}) + \varepsilon_{\perp} s_{\perp}^2 (n^2 - \varepsilon_{//}) \right] = 0 \quad (8.73)$$

The first solution couples only to excitons contributing to  $\varepsilon_{\perp}$ . The electric field is therefore parallel to the displacement current and the polariton is a transverse wave polarized perpendicular to the optical axis. This solution represents the

ordinary ray of uniaxial crystals [27], which behaves similarly to polaritons in isotropic material.

The second factor depends on the orientation  $\vartheta$  of the wavevector. Coupling also to  $\varepsilon_{//}$  the polariton is polarized in a plane that contains the optical axis and has except for  $s_{//} = 0$  a longitudinal component of the electric field. This solution represents the more interesting extraordinary ray of the uniaxial crystals. With  $\vartheta$  denoting the angle between wavevector and optical axis, the extraordinary ray obeys a simple wave equation, which shows its orientation dependence most clearly:

$$n^2 = \frac{c^2 k^2}{\omega^2} = \frac{\varepsilon_{//} \varepsilon_{\perp}}{\varepsilon_{//} \sin \vartheta + \varepsilon_{\perp} \cos \vartheta}, \quad \tan \vartheta = \frac{s_{//}}{s_{\perp}} \quad (8.74)$$

The resonance frequency of the extraordinary polariton depends on the transition energies of all excitons, obvious by expressing the dielectric constants  $\varepsilon_i$  by the Kurosawa relation [Eq. (8.64)], which involves only the energies of transverse and longitudinal excitons  $T_{ij}$  and  $L_{ij}$ :

$$n_l^2 = \varepsilon_l(\omega) = \varepsilon_l(\infty) \prod_j \frac{L_{ij}^2 - (\hbar\omega)^2}{T_{ij}^2 - (\hbar\omega)^2}, \quad l = //, \perp \quad (8.75)$$

A system with two orthogonal polarized excitons and an isotropic background dielectric constant  $\varepsilon(\infty)$  is sufficient to demonstrate the dependence of the polariton resonance on the orientation of the wavevector. One exciton  $T_{//}$  is polarized along the optical axis and  $T_{\perp}$  couples to the other axes. Resonance of the polariton, defined by a pole of the refractive index, occurs for a vanishing denominator in Eq. (8.74) and the dielectric constant in Eq. (8.75) relates resonance frequencies  $\Omega$  of the extraordinary polariton to the energies of the excitons:

$$(T_{\perp}^2 - (\hbar\Omega)^2) (L_{//}^2 - (\hbar\Omega)^2) \sin \vartheta + (T_{//}^2 - (\hbar\Omega)^2) (L_{\perp}^2 - (\hbar\Omega)^2) \cos \vartheta = 0 \quad (8.76)$$

Two transverse excitons result in two resonance frequencies  $\Omega_{1,2}$ , which depend on the orientation of the wavevector with respect to the optical axis ( $\vartheta = 0$ ), on the energy of the transverse excitons and on their coupling strength to light which determines the energy of the longitudinal exciton.

The result is shown in Fig. 8.8 for  $T_{//}$  as lowest transition. The other case,  $T_{\perp} < T_{//}$ , is obtained by exchanging the indices and replacing  $\vartheta$  by  $\pi/2 - \vartheta$ . Two cases are presented. The full lines show a very strong exciton  $T_{//}$  that opens a wide polariton gap to the longitudinal exciton  $L_{//}$ . The exciton  $T_{\perp}$  is much weaker and its longitudinal exciton  $L_{\perp}$  is below  $L_{//}$ . The resonance  $\Omega_1$  shifts with increasing  $\vartheta$  from the  $T_{//}$  to  $T_{\perp}$  while the second resonance  $\Omega_2$  moves from  $L_{\perp}$  to  $L_{//}$ . The dashed lines represent excitons of comparable strength and now  $L_{\perp}$  lies above  $L_{//}$ . The spectral shift of  $\Omega_1$  and  $\Omega_2$  crosses the same energy range but the shift is different and  $\Omega_2$  shifts now from high energy ( $L_{\perp}$ ) to low energy ( $L_{//}$ ) as  $\vartheta$  increases. By changing  $k$  from  $\vartheta = 0$  to  $90^\circ$  the electric field of the polariton rotates from per-

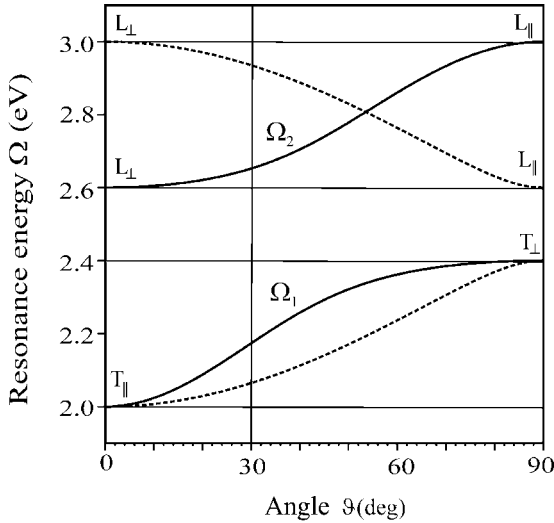


**Figure 8.8** Directional dispersion of the optical resonance in a uniaxial crystal with one transverse and longitudinal exciton for polarization parallel and perpendicular to the optical axis. The abscissa is the angle between

wavevector and optical axis. Full lines represent the case of a strong exciton  $T_{\parallel}$  and a much weaker transition  $T_{\perp}$ . Dashed lines show the case of two excitons of comparable strength.

perpendicular to parallel to the optical axis from and the resonance  $\Omega_1$  shifts between the closest pair of excitons of corresponding polarization, from  $T_{\parallel}$  to  $T_{\perp}$  or to  $L_{\parallel}$  if that comes first. The strength of the resonance, however, depends on the terminating exciton state. If the resonance shifts from  $T_{\parallel}$  to  $L_{\parallel}$  its strength vanishes for  $\vartheta = 90^\circ$  since longitudinal excitons do not couple to light. That applies also for the upper polariton resonance in Fig. 8.8, which, running between two longitudinal excitons, has strength only for intermediate angles due to some coupling to transverse excitons. In contrast to the extraordinary ray, the resonance of the ordinary ray always occurs at  $T_{\perp}$ .

The angular dependence of the resonance energy is called directional dispersion and reflects the energy shift of the induced dipoles by coupling to the longitudinal field due to a longitudinal polarization. It is unique to extraordinary polaritons in anisotropic solids and spectra calculated from conventional perturbation theory miss that shift since the longitudinal polarization is ignored. The correct resonance energy could be derived by summing up the field of induced dipoles and calculating the corresponding product of transition dipole and longitudinal field [39]. However, since the induced dipoles rotate the electric field, much iteration is needed for convergence. Elaborate sums of induced dipoles have been performed but apply only for cases where the longitudinal field is small since they implicitly assumed transverse electric fields [40].

The optical resonance frequency  $\Omega$  defines the lower edge of a polariton gap and the spectral width of the “metallic” reflectance. Figure 8.9 shows the disper-

sion  $\omega(k)$  of the extraordinary polariton in Fig. 8.8 for an angle of  $\vartheta = 30^\circ$  between optical axis and wavevector. Directional dispersion of  $\Omega_1$  moves the lower edge of the polariton gap to higher energy, while the upper edge is fixed by the longitudinal exciton  $L_{\parallel}$ . Figure 8.9a shows the wide polariton gap of the strong exciton  $T_{\parallel}$  that is interrupted by a branch running from the longitudinal exciton  $L_{\perp}$  to the second resonance  $\Omega_2$ . Figure 8.9b represents the case of a weaker exciton  $T_{\parallel}$  and the polariton represented by the dashed lines in Fig. 8.8. The polariton gap of  $\Omega_1$  starts at slightly lower energy owing to less directional dispersion and is much narrower since the longitudinal exciton  $L_{\parallel}$  has shifted to lower energy. The polariton continues with the upper branch and approaches the photon-like dispersion at high energy, crossing the second resonance  $\Omega_2$ . Another polariton gap opens, which is small since  $\Omega_2$  is close to the longitudinal exciton  $L_{\perp}$ . This case corresponds to well separated excitons. Tosatti and Harbeke found similar polariton dispersion curves in a study of the reflectivity of Wannier excitons in  $\text{PbI}_2$  and discussed also the effect of spatial dispersion and an exciton-free surface layer [41].

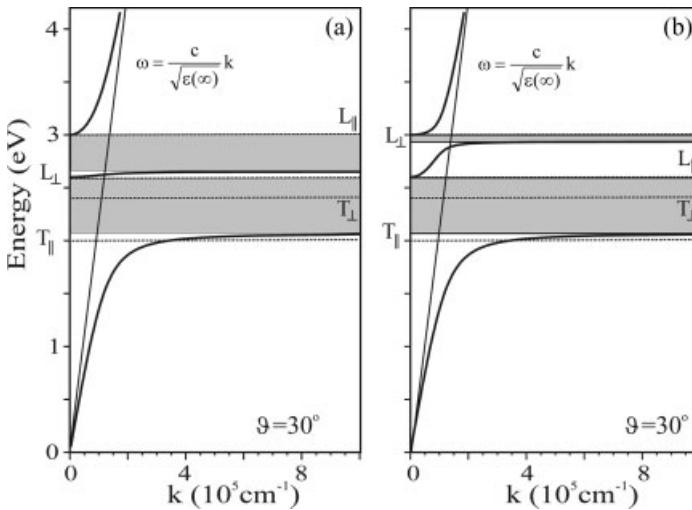


**Figure 8.9** Polariton dispersion  $\omega(k)$  of the extraordinary polariton with excitons from Fig. 8.8 for angle of  $30^\circ$  between the optical axis and the wavevector. The shaded area shows polariton gaps where electromagnetic waves cannot propagate. Dashed lines indicate the exciton energies.

Directional dispersion is a general feature of excitations in anisotropic solids and much of the dielectric theory has been developed to explain pronounced shifts observed for phonon-polaritons [13, 42]. The dipole-active oscillators in phonon-polaritons are lattice modes, which create a long-range polarization field and within the harmonic oscillator approach phonon- and exciton-polaritons show the same dispersion effects.

### 8.3.2.2 Biaxial Crystals and Axial Dispersion

The Fresnel equation for crystals of orthorhombic and lower symmetry cannot be factorized since all axes are inequivalent. We start from the Fresnel equation [Eq. 8.72)] for a diagonalized dielectric tensor, which yields two polariton modes of orthogonal polarization. Each term involves all tensor components and both polaritons couple to all excitons and propagate as extraordinary rays. Since the dielectric constants  $\epsilon_j$  vary rapidly near an exciton resonance off-diagonal elements reappear and the principal axes must be rotated to adapt to the new dielectric constants [43]. Such axial dispersion of the dielectric tensor does not occur in crystals of orthorhombic symmetry where the lattice provides a set of orthogonal axes.

Axial dispersion occurs in monoclinic and triclinic crystals. Monoclinic crystals have a symmetry axis, which being perpendicular to the other two primitive translations provides a principal axis. The dielectric tensor has only one off-diagonal element restricting axial dispersion to the plane perpendicular to the symmetry axis. The polarization induced by an electric field in a monoclinic crystal with  $z$  as symmetry axis is described by a proper dielectric tensor:

$$\begin{pmatrix} P_x \\ P_y \\ P_z \end{pmatrix} = \begin{pmatrix} \epsilon_{xx}(\omega) - 1 & \epsilon_{xy}(\omega) & 0 \\ \epsilon_{xy}(\omega) & \epsilon_{yy}(\omega) - 1 & 0 \\ 0 & 0 & \epsilon_{zz}(\omega) - 1 \end{pmatrix} \epsilon_0 \begin{pmatrix} E_x \\ E_y \\ E_z \end{pmatrix} \quad (8.77)$$

For a more detailed discussion, see Ref. [44]. If the dielectric tensor is diagonalized in a transparent region where the tensor is real, the non-diagonal element  $\epsilon_{xy}$  reappears when a transition polarized in the  $xy$ -plane changes the dielectric tensor. That component is eliminated by rotating the principal axes in the plane perpendicular to the symmetry axis by an angle  $\delta$ :

$$\tan 2\delta = \frac{2\epsilon_{xy}(\omega)}{\epsilon_{xx}(\omega) - \epsilon_{yy}(\omega)} \quad (8.78)$$

Particularly strong rotation is expected if two tensor components are near degenerate. This procedure can be extended to triclinic lattices but is not very practicable since all Eulerian angles are involved [45].

No unitary transformation diagonalizes real and imaginary part of the dielectric tensor simultaneously and only the complicated Eq. (8.71) provides the full description of optical spectra. However, the experimental results in the next section show that in the case of strong transitions an orthorhombic tensor is still a good approximation to the optical spectra of monoclinic and triclinic crystals.

## 8.4 Experimental Results

### 8.4.1 Non-Classical Absorption of Light

Polaritons as field quanta of coherently coupled radiation and polarization in solids absorb light only by inelastic scattering of the exciton. Scattering results from all interactions that are not included in the exciton–photon Hamiltonian [Eq. (8.16)]. Absorption is therefore negligible if these interactions of excitons are weaker than their coupling to photons. This case corresponds to a Rabi frequency much larger than the scattering rate and absorption should be less than predicted by Fermi’s golden rule.

Excitons of high oscillator strength and Rabi frequency seem most suitable to study such non-classical absorption. Contrary to that expectation, reduced absorption is observed only for weak excitons as for instance at low temperature in a high-quality naphthalene single crystal [46]. The absorption edge of naphthalene is determined by a weak molecular exciton, polarized parallel to the short axis, which in the monoclinic crystal splits into a Davydov doublet, separated by 18.6 meV and most of the oscillator strength is found for polarization  $E//b$ . Figure 8.10 presents the transmission spectrum of a thin single crystal for weakly absorbed light ( $E//a$ ). The sloping background of decreasing transmittance is attributed to residual absorption of the much stronger  $b$ -polarized exciton but all the strikingly sharp features belong to the  $a$ -polarized exciton at 3.9024 eV and its vibronic satellites. The  $b$ -polarized exciton also causes the broad dent marked by the arrow.

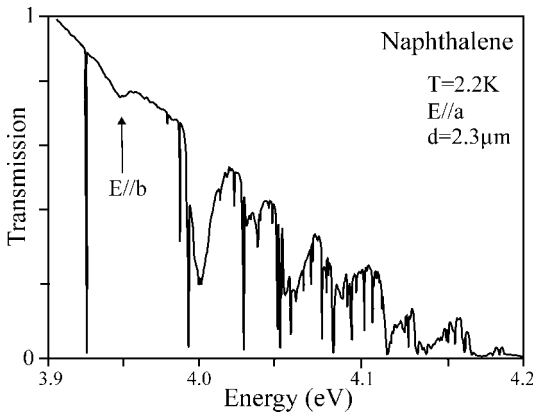


**Figure 8.10** Uncorrected transmission spectrum of a thin single crystal of naphthalene [47]. The arrow points to the residual absorption of the much stronger Davydov component for  $E//b$ .

The absorption of the weak exciton shows a rather unusual temperature dependence (Fig. 8.11). The line broadens rapidly with increasing temperature, but its height increases first indicating that the absorbance of this exciton is not determined by its oscillator strength but increases with increasing linewidth. The temperature dependence of the absorbance, determined from the integrated absorption spectrum, is shown in Fig. 8.12 together with the spectral width of the exciton [47]. The linewidth increases linearly at higher temperature owing to scattering by low-energy phonons [46]. The absorbance increases very rapidly and saturates above 15 K. From the saturation value an oscillator strength  $f \approx 10^{-5}$  is estimated and for the density of unit cells,  $4.7 \times 10^{21} \text{ cm}^{-3}$ , a Rabi frequency of 12 THz is found [Eq. (8.22)]. The corresponding Rabi time of 0.5 ps is much shorter than the coherent time of 13 ps, estimated from the spectral linewidth of  $50 \mu\text{eV}$  at 2.2 K, consistent with a reduced absorption at low temperature. In the saturation range the linewidth has increased to 1 meV and the corresponding lifetime of 0.6 ps indicates that the scattering rate has reached the Rabi frequency. The reduced absorbance at low temperature and its increase with scattering to temperatures to a saturation value when the scattering rate approaches the Rabi frequency are in full agreement with polaritons, which as eigenstate of the solid absorb light only by inelastic scattering.

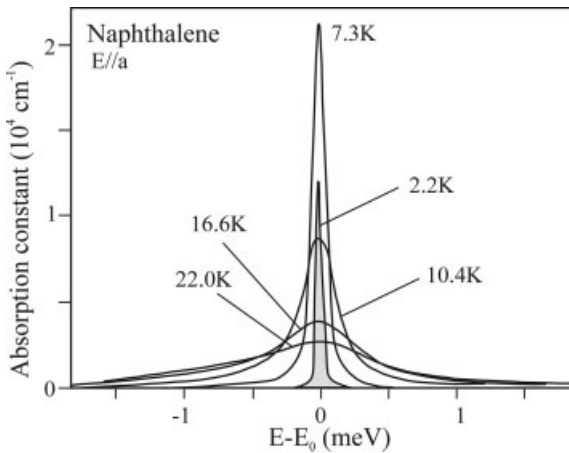


**Figure 8.11** Temperature dependence of the absorption spectrum of the weak  $a$ -polarized exciton in naphthalene [48].

The authors conjectured that thermal broadening of the spectrum was consistent with polaritons but not the absorbance. Their analysis of lifetime broadening and reduced absorbance was based on the work of Davydov and Serikov [22], who considered temporal decay of a polariton. In deriving spatial damping of light from the lifetime of the polariton excited on the surface, it was erroneously assumed that excitons move with velocity  $v$  and separate from the fast moving photons. The different speed of exciton and photon reduces within the lifetime of the exciton the coupling strength of exciton and photon by a factor  $v/c$  to a negligibly

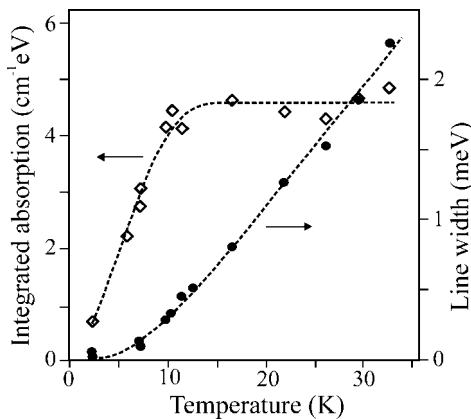


**Figure 8.12** Integrated absorption and linewidth of the *a*-polarized exciton in naphthalene [47, 48].

small value. Such separation of exciton and photon is inconsistent with a polariton as eigenstate of an optically excited homogeneous solid.

The transmission spectrum in Fig. 8.10 reveals very different linewidths of the weak *a*-polarized exciton and the much stronger *b*-polarized exciton and reduced absorption is observed only for the weak transition. Such a difference is remarkable since both derive from the same molecular state and differ only in their transition dipole moments. Obviously strong transition dipoles enhance the scattering rate. Dipolar coupling results in delocalization of the excitation via Förster transfer and excitons thus interact during their lifetime with more scattering centers. Since Förster transfer increases with the square of the dipole moment, faster than the linearly increasing Rabi frequency, large transition dipoles reduce the chance of observing reduced absorption and strong excitons obey Fermi's golden rule.

Reduced absorbance was also reported for the Wannier exciton of GaSe [48]. A 97- $\mu\text{m}$  thick sample with an estimated Rabi frequency of 20 THz shows classical absorption above 200 K. Non-classical behavior was most pronounced in thinner samples and the authors concluded that surface scattering plays an important role in the non-classical polariton absorption. No such effect is observed if photons above the bandgap of GaSe were chosen in accordance with rapid dephasing of unbound electron-hole pairs.

#### 8.4.2

#### Polaritons in Uniaxial Crystals

##### 8.4.2.1 Graphite

The spectra of the pentamethinium dye in Fig. 8.1 and other molecular solids initiated a molecular polariton model, which calculated transition energies and Davydov splitting from molecular dipoles [49], with limited success in case of strong

transitions, since the longitudinal polarization was neglected. First evidence for the importance of the longitudinal field came from angular resolved electron-loss spectra of graphite [50]. Since electrons couple to longitudinal excitons their inelastic scattering creates excitons with a longitudinal component of the field and by varying the angle of incidence the directional shift of those excitons can be studied. Since longitudinal excitons correspond to zeros of the dielectric constant  $\varepsilon$  or maxima of  $\text{Im}(-1/\varepsilon)$ , electron-loss spectra provide the same information on the dielectric response as optical data. Figure 8.13 presents the shift of the polariton resonance with the angle  $\vartheta$  between wavevector of the electron beam and the optical axis  $c$  of graphite. The particular bonds and symmetry of the lattice reduces the number of optical resonances to only two transverse excitons for each polarization  $E//c$  and  $E\perp c$ . Parallel polarized excitons correspond to transitions between  $\sigma$  and  $\pi$  states,  $\sigma \rightarrow \pi^*$  and  $\pi \rightarrow \sigma^*$ , while  $\pi \rightarrow \pi^*$  and  $\sigma \rightarrow \sigma^*$  transitions have polarization  $E\perp c$ . The sequence of transverse and longitudinal excitons has been determined from ellipsometric and electron-loss data [51, 52] and from these energies the polariton resonance can be derived from Eq. (8.75). The lowest exciton  $T_{\perp}$  belongs to  $\pi\text{-}\pi^*$  transitions and is excited by light incident parallel to the  $c$ -axis ( $\vartheta = 0$ ). As the angle of incidence rotates the polariton resonance shifts towards the longitudinal exciton  $L_{\perp}$  of  $\pi\text{-}\pi^*$  transitions, which can be excited by electrons of wavevector  $k\perp c$  ( $\vartheta = 90^\circ$ ). For oblique incidence the polariton is a mixed transverse-longitudinal mode that can be excited by light and electrons. The next polariton branch involves transitions between  $\sigma$  and  $\pi$  states which couple to light polarized parallel to the  $c$ -axis ( $E//c$ ). The transverse exciton  $T_{//}$ , excited by light of wavevector  $k\perp c$  ( $\vartheta = 90^\circ$ ) occurs near 11.5 eV, well separated from  $\pi\text{-}\pi^*$  transitions. As the wavevector rotates the polariton acquires a longitudinal field component and the resonance shifts towards the longitudinal exciton  $L_{//}$  near 14 eV, which can be excited by an electron beam parallel to the  $c$ -axis. This longitudinal exciton is degenerate with the transverse exciton  $T_{\perp}$  of  $\sigma\text{-}\sigma^*$  transitions, polarized in the layer plane and with increasing  $\vartheta$  the resonance of these transitions shifts to the corresponding longitudinal exciton  $L_{\perp}$  at 27 eV. Within that polariton gap occurs another weaker transition involving  $\sigma$  and  $\pi$  bonds with a transverse exciton  $T_{//}$  near 16 eV and the longitudinal exciton near 19 eV. At intermediate angles the resonances related to these polariton branches cross owing to directional dispersion and split since for intermediate angles both have a longitudinal field component to interact. The shift of the four optical resonances, predicted by the dielectric theory of the polariton, agrees with the data from electron-loss spectroscopy and proved the reliability of the dielectric approach to polaritons.

The simple electronic structure of graphite is responsible for the pronounced directional shift of polariton resonances since a small number of strong excitons in a wide energy range results in a number of polariton branches. Polariton dispersion is much more complicated if more excitons split the polariton into a large number of branches. Such a complex spectrum has been found in anthracene by electron-loss spectroscopy [53]. Pronounced directional dispersion is observed for a strong exciton at higher energy, derived from a molecular exciton with dipole moment parallel to the long molecular axis. At lower energy the repulsive interac-

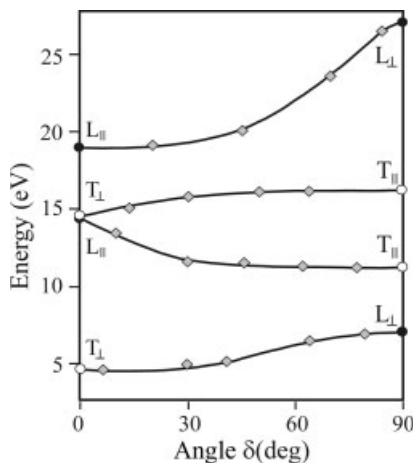


**Figure 8.13** Directional dispersion of polariton resonances of graphite [53]. Diamonds refer to data from electron-loss spectra [51] and open and filled circles to transverse and longitudinal excitons, respectively, as derived from optical data.

tion of a large number of polariton branches opens many gaps, which reduces the directional shift of the corresponding optical resonance. Although the analysis of the spectra is much more complicated than for graphite, the elaborate analysis of the data found them in full agreement with polariton dispersion theory.

#### 8.4.2.2 Dye Single-Crystal CTIP

The cyanine dye CTIP,  $\gamma$ -cyclopropyl-bis(1,3,3-trimethylindolenine-2-yl)penta-methinium tetrafluoroborate, shown in Fig. 8.14, represents a large group of linear molecules where “metallic” reflectance of crystals is common. The  $\pi$ -electrons of four double bonds are delocalized on a linear chain and the lowest transition is a strong exciton polarized parallel to the chain. The triclinic unit cell has inversion symmetry and contains two dye ions and their  $\text{BF}_4^-$  counter ion [54]. The resulting Davydov components  $\Phi$  are linear combinations of the molecular excitons  $\varphi$ :

$$\Phi_{\pm} = \frac{1}{\sqrt{2}}(\varphi_1 \pm \varphi_2) \quad (8.79)$$

Owing to inversion symmetry, the molecular dipoles are parallel and one Davydov component acquires all oscillator strength. The large transition dipole and the molecule density of  $1.466 \times 10^{21} \text{ cm}^{-3}$  result in strong polarization and shiny crystals with silvery and blue faces indicate large dispersion effects.

Figure 8.15 presents spectra of the silvery (110) face and a solution spectrum [8], which shows a strong absorption peak at 1.94 eV, followed by a shoulder due to a vibronic exciton. The (110) face shows “metallic” reflectance extending from

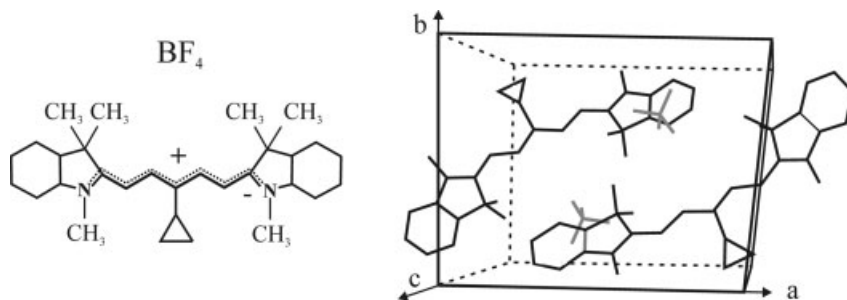


**Figure 8.14** The cyanine dye  $\gamma$ -cyclopropylbis(1,3,3-trimethylindolenin-2-yl)pentamethinium and the triclinic unit cell with two dye ions and counter ions  $\text{BF}_4^-$ .

the absorption edge near 1.65 eV to the sharp drop near 2.9 eV down to values of about 1% in the near-UV region. The high reflectance extends over the visible spectral range, which gives the (110) face its bright silvery shine. It is observed for polarization of light parallel to the projection of the transition dipole on that face. In perpendicular polarization the reflectivity reaches only 4–5% and shows no structure since the small step near 1.65 eV results from backscattered light in the range where the crystal is transparent. Such strong optical anisotropy is typical for samples where the molecules align parallel. Figure 8.15b displays spectra of the dielectric constant derived by Kramers–Kronig analysis of the reflectivity. Since the molecules are tilted only  $9.4^\circ$  out of the (110) plane, the wavevector is almost perpendicular to the exciton dipole moment and the imaginary part of the dielectric constant,  $\text{Im}(\epsilon)$ , is a good approximation of the spectral density of the exciton. The spectrum shows a single, strong and only 18 meV wide exciton at 1.73 eV that is followed by a vibronic progression of larger linewidth. The zero of the real part of the dielectric constant yields the energy of the longitudinal exciton and confirms that the 1.2 eV wide band of high reflectivity results from the polariton gap of a strong exciton. The weaker vibronic excitons, which have about 30% of the total oscillator strength, create additional polariton branches and cause the dips in the “metallic” reflectance, consistent with the model dispersion in Fig. 8.9. The dielectric constants obtained from normal incidence reflectance were confirmed by an extensive study of the surface polariton in the spectral range accessible to the method of attenuated total reflectance [55].

For a quantitative test of the polariton model, the oscillator strength  $f$  of the molecular exciton must be known, which is obtained from the sum rule applied to the spectra of  $\text{Im}(\epsilon)$  or to the molar absorption:

$$f(E) = \frac{8\pi m\epsilon_0}{e^2 h^2} \frac{1}{N} \int_0^E E' \text{Im}(\epsilon) dE' = \frac{4m\epsilon_0}{e^2 h} \frac{nc}{N} \int_0^E E' a(E') dE' \quad (8.80)$$

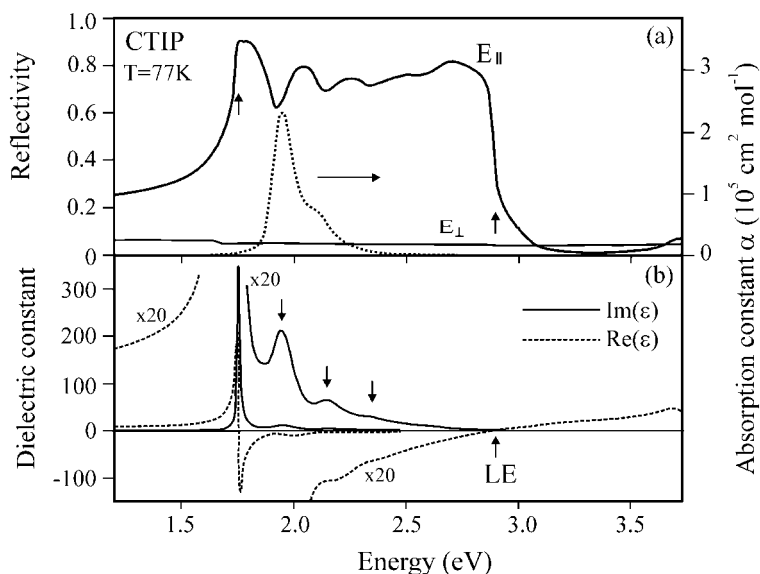


**Figure 8.15** (a) Reflectivity of CTIP observed on the (110) face for polarization of light parallel and perpendicular the projection of the molecular dipole on to that face. The dotted line shows a spectrum in methanol.

(b) Spectra of the dielectric constant derived by Kramers–Kronig transformation of the “metallic” reflectivity. Vertical arrows mark polariton resonances and the longitudinal exciton.

$N$  accounts for the density of molecules in the crystal or in solution and  $n$  is the refractive index of the solvent. The integrated spectrum of  $\text{Im}(\epsilon)$  is presented in Fig. 8.16 and shows the sharp increase due to the strong exciton and the saturation value at 3 eV, the high-energy edge of the polariton gap, yields the molecular oscillator strength  $f = 5.6$ . This large value is consistent with the value  $f = 1.8$  obtained from the solution spectrum since the random orientation of the molecules distributes the oscillator strength over three orientations. Most of the  $\pi$ -electrons of the conjugated bonds show up in a single exciton. Since the linear molecule has no orbital degeneracy, an oscillator strength far above  $f = 2$ , proves that the  $\pi$ -electrons are strongly correlated and respond to light collectively. Equation (8.18) derived from the oscillator strength and the transition energy of 1.7 eV a molecular transition dipole of  $3.54 \text{ e}\text{\AA}$  and  $5.0 \text{ e}\text{\AA}$  for the dipole of the unit cell, which has the oscillator strength of two molecules. Such dipoles are orders of magnitudes larger than those observed for Wannier excitons and result in exceptional optical properties. Since the exciton is also well separated from other transitions, CTIP provides an ideal model to test the dielectric model of strong exciton-polaritons.

Figure 8.17 compares normal incidence reflectance of three crystal faces obtained with light polarized parallel to the projection of the molecular dipole on to the respective face [56]. The angles refer to  $\vartheta$  the angle between transition dipole and wavevector, which is parallel to the face normal since normal incidence

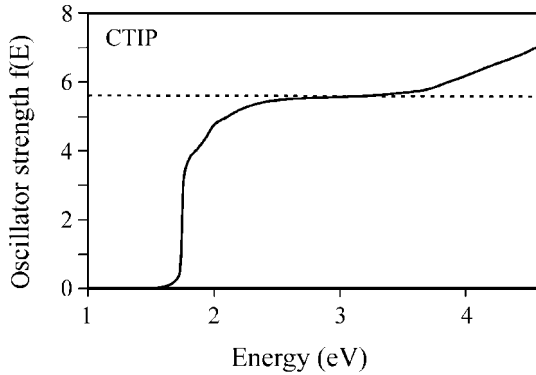


**Figure 8.16** Oscillator strength of the molecular exciton of CTIP, derived from the integrated spectrum of  $\text{Im}(\epsilon)$ .

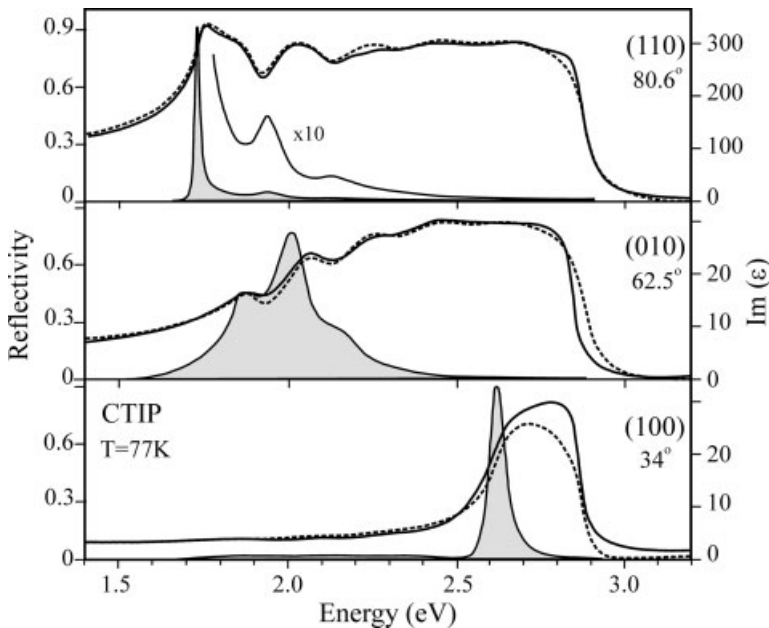


**Figure 8.17** Normal incidence reflectivity of three crystal faces of a CTIP crystal. Dashed lines compare polariton spectra calculated from the parameters in Table 8.1. Shaded areas display the spectral density, i.e. spectra of the imaginary part  $\text{Im}(\epsilon)$  of the dielectric constant.

of light maintains the orientation of the wavevector. The shaded areas are spectra of  $\text{Im}(\epsilon)$  and reveal not only a large shift of the polariton resonance but also considerable variation of the spectral lineshape. The (110) face provides the best coupling of light and exciton since the transition dipole is almost perpendicular to  $k$

and spectra of that face are used to model the dielectric tensor. The Lyddane–Sachs–Teller relation [Eq. (8.63)] suggests a uniaxial approach with the transition dipole as optical axis since the wide polariton gaps corresponds to a large change in the dielectric constant that renders anisotropy due to high-energy transitions negligible. The exciton and its satellites are represented as Lorentz oscillators with transition energies, width and strength taken from  $\text{Im}(\epsilon)$  of the (110) face and refined to improve the agreement with the experimental reflectivity. That procedure corrects also some inaccuracy of Kramers–Kronig transformation with respect to strength and linewidth of the transitions and is needed to model transitions that are too weak to be resolved in spectra of  $\text{Im}(\epsilon)$ . The dashed lines present polariton spectra calculated from the excitons in Table 8.1 and agree very well with the experimental spectrum.

**Table 8.1** Lorentz oscillators representing the exciton of CTIP and its vibronic satellites, their contribution  $\chi$  to the static dielectric constant  $\epsilon(0)$  and their linewidth  $\chi$ .

$\hbar\omega_j$ (eV)	1.69	1.81	1.93	2.13	2.33	2.53
$\chi_j$	4.0	0.2	0.4	0.15	0.03	0.005
$\hbar\gamma_j$ (meV)	18	100	100	160	160	160
$\epsilon(\infty)$	$\epsilon_{//} = 2.8$			$\epsilon_{\perp} = 2.4$		

The transverse exciton is shifted by 40 meV to lower energy compared with the peak position of  $\text{Im}(\epsilon)$  on the (110) face to account for the small directional shift. The vibronic progression starts at 1.93 eV and the energies are well defined by the dips in the reflectivity. Only two satellites are resolved in the spectrum of  $\text{Im}(\epsilon)$  but the weak transitions have significant effect on the reflectivity since by opening additional branches within the polariton gap they reduce the reflectivity. If these transitions are omitted the calculated reflectivity exceeds 90%, a significant deviation from the experimental spectrum. The narrow width of the fundamental exciton, consistent with the value derived from Kramers–Kronig transformation, is necessary to reproduce the sharp rise in the reflectivity at low energy. All vibronic states have larger width, which is expected since these excitons can scatter down in energy. The high-energy edge of the metallic reflectance is sensitive to the choice of the background dielectric constant  $\epsilon_{//}(\infty)$  and has been determined from the Lyddane–Sachs–Teller relation. The tensor component  $\epsilon_{\perp}(\infty)$  is derived from the average reflectivity for orthogonal polarization of different crystal faces.

The weak transition at 1.81 eV causes the asymmetric shape of the leading reflectance peak but is not member of the vibronic progression. The peak shows considerable variation among different samples [see Figs. 8.17 and 8.15]. Most likely it arises from molecules in the surface that should have different transition energy since the polarization field there is different from that in deeper layers.

Similar, much narrower dips have been observed at 2 K above the absorption edge of high-quality single crystals of anthracene [57] and tetracene [58]. The polariton gap is only 30–40 meV wide since the excitons are much weaker but all dips fall into that range. For anthracene it was observed that these dips shift if gas is condensed on the crystal. The most pronounced dip, occurring near the high-energy edge of the polariton band, shifts by as much as 23 meV to lower energy but returns to its former position if the condensate is removed [59], a clear indication of a state in the surface region.

The same dielectric tensor reproduces the spectra of all faces. It generates the slow rise of the reflectivity on the (010) face, its fine structure and the large shift and narrower reflectance band of the blue (100) face. The polariton spectrum reproduces the three peaks of comparable strength of  $\text{Im}(\epsilon)$  derived from the (010) face and confirms that absorption peaks in anisotropic crystals reflect neither the position nor the strength of excitons. Nevertheless, the good agreement obtained on all faces with the same broadening parameter  $\gamma_j$  of all transitions is surprising. Scattering results from coupling the exciton to other states and should be treated as self-energy corrections, which depends on the spectral density of states and the matrix elements involved. The scattering rate should change as the exciton resonance shifts over such a large range. The larger linewidth of the vibronic excitons apparently is a good approximation of the spectral variation of the imaginary part of the self-energy of the polariton, in accordance with the suggestion that coupling within the vibronic progression dominates the loss of coherence [49]. Small adjustments of the broadening parameters improve the agreement to the spectra of the (010) face where three peaks of comparable strength in the spectrum of  $\text{Im}(\epsilon)$  point to near-resonant coupling [56].

The reflectivity of strong exciton polaritons is very sensitive to the surface quality. The reflectivity of the blue (100) face increases strongly at low energy if the surface is damaged by ion bombardment and a double peak structure is observed [60]. A similar low-energy peak was observed on the poorly developed (10 $\bar{1}$ ) face and was attributed to steps of unknown orientation [61].

The directional shift of the polariton resonance calculated from Eq. (8.75) is presented in Fig. 8.18. Data points correspond to maxima of  $\text{Im}(\epsilon)$ , derived from reflectance spectra of different faces of one single crystal [61]. If there is only one exciton in that spectral range the resonance shifts smoothly from the transverse to the longitudinal exciton as due to the decreasing angle  $\vartheta$  between wavevector  $k$  and transition dipole the longitudinal polarization increases. A similar shift is observed for the lowest resonance in graphite (Fig. 8.13). The large increase of the dielectric constant from 2.6 to 7.4 by the contribution  $\chi = 4.8$  of the exciton opens the wide polariton gap from 1.7 to 2.9 eV and shifts the polariton absorption peak all over the visible range, changing the color of the crystal faces from silvery to blue. The vibronic exciton  $T_1$  opens an additional polariton branch and generates another, weaker resonance. The shift of the main peak is not much affected by additional weak transitions but the oscillator strength is redistributed near crossing points of polariton branches as observed on the (010) face.

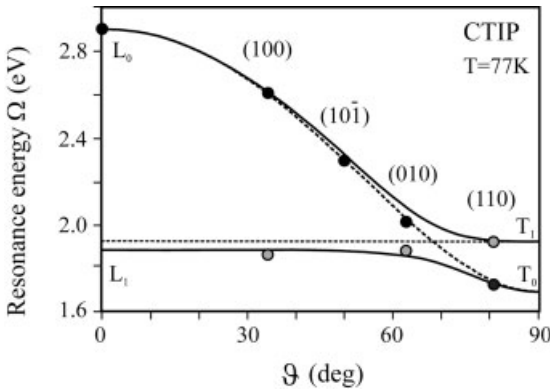


**Figure 8.18** Directional dispersion of the extraordinary polariton of CTIP. The dashed line corresponds to a single strong exciton  $T_0$ , the full curves include a vibronic exciton  $T_1$ ,

creating a second polariton resonance. Black and gray dots show the main peaks and strongest satellite, respectively, in the experimental spectra of  $\text{Im}(\epsilon)$ .

Figure 8.19 displays the polariton dispersion  $\Omega(k)$ , the “band structure” of the polariton, for three orientations of the wavevector, normal to the indicated faces. The position of the excitons in Table 8.1 is marked by arrows. The real part  $\text{Re}(k)$  of the wavevector shows the variation of the phase velocity and the small phase velocity within the polariton gap corresponds to a small refractive index  $n$ . The

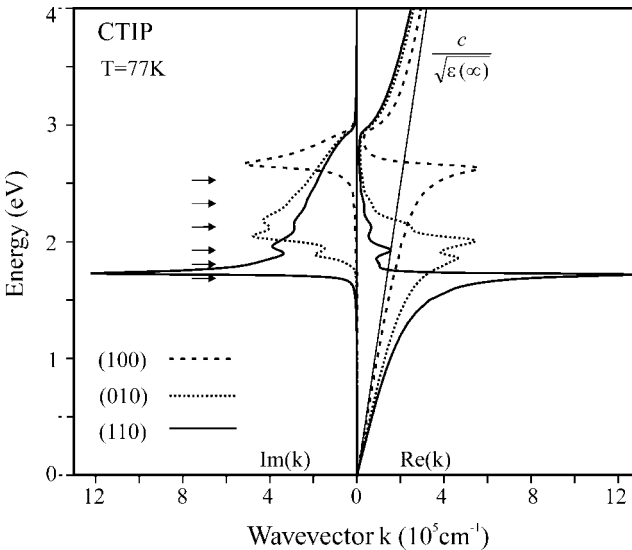


**Figure 8.19** Polariton dispersion curves  $E(k)$  for three orientation of the wavevector, defined by normal incidence on the indicated faces.  $\text{Re}(k)$  correspond to the “band structure” of the polariton and  $\text{Im}(k)$  to absorption

spectra. Arrows indicate the transition energy of excitons. The thin line displays the linear dispersion of an electromagnetic wave coupling to high-energy transitions only.

imaginary part  $\text{Im}(k)$  of the wavevector represents absorption spectra and multiplied by a factor 2 the absorption constant [Eq. (8.53)]. For wavevector normal to the (110) face, absorption peaks are close to the exciton levels since the longitudinal polarization is small ( $\vartheta = 80.6^\circ$ ). However, even in that case the absorption constant does not reflect the strength of the excitons. The weak transitions at high energy are much too strong due to a very small refractive index in that range. On the (010) face the absorption spectrum shows three closely spaced transitions of comparable strength and on the (100) face a strong peak at 2.6 eV is observed.

#### 8.4.2.3 TCNQ. Tetracyanoquinodimethane

TCNQ was the first material to show that wide polariton gaps are not peculiar to crystals of linear dye molecules but occur also for other  $\pi$ -conjugated molecules [9]. Four molecules share the monoclinic unit cell, lying nearly flat on the  $ac$  plane [62]. Figure 8.20 displays the very anisotropic reflectance spectra observed on the (010) face, which are strikingly similar to those of CTIP. A more than 1.5 eV broad band of high reflectivity is observed in the range of a single molecular exciton as shown by the solution spectrum. The transition dipole of the molecular exciton is parallel to the long molecular axis. The exciton is spectrally well separated from other transitions and shows a vibronic progression of the double bond stretch mode. The spectrum of free molecules resolves the vibronic progression better and reveals the shift of the exciton transition energy in a polarizable medium. The symmetry of the unit cell and the aggregation of the molecules result in one strong Davydov component polarized in the  $ac$  plane while the component polarized parallel to the  $b$ -axis is very weak and cannot be excited on a (010) face. The spectral features narrow considerably at low temperature but the width of the band is unchanged and Kramers–Kronig transformation of a low-temperature spectrum reveals that, like in CTIP, most of the oscillator strength is concentrated in the 0–0 transition [63]. The experimental situation is more favorable than in CTIP since the transition dipole of the strong exciton lies in the  $ac$  plane. Light incident normal to the (010) face thus excites a transverse wave, the wavevector is parallel to the symmetry axis and spectra of  $\text{Im}(\epsilon)$  thus correspond to the spectral density of the exciton and its progression, unperturbed by directional dispersion. Although the orientation of the electric field was known, attempts to calculate the reflectivity from dipole sums were not satisfactory [32], indicating how difficult it is to derive the local field from microscopic models.

Figure 8.21 presents room temperature reflectance spectra of three faces [10] and spectra of  $\text{Im}(\epsilon)$  [64]. Maxima of  $\text{Im}(\epsilon)$  found for the (010) face deliver the energy of transverse excitons and the spectrum reflects the distribution of the oscillator strength to the vibronic progression. The energy of the longitudinal exciton is derived from the zero of  $\text{Re}(\epsilon)$  and confirms a polariton gap that stretches from  $T_0$  of 2.778 eV to the longitudinal exciton  $L_0$  of 4.218, in very good agreement with low-temperature data [64]. Spectra of the other faces are again strongly modified by directional dispersion, obvious from the shift of peaks of  $\text{Im}(\epsilon)$  and the variation of the spectral density.

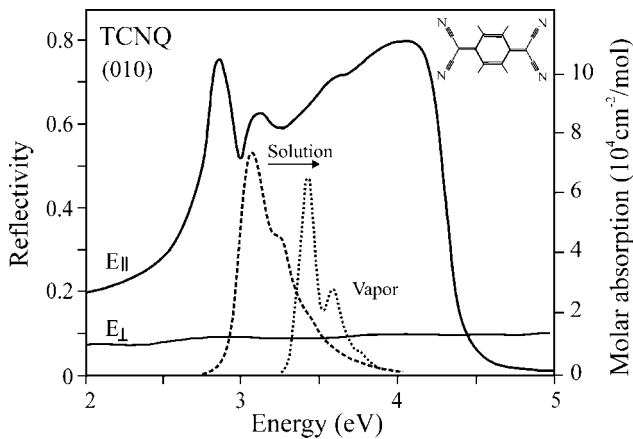


**Figure 8.20** Reflectance spectra of the (010) face of a monoclinic TCNQ crystal at room temperature and absorption spectra of molecules in the vapor phase or dissolved in chloroform [10]. The inset shows the molecular structure.

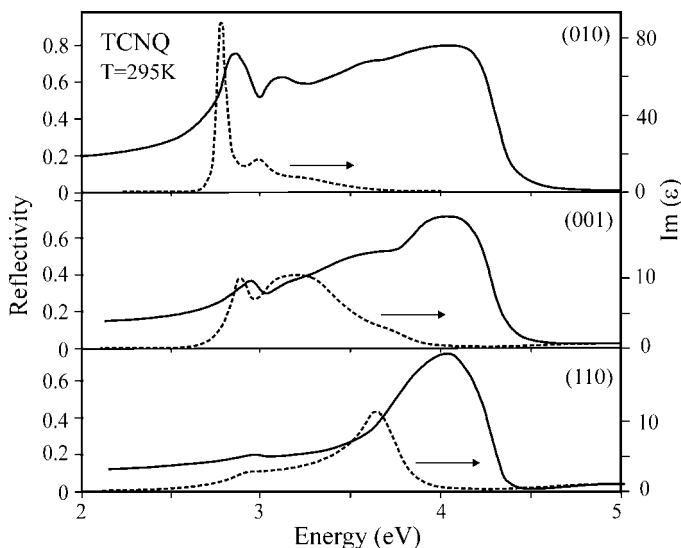


**Figure 8.21** Spectra of the reflectivity and of the imaginary part of the dielectric constant of TCNQ for three different crystal faces [9, 63].

As in CTIP, the directional shift of polariton resonances is derived from Eq. (8.75) and the energies of transverse and longitudinal exciton found in the spectrum of the (010) face. In view of the similarity of the spectra to those of CTIP is not surprising that the same behavior is observed (Fig. 8.22). The position of the main peak of  $\text{Im}(\epsilon)$  found in the spectra of three crystal faces agrees with the

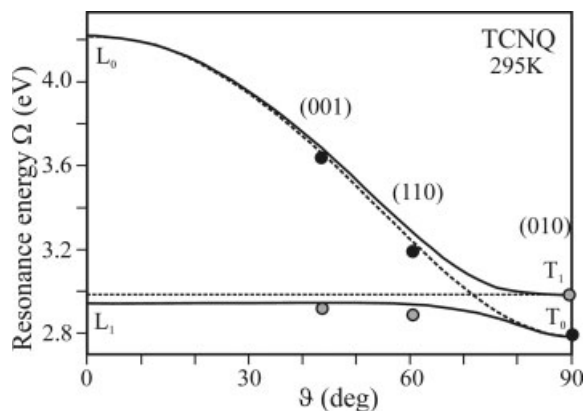


**Figure 8.22** Directional dispersion of the resonance energy of the polariton of TCNQ. The dashed line corresponds to the shift of a single strong exciton  $T_0$ , the full curves show the dispersion if a weak exciton  $T_1$  creates a

second polariton resonance. Black and gray dots show the main peaks and the strongest satellite, respectively, in the experimental spectra of  $\text{Im}(\epsilon)$ .

calculated position. A weak exciton, at about 200 meV above the fundamental exciton, opens an additional polariton branch and causes the pronounced dip in the reflectivity of the highly reflecting (010) face. Spectra of the other faces show near that energy an absorption peak, as expected when the strong resonance has shifted beyond the transition energy of a weak exciton. This transition had been attributed to a vibronic exciton [64] but it derives probably from the weak *b*-polarized exciton since the peak is strongest in the spectrum of the (001) face.

The dielectric theory based on a uniaxial tensor with the transition dipole as optical axis describes the spectra of triclinic and monoclinic crystals. This simple approach is reliable if the aggregation of molecules results in one strong transition in the spectral range of interest.

### 8.4.3

#### Polaritons in Biaxial Crystals

##### 8.4.3.1 Dye Crystal TTI: Bis(*N*-ethylthiazolin-2-yl)trimethine Cyanine Iodide

Packing of molecules frequently leads to two Davydov components of significant strength, resulting in two extraordinary polaritons with a longitudinal component of the polarization. Additional complications arise in monoclinic and triclinic systems from axial dispersion of a diagonalized dielectric tensor and non-vanishing off-diagonal elements in the absorbing region. The problem of exciting only one polariton was solved in uniaxial crystals by finding the polarization for maximum or minimum reflectance near the absorption edge. This procedure fails with biaxial crystals if the projection of the transition dipoles of the Davydov components on to the reflecting face is not orthogonal, coupling each polariton to both Davy-

dov components. Finding the proper polarization thus becomes more complicated. Polaritons are excited by photons, which have the same orientation of the field parallel to the surface. Since polaritons have orthogonal polarization a single polariton mode is excited if incident and reflected photons have the same field component parallel to the surface as the polariton and the usual boundary conditions determine the amplitude and phase shift of the reflected light. If the polarization of incident light deviates from that specific orientation a second polariton is excited and different reflection coefficients of the polaritons rotate the polarization of the reflected light while different phase introduces ellipticity. A single polariton therefore should be selected by analyzing the polarization of the reflected light and choosing that polarization which results in minimum ellipticity of the reflected light. Light of perpendicular polarization then excites the other polariton.

Such a study has been performed on TTI. The molecule, shown in Fig. 8.23, has a strong transition polarized along a conjugated chain of three double bonds. Four molecules of two different orientations in the monoclinic unit cell [65] result in two dipole-active excitons of  $B_u$  and  $A_u$  symmetry, polarized perpendicular and parallel to the monoclinic axis  $b$ , respectively. In contrast to TCNQ, the molecules are noticeably tilted out of the  $ac$  plane and the  $b$ -polarized component acquires too much strength to be ignored. The ratio of the transition dipole moments is 2.8 in favor of the  $ac$ -polarized component. Normal incidence reflectance spectra of several faces were measured with a calcite analyzer parallel to the polarization of the incident light. Measurements with crossed analyzers were used to optimize the polarization of the incident light and to investigate deviations from the ideal of exciting one polariton.

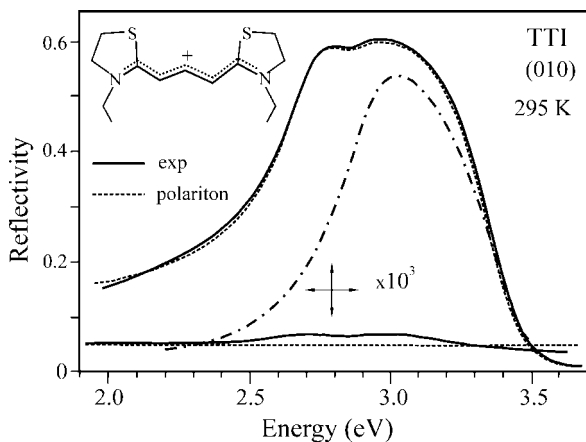


**Figure 8.23** Reflectivity of two polariton modes excited on the  $ac$  face of TTI [bis(*N*-ethylthiazolin-2-yl)trimethine cyanine iodide], measured with parallel polarization of incident and reflected light. The dashed

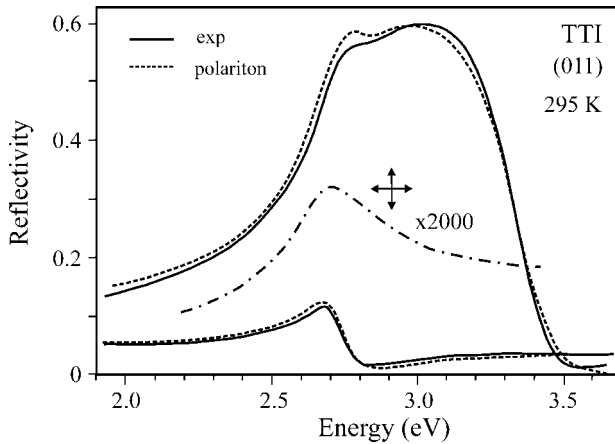
spectra are calculated from polariton dispersion and the dash-dotted line represents the spectrum of reflected light after passing crossed analyzers, with magnitude amplified as indicated.

Figure 8.23 shows the reflectance spectra of the (010) face, best suited to extract the properties of the stronger exciton ( $B_u$ ) because the dipole moment lies in the  $ac$  plane. For polarization of light parallel to this dipole ( $-72.6^\circ$  against the  $c$ -axis) a single polariton is excited and yields a band of high reflectivity. The reflectivity measured with crossed polarizers is below  $10^{-5}$  at low energy and increases to 0.06% near 3 eV. Such low ellipticity confirms not only that a single polariton is excited but also negligible axial dispersion. Kramers–Kronig analysis derives the transition energy of the transverse exciton  $T_{B_u}$  at 2.68 eV. The  $b$ -polarized exciton is not excited on that face and the nearly structureless reflectivity for orthogonal polarization of light shows that no transitions of noticeable strength couples to polarization in the  $ac$  plane. The dipole moment of the strong exciton provides an obvious choice for a principal axis in the  $ac$  plane,  $\varepsilon_1$ , and the orthogonal  $b$ -axis provides the second axis,  $\varepsilon_2$ . The third principal axis,  $\varepsilon_3$ , is again in the  $ac$  plane. The reflectivity of the  $ac$  plane for perpendicular polarization, about 5%, yields the dielectric constant  $\varepsilon_3 = 2.4$ , which is also chosen as background dielectric constant for the second axis. The dashed line shows calculated reflectance spectra based on the excitons in Table 8.2. Again, input parameters of the strong exciton and its satellites have been obtained from Kramers–Kronig transformation and refined by matching the calculated reflectivity to the “metallic” reflectivity of the  $ac$  plane.

**Table 8.2** Lorentz oscillators, representing excitons of  $B_u$  and  $A_u$  symmetry and their vibronic satellites in TTI;  $\chi_j$  and  $\gamma_j$  correspond to the strength and linewidth of the excitons, respectively.

Tensor axis	$\varepsilon_1, B_u$		$\varepsilon_2, A_u$	$\varepsilon_3$
Polarization	$\mu \perp b$		$\mu \parallel b$	$\mu \perp b$
$\hbar\omega_j$ (eV)	2.68	2.84	2.96	2.66
$\chi_j$ (eV)	1.2	0.15	0.02	0.18
$\hbar\gamma_j$ (eV)	0.16	0.24	0.3	0.16
$\varepsilon(\infty)$	2.5		2.4	2.4

Table 8.2 reveals a small Davydov splitting of the molecular exciton, not much more than the accuracy of energies derived by matching polaritons to an experimental reflectivity. The oscillator strength of the  $B_u$  exciton is obtained from the sum rule and that of the weaker exciton has been matched to agree with the ratio of transition dipole moments. Compared with CTIP the excitons contribute much less to the static dielectric constant, which is expected for a shorter conjugated chain, resulting also in a higher transition energy. The large linewidth at room temperature reduces the reflectivity of the polariton gap to about 60% and



**Figure 8.24** Reflectivity of the (011) face of TTI of polaritons coupling to either the strong or the weak Davydov component. Dashed lines represent calculated spectra of two extraordinary polaritons. The spectra measured with crossed analyzers (dash-dotted line) show negligible mixing of the polaritons.

did not allow resolution of the properties of vibronic excitons from  $\text{Im}(\epsilon)$  directly. Their properties have been derived from the fit to the reflectivity of the (010) face.

No crystal face was available to measure the properties of the  $b$ -polarized exciton unperturbed from directional dispersion. The  $b$ -exciton was therefore derived from spectra of the (011) face where the projection of the Davydov components are nearly orthogonal with angles  $\varphi_{B_a} = -0.4^\circ$  and  $\varphi_{A_a} = 90^\circ$  against the  $a$ -axis (Fig. 8.24). Polaritons excited on that face couple either to the strong or to the weak Davydov component. Spectra for polarization  $E \perp a$  yield the properties of the weak exciton, modified by directional dispersion since its dipole moment is not orthogonal to the wavevector ( $\vartheta = 65.3^\circ$ )[67]. The directional shift is small due to the modest oscillator strength. Polarization of light  $E // a$  excites an almost transverse wave due to small tilt by less than  $1^\circ$  out of the surface plane of the transition dipole of the strong Davydov component. The spectrum therefore is almost identical with that of the (010) face. Reflected light passing the crossed analyzer hardly reaches 0.01%, confirming once again negligible axial dispersion.

Since axial dispersion has not been observed, polariton spectra have been calculated from an orthorhombic dielectric tensor and the excellent agreement of calculated and experimental spectra of the (010) and (011) faces supports the choice of the exciton parameter in Table 8.2. Final confirmation for that simple approach comes from the good agreement of calculated spectra with the complicated spectra observed on (110) and  $(1\bar{1}1)$  faces. Figure 8.25 displays reflectance spectra excited of a (110) face where the projections of the strong and weak Davydov components have angles of  $62.6$  and  $90^\circ$  with the  $c$ -axis, respectively. Owing to that small difference of  $27^\circ$  each polariton couples to both excitons. The experimental spectra were measured by rotating the polarization of incident light during the

measurement to minimize the ellipticity. The polarization of the strongly reflecting mode with respect to the  $c$ -axis is shown in Fig. 8.25b. It starts in the transparent region at  $\varphi = 75^\circ$ , rotates to  $84^\circ$  near the resonance of the weak Davydov component and turns sharply back to  $62^\circ$ , settling finally at  $64^\circ$ . The rapid rotation occurs in the range where the reflectance of both polaritons is very similar and minimizing the ellipticity of reflected light seems the only way to select a single polariton. The dashed curves show the calculated reflectivity and the excellent agreement allows interpretation of the spectra in detail. Both Davydov components couple to the strongly reflecting polariton causing the double peak structure and throughout the spectrum a longitudinal field is present since the wavevector is neither perpendicular to the dipole moment of the weak ( $\vartheta = 53.3^\circ$ ) nor of the strong exciton ( $\vartheta = 40.1^\circ$ ). The first peak arises from the weak Davydov component with a small directional shift. The second peak is due to the strong Davydov component, shifted to 3.14 eV by coupling the transition dipole to the longitudinal field created by strongly tilted transition dipoles. Spectra measured with crossed analyzers show that only below 2.6 eV and above 3.1 eV the ellipticity of the reflected light can be kept negligible by proper rotation of the polarization. However, near 2.8 eV light passing the crossed analyzers reaches 0.15%, fairly large compared with 7% obtained with parallel analyzers. The electric field thus has an ellipticity of 15%. Since no axial dispersion is observed on the  $ac$  plane such ellipticity of the reflected light cannot be attributed to the neglected off-diagonal ele-

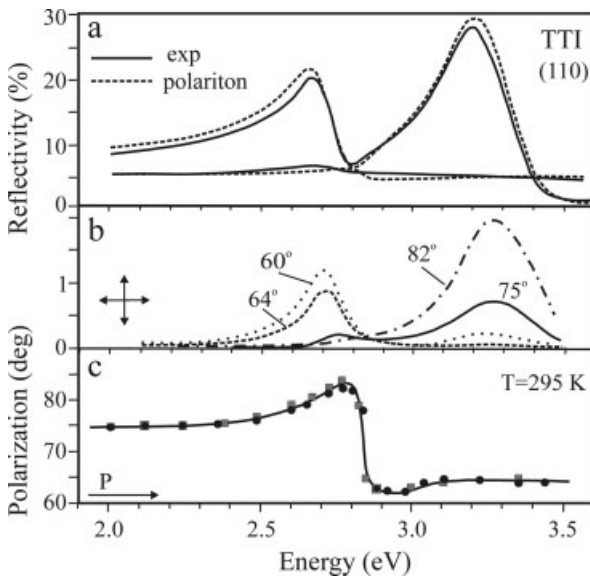


**Figure 8.25** (a) Reflectivity of the (110) face of TTI in comparison with calculated spectra; (b) reflectivity with crossed analyzers for various polarization of light with respect to the  $c$ -axis; (c) polarization with respect the  $c$ -axis,

which yields minimum ellipticity of the strongly reflected light. The arrow indicates the projection of the strong Davydov component on to that face.

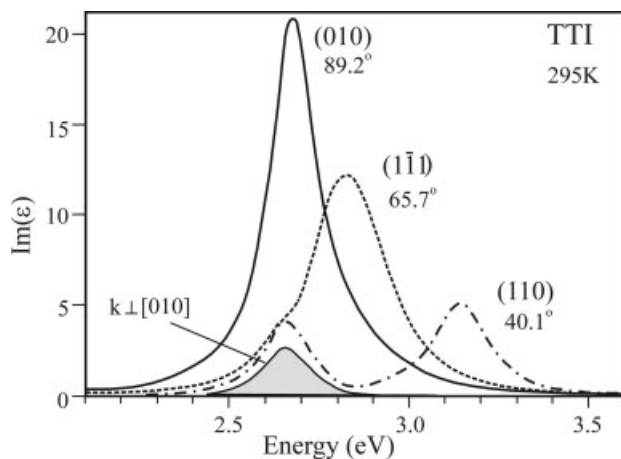


**Figure 8.26** Calculated spectra of  $\text{Im}(\epsilon)$  of TTI of the strong polariton for normal incidence on the indicated crystal faces. The angles refer to the orientation of the wavevector of light with respect to the transition dipole of

the strong Davydov component. The shaded area presents the spectral density of the weak Davydov component spectrum, polarized parallel to the  $b$ -axis.

ment  $\epsilon_{13}$  of a monoclinic tensor but points to mixing of the polariton modes. Similar ellipticity and rotation of the polarization is observed on the  $(1\bar{1}1)$  face [66].

The spectra of  $\text{Im}(\epsilon)$  in Fig. 8.26 confirm significant directional dispersion of the strong polariton. These spectra were calculated from the Lorentz oscillators in Table 8.2 and agree well with experimental spectra derived by Kramers–Kronig transformation. The shaded area shows the spectral density of the transverse exciton  $A_u$ , polarized parallel to the  $b$ -axis, which owing to lack of an appropriate crystal face could not be measured directly. This exciton appears also in the spectrum of the strong polariton, causing a peak and a shoulder on spectra of the  $(110)$  and  $(1\bar{1}1)$  faces, respectively. Mixing of the polaritons may be mediated by scattering of that common exciton.

#### 8.4.3.2 Ionic Crystals of the Dye BDH [1,7-Bis(dimethylamino)heptamethinium]

After the discovery of the “metallic” reflectivity of 1,5-bis(dimethylamino)pentamethinium perchlorate [5, 49], directional dispersion has been reported for many organic single crystals. Spectra of auramine perchlorate [67], paranitroaniline [68], adenine hydrochlorate [69], 3-ethyl-5-[2-(1,3-dithiolanylidene)]rhodanine [70], diethylcyanine iodide and chloride [71] and more pentamethinium dyes [72] show striking optical properties arising from the longitudinal field, which nevertheless was ignored in most studies. Deficits in matching the spectral lineshape were attributed to spatial dispersion [73], unlikely in the case of small intermolecular overlap, coupling to a vibronic states [49], or to significant dispersion of broad exciton bands [68]. Since the longitudinal field arises from molecular dipoles dif-

ferent aggregation should lead to different spectra, consistent with the different spectra of a squaridium dye in a triclinic and a monoclinic lattice [74]. A systematic variation of the crystal structure of the same molecule has been achieved for ionic crystals of the cyanine dye BDH by using different counter ions [75, 76]. Like CTIP, that dye has a conjugated chain of four  $\pi$ -bonds, but small methyl groups replace the bulky planar side-group and the isopropyl ring has been removed, reducing steric hindrance. Chloride and bromide counterions result in parallel stacking of the dye molecules and a 1.6-eV wide polariton gap stretching from 1.94 to 3.56 eV is observed [77]. Detailed analysis has been performed for spectra of triclinic crystals with  $\text{BF}_4^-$  ions [78]. This section presents spectra of BDH with  $\text{ClO}_4^-$  and tetraphenylborate anions,  $\text{BPh}_4^-$ , which crystallize in monoclinic and triclinic lattices, respectively [79]. Both unit cells have similar sizes ( $1.465$  and  $1.493 \text{ nm}^3$ ) but owing to the much larger size of the  $\text{BPh}_4^-$  counter ion the slightly larger triclinic cell contains only two dye molecules compared with 4 in the monoclinic cell.

The stacking of the molecules is shown in Fig. 8.27. The two molecules in the triclinic cell align parallel in dimers with a  $4.71 \text{ \AA}$  distance, which are separated by the large  $\text{BPh}_4^-$  ions. The intermolecular distances are too large for significant exchange coupling and dipolar coupling prevails. The parallel alignment of the molecules results in one optically active transition and the transition dipole parallel to the molecular axis defines the optical axis of a uniaxial tensor. The four molecules in the monoclinic crystal stack in a herringbone structure and two different orientations, related by a screw rotation  $2b$ , results in two Davydov components of  $A_u$  and  $B_u$  symmetry polarized parallel and perpendicular to the  $b$ -axis, respec-

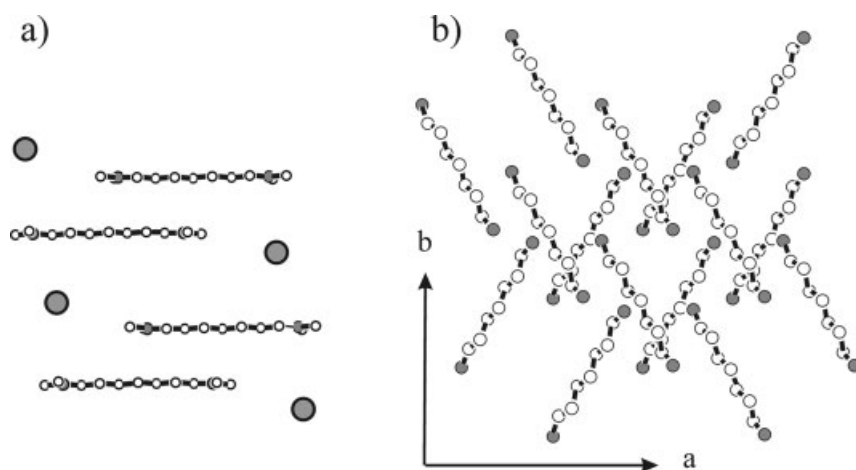


**Figure 8.27** Stacking of bis(dimethylamino)heptamethinium ions in two lattices with different counter ions. (a)  $\text{BDH}^+\text{BPh}_4^-$ ; the circles denote the boron position of the counter-ion. (b)  $\text{BDH}^+\text{ClO}_4^-$ , view on to the  $ab$ -plane; counter ions and methyl groups are omitted. Gray circles indicate the nitrogen atoms.

tively. Different from the stacking of TTI molecules, both excitons have comparable strengths with a ratio  $f_{A_u}/f_{B_u} = 1.58$  estimated from the orientation of the molecular dipoles.

Figure 8.28 shows normal incidence reflectance spectra of the triclinic lattice where all molecules are parallel. A band of high reflectivity is found for polarization of light parallel to the projection of the dipole moment on the respective face. A low and structureless reflectivity around 5% for orthogonal polarization confirms the absence of other transitions in that spectral range and a uniaxial dielectric tensor is sufficient to model the dielectric tensor. As expected for a strong exciton, the spectra vary considerably for different faces owing to directional dispersion. The angle between the wavevector of light and transition dipole is shown for each spectrum and polariton spectra calculated with a uniaxial model and the few oscillators listed in Table 8.3 describe the spectral changes satisfactorily.

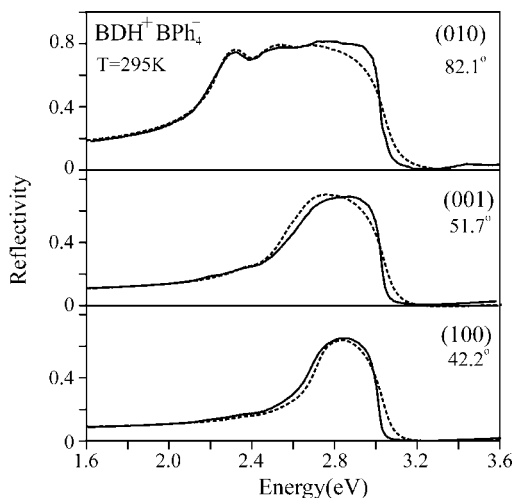


**Figure 8.28** Reflectivity of three crystal faces of BDH<sup>+</sup>BPh<sub>4</sub><sup>-</sup>. The angles refer to the orientation of the wavevector of light with respect to the transition dipole. Dashed curves present spectra calculated from parameters listed in Table 8.3 [79].

The exciton parameters were derived from the reflectivity of the (010) face where the wavevector is almost perpendicular to the dipole moment. The transverse exciton is found at 2.235 eV, followed by a vibronic progression of about 180 meV and their polariton branches cause dips in the band of high reflectivity. These features become more pronounced at low temperature and the strongest satellites are resolved in spectra of  $\text{Im}(\epsilon)$  [79]. The reflectivity increases at low temperature, reaching more than 90% before the sharp cut-off near the energy of the longitudinal exciton at 3.05 eV. As in CTIP a weak additional state, at 2.39 eV, improves the fit near the main reflectance peak. The origin is not clear but molecules in the surface layer are a most likely explanation. On the other faces the mole-

**Table 8.3** Lorentz oscillators, representing the exciton of  $\text{BDH}^+\text{BPh}_4^-$  and its vibronic satellites.

$\hbar\omega_j$ (eV)	2.235	2.39	2.425	2.61	2.79
$\chi_j$	1.90	0.05	0.10	0.015	0.0003
$\hbar\gamma_j$ (meV)	80	100	130	150	80
$\varepsilon(\infty)$	2.5				

cles are strongly inclined and directional dispersion results in narrower regions of high reflectance. The largest shift is observed for the (100) face where the polariton resonance has shifted to 2.705 eV.

The spectra of the monoclinic lattice of  $\text{BDH}^+\text{ClO}_4^-$  are more complicated since two transitions of comparable strength mix into the polariton modes. Spectra from several faces were measured which differ significantly owing to the relative orientations of wavevector and dipole moments, listed in Table 8.4.

**Table 8.4** Orientation of the transition dipoles of  $\text{BDH}^+\text{ClO}_4^-$ ;  $\vartheta$  is the angle with respect to the surface normal and  $\varphi$  the orientation of the projected dipole with respect to the indicated edge.

Face	$\vartheta_{A_u}$ (°)	$\vartheta_{B_u}$ (°)	$\varphi_{A_u}$ (°)	$\varphi_{B_u}$ (°)	Edge
(100)	90	13.8	60.1	-29.9	[011]
(001)	90	56.4	52.9	-37.1	[110]
(110)	38.8	52.5	15.7	33.2	$[\bar{1}\bar{1}0]$
( $\bar{1}\bar{1}1$ )	43.1	49.4	52.3	-38.8	[110]
( $11\bar{2}$ )	50.6	86.3	-38.6	48.3	$[\bar{1}\bar{1}0]$

The properties of a *b*-polarized  $A_u$  exciton can be derived directly from spectra of the (100) since the wavevector is normal the exciton dipole. The best face to derive the parameter of the  $B_u$  exciton is the ( $11\bar{2}$ ) face where the transition dipole is almost perpendicular to the wavevector of light. Figure 8.29 shows spectra of these two faces for polarization parallel to the projected dipole of the respective exciton. The (100) face shows a wide band of high reflectance spanning the polariton gap of the strong  $A_u$  exciton. For orthogonal polarization a faint structure near 2.6 eV is observed which is attributed to the  $B_u$  exciton. The coupling is very weak since the transition dipole is nearly parallel to the wavevector of light. The ( $11\bar{2}$ ) face shows one peak for each polarization. The peak at low energy arises from the  $B_u$

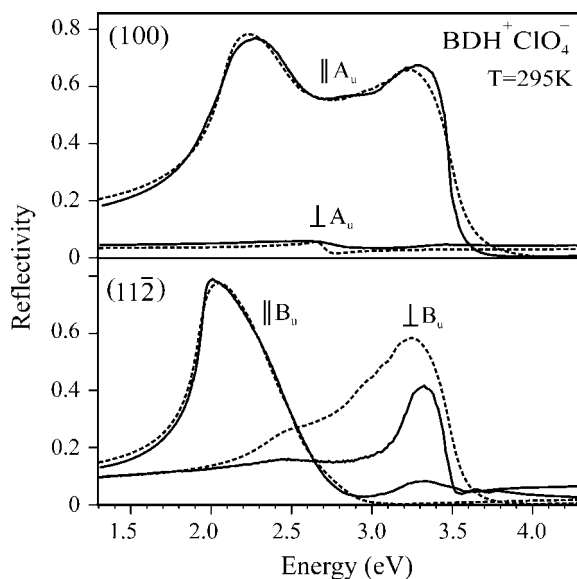


**Figure 8.29** Reflectivity of two crystal faces of  $\text{BDH}^+\text{ClO}_4^-$ , where Davydov components of the molecular exciton couple to different polaritons. Dashed curves present polariton reflectance spectra with parameters listed in Table 8.5 [79].

exciton. The peak at high energy is attributed to the  $A_u$  exciton whose resonance is shifted by directional dispersion ( $\vartheta = 50.6^\circ$ ). The spectra change little at low temperature and no clear vibronic structure emerges.

The transition dipoles of the Davydov components are used as principal axes of an orthorhombic dielectric tensor with excitons modeled by Lorentz oscillators (Table 8.5). Since vibronic states are not resolved an arbitrary progression of 90 meV was chosen to model the deep depression in the reflectivity of the polariton of the  $A_u$  exciton on the (100) face and the high-energy tail of the reflectivity of the  $B_u$  exciton on the  $(11\bar{2})$  face. A progression of 180 meV, expected from conjugated bonds, would lead to distinct dips in the reflectivity and larger broadening would decrease the reflectivity too much, washing out also the edges of the polariton band. The depression of the reflectivity without vibrational fine structure points to a broad spectrum of low-energy vibrations which couple to the excitons. A similar shape of a polariton reflectance is observed for 1,5-bis(dimethylamino)-pentamethinium perchlorate (Fig. 8.1) where all four molecules in a monoclinic cell of  $1.31\text{-nm}^3$  volume are parallel to within  $1^\circ$  [80].

The calculated spectra reproduce the strong reflectance bands of both faces. A noticeable deviation is observed for the high-energy peak on the  $(11\bar{2})$  face. Rotation of the electric field as in TTI (Fig. 8.25) is unlikely since the transition dipoles project nearly orthogonal on to that face. Since in this study the ellipticity of the reflected light was not investigated, small misalignment of the polarization of light on that small crystal face is a most probable explanation for that deviation.

**Table 8.5** Lorentz oscillators, representing the excitons of  $\text{BDH}^+\text{ClO}_4^-$  and its vibronic satellites.

Exciton	$A_u, \mu//b$							$B_u, \mu \perp b$				
$\hbar\omega_j$ (eV)	2.095	2.18	2.30	2.39	2.48	2.57	2.66	1.935	2.09	2.18	2.27	2.36
$\chi_j$	2.80	0.02	0.03	0.04	0.05	0.06	0.045	1.50	0.015	0.02	0.015	0.015
$\hbar\gamma_j$ (meV)	115	200	200	200	200	200	200	75	180	180	180	180
$\varepsilon(\infty)$	2.5											

The small peak near 3.3 eV in the other polarization, which is absent in the calculated polariton spectrum, further supports this conjecture.

Figure 8.30 demonstrates the large variance of polariton spectra of a biaxial crystal with strong excitons. The spectra of three faces agree well with polariton spectra based on the spectra of other faces. On the (001) face the spectrum polarized parallel to the dipole of the  $A_u$  exciton is almost identical with that on the (110) since a transverse mode is excited. The other polariton couples to the weaker  $B_u$  exciton and the spectrum is similar to that of the  $B_u$  exciton on the  $(11\bar{2})$  face, except for a small shift and smaller height due to a slightly different directional dispersion. On the (110) face the projection of the transition dipoles deviates by only  $18^\circ$  and both excitons couple into the stronger polariton mode. The polarization is close to that of the  $B_u$  exciton and was selected by finding at low energy the maximum of the reflectivity. Again the calculated spectra agree with the experimental spectra for both polarizations of light and allow the low-energy peak at 2.2 eV to be assigned to the dispersion-shifted resonance of the  $B_u$  exciton while the high energy peak near 3.4 eV is a resonance of the  $A_u$  exciton that is strongly shifted by the longitudinal field. On the (111) face the excitons couple to different polaritons since the projected dipoles are orthogonal. Although both transition dipoles are fairly strongly inclined, two absorption peaks are observed since the transition energy of the  $B_u$  exciton is 160 meV smaller and the smaller transition dipole causes a smaller shift in the longitudinal field.

The spectra of BDH reveal the large variety of spectra based on the same molecular exciton and are fully consistent with dielectric response theory that includes the macroscopic polarization set up by the exciton dipoles. Implicitly it was assumed that the molecular dipole is not changed by dipolar interaction. This assumption is verified by applying the sum rule to the spectra of different crystals. Figure 8.31 compiles integrated spectra of  $\text{Im}(\varepsilon)$  of the BDH cation normalized to their density in the different lattices [Eq. (8.82)]. In all cases crystal faces with negligible directional dispersion were chosen, so that  $\text{Im}(\varepsilon)$  corresponds to the spectral density of transverse excitons. The onset of the curves shows the shift of the absorption edge due to the crystal field and all curves saturate around 3 eV below the threshold to other transitions. In case of  $\text{Cl}^-$  and  $\text{BPh}_4^-$  counterions the parallel alignment of all molecules results in a single exciton and the saturation value represents the oscillator strength of the molecular exciton. In the other cases the

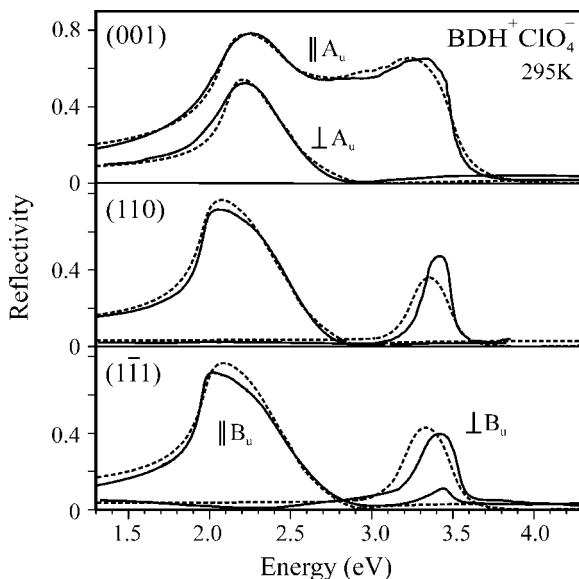


**Figure 8.30** Reflectance spectra of three crystal faces of  $\text{BDH}^+\text{ClO}_4^-$ , where both Davydov components couple into each polariton modes. Dashed curves present calculated spectra with parameters from Table 8.5 [79].

molecular oscillator strength is distributed to two Davydov components and the sum of their saturation values yields the strength of the molecular exciton. All samples yield a molecular oscillator strength in the range  $f = 5.6 \pm 0.3$  and that variation is within the experimental accuracy. The same value,  $f = 5.6$ , has been found for CTIP which is also a chain of four double bonds, suggesting that the  $\pi$ -electrons of a linear chain are not much affected by the terminating groups.

#### 8.4.4

##### Polaritons in Thin Films of Nanocrystalline Domains

The search for improved electronic devices based on  $\pi$ -conjugated molecules initiated the growth of thin films with crystalline domains. Aromatic molecules such as thiophene oligomers are widely studied and much progress has been made in growing films with crystalline order. Force microscope and X-ray studies confirm the high quality of these domains but their absorption spectra are broad and show even at low temperature not the narrow spectral features expected from excitons in a crystalline environment. Comparison of the spectra of single crystals and nanocrystalline films of sexithiophene points to polariton effects as the source of the obvious contradiction of the high structural quality of 100-nm large domains and broad structureless absorption spectra.

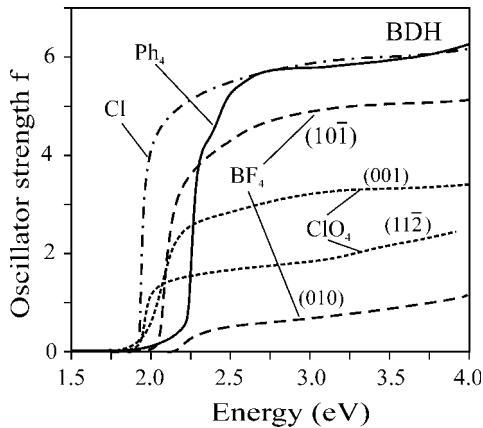


**Figure 8.31** Oscillator strength of the molecular exciton of BDH, derived from the sum rule of  $\text{Im}(\epsilon)$  of crystals with four different counterions. In all cases the sum rule has been applied to crystal faces whose normal is perpendicular or nearly perpendicular to the transition dipoles.

#### 8.4.4.1 Single Crystals of *a*-Sexithiophene (T6)

Sexithiophene crystallizes in a monoclinic lattice, the lower half of which is shown as an inset in Fig. 8.32. A pair of molecules related by a twofold rotation  $2b$  are found in this part and the remaining cell is generated by inversion on the top center [81]. The fundamental molecular exciton is polarized along the molecular axis  $L$  and the crystal symmetry generates two dipole-active states of  $A_u$  and  $B_u$  symmetry and two inactive states,  $A_g$  and  $B_g$ . Since the long axis lies almost flat on the  $ac$  plane, the  $b$ -polarized  $A_u$  exciton has a very small oscillator strength. It is the lowest transition in the crystal and gives rise to narrow absorption lines attributed to the exciton and vibronic states [82]. The  $B_u$  exciton, polarized in the  $ac$  plane, is very strong, acquiring the oscillator strength of all four molecules in the unit cell, each with a strength of  $f = 4.4$  [83]. Single crystals grow as thin platelets with the (100) face the only one of sufficient size for optical measurements. All molecules are strongly tilted out of that plane.

Figure 8.32 shows absorption spectra of a 9- $\mu\text{m}$  thin platelet. The weak  $A_u$  causes in  $E//b$  the small sharp peak at 2.273 eV and a series of similarly narrow vibronic satellites. Broader features appear above 2.5 eV, which are attributed to the  $B_u$  exciton at 2.593 eV and its vibronic progression. These excitons are polarized in the  $ac$  plane but the large oscillator strength leads to some residual absorption in the forbidden polarization  $E//b$ . In its proper polarization,  $E//c$ , the  $B_u$  exciton is accessible only to reflectance studies and Kramers–Kronig transformation of the data yields a single resonance at 3.4 eV with a height of  $2.3 \times 10^5 \text{ cm}^{-1}$ . The shift by 0.8 eV compared with the position of the  $B_u$  exciton in  $E//b$  results from directional dispersion. The dashed line shows the excellent agreement with the polariton absorption calculated in a biaxial model where the transition dipole of

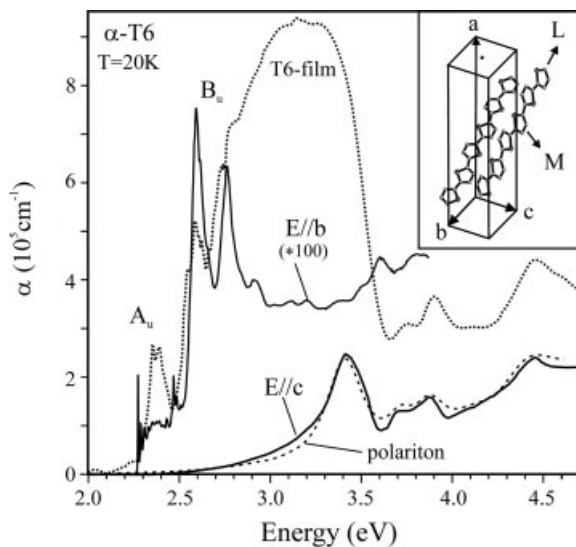


**Figure 8.32** Absorption spectra of  $\alpha$ -sexithiophene. The inset shows the lower part of the unit cell. Full lines present the spectrum of a single crystal for weakly absorbed light ( $E//b$ ) and for strongly absorbed light ( $E//c$ ) derived from reflectivity, the latter in comparison with

a calculated polariton spectrum. The dashed line shows the absorption of a 60-nm thin film of small crystalline domains. All spectral features derive from two Davydov components,  $A_u$  and  $B_u$ , of the molecular L-polarized exciton.

the strong  $B_u$  exciton defines the principal axes in the  $ac$  plane. All exciton parameters of the dielectric were taken from the experiment. The residual absorption in the forbidden polarization  $E//b$  provided the transition energy of the  $B_u$  exciton and its vibronic satellites since the weak excitation creates no significant longitudinal field. The oscillator strength was derived by integrating a solution spectrum and distributed among the exciton and its progression as estimated from the absorption spectrum [84]. The large shift results from the small angle  $\vartheta = 24.4^\circ$  between wavevector and dipole moment resulting in a large longitudinal field. It should be noted that as in naphthalene all spectral features of the strong exciton are much broader than the features of the weak exciton although both derive from the same molecular state. The larger linewidth must arise from stronger dipolar coupling of the  $B_u$  exciton, which is the only difference between the two states. Any effects based on overlap of molecular orbitals would affect both excitons equally.

Whereas the single crystal spectra are perfectly understood in a polariton model, the spectrum of a 60-nm thin nanocrystalline film with a lateral size of domains near 100 nm shows several inconsistencies at high energy. The fine structure at low energy can be attributed to the weak  $A_u$  exciton and its vibronic satellites. It is emphasized that the weak exciton couples in the single crystal to its forbidden polarization  $E//c$  by Herzberg–Teller coupling [82]. This secondary effect is sufficient to create a stronger absorption band in the forbidden polarization of light, which

has a similar shape to the spectrum of the film. However, the absorption constant of the film above 2.5 eV exceeds by far the absorption of the single crystal. This discrepancy becomes even stronger if we account for the isotropy of the film spectrum while that of the single crystal is polarized and has been measured in the proper polarization  $E//c$ .

Strong and weak excitons also respond very differently to an external electric field, as revealed by electroabsorption measurements on the single crystal [83]. Figure 8.33 shows at the top the change  $\Delta\alpha$  of the absorption constant for  $E//b$ , induced by a field  $F = 23 \text{ kV cm}^{-1}$  applied along the  $c$ -axis by two contacts evaporated on the (100) face. The spectrum of the weak  $A_u$  exciton and its vibronic states shows very narrow lines and agrees below 2.6 eV almost perfectly with the first derivative of the absorption spectrum and scaled by  $\Delta E = -0.3 \mu\text{eV}$ . This part of the spectrum is attributed to the Stark shift of the molecular exciton by its polarizability  $\beta_L$  along the molecular axis:

$$\Delta E = -\frac{\beta_L}{2} F^2 \quad (8.81)$$

From the red shift and the electric field component along the molecular axis, a polarizability  $\beta_L = 915 \text{ \AA}^3$  was obtained. Such a large molecular polarizability confirms an easy displacement of charge and is consistent with delocalization of the  $\pi$ -electrons over the molecule. The  $B_u$  exciton deriving from the same molecular

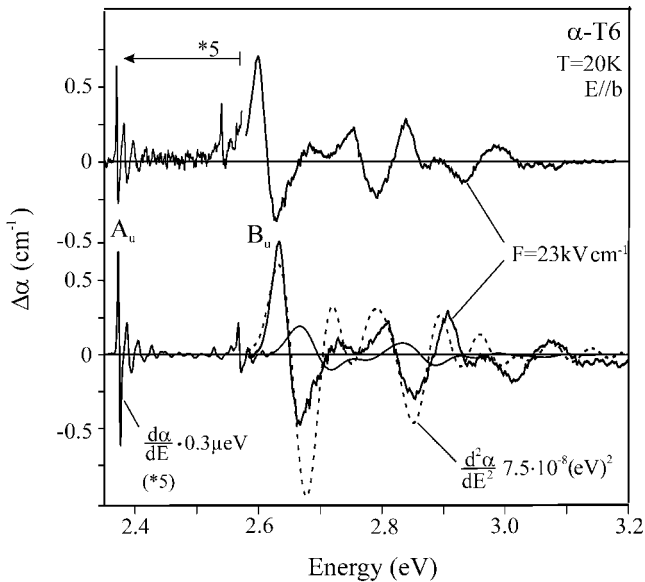


**Figure 8.33** Top: electroabsorption spectrum of the single crystal. The response of the weak  $A_u$  exciton has been enlarged as indicated. Bottom: first (thin line) and second derivative

(dotted line) of the absorption, scaled to the spectra of the  $A_u$  and  $B_u$  excitons, respectively. Note the amplification of the first derivative by a factor of 5 with respect to scale.

exciton should have the same red shift but the signal would be much smaller owing to the larger width of the spectral features. However, the response of the  $B_u$  exciton is much larger than that of the narrow  $A_u$  exciton and comparison with the first derivative shows that the Stark shift matches neither the lineshape nor the size of the modulated spectrum. The experimental spectrum is reproduced much better by the second derivative of the absorption, which yields the correct position of all spectral features. The negative peaks which occur at the maxima of the absorption constant are consistently too small which is attributed to uncorrected stray light  $I_s$ . Since  $\Delta\alpha$  is obtained from the ratio of relative change of the transmitted intensity and thickness  $d$  of the sample, stray light reduces the ratio in spectral regions of low transmittance:

$$\Delta\alpha = -\frac{1}{d} \frac{\Delta I}{I + I_s} \quad (8.82)$$

The second-derivative lineshape arises from direct coupling the coherent polarization oscillating with optical frequency  $\omega$  to the external field  $F$ . The external field  $F$  shifts the transition energy of the exciton, similar as the longitudinal field of a polaritons:

$$\Delta E(t) = \vec{\mu} \cdot \vec{F} \cos \omega t \quad (8.83)$$

The energy of the exciton thus oscillates around its zero-field position. Since the effect vanishes with the loss of phase coherence, integration over the lifetime  $\tau$  of the coherent polarization yields the observable change of the absorption in first and second order of the energy shift  $\Delta E$ :

$$\Delta\alpha = \frac{1}{\tau} \int_0^\tau \left[ \frac{\partial\alpha}{\partial E} \Delta E + \frac{1}{2} \frac{\partial^2\alpha}{\partial E^2} (\Delta E)^2 \right] dt \quad (8.84)$$

The linear term vanishes by integration but the second-order term yields a spectrum of second-derivative lineshape, corresponding to field broadening of the spectrum by the energy of the transition dipole in the electric field:

$$\Delta\alpha = \frac{\partial^2\alpha}{\partial E^2} \frac{(\vec{\mu} \cdot \vec{F})^2}{2} \quad (8.85)$$

The field-induced change of the absorption,  $\Delta\alpha$ , increases quadratically with the field as observed and is proportional to the oscillator strength of the exciton. The signal is reduced by the angle of  $65.6^\circ$  between transition dipole of the  $B_u$  exciton and the applied field. The scaling factor of the second derivative yields the transition dipole moment  $\mu = 4.1 \text{ e \AA}$ . The value is larger than the transition dipole  $\mu = 2.45 \text{ e \AA}$  of the T6

molecule but close to the value  $\mu = 4.9 e \text{ \AA}$  expected for a  $B_u$  exciton in the crystal which has the oscillator strength of all four molecules in the unit cell.

This type of field broadening is a coherent effect and different from lifetime broadening of an excited state. Its observation needs large transition dipoles and the transition dipole of the weak Davydov component  $A_u$  is too small for such a response. The properties of the weak exciton are those of the molecular exciton in a well-defined environment since the large separation of the molecules and the very small dipole moment reduce the intermolecular interaction and localize the exciton.

#### 8.4.4.2 Nanocrystalline Films

Nanocrystalline domains whose lateral size exceeds significantly the range of dipolar interaction provide most molecules with the same intermolecular coupling and should behave like single crystals. The range of coupling is estimated to a few nanometers; comparable to the Förster radius, and for larger domains the absorption should depend on the orientation of the strong molecular dipole with respect to the wavevector. The spectrum of a T6 film is thus modeled by a polariton based on the strong exciton in the single crystal. A uniaxial approach with the transition dipole of the strong  $B_u$  exciton defining the optical axis is sufficient since the weak excitons contribute negligible polarization. The exciton parameters are listed in Table 8.6 and additional weaker states at higher energy are not shown. The oscillator strength of the excitons is the same as used to calculate the polariton spectrum of the single crystal, shown in Fig. 8.32. The transition energies are slightly shifted to higher energy by 40 meV to reproduce the position of the spectral features of the electroabsorption spectrum.

**Table 8.6** Lorentz oscillators representing the  $B_u$  exciton in films of *a*-sexithiophene and its vibronic states.

$\hbar\omega_j$ (eV)	2.64	2.81	2.98	3.15	3.32	3.49
$\chi_j$	1.20	0.32	0.10	0.02	0.005	0.001
$\hbar\gamma_j$ (meV)	130	140	150	170	180	200

Figure 8.34a shows calculated spectra of T6 domains [85, 86]. Directional dispersion of the polariton resonance shifts the absorption spectrum to higher energy as the molecules rotate towards an upright orientation, thereby decreasing the angle  $\vartheta$  between the optical axis and the wavevector. It should be noted that the weak transitions above 3.5 eV show no shift.

The isotropic absorption of the film indicates random azimuthal orientation of optical axes in the nanocrystalline film but it is assumed that domain maintain the molecular orientation over the thickness of the film. Each domain has a differ-

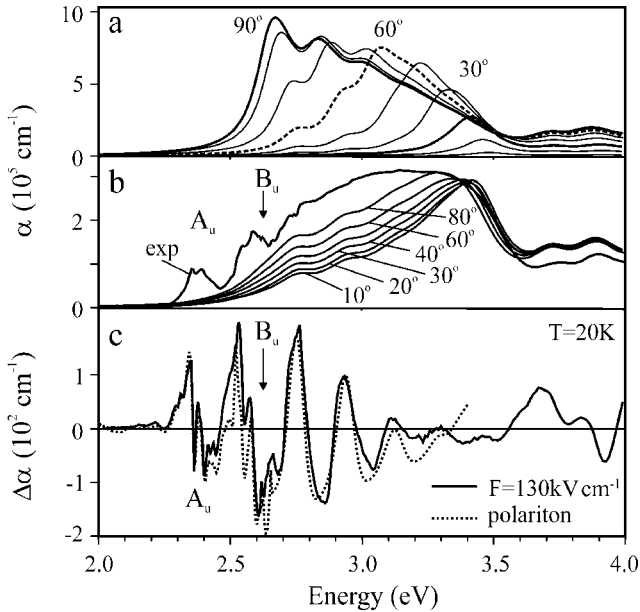


**Figure 8.34** (a) Variation of polariton absorption spectra with the angle between wavevector and transition dipole of the strong exciton in T6. (b) Absorption of a nanocrystalline film and polariton spectra calculated for different

preferential orientation of the optical axis in the domains. (c) Comparison of the electro-absorption spectrum (full line) with a spectrum calculated for a preferential orientation of  $30^\circ$  [87].

ent absorption spectrum  $a(\vartheta_j)$  and the film absorption spectrum thus depends on the distribution  $p(\vartheta_j)$  of the orientation of the optical axis  $\vartheta_j$  with respect to the wavevector. Figure 8.34b presents calculated film spectra for a smooth distribution of domain orientation,  $p(\vartheta_j - \vartheta_0) = \cos^2(\vartheta_j - \vartheta_0)$ , around a preferential orientation  $\vartheta_0$  of the optical axis. As in the experiment the absorption spectrum is obtained by summing up the transmitted light to the transmittance  $T$  of the film and the absorption constant is defined by the ratio of  $\ln T$  and film thickness,  $d = 60 \text{ nm}$ :

$$a = \frac{-1}{d} \ln \left( \frac{\sum_j p(\vartheta_j) \int_0^{\pi/2} d\varphi \exp[-a(\vartheta_j) \cos^2 \varphi \cdot d]}{\int_0^{\pi/2} d\varphi \sum_j p(\vartheta_j)} \right) \quad (8.86)$$

The spectra are calculated for optimum polarization of light ( $\varphi = 0$ ) and do not include the weak  $A_u$  exciton and its vibronic states, which cause the structure in the experimental spectrum below  $2.6 \text{ eV}$ . All calculated spectra produce a nearly structureless absorption band with a peak above  $3.2 \text{ eV}$ , well above the energy of the  $B_u$  exciton and the high energy cut-off, defined by the longitudinal exciton

near 3.5 eV. This result is a consequence of summing up the transmitted light. Domains with strongly tilted molecules (small  $\vartheta$ ) absorb less light and dominate the transmittance. Their large directional dispersion shifts the absorption peak of the film to high energy. Nevertheless, the polariton spectra do not reproduce the large absorption of the strong exciton at lower energy in the region of the strong  $B_u$  exciton.

In striking contrast to the broad absorption spectrum, the electroabsorption spectrum, shown in Fig. 8.34c, has very rich structure with some similarity to the spectrum of the single crystal in Fig. 8.33 [83]. The spectrum has been measured for polarization of light parallel to the field ( $E//F$ ) and the spectral features agree with those reported in an earlier publication and obtained in a different field configuration [87]. These authors noticed that the lineshape of their spectrum could not be fitted to derivatives of the rather structureless absorption spectrum. However, the dotted line shows a calculated electroabsorption spectrum based on the same effects as in the crystal. The narrow features below 2.4 eV agree with the first derivative of the absorption spectrum and arise from the Stark shift of the  $A_u$  exciton by  $25 \mu\text{eV}$  in a field of  $130 \text{ kV cm}^{-1}$ . This shift corresponds to a polarizability of  $425 \text{ \AA}^3$ , which is about half the value observed in the single crystal, a satisfactory agreement in view of the unknown azimuthal distribution of the dipole moments involved in the Stark effect [85, 86].

The spectrum above 2.6 eV cannot be fitted to derivatives of the absorption spectrum, thus confirming the earlier report, but coupling the transition dipoles to the electric field as in the single crystal reproduces all details. The electroabsorption spectrum  $\Delta a(\vartheta_j)$  of each domain is calculated from field broadening of the strong exciton by  $\Delta E = \mu F \cos \varphi \sin \vartheta$ , taking into account the projection of transition dipole to the electric field, including the azimuth angle  $\varphi$  between field and transition dipole. The field-induced change  $\Delta a_j$  scales with the second derivative of the corresponding polariton absorption and the square of the proper energy broadening, which is the expression in square brackets in Eq. (8.87). Summing up the resulting change of the transmitted light intensity  $\Delta I_j$  yields the electroabsorption spectrum  $\Delta a$  of the film as ratio of  $\Delta I/I$  and film thickness  $d$ :

$$\Delta I = -I d \Delta a = \frac{\sum_j \left[ \int_0^{\pi/2} d\varphi \cos^4 \varphi \sin^2 \vartheta_j \frac{1}{2} \frac{d^2 a(\vartheta_j)}{dE^2} (\mu F)^2 \right] p(\vartheta_j) \exp \left[ -a(\vartheta_j) \cdot d \right]}{\int_0^{\pi/2} d\varphi \sum_j p(\vartheta_j)} \quad (8.87)$$

The electroabsorption spectrum calculated from Eq. (8.87) reproduces all the large features between 2.6 and 3.4 eV within the polariton band of the strong  $B_u$  exciton. The preferential orientation of domains has a negligible effect on the position of these features but modifies their relative strength. The calculation in Fig. 8.34c assumed a preferential orientation  $\vartheta_0 = 30^\circ$ , similar to that in a single crystal and scaling the calculated spectrum to the size of the experimental signal yields a broadening parameter  $\Delta E \approx 10 \text{ meV}$ . The corresponding transition dipole is

5.5–10 e Å, depending on the preferential orientation of domains. Considering the sensitivity of the second derivatives to the linewidth  $\gamma_j$  and the unknown azimuth angles  $\varphi_j$ , this value is close to the expected value of 4.9 e Å. Stark shift of the weak exciton and field broadening of the strong exciton–polariton thus reproduce the complex electroabsorption spectrum of the nanocrystalline film.

The directional dispersion of the polariton resonance generates a broad absorption peak for a nanocrystalline film but fails by far to reproduce the absorption constant of the film, shown in Fig. 8.32. The experimental spectrum in Fig. 8.34b is reduced by a factor of 3 to be on the scale of the calculated spectra, which, furthermore, assumed optimum polarization of light ( $\varphi = 0$ ). The experimental absorption therefore is much larger than calculated from the data for a single crystal and this excess absorption points to additional loss of light. Domains of 50–100 nm lateral size are sufficiently large to behave like single crystals with respect to dipolar coupling and polariton resonance as shown by the appearance of Davydov components of different linewidth and different response to an external field. These domains, however, do not support coherent propagation of an electromagnetic wave of a wavelength larger than their size. Light under normal incidence excites all domains in phase and with the same orientation of wavevector and displacement current, but polaritons propagate along the Poynting vector and thus perpendicular to the electric field, which is different in neighboring domains. An electromagnetic field extending over domains of different orientation has no defined direction for energy propagation, resulting in strong scattering of the polariton and enhanced absorption, which is not determined by Fermi's golden rule and the oscillator strength of excitons. The loss of coherent coupling of exciton and light is not due to scattering of the exciton but to scattering of the radiation field, converting polaritons into an incoherent population of excitons, which diffuse slowly. Scattering of light will be strongest at low energy where the dielectric tensor, defined by the susceptibility of strong transverse excitons, varies rapidly, explaining the enhanced excess absorption at low energy into the range of the weak  $A_u$  exciton. The electroabsorption spectrum is less sensitive to that loss since the signal arises from coupling the polariton to the external field. Only polaritons reaching the back surface of the sample contribute to the electroabsorption spectrum and provide spectral information about the exciton and its satellites to the transmitted light.

Most of the scattering of the electromagnetic field seems related to azimuthal disorder in the film since nanocrystalline films of quaterthiophene (T4) oriented on a polar substrate show no excess absorption [88]. T4 domains, growing on KAP (potassium phthalate) single crystals, orient their transition dipole along a polar axis of the substrate, resulting in strongly polarized absorption spectra [89]. The structure of T4 is similar to that of T6 and four molecules with parallel long axes belong to a unit cell [90]. The azimuthal alignment of the transitions dipoles leads to much better defined samples. In most domains the molecular axis is steeply inclined with respect to the substrate ( $\vartheta = 29^\circ$ ) whereas in other domains molecules have less inclination ( $\vartheta = 61^\circ$ ) [91].

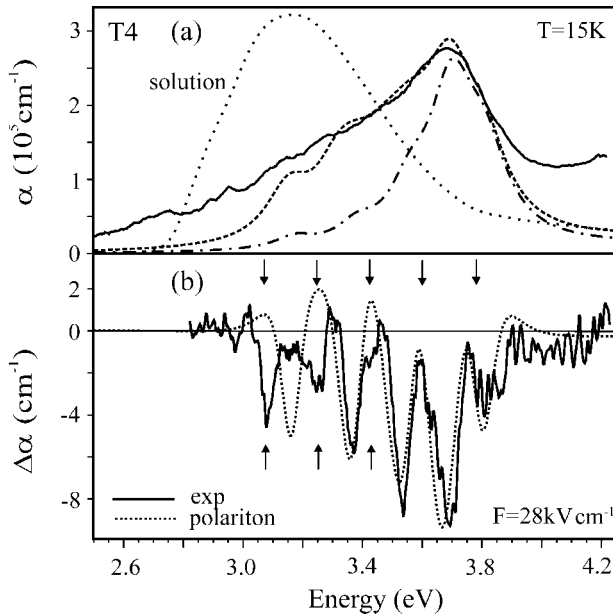


**Figure 8.35** (a) Absorption spectra of quaterthiophene in a 25-nm thick film, oriented on a polar substrate and in solution. Dashed and dash-dotted lines show calculated

polariton spectra. (b) Richly structured electroabsorption spectrum of the film in comparison with a calculated spectrum [84]. Arrows indicated the exciton transition energies.

Figure 8.35 compares spectra of an oriented 25-nm thin film [88]. The solution spectrum yields a transition dipole  $\mu = 2 e \text{ \AA}$  and oscillator strength  $f = 3.65$  of the molecular exciton which is distributed to a vibronic progression to match the richly structured electroabsorption spectrum. The arrows indicate the position of the excitons, listed in Table 8.7, together with the linewidth  $\gamma$  and the contribution  $\chi$  to the dielectric constant. Calculated polariton spectra show that directional dispersion of the polariton resonance shifts the absorption peak from the exciton transition energy at 3.07 to 3.67 eV. Assuming domains of the same orientation,  $\vartheta = 29^\circ$ , produces the correct height and peak position but a too narrow width of the absorption spectrum. Including 20% of domains with orientation  $\vartheta = 61^\circ$ , indicated by structural studies [91], agrees much better with the absorption spectrum but does still not reproduce the long absorption tail at low energy.

The electroabsorption spectrum  $\Delta\alpha$  again resolves the vibronic fine structure and has no resemblance to derivatives of the absorption spectrum. The dotted line shows the spectrum calculated from field broadening of the strong exciton by coupling its transition dipole to the external field. The calculation uses a narrow distribution of optical axes around two orientations  $\vartheta = 29$  and  $61^\circ$ . The strong features above 3.3 eV are well reproduced by the polariton spectrum and the signal size yields broadening by  $\Delta E = 1.1 \text{ meV}$  in a field of  $28 \text{ kV cm}^{-1}$ . Accounting again for the orientation of the transition dipole with respect to the field yields a transi-

**Table 8.7** Lorentz oscillators representing the  $B_u$  exciton in films of quaterthiophene and its vibronic states.

$\hbar\omega_j$ (eV)	3.070	3.247	3.424	3.600	3.780
$\chi_j$	0.78	0.32	0.09	0.03	0.01
$\hbar\gamma_j$ (meV)	160	160	170	180	180
$\varepsilon(\infty)$	2.6				

tion dipole  $\mu = 3.9 \text{ e}\text{\AA}$  for the strong Davydov component. This value is in excellent agreement with  $\mu = 4.0 \text{ e}\text{\AA}$ , expected if four molecular transition dipole moments  $\mu = 2 \text{ e}\text{\AA}$  contribute to the dipole moment of the strong exciton in the crystal.

The calculated spectrum predicts an additional peak near 3.2 eV where the experimental spectrum shows two peaks at 3.08 and 3.255 eV and a shoulder near 3.43 eV. These features match a vibronic progression of 175 meV and are very close to the transition energies of the strongest excitons in Table 8.7. These features have tentatively been attributed to flat-lying molecules from the first and probably also the second layer of the film, forced down by strong coupling to the polar axis of the substrate [89]. As the film continues to grow, coupling to the substrate weakens and molecules orient according to crystal structure of T4.

## 8.5

### Conclusion

Crystals of organic molecules with  $\pi$ -conjugated bonds have unique optical properties, which arise from the combination of spectrally isolated strong transition dipoles and the anisotropic structure. Electrons in conjugated bonds interact strongly and respond to light collectively, resulting in spectrally isolated excitons which acquire most of the oscillator strength of the  $\pi$ - $\pi^*$  transitions. This effect is particularly pronounced for linear chains.

The crystalline unit cell frequently contains two or four molecules, which splits the molecular exciton into Davydov components, the excitons of the solid. The symmetry of the cell leads to one or two orthogonal polarized excitons and owing to the large density of molecules optical excitation creates a macroscopic polarization that is an inherent part of the excited solid. The appropriate description of such excited state is the polariton, the coherently coupled state of photon and excitons. Spectrally isolated strong transitions open wide gaps for electromagnetic waves resulting in a band of high reflectivity, the polariton stop band whose width increases with the contribution of the exciton to the static dielectric constant and often exceeds 1 eV.

Aggregation of the molecules leads to optical anisotropy. Except for special cases, where the polarization and wavevector of light are parallel to axes of the

dielectric tensor, incident light creates a longitudinal polarization and a longitudinal electric field. Coupling the transition dipole to that field shifts the optical resonance over the range of the polariton gap, depending on the orientation of the wavevector with respect to the transition dipoles. Spectra measured on different crystal faces thus vary strongly and absorption spectra no longer show the transition energy and strength of the excitons. Since the directional dispersion, unique to anisotropic solids, results from electrodynamics, the properties of the excitons can be derived by solving the wave equation with a dielectric tensor defined by the excitons and comparing calculated and experimental spectra. For the spectral range of  $\pi$ - $\pi^*$  transitions the exciton dipoles derived from strong molecular transitions provide principal axes of the dielectric tensor since the susceptibility related to these excitons exceeds by far the anisotropy arising from transitions at higher energy. An orthorhombic tensor is sufficient to describe the strikingly different spectra of strong excitons observed on different crystal faces of monoclinic and triclinic crystals. If aggregation of molecules leads to one strong transition only, a uniaxial tensor with the optical axis defined by the transition dipole is sufficient, regardless of the actual crystal structure. Only in cases where the longitudinal field arising from the macroscopic polarization is small, optical spectra show the energy and strength of excitons directly.

Spatial dispersion, resulting from exchange coupling across unit cells, is negligible for molecular solids owing to the small intermolecular overlap of molecular states. Dielectric theory based on local oscillators which couple only by dipolar forces therefore describes the spectra very well. Such dominance of dipolar interaction with respect to exchange coupling is evident from the very different line-width of Davydov components of the same molecular exciton.

Directional dispersion of the polariton resonance causes broad and structureless absorption spectra of films of nanocrystalline domains of  $\pi$ -conjugated molecules. Since the dielectric response of a domain depends on the orientation of its principal axes with respect to the wavevector of light the different optical response of the domains obscures most spectral features. Azimuthal disorder of the principal axes results in isotropic absorption spectra and excess absorption if the wavelength of light is larger than the domain size. Despite a common orientation of wavevector and displacement current in the anisotropic domains polaritons are rapidly scattered since they propagate along the Poynting vector, which is different in neighboring domains. The exciton fine structure of the films can be recovered by measuring the change in transmission induced by an external electric field, which couples to the coherent polarization. Similar improved resolution is expected for other nonlinear optical experiments that are based on phase coherence.

Absorption of light occurs by inelastic scattering of propagating polaritons whose energy oscillates with the Rabi frequency between excitons and radiation field. Absorption requires breaking that coupled system by a scattering rate faster than the Rabi frequency. Although the Rabi frequency increases with the transition dipole moment, the square root of the exciton oscillator strength, reduced absorption is not observed for strong transition dipoles but for weak excitons.

This observation suggests that strong dipole moments increase the scattering rate faster than the Rabi frequency, supported also by the much larger linewidth of strong and weak Davydov components of a molecular exciton.

## References

- 1 G. H. Wannier, *Phys. Rev.* **52**, 191 (1937).
- 2 R. J. Elliott, *Phys. Rev.* **108**, 1384 (1957).
- 3 J. Frenkel, *Phys. Rev.* **37**, 17, 1276 (1931).
- 4 A. S. Davydov, *Theory of Molecular Solids*, Plenum Press, New York, 1971.
- 5 B. G. Anex, W. T. Simpson, *Rev. Mod. Phys.* **32**, 466 (1960).
- 6 B. M. Fanconi, G. A. Gerhold, W. T. Simpson, *Mol. Cryst. Liq. Cryst.* **6**, 41 (1969).
- 7 A. P. Marchetti, C. D. Salzberg, E. I. P. Walker, *J. Chem. Phys.* **64**, 4693 (1975).
- 8 H. J. Hesse, W. Fuhs, G. Weiser, L. von Szentpaly, *Chem. Phys. Lett.* **41**, 104 (1976).
- 9 C. J. Eckhardt, R. R. Penelly, *Chem. Phys. Lett.* **9**, 572 (1971).
- 10 R. R. Penelly, C. J. Eckhardt, *Chem. Phys.* **12**, 89 (1976).
- 11 K. Fuke, K. Kaya, T. Kajiwara, S. Nagakura, *J. Mol. Spectrosc.* **63**, 98 (1976).
- 12 D. L. Mills, E. Burstein, *Rep. Prog. Phys.* **37**, 817 (1974).
- 13 R. Claus, L. Merten, J. Brandmüller, *Light Scattering by Phonon-Polaritons*, Springer Tracts in Modern Physics, Vol. 75, Springer, Berlin, 1975.
- 14 G. Borstel, H. J. Falge, A. Otto, *Surface and bulk phonon-polaritons observed by attenuated total reflection*, Springer Tracts in Modern Physics, Vol. 74, Springer, Berlin, 1974.
- 15 A. Otto, *Festkörperprobleme XIV*, Vieweg, Braunschweig, 1974.
- 16 U. Fano, *Phys. Rev.* **103**, 1202 (1956).
- 17 H. Haug, S. Koch, *Quantum Theory of the Optical, Electronic Properties of Semiconductors*, World Scientific, Singapore, 1993.
- 18 W. R. Heller, A. Markus, *Phys. Rev.* **84**, 809 (1951).
- 19 D. Fox, S. Yatsiv, *Phys. Rev.* **108**, 938 (1957).
- 20 J. J. Hopfield, *Phys. Rev.* **112**, 1555 (1958).
- 21 V. M. Agranovich, V. L. Ginzburg, *Spatial Dispersion in Crystal Optics, the Theory of Excitons*, Interscience, London, 1966.
- 22 A. S. Davydov, A. A. Serikov, *Phys. Status Solidi B* **56**, 351 (1973).
- 23 M. Sargent III, M. O. Scully, W. E. Lamb Jr., *Laser Physics*, Addison-Wesley, Reading, MA, 1974.
- 24 A. Stahl, I. Balslev, *Phys. Status Solidi B* **113**, 583 (1982).
- 25 S. I. Pekar, *J. Sov. Phys. JETP* **38**, 1286, 1786 (1960).
- 26 J. J. Hopfield, D. G. Thomas, *J. Phys. Chem. Solids* **12**, 276 (1960).
- 27 M. Born, F. Wolf, *Principles of Optics*, Pergamon Press, Oxford, 1987.
- 28 M. R. Philpott, *J. Chem. Phys.* **58**, 588 (1973).
- 29 M. R. Philpott, *J. Chem. Phys.* **58**, 595 (1973).
- 30 T. Kurosawa, *J. Phys. Soc. Jpn.* **16**, 1298 (1961).
- 31 L. Merten, *Phys. Status Solidi* **30**, 449 (1968).
- 32 B. B. Johnson, W. T. Simpson, *J. Chem. Phys.* **65**, 4246 (1976).
- 33 J. J. Hopfield, D. G. Thomas, *Phys. Rev.* **132**, 563 (1963).
- 34 B. Hönerlage, A. Bivas, V. Duy Phach, *Phys. Rev. Lett.* **41**, 44 (1978).
- 35 S. I. Pekar, *Fiz. Tverd. Tela* **4**, 130 (1962); *Sov. Phys. Solid State* **4**, 953 (1962).
- 36 K. Hümmer, P. Gebhardt, *Phys. Status Solidi B* **85**, 271 (1978).
- 37 J. Lagois, *Phys. Rev. B* **23**, 5511 (1981).
- 38 A. Stahl, *Phys. Status Solidi B* **92**, 113 (1979).
- 39 M. R. Philpott, *Adv. Chem. Phys.* **23**, 227 (1973).

- 40 M. R. Philpott, P. G. Sherman, *Phys. Rev. B* **12**, 5381 (1975).
- 41 E. Tosatti, G. Harbeke, *Nuovo Cimento* **22**, 87 (1974).
- 42 L. Merten, G. Lambrecht, *Phys. Status Solidi* **39**, 573 (1970).
- 43 L. Merten, R. Claus, *Phys. Status Solidi B* **89**, 159 (1978).
- 44 R. Claus, *Phys. Status Solidi B* **88**, 683 (1978).
- 45 R. Claus, G. Borstel, *Phys. Status Solidi B* **88**, K123 (1978).
- 46 S. L. Robinette, G. J. Small, S. H. Stevenson, *J. Chem. Phys.* **68**, 4790 (1978).
- 47 S. L. Robinette, S. H. Stevenson, G. J. Small, *J. Chem. Phys.* **69**, 5236 (1978).
- 48 A. Bosacchi, S. Bosacchi, S. Franchi, *Phys. Rev.* **36**, 1086 (1976).
- 49 M. R. Philpott, *J. Chem. Phys.* **54**, 2120 (1971).
- 50 K. Zeppenfeld, *Z. Phys.* **211**, 391 (1968).
- 51 D. L. Greenaway, A. Harbeke, F. Bassani, E. Tosatti, *Phys. Rev.* **178**, 1340 (1969).
- 52 E. Tosatti, F. Bassani, *Nuovo Cimento B* **65**, 161 (1970).
- 53 S. Kunstreich, A. Otto, *Chem. Phys.* **3**, 384 (1974).
- 54 R. Allmann, T. Debaerdemaeker, Abdel-Rahman Ferwanah, W. Pressler, C. Reichardt, *Chem. Ber.* **109**, 3005 (1976).
- 55 M. R. Philpott, I. Pockrand, A. Brillante, J. D. Swalen, *J. Chem. Phys.* **72**, 2774 (1980).
- 56 G. Weiser, W. Fuhs, H. J. Hesse, *Chem. Phys.* **52**, 183 (1980).
- 57 J. M. Turllet, M. R. Philpott, *J. Chem. Phys.* **62**, 2777 (1975).
- 58 J. M. Turllet, M. R. Philpott, *J. Chem. Phys.* **62**, 4260 (1975).
- 59 J. M. Turllet, M. R. Philpott, *Chem. Phys. Lett.* **35**, 92 (1975).
- 60 W. Fuhs, D. Hauschildt, H. J. Hesse, *Phys. Status Solidi B* **91**, 447 (1979).
- 61 H. J. Hesse, W. Fuhs, G. Weiser, L. von Szentpaly, *Phys. Status Solidi B* **76**, 817 (1976).
- 62 R. E. Long, R. A. Sparks, K. N. Trueblood, *Acta Crystallogr.* **18**, 932 (1965).
- 63 M. R. Philpott, P. M. Grant, K. Syassen, J. M. Turllet, *J. Chem. Phys.* **67**, 4229 (1977).
- 64 H. J. Hesse, W. Fuhs, G. Weiser, *Chem. Phys.* **24**, 399 (1977).
- 65 R. Allmann, S. Olejnik, *Cryst. Struct. Commun.* **11**, 1175 (1982).
- 66 T. Hayne, G. Weiser, *Phys. Status Solidi B* **123**, 271 (1984).
- 67 B. G. Anex, A. V. Fratini, *J. Mol. Spectrosc.* **14**, 1 (1964).
- 68 A. Brillante, F. Bertinelli, L. A. Dissado, *Chem. Phys. Lett.* **55**, 131 (1978).
- 69 H. H. Chen, L. B. Clark, *J. Chem. Phys.* **58**, 2593 (1970).
- 70 E. I.P. Walker, A. P. Marchetti, C. D. Salzberg, *J. Chem. Phys.* **63**, 2090 (1975).
- 71 A. P. Marchetti, C. D. Salzberg, E.-I. P. Walker, *Photogr. Sci. Eng.* **20**, 107 (1976).
- 72 N. Sano, J. Tanaka, *Bull. Chem. Soc. Jpn.* **59**, 843 (1986).
- 73 G. C. Morris, M. G. Sceats, *Chem. Phys.* **1**, 259 (1973).
- 74 M. Tristani-Kendra, C. J. Eckhardt, L. Bernstein, E. Goldstein, *Chem. Phys. Lett.* **98**, 57 (1983).
- 75 L. Dähne, W. Grahn, P. G. Jones, A. Chrapkowski, *Z. Kristallogr.* **209**, 514 (1994).
- 76 L. Dähne, A. Horvath, G. Weiser, G. Reck, *Adv. Mater.* **8**, 486 (1996).
- 77 L. Dähne, K. Kamiya, J. Tanaka, *Bull. Chem. Soc. Jpn.* **65**, 2328 (1992).
- 78 L. Dähne, A. Horvath, G. Weiser, *Chem. Phys.* **178**, 449 (1993).
- 79 L. Dähne, A. Horvath, G. Weiser, *Chem. Phys.* **196**, 307 (1995).
- 80 J. O. Selzer, B. W. Matthews, *J. Phys. Chem.* **80**, 631 (1976).
- 81 G. Horowitz, B. Bachet, A. Yassar, P. Lang, F. Demanze, J. L. Fave, F. Garnier, *Chem. Mater.* **7**, 1337 (1995).
- 82 M. Muccini, E. Lunedei, A. Bree, G. Horowitz, F. Garnier, C. Taliani, *J. Chem. Phys.* **108**, 7327 (1998).
- 83 S. Möller, G. Weiser, F. Garnier, *Phys. Rev.* **61**, 15749 (2000).
- 84 G. Weiser, S. Möller *Phys. Rev.* **65**, 45203 (2002).
- 85 S. Möller, G. Weiser, C. Taliani, *Chem. Phys.* **295**, 11 (2003).
- 86 G. Weiser, *Synth. Met.* **139**, 719 (2003).

- 87 L. M. Blinov, S. P. Palto, G. Ruani, C. Taliani, A. A. Tevosov, S. G. Yudin, R. Zamboni, *Chem. Phys. Lett.* **108**, 401 (1995).
- 88 G. Weiser, S. Möller, *Org. Electron.* **5**, 91 (2004).
- 89 D. Besana, A. Borghesi, M. Campione, A. Sasella R. Tubino, M. Moret, R. Rinaldi, F. Garnier, *J. Cryst. Growth* **235**, 214 (2002).
- 90 T. Sigrist, C. Kloch, R. A. Laudise, H. E. Katz, R. C. Haddon, *Adv. Mater.* **10**, 379 (1998).
- 91 M. Campione, A. Borghesi, M. Moret, A. Sassela, B. Lotz, A. Thierry, *Org. Electron.* **5**, 141 (2004).

## 9

# Sub-5 fs Spectroscopy of Polydiacetylene

*Takayoshi Kobayashi, Mitsuhiro Ikuta and Yoshiharu Yuasa*

### 9.1

#### Introduction

##### 9.1.1

#### Ultrafast Spectroscopy

It has been a long dream of molecular physicists and chemists to visualize the structure of a molecule during its reaction and vibration, which can be a gateway to chemical reactions. Some specific molecular vibrational modes may be associated with the redistribution of electrons in the reacting molecules resulting in a configurational change or bond relocation. For such purposes ultrashort laser pulses can be used as a “flash camera” to pursue the nuclear wavepacket motions on the potential energy surfaces (PESs) to reveal photochemical reaction pathways [1–5]. Nuclear wavepackets can help in the visualization of atomic motion during a chemical reaction or molecular vibration even though too much analogy may introduce misunderstanding of the processes taking place.

Nuclear motions induced by photoexcitation through vibronic coupling modulate in turn the electronic structure with vibrational periods [6, 7]. This phenomenon can be observed as electronic spectral changes in both shape and intensity during the vibrational periods [8, 9]. If the vibration belongs to the gate mode of chemical reaction, the spectrum provides the electronic structure in the “transition state” in a broad sense. Short pulses to be used must have a broad enough spectral width to cover the spectral range of interest and a short enough duration to time resolve the vibrational motions in real time. This requires sub-5 fs Fourier transform (FT) limited pulse [10] to time-resolve most strongly and frequently coupled stretching modes of single, double and triple C–C and C–H bonds with frequencies in the range 1000–3000  $\text{cm}^{-1}$ . When materials in the condensed phase are the target of the study, there is an issue due to complications induced by inhomogeneous broadening which is found for almost all molecular systems in a condensed phase, either in a solid, in a solid matrix or in a crystalline phase. In the case of solution- and liquid-phase systems the situation is slightly different. On an extremely short time-scale, shorter than the correlation time of the polarizability

of the component molecules, the system is considered to be inhomogeneous, but on a longer time-scale it is homogeneous.

There are three problems in pump-probe experiments: (i) inhomogeneity of sample, (ii) simultaneous generation of wavepackets both in the ground and in the excited states, (iii) requirement of long-time measurement of spectral dependence of the time traces.

In a recent study [11], we were able partly to solve the above three difficulties by utilizing a sub-5 fs pulse as pump and probe sources [8] with a spiky peak in the spectra and a multi-channel detector. Especially we tackled the third problem by taking advantage of the spectral feature of the spiky structure that enables femto-second partial “hole burning” [12], to eliminate partially inhomogeneity and detect vibrational structure buried in part in the inhomogeneity. The “hole” spectrum reveals vibrational progression in the molecule with vibronic coupling [13], even though the spectrum is not a true “hole” spectrum because the burning pulse has a much broader spectrum than the homogeneous spectrum. However, this method is very useful and enabled us to track each vibrational peak in bleaching, gain and induced absorption spectra at the same time.

### 9.1.2

#### **Characteristic Spectroscopic Properties of Polymers**

The spectroscopic and electrical properties of conjugated polymers have been studied extensively because of their unique properties owing to their low dimensionality and they are considered to be model compounds of quasi-one-dimensional electronic systems. However, the primary photophysical phenomena in the relaxation kinetics of  $\pi$ -conjugated polymers are not yet fully understood in spite of their potential applications in electronics, optoelectronics and photonics [14, 15]. Examples are flexible conductors, light-emitting diodes and all-optical switches [16]. Elucidating the early electron–lattice dynamics in the vibrational non-equilibrium after photoexcitation in these systems encourages the engineering of appropriate materials for particular applications.

### 9.1.3

#### **Polydiacetylenes**

Among many existing polymers, polydiacetylenes (PDAs) have especially attracted a lot of interest, because they have many interesting features from various viewpoints. They have several phases named according to their colors, i.e. blue, yellow and red phases. They can also have various morphologies, i.e. single crystals, cast films, Langmuir films and solutions [17–20]. The ultrafast optical responses in PDAs have been intensively investigated using femtosecond spectroscopy and picosecond and femtosecond time-resolved Raman spectroscopy [3, 15, 21–32]. They are also of interest from the viewpoint of fundamental physics since they are model materials of a one-dimensional system with outstanding characteristic features due to their low dimensionality. This includes ultrafast relaxation resulting

in outstanding ultrafast large optical nonlinearity helped by their excitonic nature. Ultrafast large optical nonlinearity has been studied by nonlinear spectroscopy [22]. They exhibit several nonlinear optical effects such as phonon-mediated optical Stark effects [33], phonon-mediated hole burning [34], inverse Raman scattering [15], optical Stark effect [30] and Raman gain process [30]. These features are closely related to the formation of localized nonlinear excitations such as polarons and a self-trapped exciton (STE) formed via strong coupling between electronic excitations and lattice vibrations. An STE is sometimes called an exciton polaron or neutral bipolaron [21–23, 35–45].

Electronic states in PDA are well characterized theoretically by the Pariser–Parr–Pople–Peierls (PPPP) model [46], which includes both the electron–electron (correlation) interaction (Pariser–Parr–Pople) and the electron–lattice (Peierls) coupling, capturing essential electronic properties of the  $\pi$ -electron system. One important consequence of the electronic correlation is the reversal of the energy-level positions of the first excited  $1^1B_u$  and the second  $2^1A_g$  states [47]. Since PDAs are spatially centrosymmetric and therefore show  $C_2$  symmetry, the wavefunctions possess mirror plane and centroinversion symmetries. The group notation for mirror plane symmetries is  $A$  and  $B$  for the symmetric and the antisymmetric cases, respectively. Inversion symmetries are labeled  $g$  for the symmetric and  $u$  for the antisymmetric. The ground state is therefore labeled  $1A_g$  and the first optically active dipole has to be the  $1B_u$  state. The wavefunctions are either even ( $A_g$ ) or odd ( $B_u$ ) under inversion. Recent experimental and theoretical studies have revealed that the lowest excited singlet state in a blue-phase PDA to be an optically forbidden  $2^1A_g$  state lying  $\sim 0.1$  eV below a  $1^1B_u$ -free-exciton (FE) state [32, 48]. Blue-phase PDAs usually have much smaller fluorescence yield than red-phase PDAs. From various experimental results and discussions, this feature is well summarized in the following way [41]. First, a photoexcited  $1B_u$  free exciton (FE) generated by photoexcitation relaxes to the nonfluorescent  $1A_g$  state, which lies below the  $1B_u$  exciton in such systems with long conjugation lengths. The nonthermal  $1A_g$  state relaxes to the bottom of the potential curve and then thermalizes. The time constants of the relaxation and thermalization are about 60 fs and a few picoseconds, respectively. Finally,  $1A_g$  relaxes to the ground state with a decay time of 1.5 ps at room temperature, even before full thermalization including bulk inter-chain thermalization, which takes place only after several tens of picoseconds.

From previous extensive studies [3, 15, 21–32], the initial changes in the electronic absorption spectra and their ultrafast dynamics in a femtosecond region after photoexcitation of PDA are explained in terms of the geometric relaxation (GR) of a free exciton (FE) to an STE within 100 fs together with the internal conversion from the  $1B_u$  state to the  $1A_g$  state. STE is well established to be a geometrically relaxed state with admixture of a butatriene-type configuration  $(-CR=C=C-CR')_n$  from an acetylene-type chain  $(=CR-C\equiv C-CR')_n$  [24, 25] Here, R and R' represent substituted side-groups attached to the main chain. There are PDAs with various combinations of the substituent groups. All of the stretching vibrations of carbon atoms are considered to be coupled to the photogenerated FE and induce various nonlinear optical processes different from those in most inor-

ganic semiconductors [22, 23, 30, 41, 42, 49]. Recent experimental and theoretical studies have revealed that the lowest excited singlet state in a blue-phase PDA to be an optically forbidden  $2^1A_g$  state, because the blue-phase PDAs have long enough conjugation lengths for the  $2^1A_g$  state to be substantially stabilized. This is because the  $2^1A_g$  state with two-triplet character has a large repulsive interaction between the two triplet “components” due to the Pauli exclusion principle. These repulsive interactions stabilize  $2^1A_g$  state in a long chain and as in ordinary organics a triplet state is more stabilized than a corresponding singlet state. This  $2^1A_g$  state in blue-phase PDA lies  $\sim 0.1$  eV below a strongly allowed  $1^1B_u$ -FE state, which provides a characteristic intense blue color and metallic reflectance [35, 37, 50–53]. The internal conversion (IC) mentioned above is then explained to take place along with self-trapping [41, 42]. However, the detailed dynamic processes of IC and GR have not yet been fully characterized [41, 42]. Recent progress with femto-second pulsed lasers has permitted the study of molecular dynamics on a 10-fs time scale [3, 26]. In a previous work by Bigot and others, a wavepacket motion of a C=C stretching mode with a period of  $\sim 23$  fs was found in the photon-echo and transient bleaching signals of PDA-DCAD [poly(1,6-di(*n*-carbazolyl)-2,4-hexadiyne)] films by using 9–10-fs pulses [24, 25].

The real-time observation of the geometric relaxation in PDA has been facilitated by the recent development of sub-5-fs visible pulse generation based on a non-collinear optical parametric amplification (NOPA) system which satisfies all of the pulse-front matching, phase matching and group-velocity matching conditions [54–56]. Utilizing compressors such as a prism pair, a grating pair, chirped mirror pairs and a deformable mirror, the shortest visible–near-infrared pulses as short as 4 fs were obtained with a broad featured structure suitable for pump–probe spectroscopy [54–56]. The trace of the delay-time dependence of the normalized difference transmittance  $\Delta T(t)/T$  induced by an ultrashort pump pulse is called a “real-time spectrum”, which means a spectrum not in a frequency domain but in a time domain. By using time-resolved analysis of the Fourier transform of the real-time spectrum, the dynamic features of self-trapping, IC and coupling between stretching and bending modes in the relaxed state in a PDA have been elucidated using sub-5-fs pulses [32].

However, these experiments have a remaining problem of the possible ambiguity in the assignment of the pump–probe signals to either the ground or the excited state as mentioned previously. It is because the ultrashort laser pulse with a wide enough spectrum can drive the coherent vibrations in both ground and excited states. This prevents a well-defined discussion of the dynamics of the wavepacket after being photogenerated. In this study, we could attribute the origins of the oscillation signals in pump–probe traces to either the ground or excited state by utilizing broad spectral information of the time traces which was realized by the extremely stable sub-5-fs NOPA developed in the authors’ group.

## 9.2 Experimental

### 9.2.1 Sample

The sample used in the present study was a cast film of blue-phase PDA-3BCMU {poly[4,6-decadiyne-1,10-diolbis(*n*-butoxycarbonylmethylurethane)]} on a glass substrate. PDA-3BCMU has side-groups  $R = R' = -(CH_2)_3OCONHCH_2COO(CH_2)_3CH_3$  in the backbone chain structure of  $(=RC-C\equiv C-CR'=)_n$ . PDA-3BCMU is one of the well-known soluble PDAs. The sample was prepared in the following way.

Oxidative coupling of 4-pentyn-1-ol (purchased from Tokyo Kasei) by Hay's method [57] was used to obtain 4,6-decadiyne-1,10-diol with a yield of 79%. The diol compound reacted with butyl isocyanatoacetate at 23 °C using triethylamine in THF, resulting in the production of 3BCMU (monomer) with a yield >98%. The monomer film of 3BCMU was irradiated by solid-state polymerization of an appropriate dose of  $^{60}Co$   $\gamma$ -irradiation. The total dose was ~150 kGy. The crystal of 3BCMU after the  $^{60}Co$   $\gamma$ -irradiation process was washed with methanol to remove the unreacted monomers. The polymer obtained (PDA-3BCMU) was dried under vacuum.

A sample PDA-3BCMU film was prepared by the doctor-blade method from chloroform solution of about 0.1 wt.%. In the doctor blade method, the solution of the polymer was dropped on to a washed glass plate, stretched by a glass rod and then dried at room temperature.

### 9.2.2 Laser System

Laser output pulses with a 4.7-fs width at a 5-kHz repetition rate from a NOPA seeded by a white-light continuum were used as both pump and probe pulses [10, 31]. The duration of the NOPA output pulses was reduced with a 5-fs pulse compressor system [10, 31, 56, 58] composed of a prism pair and chirp mirrors. The source of this system is a Spitfire regenerative amplifier (Spectra-Physics), of which the pulse duration, central wavelength, repetition rate and average output power are 100 fs, 790 nm, 5 kHz and 800 mW, respectively. The spectra of the pulses covered the range 520–750 nm with a nearly constant phase, indicating that the pulses are Fourier transform limited. The pulse energies of the pump and probe were about 35 and 5 nJ, respectively. All the measurements were performed at room temperature ( $295 \pm 1$  K).

## 9.2.3

**Data Analysis**

Difference absorption spectra ( $\Delta A$ ) were calculated by Eq. (9.1) from the normalized difference transmission spectra ( $\Delta T/T$ ) at pump–probe delay times from  $-50$  to  $1949$  fs in  $1$ -fs steps.

$$\Delta A = -\log_{10}\left(1 + \frac{\Delta T}{T}\right) \quad (9.1)$$

The difference transmittances probed in a wavelength range from  $541$  to  $740$  nm (corresponding to photon energy  $1.68$ – $2.28$  eV) were detected simultaneously using a multi-channel lock-in amplifier with a  $300$  grooves  $\text{mm}^{-1}$  grating monochromator for polychromatic purposes. The spectral resolution was about  $3.6$  nm ( $10$  meV), limited by the monochromator.

## 9.3

**Results and Discussion**

## 9.3.1

**Peak Tracking Analysis**

The spectra of excitation and probe pulse laser and absorption of the blue-phase PDA-3BCMU are shown in Fig. 9.1. The vibrational energy levels of C–C double and triple bond stretching are indicated. The low-lying electronic energy states are depicted together with transitions associated with excitation, internal conversion between the excited states, induced absorption and relaxation to the ground state. A typical example of experimental data for difference absorption spectra is displayed two-dimensionally in Fig. 9.2. Several examples of the observed normalized difference transmittance [ $\Delta T(t)/T$ ] traces of the blue-phase PDA-3BCMU sample at several energies of probe photons are shown in Fig. 9.3. All of the curves show signals of a finite size of  $\Delta T(t)/T$  at negative delay times and sharp and intense peaks around zero probe-delay time. The former is due to the perturbed free induction decay process associated with the third-order nonlinearity induced by the sequential interaction of probe–pump–pump fields modified with molecular vibrations. The latter signals are due to pump–probe coupling induced by the nonlinear process of the pump–probe–pump time ordering. There is another contribution from the interference between the scattered pulses and the probe pulses the duration of which is elongated in the polychromator. The vibrational modulation observed at delay times longer than  $100$  fs is free from the distortions due to the above two mechanisms.

Here, the previously mentioned “peak-tracking” analysis developed recently by the authors’ group is explained. This is used to study the peak energies of the transient electronic transition during molecular vibrations. The authors’ group

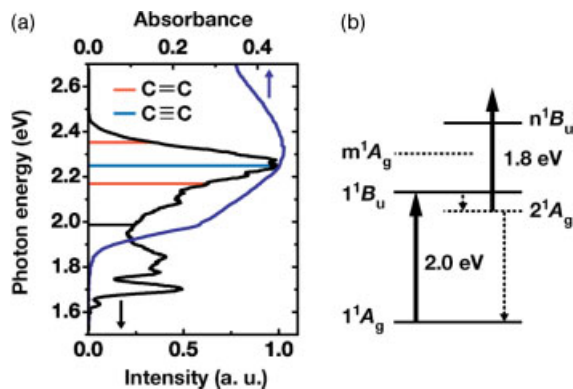


**Figure 9.1** (a) Spectra of the excitation pulses (black) and the absorption of PDA (blue) together with the lines denoting the energy of the  $1^1B_u$  state (black line) and its vibrational levels. (b) Schematic energy diagram of the essential electronic states: ground state ( $1^1A_g$ ), excited state ( $1^1B_u$ ), higher excited

state ( $m^1A_g$ ) and geometrically relaxed state ( $2^1A_g$ ), from which optical transition is allowed to another excited state ( $n^1B_u$ ) of PDA relevant to our experiment. The corresponding transition energies are also described. Dashed lines indicate radiationless transitions.

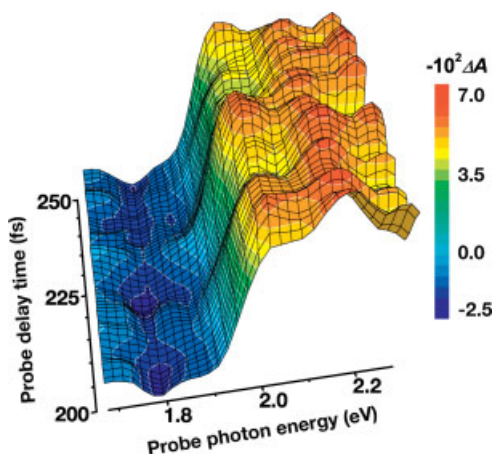


**Figure 9.2** Time evolution (200–250 fs after excitation) of the sequential difference absorption spectra of PDA-3BCMU with resolution of  $\leq 1$  fs (vertical axis) and  $\leq 10$  meV (horizontal axis) obtained by the pump–probe

measurement. Positive and negative difference absorbances are caused by the induced absorption from the  $2^1A_g$  state and the absorption saturation in the  $1^1A_g$  state, respectively.

applied this method to demonstrate the oscillations of transition peak energies in blue-phase PDA-3BCMU film [22], where 3BCMU denotes the side-chain of the conjugated polymer. Polymers composed of  $\pi$ -electrons along the one-dimensional carbon chain [59], including PDAs as a typical example, have a large ultrafast electron–lattice interaction [34] and thereby exhibit ultrafast optical response

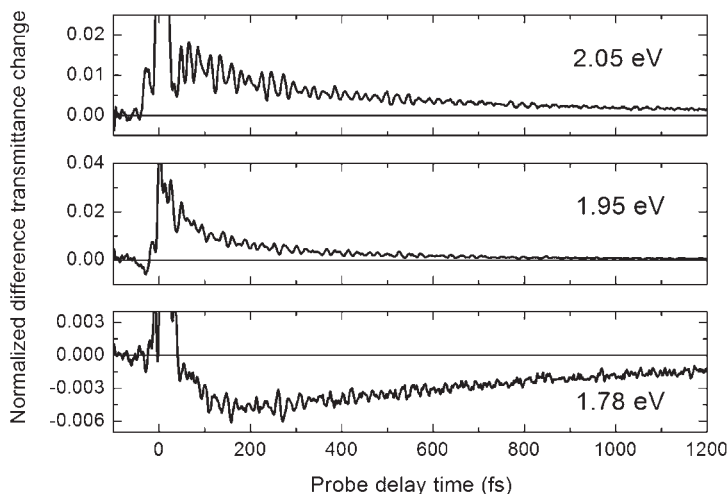


**Figure 9.3** Pump-probe delay time dependence of the normalized difference transmittance  $[\Delta T(t)/T]$  on the probe delay time at three probe photon energies.

[15]. Nonlinear optical properties in polymers including polyacetylene and PDAs can be explained in terms of four essential electronic states [60] and the ground state relevant to this experiment as shown in Fig. 9.1b. Pump pulses with the highest peak at 2.25 eV, which also corresponds to the energy of maximum absorbance in the stationary absorption spectrum, predominantly excite the allowed  $1^1A_g \rightarrow 1^1B_u$  transition coupled by  $C\equiv C$  stretching (Fig. 9.1). This creates depleted difference absorption spectra (DAS) due to the population hole generated in the ground state. The DAS has a well-defined vibronic structure including the purely electronic zero-phonon (0–0) peak around 2.0 eV [15, 22]. The broadening of the bandwidth of each peak in the bleaching spectra with increasing delay time caused by the thermalization in the ground state indicates that each peak in the bleaching spectra corresponds to a well-defined vibronic exciton–exciton transition. Another clear peak of induced absorption ( $2^1A_g \rightarrow n^1B_u$ ) around 1.8 eV [15, 22] also appears in the positive DAS (Fig. 9.2). In the figure the positive DAS is the downward signal.

These well-separated features due to the partial “hole burning” enable us to apply the “peak-tracking” method to the transition peaks. This method provides detailed information about the mechanism of the oscillating signals corresponding to all the vibronic transitions separately in DAS. For each vibronic transition the DAS signal can be analyzed in terms of two contributions: modulations of the transition energy and the transition probability. They appear in DAS as “vertical” and “horizontal” modulation with a molecular vibrational frequency,  $\Omega$ , respectively [61, 62]:

$$\Delta A(\omega) \equiv \Delta A_0(\omega) + \left[ \frac{\delta(\mu^2)}{\mu^2} \Delta A(\omega) + \delta\omega \frac{d\Delta A(\omega)}{d\omega} \right] \cos(\Omega t + \theta) \quad (9.2)$$

where  $\Delta A_0(\omega)$  is the non-oscillating component of the absorbance change [ $\Delta A(\omega)$ ] and  $\delta(\mu^2)/\mu^2$  and  $\delta\omega$  correspond to the probability and energy modulations, respectively. The modulation frequency,  $\Omega$ , and the initial phase,  $\theta$ , correspond to those of the molecular vibration. The wavepacket motion along the potential curve causes the transition energy modulation [9, 63]. The decomposed signal provides the correct time evolutions of transition energies and intensities with phase information and thus enables us to determine the relative locations of multiple PESs in the different electronic states.

The decay of the absorbance-change signal was analyzed by the global fitting method, which is to be discussed later in detail, to be classified into two components of short lifetime ( $60 \pm 3$  fs) and long lifetime ( $890 \pm 40$  fs) [22, 32]. An initial relaxation process of  $1^1B_u \rightarrow 2^1A_g$  ( $60 \pm 3$  fs) is observed as the decay of induced emission (IE) ( $1^1B_u \rightarrow 1^1A_g$ ).

At delay times longer than 100 fs when the relaxation to  $2^1A_g$  is almost fully completed since the corresponding decay time is about 60 fs, the peak-tracking analysis clarified the dynamic behavior of the sequential spectra, composed of the saturation of the stationary absorption ( $1^1A_g \rightarrow 1^1B_u$ ) and the induced absorption ( $2^1A_g \rightarrow n^1B_u$ ), which includes oscillations in the slopes between the peaks. The modulation amplitudes of transition peak energies can be related to the strengths of vibronic couplings involved in the electronic transition. Stabilization energies and Huang–Rhys factors [63] can be obtained in every direction of normal coordinates in the multidimensional configuration space, which provide the displacement of the potential hypersurface minimum of the final state with respect to that of the initial state, of the corresponding transition.

The excitonic 0-phonon transition peak near 2.0 eV ( $1^1A_g \rightarrow 1^1B_u$ ) and an IA peak near 1.8 eV ( $1^1A_g \rightarrow 1^1B_u$  transition) are tracked in Fig. 9.4. Each peak and its slopes on both sides show energy oscillation following sine and cosine functions corresponding to the wavepacket motions in the ground and the excited states [11], respectively. Two intense peaks in Fig. 9.4c indicate that the two modes of C=C ( $1460 \text{ cm}^{-1}$ ) and C $\equiv$ C ( $2080 \text{ cm}^{-1}$ ) stretching are strongly coupled with the  $1^1A_g \rightarrow 1^1B_u$  transition. However, the signal intensity of C $\equiv$ C stretching is dramatically reduced in  $2^1A_g \rightarrow n^1B_u$  (Fig. 9.4d) with a remaining strong peak of the C=C stretching mode. This indicates that the potential-minimum shift between  $2^1A_g$  and  $n^1B_u$  is largest in the C=C stretching direction, resulting in the impulsive starting of the vibrational mode. Schematic two-dimensional PESs obtained in the C=C and C $\equiv$ C stretching coordinates are plotted in Fig. 9.5.

In characterizing the dynamic behavior of the corresponding vibronic transition, we picked up a specific transition among several peaks observed in the spectra. Applying the peak-tracking method, we decomposed the two-dimensional modulation spectra into the transition-peak energy and the transition-intensity modulations. This method provides new insight into the vibrational origins relating the vibrational amplitude distributions to the spectral features in DAS and

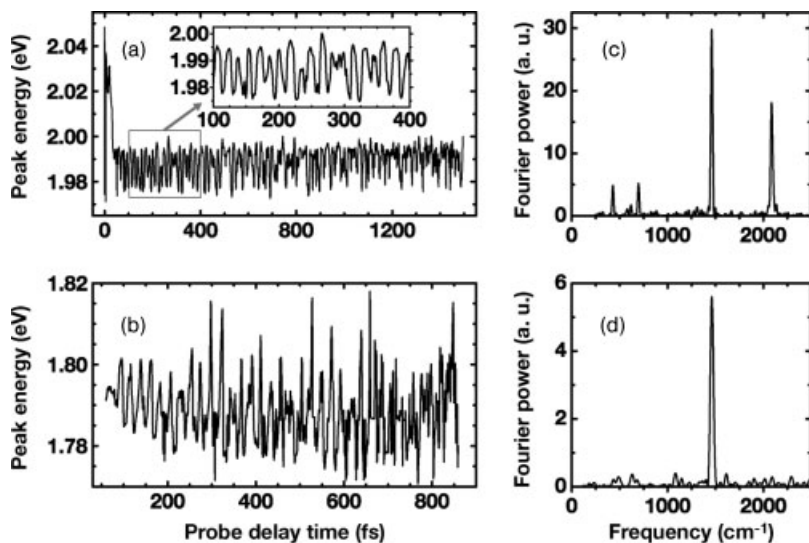


**Figure 9.4** Dynamic behaviors of transition peaks and their oscillation frequencies. Energy oscillations of the zero-phonon transition peak (a)  $1^1A_g \rightarrow 1^1B_u$  ( $\sim 1.99$  eV) and an induced absorption peak (b)  $2^1A_g \rightarrow n^1B_u$

( $\sim 1.79$  eV) and their Fourier power spectra calculated for the data of (c) 100–1500 fs and (d) 100–860 fs, respectively. The inset in (A) is the peak motion with an expanded delay-time scale from 100 to 400 fs.

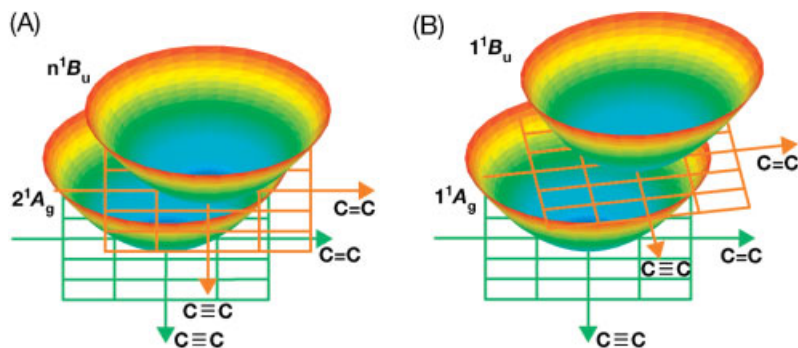


**Figure 9.5** Schematic potential energy surfaces of the two electronic states involved in (a)  $2^1A_g \rightarrow n^1B_u$  and (b)  $1^1A_g \rightarrow 1^1B_u$  transitions.

can be used as a general method to determine the multidimensional potential hypersurfaces in molecular systems in the condensed phase including organic polymers and biomolecules with multiple electronic states experiencing ultrafast dynamics and chemical reactions.

Femtosecond pulses with a wide spectrum can excite multi-vibrational levels simultaneously in-phase in the excited electronic state and thus create wavepackets on the multi-dimensional potential surfaces in the excited states. At the same

time such short pulses can generate coherent molecular vibrations in the ground state by impulsive stimulated Raman scattering. Identification and/or separation of the observed transmittance signals to these two wavepackets are sometimes difficult. Vibrational phase analysis of the wavepackets is useful for distinguishing these two effects. However, the phase profile along the probed photon energy is complicated because of the inhomogeneity of electronic transition energy to the excited states, which may be sensitive to the local environment surrounding the excitations and the phase relaxation induced by the electronic interaction. One more factor that makes it even more difficult to interpret the phase profile is that the vibrational phase to be determined by the analysis is sensitive to the frequency of the vibrational mode. Because of the homogeneous and inhomogeneous broadening of the vibrational frequency, there is a limit to the precise determination of vibrational frequency of each mode. It is also limited by the finite length of the probe delay time and finite lifetime of the corresponding excited state in cases when the modulations are due to the excited state wavepacket. Because of these limitations, the frequency determined by Fourier analysis may differ from the true value by 0.5%, namely  $5\text{ cm}^{-1}$  for a  $1000\text{ cm}^{-1}$  mode which has a corresponding 33-fs period from the time-trace data extending to the probe delay of 2000 fs. In such a case the phase obtained can be different by 15% of  $2\pi$  rad estimated by extrapolation from the center of the probe delay time, which is 1000 fs.

There is an even more difficult problem in the case of polydiacetylene considered in this chapter. There is a well-known geometric relaxation that takes place very rapidly after photoexcitation to the excited electronic state. This is because of the barrier-free feature along the potential curve between the extended free-exciton state and self-trapped exciton expected in a one-dimensional system. In order to extract the well-defined signal of vibrational coherences, we have to exclude the data during the initial geometric relaxation process when the very strong coupling between the electronic excitation and molecular vibration is exerted on the electronic transition probability and its frequency dependence. In order to discuss the effects of vibrational modes on the electronic transitions including the ground-state absorption, induced emission and induced absorption, it is of vital importance to identify the modulations with the possible candidates of electronic transitions. In the case of PDA, they are the  $1^1A_g$  ground state  $\rightarrow$   $1^1B_u$  exciton state,  $1^1B_u$  exciton state  $\rightarrow$   $m^1A_g$ -state and  $2^1A_g$  state  $\rightarrow$   $n^1B_u$  state. For identification it is necessary to investigate the dependence of the dephasing time of the vibrational amplitude of the observed modes on the probe photon energy to confirm the contributions of the vibrational coherences. The bleaching signal due to the ground-state depletion corresponding to the transition between the  $1^1A_g$  state and  $1^1B_u$  exciton and the induced absorption signals due to the absorption from the excited states to the higher excited states corresponding to the  $1^1B_u$  exciton state- $m^1A_g$  state transition and  $2^1A_g$  state- $n^1B_u$  state transition are expected to have different decay constants. They are expected to exhibit several relaxation processes in the excited state [22]. There are also possible differences in the observed dynamics at various probe photon energies due to the thermalization process among intra-chain molecular vibrational modes and inter-chain vibrational coupling including

lattice vibrations. They can appear in the signal due to the ground state and due to the excited states. The difference can be deduced from the deviation of the distribution of the population of the Franck–Condon state in the excited state generated just after the excitation from the thermal equilibrium state. The same thermalization process takes place due to the deviation of the population distribution in the ground state depopulated by excitation and populated later by the internal conversion. There is another possible origin of the difference. It may be due to the non-equilibrium state generated by the radiationless relaxation from  $1^1B_u$  excited state to the  $2^1A_g$  state associated with the geometric relaxation. The dephasing time in the excited state includes both the longitudinal and the transverse relaxations of the vibration and the electronic longitudinal decay to the ground state. On the other hand, the non-oscillating component of the transient spectra reveals the longitudinal relaxation processes of the vibrational and electronic population distributions. Clarification of the relaxation kinetics from both viewpoints is required to understand the early photophysics in the electronically delocalized system. The electronic longitudinal relaxation is expected to appear as the global change over a relatively broad spectral range in the difference absorption spectra in such a manner that the decay profile is common in the spectral range of the relevant electronic state. There can also be a blue or red shift of the weight of mass of the spectrum in cases when the initial or final state of the corresponding transition is lowered in energy due to the relaxation in the molecular geometric configuration or dielectric relaxation in the media such as the host matrix or solvent. On the other hand, the vibrational energy redistribution among various modes in the polymer is expected to show several types of change in the features in the difference absorption spectra. There can be broadening or sharpening if the initially distributed Franck–Condon state depends on the pump laser spectrum and the Franck–Condon factor has a narrower or broader distribution than that in the equilibrium state. In previous experimental studies, the transient absorption spectrum was measured with 100-fs resolution, which revealed that the spectrum of IA ( $2^1A_g \rightarrow n^1B_u$ ) is shifted to higher energy associated with the thermalization in the  $2^1A_g$  state in 0.5–1 ps [28]. However, these experiments used pump pulses with a narrow spectral width centered at 1.97 eV corresponding to the excitonic absorption peak around 2.0 eV of blue-phase PDA-3BCMU. The pump spectrum covers only the 0-phonon transition and hence the coherent vibration cannot be generated. In this study, sub-5-fs visible pulses were used as a pump and a probe. Such extremely short pulses can drive wavepacket motions associated with molecular vibrational modes with even higher frequency than  $3000\text{ cm}^{-1}$ . Their motions are along the potential hypersurfaces of the ground and excited states because of the possible vibronic coupling to many modes in both the absorption process and the impulsive stimulated Raman scattering (ISRS) process. In addition to the generation of vibrational coherence, non-equilibrium population distributions are also established in both the ground and excited states by the pump pulses with a wide spectrum covering multiple CC stretching vibrational levels in the excited state. The pump pulses induce population depletion in both the ground and excited states. The 1-fs step difference absorption spectra reveal both the vibrational dynamics and the ultrafast vibra-

tional thermalization processes in conjugated polymers. This was enabled by the extremely stable sub-5-fs NOPA system developed in our group.

### 9.3.2

#### Bleaching and Induced Absorption Spectra

We smoothed out the oscillating components from DAS by taking sequential convolutions of the data with rectangular functions of 3–101 fs time widths to investigate the non-oscillating spectral change due to molecular vibration. Then the smoothed signal can be attributed to the population dynamics of the vibrational levels in the electronic states. Figures 9.6 and 9.7 show the non-oscillating DAS in 200–1900 fs. The initial population distribution in the excited state is determined by the absorbed laser intensity.

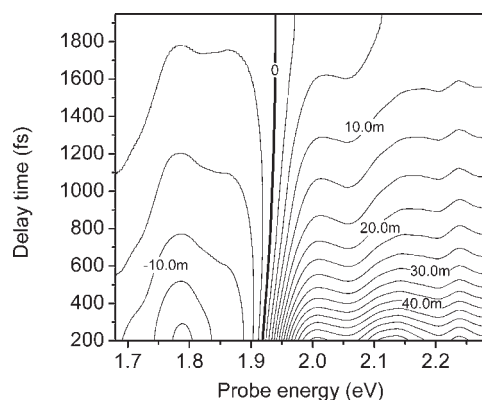


**Figure 9.6** Two-dimensional difference absorption spectrum of PDA-3BCMU after subtracting the oscillating components.

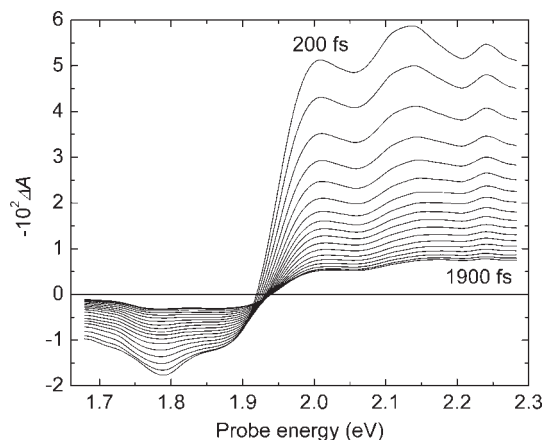


**Figure 9.7** Difference absorption spectra extracted from Fig. 9.6 at delay times of 200–1900 fs with a 100-fs interval.

Figure 9.8 shows the normalized spectra of the time derivative of DAS, which reflect the speed of the instantaneous absorbance change at each delay time and are attributed to the reduced population in the excited state, in other words, the recovered population in the ground state. The spectral changes in their shapes reveal that the two processes of the vibrational energy redistribution and the internal conversion process from the  $2^1A_g$  state to the ground state take place concurrently. The early bleaching spectrum with a vibrational progression suggests that a “hole” is induced in the inhomogeneously broadened absorption spectrum. The transient bleaching spectrum undergoes spectral changes due to the vibrational thermalization through the intra- and inter-chain interactions via the low frequency bending and torsional modes of the polymer chains. The initially prepared bleaching spectrum with a smaller inhomogeneity than that of the stationary absorbance relaxes to the thermalized spectrum with features similar to those of the stationary spectrum as shown in Fig. 9.9. The recovery of the population in the ground state also refills the “hole” with a relatively intense 0-phonon peak in the bleaching spectrum. These thermalization processes cause the spectral blue shift observed in the bleaching (negative  $\Delta A$ ) region.

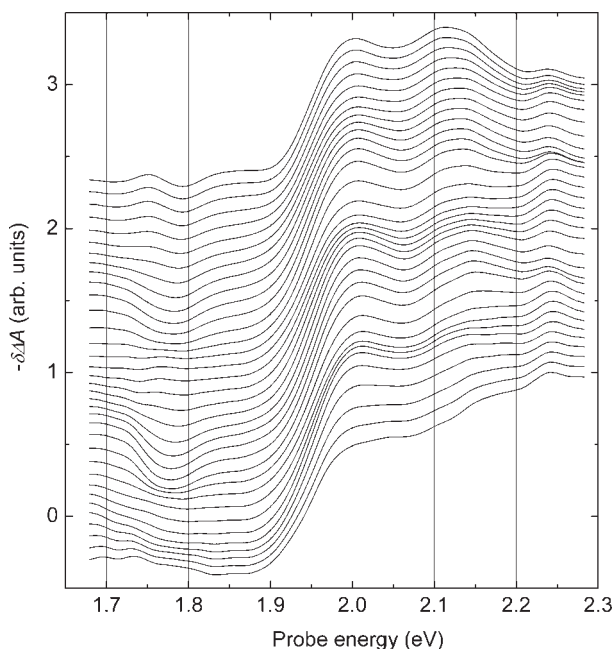


**Figure 9.8** Time derivative of the difference absorbance in Fig. 9.6. The spectrum is normalized at each delay time (200–1900 fs, 50-fs steps).

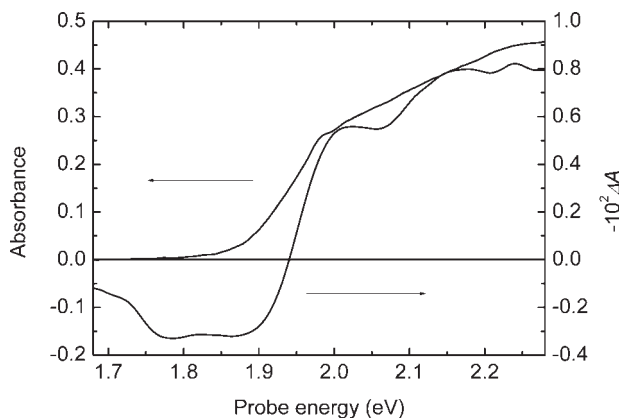


**Figure 9.9** Stationary absorption spectrum and difference absorption spectrum with a quasi-thermalized feature at 1800 fs.

### 9.3.3

#### Vibrational Thermalization in the Ground and Excited States

The non-oscillating spectra in Figs. 9.6 and 9.7 also reveal that a positive  $\Delta A$  peak due to induced absorption grows at around 1.85–1.90 eV with increasing delay time. Figure 9.10 shows the time trace of the energies of  $\Delta A = 0$  and  $d(\Delta A)/dt = 0$  points in the  $\Delta A$  spectra. The blue shift of the zero- $\Delta A$  energy, which has a single exponential decay constant of about 0.7 ps, can be ascribed to the spectral changes of both the induced absorption ( $2^1A_g \rightarrow n^1B_u$ ) and the bleaching ( $1^1A_g \rightarrow 2^1B_u$ ). The probe energy dependence of the annihilation time of  $2^1A_g$  exciton determined by biexponential fitting also exhibits a higher value of about 1.1 ps at 1.85 eV due to

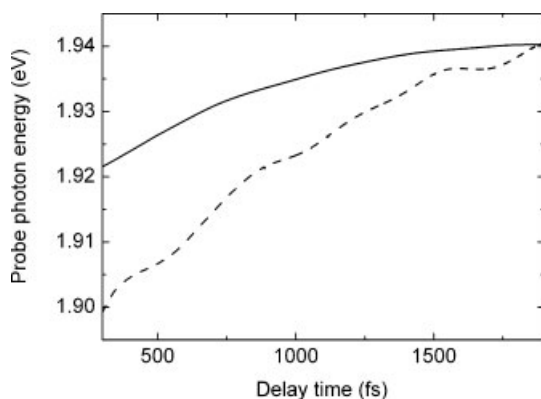


**Figure 9.10** Energy shifts of  $\Delta A = 0$  points (solid line) and intersection points between the two spectra separated by a 50 fs delay time (dashed line).

the induced absorption growth around 1.85–1.90 eV than 0.5 ps at 2.0 eV due to the bleaching decay at the 0-phonon transition energy (2.0 eV).

Thermalization processes from the non-equilibrium states both in the ground  $1^1A_g$  and the excited  $2^1A_g$  states were revealed in the long-term energy shifts of peaks and slopes in DAS. Seventeen transition energies with characteristic features in the spectra were investigated, comprising three peaks, four valleys, nine slopes and one zero  $\Delta A$  point as shown in Fig. 9.11. Each peak showed a blue or red shift due to thermalization in the  $1^1A_g$  and  $2^1A_g$  states depending on probe photon energy in Fig. 9.11. The thermalization time in which the population distribution among vibrational levels with distributed quantum numbers in various modes comes to a thermal distribution within the main chains is estimated to be

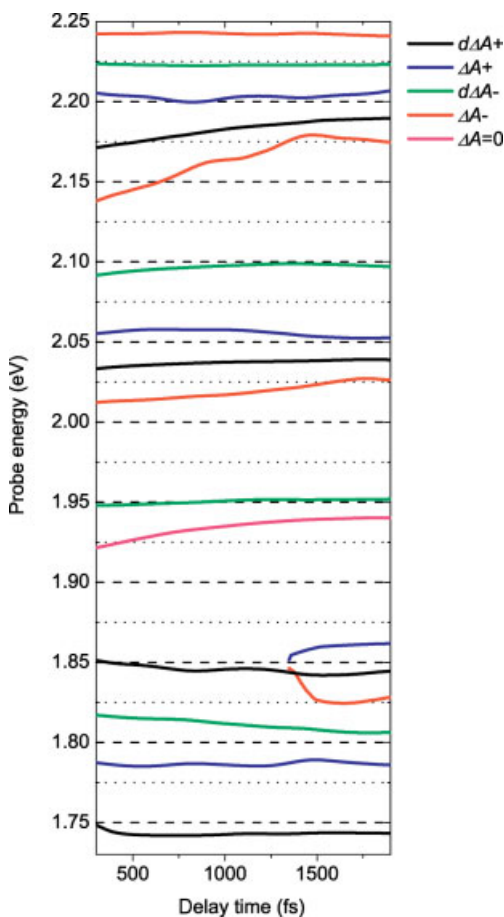


**Figure 9.11** Energy shifts of the peaks and the slopes extracted from the difference absorption spectrum in Fig. 9.6. Energies of slopes were determined by the maximum or minimum energies of the photon-energy

derivative of the spectrum at each delay time. + and – denote the positive and negative signs of the peaks and the gradient peaks, respectively.

about 0.5 ps from the time constant of the spectral shift. The value of the time constant determined here is consistent with our previous work [28].

Quantities of energy shifts of slopes in Fig. 9.11 during 1.3 ps from 0.2 to 1.5 ps are shown in Fig. 9.12, which shows that there are two regions with positive and negative energy shifts. The bandwidths of the vibrational peaks in the DAS are broadened with increasing delay time. The results may indicate the spectral diffusion in the  $2^1A_g$  excited state. The zero crossing point in Fig. 9.12 is around 1.9 eV, lower than the 0–0 transition energy by about 100 meV, which is consistent with the amount of the Stokes shift in the literature [49].

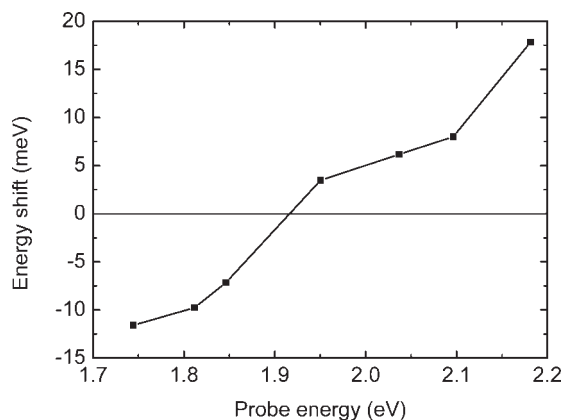


**Figure 9.12** Energy-shift quantities of gradient peaks (slopes) during 1300 fs from 200 to 1500 fs.

#### 9.3.4

##### **Singular Value Decomposition for the Analysis of Mode Dependence of Vibronic Coupling in the Excited and Ground States**

The two-dimensional normalized difference transmittance  $\Delta T(t)/T$  of the blue-phase PDA-3BCMU sample is displayed in Figure 9.2 (probe photon energy and probe delay time). Several examples of  $\Delta T(t)/T$  traces at several probe photon energies were shown in Fig. 9.3. All of the traces have signals of finite size at negative delay times and sharp and several extremely intense peaks around zero probe delay time. The former is due to the perturbed free induction decay (FID) process associated with the third-order nonlinearity of the sequential interaction of probe–pump–pump fields modified with coherent molecular vibrations. The latter signals clearly have several peaks in the signal probed at 1.95 eV and all the signals at other wavelengths with detectable signal sizes have similar features. They are due to pump–probe coupling induced by the nonlinear process of the pump–probe–pump time ordering. There is another source of artificial signal due to interference between the scattered pulses and the probe pulses, the durations of both of which are elongated by dispersion in the polychromator. The details of the vibra-

tional modulation observed at delay times longer than 100 fs are free from the signal distortions due to the above two mechanisms which are irrelevant to the mechanism of the vibronic coupling. Figure 9.13 shows the measured normalized difference transmittance spectra at a few probe delay times between 200 and 1100 fs. In the region above the probe photon energy of about 1.95 eV, the normalized difference transmittance is positive, assignable mainly to photobleaching of the  $1^1B_u$ -FE absorption peaked around 2.0 eV. In the lowest energy region this feature can be due also to induced emission in a time range shorter than 100 fs as discussed earlier. The normalized difference transmittance signals in the probe photon energy region below 1.90 eV are negative due predominantly to the photo-induced absorption transition from the geometrically relaxed  $2^1A_g$  state to the higher excited  $n^1B_u$  state. The latter state is one of the four essential states invoked to explain the characteristic features in nonlinear spectra [32, 60]. However, accompanying bleaching can modify the intensity and spectral shape. As described earlier, the  $1^1B_u$ -FE state decays within 100 fs into the geometrically relaxed  $2^1A_g$  state, which is also consistent with several previous papers [15, 49, 64].

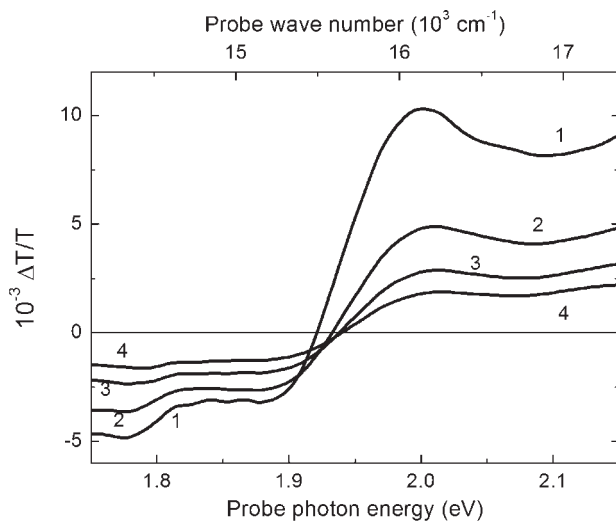


**Figure 9.13** Normalized difference transmittance spectra ( $\Delta T/T$ ); 1, delay at 200 fs; 2, 500 fs; 3, 800 fs; 4, 1100 fs.

The power spectrum of the Fourier transform of  $\Delta T(t)/T$  at 128 probe photon energies probed by using the lock-in amplifier is shown two-dimensionally in Fig. 9.14. The abscissa and ordinate of the two-dimensional description are vibrational frequency and probe photon energy, respectively. For the calculation, the signal data in the probe delay time from 400 to 900 fs were used to avoid the interference effects taking place near the zero-delay time and weak signal at longer delay. Fourier transformation was performed after high-pass step-function filtering with a cut-off frequency at  $1000 \text{ cm}^{-1}$  to avoid any slow decay due to electronic

relaxation. In the wide range of probe photon energy, three peaks were commonly observed at 1220, 1460 and 2080  $\text{cm}^{-1}$  corresponding to the C-C, C=C and C $\equiv$ C stretching modes, respectively [65, 66]. The probe photon energy dependences of the Fourier power of these modes are shown in Fig. 9.15. It is clearly seen that all three modes have peaks around 1.78, 1.92–1.96 and 2.03–2.05 eV in common. even though the intensity distribution profile is substantially different among them.

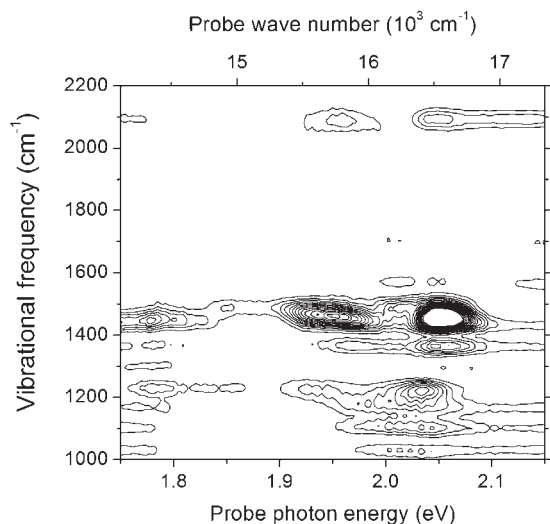


**Figure 9.14** Two-dimensional Fourier power spectra of the  $\Delta T/T$  traces.

The vibrational modes in the pump–probe signal were investigated more deeply by analysis with a linear prediction singular value decomposition (LP-SVD) method. By the LP-SVD, single or multiple mode(s) of damped oscillation were extracted from the data such as  $y(t) = A \exp(-t/\tau) \cos(\Omega t + \theta)$ , where  $A$  is the initial amplitude of the signal modulation of  $\Delta T(t)/T$  due to the molecular vibration,  $\tau$  is the decay time of the amplitude of the modulation signal,  $\Omega$  is the relevant mode frequency and  $\theta$  is the initial phase of the molecular vibration just after excitation. These parameters for the vibrational modes of C-C, C=C and C $\equiv$ C were separately extracted by the LP-SVD method from the 200–900 fs data after rectangular frequency filtering of the Fourier power spectra at 1150–1290, 1395–1535 and 2010–2150  $\text{cm}^{-1}$  at observed probe photon energies independently. The amplitudes at 300 fs of the modes are shown in Fig. 9.16. The spectrum of the amplitude of the C-C stretching mode in Fig. 9.16a does not resemble the FFT power spectrum of the C-C mode in Fig. 9.15a. The vibrational signal of the C-C stretching mode was not intense enough for the mode signal to be extracted out from the real-time data to analyze the decay time and initial phase precisely. The Fourier power spectra show modes other than C–C stretching with weaker intensities and they are presumably out-of plane bending modes [32], but they are also difficult analyze for precise detailed discussion owing to insufficient intensity. Therefore, from

here on we concentrate on only C=C and C≡C stretching modes extracted by the LP-SVD method from the pump–probe signals.

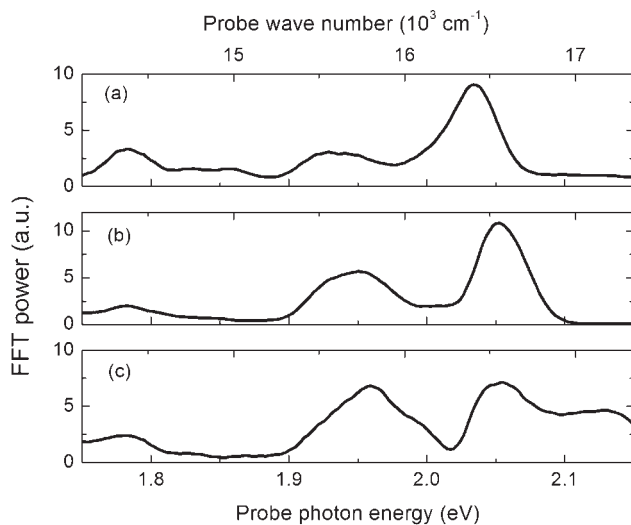


**Figure 9.15** Fast Fourier power spectra of the modes of (a) C–C, (b) C=C and (c) C≡C stretching extracted from the  $\Delta T/T$  traces.

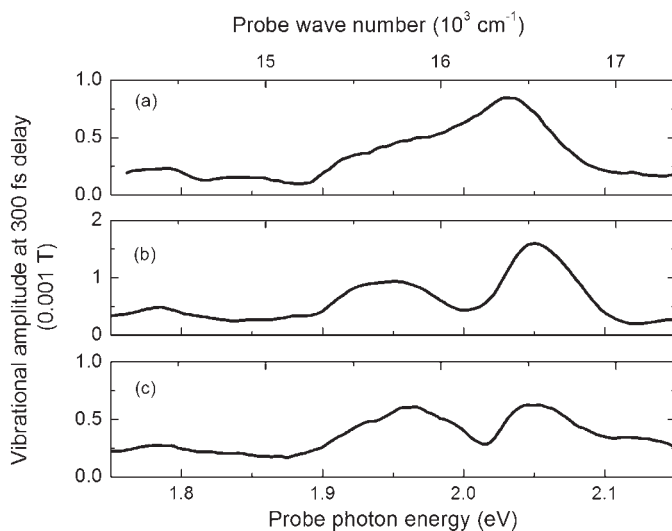


**Figure 9.16** Fourier amplitude at a probe delay of 300 fs extracted from the normalized difference transmittance by the method of LP-SVD for the modes of (a) C–C, (b) C=C and (c) C≡C stretching.

The fitted initial phase of the C=C and C≡C modes are shown as phase spectra in Fig. 9.17. This kind of phase data cannot be obtained from other time-resolved spectroscopic methods such as infrared absorption and Raman scattering, which have been developed in the last two decades and are recognized to be very useful for the identification of the ground or excited states after photoexcitation of molecules and intermediate species in photochemical processes. However, the data for the initial vibrational phases of multi-mode molecular vibration are expected to provide invaluable information about the mechanisms of chemical reactions and excited-state dynamics. This method of extraction of phase information from real-time data will be an essential and powerful spectroscopic method to describe the full chemical reaction pathways in the 21st century [5].

In order to utilize fully the information on the phases, the simple model shown in Fig. 9.18 was proposed to understand systematically the features of the phase spectra. In Fig. 18a and c, transition from the ground state to the  $1^1B_u$ -FE state and that from the geometrically relaxed  $2^1A_g$  state to the  $n^1B_u$  state, respectively, are indicated on the potential curves of PDA. The FWHM of the pulse of the NOPA output used as a pump is much shorter than the oscillation periods of C=C (23 fs) and C≡C (16 fs) vibrations. Therefore, it can generate vibrational wavepackets impulsively in the ground  $1^1A_g$  state and  $1^1B_u$ -FE state. The short pulse width of the NOPA system developed in our laboratory is thus essentially important to study the dynamic behavior of systems with such high frequencies as C≡C stretching. There are a few groups in the world where utilizing NOPA output for real-time spectroscopy with substantially broader pulse durations and the data

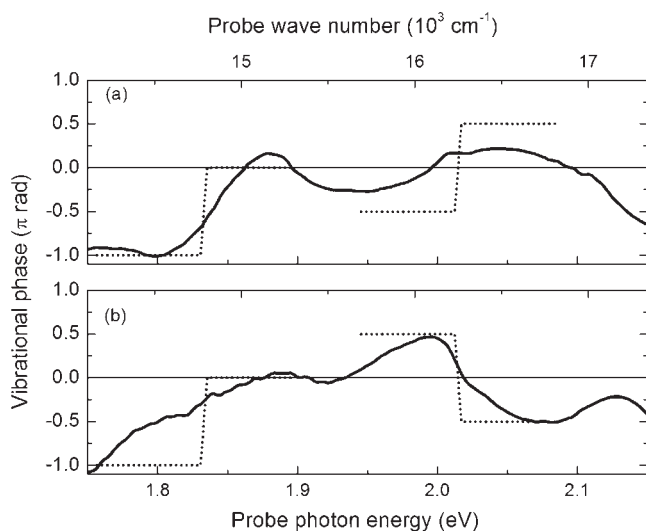


**Figure 9.17** Initial phase (solid curve) of each vibrational mode of normalized difference transmittance by the method of LP-SVD for the modes of (a) C=C and (b) C≡C stretching.

The expected phase (dotted line) of vibration from the model of the wavepacket motion in the ground state (1.95–2.07 eV) and in the excited state (1.76–1.88 eV).

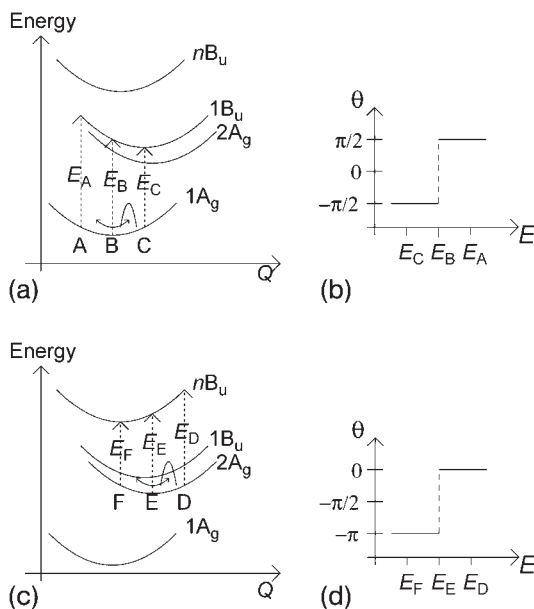


**Figure 9.18** (a) Transition from the ground states on potential energy curves of PDA. Point B is located at the bottom of the curve of the ground states. (b) The model phase of vibration by the motion of the wavepacket in the ground state.  $E_X$  is the energy of transition

from position X. (c) Transition from the excited states on potential energy diagram of PDA. Point E is located at the bottom of the curve of the ground states. (d) The model phase of vibration by the motion of the wavepacket in the excited state.

taken by using such systems are always suffering from the Fourier amplitude reduction or even disappearance of the high-frequency modes. This makes discussion of the vibronic coupling difficult or even impossible.

A wavepacket just after generation in the ground state at the bottom indicated by point B in Fig. 9.18a starts to oscillate on the potential curve along  $B \rightarrow A \rightarrow B \rightarrow C \rightarrow B \rightarrow \dots$  (or  $B \rightarrow C \rightarrow B \rightarrow A \rightarrow B \rightarrow \dots$ ). In accordance with the oscillatory motion, the absorption intensity increases when the wavepacket is located at the probe photon frequency that corresponds to the vertical transition energy at the position of the wavepacket following the Franck–Condon principle based on the adiabatic decoupling between the electronic motions and nuclear motions. Therefore, the oscillation of the wavepacket results in the modulation of normalized difference transmittance with the vibrational frequency.

If the wavepacket photoproduced at B starts to oscillate following the sequence  $B \rightarrow A \rightarrow B \rightarrow \dots$ , the transmittance at probe photon energy  $E_A$  starts to decrease initially and at the same time the transmittance at  $E_C$  starts to increase. Here  $E_X$  is the transition energy from position X ( $= A, B, C, D, E$  or  $F$ ) on the lower state to the corresponding Franck–Condon point of the potential curve of the upper state. In this case the phase of the molecular vibration of  $\Delta T(t)/T$  is  $\pi/2$  at probe photon

energies higher than  $E_B$  and it is  $-\pi/2$  at probe photon energies lower than  $E_B$ , as shown in Fig. 9.18b. When the wavepacket starts to move to the reverse direction ( $B \rightarrow C \rightarrow B \rightarrow \dots$ ) to the previous case, the phase is  $-\pi/2$  for the probe photon energies higher than  $E_B$  and  $\pi/2$  at probe photon energies lower than  $E_B$ .

Figure 9.17a shows that the phases of the C=C stretching mode determined in the probe spectral region between about 1.9 and 2.0 eV are negative whereas those between about 2.0 and 2.1 eV are positive. These features can be explained using Fig. 18a and b where  $E_B$  is 2.0 eV, which corresponds to the  $1^1B_u$ -FE absorption peak. The phase of the C=C stretching mode at a probe photon energy of 2.02 eV is clearly positive and is about  $0.3\pi$  or at least far from the zero-crossing point of 1.975 eV. On the other hand, that of the C≡C stretching mode at the same probe photon energy in Fig. 9.17b is close to zero or at least close to the zero-crossing point of 2.015 eV. This energy (2.02 eV) corresponds to the photon energy shifted by the C=C stretching energy (0.18 eV) from 2.2 eV of the peak of the probe which is expected to give a  $\pi/2$  phase shift. Therefore, it can be concluded that the phases around 2.02 eV in C=C are shifted positively owing to the contribution of the wavepacket generated by the stimulated Raman gain process. The phases of C≡C stretching are positive from about 1.93 to 2.015 eV and are negative between 2.015 and 2.15 eV. It is therefore concluded that the wavepacket of the C≡C mode generated on the ground-state potential curve initializes its motion in the reverse direction to that of the C=C mode. This means that the changes in C=C and C≡C bond lengths upon photoexcitation to the Franck–Condon state are opposite to each other. The C≡C bond length is expected to be elongated by the change in the geometric relaxation resulting in a butatriene-like configuration. The length of the C=C bond is considered to be shortened from the above discussion. This is probably due to the redistribution of the  $\pi$ -electrons of the triple bonds increasing not only C–C single bonds but also C=C double bonds neighboring the single bonds.

The phases of the C=C mode probed at about 1.95 and 2.05 eV are neither  $\pi/2$  nor  $-\pi/2$ , which can be explained in the following way. At these two spectral positions the signals of photoinduced absorption are expected to be relatively strongly modulated by the wavepacket of the C=C mode in the excited state because of the strong excitonic peak at 2.00 eV. Then the phases of the C=C mode are considered to be  $0\pi$  as expected for a wavepacket in the excited state. Therefore, it is concluded that the vibrational signal due to the ground state and that due to the excited state coexist. Therefore, the observed values of the phases are expected to correspond to the weighted averages of the two contributions, since these two contributions are incoherent with each other.

From the result of the phases at 1.95 and 2.05 eV having opposite signs to each other, it can be concluded that the vibrational amplitude peaks at 1.95 and 2.05 eV are due to the modulation of the intensity of  $1^1B_u$ -FE absorption (resonant at 2.00 eV) by the motion of the vibrational wavepacket in the ground state produced by the stimulated Raman scattering (SRS) process.

Figure 9.18c illustrates the photoinduced absorption from the “geometrically relaxed  $2^1A_g$  state”. Here it is not known whether the state  $2^1A_g$  forms or does not form an exciton, hence the use of the term “self-trapped exciton” was carefully

avoided. The pump pulse generates a wavepacket not only in the ground state but also in the  $1^1B_u$ -FE state. The photoexcited wavepacket in the  $1^1B_u$ -FE state soon ( $<100$  fs) after photogeneration relaxes into the geometrically relaxed  $2^1A_g$  state. In our group this relaxation time was determined as  $60 \pm 20$  fs [67]. This  $2^1A_g$  state has a different geometric configuration owing to its so-called “two-triplet” property. The oscillation of the wavepacket on the geometrically relaxed  $2^1A_g$  state potential curve modulates the probe signal. A wavepacket is produced at point F in Fig. 9.18c at the beginning and then starts to move as  $F \rightarrow E \rightarrow D \rightarrow E \rightarrow F \dots$ , where point E is located at the bottom of the potential curve along the corresponding stretching-mode coordinate associated with the geometrically relaxed  $2^1A_g$  state.

The expected phases of the oscillation of the photoinduced absorption signal in the case of  $E_D > E_F$  are shown in Fig. 9.18b, i.e. they are zero,  $-\pi/2$  and  $-\pi$  at probe photon energies of  $E_D$ ,  $E_E$  and  $E_F$ , respectively, in the same way as in the case of the ground state.

The absorption spectrum associated with the transition from the geometrically relaxed  $2^1A_g$  state to  $n^1B_u$  states has a peak around 1.8 eV [30]. First we consider the case when  $E_E$  is 1.83 eV. Then the phases of the C=C mode in Fig. 9.17a correspond to those in the model shown in Fig. 9.18d. The phases of the C $\equiv$ C-mode molecular vibration probed at 1.77 and 1.87 eV are  $-\pi$  and  $0\pi$ , respectively. These are the same as those of the C=C mode vibration. Therefore, it is concluded that not only the vibrational wavepacket of the C=C mode but also that of the C $\equiv$ C mode is generated in the geometrically relaxed  $2^1A_g$  state.

Figure 9.19 shows the C=C stretching-mode frequencies extracted by LP-SVD from the real-time traces at many probe photon energies between 1.78 and 2.08 eV. From the previous discussion, the signal due to the wavepacket motion in the ground state appears strongly at probe photon energies of 2.04–2.07 and 1.92–1.95 eV, which correspond to the  $E_A$  and  $E_C$  regions, respectively, in Fig. 9.18. The modulated signal due to the motion of the wavepacket in the geometrically relaxed  $2^1A_g$  state appears strongly at probe photon energies of 1.87–1.90 and 1.79–1.81 eV, indicated by regions  $E_D$  and  $E_F$  in the figure. The wavepacket motion in the geometrically relaxed  $2^1A_g$  state and that of the ground state appear nearly exclusively at 2.00 and 1.84 eV, respectively, corresponding to  $E_B$  and  $E_E$ , respectively. Figure 9.19 shows that the vibrational frequencies determined for the probe photon energy regions of  $E_B$ ,  $E_D$  and  $E_F$  are higher than those of the  $E_A$ ,  $E_C$  and  $E_E$  regions. Hence it can be concluded that the frequency of C=C stretching in the geometrically relaxed  $2^1A_g$  state is close to that determined for the  $E_B$  probe photon energy. Therefore, the frequency of the C=C stretching in the excited state is concluded to be  $1472 \pm 6$   $\text{cm}^{-1}$  and that in the ground state is  $1463 \pm 6$   $\text{cm}^{-1}$  concluded from the data for the  $E_E$  probe photon energy region. The frequency of the C $\equiv$ C stretching mode in the geometrically relaxed  $2^1A_g$  state is determined as  $2092 \pm 6$   $\text{cm}^{-1}$  and that in the ground state is  $2083 \pm 6$   $\text{cm}^{-1}$ . The errors of the differences are smaller than those of their absolute values, since the errors in the frequency determination are mainly due to the imperfect step length of the delay stage. It can then be concluded that each of the frequencies of the C=C and C $\equiv$ C stretching modes in the excited state is higher by about  $10 \pm 2$   $\text{cm}^{-1}$  than those in the ground state.

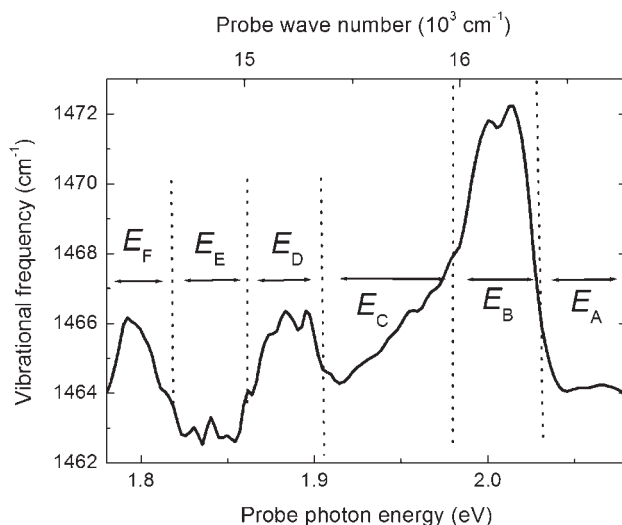


**Figure 9.19** Probe photon energy dependence of vibrational frequency of the C=C stretching mode.  $E_A$  and  $E_C$  are energy regions in which the pump-probe signal is modulated by the motion of the wavepacket in the ground state strongly rather than the excited state.  $E_D$  and  $E_F$  are energy regions in which the

pump-probe signal is modulated by the motion of the wavepacket in the ground state strongly rather than the excited state. In  $E_B$  and  $E_E$ , the signal is modulated by the motion of the wavepacket only in the excited and ground state, respectively.

## 9.4 Conclusion

We clarified the very early stage of the electronic relaxation in relation to molecular vibration, geometric relaxation and internal conversion in one of the most popular one-dimensional conjugated polymers, polydiacetylene.

Peak tracking analysis revealed the vibronic coupling to the electronic absorption corresponding to the  $1^1A_g \rightarrow 1^1B_u$  transition and  $1^12^1A_g \rightarrow n^1B_u$  transition. The peak of the 0-0 transition from the ground state in which vibrational excitation does not participate oscillates with the frequencies of the C-C stretching vibrational modes. The oscillations of energy and intensity of a peak of induced absorption to a higher excited state show different behaviors both in vibrational amplitude and phase. The results provided us with comprehensive information to determine the relative locations of the multi-dimensional potential hypersurfaces of the ground, lowest excited and higher excited states in the configuration space. The precise analysis of the time evolution of the difference absorption spectra revealed the thermalization processes due to the energy redistribution among various modes in the polymer chains in the excited and ground states.

We could also separate the ground- and excited-state contributions in the real-time vibrational signals due to the wavepacket motions from the difference trans-

mittance spectra obtained by multi-wavelength sub-5 fs spectroscopy. The wavepacket of the C=C stretching mode in the ground state was found first to start to oscillate in the opposite direction to that of the C≡C stretching mode. Also, the vibration of the C≡C stretching mode in the geometrically relaxed  $2^1A_g$  state was observed in addition to the C=C mode even after the FE has been converted to the geometrically relaxed state within 100 fs. This clearly demonstrates that the full geometrically relaxed butatriene-type structure is not formed; instead, it can still be described by the acetylene-type structure with a small admixture of a butatriene-type configuration. The frequencies of the C=C and C≡C stretching modes in the geometrically relaxed  $2^1A_g$  state were determined as 1472 and 2092  $\text{cm}^{-1}$ , respectively. The corresponding frequencies in the ground state were calculated as 1463 and 2083  $\text{cm}^{-1}$ . Each of the former is higher by about 10  $\text{cm}^{-1}$  than each of the latter.

### Acknowledgments

The authors thank T. Saito, S. Adachi, K. Nishimura, T. Taneichi and N. Ishii for enlightening discussions. This research was supported partly by a Grant-in-Aid for Specially Promoted Research (No. 14002003) and partly by the program for the “Promotion of Leading Researches” in Special Coordination Funds for Promoting Science and Technology from the Ministry of Education, Science and Culture of Japan.

### References

- 1 T. S. Rose, M. J. Rosker, A. H. Zewail, *J. Chem. Phys.* **91**, 7415 (1989).
- 2 M. H. Vos, F. Rappaport, J.-C. Lambry, J. Breton, J.-L. Martin, *Nature* **363**, 320 (1993).
- 3 Q. Wang, R. W. Schoenlein, L. A. Peteanu, R. A. Mathies, C. V. Shank, *Science* **266**, 422 (1994).
- 4 S. Pedersen, J. L. Herek, A. H. Zewail, *Science* **266**, 1359 (1994).
- 5 T. Kobayashi, T. Saito, H. Ohtani, *Nature* **414**, 531 (2001).
- 6 S. Pedersen, L. Banares, A. H. Zewail, *J. Chem. Phys.* **97**, 8801 (1992).
- 7 H. Torii, M. Tasumi, *Chem. Phys. Lett.* **260**, 195 (1996).
- 8 Y. J. Yan, S. Mukamel, *Phys. Rev. A* **41**, 6485 (1990).
- 9 A. T. N. Kumar, F. Rosca, A. Widom, P. M. Champion, *J. Chem. Phys.* **114**, 701 (2001).
- 10 A. Shirakawa, I. Sakane, M. Takasaka, T. Kobayashi, *Appl. Phys. Lett.* **74**, 2268 (1999).
- 11 M. Ikuta, Y. Yuasa, T. Kimura, H. Matsuda, T. Kobayashi, *Phys. Rev. B*, **70**, 214301 (2004).
- 12 S. A. Kovalenko, J. Ruthmann, N. P. Ernsting, *J. Chem. Phys.* **109**, 1894 (1998).
- 13 J. Friedrich, J. D. Swalen, D. Haarer, *J. Chem. Phys.* **73**, 705 (1980).
- 14 T. Kobayashi, *IEICE Trans. Fundam.* **E-75A**, 38 (1992).
- 15 M. Yoshizawa, Y. Hattori, T. Kobayashi, *Phys. Rev. B* **47**, 3882 (1993).
- 16 R. W. Carpick, D. Y. Sasaki, M. S. Marcus, M. A. Eriksson, A. R. Burns, *J. Phys.: Condens. Matter* **16**, R679 (2004).
- 17 G. Wegner, *Makromol. Chem.* **145**, 85 (1971).

- 18 G. N. Patel, R. R. Chance, J. D. Witt, *J. Chem. Phys.* **70**, 4387 (1979).
- 19 D. Bloor, in *Polydiacetylenes*, edited by D. Bloor, R. R. Chance, Martinus Nijhoff, Dordrecht, 1985.
- 20 K. Tashiro, K. Ono, Y. Minagawa, M. Kobayashi, T. Kawai, K. Yoshino, *J. Polym. Sci., Part B: Polym. Phys.* **29**, 1223 (1991).
- 21 M. Yoshizawa, T. Kobayashi, H. Fujimoto, J. Tanaka, *J. Phys. Soc. Jpn.* **56**, 338 (1982).
- 22 T. Kobayashi, M. Yoshizawa, U. Stamm, M. Taiji, M. Hasegawa, *J. Opt. Soc. Am. B* **7**, 1558 (1990).
- 23 M. Yoshizawa, K. Nishiyama, T. Kobayashi, *Chem. Phys. Lett.* **207**, 461 (1993).
- 24 J. Y. Bigot, T. A. Pham, T. Barisien, *Chem. Phys. Lett.* **259**, 469 (1996).
- 25 T. A. Pham, A. Daunois, J. C. Merle, J. Le Moigne, J. Y. Bigot, *Phys. Rev. Lett.* **74**, 904 (1995).
- 26 G. Cerullo, G. Lanzani, M. Muccini, C. Taliani, S. De Silvestri, *Phys. Rev. Lett.* **83**, 231 (1999).
- 27 A. Vierheilg, T. Chen, P. Walther, W. Kiefer, A. Materny, A. H. Zeweil, *Chem. Phys. Lett.* **312**, 349 (1999).
- 28 M. Yoshizawa, M. Taiji, T. Kobayashi, *IEEE J. Quantum Electron.* **25**, 2532 (1989).
- 29 M. Yoshizawa, A. Yasuda, T. Kobayashi, *Appl. Phys. B* **53**, 296 (1991).
- 30 M. Yoshizawa, Y. Hattori, T. Kobayashi, *Phys. Rev. B* **49**, 13259 (1994).
- 31 A. Shirakawa, I. Sakane, T. Kobayashi, *Opt. Lett.* **23**, 1292 (1998).
- 32 T. Kobayashi, A. Shirakawa, H. Matsuzawa, H. Nakanishi, *Chem. Phys. Lett.* **321**, 385 (2000).
- 33 G. J. Blanchard, J. P. Heritage, A. C. V. Lehmen, M. K. Kelly, G. L. Baker, S. Etemad, *Phys. Rev. Lett.* **63**, 887 (1989).
- 34 W. B. Bosma, S. Mukamel, B. I. Greene, S. Schmitt-Rink, *Phys. Rev. Lett.* **68**, 2456 (1992).
- 35 A. J. Heeger, S. Kivelson, J. R. Schrieffer, W. P. Su, *Rev. Mod. Phys.* **60**, 781 (1988).
- 36 W. P. Su, J. R. Schrieffer, A. J. Heeger, *Phys. Rev. Lett.* **42**, 1698 (1979).
- 37 W. P. Su, J. R. Schrieffer, A. J. Heeger, *Phys. Rev. B* **22**, 2099 (1980).
- 38 Z. Vardeny, *Physica B* **127**, 338 (1984).
- 39 L. Rothberg, T. M. Jedju, S. Etemad, G. L. Baker, *Phys. Rev. Lett.* **57**, 3229 (1985).
- 40 B. I. Greene, J. F. Mueller, J. Orenstein, D. H. Rapkine, S. Schmitt-Rink, M. Thakur, *Phys. Rev. Lett.* **61**, 325 (1988).
- 41 T. Kobayashi, M. Yasuda, S. Okada, H. Matsuda, H. Nakanishi, *Chem. Phys. Lett.* **267**, 472 (1997).
- 42 J. Kinugusa, S. Shimada, H. Matsuda, H. Nakanishi, T. Kobayashi, *Chem. Phys. Lett.* **287**, 639 (1998).
- 43 F. Zerbetto, *J. Phys. Chem.* **98**, 13157 (1994).
- 44 J. Swiatkiewicz, X. Mi, P. Chopra, P. N. Prasad, *J. Chem. Phys.* **87**, 1882 (1987).
- 45 L. X. Zheng, R. E. Benner, Z. V. Vardeny, G. L. Baker, *Synth. Met.* **49/50**, 313 (1992).
- 46 A. Race, W. Barford, R. J. Bursill, *Phys. Rev. B* **67**, 245202 (2003).
- 47 M. Y. Lavrentiev, W. Barford, *Phys. Rev. B* **59**, 15048 (1999).
- 48 B. Lawrence, W. E. Torruellas, M. Cha, M. L. Sundheimer, G. I. Stegeman, J. Meth, S. Etemad, G. Baker, *Phys. Rev. Lett.* **73**, 597 (1994).
- 49 M. Yoshizawa, A. Kubo, S. Saikan, *Phys. Rev. B* **60**, 15632 (1999).
- 50 W. P. Su, J. R. Schrieffer, A. J. Heeger, *Phys. Rev. Lett.* **68**, 1148 (1982).
- 51 S. Abe, J. Yu, W. P. Su, *Phys. Rev. B* **45**, 8264 (1992).
- 52 S. Abe, M. Schreiber, W. P. Su, J. Yu, *Phys. Rev. B* **45**, 9432 (1992).
- 53 K. Pakbaz, C. H. Lee, A. J. Heeger, T. W. Hagler, D. McBranch, *Synth. Met.* **64**, 295 (1994).
- 54 A. Shirakawa, T. Kobayashi, *Appl. Phys. Lett.* **72**, 1476 (1998).
- 55 G. Cerullo, M. Nisoli, S. Stagira, S. De Silvestri, G. Tempea, F. Krausz, K. Ferencz, *Appl. Phys. B* **70**, S253 (2000).
- 56 A. Baltuška, T. Kobayashi, *Appl. Phys. B* **75**, 427 (2002).
- 57 G. Wenz, G. Wegner, *Makromol. Chem. Rapid. Commun.* **3**, 231 (1982).
- 58 T. Kobayashi, A. Shirakawa, *Appl. Phys. B* **70**, S239 (2000).

- 59 S. Mukamel, A. Takahashi, H. X. Wang, G. Chen, *Science* **266**, 250 (1994).
- 60 S. Mazumder, D. Guo, S. N. Dixit, *Synth. Met.* **57**, 3881 (1993).
- 61 H. Kano, T. Saito, T. Kobayashi, *J. Phys. Chem. B* **105**, 413 (2001).
- 62 J. Janszky, P. Adam, An. V. Vinogradov, T. Kobayashi, *Spectrochim. Acta, Part A* **48**, 31 (1992).
- 63 K. Huang, A. Rhys, *Proc. R. Soc. London, Ser. A* **204**, 406 (1950).
- 64 M. Turki, T. Barisien, J. Y. Bigot, C. Daniel, *J. Chem. Phys.* **112**, 10526 (2000).
- 65 Z. Iqbal, R. R. Chance, R. H. Baughman, *J. Chem. Phys.* **66**, 5520 (1977).
- 66 D. Grando, S. Sottini, G. Gabrielli, *Thin Solid Films* **327–329**, 336 (1998).
- 67 Y. Yuasa, M. Ikuta, T. Kimura, H. Matsuda, T. Kobayashi, to be published in *Phys. Rev. A* (2005).

## 10

# Ultrafast Optoelectronic Probing of Excited States in Low-Dimensional Carbon – Based $\pi$ -Conjugated Materials

*T. Virgili, J. Cabanillas-Gonzalez, L. Lüer and G. Lanzani*

### 10.1

#### Introduction

Static fields (E or H) act as a perturbation on the electronic structure of molecules and solids, in a way specific to the nature of the states involved. This observation leads to modulation spectroscopy, where fields are exploited for modulating electronic transitions in molecules and solids. In general, electro-absorption detects changes in the spectra such as transition energy shift, line broadening or intensity modulation which can be caused by: (i) state mixing induced by the field; (ii) the opening up of additional decay channels, typically ionization, and (iii) symmetry breaking. Early experiments on semiconductors [1] were carried out following the predictions of Franz [2] and Keldysh [3], who independently developed a theory for band-to-band transitions in a uniform electric field. The technique of electroabsorption (EA) has been developed since then and used extensively for understanding band structure, exciton properties and carrier scattering in bulk semiconductors and more recently in quantum wells and heterostructures. In parallel, studies were carried out on atoms, molecules and molecular crystals (for a review, see Blinov et al. [4]).

EA experiments are typically run at steady-state conditions and do not provide information on the changes induced by the field onto the excited state temporal dynamics. Here, we report on new experiments, which combine EA with time-resolved spectroscopy. The latter detects transient species in photoexcited semiconductors, identifying their spectra (energy location, cross-sections and line-shapes) and dynamics (lifetime, decay paths and yields). Examples have been given in previous chapters, applied to conjugated polymers. In our case the detected signal depends on pump–probe delay, as usual in transient transmission, and on the electric field, as usual in EA, so it is a sort of double modulation. The time dependence allows ground- and excited-state effects to be separated, as the latter occurs only after the pump excitation (positive delay). Measurements are carried out on diode structures, where electrodes are used to apply the field. A sketch of the experiment is shown in Fig. 10.1. The device can be as simple as a sandwich structure or have interdigitated electrodes on top of which the sample is depos-

ited. Most experiments have been carried out in the zero-current configuration, yet in principle carrier injection can be achieved and be an interesting variable. The supply of reliable devices is a fundamental need, which explains why those techniques have become more popular only recently, once organic device engineering had reached a certain quality, stability and reproducibility of its products. This technique can also be understood as a device probe, which tests working principles under operational conditions. Optoelectronic probing can be achieved by exploiting device-related quantities, such as electric current, voltage drop or electroluminescence. In order to have time resolution in such experiments, which detect time-integrated quantities, double excitation is needed, the so-called excitation cross-correlation technique. In the following, we first provide a general physical background on electric field effects on carbon conjugated materials, then electric field-assisted spectroscopy is reviewed starting with luminescence, pump-probe and finally photoconductivity.

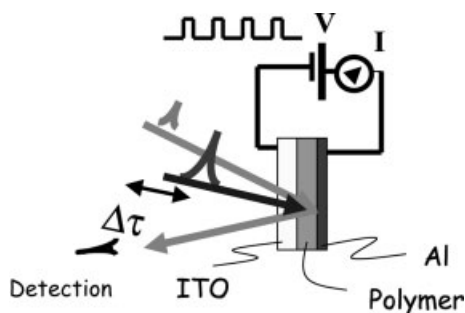


**Figure 10.1** Schematic setup for the measurement of the electromodulated pump-probe signal. Black arrows: pump pulse, grey arrows: probe pulse

## 10.2

### Physics Background: Excited States in Low-Dimensional Conjugated Carbon Materials

In previous chapters the elementary excitations of low-dimensional carbon based materials have been extensively discussed, comprising long isolated polymer chains, oligomers and their respective condensed phase, which includes crystal states such as excitons and polaritons. Here we restate part of the discussion with the purpose of highlighting those aspects relative to the effect of an electric field on the picosecond dynamics. This only partially involves the effect on the cross-section of the electronic transitions, which is the main issue in standard EA and it is focused onto the effect on the deactivation paths.

Above we mentioned briefly the Franz-Keldysh effect. This theory includes no correlation and it describes phenomena involving free carriers and band-to-band transitions. Essentially it can be understood as photon-assisted tunneling of an

electron from the valence band to the conduction band. Electron correlation and Coulomb interaction between charged states should, however, be considered in a more refined model leading to the concept of excitons, which are neutral (sometimes defined as *currentless*) states comprising a bound electron–hole (e–h) pair. Such effects become important in a number of circumstances, particularly (i) when dealing with electronic transitions at the absorption threshold in semiconductors, (ii) if experiments are carried out at low temperature, where quantum confinement enhances e–h binding and excitonic effects [5] and (iii) in organic semiconductors where correlation plays a dominant role. Here the situation is completely upside down; excitons become the primary excitations upon photon absorption and charge carriers are rarely formed. Organic and inorganic semiconductors are therefore well separated by the respective value of the exciton binding energy ( $E_b$ ), which is a measure of the strength of the electron correlation. Here dimensionality plays a crucial role, because even when electronic density and screening are comparable, in confined, low-dimensional systems correlation effects are superior. Since conjugated chains are ultimately quantum wires, whose dimensional scaling cannot be reproduced with inorganic materials, it is easily predicted that excitonic effects are going to control their excitation dynamics.  $E_b$  is usually defined as the energy difference between the neutral bound state and the lowest charge separated state. The latter can be a pair of free charges (band edge) or a polaron pair made of interacting charges (often considered as intermediate for free charges). In inorganic semiconductors an electric field of  $10^3$ – $10^5$  V cm $^{-1}$ , depending on the energy gap, is sufficient to ionize completely the exciton population [6]. In polymer semiconductors a field of 1 MV cm $^{-1}$  dissociates a few percent of the neutral state population (see below). Obviously the binding energy in the two cases is quite different. In inorganic semiconductors excitons are of Wannier–Mott type, formed by weakly bound pairs of electron and hole quasi-particles equivalent to the hydrogen atom and differing only in the values of the effective masses of the particles and dielectric constant of the medium. In this case the major effect of the electric field is to lower the lip of the Coulomb well, thereby changing discrete bound states into continuum states. A pictorial description is shown in Fig. 10.2. When the lip of the well moves below the energy of a bound level, then it takes no extra energy to separate the electron and hole and that level is said to be ionized. A secondary effect is a shift of the energy levels, in particular of the exciton ground state, to lower energy owing to a slight widening of the well. Broadening of the excitonic resonance occurs owing to the reduced lifetime resulting from ionization by the applied field. The electric field  $F_I$  capable of ionizing a Wannier–Mott exciton must provide at least a potential drop of 1 effective rydberg,  $R$ , across the effective Bohr radius,  $a$ , i.e.  $F_I = R/ea$ . At intermediate field strength, a bound state can still dissociate via tunneling through the barrier. In this regime, the dissociation rate, as evaluated in Ref. [7] is

$$\Gamma = \frac{E_b}{\hbar} \exp\left(-\frac{4E_b^{\frac{3}{2}}(m^*)^{\frac{1}{2}}}{3e\hbar F}\right) \quad (10.1)$$

where  $E_b$  is the binding energy and  $m^*$  the effective mass. Note that this expression has been used for interpreting experimental results obtained in polymer semiconductors too, based on the assumption that Wannier–Mott excitons properly described their excitation [8]. However, this remains questionable in conjugated polymers, while it is certainly a good model for other low-dimensional nanostructures such as carbon nanotubes. Alternatively, dissociation can be viewed as a carrier escape from the Coulomb attraction of the counter charge due to field-assisted thermal activation over the barrier. This model can better describe intermediate, one-dimensional excitons, such as those encountered in conjugated chains. The electric field effect is then described by the Poole–Frenkel formalism [9]. The one-dimensional analysis leads to the following expression for the quantum generation yield of charges from Coulomb escape as a function of field [10]:

$$\eta(F) = \left[ A \exp\left(-\beta F^{\frac{1}{2}}/kT\right) - 1 \right]^{-1} \quad (10.2)$$

where  $A$  is parameter which contains an attempt frequency determined by material properties and

$$\beta = (e^3/\pi\epsilon\epsilon_0)^{\frac{1}{2}} \quad (10.3)$$

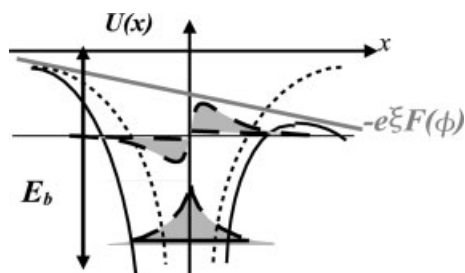


**Figure 10.2** Influence of a static electric field of the potential curve of an electronic state. Two vibronic levels are given.

In small-molecule organic semiconductors, the lowest energy neutral excited state is understood as a tightly bound excitation, localized on the molecular unit, whose internal structure is not discussed because electron and hole wavefunctions are fully overlapped and cannot be physically singled out. Such molecular states can still lead to wave-like, collective excitations, but only in ordered solids with a periodic lattice, provided that some intermolecular interaction exists. When this holds true, splitting of the molecular state, induced by the interaction, generates the Frenkel exciton band [11]. In most cases, organic solids are disordered and excited states discrete and localized. Bands arise from inhomogeneous broadening and propagation is incoherent, by hopping. Elementary excitations are then those of large organic molecules, singlet, triplet and charged states (in terms of

spin quantum number  $S = 0$ ,  $S = 1$  and  $S = 1/2, 3/2$ , etc., respectively). All these can be labeled, independently from theoretical models, as  $S_k$ ,  $T_k$  and  $D_k$ , where  $S$  stands for singlet,  $T$  for triplet and  $D$  for doublet, the last being charged (we neglect at present the case of spinless charge carriers [12]) and  $k$  is an integer giving the order in energy. Dissociation can still occur when the electric field induces a charge-transfer (CT) reaction across the high potential barrier, from either a molecular or Frenkel state. It is important to note that in this case one does not generally consider a full dissociation of free carriers, but the generation of near charge pairs, still bonded, at a distance  $r$ , with energy  $e^2/4\pi\epsilon\epsilon_0 r$ . Such a CT complex can be viewed as an intermediate step in charge separation. CT reactions are usually supposed to take place between well-separated units. If wavefunction overlap can be disregarded, a rate coefficient can describe the probability of a jump, depending on, among other parameters, the energy difference between “donor” and “acceptor”. This is a well-known system, studied in detail for small molecules in chemical physics. As a good reference one can look at the work of Marcus, who received the Nobel Prize in Chemistry in 1992 for theory and experiments on electron transfer [13]. In the solid state, where “equal” molecules are packed, an electric field can help electron transfer because of level shifting, thus introducing donor and acceptor sites even in homogeneous samples. The energy involved is  $eF\Delta r$ , where  $e$  is the electron charge,  $F$  the field amplitude and  $\Delta R$  the donor–acceptor separation. The idea is sketched in Fig. 10.3, following a study reported in 1996. The concept is, however, very old; it can be found, for instance, in Ref. [14] for molecular solids.

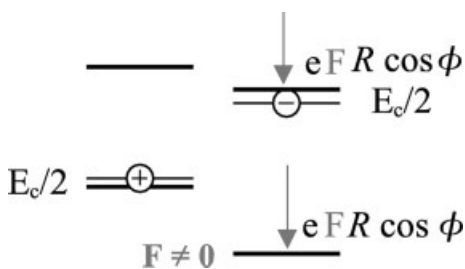


**Figure 10.3** Dependence of energies of electronic states on the amount and direction of the electric field.

In conjugated polymers a mixed scenario occurs, as along the chain dielectric screening can be high enough to support the weak electron–hole interaction picture (Wannier–Mott exciton), while inter-chain interaction is weak, giving rise to a smaller dielectric constant and tightly bound states. Note, however, that 1D excitons represent only one class of excitations in a wider scenario, which corresponds to “ionic” excitations in the quantum chemistry language. Covalent states, which at low energy can be approximated by spin–wave excitations, are not represented, yet they play an important role, especially in non-emitting moieties. Intra-chain excitons, which propagate coherently along the conjugated segment, hop incoher-

ently from one chain to the other. The simultaneous presence of these two scenarios gave rise to a number of models for describing field-induced dissociation [15–17], from one extreme to the other, basically choosing between intra- or inter-chain separation. Note that the dual interpretation brings ambiguity also in the final state, which is generated following dissociation. Charges may be on the same conjugated segment or can be dwelling on separate segments (on either the same or different chains). So far we have discussed the possibility of ionization of the lowest singlet state  $S_1$ . However, it appears now well documented that higher lying states ( $S_n$  with  $n > 1$ ) can dissociate more easily than lower ones, in close similarity with autoionization in molecular crystals. This has consequences: (1) additional charge generation pathways, starting from higher lying states, should be considered, e.g., sequential excitation, two-photon absorption and bimolecular singlet annihilation, (2) a description of higher lying states is required and (3) an experimental estimate of the binding energy ( $E_b$ ) should be carefully considered. Whether  $S_n$  prevails over  $S_1$  dissociation depends on a number of boundary conditions. Among others, one important factor is the inter-chain interaction, which can probably modulate the dissociation rate. For instance, as seen below, we find that field-induced ionization occurs predominantly from  $S_n$  in polyfluorene, but from  $S_1$  in ladder polymers. In general it appears that long conjugated chains have a lower exciton binding energy and may easily involve the lowest neutral state  $S_1$ . In oligomers and small molecules, only intermolecular separation makes sense. Here  $S_n$  appears as the unique path to charge separation, because of the high binding energy in  $S_1$ .

### 10.3

#### Electromodulation of Steady-State Fluorescence in Organic Solids

##### 10.3.1

##### Introduction

As stated above, in the last 20 years different spectroscopic techniques combined with electric fields have been developed to elucidate the fundamentals of charge generation and recombination in organic semiconductors and many of them involve state luminescence. The first reports concerning field-induced quenching of the steady-state photoluminescence in organic solids date from the mid-1980s [18, 19]. Since then, different electromodulation techniques have been developed in order to identify the different mechanisms which cause fluorescence quenching in OLEDs.

Although there are few examples in literature of fluorescence quenching studies employing steady-state electric fields, the use of electromodulation techniques introduces two major advantages. First, it allows one to separate external contributions to the fluorescence quenching signal from those strictly induced by the electric field. Second, changing the phase and frequency detection with respect to the electric field also allows one to discriminate the different mechanisms of fluorescence quenching that coexist in OLEDs.

In devices used for electromodulated fluorescence (EMF) there exist two electric fields: one “internal” ( $F_i$ ) caused by interface potential and the other external due to the applied voltage.  $F_i$  can be induced by workfunction differences of electrodes and also residual charges contained in the bulk or by dipole layers formed by CT reactions. Although this internal field is often considered to be constant across the device, the presence of large current densities under operating conditions may lead to local fluctuations. As a result, it becomes difficult to interpret the fluorescence quenching signal since the effective electric field is given by a superposition of both external and internal fields, the latter being different at each point in the sample. In order to account for this effect, Kalinowski et al. [10] developed a modulation scheme which allows one to evaluate the contribution of the internal field to the overall EMF. The technique consists of the application of an electric field with a sinusoidal profile (Fig. 10.4a) and the detection of the fundamental and second harmonic components of the EMF signal. The in-phase ( $\phi = 0$ ) first harmonic component is observed to follow a profile identical with that of the electric field. At positive fields the fluorescence is enhanced or diminished as it is the module of the electric field, suggesting a situation of *fluorescence enhancement*, (see Fig. 10.4b). At negative fields however, the dependence of the EMF signal on the module is reversed. Alternately, an EMF signal detected at an angle of  $\phi = \pi$  can be referred as *fluorescence quenching*, since in this configuration the fluorescence intensity diminishes when the electric field is enhanced in the positive direction (see Fig. 10.4c). Again, the opposite dependence holds for fields applied in the negative direction. Therefore, a non-zero EMF signal collected using these detection schemes must be dependent on the module in addition to the direction of the electric field. If we attain to a situation of absence of internal fields, application of electric fields in the positive and negative directions must lead to symmetric configurations and a negligible first harmonic component. In contrast, detection of a non-zero first harmonic component would otherwise imply a preferred direction of polarization. Assuming the medium to be isotropic, such a possibility can only be attributed to the presence of an internal field across the device.

The out-of-phase ( $\phi = \pi/2$ ) second harmonic component contains exclusively *fluorescence quenching* information. Differing from the fundamental component of the EMF signal, the profile of the second harmonic suggests a fluorescence decrease upon increasing the module of the electric field, no matter in which direction the field is (Fig. 4d). In other words this detection configuration provides a internal field-free EMF signal suitable for evaluation of different charge photogeneration models.

Kalinowski's group applied this technique to study field-induced exciton separation in different molecular systems such as crystalline thionaphthenindole (TNI) [10] or 8-hydroxyquinoline ( $Alq_3$ ) [20]. For the case of TNI, the fundamental and second Fourier component of the EMF signal show a superlinear dependence on the module of the electric field different from the quadratic dependence expected for the Stark effect (Fig. 10.5). The possibility of quenching induced by exciton-carrier interaction was also excluded on the basis of the large magnitude of the quenching signal and the low mobility of singlet excitons in polycrystalline TNI.

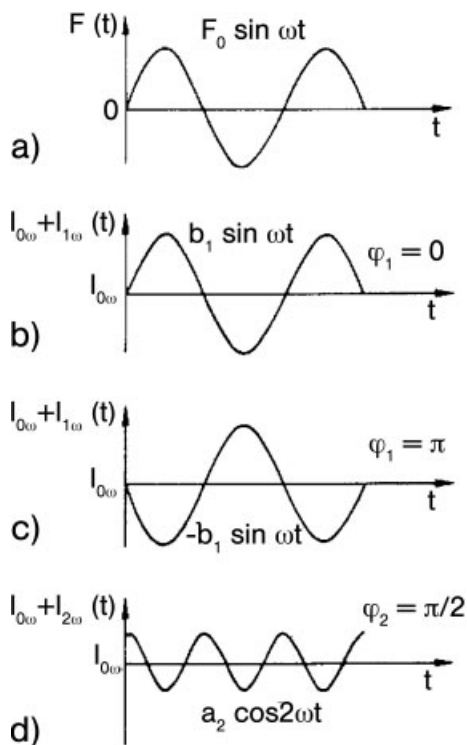


**Figure 10.4** (a) Applied electric field with sinusoidal profile; (b) and (c) fluorescence response at the first harmonics with two different phase shifts; (d) out-of-phase second harmonic component of the fluorescence response. After Ref. [10].

Accordingly, the fluorescence quenching signal was attributed to an electric field modulation of charge separation from a singlet state which was evaluated according to the different established theoretical models. The results were understood in terms of a macrotrap model. According to this model, singlet excitons are trapped in their diffusion movement by chemical or structural traps forming a trapped singlet. Whether additional free energy is available, charge separation on to a nearest neighbor leads to the formation of a trapped CT exciton. This state may either decay radiatively or alternatively extend its delocalization by hopping of the electron or the hole towards more distant molecules. The action of the electric field eventually facilitates electron–hole separation and formation of a pair of free carriers.

The experimental data were also extrapolated to high electric fields in the electroluminescent regime in order to estimate the percentage of quenched excitons in OLEDs. This value was found to be particularly large in certain materials such as  $\text{Alq}_3$  (60% of singlets are quenched at fields over  $3.5 \times 10^6 \text{ Vcm}^{-1}$ ) [20], and could be one of the causes of the low electroluminescence quantum yield exhibited by OLEDs fabricated from this organic compound.

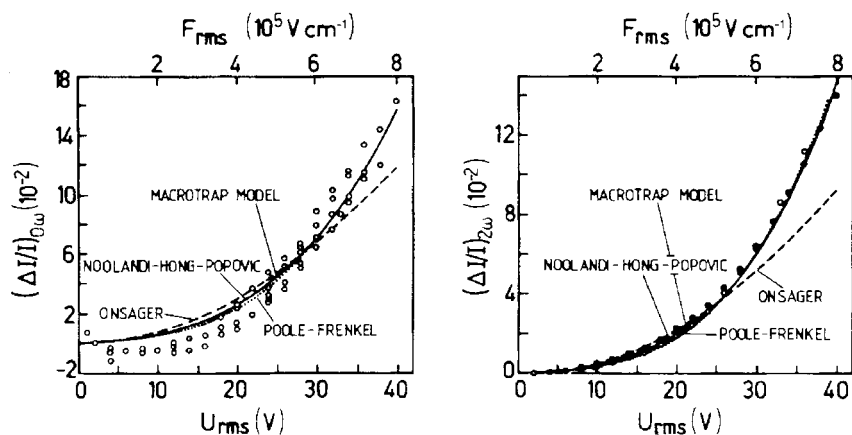


**Figure 10.5** Zeroth and second Fourier components of the fluorescence quenching signal for different electric field amplitudes across the device. After Ref. [10].

### 10.3.2

#### Electric Field-Assisted Photoluminescence Up-Conversion

Within the framework of the one-dimensional (1D) semiconductor description established by Su et al. [21], photoluminescence in conjugated polymers is the result of radiative recombination of two oppositely charges directly photogenerated into the  $\pi$ -valence and conduction bands. Differing from inorganic semiconductors, strong electron phonon interaction would lead to rapid self-localization of the charged species (*polarons*) and a considerable red shift between absorption and photoluminescence spectra. In 1990, the validity of the 1D semiconductor approach was challenged by Bässler and co-workers [22]. They demonstrated the existence of a polarization memory in the photoluminescence of PPV, even upon excitation above the localization threshold. This evidence is incompatible with the band model since excitation over the localization threshold leads to formation of uncorrelated e-h pairs and point towards the formation of excitons where geminate e-h pairs are bound by their mutual coulombic interaction. Additional proofs of the excitonic nature of photoexcitations in conjugated polymers came from time-resolved photoluminescence up-conversion in PPV [23, 24]. Kersting et al. reported a comparative study of the transient PL in PPV and model oligomer OPV compounds [23]. On the assumption that both PPV and OPVs show the same type of vibrations responsible for vibronic progressions in the optical spectra, they demonstrated that the larger red shift of the PL spectra of PPV cannot be explained as due to vibrational relaxation. Moreover, the observation of energy-dependent luminescence decay, faster in the blue in PPV (spectral migration), further confirms incoherent hopping of excitons between chromophores with different energies. Emission occurs preferentially from lower energy sites, account-

ing for the observed red shift. Inhomogeneity within polymer films arises from the variation of length and environment of conjugated segments, producing a band energy density of states. Indeed, below the localization energy (i.e. the minimum energy for observing spectral migration) resonant emission was found. This points to a negligibly small relaxation energy, if any at all.

These important findings provided the motivation for further investigations on the origin of photoexcitations in PPV. An opposite approach, however, was followed this time: if excitons were the primary photoexcitations in PPV, it would be possible to obtain traces of its nature by monitoring their likely dissociation under an applied electric field. Within the 1D semiconductor model, the decrease in the photoluminescence quantum yield under an electric field would be attributed solely to field-induced reduction of the oscillator strengths associated with the electronic transitions (also known as Stark shift). Since this effect is quasi-instantaneous, observation of a time-resolved reduction of the photoluminescence would imply a different quenching mechanism. The experimental setup employed for this purpose was electric field-assisted photoluminescence up-conversion (Fig. 10.6).

Essentially, photoluminescence up-conversion is a technique which consists of mixing the luminescence frequency emitted by the sample with an optical pulse (gate) inside a nonlinear crystal. Upon conditions of phase matching, the outgoing signal frequency is equal to the sum or difference in frequencies from both

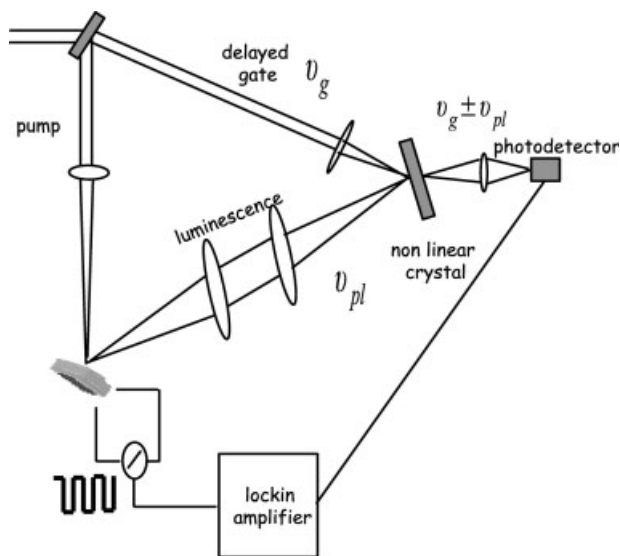


**Figure 10.6** Experimental setup of electric field assisted up-conversion. The sample is excited by 150-fs pulses delivered by a frequency-doubled Ti:sapphire laser. The luminescence is focused with the delay gate pulse

on to a nonlinear beta barium borate crystal. Phase-sensitive detection allows one to determine the effect of the applied electric field on the photoluminescence signal.

incident light sources. Accordingly, the luminescence can be resolved in time by changing the gate delay. Since sum or difference frequency is only generated during the time that the gate is present at the crystal, the total time resolution is comparable to the temporal width of the gate (typically few hundred femtoseconds). Changes on the photoluminescence signal induced by the electric field are probed by applying a reverse modulated signal and referring the detection to its frequency by means of a lock-in amplifier.

Kersting et al. performed the experiment in PPPV, a soluble PPV derivative, blended in a polycarbonate (PC) matrix. Dilution of the polymer chains in an inert matrix leads to slowing down of the exciton hopping rate by a factor of three with respect to the pure polymer, which facilitates the time monitoring of the dissociation process [24]. According to this, the PL quenching process was resolved in time during the first 100 ps after photoexcitation (see Fig. 10.7). According to their findings, PPPV photoluminescence decreases gradually in the first 5 ps under the influence of an electric field of  $1.7 \text{ MV cm}^{-1}$ . At early time-scales far beyond the time resolution of the experiment, a photoluminescence reduction of less than 1% is already appreciable. This “instantaneous” photoluminescence quenching is assigned to reduction of the oscillator strength induced by the electric field. Following this, the photoluminescence experiences a gradual decrease in the next 5 ps, approaching the 13% reduction measured for the steady-state photoluminescence. Saturation in the quenching process is appreciable from the similar quenching values found at 5, 10 and 20 ps. These results were interpreted in terms of dissociation of excitons photogenerated at high-energy sites within the homogeneous broadened density of states (see Fig. 10.8). Spectral relaxation drives excitons on to the bottom of the density of states, leading to the saturation in the dissociation process detected beyond 5 ps.

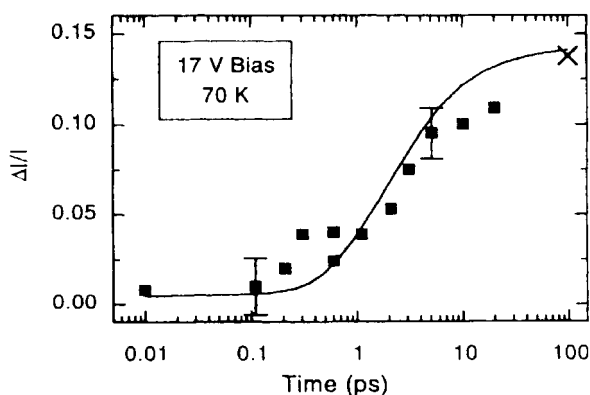


**Figure 10.7** Transient photoluminescence quenching in PPPV dispersed in solid polycarbonate (PC) matrix. Measurements were performed at 70 K under an electric field of  $1.7 \text{ MV cm}^{-1}$ .  $\Delta I/I$  holds for the modulated photoluminescence intensity detected at the

fundamental frequency of the electric field. The experimental data are denoted with filled squares. The cross indicates the quenching level of the steady state photoluminescence. After Ref. [24].

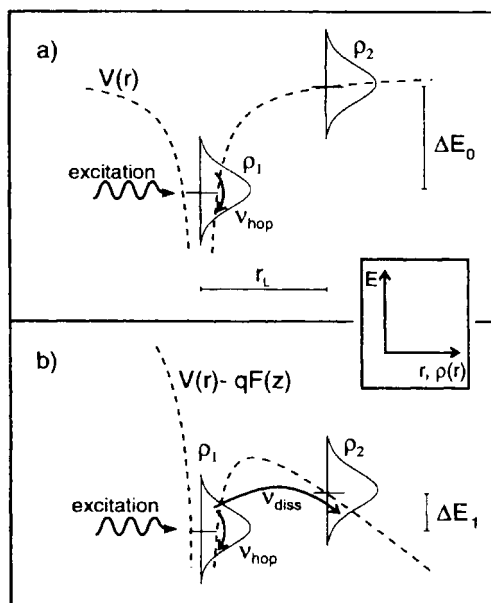


Figure 10.8 The exciton dissociation process in PPPV. After Ref. [24].

According to the interpretation provided by Arkhipov et al. [16], dissociation of excitons proceeds through the intermediate formation of off-chain loosely bound excitons, these species being generated by diffusion of on-chain excitons photo-generated with an energy excess towards the bottom of the density of states. A schematic diagram of the field-induced exciton dissociation mechanism is displayed in Fig. 10.8. According to the diagram, population is optically generated in  $\rho_1$ , which relax towards the bottom of the *density of states* (DOS) by inter-chain hopping. During their Brownian motion, excitons find low-energy sites where they can transfer an electron or hole forming a charge transfer exciton  $\rho_2$ . In absence of electric field the large energy separation between  $\rho_1$  and  $\rho_2$  prevents e–h separation. However, application of an electric field induces a potential asymmetry which contributes to lowering the differences in energy between the neutral  $\rho_1$  and charged  $\rho_2$  states, as discussed in Section 10.2. Dissociation therefore becomes energetically feasible for excitations located in the upper part of the DOS. Once vibrational relaxation proceeds the dissociation process becomes improbable. Such observation is experimentally justified by the saturated value of  $\Delta I/I$  at timescales beyond 10 ps.

This picture appears to be idealistic since it was demonstrated by Vissenberg et al. that the dissociation rate values at early timescales reported by Kersting et al. [24] can be fitted by a model which considers exclusively on-chain exciton dissociation [17]. This effect leads, however, to saturation of the dissociation rate over 1 ps. The large time dispersion observed over 1 ps thus seems to be attributed exclusively to inter-chain migration. A more general description of exciton dissociation

in conjugated polymers therefore requires us to take into account not only inter-chain migration but also ultrafast on-chain dissociation in addition to the effects of charge recombination. As a concluding remark one should note that EMF does not explicitly detect the by-product of the emitting states quenching. Charge generation is at this stage a conjecture of the model. Pump-probe experiments provide a more direct description.

## 10.4

### Electric Field-Assisted Pump-Probe

The pump-probe technique is the basic answer for studying photoinduced phenomena in the temporal domain. Its concept is very simple and straightforward. A pump excites the sample at time zero. A probe, at any later time, interrogates the modified material, providing a time-dependent description of the pump-induced changes. Time resolution is only limited by pulse duration and not by the electronics, through the optical correlation scheme. The technique can, at least in principle, address both radiative and non-radiative processes. In particular it is relevant to the application described here that charged states, which usually have well-defined spectroscopic signatures in organic semiconductors, could be directly monitored, as is true for any other excitation. In the process of neutral state dissociation, for instance, one may obtain a full description, whereby neutral state population depletion and charge state formation are directly measured, at variance with indirect techniques such as PL quenching. The drawback is the low sensitivity of the experiment; certainly lower than PL. Essentially the constraint derives from the fact that, in pump-probe experiments, one collects small amplitudes on top of a large signal. In addition, the experimental setup is of considerable complexity. In order to have suitable pump and probe pulses, broad range tunability is required, while keeping the time duration comparable throughout the entire spectrum. Details on the experimental technique concerning both pulse generation and detection can be found in a number of review papers and books; see, for instance, Ref. [25].

#### 10.4.1

##### Interpretation of the Pump-Probe Experiment

The pump-induced relative transmission change, differential transmission  $\Delta T$ , is measured by a lock-in amplifier, which is referenced to the modulated pump pulse train and normalized to yield  $\Delta T/T$ . On a first level the interpretation of this experiment can be done by disregarding coherent effects (these require the full third-order nonlinear response function in the field interaction picture), focusing on the population dynamics. From the previous discussion on the nature of the excited state, it is convenient to adopt a simple approach, which is straightforward, where one considers well-defined “states” and associated populations. These can be excitons with delocalized wavefunctions or localized molecular states. Let us

consider an electronic transition between two levels,  $i$  and  $j$ . The absorption coefficient is  $a_{ij}(\lambda) = \sigma_{ij}(\lambda)(N_i - N_j)$ , where  $\sigma_{ij}(\lambda)$  is the cross-section (in  $\text{cm}^2$ ), containing the dipole moment of the transition and the lineshape and  $N_i$  and  $N_j$  are the populations of the initial and final states, respectively. Accordingly, we find  $a > 0$  for absorption,  $a < 0$  for gain (i.e. when  $N_j > N_i$ ). This expression can be extended to a set of levels as

$$a = \sum_{ij} \sigma_{ij}(\lambda)(N_i - N_j) = \sum_j \left[ \sum_i \sigma_{ij}(\lambda)N_j \right] \quad (10.4)$$

In the last sum we take  $\sigma$  as positive for upward transitions and negative for downward transitions. Grouping index as in Eq. (10.4) counts all the final states  $i$  for each starting state  $j$ . The pump pulse acts on the sample by changing level occupation,  $N_i \rightarrow N_i(t)$ , where  $t$  is the time and  $N_i$  the equilibrium population (which is zero for most cases, except the ground state). With appropriate initial conditions, the time-dependent population can be obtained from rate equations such as

$$\frac{dN_i}{dt} = G_i(t) - R_i(t) \quad (10.5)$$

where  $G(t)$  and  $R(t)$  are the generation and deactivation rate, respectively. For instance, if the state  $i$  is directly populated by the pump pulse via one photon transition from the ground state, the generation term will be

$$G_i(t) = \sigma_{0i}N_0(t)I_{\text{pu}}(t) \quad (10.6)$$

where  $\sigma_{0i}$  is the cross-section for the one-photon transition  $0 \rightarrow i$ ,  $N_0(t)$  the time-dependent ground-state population, which gets depleted, and  $I_{\text{pu}}(t)$  the temporal pump photon intensity distribution, usually being approximated by a Gaussian function of temporal width  $\tau_p$ .

The measured quantity is the normalized change in probe transmission. For a delta-like probe pulse (time duration much shorter than any dynamics in the material), the expression derived from the Beer–Lambert relation within a small signal approximation turns out to be

$$\frac{\Delta T}{T} = - \sum_{ij} \sigma_{ij}(\lambda)\Delta N_j(t)d \quad (10.7)$$

where  $d$  is the sample thickness;  $j$  describes all possible excited states, irrespective of their charge or spin state, including each vibrational replica of the bare electronic ones and  $\Delta N_j$  is the pump-induced change of population. The spectrum associated with the state (or species)  $j$  is  $A_j(\lambda) = \sum_i \sigma_{ij}(\lambda)d$  and Eq. (10.7) can be

also written as  $\Delta T/T = -\sum_j A_j(\lambda)N_j(t)$ , an expression often used in global fitting analysis. This equation shows that the typical  $\Delta T/T$  signal is a superposition of individual contributions from several photoexcited states. Analogously to the case of photokinetics under cw irradiation, time-dependent data must be taken at various probe wavelengths in order to single out the various contributions. If the pulse duration is of the order of the observed decay kinetics, the correct behavior is obtained by working out the correlation  $\Delta N_j(t) \otimes I_{\text{pu}}(t)$  with the probe pulse time profile  $I_{\text{pu}}(t)$ .

Out of a huge number of states, only those transitions between dipole-coupled states have non-negligible cross-section, hence the expression usually contains a limited number of terms. In addition, it is of interest only for the wavelength range actually explored by the probe pulse, so few transitions have to be considered in practice. For  $j=0$ , ground-state depletion is depicted, named photobleaching (PB). PB corresponds to positive  $\Delta T$  and has the spectral shape of ground-state absorption when thermalization, which is usually very fast, is over. For all the other levels ( $j>0$ ) both upward and downward transitions are possible [i.e.  $A(\lambda)$  can be positive and negative]. In particular, transitions from a level populated by the pump pulse to a higher lying level give rise to photoinduced absorption (PA). One should keep in mind, however, that internal conversion normally is very fast (about 100 fs), so in most cases one probes the thermalized sample with occupation of the lowest states only. When the lowest singlet excitation ( $S_1$ ) is dipole-coupled to  $S_0$ , i.e. the system is luminescent, stimulated emission (SE) is taking place. Yet this does not mean that positive  $\Delta T$  is necessarily observed in the region of emission, as it depends on the spectral overlap with other absorbing transitions (often there) and on the relative cross-sections involved. As a result, SE may not appear at all even in light-emitting materials.

Here we shall focus on a number of materials that have been thoroughly studied: We will present results for two different polymers, methyl-substituted ladder-type poly(*p*-phenylene) (m-LPPP) and polyfluorene (PFO). Since the torsional motion of the former is blocked synthetically, a comparison of these two materials will give insight into the influence of conformational degrees of freedom on charge carrier photogeneration and -recombination. We will also give results on two samples of short oligomers: trimers of oligo(phenylenevinylene) (3PV) and polyfluorene (3F8). Comparing the results obtained in polymers with those obtained in short oligomers will allow us to separate 1D (on-chain) processes from higher dimensional (off-chain) processes. Chirp-free  $\Delta T/T$  spectra of all those compounds are shown in Fig. 10.9 at 1 ps pump-probe delay. All compounds show a PA peak below the optical band-gap in the near-infrared spectral region, assigned to the  $S_1 \rightarrow S_n$  transition. The second peak below the optical bandgap, but in the visible spectral region, is assigned to charged states. Approaching the optical bandgap, positive  $\Delta T/T$  signals are obtained due to SE and in the case of m-LPPP also due to PB. All the spectra conform to a universal behavior, shifted from one another owing to differences in effective conjugation length. m-LPPP, where inter-ring torsional motion is hampered, shows superior

spectral resolution, indicating that indeed intra-chain conformers are major source of disorder. Also evident is the better resolution in oligomers (see the spectrum for 3PV), even if the analogous comparison with 3F8 and PFO is not so striking, owing to the disorder typical of the solid-state phase of oligofluorenes.

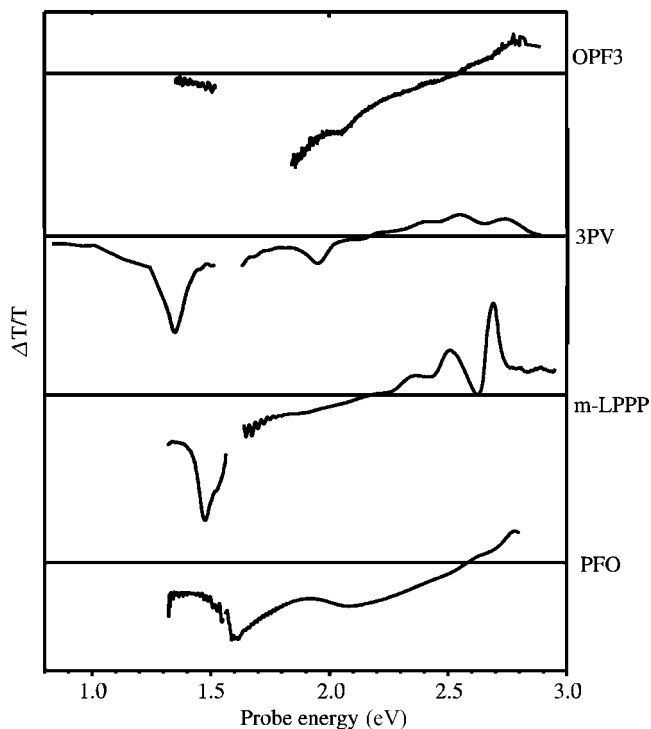


**Figure 10.9** Chirp-free transient absorption spectra of different compounds are shown at 1 ps probe delay.

#### 10.4.2

##### Interpretation of the Electric Field-Assisted Pump-Probe Experiment

Considering Eq. (10.7) as our starting point, let us now assume that an electric field is applied to the sample, then the change in  $\Delta T/T$  due to the electric field is  $(\Delta T/T)_F - (\Delta T/T)_0$ , expressed as

$$\frac{\Delta^2 T}{T} = - \sum_{ij} \Delta(\sigma_{ij} \Delta N_j d) = - \sum_{ij} \Delta \sigma_{ij}(\omega) \Delta N_j d - \sum_{ij} \sigma_{ij}(\omega) \Delta^2 N_j d \quad (10.8)$$

The first term comprises changes in the cross-section of the transitions involved, due to electroabsorption of the ground state and/or excited states. The second term represents changes in the population. This will, for instance, account for sin-

plet state dissociation ( $\Delta N_s < 0$ ) and charge formation ( $\Delta N_p > 0$ ). The square differential indicates the two perturbation factors acting on the sample, the pump beam and the electric field. To understand correctly the meaning of the sign in  $\Delta^2 T$ , Fig. 10.10 reports two examples. The reduction of the  $\Delta T/T$  signal, when an electric field is applied to the device, results in a  $\Delta^2 T/T$  with an opposite sign with respect to that without field (see Fig. 10.10a). An increase in the  $\Delta T/T$  signal instead results in a  $\Delta^2 T/T$  with the same sign with respect to that without field (see Fig. 10.10b). In the experiment we replace the chopper modulating the pump in standard devices with an a.c. voltage source applied to the diode sample. In this way the lock-in signal detects only changes in  $\Delta T/T$  due to the field.

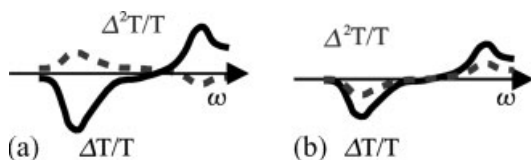


**Figure 10.10** Comparison between pump and probe ( $\Delta T/T$ ) and electromodulated pump and probe ( $\Delta^2 T/T$ ) signal as discussed in the text.

### 10.4.3

#### Review of Experimental Results

We discuss experimental results obtained for long-chain polymers with extended  $\pi$ -delocalization (m-LPPP and PFO) and in short-chain oligomers [trimers of oligo(phenylenevinylene) (3PV) and polyfluorene (3F8)]. In both the effect of the electric field is understood in terms of population changes due to ionization of neutral states. Comparison of results from polymers and short oligomers will enable us to discriminate inter-chain processes (possible in both oligomers and polymers) from on-chain processes (possible only in polymers whose conjugated segments exceed the extension of neutral and charged excited states). However, owing to the mixed scenario prevalent in polymers, the distinction cannot be absolutely clear-cut.

#### 10.4.3.1 Methyl-Substituted Ladder-Type Poly(*p*-Phenylene) (m-LPPP)

m-LPPP is commonly used as active layer in LEDs device and its photophysics is well known [26]. Figure 10.11 shows the absorption, the luminescence spectrum and the chemical structure of the polymer. Different excitation densities ( $1.2 \text{ mJ cm}^{-2}$  in Ref. [27] and  $14 \mu\text{J cm}^{-2}$  in Ref. [28]) have been used and different electric field strengths were applied ranging between  $0.5$  and  $2 \text{ MV cm}^{-1}$  to study the photophysics of this polymer under an applied field. Graupner et al. [27] were the first to use the field-assisted pump-probe technique to observe directly charge formation by singlet exciton breaking in the prototypical conjugated polymer

m-LPPP. They used a polymer film placed between two electrodes, ITO (indium tin oxide) and aluminum. Figure 10.12 shows the field-induced transient absorption at different probe delays obtained by collecting white light spectra with and without applied field. The dashed line represents the cw absorption spectrum of the charged states created by chemical doping of the polymer for reference.

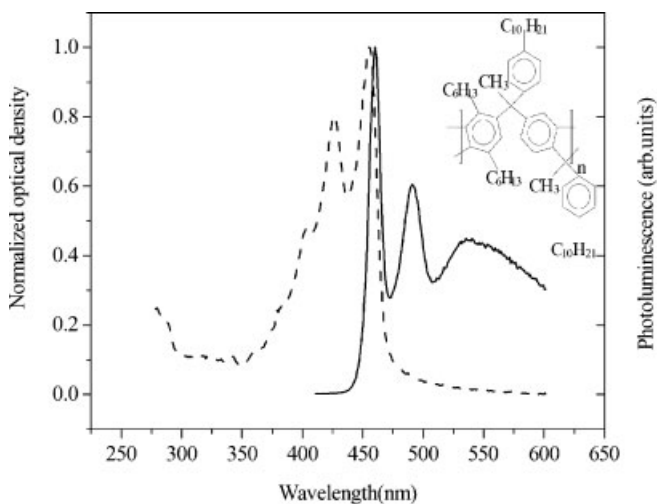


**Fig. 10.11** Absorption (dotted line) and photoluminescence (solid line) spectra of methyl-substituted ladder-type poly(*p*-phenylene) (m-LPPP; chemical structure in the inset).

The comparison suggests a straightforward interpretation: singlet excitons are ionized forming charged (polaron) states. The reduced singlet population is detected as a lower singlet absorption ( $\Delta T^2 > 0$  below 1.8 eV) and lower SE ( $\Delta T^2 < 0$  above 2.3 eV). Graupner et al. observed a quadratic field dependence of polaron generation. The rate of dissociation of singlets into polaron pairs,  $\gamma(t)$ , was derived directly from the experimental data, so to avoid any dependence on mathematical modeling. The result is a time-dependent rate, which shows higher value at the beginning, decaying to a plateau in about 5 ps; see Fig. 10.13. Hence, the action of two different charge generation mechanisms was suggested. One is highly dispersive and takes place within the first 5 ps. The other is only weakly time dependent and persists for the whole lifetime of the  $S_1$  states. A possible contribution of polaron generation by bimolecular singlet annihilation has been suggested by other authors [29]. Note, however, that in the original work by Graupner et al. no intensity dependence was detected. The initial rate could then be assigned to a hot, non-equilibrium state. One possibility is CPG driven by exciton migration towards lower energy sites within the disorder-induced density of state (DOS). During such thermalization hot excitons reach “dissociation sites” whereby charge generation takes place either on-chain or inter-chain. With this

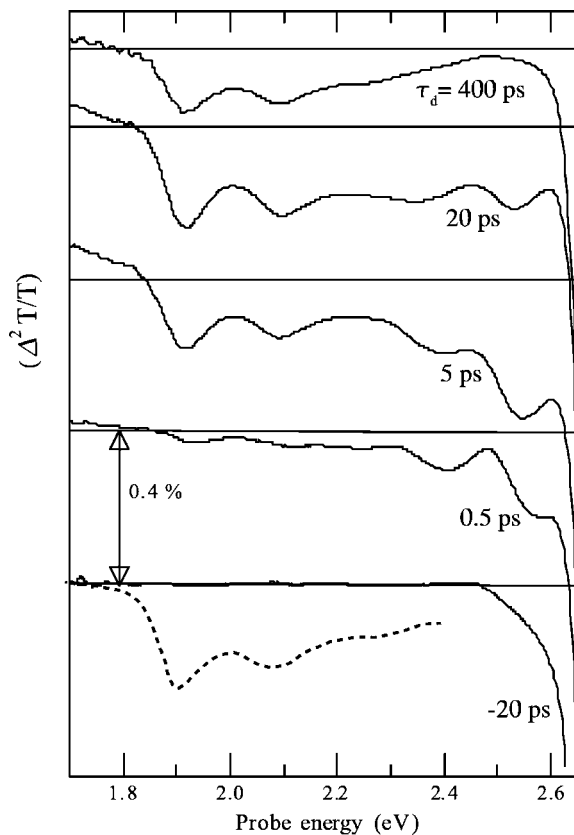


**Figure 10.12** Field-induced transient absorption of m-LPPP at different probe delays are shown. The spectrum shown by a dashed line represents the absorption spectrum of the charges created by chemical doping of the polymer.

model, CPG is reduced once the excitons have reached the bottom of their density of states distribution and their mobility is very low. Alternative vibrational energy dissipation may set the required time-scale, assuming that locally hot chains, i.e. with excess phonon energy, have higher dissociation rates.

In Fig. 10.14, we compare the time-dependent charge generation rates  $\gamma(t)$  obtained on the polymer m-LPPP using different excitation pump wavelengths  $\lambda_{\text{exc}}$  and excitation energy density  $E_{\text{pump}}$ . It is evident that for  $t > 3$  ps, the value is almost constant at  $\sim 0.01 \text{ ps}^{-1}$ . This is a nice proof of the reliability of the methods of measurement and also for sample preparation. The fact that the  $\gamma(t)$  value remains constant for most of the decay time points to the low level of energetic dispersion in the m-LPPP films. The measurements differ in the early time regime of  $t < 3$  ps. Weak time dependence is found if the samples are pumped at both low intensity [29] and energy [28]. In contrast, a strong time dependence of  $\gamma(t)$  is found upon pumping at either high intensity [27] or high energy [29]. Note

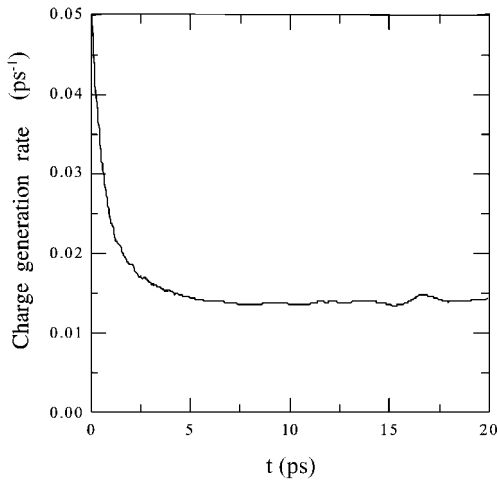


**Figure 10.13** Time dependence of the field-induced dissociation rate of singlets into polaron pairs,  $\gamma(t)$ .

that higher intensity may lead to multi-photon transitions, while higher photon energy directly populates higher lying states. In both cases, excess energy is provided, which is the key point: this helps charge separation. Be this purely electronic, assisted by disorder or due to the phonon bath remains to be assessed.

An interesting variation of the field-induced pump-probe experiment was performed by Gulbinas et al., who looked at the Stark shift in the photobleaching spectral region of the  $\Delta^2 T/T$  spectra [30]. Since the latter refers to the ground state,

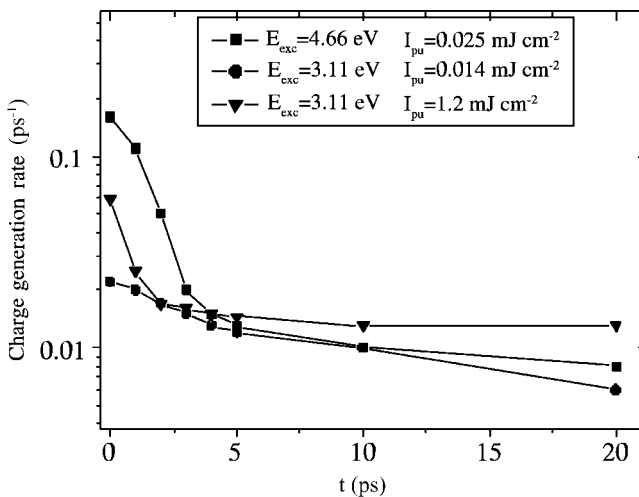


**Figure 10.14** Time-dependent charge generation rates  $\gamma(t)$  obtained on the polymer m-LPPP using different excitation pump wavelengths  $\lambda_{\text{exc}}$  and excitation energy densities  $E_{\text{pump}}$ . ■ and ●: data taken from [30].

the population contribution [last sum in Eq. (10.8)] can be neglected in this case and only the field-induced variation of cross-sections is observed. Gulbinas et al. monitored the transient Stark shift of the ground-state absorption in m-LPPP to gain insight into the temporal and spatial evolution of photogenerated but still coulombically bound charged pairs. They were able to trace the increase in the average intra-pair distance from 0.6 to 3 nm in an interval of 800 ps. Modeling of the phenomenon allows extracting information on the carrier mobility in a clean, contactless way.

#### 10.4.3.2 Polyfluorene

Polyfluorene has been studied because of its large use in different applications such as LEDs, photodiodes and solar cells. Figure 10.15 shows its absorption and photoluminescence band (in the inset its chemical structure is shown). The excitation density used by Virgili et al. [31] to study the photophysics of this polymer under an applied field of  $1.7 \text{ MV cm}^{-1}$  is  $0.39 \text{ mJ cm}^{-2}$ . In PFO the generation of charges from singlet breaking is instantaneous (limited by the temporal duration of the pulse), with an estimated efficiency of 3%. Figure 10.16 shows the corresponding  $\Delta^2 T/T$  for the PFO LED at two different probe delays, namely 2 ps (filled squares + solid line) and 200 ps (filled triangles + dashed line). The resulting spectral variations help to identify the origin of the field-induced changes in the visible and near-infrared regions at fixed pump-probe delay.

At a 2 ps probe delay, the  $\Delta^2 T/T$  signal is negative at wavelengths corresponding to the stimulated emission (SE) and charges photoinduced absorption ( $\text{PA}_2$ ) and positive in the region of the  $\text{PA}_1$  band due to neutral singlets. These results are readily interpreted: the electric field within the LED dissociates singlet states and consequently reduces SE and  $S_1$ - $S_n$  absorption ( $\text{PA}_1$ ). There is a corresponding increase in the signal at 580 nm ( $\text{PA}_2$ ), which indicates that polarons result from

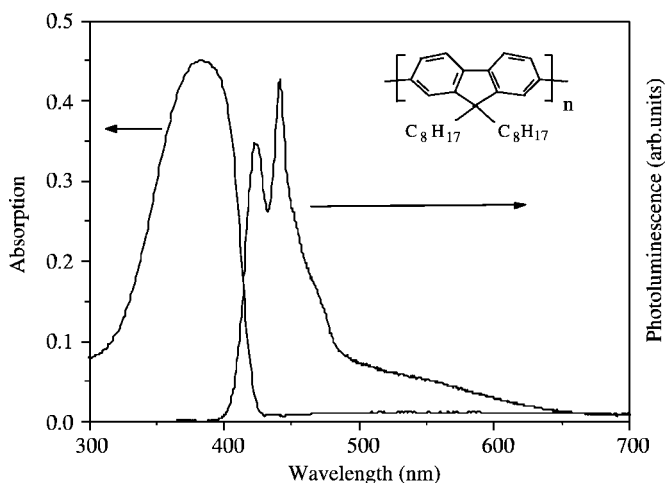


**Fig. 10.15** Absorption and the photoluminescence spectra of polyfluorene (PFO). The inset shows its chemical structure.

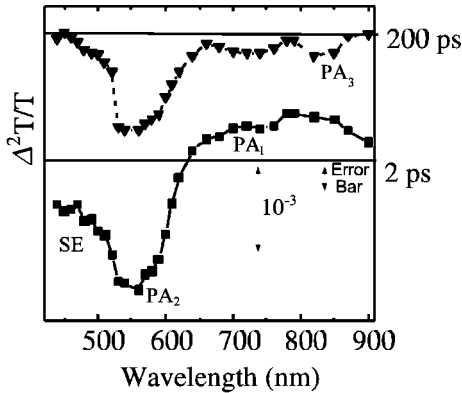


**Figure 10.16** Field-induced transient absorption ( $\Delta^2 T/T$ ) spectra at different pump-probe delays for a PFO light-emitting diode.

singlet dissociation. At a 200 ps probe delay the  $\Delta^2 T/T$  signal at the  $PA_2$  band position decreases in strength. The  $\Delta^2 T/T$  signal at SE wavelengths is no longer apparent, indicating that changes in the singlet population are recovered. There is, however, an interesting change of sign for the  $\Delta^2 T/T$  signal in the spectral region beyond 650 nm. This indicates the presence, at long probe delays, of a new absorption band (labeled  $PA_3$ ), apparently not correlated with SE and singlets.

These features are more evident from the data in Fig. 10.17, which shows the temporal evolution of the (normalized)  $\Delta^2 T/T$  signal at two wavelengths: 680 nm (solid line) and 820 nm (open squares and line). The inset shows the corresponding evolution of the (normalized)  $\Delta T/T$  signal (no field applied) at the same wavelengths. Whereas in the latter case both signals have the same dynamics, consistent with their common origin in the singlet exciton population, the two  $\Delta^2 T/T$  signals show different behavior. The signal at 820 nm changes sign after about 50 ps at which point that at 680 nm has already decayed to zero. The transitions responsible for the negative  $\Delta^2 T/T$  signal therefore cannot be attributed to the singlet exciton population. A triplet PA band has been observed in the same wavelength range by Cadby et al. [32] using (quasi-) steady-state photoinduced absorption spectroscopy. This result allows us to postulate that the new  $PA_3$  absorption band arises from the formation of a triplet population, in about 50 ps, by non-geminate recombination of the initially field-induced polarons. Geminate recombination of singlet polaron pairs cannot lead to triplet states on this time-scale for at least two reasons; the spin flip rate for doublet states has a time-scale of the order of 1  $\mu$ s [33], and intersystem crossing in PFO is negligible.

With this interpretation it is possible to model the  $\Delta^2 T/T$  data to determine the efficiency,  $\beta$ , for polaron recombination into singlets and hence also that for triplet generation ( $1 - \beta$ ). The formation of triplet states in the presence of an external field can be rationalized by the generation of free charges from singlet dissociation due to the applied electric field (see Fig. 10.18).

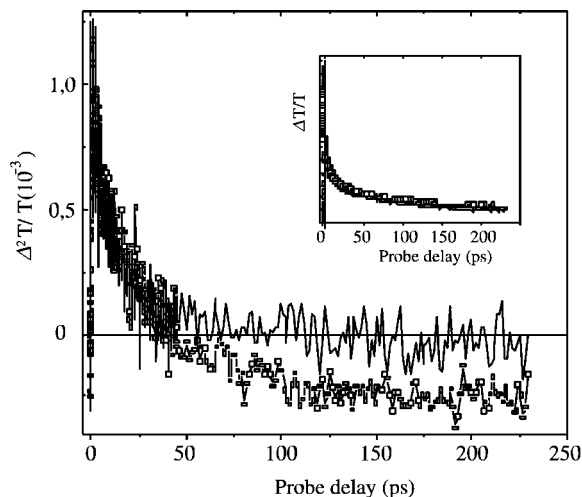
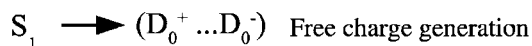


**Figure 10.17** Temporal evolution of the (normalized)  $\Delta^2 T/T$  signal at two wavelengths: 680 nm (solid line) and 820 nm (open squares and line). The inset shows the corresponding evolution of the (normalized)  $\Delta T/T$  signal (no field applied) at the same wavelengths (same symbols are applied).

Electric field dissociation of neutral singlet states



Field-induced polaron recombination:

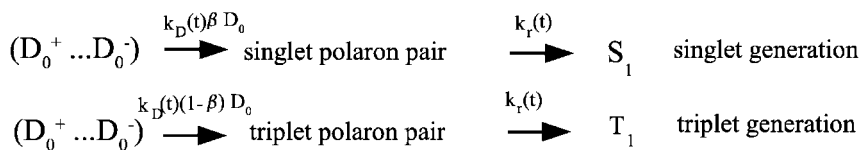


**Figure 10.18** Schematic diagram of field-induced processes in PFO films.

These charges, in a very short time, undergo a *pairing* process. Such intermediate pairs will eventually decay, without further interaction, into lowest neutral states (singlets and triplets). During the pairing of the free charges a fraction  $\beta$  will form singlet polaron pairs and the remaining ones will form triplet polaron pairs. With this numerical fitting to the experimental data it is possible to find the value of the branching ratio  $\beta$  if one assumes that all the dissociated singlets generate free pairs. This is, however, a rather strong proposition.

Figure 10.19 shows the decay traces of the polaron population at 580 nm in an LED structure ( $\Delta^2 T/T$ ) with an applied field at three different excitation densities:  $1.67 \text{ mJ cm}^{-2}$  (filled squares),  $0.44 \text{ mJ cm}^{-2}$  (open squares) and  $0.18 \text{ mJ cm}^{-2}$  (solid

line). Even though the population of polarons grows with excitation density, showing that saturation is not taking place, the decay kinetics do not change. This is due to the fact that bimolecular recombination occurs on the excitation time-scale (200 fs), whereas what is observed is the recombination of monomolecular pairs, possibly owing to intra-pair electron tunneling.

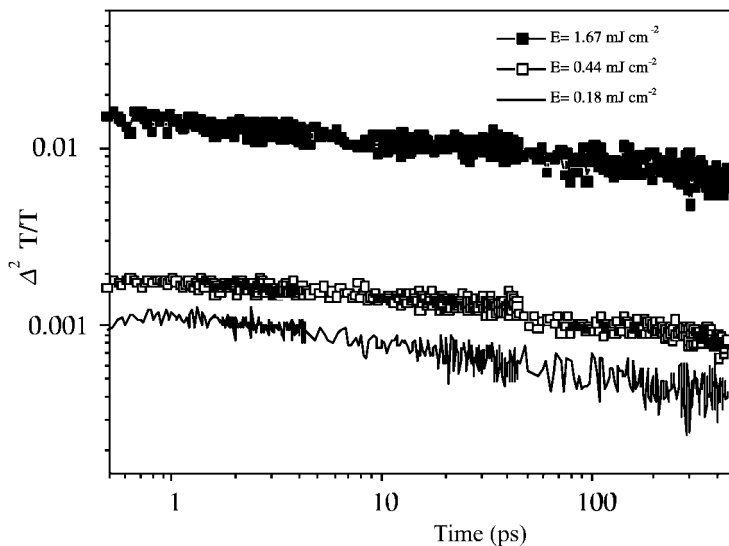


**Figure 10.19** Field-induced decay traces ( $\Delta^2 T/T$ ) of the polaron population at 580 nm in a PFO LED structure at three different excitation densities: 1.67 (filled squares), 0.44 (open squares) and 0.18 mJ cm<sup>-2</sup> (solid line).

A kinetic analysis of the  $\Delta T/T$  and  $\Delta^2 T/T$  decay traces was carried out in order to extract quantitative information, in particular on the polaron recombination rate and the corresponding singlet–triplet branching ratio (see Fig. 10.18). Since the dependence of the  $\Delta T/T$  decay kinetics on pump pulse intensity is weak, we exclude any significant contribution from bimolecular decay channels to the  $\Delta T/T$  decay kinetics of singlets. It is assumed that under the influence of an electric field, predominantly free charge carriers  $D_F$  during the pump pulse are formed, which subsequently undergo non-geminate *pairing* according to second-order kinetics with rate constant  $k_D$  to form singlet and triplet polaron pairs in a ratio  $\beta/(1 - \beta)$ . Since the initial concentration of free carriers is about  $10^{18}$  cm<sup>-3</sup>, the mean separation of charge carriers is  $r_{av} \approx 10$  nm. This is less than the typical Coulomb capture radius in films of pure hydrocarbons,  $r_c \approx 20$  nm. Therefore, each charge carrier is subject to multiple interactions with non-geminate carriers. The prevalence of non-geminate recombination shows that the initial intrapair separation  $r_0$  must be larger than  $r_{av}$ , which can be explained by the high amount of excess energy due to the sequential excitation mechanism and by the initial delocalization of the 1D singlet exciton. Free carriers can thus interact given their

high mobility; this early charge carrier mobility ( $\mu$  is estimated by the Langevin law [ $\mu = \epsilon\epsilon_0 k_d(t)/(2e)$ , where  $e$  is the unit charge,  $\epsilon\epsilon_0$  is the dielectric constant and  $k_d(t)$  is the rate coefficient of the dispersive motion of the polarons] to be  $5 \text{ cm}^2 \text{ V}^{-1} \text{ s}^{-1}$ . This population of polaron pairs decays with first-order kinetics at a rate  $k_r(t)$  [the time dependence of the rate constant  $k_r(t)$  is  $k_r(t) = k_{r,0.2 \text{ ps}} (t/1 \text{ ps})^{-m}$ ] to singlet and triplet states. This decay does not depend on the pump intensity as seen in Fig. 10.19. The singlet efficiency,  $\beta$ , can be varied in order to fit  $\Delta^2 T/T$ , once other parameters are determined by fitting the no-field ( $\Delta T/T$ ) data and the  $\Delta^2 T/T$  polaron data. The best fit is found for  $\beta = 0.7 \pm 0.1$ . Under the approximation discussed above, this work finds a  $\beta$  value that is unquestionably larger than the 0.25 expected for a spin-independent recombination process. Qualitatively, this is consistent with the results of Wohlgenannt et al. [34], namely  $\beta = 0.57$ , as exhaustively discussed in Section 10.5.

#### 10.4.3.3 Fluorene Trimers (3F8)

The absorption and the photoluminescence spectrum of 3F8 amorphous films together with its chemical structure are shown in Fig. 10.20. Both spectra are blue shifted with respect to the polymer as a consequence of the smaller size of the conjugation length. In this short  $\pi$ -conjugated system, ultrafast on-chain dissociation is prevented since its short conjugation length is insufficient to accommodate two separated charged quasi-particles.

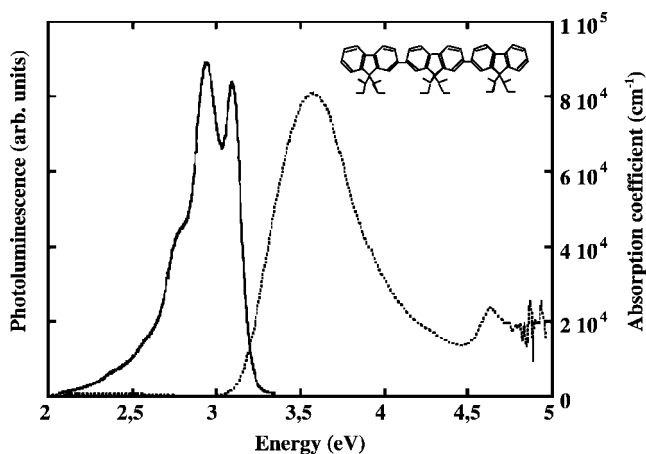
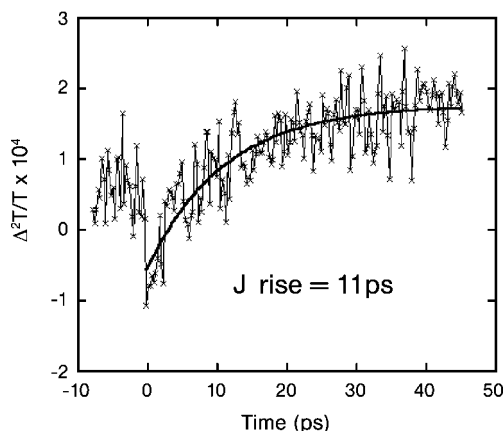


Fig. 10.20 Absorption and the photoluminescence spectra of the oligomer 3F8 is shown. The inset shows its chemical structure.

Comparison between 3F8 [35] and PFO provides a very different scenario. First, in 3F8 we detected a Stark shift of the excited state electronic transition. In PFO, a Stark shift is not observable owing to superposition with instantaneous changes of the singlet and polaron populations via a sequential mechanism. At early time-

scales the electric field pump–probe dynamics are characterized by an instantaneous negative signal attributed to Stark shift of the upper lying energy levels; see Fig. 10.21. The negative sign of  $\Delta^2 T/T$  implies a field-induced increase in excited state absorption motivated by the shift of the excited state transitions towards lower energies. The magnitude of the change  $\Delta a$  of the absorption coefficient  $a$ , taking into account the value of the electric field ( $F$ ) and the quadratic Stark shift, is

$$\Delta a \approx ca + \frac{1}{2} \Delta p F^2 \frac{\partial a}{\partial E} + \dots \quad (10.9)$$

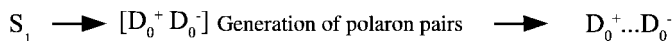


**Figure 10.21** Instantaneous shift experienced by the dynamics at 1.5 eV under an electric field. The 11 ps rise was calculated from a fit of the type  $A - B \exp(-t/\tau)$ . Redrawn after Ref. [36].

For the difference in polarizability between the initial and final states, a value of  $\Delta p = 0.43 \times 10^{-19} \text{ eV m}^2 \text{ V}^{-2}$  was obtained [36]. This value is  $\sim 15$  times lower than the difference in polarizability between the  $1A_g$  and  $1B_u$  states of PFO [37] and in the range of polarizabilities which have been reported in other conjugated systems such as *p*-(hexaphenyl) (PHP) [38]. Note that pump–probe spectroscopy is employed as a complementary technique to conventional electroabsorption. While the latter provides information on ground-state transitions, here we obtain the field-induced change of excited state transitions.

Regarding the singlet dissociation process in 3F8, the electric field-induced effect is never instantaneous as a first difference with the polymer. Second, there is evidence for field-induced polaron-pairs as precursor species of free carriers, as depicted in Fig. 10.22. The field-induced charge generation can be described by a two-step process consisting of singlet splitting into intermediate polaron pairs and their further dissociation into free carriers. The estimated efficiency of singlet splitting into polaron pairs, under similar experimental conditions to those used in PFO, is a factor of 6 smaller, around 0.5%. The dissociation yield into free

Electric field dissociation of neutral singlet states:



Field-induced free charge recombination:

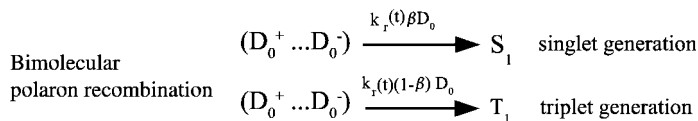


**Figure 10.22** Schematic diagram of field-induced processes in 3F8 films.

carriers from the intermediate pair is as high as about 50%, indicating that the binding energy is appreciably lower in these pairs with respect to on-chain excitons. Thereby, the total quantum yield for free carrier generation under an applied field is only 0.25%, one order of magnitude lower than PFO. Figure 10.23a shows the electric field pump-probe dynamics at 2.2 eV (560 nm) where charges are placed and Fig. 10.23b shows the electric field pump-probe dynamics at 1.5 eV (820 nm) where the PA band of singlets appears. The fit according to the model above is shown by the solid line. On the basis of this process, a certain number of polaron pairs undergo geminate recombination towards  $S_1$ , therefore being lost for free carrier photogeneration. The result is a lower free polaron population, which reduces the effects of fast bimolecular recombination. Dissociation of singlets proceeds gradually in the trimer, extending over timescales beyond 50 ps.

From the comparison between PFO and 3F8, it appears that ultrafast dissociation (via sequential excitation) is peculiar to long conjugated segments. This suggests that the process is intra-chain, as recently confirmed by experiments on isolated PFO chains [39].

#### 10.4.3.4 Oligo(phenylenevinylene)s

Different from the materials considered so far, OPV films have nanocrystalline morphology. This implies that there is crystal physics, with peculiar excitation and propagation phenomena and interface, boundary physics, similar to what was discussed before with 3F8, which is amorphous. Thin films of oligo PPV (3PV) were prepared by high-vacuum deposition on to ITO glass substrates [40]. Partially ordered thin films were obtained, also including amorphous regions. The chain length is short enough, so that on-chain formation of geminate pairs can be excluded. From detailed photophysical investigations, it was demonstrated that charge pairs are formed during the pump pulse by a sequential mechanism [40]. Here collective excitation within the crystal compensates for the lack of intra-chain interaction, and for this reason the process of charge separation should be inter-chain. Figure 10.24b shows the transient transmission spectra of the oligomer, without electric field, at different probe delays. The spectra are characterized by

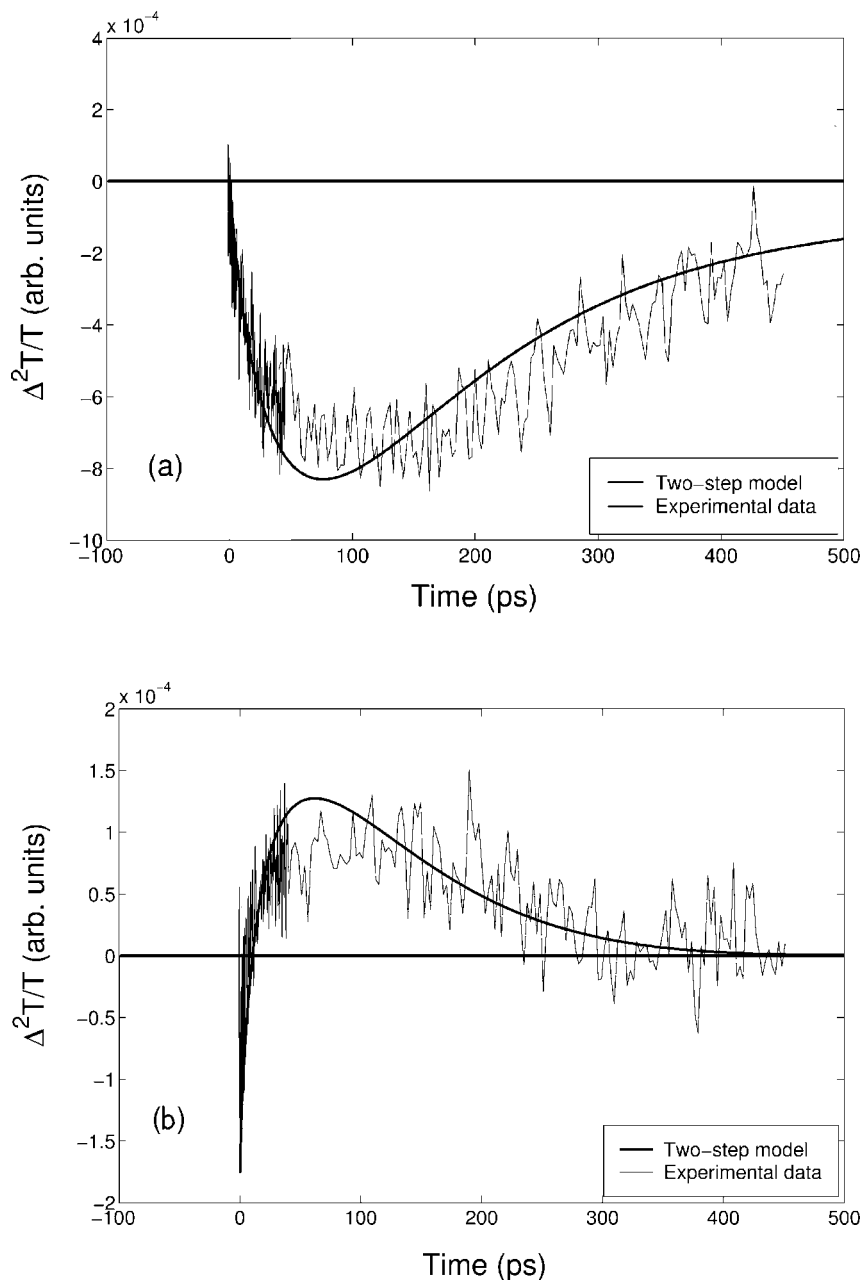


**Figure 10.23** Field-induced decay traces ( $\Delta^2 T/T$ ) in 3F8. (a) At 560 nm (polaron absorption); (b) at 820 nm (absorption of singlet state). Smooth lines give numerical fits according to the model described in the text.

three different photoinduced absorption bands: the first one is centered at 630 nm is due to triplet-triplet absorption; the second one at 900 nm is assigned to photoinduced absorption from the  $S_1$  state; the third one is at around 1400 nm representing the lowest electronic polaron transition. During the first 250 fs after excitation, geminate recombination of charged pairs can be observed (see Fig. 10.26d; compare also Fig. 10.35). After that time the decay of charged pairs is nongeminate and dispersive. The early charge carrier mobility is estimated by the Langevin law (see above) to be  $0.02 \text{ cm}^2 \text{ V}^{-1} \text{ s}^{-1}$ . Geminate recombination requires the initial separation distance  $r_0$  of charge pairs be smaller than the average distance  $r_{av}$  between pairs. This distance can be estimated as inverse of the initial density of charged states, the latter being related to the amplitude of the associated PA and it was found to be between 4 and 12 nm, depending on pump intensity. Since geminate recombination was observed up to the highest applied pump intensities, it follows that in 3PV  $r_0$  must be smaller than 4 nm.

Fig. 24a shows the transient transmission spectrum of the oligomer with an applied electric field at different probe delays. In the presence of a strong electric field ( $1 \text{ MV cm}^{-1}$ ), photoinduced charges and triplet generation are enhanced on the expense of the population of the thermalized singlet excitons (see Fig. 10.26a). Field-induced singlet exciton breaking is a bimolecular process in the singlet population and competes with singlet annihilation (a schematic diagram of those proposed mechanism is shown in Fig. 10.25). Direct electron transfer between two relaxed  $S_1$  states is proposed as the underlying mechanism. In ordered oligomer

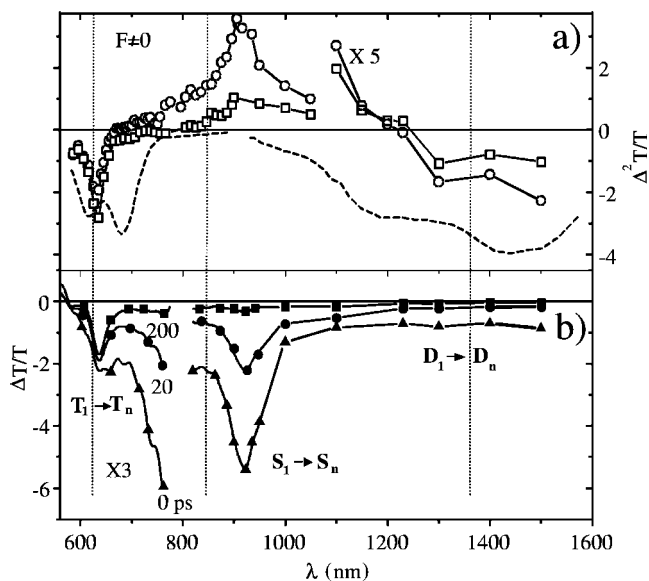


**Figure 10.24** Pump and probe spectra of 3PV at various pump probe delays, as indicated. (a) Field-induced differential transmission ( $\Delta^2 T/T$ ); (b) differential transmission  $\Delta T/T$

without applied field. The nature of the transitions is indicated. Dashed line:  $3PV^+$  cations of single molecules adsorbed on silica gel.

samples the dispersion is weak, the corresponding density of states (DOS) profiles are very sharp and significantly higher field strengths are necessary to equalize the state energies of singlet and charged states. Field-induced CPG in oligomer samples can therefore only proceed with the energy of two  $S_1$  states.

**Electric field dissociation of neutral singlet states**

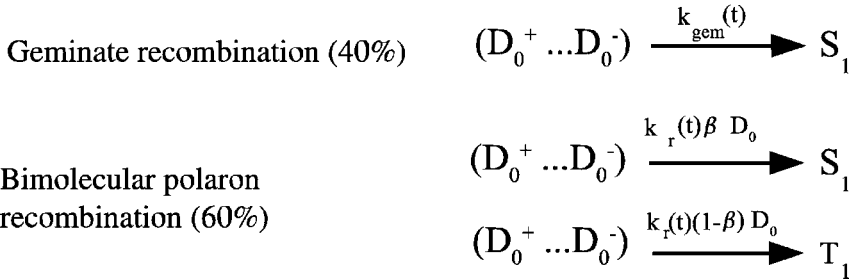
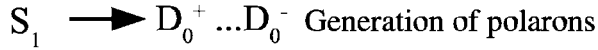


**Figure 10.25** Schematic diagram of field-induced processes in 3PV films.

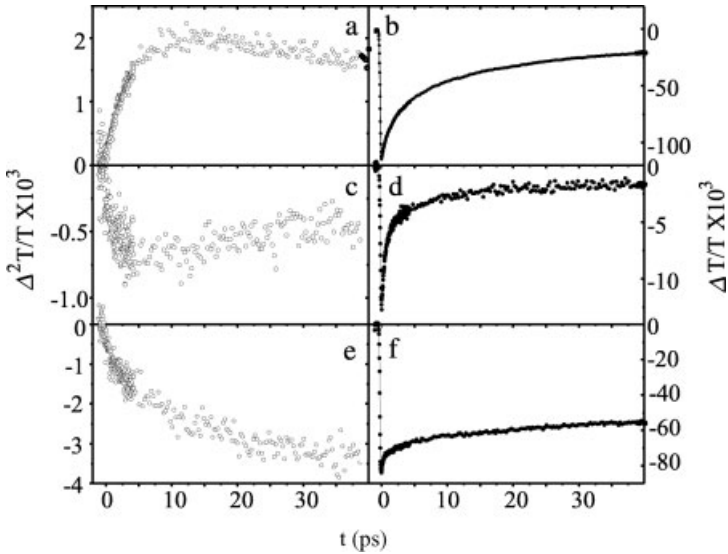


**Figure 10.26** Pump-probe decay traces in 3PV at fixed probe wavelengths: (a, b) 870 nm (singlet absorption); (c, d) 1400 nm (polaron absorption); (e, f) 630 nm (triplet absorption with singlet contribution). (a, c, e) Field-induced differential transmission ( $\Delta^2 T/T$ ); (b, d, f) differential transmission without field ( $\Delta T/T$ ).

## 10.5

### Photocurrent Cross-Correlation: Real-Time Tracing of Mobile Charge Carrier Formation

Photocurrent cross-correlation (PCC) is a variation of the pump–probe technique discussed before. Instead of interrogating the electronic spectra of the pump-induced photoexcitations by a delayed white probe pulse, we record the change in steady-state photocurrent induced by the action of a delayed narrow-band pulse. Since photocurrent is brought about by mobile charge carriers, this technique enables us to study the *precursor-specific formation of mobile charge carriers with femtosecond resolution* (a possible displacement current due to ultrafast polarization of neutral species will be suppressed if the external RC response is much slower than the lifetime of these species [41]). Mobile charge carriers are interesting because, they form the working principle of photovoltaic cells [42, 43]; they can escape geminate recombination and become trapped and therefore live for hours [44]. These long-lived polarons decrease the efficiency of organic lasers [45] and field-effect transistors [46]. It is therefore important to study by which processes mobile charge carriers are formed and how they recombine or become trapped. Moreover, since PCC is precursor specific, the mobile charge carriers can also be used to *probe the state of the precursor*, e.g. during dispersive motion. Important issues that are to be addressed for device optimization are the amount of the exciton binding energy, the importance of energetic dispersion for the formation of mobile charge carriers and the importance and characteristics of geminate and nongeminate recombination.

If femtosecond laser pulses are absorbed by a semiconductor connected to two electrodes, we will be able to measure a photocurrent, given by

$$I_{\text{PC}} = AE \left( n\mu_n + p\mu_p \right) e \quad (10.10)$$

where  $A$  is the active electrode area,  $E$  the electric field strength,  $e$  the unit charge,  $n$  and  $p$  are the concentrations of positive and negative polarons, respectively, and  $\mu_n$  and  $\mu_p$  are their respective mobilities. Unfortunately, electronic circuitry is not capable of real-time tracing the photocurrent after pulsed irradiation with femtosecond resolution. The relaxation time of an electrical circuit is given by  $\tau = 1/RC$ . In sandwich structures terminated with  $50\ \Omega$ ,  $\tau > 10$  ns. Working in surface cell alignment with a  $50\text{-}\Omega$  transmission line, relaxation times down to 25 ps can be realized owing to very small capacitive areas [47]. However, problems with internal and external photoemission arise in this setup [48], which must be dealt with by working in an atmosphere of  $\text{SbF}_6$  and  $\text{CO}_2$  [49]. Furthermore, most charge generation pathways take place in the femtosecond to lower picosecond regime, being out of reach for direct electrical kinetic measurements.

These problems can be circumvented if instead of the temporally resolved photocurrent, its time-averaged value is monitored during pulsed laser irradiation. Femtosecond temporal resolution is obtained if the average photocurrent caused by two femtosecond laser pulses is studied as a function of the time delay between

the two laser pulses. Depending on its wavelength, the second pulse will remove or re-excite photoexcitations that have been generated by the first pulse. A concomitant change in average photoconductivity due to these actions can therefore be used to study specific formation pathways of mobile charge carriers with femtosecond temporal resolution. In this way, the formation of mobile charge carriers by exciton dissociation and exciton re-excitation has been studied. Mobile charge carriers can also be formed by re-excitation of charged states. These results will be presented in the following. Before that, we discuss the general setup for the measurement of photocurrent cross-correlation and present a general theory for the observed signal.

### 10.5.1

#### Experimental Setup

The setup for the measurement of photocurrent cross-correlation is analogous to the pump-probe spectrometer shown in Fig. 10.1. However, instead of broadband “white” pulses, monochromatic pulses of various wavelengths are being used as probe pulses. Typically, optical parametric amplifiers are used to provide for tunable monochromatic pulses. The fundamental beam (typically of a Ti:sapphire laser with photon energy at 1.6 eV) can also be used directly as a second pulse; this pulse is resonant with singlet-singlet absorption in the materials under consideration; see Fig. 10.9. Both pump and probe beams are brought to overlap on the sample, which consists of a semiconducting material sandwiched between two electrodes. One of these should be at least semi-transparent; often ITO is used as a transparent anode. Usually, both electrodes are connected to the current input of a lock-in amplifier without an external voltage source; the built-in field of sandwich cells with different anode and cathode (the authors give values around  $F = 10^4 \text{ V cm}^{-1}$ ) is used as a driving force. The lock-in amplifier is referenced to a mechanical chopper that periodically blocks the probe pulse train. The signal is therefore the effect of the probe pulse on the photoconductivity. Some authors use a slow chopper frequency ( $f \approx 20 \text{ Hz}$ ) [41], whereas some remove every second probe pulse ( $f \approx 500 \text{ Hz}$ ) [50].

Alternative approaches are described in the literature. Instead of using a lock-in-technique, it is also possible to read out the total averaged photocurrent [51]. In this case, the time trace is usually normalized to its value for negative pump-probe delay (i.e. when the pump arrives *before* the probe). In order to draw quantitative conclusions, often the pump-probe differential transmission is recorded for comparison. Some authors record the integrated fluorescence as a function of pump-probe delay to trace the probe-dependent singlet exciton concentration [51, 52].

### 10.5.2

#### Photocurrent Cross-Correlation: the Signal

For simplicity, let us assume that the chopper frequency is set exactly to half of the pulse frequency so that every second probe pulse is blocked. A lock-in ampli-

fier determines the amplitude and phase of the Fourier component with the reference frequency. If the probe pulse has any influence on the measurable photocurrent, the input signal will be current decay traces of alternating height and kinetics, depending on whether the probe pulse is blocked or not. The amplitude of the Fourier component in this case is given by the difference in the *average* photocurrent if the probe is on or off. The definition of the photocurrent cross-correlation is as follows:

$$\Delta I = v_{\text{rep}} \left[ \int I_{\text{on}}(\tau) d\tau - \int I_{\text{off}}(\tau) d\tau \right] = v_{\text{rep}} (G_{\text{on}} - G_{\text{off}}) \quad (10.11)$$

where  $\tau$  is the elapsed time since the arrival of the pulses (since the time constant of the electronic circuit is in the nanosecond range, the ultrashort pump–probe delay need not be considered here),  $v_{\text{rep}}$  is the laser repetition rate (1000 Hz),  $I_{\text{on}}(\tau)$  and  $I_{\text{off}}(\tau)$  are the current decay traces with the second beam on or off, respectively, and  $G_{\text{on}}$  and  $G_{\text{off}}$  are the areas under the current traces  $I(\tau)$  with the probe pulse on or off, respectively.

Since we are going to study the generation of free charge carriers, we are interested in the functional dependence of  $\Delta I$  on the change of the initial concentration of free charge carriers,  $\Delta c_0 = \Delta(n_0 + p_0) = c_0^{\text{on}} - c_0^{\text{off}}$ , generated by the second pulse, before any recombination takes place. However, the integrals  $G_{\text{on}}$  and  $G_{\text{off}}$  in Eq. (10.11) extend over the whole current decay trace and therefore will contain also recombination information. Since in general, recombination will be affected by a change in  $c_0$ ,  $G$  will be a nonlinear function of  $c_0$  with unknown behavior. However, every differentiable nonlinear function can be approximated by a straight line on short intervals. This is the core of the *small-signal limit*: As long as  $G_{\text{on}} - G_{\text{off}} \ll G_{\text{off}}$ ,

$$\Delta I/I \approx a \Delta c_0 / c_0 \quad (10.12)$$

where  $a$  is the slope of the  $G(c_0)$  curve. If the dependence of  $G$  on  $c_0$  is linear, then  $a = 1$ . In this case, the relative change in photocurrent equals the relative change in free carrier concentration.

### 10.5.3

#### Precursor Populations and the Precursor-Specific Free Carrier Yield

Equation (10.12) enables us to trace  $\Delta c_0$ , the free carrier concentration change induced by the probe pulse, via the observation of  $\Delta I/I$ . The probe pulse will induce population changes among the precursor states for free charge generation. It can *push* singlet and triplet excitons to form higher excited states (Section 10.5.4), it can *dump* excited states to the ground state via stimulated emission (Section 10.5.5) and it can *detrap* polaron pairs to form free charge carriers (Section 10.5.6). Figure 10.27 gives an overview on the precursors that form free charge carriers and on the interaction of these precursors with probe pulses of appropri-

ate energy. Free charge carriers can be formed from hot singlet states  $S_n$ , from thermalized singlet states  $S_1$  and also from detrapped polaron pairs PP. The efficiencies of these paths (given as dashed lines in Fig. 10.27) are defined by

$$c_0^i(t) = \int_{t'=0}^t \beta^i(t') c_p^i(t') dt' \quad (10.13)$$

where  $i = S_n, S_1$  or PP and  $\beta^i(t)$  and  $c_p^i(t)$  are the time-dependent efficiency and precursor concentration of path  $i$ , respectively. The quantity  $c_0^i$  is the population of free charge carriers generated by path  $i$  from the moment of precursor formation (pump pulse at  $t = 0$ ) up to time  $t$ , such that

$$c_0(t) = \sum_i c_0^i(t) \quad (10.14)$$

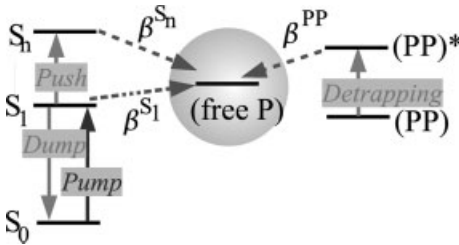


**Figure 10.27** Change of free polaron population by action of second laser pulse (dashed arrows) on the precursors.

By comparing the temporal evolution of precursor population (accessible via pump–probe or time-resolved fluorescence measurements) with that of  $\Delta I_{CC}$ , it is thus possible to obtain the temporal evolution of the *precursor-specific free carrier yield*  $\beta^i(t)$ . This is an important material property, because it allows one to verify postulations on charge carrier formation and separation mechanisms.

#### 10.5.4

##### Stimulated Emission Dumping

In this type of experiment, a fraction of the  $S_1$  population that have been generated by the pump pulse are “dumped” back to the ground state. Since we know that only the  $S_1$  population will be influenced by the action of the dump pulse, we can write

$$\Delta c_0 = c_0^{\text{on}} - c_0^{\text{off}} = \eta [c_0^{S_1}(t_0) - c_0(\infty)] + \sum_{i \neq S_1} c_0^i(\infty) \quad (10.15)$$

with  $\eta$  as the dump efficiency, defined as

$$\eta = 1 - \left[ \lim_{t \rightarrow t_0^+} c_p^{S_1}(t) / \lim_{t \rightarrow t_0^+} c_p^{S_1}(t) \right] \quad (10.16)$$

and  $t_0$  is the pump-dump delay. We stress that  $t_0$  is very small (femtoseconds to picoseconds) compared with  $\tau$  in Eq. (10.11) (microseconds), so it need not be considered there. Equation 10.15 can be made plausible considering Fig. 10.28: if the dumping is complete,  $\eta = 1$ , then the  $S_1$  population is brought to zero at  $t_0$ . The final population of free charge carriers produced by singlet dissociation is the one that had been reached up to  $t_0$ :

$$c_0^{S_1}(\infty) = c_0^{S_1}(t_0) \tag{10.15a}$$

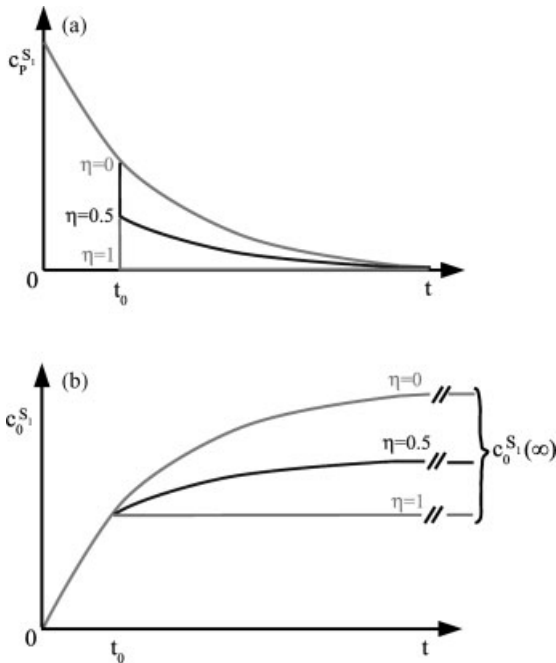


**Figure 10.28** Illustration of Eqs. (10.8) and (10.9): at time  $t_0$ , the dump pulse reduces the  $S_1$  population (a), depending on the dump efficiency  $\eta$ . As a consequence, also the concentration of free carriers formed by  $S_1$  states increases more slowly.

If  $\eta < 1$ , then a fraction of the  $S_1$  population will still be able to increase  $c_0^{S_1}$  even after the dump pulse. The decay of  $S_1(t)$  as well as the build-up of  $c_0^{S_1}(t)$  after  $t_0$  will therefore be compressed replicas of the dump-free case at  $\eta = 0$ . This leads straightforwardly to Eq. (10.15). We must, however, be sure that  $S_1$  decay does not depend on the initial population, i.e. we must exclude bimolecular annihilation. On the other hand, even if the  $S_1$  decay shows non-Markovian behavior, Eq. (10.15) remains perfectly valid. Introduction of Eq. (10.15) into Eq. (10.12) gives

$$\Delta I/I(t_0) = a\eta [c_0^{S_1}(t_0)/c_0(\infty) - 1] + \sum_{i \neq S_1} c_0^i(\infty)/c_0(\infty) \tag{10.17}$$

Rothberg et al. were the first to study the formation of mobile charge carriers with 300 fs time resolution in 1995 [51]. The material under investigation was MEH-PPV, in the form of a thin film spun on to interdigitated electrodes. Tuning the probe pulse to the stimulated emission region, the authors were able to dump a certain amount of the singlet exciton population. Sampling the average fluorescence intensity, the efficiency of this dumping was obtained as a function of pump-dump delay in the form of relative dump-induced photoluminescence quenching ( $\Delta PL/PL$ ). In parallel, they recorded the relative dump-induced change in photoconductivity ( $\Delta I/I$ ). They found that dumping part of the excited states to the ground state results in a *decrease* in the average photoconductivity. This clearly shows that singlet excitons can form mobile charge carriers by exciton breaking. Since the photocurrent varies linearly with applied voltage, it is concluded that the exciton breaking is not field-assisted; this is in accordance with measurements shown by Kersting et al. [24]. At  $t = 0$ , when pump and dump pulses arrive at the same time,  $\Delta PL/PL \approx \Delta I/I(t = 0)$  was obtained: a removal of 7% of the singlet excitons directly after formation results in a decrease of 7% of average photoconductivity (see Fig. 10.29). In other words, the dumping efficiency equals the negative photocurrent cross-correlation:

$$\Delta I/I(t = 0) = -\eta \quad (10.18)$$

Inserting Eq. (10.18) into Eq. (10.17) yields

$$-\eta = \eta[0/c_0(\infty) - 1] + \sum_{i \neq S_1} c_0^i(\infty)/c_0(\infty), \quad (10.19)$$

where the condition  $a = 1$  has been verified by the authors. Equation (10.19) can be solved only if the sum term is zero. Therefore, Rothberg et al. concluded that *dissociation of thermalized singlet excitons is the predominant pathway for the generation of mobile charges in MEH-PPV*.

The charge generation efficiency is not constant throughout the singlet exciton lifetime: whereas  $\Delta PL/PL$  describes the exciton decay with a lifetime in the range of 50 ps,  $\Delta I/I(t)$  approaches zero at much shorter times; see Fig. 10.29. We can obtain a normalized generation efficiency by rewriting Eq. (10.13) for an efficiency normalized to its value at  $t = 0$ :

$$\frac{\beta^{S_1}(t)}{\beta^{S_1}(0)} = \frac{-[dc_0^{S_1}(t)/dt]^{\text{norm}}}{[dc_p^{S_1}(t)/dt]^{\text{norm}}} \quad (10.20)$$

The denominator of Eq. (10.20) is experimentally accessible via time-resolved stimulated emission (SE) or photoluminescence (PL) measurements. The numerator is obtained simply as the normalized first derivative of the photocurrent cross-correlation; see Eq. (10.16).

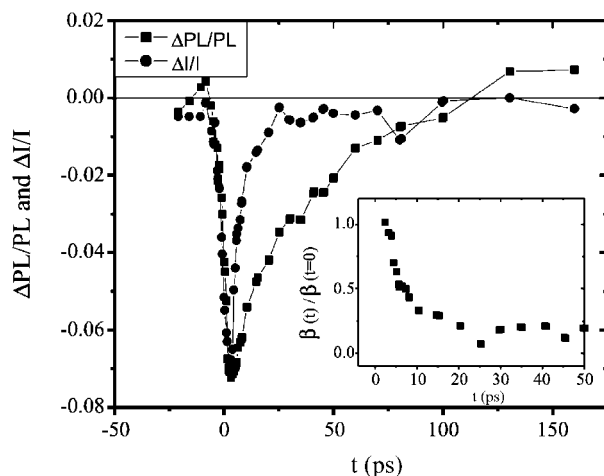


**Figure 10.29** Dump-induced change in photoluminescence,  $\Delta PL/PL$  (squares) and photocurrent  $\Delta I/I$  (circles) in an MEH-PPV film. The relative time-dependent charge carrier generation yield,  $\beta(t)/\beta(t=0)$ , calculated according to Eq. (10.13), is given in the inset. Redrawn after Ref. [51].

The free carrier yield, calculated according to Eq. (10.20), decreases to about one-tenth of its initial value on a time-scale of 20 ps; see inset in Fig. 10.29. It is concluded that the singlet exciton can only generate mobile charge carriers as long as it is still furnished with excess energy. Since a linear dependence on pump pulse energy was measured, a possible contribution of bimolecular singlet annihilation to mobile charge carrier formation can be excluded. The loss of excess energy is readily explained by dispersive hopping of the singlet excitons in a distribution of site energies [53]. As long as the exciton is energetically near the center of the distribution, there will be sites nearby with lower energy so that the exciton binding energy  $E_b$  can be furnished. However, once arrived at the low-energy end of the distribution, the exciton will be surrounded by states where charge carrier formation is at least on the expense of  $E_b$  or more; the fact that very few free charge carriers are formed after a few picoseconds suggests that  $E_b \gg kT$ .

It is interesting to compare the results of Rothberg et al. with more recent findings by Müller et al. [52]. They performed the same measurements in films of m-LPPP. Owing to its rigid structure, this material is expected to show much less dispersion effects than other polymers. Müller et al. used very low pump pulse intensities to exclude bimolecular exciton annihilation. At  $t = 0$ , a dumping of 2.5% of the singlet excitons to the ground state results in a reduction of photoconductivity by 1.8%, as shown in Fig. 10.30. Analogously to the case of MEH-PPV, this shows that dissociation of excitons is the prominent channel for mobile charge carrier formation.

The kinetics of  $\Delta PL/PL$  is given by an exponential function with a time constant of  $\tau \approx 180$  ps, see Fig. 10.30. The kinetics of  $\Delta I/I$  are given by an exponential func-

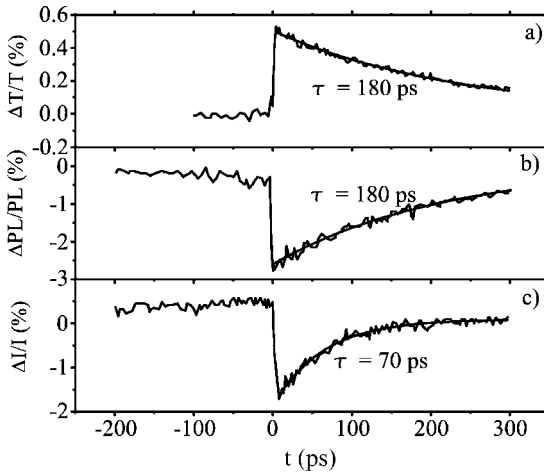


**Figure 10.30** Transient signals in MLPPP measured with the second laser pulse tuned to 2.49 eV. (a) Differential transmission; (b) photoluminescence changes due to the second pulse; (c) photocurrent changes due to the second pulse versus time delay after

excitation, normalized to the value observed in the absence of the second pulse. Both beams are polarized parallel to each other. Solid lines are exponential fits with time constants displayed in the figure. Redrawn after Ref. [52]).

tion as well, however with a time constant of  $\tau \approx 70$  ps, being much smaller than the one measured for  $\Delta PL/PL$ . This result is analogous to the one obtained by Rothberg et al. [51]. Applying Eq. (10.19) using curves (b) and (c) in Fig. 10.30 would result in an exponential function for  $\beta(t)/\beta(t=0)$  with a 115 ps decay time. However, Müller et al. explained this discrepancy between  $\Delta I/I$  and  $\Delta PL/PL$  by assuming different spatial origins for the respective signals: whereas  $\Delta PL/PL$  is a bulk effect, only those excitons in the vicinity of the Al electrode contribute to PC. Therefore,  $\Delta I/I$  samples the exciton decay near to the Al electrode, being enhanced due to electrode quenching. Following this line of reasoning, singlet excitons close to the Al electrode generate mobile charge carriers with constant efficiency throughout their entire lifetime,  $\beta(t) = \beta(t=0)$ . This finding is strictly different from the result of Rothberg's group (Rothberg et al. [51] did not need to consider this phenomenon because they used interdigitated electrodes, where the photocurrent is predominantly a bulk effect due to the much larger electrode spacing compared with the sandwich structures used by Müller et al. [52]). A charge carrier generation efficiency which is independent of exciton excess energy can either be explained by a vanishing exciton binding energy or by additional free energy which is not decreasing on the time scale of exciton decay. Since many experimental facts place  $E_b$  higher than  $kT$  [54], the first hypothesis is discarded. Additional free energy can either be furnished by traps or by the electric field. However, if dispersive motion prevails then traps cannot explain a time-independent generation efficiency because exciton mobility decreases over time. Therefore, the authors suggested field-induced exciton breaking. In consequence, it

must be concluded that in m-LPPP, the exciton binding energy is much lower (or tunneling is much more efficient) than in PPV, where substantially higher field strengths are needed to observe field-induced exciton breaking [24]. From the viewpoint of device technology, this suggests that the degree of dispersion and/or molecular orientation might be a powerful tool to customize this important parameter. Comparative morphology-dependent studies are highly in demand to clarify this possibility further.

### 10.5.5

#### Formation of Mobile Charge Carriers by Re-Excitation (Pushing) of Singlet Excitons

In this type of experiment, the probe pulse is tuned to the lowest energetic excited state absorption of the singlet exciton. Thus, part of the singlet states are “pushed” to form a higher lying neutral excitation  $S_n$  with an excess energy of 1.2–1.6 eV, depending on the material. Since  $E_b$  is typically below 1 eV, one expects that from this state,  $\beta_{S_n}(t)$  is much higher than  $\beta_{S_1}(t)$  from the singlet exciton if the competing thermalization mechanisms are not too efficient. In fact, three-pulse experiments [55] in polymers as well as near-infrared pump–probe data in oligomers [40] demonstrate the importance of excess energy in charge carrier generation. Since the lifetime of the  $S_n$  states is of the order of the pulse widths or shorter, the action of the push pulse at time  $t_0$  can be described by a delta pulse generating a certain amount of higher excited singlet states  $S_n$ :

$$S_n(t_0) = \sigma_{ps} I_{ps} S_1(t) \quad (10.21)$$

where  $\sigma_{ps}$  is the cross-section of the  $S_1 \rightarrow S_n$  transition and  $I_{ps}$  the intensity of the push pulse. Without measurable time delay, these  $S_n$  states decay back to the  $S_1$  state leaving a certain amount of free charge carriers  $c^{S_n}(t_0)$ . It is therefore appropriate to define the free charge carrier yield in an integral manner:

$$\beta(t_0) = c^{S_n}(t_0)/S_n(t_0) \quad (10.22)$$

According to this definition, the free carrier yield depends on the time  $t_0$  when the  $S_n$  states have been created. A possible additional time dependence of the differential free carrier yield during  $S_n$  is not considered since only the resulting free carrier concentration  $c(t_0)$  after complete  $S_n$  decay has been experimentally accessed. Under consideration of Eqs. (10.21) and (10.22), the relative free charge carrier yield from  $S_n$  dissociation is simply obtained by

$$\frac{\beta(t)}{\beta(t=0)} = \frac{c^{S_n}(t)}{S_1(t)} \cdot \frac{S_1(t=0)}{c^{S_n}(t=0)} \approx \left( \frac{\Delta I}{I} \right)_t / \left( \frac{\Delta T}{T} \right)_{t,\text{norm}} \quad (10.23)$$

where  $(\Delta T/T)_{t,\text{norm}}$  is the normalized differential transmission in the  $S_1 \rightarrow S_n$  optical transition, which in the small signal limit is proportional to the normalized  $S_1$  population. Equation (10.23) is similar to Eq. (10.20); however, no derivatives are

involved. Furthermore, the constraint of monomolecular exciton decay, required in the derivation of Eq. (10.20), is not necessary here.

Photocurrent-cross-correlation experiments generally show an enhancement of the photocurrent upon re-excitation of the singlet exciton [16, 50, 56, 57], although a decrease may sometimes be observed [58]. In general, the kinetics of  $\Delta I_{PC} = f(t)$  deviate from the kinetics of singlet exciton decay, monitored via its time-dependent differential transmission. The deviations are explained either by assuming a time-dependence of the charge carrier generation efficiency  $\beta(t)$  or by assuming different spatial regions being sampled by the respective probes.

Photocurrent cross-correlation by re-excitation of singlet excitons in m-LPPP films was investigated by a number of authors. In all cases, it is found that the strongest  $\Delta I/I$  enhancement is at  $t = 0$ . It can reach values up to 60%. Since the pump and push pulse intensities are known, one can arrive at an estimate for the enhancement of mobile charge carrier formation. Zenz et al. [50] estimated an enhancement by a factor of 7. This in turn sets the upper limit of the mobile charge carrier generation efficiency *without* re-excitation to 15%. This value is in accordance with that published by Müller et al. (5–25%) [52].

Lanzani et al. [59] and Zenz et al. [50] show that  $\Delta I/I$  decays much faster than the singlet exciton concentration  $\Delta T/T$ ; see Fig. 10.31. The relative free charge carrier yield, calculated according to Eq. (10.16), is given in the inset. It decays to one-fifth of its initial value during 4 ps. A biexponential fit to  $\beta(t)$  yields an ultrafast ( $\tau_1 = 0.5$  ps) and a slower ( $\tau_2 = 9$  ps) time constant. The question arises why the free carrier yield from  $S_n$  dissociation, as given here, should depend on the time of their formation. A direct energetic memory effect can be excluded: even if the energy of the  $S_n$  state depends on the energy of its precursor  $S_1$  state, it should not influence the charge carrier yield. The re-excitation of even the energetically relaxed  $S_1$  state would yield 1.4 eV of excess energy, more than enough to form free charge carriers. However, the energy of the precursor  $S_1$  influences also its mobility. The time dependence of  $\beta(t)$  can therefore be explained straightforwardly by an *indirect energetic memory effect* if one assumes that an  $S_1$  state must be mobile in order to dissociate. The authors therefore concluded that the presence of trap sites is necessary to generate free charge carriers and identify the “dark zone” near the Al electrode as the origin of the mobile charge carriers. In this zone, the luminescence is efficiently quenched by additional traps and by energy transfer to the electrode itself [60]. The biexponential decay is rationalized by the assumption of two temporally separated charge generation pathways. They assume that, in order to generate mobile charge carriers, the exciton must reach a dissociation center. The generation efficiency will therefore be intimately related to the exciton mobility. The fast process with a time constant of  $\tau \approx 0.5$  ps is therefore given by an exciton still near the center of the DOS and thus very mobile, whereas the slow process refers to immobile excitons that have reached the low-energetic tail of the DOS. Re-excitation does not change the mobility but allows charge carrier formation in case a dissociation center is encountered. The authors show that  $\beta(t)$  decays with the same kinetics as the anisotropy of the differential transmission; see inset of Fig. 10.31. Time-dependent anisotropy loss in solid films is a secure

probe for exciton motion, if bimolecular annihilation can be excluded [61]. The results suggest that at least for the first 4 ps, a decrease in exciton mobility can be inferred. A slight error in the calculation of  $\beta(t)$  arises from the fact that  $\Delta T/T$ , as used in Eq. (10.22), is proportional to the integral  $S_1$  decay. Assuming a strongly confined spatial region with enhanced exciton decay as the zone of free charge carrier generation, makes it necessary to use a probe for  $S_1(t)$  in that same region in order to calculate  $\beta(t)$ . Such a probe is difficult to obtain.

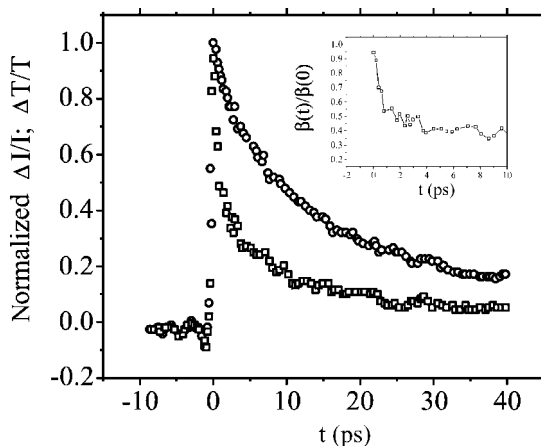


**Figure 10.31** Normalized  $\Delta T/T$  and  $\Delta I/I$  traces (circles and squares, respectively) in m-LPPP at a probe photon energy of 1.6 eV singlet state absorption. In the inset, the free charge generation efficiency  $\beta(t)$ , normalized to its value at  $t = 0$ , is given.

Lüer et al. investigated photocurrent cross-correlation in oligo-phenylenevinylene (OPV) films [57]. They applied high pump pulse intensities so that bimolecular exciton annihilation is the most prominent exciton decay channel; the underlying mechanisms have been quantified in several studies [35, 62]. The authors measured both  $\Delta I/I$  and  $\Delta T/T$  upon re-excitation of the singlet exciton analogously to the experiments previously described for m-LPPP. They found an increase in PC upon singlet exciton re-excitation with a maximum at  $t = 0$  where the exciton concentration was highest. The probe pulse energy was adjusted such that the experiment stayed within the low-signal limit. Comparing the kinetics of the cross-correlation and the differential transmission gave the opposite result as in the case of m-LPPP:  $\Delta I/I$  decays more slowly than  $\Delta T/T$  (Fig. 10.32). The same holds true for the comparison of the anisotropy loss of both signals. Obviously, the application of Eq. (10.22) would yield a free charge carrier yield  $\beta(t)$  that increases over time. Such a behavior is not easy to justify physically. The authors present a different explanation for the discrepancy between  $\Delta I/I$  and  $\Delta T/T$  assuming that mobile charge carriers are only formed in a thin sheet near the Al electrode. This is the same assumption as made by Müller et al. [52] and by

Zenz et al. [50]; however, the presence of bimolecular singlet annihilation provides a probe for this assumption in this case: Since the electrode is illuminated through the ITO electrode and absorption of the pump pulse is strong, the singlet exciton concentration is lowest in the vicinity of the Al back electrode. In the case of bimolecular annihilation, the decay in the vicinity of the Al electrode will be slower than the spatial average. In 3PV, bimolecular annihilation causes  $S_1(t)$  kinetics of the form [[62]

$$S_1(t) = \left[ 1/S_1(t=0) + \frac{\beta}{kA\tau^2} + \frac{\beta}{\kappa AA\tau} \right]^{-1} \quad (10.24)$$

Normalized reciprocal traces are then

$$\frac{S_1(t=0)}{S_1(t)} = 1 + S_1(t=0) \left( \frac{\beta}{kA\tau^2} + \frac{\beta}{\kappa AA\tau} \right) \quad (10.25)$$

In Eq. (10.25), the starting population  $S_1(t=0)$  scales the slope of the curves retaining the overall curve form. As is shown in Fig. 10.33, the reciprocal representation of  $\Delta I/I$  can be nicely projected on to the reciprocal representation of  $\Delta T/T$  by applying a factor of 1.7 to its time-dependent part. According to Eq. (10.25), this can be interpreted in the following way: both  $\Delta I/I$  and  $\Delta T/T$  trace bimolecular exciton decay and hence show curves of the form of Eq. (10.25); however, the starting  $S_1$  population sampled by  $\Delta T/T$  (bulk of film) is a factor of 1.7 higher than that sampled by  $\Delta I/I$  (region near backside Al electrode where starting population is less according to the Beer–Lambert law). The good congruence of this model with experiment makes the assumption of a time-dependent free charge carrier yield unnecessary. A constant value for  $\beta(t)$  is in accordance with the low level of energetic dispersion in polycrystalline films of short oligomers. From geometric considerations, the authors arrived at a higher factor than 1.7; they discussed possible reasons for this discrepancy.

The measured anisotropy decay, as displayed in Fig. 10.32c, presents additional proof for the above model. It is known that in samples with crystalline domains, bimolecular annihilation can induce intensity-dependent anisotropy loss [61]: those crystallites with their transition moments parallel to the exciting light vector will show the highest initial exciton density but will also be subject to the fastest annihilation. At low-level excitation, anisotropy loss in similar OPV films is on the order of several hundred picoseconds [63]. In contrast, the anisotropy loss of the  $\Delta T/T$  signal proceeds on the order of 10 ps. This clearly shows that in 3PV, anisotropy loss is indeed intensity dependent. Since the anisotropy loss of the  $\Delta I/I$  signal is much slower than that of  $\Delta T/T$  (but still much faster than that obtained at low-level excitation), this presents an additional hint that the starting population sampled by the  $\Delta I/I$  signal is lower than that sampled by  $\Delta T/T$ .

In conclusion, the literature considered shows that re-excitation of singlet excitons leads to a strongly enhanced generation of mobile charge carriers. It is demonstrated in several ways that photoconductivity in sandwich-type devices is not a

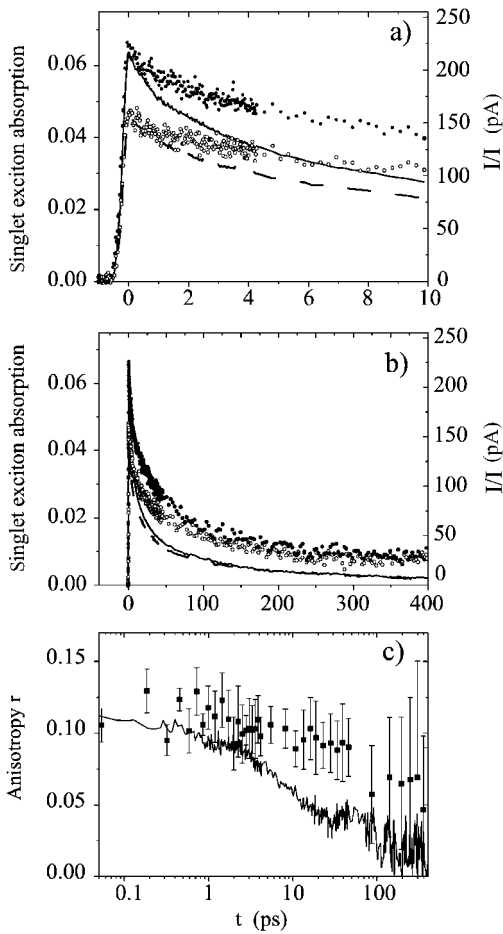


**Figure 10.32** Decay curves of  $\Delta I/I$  (symbols) and absorption of the singlet exciton at 1.45 eV (lines), measured with pump and push beams polarized parallel (full symbols/solid lines) and perpendicular (open

symbols/dashed lines). (b) Same as (a) on a longer time-scale. (c) Anisotropy of singlet exciton absorption at 1.45 eV (line) and  $\Delta I/I$  at a push energy of 1.6 eV (symbols with error bars).

bulk effect but originates from only a small sheet near to the Al electrode. It seems that in materials of strong dispersion of site energies, the efficiency for mobile charge carrier formation decreases over time, whereas in the more ordered samples of m-LPPP and in 3PV, the efficiency is constant. A time-dependent efficiency in the case of exciton re-excitation cannot be explained by a single-step process. Owing to dispersive motion in a distribution of site energies, the exciton will on average lose energy during its motion. However, irrespective of the actual exciton energy at a given time, the push pulse will always supply enough energy for the formation of a polaron pair. However, it will depend on the *surrounding*

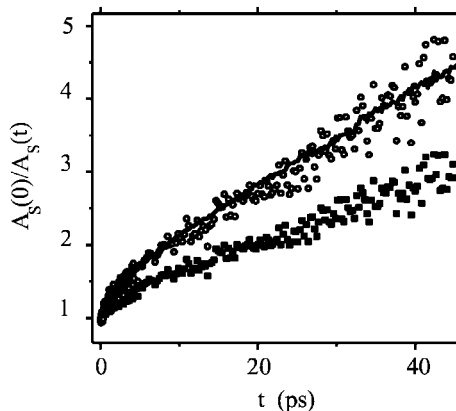


**Figure 10.33** Reciprocal, normalized representations of singlet exciton absorption at 1.45 eV and  $\Delta I$  signal at a push energy of 1.6 eV (line and squares, respectively). Circles: as squares, but curve stretched by factor of 1.7.

whether this polaron pair will be stable. If the exciton is still in the center of the DOS, the polaron pair, also moving in the DOS, will with high probability find sites with lower energies (be them tail states of the ideal DOS or extrinsic trap states), preventing it from recombination. If, on the other hand, the exciton itself is in a tail state, it can still form a polaron pair; however, this pair cannot escape their mutual attraction because each hopping step leads to even higher energy additional to the increase in Coulomb energy. Therefore, this polaron pair will recombine probably within a few vibrational periods. This scenario predicts that the broader the dispersion of site energies, the more time-dependent becomes the charge *separation* efficiency, whereas the charge *generation* efficiency is probably not influenced strongly. The product of both, in turn, is the mobile charge carrier efficiency and the experiments under consideration have shown that it tends to be time dependent for samples with a higher energetic dispersion.

#### 10.5.6

#### Mobile Charge Carrier Generation by Re-Excitation of Charged States (Detrapping)

Owing to strongly changed electron–electron correlation, negative and positive polarons show optical absorption bands that are strongly red shifted with respect to singlet excitons. The lowest energetic polaron absorption is below 1 eV. Applying a push pulse in resonance with this absorption band would therefore selectively re-excite polarons. Unfortunately, owing to the lack of high energetic monochromatic pulses in the near-infrared region, such measurements are not described in the literature. The groups that studied the re-excitation of charged states up to now either irradiated into the second [40, 52] or an even higher [41] polaron absorption band. Ambiguities result because of spectral overlap with singlet and triplet exciton absorption, being resolved by considering kinetics and/or

anisotropy arguments. Generally, it is observed that re-excitation of polarons leads to an enhancement of photoconductivity. Clearly, the concentration of charge carriers is not changed directly by the act of re-excitation; however, during the course of geminate recombination, the escape probability can be strongly influenced by re-excitation. This in turn leads to a change in average charge carrier concentration and therefore a change in the average photoconductivity.

Müller et al. irradiated into the second polaron absorption band (1.9 eV) in an m-LPPP film and found a strong enhancement of photoconductivity [52], the enhancement being strongest for  $t = 0$ . The  $\Delta I/I$  signal shows an ultrafast decay of the order of 1 ps, accompanied by strong anisotropy loss (Fig. 10.34). On a longer time-scale, the decay of both  $\Delta I/I$  and  $\Delta T/T$  becomes exponential with time constants of 290 and 200 ps, respectively. Considering the initial high anisotropy of the  $\Delta I/I$  signal, the authors assigned the enhancement of photoconductivity at 1.9 eV to dissociation of coulombically bound on-chain polaron pairs. The fact that singlet exciton breaking is the predominant source for free charge carriers in m-LPPP (see Section 10.5.4), shows that without re-excitation, these polaron pairs do not contribute significantly to photoconductivity and hence have a recombination probability near unity. The ultrafast anisotropy loss is attributed to hopping of either a single polaron or a complete polaron pair to a neighboring chain with different orientation. They authors gave no details on the possible mechanism of the dissociation process. In the Onsager picture, geminate recombination in a one-dimensional case indeed results in a recombination probability of 100% whereas a non-zero escape probability is obtained at higher dimensionality [64]. The effect of the push pulse could be to generate off-chain polaron pairs (via supplying excess energy for the inter-chain hopping of one polaron), thus increasing the *dimensionality* of the recombination problem.

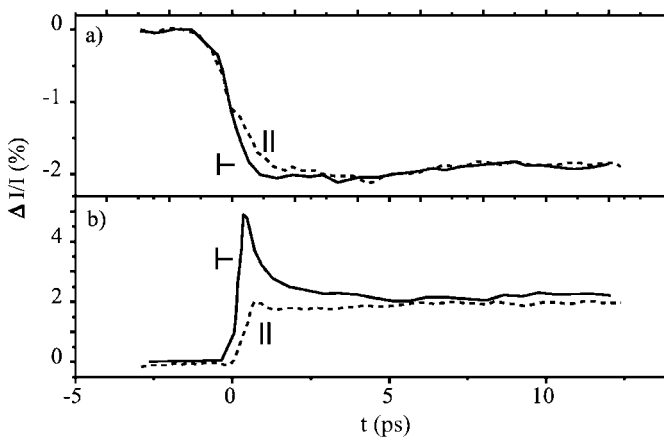


**Figure 10.34** Normalized photocurrent change in m-LPPP for the second pulse tuned to (a) 2.49 and (b) 1.9 eV. The data for parallel polarized pulses (solid line) and perpendicular polarized pulses (dashed line) are shown in comparison. Redrawn from Ref. [52].

Müller et al. were able to calculate the ultrafast formation yield of polarons to be between 5 and 25%. This is in accordance with polaron yields in other materials, determined by quantitative absorption of infrared-active vibrational modes (IRAV) [65] or field-assisted pump–probe measurements [31, 40].

Re-excitation of charged states in films of short-chain OPV was studied by Lürer et al. and explained in the framework of geminate recombination [57]. The push pulse energy was 1.9 eV. In this spectral region, the second optical transition of charged states overlaps with the lowest energetic triplet absorption. In order to resolve ambiguities in the assignment, the authors compared the kinetics of  $\Delta I/I$  with the  $\Delta T/T$  signal at 0.8 eV, representing the pure polaron decay (Fig. 10.35). The  $\Delta T/T$  decay was measured at various pump pulse intensities. It was found that polaron decay consists of two regimes: An ultrafast contribution, which is independent of intensity, reaches a plateau of about 60% of the initial density. An intensity-dependent slower contribution follows, taking the polaron concentration to zero. The  $\Delta I/I$  kinetics are equal to the kinetics of the intensity-independent contribution to  $\Delta T/T$ . The authors concluded that the photocurrent cross-correlation signal probes the *current progress* of geminate recombination. One can define the time-dependent recombination probability as the probability for a polaron that survived until time  $t$  to recombine at a later time. It is given by  $P_r(t) = [c(t) - c_\infty]/c_0$ , where  $c(t)$  is the time-dependent polaron concentration,  $c_0$  its initial and  $c_\infty$  its final value (in the absence of other recombination types). Re-excitation can decrease the recombination probability by a certain amount, thereby increasing the number of free charge carriers and thus the PC. However, this increase will be proportional to  $P_r(t)$ . If the push arrives at a time when the recombination probability is close to zero, re-excitation will have no effect. Escape cannot be enhanced if all polarons are already escaped. Therefore, the  $\Delta I/I$  signal should show the same kinetics as  $P_r(t)$ , which can be gained by simply normaliz-

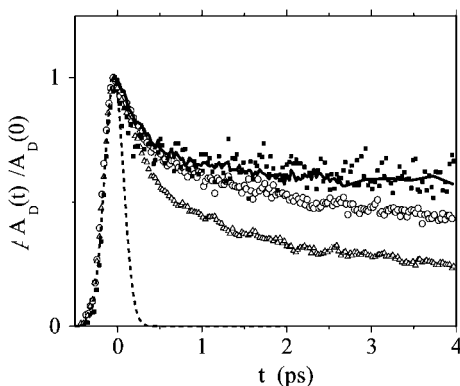


**Figure 10.35** Decay traces of charged state absorption in 3PV, measured at 0.89 eV probe energy, at various pump pulse intensities:  $J_{pu} = 0.19$  (full squares), 0.64 (circles) and 1.78 (triangles)  $\text{mJ cm}^{-2}$ , normalized to their

respective maximum. Solid line: fast part of PC cross-correlation at a push energy of 1.95 eV, compressed according to Eq. (10.9) with  $a = 0.45$ . The dashed line shows the pump pulse autocorrelation.

ing the  $\Delta T/T$  signal and removing the plateau. In comparing  $\Delta I/I$  with  $\Delta T/T$ , the latter being a bulk effect, the authors assumed that the measured  $\Delta I/I$  is a bulk effect too.

In conclusion, it is found that geminate recombination of initially formed polaron pairs is important for both polymers and oligomers. Whereas in m-LPPP geminate recombination is almost complete, it amounts to only 40% in 3PV. This result is in accordance with Onsager theory and points to the different dimensionality in polymers and short molecules. Re-excitation of polarons leads to an enhancement of their escape probability. For 3PV, this has been shown quantitatively because  $\Delta I/I$  shows the same kinetics as geminate recombination, obtained directly by pump-probe measurements at low pump intensity.

## References

- 1 K. W. Boer, H. J. Hansche, V. Kummel, *Z. Phys.* **155**, 170 (1959).
- 2 W. Franz, *Z. Naturforsch., Teil A* **13**, 484 (1958).
- 3 L. V. Keldysh, *Sov. Phys. JETP* **7**, 788 (1958).
- 4 L. M. Blinov, S. P. Palto, S. G. Yudin, *Mol. Mater.* **1**, 183 (1992).
- 5 D. A. B. Miller et al., *Phys. Rev. B* **32**, 1043 (1985).
- 6 D. F. Blossey *Phys. Rev. B* **2**, 3976 (1979); F. Evangelisti, A. Frova, J. U. Fischbach, *Phys. Rev. Lett.* **29**, 1001 (1972).
- 7 N. Kirova, S. Brazovskii, A. R. Bishop, *Synth. Met.* **100**, 29 (1999).
- 8 D. Moses, et al., *Proc. Natl. Acad. Sci. USA* **98**, 13496 (2001); D. Moses, R. Schmechel, A. J. Heeger, *Synth. Met.* **139**, 807 (2003).
- 9 J. Frenkel, *Phys. Rev.* **54**, 647 (1938).
- 10 J. Kalinowski, W. Stampor, P. G. Di Marco, *J. Chem. Phys.* **96**, 4136 (1992).
- 11 Ya. I. Frenkel, *Phys. Rev.* **37**, 1276 (1931).
- 12 A. J. Heeger, S. Kivelson, J. R. Schrieffer, W. P. Su, *Rev. Mod. Phys.* **60**, 781 (1988).
- 13 R. A. Marcus, *Rev. Mod. Phys.* **65**, 599 (1993).
- 14 F. Gutman and L. E. Lyons, *Organic Semiconductors*, Wiley, New York, 1967.
- 15 D. M. Basko, E. M. Conwell, *Phys. Rev. B* **66**, 155210 (2002).
- 16 V. I. Arkhipov, H. Bässler, M. Deussen, E. O. Göbel, R. Kersting, H. Kurz, U. Lemmer, R. F. Mahrt, *Phys. Rev. B* **52**, 4932 (1995).
- 17 M. C. J. M. Vissenberg M. J. M. de Jong, *Phys. Rev. Lett.* **77**, 4820 (1996).
- 18 J. Ristein, G. Weiser, *Philos. Mag. B* **54**, 5330 (1986).
- 19 Z. D. Popovic, *J. Chem. Phys.* **78**, 1552 (1983).
- 20 W. Stampor, J. Kalinowski, P. di Marco, V. Fattori, *Appl. Phys. Lett.* **70**, 1935 (1997).
- 21 W. P. Su, J. R. Schrieffer, A. J. Heeger, *Phys. Rev. Lett.* **42**, 1698 (1979).
- 22 U. Rauscher, H. Bässler, D. D. C. Bradley, M. Hennecke, *Phys. Rev. B* **42**, 9830 (1990).
- 23 R. Kersting, U. Lemmer, R. F. Mahrt, K. Leo, H. Kurz, H. Bässler, E. O. Göbel, *Phys. Rev. Lett.* **70**, 3820 (1993).
- 24 R. Kersting, U. Lemmer, M. Deussen, H. J. Bakker, R. F. Mahrt, H. Kurz, V. I. Arkhipov, H. Bässler, E. O. Göbel, *Phys. Rev. Lett.* **73**, 1440 (1994).
- 25 C. Rulliere, editor, *Femtosecond Laser Pulses*, Springer, Berlin, 1998, Chapt. 8, p. 203.
- 26 S. Tasch et al., *Phys. Rev. B* **55**, 5079 (1997); G. Cerullo et al., *Phys. Rev. B* **57**, 12806 (1998).
- 27 W. Graupner et al., *Phys. Rev. Lett.* **81**, 153259 (1998).
- 28 Gulbinas et al., *Phys. Rev. Lett.* **89**, 107401 (2002).
- 29 Gulbinas et al., *Phys. Rev. B* **70**, 035215 (2004).
- 30 V. Gulbinas, R. Kananavicius, L. Valkunas, H. Bässler, *Phys. Rev. B* **66**, 233203 (2002).

- 31 T. Virgili, G. Cerullo, L. Lüer, G. Lanzani, C. Gadermaier, D. D. C. Bradley, *Phys. Rev. Lett.* **90**, 247402 (2003).
- 32 A. J. Cadby, P. A. Lane, H. Mellor, S. J. Martin, M. Grell, C. Giebeler, D. D. C. Bradley, M. Wohlgenannt, C. An, Z. V. Vardeny, *Phys. Rev. B* **62**, 15604 (2000).
- 33 N. Dediu et al., *Solid State Commun.* **122**, 181 (2002).
- 34 M. Wohlgenannt et al., *Nature* **409**, 494 (2001).
- 35 J. Cabanillas-Gonzalez et al., *Phys. Rev. B* **71**, 155207 (2005).
- 36 J. Cabanillas-Gonzalez, M. R. Antognazza, T. Virgili, G. Lanzani, M. Sonntag, P. Strohrriegel, *Synth. Met.* submitted.
- 37 A. J. Cadby, P. A. Lane, H. Mellor, S. J. Martin, M. Grell, C. Giebeler, D. D. C. Bradley, M. Wohlgenannt, C. An, Z. V. Vardeny, *Phys. Rev. B* **62**, 15604 (2000).
- 38 W. Graupner, G. Lanzani, G. Cerullo, C. Zenz, E. J. W. List, G. Leising, S. De Silvestri, *Synth. Met.* **101**, 277 (1999).
- 39 T. Virgili, D. Marinotto, C. Manzoni, G. Cerullo, G. Lanzani *Phys. Rev. Lett.* **94**, (2005).
- 40 L. Lüer, H.-J. Egelhaaf, D. Oelkrug, C. Gadermaier, G. Cerullo, G. Lanzani *Phys. Rev. B* **68**, 155313 (2003).
- 41 R. Hidayat, Y. Nisihara, A. Fujii, M. Ozaki, K. Yoshino, E. Frankevich, *Phys. Rev. B* **66**, 075214 (2002).
- 42 M. Al-Ibrahim, H.-K. Roth, U. Zhokhavets, G. Gobsch, S. Sensfuss, *Solar Energy Mater. Solar Cells* **85**, 13 (2005).
- 43 H. J. Snaith, R. H. Friend, *Synth. Met.* **147**, 105 (2004).
- 44 L. Luer, H.-J. Egelhaaf, D. Oelkrug, *Opt. Mater.* **9**, 454 (1998).
- 45 N. Tessler, *Adv. Mater.* **11**, 363 (1999).
- 46 E. J. Meijer, A. V. G. Mangnus, B.-H. Huisman, G. W. 't Hooft, D. M. DeLeeuw, T. M. Klapwijk, *Synth. Met.* **142**, 53 (2004).
- 47 D. Moses, J. Wang, A. Dogariu, D. Fichou, C. Vidélot, *Synth. Met.* **101**, 421 (1999).
- 48 B. R. Wegewijs, G. Dicker, J. Piris, et al, *Chem. Phys. Lett.* **332**, 79 (2000).
- 49 D. Moses, C. Soci, P. Miranda, A. J. Heeger, *Chem. Phys. Lett.* **350**, 531 (2001).
- 50 C. Zenz, G. Lanzani, G. Cerullo, W. Graupner, G. Leising, S. De Silvestri, *Chem. Phys. Lett.* **341**, 63 (2001).
- 51 L. J. Rothberg, M. Yan, A. W. P. Fung, T. M. Jedju, E. W. Kwock, M. E. Galvin, *Synth. Met.* **84**, 537 (1997).
- 52 J. G. Müller, U. Lemmer, J. Feldmann, U. Scherf, *Phys. Rev. Lett.* **88**, 147401 (2002).
- 53 M. Scheidler, U. Lemmer, R. Kersting, S. Karg, W. Riess, B. Cleve, R. F. Mahrt, H. Kurz, H. Bässler, E. O. Göbel, P. Thomas, *Phys. Rev. B* **54**, 5536 (1996).
- 54 V. I. Arkhipov, H. Bässler, M. Deussen, E. O. Göbel, R. Kersting, H. Kurz, U. Lemmer, R. F. Mahrt, *Phys. Rev. B* **52**, 4932 (1995), and references cited therein.
- 55 C. Gadermaier, G. Cerullo, G. Sansone, G. Leising, U. Scherf, G. Lanzani, *Phys. Rev. Lett.* **89**, 117402 (2002).
- 56 J. G. Müller, U. Scherf, U. Lemmer, *Synth. Met.* **119**, 395 (2001).
- 57 L. Lüer, G. Cerullo, M. Zavelani-Rossi, G. Lanzani, *Chem. Phys. Lett.* **381**, 751 (2003).
- 58 E. Frankevich, H. Ishii, Y. Hamanaka, T. Yokohama, A. Fujii, S. Li, K. Yoshino, A. Nakamura, K. Seki, *Phys. Rev. B* **62**, 2505 (2000).
- 59 G. Lanzani, C. Zenz, G. Cerullo, W. Graupner, G. Leising, U. Scherf, S. De Silvestri, *Synth. Met.* **111–112**, 493 (2000).
- 60 F. Kouki, P. Spearman, G. Horowitz, P. Delannoy, P. Velat, V. Wintgens, F. Garnier, *Synth. Met.* **102**, 1071 (1999).
- 61 I. G. Sheblykin, O. P. Varnavsky, M. M. Bataiev, O. Sliusarenko, M. Van der Auweraer, A. G. Vitukhnovsky, *Chem. Phys. Lett.* **298**, 341 (1998).
- 62 G. Cerullo, G. Lanzani, S. De Silvestri, H.-J. Egelhaaf, L. Lüer, D. Oelkrug, *Phys. Rev. B* **62**, 2429 (2000).
- 63 J. Gierschner, H.-J. Egelhaaf, D. Oelkrug, K. Mullen, *J. Fluoresc.* **8**, 37 (1998).
- 65 D. Moses, A. Dogariu, A. J. Heeger, *Phys. Rev. B* **61**, 9373 (1999).

## Index

### a

- absorption
  - vibronic structure 239
  - coefficient 198
  - photoluminescence 253
- absorption spectrum 230
  - Franck-Condon type 321
- Airy unit 155
- amplitude mode model 229 f
- anthracene 218, 367, 369 f, 461, 467
- anti-resonance 228, 230, 241, 254
  - Fano-type AR 196
- autocorrelation 29, 32
  - function 9
- autoionization 264
- avalanche photodiode 20

### b

- 1,1-bis(ditolylaminophenyl)cyclohexane 313, 339 ff
- $1^1B_u$ , free-exciton 499
- band gap 369
- band transport, trap-controlled 284
- biexciton 194
- bimolecular recombination 207, 235 f, 247, 252 f
  - DBR 209
  - kinetics 232
  - non-dispersive 232
  - rate constant 319
- biphenylamine 350 f
- bipolaron 190
- Boltzmann distribution 204
- broadening homogeneous 507
- broadening inhomogeneous 507
- bulk conductivity 325

### c

- carbon nanotube 381, 391 ff, 395
- carrier
  - density 282
  - dynamics 395
- carrier jump
  - backward 285 f
  - rate 273
- carrier mobility 280, 293, 302, 381, 408, 410 f
  - single-carrier (TOF) 294
- carrier packet 283
  - dispersion 277
  - field-assisted spreading 285
- carrier transport 391
  - band-like 370
  - trap-controlled 279
- charge carrier
  - concentration 318
  - equilibration 275
  - generation 318
  - hopping 265
  - optical 320
- charge carrier generation
  - delayed 320
  - optically detected 320
- charge carrier hopping, trapping effect 342
- charge carrier mobility 304
  - determination 325
  - effective 315
  - P3HT 354
- charge carrier motion
  - in a FET 326
  - ultrafast monitoring 327
- charge carrier transport 368
  - in disordered organic materials 314
- charge coupled device 16 f
- charge density wave 229 f
  - approximation 196

- charge generation 262
  - efficiency 400
  - rate 543
- charge photogeneration efficiency 407 f, 410, 418
- charge transfer
  - complex 529
  - overlap integral 192
  - transition 192
- charge transport 261
  - ambipolar 171, 175, 178
  - chemical and morphological aspects 350
  - effect of positional disorder 339
  - random organic solid with energetic disorder 328
  - unipolar 171
- charged excitation, optical transition 190
- Child's law 323
- co-evaporation 178
- Cole-Cole model 213, 387
- Cole-Davidson model 387
- conductivity 396
  - complex 373
  - model 381
  - spectrum 197
- conjugated polymer 49 f, 57, 131, 134 ff, 183, 302, 338, 347
  - correlations, electronic 49 f, 98 f, 135
  - electron-electron interactions 49 f, 98 f, 135
  - electron-phonon interactions 49 f, 121 134
  - ordered reference state 50
  - photoexcitation 187
  - self-trapping 134
- conjugation length 239 f, 241 f, 250, 254
- continuity equation, Fokker-Planck type 275
- continuous time random walks 265
- Coulomb
  - binding energy 290
  - center 326
  - potential 290
  - potential well 293
  - trap 290, 292 ff
- cryostat 30
  - optical 24
- Curie susceptibility 187
- current flow, space charge-limited 323
  
- d**
- dark count 21
- DAST 374, 376
- Davydov
  - component 430, 445, 458, 462, 469, 471, 474 f, 477, 480, 490, 492 f
  - splitting 239, 460, 473
- degradation 163
- density of state 275 ff, 536, 542
  - distribution 278
  - function 281
  - Gaussian 279, 284, 287, 314
  - Gaussian function 276
  - maximum 280
- device
  - electronic 153
  - optoelectronic 171
- diacetylenes 50, 56, 64 ff, 137 ff
  - 3- and 4-BCMU monomer 53, 59, 64 ff
  - BCMU crystal structures 142 ff
  - polymerization, topochemical 51, 64, 137 ff
  - side-groups 53 ff, 60, 66, 139
- diacetylenes, polymerization
  - energetics 141 f
  - initiation 51 f, 137, 139
  - propagation 51 f, 54, 138, 140
  - strain, and effect of 54 f, 57, 71, 141, 144 f
  - structural requirements 54, 138 ff
- disorder 49, 51, 54 ff, 63, 125 ff, 136 f
- dichroic beam splitter 17, 20
- dielectric tensor 442, 445 f, 453, 457, 466 f, 478, 480, 490, 493
  - aggregation 430, 463, 469, 471, 477, 483, 492
  - optical axis 445, 453 f, 456, 461, 466, 471, 477, 487, 491
  - principal axes 446, 453, 457, 473, 480, 484, 492
- dielectric theory 439, 471, 481
  - absorption constant 443, 449, 469, 485, 488
  - boundary conditions 443, 451 f, 472
  - exciton-free layer 452, 456
  - Fermi's golden rule 429, 438 f, 458, 460, 490
  - dielectric constant 440, 442 ff, 447, 449, 453 f, 466, 473
  - dielectric susceptibility 443, 447, 490
  - local field 445, 469
  - material equations 440
  - permeability 440
  - plasma frequency 437, 438, 447
  - polarizability 444, 445, 485, 489
  - polarization, macroscopic 429 ff, 443 f, 446, 462, 481, 492
  - Poynting vector 440 f, 490, 492
  - reflectivity 443 f, 449
  - refractive index 440, 442 f, 452, 454, 468

- solvent shift 445
  - sum rule 463, 481, 483
  - transmittance 444, 488 f
  - diethylaminobenzaldehyde diphenylhydrazone 345
  - difference absorption spectra 504
  - diffusion coefficient 280
  - dimer 192
  - disorder model
    - correlated 271, 305
    - Gaussian 271
  - disordered organic materials, in presence of traps 314
  - dispersive process 213
  - dispersive recombination 213
  - ditolylphenylamine 345
  - drift mobility
    - electric field dependence of 2, 303
    - temperature dependence 299
    - zero-field effective 309
  - Drude model 381 ff
    - generalized 387 f
    - localized-modified 388, 390 ff
    - relaxation time 381 f
    - response 403
  - Drude-Lorentz model 385, 394
  - Drude-Smith model 387 f, 390, 415 f
- e**
- effective medium approximation 270, 308, 314
    - hopping charge-carrier transport 295
    - theory 297
  - effective medium model 284
  - Einstein relation 273, 277, 322
  - electrically detected magnetic resonance 206
  - electric field-assisted photoluminescence up-conversion 533 ff
    - experimental setup 534
  - electric field-assisted pump-probe 537 ff
    - differential transmission 537
    - interpretation 537
    - popular dynamics 537
  - electric field-assisted up-conversion, PPPV 535
  - electroabsorption 185, 525
  - electrodynamics
    - electric field 439 ff, 453, 454, 486
    - energy density 440 f, 442
    - energy flux 439 f, 450, 490
    - energy velocity 440 f
    - displacement current 439, 441 ff, 452 f, 490, 492
    - induction 439
    - magnetic field 439 f
    - Maxwell's equations 439 ff, 446
    - normal mode 433 f, 439, 443
    - phase velocity 440 f, 468
    - polarization, longitudinal 446, 455, 461, 467, 476, 484, 492
    - polarization of light 439, 442, 476, 480 f
    - spatial damping 434, 439, 443, 449, 459
    - temporal damping 434, 439, 443, 459
    - wave vector 433 f, 442 f, 445 ff, 451, 453 f, 456, 467, 475, 478 f, 490, 492
  - electroluminescence 175, 178
  - electromodulation 530
  - electron
    - correlation 191
    - spin 201
    - spin resonance 200 ff
    - spin transition 200
    - trap 263
  - electron-electron interaction 184
  - electron-hole
    - pair 263 f
    - recombination 319
  - electronic coupling 32 ff
  - electronic relaxation 521
  - electron-lattice dynamics 498
  - electron-photon interaction 184
  - electron-spin resonance, light-induced 187
  - electro-optic sampling 376
  - emission 103 ff, 130
    - excitation spectrum 104
    - lifetime, non-radiative 113 ff
    - lifetime, radiative 112 f, 130
    - quantum yield 109 f
    - rate 8
    - resonance emission 104 ff
    - resonant vs non-resonant excitation 117 f, 128 ff
    - spectrum 125
    - vibronic lines 103 f, 117 f, 123, 126
  - energetic disorder 328
  - ergodic hypothesis 295
  - excitation binding energy 369
  - excitation, long-lived 205
  - excitation transfer interaction 12
  - exciton 61 ff, 99 f, 193, 268, 386, 408, 429, 431, 433 f, 436, 438, 446 f, 452, 458, 460, 463, 469, 490, 527 ff
    - binding energy 63, 99 f, 132
    - Davydov component, *see* Davydov
    - density fluctuation 434

- dipole moment 434, 436 f, 452, 473, 475, 479, 486, 492 f
  - energy 99 f
  - Förster transfer 460, 487
  - formation 220
  - Herzberg-Teller coupling 484
  - high-energy 93 ff
  - hybridization 450, 484, 492
  - longitudinal exciton 434, 447 ff, 451, 454 ff, 461, 467, 469 f, 488
  - Lorentz oscillation, *see* Lorentz
  - Lorentz screening, *see* Lorentz
  - oscillator strength 430, 437 f, 447, 453, 458 f, 462 ff, 467, 473 f, 481 ff, 486 f, 491
  - radius 63, 99
  - relaxation 101
  - scattering 438 f, 449 f, 452, 458 ff, 467, 476, 490, 492
  - Stark effect 436, 485
  - surface states 452, 466 f, 478
  - transition dipole, *see* transition dipole
  - transverse 434, 447 ff, 451, 454, 461, 467, 469 f, 473, 476, 478, 490
  - vibronic exciton 448, 462 f, 469, 473
  - virtual transition 444
  - Wannier exciton, *see* Wannier
  - exciton, bands 528
    - binding energy 262, 527
    - dissociation 178, 263, 535 ff
    - Frenkel exciton, *see* Frenkel
    - migration 542
    - self-trapping 194
    - trap 334
    - trapped CT 532
    - vibrationally relaxed 263
    - Wannier-Mott exciton, *see* Wannier-Mott
  - exciton, singlet 73 ff, 96 ff, 117–136, 243, 246, 255
    - 1-D band 112, 117 ff
    - binding energy 76 f, 96 ff
    - coherence time 121 f
    - effective mass 76, 78, 113, 130
    - energy 72, 76 f
    - exciton-phonon interactions 130 ff
    - exciton-photon interaction (Rabi period) 129 ff
    - fission 89 ff, 96, 134
    - non radiative relaxation 82–88, 96
    - radius, or size 76, 96, 98, 133
    - relaxation 109
    - self-trapping, and absence of 82, 88, 93
  - exciton, triplet 88 ff, 133
    - energy 91
    - modulation frequency 235
    - transport 92 f, 97
  - triplet-triplet exciton annihilation 207
  - T-T\* transition 84, 89, 91, 194, 207, 225, 232, 240 f, 243, 246, 255
  - extinction coefficient 198
- f**
- far-infrared 370, 393
  - fast Fourier power spectrum 515
  - femtosecond laser source 377
  - femtosecond spectroscopy 498
  - Fermi
    - energy 284, 286 f
    - level 286 f, 292
  - Fermi-Dirac
    - distribution 286
    - function 283
  - field
    - drift mobility 303, 305
    - effective polaron mobility 306
    - external 290
    - strong 290
    - weak 290
  - field dependence, Pool-Frenkel type 270 f
  - field-effect transistor 326 ff
    - mobility 327
  - field-induced pump-probe, Stark shift 544
  - film
    - co-evaporated 174
    - vacuum sublimed 162
  - fluorene trimers 539, 549
    - polarization of initial and final states 550
    - singlet dissociation 550
  - fluorescence 79 ff, 193, 531
    - site-effective 272
    - lifetime 36, 80 f, 96 f
    - quenching 264, 531
    - resonance energy transfer 11
    - Stokes shift, absence of 80, 96
    - vibronic lines 79
  - Fourier transform IR spectrometer 241
  - Franck-Condon
    - point 518
    - principle 518
    - state 264, 508
    - transition 321
  - Franz-Keldysh effect 73, 75, 77 ff, 102, 357
  - free carrier absorption 370
  - free carrier yield 557
  - free induction decay 513
  - Frenkel
    - excitation 368

- exciton 429, 439
- exciton band 528
- Frenkel-type exciton 262
- Fresnel equation 442 f, 451, 453, 457, 492
- biaxial 457, 483
- isotropic 446 f
- uniaxial 453

**g**

- gallium arsenide 373
- Gaussian distribution, double-peak 288
- Gaussian envelope function 268
- generalized coordinates 234, 252
- geometric relaxation 500
- geometrically relaxed  $2^1 A_g$  state 519
- Gill equation 266, 269
- grain boundary 412

**h**

- 8-hydroxyquinoline, field-induced exciton separation 531
- H-aggregate 12
- heterojunction, bulk 171, 171 ff, 175, 177 f
- higher lying state 530
- Hoesterey-Letson formalism 314, 316
- hole burning 498
- hole mobility 332
- in substituted tritolyamines and biphenylamines 352
- hole transport 343
- in polyfluorene films 356
- non-dispersive to dispersive 329
- HOMO 188, 226, 346
- hopping
- conductivity 286
- Coulomb effects 289
- downward 275
- in a doped organic material 289
- master equation 297
- mobility 274
- model 267
- neighbors 277 f, 285
- parameter 274 f
- rate 280
- relaxation 276
- sites 287, 316
- thermally activated variable-range 277
- transition 296
- hopping charge-carrier transport, EMA theory 295
- hopping mobility, equilibrium 284, 287
- hopping state distribution 268
- hopping theory, stochastic 273

- hopping transport
- dispersive 281
- equation 283
- equilibrium 283 ff
- in organic solids 306
- low-field 308
- trap-controlled 315 ff
- trap-to-trap 315 ff
- hot excitation 413
- dissociation 368
- Huang-Rhys factor 251, 272, 347, 505
- Hückel model 185

**i**

- imaging
- photoluminescence 161, 168
- topographic 161
- inorganic glass 328
- in-phase quadrature 200
- intensity correlation function 27
- interchain excitation 186
- interchain interaction 221, 240, 254, 530
- interface 153
- internal conversion 500
- intersystem crossing 7, 225
- IR-active vibration 188, 195, 222, 228 ff, 232, 254

**j**

- J-aggregate 12, 239
- jump rate 280
- Markus theory 296, 306
- Miller Abrahams 198, 298

**l**

- ladder-type polyphenylene 264, 334 ff, 357, 539
- ladder-type polyphenylene, methylated 243
- anisotropy loss 569
- geminate recombination 569
- re-excitation of charged state 569
- re-excitation of singlet exciton 564
- ladder-type polyphenylene, methyl-substituted 541 ff
- field-assisted pump-probe 541
- Landé factor 203
- Langevin's equation 319
- Larmor frequency 203
- laser 158
- femtosecond 158
- lens, aperture angle 155
- lifetime, mean 214
- lifetime distribution function 216

- light-induced electron spin resonance 187
- linear prediction singular value decomposition 515
- lineary increasing voltage 325
- Lorentz
  - oscillator 384 ff, 408, 415 f, 444, 446, 466 f, 479 ff, 487, 492
  - screening 445
- LT-GaAs 375
- LUMO 188, 226, 346
  
- m**
- magnetic dipole moment 202
- magnetic moment 202
- magnetic quantum number 201
- magnetic resonance 205, 245, 248 f
  - spectroscopy 204
- Marcus
  - jump rate 296, 306
  - model 309
- mean lifetime 214
- methoxyspirofluorenearylamine 330
- microscope
  - confocal laser scanning 157 f
  - objective 19
- microscopy
  - $4\pi$  21
  - atomic force 154, 161, 164
  - confocal 24 ff, 155, 157
  - confocal laser scanning 178
  - confocal laser scanning fluorescence 154
  - epifluorescence 14 ff
  - optical 153
  - photoluminescence 164
  - scanning confocal optical 18 ff
  - scanning near-field optical 22
  - stimulated emission depletion 21
  - total internal reflection 18
  - two-photon 21
- microwave conductivity 356
  - time-resolved 370
- microwave technique, time-resolved 327
- Miller-Abrahams
  - assumption 269
  - equation 278
  - form 314
  - formalism 296, 298
  - jump rate 198, 298
  - model 309
  - rate 271
- mobility 220, 367
  - field-effect 176
  - transient 332
- modulation frequency 210
- molecular dimers 32 ff
- molecular excitation model 369
- molecular exciton model 368
- molecular orientation 153, 165
- molecular weight 241
- monomolecular recombination 207
  - DMR 209
- mononuclear recombination 252
- Monte Carlo simulation 267, 270 f, 279, 284
- morphology 153, 162, 164, 171, 173
- Mott law 292
- multi-phonon approximation 296
  
- n**
- naphthalene 367 f, 369, 408, 458 f
- neutral exciton, optical transition 193
- N, N'-ditridecylperylene-3,4,9,10-tetracarboxylic diimide 172
- non-collinear optical parametric amplification 500
- noncrystalline organic material 265
- non-degenerated ground state polymers 184
- non-equilibrium state 510
- nonlinear optical property 504
- nonlinear optical spectroscopy 194
  
- o**
- objective, numerical aperture 156
- occupational density of state 297, 314
- occupational probability 275
- oligoacenes 368
- oligomer 186, 241 f, 243, 249 f, 255
- oligo(phenylenevinylene) 242, 348, 539, 551 ff
  - anisotropy decay 566
  - early charge carrier mobility 553
  - field-induced singlet exciton breaking 553
  - geminate recombination of charged pairs 553
  - photoinduced absorption bands 553
  - re-excitation of charged state 570
  - re-excitation of singlet exciton 565
- oligophenyls 242
- oligo(thienylenevinylene)s 242
- oligothiophenes 242 f
- one-dimensional system 507
- Onsager theory 186
- optical absorption 188, 252
  - band 200
- optical Bloch equation 7
- optical gap 241
  - optical microscopy, near- and far-field 153

- optical properties
    - absorption coefficient 379
    - complex conductivity 380
    - complex dielectric constant 380
    - conductivity 397
    - effective medium model 393 f
    - extinction coefficient 380
    - refractive index 379
  - optical rectification 373 f
  - optical resolution 154
  - optical sectioning 160 f
  - optical selection rule 191
  - optically detected magnetic resonance 200 f, 246, 248, 251 f, 255
    - spectroscopy 243
  - optoelectronic probing 526
  - organic light-emitting diode 183, 218, 251 f
  - organic material
    - doped 286
    - disordered, in presence of traps 314
    - organic molecular crystal 367
  - organic solid 306
  - organic thin film, semiconductor 154
  - orientation factor 11
  - oscillation, coupled 10
  - overlap integral 12
- p**
- P13 173
  - paramagnetic species 203
  - peak-tracking 502
  - Peierls gap 184
  - pentacene 367, 370, 375, 404, 406, 409 f, 414
    - functionalized 370, 395, 404 f, 407, 409
    - thin films 370
  - percolation energy 314
  - percolation threshold 296, 301
  - percolation-type theory 273
  - perylene 367
  - phase segregation 171
  - phase separation 173
  - phase-sensitive lock-in detection 210
  - phonon peak 510
  - phonon-polariton 431, 456
  - phonon replica 222
  - phonon transition 505
  - phosphorescence 194, 219
  - photoabsorption 239, 242 f, 246, 249 f, 252 f
  - photobleaching 39
  - photoconductive switch 373
  - photoconductivity 187, 261 ff, 369 f
    - transient 370, 393, 395, 399 f, 404, 406, 414
  - photoconductor, disordered organic 316
  - photocurrent
    - stationary 318
    - transient 320 f
  - photocurrent cross-correlation 555 ff
    - experimental setup 556
    - re-excitation of charged state 568
    - stimulated emission dumping 558
  - photodegradation 37
  - photoexcitation
    - optical transition 188
    - density 208
    - lifetime 206
  - photogenerated species 200
  - photogeneration 185, 261
    - efficiency 410
  - photoinduced absorption 199, 225 f, 228 ff, 232, 234 f
    - spectroscopy 255
  - photoinduced absorption-detected magnetic resonance 187, 204, 224, 241, 246 ff, 249, 255
    - spectroscopy 243 ff
  - photoinduced absorption, kinetics 232
    - modulation frequency dependence 232
    - pump intensity dependence 232
  - photoinduced carrier density 197
  - photoluminescence 155, 185, 238 f, 241, 246 f
    - decay 178
    - quenching 177
    - spatially resolved 166, 169
    - spectroscopy, time-resolved 178
  - photoluminescence-detected magnetic resonance 204, 246 f
  - photoluminescence, intersystem crossing 222
    - quantum efficiency 222, 253
    - RRA-P3HT and RR-P3HT 221
    - time-resolved 172
  - photoluminescence spectrum, vibronic structure 239
  - photoluminescence up-conversion 533 ff
  - photoluminescent efficiency 220
  - photomodulation 186, 222, 224, 252
    - spectroscopy 198
  - photomultiplier tube 20
  - photon
    - antibunching 9, 27
    - bunching 9, 29
    - propagator 196
  - photonics 367
  - point spread function 20, 154
  - Poisson
    - distribution 281
    - probability 275

- statistics 274
- equation 323
- polariton 429, 431, 434, 437, 439, 443, 445, f, 450 f, 458, 460, 490, 492
  - absorption, non-classical 439, 458 ff
  - Boson 432 f
  - exciton-polariton 431, 446, 456, 467
  - Fermion 432 f
  - Hamiltonian 432 ff, 436, 458
  - harmonic oscillators 432
  - nanocrystals 482, 487 ff, 492
  - polarization quanta 436
  - radiation field 429, 434 ff, 438, 443, 445, 490
  - self-energy correction 467
  - spectral density 463, 465, 467, 469, 481
  - surface polariton 431, 463
- polariton dispersion 446 ff, 456, 461
  - axial dispersion 457, 471, 473 ff
  - directional dispersion 453, 455 f, 461 f, 468 f, 474, 476, 478 f, 483, 487, 489 ff
  - extraordinary ray 454 ff, 471
  - field-broadening 486 f, 489, 491
  - Kurosawa relation 449, 454
  - Lyddane-Sachs-Teller relation 448, 451, 466
  - ordinary ray 454 f
  - polariton gap 447 f, 452 f, 455 f, 466 f, 469, 477
  - reflectivity, metallic 430 f, 447, 455, 462 f, 466, 473, 476, 478
  - resonance frequency 454 f, 461, 465, 467, 481, 483, 491
  - spatial dispersion 450 ff, 456, 476, 492
  - spectral shift 454, 461, 466 f, 470, 474 f, 484, 492
  - stop band 447, 489, 492
- polariton spectra 464 ff, 478, 488
  - anthracene 461, 467
  - BDP 430, 480
  - BDH 477 ff
  - CTIP 462 ff, 468
  - electroabsorption 485 ff
  - electron-loss spectra 461 f
  - elliptic polarization 472 f, 475 f, 480
  - graphite 460 ff
  - lineshape 449, 465, 476, 486, 488
  - linewidth 459, 460, 463, 467, 473, 484, 493
  - naphthalene 458 f
  - quaterthiophene 490 ff
  - polariton selection 471 f, 475
  - sexithiophene 482 ff, 487 ff
  - TCNQ 469 ff
  - tetracene 467
- TTI 471 ff
- normal incidence 445, 464, 469, 490
- polarization 18 f
- polaron 190, 225 f, 229 f, 240 f, 243, 248, 250, 272, 369, 410
  - activation energy 307
  - absorption 223
  - delocalized 192, 221, 224 f, 253
  - effect 306, 347
  - hopping transport 306
  - modulation frequency dependence 236
  - PA spectrum 241
  - photoabsorption 247
  - relaxation energy 198, 225 f
  - small molecular 409
- polaron excitation, trapped 197
- polaron mobility
  - Arrhenius activation energy 307
  - in electric fields 306
- polaron pair 193, 246, 249
  - geminate 243
  - non-geminate 245
- polaron recombination 218, 243, 255
  - non-geminate 248
  - process 219
- polaron transport 272
- polaron vibrational pinning parameter 196
- polaronic exciton 195
- polyacetylene
  - cis 183
  - trans 183
- polyarylenevinylenes 272
- polycarbonate 266, 313
- polydiacetylene 262 f, 498
  - 3BCMU 501 f
  - crystalline 356
- polydiacetylene, bulk crystal 60 ff, 99 ff
  - $A_g$  excited states 64, 75
  - absorption and reflection spectra 56 f, 61
  - blue and red states 56 f, 66
  - chain geometry and conformation 58 f
  - electroreflectance 62, 74 f
  - interchain interactions 79, 100
  - ionized states 102
  - triplet states 102
- polydiacetylene ionized states 73 ff
  - band gap 77, 96
  - effective mass 78
  - coherence length 78
- polydiacetylene, isolated chains, blue 50, 67–102
  - $A_g$  excited states 82, 88, 93, 96 ff, 133, 135
  - $A_g$  triplets, excited 88, 91

- absorption 67 ff
  - absorption low energy lines 71, 74, 145 f
  - electroabsorption 73 ff, 79, 95, 145
  - polydiacetylene, isolated chains, red 103 f
    - absorption 105 ff
    - absorption cross-section 127
    - electroabsorption 107
  - polydiacetylene, single chain emission 116–130
    - spatial extension 124 ff
  - polydiacetylene solution 56 f, 65 f, 133
    - absorption spectrum 57, 68
    - chain length, mol. weight 65 f
  - poly(dibutylsilylene) 312
  - poly(dioctylfluorene) 304
  - poly(ethylenedioxythiophene) 330
  - polyfluorene 184, 270, 338, 539, 545 ff
    - phase 254
  - polyfluorene, charge carrier mobility 549
    - field-induced process 547
    - morphological behavior 237
    - non-geminate pairing 548
    - phase 238 f, 240 f
  - polyfluorene film 338
    - hole transport 356
  - polyfluorene, singlet efficiency 549
    - thermal cycling 240 f
    - triplet state 546
  - polyfluorene-phenyl-butyric acid ester 346
  - poly(3-hexylthiophene) 192, 355
    - regio-random 220, 222, 246, 253
    - regio-regular 220, 224 ff, 253
  - polymer 241, 243, 249, 255
    - conducting 391
  - polymethylphenylsilylene 348
  - poly(3-methylthiophene) 381, 391 f
  - poly(phenylenevinylene) 184, 235 f, 246 f, 254, 266, 353, 375
  - poly(phenylenevinylene), MEH substituted 375, 381, 395, 403, 416 ff
    - free carrier field 561
  - polypyrrole 381, 391, 391 f
  - polystyrene
    - doped 345
  - polystyrene sulfonic acid 330
  - polythiophene 184, 253, 272, 325
  - poly(toluenesulfonate-diacetylene) 357
  - polyvinylcarbazole 266, 345
  - Poole-Frenkel
    - effect 266
    - factor 307
    - formalism 528
    - law 266, 271, 311
    - regime 271
  - positional disorder, effect 339
  - potential hypersurface 505
  - power-law
    - behavior 407
    - decay 413 f
  - primary photoexcitation 368 f, 411
  - proton-deprotonation process 230, 254
  - pump intensity 213, 216
  - pump-pump coupling 513
  - pyridylene/vinylene polymer 230
- q**
- quantized angular momentum 201
  - quantum efficiency 200, 219
    - internal electroluminescence 218
  - quantum interference 197 f
  - quantum wire, or 1D 55, 98, 120, 132 f, 136
    - lateral confinement 49, 98, 132
  - quinquethiophene 172
- r**
- Rabi
    - coupling 438
    - frequency 7, 435 f, 438, 458 f, 492
    - oscillation 10, 436
    - splitting 435 f
  - Raman
    - active mode 195
    - active vibration 195
  - Raman scattering
    - impulsive stimulated 508
    - dispersion 195
    - resonant 229
  - Raman spectroscopy, time-resolved 498
  - random organic solid, charge transport analysis in 328
  - random phase approximation 196
  - raster scanning 156
  - Rayleigh resolution 155
  - real-time spectrum 500
  - recombination rate distribution 213, 212
  - re-excitation of singlet excitons 563
  - refractive index 156
  - relaxation time 393
  - resolution, depth 155
    - in-plane 155
  - retinal 378 f
  - RRS 230
  - rubrene 367, 370

**s**

saturation intensity 9  
 saturationless recombination kinetics 212  
 scanning head 157  
 second-harmonic generation 158  
 semiconductor 395  
 – band model 321, 369  
 – organic 153, 164, 367  
 – organic thin-film 154  
 sexithiophene 164, 370  
 – unit cell 164  
 sexithiophene film, sub-monolayer 170  
 signal-to-noise ratio 13, 28  
 simple-rate-equation 220  
 single molecule, orientation 41  
 single molecule spectroscopy 13  
 – cryogenic temperature 23  
 single-phonon approximation 296  
 single rate equation 208  
 singlet 244  
 – excitation 193  
 – exciton, *see* exciton, singlet  
 singlet-singlet annihilation 38, 40  
 singlet-triplet  
 – annihilation 38, 40  
 – formation 220  
 – ratio in OLED 251 f  
 site correlation effect 270  
 soliton 184  
 – optical transition 189  
 – soliton-antisoliton pair 185  
 SOMO 188  
 space charge limited current 323 ff  
 – stationary 323  
 – transient 324  
 spectral relaxation 535  
 spectroscopy  
 – femtosecond 498  
 – nonlinear optical 194  
 – optically detected magnetic resonance 243  
 – photoinduced absorption 255  
 – photoinduced absorption-detected magnetic resonance 243 ff  
 – photoluminescence 153  
 – single molecule 13  
 – terahertz puls 327  
 – terahertz time-domain 377  
 – spatially resolved 154  
 – spatially resolved PL 164  
 – time-resolved 158  
 – time-resolved PL 159  
 – time-resolved Raman 498

spin 202  
 – angular momentum 201  
 – degeneracy 219  
 – polarization 201  
 spin-dependent exciton formation 243, 248  
 – cross-section 220  
 spin-dependent polaron recombination 247  
 spin-dependent recombination rate 243  
 spin-lattice relaxation time 206  
 spin-orbit coupling 219  
 static disorder 13  
 stimulated emission 203  
 stimulated emission dumping  
 – MEH-PPV 560  
 – m-LPPP 561  
 streak camera 159  
 superimposed disorder, organic solids 306  
 superradiance 34 f  
 supramolecular arrangement 153  
 supramolecular organization 165, 168, 171  
 Su-Schrieffer-Heeger model 185  
 SWNT 393

**t**

T13 178  
 T5 173, 178  
 teracene 367  
 terahertz pulse 327, 367, 370, 373  
 terahertz spectroscopy 327  
 – time-resolved 370 ff, 393  
 terahertz time-domain spectroscopy 377  
 tetracene 370  
 thermal cycling 254  
 thermal excitation, Boltzmann type 273  
 thin film 153, 163, 367, 409  
 – transistor 286  
 thionaphthenindole, field-induced exciton separation 531  
 three-level system 6  
 time-of-flight currents 346  
 time-of-flight technique 321  
 transcendental equation yield 277  
 transistor  
 – light-emitting 175  
 – light-emitting field-effect 171  
 transition dipole 167, 429, 433, 444 ff, 451, 460, 463 ff, 469, 472, 477, 481, 486 f, 491  
 transition rate  
 – effective 308  
 – two-site 308  
 transport, band-like 367, 407 ff  
 transport regime, dispersive 282

trap  
– concentration 315  
– density 208  
– depth 342  
– distribution 323  
– exciton 334  
– monoenergetic 323  
trap-filling effect 286  
trapping effect, on charge carrier hopping 342  
trinitrofluorene 345  
triplet 244  
triplet excitation 236, 254  
– absorption 223  
– pump intensity dependence 235  
tritolyamine 343, 350 f  
two-photon absorption 194  
two-triplet property 520

**u**

ultrafast 368 ff  
ultra-thin film 164 f  
– organic 171

**v**

vibration  
– coherent 500  
– torsional 379  
vibrational mode 379  
vibronic sideband 241

**w**

wave  
– absorption 202  
– radiation 203  
wave packet motion 505  
Wannier exciton 429, 439, 451, 456, 460, 464  
Wannier-Mott exciton 527

**x**

xerographic discharge technique 324

**z**

Zeeman  
– Hamiltonian 203  
– level 203  
– splitting 202